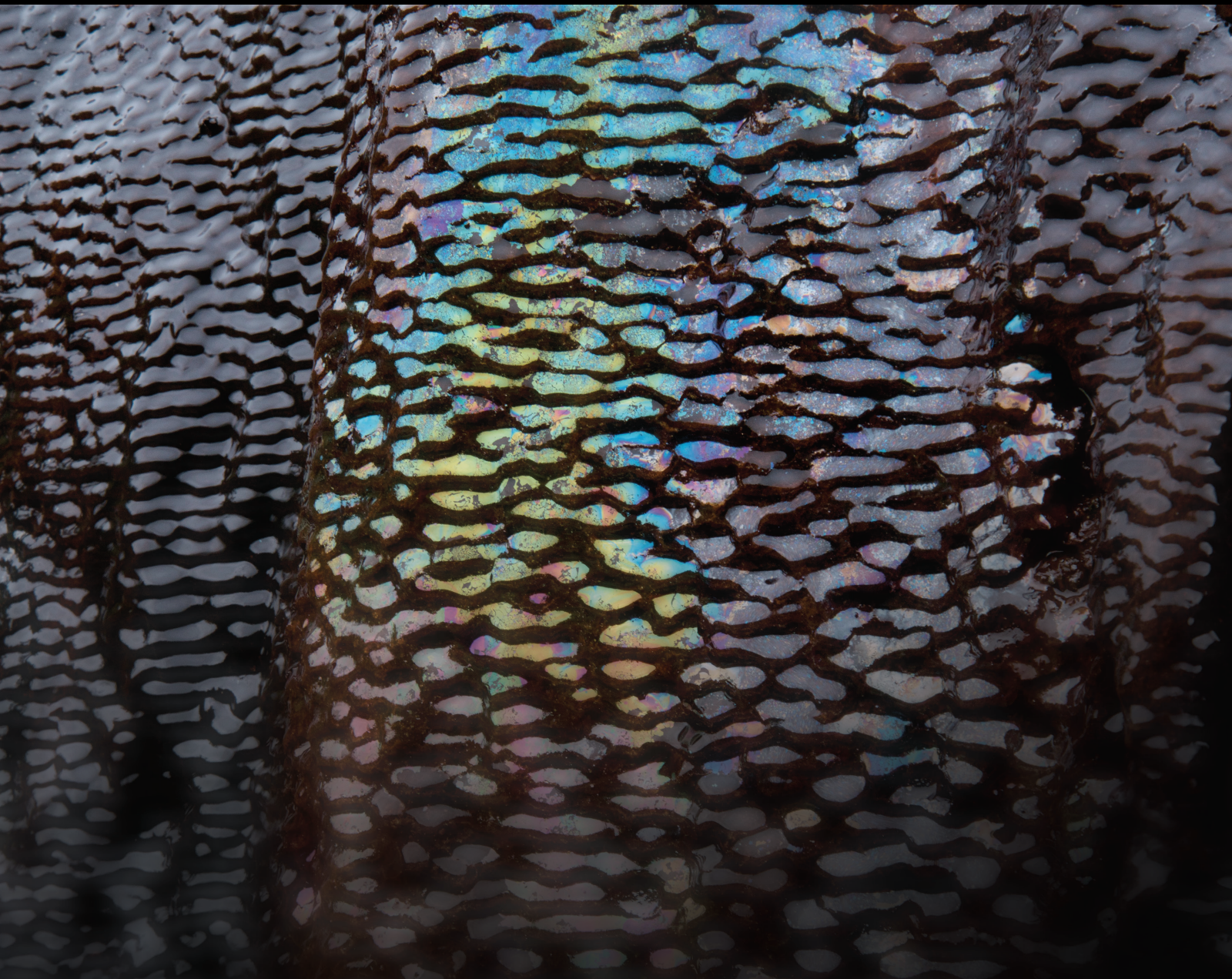


Advances in Rock Mass Structural Geomechanics Related to Hydro-Mechanical Effects

Lead Guest Editor: Yu Wang

Guest Editors: Changhong Li, Rihong Cao, and Zhengyang Song





**Advances in Rock Mass Structural
Geomechanics Related to Hydro-Mechanical
Effects**

Geofluids

**Advances in Rock Mass Structural
Geomechanics Related to Hydro-
Mechanical Effects**

Lead Guest Editor: Yu Wang

Guest Editors: Changhong Li, Rihong Cao, and
Zhengyang Song







Copyright © 2021 Hindawi Limited. All rights reserved.

This is a special issue published in "Geofluids." All articles are open access articles distributed under the Creative Commons Attribution License, which permits unrestricted use, distribution, and reproduction in any medium, provided the original work is properly cited.



























Chief Editor

































Umberta Tinivella, Italy

Associate Editors

Paolo Fulignati , Italy
Huazhou Li , Canada
Stefano Lo Russo , Italy
Julie K. Pearce , Australia

Academic Editors

Basim Abu-Jdayil , United Arab Emirates
Hasan Alsaedi , USA
Carmine Apollaro , Italy
Baojun Bai, USA
Marino Domenico Barberio , Italy
Andrea Brogi , Italy
Shengnan Nancy Chen , Canada
Tao Chen , Germany
Jianwei Cheng , China
Paola Cianfarra , Italy
Daniele Cinti , Italy
Timothy S. Collett , USA
Nicoló Colombani , Italy
Mercè Corbella , Spain
David Cruset, Spain
Jun Dong , China
Henrik Drake , Sweden
Farhad Ehya , Iran
Lionel Esteban , Australia
Zhiqiang Fan , China
Francesco Frondini, Italy
Ilaria Fuoco, Italy
Paola Gattinoni , Italy
Amin Gholami , Iran
Michela Giustiniani, Italy
Naser Golsanami, China
Fausto Grassa , Italy
Jianyong Han , China
Chris Harris , South Africa
Liang He , China
Sampath Hewage , Sri Lanka
Jian Hou, China
Guozhong Hu , China
Lanxiao Hu , China
Francesco Italiano , Italy
Azizollah Khormali , Iran
Hailing Kong, China

Karsten Kroeger, New Zealand
Cornelius Langenbruch, USA
Peter Leary , USA
Guangquan Li , China
Qingchao Li , China
Qibin Lin , China
Marcello Liotta , Italy
Shuyang Liu , China
Yong Liu, China
Yueliang Liu , China
Constantinos Loupasakis , Greece
Shouqing Lu, China
Tian-Shou Ma, China
Judit Mádl-Szonyi, Hungary
Paolo Madonna , Italy
Fabien Magri , Germany
Micòl Mastroicco , Italy
Agnes Mazot , New Zealand
Yuan Mei , Australia
Evgeniy M. Myshakin , USA
Muhammad Tayyab Naseer, Pakistan
Michele Paternoster , Italy
Mandadige S. A. Perera, Australia
Marco Petitta , Italy
Chao-Zhong Qin, China
Qingdong Qu, Australia
Reza Rezaee , Australia
Eliahu Rosenthal , Israel
Gernot Rother, USA
Edgar Santoyo , Mexico
Mohammad Sarmadivaleh, Australia
Venkatramanan Senapathi , India
Amin Shokrollahi, Australia
Rosa Sinisi , Italy
Zhao-Jie Song , China
Ondra Sracek , Czech Republic
Andri Stefansson , Iceland
Bailu Teng , China
Tivadar M. Tóth , Hungary
Orlando Vaselli , Italy
Benfeng Wang , China
Hetang Wang , China
Wensong Wang , China
Zhiyuan Wang , China
Ruud Weijermars , Saudi Arabia

Bisheng Wu , China
Da-yang Xuan , China
Yi Xue , China
HE YONGLIANG, China
Fan Yang , China
Zhenyuan Yin , China
Sohrab Zendeboudi, Canada
Zhixiong Zeng , Hong Kong
Yuanyuan Zha , China
Keni Zhang, China
Mingjie Zhang , China
Rongqing Zhang, China
Xianwei Zhang , China
Ye Zhang , USA
Zetian Zhang , China
Ling-Li Zhou , Ireland
Yingfang Zhou , United Kingdom
Daoyi Zhu , China
Quanle Zou, China
Martina Zucchi, Italy

Contents


Energy Characteristics of Seismic Waves on Cardox Blasting Tube

Xuejiao Cui, Bo Ke, Songtao Yu , Ping Li, and Mingsheng Zhao
Research Article (13 pages), Article ID 9919764, Volume 2021 (2021)



Study on the Settlement Mechanism with Effect of Backfilling Method of an Underground Mine

Dequan Xuan , Zhiming Liu , Gang Huang , Jianhua Zhang , Tingting Jiang , and Bo Ke 
Research Article (13 pages), Article ID 5929116, Volume 2021 (2021)




Analysis of Laterally Loaded Piles in Undrained Clay Concave Slope

Chong Jiang , Xintai Li, Pan Liu, and Li Pang
Research Article (13 pages), Article ID 8580748, Volume 2021 (2021)

Effect of Microwave Pretreatment on Grindability of Lead-Zinc Ore

Qing Yu, Dexin Ding, Wenguang Chen, Nan Hu, Lingling Wu, Qiucui Zhang, Yulong Liu, Zhijun Zhang , Feng Li, Xilong Xue, Zhaopeng Li, and Guicheng He 
Research Article (13 pages), Article ID 4418684, Volume 2021 (2021)


Temporal-Spatial Characteristics of Ground and Pile Responses to Twin Shield Tunneling in Clays

Minghong Sheng, Jinjin Gao , Panpan Guo , Rihong Cao, and Yixian Wang 
Research Article (15 pages), Article ID 2373456, Volume 2021 (2021)

Experimental Investigation into Limit Void Ratio Characteristics of Calcareous Sands considering Various Factors

Baojian Li , Gang Lei , Panpan Guo , Gaoyun Zhou, Zhe Wang, and Xiaonan Gong
Research Article (9 pages), Article ID 3686852, Volume 2021 (2021)

Intelligent Prediction Model of the Triaxial Compressive Strength of Rock Subjected to Freeze-Thaw Cycles Based on a Genetic Algorithm and Artificial Neural Network

Xin Xiong , Feng Gao , Keping Zhou, Yuxu Gao, and Chun Yang 
Research Article (12 pages), Article ID 1250083, Volume 2021 (2021)



Laboratory Study on the Effect of Fluid Pressurization Rate on Fracture Instability

Xinyao Wang , Quanchen Gao , Xiao Li , and Dianzhu Liu 
Research Article (8 pages), Article ID 6084032, Volume 2021 (2021)


Analytical and Experimental Investigations on Mechanical Properties of Weak Plane Bedding in Mudstone

Yijin Zeng, Hailong Jiang , Shidong Ding, Junhai Chen, Yi Wang, and Jie Zheng
Research Article (5 pages), Article ID 5408701, Volume 2021 (2021)

Cylindrical Caved Space Stability Analysis for Extension Prediction of Mining-Induced Surface Subsidence

Yang Liu , Yongxiang Ge, Congrui Zhang, Fengyu Ren, Junsheng Ma, and Gaofeng Ren 
Research Article (13 pages), Article ID 4309530, Volume 2021 (2021)

Analysis of Vertical Response of Drilled Pile at the Crest of Rock Slope Based on Shear Behavior

Chong Jiang , Ju Fang, and Bowen Sun



Research Article (12 pages), Article ID 9922653, Volume 2021 (2021)

Grouting Reinforcement Mechanism and Multimodel Simulation Analysis of Longwall Goaf

Xueliang Li , Xiaoli Guo, and Guang Sun




Research Article (13 pages), Article ID 9943596, Volume 2021 (2021)

Shale Permeability under Shale Components' Thermal Swelling

Xiang Ao , Jiren Tang, Hai Qu , and Zuping Xiang


Research Article (7 pages), Article ID 9930241, Volume 2021 (2021)

Fracture Characteristics and Fatigue Damage of Noncoplanar Fractured Rocklike Specimens under Uniaxial Graded Cyclic Loading and Unloading

Gui-cheng He, Wen-yuan Wu , Yun Wang, Yong-ming Xue , Bing Dai, and Zhi-jun Zhang 

Research Article (13 pages), Article ID 9993195, Volume 2021 (2021)

Macro-Micro Response Characteristics of Surrounding Rock and Overlying Strata towards the Transition from Open-Pit to Underground Mining

Xiaoshuang Li, Shun Yang , Yunmin Wang, Wen Nie, and Zhifang Liu

Research Article (18 pages), Article ID 5582218, Volume 2021 (2021)

Coupled Effects of Water and Low Temperature on Quasistatic and Dynamic Mechanical Behavior of Sandstone

Zilong Zhou, Yude E , Xin Cai , and Jing Zhang 


Research Article (12 pages), Article ID 9926063, Volume 2021 (2021)

Numerical Study on the Mechanism and Application of Artificial Free Surfaces in Bedrock Blasting of Shield Tunnels

YanJun Qi , Linming Dou , Zhaoxing Dong , Zheng Jiang, Bo Meng, and Junzhong Zhang



Research Article (21 pages), Article ID 9988120, Volume 2021 (2021)

Crack Evolution Characteristics and Cracking Mechanism of Red Beds in Central Sichuan during Seepage and Swelling

Zhe Zhou, Shanxiong Chen, Yinhui Wang, and Zhangjun Dai 




Research Article (19 pages), Article ID 9981046, Volume 2021 (2021)

Experimental Study on Fluid Properties of Cement-Fly Ash Slurry Subjected to Multifactors

Tian Huang , Feng Huang , and Huifeng Zhou

Research Article (17 pages), Article ID 9924895, Volume 2021 (2021)




Numerical Analysis of the Mud Inflow Model of Fractured Rock Mass Based on Particle Flow

Yongjian Pan, Huajun Wang, Yanlin Zhao , Qiang Liu , and Shilin Luo 

Research Article (16 pages), Article ID 5599748, Volume 2021 (2021)






Contents

The Elastoplastic Solutions of Deep Buried Roadway Based on the Generalized 3D Hoek-Brown Strength Criterion considering Strain-Softening Properties

Rui Wang , Jian-biao Bai , Shuai Yan , Zhi-guo Chang, Yuan-ba Song, Wei-guang Zhang, and Jun Xu


Research Article (15 pages), Article ID 5575376, Volume 2021 (2021)

Experimental Investigation into Compressive Behaviour and Preconsolidation Pressure of Structured Loess at Different Moisture Contents

Yali Xu , Panpan Guo , Chengwei Zhu , Gang Lei , and Kang Cheng 

Research Article (9 pages), Article ID 5585392, Volume 2021 (2021)

Investigation on Nonuniform Extension of Hydraulic Fracture in Shale Gas Formation

Zhiheng Zhao , Youcheng Zheng, Yili Kang, Bo Zeng, and Yi Song



Research Article (11 pages), Article ID 5516040, Volume 2021 (2021)

Predicting Response of Constructed Tunnel to Adjacent Excavation with Dewatering

Panpan Guo , Feifei Liu, Gang Lei , Xian Li , Cheng-wei Zhu , Yixian Wang , Mengmeng Lu, Kang Cheng , and Xiaonan Gong

Research Article (17 pages), Article ID 5548817, Volume 2021 (2021)

Research on the Deformation Law of Jointed Surrounding Rock during Tunnel Excavation Based on Hydromechanical Coupling

Yan Wang  and Mingfei Li 



Research Article (13 pages), Article ID 5583940, Volume 2021 (2021)

Numerical Simulation on Mesoscale Mechanism of Seepage in Coal Fractures by Fluid-Fluid Coupling Method

Kai Si , Ruidong Peng , Leilei Zhao , Yan Zhao , Yaheng Zhu , Zhendong Cui , and Jianyong Zhang 

Research Article (11 pages), Article ID 5562149, Volume 2021 (2021)

Laboratory Model Tests on Flow Erosion Failure Mechanism of a Slope Consisting of Anqing Group Clay Gravel Layer

Kang Huang, Haipeng Duan, Yuelin Yi, Fei Yu , Shanxiong Chen, and Zhangjun Dai 






Research Article (14 pages), Article ID 5559052, Volume 2021 (2021)

Model Test Study on Dynamic Response of Expressway Plastic-Reinforced Earth Embankment under Earthquake

Xue Han , Pengyue Ji, Qichen Gu, and Guangsen Mu

Research Article (12 pages), Article ID 5551699, Volume 2021 (2021)

Experimental Investigation of Permeability Evolution on Sandstone in Triaxial and Long-Term Dissolution Experiment

Ji Shi , Jianhua Zhang , Chunyang Zhang , Tingting Jiang , and Gang Huang 

Research Article (12 pages), Article ID 5580185, Volume 2021 (2021)

Effect of Bedding Structure on the Energy Dissipation Characteristics of Dynamic Tensile Fracture for Water-Saturated Coal

Shuang Gong , Lei Zhou , Zhen Wang, and Wen Wang

Research Article (10 pages), Article ID 5592672, Volume 2021 (2021)

Research Article

Energy Characteristics of Seismic Waves on Cardox Blasting Tube

Xuejiao Cui,^{1,2} Bo Ke,³ Songtao Yu ,^{1,4} Ping Li,³ and Mingsheng Zhao²

¹School of Resource and Safety Engineering, Central South University, Changsha, Hunan 410083, China

²Poly Xinlian Blasting Engineering Group Co, Ltd, Guiyang 550001, China

³School of Resources and Environmental Engineering, Wuhan University of Technology, Wuhan 430070, China

⁴School of Emergency Management, Jiangxi University of Science and Technology, Ganzhou 341000, China

Correspondence should be addressed to Songtao Yu; yusongtao92@163.com

Received 1 April 2021; Accepted 14 September 2021; Published 13 October 2021

Academic Editor: Yu Wang

Copyright © 2021 Xuejiao Cui et al. This is an open access article distributed under the Creative Commons Attribution License, which permits unrestricted use, distribution, and reproduction in any medium, provided the original work is properly cited.

In order to study the energy characteristics of seismic waves on the liquid CO₂ blasting system, the blasting seismic wave signal of liquid CO₂ blasting was obtained by on-site microseismic monitoring tests. The adaptive optimal kernel time-frequency analysis method was used to study the basic time-frequency properties of the seismic wave signal. Combining wavelet packet transform decomposition and reconstruction and adaptive optimal kernel time-frequency analysis method, the liquid CO₂ energy distribution of the seismic wave signal was further analyzed. And the energy regression model of seismic wave source of liquid CO₂ blasting system was discussed. The results show that the vibration velocity is at a low level, and the main frequency range is between 30 and 70 Hz, and the duration is about 20-30 ms. The energy is mainly distributed in 0-125 Hz, which is composed of two main regions. The power function model can be used to describe the attenuation law of the seismic wave energy. The energy conversion coefficient and characteristic coefficient of the source of liquid CO₂ blasting system were defined and analyzed. Combined with the empirical formula of the Sadovsky vibration velocity, the energy regression model of the seismic wave source of liquid CO₂ blasting system was obtained.

1. Introduction

The cyclic nature of the drill-and-blast method, increasing excavation demands, environmental concerns, and trends towards safety, necessitates the development and exploration of the potential of new and improved concepts of rock excavation. One of the promising and nonexplosive concepts that warrants in-depth evaluation as a tool for rock fragmentation is the “Penetrating Cone Fracture” (PCF) method [1]. Liquid CO₂ blasting system is one of the nonexplosive blasting technologies, which is based on liquid carbon dioxide being converted to high-pressure carbon dioxide gas or fluid with the ignition. The gas spreads through fissures and microcracks in the rock and breaks it in tension, rather than compression as with explosives, and the damage at lower tensile stress levels is more efficient in the utilization of energy, less vibration, pollution-free, reduce the damage of the surrounding rock mass, and destruction of the environment. Figure 1 shows a schematic diagram of the compo-

nents which make up the cartridge. The chemical energizer is activated by a small electrical charge which causes the blasting [2].

In the past, researches on liquid CO₂ blasting technology mainly concentrated on the blasting equipment and its applications. The gas pressures and the velocities of blast waves that travel through the sandy shale were determined by field tests [3]. Other important applications of this technology are in the fields of environment-friendly blasting, such as urban underground construction [4], neighbor rock breaking of the forest [5], highway construction for the cold region [6], and controlled blasting [7, 8]. Recently, with the wide application of this technology, many scholars have done a lot of research on coal seam permeability improvement [9–17], energy calculation [2, 18], pressure characteristics [19, 20], and mechanism of fracture [13, 21–25] and its application.

Liquid CO₂ blasting fracturing technology is a new green blasting excavation method, which can effectively reduce the vibration effect compared with the traditional explosive

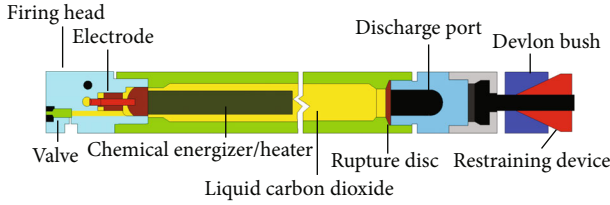


FIGURE 1: Schematic diagram of a liquid CO₂ blasting system [2].

blasting. Blasting vibration signal is the carrier and physical manifestation of blasting seismic waves, which determines the crack geometrical form and propagation mode of the rock mass. However, the time-frequency characteristics and energy distribution of seismic wave signals of liquid CO₂ blasting are not clear from above literature review.

The blasting seismic waves of liquid CO₂ blasting are nonstationary signals, and time-frequency analysis/distribution is an important mean of analyzing such nonstationary signals. The time-frequency analysis technique can be divided into two categories: linear time-frequency analysis and nonlinear time-frequency analysis. The linear time-frequency analysis includes short-time Fourier transform (STFT), Gabor expansion, wavelet transform (WT), and S transform. The nonlinear time-frequency analysis includes bilinear time-frequency analysis and adaptive optimal kernel (AOK) [26, 27] time-frequency analysis [28]. Moreover, based on the simulation signal of blasting vibrations and seismic waves, the STFT, WT, S transformation, Wigner-Ville distribution, smooth pseudo-Wigner distribution, cone-shaped kernel time-frequency distribution, and the distribution of the AOK time-frequency analysis were used for the signal processing in the MATLAB software. The results of the comparative analysis show that the kernel function of AOK is adaptive with the change of time, which can effectively suppress the cross term and realize the time-frequency localization with the best precision. Published researches that mainly focused on the signals of blasting vibrations and seismic waves processed by the AOK time-frequency analysis found in the literature were those of Zhao et al. [28], Wang et al. [29], Sejdić et al. [30], and Sun et al. [31].

In the analysis method of signal decomposition and reconstruction, compared with wavelet analysis, wavelet packet transform analysis provides a more refinement analysis method for signals [32–34]. The frequency band can be divided into different levels; according to the characteristics of the analyzed signal, the corresponding frequency band is adaptively selected to match with the signal spectrum, which can improve the time-frequency resolution. The signal was decomposed and reconstructed in multiscale and multiresolution by the wavelet packet, which can better express the energy distribution characteristics of the frequency band. However, the signal reconstruction of time-frequency analysis still uses the linear summation calculation method to analyze the different frequency band energy, instead of nonlinear calculation on the double integral of time and frequency to analyze the signal energy, which resulting in a relatively low accuracy of calculation results.

In this work, the research is conducted by microseismic tests of blasting seismic signals of liquid CO₂ blasting as the foundation after reviewing the signal processing and analysis methods. Firstly, the basic time-frequency characteristics of the seismic signals were analyzed through the adaptive optimal kernel time-frequency analysis method. Secondly, combining wavelet packet transform decomposition and reconstruction and adaptive optimal kernel time-frequency analysis method, the energy distribution of the seismic wave signals from liquid CO₂ blasting was further analyzed. Finally, an energy regression model of the seismic wave source of the liquid CO₂ blasting system was obtained. These findings can provide a theoretical basis for the propagation law of shock waves of supercritical CO₂ jet in the rock mass and for the design of liquid CO₂ blasting.

2. Experimental Methodology

2.1. Test Scheme and Design. Since the seismic waves from liquid CO₂ blasting (principle and equipment can be referred to in reference [1]) are weak, the microseismic monitoring system was adopted to monitor the blasting seismic waves. The tests were divided into two parts: one part is for the analysis and research of time-frequency characteristics of the blasting source signals, and the other part is for the analysis of seismic wave attenuation law, as shown in Figure 2, the layout plan of the microseismic test station.

- (1) *Analysis of Time-Frequency Characteristics.* From Figure 2, the monitoring points are arranged as a circle with a total of 8 stations. There are five blasting points; one blasting point is arranged in the center of the circle, and the other four blasting points are arranged in a square at a distance of 0.5 meters from the center of the circle. The distance between the 8 monitoring points and the center is 12 meters
- (2) *Study on the Attenuation Law of Seismic Waves.* Monitoring points are arranged in a “straight line” pattern, with a total of 4 monitoring points. The first monitoring point is 12 meters away from the blasting source, and the distance between each monitoring point is 12 meters

2.2. Implementation of the Test Plan

2.2.1. Test Equipment and Installation. As shown in Figure 3, the monitoring point equipment used in the experiment consists of three parts: sensor, collector, and battery. The sensor is installed by deep drilling, with a hole depth of 1 meter and a diameter of 90 mm. After the installation of the whole monitoring point, the monitoring software can be used to check its background noise. Generally, the background noise should be no more than E-5 V. The sensor and the hole wall adopt the yellow mud coupling.

2.2.2. Program Implementation. A total of 5 blasting tests were carried out in this test, and the phase change blasting parameters of liquid CO₂ are shown in Table 1, which were obtained from the laboratory at Central South University

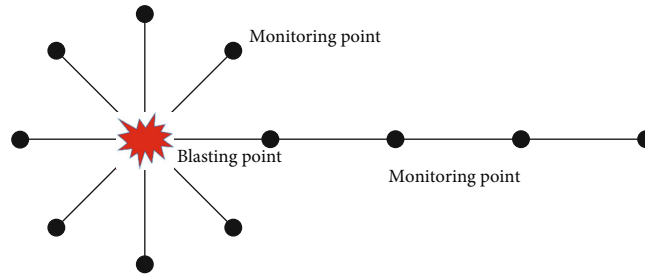


FIGURE 2: Microseismic monitoring schematic diagram of the test scheme.



FIGURE 3: Equipment installation at site monitoring points.

TABLE 1: Phase change blasting parameters of liquid CO₂.

Serial number	CO ₂ quality	Stomatal direction	Burst disc pressure	Blasting rod
1	0.452 kg	East and west	150 MPa	1 bar
2	0.526 kg	South and north	150 MPa	1 bar
3	0.454 kg	East and west	150 MPa	2 bar
4	0.498 kg	East and west	150 MPa	1 bar
5	0.448 kg	East and west	150 MPa	2 bar

(see the reference [2]). Test 1, test 2, and test 3 were carried out to discuss the time-frequency characteristics, and test 4 and test 5 were carried out to analyze the attenuation law of seismic waves. The recording sampling rate of the test data was 4000 Hz. A total of 8 microseismic instruments were used to record seismic wave data, and the sensitivity of the sensor was set at 200 V/m/s.

3. Decomposition and Reconstruction of Signal and Time-Frequency Analysis Techniques

3.1. Wavelet Packet Decomposition and Reconstruction. The time-frequency local property of a seismic wave is the most fundamental and key property of a nonstationary signal. The traditional Fourier transform signal analysis cannot well describe this property. Therefore, in order to analyze and process a nonstationary signal, researchers have improved or created new signal analysis theories based on the Fourier transform. Wavelet analysis and wavelet packet analysis are widely used in seismic signal analysis. The understanding of wavelet analysis and wavelet packets analysis is illustrated by three layers structure diagram of the wavelet analysis tree and wavelet packet analysis tree shown in Figures 4(a) and 4(b).

Wavelet transform has the characteristics of multiresolution analysis and can represent the local features of signals in both time and frequency domains. In Figure 4, A represents the low frequency parts, and D represents the high frequency parts, and they are followed by the number of layers (i.e., scale number) of decomposition. As can be seen from Figure 4(a), the low-frequency part is continuously decomposed by wavelet analysis, while the high-frequency part is not considered. The final signal consists of $A_3 + D_3 + D_2 + D_1$. Figure 4(b) shows the structure diagram of the wavelet packet analysis tree. The decomposition relation of signal [34] is $S = AAA_3 + DAA_3 + ADA_3 + DDA_3 + AAD_3 + DAD_3 + ADD_3 + DDD_3$.

From the previous analysis, it can be seen that the wavelet packet analysis can provide a more detailed analysis for the signals, by dividing the frequency band into multiple levels. Decompose the high-frequency part without subdivision of the multiresolution analysis, and adaptively select the corresponding frequency band according to the characteristics of the analyzed signal, so that it can match with the signal spectrum, thus improving the time-frequency resolution. In this paper, wavelet packet analysis is selected for signal decomposition and reconstruction.

3.2. Time-Frequency Analysis of Nonstationary Signals. Adaptive optimal kernel time-frequency analysis (AOK) is a nonlinear time-frequency distribution analysis method proposed by Jones and Baraniuk [26], which uses short-time fuzzy function and time-varying adaptive kernel function to distinguish the details of multicomponent signals in the time-frequency distribution. AOK is an optimal time-frequency method in time-frequency matching. Its kernel function changes in an adaptive manner with the change of time, which is characterized by the optimal accuracy of both cross term suppression and time-frequency localization. This

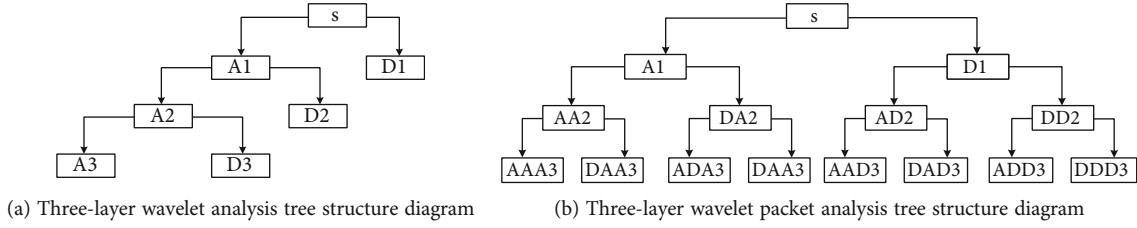


FIGURE 4: Structure diagram of wavelet analysis and wavelet packet analysis decomposition.

ability of good localization in both time and frequency domains is suitable for the analysis of time-frequency characteristics of seismic signals. The AOK is used to analyze signal in the time-frequency domain.

The AOK distribution of signals at as $s(t)$ can be expressed as follows.

$$P_{AOK}(t, f) = \frac{1}{2\pi} \int_{-\infty}^{+\infty} \int_{-\infty}^{+\infty} A(t; \theta, \tau) \Phi_{opt}(t; \theta, \tau) e^{-j\theta\tau - j\tau\omega} d\theta d\tau. \quad (1)$$

In the equation, $A(t; \theta, \tau)$ is the short fuzzy function of the signal; $\Phi_{opt}(t; \theta, \tau)$ is the corresponding optimal kernel function.

$$A(t; \theta, \tau) = \int_{-\infty}^{+\infty} h\left(u - \frac{\tau}{2}\right) w\left(u - t - \frac{\tau}{2}\right) h\left(u + \frac{\tau}{2}\right) f\left(u - t + \frac{\tau}{2}\right) e^{j\theta u} du. \quad (2)$$

In the formula, $w(u)$ is the symmetric window function, and t is the central position of $w(u)$. When $w(u) = 0$, only the signal in the range of $[t - T, t + T]$ can calculate its kernel function. For any detail part of the signal, the short-time ambiguity function can be accurately described. With the definition of the short-time fuzzy function, it is easy to calculate the corresponding $\Phi_{opt}(t; \theta, \tau)$. The short-time fuzzy function varies with time, so the optimal kernel also varies with time.

$\Phi_{opt}(t; \theta, \tau)$ can be obtained by solving the following optimization problems:

$$\max_{\Phi} \int_0^{2\pi} \int_0^{+\infty} |A(t; r, \varphi) \Phi(t; r, \varphi)|^2 r dr d\varphi. \quad (3)$$

The constraint conditions are

$$\left. \begin{aligned} \Phi(t; r, \varphi) &= \exp\left(-\frac{r^2}{2\sigma^2(\varphi)}\right) \\ \frac{1}{2\pi} \int_0^{2\pi} \int_0^{+\infty} |\Phi(t; r, \varphi)|^2 r dr d\varphi &= \frac{1}{2\pi} \int_0^{2\pi} \sigma^2(\varphi) d\varphi \leq \alpha, \alpha \geq 0 \end{aligned} \right\} \quad (4)$$

In which, $\sigma(\varphi)$ is the extension of the radial Gaussian function in the direction of the radial angle φ , which is called the expansion function. The φ is the angle between the radial and the horizontal $\varphi = \arctan(\tau/\theta)$, $r = \sqrt{\theta^2 + \tau^2}$. θ is the

polar coordinate angle of ambiguity function, τ is the time interval, and f is frequency, which is the energy volume of radial Gaussian kernel function. If α is too small, the kernel function will filter out some self-components. If α is too large, the kernel function can not effectively remove the influence of cross components. The proper selection of α is taken according to the actual signal, and the range of values is generally $1 \leq \alpha \leq 5$ Gaussian window, and radial Gaussian function was adopted in time-frequency analysis. The energy volume variable 128×128 is 2 [35, 36]; the output resolution is 512.

Nonlinear time-frequency representation (TFR) analysis method of a nonstationary signal $s(t)$ has the following properties [37]:

- (1) TFR is a real value and positive, indicating the change of energy
- (2) TFR gives the signal energy of the double integration of time and frequency, namely

$$E = \int_{-\infty}^{+\infty} \int_{-\infty}^{+\infty} \text{TFR}(t, f) df dt. \quad (5)$$

According to equation (5), time and frequency distribution (TFR) is the two-dimensional spatial distribution of signal energy in time and frequency, which has a clear physical meaning of joint distribution of signal energy in time and frequency domain.

3.3. Detailed Analysis of Energy Distribution Characteristics of Blasting Seismic Waves. Although AOK time-frequency analysis can obtain the main frequency information and the frequency range of energy concentration, it cannot show the detailed information of energy distribution in different frequency bands. Wavelet packet transform can be achieved by signal decomposition, and reconstruction can show good energy distribution of different frequency bands after detail, but the energy calculation is the signal amplitude linear summation, and the time-frequency distribution (TFR) is the signal energy in time and frequency; compared to 2d space distribution, it does not have clear physical meaning when the signal energy in frequency domain on the joint distribution. In this paper, seismic waves are decomposed and reconstructed in different frequency bands by wavelet packet transformation, and then, the time-frequency characteristics and energy of reconstructed signals in each frequency band

are analyzed in detail by using AOK time-frequency analysis method. The method combining wavelet packet transform and AOK time-frequency analysis can make up for each other's shortcomings and accurately analyze the magnitude and distribution rule of different frequency band energy of liquid CO₂ blasting seismic wave signals.

Wavelet packet decomposition and reconstruction analysis of signals can be realized directly on the MATLAB platform. AOK time-frequency analysis technology adopts the AOK time-frequency analysis toolbox (TFTB, Time-Frequency Toolbox); a time-frequency analysis toolbox developed by professor (CNRS, The National Center for Scientific Research) François Auger [38] of France National Center for Scientific Research was used to calculate the band energy of reconstructed signals. The above analysis is all independent individual analysis, which needs to be further compiled on MATLAB software platform to complete the wavelet packet decomposition and reconstruction of seismic wave signal, AOK time-frequency analysis, and energy calculation. The flow chart of the MATLAB program for signal decomposition and reconstruction, AOK time-frequency analysis, and energy calculation is shown in Figure 5. Firstly, the signal is decomposed and reconstructed by the wavelet packets, and then, the energy calculation formula (5) is added to the AOK time-frequency analysis program to calculate the energy of each frequency band. Finally, the energy normalization, calculation, and analysis of the energy distribution in different frequency bands are carried out.

4. Results and Discussions

4.1. Basic Characteristics and Energy Distribution Analysis of Blasting Seismic Wave Signal. The microseismic monitors have been arranged as a circle in Figure 2 of the test plan. Three blasting tests have been carried out. 24 sets of signals from blasting earthquakes have been received by the monitoring equipment of 8 stations, each of which has component data in three directions (*D*, *B*, and *Z* directions). In this paper, the time-frequency analysis of liquid CO₂ blasting seismic wave signal is carried out by taking the typical test data obtained from the No. 1 test as an example.

As shown in Figure 6, the seismic wave signal of the No. 1 test is shown. It can be seen from the diagram that the direct wave energy of liquid CO₂ blasting signal is strong, and the attenuation speed is fast. No obvious S wave is found in the blasting process, and the attenuation law of seismic signal waveform accords with the characteristics of the explosive blasting signal. The amplitude of blasting vibration of seismic wave signals in three directions is 0.01-0.04 cm/s, and the vibration velocity is at a lower level. In order to analyze and study seismic wave signals from time domain and frequency domain, this paper selects three components of M1 seismic wave signal in the No. 1 test as typical test data and uses AOK time-frequency analysis technology to analyze seismic wave signal based on signal analysis MATLAB processing platform. AOK time-frequency analysis method adopts program and toolbox compiled by Jones et al. [26] of (Rice University) of Rice University. The time-frequency distribution (TFR) contours and three-dimensional dia-

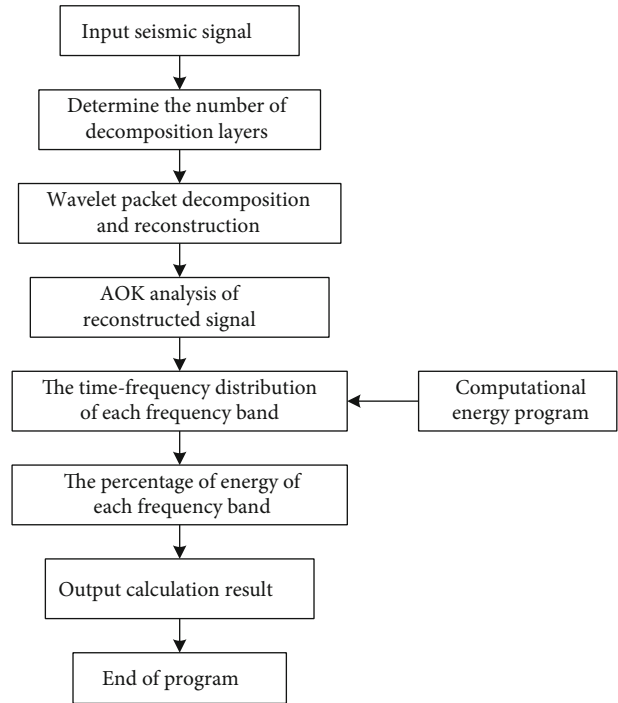


FIGURE 5: Flow chart of the MATLAB program for signal reconstruction and AOK time-frequency analysis.

grams of the three-component signals of the M1 station of the No. 1 test station are shown in Figure 7 by using the toolbox.

As can be seen from Figure 7, the AOK time-frequency analysis method can localize the time domain and frequency domain of the three-component signals and can obtain the main frequency information and duration of the seismic wave signal. The main frequency of the three components of the M1 station in test 1 is 60 Hz, 54 Hz, and 47 Hz, and the frequency band with large energy is between 30 and 70 Hz. The duration is about 20-30 ms. The frequency range of the *D* component signal is between 0 and 250 Hz, the frequency range of the *B* component signal is between 0 and 125 Hz, the frequency range of the *Z* component signal is between 0 and 200 Hz, and the duration of three-component signals is about 0.1 s.

The sampling frequency of the microseismic monitoring system is 4000 Hz. According to the sampling theorem, the sampling frequency of Nyquist is 2000 Hz. When the wavelet packets are used to process the seismic wave signal, the selection of wavelet basis function directly determines the accuracy of signal processing and analysis results. Daubechies wavelet (DB wavelet) basis function series can better reflect the unstable change process of the seismic wave signal in time and frequency distribution. db8 wavelet is often used to transform blasting vibration signal by wavelet packet transform. In the study of blasting seismic wave signals analysis, most of them adopted 8, 16, 32, 64 as the minimum decomposition frequency band. Combined with the Nyquist sampling frequency, the wavelet packet decomposition and reconstruction signal are decomposed by using the db8 wavelet series as the basis function. A total of 256

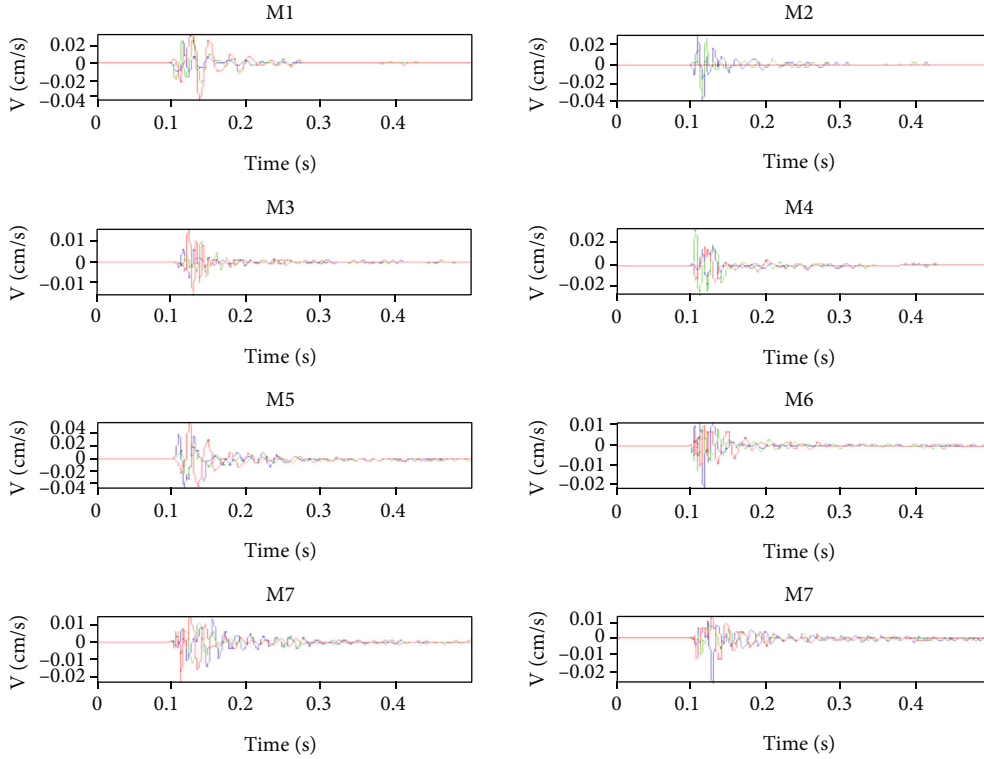


FIGURE 6: Seismic wave of blasting test 1.

subbands is obtained, the minimum frequency band is 0.0000 Hz~7.8125 Hz, the highest frequency band is 1992.1875 Hz~2000 Hz, and the intermediate frequency band is increased with 7.8125 Hz as the equal difference sequence.

The AOK time-frequency domain analysis of 256 seismic waves with different frequency bands after wavelet packet reconstruction is carried out. The `margtfr` function in the time-frequency analysis toolbox is used to calculate the time-frequency distribution TFR, time t , and frequency f after AOK time-frequency analysis. The return value is the energy of the signal, and the function expression is $[\text{margt}, \text{margf}, E] = \text{margtfr}(\text{tfr}, t, f)$, E as the energy of the signal.

Based on the above analysis flow and analysis method, combined with the time-frequency analysis toolbox, the three components recorded in the M1 test station were decomposed and reconstructed by the wavelet packets, and then, AOK time-frequency analysis and energy calculation were carried out, and 256 band energy distribution percentages are obtained as shown in Table 2 and Figure 8.

As can be seen from Table 2 and Figure 8, the frequency band energy distribution of liquid CO₂ blasting seismic wave signal is as follows:

- (1) It can be arranged from the figure that the energy of the signal is mainly concentrated in the 1-16 frequency band (0-125 Hz). The energy distribution of the three signal components in the first 16 frequency bands is, respectively, 87.74%, 98.42%, and 99.72%, and the maximum value occurs in the frequency band where the main frequency is located. The

energy distribution of 125 Hz-250 Hz is 11.04%, 1.5%, and 0.24%, respectively. After the frequency of 250 Hz, the energy distribution of the three components is 1.22%, 0.08%, and 0.04%, respectively. It indicates that the energy of the seismic wave signal is very concentrated, and the energy of the high-frequency part decays very rapidly, although the high-frequency part of the energy decays rapidly but still occupies a certain proportion of the distribution

- (2) In the 16 frequency bands, the energy distribution is divided into two regions, the 1-8 frequency band region and the 11-16 frequency band region. The energy of the three-component signals distributed in the 1-8 frequency is 63.24%, 80.85%, and 95.97%. The energy of the three-component signals distributed in the 11-16 frequency is 24.02%, 16.59%, and 3.7%, respectively.

4.2. Energy Calculation of Measuring Point. According to the linear arrangement of the test scheme, a total of 4 monitoring points and two blasting tests were set up, and a total of 8 groups of test data were set up. Each group of test data included the vibration signal components in D , B , and Z directions. Because of the poor signal-to-noise ratio (SNR) of the signal recorded by station 2, a total of 18 data amounts were obtained in this experiment. According to the waveform information of the blasting signal recorded by the monitoring network, the PPV value of each component of each station is

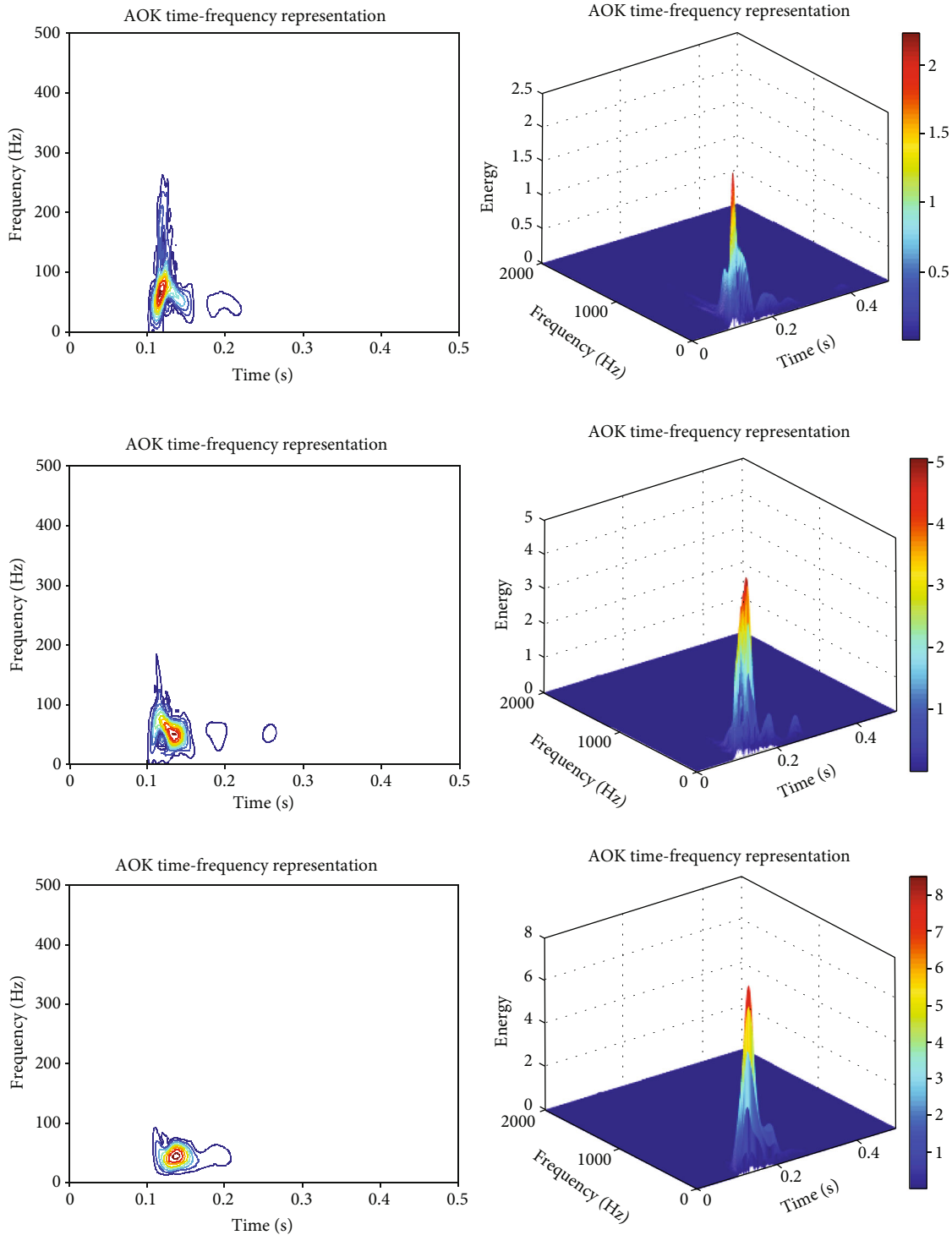


FIGURE 7: Time-frequency distribution (TFR) contours and three-dimensional maps of the three component signals for station M1 (in turn, *D*, *B*, and *Z* components, respectively).

calculated. Table 3 is the PPV table of three directional components of the seismic wave in two explosion tests.

Figure 9 shows the trend diagram that the PPV of the three directional components of seismic waves decreases with the increase of distance. It can be seen from the diagram that the whole vibration velocity is at a lower level. With the increase of distance, the vibration velocity decays

rapidly, in which the attenuation speed of vibration velocity in *D* and *B* directions is first fast and then slow; 24 meters is the inflection point of velocity attenuation rate, and the attenuation rate of vibration velocity in *Z* direction shows a trend of rapid decrease. When the vibration velocity decreases to the micron level at 48 meters, the vibration velocity in three directions tends to be similar.

TABLE 2: The percentage of energy distribution for three-component signals in different frequency bands.

Serial number	Frequency band (Hz)	D Distribute (%)	B Distribute (%)	Z Distribute (%)	Frequency band	Distribute (Hz)	D Distribute (%)	B Distribute (%)	Z Distribute (%)
1	0-7.8125	0.42	0.48	0	10	70.3125-78.125	0.3	0.45	0.04
2	7.8125-15.625	0.56	0.83	0.04	11	78.125-85.9375	1.48	1.2	0.18
3	15.625-23.4375	5.86	2.59	4.23	12	85.9375-93.75	0.65	0.34	0.11
4	23.4375-31.25	1.41	1.14	0.74	13	93.75-101.5625	9.03	3.18	0.38
5	31.25-39.0625	11.32	20.5	1.82	14	101.5625-109.375	7.26	5.58	1.54
6	39.0625-46.875	6.06	10.05	13.94	15	109.375-117.1875	1.39	0.52	0.31
7	46.875-54.6875	4.85	30.69	57.7	16	117.1875-125	4.22	5.78	1.19
8	54.6875-62.5	32.76	14.57	17.5	17-32	125-250	11.04	1.5	0.24
9	62.5-70.3125	0.18	0.52	0.01	33-256	250-2000	1.22	0.08	0.04

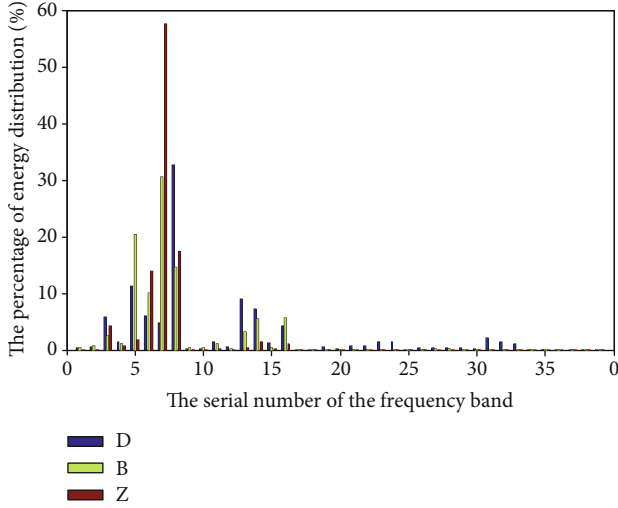


FIGURE 8: The percentage of energy distribution for three-component signals of station M1 in different frequency bands.

TABLE 3: PPV of three direction components of seismic waves in two explosion tests.

Serial number	Recording station	D-PPV (mm/s)	B-PPV (mm/s)	Z-PPV (mm/s)
4	a1	0.064	0.111	0.127
	a2	0.0395	0.067	0.039
	a4	0.009	0.0055	0.0001159
	a1	0.04	0.1	0.107
5	a2	0.02	0.0461	0.033
	a4	0.00523	0.0035	0.00012

As can be seen from Table 4, the AOK time-frequency distribution method can localize the time domain and frequency domain of the three components of the signal, which can obtain the main frequency information and duration of the seismic wave signal. The main frequency of the three-component signals of the 4 test a1, a2, and a4 stations is mainly distributed between 30 and 53 Hz, the duration is about 20-50 ms, all the seismic wave component signals are concentrated in the frequency domain, and the frequency range is between 0 and 250 Hz. The duration of the signal is about 0.1 s. With the increase of distance, the main frequency decreases, and the energy decreases gradually.

In the process of seismic wave propagation, it is very difficult to accurately calculate the seismic wave energy density at each geophone position. In engineering, the maximum peak vibration velocity and the square (discrete signal) of the amplitude of each sampling point in the seismic wave duration are usually used to represent the energy of the measuring point. Table 5 shows the seismic wave energy parameters of the liquid CO₂ blasting system, and Figure 10 shows the correlation curve between the peak vibration velocity of the measuring point and the double integral energy of TFR to time and frequency. It can be seen from the diagram that the correlation curve of the two parameters has a high linear

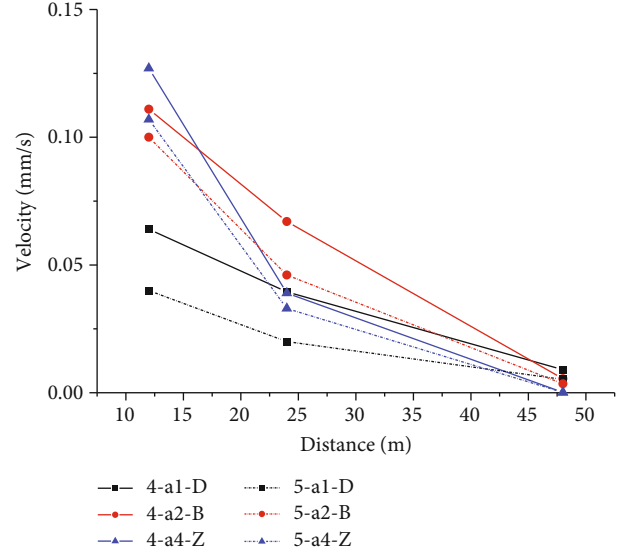


FIGURE 9: Relationship between PPV and distance of three directional components of seismic waves in two explosion tests.

TABLE 4: Main frequency of three directional components of seismic wave in explosion test 4.

Serial number	Recording station	D (Hz)	B (Hz)	Z (Hz)
4	a1	53	41	47
	a2	41	39	50
	a4	30	39	35

correlation. The correlation coefficient is $R^2 = 0.90$. Therefore, it can be considered that the peak velocity of the measuring point can reflect the energy of the measuring point for liquid CO₂ and explosive blasting seismic wave, and it is not necessary to calculate the energy obtained by the double integration of time and frequency of TFR in the whole time period of the event. In the process of analyzing the law of seismic wave energy attenuation in liquid CO₂ blasting system, on the one hand, it can automatically pick up and calculate the peak velocity and reduce the calculation workload; on the other hand, it can improve the efficiency of evaluating the damage and attenuation degree of seismic wave energy.

4.3. *Energy Attenuation Law.* The regression models that can be used for seismic wave energy attenuation can be divided into two categories [39]: (1) exponential function form, see formula (6), and (2) power function form, see formula (7).

$$E = E_0 e^{-\alpha r}, \tag{6}$$

$$E = E_0 r^{-\alpha}. \tag{7}$$

In the formula, r is the distance between the measuring point and the source, E_0 is the initial energy of the source, E is the energy at r , and α is the attenuation coefficient. Here, E_0 is only the initial energy of the source obtained by the regression curve or the initial energy of the virtual source.

TABLE 5: Seismic wave energy parameters of the liquid CO₂ blasting system.

Measure point	Distance (m)	PPV (cm/s)			Energy (cm ² /s ²)		
		<i>D</i>	<i>B</i>	<i>Z</i>	<i>D</i>	<i>B</i>	<i>Z</i>
4-a1	12	0.0064	0.0111	0.0127	0.0156	0.029281	0.022842
4-a2	24	0.00395	0.0067	0.0039	0.004070286	0.011159	0.006034
4-a4	48	0.0009	0.00055	0.00001159	0.000481786	0.000205	4.99E-08

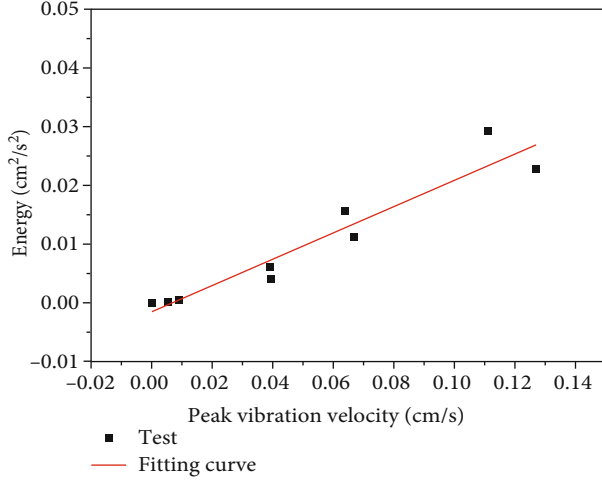


FIGURE 10: Regression curve between peak vibration velocity and energy.

Use the data in Table 5 to compare the exponential function with the fitting curve of the power function according to the above formula. As shown in Figure 11, the parameter coefficients and correlation coefficients of the exponential function model and the power function are shown in Table 6. It can be seen from the table that both the exponential function model and the power function model are suitable to describe the energy attenuation law of seismic waves produced by the liquid CO₂ blasting system. From the point of view of correlation coefficient alone, the exponential function model is more suitable for seismic wave attenuation law of liquid CO₂ blasting system, but the initial energy E_0 of the source is small or has little difference with the energy at the measuring point of 12 meters and is in the same order of magnitude. Although the correlation coefficient of the power function model is smaller than that of the exponential function model, it is closer to the real value from the initial energy E_0 of the source. To sum up, the power function is more suitable to describe this typical attenuation law of explosive seismic wave: with the increase of the distance from the source, the early attenuation is rapid, and the late attenuation is slow. The attenuation of explosion seismic wave energy in lithe quid CO₂ blasting system is similar to that of explosive explosion seismic wave energy.

Although the data are few here, while the relationship between energy and distance in this paper conforms to the general law of energy characteristics of blasting seismic waves. Therefore, in a sense, we just proved this relationship, if data points are more in the future work, the other analyt-

ical method such as the analysis of variance (ANOVA) can be conducted to deep investigate the influence of distance on energy.

4.4. Source Energy Regression Model

4.4.1. *The Empirical Formula of Vibration Velocity of Sadovsky.* The velocity attenuation law of particle vibration in blasting engineering is commonly expressed by Sadovsky's empirical formula [39], that is,

$$V = K \left(\frac{\sqrt[3]{Q}}{r} \right)^\alpha = V_0 r^{-\alpha}. \quad (8)$$

In the formula, the particle vibration velocity is the particle vibration velocity, the cm/s; V is the site coefficient; K is the charge, kg; r and α are the same as above; V_0 is the initial vibration velocity of the source; and the same V_0 of cm/s is the vibration velocity of the virtual source here. For the data in Table 5, combined with the formula (8), the average energy of liquid CO₂ blasting tube in reference [2] is 0.030 kg TNT. The regression analysis shows that $K = 4.924$ and $\alpha = 1.0526$.

4.4.2. *Energy Conversion Factor.* It is not convenient for Sadovsky's formula to be directly used to calculate the energy of the microseismic source. The site coefficient K is related to the source medium and blasting parameters. The seismic wave energy corresponding to explosive quantity Q also needs to be converted. In solid media, only a very small part of explosive explosion energy is converted into the seismic wave. Here is a concept of energy conversion coefficient η that needs to be explained and defined. The ratio of seismic wave energy to total energy produced by the explosive explosion is defined as the seismic wave energy conversion coefficient of explosive blasting. According to this theory, this paper also represents the ratio of seismic wave energy E_c to TNT equivalent total energy produced by liquid CO₂ blasting according to this theory that liquid CO₂ blasting system has a similar seismic wave energy conversion coefficient E_T [39].

$$\eta_c = \frac{E_c}{E_T}. \quad (9)$$

Through theoretical analysis and a large number of experimental data, the energy conversion coefficient of explosive was discussed and analyzed in detail and put forward the formula for calculating the energy conversion coefficient of explosive earthquake based on the statistical

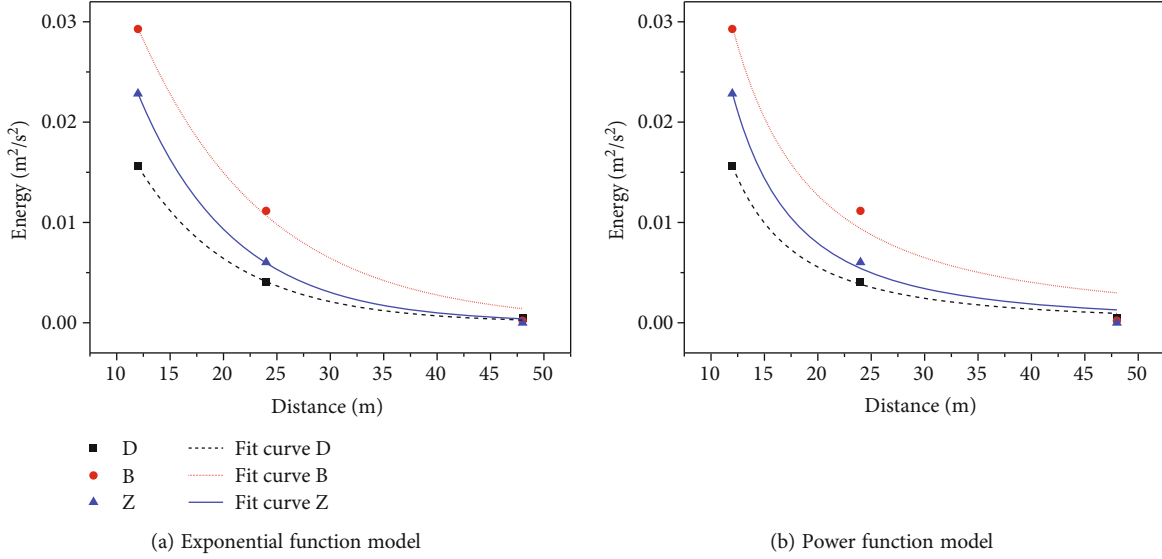


FIGURE 11: Regression model of energy with distance.

TABLE 6: Parameter of exponential function model and power function model from the regression curves in Figure 11.

Formula	$E = E_0 e^{-\alpha r}$		Formula	$E = E_0 r^{-\alpha}$			
R^2	0.999	0.992	0.999	R^2	0.996	0.949	0.986
D	E_0	0.05929	D	E_0	2.3994		
	α	0.1112		α	2.0253		
B	E_0	0.08088	B	E_0	1.79948		
	α	0.08434		α	1.65352		
Z	E_0	0.08777	Z	E_0	4.00521		
	α	0.11212		α	2.078		

parameters K and α based on explosive seismic effect (the unit of Q is m of kg, r and the unit of V is cm/s) and the formula for the energy conversion coefficient of explosive as follow [39, 40]:

$$\eta_c = (K \cdot 10^{-2})^{3/\alpha} \cdot 10^{-3}. \quad (10)$$

The seismic wave energy conversion coefficient $C = 1.88E - 07$ of the liquid CO_2 blasting system is obtained by using $A = 4.924$ and $B = 1.0526$ generation (15).

4.4.3. *Source Energy Characteristic Coefficient.* The total energy generated by the explosion of TNT with a mass of Q is

$$E_T = Q * Q_V. \quad (11)$$

Q_V is the explosion heat of TNT, 4150.2 kJ/kg.

The seismic wave energy is obtained by replacing formula (11) with (9).

$$E_c = Q * Q_V * \eta_c. \quad (12)$$

Then, the Q , Q_V , and η_c parameters are substituted into (12) to obtain the elastic wave energy of liquid CO_2 blasting source $E_c = 0.0232$ J. Replace formula (12) with (8) to get

$$V = \frac{K}{(Q_V \eta_c)^{\alpha/3}} \left(\frac{\sqrt[3]{E_c}}{r} \right)^\alpha = \frac{V_0}{E_c^{\alpha/3}} \left(\frac{\sqrt[3]{E_c}}{r} \right)^\alpha. \quad (13)$$

Assume

$$K_c = \frac{K}{(Q_V \eta_c)^{\alpha/3}} = \frac{V_0}{E_c^{\alpha/3}}. \quad (14)$$

The K_c is defined as the energy characteristic coefficient of the source, and formula (10) is obtained by replacing formula (14) with the energy characteristic coefficient of the source.

$$K_c = \frac{10^{2+\alpha}}{Q_V^{\alpha/3}}. \quad (15)$$

From formulas (14) and (15), it can be seen that the value of K_c is mainly related to the dynamic characteristics of the source medium but independent of the specific blasting mode. That is to say, K_c reflects the proportional relationship between the source elastic wave energy E_c and the initial peak vibration velocity V_0 of the source. Under the same experimental conditions, the stability of K_c is better than that of site coefficient. The energy characteristic coefficient K_c of the source of liquid CO_2 blasting system is 5.376 by replacing K , Q_V , η_c , and (14).

4.4.4. *Source Energy Regression Model.* The relationship between the peak vibration velocity of particles and the energy of the seismic wave is obtained by replacing formula (14) with (13).

$$V = K_c \left(\frac{\sqrt[3]{E_c}}{r} \right)^\alpha \quad (16)$$

After determining the energy characteristic coefficient K_c , formula (16) is used as the regression model of seismic wave energy attenuation in the liquid CO₂ blasting system. Taking the peak vibration velocity V and attenuation coefficient α as parameters, the source energy of liquid CO₂ blasting system is directly obtained by the least square method, and the seismic wave source energy $E_c = 0.0234$ J is obtained by regression of Table 5 experimental data. The deviation of elastic wave energy between liquid CO₂ blasting source and formula (12) is 8.55%.

5. Conclusions

In order to study the time-frequency and energy characteristics of seismic waves in the liquid CO₂ blasting system, the liquid CO₂ blasting seismic wave signal is obtained by field microseismic monitoring test. According to the nonstationary characteristics of the blasting seismic wave signal, the basic time-frequency characteristics of the seismic wave signal are studied by adaptive optimal kernel time-frequency analysis method. On this basis, combined with wavelet packet transform decomposition and reconstruction technology and adaptive optimal kernel time-frequency analysis method, the energy distribution of the seismic wave signal is analyzed in detail. The main conclusions are as follows:

- (1) The direct wave energy of the blasting signal is strong, and the attenuation speed is fast. There is no obvious S wave in the blasting process. The amplitude of blasting vibration of seismic wave signals in three directions is 0.01–0.04 m/s at about 12 m, and the vibration velocity is at a lower level. The main frequency range is between 30 and 70 Hz, and the duration is about 20–30 ms. The energy is mainly distributed in 0–125 Hz, the main frequency appears in the frequency band with the maximum energy, and the energy in the high-frequency part decays rapidly, and there are two main regions in the energy distribution, which indicates that two different peak pressures will be produced in the process of liquid CO₂ blasting, which is consistent with the experimental data of the pressure response of the free explosion field in reference [2]
- (2) The attenuation of explosion seismic wave energy in the liquid CO₂ blasting system is similar to that of explosive explosion seismic wave energy. The power function model can be used to describe the attenuation law of seismic wave energy: with the increase of distance from the source, the early attenuation is rapid, and the later attenuation is slow
- (3) The energy conversion coefficient and characteristic coefficient of the source of liquid CO₂ blasting system are defined and analyzed. Combined with the

empirical formula of Sadovsky vibration velocity, the energy regression model of seismic wave source of liquid CO₂ blasting system is given

Data Availability

The data presented in this study are available on request from the corresponding author.

Conflicts of Interest

The authors declare no conflict of interest.

Authors' Contributions

Xuejiao Cui and Bo Ke contributed to the conceptualization. Bo Ke and Songtao Yu contributed to the data curation. Xuejiao Cui and Ping Li contributed to the formal analysis. Mingsheng Zhao contributed to the investigation. Xuejiao Cui, Songtao Yu, and Ping Li contributed to the methodology. Bo Ke and Ping Li contributed to the software. Bo Ke and Songtao Yu contributed to the validation. Mingsheng Zhao contributed to the visualization. Xuejiao Cui, Bo Ke, and Ping Li contributed to the writing—original draft. Xuejiao Cui and Songtao Yu contributed to the writing—review and editing. All authors have read and agreed to the published version of the manuscript.

Acknowledgments

This work was supported by the National key research and development projects (No. 2018YFC0808405), the China Postdoctoral Science Foundation (No. 2018M632936), the National Natural Science Foundation of China (No. 52064003), and the Fundamental Research Funds for the Central Universities (WUT: 2019IVA092).







References

- [1] S. P. Singh, "Non-explosive applications of the PCF concept for underground excavation," *Tunnelling and Underground Space Technology*, vol. 13, no. 3, pp. 305–311, 1998.
- [2] B. Ke, K. Zhou, C. Xu, G. Ren, and T. Jiang, "Thermodynamic properties and explosion energy analysis of carbon dioxide blasting systems," *Mining Technology*, vol. 128, no. 1, pp. 39–50, 2019.
- [3] B. Davies and I. Hawkes, *The Mechanics of Blasting Strata Using the Cardox and Air Blasting Systems*, Toothill Press, London, 1984.
- [4] R. Pesch and A. Robertson, *Drilling and Blasting for Underground Space*, 2007, <https://www.coffey.com.au>.
- [5] A. Parsakhoo and M. Lotfalian, "Demolition agent selection for rock breaking in mountain region of hyrcanian forests," *Research Journal of Environmental Sciences*, vol. 3, no. 3, pp. 384–391, 2009.
- [6] A. Parsakhoo, M. Lotfalian, and S. A. Hosseini, "Forest roads planning and construction in Iranian forestry," *Journal of Civil Engineering and Construction Technology*, vol. 1, no. 1, pp. 14–18, 2010.
- [7] S. Durga and R. Swetha, "Disaster prevention and control management," *Energy Economics*, vol. 128, pp. 528–536, 2015.

- [8] T. Bajpayee, T. R. Rehak, G. L. Mowrey, and D. K. Ingram, "Blasting injuries in surface mining with emphasis on flyrock and blast area security," *Journal of Safety Research*, vol. 35, no. 1, pp. 47–57, 2004.
- [9] T. K. Lu, Z. Wang, H. Yang, P. Yuan, Y. Han, and X. Sun, "Improvement of coal seam gas drainage by under-panel cross-strata stimulation using highly pressurized gas," *International Journal of Rock Mechanics and Mining Sciences*, vol. 77, pp. 300–312, 2015.
- [10] L. P. Zhao, "Technology of liquid carbon dioxide deep hole blasting enhancing permeability in coal seam," *Saf. Coal Mines*, vol. 44, no. 12, pp. 76–78, 81, 2013.
- [11] Z. F. Wang, X. M. Sun, T. K. Lu, and Y. B. Han, "Experiment research on strengthening gas drainage effect with fracturing technique by liquid CO₂ phase transition," *Journal of Henan Polytechnic University(Natural Science)*, vol. 34, no. 1, pp. 1–5, 2015.
- [12] H. D. Chen, Z. Wang, X. Chen, X. Chen, and L. Wang, "Increasing permeability of coal seams using the phase energy of liquid carbon dioxide," *Journal of CO₂ Utilization*, vol. 19, pp. 112–119, 2017.
- [13] G. Z. Hu, W. He, and M. Sun, "Enhancing coal seam gas using liquid CO₂ phase- transition blasting with cross-measure borehole," *Journal of Natural Gas Science and Engineering*, vol. 60, pp. 164–173, 2018.
- [14] J. Kang, F. Zhou, Z. Qiang, and S. Zhu, "Evaluation of gas drainage and coal permeability improvement with liquid CO₂ gasification blasting," *Advances in Mechanical Engineering*, vol. 10, no. 4, 2018.
- [15] H. D. Wang, Z. Cheng, Q. Zou et al., "Elimination of coal and gas outburst risk of an outburst-prone coal seam using controllable liquid CO₂ phase transition fracturing," *Fuel*, vol. 284, p. 119091, 2021.
- [16] Z. Shang, H. Wang, B. Li et al., "Experimental investigation of BLEVE in liquid CO₂ phase- transition blasting for enhanced coalbed methane recovery," *Fuel*, vol. 292, article 120283, 2021.
- [17] X. F. Liu, B. Nie, K. Guo, C. Zhang, Z. Wang, and L. Wang, "Permeability enhancement and porosity change of coal by liquid carbon dioxide phase change fracturing," *Engineering Geology*, vol. 287, article 106106, 2021.
- [18] Y. Zhang, J. Deng, B. Ke, H. Deng, and J. Li, "Experimental study on explosion pressure and rock breaking characteristics under liquid carbon dioxide blasting," *Advances in Civil Engineering*, vol. 2018, Article ID 7840125, 9 pages, 2018.
- [19] B. Ke, K. Zhou, G. Ren, J. Shi, and Y. Zhang, "Positive phase pressure function and pressure attenuation characteristic of a liquid carbon dioxide blasting system," *Energies*, vol. 12, no. 21, p. 4134, 2019.
- [20] X. Huang, Q. Li, X. Wei et al., "Indoor test system for liquid CO₂ phase change shock wave pressure with PVDF sensors," *Sensors*, vol. 20, no. 8, p. 2395, 2020.
- [21] F. Gao, L. Tang, K. Zhou, Y. Zhang, and B. Ke, "Mechanism analysis of liquid carbon dioxide phase transition for fracturing rock masses," *Energies*, vol. 11, no. 11, p. 2909, 2018.
- [22] Y. Zhang, J. Deng, H. Deng, and B. Ke, "Peridynamics simulation of rock fracturing under liquid carbon dioxide blasting," *International Journal of Damage Mechanics*, vol. 28, no. 7, pp. 1038–1052, 2019.
- [23] Y. Chen, H. Zhang, Z. Zhu et al., "A new shock-wave test apparatus for liquid CO₂ blasting and measurement analysis," *Measurement and Control*, vol. 52, no. 5-6, pp. 399–408, 2019.
- [24] Q. Y. Li, G. Chen, D. Y. Luo, H. P. Ma, and Y. Liu, "An experimental study of a novel liquid carbon dioxide rock-breaking technology," *International Journal of Rock Mechanics and Mining Sciences*, vol. 128, p. 104244, 2020.
- [25] Z. W. Liao, X. Liu, D. Song et al., "Micro-structural damage to coal induced by liquid CO₂ phase change fracturing," *Natural Resources Research*, vol. 30, no. 2, pp. 1613–1627, 2021.
- [26] D. L. Jones and R. G. Baraniuk, "An adaptive optimal-kernel time-frequency representation," *IEEE Transactions on Signal Processing*, vol. 43, no. 10, pp. 2361–2371, 1995.
- [27] D. L. Jones, R. G. Baraniuk, and E. Winkler, "Adaptive optimal-kernel TFR (AOK) TFR," <http://www-dsp.rice.edu/software/time-frequency-analysis>.
- [28] M. S. Zhao, K. S. Liang, and B. W. Li, "Influence of deck charge on time-frequency characteristics of a blasting vibration signal," *Vibration and Shock*, vol. 31, no. 7, pp. 85–88, 2012.
- [29] X. Wang, J. Gao, W. Chen, W. Zhao, X. Jiang, and Z. Zhu, "Seismic attenuation qualitative characterizing method based on adaptive optimal-kernel time-frequency representation," *Journal of Applied Geophysics*, vol. 89, pp. 125–133, 2013.
- [30] E. Sejdić, I. Djurović, and J. Jiang, "Time-frequency feature representation using energy concentration: an overview of recent advances," *Digit Signal Process*, vol. 19, no. 1, pp. 153–183, 2009.
- [31] B. Sun, E. Wang, Y. Ding, H. Bai, and Y. Huang, "Time-frequency signal processing for gas-liquid two phase flow through a horizontal venturi based on adaptive optimal-kernel theory," *Chinese Journal of Chemical Engineering*, vol. 19, no. 2, pp. 243–252, 2011.
- [32] M. S. Zhao, K. S. Liang, and L. I. Ben-Wei, "Influence of deck charge on time-frequency characteristics of a blasting vibration signal," *Journal of Vibration and Shock*, vol. 31, no. 7, pp. 85–88, 2012.
- [33] Z. Liu, S. Zou, Z. Li, and W. Ju, "Wavelet energy features of acoustic emission signals under centrifugal pump cavitation conditions," *Transactions of the Chinese Society of Agricultural Engineering*, vol. 31, no. 8, pp. 99–103, 2015.
- [34] T. H. Lin, Y. C. Liao, and S. Zhang, "Application of wavelet packets method in frequency bands energy distribution on rock acoustic emission signals under impact loading," *Shock and Vibration*, vol. 29, no. 10, 130 pages, 2010.
- [35] S. W. Ma, W. Q. Xie, X. J. Zhu, and G. H. Chen, "Instantaneous frequency estimation based on parametric adaptive time-frequency distribution," *Chinese Journal of Scientific Instrument*, vol. 27, no. 11, pp. 1373–1377, 2006.
- [36] X. K. Wang, J. H. Gao, and Y. Y. He, "Time-frequency analysis based on time-frequency-adaptive optimal-kernel," *Systems Engineering and Electronics*, vol. 32, no. 1, pp. 22–26, 2010.
- [37] Q. J. Zhu, F. X. Jiang, Z. X. Yu, Y. M. Yin, and L. Lv, "Study on energy distribution characters about blasting vibration and rock fracture microseismic signal," *Chinese Journal of Rock Mechanics and Engineering*, vol. 31, no. 4, pp. 723–730, 2012.
- [38] F. Auger, O. Lemoine, P. Gonçalves, and P. Flandrin, "The Time-Frequency Toolbox (TFTB)," <http://tftb.nongnu.org>.
- [39] Z. Li, R. G. Zhu, Z. L. Hu, Y. M. Chen, J. X. Yang, and J. X. Cai, "Studies on the characteristic coefficient and attenuation index in the measurement of blasting seismic wave," *Explosion, and Shock Waves*, vol. 6, no. 3, pp. 221–229, 1986.
- [40] J. Q. Wang, N. L. Hu, F. X. Jiang, W. S. Lv, and X. C. Qu, "Calculation method for the seismic wave energy of microseismic hypocenters," *Journal of University of Science and Technology Beijing*, vol. 35, no. 6, pp. 703–708, 2013.

Research Article

Study on the Settlement Mechanism with Effect of Backfilling Method of an Underground Mine

Dequan Xuan ^{1,2}, Zhiming Liu ^{1,2}, Gang Huang ^{1,2}, Jianhua Zhang ^{1,2},
Tingting Jiang ^{1,2} and Bo Ke ^{1,2}

¹School of Resources and Environmental Engineering, Wuhan University of Technology, Wuhan, Hubei 430070, China

²Hubei Key Laboratory of Mineral Resources Processing and Environment, Wuhan, Hubei 430070, China

Correspondence should be addressed to Gang Huang; huanggang2016@whut.edu.cn

Received 11 May 2021; Accepted 19 July 2021; Published 6 August 2021

Academic Editor: Yu Wang

Copyright © 2021 Dequan Xuan et al. This is an open access article distributed under the Creative Commons Attribution License, which permits unrestricted use, distribution, and reproduction in any medium, provided the original work is properly cited.

The study on the subsidence of backfill mining block has been a concern of many scholars. A mechanical model of plate subsidence is established by studying the roof of a filling mining area in Luo Iron Mine in this paper. The boundary conditions are given, and the Navier method is used to solve the problem. Based on the thin plate model, the subsidence distribution map of the roof of the underground plate area is obtained. Based on the basic calculation parameters, the influence of a different foundation coefficient, mining depth, length-width ratio of plate area, elastic modulus of roof rock, and thickness of roof on the subsidence of roof is studied. According to the deflection calculation formula obtained, the expression of the internal force and stress is deduced, and the distribution of stress and shear stress on the upper and lower surfaces of the roof is analyzed. The dangerous area of the roof can be obtained, which provides a theoretical basis for the daily maintenance of mine safety.

1. Introduction

Mineral resources are the important material basis of social development and construction. With the development and depletion of shallow mineral resources, more and more minerals are converted to underground mining. Filling mining technology can not only maintain stope stability but also effectively control surface subsidence and protect ecological environment, which has significant safety and environmental benefits [1]. In this paper, the roof of the filling mining panel in the Luoshan iron mine is taken as the research object. According to the theory of elastic-plastic mechanics and the characteristics of underground panel, the mechanical model of roof settlement is established to analyze the settlement law of the underground panel roof, which is expected to provide a theoretical basis for the daily maintenance of mine safety.

The Luohe iron mine is mined in two phases, one in the East and the other in the West. The design scale of phase I is 3 million t/a, which is divided into two stages

of -560 m and -620 m. The stage height of -560 m is 120 m, the stage height of -620 m is 60 m, and the first stage is -560 m. The original mining method was sublevel caving without sill pillar. Due to the difficulty of land acquisition and relocation, the mining method is the filling method [2]. According to the characteristics of the underground mining panel, combined with the original solid mechanics theory and various research methods, the paper studies the deformation of overlying strata and surface settlement law in the process of mine filling, which can provide reference for optimizing mining and filling sequence and stope structure parameters, and realize low-cost, efficient, and safe mining [3].

2. Physical Model Description

The buried depth of the Luohe iron ore body is -382 m ~ -864 m. Mining is divided into two stages, first up and then down. Each panel is 126 m long along the strike of the ore body, which is divided into 7 rooms, each room is 18 m,

and the mining method of “mining every other one” is adopted. There are 18 m pillars between each panel to support the roof and overburden. The width of each panel is 100 m, and the height is 120 m. The roof rock mass is layered. According to the theory of thin plate, when the ratio of the thickness h to the characteristic dimension L is about 1/80~1/5, it can be called a thin plate. According to the lithology and strata thickness of 13# geological section in the Luohe iron mine, a single panel and its roof can be regarded as a thin plate model.

The filling body can be regarded as an elastic foundation, and the supporting force is transferred to the basic roof through the direct roof [4]. Therefore, the basic roof can be regarded as a plate with the upper part bearing the load of the overlying strata and the lower part supported by the filling body and the surrounding pillars [5]. The schematic diagram of establishing the settlement mechanics model is shown in Figure 1.

3. Mathematical Models

3.1. Basic Equations of Solid Mechanics Model

3.1.1. Equilibrium Differential Equation. When the interior of the object is in a state of equilibrium, it needs to meet the equilibrium conditions [6], and the equilibrium equation is shown in

$$\begin{cases} \frac{\partial \sigma_x}{\partial x} + \frac{\partial \tau_{xy}}{\partial y} + \frac{\partial \tau_{xz}}{\partial z} + X = 0 \text{ or } \left(\rho \frac{\partial^2 u}{\partial t^2} \right), \\ \frac{\partial \tau_{yx}}{\partial x} + \frac{\partial \sigma_y}{\partial y} + \frac{\partial \tau_{yz}}{\partial z} + Y = 0 \text{ or } \left(\rho \frac{\partial^2 v}{\partial t^2} \right), \\ \frac{\partial \tau_{zx}}{\partial x} + \frac{\partial \tau_{zy}}{\partial y} + \frac{\partial \sigma_z}{\partial z} + Z = 0 \text{ or } \left(\rho \frac{\partial^2 w}{\partial t^2} \right), \end{cases} \quad (1)$$

or abbreviated as

$$\sigma_{ij,j} + X_i = 0 \text{ or } \left(\rho \frac{\partial^2 u}{\partial t^2} \right), \quad (2)$$

where σ_{ij} is the second-order stress tensor inside the body; $X, Y,$ and Z are the components of the physical force in three coordinates; $u, v,$ and w are the components of the displacement vector at any point in the body in three coordinate directions; and ρ is the density of the body.

3.1.2. Geometric Equation. Because it does not involve the cause of deformation and the material properties of the object, they are generally applicable equations [7]. The geo-

metric equation is as follows:

$$\varepsilon_{ij} = \frac{1}{2} (u_{i,j} + u_{j,i}), \quad (3)$$

where ε_{ij} is the strain tensor inside the body.

3.1.3. Strain Compatibility Equation (Saint Venant Equation). In order to make the geometric equations not contradictory, the six strain components must satisfy certain conditions. Therefore, the strain compatibility equation is obtained:

$$\varepsilon_{ij,kl} + \varepsilon_{kl,ij} = \varepsilon_{ik,jl} + \varepsilon_{jl,ik}. \quad (4)$$

3.1.4. Constitutive Equation

(1) Elastic Stage. There are two forms that can transform each other in this stage [8]:

(a) Expression of the strain component by the stress component:

$$\varepsilon_{ij} = \frac{1+\nu}{E} \sigma_{ij} - \frac{\nu}{E} \sigma_{kk} \delta_{ij} \quad (5)$$

(b) Expression of the stress component by the strain component

$$\sigma_{ij} = \lambda \varepsilon_{kk} \delta_{ij} + 2\mu \varepsilon_{ij} = \lambda \Theta \delta_{ij} + 2\mu \varepsilon_{ij} \quad (6)$$

(2) Plastic Stage. The constitutive equation for elastoplastic materials is as follows:

$$d\varepsilon_{ij} = \frac{1}{2G} dS_{ij} + d\lambda S_{ij} + \frac{1-2\nu}{3E} d\sigma_{kk} \delta_{ij} \quad (7)$$

where E is the modulus of elasticity, Pa; G is the shear modulus, Pa; ν is Poisson's ratio; δ_{ij} is the unit tensor; μ, λ is the lame constant; Θ is the volumetric strain, where $\Theta = \varepsilon_x + \varepsilon_y + \varepsilon_z$; S_{ij} is the partial stress tensor; K is the bulk modulus; $d\lambda$ is the proportional factor greater than zero related to the loading history; e_{ij} is the total strain in the plastic stage; and Θ is the total strain in the plastic stage; σ_m is called the average stress, $\sigma_m = (\sigma_x + \sigma_y + \sigma_z)/3$

For the plastic region, it also needs to satisfy three equilibrium differential equations and six geometric and constitutive equations. The problem can still be solved by adding an increment $d\lambda$ and a uniform condition $f(\sigma_{ij}) = 0$. In the plastic region, the constitutive equation is nonlinear.

3.2. Elastic Thin Plate Theory. Thin plate refers to the plate whose thickness h is approximately 1/80~1/5 of the characteristic dimension l . For thin plate bending problems,

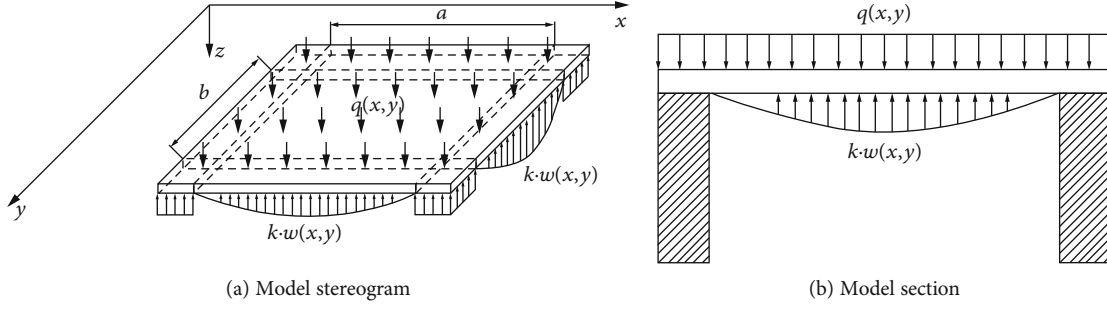


FIGURE 1: Mechanical model of roof settlement.

the following assumptions should be introduced on the basis of continuous [9], uniform, and isotropic assumptions:

- (1) Any straight line segment perpendicular to the middle plane before deformation remains a straight line after deformation and is perpendicular to the middle plane after bending deformation, and the length remains unchanged. That is, $\gamma_{zx} = \gamma_{xz} = 0$, $\varepsilon_z = 0$
- (2) The normal stress perpendicular to the middle plane of the thin plate is relatively small and neglected, $\sigma_z = 0$
- (3) There is no in-plane expansion and shear deformation in the thin plate, i.e., $u(x, y, 0) = v(x, y, 0) = 0$.

3.2.1. Constitutive Relation

(1) *Stress-Deformation Relationship.* According to the hypothesis, the relationship between the strain component and the midplane deflection w can be obtained as shown in equation (8), and the generalized Hooke's law [9] can be written as the relationship between the principal stress component and the midplane deflection w as shown in equation (9):

$$\begin{cases} \varepsilon_x = -z \frac{\partial^2 w}{\partial x^2}, \\ \varepsilon_y = -z \frac{\partial^2 w}{\partial y^2}, \\ \varepsilon_{xy} = -2z \frac{\partial^2 w}{\partial x \partial y}, \end{cases} \quad (8)$$

$$\begin{cases} \sigma_x = -\frac{Ez}{1-\nu^2} \left(\frac{\partial^2 w}{\partial x^2} + \frac{\partial^2 w}{\partial y^2} \right), \\ \sigma_y = -\frac{Ez}{1-\nu^2} \left(\frac{\partial^2 w}{\partial y^2} + \frac{\partial^2 w}{\partial x^2} \right), \\ \tau_{xy} = -\frac{Ez}{1+\nu} \frac{\partial^2 w}{\partial x \partial y}. \end{cases} \quad (9)$$

(2) *Internal Force-Deformation Relationship.* The relationship between the internal force and deformation can be

TABLE 1: Calculation parameter value.

Number	Parameter name (unit)	Parameter value
1	Average density of rock (kg/m ³)	2800
2	Elastic modulus (GPa)	30
3	Foundation coefficient (MPa/m)	40
4	Panel length (m)	126
5	Panel width (m)	60
6	Roof thickness (m)	10
7	Buried depth (m)	450
8	Poisson's ratio	0.25

expressed as

$$\begin{cases} M_x = -D \left(\frac{\partial^2 w}{\partial x^2} + \nu \frac{\partial^2 w}{\partial y^2} \right), \\ M_y = -D \left(\frac{\partial^2 w}{\partial y^2} + \nu \frac{\partial^2 w}{\partial x^2} \right), \\ M_{xy} = M_{yx} = -D(1-\nu) \frac{\partial^2 w}{\partial x \partial y}, \\ Q_x = \int_{h/2}^{h/2} \tau_{xz} dz = -D \frac{\partial}{\partial x} \nabla^2 w, \\ Q_y = \int_{h/2}^{h/2} \tau_{yz} dz = -D \frac{\partial}{\partial y} \nabla^2 w, \end{cases} \quad (10)$$

where D is the bending rigidity of thin plate, expressed as $D = Eh^3/12(1-\nu)$; M_x and M_y are bending moment per unit length of the thin plate cross-section; M_{xy} are M_{yx} the torque per unit length of the thin plate cross-section, respectively; and Q_x and Q_y are the transverse shear force per unit length of the cross-section.

(3) *Bending Differential Equation of Thin Plate.* After the underground stope is filled, the roof is located on the continuous elastic foundation and is ballasted by the load $q(x, y)$ perpendicular to the slab [10]. When the deflection value is small, according to the Winkler foundation assumption, the reaction force of the filling body at any

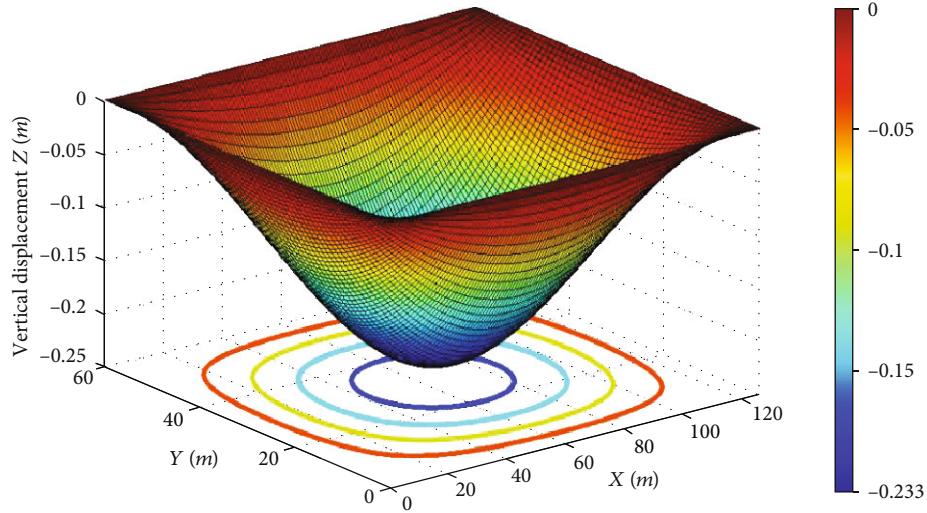


FIGURE 2: Distribution of roof settlement under basic parameters.

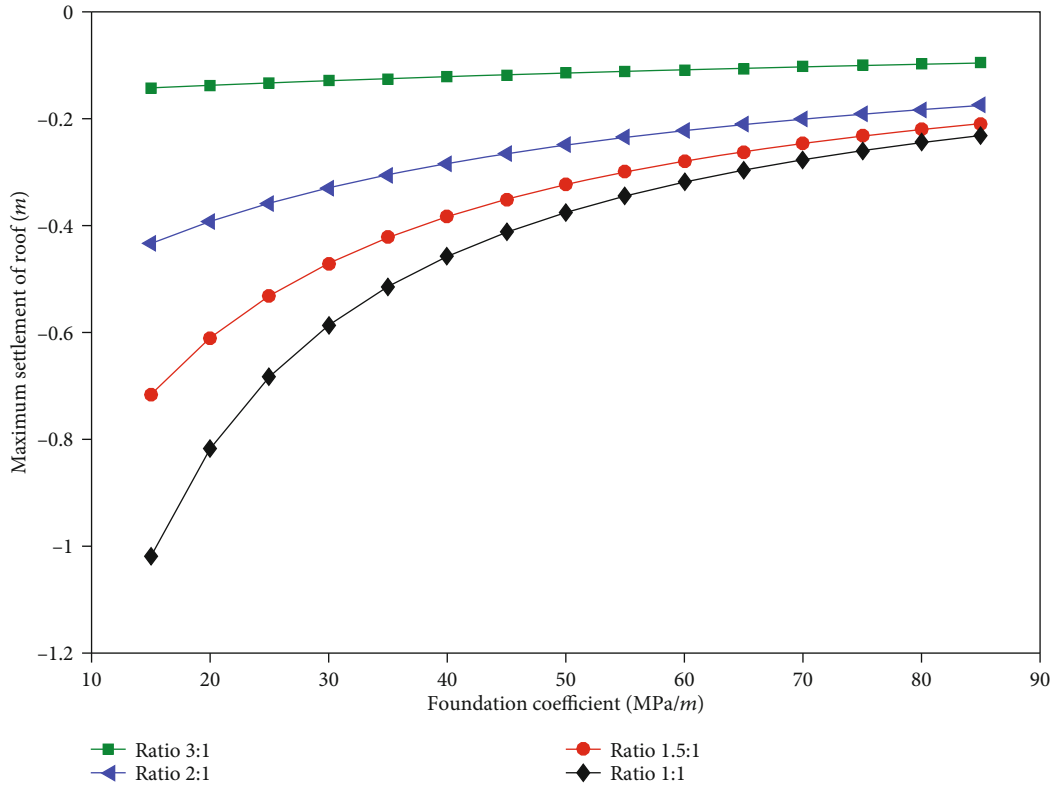


FIGURE 3: Curve of the maximum settlement of roof with the variation of foundation coefficient.

point under the roof can be expressed as proportional to the deflection of the point, so the load strength of each point of the plate is

$$Q(x, y) = q(x, y) - k \cdot w(x, y), \quad (11)$$

where k is the coefficient of elastic foundation.

Therefore, the differential equation of the roof bending surface can be expressed as

$$\frac{\partial^4 w}{\partial x^4} + 2 \frac{\partial^4 w}{\partial x^2 \partial y^2} + \frac{\partial^4 w}{\partial y^4} = \frac{q(x, y) - k \cdot w(x, y)}{D}. \quad (12)$$

3.3. *Solution of Mechanical Model of Roof Settlement.* According to the above modeling analysis, formula (12) is

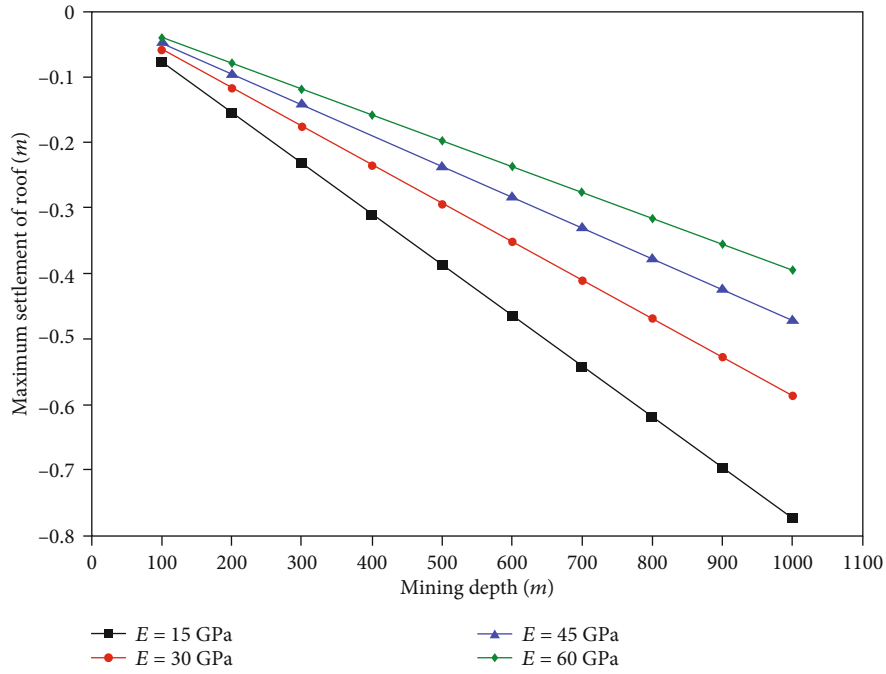


FIGURE 4: Influence of different mining depths on roof settlement.

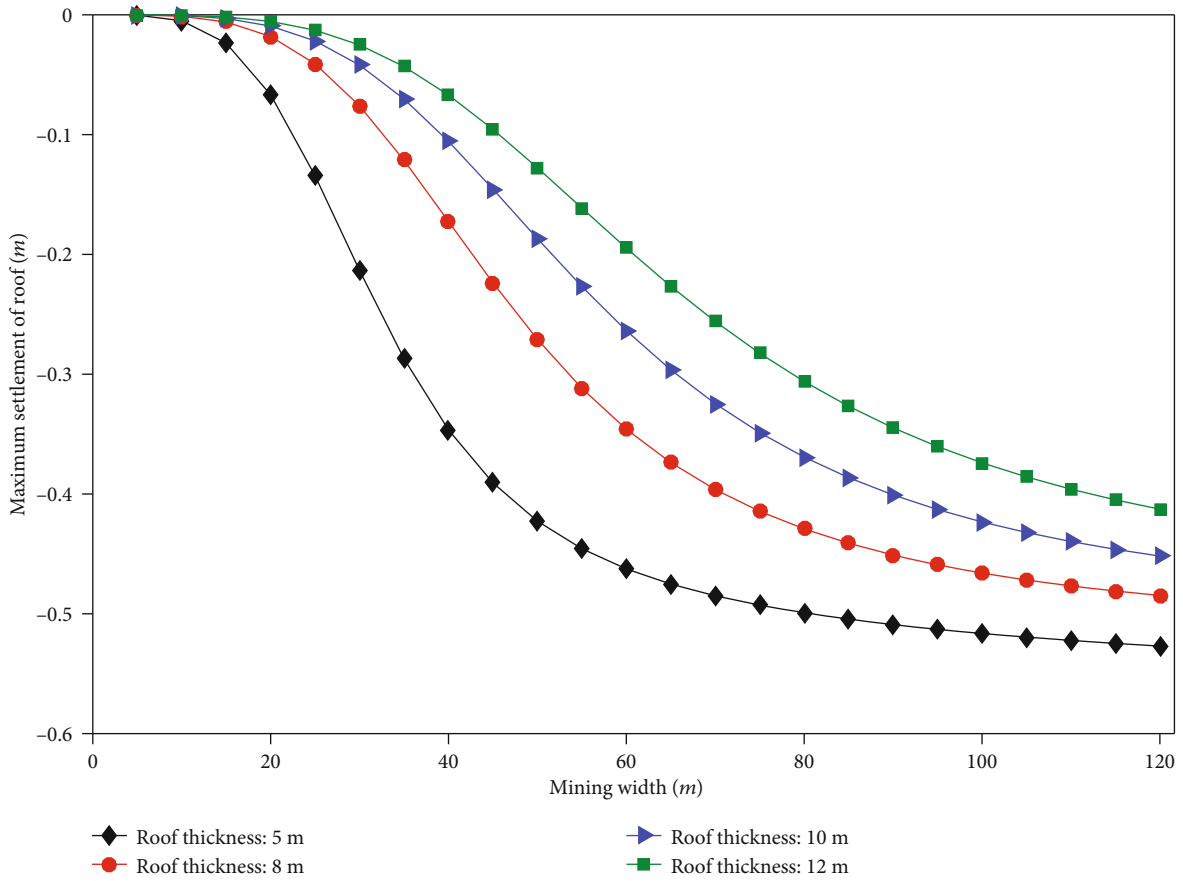


FIGURE 5: Influence of different aspect ratios of the panel on roof settlement.

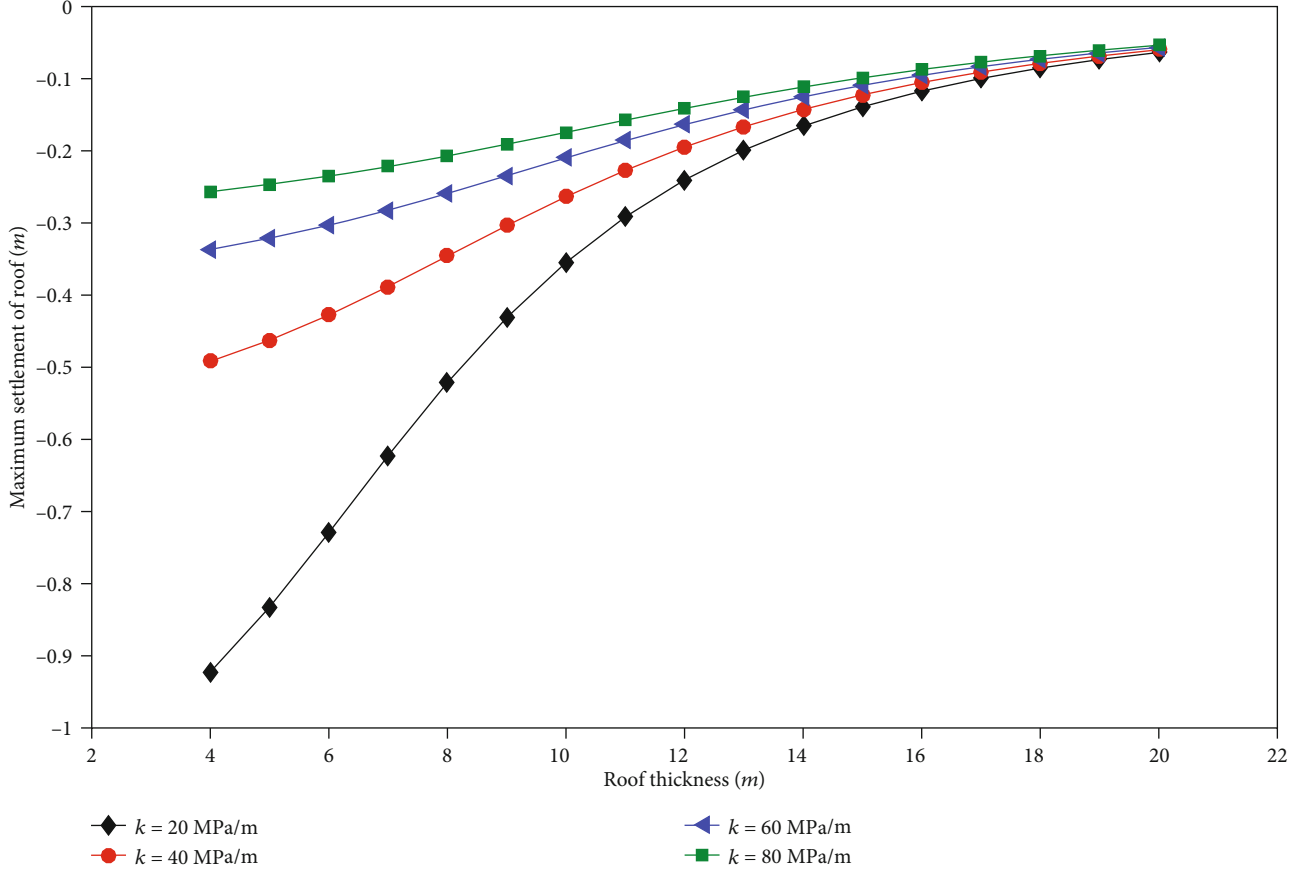


FIGURE 6: Influence of different roof thicknesses on roof settlement.

obtained, which is the differential equation of the roof settlement mechanics model. The equation is a high-order partial differential equation, which requires a special solution to obtain the deflection and internal force expressions of the model [11]. Firstly, the boundary conditions of the model are given.

3.3.1. Boundary Conditions. The boundary conditions at $x = 0$ and $x = a$, $y = 0$ and $y = b$ of the model are fixed, and the deflection and rotation angle are both 0, so the boundary conditions can be written as

$$\begin{cases} w|_{x=0} = w|_{x=a} = 0, \\ \frac{\partial w}{\partial x}|_{x=0} = \frac{\partial w}{\partial x}|_{x=a} = 0, \\ w|_{y=0} = w|_{y=b} = 0, \\ \frac{\partial w}{\partial y}|_{y=0} = \frac{\partial w}{\partial y}|_{y=b} = 0. \end{cases} \quad (13)$$

3.3.2. Navier Method for Mechanical Model of Thin Plate. The Navier method is often used to solve the problem of plate deflection in mechanics, that is, double trigonometric series

can be used to express the deflection of the thin plate:

$$w(x, y) = \sum_{m=1}^{\infty} \sum_{n=1}^{\infty} A_{mn} \sin \frac{m\pi x}{a} \sin \frac{n\pi y}{b}, \quad (14)$$

where m and n are any positive integers, A_{mn} is the undetermined coefficient, a and b are length and width of the thin plate model, respectively, m.

From the deflection formula, bending moment, and torque formula, the stress components in the thin plate can be obtained as follows:

$$\begin{cases} \sigma_x(x, y, z) = \frac{12M_x}{h^3} z, \\ \sigma_y(x, y, z) = \frac{12M_y}{h^3} z, \\ \sigma_{xy}(x, y, z) = \frac{12M_{xy}}{h^3} z. \end{cases} \quad (15)$$

4. Study on Factors Affecting Roof Settlement

Through the assignment of each parameter, the settlement of different positions of the roof can be calculated [12]. According to the geological data of a mine, the values of basic parameters are shown in Table 1.

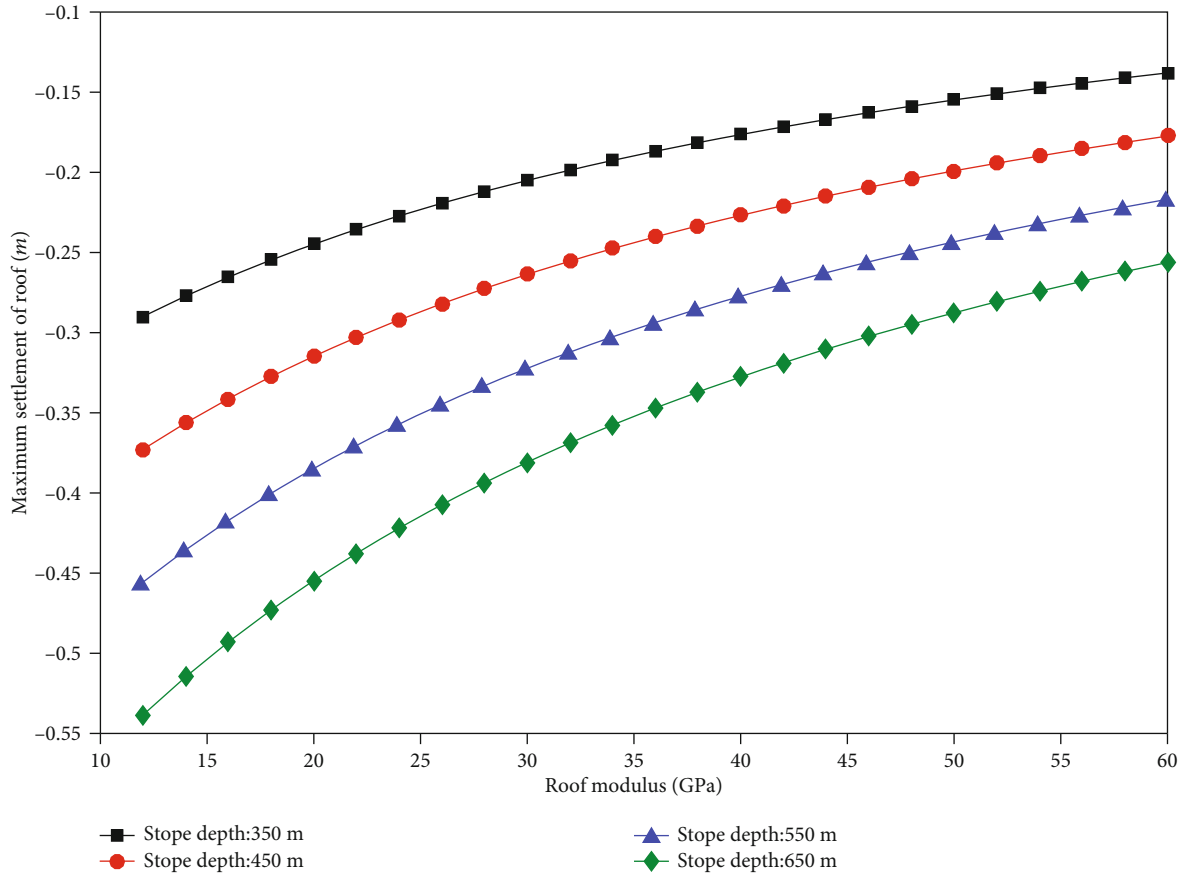


FIGURE 7: Influence of different elastic moduli of the roof rock on roof settlement.

The distribution of roof settlement under this parameter is shown in Figure 2.

In Figure 2, the X direction represents the advancing direction of the stope, and the Y direction represents the width of the panel area. It can be seen from the figure that the maximum settlement occurs at $x = 63$ m and $y = 30$ m. The maximum settlement is 23.3 cm. The roof boundary is limited by boundary conditions, so the displacement is zero. The following is to analyze the influence of different parameters on the roof settlement. It can be seen from the figure that the maximum roof settlement occurs in the middle of the stope. Therefore, based on the basic parameters, the influence of different factors on the maximum roof settlement is studied.

4.1. Foundation Coefficient. The foundation coefficient in the model is used to express the supporting force coefficient of the filling body to the roof after the panel is filled [13]. Different foundation coefficients represent different strength backfills. The variation curve of the maximum settlement of the roof with the foundation coefficient is shown in Figure 3.

The influence degree of different panel length to width ratios on the roof settlement curve is also different. When the ratio of length to width is 3 : 1, the influence of the foundation coefficient on settlement is small. When the length to width ratio is 1 : 1, the maximum settlement of roof is greatly affected by the foundation coefficient. The influence of the

foundation coefficient is larger in the initial stage and gradually slows down with the increase of the foundation coefficient.

4.2. Mining Depth. With different mining depths, the load on the roof is different, so the study of different mining depths on the roof settlement is of great significance for mine work. Under different elastic moduli of the roof, the curve of the maximum roof settlement with mining depth is shown in Figure 4.

According to the theory of in situ stress, the load on the roof is equal to the weight of the overburden, so the deeper the mining depth is, the greater the $q(x, y)$ is. It can be seen from the curve in the figure that the maximum roof settlement increases approximately linearly with the increase of depth, because the influence of lateral stress is not considered in the model. The influence of the roof elastic modulus on the maximum settlement of the roof shows that the smaller the elastic modulus is, the greater the growth rate of settlement is.

4.3. Aspect Ratio of Panel. The aspect ratio of the panel is an important parameter for mine design and evaluation of stope safety. In order to study its influence on roof settlement, the variation curves of the maximum roof settlement with panel width under different roof thicknesses are calculated, as shown in Figure 5.

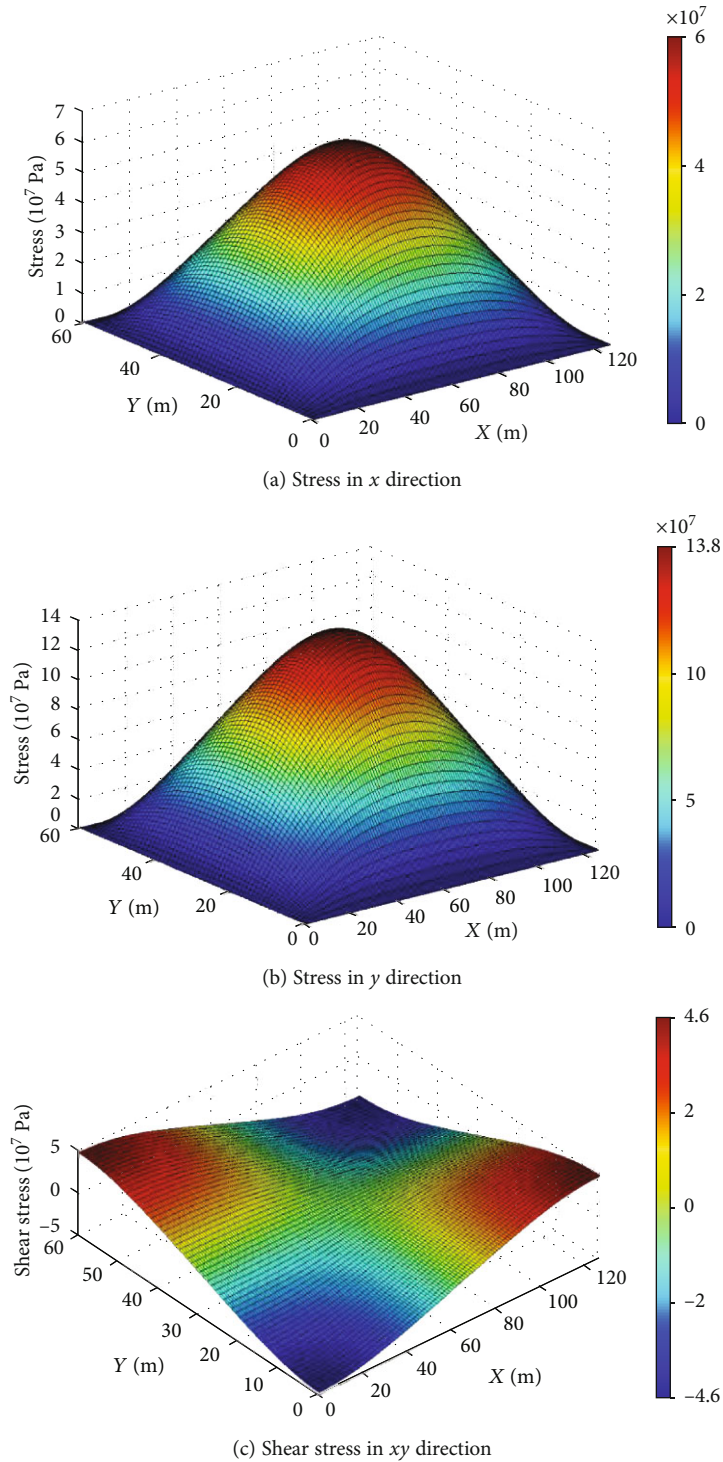


FIGURE 8: Stress diagram at $z = h/2$.

According to the mining design of the mine, the length of a panel is 126 m, so when the stope length is unchanged and the stope width increases from 10 m to 120 m, the variation curve of the maximum roof settlement under different roof thicknesses is obtained. It can be seen from the figure that the maximum roof settlement increases rapidly with the increase of the stope width. When the ratio of stope length to width decreases to 1.5:1, the increase slows down. Com-

paring the curves of different roof thicknesses, it can be seen that the greater the thickness is, the slower the maximum roof settlement increases with the increase of stope width.

4.4. Panel Roof Thickness. The thickness of the roof has an important impact on the safety of the stope. The thickness of the roof depends on the thickness of the direct roof of the panel [1]. Therefore, the parameters of the underground

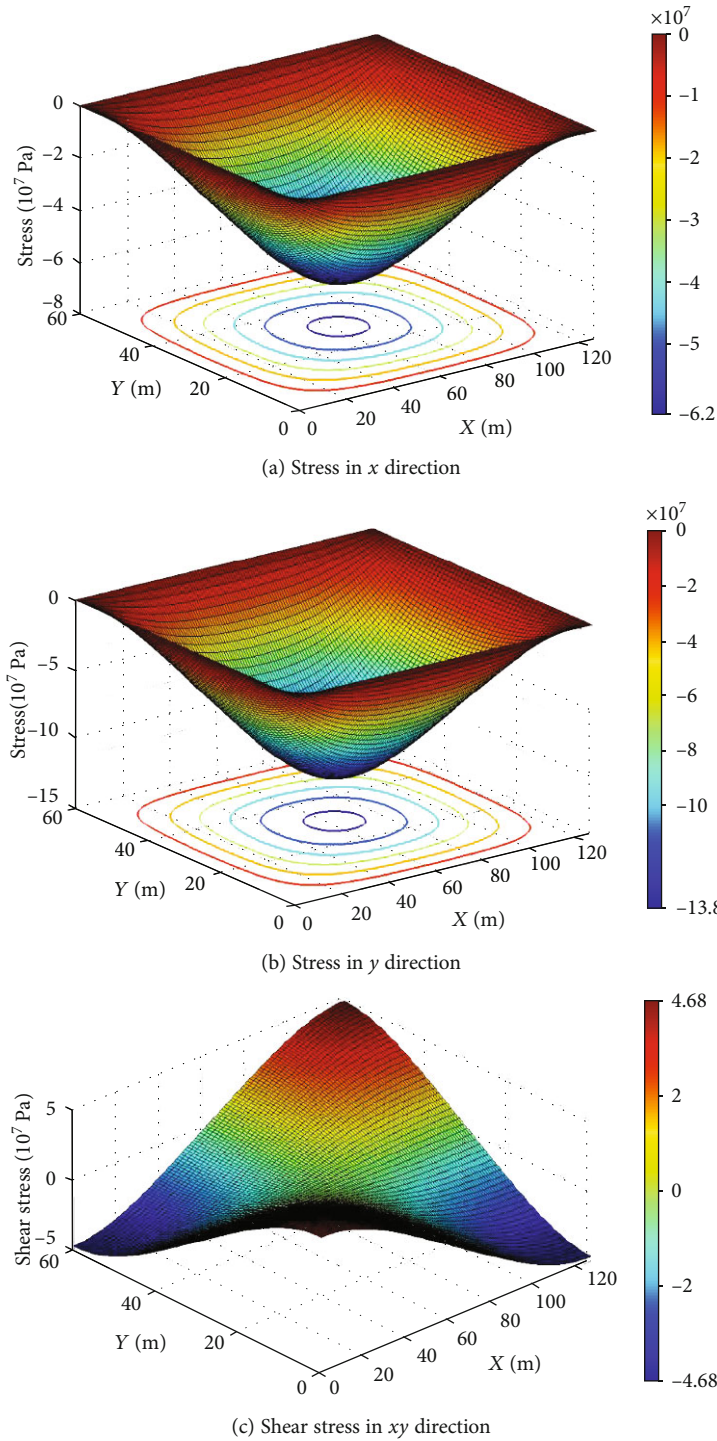


FIGURE 9: Stress diagram at $z = -h/2$.

stope can be understood according to the geological data to evaluate and predict the maximum settlement of the roof. In this model, when the roof thickness increases from 4 m to 20 m, the maximum settlement curve of the roof is shown in Figure 6.

It can be seen from the figure that the roof settlement decreases with the increase of the thickness of the roof and decreases rapidly in the initial stage. When the thickness increases to a certain value, the maximum settlement of the

roof does not decrease significantly [14]. When the foundation coefficient is 20 MPa/m, it can be seen that the roof thickness has a great influence on the maximum settlement [15]. Therefore, the foundation coefficient is a sensitive parameter when studying the relationship between the maximum settlement and the thickness of the roof.

4.5. Elastic Modulus of Roof Rock. The elastic modulus is an indicator of rock strength [16]. The curve of maximum roof

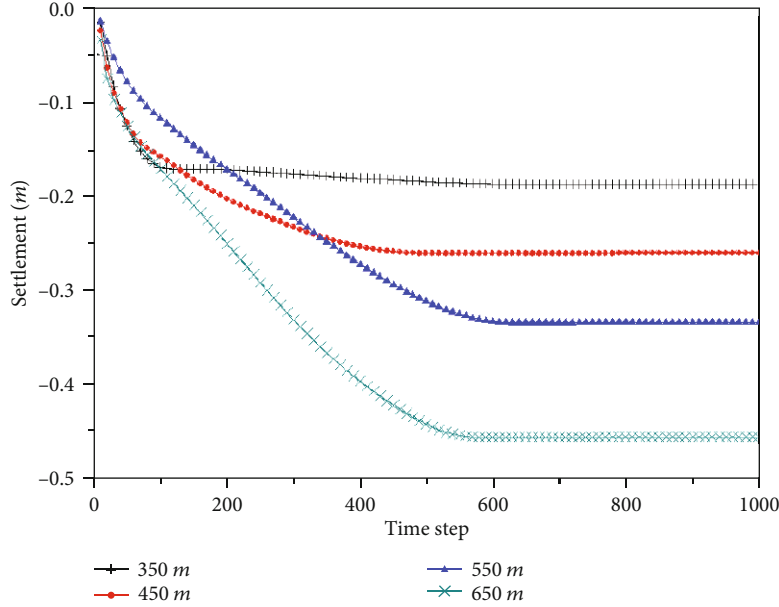


FIGURE 10: Maximum roof settlement displacement curve under different mining depths.

settlement is shown in Figure 7 when the elastic modulus increases from 12 GPa to 60 GPa.

It can be seen from the figure that the larger the elastic modulus is, the smaller the roof settlement is. When the elastic modulus increases linearly, the maximum roof settlement decreases nonlinearly. From the influence of different stope depths on settlement, we can see that the influence of stope depth is linear. In underground mining, due to different geological conditions, the elastic modulus of rock is different, so it is very important to understand the influence of the rock elastic modulus on the maximum roof settlement.

5. Stress Analysis

After analyzing the influencing factors of the roof settlement, the deflection formula can be substituted into the internal force formula to get the stress component and internal force of the roof [17]. According to the assumption of the model, the stress at $z = 0$ is 0, so the stress changes at different z will be analyzed below.

5.1. Stress at $z = h/2$. It can be seen from Table 1 that the thickness of the thin plate is 10 m, so when $z = 5$ m, it is the upper surface of the thin plate, and the plate is concave downward, so the stress in the upper part is compressive stress, and the stress in the lower part is tensile stress. According to the calculation, the stress distribution is shown in Figure 8.

The stress in x and y directions and shear stress in xy direction in the upper surface of the thin plate are, respectively, shown in Figures 8(a) and 8(b) showing that the maximum stress in the thin plate occurs in the middle of the plate, that is, the position of the maximum settlement. The maximum stress in the x direction is 60 MPa, while the maximum stress in the y direction is 138 MPa, because the model takes 126 m in the x direction and 60 m in the y direction. It

TABLE 2: Data comparison between the mathematical model calculation and numerical simulation results.

Influence factor	Parameter	Calculated value of the model (m)	Numerical simulation value (m)	Difference rate (%)
Mining depth	350 m	0.180	0.188	4.4
	450 m	0.233	0.261	12.0
	550 m	0.285	0.334	17.2
	660 m	0.337	0.456	35.3
Aspect ratio	3 : 1	0.100	0.127	27.0
	2 : 1	0.233	0.261	12.1
	1.5 : 1	0.310	0.289	-6.8
Roof thickness	1 : 1	0.370	0.317	-14.3
	5 m	0.378	0.296	-21.7
	8 m	0.296	0.280	-5.4
	10 m	0.233	0.261	12.0
Elastic modulus	12 m	0.177	0.240	35.6
	15 GPa	0.298	0.305	2.3
	30 GPa	0.233	0.261	12.0
	45 GPa	0.192	0.196	2.1
	60 GPa	0.160	0.145	-9.4

Note: difference rate = (simulation value - calculated value)/(calculated value) * 100%.

can be seen that the panel parameters have a great influence on the roof stress. According to the boundary conditions, the stress around the thin plate is 0.

Figure 8(c) shows the shear stress in the xy direction in the thin plate. It can be seen from the figure that the shear stress at the four vertices is the largest, reaching 46 MPa, while the shear stress at the most central position of the plate is 0. The shear stresses at two adjacent vertices are equal in magnitude and opposite in direction. Therefore, it can be

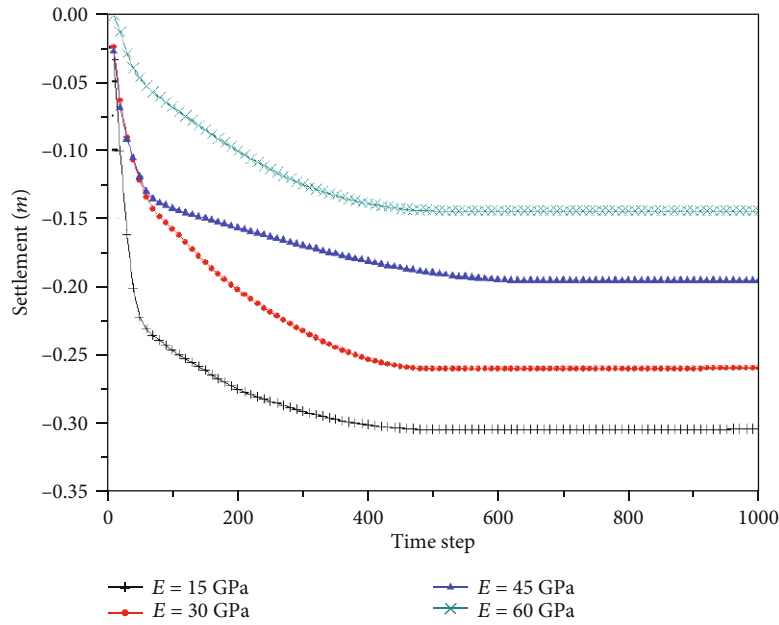


FIGURE 11: Maximum settlement displacement curve of roof under different elastic moduli of rock.

seen that the most dangerous part of the roof occurs in the center and four corners of the plate, which is prone to fracture and torsion.

5.2. *Stress at $z = -h/2$.* In the last section, the distribution of stress and shear stress on the upper surface of the roof is investigated. The symmetrical position of the surface is at $z = -h/2$, and the distribution of stress and shear stress is shown in Figure 9.

The three figures in Figure 9 show that the distribution of internal stress and shear stress is similar to that in Figure 8, but the directions are opposite. The stress in x and y directions is -62 MPa and -138 MPa, respectively. It means that the plate bears tensile stress. The magnitude and distribution of shear stress are the same, but the direction is opposite. The damage prone parts are also the center and four corners.

6. Study on Influencing Factors of Overburden Stability

Combined with the mechanical model of underground mining panel roof settlement established above, the numerical simulation method is used to study the influence of different mining depths, panel length to width ratios, roof thicknesses, and roof rock elastic moduli on roof settlement. The applicability of the settlement model can be verified by comparison [5].

6.1. Simulation Results of Influencing Factors of Maximum Roof Settlement

6.1.1. *Influence of Mining Depth on Maximum Displacement of Roof.* The deeper the mining depth is, the greater the pressure on the panel roof is, and the in situ stress increases correspondingly. Using the simulation method, the settlement curve of the maximum displacement of the panel roof with

the calculation step length under the mining depth of 350 m, 450 m, 550 m, and 650 m is simulated, as shown in Figure 10.

6.1.2. *Influence of Length to Width Ratio of Panel on Maximum Displacement of Roof.* In underground mining, the ratio of length to width determines the exposed area of the stope when the panel length is fixed [18]. The larger the exposed area, the worse the stability of stope. Therefore, in the mathematical model and numerical simulation, the length of the panel is set as 126 m, and the maximum displacement of the panel roof is simulated when the panel width is 40 m, 60 m, 80 m, and 120 m (length to width ratio is 3:1, 2:1, 1.5:1, and 1:1, respectively). For each stope width, the results are shown in Table 2.

6.1.3. *Influence of Panel Roof Thickness on Maximum Displacement of Roof.* The maximum displacement of the roof is simulated when the thickness of the roof is 5 m, 8 m, 10 m, and 12 m, respectively. The results are shown in Table 2.

6.1.4. *Influence of Elastic Modulus on Maximum Displacement of Roof.* The variation of roof displacement with time step is simulated when the elastic modulus of roof rock is 15 GPa, 30 GPa, 45 GPa, and 60 GPa, respectively. The curve of the maximum displacement point of the roof is shown in Figure 11.

6.2. *Comparative Analysis of Mathematical Model Calculation and Numerical Simulation Results.* It can be seen from Figure 11 that when the mining depth increases linearly, the increase of the maximum displacement of the panel roof is nonlinear. When the mining depth increases from 550 m to 650 m, the maximum displacement of the roof increases from 0.34 m to 0.46 m, with an increase of 35%. It can be seen that in the process of deep mining, the pressure

around the panel increases sharply, and the potential safety hazard also increases. As for the influence of the panel aspect ratio, it can be seen from Table 2 that the influence of the panel aspect ratio and roof thickness is as follows: with the increase of panel width, the exposed area of the panel increases, so the maximum displacement of the roof increases gradually; the greater the thickness of roof, the smaller the settlement.

Through the analysis and comparison of the calculation results of the mathematical model and the numerical simulation results, it can be seen from Table 2 that the influence law of the mining depth and other four factors on the maximum displacement of the panel roof is consistent. In order to verify the accuracy of the mathematical model, the difference between the two results is calculated, and the difference rate is shown in the table. It can be seen that most of the calculated results are within 15%, and only a few of them are 20%~30%. Generally speaking, the mathematical model can be used to calculate the settlement of the panel roof.

7. Conclusion

- (1) Based on the previous research and the theory of elastic-plastic mechanics, this paper analyzes the factors and laws of filling mining affecting overburden settlement. By establishing the mechanical model of panel roof settlement, the boundary conditions are given and solved by the Navier method; the deflection formula and internal force formula of panel roof settlement are obtained. After analysis, the settlement distribution map of the underground panel roof based on the thin plate model is obtained.
- (2) Based on the basic calculation parameters, the influence of different foundation coefficients, mining depths, panel length to width ratios, roof rock elastic moduli, and roof thicknesses on roof settlement is studied. According to the obtained deflection calculation formula, the expressions of internal force and stress are deduced, and the distribution of stress and shear stress on the upper and lower surface of the roof is analyzed. The dangerous area of the roof can be obtained, which provides a theoretical basis for the daily maintenance of mine safety.

Data Availability

All data used in this study can be obtained by contacting the corresponding author (Gang Huang) (email address: huanggang2016@whut.edu.cn).

Conflicts of Interest

The authors declare that they have no conflicts of interest.

Acknowledgments

The authors gratefully acknowledge the financial support by the National Nature Science Foundation of China under

Grant 51804235 and the National Key R&D Plan under Grant Nos. 2018YFC0808405 and 2018YFC0604401.

References

- [1] R. Zhang and S. P. Lu, "Kinematic analysis of shallow tunnel in layered strata considering joined effects of settlement and seepage," *Journal of Central South University*, vol. 25, no. 2, pp. 368–378, 2018.
- [2] Y. Wang, B. Zhang, B. Li, and C. H. Li, "A strain-based fatigue damage model for naturally fractured marble subjected to freeze-thaw and uniaxial cyclic loads," *International Journal of Damage Mechanics*, vol. 6, no. 5, pp. 12817–92136, 2021.
- [3] Z. Wang, Y. S. Luo, and S. H. Tang, "Mechanism and calculation method of rheological settlement of high-filled embankment," *Journal of Central South University of Technology*, vol. 15, no. S1, pp. 381–385, 2008.
- [4] Y. Zhou, J. Zuo, C. Hu, G. Liu, Y. Shi, and H. Liu, "Strata movement model of filling coal mining based on two-parameter elastic foundation," *Geotechnical and Geological Engineering*, vol. 38, no. 4, pp. 3631–3641, 2020.
- [5] C. Ma, H. Li, and P. Zhang, "Subsidence prediction method of solid backfilling mining with different filling ratios under thick unconsolidated layers," *Arabian Journal of Geosciences*, vol. 10, no. 23, p. 511, 2017.
- [6] X. Yang and C. B. Qin, "Limit analysis of supporting pressure in tunnels with regard to surface settlement," *Journal of Central South University*, vol. 22, no. 1, pp. 303–309, 2015.
- [7] K. Zhao, Q. Wang, S. Gu et al., "Mining scheme optimization and stope structural mechanic characteristics for a deep and large ore body," *JOM*, vol. 71, no. 11, pp. 4180–4190, 2019.
- [8] H. Zhao, F. Ma, Y. Zhang, and J. Guo, "Monitoring and mechanisms of ground deformation and ground fissures induced by cut-and-fill mining in the Jinchuan Mine 2, China," *Environmental Earth Sciences*, vol. 68, no. 7, pp. 1903–1911, 2013.
- [9] S. M. Dasaka, A. Jain, and Y. A. Kolekar, "Effect of uncertainties in the field load testing on the observed load-settlement response," *Indian Geotechnical Journal*, vol. 44, no. 3, pp. 294–304, 2014.
- [10] X. Deng, J. Zhang, B. Klein, B. de Wit, and J. Zhang, "Time-dependent lateral pressure of the filling barricade for roadway cemented backfill mining technology," *Mechanics of Time-Dependent Materials*, vol. 24, no. 1, pp. 41–58, 2020.
- [11] J. Guo, K. Ding, and Y. Jian, "Study on compaction characteristics of paste filling and its application," *Geotechnical and Geological Engineering*, vol. 37, no. 3, pp. 1185–1194, 2019.
- [12] M. Gao, Z. L. Zhang, Z. Q. Qiu, C. Xu, and J. Zhao, "The mechanism of hysteretic ground settlement caused by shield tunneling in mixed-face conditions," *Geomechanics and Geophysics for Geo-Energy and Geo-Resources*, vol. 4, no. 1, pp. 51–61, 2018.
- [13] R. Balin and K. E. Jansen, "Direct numerical simulation of a turbulent boundary layer over a bump with strong pressure gradients," *Journal of Fluid Mechanics*, vol. 918, no. 414, 2021.
- [14] X. Yang and R. Zhang, "Limit analysis of stability of twin shallow tunnels considering surface settlement," *KSCE Journal of Civil Engineering*, vol. 22, no. 5, pp. 1967–1977, 2018.
- [15] F. Wang, Q. Ren, B. Chen et al., "Numerical investigation on safe mining of residual pillar in goaf: a case study of Panlong Lead-zinc mine," *Geotechnical and Geological Engineering*, vol. 38, no. 4, pp. 4269–4287, 2020.

- [16] B. Yan, S. Che, D. D. Tannant, F. Ren, and P. Wang, "Application of double-yield model in numerical simulation of stability of mining filling body," *Arabian Journal of Geosciences*, vol. 12, no. 16, p. 515, 2019.
- [17] Y. Wang, Y. F. Yi, C. H. Li, and J. Q. Han, "Anisotropic fracture and energy characteristics of a Tibet marble exposed to multi-level constant-amplitude (MLCA) cyclic loads: a lab-scale testing," *Engineering Fracture Mechanics*, vol. 244, p. 107550, 2021.
- [18] X. Wu, X. W. Jiang, Y. F. Chen, H. Tian, and N. X. Xu, "The influences of mining subsidence on the ecological environment and public infrastructure: a case study at the Haolaigou Iron Ore Mine in Baotou, China," *Environmental Earth Sciences*, vol. 59, no. 4, pp. 803–810, 2009.

Research Article

Analysis of Laterally Loaded Piles in Undrained Clay Concave Slope

Chong Jiang , Xintai Li, Pan Liu, and Li Pang

School of Resources and Safety Engineering, Central South University, Changsha, 410083 Hunan, China

Correspondence should be addressed to Chong Jiang; jiang4107@sohu.com

Received 14 May 2021; Accepted 1 July 2021; Published 23 July 2021

Academic Editor: Yu Wang

Copyright © 2021 Chong Jiang et al. This is an open access article distributed under the Creative Commons Attribution License, which permits unrestricted use, distribution, and reproduction in any medium, provided the original work is properly cited.

A concave slope is a common type of slope. This paper proposes a simplified method to study the effect of a clay concave slope on laterally loaded piles. The hyperbolic p - y curve model is selected as the lateral pile-soil interaction model of the concave slope. Considering the two angles of the concave slope, the variation of the ultimate soil resistance with depth is divided into two parts, and the ultimate soil resistance varies nonlinearly with depth. The reduction factor method and normalization method are used to obtain the initial stiffness. The theoretical results will be compared with the calculation results of the 3D FE analysis to prove the rationality of this method. Finally, the simplified method is used to analyze the response of laterally loaded piles under different parameters.

1. Introduction

Pile foundation is one of the most commonly used foundations in bridge engineering, offshore drillings, and offshore wind turbines. These pile foundations are often used on sloping ground, such as river valleys and the seabed [1, 2]. The pile foundation will be subjected to lateral loads caused by traffic loads, lateral wind, and waves.

The bearing capacity of pile foundations depends on the bearing capacity of the rock and soil around the pile. There are three main approaches to study the bearing capacity of rock and soil around the pile: theoretical methods [3, 4], numerical simulations [5], and experimental methods [6]. In the past few decades, the p - y curve method is often used to study the response of pile foundation bearing lateral load. The main research includes the influence of laterally loaded piles in flat ground and sloping ground. For the flat grounds, many scholars and institutions proposed p - y curves for different types of soil [7–9]. For the sloping ground, the soil in front of the pile is weakened, and the damage model of soil is different from that in the horizontal ground [10–12]. Therefore, Reese et al. [13] proposed p - y curves that were suitable for sand and clay sloping ground, respectively. Based

on the 3D FE analysis, Georgiadis and Georgiadis [14, 15] obtained the p - y curves suitable for clay sloping ground. On this basis, the p - y curves of clay sloping ground were proposed, which considered the distance between the slope and pile. But all the p - y methods mentioned above only considered level ground and single-angle slope.

However, due to the influence of external factors such as rain erosion and soil accumulation, the slope has more than two angles. Wu et al. [16] and Fan et al. [17] pointed out that slope shapes could be roughly divided into four types, which were the straight type with a single angle, the convex type (the upper slope angle is smaller than the lower slope angle), the concave type (the upper slope angle is greater than the lower slope angle), and a mixed type.

The p - y method is widely used in engineering because of its simple calculation and short calculation time. However, compared to a slope with a single angle, the distribution law of the concave slope's ultimate soil resistance and initial stiffness will change. But unfortunately, the existing p - y curves of sloping ground can only consider the change law of ultimate soil resistance and initial stiffness under a single angle. It leads to errors in the analysis of the horizontal bearing characteristics of piles using the existing p - y curve.

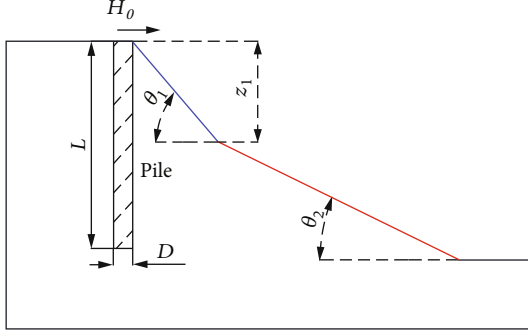


FIGURE 1: Analysis model of a laterally loaded pile on a concave slope. Here, L is the length of the pile embedded in the soil, D is the pile diameter, H_0 is the lateral load on the pile head, θ_1 is the upper slope angle, θ_2 is the lower slope angle, and Z_1 is the upper slope height.

Therefore, it is necessary to carry out further research on the lateral load characteristics and calculation methods of concave slope piles.

This paper focuses on giving a nonlinear analysis method considering the bearing characteristics of the laterally loaded pile in concave sloping ground. In this method, the pile-soil interaction model adopts the hyperbolic p - y curve model. And the calculation formula of the ultimate soil resistance and the initial stiffness varying with depth in the concave slope is given. Then, the derived p - y curve is brought into MATLAB for a differential calculation to obtain the nonlinear response of the pile under a lateral load. To prove the correctness, the method is verified by the results of three-dimensional finite element analysis considering the concave clay slope. Furthermore, this article discusses the influence of the different slope angles and upper slope height and obtains the response law of piles under the influence of different parameters.

2. Establish a p - y Curve of Clay Concave Slope

At present, the p - y curve method, which regards soil as a nonlinear spring, is widely used to study the lateral load response of the horizontal ground piles. There are many kinds of mathematical models of the p - y curve. One of the most widely used is the hyperbolic p - y curve [18–21]. The expression is shown as follows:

$$p = \frac{y}{(1/k_i) + (y/p_u)}, \quad (1)$$

where p_u = ultimate soil resistance of the soil along the pile, K_i = initial stiffness of the foundation.

Yang [22] compared different types of p - y curves and concluded that the hyperbolic p - y curve has the best fitting effect with the data obtained from field experiments. Therefore, this article adopts a hyperbolic p - y curve.

2.1. Basic Assumption. To analyze the influence of the concave slope which has two angles on the horizontal bearing

characteristics of the pile, an analysis model is established, as shown in Figure 1.

For simplicity, the following assumptions are made:

- (1) The slope is stable without a sliding surface, and slope failure and instability are not considered in the calculation
- (2) The soil resistance along the pile changes nonlinearly with the increase in lateral displacement. When the ultimate soil resistance is achieved, its value remains constant as the increase in lateral displacement
- (3) This article only considers concave slopes, the upper slope angle is larger than the lower slope angle, $\theta_1 > \theta_2$

2.2. Ultimate Soil Resistance of Concave Slope Varying with Depth. For the ultimate soil resistance p_u , its expression is as follows:

$$p_u = N_p c_u D, \quad (2)$$

where N_p is the ultimate soil-resistance-bearing factor, c_u is the undrained shear strength of soil, D is the pile diameter.

Equation (3) shows that the value of N_p changes nonlinearly with the increase in depth [14]. The initial value of N_p is $N_{p0} \cos(\theta)$ at the ground surface, and the maximum value is N_{pu} :

$$N_p = N_{pu} - (N_{pu} - N_{p0} \cos(\theta)) e^{((-\lambda(z/D))/(1+\tan(\theta)))}. \quad (3)$$

The value of N_{p0} , N_{pu} , and λ are related to the adhesion factor α of the pile-soil interface [23, 24].

The adhesion factor α is the ratio of the interface shear strength to the undrained shear strength of the soil. In this article, α can be obtained from Figure 2 [14].

When $0 \leq c_u < 25$, we have

$$\alpha = 1. \quad (4)$$

When $25 \leq c_u < 80$, we have

$$\alpha = \frac{14}{11} - \frac{3}{275} c_u. \quad (5)$$

When $80 \leq c_u < 200$, we have

$$\alpha = 0.5 - \frac{1}{800} c_u. \quad (6)$$

λ is a dimensionless parameter that changes with the adhesion factor. For smooth piles, λ is 0.55 ($\alpha = 0$); for rough piles, λ is 0.4 ($\alpha = 1$):

$$\lambda = 0.55 - 0.15\alpha. \quad (7)$$

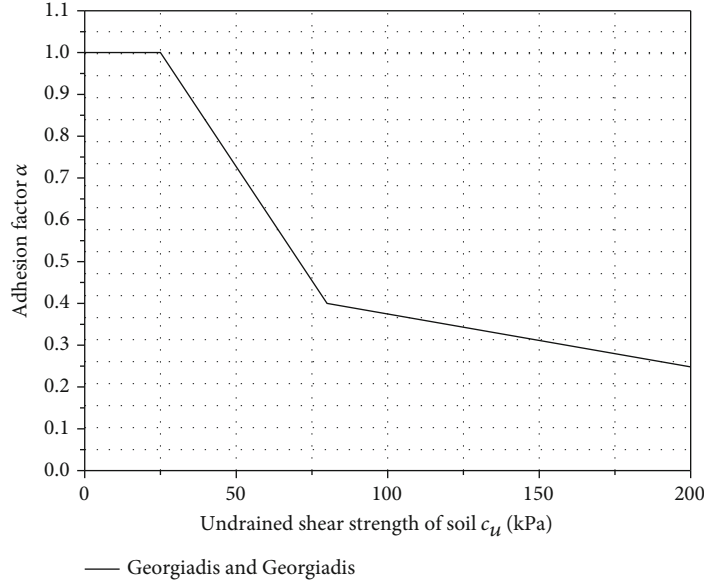


FIGURE 2: The relationship between α and c_u .

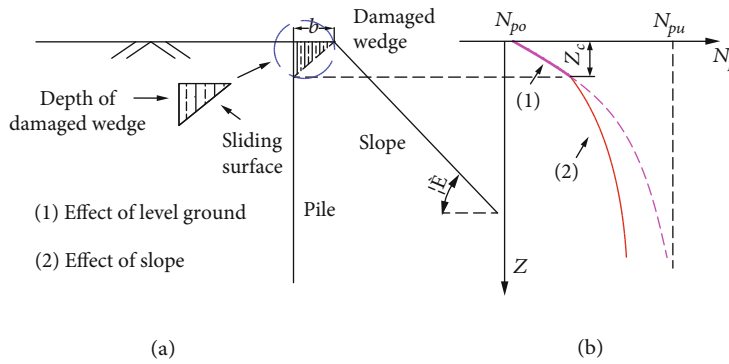


FIGURE 3: Ultimate soil resistance analytical model with the distance of piles from the crest of the slope. (a) Damaged wedge model of the laterally loaded piles. (b) The N_p curve varying with the depth.

N_{po} is the ultimate soil-resistance-bearing factor at the ground surface:

$$N_{po} = 2 + 1.5\alpha. \quad (8)$$

N_{pu} is the ultimate soil-resistance-bearing factor based on the deep soil flow failure model by Randolph and Houlsby [25]:

$$N_{pu} = \pi + 2\Delta + 2 \cos \Delta + 4 \left(\cos \frac{\Delta}{2} + \sin \frac{\Delta}{2} \right), \quad (9)$$

where $\Delta = \sin^{-1}\alpha$.

To obtain the ultimate soil resistance along the pile in concave sloping ground, the ultimate soil-resistance-bearing factor N_p is the key.

Jiang et al. [26] found that with the increase in the lateral displacement of the pile in sloping ground, the stress and strain of the soil show a wedge-shaped distribution in the

three-dimensional numerical simulation. Similarly, Georgiadis and Georgiadis [15] found the same rule when studying the influence of the distance between the pile and slope on laterally loaded piles, as shown in Figure 3.

It shows in Figure 3(a) that when the pile head deflection is small, the soil has a damaged wedge in a shallow soil. The sliding surface of the damaged wedge only intersects with the level ground. Therefore, the slope will not affect the ultimate soil resistance near the mudline. As the pile head deflection augments, the depth of the damaged wedge increases. When the depth of the damaged wedge reaches Z_c , the sliding surface of the wedge spreads to the slope. As shown in Figure 3(b), when the depth of the damaged wedge is less than Z_c , the expression of the ultimate soil-resistance-bearing factor N_p is the same as that of the flat ground since the pile is only affected by the level ground. When the sliding surface of the damaged wedge intersects with the slope surface, the ultimate soil resistance along the pile is weakened compared to the level ground. The expression of N_p needs to consider the influence of the slope.

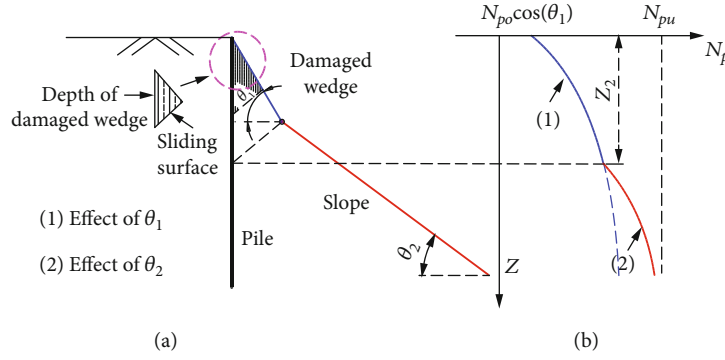


FIGURE 4: Ultimate soil resistance analytical model of the concave sloping ground. (a) Damaged wedge model of laterally loaded piles on the concave slope. (b) The N_p curve along the pile on concave slope.

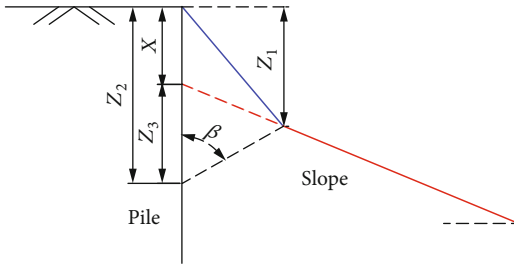


FIGURE 5: The definition of height difference X .

Georgiadis and Georgiadis [15] believed that the depth of the damaged wedge would change with the increase of lateral load, and it had a nonlinear relationship with the distance of pile from the crest of the slope. When the sliding surface intersects with the slope crest, the critical depth Z_c is expressed as follows:

$$\frac{Z_c}{D} = 8.5 - 10 \log_{10} \frac{(8 - b)}{D}, \quad (10)$$

where b indicates the distance from the pile core to the crest of the slope. When $b = 0.5D$, the pile is at the crest of the slope.

For concave slopes, this article will use the same method to get the expression of N_p , as shown in Figure 4.

Figure 4(a) shows that the sliding surface of the damaged wedge intersects the slope with the angle of θ_1 when $0 \leq Z < Z_2$, and the ultimate soil resistance is only affected by the upper slope. When the depth reaches Z_2 , the sliding surface of the wedge intersects with the intersection of the upper slope and lower slope. When the depth is greater than Z_2 , the sliding surface intersects the slope with the angle of θ_2 , and the lower slope begins to affect the ultimate soil resistance. It is pointed out in Figure 4(b) the changing law of N_p in the concave slope with two angles. The expression of N_p is only controlled by θ_1 when the depth of the damaged wedge is less than Z_2 . When the depth is greater than Z_2 , the expression of N_p is affected by θ_2 . It is reasonable that the value of N_p increases at Z_2 relative to that of the single-angle slope (θ_1) because the lower slope increases

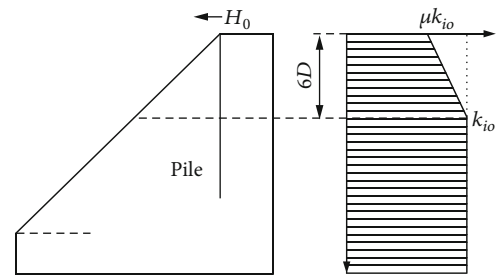


FIGURE 6: Initial stiffness model of slope foundation.

the volume of soil in front of the pile. To determine the critical depth Z_2 , this paper adopts the modified critical depth expression:

$$Z_2 = \left[8.5 - 10 \log_{10} \left(8 - \frac{(Z_1/\tan(\theta_1)) + 0.5D}{D} \right) \right] D + Z_1. \quad (11)$$

Because the slope is a homogeneous medium, the expression of the ultimate soil resistance is continuous and derivable when the depth increases, and there will be no sudden change point. Therefore, when the depth reaches the critical depth (Z_2), the piecewise function of N_p should be the same value $N_p(Z_2)$, as shown in Figure 4(b). When the value of N_p is $N_p(Z_2)$, the corresponding depths are Z_2 for the slope with angle θ_1 and Z_3 for the slope with angle θ_2 . And the difference between Z_2 and Z_3 is defined as X , as shown in Figure 5.

When the depth is less than Z_2 , the expression of N_{p1} is as follows:

$$N_{p1} = N_{pu} - (N_{pu} - N_{po} \cos(\theta_1)) e^{((-\lambda(z/D))/(1+\tan(\theta_1)))}. \quad (12)$$

When the depth is greater than Z_2 , the expression of N_{p2} is as follows:

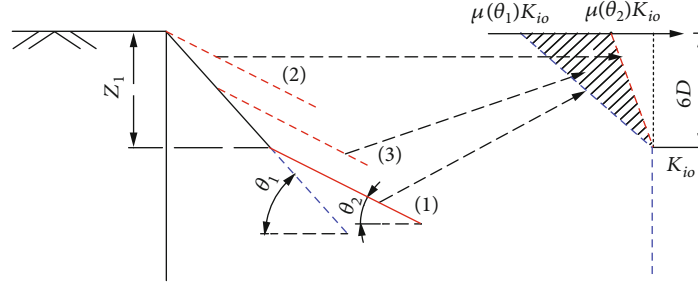


FIGURE 7: Initial stiffness model of concave sloping ground. (a) The concave sloping ground under 3 cases. (b) The value of initial stiffness under 3 cases.

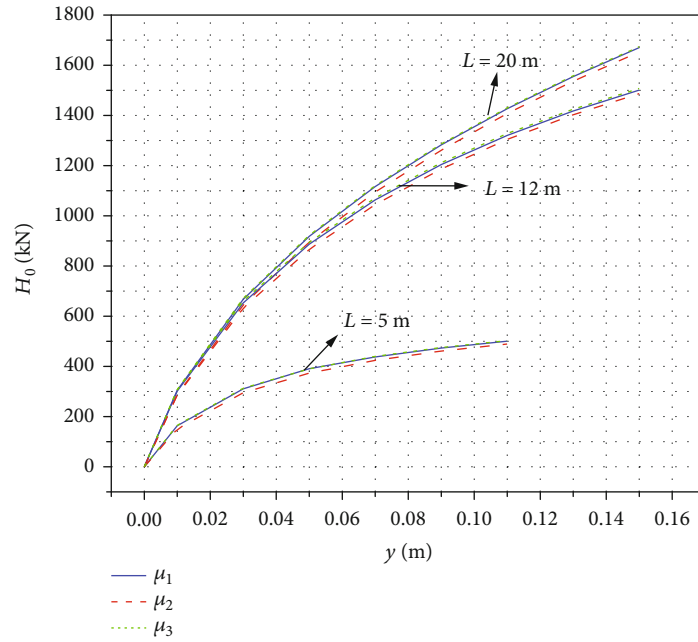


FIGURE 8: Effect of initial stiffness reduction factor on pile head deflection.

$$\begin{aligned}
 N_{p2} &= N_{pu} - (N_{pu} - N_{po} \cos(\theta_2)) e^{((-\lambda(Z-x))/D)/(1+\tan(\theta_2))}, \\
 N_p(Z_2) &= N_{pu} - (N_{pu} - N_{po} \cos(\theta_1)) e^{((-\lambda Z_2)/D)/(1+\tan(\theta_1))}, \\
 Z_3 &= \ln \left[\frac{N_{pu} - N_p(Z_2)}{N_{pu} - N_{po} \cos(\theta_2)} \right] \frac{D(1 + \tan(\theta_2))}{-\lambda}, \\
 X &= Z_2 - Z_3.
 \end{aligned} \tag{13}$$

2.3. Initial Stiffness of Concave Slope Varying with Depth. Carter [27] proposed the expression of the initial stiffness \$K_{io}\$ of the clay level ground, and believed that the initial stiffness is related to the initial elastic modulus of the soil, Poisson's ratio, and other factors:

$$K_{io} = \frac{1.0E_i D}{(1 - \nu_s^2) D_{ref}} \left(\frac{E_i D^4}{E_p I_p} \right)^{1/12}, \tag{14}$$

where \$D\$ is the pile diameter; \$D_{ref}\$ is the pile diameter reduction factor, usually taken as 1; \$E_p I_p\$ is the bending stiffness of the pile; \$\nu_s\$ is the Poisson's ratio of the soil; \$E_i\$ is the initial elastic modulus of the soil.

Kondner and Robertson et al. [28, 29] proposed the equation of elasticity modulus \$E_{50}\$ and believed that the initial elastic modulus \$E_i\$ can be related to the elasticity modulus at fifty percent of the failure stress \$E_{50}\$:

$$E_{50} = E_i \left(1 - \frac{R_f \sigma}{\sigma_f} \right), \tag{15}$$

where \$\sigma\$ is deviatoric stress; \$E_{50}\$ is elasticity modulus; \$\sigma_f\$ is deviatoric failure stress; \$R_f\$ is the ratio of deviatoric failure stress over deviatoric ultimate stress, usually taken equal to 0.8.

Setting \$R_f = 0.8\$, \$\sigma/\sigma_f = 0.5\$, and \$\nu_s = 0.5\$, equation (14) becomes

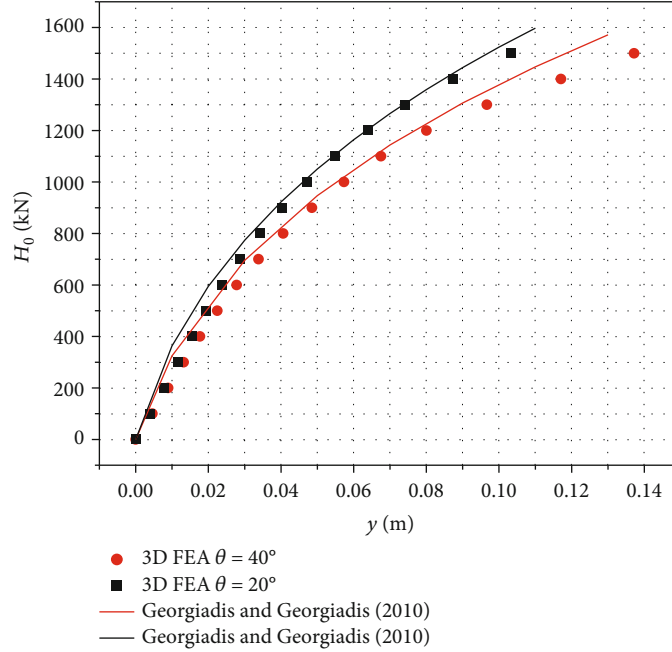


FIGURE 9: Deflection curve of pile head for comparison.

TABLE 1: Summary of three-dimensional numerical analysis conditions.

	L (m)	D (m)	θ_1	θ_2	Z_1 (m)
Case 1	20	1	40°	0°	1, 3
Case 2	20	1	$50^\circ, 40^\circ$	30°	2
Case 3	12	1	40°	30°	1
			45°	30°	2

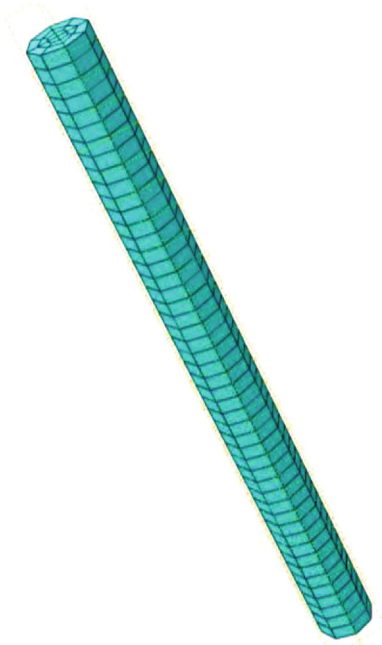


FIGURE 10: Three-dimensional model of the pile.

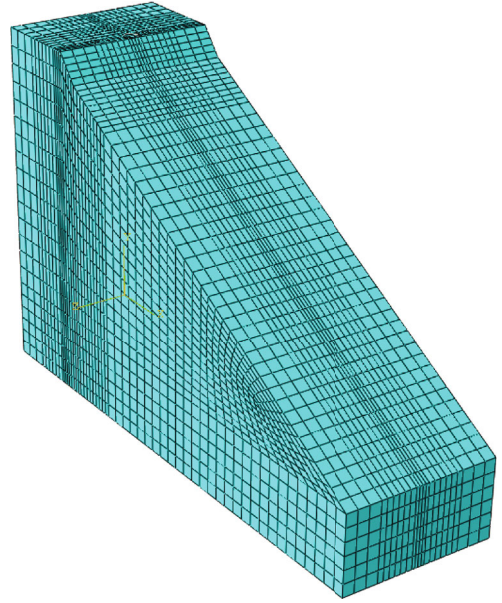


FIGURE 11: Three-dimensional model of concave slope.

$$K_{io} = 2.3DE_{50} \left(\frac{E_{50}D^4}{E_p I_p} \right)^{1/12}. \quad (16)$$

Equation (16) reveals that the initial stiffness of the foundation is only related to the characteristics of the soil and the pile. The normalization method is commonly used to obtain the initial stiffness expression of the sloping ground. On the basis of the initial stiffness expression of the level ground, many scholars adopt the reduction factor μ to establish the initial stiffness expression of the sloping ground [14, 30]:

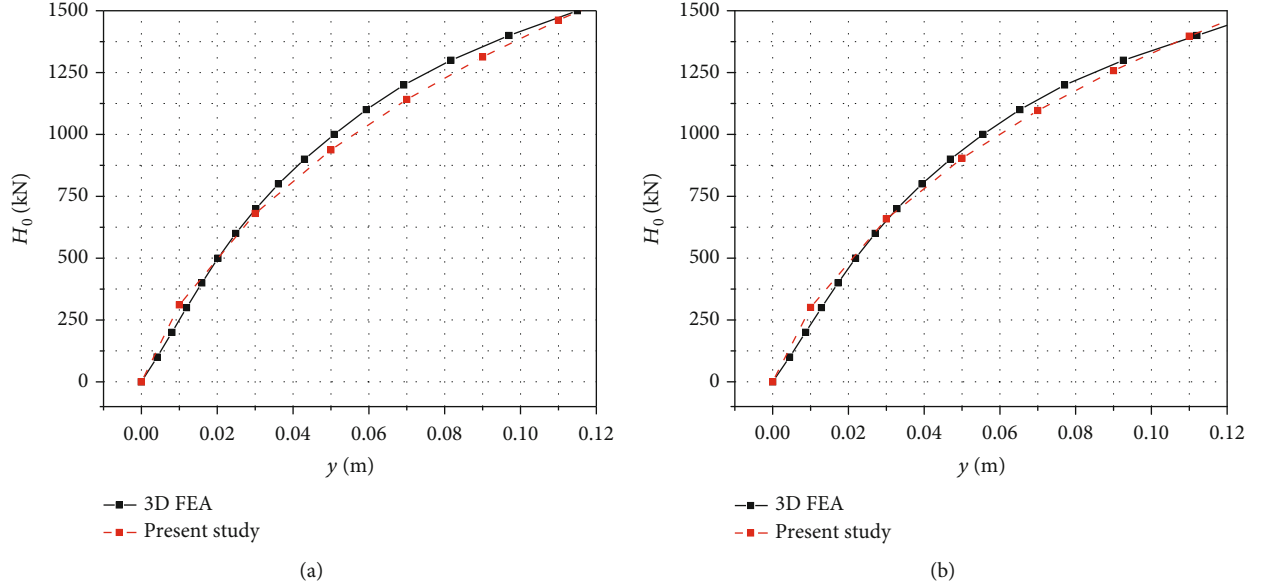


FIGURE 12: Load and displacement curve of pile head predicted for Case 2. (a) Considering $Z_1 = 1$ m. (b) Considering $Z_1 = 3$ m.

$$\mu = \frac{K_i}{K_{io}} \leq 1, \quad (17)$$

where K_i is the initial stiffness of the sloping ground; K_{io} is the initial stiffness of the level ground.

When studying the influence of the initial stiffness of the sloping ground, Georgiadis and Georgiadis [14] proposed that the initial stiffness reduction factor is related to the depth of the slope, as shown in equation (18). The reduction factor μ changes linearly with the increase of depth, as shown in Figure 6. For slopes at an arbitrary angle, when the depth Z is less than $6D$, the slope weakens the initial stiffness, and the degree of weakening decreases when the depth becomes greater. When the depth is greater than $6D$, the initial stiffness of the sloping ground is the same as that in level ground, and remains constant with the increase of depth:

$$\mu = \cos(\theta) + \frac{Z}{6D}(1 - \cos(\theta)). \quad (18)$$

As shown in Figure 7, for a concave slope, when the value of Z_1 exceeds $6D$ (red line (1) in Figure 7(a)), the initial stiffness of the concave sloping ground at Z_1 reaches the value of that in level ground. The lower slope does not affect the initial stiffness, and the reduction factor μ is only controlled by the upper slope (blue line in Figure 7(b)). When Z_1 is 0, the concave slope becomes a single-angle slope with θ_2 (red line (2) in Figure 7(a)). The reduction factor μ is controlled by the slope with angle θ_2 (red line in Figure 7(b)). When Z_1 ranges from 0 to $6D$ (red line (3) in Figure 7(a)), the reduction factor μ varies with depth in the range between the two limit conditions (shaded part in Figure 7(b)). Georgiadis and Georgiadis [14] point out that the reduction factor has a small effect on both pile head deflection and maximum bending moment. This paper assumes that the initial value of the reduction

factor changes uniformly from $\mu(\theta_2)$ to $\mu(\theta_1)$ as Z_1 increases from 0 to $6D$.

When $0 < Z_1 < 6D$, we have

$$\begin{aligned} \mu_1 &= u_1 + \frac{Z}{6D}(1 - u_1), \\ u_1 &= \cos(\theta_1) + (\cos(\theta_2) - \cos(\theta_1)) \frac{6D - Z_1}{6D}. \end{aligned} \quad (19)$$

When $Z_1 \geq 6D$, we have

$$\mu_1 = \cos(\theta_1) + \frac{Z}{6D}(1 - \cos(\theta_1)). \quad (20)$$

And the initial stiffness of concave sloping foundation $K_{i\theta}$ can be expressed as follows:

$$K_{i\theta} = \mu_1 K_{io}. \quad (21)$$

To verify the rationality of the above assumptions, three cases of reduction factors μ are used to obtain the pile head load-displacement curve. μ_1 is calculated by the method in this paper, μ_2 is obtained by the calculation method considering the single-angle slope with angle θ_1 , and μ_3 is obtained from the calculation method considering the single-angle slope with angle θ_2 . Undrained shear strength $c_u = 70$ kPa, and elastic modulus of soil E_{50} is 14 MPa. Pile diameter $D = 1$ m; pile length $L = 5$ m, 12 m, and 20 m; and elastic modulus of piles $E_p = 2.9 \times 10^7$ kPa. $\theta_1 = 40^\circ$; $\theta_2 = 20^\circ$; and upper slope height $Z_1 = 1$ m. The load-displacement curve of the pile head under different conditions is shown in Figure 8. It indicates that the load-displacement curve of the pile head is almost unchanged even if μ is taken as two limit conditions (μ_2, μ_3). For the pile length $L = 5$ m, the maximum discrepancies are only 16%. The above simplifying method is sufficient for determining the reduction factor.

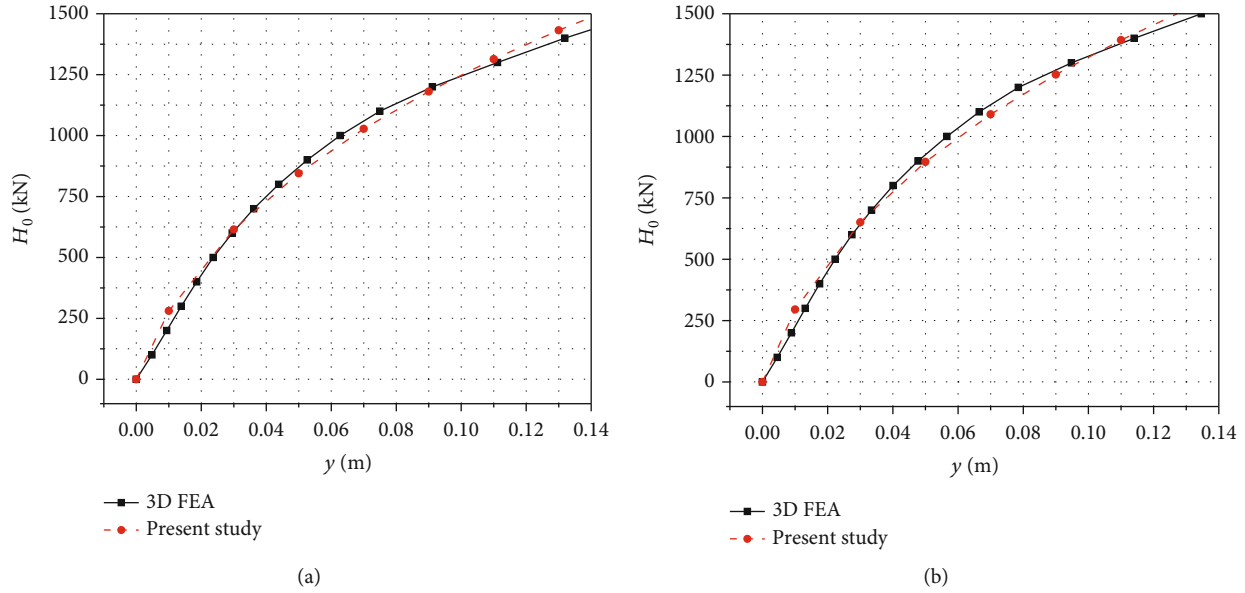


FIGURE 13: Load and displacement curve of pile head predicted for Case 2. (a) Considering $\theta_1 = 50^\circ$. (b) Considering $\theta_1 = 40^\circ$.

3. Approach Verification

A series of three-dimensional finite element analysis models of the laterally loaded pile in a concave slope is established to verify the correctness of the calculation method in this paper.

3.1. Establishment and Verification of 3D FEA Model. All the basic parameters of the 3D finite element analysis model in this paper are obtained from the literature [5, 14]. The basic parameters of the pile are set as follows: pile length $L = 20$ m; diameter $D = 1$ m; elastic modulus of pile $E_p = 2.9 \times 10^7$ kPa; Poisson's ratio of pile ν_p is 0.1; and the density of pile ρ_l is 2500 kg/m^3 . Piles are all embedded in the soil, the load is applied at the pile head, and the pile head is free. Slope angles are 20° and 40° . The undrained shear strength of the soil c_u is 70 kPa, elastic modulus of the soil at 50% ultimate stress E_{50} is 14 MPa, Poisson's ratio of soil ν_s is 0.49, and bulk unit weight γ_s is 18 kN/m^3 . C3D8R grids are used for piles and soil. In addition, there is more detailed meshing around the pile. The number of meshes in all models is approximately 25,000. The bottom boundary of the model is fixed in all directions, and the other boundaries, except for the top boundary, are only fixed in the normal direction. The soil is established based on the Mohr-Coulomb model. The contact surface between pile and soil adopts normal behavior and tangential behavior. Normal behavior is set as a "hard" contact mode, and tangential behavior is set as "penalty" function. The "penalty" factor of the pile side is 0.5, and that between pile tip and pile-tip soil is considered to approach 1 for the slender pile, and assumed to be 0.5 for rigid pile. The friction angle is taken as a smaller value. In this paper, the friction angle is taken as 10° and the results obtained from the 3D FEA model for different working conditions are fitted to the data from Georgiadis and Georgiadis, as shown in Figure 9. In general, the fitting is well for any working conditions, proving that the model-

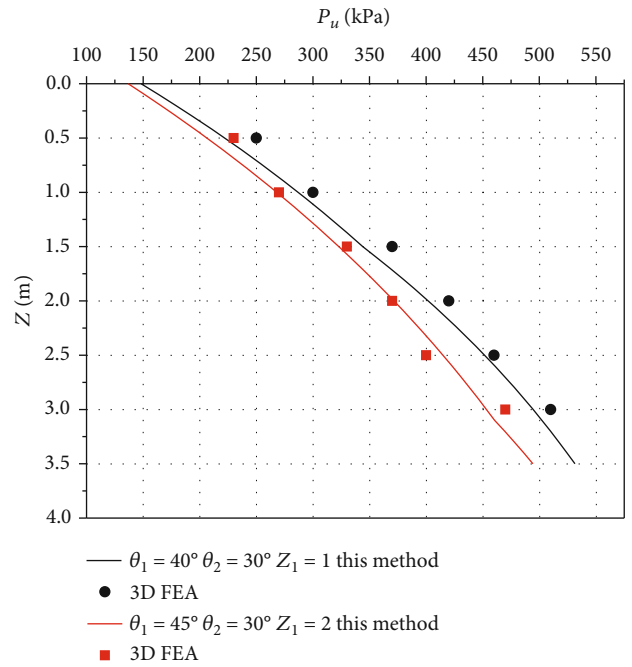


FIGURE 14: Curve of ultimate soil resistance versus depth.

ing method and the selection of parameters in this paper are reasonable and correct.

3.2. Verification of the Calculation Method. In this section, the proposed method is validated by comparing the load-displacement curve of the pile head and the ultimate soil resistance with the 3D FE analysis results of three cases, respectively. The three cases are shown in Table 1. The modeling method and correlation parameters are the same as those in Section 3.1. Figures 10 and 11 show the pile and soil three-dimensional model of case 2 ($\theta_1 = 50^\circ$; $\theta_2 = 30^\circ$; and $Z_1 = 2$ m).

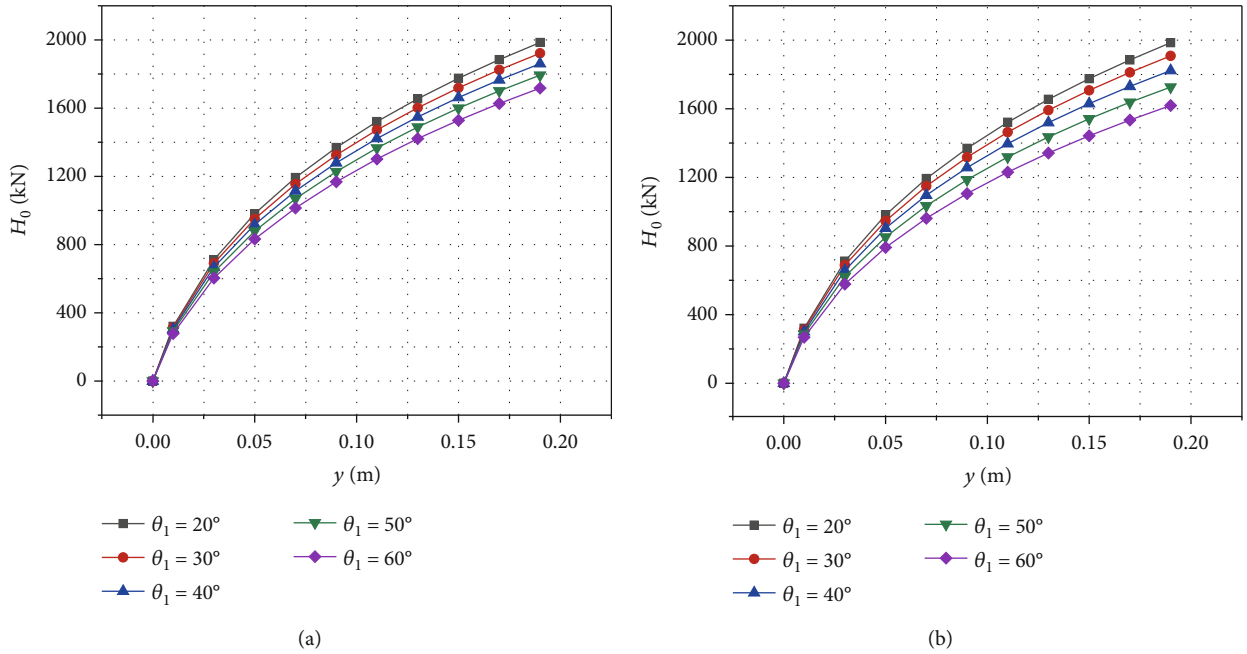


FIGURE 15: Load and displacement curve of pile head under the effect of θ_1 . (a) Considering $Z_1 = 1$ m. (b) Considering $Z_1 = 2$ m.

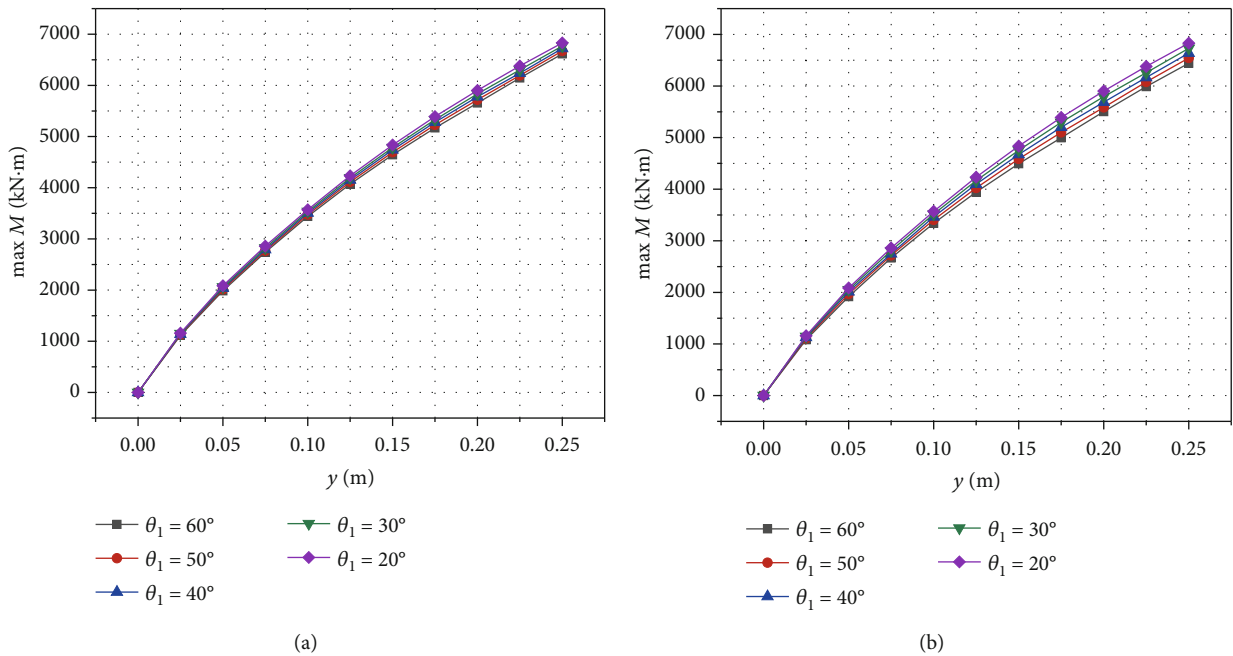


FIGURE 16: Effect of θ_1 on maximum bending moment. (a) Considering $Z_1 = 1$ m. (b) Considering $Z_1 = 2$ m.

Case 1 considers two upper slope heights ($Z_1 = 1$ m, 3 m) as variates under the same slope angle ($\theta_1 = 40^\circ$; $\theta_2 = 0^\circ$). The pile head displacement of Case 1 is shown in Figure 12. The theoretical calculation has a good agreement with the result of the 3D FE analysis. And Figure 13 shows the load-displacement curve of the pile head of Case 2. In Case 2, two upper slope angles ($\theta_1 = 50^\circ$, $\theta_1 = 40^\circ$), one lower slope angle ($\theta_2 = 30^\circ$), and one upper slope height ($Z_1 = 2$ m) are considered. The verification result is good.

Case 3 carries out a verification between the theoretical ultimate soil resistance and the results of 3D FE analysis under different angles and heights. A higher degree polynomial is used to accurately fit the shearing force curve of the pile which is obtained from the three-dimensional model [26, 31]. The curve of soil resistance p versus pile depth Z under different lateral load H_0 is obtained by differentiating the fitted shearing force curve of the pile. Through combining $p - Z$ curves and the pile displacement curves under

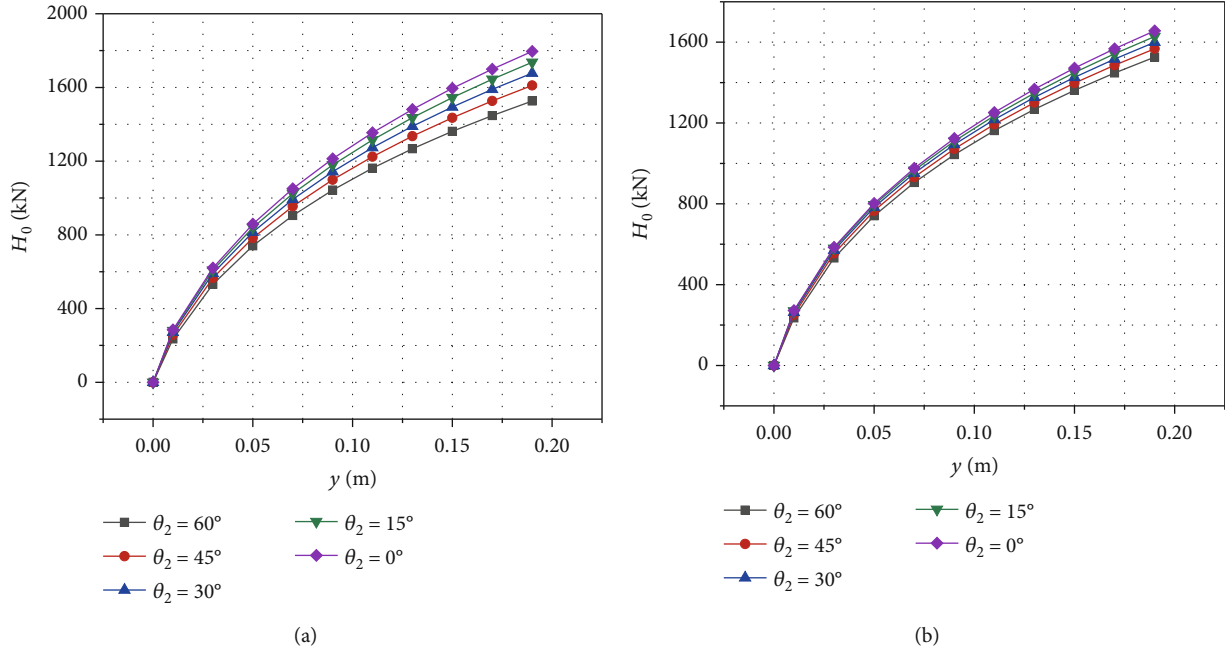


FIGURE 17: Effect of θ_2 on the load-displacement curve of pile head. (a) Considering $Z_1 = 1$ m. (b) Considering $Z_1 = 2$ m.

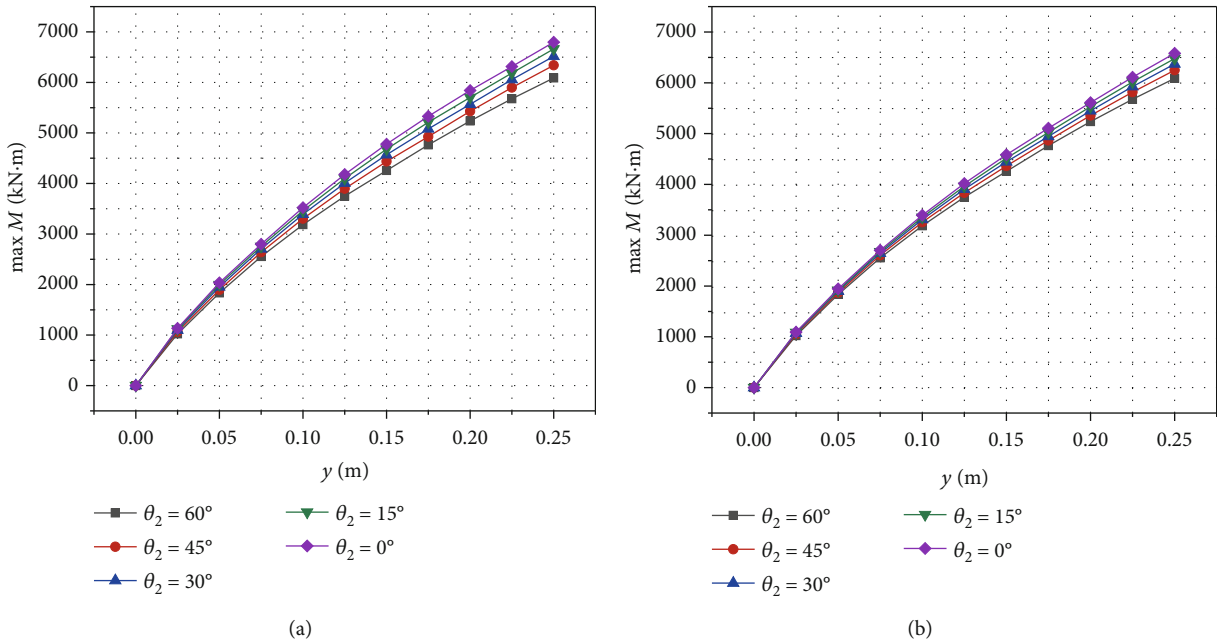


FIGURE 18: Effect of θ_2 on maximum bending moment. (a) Considering $Z_1 = 1$ m. (b) Considering $Z_1 = 2$ m.

different lateral loads H_0 , the ultimate soil resistance of each point of the pile is obtained. The verification result is displayed in Figure 14. The theoretical result is in good agreement with the data of 3D FE analysis.

4. Parameter Analysis

4.1. *The Effect of Upper Slope Angle θ_1 .* In this section, the effect of θ_1 on the pile under lateral load is discussed for the case of $\theta_2 = 20^\circ$, and the height of upper slope $Z_1 = 1$ m and

2 m by selecting 5 values of $\theta_1 = 60^\circ, 50^\circ, 40^\circ, 30^\circ, 20^\circ$ as variables. And calculation parameters are pile length $L = 15$ m, diameter $D = 1$ m, elastic modulus of pile $E_p = 2.9 \times 10^7$ kPa, the undrained shear strength of the soil $c_u = 70$ kPa, and the elastic modulus $E_{50} = 14$ MPa.

Figures 15(a) and 15(b) show the influence of different θ_1 on the load-displacement curve for the case of $Z_1 = 1$ m and 2 m, respectively. Under the same lateral load, the deflection of the pile head increases with the increment of θ_1 . And the deflection growth rate of the pile head is greater when the

lateral load becomes larger. In addition, with the augmentation of Z_1 , the influence of the upper slope is enhanced, and the dispersion of load-displacement curves under different slope conditions becomes larger. For example, considering that θ_1 goes up from 0° to 60° , the pile head deflection increases by 34.3% under the condition that the lateral load is 1500 kN and $Z_1 = 1$ m. And the maximum growth rate can reach 51% for the case of $Z_1 = 2$ m.

Figure 16 investigates the curve of maximum bending moment varying with the pile head displacement under the effect of θ_1 . Compared with the load-displacement curve, θ_1 has a similar but smaller influence on the maximum bending moment of the pile. The maximum bending moment of the pile becomes larger when the angle θ_1 decreases under the same displacement of the pile head. And the dispersion of curves is pronounced for larger Z_1 . At a pile head displacement $y = 0.2$ m, the maximum bending moment of the pile for $\theta_1 = 20^\circ$ is higher than that for $\theta_1 = 60^\circ$ by 4.4% and 7.2% for the $Z_1 = 1$ m and $Z_1 = 2$ m, respectively.

4.2. *The Effect of Lower Slope Angle θ_2 .* In order to investigate the influence of θ_2 on the laterally loaded pile, $\theta_2 = 0^\circ, 15^\circ, 30^\circ, 45^\circ,$ and 60° are selected as variables in this section. When $Z_1 = 1$ m, 2 m, and θ_1 is 60° , the variation rules of pile head deflection and maximum bending moment are analyzed. The calculation parameters of pile and soil are the same as those in Section 4.1.

Figures 17(a) and 17(b) show the influence of different θ_2 on the load-displacement curve under the different upper slope heights Z_1 , respectively. The figures represent that as the angle θ_2 increases, the displacement of the pile head under the same load raises nonlinearly. And the growth rate of deflection is positively correlated with θ_2 . Besides, the influence of the lower slope can be weakened, and the dispersion of load-displacement curves under different slope conditions becomes smaller when the upper slope height Z_1 increases. Considering that θ_2 goes up from 0° to 60° , the pile head deflection increases by 40% under the condition that the lateral load is 1500 kN and $Z_1 = 1$ m. When Z_1 is 2 m, the maximum growth rate is 20%.

Figure 18 shows the effect of θ_2 in the maximum bending moment. The maximum bending moment of the pile becomes larger when the angle θ_2 decreases under the same displacement of the pile head. And the dispersion of curves is smaller for larger Z_1 . At a pile head displacement $y = 0.2$ m, the maximum bending moment of the pile for $\theta_2 = 0^\circ$ is higher than that for $\theta_2 = 60^\circ$ by 11.6% and 7.1% for the $Z_1 = 1$ m and $Z_1 = 2$ m, respectively.

4.3. *The Effect of the Normalized Height Z_1/D .* To study the influence of the normalized height Z_1/D , this section considers Z_1/D as 0, 0.5, 1.0, 2.0, 4.0, and 5.0. And upper slope angle $\theta_1 = 60^\circ$, lower slope angle $\theta_2 = 30^\circ$. Other calculation parameters of pile and soil are the same as in Section 4.1.

Figure 19 shows the load-displacement curves of the pile head considering different sloping conditions. It indicates that the augmentation in Z_1/D increases the deflection of the pile head. When the normalized height Z_1/D changes from 0 to 2, the pile head deflection increases

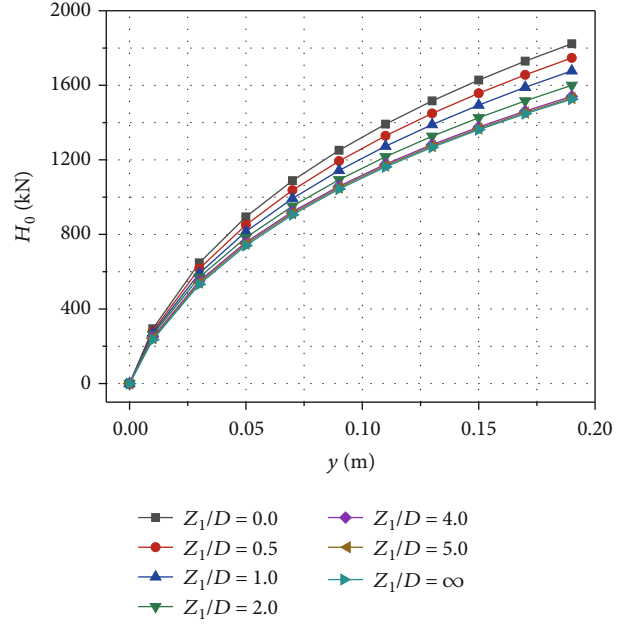


FIGURE 19: Effect of Z_1/D on the deflection of the pile head.

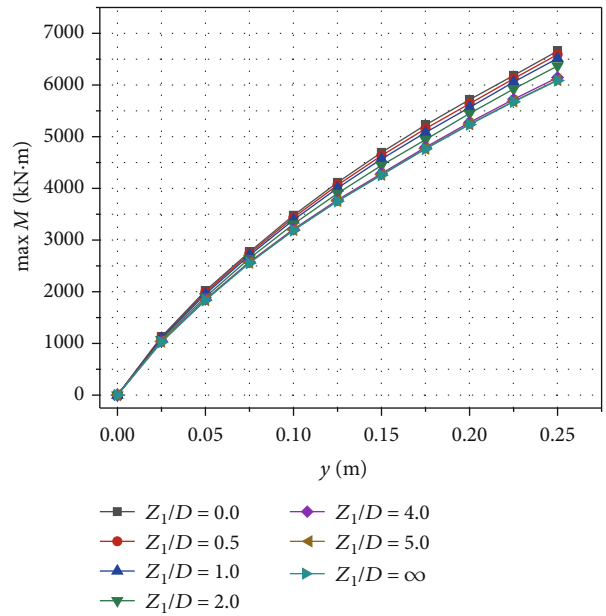


FIGURE 20: Effect of Z_1/D on maximum bending moment.

rapidly. For the lateral load $H_0 = 1500$ kN, the growth rate of pile head deflection is 32%. When the normalized height is greater than 2, the growth rate of deflection gradually becomes flat. For $Z_1/D = 5$ and applied load $H_0 = 1500$ kN, the deflection of the pile head is only 10% higher than that for $Z_1/D = 2$ m. It also can be seen that the deflection of the pile head is similar to that for the case of $Z_1/D = \infty$ when the normalized height Z_1/D exceeds 5 in Figure 19.

The influence of the normalized height Z_1/D on the maximum bending moment of the pile is illustrated in Figure 20.

The maximum bending moment is smaller for larger Z_1/D under the same deflection of the pile head. The max M of a pile decreases steeply first and then gently with the increase of the normalized height Z_1/D . When the value of Z_1/D exceeds 5, the normalized height has no effect on the maximum bending moment. However, the effect of the increase in Z_1/D on max M is quite small. When the displacement of the pile head $y = 0.2$ m, the growth rate of maximum bending moment of the pile is only 9.2% with the normalized height Z_1/D range 0 to ∞ .

5. Conclusion

This paper has proposed the p - y curve which is suitable for a concave slope, and the lateral response of a pile has been studied. Equations of initial stiffness K_i varying with depth were obtained through the reduction coefficient method and the normalization method. The nonlinear formulas of the ultimate soil resistance with depth were obtained by using the soil damaged model in front of piles. The rationality of the theory in this paper was verified by comparing the result of three-dimensional finite element analysis. The upper slope angle θ_1 , the lower slope angle θ_2 , and the normalized height Z_1/D were discussed. The following conclusions can be drawn:

- (1) Both ultimate soil resistance and deflection of pile head were predicted using a new method in this paper, which is in good agreement with those calculated by 3D FE analysis
- (2) The slope angle (θ_1, θ_2) has a significant effect on the pile head deflection and a moderate effect on the maximum bending moment. Both deflection and maximum bending moment increase with the increase in slope angle. In addition, the effects of the angle and the height of the upper slope are mutual. As Z_1 increases, the influence of the lower slope angle θ_2 weakens and that of the upper slope angle θ_1 enhances
- (3) The normalized height Z_1/D is also a remarkable factor for the concave slope. The increase of the deflection and maximum bending moment is greater for larger Z_1/D under the same load. And the influence scope of Z_1/D is 0 to 5
- (4) The response of lateral load piles on concave slopes differs markedly from the response of lateral load piles on single-angle slopes. There is a large error using the existing p - y curves to predict the response of the laterally loaded pile on the concave slope. Thus, the proposed p - y curve of a concave slope in this paper has practical value

Data Availability

The data used to support the findings of this study are available from the corresponding author upon request.

Conflicts of Interest

The authors declare that there are no conflicts of interest regarding the publication of this paper.

Acknowledgments

This work is supported by National Natural Science Foundation of China (Grant Nos. 51678570 and 51978665).

References

- [1] H. G. Poulos and E. H. Davis, *Pile Foundation Analysis and Design*, John Wiley & Sons, New York, NY, 1980.
- [2] L. Zhang, *Drilled Shafts in Rock-Analysis and Design*, Balkema, London (UK), 2005.
- [3] P. Liu, C. Jiang, M. Lin, L. Chen, and J. He, "Nonlinear analysis of laterally loaded rigid piles at the crest of clay slopes," *Computers and Geotechnics*, vol. 126, p. 103715, 2020.
- [4] P. Liu, L. Chen, C. Huawei, and C. Jiang, "A method for predicting lateral deflection of large-diameter monopile near clay slope based on soil-pile interaction," *Computers and Geotechnics*, vol. 135, article 104180, 2021.
- [5] L. J. Chen, C. Jiang, L. Pang, and P. Liu, "Lateral soil resistance of rigid pile in cohesionless soil on slope," *Computers and Geotechnics*, vol. 135, p. 104163, 2021.
- [6] Y. Wang, Y. F. Yi, C. H. Li, and J. Q. Han, "Anisotropic fracture and energy characteristics of a Tibet marble exposed to multi-level constant-amplitude (MLCA) cyclic loads: a lab-scale testing," *Engineering Fracture Mechanics*, vol. 244, no. 10, p. 107550, 2021.
- [7] L. C. Reese and W. F. Van Impe, *Single Piles and Pile Group under Lateral Loading*, A. A. Balkema, Ed., CRC press, Rotterdam, 2001.
- [8] H. Matlock, "Correlations for design of laterally loaded piles in soft clay," *Proceedings 2nd Offshore Technology Conf.*, 1970, pp. 577–594, OTC, Houston, 1970.
- [9] API (American petroleum institute), *Recommended Practice for Planning, Designing and Constructing Fixed Offshore Platforms. API RP-2A*, API, Washington DC, 15th edition, 1984.
- [10] L. U. Cheng, X. C. Xu, and S. X. Chen, "Model test and numerical simulation of horizontal bearing capacity and impact factors for foundation piles in slope," *Rock and Soil Mechanics*, vol. 9, no. 26, pp. 85–91, 2014.
- [11] Y. I. Ping-bao, Z. H. Ming-hua, Z. H. Heng, and H. E. Wei, "Stability analysis of pile column bridge pile considering slope effect," *Journal of Hunan University*, vol. 43, no. 11, pp. 20–25, 2016.
- [12] Y. S. Deng, M. H. Zhao, and X. J. Zhou, "Research progress of bearing characteristics of pile column at steep slope in mountain areas," *Journal of Highway and Transportation Research and Development*, vol. 29, no. 6, pp. 37–45, 2012.
- [13] L. C. Reese, W. R. Cox, and F. D. Koop, "Field testing and analysis of laterally loaded piles in stiff clay," in *Proceedings 7th Offshore Technology Conference, OTC*, pp. 671–690, Houston, 1975.
- [14] K. Georgiadis and M. Georgiadis, "Undrained lateral pile response in sloping ground," *Journal of Geotechnical and Geoenvironmental Engineering*, vol. 136, no. 11, pp. 1489–1500, 2010.

- [15] K. Georgiadis and M. Georgiadis, "Development of p - y curves for undrained response of piles near slopes," *Computers and Geotechnics*, vol. 40, pp. 53–61, 2012.
- [16] C. Y. Wu, J. P. Qiao, and L. B. Lan, "Research on slope shape of landslide based on GIS technique," *Journal of Natural Disasters*, vol. 2005, no. 3, pp. 34–37, 2005.
- [17] H. M. Fan, T. L. Wang, and L. L. Zhou, "Study on temporal and spatial variation of current velocity on different form slopes," *Journal of Soil and Water Conservation*, vol. 21, no. 6, pp. 35–38, 2007.
- [18] M. Georgiadis, C. Anagnostopoulos, and S. Safflekou, "Interaction of laterally loaded piles," in *Proceedings, Foundations Profondes, Ponts et Chaussées*, pp. 177–184, Paris, 1991.
- [19] S. S. Rajashree and T. G. Sitharam, "Nonlinear finite-element modeling of batter piles under lateral load," *Journal of Geotechnical and Geoenvironmental Engineering*, vol. 127, no. 7, pp. 604–612, 2001.
- [20] B. T. Kim, N. K. Kim, W. J. Lee, and Y. S. Kim, "Experimental load-transfer curves of laterally loaded piles in Nak-Dong river sand," *Journal of Geotechnical and Geoenvironmental Engineering*, vol. 130, no. 4, pp. 416–425, 2004.
- [21] R. Liang, K. Yang, and J. Nusairat, " P - Y criteria for rock mass," *Journal of Geotechnical and Geoenvironmental Engineering*, vol. 135, no. 1, pp. 26–36, 2009.
- [22] K. Yang, "Analysis of laterally loaded drilled shafts in rock," Department of Civil Engineering, Univ. of Akron, 2006, Ph.D. dissertation.
- [23] J. D. Murff and J. M. Hamilton, " P -ultimate for undrained analysis of laterally loaded piles," *Journal of Geotechnical Engineering*, vol. 119, no. 1, pp. 91–107, 1993.
- [24] C. M. Martin and M. F. Randolph, "Upper-bound analysis of lateral pile capacity in cohesive soil," *Géotechnique*, vol. 56, no. 2, pp. 141–145, 2006.
- [25] M. F. Randolph and G. T. Houlsby, "The limiting pressure on a circular pile loaded laterally in cohesive soil," *Géotechnique*, vol. 34, no. 4, pp. 613–623, 1984.
- [26] C. Jiang, J. L. He, L. Liu, and B. W. Sun, "Effect of loading direction and slope on laterally loaded pile in sloping ground," *Advances in Civil Engineering*, vol. 2018, no. 4, pp. 1–12, 2018.
- [27] D. P. Carter, *A Non-Linear Soil Model for Predicting Lateral Pile Response*, Dept. of Civil Engineering, Univ. of Auckland, 1984, Ph.D. dissertation.
- [28] R. L. Kondner, "Hyperbolic stress-strain response: cohesive soils," *Journal of Soil Mechanics and Foundation Engineering Division*, vol. 89, no. 1, pp. 115–143, 1963.
- [29] P. K. Robertson, M. P. Davies, and R. G. Campanella, "Design of laterally loaded driven piles using the flat dilatometer," *Geotechnical Testing Journal*, vol. 12, no. 1, pp. 30–38, 1989.
- [30] M. H. Yang, B. Deng, and M. H. Zhao, "Experimental and theoretical studies of laterally loaded single piles in slopes," *Journal of Zhejiang University-SCIENCE A*, vol. 20, no. 11, pp. 838–851, 2019.
- [31] S. Mezazigh and D. Levacher, "Laterally loaded piles in sand: slope effect on p - y reaction curves," *Canadian Geotechnical Journal*, vol. 35, no. 3, pp. 433–441, 1998.

Research Article

Effect of Microwave Pretreatment on Grindability of Lead-Zinc Ore

Qing Yu,^{1,2,3} Dexin Ding,^{1,2} Wenguang Chen,² Nan Hu,^{1,2} Lingling Wu,¹ Qiucui Zhang,¹ Yulong Liu,² Zhijun Zhang¹,,¹ Feng Li,^{1,2} Xilong Xue,¹ Zhaopeng Li,⁴ and Guicheng He^{1,2}

¹School of Resources Environment and Safety Engineering, University of South China, Hengyang 421001, China

²Key Discipline Laboratory of Defense Biotechnology in Uranium Mining and Hydrometallurgy, University of South China, Hengyang 421001, China

³State Key Laboratory of Safety and Health for Metal Mines, Maanshan 243000, China

⁴School of Resources and Safety Engineering, Central South University, Changsha 410083, China

Correspondence should be addressed to Guicheng He; hegc9210@163.com

Received 10 May 2021; Revised 24 May 2021; Accepted 17 June 2021; Published 16 July 2021

Academic Editor: Zhengyang Song

Copyright © 2021 Qing Yu et al. This is an open access article distributed under the Creative Commons Attribution License, which permits unrestricted use, distribution, and reproduction in any medium, provided the original work is properly cited.

The influence of microwave pretreatment on grindability of lead-zinc ore was studied through comparison analysis on the changes of particle size distribution, percentage of below 0.074 mm, energy consumption, and other indexes of grinding products before and after microwave pretreatment in the ball milling process. The results showed that the grindability of lead-zinc ore was improved obviously by microwave pretreatment. The particle size distribution curve of the grinding products was obviously higher than that of the samples without microwave irradiation. The yield of size fraction below 0.074 mm was also improved in a certain degree. Pulsed microwave irradiation was more effective than continuous microwave irradiation when other microwave parameters were consistent. The comprehensive energy consumption of lead-zinc ore pretreated by different microwave parameters was lower than that without microwave irradiation under the same grinding fineness. The total energy consumption was down by 30.1% when irradiated for 15 s at 7 kW power, and it was lower than that without microwave irradiated. The results showed that pulsed microwave pretreatment was more effective in reducing the comprehensive energy consumption of grinding process for lead-zinc ore. And water quenching after microwave irradiation can improve the grindability and reduce the energy consumption of grinding for lead-zinc ore.

1. Introduction

The crushing and grinding of ore is considered to be a process of high energy consumption and low efficiency. There are two indicators to evaluate the efficiency of grinding. One is the particle size distribution, and the other is the liberation degree of grinding products [1]. The essence of grinding is ore properties. Changing the mechanical properties of ore [2, 3], improving the liberation degree of useful minerals, and enhancing the grinding efficiency have always been the focus of scholars [4, 5].

Previous studies indicate that the heat pretreatment can reduce the energy consumption of grinding effectively and improve the liberation degree of useful minerals [6–8].

Compared with conventional heating, microwave pretreatment has the advantages of fast heating rate [9, 10], selective heating, uniformity heating, and so on [11]. Because of the different dielectric loss factors of different minerals, the microwave absorption capacity of mineral particles is not the same [12, 13]. Thus, thermal stress is induced by the temperature difference between mineral particles, which leads to cracks in the grain boundary of mineral particles and promotes grinding and dissociating of useful minerals [14, 15].

Microwave pretreatment can improve the grinding property and grinding efficiency of ore [16]. However, most researchers pretreat ore with continuous microwave [17, 18]. From the pretreatment effect of the ore [19], it has the

disadvantage of high energy consumption for continuous microwave irradiation, and high temperature may even cause changes in the crystal structure of some useful minerals, thus affecting the efficiency of subsequent processes.

It is found that pulse microwave irradiation is a more effective method to reduce the mechanical strength of ore and improve the degree of mineral dissociation. [20] found that microcracks produced in breccia uranium ore with pulsed microwave pretreatment was the fundamental reason for improving its grindability. [21] found that pulsed microwave with high power would be more efficient than continuous microwave for treating fine-grained ores. [22] irradiated pyrite with continuous microwave and pulsed microwave, respectively, and found pulsed microwave could be more effective on weakening the ore. In addition, it was found that the grinding property and energy consumption of the metallurgical coke pretreated by pulsed microwave for a short time were better than by continuous microwave pretreatment [23]. So it can be seen pulsed microwave pretreatment is an important subject in the area of improving the grinding of ore, which has a wide range of potential applications. Pulsed microwaves are obtained by applying high-voltage pulses of microsecond to millisecond width to a magnetron. Its pulse power can reach tens of kilowatts or even several megawatts, while the average power is only a few kilowatts. When such microwave energy is added to the treated ore, the ore will be irradiated by high-energy microwave in a very short period of time, and the grain boundary fracture will occur to various wave-absorbing minerals in the ore under the action of thermal stress, thus reducing the mechanical strength of the ore [24] and improving the degree of mineral dissociation. At present, there are few researches on the grinding ability of pulsed microwave pretreatment for lead-zinc ore, which points out the direction of this experiment.

So the objective of this research was to compare and analyze the changes of the particle size distribution, percentage of below 0.074 mm [25], grinding energy consumption, and other indexes before and after the continuous and pulsed microwave pretreatment of lead-zinc ore and to reveal the influence of microwave pretreatment on the grindability of lead-zinc ore.

2. Experimental

2.1. Raw Materials. The lead-zinc ore from Hunan province in China was crushed to 1-2 mm by the jaw crusher and then divided by the cone quartering method for grinding test. The mineral composition of lead-zinc ore was analyzed by X-ray diffractometer (XRD), and the results are shown in Figure 1. Microwave digestion was used, hydrochloric acid and hydrogen peroxide solution was used to digest the lead-zinc ore sample, and then, atomic absorption spectrograph was used to determine the content of lead, zinc, and other metals in the digestion solution. Through chemical test and analysis, the chemical composition of lead and zinc ores is shown in Table 1. Table 1 shows that the petrochemical composition complex, lead-zinc mine of valuable element content is 2.9% and 4.80% of lead and zinc, respectively, and contains a lot of sulfur, iron, and silicon; there is a small amount of

calcium; the content is 30.29%, 18.68%, 17.98%, and 2.03%, respectively; the ore belongs to contain lead and zinc sulfide ores; the main metal mineral of galena and sphalerite and gangue minerals are mainly quartz.

2.2. Equipment. The box-type microwave heating device used in this experiment was developed independently by the key discipline laboratory for national defense for biotechnology in uranium mining and hydrometallurgy from university of South China. Its power is continuously adjustable in the range of 1-70 kW, and the frequency is 2450 MHz. As shown in Figure 2, the size of sagger used to load the ore for microwave irradiation is 168 × 130 × 45 mm, and the loading capacity of each sagger is 2.5 kg. 1 is the magnetron, 2 is the door of cavity, 3 is the platform, 4 is touch screen of human-machine interface operation, 5 is the power supply of the microwave tube, 6 is the frequency converter, 7 is the cooling water tube, and 8 is the microwave resonant heating cavity. The grinding test was carried out by planetary ball mill from German Retsch company, as shown in Figure 3.

2.3. Test Plan. The lead-zinc ore was crushed to 1-2 mm by the jaw crusher and then divided by the cone quartering method for grinding test. Seven parts of ore samples were marked as 1#, 2#, 3#, 4#, 5#, 6#, and 7#, respectively. The detailed test plan was shown in Table 2. Seven parts of lead-zinc ore samples were pretreated under microwave with different irradiation parameters. Each part was weighed 200 grams and put into planetary ball mill to grind for 10 min with speed of 400 rad/min.

The yield of each particle was obtained by analyzing the ore grinding products with standard sieves of 24 mesh, 28 mesh, 40 mesh, 55 mesh, 60 mesh, 80 mesh, 100 mesh, 120 mesh, 150 mesh, 190 mesh, and 200 mesh, respectively. Repeat the experiment many times, particle size distribution curves of lead-zinc ore were drawn for different microwave irradiation parameters, and it revealed the influence law of microwave pretreatment and cooling methods on the particle size of lead-zinc ore after ball milling.

3. Results and Discussion

It can be seen that the coarse fraction was relatively large, and the percentage of below 0.074 mm after ball milling was only 36.08% without microwave pretreatment. The content of coarse fraction with microwave pretreatment after ball grinding for 10 minutes decreased gradually. The grinding products were finer, and the percentage content of grinding products below 0.074 mm was larger by increasing microwave power and changing the cooling method when the rest grinding conditions were completely the same.

3.1. Effect of Continuous Microwave Pretreatment on Particle Size of Grinding Products. Figure 4 showed the effect of continuous microwave pretreatment on size fraction distribution of grinding products for lead-zinc ore. It can be seen that the contents of coarse and medium size fraction (380-600 μm and 106-120 μm) were 6.93% and 7.90%, respectively, after ball milling without microwave irradiation, and the content of fine fraction below 74 μm was 36.08%. When the lead-

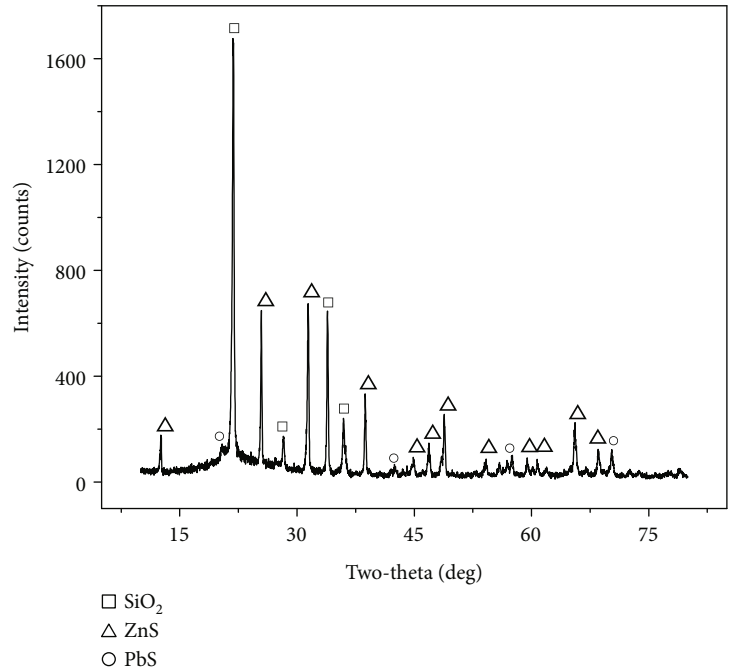


FIGURE 1: X-ray diffraction pattern of lead-zinc ore for grinding test.

TABLE 1: Main chemical composition of lead-zinc ore.

Component	Pb	Zn	S	Fe	Si	O	Ca	C	Cu
Content (%)	4.80	2.90	30.29	18.68	17.98	19.32	2.03	1.42	0.30
Component	P	F	As	Al	Ba	K	Mg	Na	
Content (%)	0.31	0.05	0.17	0.81	0.06	0.40	0.31	0.18	

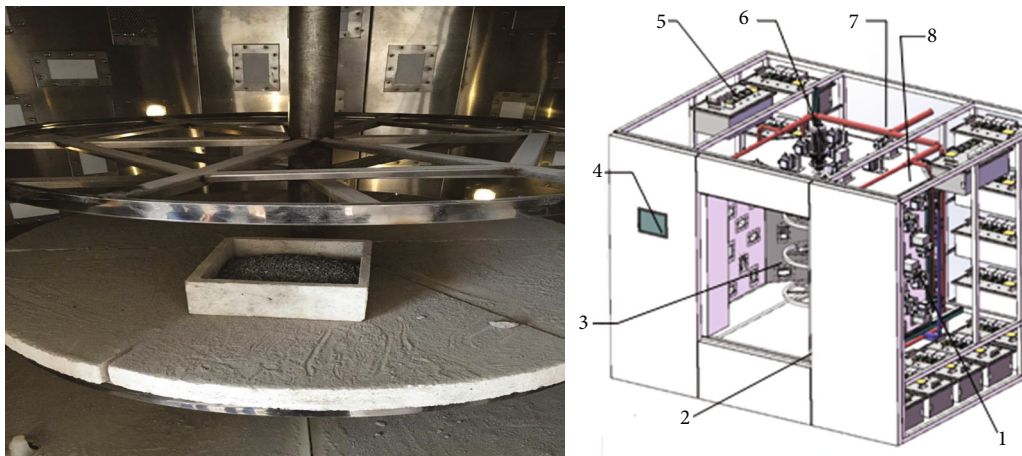


FIGURE 2: Internal diagram and three-dimensional diagram of the microwave heating device.

zinc ore was irradiated by continuous microwave with power of 800 W, the contents of coarse and medium size fraction decreased gradually after natural cooling, but not so obvious. For example, the contents of size fraction (380-600 μm and 106-120 μm) were 5.86% and 5.19%, respectively, but the content of fine fraction below 74 μm was 41.36%, which increased obviously. As the power of continuous

microwave was increased to 7kW, the content of coarse and medium size fraction decreased gradually, and the fine fraction content increased gradually, where the content of below 74 μm increased to 48.61%. By comparing the effects of 800 W and 7kW microwave power on the ore size distribution after grinding, it could be seen that the ore treated by 7 kW microwave power was more conducive to grinding



FIGURE 3: Planetary ball mill with four platforms.

and thus to mineral disintegration under less irradiation time.

Figure 5 reflected the influence of continuous microwave pretreatment on the particle size cumulative percentage of grinding products for lead-zinc ore. As shown in Figure 5, the particle size distribution curve of the grinding products after continuous microwave pretreatment was above that without microwave irradiation obviously. It is indicated that continuous microwave pretreatment can improve the grindability of lead-zinc ore, and the particle size of ore samples becomes finer with the increase of microwave power. It could be that the lead-zinc minerals were easy to absorb microwave energy and converted it into thermal energy under microwave irradiation, but the gangue minerals were not easy to absorb microwave energy. Then, thermal stress was formed in the ore due to the temperature gradient, which led to microcracks in the grain boundary of different minerals, reducing the mechanical strength of the ore and improving the grinding effect.

The surface of lead-zinc ore was characterized by scanning electron microscopy (SEM) and energy dispersive spectroscopy (EDS) after continuous microwave irradiation, as shown in Figure 6. The results of SEM and EDS analyses were as follows. Figure 6(a) showed that the bright zone contained Pb and S elements, which should be galena, and there were a lot of cracks on the surface of the bright zone, which may be caused by thermal stress between the metallic minerals and gangue minerals after microwave irradiation. Figure 6(b) showed that the dark zone contained Zn and S elements, which should be sphalerite, and there were also some cracks

on its surface. In addition, under the scanning electron microscope, there were clear cracks appearing on the bright and dark borders between the two metallic minerals. It proved that the microwave treatment caused cracks between different minerals in the lead-zinc ore, which could effectively promote the dissociation of metallic minerals and gangue minerals, leading to the reduction of the strength of lead-zinc ore, improving the grinding effect.

3.2. Effect of Pulsed Microwave Pretreatment on Particle Size of Grinding Products. The influence of pulsed microwave pretreatment on size fraction distribution of grinding products for lead-zinc ore was shown in Figure 7. It can be seen that the contents of coarse and medium size fraction ($250\text{-}260\ \mu\text{m}$ and $106\text{-}120\ \mu\text{m}$) were 6.48% and 7.90%, respectively, after ball milling without microwave irradiation, and the content of fine fraction below $74\ \mu\text{m}$ was 36.08%. When the lead-zinc ore was irradiated by pulsed microwave with nature cooling under the condition of pulsed microwave of 7 kW, pulse width of 1 ms, and working frequency of 500 Hz, the contents of size fraction ($250\text{-}260\ \mu\text{m}$ and $106\text{-}120\ \mu\text{m}$) were 2.07% and 2.93%, respectively, and the content of fine fraction below $74\ \mu\text{m}$ was 49.58% which increased obviously.

Figure 7 shows the influence of pulsed microwave pretreatment on the percentage of particle size accumulation of lead-zinc ores. It can be seen that the particle size distribution curve of the grinding products with pulsed microwave pretreatment was above that without microwave irradiation obviously. It indicates that pulsed microwave pretreatment also can improve the grinding efficiency of lead-zinc ore.

3.3. Effect of Cooling Method on Particle Size of Grinding Products. Figure 8 showed the influence of cooling method on size fraction distribution of grinding products after continuous microwave pretreatment. It can be seen from Figure 8 that water quenching had a significant influence on the grinding effect of lead-zinc ore irradiated by continuous microwave with power of 800 W for 70 seconds. The yield of fine fraction of grinding products after water quenching was obviously higher than natural cooling. The effect of water quenching on grinding was more remarkable than that of natural cooling when lead-zinc ore was irradiated by continuous microwave with power of 7 kW for 15 seconds. The yields of the size fraction ($380\text{-}600\ \mu\text{m}$) with water quenching after continuous microwave pretreatment decreased from 5.19% to 3.83%, and the yields of the fine fraction below $74\ \mu\text{m}$ increased from 48.61% to 51.46% compared to natural cooling. The effect of water quenching on the grinding of lead-zinc ore was more remarkable than natural cooling whether it was pretreated by continuous microwave or pulsed microwave. It could be that the water quenching can prevent healing microcracks formed along the mineral grains due to thermal stress generated by microwave irradiation. At the same time, water quenching also caused a sudden drop in temperature in and outside the ore, which further expanded the original grain boundary cracks of the minerals.

Figure 9 showed the influence of cooling method on size fraction distribution of grinding products after pulsed microwave pretreatment with high power. As shown in Figure 9,

TABLE 2: Grinding test plan of lead-zinc ore with microwave pretreatment.

Test label	Microwave pretreatment parameters			Grinding parameters		
	Microwave type	Power (kW)	Time (s)	Cooling method	Speed (rad/min)	Grinding time (min)
1#	No microwave irradiation	/	/	/	400	10
2#	Continuous microwave	0.8	70	Nature cooling	400	10
3#	Continuous microwave	0.8	70	Water quenching	400	10
4#	Continuous microwave	7	15	Nature cooling	400	10
5#	Continuous microwave	7	15	Water quenching	400	10
6#	Pulsed microwave, pulse width was 1 ms, working frequency was 500 Hz	7 (peak)	15	Nature cooling	400	10
7#	Pulsed microwave, pulse width was 1 ms, working frequency was 500 Hz	7 (peak)	15	Water quenching	400	10

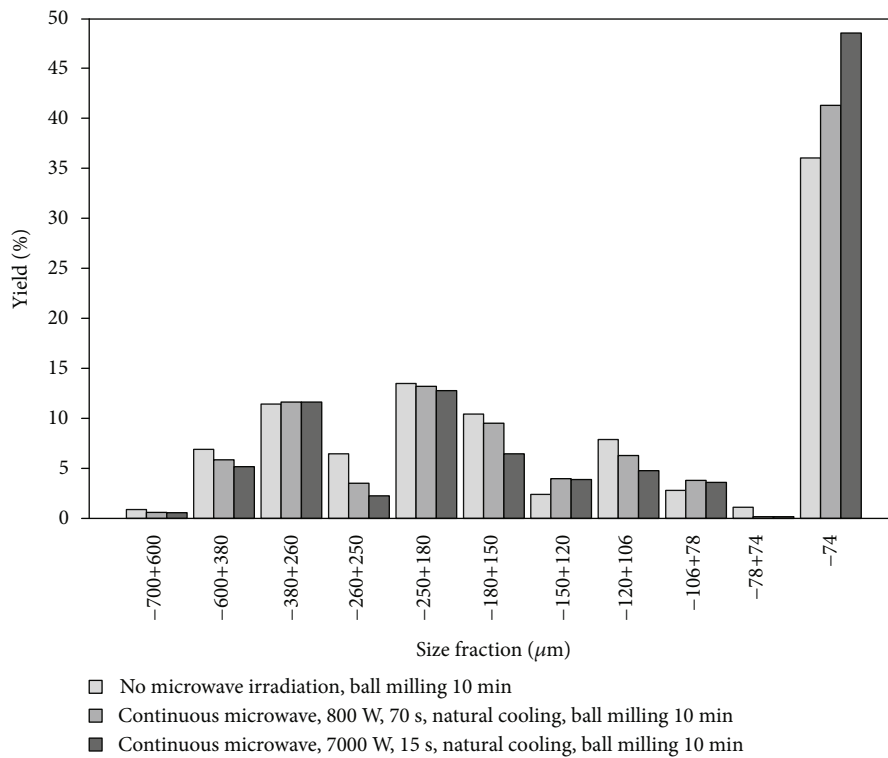


FIGURE 4: Effect of continuous microwave pretreatment on size fraction distribution of grinding products for lead-zinc ore.

water quenching can improve grinding better than natural cooling. When the lead-zinc ore was irradiated by pulsed microwave with power of 7kW for 15 seconds, the yields of the coarse fraction (260-380 μm) with water quenching decreased from 11.54% to 10.59% compared with natural cooling, and the yields of fine fraction below 0.074 mm increased from 49.58% to 52.71%.

3.4. Analysis and Comparison between the Effect of Continuous Microwave and Pulsed Microwave on the Particle Size of Grinding Products. Figure 10 showed the comparison diagrams of size fraction distribution of grinding products under different cooling methods with continuous and pulsed microwave pretreatment. It can be seen from

Figure 10 that the grinding effect after pulsed microwave pretreatment was better than that of continuous microwave pretreatment in both natural cooling and water quenching, and the percentage composition of coarse and medium size fraction is less than that by continuous microwave pretreatment. The content of fine fraction below 0.074 mm after pulsed microwave pretreatment was all larger than that by continuous microwave pretreatment, which increased by 0.97% under natural cooling and increased by 1.25% under water quenching.

In summary, the grindability of the ore after pulsed microwave pretreatment was improved compared with continuous microwave pretreatment under the same microwave power and irradiation time. The yields of size fraction below

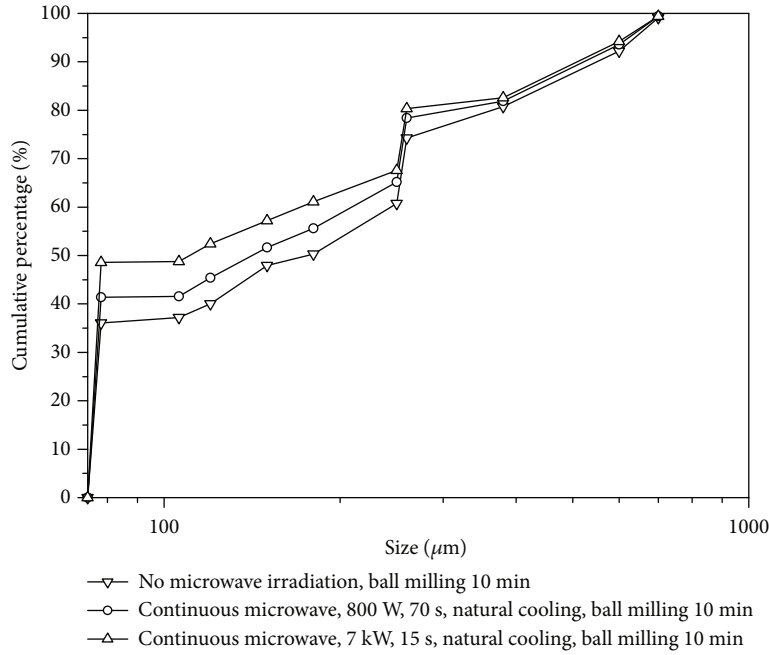


FIGURE 5: Effect of continuous microwave pretreatment on the particle size cumulative percentage of grinding products for lead-zinc ore.

0.074 mm increased at different degrees. It produced hysteresis phenomenon of rebound deformation because of the thermal stress formed by pulsed microwave pretreatment loads and unloads. And it caused irreparable residual deformation in the ore. The fatigue failure occurred in the ore promoted the grinding of lead-zinc ore as the circulation of load and unload increased. Therefore, the effect of pulsed microwave pretreatment on the grinding of lead-zinc ore was improved compared with continuous microwave pretreatment.

3.5. Effect of Microwave Pretreatment on Grinding Fineness. The lead-zinc ore was pretreated by microwave under different conditions, and then, it was milled for 10 minutes by planetary ball mill. Finally, the grinding fineness under different microwave pretreatment conditions was achieved by comparing and analyzing the yields of below 0.074 mm.

It can be seen from Figure 9 that the particle size yield of below 0.074 mm was 36.08% after grinding without microwave irradiation. When the continuous microwave irradiation was applied for 70 seconds with power of 800 W, the particle size yield of grinding products below 0.074 mm after natural cooling was 41.38%, improved by 5.30% compared with the untreated. The grinding fineness of the samples with pulsed microwave pretreatment was also higher than that with continuous microwave pretreatment under the same condition. This indicated that the lead-zinc ore pretreated by pulsed microwave could save more energy and improve the grinding fineness of the samples. For example, the particle size yield of grinding products below 0.074 mm was 52.71% after water quenching when the pulsed microwave was 7 kW and the irradiation duration was 15 seconds. This was higher than that with continuous microwave pretreatment under the same condition. And it was improved by

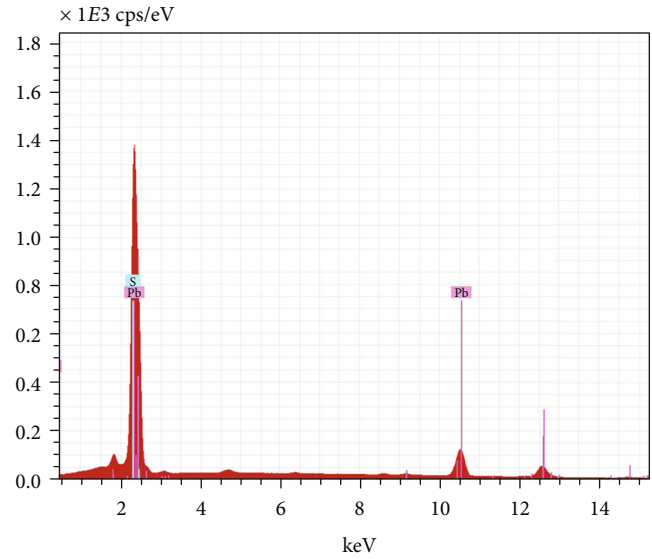
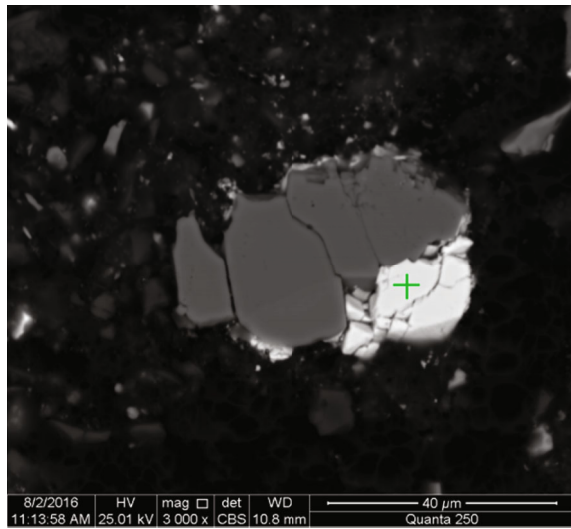
16.63% compared with the untreated, improving the grinding fineness of lead-zinc ore greatly.

3.6. Effect of Microwave Pretreatment on Energy Consumption of Grinding. In order to compare and analyze the energy consumption of grinding for lead-zinc ore under different microwave pretreatment conditions, the target grinding fineness which the yield of below 0.074 mm was set as 50%. According to the results of grinding tests, the ball milling time before reaching the target fineness and the energy consumption of grinding, under different microwave pretreatment conditions, was determined and calculated. Under the condition of the same grinding fineness, the energy consumption of the ore samples without microwave irradiation (E_1) mainly comes from the ball mill, and the calculation formula is shown in Eq. (1). The energy consumption of the samples pretreated by microwave (E_2) was mainly composed of the energy consumption of the ball mill during grinding (E_0) and the energy consumption generated during microwave pretreatment (E_m). It was calculated by Eq. (2).

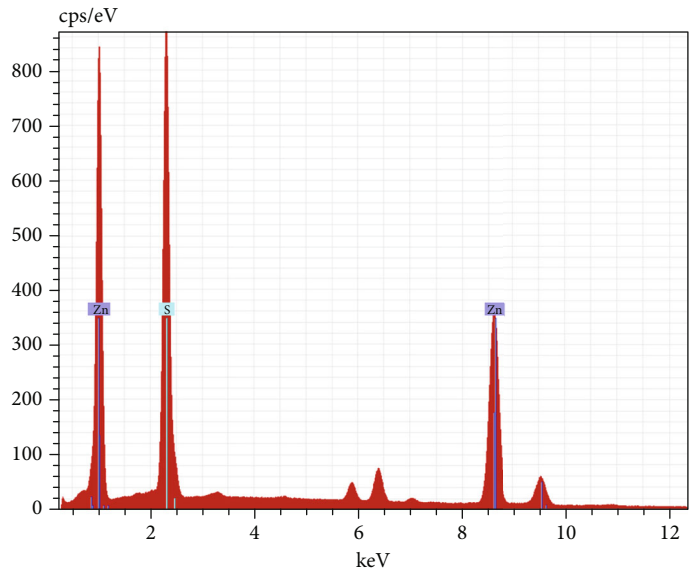
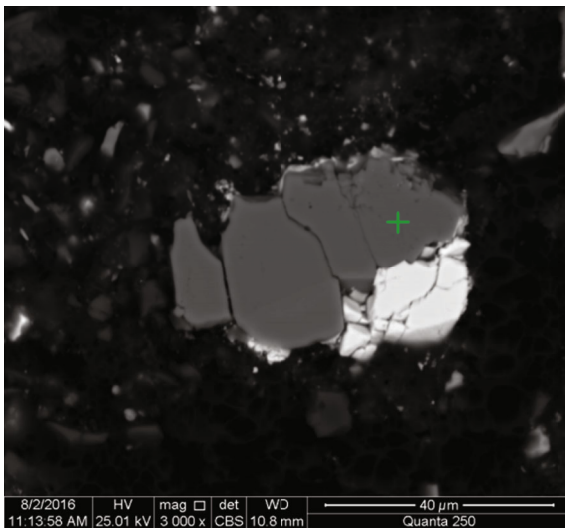
$$E_1 = P_1 t_1, \quad (1)$$

$$E_2 = E_0 + E_m = P_1 t_2 + P_2 \tau \frac{Q}{q}. \quad (2)$$

In Eq. (1) and Eq. (2), P_1 was the power of ball mill (kW), t_1 was the grinding time reaching the target fineness without microwave pretreatment (hour), t_2 was the grinding time reaching the target fineness with microwave pretreatment (hour), P_2 was the power of microwave (kW), τ was time of the microwave pretreatment (hour), Q was the give ore amount of ball mill, which were both 0.8 kg, and q was the



(a)



(b)

FIGURE 6: SEM and EDS images of lead-zinc ore after continuous microwave pretreatment.

weight of ore samples with microwave pretreatment, which were both 1 kg.

The grinding fineness of lead-zinc ore with different grinding time under different microwave irradiation process was shown in Table 3.

Figure 11 showed the influence of different ball milling time on the grinding fineness of lead-zinc ore after microwave pretreatment. It can be seen from Figure 11 that the yields of below 0.074 mm increased gradually with the increase of grinding time. The ball milling time for reaching the target fineness without microwave pretreatment was 15 minutes. When the power of continuous microwave was 800 W and the irradiation time was 70 seconds, the ball milling time for reaching the target fineness was 13 minutes, saving 2 minutes compared with that without microwave

pretreatment. The ball grinding time to reach the target grinding fineness was 12 minutes and 10 minutes, respectively, with continuous microwave pretreatment and pulsed microwave pretreatment when the power of microwave was 7 kW and the irradiation time was 15 seconds, which were 3 minutes and 5 minutes shorter than that without microwave pretreatment.

It suggested the grinding time of lead-zinc ore after microwave pretreatment was greatly shortened when the same target fineness was achieved compared with that without microwave irradiation, and the energy consumption of grinding was also saved when the grinding efficiency was improved.

In the laboratory condition, 1.0 kg of ore samples was pretreated by microwave each time. The give ore amount of

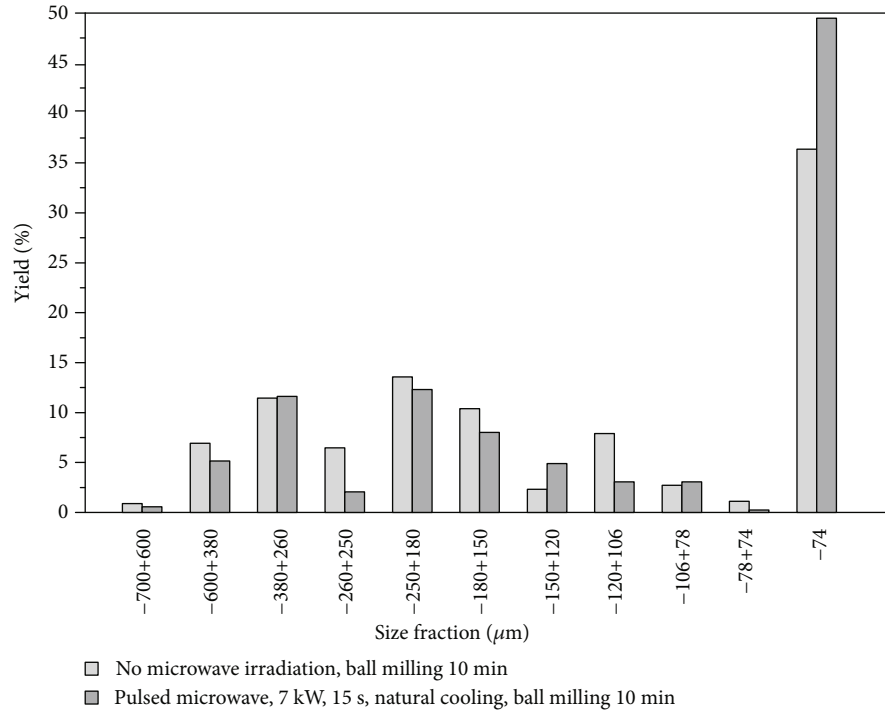


FIGURE 7: Effect of pulsed microwave pretreatment on size fraction distribution of grinding products for lead-zinc ore.

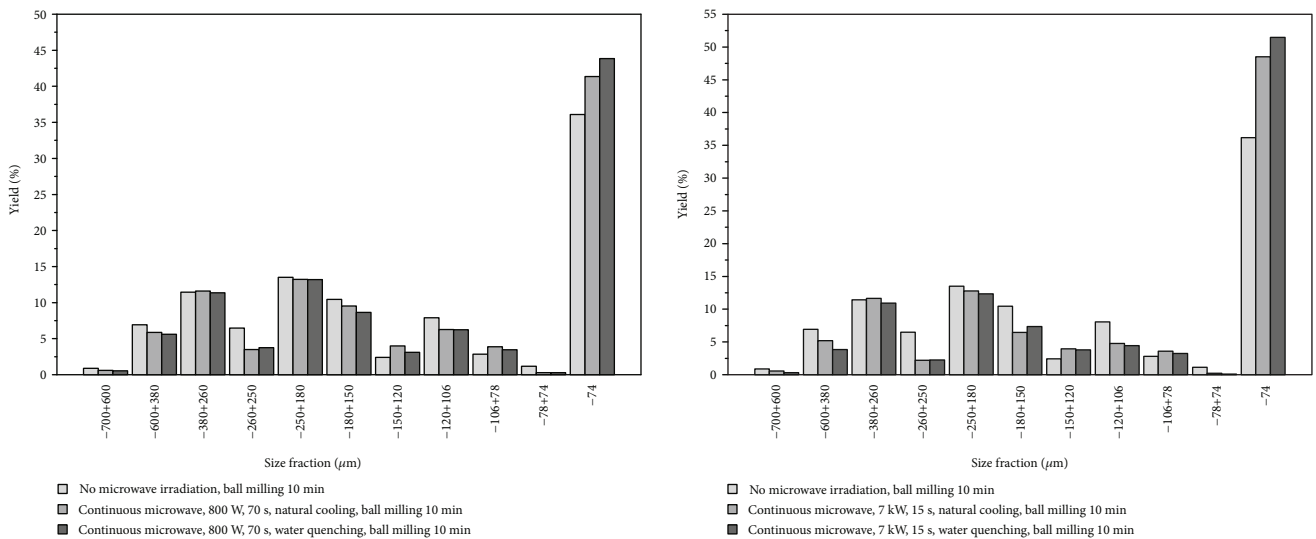


FIGURE 8: Effect of cooling method on the size fraction distribution of grinding products after continuous microwave pretreatment.

each ball grinding was 800 g, and the power of the ball mill was 2.2 kW. The calculation results of energy consumption and the total energy consumption distribution of reaching the target grinding fineness for lead-zinc ore under different microwave pretreatment conditions were shown in Figure 12.

It can be seen from Figure 12 that the energy consumption of lead-zinc samples without microwave irradiation was 0.55 kW·h when the target grinding fineness was reached. When the power of continuous microwave was

800 W and the irradiation time was 70 seconds, the total energy consumption of reaching the target grinding fineness was reduced to 0.49 kW·h, in which the energy consumption of microwave pretreatment was 0.01 kW·h and the energy consumption of grinding was 0.48 kW·h. In addition, the total energy consumption was reduced by 10.9% compared to that without microwave irradiation. The microwave pretreatment could reduce the comprehensive energy consumption of grinding process for the lead-zinc ore obviously. When the power of continuous microwave was 7 kW and the

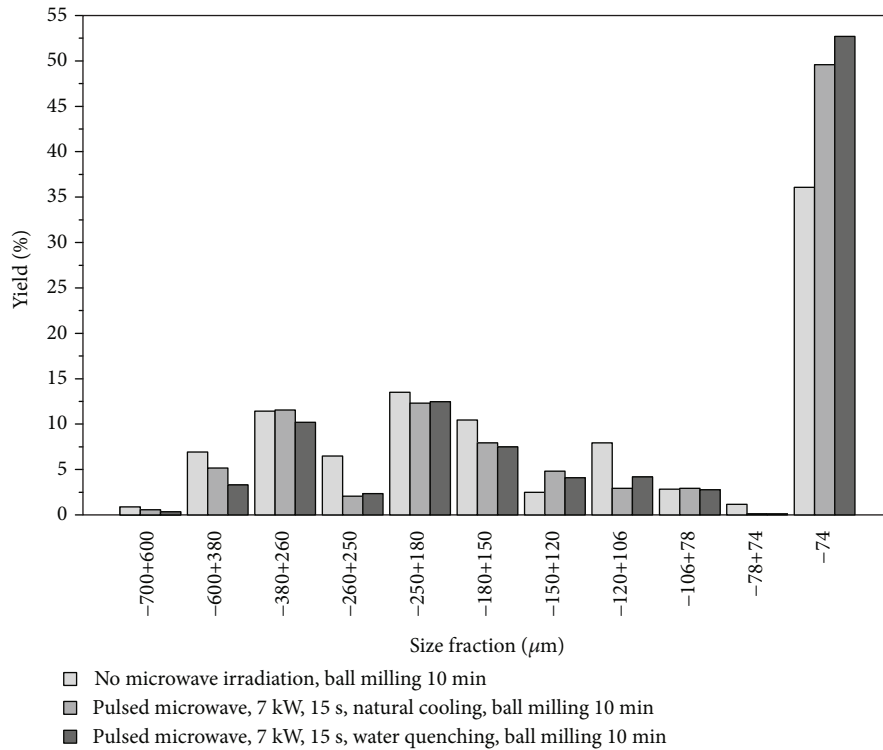


FIGURE 9: Effect of cooling method on size fraction distribution of grinding products after pulsed microwave pretreatment.

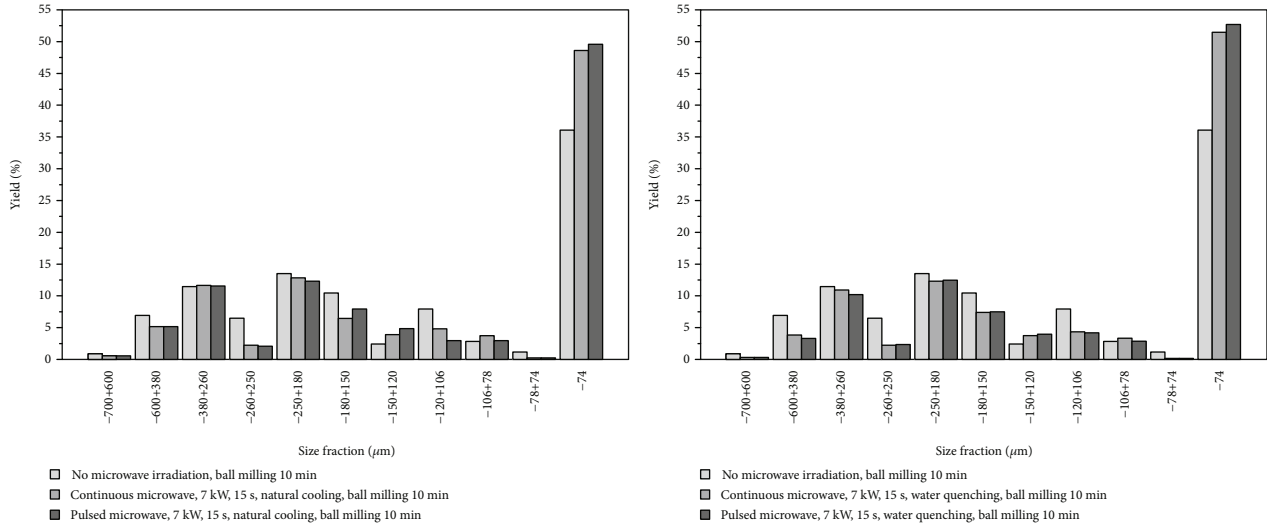


FIGURE 10: Comparison diagrams of the size fraction distribution of grinding products under natural cooling and water quenching after continuous and pulsed microwave pretreatment.

irradiation time was 15 seconds, the total energy consumption was 0.46kW·h, which was 16.4% lower than that without microwave irradiation. It showed that the comprehensive energy consumption decreased more obviously with the increase of power of continuous microwave. When the power of pulsed microwave was 7kW and the irradiation time was 15 seconds, the total energy consumption of reaching the target grinding fineness was only

0.38kW·h. It was 30.1% lower than that without microwave irradiation, and the energy consumption decreased the most. Pulsed microwave pretreatment was more effective in reducing the comprehensive energy consumption of grinding process of lead-zinc ore compared with continuous microwave pretreatment.

In conclusion, under the condition of achieving the same target grinding fineness, the energy consumption of grinding

TABLE 3: Grinding fineness of lead-zinc ore with different grinding time under different microwave pretreatment conditions.

Pretreatment conditions	Pretreatment time τ (s)	Grinding time t (min)	Give ore amount Q (kg)	The yields of below 0.074 mm (%)
No microwave irradiation	0	10	0.8	37.80
	0	11	0.8	40.04
	0	12	0.8	42.88
	0	13	0.8	45.31
	0	14	0.8	47.80
	0	15	0.8	50.23
Continuous microwave, power of microwave was 800 W, natural cooling	70	10	0.8	42.03
	70	11	0.8	43.99
	70	12	0.8	46.27
	70	13	0.8	49.84
	70	14	0.8	51.07
Continuous microwave, power of microwave was 7 kW, natural cooling	15	10	0.8	46.55
	15	11	0.8	48.13
	15	12	0.8	49.87
Pulsed microwave, power of microwave was 7 kW, pulse width was 1 ms, working frequency was 500 Hz, natural cooling	15	13	0.8	51.34
	15	10	0.8	49.53
	15	11	0.8	52.38

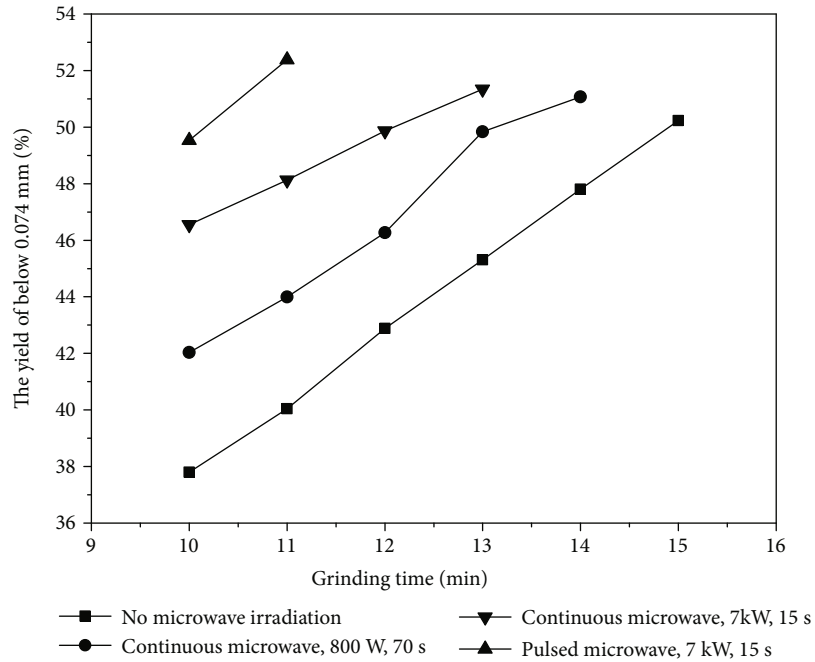


FIGURE 11: The influence of ball milling time on the grinding fineness of lead-zinc ore after microwave pretreatment.

for the lead-zinc ore samples without microwave pretreatment was greater than the sum of the energy consumption of microwave pretreatment and the energy consumption of ball milling. It indicated that the microwave pretreatment could assist in grinding and reducing energy consumption in the process of lead-zinc ore.

4. Conclusions

The pretreatment of lead-zinc ore with different microwave parameters was carried out. The conclusion can be reached as the following by analyzing the changes of particle size distribution, energy consumption of grinding, and the yields of

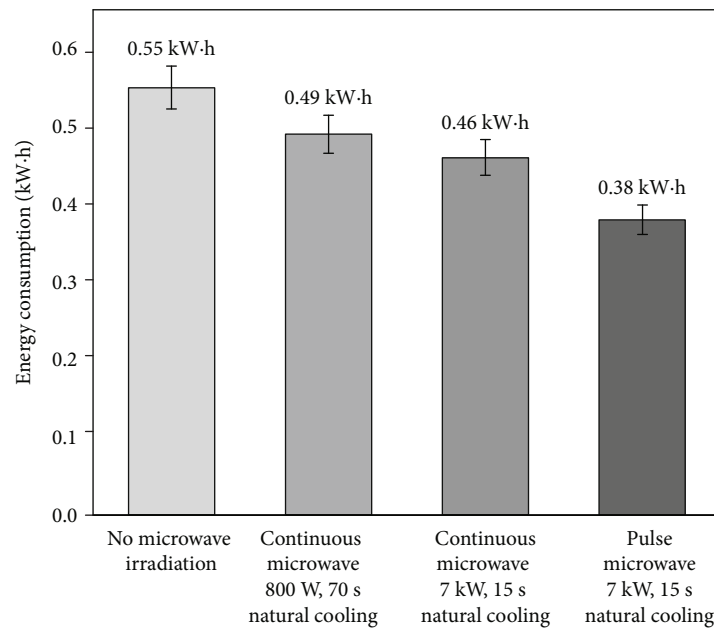


FIGURE 12: The total energy consumption of reaching the target fineness for lead-zinc ore under different microwave pretreatment conditions.

grinding products below 0.074 mm before and after microwave pretreatment.

- (1) Continuous microwave pretreatment could improve the grinding efficiency of lead-zinc ore, and the particle size of grinding products became finer with the increase of microwave power. The yield of grinding products below 0.074 mm was 36.08% without microwave irradiation. When the power of continuous microwave was 800 W and the irradiation time was 70 seconds, the yield of grinding products below 0.074 mm after natural cooling was 41.36%, which was 5.28% higher than that of untreated. And the particle size distribution curve of grinding products was obviously above that without microwave irradiation. This was because the lead-zinc minerals were easy to absorb microwave energy and converted the energy into thermal energy under microwave irradiation, while the gangue minerals were not easy to absorb microwave energy. Then, thermal stress was formed in the ore due to the temperature gradient, which led to microcracks along the grain boundary of minerals, reduced the mechanical strength of the ore, and improved the grinding effect
- (2) In summary, the grindability of the ore after pulsed microwave pretreatment was improved compared with continuous microwave pretreatment under the same microwave power and irradiation time. The yield of size fraction below 0.074 mm increased in certain degree. It produced hysteresis phenomenon of rebound deformation because of the thermal stress formed by pulsed microwave pretreatment loads and

unloads. And it caused irreparable residual deformation in the ore. The fatigue failure occurred in the ore which promoted the grinding of lead-zinc ore as the times of load and unload increased. Therefore, the effect of pulsed microwave pretreatment on the grinding of lead-zinc ore was improved compared with continuous microwave pretreatment

- (3) The effect of water quenching on the grinding of lead-zinc ore was more remarkable than that of natural cooling whether it was pretreated by continuous microwave or pulse microwave. It was because that the water quenching can prevent healing microcracks formed along the mineral grains' boundaries due to thermal stress generated by microwave irradiation. At the same time, water quenching also causes a sudden drop in temperature in and outside the ore, which further expands the original grain boundary cracks of the minerals inside the ore
- (4) Under the condition of achieving the same target grinding fineness, the energy consumption of grinding for the lead-zinc ore samples without microwave pretreatment was greater than the sum of the energy consumption of microwave pretreatment and the energy consumption of ball milling. When the power of continuous microwave was 800 W and the irradiation time was 70 seconds, the total energy consumption of reaching the target grinding fineness was reduced to 0.49 kW·h, which was reduced by 10.9% relative to that without microwave irradiation. When the power of continuous microwave was 7 kW and the irradiation time was 15 seconds, the total energy consumption was 0.46 kW·h, which was 16.4% lower

than that without microwave irradiation. When the power of pulsed microwave was 7 kW and the irradiation time was 15 seconds, the total energy consumption of reaching the target grinding fineness was only 0.38 kW·h. It was 30.1% lower than that without microwave irradiation, and the energy consumption decreased the most. Pulsed microwave pretreatment was more effective in reducing the comprehensive energy consumption of grinding process of lead-zinc ore compared with continuous microwave pretreatment

Data Availability

All data used in this study can be obtained by contacting the corresponding author.

Conflicts of Interest

The authors declare that they have no conflicts of interest.

Acknowledgments

This project was financially supported by the National Natural Science Foundation of China (Nos. 51974163 and 51804164), the Natural Science Foundation of Hunan Province of China (Nos. 2018JJ2329, 2018JJ3448, and 2019JJ50498), the Key Research and Development Project of Hunan Province of China (No. 2020SK2024), and the Education Department of Hunan Province of China (Nos. 18A248, 18A247, 18B266, and 18B276).

References

- [1] Z. H. Huang, "Application of grindability index in selection of vertical mill for manganese ore," *China's Manganese Industry*, vol. 34, no. 2, pp. 46–50, 2016.
- [2] W. Dang, J. Chen, and L. Huang, "Experimental study on the velocity-dependent frictional resistance of a rough rock fracture exposed to normal load vibrations," *Rock Mechanics and Rock Engineering*, vol. 16, no. 7, pp. 2189–2202, 2021.
- [3] W. Dang, W. Wu, H. Konietzky, and J. Qian, "Effect of shear-induced aperture evolution on fluid flow in rock fractures," *Computers and Geotechnics*, vol. 114, article 103152, 2019.
- [4] Z. Moravvej, A. Mohebbi, and S. Daneshpajouh, "The microwave irradiation effect on copper leaching from sulfide/oxide ores," *Materials & Manufacturing Processes*, vol. 33, no. 1, pp. 1–6, 2016.
- [5] R. S. John, A. R. Batchelor, D. Ivanov et al., "Understanding microwave induced sorting of porphyry copper ores," *Minerals Engineering*, vol. 84, pp. 77–87, 2015.
- [6] A. J. Buttress, J. M. Rodriguez, A. Ure, R. S. Ferrari, C. Dodds, and S. W. Kingman, "Production of high purity silica by microfluidic-inclusion fracture using microwave pre-treatment," *Minerals Engineering*, vol. 131, pp. 407–419, 2019.
- [7] Z. Y. Ma, Y. Liu, J. K. Zhou, M. D. Liu, and Z. Z. Liu, "Recovery of vanadium and molybdenum from spent petrochemical catalyst by microwave-assisted leaching," *International Journal of Minerals, Metallurgy, and Materials*, vol. 26, no. 1, pp. 33–40, 2019.
- [8] G. M. Qian, B. Zhang, M. M. Li, R. Yan, and H. L. Zhang, "Effect of microwave pretreatment on grinding efficiency of oolitic hematite in western Hubei Province," *Journal of Wuhan University of Science and Technology*, vol. 39, no. 1, pp. 1–6, 2015.
- [9] A. Mehdilo and M. Irannajad, "Comparison of microwave irradiation and oxidation roasting as pretreatment methods for modification of ilmenite physicochemical properties," *Journal of Industrial and Engineering Chemistry*, vol. 33, pp. 59–72, 2016.
- [10] M. Omran, T. Fabritius, A. M. Elmahdy, N. A. Abdel-Khalek, and S. Gornostayev, "Improvement of phosphorus removal from iron ore using combined microwave pretreatment and ultrasonic treatment," *Separation and Purification Technology*, vol. 156, pp. 724–737, 2015.
- [11] E. Charikinya and S. M. Bradshaw, "An experimental study of the effect of microwave treatment on long term bioleaching of coarse, massive zinc sulphide ore particles," *Hydrometallurgy*, vol. 173, pp. 106–114, 2017.
- [12] A. R. Batchelor, A. J. Buttress, D. A. Jones et al., "Towards large scale microwave treatment of ores: part 2-metallurgical testing," *Minerals Engineering*, vol. 111, pp. 5–24, 2017.
- [13] N. Hu, W. Chen, D. X. Ding et al., "Role of water contents on microwave roasting of gold bearing high arsenic sulphide concentrate," *International Journal of Mineral Processing*, vol. 161, pp. 72–77, 2017.
- [14] R. K. Amankwah, A. U. Khan, C. A. Pickles, and W. T. Yen, "Improved grindability and gold liberation by microwave pretreatment of a free-milling gold ore," *Mineral Processing and Extractive Metallurgy*, vol. 114, no. 1, pp. 30–36, 2005.
- [15] M. Toifl, P. Hartlieb, R. Meisels, T. Antretter, and F. Kuchar, "Numerical study of the influence of irradiation parameters on the microwave-induced stresses in granite," *Minerals Engineering*, vol. 103–104, pp. 78–92, 2017.
- [16] J. Wang, T. Jiang, Y. Liu, and X. Xue, "Effect of microwave irradiation on the grinding and magnetic separation characteristics of vanadium titanomagnetite," *Metallurgical Research & Technology*, vol. 116, no. 4, p. 419, 2019.
- [17] R. Rajavaram, J. Lee, J. S. Oh, H. G. Kim, and J. Lee, "Microwave heating characteristics of magnetite ore," *Metals and Materials International*, vol. 22, no. 6, pp. 1116–1120, 2016.
- [18] K. Yang, S. W. Li, L. B. Zhang et al., "Microwave roasting and leaching of an oxide-sulphide zinc ore," *Hydrometallurgy*, vol. 166, pp. 243–251, 2016.
- [19] V. Madakkaruppan, A. Pius, T. Sreenivas, N. Giri, and C. Sarbajna, "Influence of microwaves on the leaching kinetics of uraninite from a low grade ore in dilute sulfuric acid," *Journal of Hazardous Materials*, vol. 313, pp. 9–17, 2016.
- [20] S. H. Jiang, N. Hu, H. Zhang, W. Hou, and D. X. Ding, "Effect of pulse microwave pretreatment parameters on crushing and grinding properties of brecciate uranium ore," *Uranium Mining and Metallurgy*, vol. 36, no. 3, pp. 192–200, 2017.
- [21] A. Y. Ali and S. M. Bradshaw, "Bonded-particle modelling of microwave-induced damage in ore particles," *Minerals Engineering*, vol. 23, no. 10, pp. 780–790, 2010.
- [22] D. A. Jones, S. W. Kingman, D. N. Whittles, and I. S. Lowndes, "The influence of microwave energy delivery method on strength reduction in ore samples," *Chemical Engineering &*

- Processing Process Intensification*, vol. 46, no. 4, pp. 291–299, 2007.
- [23] E. Ruisanchez, A. Arenillas, E. J. Juarez-Perez, and J. A. Menéndez, “Pulses of microwave radiation to improve coke grindability,” *Fuel*, vol. 102, no. 6, pp. 65–71, 2012.
- [24] W. Dang, H. Konietzky, T. Frühwirt, and M. Herbst, “Cyclic frictional responses of planar joints under cyclic normal load conditions: laboratory tests and numerical simulations,” *Rock Mechanics and Rock Engineering*, vol. 53, no. 1, pp. 337–364, 2020.
- [25] W. Xia, J. Yang, and B. Zhu, “The improvement of grindability and floatability of oxidized coal by microwave pre-treatment[J],” *Energy Sources Part A-recovery Utilization and Environmental Effects*, vol. 36, no. 1, pp. 23–30, 2014.

Research Article

Temporal-Spatial Characteristics of Ground and Pile Responses to Twin Shield Tunneling in Clays

Minghong Sheng,^{1,2} Jinjin Gao ,³ Panpan Guo ,⁴ Rihong Cao,⁵ and Yixian Wang ⁶

¹School of Management, Hefei University of Technology, Hefei 230009, China

²Anhui Road & Bridge Group Co. Ltd., Hefei 210029, China

³Center for Strategic Studies, Chinese Academy of Engineering, Beijing 100088, China

⁴Research Center of Coastal and Urban Geotechnical Engineering, Zhejiang University, Hangzhou 310058, China

⁵The University of Western Australia, Perth WA 6009, Australia

⁶School of Civil Engineering, Hefei University of Technology, Hefei 230009, China

Correspondence should be addressed to Jinjin Gao; gjj@cae.cn and Yixian Wang; wangyixian2012@hfut.edu.cn

Received 8 April 2021; Revised 3 June 2021; Accepted 21 June 2021; Published 7 July 2021

Academic Editor: Afshin Davarpanah

Copyright © 2021 Minghong Sheng et al. This is an open access article distributed under the Creative Commons Attribution License, which permits unrestricted use, distribution, and reproduction in any medium, provided the original work is properly cited.

This paper investigates the temporal-spatial characteristics of ground displacements as well as vertical and horizontal displacements and axial forces in existing piles induced by twin shield tunneling in clays. To that end, a case study and three-dimensional (3D) finite element (FE) analysis were performed. Based on the *in situ* monitoring data from the presented twin tunneling case history with existing piles beneath, the adopted 3D FE method was validated to be competent to yield reasonable simulation results. The validated 3D FE method was then used to analyze the effects of the distance between the tunnel and the pile, the distance between tunnel faces, and the pile length on the horizontal and vertical displacements and axial stresses in piles. It was found that the horizontal displacement distribution forms along the pile shaft for the front piles are similar to that for the back piles, whereas the magnitudes of the horizontal displacements of the front piles are slightly larger than that of the back piles. The interactions between piles in the pile group provide protection of the middle piles in the pile group against twin tunneling effects. With a reduction in the distance between the tunnel and the pile, the pile displacements and stresses increase nonlinearly. With an increase in the distance between tunnel faces, the maximum positive pile displacements and the maximum and minimum axial pile stresses increase, while the maximum negative pile displacements and the difference between the maximum and minimum axial pile stresses decrease.

1. Introduction

In congested urban cities, one of the effective means of relieving traffic pressure is to construct metros. The metro tunnels, in many cases, are adjacent to pile-supported structures [1, 2]. Studies have indicated that tunneling adjacent to pile-supported structures can induce ground movements [3], excessive lateral pile displacements [4], and reduction in structure bearing capacity and stability [5]. This will pose serious risks to people's lives and properties. Consequently, it is significant to investigate tunneling-induced ground movements and pile group responses [6–11].

Prediction of ground movements induced by tunneling can be made employing numerical analyses [12, 13], analytical expressions [14–16], artificial neural networks [17], and empirical methods [18]. The empirical methods have been proposed on the basis of the Gaussian error function [19–22] and are widely used in engineering practices because of convenience and simplicity [23]. However, limitations of the empirical methods exist, which include taking no account of the tunnel geometry, ground condition, and construction technique and providing insufficient information about subsurface settlements and horizontal displacements [24, 25].

Tunneling-induced ground movements affect the responses of the adjacent pile group because of the tunnel-

soil-structure interaction effect [26, 27]. This effect is dependent on factors such as the location of the pile relative to the tunnel, pile working load, cover-to-diameter ratio, and pile and tunnel dimensions [28]. To better understand this vital issue, researchers have carried out numerous studies based on different methods such as field monitoring [29], theoretical analysis [30], numerical simulation [31], and experimental investigation [32]. Actually, each of these methods has its own merits. The merits of numerical simulation, for example, are being able to account for the tunnel-soil-pile interaction effect, soil heterogeneity, and complex boundary conditions [33].

Pile group responses to tunneling can vary slightly, depending on the characteristics of the stratum in which tunneling occurs [34–36]. Studies on pile group responses to tunneling in a clay stratum are available in the literature. Ieronymaki et al. [37] conducted a comparative study into the effects of methods of tunneling in stiff clay on ground movements. It was found that the closed-face method controlled best the volume loss, while the open-face shield excavation method produced the largest tunnel cavity ovalization. Cattoni et al. [38] investigated the coupled hydromechanical processes related to shield tunneling in soft clays. A new method for predicting the displacement and internal force of constructed tunnels induced by adjacent excavation with dewatering was proposed by Guo et al. [35]. Using the force relaxation technique and finite difference program, Shiau et al. [39] analyzed the ground settlements induced by circular tunneling in soft clay. Son [40] made an analysis of structure responses to ground movements induced by tunneling in clay soils. Wang and Li [36] investigated the deformation and failure of surrounding rock after tunnel excavation under different joint network and groundwater conditions. Laver et al. [41] proposed a new method of estimating long-term ground movements induced by tunneling in London clay. Sun et al. [42] performed three-dimensional coupled consolidation finite element analyses to study the influence of consolidation on the tunnel response to excavation. However, the focus of most of these studies is on single-line tunnels. The effects of twin tunneling in a thick clay stratum on ground movements and pile group responses have not been fully captured.

Twin tunneling is becoming common with the development of urban underground traffic systems [43–45]. However, the number of studies available into the effects of twin tunneling on ground movements and pile group responses is limited. Moreover, most of the studies available are mainly focused on the effects of twin tunneling in dry sand [46–48]. Thus, twin tunneling-induced ground movements and pile group responses still remain poorly understood, especially for twin tunneling in a thick clay stratum.

The present study is targeted at investigating the ground surface settlements and pile group responses induced by twin tunneling in clays. 3D finite element analysis was performed to capture the development of ground surface settlements and pile group responses with advancing tunneling steps and to ascertain the effects of the distance between the tunnel and the pile, the distance between tunnel faces, and the pile length on the pile group responses on completion of tunnel-

ing. The performance of the 3D finite element analysis has been verified by the *in situ* monitoring data. The results obtained in this study have the potential to guide the protection of the pile group adjacent to twin tunneling.

2. Case History

2.1. Overview. The considered case history is a twin tunneling-by-shield tunneling machine for the construction of Hefei Metro Line 2 in Hefei, China. The twin tunneling passes underneath the Wulidun Overpass in the mileage range of SK26+050–SK26+450 between Qingyang Road Station and Xiyuan Road Station. The Wulidun Overpass, supported by a pile group, is located at the intersection of West Changjiang Road, Tunxi Road, and Hezuohua Road. It has connected the traffic in 17 flow directions. The maximum height of the Wulidun Overpass is 21 m from the ground surface. The superstructure of the Wulidun Overpass is a continuous beam on many supports. Figure 1 shows the location of the engineering site.

2.2. Parameters for the Ground, Tunnel, and Pile Group. The twin tunnels (i.e., the right and left tunnels) were excavated in a thick clay stratum and have a cover depth of 20 m, as depicted in Figure 2. The clay's engineering properties have been investigated by the authors and reported elsewhere [49–52]. The horizontal distance between the tunnel axes of the left and right tunnels is 28 m. The pile group foundation is composed of 8 bored concrete piles of 1 m in diameter and 30 m in length. The distance between the centers of any two adjacent piles in the pile group foundation is 3 m. The shortest distance between the pile group foundation and the left tunnel is 3 m. Three different strata (i.e., backfill soil, clay, and weathered rock) are penetrated by the pile group foundation. The pile cap is 12 m in length, 6 m in width, and 1 m in height. Besides, the tunnel segments' internal diameter, thickness, and ring width are 5.4, 0.3, and 1.5 m, respectively. The thickness of the grouting in the TBM tail interspace is 0.1 m.

2.3. Instrumentation. To ensure stability and safety for tunneling construction and the adjacent pile group, instruments of different types were installed at various positions to monitor the responses of the tunnel structure, ground surface, and pile group at different tunneling steps. The measurement items, instruments, and monitoring point arrangement for the considered case history are summarized in Table 1. As shown in the table, the measurement items include the ground surface settlement, tunnel vertical displacement, tunnel peripheral convergence, pile cap settlement, pile cap tilt, pile cap differential settlement, pile cap fissure, and Wulidun Overpass beam stress. The adopted instruments consist of the precise leveling instrument, steel ruler, convergence gauge, laser range finder, total station, reflector, crack gauge, vernier caliper, and taseometer. Figure 3 depicts the arrangement of the monitoring points in the field. The distance between two neighboring monitoring points can be 2.5, 3.5, or 5 m. The symbol “DBC” represents the instrumented section in the transverse direction

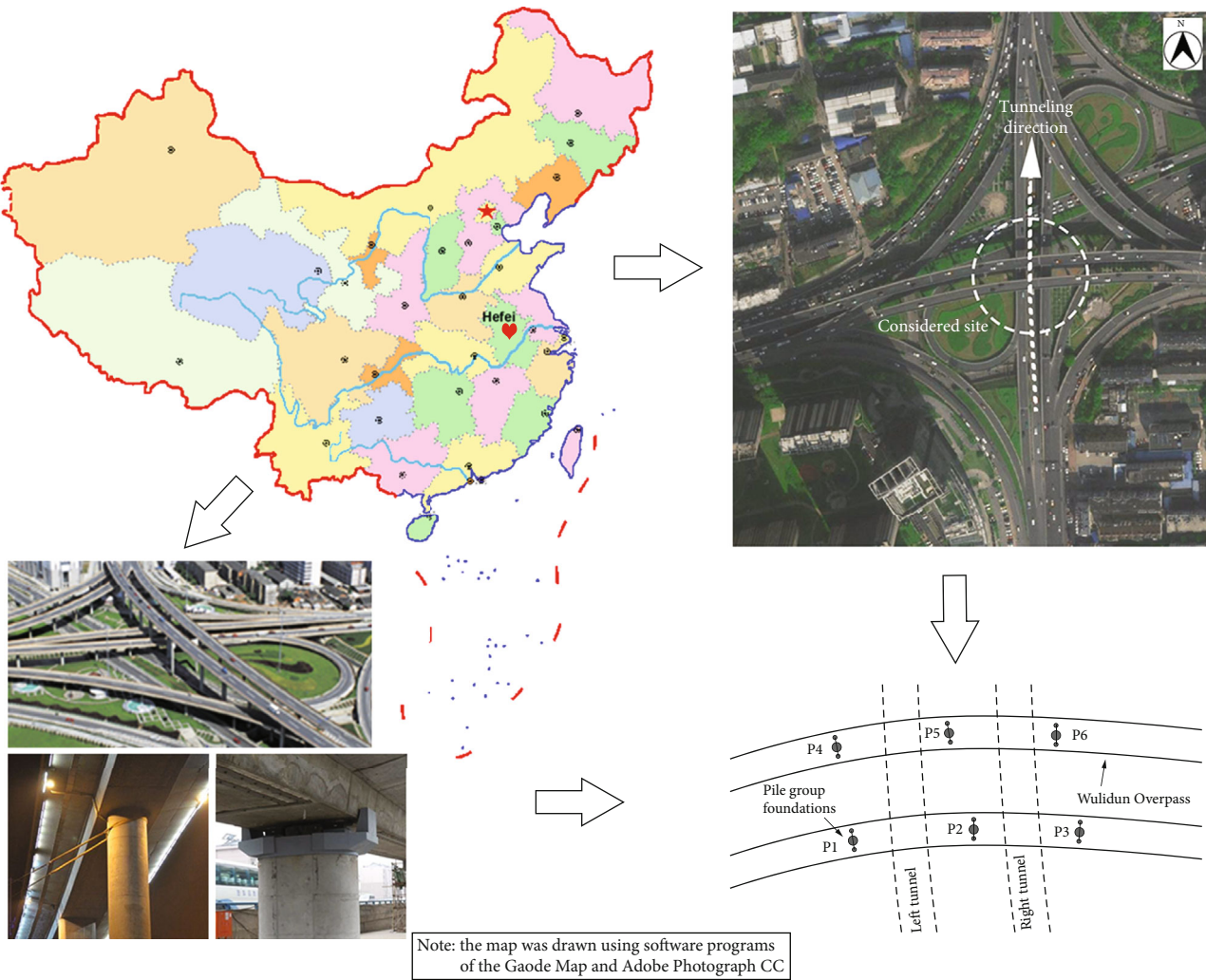


FIGURE 1: Engineering site.

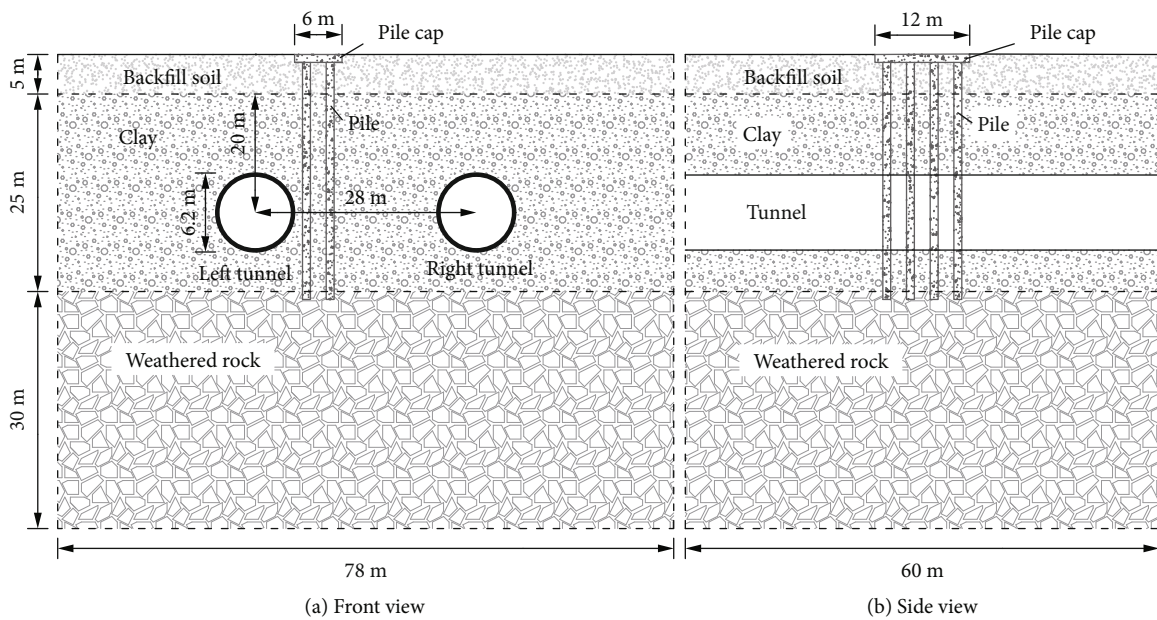
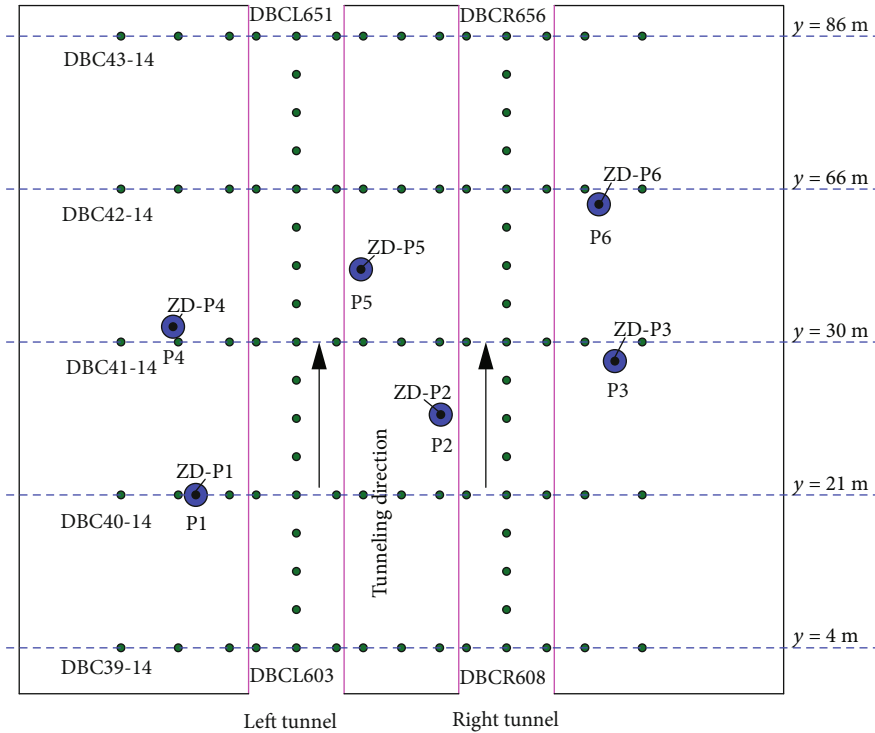


FIGURE 2: Front and side views of the considered engineering case.

TABLE 1: Summary of the *in situ* monitoring information.

Item	Instrument	Arrangement
Ground surface settlement	Precise leveling instrument; steel ruler	Interval of instrumented sections = 20 m; built-up areas
Tunnel vertical displacement	Precise leveling instrument; steel ruler	Interval of instrumented sections = 5 m
Tunnel peripheral convergence	Convergence gauge; laser range finder	Interval of instrumented sections = 5 m
Pile cap settlement	Precise leveling instrument; steel ruler	On the two sides of each pier perpendicular to the tunnel axis
Pile cap tilt	Total station; reflector	On the two sides of each pier perpendicular to the tunnel axis
Pile cap differential settlement	Precise leveling instrument; steel ruler	Each pier
Pile cap fissure	Crack gauge; vernier caliper	On the two sides of each fissure
Wulidun Overpass beam stress	Taseometer	In the middle of the bridge beam and slab structure

FIGURE 3: Schematic diagram of the *in situ* monitoring point arrangement.

along the tunnel axis. “DBCL” and “DBCR” denote, respectively, instrumented sections in the tunnel axis direction above the left and right tunnels.

3. Three-Dimensional Finite Element Analysis

3.1. Modeling of the Pile Group, Strata, and Their Interaction. Numerical modeling of the pile group, soil strata, and pile-soil interaction is established using the finite element method. Figure 4 shows the meshing of the numerical models based on MIDAS GTS NX [53]. A spatial model size of 78 m × 60 m × 60 m (i.e., $x \times y \times z$) is selected for the purpose of minimizing the potential boundary effects as much as possible. As for the model boundary conditions, normal restraints are applied to the four vertical boundaries and base boundary, while the top boundary is free. Therefore, there is no normal movement for the vertical boundaries and no movement for the base bound-

ary. Tetrahedral elements are adopted here to mesh the soil, pile cap, lining segments, and bored concrete piles. The TBM shell and grouting are modeled using shell elements. Table 2 summarizes the mechanical parameters of the materials used in numerical modeling. In this table, the parameters for the geomaterials, including backfill soil, clay, and weathered rock, were obtained by performing *in situ* and laboratory tests. It is noted that the elasticity modulus of the weathered rock is significantly greater than that of the backfill soil and the clay, whereas the difference among the other four parameters of the three types of soils is not very significant. For the artificial materials (i.e., grouting, segment, shield, and pile), the parameters were obtained from design specifications or from empirical values. Note that there are no cohesion and no internal friction angle for these artificial materials as their constitutive behavior was simulated with a linear elastic model in the numerical analysis.

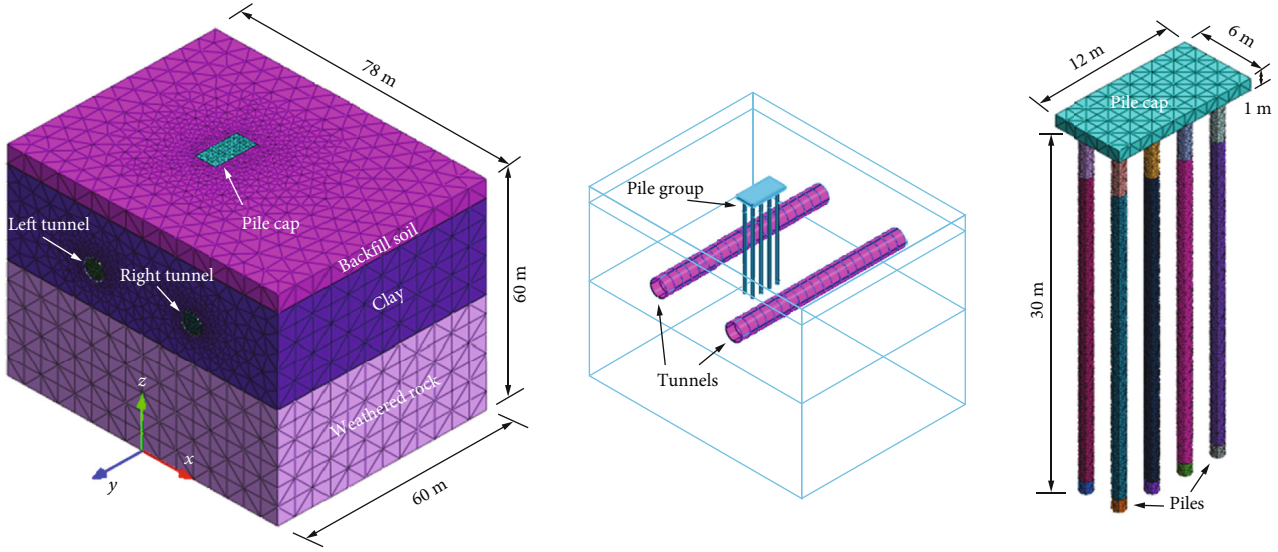


FIGURE 4: Meshing of numerical models.

TABLE 2: Material parameters for numerical analysis.

Material	Elasticity modulus (MPa)	Unit weight (kN/m ³)	Poisson's ratio	Cohesion (kPa)	Internal friction angle (°)
Backfill soil	13	19	0.35	10	8
Clay	37	20.3	0.33	40	20
Weathered rock	100	26	0.3	35	30
Grouting	10	23.6	0.3	/	/
Segment	30000	24.5	0.2	/	/
Shield	200000	78.5	0.3	/	/
Pile	33000	25	0.2	/	/

In numerical modeling, the interaction between the pile and the surrounding soil is simulated by generating interface elements in the pile-soil interface based on the Coulomb friction theory. A summary of the parameters for the interface elements generated in numerical modeling is presented in Table 3. As presented in Table 3, there are in total four different parameters required for the contact elements. Considerations on determining the magnitudes of the interfacial shear modulus, normal modulus, cohesion, and internal friction angle are presented as follows. The interface elements have a shear modulus of 80% of the elastic modulus of the piles. The normal modulus of the interface elements is taken as 10 times the shear modulus of the interface elements. For convenience, the cohesion and internal friction angle for the interface elements are regarded approximately to be equivalent to that of the surrounding soil in contact with the piles.

3.2. Modeling of Twin Tunneling. For numerically simulating the twin tunneling process, several assumptions have to be made. First, take no account of the effects of permeation and hydraulic pressure induced by groundwater. Second, assume that the soil strata are isotropic, homogeneous, elastic, perfectly plastic materials. Third, take no account of the ultimate consolidation settlement of soil.

Before tunneling, initial gravity stress is applied to soil strata. Then, reset the displacement of soil strata to zero. The weight of the overpass supported by the pile group is equivalent to a uniform load of 2 MPa applying on the pile cap. Twin tunneling starts from $y = 0$ m and progresses step by step until reaching $y = 60$ m. The length of two segments (i.e., 3 m) is selected as the progressing distance of each step. During twin tunneling, the tunnel face of the left tunnel gets ahead of the tunnel face of the right tunnel with a distance of 30 m between these two tunnel faces, as shown in Figure 5.

The procedure for numerically simulating twin tunneling is as follows. First, remove the initial soil elements included in a progressing distance (i.e., 3 m), apply a normal compressive stress of 0.2 MPa on the tunnel face, and install two pieces of lining segments under the protection of the TBM shell. Second, progress the TBM for a progressing distance of 3 m and grout in the interspace of the TBM tail with a grouting pressure of 0.2 MPa. Third, release the grouting pressure after the hardening of the grout is achieved. Repeat the aforementioned three steps until finishing twin tunneling.

3.3. Parametric Analysis. The finite element method has been used in this research work for the analysis of pile group responses to twin tunneling at different distances between

TABLE 3: Parameters for contact elements.

Parameter	Value
Shear modulus (MPa)	26400
Normal modulus (MPa)	264000
Cohesion (kPa)	36
Internal friction angle ($^{\circ}$)	28

the tunnel and the pile, different distances between tunnel faces, and different pile lengths. Keeping the distance between the left and right tunnels constant, five different distances between the tunnel and the pile which are 3 m (i.e., $0.5D$ (D is the tunnel diameter)), 6 m (i.e., $1D$), 9 m (i.e., $1.5D$), 12 m (i.e., $2D$), and 15 m (i.e., $2.5D$) are considered. Note that the distance between the tunnel and the pile is the minimum horizontal distance between the left tunnel and the pile group. Also, five different distances between tunnel faces, defined as the difference in the y -coordinate values of the left tunnel face and the right tunnel face, are considered for capturing the effects of this parameter on the displacement and stress behavior of the pile group. The considered distances between tunnel faces are 10, 20, 30, 40, and 50 m. The considered four different pile lengths are 10, 20, 30, and 40 m.

4. Development of Ground and Pile Responses with Advancing Tunneling Steps

4.1. Ground Surface Settlements. The tunneling-induced ground surface settlements at $y = 21$ m by the 3D finite element analysis and *in situ* monitoring are shown in Figure 6. In general, a good agreement between the 3D finite element analysis and *in situ* monitoring results can be observed. This indicates that the 3D finite element method adopted in this study has the ability to well capture the responses of the ground surface to twin tunneling at different tunneling steps. Moreover, it can be seen that as the tunnel face approaches $y = 21$ m, the ground surface settlements increase gradually. However, the rates of increases in the ground surface settlements decrease as the tunnel face exceeds $y = 21$ m. The settlement versus step curves of steps 5 to 9 show that, when the distance between the left tunnel face and $y = 21$ m is less than $1D$, the variation of the ground surface settlements reaches the maximum, which is 3.2 mm. However, when that distance is larger than $2D$, the variation of the ground surface settlements with progressing tunneling steps is relatively small with a maximum value of 1.3 mm, as indicated by ground settlements of steps 13 to 32. Particularly, no matter what the tunneling step is, the ground surface settlement at the tunnel axis is larger than that at other locations. The maximum ground surface settlement, which is 6.9 mm, is achieved at the left tunnel axis at tunneling step 32.

The ground surface settlements at the right tunnel axis are similar in tendency to that at the left tunnel axis. However, the maximum variation of the ground surface settlements at the right tunnel axis when the right tunnel face is in the area of $\pm D$ with respect to $y = 21$ m is 3.6 mm, which is slightly larger than that at the left tunnel (i.e., 3.2 mm). The ultimate ground surface settlement at the right tunnel

axis is the maximum, which is 8.4 mm. In addition, previous studies have indicated that the tunneling influence zones depend primarily on parameters such as the tunnel diameter, tunnel cover depth, and soil parameters [54–56]. Based on the calculation methods used in the literature and the practical conditions presented in this research work, the diameter of the tunneling influence zones for twin tunneling is approximately 23 m. Thus, obvious superimposed effects can be observed for the ground surface settlements between the two axes of the left tunnel and the right tunnel.

Due to the fact that the pile group is nearer to the left tunnel than to the right tunnel, the inhibiting effects of the pile cap on the ground surface settlement are more observable at the left tunnel axis compared to the right tunnel axis. Hence, the maximum superimposed effects of twin tunneling-induced ground settlements occur at a data collection point that is nearer to the left tunnel than to the right tunnel.

Figure 7 presents the ground surface settlements at $y = 4$ m obtained by the 3D finite element analysis and *in situ* monitoring for various tunneling steps. A comparison between Figures 6 and 7 indicates that the settlement curves presented in Figure 6 are in a better symmetry with respect to $x = 0$ compared to the settlement curves presented in Figure 7. It is indicated by Figure 7 that the ultimate ground surface settlements at the left tunnel axis and at the right tunnel axis are, respectively, 6.9 mm and 8.6 mm. The maximum superimposed effects of twin tunneling-induced ground surface settlements occur almost in the lateral middle of the two tunnels, which is in good agreement with the ground surface settlements' tendency predicted using the Peck formula. Consequently, the pile-to-tunnel distance affects significantly the twin tunneling-induced ground surface settlements.

A comparison of the ground surface settlement at Point A and the pile cap settlement at Point B by the 3D finite element analysis and *in situ* monitoring is shown in Figure 8. Points A and B are at $y = 30$, as depicted in Figure 5. The comparison indicates that when the distance between the left tunnel face and $y = 30$ is less than $2.5D$, the settlements at Points A and B increase with progressing tunneling steps at a relatively high rate. However, when that distance is larger than $2.5D$, the rate of increase in the settlements at Points A and B reduces gradually until reaching a steady settlement. The ultimate settlements at Points A and B are, respectively, 3.6 mm and 4.6 mm. During the whole tunneling process, the settlement at Point A is consistently larger than that at Point B. This is because the pile cap stiffness is greater than the ground stiffness. The stability of the pile group is reduced due to the relative displacement between the pile and the soil around the pile resulting from the differential settlements between them. Thus, special attention should be paid to that issue in practical engineering so as to avoid undesirable accidents.

4.2. Horizontal Pile Displacement. The finite element analysis results indicate comparable horizontal displacements for different piles in the group. Therefore, for convenience, in this section, only the horizontal displacement of Pile 1 is discussed. Figure 9 shows the variation of the horizontal

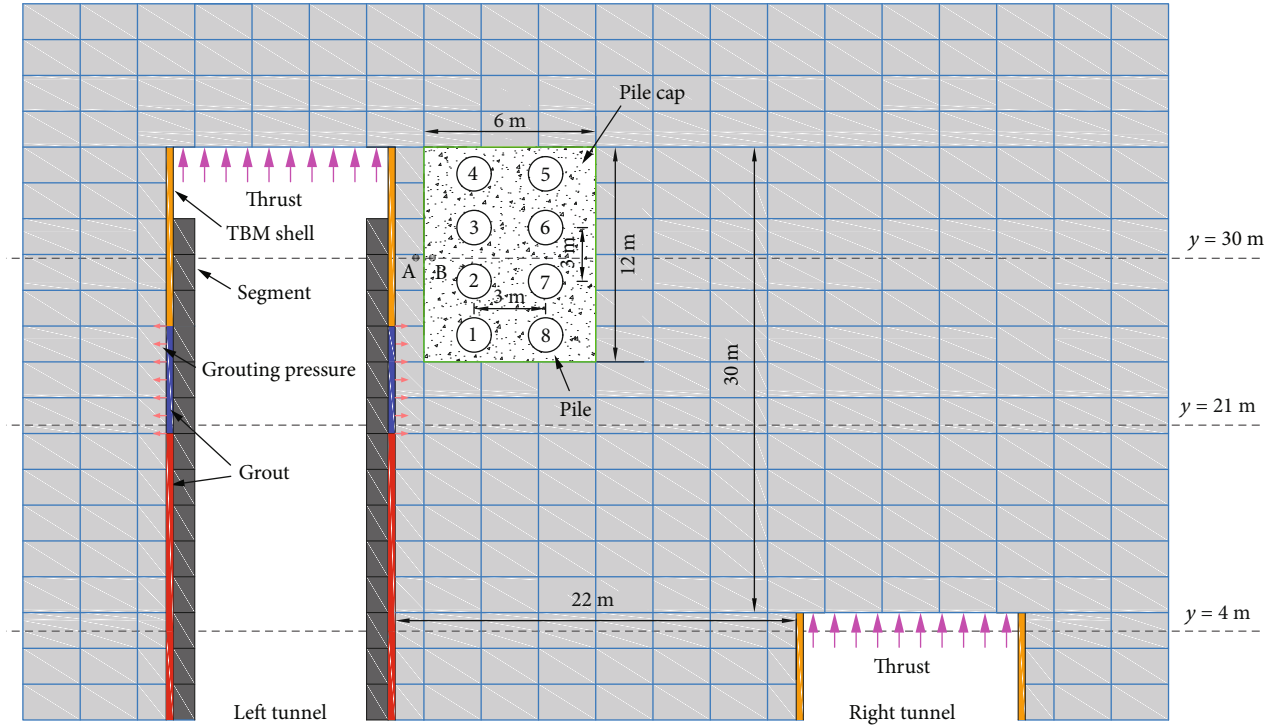


FIGURE 5: Schematic diagram of twin tunneling.

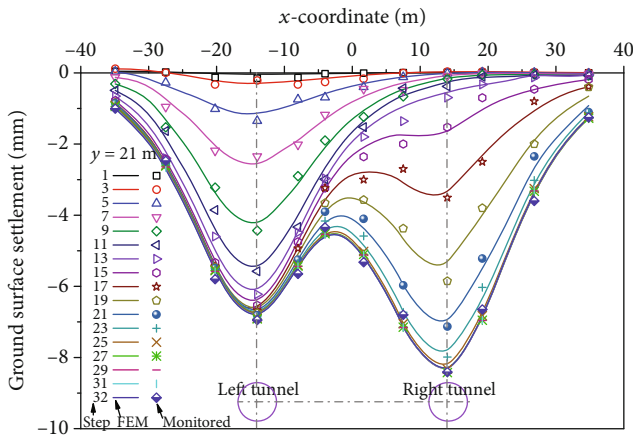


FIGURE 6: Ground surface settlement troughs at $y = 21$ m by the finite element method (FEM) and *in situ* monitoring.

displacement of Pile 1 with tunneling steps. Note that in Figure 9, the monitored horizontal pile displacement is only available at the pile top due to the difficulty in installing instruments on the pile shaft below the ground surface. It can be indicated that the horizontal displacement of Pile 1 is relatively small at tunneling steps 1 to 7. During these tunneling steps, the shortest distance between the tunnel face and the pile group is larger than $2D$. When this distance decreases from $2D$ to $1.5D$, the horizontal displacement of Pile 1 increases gradually. In addition, the distribution along the pile shaft of the horizontal displacement of Pile 1 is approximately S-shaped, with the horizontal displacements

at the pile top and bottom being negative and at the cover depth of the tunnel centerline being positive.

During tunneling steps 7 to 10, when the shortest distance between the tunnel face and the pile group is no more than $1D$, the variation of the horizontal displacement of Pile 1 is the maximum. Similarly, the variation of the horizontal displacement of Pile 1 at the cover depth of the tunnel centerline reaches the maximum (i.e., 1.3 mm). The maximum horizontal displacement of Pile 1 at the cover depth of the tunnel centerline (i.e., 1.9 mm) is achieved at tunneling step 10. The negative displacements at the pile top and pile bottom remain increasing when the tunneling step progresses from 7 to 10. Because the pile bottom is penetrated into bedrock, the horizontal displacement of the pile bottom is slightly smaller than that of the pile shaft above the pile bottom, which results in a point of inflection for the pile shaft. Progressing tunneling steps from 11 to 15, it is found that the positive horizontal displacement at the cover depth of the tunnel centerline decreases, while the negative horizontal displacements at the pile top and pile bottom increase. The maximum negative horizontal displacement is 2.4 mm. No apparent variation occurs of the horizontal displacement of Pile 1 after reaching tunneling step 15, when the shortest distance between the tunnel face and the pile group is larger than $3D$. A point of inflection is generated at the pile shaft of the cover depth being slightly smaller than that of the tunnel centerline. The horizontal displacements of the pile shaft above the point of inflection decrease with an increase in the tunneling steps due to a relatively looser constraint that back-fill soil poses on the pile shaft than clay.

In fact, during the whole tunneling process, the primary reason for a gradual increase in the positive horizontal

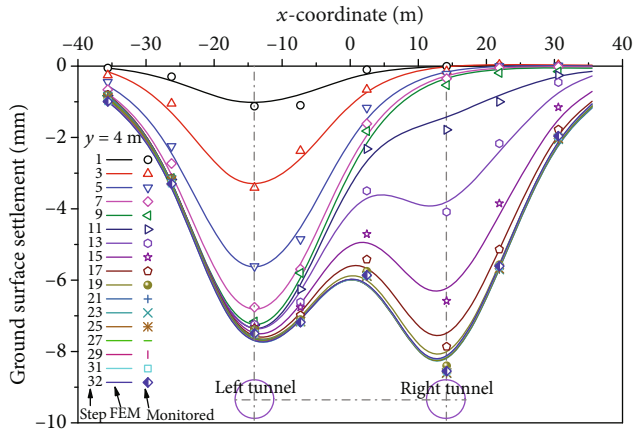


FIGURE 7: Ground surface settlement troughs at $y = 4$ m by the finite element method (FEM) and *in situ* monitoring.

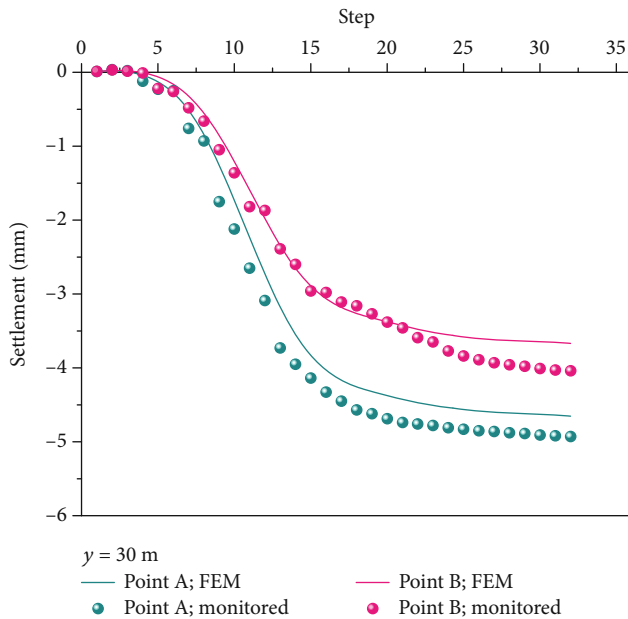


FIGURE 8: Settlements at Points A and B by the finite element method (FEM) and *in situ* monitoring.

displacement of Pile 1 is that the support pressure of the left tunnel is larger than the stress-releasing effects of the soil around the left tunnel induced by the left tunneling. However, the positive horizontal displacement of Pile 1 will be restrained and even reduced due to the gradual decrease in the left tunnel support pressure caused by the TBM shell's absence and hardening of the grout and due to the support pressure induced by the right tunneling.

Figure 10 shows horizontal displacements of different piles in the pile group foundation at tunneling step 32. For convenience, Piles 1, 2, 3, and 4, which are nearer to the left tunnel compared to the other four piles, are termed the front piles, and the other four piles (i.e., Piles 5, 6, 7, and 8) are termed the back piles. It can be seen from Figure 10 that the ultimate horizontal displacements of the front piles are

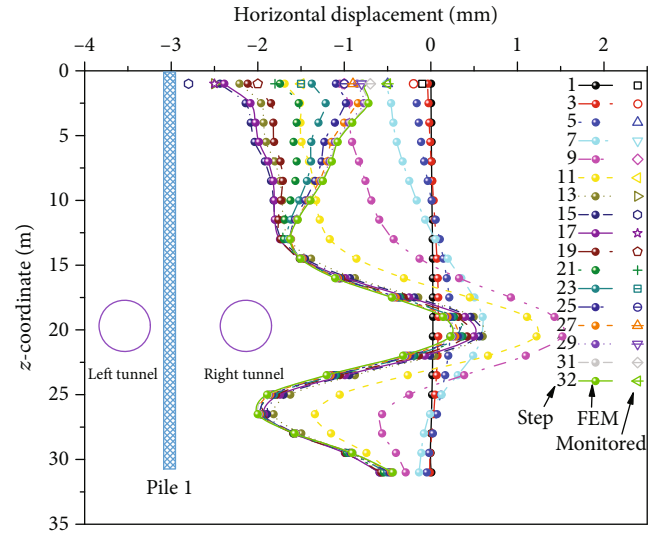


FIGURE 9: Horizontal displacements of Pile 1 at different tunneling steps.

generally larger than that of the back piles, although their distributions along the pile shaft of the ultimate horizontal displacements are similar in form. The positive horizontal displacements of the front piles at the cover depth of the tunnel centerline are larger than that of the back piles, resulting from a larger support pressure of the left tunnel subjected by the front piles than by the back piles due to a relatively smaller distance between the front pile and the left tunnel.

Figure 10 also indicates that the negative horizontal displacements at pile tops and pile bottoms of the front piles are larger than that of the back piles. This involves two reasons, which are, first, a relatively larger value for the left tunneling-induced stress-releasing effects subjected by the front piles than by the back piles and, second, a smaller value for both the right tunneling-induced stress-releasing effects and the support pressure of the right tunnel resulting from the shielding effects of the back piles. Consequently, the distributions along the pile shaft of the horizontal displacement are similar in form between the front and back piles, but the magnitude of the horizontal displacement of the front piles is slightly larger than that of the back piles.

4.3. Vertical Pile Displacement. Figure 11 shows the variation of the vertical displacement of Pile 1 with tunneling steps. It is indicated that the pile top settles most, and the settlements at the pile shaft decrease gradually with an increase in the cover depth till reaching maxima at a cover depth. After this, the pile shaft heaves slightly. The settlement of Pile 1 is no more than 1 mm from tunneling steps 1 to 5 when the shortest distance between the tunnel face and the pile group exceeds $2D$. The rate of increase in the vertical displacement of Pile 1 increases with progressing tunneling steps from 5 to 11, during which the shortest distance between the tunnel face and the pile group reduces from $2D$ to $1D$. After reaching tunneling step 11, the rate of increase in the vertical displacement of Pile 1 starts to reduce until tunneling step 15, after which the vertical displacement of Pile 1 turns to be an

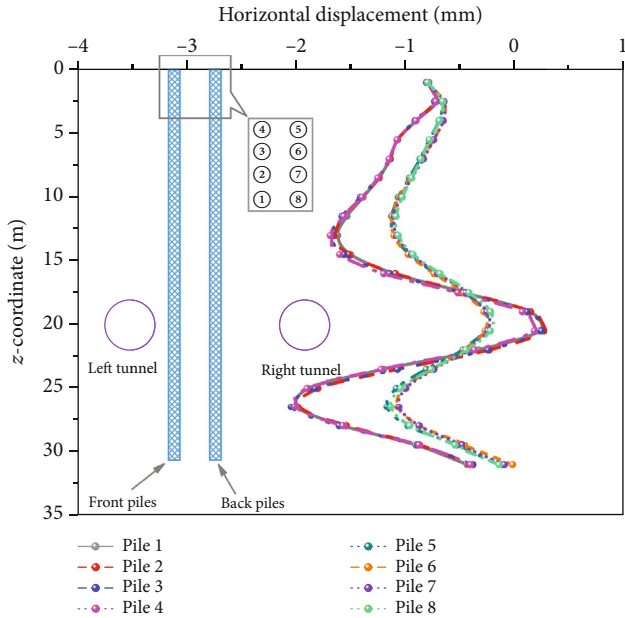


FIGURE 10: Horizontal pile displacements on completion of twin tunneling.

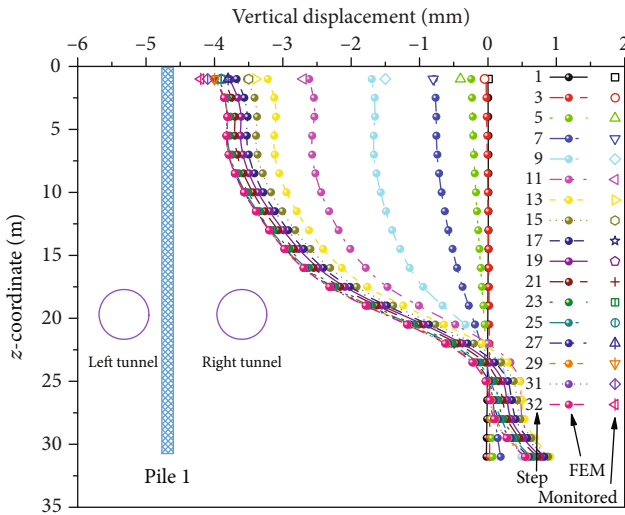


FIGURE 11: Vertical displacements of Pile 1 at different tunneling steps.

almost steady value. At last, the pile top settlement reaches the maximum with a value of 3.9 mm, while a maximum heave (i.e., 0.5 mm) appears at the pile bottom.

The vertical displacement of the pile and its distribution along the pile shaft are attributed to the tunneling-induced stress-releasing effects subjected by the soil around the tunnel, which can induce movements of the soil around the tunnel and of the pile penetrated in the soil to the tunnel centerline. Moreover, the magnitude and direction of this movement of the pile depend primarily on the relative location and distance between the tunnel centerline and the pile shaft.

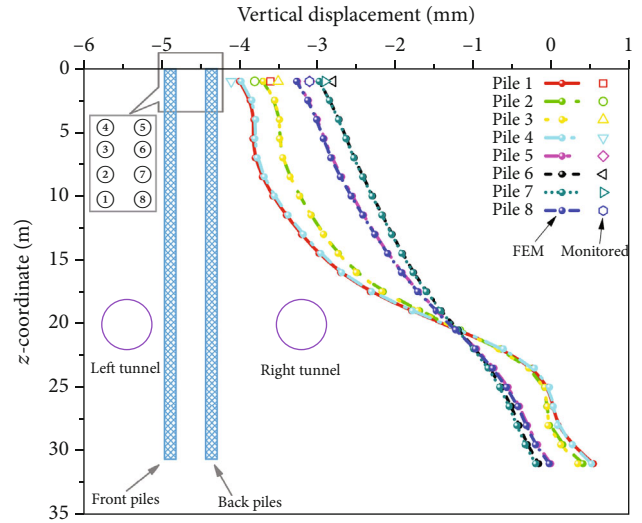


FIGURE 12: Vertical pile displacements on completion of twin tunneling.

It is observed from Figure 12 that the vertical displacements of the front piles are larger in magnitude than that of the back piles. Among the front piles, the two corner piles (i.e., Piles 1 and 4) settle most compared to the other front piles. But the vertical displacements of Piles 6 and 7 in the back piles are the minima. Nevertheless, the distributions along the pile shaft of the vertical displacement of all the piles in the pile group are almost identical. Thus, twin tunneling-induced pile responses are varied for different piles in the pile group. By comparison, the corner piles in the pile group are more susceptible to twin tunneling than the middle piles, demonstrating that the interactions between piles in the pile group provide protection of the middle piles in the pile group against twin tunneling effects.

4.4. Axial Pile Stress. The distributions along the pile shaft of the axial stresses of different piles in the pile group are presented in Figure 13. It is observed that all the piles are under compression over the entire pile shaft with a most identical distribution form of axial pile stress. The compressive stress along the pile shaft increases from the ground surface to the cover depth of the tunnel centerline. After reaching the cover depth of the tunnel centerline, the magnitude of the compressive stress decreases with a further increase in the cover depth. Hence, the maximum compressive stress in Pile 1 (i.e., 17.3 MPa) is achieved at the cover depth of the tunnel centerline, while the compressive stress at the bottom of Pile 13, which is 9.3 MPa, is the minimum.

Before twin tunneling, initial compressive stress exists in the pile group, which is generated by the pile weight and the uniform load applied on the pile cap. However, this initial compressive stress has been changed since the beginning of twin tunneling, resulting from the relative displacement between the pile shaft and the soil around the pile induced by the soil's stress-releasing effects. The magnitude of the relative displacement in the pile-soil interface depends primarily on the cover depth of the pile shaft. Above the pile shaft of the cover depth of the tunnel centerline, the relative

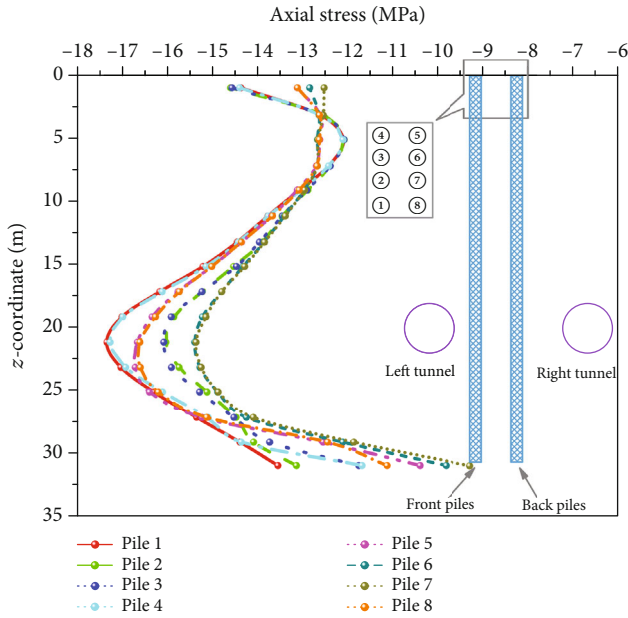


FIGURE 13: Axial pile stresses on completion of twin tunneling.

displacement in the pile-soil interface induces negative friction along the pile-soil interface, and the magnitude of which increases with an increase in the cover depth. On the contrary, positive friction has been induced along the pile-soil interface below the pile shaft of the cover depth of the tunnel centerline. Consequently, the magnitude of the twin tunneling-induced compressive stress increases with an increase in the cover depth of the pile shaft until reaching the cover depth of the tunnel centerline, after which a further increase in the cover depth of the pile shaft results in a reduction in the compressive stress along the pile shaft.

5. Discussion

5.1. Effect of the Distance between the Tunnel and the Pile. Figure 14 shows the variation of the twin tunneling-induced horizontal displacement of Pile 1 with the distance between the tunnel and the pile. When the distance between the tunnel and the pile increases from 3 m to 9 m, Pile 1 moves more further to the left tunnel, which means a reduction in the horizontal displacement of Pile 1. Particularly, the variation of the maximum horizontal displacement of Pile 1 is larger than that of any other horizontal displacement of the pile shaft. A rather small horizontal displacement ranging from -0.3 to 0.2 mm is produced of Pile 1 at a pile-to-tunnel distance of 9 m. The pile group approaches the right tunnel gradually when the pile-to-tunnel distance increases from 9 to 15 m. At this time, the horizontal displacement distribution along the pile shaft of Pile 1 becomes apposite to the case where the pile-to-tunnel distance is 3 or 6 m.

Figure 15 presents the vertical displacements of Pile 1 induced by twin tunneling at different distances between the tunnel and the pile. Pile settlement occurs at all the considered distances between the tunnel and the pile. The effects of the left tunneling on pile settlement decrease with an

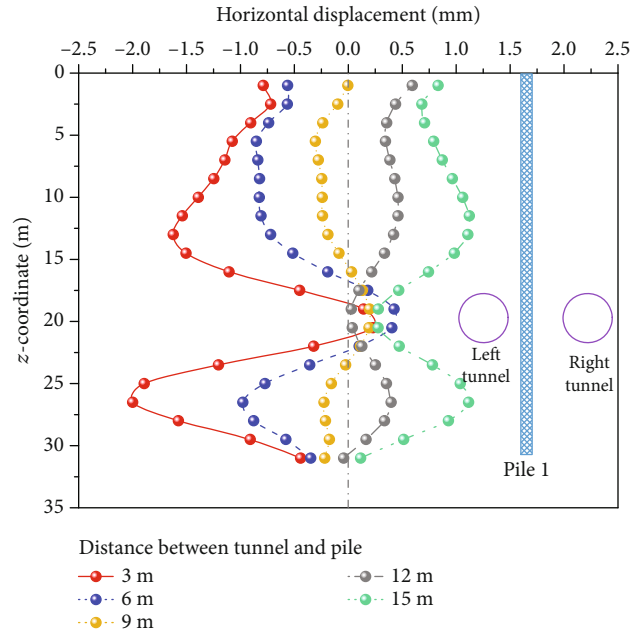


FIGURE 14: Horizontal displacements of Pile 1 on completion of twin tunneling at different pile-to-tunnel distances.

increase in the distance between the tunnel and the pile, which is characterized by a reduction in the vertical pile displacement. The pile top settlement reduces from 3.9 to 3 mm, and the vertical displacement at the pile bottom changes from 0.5 to -0.1 mm when increasing the distance between the tunnel and the pile from 3 to 12 m. The pile group becomes closer to the right tunnel than to the left tunnel at a distance between the tunnel and the pile of 15 m. In this circumstance, the vertical pile displacement is affected predominantly by the right tunnel rather than the left tunnel.

The axial stress of Pile 1 induced by twin tunneling at different distances between the tunnel and the pile is shown in Figure 16. It is shown that the axial stress distributions along the pile shaft are consistent at different distances between the tunnel and the pile. The maximum axial pile stress reduces slightly with an increase in the distance between the tunnel and the pile due to a lower magnitude of the relative displacement in the pile-soil interface.

Consequently, the horizontal pile displacement is most susceptible to the distance between the tunnel and the pile compared to the other responses of the pile group to twin tunneling. Thus, in engineering practices, a larger distance between the tunnel and the pile is recommended for twin tunneling adjacent to an existing pile group foundation. Moreover, it should be taken into consideration that the distance between the left and right tunnels is subjected to constraints. By comparison, the optimal distance between the tunnel and the pile for the engineering case presented herein is 9 m. More importantly, a recommendation can be made for the design of twin tunneling adjacent to an existing pile group that the pile group should be placed in the middle of the left and right tunnels in order to minimize the adverse effects of twin tunneling on pile group responses.

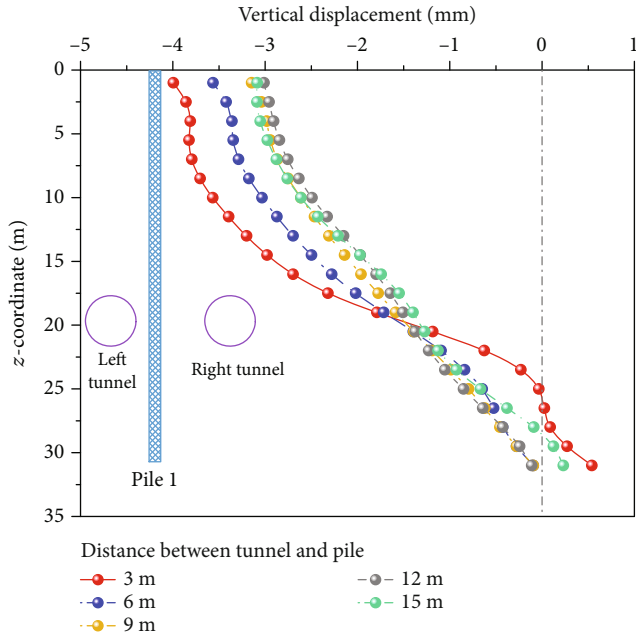


FIGURE 15: Vertical displacements of Pile 1 on completion of twin tunneling at different pile-to-tunnel distances.

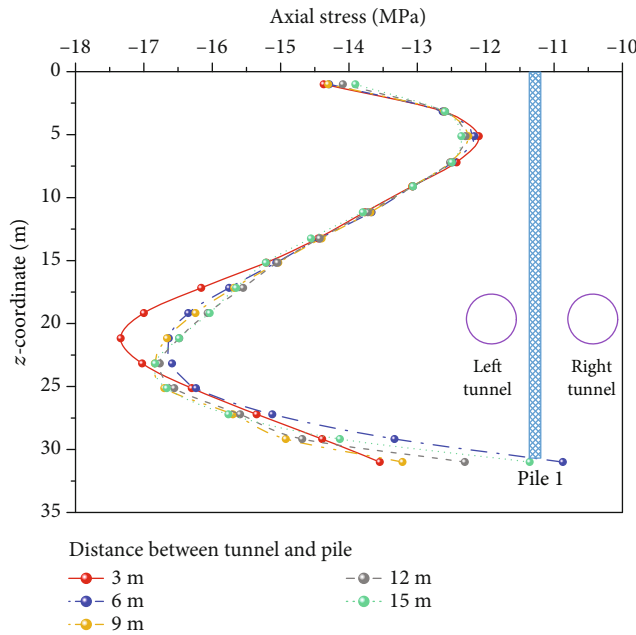


FIGURE 16: Axial displacements of Pile 1 on completion of twin tunneling at different pile-to-tunnel distances.

5.2. *Effect of the Distance between Tunnel Faces.* Figure 17 shows the variations of the maximum positive and negative horizontal displacements of Pile 1 on completion of twin tunneling with the distance between tunnel faces. From this figure, it can be indicated that both the maximum positive and negative horizontal displacements increase nonlinearly with an increase in the distance between tunnel faces. However, the rate of the increase becomes smaller at a larger mag-

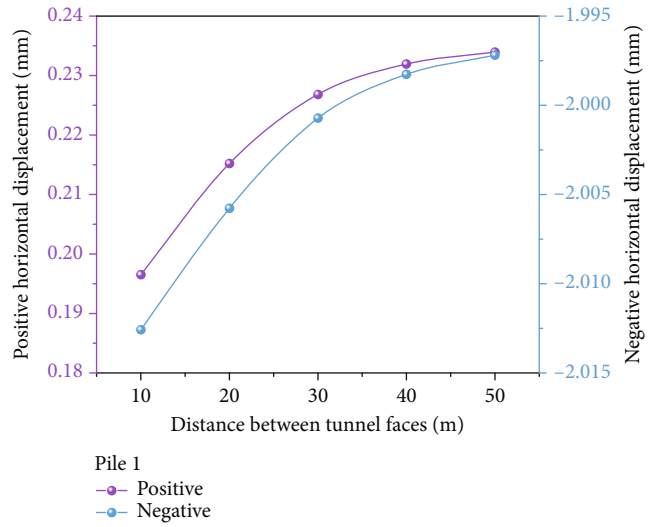


FIGURE 17: Maximum horizontal displacements of Pile 1 on completion of twin tunneling at different tunnel face-to-face distances.

nitude of the distance between tunnel faces. When the distance increases from 10 to 50 m, the maximum positive and negative horizontal displacements increase, respectively, from approximately 0.195 mm to about 0.235 mm and from approximately 0.185 mm to about -2.0175 mm to about -1.9975 mm. Nevertheless, the effect of the distance between tunnel faces on the maximum horizontal displacement of Pile 1 is negligible, as the variations in these values are generally less than 0.1 mm which can be also neglected.

Figure 18 presents the variations of the maximum positive and negative vertical displacements of Pile 1 on completion of twin tunneling with the distance between tunnel faces. It is shown that when the distance between tunnel faces increases from 10 to 50 m, the variation of the maximum positive vertical displacement is less than 0.01 mm, while the variation of the maximum negative vertical displacement is less than 0.25 mm. These extremely small variations demonstrate that the distance between tunnel faces has a trivial effect on the maximum positive and negative vertical pile displacements induced by twin shield tunneling in clays. In addition, a further comparison between the variational trends in Figures 17 and 18 indicates that the maximum positive displacements in both the horizontal and vertical directions are one order of magnitude lower than the maximum negative displacements in both the horizontal and vertical directions. Hence, increasing the distance between tunnel faces within certain limits does benefit the stability of the pile group.

The variations of the maximum and minimum axial stresses of Pile 1 on completion of twin tunneling with the distance between tunnel faces are shown in Figure 19. It is observed that the maximum and minimum axial pile stresses increase slightly, while the difference between the maximum and minimum axial pile stresses decreases with an increase in the distance between tunnel faces. This demonstrates that a relatively uniform distribution of the axial pile stress along the pile shaft can be achieved by increasing the distance

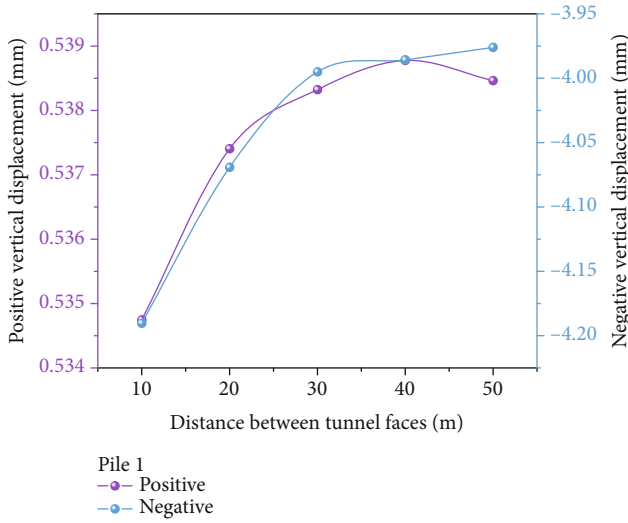


FIGURE 18: Maximum vertical displacements of Pile 1 on completion of twin tunneling at different tunnel face-to-face distances.

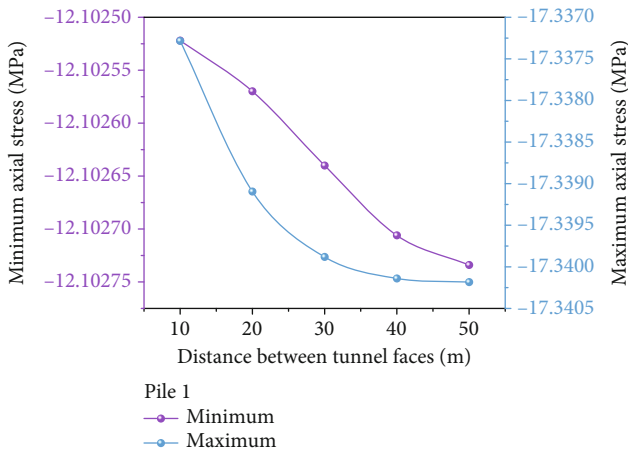


FIGURE 19: Maximum and minimum axial stresses of Pile 1 on completion of twin tunneling at different tunnel face-to-face distances.

between tunnel faces. After the distance between tunnel faces exceeds 30 m, a further increase in the distance between tunnel faces results in no apparent variation in the horizontal and vertical displacements and axial pile stress. Moreover, a shorter construction period is favored in practical engineering practices for maximizing the economic benefits. Thus, 30 m has been chosen as the optimal distance between tunnel faces for the twin tunneling engineering case presented in this study for the purpose of achieving a balance between maximizing economic benefits and minimizing pile group responses induced by twin tunneling.

5.3. Effect of the Pile Length. Figure 20 presents the variation of the pile settlement with the cover depth for various pile lengths. It is found that the maximum pile settlement occurs at the pile bottom at relatively low pile lengths (i.e., 10 and 20 m). At relatively high pile lengths (i.e., 30 and 40 m), the

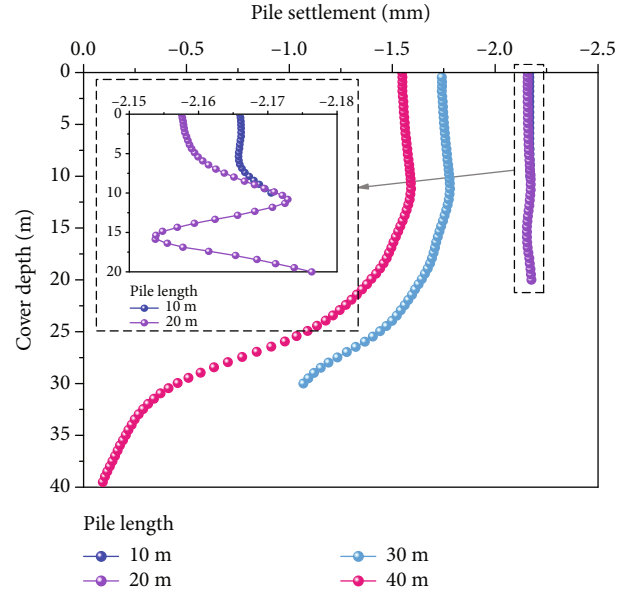


FIGURE 20: Variation of the pile settlement with the cover depth for different pile lengths.

maximum pile settlement occurs at a cover depth of appropriately 10 m. In general, the maximum pile settlement decreases with an increase in the pile length. This is mainly because a higher pile length corresponds to a larger side friction between the pile and the soil and a greater bearing capacity of the soil at the pile bottom. Moreover, the difference between the settlements at the pile top and bottom increases with an increase in the pile length. At the pile length of 10 m, the difference between the settlements at the pile top and bottom is 0.01 mm. This value increases to 1.5 mm at the pile length of 40 m. Nevertheless, an increase in the pile length from 10 m to 40 m leads to a decrease in the maximum pile settlement of 0.62 mm which is negligible. Therefore, it can be noted that the effect of the pile length is trivial on the magnitude of the pile settlement and is significant on the distribution of the pile settlement.

Figure 21 presents the variation of the horizontal pile displacement with the cover depth for different pile lengths. It can be seen that the distribution of the horizontal pile displacement along the pile shaft is similar at different pile lengths. At a pile length, the horizontal pile displacement decreases with an increase in the cover depth until reaching the cover depth of the twin tunnels (i.e., 20 m). After this, the horizontal pile displacement increases with an increase in the cover depth until reaching a cover depth of appropriately 30 m. With an increase in the pile length, the horizontal displacement at the pile top decreases till reaching the pile length of 30 m and then increases again when the pile length increases from 30 to 40 m. Moreover, it seems that an increase in the pile length has a tendency to reduce the maximum negative horizontal pile displacement. However, the reduction in the maximum negative horizontal pile displacement due to an increase in the pile length is negligible.

Figure 22 presents the variations of the maximum and minimum axial pile stresses with the pile length. It is clear

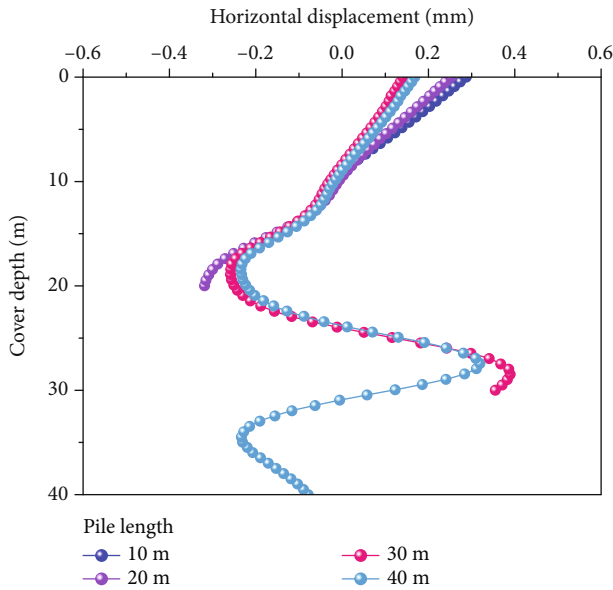


FIGURE 21: Variation of the horizontal pile displacement with the cover depth for different pile lengths.

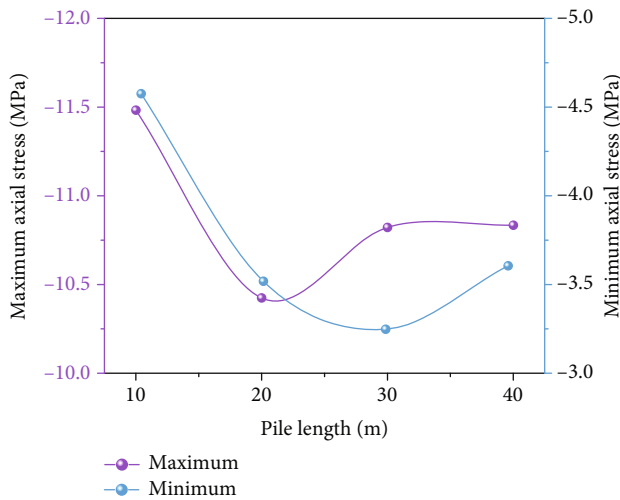


FIGURE 22: Variation of the maximum and minimum axial pile stresses with the pile length.

in Figure 22 that the relatively low maximum and minimum axial pile stresses can be achieved at a pile length ranging between 20 and 30 m. At the pile length of 10 m, the maximum and minimum axial pile stresses are far beyond that at the other three pile lengths. The reason for this is that the side friction between the pile and the soil is greater at a relatively low pile length.

6. Conclusions

Ground surface settlements and pile group responses induced by twin tunneling in clays have been investigated by performing 3D finite element analysis validated with the *in situ* monitoring data. The characteristics of the develop-

ment of twin tunneling-induced ground surface settlements, horizontal and vertical pile displacements, and axial pile stresses with advancing tunneling steps were captured. The effects of the distance between the tunnel and the pile, the distance between tunnel faces, and the pile length on the pile group responses were discussed. The main conclusions that can be drawn from this study are summarized as follows:

- (i) The ground surface settlements increase nonlinearly with progressing tunneling steps. The rates of increases in the ground surface settlements achieve maxima when the tunnel faces reach the positions under consideration. At any of the tunneling steps, the ground surface settlements are greater at the tunnel centerlines compared to the other positions. The maximum ground surface settlements at the centerlines of the left tunnel and right tunnel are, respectively, 7.9 mm and 8.6 mm
- (ii) The horizontal pile displacements change from being negative at the pile tops to being positive at the cover depth of the tunnel centerline. A maximum horizontal pile displacement of 1.5 mm is achieved at tunneling step 9. The vertical pile displacements decrease with an increase in the cover depth until reaching a cover depth of approximately 23 mm, after which a pile heave occurs. The distributions along the pile shafts of axial pile stresses are similar for different piles in the pile group
- (iii) Compared to the vertical pile displacements and axial pile stresses, the horizontal pile displacements are more susceptible to the distance between the tunnel and the pile. A distance between the tunnel and the pile of 9 m is found to be optimum for the considered engineering case. An increase in the distance between tunnel faces reduces the maximum negative horizontal and vertical pile displacements, improves the pile group stability, and facilitates a more uniform distribution along the pile shaft of the axial pile stress. The optimum distance between tunnel faces is found to be 30 m. The effect of the pile length is more significant on the distribution of the pile settlement than on the magnitude of the pile settlement. The axial pile stresses reach the minimum when the pile length is slightly greater than the cover depth of the twin tunnels

Data Availability

Some or all data, models, or codes generated or used during the study are available from the corresponding authors by request.

Conflicts of Interest

The authors declare that they have no conflicts of interest.

Acknowledgments

This research work was funded by the National Natural Science Foundation of China (51774107, 42077249) and the Opening Project of State Key Laboratory of Explosion Science and Technology, Beijing Institute of Technology (KFJJ21-03Z).

References

- [1] Y. Xiang, S. He, Z. Cui, and S. Ma, "A subsurface "drift and pile" protection scheme for the construction of a shallow metro tunnel," *Tunnelling and Underground Space Technology*, vol. 20, no. 1, pp. 1–5, 2005.
- [2] Q. Fang, D. Zhang, and L. N. Y. Wong, "Shallow tunnelling method (STM) for subway station construction in soft ground," *Tunnelling and Underground Space Technology*, vol. 29, pp. 10–30, 2012.
- [3] K. H. Park, "Elastic solution for tunneling-induced ground movements in clays," *International Journal of Geomechanics*, vol. 4, no. 4, pp. 310–318, 2004.
- [4] M. Nematollahi and D. Dias, "Three-dimensional numerical simulation of pile-twin tunnels interaction – case of the Shiraz subway line," *Tunnelling and Underground Space Technology*, vol. 86, pp. 75–88, 2019.
- [5] F. Basile, "Effects of tunnelling on pile foundations," *Soils and Foundations*, vol. 54, no. 3, pp. 280–295, 2014.
- [6] C. Liu, Z. Zhang, and R. A. Regueiro, "Pile and pile group response to tunnelling using a large diameter slurry shield – case study in Shanghai," *Computers and Geotechnics*, vol. 59, pp. 21–43, 2014.
- [7] Y. Wang, C. H. Li, and J. Q. Han, "On the effect of stress amplitude on fracture and energy evolution of pre-flawed granite under uniaxial increasing-amplitude fatigue loads," *Engineering Fracture Mechanics*, vol. 240, article 107366, 2020.
- [8] A. Davarpanah, R. Shirmohammadi, B. Mirshekari, and A. Aslani, "Analysis of hydraulic fracturing techniques: hybrid fuzzy approaches," *Arabian Journal of Geosciences*, vol. 12, no. 13, p. 402, 2019.
- [9] L. Cao, D. Zhang, X. Shen, J. Su, H. Fang, and D. Su, "Horizontal mechanical responses of single pile due to urban tunnelling in multi-layered soils," *Computers and Geotechnics*, vol. 135, article 104164, 2021.
- [10] F. Peng and S. Ma, "Analysis of experimental data on the effect of double-line parallel shield tunneling on the deformation of adjacent buildings," *Alexandria Engineering Journal*, vol. 60, no. 4, pp. 3957–3963, 2021.
- [11] Y. Wang, Y. F. Yi, C. H. Li, and J. Q. Han, "Anisotropic fracture and energy characteristics of a Tibet marble exposed to multi-level constant-amplitude (MLCA) cyclic loads: a lab-scale testing," *Engineering Fracture Mechanics*, vol. 244, p. 107550, 2021.
- [12] G. Mollon, D. Dias, and A.-H. Soubra, "Probabilistic analyses of tunneling-induced ground movements," *Acta Geotechnica*, vol. 8, no. 2, pp. 181–199, 2013.
- [13] Z. Zhang, M. Huang, Y. Pan et al., "Analytical prediction of time-dependent behavior for tunneling-induced ground movements and stresses subjected to surcharge loading based on rheological mechanics," *Computers and Geotechnics*, vol. 129, p. 103858, 2021.
- [14] J.-F. Zhu, R.-Q. Xu, and G.-B. Liu, "Analytical prediction for tunnelling-induced ground movements in sands considering disturbance," *Tunnelling and Underground Space Technology*, vol. 41, pp. 165–175, 2014.
- [15] M. Zhu, L. Yu, X. Zhang, and A. Davarpanah, "Application of implicit pressure-explicit saturation method to predict filtrated mud saturation impact on the hydrocarbon reservoirs formation damage," *Mathematics*, vol. 8, no. 7, article 1057, 2020.
- [16] S. Sun, M. Zhou, W. Lu, and A. Davarpanah, "Application of symmetry law in numerical modeling of hydraulic fracturing by finite element method," *Symmetry*, vol. 12, no. 7, article 1122, 2020.
- [17] K. M. Neaupane and N. R. Adhikari, "Prediction of tunneling-induced ground movement with the multi-layer perceptron," *Tunnelling and Underground Space Technology*, vol. 21, no. 2, pp. 151–159, 2006.
- [18] Y.-S. Fang, C.-T. Wu, S.-F. Chen, and C. Liu, "An estimation of subsurface settlement due to shield tunneling," *Tunnelling and Underground Space Technology*, vol. 44, pp. 121–129, 2014.
- [19] R. B. Peck, "Deep excavation and tunneling in soft ground," in *Proceedings of the 7th International Conference on Soil Mechanics and Foundation Engineering*, pp. 225–290, Mexico City, 1969.
- [20] R. J. Mair, M. J. Gunn, and M. P. O'Reilly, "Ground movements around shallow tunnels in soft clay," in *Proceedings of the 10th international conference on soil mechanics and foundation engineering*, pp. 323–328, Stockholm, Sweden, 1981.
- [21] B. M. New and M. P. O'Reilly, "Tunnelling induced ground movements, predicting their magnitude and effects," in *Proceedings of the 4th Conference on Ground Movements and Structures*, pp. 671–697, Cardiff, 1991.
- [22] L. Z. Wang, L. L. Li, and X. J. Lv, "Complex variable solutions for tunneling-induced ground movement," *International Journal of Geomechanics*, vol. 9, no. 2, pp. 63–72, 2009.
- [23] M. N. Vu, W. Broere, and J. Bosch, "Effects of cover depth on ground movements induced by shallow tunnelling," *Tunnelling and Underground Space Technology*, vol. 50, pp. 499–506, 2015.
- [24] N. Loganathan and H. G. Poulos, "Analytical prediction for tunneling-induced ground movements in clays," *Journal of Geotechnical and Geoenvironmental Engineering*, vol. 124, no. 9, pp. 846–856, 1998.
- [25] T. B. Celestino, R. A. M. P. Gomes, and A. A. Bortolucci, "Errors in ground distortions due to settlement trough adjustment," *Tunnelling and Underground Space Technology*, vol. 15, no. 1, pp. 97–100, 2000.
- [26] Y. Shi, J. Fu, J. Yang, C. Xu, and D. Geng, "Performance evaluation of long pipe roof for tunneling below existing highway based on field tests and numerical analysis: case study," *International Journal of Geomechanics*, vol. 17, no. 9, article 04017054, 2017.
- [27] P. Guo, X. Gong, and Y. Wang, "Displacement and force analyses of braced structure of deep excavation considering unsymmetrical surcharge effect," *Computers and Geotechnics*, vol. 113, article 103102, 2019.
- [28] P. Jongpradist, T. Kaewsri, A. Sawatpanich et al., "Development of tunneling influence zones for adjacent pile foundations by numerical analyses," *Tunnelling and Underground Space Technology*, vol. 34, pp. 96–109, 2013.
- [29] S. W. Jacobsz, K. H. Bowers, N. A. Moss, and G. Zanardo, "The effects of tunnelling on piled structures on the CTRL," in

- Geotechnical Aspects of Underground Construction in Soft Ground*, pp. 115–122, Taylor & Francis Group, Amsterdam, 2005.
- [30] J. Zhou, X. Shi, K. Du, X. Qiu, X. Li, and H. S. Mitri, “Feasibility of random-forest approach for prediction of ground settlements induced by the construction of a shield-driven tunnel,” *International Journal of Geomechanics*, vol. 17, no. 6, article 04016129, 2017.
- [31] M. A. Soomro, Y. Hong, C. W. W. Ng, H. Lu, and S. Peng, “Load transfer mechanism in pile group due to single tunnel advancement in stiff clay,” *Tunnelling and Underground Space Technology*, vol. 45, pp. 63–72, 2015.
- [32] Y. Xu and P. Guo, “Disturbance evolution behavior of loess soil under triaxial compression,” *Advances in Civil Engineering*, vol. 2020, Article ID 4160898, 14 pages, 2020.
- [33] R. Zhang, J. Zheng, and S. Yu, “Responses of piles subjected to excavation-induced vertical soil movement considering unloading effect and interfacial slip characteristics,” *Tunnelling and Underground Space Technology*, vol. 36, pp. 66–79, 2013.
- [34] Y. X. Wang, S. B. Shan, C. Zhang, and P. P. Guo, “Seismic response of tunnel lining structure in a thick expansive soil stratum,” *Tunnelling and Underground Space Technology*, vol. 88, pp. 250–259, 2019.
- [35] P. Guo, F. Liu, G. Lei et al., “Predicting response of constructed tunnel to adjacent excavation with dewatering,” *Geofluids*, vol. 2021, Article ID 5548817, 17 pages, 2021.
- [36] Y. Wang and M. Li, “Research on the deformation law of jointed surrounding rock during tunnel excavation based on hydromechanical coupling,” *Geofluids*, vol. 2021, Article ID 5583940, 13 pages, 2021.
- [37] E. Ieronymaki, A. J. Whittle, and H. H. Einstein, “Comparative study of the effects of three tunneling methods on ground movements in stiff clay,” *Tunnelling and Underground Space Technology*, vol. 74, pp. 167–177, 2018.
- [38] E. Cattoni, C. Miriano, L. Boco, and C. Tamagnini, “Time-dependent ground movements induced by shield tunneling in soft clay: a parametric study,” *Acta Geotechnica*, vol. 11, no. 6, pp. 1385–1399, 2016.
- [39] J. S. Shiau, M. S. Sams, J. Zhang, and R. J. Kemp, “Settlement analyses of underground circular tunneling in soft clay,” in *8th International Symposium on Geotechnical Aspects of Underground Construction in Soft Ground*, Seoul, South Korea, 2014.
- [40] M. Son, “Response analysis of nearby structures to tunneling-induced ground movements in clay soils,” *Tunnelling and Underground Space Technology*, vol. 56, pp. 90–104, 2016.
- [41] R. G. Laver, Z. Li, and K. Soga, “Method to evaluate the long-term surface movements by tunneling in London clay,” *Journal of Geotechnical and Geoenvironmental Engineering*, vol. 143, article 06016023, 2016.
- [42] H. Sun, J. Zhang, G. Zhao, and H. Wang, “Tunnel behaviour caused by basement excavation in clay,” *Geofluids*, vol. 2021, Article ID 5570846, 11 pages, 2021.
- [43] T. I. Addenbrooke and D. M. Potts, “Twin tunnel interaction: surface and subsurface effects,” *International Journal of Geomechanics*, vol. 1, no. 2, pp. 249–271, 2001.
- [44] A. Mirhabibi and A. Soroush, “Effects of building three-dimensional modeling type on twin tunneling-induced ground settlement,” *Tunnelling and Underground Space Technology*, vol. 38, pp. 224–234, 2013.
- [45] P. Guo, X. Gong, Y. Wang, H. Lin, and Y. Zhao, “Minimum cover depth estimation for underwater shield tunnels,” *Tunnelling and Underground Space Technology*, vol. 115, p. 104027, 2021.
- [46] Y. Hong, M. A. Soomro, and C. W. W. Ng, “Settlement and load transfer mechanism of pile group due to side-by-side twin tunnelling,” *Computers and Geotechnics*, vol. 64, pp. 105–119, 2015.
- [47] C. W. W. Ng, H. Lu, and S. Y. Peng, “Three-dimensional centrifuge modelling of the effects of twin tunnelling on an existing pile,” *Tunnelling and Underground Space Technology*, vol. 35, pp. 189–199, 2013.
- [48] M. A. Soomro, C. W. W. Ng, N. A. Memon, and R. Bhanbhro, “Lateral behaviour of a pile group due to side-by-side twin tunnelling in dry sand: 3D centrifuge tests and numerical modelling,” *Computers and Geotechnics*, vol. 101, pp. 48–64, 2018.
- [49] Y. Wang, P. Guo, F. Dai, X. Li, Y. Zhao, and Y. Liu, “Behavior and modeling of fiber-reinforced clay under triaxial compression by combining the superposition method with the energy-based homogenization technique,” *International Journal of Geomechanics*, vol. 18, no. 12, article 04018172, 2018.
- [50] Y. Wang, P. Guo, X. Li, H. Lin, Y. Liu, and H. Yuan, “Behavior of fiber-reinforced and lime-stabilized clayey soil in triaxial tests,” *Applied Sciences*, vol. 9, no. 5, p. 900, 2019.
- [51] Y. X. Wang, P. P. Guo, W. X. Ren et al., “Laboratory investigation on strength characteristics of expansive soil treated with jute fiber reinforcement,” *International Journal of Geomechanics*, vol. 17, no. 11, article 04017101, 2017.
- [52] Y. Wang, P. Guo, S. Shan, H. Yuan, and B. Yuan, “Study on strength influence mechanism of fiber-reinforced expansive soil using jute,” *Geotechnical and Geological Engineering*, vol. 34, pp. 1079–1088, 2016.
- [53] M. P. Komu, U. Guney, T. E. Kilickaya, and C. Gokceoglu, “Using 3D numerical analysis for the assessment of tunnel-landslide relationship: Bahce-Nurdag tunnel (south of Turkey),” *Geotechnical and Geological Engineering*, vol. 38, no. 2, pp. 1237–1254, 2020.
- [54] S. L. Chen, M. W. Gui, and M. C. Yang, “Applicability of the principle of superposition in estimating ground surface settlement of twin- and quadruple-tube tunnels,” *Tunnelling and Underground Space Technology*, vol. 28, pp. 135–149, 2012.
- [55] D. Jin, Z. Zhang, and D. Yuan, “Effect of dynamic cutterhead on face stability in EPB shield tunneling,” *Tunnelling and Underground Space Technology*, vol. 110, p. 103827, 2021.
- [56] D. Selemetas, “The response of full-scale piles and pile structures to tunneling, [Ph.D. thesis],” Cambridge University, 2005.

Research Article

Experimental Investigation into Limit Void Ratio Characteristics of Calcareous Sands considering Various Factors

Baojian Li ¹, Gang Lei ^{1,2}, Panpan Guo ¹, Gaoyun Zhou,¹ Zhe Wang,³ and Xiaonan Gong¹

¹Research Center of Coastal and Urban Geotechnical Engineering, Zhejiang University, Hangzhou 310058, China

²Beijing Urban Construction Design & Development Group Company Limited, Beijing 100037, China

³College of Civil Engineering and Architecture, Zhejiang University of Technology, Hangzhou 310023, China

Correspondence should be addressed to Gang Lei; 11812105@zju.edu.cn

Received 14 May 2021; Accepted 15 June 2021; Published 25 June 2021

Academic Editor: Yu Wang

Copyright © 2021 Baojian Li et al. This is an open access article distributed under the Creative Commons Attribution License, which permits unrestricted use, distribution, and reproduction in any medium, provided the original work is properly cited.

Relative density is an important index affecting the mechanical behaviors of calcareous sands. The dense sands present softening strength, whereas the loose sands exhibit hardening strength. Furthermore, the relative density is determined based on the maximum and minimum void ratios obtained by using the maximum and minimum dry density test. In this study, a series of tests were carried out on various mixed graded sands to explore their material properties and the relationship between the limit void ratio, considering the effects of test methods, equipment, and fine content. It is shown that a more accurate maximum void ratio can be attained by using the 1000 mL measuring cylinder with low rotation speed. In addition, in order to avoid particle breakage of calcareous sands, it is suggested that the minimum void ratio should be obtained with the 1000 mL compaction cylinder combining vibration with hit. The results also show that a linear relationship exists among the limit void ratio of various mixed graded sands. Besides, the void ratio is significantly affected by the fine content. 40% is the critical fine content corresponding to the lowest value of the limit void ratio.

1. Introduction

Calcareous sands are special soils, which are biogenic sediments and skeletal remains of marine organisms. The main composition is calcium carbonate with a lower hardness than silica sands [1–6]. They are widely distributed in shallow, warm, and continental shelf seas. Calcareous sands are characterized by high crushability, irregular particle shape, high intraparticle void, and complex microstructure. Therefore, their mechanical behaviors are quite different from that of terrigenous sands [7–10]. With the implementation of the Belt and Road Initiative, calcareous sands have been a topic of interest among geotechnical researchers recently. However, they tend to concern particle shape and breakage [11–13], biocementation [14–16], and bearing capacity of pile foundations [17–19]. There

are few papers on maximum and minimum void ratios and relative density of calcareous sands.

Relative density, D_r , is a crucial indicator reflecting the compactness of noncohesive soil, which has been proposed and widely used by domestic and foreign scholars since the 1940s [20]. It is a state parameter indicating how dense a given sand sample or deposit is with respect to its range of possible densities. It has a governing influence on strength and stability of sand in filling engineering, such as embankment, retaining wall, and ground improvement [21–23]. Nevertheless, the determination of the maximum and minimum void ratios is the prerequisite for calculating the relative density. Two parameters, e_{\min} and e_{\max} , cannot be directly measured and must be determined by the maximum and minimum dry densities of sand. Generally, the minimum dry density $\rho_{d\min}$ is often measured by the funnel methods

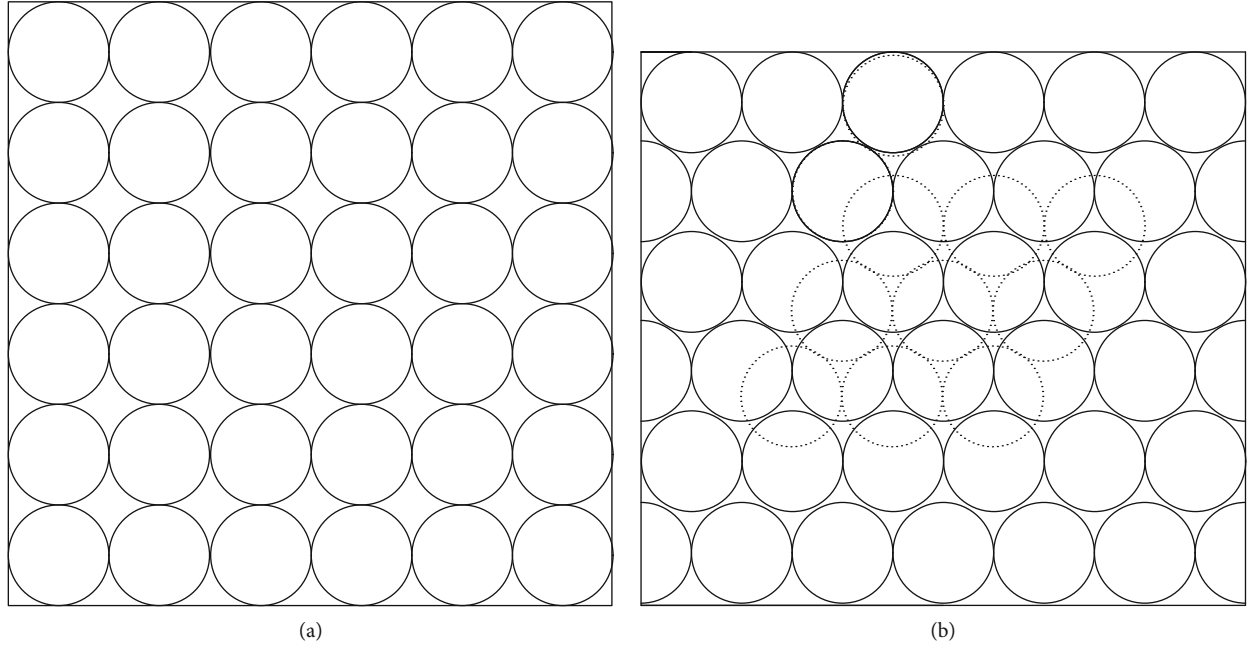


FIGURE 1: Schematic illustration of packing of single-size spheres: (a) loosest state and (b) densest state.

or the measuring cylinder method, and the maximum dry density ρ_{dmax} is usually measured by the vibration-hammer method [24, 25].

Experimental research shows that the main factors affecting the maximum and minimum dry densities of sand are particle shape, uniformity coefficient, fine content, instrument size, test method, and so on. The formula for calculating the maximum and minimum dry densities of noncohesive soil is proposed, considering compaction power, particle composition and shape, and particle filling [26–28]. Unfortunately, the result is far from satisfactory, because of idealized assumptions. Meanwhile, some improved methods are found to measure the maximum and minimum dry densities of terrigenous sands [29, 30]. Previous researches mainly focus on clean sand. In particular, characteristics of e_{max} and e_{min} have been studied in the context of applicability and accuracy of the relative density. Other studies have investigated the relation between the material properties and e_{max} or e_{min} of sand. Recently, effects of fines on the limit void ratio (e_{max} and e_{min}) have been a new theme to examine the influence of fines on the physical and mechanical properties of quartz sands among geotechnical scholars [31–34]. A large number of test data on silty sand were examined, and a set of empirical equations were proposed to show the effect of fine content on the minimum void ratio [35]. Apart from these studies, computer simulation analyses using the discrete element method have also been carried out to study the characteristics of the limit void ratio of particle mixtures. The trend of computer simulation results resembles that obtained from experimental tests [36–38].

Above all, compared to the number of studies on mechanical behaviors of calcareous sands and influence factors of relative density, the impact on the relative density of test methods and fine content of calcareous sands is rather limited. In the present study, we aim to examine the void

ratio characteristics for calcareous sands including clean sands and sands containing a small amount of fine-size particles (diameter < 0.075 mm). Specifically, the study highlights the influence of test methods and equipment on e_{max} , e_{min} , and D_r . In what follows, binary relationships between the maximum and minimum void ratios are obtained. The results supplement the relevant provisions of the national regulations, which can improve the availability of the laboratory test.

2. Idealized Packing of Spherical Grains

Analyzing the idealized packing of spherical grains is an effective way to understand the characteristics of soil. At the same time, it is suitable for sand to build the physical model based on spherical particles [39–43]. For convenience, in theoretical calculation, it was assumed that the sand particle is completely incompressible.

2.1. Single-Size Spheres. For single-size spheres, the loosest possible packing is shown in Figure 1(a), with the corresponding maximum void ratio being calculated according to the following equations:

$$\begin{aligned}
 V &= 6D \times 6D \times D = 36D^3, \\
 V_s &= 6 \times 6 \times \frac{4}{3}\pi \left(\frac{D}{2}\right)^3 = 6\pi D^3 \approx 18.85D^3, \\
 V_v &= V - V_s \approx 17.15D^3, \\
 e_{max} &= \frac{V_v}{V_s} = 0.9098,
 \end{aligned} \tag{1}$$

where D is the diameter of sand particles and V , V_s , and V_v are the volume of sand, sand particles, and void.

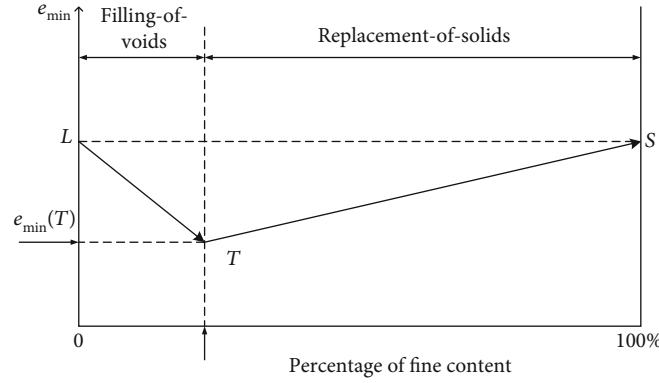


FIGURE 2: Effect of fines on binary packing of spherical particles in e_{\min} .

On the other hand, Figure 1(b) displays the void ratio of densest packing. The volume of sand is composed of 3 parts: V_{s1} = the volume of complete sphere particles, V_{s2} = the volume of sand embedded in the pores above the first layer and below the sixth layer, and V_{s3} = the volume of sand embedded in the pores among three balls between the upper and lower sides. The minimum void ratio is computed by Equations (2)–(8). It is obvious from the above results that the maximum and minimum void ratios are independent of the size in the certain number of idealized single-sized spheres:

$$V = 6D \times \left(\frac{5\sqrt{3}}{2} + 1 \right) D \times D = 31.98D^3, \quad (2)$$

$$V_{s1} = 6 \times 6 \times \frac{4}{3} \pi \left(\frac{D}{2} \right)^3 = 6\pi D^3 \approx 18.85D^3, \quad (3)$$

$$\begin{aligned} V_{s2} &= 12 \times V_{s2}' = 12 \times \frac{1}{4} \\ &\times \left\{ \frac{\pi}{6} D^3 - \left[\left(\frac{\sqrt{3}D}{2} - \frac{D}{2} \right) \times 2 \right]^3 \right\} \\ &\approx 0.384D^3, \end{aligned} \quad (4)$$

$$\begin{aligned} V_{s3} &= 120 \times V_{s3}' = 120 \\ &\times \left[\frac{\pi}{36} D^3 - \frac{1}{3} \times 0.471 \times \left(\frac{\sqrt{6}}{3} - \frac{1}{2} \right) D^3 \right] \\ &\approx 4.51D^3, \end{aligned} \quad (5)$$

$$V_s = V_{s1} + V_{s2} + V_{s3} = 23.74D^3, \quad (6)$$

$$V_v = V - V_s = 8.24D^3, \quad (7)$$

$$e_{\min} = \frac{V_v}{V_s} = 0.347. \quad (8)$$

2.2. Mixtures of Two Grain Sizes. When mixing two spherical particles of different sizes, the packing is influenced by the proportion of large and small particles in the total volume of solids as well as by the relative sizes of the large and small

spheres. Figure 2 schematically shows the corresponding change in e_{\min} with the percentage of fine content.

The point L expresses the densest packing of the larger spherical particles. At first, adding smaller-size spheres to the densest packing of large spheres results in a decrease in the volume of void for small particles fill in the void among the large particles, which is denoted the filling-of-voids process with the path $L-T$ in the diagram. When the content of small spheres exceeds the threshold percentage corresponding to point T , a reverse trend is evident in which the volume of void increases with the percentage of the small-size content. Subsequently, in the so-called replacement-of-solids phase, the large-size spheres are separated and increasingly replaced by the small-size particles until the solid is composed of the smaller particles (point S). So, we can see that e_{\min} decreases during the filling-of-voids phase and reaches its minimum value at a certain percentage T . Then, e_{\min} steadily increases in the course of the replacement-of-solids phase, with the path $T-S$. In practice, the value of $e_{\min(L)}$ is similar to that of $e_{\min(S)}$ since the voids have no concern with the size of spherical particles.

Obviously, e_{\max} of mixtures of two grain sizes may change with the fine content similar to e_{\min} in Figure 2. But the value may be nearly constant or slightly increase with an addition of a very small amount of fines because the small particles do not fill the void formed by the large spheres yet.

3. Materials and Methods

3.1. Experimental Materials. The sand samples as shown in Figure 3 are biogenic sediments and skeletal remains of marine organisms retrieved from the reef reclamation site in Nansha Island, South China Sea. The total area of coral reef in the South China Sea is about $3.8 \times 10^4 \text{ km}^2$, accounting for 5% of the total amount all around the world [44]. Most of the coral reef is located in the region of Nansha Island in our country. Figure 4 displays the grain size distribution curve of calcareous sands collected from Nansha Island. A natural grading with grain diameter less than 5.0 mm was retained for the test. The physical parameters are shown in Table 1. According to the characteristics of particle sizes, the investigated materials include coarse and medium

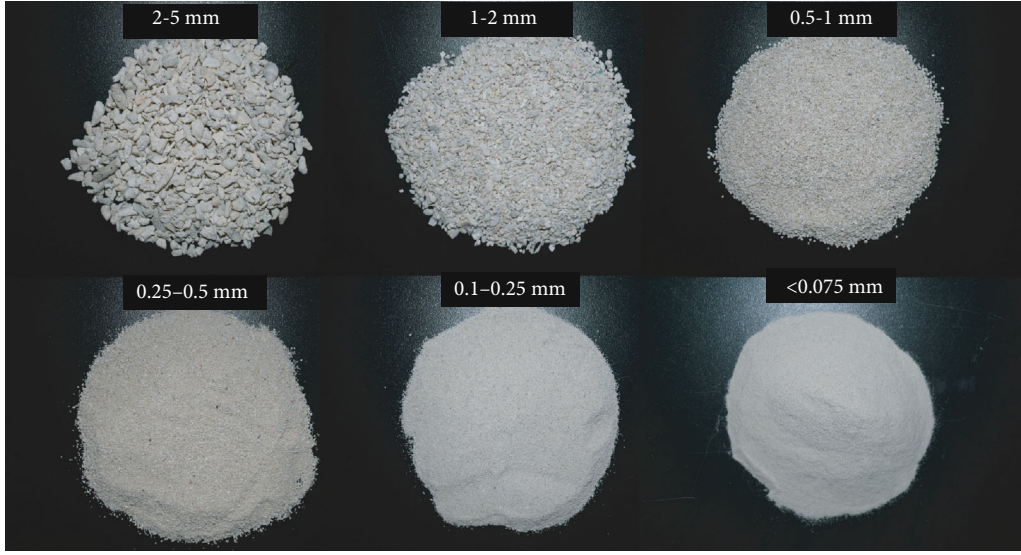


FIGURE 3: Sand samples of different grain sizes.

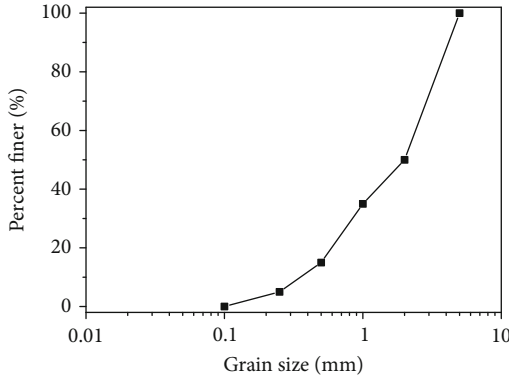


FIGURE 4: Grain size distribution curves of calcareous sands.

TABLE 1: Physical properties of calcareous sands.

G_s	d_{60} (mm)	d_{30} (mm)	d_{10} (mm)	C_u	C_c
2.79	2.60	0.88	0.38	6.84	0.78

Note. G_s = specific gravity; d_{60} = limited particle size; d_{30} = median particle size; d_{10} = effective particle size; C_u = coefficient of uniformity; C_c = coefficient of curvature.

sand without fine particles. The main reasons are sampling location and construction characteristics of hydraulic filling. In the process of reef reclamation, under the action of hydraulic screening and particle gravity, the coarse sand particle tends to accumulate near the mouth of the reclamation site, while the fine particle tends to accumulate downstream with the flow of water, resulting in the uneven distribution. The sand sample used in this experiment was taken from the shallow surface upstream. Therefore, it is poor distribution without particles below 0.1 mm.

3.2. The Minimum and Maximum Dry Density Test. As is mentioned above, relative density is an important parameter of sand, which is analyzed by Equation (9). Nevertheless, the

limit void ratio is difficult to measure directly and needs to be computed using Equations (10) and (11). Namely, relative density can be obtained by measuring the maximum and minimum dry densities:

$$D_r = \frac{e_{\max} - e}{e_{\max} - e_{\min}}, \quad (9)$$

$$e_{\max} = \frac{\rho_w G_s}{\rho_{d\min}} - 1, \quad (10)$$

$$e_{\min} = \frac{\rho_w G_s}{\rho_{d\max}} - 1, \quad (11)$$

where ρ_w is the density of water (kg/m^3), $\rho_{d\min}$ is minimum dry density, and $\rho_{d\max}$ is maximum dry density.

The standard [24] suggests that the minimum dry density should be obtained by the funnel method or the measuring cylinder method. The volume of the measuring cylinder is 500 mL or 1000 mL, and the mass of sand samples is 700 g. In order to study the influence of the volume of measuring cylinder and test methods on the minimum dry density, 3 different volume ranges (250, 500, and 1000 mL) were used in the experiment. The sand samples were experimented with by the funnel method (M_1), fast measuring cylinder method (M_2), and slow measuring cylinder method (M_3). The speed of sand falling into the measuring cylinders through funnels was approximately 5g/s. The inversion speeds of measuring cylinders in M_2 and M_3 were, respectively, 30 s/180° and 60 s/180°. Each group of tests was repeated 3 times, and the average value was taken as the final results.

On the other hand, for the determination of maximum dry density, there is no internationally uniform method. China geotechnical engineers often use the vibration-hammer method. During the test, the sand samples were compacted and hammered to obtain the idealized maximum dry density. In order to analyze the influence of test equipment on maximum dry density, the compaction cylinder

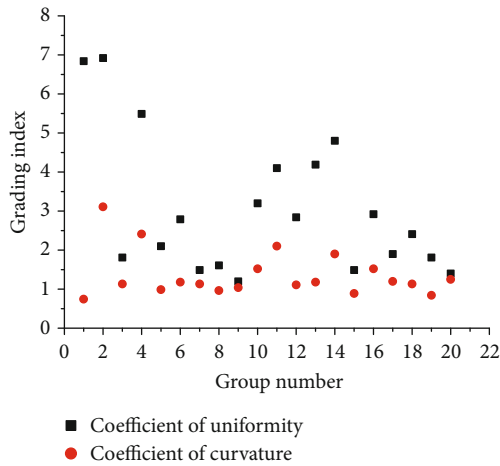


FIGURE 5: Grading indexes of experimental sands.

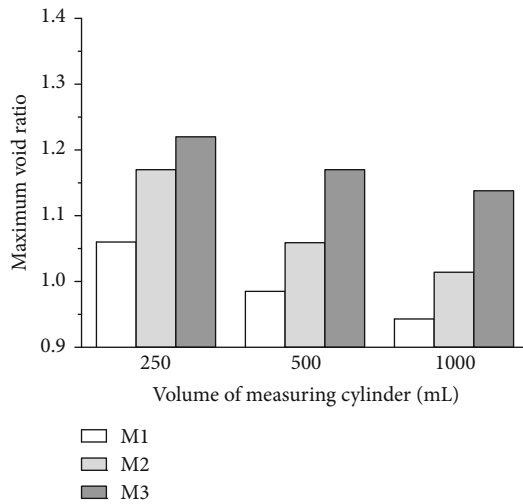


FIGURE 6: Maximum void ratio in different volumes of measuring cylinder.

with a volume of 250 and 1000 mL was selected for layered compaction. When sand samples reached a constant value, the mass was weighed and the corresponding maximum dry density was calculated. Similarly, every experiment was conducted 3 times, and the average value was considered the final results.

3.3. Test on the Relationship between the Maximum and Minimum Void Ratios. It is well known that maximum and minimum void ratios of sand are evaluated from laboratory tests through two independent test methods for the minimum and maximum dry densities, respectively. But previous studies have reported that a linear correlation was derived to express the relationship between e_{max} and e_{min} of terrigenous sands [45]. For the sake of exploring the relationship of calcareous sands, the experimental sand samples of various distributions were mixed at random. 20 groups of sand with diverse grading indexes shown in Figure 5 were configured.

3.4. Test on the Influence of Fine Content on the Limit Void Ratio. Fine contents are a critical factor affecting the void

ratio of sand. For a further study, calcareous sands were mixed with 10%, 20%, 30%, 40%, 50%, 60%, 70%, 80%, 90%, and 100% of fine particles to produce 10 groups with diverse grain compositions. The following was determining the minimum and maximum dry densities and computing the limit void ratio. Before the test, sand was washed with clean water to remove fine and clay particles on the surface and in the inner pore of large particles.

4. Results and Discussion

4.1. The Effects of Test Methods and Equipment on Maximum and Minimum Void Ratios. Before exploring the maximum and minimum void ratios of sand, it is necessary to address several important issues related to the determination procedures and applicability of minimum and maximum dry densities. According to the funnel method and measuring cylinder method to estimate minimum dry density of calcareous sands, the maximum void ratio was acquired. The results in Figure 6 indicate that the value of the funnel method was the largest, followed by the fast measuring cylinder method, and the slow measuring cylinder method was the smallest in the same volume of measuring cylinder. What is more, the larger the volume, the smaller the void ratio in the similar test method.

It can also be seen that the void ratio measured by the funnel method (M_1) was smaller than that of the measuring cylinder methods (M_2 and M_3), which was caused by the different determination operations. In the process of M_1 , since the particles dropping from the funnel had a certain falling speed, the void between particles and between the particles and measuring cylinder was small. In particular, due to the limitation of the funnel size, the given large particles almost slowly fall one by one, leading to a tight sand sample. For M_3 , the entire operation being carried out slowly, it only changed the relative position of particles inside the samples. The void was more than that measured by M_1 . Besides, different volumes of measuring cylinders had a certain impact on the experimental results. When the volume was smaller, sand particles were more likely to be arranged in layers, which made a higher value of the maximum void ratio. Therefore, we should choose the slow measuring cylinder method and a large volume of measuring cylinder to evaluate the minimum void ratio in the laboratory test. Strangely, the idealized value of the maximum void ratio was unexpectedly lower than the measured one. The main reason is that the natural sand particles are not regular spherical, and there are arching and cavitation inside them during determination procedures. And particles of calcareous sands are rich in the inner pore, displayed in Figure 7 (50 and 2000 magnification times, respectively), simultaneously resulting in the peculiar phenomenon.

Table 2 presents the maximum dry density and minimum void ratio of sand measured by the vibratory hammer method using a compaction cylinder with a volume of 250 and 1000 mL. It is found that under the same condition, the measured minimum void ratio with a volume of 250 mL is significantly lower than that of the 1000 mL compaction cylinder.

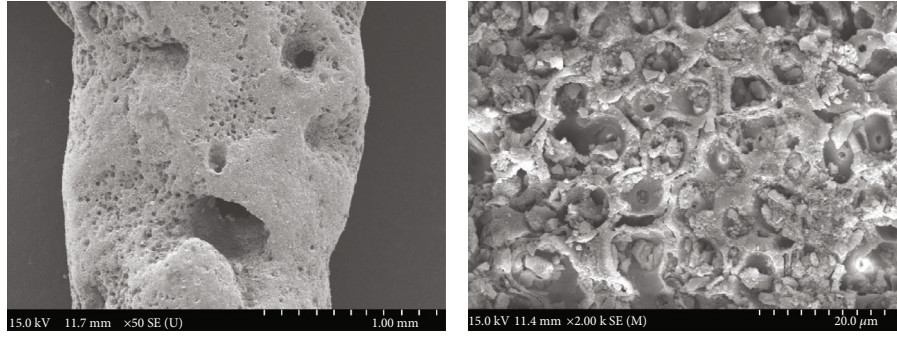


FIGURE 7: SEM scanning images of calcareous sands.

TABLE 2: Maximum dry density and minimum void ratio under the volume of 250 and 1000 mL.

V (mL)	m_s (g)	ρ_{dmax} (g/cm ³)	ρ'_{dmax} (g/cm ³)	e_{min}	$e_{min(I)}$
250	389.5	1.558	1.561	0.78	0.347
	392.5	1.570			
	388.7	1.555			
1000	1503.2	1.503	1.493	0.87	
	1485.1	1.485			
	1491.4	1.491			

Note. V = volume of compaction cylinder; m_s = mass of sand; ρ'_{dmax} = average value of maximum dry density; $e_{min(I)}$ = minimum void ratio of idealized single-size spheres.

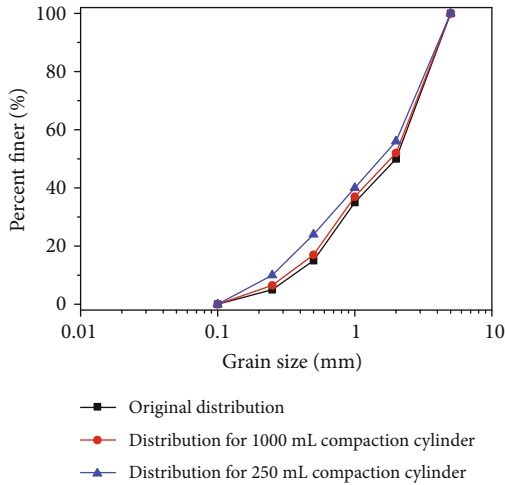


FIGURE 8: Grain size distribution curves for 250 and 1000 mL compaction cylinders.

The grain size distribution curves of calcareous sands before and after vibration hammering are shown in Figure 8. For the 250 mL compaction cylinder, due to the small inner diameter, the compaction energy was more likely to accumulate, making the coarse particles easy to break, which resulted in an increase in the maximum dry density and a decrease in the minimum void ratio. Compaction energy had a significant effect on the crushing of medium and coarse particles. However, the grading curve did not change significantly after being hammered in a compaction

cylinder with a volume of 1000 mL. So, for the vibration-hammer method to determine the maximum dry density of sand, in order to be more similar to the given graded sand, it is recommended that a 1000 mL compaction cylinder should be used. In addition, compared with the idealized minimum void ratio, the experimental value converted from the test on maximum dry density was different from the theoretical one. This is because the premise of theoretical calculation is that the sand particles are assumed to have a uniform sphere. The shape of actual sand particles is irregular, and the arrangement is also different.

In summary, the maximum and minimum void ratios of a given sandy soil are not unique, but rather, they rest with the test methods and equipment used to determine them. For this reason, when comparing the limit void ratio of various soils, it is an essential and prerequisite condition that e_{max} or e_{min} of all soils are measured using the same test procedures (including methods, equipment, and experimental steps) for ρ_{dmin} or ρ_{dmax} , respectively. Although these procedures tend to identify the limited dry density of given sand, it would be difficult to determine the minimum and maximum densities in the true sense.

4.2. A Linear Relationship between Maximum and Minimum Void Ratios. The maximum and minimum dry density test was carried out on these 20 groups of sands. Even though the limit void ratio was obtained from two independent tests that have opposite targets, namely, to produce the loosest state and the densest state of a sand sample, respectively, yet Figure 9 indicates that there is a linear relationship between e_{max} and e_{min} of the compiled sands evidently. However, when the value of e_{min} was in a lower range of 0.6 to 0.75, the distribution of e_{max} was relatively discrete, which made the linear relationship between the maximum and minimum void ratios a little weaker. As the range of e_{min} increases, e_{max} of the sand samples became a more and more well-defined relationship. This is consistent with the results of Cubrinovski and Ishihara, Yilmaz, and Muszynski [35, 41, 46].

4.3. Discussion on Influence of Fine Content on Limit Void Ratio. For each type of composite sands, the maximum and minimum void ratios have been determined according to the above laboratory procedures. Therefore, it is possible to plot the values of e_{max} and e_{min} as a function of the fine

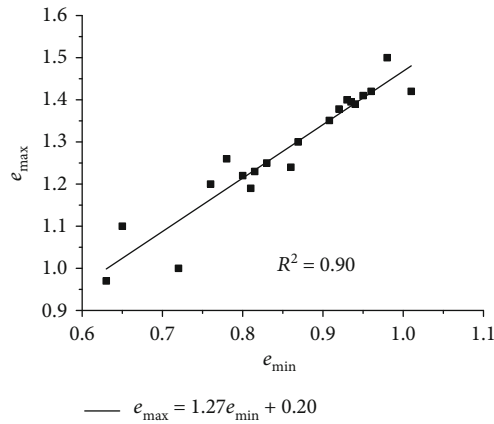


FIGURE 9: Correlation between e_{\max} and e_{\min} of calcareous sands.

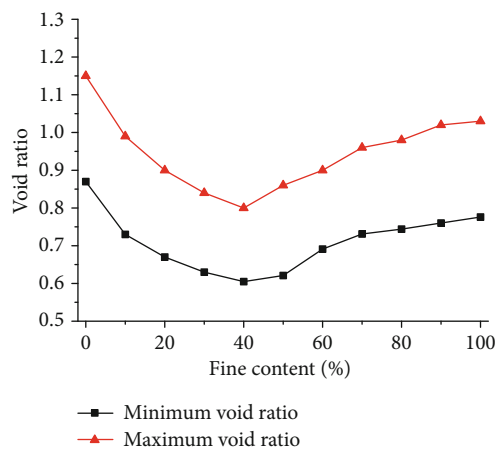


FIGURE 10: Variation in e_{\max} and e_{\min} with fine content.

content for each of the composite soils, as shown in Figure 10. It is observed that both e_{\max} and e_{\min} initially decreased as the fine content increased from 0% to about 30%. Within the range of 30 to 50% fines, the correlations presented a change of form indicating a transition from the filling-of-voids to the replacement-of-solids process. Above 60% fines, the maximum and minimum void ratios were seen to steadily increase until they eventually reached 100% fine content. It is indicated that the variation of e_{\max} and e_{\min} with the fine content in Figure 10 closely resembled that of the spherical particles shown in Figure 2. But e_{\max} and e_{\min} of the nature sands without fines were higher than that with 100% fine content, which differed from the idealized values and previous studies [47]. Maybe there are 2 main reasons. On the one hand, the original sands are full of void among particles, leading to poor distribution. Besides, compared with fine fractions, the nature sands without fines are rich in intraparticle voids.

5. Conclusions

A series of data were acquired by the maximum and minimum dry density test on various mixed sand. The main conclusions drawn from this study can be summarized as follows.

- (1) The maximum and minimum dry density test should adopt the vibration-hammer method and slow measuring cylinder methods, respectively. To avoid the influence of equipment on experimental results, measuring cylinder and compaction cylinder with a volume of 1000 mL should be used
- (2) An almost linear relationship exists between the maximum and minimum void ratios of various mixed graded sand. The relationship has a high correlation coefficient of 0.9 and can be used to approximately evaluate e_{\max} from e_{\min} and vice versa
- (3) The maximum and minimum void ratios are significantly affected by the fine content in a way that the limit void ratio decreases from 0% to 30% during the filling-of-voids phase and increases within the range of 50% to 100% in the course of the replacement-of-solids phase. Near 40% is a certain percentage showing a change of pattern indicating the transition
- (4) The maximum and minimum void ratios of a given sandy soil are not unique, but rather they rest with the test methods and equipment used to determine them. Therefore, when comparing the limit void ratio of various soil, it is an essential and prerequisite condition that e_{\max} or e_{\min} of all soil are measured using the same test procedures. Besides, the void ratio characteristics should not be regarded as an isolated feature of the packing of sand, but rather, they should be looked upon as the fact that the particle structure is directly reflected in the mechanical properties of sand

Data Availability

The data used to support the findings of this study are available from the corresponding author upon request.

Conflicts of Interest

The authors declare that they have no known competing financial interests or personal relationships that could have appeared to influence the work reported in this paper.

Acknowledgments

This paper gets its funding from a project (Grant Nos. 51778585 and 5207080379) supported by the National Natural Science Foundation of China and Joint Fund of Zhejiang Natural Science Foundation Committee Power China Huadong Engineering Corporation (Grant No. LHZ19E090001).

References

- [1] C.-l. Zhu, J.-x. Zhang, N. Zhou, M. Li, and Y.-b. Guo, "Permeability of sand-based cemented backfill under different stress conditions: effects of confining and axial pressures," *Geofluids*, vol. 2021, Article ID 6657662, 13 pages, 2021.

- [2] Z.-h. Yan, C. Cao, M.-y. Xie et al., "Pressure behavior analysis of permeability changes due to sand production in offshore loose sandstone reservoirs using boundary-element method," *Geofluids*, vol. 2021, Article ID 6658875, 10 pages, 2021.
- [3] M. R. Coop, "The mechanics of uncemented carbonate sands," *Géotechnique*, vol. 40, no. 4, pp. 607–626, 1990.
- [4] M. R. Coop, K. K. Sorensen, T. B. Freitas, and G. Georgoutsos, "Particle breakage during shearing of a carbonate sand," *Géotechnique*, vol. 54, no. 3, pp. 157–163, 2004.
- [5] S. Donohue, C. O'Sullivan, and M. Long, "Particle breakage during cyclic triaxial loading of a carbonate sand," *Géotechnique*, vol. 59, no. 5, pp. 477–482, 2009.
- [6] V. Fioravante, D. Giretti, and M. J. Kowski, "Small strain stiffness of carbonate Kenya sand," *Engineering Geology*, vol. 161, pp. 65–80, 2013.
- [7] D. Kong and J. Fonseca, "Quantification of the morphology of shelly carbonate sands using 3D images," *Géotechnique*, vol. 68, no. 3, pp. 249–261, 2018.
- [8] Y. Wu, N. Li, X.-z. Wang, and J. Cui, "Experimental investigation on mechanical behavior and particle crushing of calcareous sand retrieved from South China Sea," *Engineering Geology*, vol. 280, p. 105932, 2020.
- [9] Y. Qin, T. Yao, R. Wang, C.-q. Zhu, and Q.-s. Meng, "Particle breakage-based analysis of deformation law of calcareous sediments under high-pressure consolidation," *Rock and Soil Mechanics*, vol. 35, no. 11, pp. 3123–3128, 2014.
- [10] H.-y. Chen, R. Wang, J.-g. Li, and J.-m. Zhang, "Grain shape analysis of calcareous soil," *Rock and Soil Mechanics*, vol. 26, no. 9, pp. 1389–1392, 2005.
- [11] S.-j. Rui, Z. Guo, T.-l. Si, and Y.-j. Li, "Effect of particle shape on the liquefaction resistance of calcareous sands," *Soil Dynamics and Earthquake Engineering*, vol. 137, article 106302, 2020.
- [12] Y.-r. Lv, X. Li, and Y. Wang, "Particle breakage of calcareous sand at high strain rates," *Powder Technology*, vol. 366, pp. 776–787, 2020.
- [13] Y. Peng, X.-m. Ding, Y. Zhang, C.-l. Wang, and C. Y. Wang, "Evaluation of the particle breakage of calcareous sand based on the detailed probability of grain survival: an application of repeated low-energy impacts," *Soil Dynamics and Earthquake Engineering*, vol. 141, article 106497, 2020.
- [14] L. Wang, X. Jiang, X. He et al., "Crackling noise and biocementation," *Engineering Fracture Mechanics*, vol. 247, article 107675, 2021.
- [15] M. Oualha, S. Bibi, M. Sulaiman, and N. Zouari, "Microbially induced calcite precipitation in calcareous soils by endogenous *Bacillus cereus*, at high pH and harsh weather," *Soil Dynamics and Earthquake Engineering*, vol. 257, article 109965, 2020.
- [16] S. T. O'Donnell and E. K. Jr, "Stiffness and dilatancy improvements in uncemented sands treated through MICP," *Journal of Geotechnical and Geoenvironmental*, vol. 141, article 02815004, 2015.
- [17] J. D. Murff, "Pile capacity in calcareous sands: state of the art," *Journal of Geotechnical Engineering*, vol. 113, no. 5, pp. 490–507, 1987.
- [18] B. R. Danzigier, A. M. Costa, F. R. Lopes, and M. P. Pacheco, "Back analysis of offshore pile driving with an improved soil model," *Géotechnique*, vol. 49, no. 6, pp. 777–799, 1999.
- [19] H. Jiang, R. Wang, Y.-h. Lv, and Q.-s. Meng, "Test study of model pile in calcareous sands," *Rock and Soil Mechanics*, vol. 31, no. 3, pp. 780–784, 2010.
- [20] F. Tavenas and P. Rochelle, "Accuracy of relative density measurements," *Géotechnique*, vol. 22, no. 4, pp. 549–562, 1972.
- [21] P. Guo, F. Liu, G. Lei et al., "Predicting response of constructed tunnel to adjacent excavation with dewatering," *Geofluids*, vol. 2021, Article ID 5548817, 17 pages, 2021.
- [22] P. Guo, X. Gong, and Y. Wang, "Displacement and force analyses of braced structure of deep excavation considering unsymmetrical surcharge effect," *Computers and Geotechnics*, vol. 113, p. 103102, 2019.
- [23] P. Guo, X. Gong, Y. Wang, H. Lin, and Y. Zhao, "Minimum cover depth estimation for underwater shield tunnels," *Tunnelling and Underground Space Technology*, vol. 115, p. 104027, 2021.
- [24] GB/T 50123—2019, *Standard for Soil Test Method*, pp. 48–50, 2019.
- [25] B. Das and K. Sobhan, *Principles of Geotechnical Engineering*, Cengage Learning, 2010.
- [26] H. W. Humphres, "A method for controlling compaction of granular materials," *Highway Research Board Bulletin*, vol. 159, pp. 41–57, 1957.
- [27] Q.-g. Guo and Z.-c. Liu, "Approximation of maximum density of coarse-grained soils," *Water Resources & Water Engineering*, vol. 3, no. 1, pp. 12–21, 1992.
- [28] Y. Wang, C. H. Li, and J. Q. Han, "On the effect of stress amplitude on fracture and energy evolution of pre-flawed granite under uniaxial increasing-amplitude fatigue loads," *Engineering Fracture Mechanics*, vol. 240, p. 107366, 2020.
- [29] M.-h. Fan and D.-z. Kong, "Improvement on method for relative density of sand experiments," *Rock and Mineral Analysis*, vol. 26, no. 5, pp. 67–68, 2007.
- [30] S. Li, D.-y. Li, and Y.-g. Gao, "Determination of maximum and minimum void ratios of sands and their influence factors," *Chinese Journal of Geotechnical Engineering*, vol. 40, no. 3, pp. 554–561, 2018.
- [31] D. C. Bobei, S. R. Lo, D. Wanatowski, C. T. Gnanendran, and M. M. Rahman, "Modified state parameter for characterizing static liquefaction of sand with fines," *Canadian Geotechnical Journal*, vol. 46, no. 3, pp. 281–295, 2009.
- [32] C. A. Stamatopoulos, "An experimental study of the liquefaction strength of silty sands in terms of the state parameter," *Soil Dynamics and Earthquake Engineering*, vol. 30, no. 8, pp. 662–678, 2010.
- [33] C. S. Chang and M. Meidani, "Dominant grains network and behavior of sand-silt mixtures: stress-strain modeling," *International Journal for Numerical and Analytical Methods*, vol. 37, no. 15, pp. 2563–2589, 2013.
- [34] A. Ekinci, M. Hanafi, and P. M. V. Ferreira, "Influence of initial void ratio on critical state behaviour of poorly graded fine sands," *Indian Geotechnical Journal*, vol. 50, no. 5, pp. 689–699, 2020.
- [35] M. Cubrinovski and K. Ishihara, "Maximum and minimum void ratio characteristics of sands," *Soils and Foundations*, vol. 42, no. 6, pp. 65–78, 2002.
- [36] X.-z. An, "Densification of the packing structure under vibrations," *International Journal of Minerals, Metallurgy, and Materials*, vol. 20, no. 5, pp. 499–503, 2013.
- [37] H. K. Dash, T. G. Sitharam, and B. A. Baudet, "Influence of non-plastic fines on the response of a silty sand to cyclic loading," *Soils and Foundations*, vol. 50, no. 5, pp. 695–704, 2010.

- [38] C. S. Chang, J. Y. Wang, and L. Ge, "Modeling of minimum void ratio for sand-silt mixtures," *Engineering Geology*, vol. 196, pp. 293–304, 2015.
- [39] R. K. Mcgeary, "Mechanical packing of spherical particles," *Journal of the American Ceramic Society*, vol. 44, no. 10, pp. 513–522, 1961.
- [40] B. Aberg, "Void ratio of noncohesive soils and similar materials," *Journal of Geotechnical Engineering*, vol. 118, no. 9, pp. 1315–1334, 1992.
- [41] Y. Yilmaz, "A study on the limit void ratio characteristics of medium to fine mixed graded sands," *Engineering Geology*, vol. 104, no. 3-4, pp. 290–294, 2009.
- [42] Y. Wang, Y. F. Yi, C. H. Li, and J. Q. Han, "Anisotropic fracture and energy characteristics of a Tibet marble exposed to multi-level constant-amplitude (MLCA) cyclic loads: a lab-scale testing," *Engineering Fracture Mechanics*, vol. 244, p. 107550, 2021.
- [43] C. S. Chang and J. Y. Wang, "Maximum and minimum void ratios for sand-silt mixtures," *Engineering Geology*, vol. 211, pp. 7–18, 2016.
- [44] Y. Dong, Y. Liu, C. Hu, and B. Xu, "Coral reef geomorphology of the Spratly Islands: a simple method based on time-series of Landsat-8 multi-band inundation maps," *ISPRS Journal of Photogrammetry and Remote Sensing*, vol. 157, pp. 137–154, 2019.
- [45] M. Cubrinovski and K. Ishihara, "Empirical correlation between SPT N_{60} value and relative density for sandy soils," *Soils and Foundations*, vol. 39, no. 5, pp. 61–71, 1999.
- [46] M. R. Muszynaki, "Determination of maximum and minimum density of poorly graded sands using a simplified method," *Geotechnical Testing Journal*, vol. 29, no. 3, pp. 263–272, 2006.
- [47] A. Papadopoulou and T. Tika, "The effect of fines on critical state and liquefaction resistance characteristics of non-plastic silty sands," *Soils and Foundations*, vol. 48, no. 5, pp. 713–725, 2008.

Research Article

Intelligent Prediction Model of the Triaxial Compressive Strength of Rock Subjected to Freeze-Thaw Cycles Based on a Genetic Algorithm and Artificial Neural Network

Xin Xiong ^{1,2}, Feng Gao ^{1,2}, Keping Zhou,^{1,2} Yuxu Gao,¹ and Chun Yang ^{1,2}

¹School of Resources and Safety Engineering, Central South University, Changsha, Hunan 410083, China

²Research Center for Mining Engineering and Technology in Cold Regions, Central South University, Changsha, Hunan 410083, China

Correspondence should be addressed to Feng Gao; csugaofeng@csu.edu.cn

Received 11 April 2021; Accepted 3 June 2021; Published 17 June 2021

Academic Editor: Yu Wang

Copyright © 2021 Xin Xiong et al. This is an open access article distributed under the Creative Commons Attribution License, which permits unrestricted use, distribution, and reproduction in any medium, provided the original work is properly cited.

Rock compressive strength is an important mechanical parameter for the design, excavation, and stability analysis of rock mass engineering in cold regions. Accurate and rapid prediction of rock compressive strength has great engineering value in guiding the efficient construction of rock mass engineering in a cold regions. In this study, the prediction of triaxial compressive strength (TCS) for sandstone subjected to freeze-thaw cycles was proposed using a genetic algorithm (GA) and an artificial neural network (ANN). For this purpose, a database including four model inputs, namely, the longitudinal wave velocity, porosity, confining pressure, and number of freeze-thaw cycles, and one output, the TCS of the rock, was established. The structure, initial connection weights, and biases of the ANN were optimized progressively based on GA. After obtaining the optimal GA-ANN model, the performance of the GA-ANN model was compared with that of a simple ANN model. The results revealed that the proposed hybrid GA-ANN model had a higher accuracy in predicting the testing datasets than the simple ANN model: the root mean square error (RMSE), mean absolute error (MAE), and R squared (R^2) were equal to 1.083, 0.893, and 0.993, respectively, for the hybrid GA-ANN model, while the corresponding values were 2.676, 2.153, and 0.952 for the simple ANN model.

1. Introduction

The distribution of permafrost and seasonal permafrost in China, mainly in the west and north, accounts for more than 70% of the total land area [1]. With Western development and the in-depth implementation of the “belt and road” national strategy, mineral resource development and engineering construction in cold regions are steadily increasing [2]. The rock masses addressed in geotechnical engineering in cold regions are subject to freeze-thaw cycling caused by day-night and seasonal temperature changes [3, 4]. Because of the unique stress field and environment, microdefects inside the rock will continue to form and expand. The macroscopic effect of the damage accumulation is represented by the deformation and destruction of the rock, which causes potential damage to rock mass engineering. Therefore, the

study of the mechanical properties of rocks in cold regions has important engineering value for the stability of rock mass engineering.

The triaxial compressive strength (TCS) of rock is a key rock mechanics parameter to be considered in rock mass engineering. It is considered in the design, excavation, and support of rock mass engineering. Many researchers have conducted a considerable amount of research on the mechanical properties of rocks subjected to freeze-thaw cycles based on laboratory tests. Tan et al. [5] and Hosseini and Khodayari [6] performed triaxial compression tests of granite and sandstone, respectively, subjected to different numbers of freeze-thaw cycles. It was found that with the increase in the number of freeze-thaw cycles, the TCS of the rock decreases, and with the increase in the confining pressure, the TCS of the rock increases. Shen and Wang [7]

analyzed the freeze-thaw damage mechanism of rocks in cold regions, expounded the freeze-thaw damage process of the rock, and analyzed the influence of external influencing factors such as the freeze-thaw temperature, number of freeze-thaw cycles, and stress state on rock freeze-thaw damage in detail. Bai et al. [8] carried out uniaxial and triaxial compression tests of saturated sandstone at different frozen temperatures. The effects of frozen temperature on peak strength, elastic modulus, cohesion, and internal friction angle were analyzed, and the relationships between the confining pressure and the peak strength and elastic modulus were obtained. These work has important guiding significance for the study of the factors influencing the compressive strength of rock in freeze-thaw environments.

Although many of these influencing factors have been investigated in freeze-thaw experiments, it is difficult to obtain the TCS of rocks subjected to any number of freeze-thaw cycles because of the lack of a precise prediction model. This has driven scholars to search for easy and reliable methods to predict the mechanical properties of rocks subjected to freeze-thaw cycles. Bayram [9] developed a statistical model to estimate the reduction in the uniaxial compressive strength of limestone after freeze-thaw cycle treatment. İnce and Fener [10] investigated various rock index properties after freeze-thaw cycle treatment, including the dry density, ultrasonic velocity, point load strength, and slake-durability test indices, and proposed a statistical model to predict the uniaxial compressive strength of deteriorated pyroclastic rocks. Liu et al. [11] improved an empirical equation to determine the uniaxial compressive strength of rocks subjected to freeze-thaw cycles based on a fatigue damage model. Fu et al. [12] and Seyed Mousavi et al. [13] proposed a TCS prediction model for transversely isotropic rocks subjected to freeze-thaw cycles based on the single discontinuity theory. However, the unknown parameters in those models should be determined by experimental tests. Because the experiment is expensive, time-consuming, and laborious, it is difficult to provide rapid guidance for engineering design and construction. In addition, the prediction models are based on specific hypothetical function forms, the prediction results show good consistency under specific conditions, but the prediction results are poor when these models are applied to other rock types.

It was highlighted that artificial intelligence (AI) techniques have an impressive potential for use in geotechnical engineering [14–16], especially in solving rock mechanics problems [17, 18]. To the best of the authors' knowledge, no study has developed a hybrid GA-ANN model for TCS prediction of rocks subjected to freeze-thaw cycles. Therefore, in this paper, to solve this problem, a hybrid GA-ANN prediction model is constructed and proposed. First, a database of 60 datasets is prepared and used in the modeling. From this database, the longitudinal wave velocity, porosity, confining pressure, and number of freeze-thaw cycles are utilized as model inputs. Furthermore, the developed models, including a simple ANN model and hybrid GA-ANN model, are compared to select the best model for estimating TCS of rocks subjected to freeze-thaw cycles.

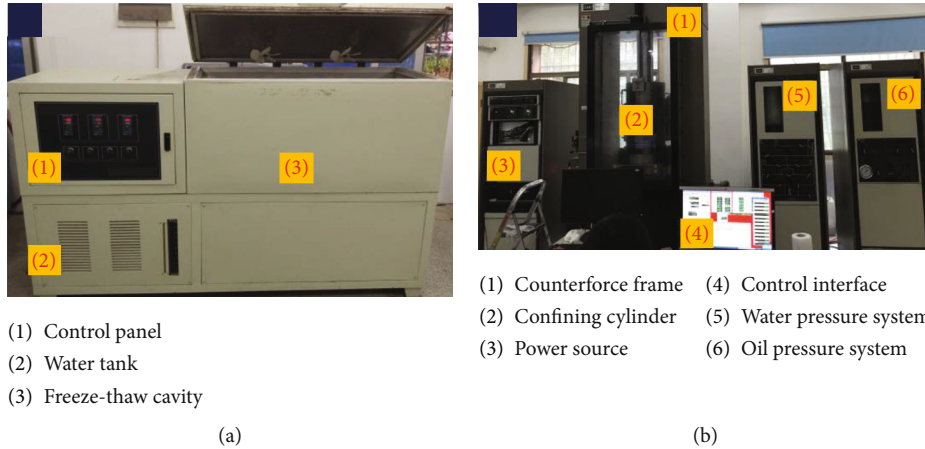
2. Laboratory Tests and Collect Datasets

The rock specimens used in this test were sandstone taken from the Jiama open-pit copper mine located in the Tibet Autonomous Region of China. According to the Commission on Testing Methods of the International Society for Rock Mechanics, all the sandstone specimens were cylindrical samples with diameters of 50 mm and the end surfaces were polished to ensure that the flatness was less than 0.05 mm. Careful preparations ensured that the maximum deviations of the specimen diameters and heights were less than 0.3 mm and that the vertical deviation was less than 0.25°. Sixty sandstone specimens with a length/diameter ratio of 2.0 were used in the freeze-thaw cycle tests and conventional triaxial compression tests.

2.1. Determination of Input and Output Variables. When using machine learning to predict rock mechanical properties, the choice of input variables (influencing factors) is very important. The selection of general input variables needs to follow the following rules: (1) the physical meaning of the parameters is clear, (2) the parameter values are easy to obtain, and (3) the characteristics of the output variables can be comprehensively reflected. The TCS of the rock is combined with other factors, such as the pore structure, deposition environment, and ground stress. In this paper, we establish a lossless intensity prediction model and then select variables that are easy to measure and control, such as the confining pressure, porosity, longitudinal wave velocity, and number of freeze-thaw cycles, as input variables to predict the TCS of the sandstone. Among them, the confining pressure reflects the magnitude of rock mass stress, the porosity and longitudinal wave velocity reflect the rock integrity, and the number of freeze-thaw cycles reflects the natural environmental factors in alpine regions.

2.1.1. Determination of Freeze-Thaw Cycles. Because of the day-night and seasonal temperature changes, rocks in cold regions undergo repeated freeze-thaw cycling. The 60 sandstone specimens were divided into 5 groups (labeled A through E), and each group comprised 12 rock specimens (labeled 1 through 12). The sandstone specimens from groups A, B, C, D, and E were treated for 0 cycles, 10 cycles, 20 cycles, 30 cycles, and 40 cycles, respectively. The freeze-thaw weathering process was simulated with a TDS-300 automatic freeze-thaw test machine (Figure 1(a)). Based on the local climate of the mine site, one freeze-thaw weathering cycle in our tests included freezing the saturated rock specimens at -20°C for four hours and then thawing them in water at $+20^{\circ}\text{C}$ for four hours. Therefore, one freeze-thaw weathering cycle lasted for 10 hours, including the cooling time and warming time.

2.1.2. Determination of Porosity. Porosity is an important quantitative criterion for rock cracks and voids. There are many microcracks and microvoids inside rocks. When the temperature drops below 0°C , the water in these microdefects freezes into ice and its volume expands by approximately 9%, which produces pressure on the pore walls. When the pressure on the walls exceeds the tensile strength of the rock



- (1) Control panel
 (2) Water tank
 (3) Freeze-thaw cavity

(a)

- (1) Counterforce frame (4) Control interface
 (2) Confining cylinder (5) Water pressure system
 (3) Power source (6) Oil pressure system

(b)

FIGURE 1: Experimental apparatus. (a) TDS-300 automatic freeze-thaw test machine. (b) MTS815 electrohydraulic servocontrolled rock testing machine.

[19], it causes defect development and the porosity increases. When the frozen water melts, water will be absorbed into the defect spaces before the next freezing step [20]. Repeated freeze-thaw cycles can cause rapid deterioration of the physical and mechanical properties of rocks. Therefore, porosity has a great influence on rock strength after freeze-thaw cycle treatment. According to the literature [21, 22], porosity can be measured by nuclear magnetic resonance (NMR). Hence, in this study, after the corresponding freeze-thaw cycles of the specimens were completed, the AniMR-150 NMR imaging system was used to perform measurements.

2.1.3. Determination of Longitudinal Wave Velocity. Stress influences the distribution and orientation of microcracks inside rocks, which leads to a change in the macroscopic physical properties and the longitudinal wave velocity of the rock. Therefore, longitudinal wave velocity is a powerful indicator of the distribution of cracks inside rocks. After the corresponding freeze-thaw cycles of the specimens were completed and dried, the longitudinal wave velocity of the sandstone specimens was determined using an HS-YS4A rock acoustic wave parameter test system.

2.1.4. Determination of Confining Pressure. Confining pressure is an important factor affecting the TCS of rock. Therefore, in this study, based on the in situ geological data and laboratory conditions, the tested confining pressures were 3 MPa, 6 MPa, 9 MPa, and 12 MPa, corresponding to specimens 1–3, 4–6, 7–9, and 10–12 in each group.

2.1.5. Determination of Triaxial Compressive Strength. The TCS of the rock specimens was determined by performing conventional triaxial compression tests. Each sandstone specimen was compressed at a constant confining pressure, and then, the axial load was increased until the specimen failed. The conventional triaxial compression tests were conducted on an MTS815 electrohydraulic servocontrolled rock testing machine (as shown in Figure 1(b)) with a maximum loading capability of 2600 kN. The displacement-control

loading mode was used in the experiment, and the loading rate was 0.1 mm/min.

Figure 2 shows the TCS results of the sandstone specimens under different combinations of influencing variables (number of freeze-thaw cycles and confining pressure) with a detailed illustration of the specimens in group E (40 cycles). As expected, the TCS of the sandstone decreased with increasing number of freeze-thaw cycles; the TCS of the sandstone increased with increasing confining pressure. The strength characteristics of the sandstone under different influencing variables found in this paper agree with findings presented in the literature [5, 6].

2.2. Database. As mentioned above, to achieve the goal of this study, a series of rock tests, including tests of the porosity, longitudinal wave velocity, and TCS, were carried out on sandstone specimens. In total, a database of 60 datasets was prepared for further analyses. More statistical information regarding the established database, i.e., the maximum, minimum, and mean results, is presented in Table 1.

3. Methods

3.1. Artificial Neural Network. ANNs are one of the most important methods in artificial intelligence. ANN is a multi-layer perceptron model composed of directional interconnected neurons and is used to determine the nonlinear relationship between input variables and output variables. Each neuron is a basic computing unit such as $y = \max(0, \sum_i w_i x_i + b)$, in which $\{x_i\}$ is the input value of the neuron, $\{w_i\}$ is the corresponding weight value of each input variable, b is the bias, and y is the output of the neuron. For each neuron, a summation operation is first performed for the inputs that are multiplied by the appropriate weights, and then, the output is produced with the use of an “activation function.” The output should be in the range $[0, 1]$ and exhibit a behavior comparable to that of the activation of a biological neuron [23]. Therefore, a function with a sigmoid curve shape, such as a hyperbolic tangent function, is selected. The basic element of an ANN is the determination

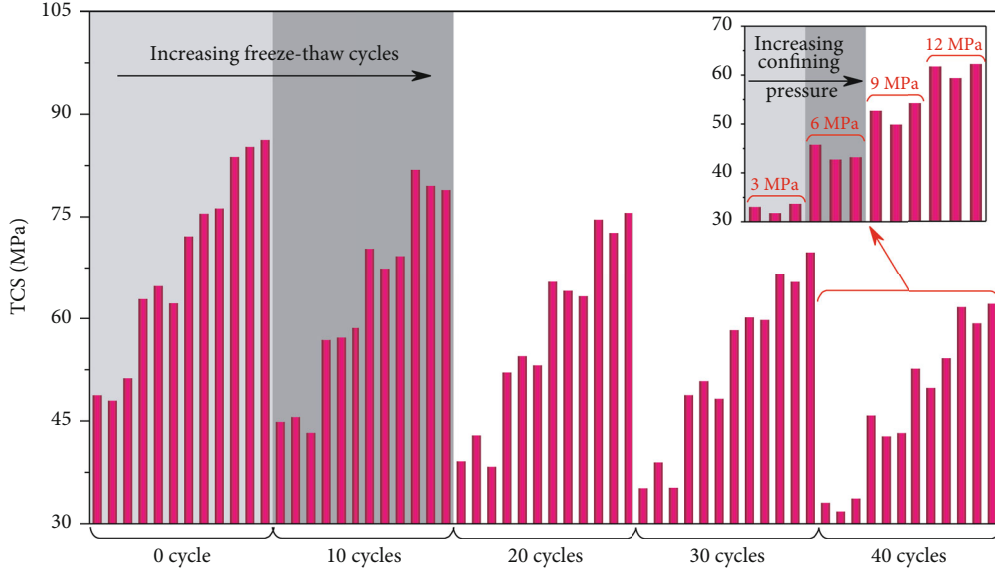


FIGURE 2: TCS test results with enlarged figures for sandstone specimens in group E (40 cycles).

TABLE 1: Statistical information regarding the established database.

Parameter	Unit	Category	Min	Max	Mean
Number of freeze-thaw cycles	Times	Input	0	40	20
Porosity	%	Input	7.49	10.23	8.67
Longitudinal wave velocity	m/s	Input	1961.53	2604.19	2327.91
Confining pressure	MPa	Input	3.0	12.0	7.5
TCS	MPa	Output	31.78	86.83	58.11

of weights, which are related to the connection mode between neurons of different layers, that is, the ANN structure [24]. At present, there are many methods available to determine the ANN structure such as the empirical formula method [25] and coupling optimization algorithm [26].

The ANN training process can be divided into three steps. Datasets are usually divided into three sets: a training set, validation set, and test set. First, the weights and biases are determined based on the training set; then, the weights and biases are adjusted by feedback based on the validation set until the error stops falling; finally, the generalization ability of the model, that is, the ability to predict unknown inputs, is tested by the test set. The RMSE is usually used to reflect the prediction error of an ANN, as shown in equation (2).

3.2. Genetic Algorithm. The genetic algorithm is a computational model that simulates the natural selection and genetic mechanism of Darwin's biological evolution theory. It solves for an optimal solution by simulating the natural evolution process. It was first proposed by Holland [27] in 1973 and was further developed by researchers such as Goldberg [28]. Since its inception, GA has been successfully applied in various fields and has been used to solve different optimization problems, whether the objective (fitness) function is static or dynamic, linear or nonlinear, continuous or discontinuous. However, the rational mathematical expression of

the fitness function and gene selection method are the key points in the application of genetic algorithms. In addition, the improper selection of population size and genetic operator rate will also affect the convergence of the algorithm. Therefore, a reasonable fitness function and appropriate parameter settings should be selected for different optimization objectives. The implementation process of GA is shown in Figure 3(a).

Generally, the process of the standard genetic algorithm can be described by the following steps:

- (1) In the initial population, n chromosomes are randomly generated, i.e., n solutions of the objective function
- (2) Evaluate all chromosomes in the initial population, and rank them according to the objective function
- (3) Selection operator: according to the specific selection method, chromosomes with high adaptability are selected to enter the next generation population and some chromosomes are eliminated
- (4) Crossover operator: random selection of parent chromosomes and exchange of gene fragments to generate new chromosomes (children) in the next generation to supplement the individuals eliminated in the selection, as shown in Figure 3(b)

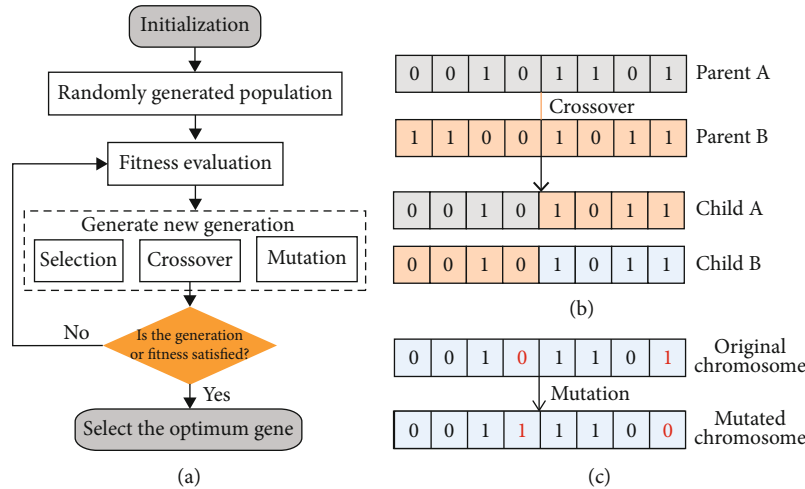


FIGURE 3: GA process and interpretation.

- (5) Mutation operator: to simulate the gene mutation behavior in population reproduction, some genes of the chromosomes (in a certain proportion) of each generation are mutated, as shown in Figure 3(c). Increasing the diversity of chromosomes with population iteration can effectively avoid falling into the dilemma of local optimal solutions
- (6) Repeat steps 2 to 5 until a predetermined stopping condition is satisfied, usually to the maximum multiplication algebra set in advance. Finally, the chromosome with the highest fitness is selected as the optimal solution of the objective function and the chromosome is transformed into the actual solution by coding language

There are many choice operators in GA, and the mechanisms are different. Among them, roulette selection, elite selection, and tournament selection are the most popular. The roulette selection method is a replay-type random sampling method. The probability that a chromosome in a population is selected is proportional to its corresponding fitness (adaptive function value). By accumulating and then normalizing the fitness values of all the individuals in the population and generating random numbers, according to the area where the random numbers fall, select the corresponding individuals as parents. The elite selection method, also known as the best retention method, completely copies the most adaptive chromosomes in the current population to the next-generation group. The tournament selection method is also called the random competition selection method. Each time, a pair of chromosomes is selected by roulette, competition occurs, and the chromosome with the highest fitness is selected to enter the next generation until all the chromosomes in the tournament have participated and the preset threshold is reached. The elite selection method and the tournament selection method are improved versions of the roulette selection method, and their selection error is better than that of the roulette selection method. The retention mechanism of the elite selection method makes it

difficult to guarantee chromosome diversity in reproduction, so a certain probability will lead to a local optimal solution. The literature [29] compares these three selection operators to prove that the tournament selection method performs better than the other two methods. Therefore, the tournament method is used here as the embedded algorithm of the selection operator.

3.3. *GA-ANN Combination.* As mentioned above, the main problems that ANN needs to solve in the application include the following: (1) determining the optimal parameters in a machine learning algorithm. Most studies use the grid search method [30] or empirical formula method [24], but both of these methods have serious defects that are difficult to overcome: the grid search method is an exhaustive search method. The possible values of each parameter are arranged and combined, and all the combinations are used as input parameters for the modeling, which is time-consuming and inefficient. The neural network structure based on the empirical formula method has a good generalization ability, but the application items and data distribution of the neural network often have great differences because the accuracy of the model constructed by this method is often poor. (2) Determine the optimal initial weights and biases. The default initial weights and biases are random numbers between $[-1, 1]$. The blindness of their setting will increase the number of iterations in model training, which will slow the convergence speed of the model and seriously affect the accuracy and application effect of the model. Therefore, it is necessary to solve such problems with an optimization algorithm.

Regarding the optimization study of ANNs, researchers have adopted a method of coupling GA and ANN in various scientific studies, namely, the GA-ANN method. Arifovic and Gencay [29] used GA to optimize the neural network structure and verified that this method is superior to Schwarz and Akaike’s empirical criteria. Bahnsen and Gonzalez [31] used not only GA to tune the number of hidden layers and neurons but also the type of activation function for hidden and output layers and the bias terms, and compared with

the optimization performance of binary particle swarm optimization algorithm (BPSO), the research proved that the GA optimization approach was superior to that of the default process of network structure determination and that this approach led to a solution that is very close to the global optimum based on GA-MLP. Boithias et al. [32] used GA-ANN to predict indoor discomfort and energy consumption. They used GA to optimize the parameters of the ANN structure and training process. First, the GA was used to realize variable selection and the variables that have a small influence on ANN training was eliminated. Finally, a model with considerable accuracy was obtained. Idrissi et al. [33] used GA to optimize the ANN, with a view to minimize the number of hidden layers and neurons while having the lowest MSE. Jeong et al. [34] employed a generalized additive model (GAM) and GA to tune the structure and decay coefficient of the ANN model. Based on the optimal structure and decay coefficient value, the proposed approach was compared to other classification methods, as well as to a nontuned ANN, and it was found that the GA-ANN performed better than other approaches. Efkolidis et al. [23] used GA-ANN to predict the thrust (Fz) and torque (Mz) during the drilling of St60 work pieces. The structure, connection weights, and training algorithms of an ANN were optimized in turn based on GA. The superiority of ANN progressive optimization is verified. However, in this paper, when considering only the prediction accuracy, the double-hidden-layer structure is the optimal model but the authors have not further optimized the multiple-hidden-layer ANN model.

Of the many researchers of GA-ANN, few scholars have considered progressive optimization from the aspects of the ANN structure and connection weight, especially after determining the optimal structure of a multiple-hidden-layer ANN. Few studies have further optimized the initial connection weights and biases. In view of this, a new GA-ANN method is proposed in this paper to accurately predict the TCS of sandstone subjected to freeze-thaw cycles. The model explores the nonlinear relationship between TCS (output) and confining pressure, number of freeze-thaw cycles, porosity, and longitudinal wave velocity (four inputs). The research includes two-step optimization of the structure, weights and biases of an ANN by GA, and the prediction performance is compared with the ANN model created in a simpler way. Therefore, this paper studies the optimal structure of an ANN for predicting the TCS of sandstone and compares it with the empirical formula method. Then, on the basis of the ANN optimal structure, the initial connection weights and biases are further optimized and a final GA-ANN model is obtained.

4. Details of the Development of ANN Models

4.1. Data Preprocessing. It can be seen from the data statistics in Table 1 that there are large differences between the dimensions and magnitudes of the five variables. To speed up the learning of neural networks and avoid singular samples, before the ANN modeling, the dataset should be normalized by equation (1) [35] and the output of the prediction result should be inversely normalized for comparison with the

experimental values.

$$X_{\text{norm}} = \frac{(X - X_{\min})}{(X_{\max} - X_{\min})}, \quad (1)$$

where X and X_{norm} are the experimental value and the normalized value, respectively, and X_{\max} and X_{\min} are the maximum value and the minimum value, respectively.

In addition, in supervised learning, the dataset needs to be divided into training samples (i.e., training set and validation set) and test samples, wherein the training samples are used to optimize the model learning and model parameter tuning; the test samples are used to test the generalization ability and reflect the prediction performance of the model. Based on the analysis results from the literature [36], the dataset is divided into a training sample set and a test sample set according to a ratio of 7:3.

4.2. Verification Method. The k -fold crossvalidation method is applied as a verification method for model training. In k -fold crossvalidation, the training dataset D is divided into k mutually exclusive subsets of similar size: $D = D_1 \cup D_2 \cup \dots \cup D_k$, and $D_i \cap D_j = \emptyset (i \neq j)$. To reduce the impact of sample randomness on the prediction model, each subset maintains the consistency of the data distribution as much as possible, i.e., by stratified sampling. This subset is selected as the verification sample, the remaining $k - 1$ sets are used as the training set, and finally, the mean value of the k verification results is returned. The amount of data in this paper is small, and a 5-fold crossvalidation method is selected.

4.3. Simple ANN Model. The ANN capabilities are dependent directly on the ANN structure [16]. Therefore, to establish an ideal neural network model, a structural optimization design must be carried out. As mentioned above, there are many studies on empirical formulas of the ANN model structure. The empirical formula method suggests that for small- and medium-sized datasets, an ANN model with a single hidden layer can evaluate any nonlinear relationship [37, 38]. Table 2 lists several ANN structure empirical formulas for calculating the number of neurons in a single hidden layer. In this study, four input variables and one output variable were used in the prediction model; hence, $N_i = 4$ and $N_0 = 1$. It can be seen from the calculation that the ANN structure constructed by several different formulas is very different.

The most well-recognized formula is from Zhang et al. [39]. Therefore, based on the trial-and-error method, 11 single-hidden-layer ANN models for predicting TCS were constructed and the number of neurons in the hidden layer ranged from 3 to 13. According to the study results from the literature [23], the Levenberg-Marquardt (LM) algorithm was selected as the training algorithm. Taking RMSE as the ANN model performance measurement standard, the lower the RMSE is, the better the model performance. To reduce the error, all the ANN models were trained five times and the average RMSE values were considered in the following analysis. Table 3 shows that model 10 has the best prediction performance for the TCS of sandstone subjected to freeze-thaw cycles, and the corresponding RMSE (3.52) is the

TABLE 2: Empirical formulas of the ANN structure.

Reference	Equations	Computational results	Parameter
Zhang [39]	$\sqrt{N_i + N_0} + a, a \in [0, 10]$	$3 \leq n \leq 13$	
Hecht-Nielsen [37]	$\leq 2 \times N_i + 1$	$n \leq 9$	
Ripley [40]	$(N_i + N_0)/2$	$n = 3$	
Paola [41]	$(2 + N_0 \times N_i + 0.5N_0 \times (N_0^2 + N_i) - 3)/N_i + N_0$	$n = 8$	N_i and N_0 are the numbers of neurons in the input layer and output layer, respectively, which are both 3 in these paper.
Wang [42]	$2N_i/3$	$n = 3$	
Masters [43]	$\sqrt{N_i \times N_0}$	$n = 3$	
Kaastra and Boyd [44], Kanellopoulos and Wilkinson [45]	$2N_i$	$n = 8$	

lowest. The structure of the model is (4-12-1). Later, we use (4-12-1) as the optimal model for TCS prediction with a simple ANN model and compare its performance with that of the ANN model based on GA structure optimization.

4.4. GA-ANN Model. The GA-ANN presented in this paper summarizes the process of determining the optimum network structure and the optimum initial weights and biases for predicting the TCS of sandstone subjected to freeze-thaw cycles. The prediction errors are minimized by changing the network structure and other parameters. This process will be implemented in two steps in this section. The GA parameter settings in the two-step optimization process are shown in Table 4.

4.4.1. ANN Structure Tuning Based on GA. GA is a powerful optimization technique for finding a global optimum in a multidimensional searching space. The global optimization ability of the GA algorithm was used to perform ANN structural tuning. The global search scope of the ANN structure should be determined first. If the search range is set too large, the number of calculations will be too large and the convergence speed will be slow. When the search range is set too small, the optimal ANN structure may be missed. Therefore, setting reasonable search boundaries is important for the performance of the model. The expert-level model can be obtained by setting appropriate parameters. Therefore, according to the relevant reference [26], the learning rate and structural boundary settings of the ANN are as follows (see Table 5). In this process, because the performance of the model is inversely related to the RMSE, the fitness function is set to the reciprocal form of the RMSE, i.e., $1/\text{RMSE}$. According to the literature [46], the number of maximum generations is set to 20, the selection operator is the tournament selection method, the crossover rate and the mutation rate are 0.8 and 0.1, respectively, and the population number is 200. The process stops when it iterates to the maximum reproductive value (20). See Table 4 for the details of the GA.

Figure 4 shows the changing process of the minimum RMSE (corresponding to the optimal chromosome) in each generation of populations when using different numbers of hidden layers. It can be seen from the four curves that the minimum RMSE value of each generation shows a significant downward trend with population reproduction, which

proves the effectiveness of the GA for the structural optimization of ANN. Figure 4(a) is the optimization process of the ANN model structure for predicting TCS of sandstone subjected to freeze-thaw cycles. After one iteration, the minimum RMSE of the population is greatly reduced; after that, the minimum RMSE in every generation progressively reduces in the first 15 iterations and the lowest RMSE was achieved by the ANN model with two hidden layers (14 neurons in the first layer and 11 neurons in the second). The RMSE value (1.562) is much lower than the minimum RMSE (3.52) corresponding to the simple ANN based on the empirical formula method. Although the simple ANN can map any nonlinear relationship, it is not the optimal choice. Figure 4(b) shows the ANN structure after the optimization of the GA, which is used for further optimization, as described below. Therefore, the optimal structure of the ANN is determined to be (4-14-11-1).

4.4.2. ANN Initial Connection Weight and Bias Tuning Based on GA. After determining the ANN structure, the initial connection weights and biases of the ANN are optimized. The initial connection weights and biases are generally chosen as random numbers between $(-1, 1)$. Because of the randomness of the initial weight and bias setting process, the learning time and final connection weights of the model keep changing due to the number of training iterations. Therefore, even if specific ANN structural parameters are determined, the trained final ANN model is not unique, which often leads to the ANN model falling into a local optimal deadlock, thus affecting the accuracy of the model. In addition, the blindness of the initial weight and bias setting will increase the number of iterations of the model training, resulting in slower convergence of the model. This process seriously affects the accuracy and application effect of the model. Therefore, it is necessary to further apply GA to tune the initial weights and biases of the ANN model, which possesses the optimal structure.

The number of optimization objects (connection weights and biases) is consistent with the length of the chromosomes in the GA. For the ANN structure (4-14-11-1) identified above, the connection weights and biases of the model are calculated by stratification and the total number is $(4 \times 14) + (14 \times 11) + (11 \times 1) + (14 + 11 + 1) = 247$, where (4×14) is the connection weights between the 4 input neurons and

TABLE 3: Simple ANN optimal network structure and prediction results.

Model no.	TCS	
	Nodes in hidden layer	Average RMSE
1	3	9.266
2	4	6.165
3	5	7.381
4	6	5.244
5	7	5.038
6	8	4.157
7	9	5.284
8	10	4.753
9	11	5.021
10	12	3.522
11	13	4.320

the 14 hidden neurons in the first hidden layer, (14×11) is the connection weights between the 14 neurons in the first hidden layer and the 11 neurons in the second hidden layer, and (11×1) is the connection weights between the 11 neurons in the second hidden layer and the output neuron; 14, 11, and 1 are the total number of biases on the first hidden layer, the second hidden layer, and output layer, respectively. Considering that the chromosomes are a floating point type and that the number of chromosomes is large, to determine the optimal population number, the population size should be 50, 100, 150, and 200 in turn and the maximum iteration should be set to 500 to ensure the realization of the global optimal solution. The parameters of GA are specified in Table 4.

Figure 5 shows the iterative process of the initial weight and bias tuning of the ANN model with the optimal structure. Although there are great differences among the four iteration curves (dashed lines) corresponding to different population sizes, the maximum RMSE is less than the RMSE (1.562). The RMSE corresponding to population chromosome number 150 is the lowest. Therefore, the population size of the GA-ANN model selected in the following training is 150. Compared with the optimization results in the previous section, the prediction error of the ANN is greatly reduced and the model performance is improved.

5. Evaluation of the Performance of the Model

In the process of GA-ANN model training, the inclusion of the GA can significantly improve the prediction performance of ANN. The database is randomly divided into a training set and testing set at a ratio of 7 : 3 and repeated five times. Based on the five datasets, five ANN models and five GA-ANN models are established with the optimal parameters determined above. To further verify the superiority of GA-ANN, RMSE, MAE, and R^2 are used to test the performance of the model. The calculation methods are as follows:

$$\text{RMSE} = \sqrt{\frac{1}{n} \sum_{i=1}^n (y_{\text{exp},i} - y_{\text{pred},i})^2}, \quad (2)$$

$$\text{MAE} = \frac{1}{n} \sum_{i=1}^n |y_{\text{exp},i} - y_{\text{pred},i}|, \quad (3)$$

$$R^2 = 1 - \frac{\sum_{i=1}^n (y_{\text{pred},i} - y_{\text{exp},i})^2}{\sum_{i=1}^n (y_{\text{exp},i} - \overline{y_{\text{exp},i}})^2}, \quad (4)$$

where n is the number of test samples, $y_{\text{exp},i}$ is the experimental value, $y_{\text{pred},i}$ is the predicted value of the test samples, and $\overline{y_{\text{exp},i}}$ is the average value of the test samples. The RMSE and MAE are used to measure the degree of deviation between the predicted value and the true value. The smaller the RMSE or MAE is, the smaller the prediction error of the model. R^2 is between $[0, 1]$, and the larger R^2 is, the better the prediction ability of the model.

Table 6 lists the obtained values of the performance indices for the proposed simple ANN and hybrid GA-ANN models. The prediction of testing data can reflect the application performance and generalization ability of the model; hence, these results are presented based on the test set. To select the best datasets of ANN and GA-ANN, a ranking technique proposed by Zorlu et al. [47] was used. As shown in Table 6, when a GA is incorporated into the ANN, the prediction performance of the model is significantly improved. According to the total score, the ANN based on the empirical formula has the best prediction performance for dataset 2, for which the RMSE, MAE, and R^2 are 2.676, 2.153, and 0.952, respectively. The GA-ANN based on dataset 5 has the best performance, with RMSE, MAE, and R^2 scores of 1.083, 0.893, and 0.993, respectively. The performance of the GA-ANN model is better than that of the simple ANN model based on any evaluation criterion.

Based on datasets 2 and 5, with the true value (experimental value) as the abscissa and the predicted value as the ordinate, a scatter point figure is made (Figure 6). Figures 6(a) and 6(b) show the relationship between the predicted and measured values of the simple ANN model and GA-ANN model, respectively. Line $y = x$ is the ideal prediction model. The closer the scatter points are to the straight line, the more accurate the prediction results are. Comparisons show that the fitness between the scatter points and ideal straight lines in Figure 6(b) is much greater than that in Figure 6(a).

6. Superiority and Limitations

The primary strength of this study is the verification of the GA-ANN method for the prediction of TCS of sandstone subjected to freeze-thaw cycles. Advantages of the GA-ANN method over conventional experimental tests include its low cost, low time consumption, and nondestructive process, which will become more evident when a larger rock dataset is available. Even compared with existing models, the GA-ANN still has the following advantages: (1) the

TABLE 4: GA parameter settings.

GA parameter	Values	
Scenarios	Optimization of ANN structure	Optimization of initial weights and biases
Fitness function	1/RMSE	1/RMSE
Selection method	Tour	Tour
Genetic possibility	Crossover (0.8), mutation (0.1)	Crossover (0.8), mutation (0.1)
Stop criteria	Maximum generation	Maximum generation
Number of chromosomes	200	50/100/150/200
Type of chromosomes	Integer	Float
Number of generation	20	500

TABLE 5: ANN parameters and tuning range.

Hyper parameters	Explanation	Type	Tuning range
Max_neuron	Maximum number of neurons in every hidden layer	Integer	1–40
Number_hidden_layers	Maximum number of hidden layers	Integer	1–4
Input_layer_neuron	Number of neurons in the input layer	Integer	3
Output_layer_neuron	Number of neurons in the output layer	Integer	3
Learning rate	Weight reduction due to updating in feedback training	Float	0.01

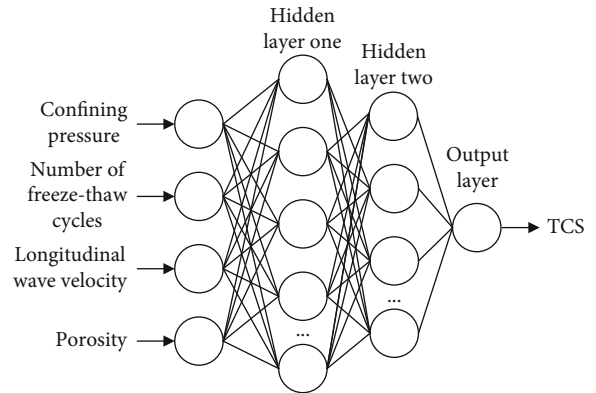
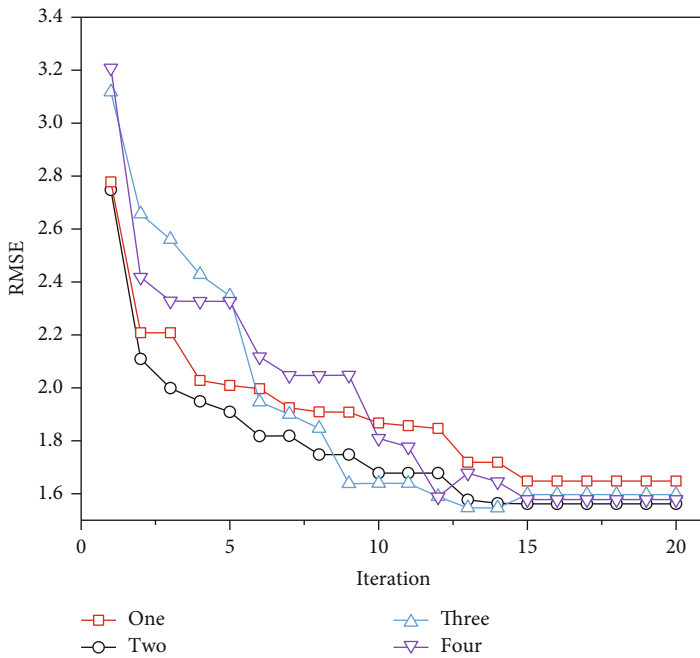


FIGURE 4: Structure parameter tuning: (a) minimum RMSE versus iteration with 1–4 hidden layers; (b) optimal ANN structure.

GA-ANN method requires no mechanical tests, as the prediction is made directly from the influencing variables of the TCS, (2) the generalization capability of the GA-ANN method might be better than existing models, which need to be fit based on a specific dataset, and a general model can be easily built and updated using a more comprehensive dataset, and (3) most importantly, such predictions can pro-

mote the establishment of “intelligent management for engineering” in the future.

The omission of other influencing variables of the TCS of sandstone, such as the addition of freeze-thaw temperature, rock mineralogical composition, and water saturation degree, is a clear limitation of the current study. A larger dataset containing more types and mineralogical composition variables

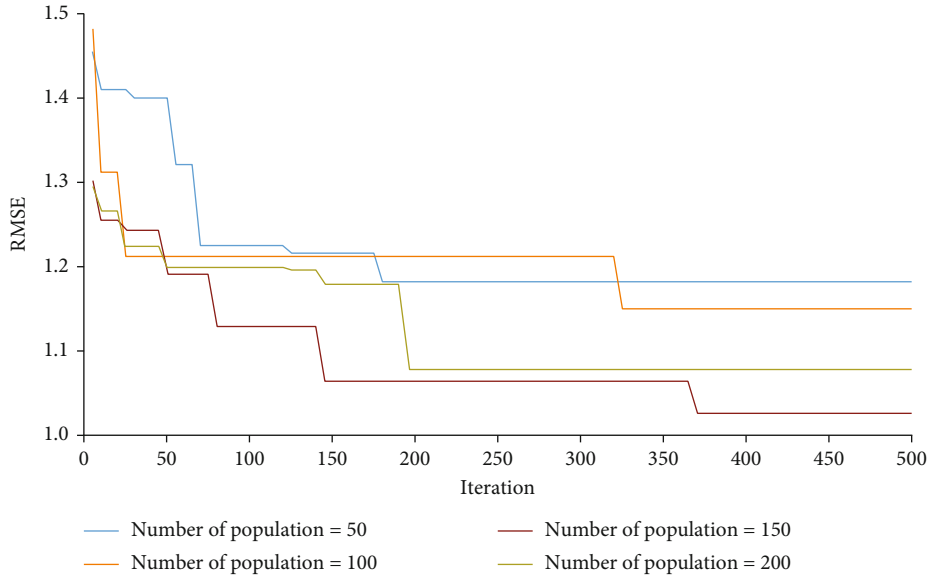
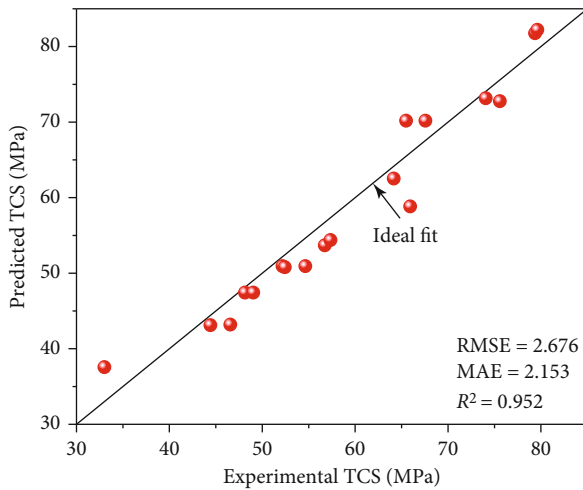


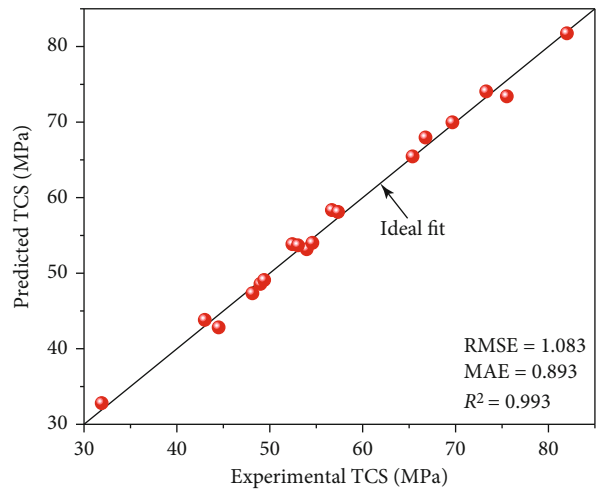
FIGURE 5: Initial connection weight and bias parameter tuning.

TABLE 6: Results of the performance indices of the ANN and GA-ANN models.

Method	Model	RMSE	MAE	R^2	Rating for RMSE	Rating for MAE	Rating for R^2	Rank value
ANN	1	3.408	2.395	0.925	1	4	1	6
	2	2.676	2.153	0.952	5	5	3	13*
	3	3.123	2.426	0.937	4	3	2	9
	4	3.301	2.524	0.953	2	2	4	8
	5	3.186	2.626	0.958	3	1	5	9
GA-ANN	1	1.139	0.866	0.992	4	5	4	13
	2	1.165	0.899	0.991	3	3	3	9
	3	1.302	1.004	0.989	1	1	1	3
	4	1.206	0.949	0.990	2	2	2	6
	5	1.083	0.893	0.993	5	4	5	14*



(a)



(b)

FIGURE 6: Comparison of the predicted and experimental TCS values: (a) simple ANN model; (b) GA-ANN model.

of rocks is being collected in the hope that the generalization capability of the trained ANN model can be improved once physical-mechanical characteristics are used as inputs.

7. Conclusions

This paper established a new AI model (GA-ANN) for estimating the TCS of sandstone subjected to freeze-thaw cycles. A database consisting of 60 datasets was prepared, and in each dataset, the longitudinal wave velocity, porosity, confining pressure, and number of freeze-thaw cycles were considered inputs and the TCS was set as the system output. First, the ANN structure was optimized based on the GA. When there were 2 hidden layers, the first hidden layer and the second hidden layer had 14 and 11 neurons, respectively, and the RMSE was reduced to 1.562, which was much lower than the RMSE (3.522) based on the simple ANN model. Then, based on the optimal ANN structure (4-14-11-1), the initial connection weights and biases of the ANN were further optimized based on GA and the RMSE was minimized (1.083); thus, the optimal ANN model was obtained. After proposing the AI systems, to determine the accuracy level of the developed models, three performance indices including RMSE, MAE, and R^2 were used and computed. The RMSE, MAE, and R^2 equal to 1.083, 0.893, and 0.993, respectively, for testing datasets revealed the highest accuracy of the hybrid GA-ANN model in predicting TCS of sandstone subjected to freeze-thaw cycles, while these values were 2.676, 2.153, and 0.952 for the simple ANN model. These results indicated the superiority of the hybrid GA-ANN model in predicting TCS of sandstone subjected to freeze-thaw cycles in comparison with the simple ANN model.

Data Availability

The data are presented in the manuscript.

Conflicts of Interest

The authors declare that they have no conflict of interest.

Acknowledgments

This work was supported by the National Natural Science Foundation of China (Grant no. 51774323), the Hunan Provincial Natural Science Foundation of China (Grant no. 2020JJ4704), and the fundamental research funds for the central universities of Central South University, China (Grant no. 2021zzts0279).

References

- [1] W. Chen, X. Tan, H. Yu, K. Yuan, and S. Li, "Advance and review on thermo-hydro-mechanical characteristics of rock mass under condition of low temperature and freeze-thaw cycles," *Chinese Journal of Rock Mechanics and Engineering*, vol. 30, no. 7, pp. 1318–1336, 2011.
- [2] R.-H. Cao, C. Wang, R. Yao et al., "Effects of cyclic freeze-thaw treatments on the fracture characteristics of sandstone under different fracture modes: laboratory testing," *Theoretical and Applied Fracture Mechanics*, vol. 109, p. 102738, 2020.
- [3] H. Zhang, C. Yuan, G. Yang et al., "A novel constitutive modeling approach measured under simulated freeze-thaw cycles for the rock failure," *Engineering with Computers*, vol. 37, pp. 779–792, 2019.
- [4] F. Gao, X. Xiong, C. Xu, and K. Zhou, "Mechanical property deterioration characteristics and a new constitutive model for rocks subjected to freeze-thaw weathering process," *International Journal of Rock Mechanics and Mining Sciences*, vol. 140, p. 104642, 2021.
- [5] X. Tan, W. Chen, J. Yang, and J. Cao, "Laboratory investigations on the mechanical properties degradation of granite under freeze-thaw cycles," *Cold Regions Science and Technology*, vol. 68, no. 3, pp. 130–138, 2011.
- [6] M. Hosseini and A. R. Khodayari, "Effect of freeze-thaw cycle on strength and rock strength parameters (a Lushan sandstone case study)," *Journal of Mining and Environment*, vol. 10, no. 1, pp. 257–270, 2019.
- [7] Y. Shen and X. Wang, "Study on freeze thawing and damage mechanism of rock in Western cold and dry area," *Urban Roads Bridges and Flood Control*, vol. 7, no. 9, pp. 223–224, 2017.
- [8] Y. Bai, R. Shan, Y. Ju, Y. Wu, P. Sun, and Z. Wang, "Study on the mechanical properties and damage constitutive model of frozen weakly cemented red sandstone," *Cold Regions Science and Technology*, vol. 171, p. 102980, 2020.
- [9] F. Bayram, "Predicting mechanical strength loss of natural stones after freeze-thaw in cold regions," *Cold Regions Science and Technology*, vol. 83–84, pp. 98–102, 2012.
- [10] İ. İnce and M. Fener, "A prediction model for uniaxial compressive strength of deteriorated pyroclastic rocks due to freeze-thaw cycle," *Journal of African Earth Sciences*, vol. 120, pp. 134–140, 2016.
- [11] Q. Liu, S. Huang, Y. Kang, and X. Liu, "A prediction model for uniaxial compressive strength of deteriorated rocks due to freeze-thaw," *Cold Regions Science and Technology*, vol. 120, pp. 96–107, 2015.
- [12] H. Fu, J. Zhang, Z. Huang, Y. Shi, and W. Chen, "A statistical model for predicting the triaxial compressive strength of transversely isotropic rocks subjected to freeze-thaw cycling," *Cold Regions Science and Technology*, vol. 145, pp. 237–248, 2018.
- [13] S. Z. Seyed Mousavi, H. Tavakoli, P. Moarefvand, and M. Rezaei, "Assessing the effect of freezing-thawing cycles on the results of the triaxial compressive strength test for calc-schist rock," *International Journal of Rock Mechanics and Mining Sciences*, vol. 123, p. 104090, 2020.
- [14] D. J. Armaghani and E. Momeni, "Feasibility of ANFIS model for prediction of ground vibrations resulting from quarry blasting," *Environmental Earth Sciences*, vol. 74, no. 4, pp. 2845–2860, 2015.
- [15] M. Monjezi, Z. Ahmadi, A. Y. Varjani, and M. Khandelwal, "Backbreak prediction in the Chadormalu iron mine using artificial neural network," *Neural Computing and Applications*, vol. 23, pp. 1101–1107, 2012.
- [16] M. Khandelwal and T. N. Singh, "Predicting elastic properties of schistose rocks from unconfined strength using intelligent approach," *Arabian Journal of Geosciences*, vol. 4, pp. 435–442, 2011.
- [17] E. T. Mohamad, D. J. Armaghani, E. Momeni, A. H. Yazdavar, and M. Ebrahimi, "Rock strength estimation: a PSO-based BP

- approach,” *Neural Computing and Applications*, vol. 30, pp. 1635–1646, 2018.
- [18] D. Jahed Armaghani, M. F. Mohd Amin, S. Yagiz, R. S. Fardoneh, and R. A. Abdullah, “Prediction of the uniaxial compressive strength of sandstone using various modeling techniques,” *International Journal of Rock Mechanics and Mining Sciences*, vol. 85, pp. 174–186, 2016.
- [19] A. Momeni, Y. Abdilor, G. R. Khanlari, M. Heidari, and A. A. Sepahi, “The effect of freeze–thaw cycles on physical and mechanical properties of granitoid hard rocks,” *Bulletin of Engineering Geology and the Environment*, vol. 75, pp. 1649–1656, 2015.
- [20] X.-C. Qin, S.-P. Meng, D.-F. Cao et al., “Evaluation of freeze-thaw damage on concrete material and prestressed concrete specimens,” *Construction and Building Materials*, vol. 125, pp. 892–904, 2016.
- [21] Z. Pan, K. Zhou, R. Gao et al., “Research on the pore evolution of sandstone in cold regions under freeze-thaw weathering cycles based on NMR,” *Geofluids*, vol. 2020, Article ID 8849444, 12 pages, 2020.
- [22] J.-L. Li, K.-P. Zhou, W.-J. Liu, and H.-W. Deng, “NMR research on deterioration characteristics of microscopic structure of sandstones in freeze-thaw cycles,” *Transactions of Non-ferrous Metals Society of China*, vol. 26, no. 11, pp. 2997–3003, 2016.
- [23] N. Efkolidis, A. Markopoulos, N. Karkalos, C. G. Hernández, J. L. H. Talón, and P. Kyratsis, “Optimizing models for sustainable drilling operations using genetic algorithm for the optimum ANN,” *Applied Artificial Intelligence*, vol. 33, no. 10, pp. 881–901, 2019.
- [24] M. Khandelwal, A. Marito, S. A. Fatemi et al., “Implementing an ANN model optimized by genetic algorithm for estimating cohesion of limestone samples,” *Engineering with Computers*, vol. 34, pp. 307–317, 2018.
- [25] Z. Shao, D. Jahed Armaghani, B. Yazdani Bejarbaneh, M. A. Mu’azu, and E. Tonnizam Mohamad, “Estimating the friction angle of black shale core specimens with hybrid-ANN approaches,” *Measurement*, vol. 145, pp. 744–755, 2019.
- [26] C. Qi, A. Fourie, and Q. Chen, “Neural network and particle swarm optimization for predicting the unconfined compressive strength of cemented paste backfill,” *Construction and Building Materials*, vol. 159, pp. 473–478, 2018.
- [27] J. H. Holland, “Genetic algorithms and the optimal allocation of trials,” *SIAM Journal on Computing*, vol. 2, no. 2, pp. 88–105, 1973.
- [28] D. E. Goldberg, *Genetic Algorithm in Search, Optimization, and Machine Learning*, The University of Alabama, Addison-Wesley Publishing Company, 1989.
- [29] J. Arifovic and R. Gencay, “Using genetic algorithms to select architecture of a feedforward artificial neural network,” *Physica A: Statistical Mechanics and its Applications*, vol. 289, no. 3–4, pp. 574–594, 2001.
- [30] Q. H. Doan, T. Le, and D.-K. Thai, “Optimization strategies of neural networks for impact damage classification of RC panels in a small dataset,” *Applied Soft Computing*, vol. 102, p. 107100, 2021.
- [31] A. C. Bahnsen and A. M. Gonzalez, “Evolutionary algorithms for selecting the architecture of a MLP neural network: a credit scoring case,” in *2011 IEEE 11th International Conference on Data Mining Workshops*, pp. 725–732, 2011.
- [32] F. Boithias, M. El Mankibi, and P. Michel, “Genetic algorithms based optimization of artificial neural network architecture for buildings’ indoor discomfort and energy consumption prediction,” *Building Simulation*, vol. 5, no. 2, pp. 95–106, 2012.
- [33] J. Idrissi, R. Hassan, C. Youssef, and E. Mohamed, *Genetic Algorithm for Neural Network Architecture Optimization*, Third International Conference on Logistics Operations Management, IEEE, 2016.
- [34] C. Jeong, J. H. Min, and M. S. Kim, “A tuning method for the architecture of neural network models incorporating GAM and GA as applied to bankruptcy prediction,” *Expert Systems with Applications*, vol. 39, no. 3, pp. 3650–3658, 2012.
- [35] M. Khandelwal, “Blast-induced ground vibration prediction using support vector machine,” *Engineering with Computers*, vol. 27, pp. 193–200, 2011.
- [36] X. Lu, W. Zhou, X. Ding, X. Shi, B. Luan, and M. Li, “Ensemble learning regression for estimating unconfined compressive strength of cemented paste backfill,” *IEEE Access*, vol. 7, pp. 72125–72133, 2019.
- [37] R. Hecht-Nielsen, *Kolmogorov’s Mapping Neural Network Existence Theorem*, The first IEEE international conference on neural networks, IEEE, 1987.
- [38] K. Hornik, M. Stinchcombe, and H. White, “Multilayer feed-forward networks are universal approximators,” *Neural Networks*, vol. 2, no. 5, pp. 359–366, 1989.
- [39] Z. H. Zhang, D. N. Yan, J. T. Ju, and Y. Han, “Prediction of the flow stress of a high alloyed austenitic stainless steel using artificial neural network,” *Materials Science Forum*, vol. 724, pp. 351–354, 2012.
- [40] B. D. Ripley, *Statistical Aspects of Neural Networks*, Springer, USA, 1993.
- [41] J. Paola, *Neural network classification of multispectral imagery*, [M.S. thesis], The University of Arizona, USA, 1994.
- [42] C. Wang, *A theory of generalization in learning machines with neural application*, [Ph.D. thesis], The University of Pennsylvania, USA, 1994.
- [43] T. Masters, *Practical Neural Network Recipes in C++*, Academic Press, USA, 1993.
- [44] I. Kaastra and M. Boyd, “Designing a neural network for forecasting financial and economic time series,” *Neurocomputing*, vol. 10, pp. 215–236, 1996.
- [45] I. Kanellopoulos and G. G. Wilkinson, “Strategies and best practice for neural network image classification,” *International Journal of Remote Sensing*, vol. 18, no. 4, pp. 711–725, 2010.
- [46] C. Qi, Q. Chen, A. Fourie, and Q. Zhang, “An intelligent modelling framework for mechanical properties of cemented paste backfill,” *Minerals Engineering*, vol. 123, pp. 16–27, 2018.
- [47] K. Zorlu, C. Gokceoglu, F. Ocakoglu, H. A. Nefeslioglu, and S. Acikalin, “Prediction of uniaxial compressive strength of sandstones using petrography- based models,” *Engineering Geology*, vol. 96, no. 3–4, pp. 141–158, 2008.

Research Article

Laboratory Study on the Effect of Fluid Pressurization Rate on Fracture Instability

Xinyao Wang ¹, Quanchen Gao ¹, Xiao Li ², and Dianzhu Liu ¹

¹School of Mechanics and Civil Engineering, China University of Mining and Technology (Beijing), Beijing 100083, China

²Key Laboratory of Shale Gas and Geoengineering, Institute of Geology and Geophysics, Chinese Academy of Sciences, Beijing 100029, China

Correspondence should be addressed to Xinyao Wang; lnwangxinyao@126.com

Received 5 April 2021; Accepted 20 May 2021; Published 9 June 2021

Academic Editor: Yu Wang

Copyright © 2021 Xinyao Wang et al. This is an open access article distributed under the Creative Commons Attribution License, which permits unrestricted use, distribution, and reproduction in any medium, provided the original work is properly cited.

Fluid injection-induced earthquakes have been a scientific and social issue of wide concern, and fluid pressurization rate may be an important inducement. Therefore, a series of stepwise and conventional injection-induced shear tests were carried out under different fluid pressurization rates and effective normal stresses. The results show that the magnitude of fluid pressure is the main factor controlling the initiation of fracture slipping. The contribution of fluid pressure heterogeneity and permeability evolution on the initiation of fracture slipping is different with the increase of fluid pressurization rate. When the fluid pressurization rate is small, permeability evolution plays a dominant role. On the contrary, the fluid pressure heterogeneity plays a dominant role. The increase of fluid pressurization rate may lead to the transition from creep slip mode to slow stick-slip mode. Under the laboratory scale, the fluid pressure heterogeneity causes the coulomb failure stress to increase by about one times than the predicted value at the initiation of fracture slipping, and the coulomb stress increment threshold of 1.65 MPa is disadvantageous to the fracture stability.

1. Introduction

In the last 10 years, the worldwide exponential increase of fluid injection-induced earthquakes has become a widely concerned scientific and social problem. This is due to hydraulic fracturing, enhanced geothermal stimulation, and saltwater disposal engineering operations which result in the reactivation of faults [1]. However, the role of fluid injection procedures in induced earthquakes remains controversial, and the key knowledge gaps in risk management remain. Understanding the mechanism by which fluid injection procedures induced fault slip is important for improving seismic risk associated with large-scale fluid injection.

According to the effective stress principle and Mohr-Coulomb failure criterion, fault instability occurs when the shear stress on a rock fracture exceeds the product of the friction coefficient and effective normal stress, which is given by the difference between the normal stress and fluid pressure. Elevating the fluid pressure during fluid injection decreases the effective normal stress, resulting in fault instability [2–

6]. However, this is restricted to fault slip initiation caused by fluid overpressure. Recent studies showed that fluid overpressure is not the only parameter governing fault reactivation and the associated seismicity. The fluid pressurization rate and the fluid pressure heterogeneity are also closely related to the fault slip initiation and slip mode [7]. French et al. performed axial compression and lateral relaxation tests on permeable sandstones with saw-cut surfaces. Fluid injection into a saw-cut granite sample in stress relaxation test shows that the onset of fault activation may not be predicted by the principle of effective stress at high injection rates [8]. This is presumably caused by a significantly heterogeneous distribution of fluid pressure on the fault plane [9, 10]. In addition, the influence of permeability evolution on fracture slip has also been concerned, and it has been regarded as a supplementary mechanism of fluid injection induced fault slip. However, the physical mechanisms controlling fault slip initiation and slip mode in response to fluid pressurization are still a matter of debate. The mismatch between seismic time and fluid injection time is still not clear.

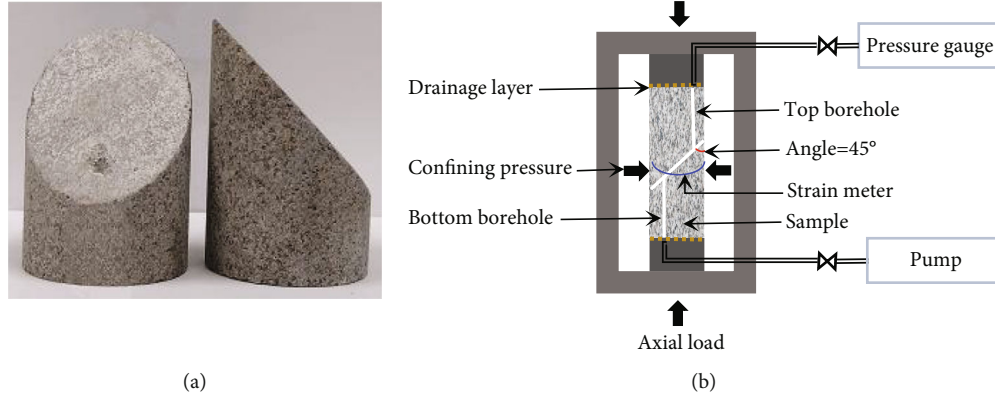


FIGURE 1: Experimental material and configuration. (a) Saw-cut sandstone fracture. (b) Sketch of sample assembly installed inside the triaxial pressure vessel.

The objective of this study is to unravel the slip characteristics of a critically stressed fracture associated with fluid pressurization rate. We conducted injection-induced fracture slip experiments on saw-cut permeable sandstones using different fluid injection schemes. The influence of fluid pressurization rate on fracture slip mode and displacement evolution process under different fluid injection rates is compared and analyzed. In addition, we also analyzed the influence of fluid pressure heterogeneity and permeability evolution on fracture slip initiation.

2. Experimental Configuration and Method

2.1. Experimental Material and Configuration. The cylindrical samples of sandstone of 50 mm in diameter were cored and then cut and precisely ground to a length of 100 mm. The sample was then cut at 45° with respect to its axis to create an elliptical saw cut fracture interface of 50 mm in width and 70 mm in length along strike (Figure 1(a)). The fracture surfaces were then polished using sandpaper with $300\ \mu\text{m}$ particle size. Two 3 mm diameter boreholes were drilled parallel to the core axis at the sample ends to maximize the fluid diffusion distance along the fracture. The fractured sample was placed in two heat shrinkable tubes and equipped with axial and radial extensometers (Figure 1(b)). The tests were carried out using the TAW-2000 electrohydraulic servo rock triaxial testing machine, from Key Laboratory of Shale Gas and Geological Engineering, Institute of Geology and Geophysics, Chinese Academy of Sciences at ambient temperature (25°C). The testing machine has an independent closed-loop control system of axial pressure, confining pressure, and pore water pressure. The range of axial pressure is 0-2000 kN, confining pressure is 0-100 MPa, and pore water pressure is 0-60 MPa. The whole process test of uniaxial and triaxial strain, cyclic loading, and other tests with the diameter of the specimen ranging from 25 mm to 100 mm can be conducted to record the whole process of the test in real-time. Water and silicon oil were used as the pore and confining fluids, respectively. The normal and shear stresses were obtained by resolving the triaxial stress state onto the fracture plane [11]. In addition, the normal and shear stresses were corrected by considering the change in fractured con-

tact area and the deformation of Teflon drainage layers [12]. Fracture slip was computed by projecting the sample axial shortening onto the fracture direction.

2.2. Experimental Method and Program. Tests were conducted by adjusting the injection rate (IR) and fluid pressurization rate (PR) under different effective normal stress. The initial pore pressure (P_0) was set to 1 MPa. The shear strength at the onset of fault slip under constant pore pressure conditions, denoted τ_s , was determined by conducting an axial displacement loading test (Figure 2: stage1 (gray area)). Subsequently, we applied the shear stress τ_0 , equivalent to 93% of the shear strength, and fixed the normal stress (σ_n), assumed the fracture approaching a critical stress state (Figure 2: stage2 (yellow area)). Finally, the fluid pressure was applied from the bottom end of the sample by advancing the downstream syringe pump under constant effective normal stress (σ_{eff}) until a fracture slip occurred (Figure 2: stage3 (white area)). While the top end of the sample was connected to an intelligent digital pressure gauge, resulting in undrained boundary condition (Figure 1(b)). The fluid pressure in the top and bottom boreholes was monitored to observe fluid pressure distribution on the fracture. Note that confining pressure σ_3 remained constant throughout the fluid injection. We applied two different fluid injection schemes in the tests SW-1 and SW-2. The fluid pressure was increased stepwise from 1 to 7 MPa with a rate of 0.04 MPa/s in test SW-1 and 0.005 MPa/s in test SW-2 (Figure 3). Each fluid injection phase lasted for 8 min. For tests SW-1 and SW-2, fluid pressure was increased stepwise by 2 MPa, with each step lasting 1 and 7 min, respectively. Subsequently, the fluid pressure was held constant for 7 and 1 min for tests SW-1 and SW-2, respectively. In addition, three nonstepping injection-induced shear tests were carried out under 10 MPa, 20 MPa, and 26 MPa effective normal stresses, respectively. The experiment program is depicted in Table 1.

3. Experimental Results

3.1. The Role of Fluid Pressurization Rate. As shown in Figure 2(a) and Figure 2(b), the shear stress on the fracture surface showed a nearly linear increase during the initial

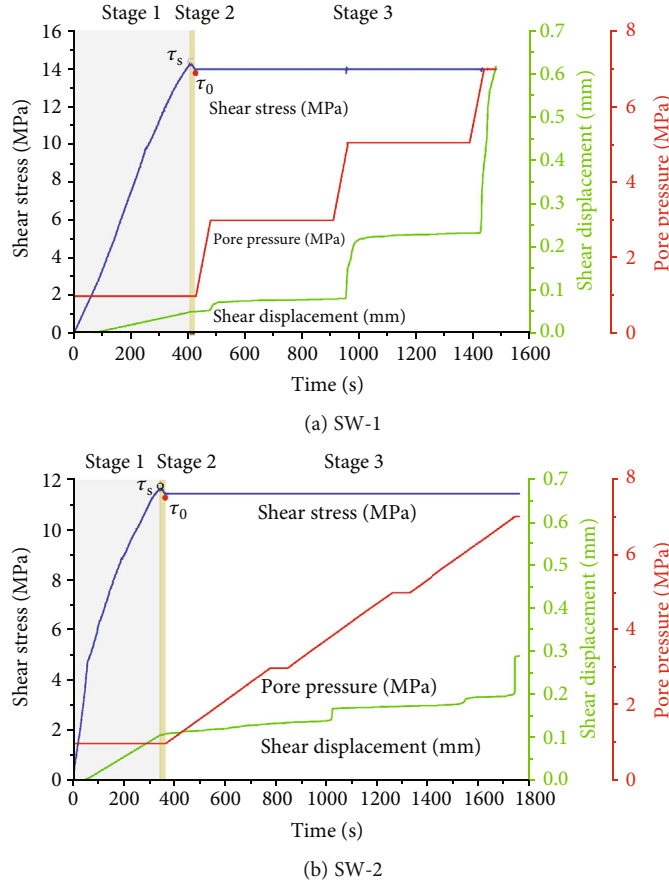


FIGURE 2: Stress-displacement evolution in stepping injection-induced shear tests. Please notice the difference in the coordinate scale.

loading stage (stage1), and the fracture slip rate gradually accelerated. Under $\sigma_n = 27$ MPa and $P_0 = 1$ MPa, the peak shear strength (τ_s) of tests SW-1 and SW-2 are very close ($\tau_s \approx 14$ MPa, $\tau_s \approx 12$ MPa), and then, the peak shear strength (τ_s) is reduced to about $0.93 \times \tau_s$ before injection. In the test SW-1, the saw-cut samples with critical stress begin to slip approximately at the end of the first fluid injection phase ($P_0 \approx 3.0$ MPa), slight slip hysteresis was detected, and there is no further slip during the pressure holding phase. This indicates that the magnitude of fluid pressure may control the onset of fracture slip. At a relatively fast fluid pressurization rate, slow stick-slip events were observed (slow stick-slip events are defined as peak slip speeds of less than 1 mm/s). Slip abruptly accelerated to peak velocity and then decelerated slowly. Subsequently, a slight hysteresis slipping of the fracture was induced at the end of each fluid pressurization phase. By contrast, in the test SW-2, saw-cut samples with critical stress did not show significant slip after the first fluid injection phase ($P_0 \approx 3.0$ MPa). Instead, it shows a significant slipping hysteresis, which may be due to the combined action of fluid pressure heterogeneity and fracture surface permeability evolution. In addition, compared with the test SW-1, fluid injection rate is 8 times slower, almost continuous fracture creep was observed, which indicates that the fluid pressurization rate may control the fracture slip mode.

3.2. Deformation Characteristics of Fracture during Fluid Injection. As shown in Figures 2(a) and 2(b), the shear displacement increases gradually at each stage of fluid injection. One aspect, the shear creep behavior occurs under constant shear stress, resulting in an increase in shear displacement. The other aspect, fluid injection reduces the effective normal stress and frictional resistance, so the fracture is more likely to slip as the shear displacement increases. In the test SW-1, episodic slow stick-slip events were observed, the slipping speed is less than $2 \mu\text{m/s}$ for long slipping duration of 60 seconds or more. In the SW-2, the slip at the low-pressure rate is apparently intermittent, and a number of small slips accumulate leading to eventual instability. But the slipping speed increases with the maximum $< 0.2 \mu\text{m/s}$ while slowly increasing and decreasing. Seismic (unstable) slip for natural faults generally shows high slip velocities (≥ 0.1 m/s) [13]. Thus, in these experiments, fluid pressure may promote steady and slow slipping [14–16]. It can also be seen that the fracture does not expand significantly during the initial injection stage. With the increase of injection pressure, fracture expansion occurred and gradually accelerated, indicating that fracture opening occurred during the slipping process. This condition may reflect surface roughness and associated shear dilation under the combined action of shear stress and continuous injection [17]. After that, the rate of expansion

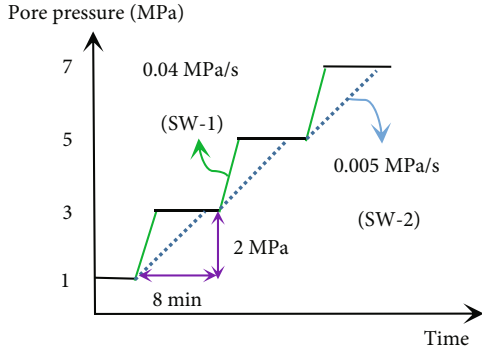


FIGURE 3: Stepping injection process.

TABLE 1: Experimental program and parameter setting.

Test no.	σ_n (MPa)	P_0 (MPa)	σ_{eff} (MPa)	IR (MPa/s)
SW-1	27	1	26	0.04
SW-2	27	1	26	0.005
T-1	11	1	10	0.005
T-2	21	1	20	0.005
T-3	27	1	26	0.005

increased dramatically. When the fracture is activated, the shear displacement remains stable at the current position due to a combination of reduced injection pressure and shear creep behavior. However, when the injection pressure is unloaded, the fracture tends to close. The normal displacement recovery also has the hysteresis phenomenon. Therefore, in this case, injection-induced fracture activation can be well characterized by the mechanism of deformation.

3.3. Influence of Fluid Pressure Heterogeneity. In order to study the influence of fluid pressure heterogeneity on fault slip, three tests were carried out at a water injection rate of 0.005 MPa/s under an effective normal stress of 10 MPa, 20 MPa, and 26 MPa, respectively. As shown in Figures 4(a)–4(c), the Mohr-Coulomb failure envelope was constructed by shear strength (Figure 4(d); solid red circle), and the friction coefficient μ was 0.62.

As shown in Figure 4(d), the stress state of the saw-cut fracture is represented by a solid green five-pointed star, which is located below the Mohr failure envelope. When loaded at a constant fluid rate, the effective normal stress gradually decreases until the fracture slips unsteadily (solid pink five-pointed star). Obviously, the measured fluid pressure in the water injection hole is greater than that predicted by the failure criterion. The deviation between them increases with the increase of effective normal stress and water injection rate. Through analysis, we believe that when the effective normal stress and fluid injection rate are high, the compression of fracture aperture becomes smaller and the fracture surface permeability increases, which leads to the amplification of the heterogeneity of fluid pressure. In order to verify the analysis results, the Coulomb failure stress change ($\mu\Delta P$) can be obtained from equation (1) [18], which is caused by the change of pore pressure. The calculated cou-

lomb stress at the beginning of fracture slipping is about one time larger than that predicted by the failure criterion. The increment of Coulomb fracture stress value is greater than 1.65 MPa during each test process of fluid injection-induced fracture instability. It fully shows that the cause of fracture instability is related to the variation of Coulomb fracture stress caused by pore pressure, and the influence is amplified by the fluid pressure heterogeneity.

$$\Delta\text{CFS} = \Delta\tau - \mu\Delta\sigma_{\text{eff}}, \quad (1)$$

where ΔCFS is the variation of Coulomb fracture stress, $\Delta\tau$ is the variation of shear stress, μ is the friction coefficient, and $\Delta\sigma_{\text{eff}}$ is the effective normal stress.

3.4. Influence of Permeability Changes. In order to study the influence of permeability evolution on fracture instability, the cubic law is used to calculate the permeability K_m (m^2) on the fracture surface (equations (2) and (3)) [19, 20].

$$b_m = -\left(\frac{12\eta \cdot L(t) \cdot Q(t)}{W \cdot \Delta P}\right)^{\frac{1}{3}}, \quad (2)$$

$$K_m = \frac{b_m^2}{12}, \quad (3)$$

where b_m (m) is the averaged hydraulic aperture, η (Pa·s) is the viscosity of fluid, $L(t)$ (m) is the contact length of the fracture surface, W (m) is the fracture width, $Q(t)$ (m^3/s) is the measured flow rate, and ΔP (Pa) is the differential pressure between the upstream and downstream extent of the fracture.

Figure 5 shows the variation of the friction coefficient and permeability on the fracture surface with slipping displacement and pore pressure at different fluid pressurization rates. In the test SW-1, when the fluid pressurization rate is high, the friction coefficient increases almost linearly with the increase of slipping displacement and, then, remains relatively stable after reaching the peak value, while the permeability of the fracture surface decreases almost linearly (Figure 5(a)). Compared with the test SW-1, the permeability of the fracture surface decreases relatively slowly and the average permeability is higher with the increase of the slipping displacement in test SW-2. When the slip displacements are 0.55 mm and 0.7 mm, respectively, the permeability is hysteresis and beyond the fracture slipping initial point of the second and third stages and, suddenly, decreases. The friction coefficient gradually increased to a peak during the stage1 of fluid injection and then decreased, until remained relatively stable (Figure 5(b)). The reduction of fracture surface permeability may be due to roughness degradation. Due to shear expansion, a sudden increase in the slipping rate temporarily increases the fracture permeability, but as the wear products fill the pore space, the permeability decreases with the increase of the slipping displacement. In addition, Figures 5(c) and 5(d) also show the change of friction coefficient and permeability with the increase of pore pressure. In SW-1 test, the permeability increases linearly and slowly with pore pressure until it suddenly increases at 3 MPa and 5 MPa

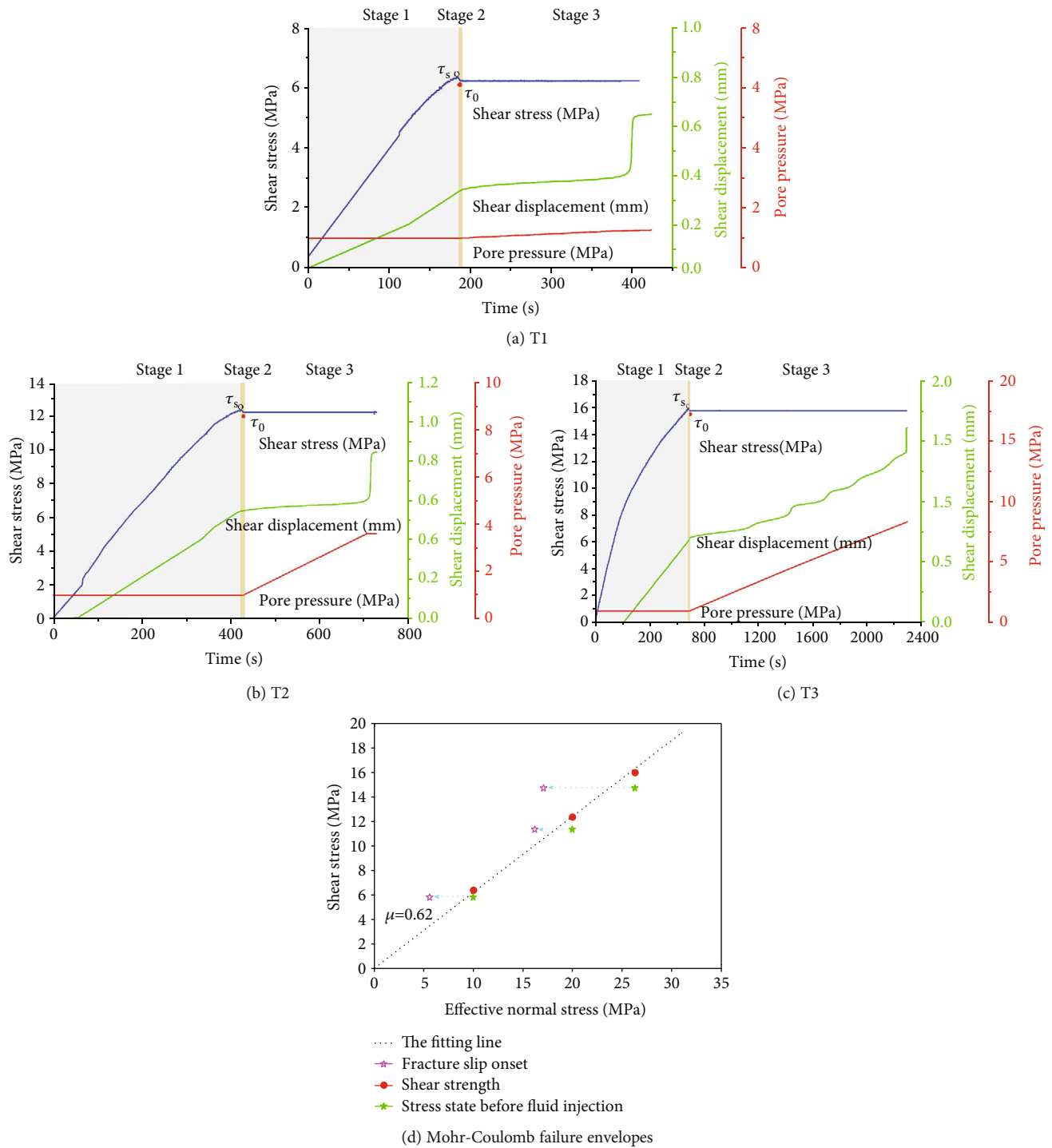


FIGURE 4: Stress-displacement evolution in nonstepping injection-induced shear tests. (a–c) Tests T1, T2, and T3. (d) Mohr-Coulomb failure envelopes obtained by fitting the shear strengths (solid red circle) from the displacement-driven shear tests, and the stress states of sawcut fractures before the fluid injection (solid green five-pointed star) and at the onset of injection-driven fracture instability (solid pink five-pointed star). Please notice the difference in the coordinate scale.

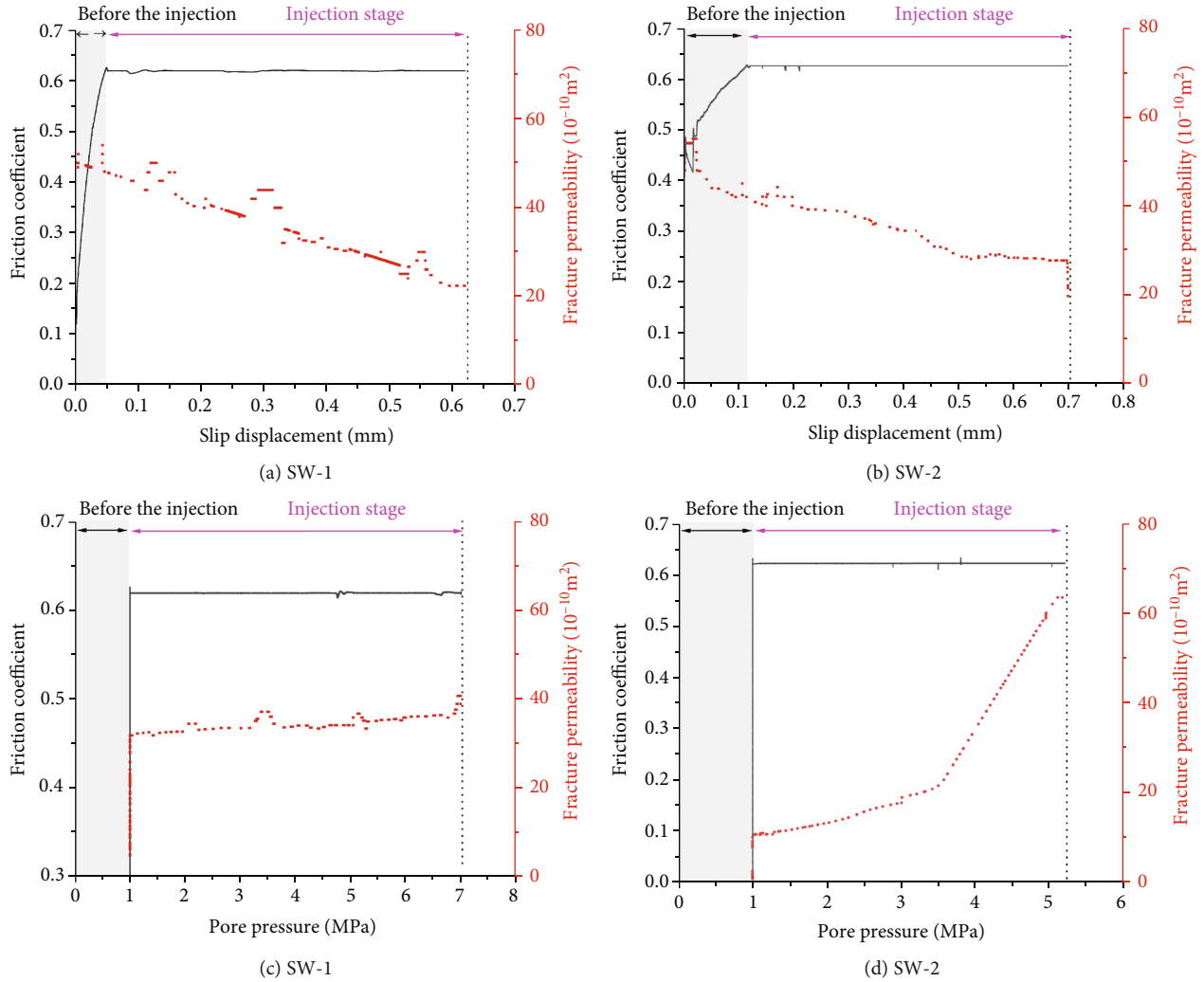


FIGURE 5: Friction coefficient and permeability evolution. (a, b) The friction coefficient and fracture surface permeability in SW-1 and SW-2 tests as functions of slip displacement, respectively. (c, d) The friction coefficient and fracture surface permeability as a function of pore pressure in SW-1 and SW-2 tests, respectively.

and, then, continues to grow slowly and relatively steadily. Slight infiltration lag was detected during injection pressure loading and holding. In contrast, in test SW-2, the permeability increased rapidly throughout the injection process, and there was no obvious sudden increase at 3 MPa and 5 MPa. However, significant permeability hysteresis was detected during injection pressure loading and holding stages.

In view of the above experimental phenomenon, when the fluid pressurization rate is small, the permeability increases rapidly with the increase of fluid pressure and decreases slowly with the increase of slipping displacement. This results in the fracture surface being able to maintain relatively high average permeability and weak fluid pressure heterogeneity. On the contrary, when the fluid pressurization rate is high, the permeability increases slowly with the increase of fluid pressure and decreases rapidly with the increase of slipping displacement. This results in the fracture surface being able to maintain relatively low average permeability and strong fluid pressure heterogeneity. Note that we

are studying the entire process of fracture slipping, not the local features.

4. Conclusions

In order to understand the influence of fluid pressurization rate on rock fracture slip, a series of injection-induced shear tests were carried out. The influence of fluid pressurization rate on fracture slip mode and displacement evolution process under different fluid injection rates is compared and analyzed. Then, we aim at the phenomenon of fracture slipping hysteresis at fluid pressurization rate; further analysis is made from two aspects of fluid pressure heterogeneity and permeability evolution. The main conclusions are summarized as follows:

- (1) The magnitude of fluid pressure may control the initiation of fracture slip, while the fluid pressurization rate may control the fracture slip mode. The fracture exhibits a slow stick-slip mode at a relatively fast fluid

pressurization rate, whereas the fracture exhibits an almost continuous creep mode at a relatively slow fluid pressurization rate

- (2) The contribution of fluid pressure heterogeneity and permeability evolution to fracture slip initiation is different with the increase of fluid pressurization rate. Under low fluid pressurization rate, fracture slipping shows obvious hysteresis phenomenon, which may be caused by the combined action of fluid pressure heterogeneity and permeability evolution. When the fluid pressurization rate is low, the fluid pressure heterogeneity is weak, and the permeability growth rate is fast. The influence of permeability on fracture slipping initiation may be more significant than the fluid pressure heterogeneity. With the increase of fluid pressurization rate, the fluid pressure heterogeneity may play a more significant role than permeability. This provides a supplementary insight for revealing the mechanism of seismogenic time lag behind fluid injection time
- (3) Under the experimental scale, the Coulomb fracture stress at the initiation of fracture instability is magnified by about one time than that predicted by the failure criterion due to the fluid pressure heterogeneity. In addition, the increment of Coulomb fracture stress during the test is greater than 1.65 MPa, which indicates that the heterogeneity of fluid pressure is closely related to fracture slip, and the increment of Coulomb fracture stress value greater than 1.65 MPa may be detrimental to fracture stability

Data Availability

For more information regarding the data availability, please reach out to the corresponding author.

Conflicts of Interest

The authors declare no conflict of interest.

Acknowledgments

This research was funded by the Special Fund for Formation and Evolution of Reservoir Fracture Networks, grant number Y411708117.

References

- [1] G. M. Atkinson, D. W. Eaton, and N. Igonin, "Developments in understanding seismicity triggered by hydraulic fracturing," *Nature Reviews Earth & Environment*, vol. 1, no. 5, pp. 264–277, 2020.
- [2] W. L. Ellsworth, "Injection-induced earthquakes," *Science*, vol. 341, no. 6142, article 1225942, 2013.
- [3] Y. Ji, W. A. M. Wanniarachchi, and W. Wu, "Effect of fluid pressure heterogeneity on injection-induced fracture activation," *Computers and Geotechnics*, vol. 123, article 103589, 2020.
- [4] A. A. Holland, "Earthquakes triggered by hydraulic fracturing in south-central Oklahoma," *Bulletin of the Seismological Society of America*, vol. 103, no. 3, pp. 1784–1792, 2013.
- [5] Y. Wang, W. K. Feng, R. L. Hu, and C. H. Li, "Fracture evolution and energy characteristics during marble failure under tri-axial fatigue cyclic and confining pressure unloading (FC-CPU) conditions," *Rock Mechanics and Rock Engineering*, vol. 54, no. 2, pp. 799–818, 2021.
- [6] M. Kozłowska, M. R. Brudzinski, P. Friberg, R. J. Skoumal, N. D. Baxter, and B. S. Currie, "Maturity of nearby faults influences seismic hazard from hydraulic fracturing," *Proceedings of the National Academy of Sciences*, vol. 115, no. 8, pp. E1720–E1729, 2018.
- [7] L. Wang, G. Kwiatek, E. Rybacki, M. Bohnhoff, and G. Dresen, "Injection-induced seismic moment release and laboratory fault slip: implications for fluid-induced seismicity," *Geophysical Research Letters*, vol. 47, no. 22, pp. 1–11, 2020.
- [8] Y. Ji and W. Wu, "Injection-driven fracture instability in granite: mechanism and implications," *Tectonophysics*, vol. 791, pp. 1–12, 2020.
- [9] C. Noël, F. X. Passelègue, C. Giorgetti, and M. Violay, "Fault reactivation during fluid pressure oscillations: transition from stable to unstable slip," *Journal of Geophysical Research: Solid Earth*, vol. 124, no. 11, pp. 10940–10953, 2019.
- [10] F. X. Passelègue, N. Brantut, and T. M. Mitchell, "Fault reactivation by fluid injection: controls from stress state and injection rate," *Geophysical Research Letters*, vol. 45, no. 23, pp. 12837–12846, 2018.
- [11] J. C. Jaeger, N. G. Cook, and R. Zimmerman, *Fundamentals of Rock Mechanics*, John Wiley & Sons, Oxford, UK, 2009.
- [12] A. H. Kohli and M. D. Zoback, "Frictional properties of shale reservoir rocks," *Journal of Geophysical Research: Solid Earth*, vol. 118, no. 9, pp. 5109–5125, 2013.
- [13] R. Bürgmann, "The geophysics, geology and mechanics of slow fault slip," *Earth and Planetary Science Letters*, vol. 495, pp. 112–134, 2018.
- [14] F. Cappa, M. M. Scuderi, C. Collettini, Y. Guglielmi, and J. P. Avouac, "Stabilization of fault slip by fluid injection in the laboratory and in situ," *Science Advances*, vol. 5, pp. 1–8, 2019.
- [15] M. E. French, W. Zhu, and J. Banker, "Fault slip controlled by stress path and fluid pressurization rate," *Geophysical Research Letters*, vol. 43, no. 9, pp. 4330–4339, 2016.
- [16] Y. Wang, Y. F. Yi, C. H. Li, and J. Q. Han, "Anisotropic fracture and energy characteristics of a Tibet marble exposed to multi-level constant-amplitude (MLCA) cyclic loads: a lab-scale testing," *Engineering Fracture Mechanics*, vol. 244, article 107550, 2021.
- [17] B. Derode, Y. Guglielmi, L. De Barros, and F. Cappa, "Seismic responses to fluid pressure perturbations in a slipping fault," *Geophysical Research Letters*, vol. 42, no. 9, pp. 3197–3203, 2015.
- [18] X. Lei, G. Yu, S. Ma, X. Wen, and Q. Wang, "Earthquakes induced by water injection at ~3 km depth within the Rongchang gas field, Chongqing, China," *Journal of Geophysical Research: Solid Earth*, vol. 113, no. B10, pp. 1–12, 2008.
- [19] F. Cappa, Y. Guglielmi, C. Nussbaum, and J. Birkholzer, "On the relationship between fault permeability increases, induced stress perturbation, and the growth of aseismic slip during

fluid injection,” *Geophysical Research Letters*, vol. 45, no. 20, pp. 11012–11020, 2018.

- [20] Z. Ye and A. Ghassemi, “Injection-induced shear slip and permeability enhancement in granite fractures,” *Journal of Geophysical Research: Solid Earth*, vol. 123, no. 10, pp. 9009–9032, 2018.

Research Article

Analytical and Experimental Investigations on Mechanical Properties of Weak Plane Bedding in Mudstone

Yijin Zeng,¹ Hailong Jiang ,^{1,2} Shidong Ding,¹ Junhai Chen,¹ Yi Wang,¹ and Jie Zheng²

¹State Key Laboratory of Shale Oil and Gas Enrichment Mechanisms and Effective Development, Beijing 100083, China

²College of Mechanical Engineering, Xi'an Shiyou University, Xi'an, Shannxi 710065, China

Correspondence should be addressed to Hailong Jiang; jianghl_xapi@126.com

Received 19 April 2021; Accepted 22 May 2021; Published 4 June 2021

Academic Editor: Yu Wang

Copyright © 2021 Yijin Zeng et al. This is an open access article distributed under the Creative Commons Attribution License, which permits unrestricted use, distribution, and reproduction in any medium, provided the original work is properly cited.

Wellbore instabilities frequently occur in mudstone formation with weak plane bedding because of strong anisotropies. The mechanics parameters of weak plane bedding are of vital significance to the wellbore stability analysis for mudstone formations. The conventional method for determining the mechanics parameters is to fit lots of triaxial test data due to the blindness of coring. In this paper, an evaluation method of the mechanics parameters of weak plane bedding is proposed to improve the accuracy of weak plane bedding mechanical properties. The mechanics parameters of weak plane bedding are obtained by combing the single-weak plane failure criterion with the compressive strength of rock obtained by the triaxial test of cores with different coring angles. It is seen that the new evaluation method is simple and convenient. On the other hand, a validation method of the mechanics parameters of weak plane bedding is proposed to ensure their accuracy. The compressive strength obtained from the core with the special coring angle is compared with the theoretical compressive strength for verifying the accuracy of weak plane bedding mechanical properties. It is observed that the proposed evaluation and validation methods can be used to measure the value of weak plane bedding mechanical properties precisely. The proposed methods are general and can be used for measuring the mechanical properties of fracture weak-plane and joint weak-plane.

1. Introduction

The anisotropic rock (mudstone, shale, etc.) formed by the weak plane (bedding, joint, etc.) can be weaker than the intact rock. The current research focuses on the failure criterion of the anisotropic rock, such as the Mohr-Coulomb, Drucker-Prager, the Modified Lade, Hoek-Brown, single-weak plane failure criterion, and 3D criteria (Mogi-Coulomb, Wiebols-Cook, Desai-Salami, 3D Hoek-Brown) [1–4]. The 3D criteria focus on the effects of the intermediate principal stress, which is usually difficult in practice to analyze the wellbore stability because of the more required input parameters. One of the most widely used empirical criteria in the anisotropic rock is the single-weak plane failure criterion. Since its first introduction by Jaeger [2] in extending the earlier work of Bott [1], the single-weak plane failure criterion has been used successfully in evaluating wellbore stability [5–13]. In this criterion, the failure of both the bedding planes and rock matrix is described by using the Mohr-Coulomb criterion by two dif-

ferent sets of intact rock and weak plane constants. Then, the mechanics parameters of weak plane bedding are important parameters required for use of the single-weak plane failure criterion in evaluation wellbore stability. The conventional method for determining the mechanics parameters is to fit lots of triaxial test data of anisotropic rocks [14–19]. Donath [14] tested the several rocks with different types of planar anisotropy with seven different δ , where δ is the inclination of anisotropy, bedding planes. Chenevert and Gatlin [15] early showed the rock properties of coefficient of internal friction can vary with direction, depending on the particular rock tested. Duveau and Shao [16] performed 78 triaxial compression tests in order to investigate the schist strength anisotropy. The cohesion and friction of weakness planes are determined from failure stresses obtained in triaxial tests with the loading orientation resulting in the minimum strength. Heng et al. [17] analyzed the mechanical properties of the bedding plane based on the experimental data of shale with four different α , where α is the angle

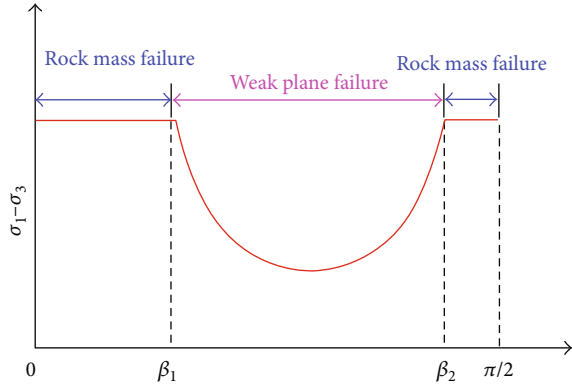


FIGURE 1: Relation between the failure mode of the anisotropic mudstone and β .

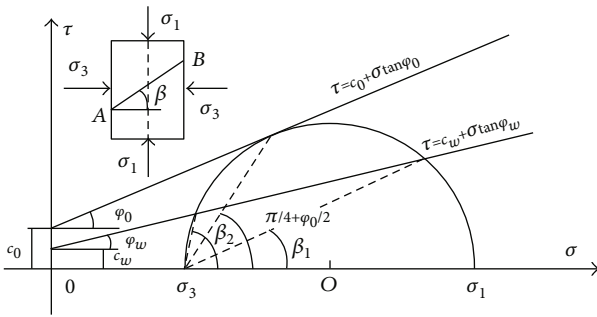


FIGURE 2: Weak plane failure curves based on the Mohr-Coulomb failure criterion. The line AB is defined as the weak plane. τ is the shear stress at failure.

between the bedding planes and the coring orientation. Wasantha et al. [18] studied the mechanics property of sandstone specimens with six different interconnected joint patterns under three different combinations of confining pressure and initial pore-water pressure. Liu et al. [19] found that the presence of the weak plane greatly reduced the mechanical strength of the shale. Although the above experimental methods can measure the value of the mechanical properties of the weak plane, lots of triaxial test data is necessary to fit the properties.

In this paper, an evaluation method of the mechanics parameters of weak plane bedding is proposed to improve the accuracy of weak plane bedding mechanical properties. On the other hand, a validation method of the mechanics parameters of weak plane bedding is proposed to ensure their accuracy. It is observed that the proposed evaluation and validation methods can be used to measure the value of weak plane bedding mechanical properties precisely and avoid blindness of coring operation. Rock mechanical properties of the mudstone specimen are measured using an RTR-1500 triaxial rock testing system with an axial strain loading rate of 0.05% per minute under successively higher confining pressures. The frame stiffness, axial load, and cell pressure of the RTR-1500 triaxial rock testing system are 0MN/mm, Max. 1500 kN, and Max. 140 MPa, respectively. Experimental results show that the proposed evaluation and validation methods can be used to measure the value of weak plane bed-

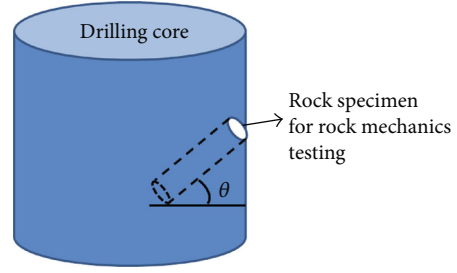


FIGURE 3: Sketch for the drilling core and rock specimen.

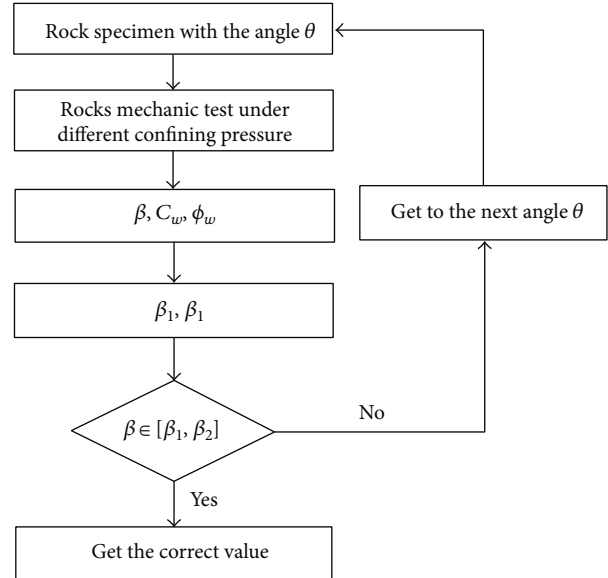


FIGURE 4: A flow chart for the determination of the cohesion and friction angle of the weak plane.

ding mechanical properties precisely. The proposed methods are general and can be used for measuring the mechanical properties of fracture weak-plane and joint weak-plane.

2. Weak Plane Failure Criterion

The weak plane failure criterion which is that the failure condition of the anisotropic mudstone depends on sets of the single weak plane parameters was the first presented by Jaeger with the most extensive triaxial tests [1]. There are an upper limit and a lower limit for the compressive strength of the anisotropic mudstone with the weak plane. The upper limit is corresponding to the compressive strength depending on the rock mass. The lower limit is corresponding to the compressive strength depending on the weak plane. β is the angle between maximum principal stress and weak plane normal, related to the failure mode of the anisotropic mudstone with the weak plane (Figures 1 and 2). For $\beta_1 \leq \beta \leq \beta_2$, the failure mode is conducted by the weak plane failure.

The weak plane failure criterion for $\beta_1 \leq \beta \leq \beta_2$ is defined as

$$\sigma_1 - \sigma_3 = \frac{2(C_w + \tan \phi_w \sigma_3)}{(1 - \tan \phi_w \cot \beta) \sin 2\beta}, \quad (1)$$

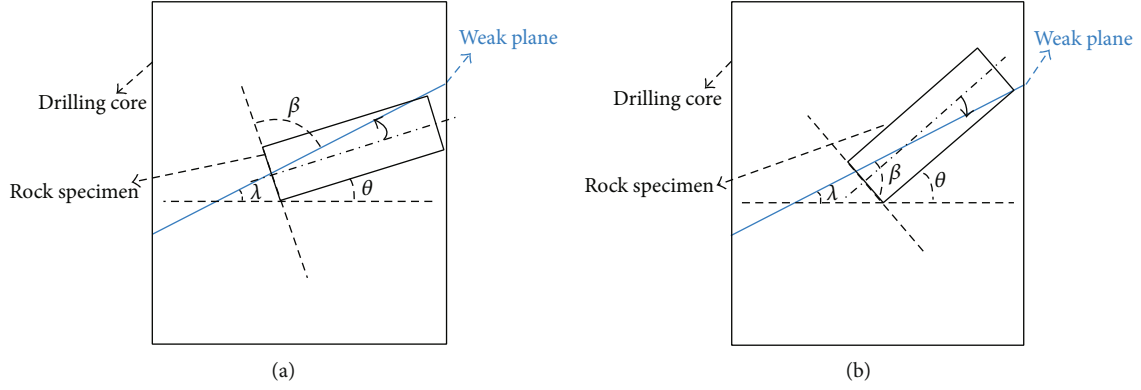


FIGURE 5: Geometric sketch for the original angle of λ . (a) The orientation from the axis of the tested rock to the weak-plane line is anticlockwise, $\theta < \lambda$. (b) The orientation from the axis of the tested rock to the weak-plane line is clockwise, $\theta > \lambda$.

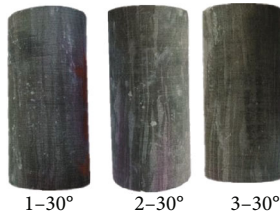


FIGURE 6: Standard cylinder (ϕ 25 mm \times 50 mm).



FIGURE 8: Original weak plane bedding for the drilling core.



FIGURE 7: RTR-1500 Rock triaxial experiment system.

TABLE 1: Compressive strength from triaxial test.

Specimen number	θ (°)	Confining pressure (MPa)	Compressive strength (MPa)
1-30°	30	0	59.958
2-30°	30	20	144.852
3-30°	30	30	188.185

where C_o is the cohesion of the rock and ϕ_o is the friction angle of the rock.

3. Evaluation Method of the Weak Plane Mechanical Properties

θ is defined as the complementary angle of the angle between the axis of the drilling core and that of the rock specimen for rock mechanics testing (Figure 3). It is assumed that the angle β of the drilling core is between β_1 and β_2 . Hence, the failure mode of this rock specimen should be determined by the weak plane. The triaxial tests are run on the three rock specimens with the same θ at three different confining pressures; then, we can get three compressive strengths. The parameters C_w , ϕ_w , and β can be got by combining equation (1) with the three compressive strengths. β_1 and β_2 can be easily computed using equations (2) and (3). If $\beta \in [\beta_1, \beta_2]$, we will get the correct cohesion and friction angle of the weak plane, or else will increase the angle θ . Figure 4 shows the algorithms with which the required cohesion and friction angle of the weak plane can be obtained.

$$\beta_1 = \frac{\phi_w}{2} + \frac{1}{2} \arcsin \left[\frac{(\sigma_1 + \sigma_3 + 2C_w \cot \phi_w) \sin \phi_w}{\sigma_1 - \sigma_3} \right], \quad (2)$$

$$\beta_2 = \frac{\pi}{2} + \frac{\phi_w}{2} - \frac{1}{2} \arcsin \left[\frac{(\sigma_1 + \sigma_3 + 2C_w \cot \phi_w) \sin \phi_w}{\sigma_1 - \sigma_3} \right], \quad (3)$$

where σ_1 and σ_3 is the maximum and minimum principal stress, respectively. C_w is the cohesion of the weak plane. ϕ_w is the friction angle of the weak plane [11].

The Mohr-Coulomb failure criterion for $\beta < \beta_1$ or $\beta > \beta_2$ is defined as

$$\sigma_1 = \sigma_3 \tan^2 \left(\frac{\pi}{4} + \frac{\phi_o}{2} \right) + 2C_o \tan \left(\frac{\pi}{4} + \frac{\phi_o}{2} \right), \quad (4)$$

4. Validation Method of the Weak Plane Mechanical Properties

λ is defined as the original angle which is the angle between the axis of the drilling core and weak plane normal. The original angle can be given by the geometric relationship. When the orientation from the axis of the tested rock to the weak-plane line is anticlockwise, $\lambda = \theta - \beta + (\pi/2)$ (Figure 5(a)). When the orientation from the axis of the tested rock to the weak-plane line is clockwise, $\lambda = \theta + \beta - \pi/2$ (Figure 5(b)). We can change the angle θ to make the angle β meet $\beta \in [\beta_1, \beta_2]$. The rock specimen with this angle θ will be conducted with a triaxial test. It can be seen from equations (2) and (3) that the failure model of the rock specimen with this angle θ will be the weak plane failure. If the value of the compressive strength from the triaxial test is close to that from the theoretic calculation of the weak plane failure criterion, the previous cohesion and friction angle of the weak plane got by the method of evaluating the weak plane mechanical properties will be accurate.

5. Experiments and Discussions on Weak Plane Mechanical Properties

5.1. Materials and Experimental Methodology. Mudstone samples buried to 6670-6678 m were obtained from the Sangtamu formation in Tarim Basin, Northwest China. The Tarim Basin has abundant hydrocarbons and is currently the largest natural gas-producing region in the country. The complex situations in the process of drilling are liable to occur while drilling in the Sangtamu formation in Tarim Basin. Rock mechanical properties of weak plane bedding in mudstones are of vital significance to these situations because of the poor mechanical properties of weak plane bedding. The rock specimens are from the drilling core according to the angle depicted in Figure 3. The geometry size of these rock specimens is 50 mm in length and 25 mm in diameter (Figure 6). Rock mechanics of these rock specimens are tested with an RTR-1500 triaxial rock testing system with an axial strain loading rate of 0.05% per minute under successively higher confining pressures (Figure 7).

5.2. Experimental Results and Analysis

5.2.1. Experiment for Evaluation Method of the Weak Plane Mechanical Properties. We can find that the original angle λ is 10° when the drilling core is coring along with the horizontal or vertical direction (Figure 8). We choose to conduct the triaxial test for the rock specimens with $\theta = 30^\circ$. The compressive strength values of these rock specimens are listed in Table 1. The stress-strain curves of these rock specimens are as shown in Figure 9. By equation (1), we can obtain that $\beta = 69.3697^\circ$, $c_w = 13.0318\text{MPa}$, and $\phi_w = 37.7435^\circ$. Then, β_1 and β_2 can be given by equations (2) and (3), which are listed in Table 2. It can be easily verified that $\beta \in [\beta_1, \beta_2]$. Therefore, $c_w = 13.0318\text{MPa}$ and $\phi_w = 37.7435^\circ$ are the required cohesion and friction angle of the weak plane.

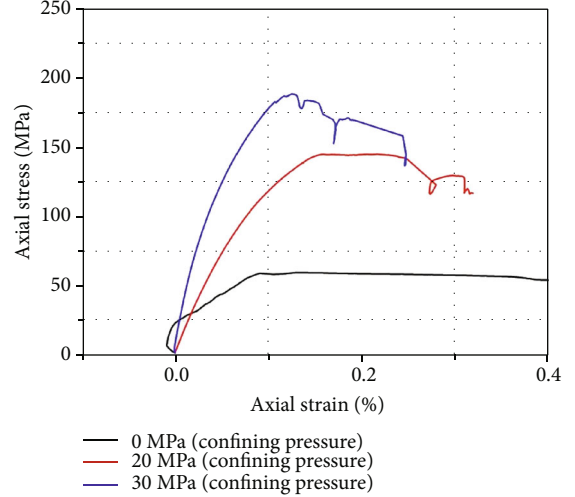


FIGURE 9: Stress-strain curves of rock specimens from Sangtamu mudstone formation.

TABLE 2: Relationship among β , β_1 , and β_2 .

Specimen number	β_1 ($^\circ$)	β_2 ($^\circ$)	β ($^\circ$)
1-30 $^\circ$	55.3291	72.4144	69.3697
2-30 $^\circ$	57.2389	70.5046	69.3697
3-30 $^\circ$	57.4011	70.3424	69.3697

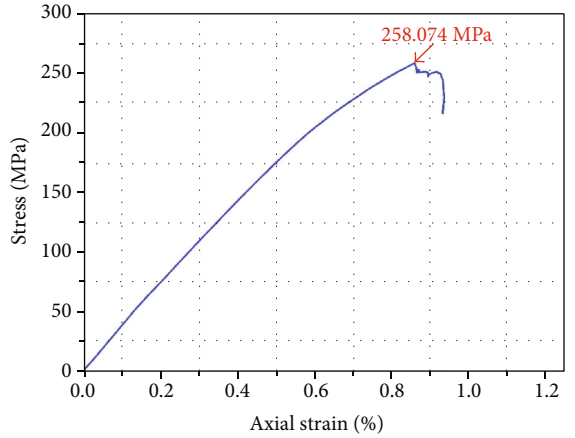


FIGURE 10: Stress-strain curves of the verified rock specimen with $\theta = 35.4980^\circ$.

5.2.2. Experiment for Validation Method of the Weak Plane Mechanical Properties. As $\lambda = \theta + \beta - 90^\circ$, we have $\theta = 30^\circ$, $\beta = 69.3697^\circ$, and so $\lambda = 9.3697^\circ$. We should drill the rock specimen with $\theta = 35.4980^\circ$ again, according to the validation method of the weak plane mechanical properties described in Section 4. The compressive strength of this rock specimen is measured with an RTR-1500 three-axial rock testing system for checking the difference between the experimental value of compressive strength and the calculated value of that from the weak plane failure criterion. The stress-strain curve of this rock specimen is as shown in Figure 10. The

experimental value of compressive strength is 258.074 MPa, and the calculated value of that is 260.9528 MPa. The relative error between the results of the theoretic calculation and experiment is only 1.12%. Therefore, the previously obtained weak plane mechanical properties by the evaluation method of the weak plane mechanical properties is accurate.

6. Conclusions

In this paper, we investigated both the evaluation method and the validation method of the weak plane mechanical properties by the theory analysis and experimental investigation in mudstone with the weak plane bedding. The evaluation method of the weak plane mechanical properties is proposed, based on the weak plane failure criterion. This method can guide the measurement of the weak plane mechanical properties to avoid blindness of coring operation. The validation method of the weak plane mechanical properties is proposed, equally based on the weak plane failure criterion. The validation method can further ensure the correctness of the weak plane mechanical properties which is previously obtained by the evaluation method of the weak plane mechanical properties. Both methods are general and can be used for measuring the mechanical properties of fracture weak-plane or joint weak-plane.

Data Availability

The manuscript is a data self-contained article, whose results were obtained from the laboratory analysis, and the entire data are presented within the article.

Conflicts of Interest

The authors declare that there is no conflict of interest regarding the publication of this paper.

Acknowledgments

This study is supported by the Open Fund of State Key Laboratory of Shale Oil and Gas Enrichment Mechanisms and Effective Development (Program No. 20-YYGZ-KF-GC-15), Natural Science Basic Research Plan in Shaanxi Province of China (Program No. 2021JM-407), and National Natural Science Foundation of China (Grant No. 52004215).

References

- [1] M. H. P. Bott, "The mechanics of oblique slip faulting," *Geological Magazine*, vol. 96, no. 2, pp. 109–117, 1959.
- [2] J. C. Jaeger, "Shear failure of anisotropic rocks," *Geological Magazine*, vol. 97, no. 1, pp. 65–72, 1960.
- [3] E. Hoek, C. Carranza-Torres, and B. Corkum, "Hoek-Brown failure criterion-2002 edition," in *Proceedings of NARMS-Tac*, vol. 1, pp. 267–273, 2002.
- [4] Y. Wang, Y. F. Yi, C. H. Li, and J. Q. Han, "Anisotropic fracture and energy characteristics of a Tibet marble exposed to multi-level constant-amplitude (MLCA) cyclic loads: a lab-scale testing," *Engineering Fracture Mechanics*, vol. 244, article 107550, 2021.
- [5] B. S. Aadnoy, "Modeling of the stability of highly inclined boreholes in anisotropic rock formations (includes associated papers 19213 and 19886)," *SPE Drilling Engineering*, vol. 3, no. 3, pp. 259–268, 1988.
- [6] B. S. Aadnoy and K. Larson, "Method for fracture-gradient prediction for vertical and inclined boreholes," *SPE Drilling Engineering*, vol. 4, no. 2, pp. 99–103, 1989.
- [7] S. H. Ong and J. C. Roegiers, "Influence of anisotropies in borehole stability," *International Journal of Rock Mechanics and Mining Sciences & Geomechanics Abstracts*, vol. 30, no. 7, pp. 1069–1075, 1993.
- [8] T. Popp, K. Salzer, and W. Minkley, "Influence of bedding planes to EDZ-evolution and the coupled HM properties of Opalinus Clay," *Physics and Chemistry of the Earth, Parts A/B/C*, vol. 33, no. s1, pp. S374–S387, 2008.
- [9] H. Lee, S. H. Ong, M. Azeemuddin, and H. Goodman, "A wellbore stability model for formations with anisotropic rock strengths," *Journal of Petroleum Science & Engineering*, vol. 96–97, pp. 109–119, 2012.
- [10] J. Zhang, "Borehole stability analysis accounting for anisotropies in drilling to weak bedding planes," *International Journal of Rock Mechanics & Mining Sciences*, vol. 60, pp. 160–170, 2013.
- [11] C. Liang, M. Chen, Y. Jin, and Y. Lu, "Wellbore stability model for shale gas reservoir considering the coupling of multi-weakness planes and porous flow," *Journal of Natural Gas Science and Engineering*, vol. 21, pp. 364–378, 2014.
- [12] Y. Wang, C. H. Li, and J. Q. Han, "On the effect of stress amplitude on fracture and energy evolution of pre-flawed granite under uniaxial increasing-amplitude fatigue loads," *Engineering Fracture Mechanics*, vol. 240, article 107366, 2020.
- [13] W. Feng, D. Li, G. Wang, and Y. Song, "Wellbore Stability of a Deep-Water Shallow Hydrate Reservoir Based on Strain Softening Characteristics," *Geofluids*, pp. 1–11, 2020.
- [14] F. A. Donath, "Experimental study of shear failure in anisotropic rocks," *Geological Society of America Bulletin*, vol. 72, no. 6, pp. 985–989, 1961.
- [15] M. E. Chenevert and C. Gatlin, "Mechanical anisotropies of laminated sedimentary rocks," *Society of Petroleum Engineers Journal*, vol. 5, no. 1, pp. 67–77, 1965.
- [16] G. Duveau and J. F. Shao, "A modified single plane of weakness theory for the failure of highly stratified rocks," *International Journal of Rock Mechanics and Mining Sciences*, vol. 35, no. 6, pp. 807–813, 1998.
- [17] S. Heng, Y. Guo, C. Yang, J. J. Daemen, and Z. Li, "Experimental and theoretical study of the anisotropic properties of shale," *International Journal of Rock Mechanics & Mining Sciences*, vol. 74, pp. 58–68, 2015.
- [18] P. L. P. Wasantha, P. G. Ranjith, and D. R. Viete, "Hydro-mechanical behavior of sandstone with interconnected joints under undrained conditions," *Engineering Geology*, vol. 207, pp. 66–77, 2016.
- [19] T. Liu, H. Liu, Y. Meng, X. Han, S. Cui, and A. Yu, "Multi-coupling stress field and evaluation of borehole stability in deep brittle shale," *Arabian Journal of Geosciences*, vol. 13, no. 21, pp. 1–9, 2020.

Research Article

Cylindrical Caved Space Stability Analysis for Extension Prediction of Mining-Induced Surface Subsidence

Yang Liu ^{1,2}, Yongxiang Ge,¹ Congrui Zhang,^{1,2} Fengyu Ren,³ Junsheng Ma,⁴ and Gaofeng Ren ^{1,2}

¹School of Resource and Environmental Engineering, Wuhan University of Technology, Wuhan, Hubei 430070, China

²Key Laboratory of Mineral Resources Processing and Environment of Hubei Province, Wuhan University of Technology, Wuhan, Hubei 430070, China

³School of Resources and Civil Engineering, Northeastern University, Shenyang, Liaoning 110819, China

⁴China Enfi Engineering Corporation, Beijing 100038, China

Correspondence should be addressed to Gaofeng Ren; rengf110@whut.edu.cn

Received 9 April 2021; Accepted 14 May 2021; Published 27 May 2021

Academic Editor: Yu Wang

Copyright © 2021 Yang Liu et al. This is an open access article distributed under the Creative Commons Attribution License, which permits unrestricted use, distribution, and reproduction in any medium, provided the original work is properly cited.

Subsequent extension of surface subsidence after vertical caving leads to large-scale surface destruction, as well as associated geological hazards. The extension prediction for cylindrical caved space, which appears circular surface subsidence, is still an intractable issue, due to the absence of robust models. To fill such a research gap, this paper provides an analytical model for the depth and orientation where the shear failure of isotropic rocks around the caved space is firstly observed. The anisotropy of surrounding rocks is further involved to enable this model to analyze the slip failure along discontinuities in anisotropic stress state. The prediction for the extension of the surface subsidence in Xiaowanggou iron mine is conducted, and the comparison between the prediction and the observation in satellite images demonstrates the validity of the proposed model. Even though this model cannot provide a definite boundary after extension, the prediction for the orientation surface subsidence extends to contribute to mitigating the effect of geological hazards. Another contribution of this work is to provide guidance to mitigate the impact of surface subsidence on safety and environment, such as filling the interspace between large-sized caved rocks by dumping small-sized waste rocks or backfilling the caved space with waste rocks.

1. Introduction

The geological hazards due to mining-induced surface subsidence raise public concerns [1, 2]. The employment of caving mining is restricted because of the surface subsidence [3, 4], even though it is being favored in underground mining projects due to high cost efficiency [5]. On the other hand, in situ observations have demonstrated that the surface subsidence is likely to take place in open-stope-based mines [6], even in the filling-based ones [7, 8]. Such mining-induced surface subsidence can be categorized into 6 types, such as crown hole, chimney caving, plug subsidence, solution cavities, block caving, and progressive caving [9]. The progressive caving indicates the process that surrounding rocks progres-

sively cave into the original caved space formed after chimney caving, plug subsidence, or block caving; meanwhile, the caved space will be extended accordingly during such process. In situ or remote monitoring from many mining projects shows the progressive caving is a primary contributor to the large-scale extension of surface subsidence [10–13].

To predict the progressive caving, as well as the extension of surface subsidence, some analytical solutions have been proposed. The most commonly cited is the limiting equilibrium analysis by Hoek [14]. This model relates the stability of the hanging wall of caved space to the effective cohesion of rock mass, thrust on shear plane due to caved rocks, and the base area and weight of wedge of sliding rock mass. Brown and Ferguson [15] extended Hoek's model by

involving the impact of water pressure and sloping ground surface on shear failure plane. Lupo [16] modified Hoek's model to enable it to predict the rock failure on both hanging wall and footwall. Yet despite having been successfully applied in many mining projects, such as Kiruna iron mine in Sweden, El Teniente copper mine in Chile, Río Blanco copper mine in Peru, and Gaths asbestos mine in Zimbabwe, the employment of both Hoek's and extended models is still restricted because of some basic assumptions: (1) the rock failure and associated surface subsidence occur for a long distance compared with the cross section normal to the strike of ore body, and the analysis can be reduced to a two-dimension problem; (2) the rock mass has homogeneous and isotropic mechanical property, which means the discontinuities (e.g., faults, joints, or beddings) are not taken into account. Such assumptions mean Hoek's and extended models are invalid to analyze progressive caving either around the cylindrical caved space or with the consideration of the rock anisotropy due to discontinuities.

Both in situ monitoring [17, 18] and numerical simulations [7, 19, 20] show the evident impact of discontinuities on the progressive caving. On the other hand, the cylindrical surface subsidence formed after chimney caving, plug subsidence, or block caving has been observed not only in caving-based projects (e.g. Northparkes copper-gold mine, Kimberley diamond mine, and Xiaowanggou iron mine; Figure 1) but also in filling-based one (e.g., Jinchuan nickel mine) [9]. However, the analytical prediction for the progressive caving, as well as the associated extension of surface subsidence in these projects, is still an intractable issue, due to the absence of robust model, especially when the rock anisotropy due to discontinuities is taken into consideration.

Therefore, to fill such a research gap, we introduce an analytical model to relate the rock shear failure around the cylindrical caved space, which accounts for extension of surface subsidence, to in situ stress, and the property of surrounding rocks and caved rocks. Additionally, the rock anisotropy due to inherent discontinuities is involved to enable the proposed model to analyze the extension of surface subsidence because of the slip failure along discontinuities. The rest of this paper is organized as follows. Section 2 introduces the solutions to test stability of the isotropic rocks around cylindrical caved space. Section 3 provides the solution to predict the slip failure along discontinuities around the caved space. In Section 4, employing the proposed model, we calculated the depth and orientation where the shear or slip failure take place at the intact rocks around caved space in Xiaowanggou iron mine (Figure 1(c)), and the associated extension of surface subsidence is predicted. Additionally, some implications regarding the proposed model and case study are discussed in this section. Finally, the conclusions and contributions are summarized in Section 5.

2. Stability Analysis for Surrounding Isotropic Rocks of Cylindrical Caved Space

The stability analysis for the surrounding isotropic rocks of cylindrical caved space is primarily to establish a relationship to test whether rock failure will take place, by comparing the redistributed stress after vertical caving (e.g., chimney caving,

plug subsidence, or block caving) with rock strength by an appropriate failure criterion. To conduct such analysis, the caved space, observed as circular subsidence area on ground surface (Figure 1), is assumed as a vertical and cylindrical excavation filled with caved rocks (Figure 2(a)).

When the rocks situated in the in situ stress state caves in the void after deposit excavation, the stress redistribution takes place near the caved space. To analyze the rock shear failure surrounding rocks of caved space, the following inputs are involved, such as rock strength, in situ stress, and the impact of caved rocks. Conventionally, rock strength, in situ stress, and associated orientations can be obtained by some robust methods [21–24]. However, the analysis for the impact of caved rocks is rarely reported.

2.1. Impact of Caved Rocks on Stability of Cylindrical Caved Space. In the analytical models proposed in existing literature [14–16], the caved rocks provide thrust to the sliding rocks, which contribute to enhancing the stability of surrounding rocks of caved space. Under the assumption that the subsidence occurs for a long distance compared with the cross section normal to the strike of ore body, this thrust can be expressed as a function of the density and height of caved rocks. Hence, numerous literatures have demonstrated such contribution; Laubscher [13] proposed an empirical solution to describe the effect of the density and height of caved rocks. To describe the stress from caved rocks to the surrounding rocks in a confined space, Ren et al. [25] conduct the scaled laboratory tests, and the results reveal this stress matches the solution for granular materials by Janssen [26]:

$$\sigma_b = C\rho_b g r_b (1 - e^{-z_b/4r_b}), \quad (1)$$

where σ_b is the horizontal stress from caved rocks to the surrounding rocks, ρ_b is the average density of caved rocks, g is the gravity of earth, r_b is the radius of the cross section of caved space, z_b is a variable representing the depth measured from the free surface of caved rocks, and C is a constant that can be obtained by in situ or laboratory tests.

2.2. Shear Failure at Isotropic Surrounding Rocks. For the cylindrical excavation (Figure 2(a)), the in situ stress and redistributed local stress are illustrated in Figures 2(b) and 2(c), respectively. Such redistributed local stress near the rocks around the cylindrical caved space can be expressed in polar system (θ, z, r) , original due to Krisch:

$$\begin{aligned} \sigma_r &= \frac{\sigma_H + \sigma_h}{2} \left(1 - \frac{r_b^2}{r^2}\right) + \frac{\sigma_H - \sigma_h}{2} \left(1 - 4\frac{r_b^2}{r^2} + 3\frac{r_b^4}{r^4}\right) \cos 2\theta + \sigma_b \frac{r_b^2}{r^2}, \\ \sigma_\theta &= \frac{\sigma_H + \sigma_h}{2} \left(1 + \frac{r_b^2}{r^2}\right) - \frac{\sigma_H - \sigma_h}{2} \left(1 + 3\frac{r_b^4}{r^4}\right) \cos 2\theta - \sigma_b \frac{r_b^2}{r^2}, \\ \sigma_z &= \sigma_V - 2\nu(\sigma_H - \sigma_h) \frac{r_b^2}{r^2} \cos 2\theta, \\ \tau_{rz} &= \tau_{r\theta} = \tau_{\theta z} = 0, \end{aligned} \quad (2)$$

where σ_r , σ_θ , and σ_z are the radial, tangential, and axial local normal stress near the rocks around the cylindrical

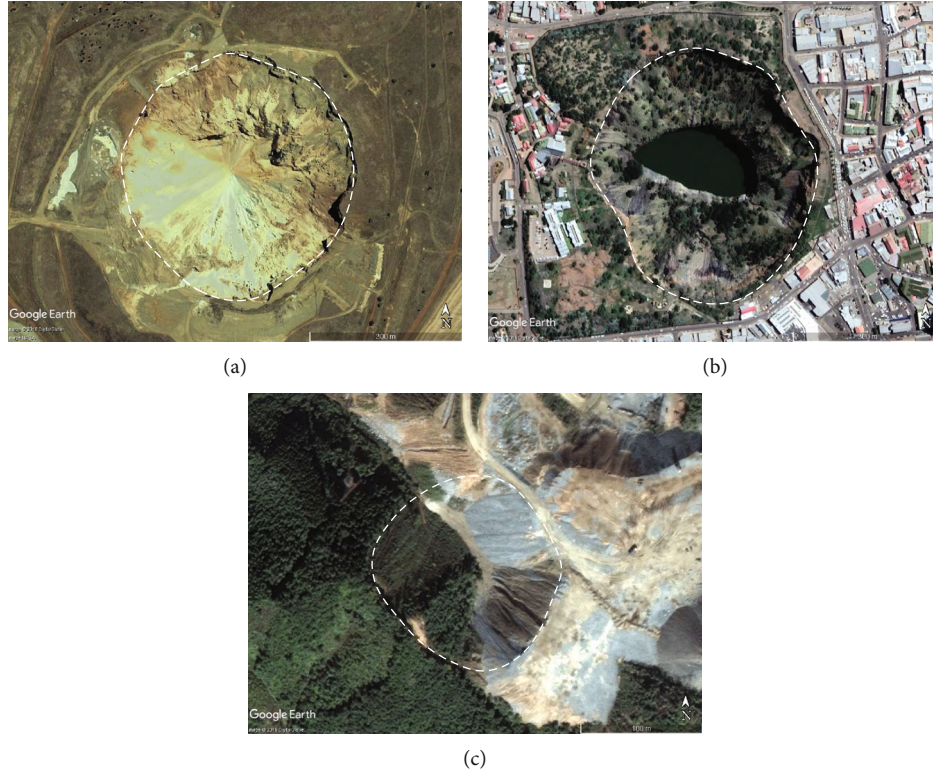


FIGURE 1: Circular surface subsidence observed visually in Google Earth satellite images: (a) Northparkes copper-gold mine, Australia; (b) Kimberley diamond mine, South Africa; (c) Xiaowanggou iron mine, China.

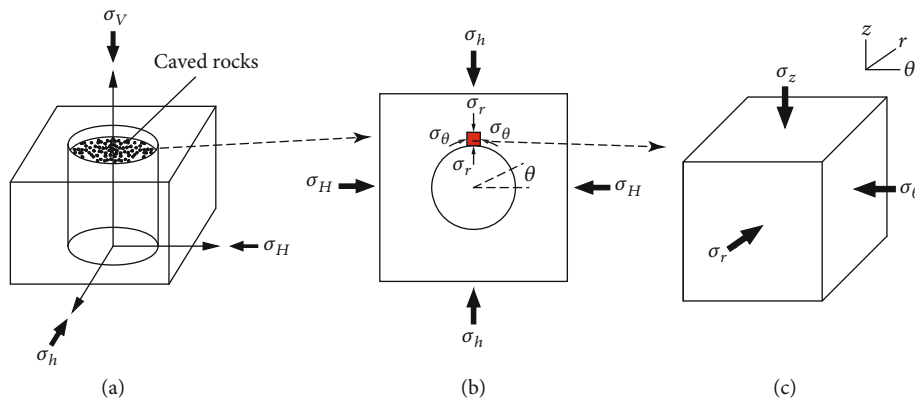


FIGURE 2: Coordinates' transformation from in situ stress ($\sigma_H, \sigma_V, \sigma_h$) into the local stress at surrounding intact rocks ($\sigma_\theta, \sigma_z, \sigma_r, \tau_{\theta z}, \tau_{r\theta}, \tau_{rz}$) in polar system (θ, z, r). (a) Three-dimension (3D) view of the caved space. (b) Local stress at the surrounding rocks in the cross section of caved space. (c) An element illustrating the local stress at surrounding rocks.

excavation, respectively, $\tau_{r\theta}, \tau_{rz}$, and $\tau_{\theta z}$ are the radial, tangential, and axial local shear stress, respectively, and σ_V, σ_H , and σ_h are the vertical, maximum, and minimum horizontal in situ stress, respectively; the in situ stress linearly varies with the depth from ground surface (z) and can be expressed as $\sigma_V = a_V z + b_V$, $\sigma_H = a_H z + b_H$, and $\sigma_h = a_h z + b_h$; a_V, b_V, a_H, b_H, a_h , and b_h are constants which can be obtained by regressing the results from in situ test (e.g., overcoring and hydraulic

fracturing) or core-based test (e.g., anelastic strain recovery, differential strain curve analysis, and acoustic emission); r is a variable that indicates the distance between the position stress redistribution that occurs and the axis of the cylindrical excavation; θ is the orientation around the cylindrical excavation measured from the direction of maximum horizontal in situ stress (i.e., σ_H , as illustrated in Figure 2(b)); $\theta = 0^\circ$ represents the direction of maximum horizontal in situ stress (σ_H), and $\theta =$

90° represents the direction of minimum horizontal in situ stress (σ_h); ν is Poisson's ratio of the surround rocks.

The normal and shear stress at caved space wall ($r = r_b$) can be accordingly calculated from Equation (2):

$$\begin{aligned}\sigma_r &= \sigma_b, \\ \sigma_\theta &= \sigma_H + \sigma_h - 2(\sigma_H - \sigma_h) \cos 2\theta - \sigma_b, \\ \sigma_z &= \sigma_V - 2\nu(\sigma_H - \sigma_h) \cos 2\theta, \\ \tau_{rz} &= \tau_{r\theta} = \tau_{\theta z} = 0.\end{aligned}\quad (3)$$

Equation (3) reveals that the relationship between the three principal stress (σ_θ , σ_z , and σ_r) depends on not only the constants from in situ or laboratory test (e.g., a_V , b_V , a_H , b_H , a_h , b_h , ρ_b , and r_b) but also the depth (z) and direction (θ) at the surrounding rocks. Even though the tangential principal stress (σ_θ) is the maximum principal stress, it is intractable to determine the relationship between the radial and axial principal stress (i.e., σ_r and σ_z , respectively). For instance, in shallow depth, the principal stress is likely to satisfy $\sigma_\theta > \sigma_r > \sigma_z$. However, when the depth increases, the relationship of $\sigma_\theta > \sigma_z > \sigma_r$ can be satisfied, because σ_b will be near to its ultimate value ($\lim_{z_b \rightarrow +\infty} \sigma_b = C\rho_b g r_b$). Therefore,

to analyze the rock failure around the cylindrical caved space in varying depths, we employ the extended Mohr-Coulomb failure criterion for the problems in 3D space [27]

$$\begin{aligned}\sigma_c + q\sigma_3 - \sigma_1 &\geq 0, \\ \sigma_c + q\sigma_1 - \sigma_3 &\geq 0, \\ \sigma_c + q\sigma_2 - \sigma_1 &\geq 0, \\ \sigma_c + q\sigma_1 - \sigma_2 &\geq 0, \\ \sigma_c + q\sigma_3 - \sigma_2 &\geq 0, \\ \sigma_c + q\sigma_2 - \sigma_3 &\geq 0,\end{aligned}\quad (4)$$

where σ_1 , σ_2 , and σ_3 are the maximum, intermediate, and minimum applied principal stress, respectively; σ_c is rock strength; σ_c can be replaced by long-term strength of rocks (σ_{cd}), if this criterion is utilized to analyze rock stability in a long duration of time [28]; the long-term strength of rocks (σ_{cd}) can be converted from the rock strength without time effect (σ'_c) by $\sigma_{cd} = \alpha\sigma'_c$; $\alpha = 0.4 \sim 0.6$, for the intact rocks without preexisting fractures [29]; $q = (1 + \sin \phi)/(1 - \sin \phi)$; ϕ is the internal friction angle of rocks.

Assuming the tangential, radial, and axial principal stress (i.e., σ_θ , σ_r , and σ_z) are the maximum, intermediate, and minimum applied principal stress (i.e., σ_1 , σ_2 , and σ_3), respectively, by substituting Equation (3) into Equation (4), noticing $\sigma_1 = \sigma_\theta$, $\sigma_2 = \sigma_r$, and $\sigma_3 = \sigma_z$, we obtain the following relationships, which should be satisfied, if the surrounding rocks are expected to maintain stable in a long duration of time

$$\begin{aligned}\sigma_{cd} + q[\sigma_V - 2\nu(\sigma_H - \sigma_h) \cos 2\theta] - [\sigma_H + \sigma_h - 2(\sigma_H - \sigma_h) \cos 2\theta - \sigma_b] &\geq 0, \\ \sigma_{cd} + q[\sigma_H + \sigma_h - 2(\sigma_H - \sigma_h) \cos 2\theta - \sigma_b] - [\sigma_V - 2\nu(\sigma_H - \sigma_h) \cos 2\theta] &\geq 0, \\ \sigma_{cd} + q\sigma_b - [\sigma_H + \sigma_h - 2(\sigma_H - \sigma_h) \cos 2\theta - \sigma_b] &\geq 0, \\ \sigma_{cd} + q[\sigma_H + \sigma_h - 2(\sigma_H - \sigma_h) \cos 2\theta - \sigma_b] - \sigma_b &\geq 0, \\ \sigma_{cd} + q[\sigma_V - 2\nu(\sigma_H - \sigma_h) \cos 2\theta] - \sigma_b &\geq 0, \\ \sigma_{cd} + q\sigma_b - [\sigma_V - 2\nu(\sigma_H - \sigma_h) \cos 2\theta] &\geq 0.\end{aligned}\quad (5)$$

Because the tangential principal stress (σ_θ) is the maximum applied principal stress (i.e., either $\sigma_\theta > \sigma_r > \sigma_z$ or $\sigma_\theta > \sigma_z > \sigma_r$ is satisfied), Equation (5) can be reduced to the following equations:

$$\begin{aligned}\sigma_{cd} + q[\sigma_V - 2\nu(\sigma_H - \sigma_h) \cos 2\theta] \\ - [\sigma_H + \sigma_h - 2(\sigma_H - \sigma_h) \cos 2\theta - \sigma_b] &\geq 0,\end{aligned}\quad (6a)$$

$$\sigma_{cd} + q\sigma_b - [\sigma_H + \sigma_h - 2(\sigma_H - \sigma_h) \cos 2\theta - \sigma_b] \geq 0.\quad (6b)$$

Substituting $\sigma_H = a_H z + b_H$, $\sigma_h = a_h z + b_h$, $\sigma_V = a_V z + b_V$, $\sigma_{cd} = \alpha\sigma'_c$, and Equation (1) into Equations (6a) and (6b), we obtain the following equations to test the stability of the rocks around the cylindrical excavation:

$$\begin{aligned}\sigma_{cd} + C\rho_b g r_b \left(1 - e^{-(z-z_0)/4r_b}\right) \\ + [qa_V - (a_H + a_h) + 2(1 - q\nu)(a_H - a_h) \cos 2\theta]z \\ + qb_V - (b_H + b_h) + 2(1 - q\nu)(b_H - b_h) \cos 2\theta &\geq 0,\end{aligned}\quad (7a)$$

$$\begin{aligned}\sigma_{cd} + (1 + q)C\rho_b g r_b \left(1 - e^{-(z-z_0)/4r_b}\right) \\ - [(a_H + a_h) - 2(a_H - a_h) \cos 2\theta]z \\ + 2(b_H - b_h) \cos 2\theta - (b_H + b_h) &\geq 0,\end{aligned}\quad (7b)$$

where z is a variable that indicates the depth from ground surface and z_0 is the depth of the free surface of caved rocks from ground surface.

Equations (7a) and (7b) enable the prediction for the depth (z) where rock failure will take place around the cylindrical excavation (θ). If the depth of implemented undercut exceeds the results by Equations (7a) and (7b), rock failure and associated extension of surface subsidence can be expected to take place. On the other hand, Equations (7a) and (7b) also reveal the predicted depth for rock failure varies in different orientations. For instance, when $\sigma_\theta > \sigma_z > \sigma_r$ is satisfied (i.e., Equations (6b) and (7b) are valid to conduct such prediction), rock failure and associated extension of surface subsidence are most likely to take place in the direction of minimum in situ stress, i.e., $\theta = 90^\circ$ is satisfied. This means the extension of surface subsidence due to the rock shear failure can be expected to be anisotropic.

On the other hand, Equations (6a) and (6b) reveal that the stability of surrounding rocks heavily depends on not only the rock strength (σ_{cd}) but also the stress due to caved rocks (σ_b). Equations (7a) and (7b) provide more details regarding the

contribution of the caved rocks. Because of $q > 0$ and $C > 0$, the increase of the density (i.e., ρ_b increases) or height (i.e., z_0 decrease) of caved rocks facilitates the stability of surrounding rocks. This provides some measures to prevent the rock failure and associated extension of surface subsidence: (1) filling the interspace between large-sized caved rocks by dumping small-sized waste rocks to increase the average density of the materials in the caved space or (2) backfilling the caved space with waste rocks to increase the height of caved rocks. Some discussions for such measures should be noted. Equation (1) shows the ultimate value of stress due to caved rocks ($\lim_{z_b \rightarrow +\infty} \sigma_b = C\rho_b g r_b$) will increase, if measure (1) is implemented. This means that this measure contributes to the stability of surrounding rocks in all depth. However, the effect of measure (2) only works in shallow depth, because the ultimate value of the horizontal stress due to caved rocks maintains constant when the height of caved rocks changes.

3. Stability Analysis for Caved Space with Anisotropic Rocks due to Discontinuities

3.1. The Impact of Discontinuities on Rock Strength. Inherent discontinuities (e.g., faults, joints, and beddings) are the primary cause for rock strength weakening. Laboratory tests of the failure behavior in anisotropic rocks with polyaxial or triaxial compression demonstrate that the strength of anisotropic rocks varies significantly with the orientation of discontinuities [30–33].

Figure 3(a) shows such variation of the peak strength of anisotropic rocks, which can be obtained by the experimental method illustrated in Figure 3(b), at a constant confining pressure with the angle (i.e., β illustrated in Figure 3(b)) between the maximum applied stress (σ_1) and the normal to the discontinuities. The slip failure along the discontinuities is most likely to take place, when β satisfies

$$\beta = \frac{\pi}{4} + \frac{\phi'}{2}, \quad (8)$$

where β is the angle between the maximum applied stress and the normal to the discontinuities, as illustrated in Figure 3(b), and ϕ' is the internal friction angle on the discontinuities.

To analyze this slip failure along the inherent discontinuities, Jaeger et al. [34] extended Coulomb's failure criterion and proposed a new relationship for such analysis. The slip failure along discontinuities is expected to be prevented, if the following relationship is satisfied:

$$\sigma_1 \leq \frac{2(c' + \mu' \sigma_3)}{(1 - \mu' \cot \beta) \sin 2\beta} + \sigma_3, \quad (9)$$

where c' is the cohesion of discontinuities, μ' is the coefficient of internal friction on discontinuities, and $\mu' = \tan \phi'$. When β tends to ϕ' or 90° , the maximum applied principal stress (σ_1), which accounts for the slip failure, tends to infinity.

Jaeger's model is valid to analyze the slip failure of surrounding rocks, when the discontinuities are parallel to the cylindrical excavation. This is because the analysis for the slip failure can be reduced to a 2D problem on a plane which is perpendicular to the axis of the excavation. The validity of Jaeger's model has been demonstrated in a lot of underground engineering, such as borehole drilling [35] and reinforcement for underground tunnels [36]. However, when the discontinuities distribute inclining towards excavation's axis, Jaeger's model is no longer valid to conduct such analysis, because the stress accounting for the slip failure varies in the 3D space. For instance, as illustrated in Figure 3(c), with the confining stress σ_3 , the slip failure along discontinuities due to σ_2 ($\beta_{\sigma_2-\sigma_3}$) is likely to take place before the slip failure due to σ_1 ($\beta_{\sigma_1-\sigma_3}$), because of the anisotropy of rock strength in different orientations.

Therefore, we extend Jaeger's model to enable it to analyze the slip failure along inclined discontinuities with anisotropic applied principal stress ($\sigma_1 > \sigma_2 > \sigma_3$) in 3D space, as illustrated in Figure 3(c). Assuming the redistributed stress is homogenous after vertical caving, an extended model after Jaeger's is proposed for the slip failure along inclined discontinuities, based on the extended Mohr-Coulomb failure criterion in 3D space (i.e., Equation (4)):

$$\begin{aligned} \frac{2(c' + \mu' \sigma_3)}{(1 - \mu' \cot \beta_{\sigma_1-\sigma_3}) \sin 2\beta_{\sigma_1-\sigma_3}} + \sigma_3 - \sigma_1 &\geq 0, \\ \frac{2(c' + \mu' \sigma_1)}{(1 - \mu' \cot \beta_{\sigma_3-\sigma_1}) \sin 2\beta_{\sigma_3-\sigma_1}} + \sigma_1 - \sigma_3 &\geq 0, \\ \frac{2(c' + \mu' \sigma_2)}{(1 - \mu' \cot \beta_{\sigma_1-\sigma_2}) \sin 2\beta_{\sigma_1-\sigma_2}} + \sigma_2 - \sigma_1 &\geq 0, \\ \frac{2(c' + \mu' \sigma_1)}{(1 - \mu' \cot \beta_{\sigma_2-\sigma_1}) \sin 2\beta_{\sigma_2-\sigma_1}} + \sigma_1 - \sigma_2 &\geq 0, \\ \frac{2(c' + \mu' \sigma_3)}{(1 - \mu' \cot \beta_{\sigma_2-\sigma_3}) \sin 2\beta_{\sigma_2-\sigma_3}} + \sigma_3 - \sigma_2 &\geq 0, \\ \frac{2(c' + \mu' \sigma_2)}{(1 - \mu' \cot \beta_{\sigma_3-\sigma_2}) \sin 2\beta_{\sigma_3-\sigma_2}} + \sigma_2 - \sigma_3 &\geq 0, \end{aligned} \quad (10)$$

where $\beta_{\sigma_i-\sigma_j}$ is angle between the stress that accounts for the slip failure (σ_i) and the normal to the discontinuities on the plane consisted by confining stress (σ_j) and the stress accounts for the slip failure (σ_i).

3.2. Slip Failure along Discontinuities at Caved Space Wall. The extended Jaeger model (i.e., Equation (10)) is employed to test the stability of the anisotropic rocks around the cylindrical caved space. Assuming the tangential, radial, and axial principal stress (i.e., σ_θ , σ_r , and σ_z) are the maximum, intermediate, and minimum applied principal stress

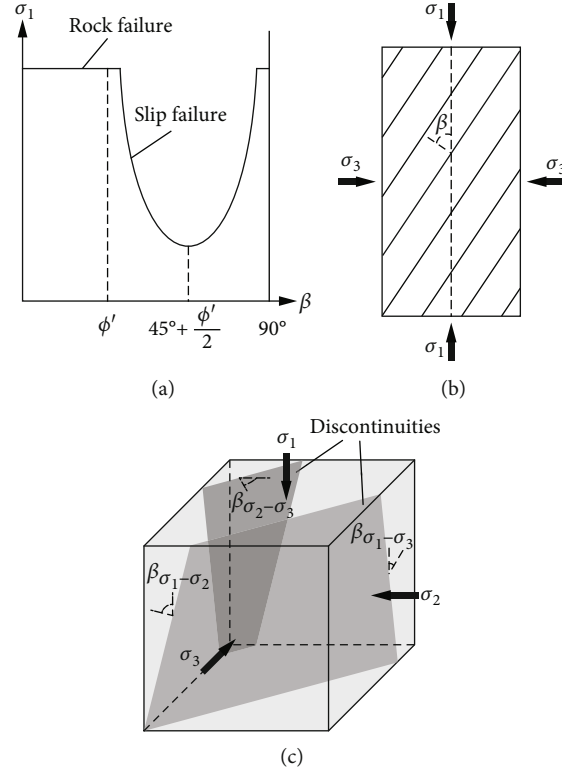


FIGURE 3: (a) Variation of the peak rock strength with β , at a constant confining pressure. (b) Transversely isotropic specimen in triaxial compression. (c) 3D view of a specimen with inclined discontinuities in anisotropic stress state.

(i.e., σ_1 , σ_2 , and σ_3), respectively, we substitute Equation (3) into Equation (9), noticing $\sigma_1 = \sigma_\theta$, $\sigma_2 = \sigma_r$, and $\sigma_3 = \sigma_z$; we obtain the following relationships, which should be satisfied, if the surrounding rocks are expected to keep stable from the slip failure along discontinuities:

$$\begin{aligned}
& \frac{2c' + 2\mu'[\sigma_V - 2\nu(\sigma_H - \sigma_h) \cos 2\theta]}{(1 - \mu' \cot \beta_{\sigma_\theta - \sigma_z}) \sin 2\beta_{\sigma_\theta - \sigma_z}} + [\sigma_V - 2\nu(\sigma_H - \sigma_h) \cos 2\theta] - [\sigma_H + \sigma_h - 2(\sigma_H - \sigma_h) \cos 2\theta - \sigma_b] \geq 0, \\
& \frac{2c' + 2\mu'[\sigma_H + \sigma_h - 2(\sigma_H - \sigma_h) \cos 2\theta - \sigma_b]}{(1 - \mu' \cot \beta_{\sigma_z - \sigma_\theta}) \sin 2\beta_{\sigma_z - \sigma_\theta}} + [\sigma_H + \sigma_h - 2(\sigma_H - \sigma_h) \cos 2\theta - \sigma_b] - [\sigma_V - 2\nu(\sigma_H - \sigma_h) \cos 2\theta] \geq 0, \\
& \frac{2c' + 2\mu' \sigma_b}{(1 - \mu' \cot \beta_{\sigma_\theta - \sigma_r}) \sin 2\beta_{\sigma_\theta - \sigma_r}} + \sigma_b - [\sigma_H + \sigma_h - 2(\sigma_H - \sigma_h) \cos 2\theta - \sigma_b] \geq 0, \\
& \frac{2c' + 2\mu'[\sigma_H + \sigma_h - 2(\sigma_H - \sigma_h) \cos 2\theta - \sigma_b]}{(1 - \mu' \cot \beta_{\sigma_r - \sigma_\theta}) \sin 2\beta_{\sigma_r - \sigma_\theta}} + [\sigma_H + \sigma_h - 2(\sigma_H - \sigma_h) \cos 2\theta - \sigma_b] - \sigma_b \geq 0, \\
& \frac{2c' + 2\mu'[\sigma_V - 2\nu(\sigma_H - \sigma_h) \cos 2\theta]}{(1 - \mu' \cot \beta_{\sigma_r - \sigma_z}) \sin 2\beta_{\sigma_r - \sigma_z}} + [\sigma_V - 2\nu(\sigma_H - \sigma_h) \cos 2\theta] - \sigma_b \geq 0, \\
& \frac{2c' + 2\mu' \sigma_b}{(1 - \mu' \cot \beta_{\sigma_z - \sigma_r}) \sin 2\beta_{\sigma_z - \sigma_r}} + \sigma_b - [\sigma_V - 2\nu(\sigma_H - \sigma_h) \cos 2\theta] \geq 0.
\end{aligned} \tag{11}$$

Because the tangential principal stress (σ_θ) is the maximum applied principal stress (i.e., either $\sigma_\theta > \sigma_r > \sigma_z$ or $\sigma_\theta > \sigma_z > \sigma_r$ is satisfied), Equation (10) can be reduced to the following equations:

$$\begin{aligned}
& \frac{2c' + 2\mu'[\sigma_V - 2\nu(\sigma_H - \sigma_h) \cos 2\theta]}{(1 - \mu' \cot \beta_{\sigma_\theta - \sigma_z}) \sin 2\beta_{\sigma_\theta - \sigma_z}} + [\sigma_V - 2\nu(\sigma_H - \sigma_h) \cos 2\theta] - [\sigma_H + \sigma_h - 2(\sigma_H - \sigma_h) \cos 2\theta - \sigma_b] \geq 0, \\
& \frac{2c' + 2\mu'\sigma_b}{(1 - \mu' \cot \beta_{\sigma_\theta - \sigma_r}) \sin 2\beta_{\sigma_\theta - \sigma_r}} + \sigma_b - [\sigma_H + \sigma_h - 2(\sigma_H - \sigma_h) \cos 2\theta - \sigma_b] \geq 0, \\
& \frac{2c' + 2\mu'[\sigma_V - 2\nu(\sigma_H - \sigma_h) \cos 2\theta]}{(1 - \mu' \cot \beta_{\sigma_r - \sigma_z}) \sin 2\beta_{\sigma_r - \sigma_z}} + [\sigma_V - 2\nu(\sigma_H - \sigma_h) \cos 2\theta] - \sigma_b \geq 0, \\
& \frac{2c' + 2\mu'\sigma_b}{(1 - \mu' \cot \beta_{\sigma_z - \sigma_r}) \sin 2\beta_{\sigma_z - \sigma_r}} + \sigma_b - [\sigma_V - 2\nu(\sigma_H - \sigma_h) \cos 2\theta] \geq 0.
\end{aligned} \tag{12}$$

Substituting $\sigma_H = a_H z + b_H$, $\sigma_h = a_h z + b_h$, $\sigma_V = a_V z + b_V$, and Equation (1) into Equation (12), we obtain the following equations to test whether the slip failure along discontinuities will take place around the cylindrical caved space:

$$\begin{aligned}
& 2c' + (1 - \mu' \cot \beta_{\sigma_\theta - \sigma_z}) \sin 2\beta_{\sigma_\theta - \sigma_z} C\rho_b g r (1 - e^{-(z-z_0)/4r_b}) \\
& + [2\mu' + (1 - \mu' \cot \beta_{\sigma_\theta - \sigma_z}) \sin 2\beta_{\sigma_\theta - \sigma_z}] (a_V z + b_V) \\
& + [2(1 - \nu)(1 - \mu' \cot \beta_{\sigma_\theta - \sigma_z}) \sin 2\beta_{\sigma_\theta - \sigma_z} - 4\nu\mu'] \\
& \quad [(a_H - a_h)z + b_H - b_h] \cos 2\theta \\
& - (1 - \mu' \cot \beta_{\sigma_\theta - \sigma_z}) \sin 2\beta_{\sigma_\theta - \sigma_z} [(a_H + a_h)z + b_H + b_h] \geq 0,
\end{aligned} \tag{13a}$$

$$\begin{aligned}
& 2c' + 2[2\mu' + (1 - \mu' \cot \beta_{\sigma_\theta - \sigma_r}) \sin 2\beta_{\sigma_\theta - \sigma_r}] C\rho_b g r (1 - e^{-(z-z_0)/4r_b}) \\
& - [(1 - \mu' \cot \beta_{\sigma_\theta - \sigma_r}) \sin 2\beta_{\sigma_\theta - \sigma_r}] \\
& \quad [(a_H + a_h)z - 2(a_H - a_h)z \cos 2\theta \\
& + (b_H + b_h) - 2(b_H - b_h) \cos 2\theta] \geq 0,
\end{aligned} \tag{13b}$$

$$\begin{aligned}
& 2c' - [(1 - \mu' \cot \beta_{\sigma_r - \sigma_z}) \sin 2\beta_{\sigma_r - \sigma_z}] C\rho_b g r_b (1 - e^{-z_b/4r_b}) \\
& + [2\mu' + (1 - \mu' \cot \beta_{\sigma_r - \sigma_z}) \sin 2\beta_{\sigma_r - \sigma_z}] \\
& \quad [a_V z + b_V - 2\nu(a_H - a_h)z \cos 2\theta - 2\nu(b_H - b_h) \cos 2\theta] \geq 0,
\end{aligned} \tag{13c}$$

$$\begin{aligned}
& 2c' + [2\mu' + (1 - \mu' \cot \beta_{\sigma_z - \sigma_r}) \sin 2\beta_{\sigma_z - \sigma_r}] C\rho_b g r_b (1 - e^{-z_b/4r_b}) \\
& - (1 - \mu' \cot \beta_{\sigma_z - \sigma_r}) \sin 2\beta_{\sigma_z - \sigma_r} \\
& \quad [a_V z + b_V - 2\nu(a_H - a_h)z \cos 2\theta - 2\nu(b_H - b_h) \cos 2\theta] \geq 0.
\end{aligned} \tag{13d}$$

Equation (12) enables the prediction for orientation (θ) and depth (z) where slip failure along the inclined discontinuities will take place, and it shows the occurrence of slip failure heavily depends on the property (c' and μ') of discontinuities. This means the slip failure along discontinuities and associated extension of surface subsidence may suddenly occur due to the dramatic decrease of discontinuities' cohesion, such as when the infill in discontinuities is saturated because of heavy precipitation or underground water [37]. Additionally, laboratory tests have demonstrated the strength of discontinuities will reduce after the slip failure [38]. This reduction will deteriorate the stability of surrounding rocks, because the initial slip failure in one dimension (e.g., when $\beta_{\sigma_\theta - \sigma_r} = (\pi/4) + (\phi'/2)$ is satisfied) is likely to lead to the subsequent failure in other directions (e.g., $\beta_{\sigma_\theta - \sigma_z} = (\pi/4) + (\phi'/2)$ or $\beta_{\sigma_z - \sigma_r} = (\pi/4) + (\phi'/2)$ is satisfied).

On the other hand, Equations (13a)–(13d) show the impact of caved materials on the stability of surrounding rocks. Because of $\phi' < \beta_{\sigma_r - \sigma_j} < 90^\circ$, the caved rocks contribute to keeping the surrounding rocks from slip failure (i.e., Equations (13a), (13b), and (13d)), apart from the condition that the radial principal stress (σ_b) accounts for the slip failure (i.e., Equation (13c)). This means the measures to prevent the shear failure of isotropic surrounding rocks (i.e., (1) filling the interspace between large-sized caved rocks by dumping small-sized waste rocks or (2) backfilling the caved space

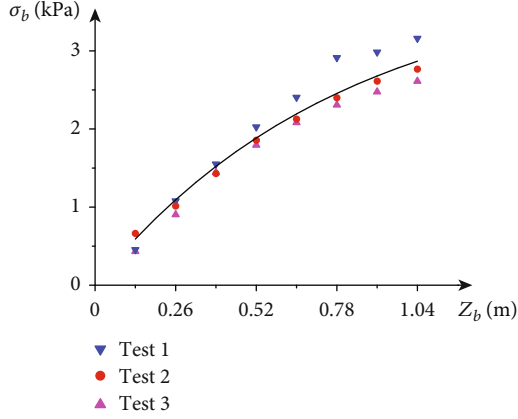


FIGURE 4: The variation of σ_b with the depth from the free surface of caved rocks by laboratory tests.

with waste rocks) are also valid to enhance the stability of anisotropic surrounding rocks, as well as to mitigate the extension of surface subsidence, if the rock failure is due to tangential principal stress (σ_θ) or axial principal stress (σ_z).

4. Case Study for Extension of Surface Subsidence in Xiaowanggou Iron Mine

Herein is presented a case study for Xiaowanggou iron mine. Some implications from the proposed model and case study are discussed.

4.1. Prediction for Subsequent Extension of Surface Subsidence after Vertical Caving. Xiaowanggou iron mine is located in Liaoyang, Liaoning of China, whose deposit is extracted by sublevel caving method. The surface subsidence appears circular after the vertical caving. To predict the extension of surface subsidence, the proposed model is employed. The inputs should be noted firstly, such as in situ stress, rock strength, property of caved materials, and the distribution of discontinuities in 3D space.

We conducted the point load test for the strength of surrounding rocks, and it is converted to the long-term strength to analyze the stability of caved space in a long duration of time [22]. On the other hand, we also collected the caved rocks in situ, and scaled laboratory tests are thus conducted for the constant (i.e., C) in Equation (1). By regressing 3 sets of laboratory test data, the results demonstrate $C = 0.991$ ($R^2 = 0.993$), as illustrated in Figure 4.

The in situ stress is obtained by regressing 12 sets of data by anelastic strain recovery and hydraulic fracturing methods, which is provided by the Fundamental Database of Crustal Stress Environment in continental China. The direction of the maximum in situ stress is N80°E [39]. The in situ stress in Xiaowanggou iron mine can be expressed as follows:

$$\begin{aligned}\sigma_H &= 0.0304z + 2.9033, \\ \sigma_V &= 0.0244z + 1.1593, \\ \sigma_h &= 0.0149z + 2.6795.\end{aligned}\quad (14)$$

The in situ investigation shows the strike and inclination of the discontinuities are N15°E and 76°, respectively. Figure 5 shows the distribution of caved space, in situ stress, and discontinuities in 3D space.

Table 1 lists the inputs to calculate the critical depth of undercut, above which either rock shear failure or slip failure along discontinuities can be prevented, if the implemented undercut locates.

The in situ stress and involved parameters reveal the three principal stress (σ_θ , σ_z , σ_r) satisfies $\sigma_\theta > \sigma_z > \sigma_r$ under the free surface of caved rocks ($z_0 = 45$ m). This means Equations (13a), (13b), (13d), and (7a) are valid to predict the slip failure along discontinuities and the shear failure occurring at the surrounding rock of caved space, respectively. Additionally, the calculation for the angles related to slip failure, i.e., $\beta_{\sigma_\theta-\sigma_r}$, $\beta_{\sigma_\theta-\sigma_z}$, and $\beta_{\sigma_z-\sigma_r}$, should be noted. The angle δ is defined to describe the distribution of in situ stress and the strike of the discontinuities on the plane constituted by the maximum and minimum in situ stress (Figure 5(a)), and the angles related to the slip failure in Xiaowanggou iron mine can be calculated by the following equations:

$$\begin{aligned}\beta_{\sigma_\theta-\sigma_r} &= |\theta - \delta|, \\ \beta_{\sigma_\theta-\sigma_z} &= \arctan \frac{1}{\tan \eta \cdot \cos \theta}, \\ \beta_{\sigma_z-\sigma_r} &= \arctan (\tan \eta \cdot \sin \theta),\end{aligned}\quad (15)$$

where δ is the angle between discontinuities' strike and the maximum in situ stress (σ_H) on the plane constituted by the maximum and minimum in situ stress and η is the inclination of the discontinuities.

Therefore, we calculate the critical depth of undercut around the caved space, above which the surrounding wall maintains stable from either rock shear failure or slip failure along discontinuities. Because of symmetry, we only present the results in a half circumference, i.e., θ varies from 0° to 180°, as shown in Figure 6.

As expected, the variation of the critical depth related to rock shear failure (i.e., “shear failure” in Figure 6) is symmetric on either sides of the direction where the maximum effective principal stress (σ_θ) has maximum value (i.e., $\theta = 90^\circ$, N10°W, or the direction of minimum in situ stress). The minimum value of such critical depth appears at $z = 406$ m, in the direction of minimum in situ stress. However, the depth of implemented undercut locates at $z = 168$ m, and this means rock shear failure is not responsible for extension of surface subsidence in Xiaowanggou iron mine.

On the other hand, Figure 6 provides the results of the critical depth of undercut related to the slip failure along discontinuities. The results indicate the slip failure due to σ_θ , with the confining stress σ_z , will not take place above the depth $z = 2500$ m in this project. When the σ_r serves as the confining stress, the critical depth related to the slip failure due to σ_θ (i.e., “slip failure due to σ_θ ” in Figure 6) or σ_z (i.e., “slip failure due to σ_z ” in Figure 6) presents an asymmetrical distribution. Their ultimate value of the critical depth appears near the direction where Equation (8) is satisfied

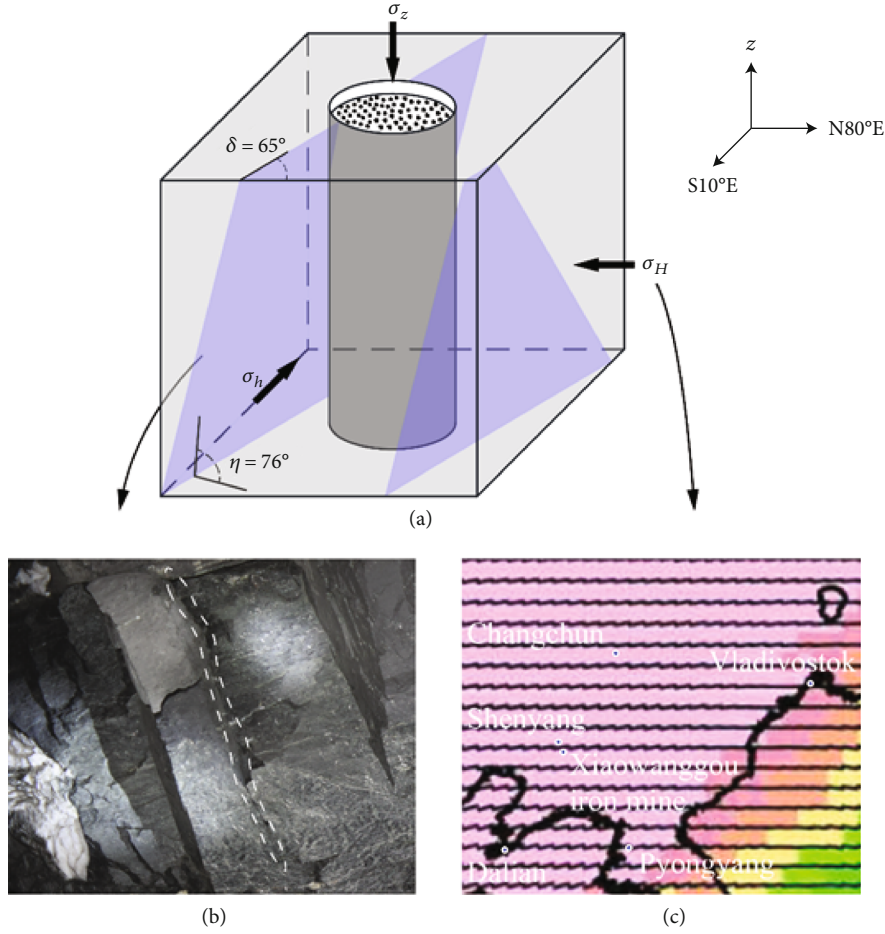


FIGURE 5: (a) The distribution of caved space, in situ stress, and discontinuities in 3D space. (b) In situ observation for the discontinuities in the undercut in Xiaowanggou iron mine. (c) The orientation of mean maximum horizontal in situ stress (represented by black bar) around Xiaowanggou iron mine.

TABLE 1: Parameters of the surrounding intact rocks, caved rocks, and discontinuities.

Surrounding intact rocks				Discontinuities			Caved rocks		
I_{s50} (MPa)	σ_{cd} (MPa)	ϕ ($^\circ$)	ν	c' (MPa)	ϕ' ($^\circ$)	ρ_B (t/m 3)	C	r_B (m)	z_0 (m)
4.093	32.744	35	0.25	3.25	20	1.77	0.991	77.05	45

(i.e., $\beta_{\sigma_\theta-\sigma_r} = 55^\circ$ or $\beta_{\sigma_z-\sigma_r} = 55^\circ$), but the offset towards the direction of minimum in situ stress can be observed. The variation of σ_θ and σ_z around the caved space is responsible to this offset, as well as the difference of the ultimate value of critical undercut depth in each distribution interval (e.g., the ultimate value of critical undercut depth due to σ_θ between $\theta = 0^\circ$ and $\theta = 40^\circ$ is smaller than the one between $\theta = 90^\circ$ and $\theta = 150^\circ$). The minimum critical depth of undercut appear at $z = 55$ m when $\theta = 115^\circ$, i.e., N35°W, and this value is smaller than the depth of implemented undercut. This means the slip failure along discontinuities and the associated extension of surface subsidence are likely to be firstly observed in N35°W, as well as in S35°E due to symmetry. Therefore, the extension of surface subsidence in Xiaowanggou iron mine is predicted. In the depth of the free surface of

caved rocks (i.e., $z = 45$ m or “caved rocks surface” in Figure 6), the surrounding rocks of the caved space maintain stable from either rock shear failure or slip failure along discontinuities. In the depth of implemented undercut (i.e., $z = 168$ m or “undercut depth” in Figure 6), Figure 6 shows the slip failure due to σ_θ will take place between $\theta = 98^\circ$ and $\theta = 135^\circ$, i.e., between N18°W and N55°W, as well as between S18°E and S55°E due to symmetry. This means the surface subsidence is likely to extend to such orientations. To test the validity of this prediction, we compared it with the satellite images by Google Earth, as illustrated in Figure 7.

The extension process of surface subsidence is illustrated in Figure 7, and the blue shadow indicates the predicted orientation that the surface subsidence extends to by the proposed model. Figure 7 shows the observed extension of

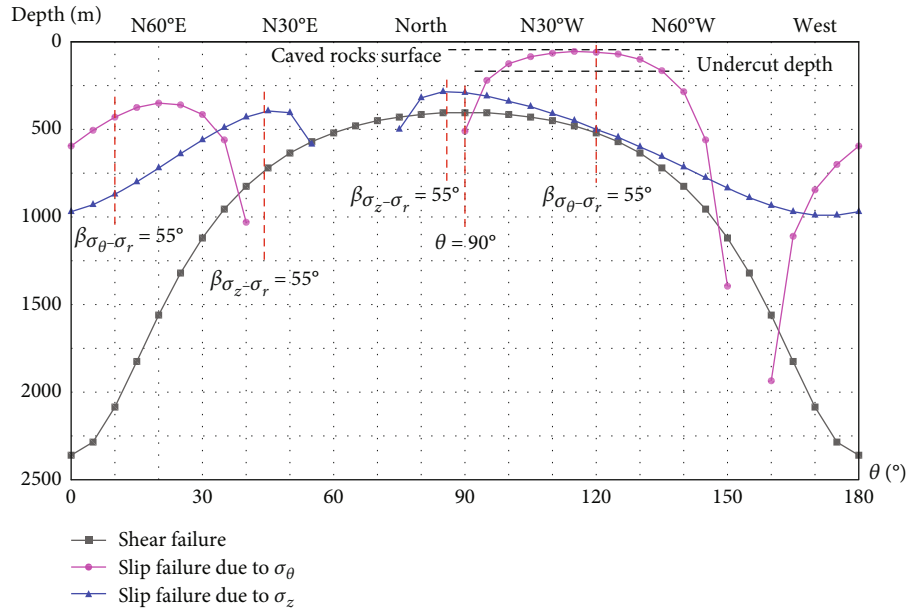


FIGURE 6: The variation of the critical depth of undercut around the cylindrical caved space, above which the surrounding rocks maintain stable from either rock shear failure (i.e., “shear failure”), or the slip failure along discontinuities (i.e., “slip failure due to σ_θ ” or “slip failure due to σ_z ”). The undercut locates at the depth of 168 m (i.e., “undercut depth”), and the slip failure of surrounding rocks along discontinuities will take place at the direction between N18°W and N55°W, as well as between S18°E and S55°E due to symmetry, because the critical depth of undercut to prevent slip failure due to σ_θ (i.e., magenta line) locates above the depth of implemented undercut in these ranges of direction.

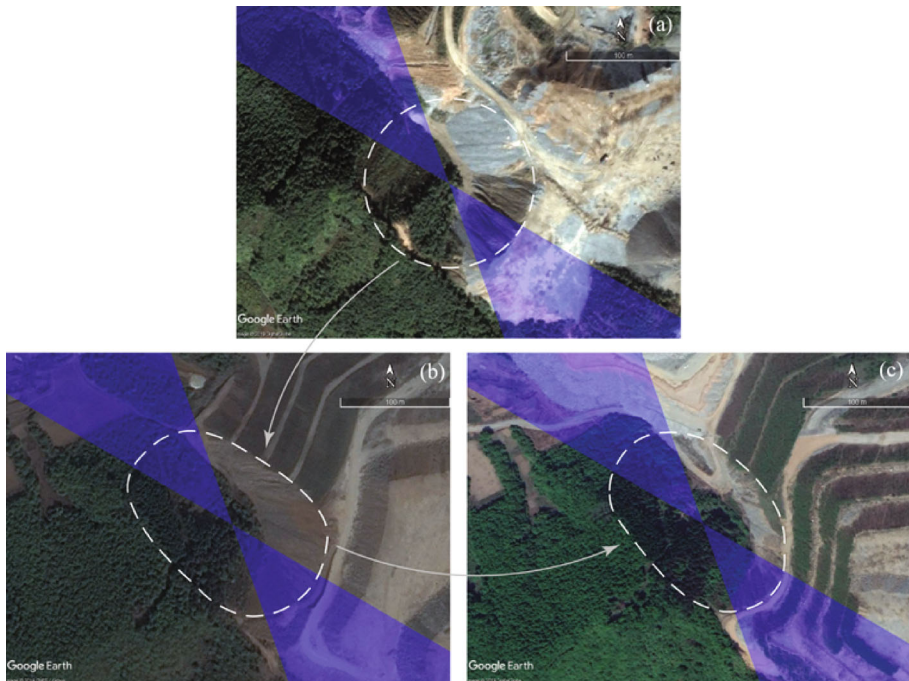


FIGURE 7: The comparison between the prediction by the proposed model and the observation in Google Earth satellite images for the surface subsidence extension in Xiaowanggou iron mine (41.39°N, 123.63°E). (a) The circular surface subsidence observed after vertical caving on October 1, 2012. (b) The extended surface subsidence area observed on April 25, 2014. (c) The extended surface subsidence area on May 8, 2017. The blue shadow illustrated indicates direction that the surface subsidence extends to, which is obtained from Figure 6, by comparing the depth of implemented undercut to critical depth of undercut to maintain the surrounding rocks from either rock shear failure or slip failure along the discontinuities.

surface subsidence generally matches the prediction, even though the observed range of orientation that surface subsidence extends to is larger than the predicted. Such results demonstrate the validity of the proposed model for the prediction of subsequent extension of surface subsidence after vertical caving.

4.2. Implications from the Proposed Model and Illustrative Example. Herein is presented some implications regarding the proposed model and illustrative example. The difference of orientation range, where surface subsidence extends to, between the observation in satellite image and the prediction by proposed model should be discussed first. The long-term strength is involved to test the stability of surrounding isotropic rock in a long duration of time because of the consideration of time effect, such as rock creep or the saturation by surface or underground water. However, rare analytical solutions regarding long-term strength of discontinuities have been reported, even though the impact of time on discontinuities' strength has been commonly observed [40, 41]. Thus, the time effect is not involved in the proposed model for the slip failure (Equations (11), (12), and (13a)–(13d)), and this leads to observed orientation range where surface subsidence extension that takes place is larger than the predicted. Meanwhile, the absence of the consideration for the impact of time on discontinuities' strength is a limitation of the proposed model.

The comparison for surface subsidence extension between the observation in satellite images and the analytical prediction demonstrates the validity of the proposed model. Compared with the existing models [13–16], the proposed targets predict the subsequent extension of surface subsidence after vertical caving, which is rarely analyzed in previous literatures. Both rock shear failure and slip failure along discontinuities are involved in this model, and the case study shows such two failures are likely to take place either in the direction of minimum in situ stress or near the direction where the anisotropic rocks have minimum strength, respectively. Moreover, the impact of caved rocks on the stability of surrounding rocks of caved space is addressed, and some approaches to prevent the extension of surface subsidence are thus suggested, e.g., filling the interspace between large-sized caved rocks by dumping small-sized waste rocks or backfilling the caved space with waste rocks.

5. Conclusion

Surface subsidence due to underground mining leads to severe geological hazards. The extension of surface subsidence after vertical caving is a primary contributor to the large-scale ground destruction, as well as the associated geological hazards. However, it is still intractable to analytically predict the extension of circular surface subsidence, because of the absence of robust model.

To fill such a research gap, employing in situ stress, property of surrounding intact rock, inherent discontinuities, and caved rocks, an analytical model is proposed to calculate the depth around the cylindrical caved space, above which the surrounding rocks maintain stable from either rock shear failure or the slip failure along discontinuities. The compari-

son between the predicted extension of circular surface subsidence in Xiaowanggou iron mine and the in situ observation demonstrates the validity of the proposed model. The proposed model reveals the surface subsidence tends to extend to the direction of minimum in situ stress, when the rock shear failure accounts for such extension. Meanwhile, the extension of surface subsidence due to slip failure along discontinuities is most likely to take place near the direction where the anisotropic rocks have minimum strength. On the other hand, the impact of caved rocks clarified by the proposed model shows the increase of either density or height of caved rocks facilitates the stability of the rocks around the caved space. Some measures are accordingly suggested to prevent the extension of surface subsidence, including filling the interspace between large-sized caved rocks by dumping small-sized waste rocks or backfilling the caved space with waste rocks.

Finally, the contribution of this study should be addressed. Theoretically, this paper proposed an analytical solution to predict the subsequent surface subsidence after vertical caving, by analyzing either rock shear failure or slip failure along discontinuities that occurred at surrounding rock. Practically, the validity of this solution has been validated, which means it has the potential to guide the underground metal mines to mitigate the impact of surface subsidence on safety and environment.

Data Availability

The data used to support the findings of this study are included within the article.

Conflicts of Interest

The authors declare that they have no conflicts of interest.

Acknowledgments

This study was funded by the Fundamental Research Funds for the Central Universities (grant numbers 2020IVA083 and WUT2019III187), the National Key R&D Plan (grant numbers 2018YFC0808405 and 2018YFC0604401), and the Natural Science Foundation of China (grant number 51774220). The authors would like to thank the Institute of Crustal Dynamics (ICD), China Earthquake Administration, for providing the in situ stress data near Xiaowanggou iron mine.

References

- [1] P. Tzampoglou and C. Loupasakis, "Mining geohazards susceptibility and risk mapping: the case of the Amyntaio open-pit coal mine, West Macedonia, Greece," *Environment and Earth Science*, vol. 76, no. 15, p. 542, 2017.
- [2] Z. Dawei, W. Kan, B. Zhihui et al., "Formation and development mechanism of ground crack caused by coal mining: effects of overlying key strata," *Bulletin of Engineering Geology and the Environment*, vol. 78, no. 2, pp. 1025–1044, 2019.
- [3] W. X. Li, L. Wen, and X. M. Liu, "Ground movements caused by deep underground mining in Guan-Zhuang iron mine, Luzhong, China," *International Journal of Applied Earth*

- Observation and Geoinformation*, vol. 12, no. 3, pp. 175–182, 2010.
- [4] Y. Y. Deng, C. X. Chen, K. Z. Xia, K. Y. Yang, C. Y. Sun, and X. W. Zheng, “Investigation on the characteristics of overlying strata caving in the Chengchao Iron Mine, China,” *Environment and Earth Science*, vol. 77, no. 10, p. 362, 2018.
 - [5] J. P. Hurtado, N. Díaz, E. I. Acuna, and J. Fernandez, “Shock losses characterization of ventilation circuits for block caving production levels,” *Tunnelling and Underground Space Technology*, vol. 41, pp. 88–94, 2014.
 - [6] Y. S. Wang, G. P. Zheng, and X. Wang, “Development and application of a goaf-safety monitoring system using multi-sensor information fusion,” *Tunnelling and Underground Space Technology*, vol. 94, p. 103112, 2019.
 - [7] M. Sepehri, D. B. Apel, and R. A. Hall, “Prediction of mining-induced surface subsidence and ground movements at a Canadian diamond mine using an elastoplastic finite element model,” *International Journal of Rock Mechanics and Mining Sciences*, vol. 100, pp. 73–82, 2017.
 - [8] K. Ding, F. S. Ma, J. Guo, H. J. Zhao, R. Lu, and F. Liu, “Investigation of the mechanism of roof caving in the Jinchuan nickel mine, China,” *Rock Mechanics and Rock Engineering*, vol. 51, no. 4, pp. 1215–1226, 2018.
 - [9] B. H. G. Brady and E. T. Brown, *Rock Mechanics for Underground Mining*, Springer, Dordrecht, 2004.
 - [10] T. Villegas, E. Nordlund, and C. Dahner-Lindqvist, “Hanging-wall surface subsidence at the Kiirunavaara Mine, Sweden,” *Engineering Geology*, vol. 121, no. 1-2, pp. 18–27, 2011.
 - [11] K. S. Woo, E. Eberhardt, D. Elmo, and D. Stead, “Empirical investigation and characterization of surface subsidence related to block cave mining,” *International Journal of Rock Mechanics and Mining Sciences*, vol. 61, pp. 31–42, 2013.
 - [12] L. C. Li, C. A. Tang, X. D. Zhao, and M. Cai, “Block caving-induced strata movement and associated surface subsidence: a numerical study based on a demonstration model,” *Bulletin of Engineering Geology and the Environment*, vol. 73, no. 4, pp. 1165–1182, 2014.
 - [13] D. H. Laubscher, “Cave mining - the state of the art,” *Journal of the Southern African Institute of Mining and Metallurgy*, vol. 94, pp. 279–293, 1994.
 - [14] E. Hoek, “Progressive caving induced by mining an inclined orebody,” *Trans Instn Min Metall*, vol. 83, pp. 33–39, 1974.
 - [15] E. T. Brown and G. A. Ferguson, “Progressive hangingwall caving at Gath’s mine, Rhodesia,” *T I Min Metall A*, vol. 88, pp. 92–105, 1979.
 - [16] J. F. Lupo, “Progressive failure of hanging wall and footwall Kiirunavaara Mine, Sweden,” vol. 34, no. 3-4, pp. 184.e1–184.e11, 1997.
 - [17] L. Nie, H. F. Wang, and Y. Xu, “Application of the arctangent function model in the prediction of ground mining subsidence deformation: a case study from Fushun City, Liaoning Province, China,” *Bulletin of Engineering Geology and the Environment*, vol. 76, no. 4, pp. 1383–1398, 2017.
 - [18] K. Z. Xia, C. X. Chen, Y. Y. Deng et al., “In situ monitoring and analysis of the mining-induced deep ground movement in a metal mine,” *International Journal of Rock Mechanics and Mining Sciences*, vol. 109, pp. 32–51, 2018.
 - [19] G. W. Cheng, C. X. Chen, L. C. Li et al., “Numerical modelling of strata movement at footwall induced by underground mining,” *International Journal of Rock Mechanics and Mining Sciences*, vol. 108, pp. 142–156, 2018.
 - [20] P. Hamdi, D. Stead, D. Elmo, and J. Toyra, “Use of an integrated finite/discrete element method-discrete fracture network approach to characterize surface subsidence associated with sub-level caving,” *International Journal of Rock Mechanics and Mining Sciences*, vol. 103, pp. 55–67, 2018.
 - [21] E. Hoek and E. T. Brown, *Underground Excavations in Rock*, The institute of mining and metallurgy, London, 1980.
 - [22] J. A. Franklin, “Suggested method for determining point load strength,” *International Journal of Rock Mechanics and Mining Sciences & Geomechanics Abstracts*, vol. 22, no. 2, pp. 51–60, 1985.
 - [23] A. Funato and T. Ito, “A new method of diametrical core deformation analysis for in-situ stress measurements,” *International Journal of Rock Mechanics and Mining Sciences*, vol. 91, pp. 112–118, 2017.
 - [24] H. Roshan, H. Masoumi, Y. H. Zhang et al., “Microstructural effects on mechanical properties of shaly sandstone,” *Journal of Geotechnical and Geoenvironmental Engineering*, vol. 144, no. 2, article 06017019, 2018.
 - [25] F. Y. Ren, Y. Liu, J. L. Cao et al., “Prediction of the caved rock zones’ scope induced by caving mining method,” *PLoS One*, vol. 13, no. 8, article e0202221, 2018.
 - [26] S. Mahajan, M. Tennenbaum, S. N. Pathak et al., “Reverse Janssen effect in narrow granular columns,” *Physical Review Letters*, vol. 124, no. 12, p. 128002, 2020.
 - [27] E. A. S. Neto, D. Peric, and D. R. J. Owen, *Computational Methods for Plasticity Theory and Applications*, Wiley, Chichester, UK, 2008.
 - [28] N. Brantut, M. J. Heap, P. G. Meredith, and P. Baud, “Time-dependent cracking and brittle creep in crustal rocks: a review,” *Journal of Structural Geology*, vol. 52, pp. 17–43, 2013.
 - [29] B. Damjanac and C. Fairhurst, “Evidence for a long-term strength threshold in crystalline rock,” *Rock Mechanics and Rock Engineering*, vol. 43, no. 5, pp. 513–531, 2010.
 - [30] A. Serrano and C. Olalla, “Ultimate bearing capacity of an anisotropic discontinuous rock mass. Part I: basic modes of failure,” *International Journal of Rock Mechanics and Mining Sciences*, vol. 35, no. 3, article S0148906297003379, pp. 301–324, 1998.
 - [31] Y. M. Tien and M. C. Kuo, “A failure criterion for transversely isotropic rocks,” *International Journal of Rock Mechanics and Mining Sciences*, vol. 38, no. 3, pp. 399–412, 2001.
 - [32] A. Ghazvinian, R. G. Vaneghi, M. R. Hadei, and M. J. Azinfar, “Shear behavior of inherently anisotropic rocks,” *International Journal of Rock Mechanics and Mining Sciences*, vol. 61, pp. 96–110, 2013.
 - [33] M. Singh, N. K. Samadhiya, A. Kumar, V. Kumar, and B. Singh, “A nonlinear criterion for triaxial strength of inherently anisotropic rocks,” *Rock Mechanics and Rock Engineering*, vol. 48, no. 4, pp. 1387–1405, 2015.
 - [34] J. C. Jaeger, N. G. W. Cook, and R. W. Zimmerman, *Fundamentals of Rock Mechanics*, Wiley-Blackwell, Oxford, 4th ed edition, 2007.
 - [35] J. Zhang, “Borehole stability analysis accounting for anisotropies in drilling to weak bedding planes,” *International Journal of Rock Mechanics and Mining Sciences*, vol. 60, pp. 160–170, 2013.
 - [36] O. Aydan, *Rock Reinforcement and Rock Support*, CRC Press, London, UK, 2018.
 - [37] L. B. Gong, J. Nemicik, and T. Ren, “Numerical simulation of the shear behavior of rock joints filled with unsaturated soil,”

International Journal of Geomechanics, vol. 18, no. 9, article 04018112, 2018.

- [38] E. E. Alonso and N. M. Pinyol, "Slope stability in slightly fissured claystones and marls," *Landslides*, vol. 12, no. 4, pp. 643–656, 2015.
- [39] X. P. Hu, A. N. Zang, O. Heidbach, X. F. Cui, F. R. Xie, and J. W. Chen, "Crustal stress pattern in China and its adjacent areas," *Journal of Asian Earth Sciences*, vol. 149, pp. 20–28, 2017.
- [40] L. M. Vick, M. Bohme, L. Rouyet, S. G. Bergh, G. D. Corner, and T. R. Lauknes, "Structurally controlled rock slope deformation in northern Norway," *Landslides*, vol. 17, no. 8, pp. 1745–1776, 2020.
- [41] A. Liu, W. L. Lin, and J. C. Jiang, "Investigation of the long-term strength properties of a discontinuity by shear relaxation tests," *Rock Mechanics and Rock Engineering*, vol. 53, no. 2, pp. 831–840, 2020.

Research Article

Analysis of Vertical Response of Drilled Pile at the Crest of Rock Slope Based on Shear Behavior

Chong Jiang , Ju Fang, and Bowen Sun

School of Resources and Safety Engineering, Central South University, Changsha, 410083 Hunan, China

Correspondence should be addressed to Chong Jiang; jiang4107@sohu.com

Received 31 March 2021; Accepted 8 May 2021; Published 26 May 2021

Academic Editor: Yu Wang

Copyright © 2021 Chong Jiang et al. This is an open access article distributed under the Creative Commons Attribution License, which permits unrestricted use, distribution, and reproduction in any medium, provided the original work is properly cited.

This paper proposed a method for analysis of a drilled pile under vertical load at the crest of rock slope. Based on wedge theory, a modified model of normal stiffness of socket wall affected by the slope is obtained. Analyze the shear behaviors of the pile-rock interface, an analytical solution of load transfer of pile at the crest of rock slope is obtained. To evaluate the accuracy of the new method, this method is compared with the results of finite difference analysis. Finally, the method is used to analyze the effect of slope, pile, and rock properties on the unit side resistance and axial force.

1. Introduction

Piles, which are widely used in offshore drillings, bridges, and other structures, are often embedded in rocks. Foundations constructed in level ground near continental, nearshore slopes, or man-made slope are inevitable in engineering practice. Because of slope, increase in settlement is observed [1, 2].

To analyze load transfer of pile under vertical loads, a series of method have been proposed. Laboratory test [3–7] could evaluate the vertical behaviors of pile; however, there are differences between small scale model pile test and engineering practice. Numerical method [1, 2, 8, 9] could simulate various engineering conditions, but parameters of sophisticated soil constitutive relations are hard to obtain. Theoretical method [10–23] could quickly obtain the relationship between load and settlement under various working conditions.

Jiang et al. [1, 2] used theoretical method to investigate the behaviors of rigid piles in sloping ground and obtained the effect of slope on the settlement. Jesmani et al. [24] investigated the effect of different types of clayey slopes on vertical bearing capacity based on finite element. All these methods applied to the soil slope; however, there are differences between soil and rock. For short pile in soil, structural loads are carried by base resistance, but for long pile embedded

in rock, the bearing capacity almost depends on side resistance.

Johnston and Lam [25] analyzed pile-rock surface and proposed the theory of dilation energy. Based on the theory of dilation energy, many scholars [26–29] have studied the shear behavior of pile-rock interface. Zhao MH et al. [30], Xing HF et al. [31], and Zhao H [32] investigated the principal mechanisms of shear transfer between piles and rock, and the failure surfaces were assumed to line and slip-line field, respectively. All these methods obtained the effect of the concrete-rock surface on the behaviors. But for the pile at the crest of rock slope, because of slope, the normal stiffness of socket wall will decrease. To accurately evaluate the behaviors of pile at the crest of rock slope, the decrease of normal stiffness of socket wall is the key to the principal mechanisms of shear transfer between piles and rock.

To obtain the effect of slope on normal stiffness of socket wall, the wedge theory is used to illustrate it. An analytical solution of load transfer of pile at the crest of rock slope is obtained by analyzing the shear behaviors of the pile-rock interface. To evaluate the accuracy of the new method which is analysis of a drilled pile under vertical load at the crest of rock slope, this method is compared with the results of finite element analysis. Finally, the method is used to analyze the effect of slope, pile, and rock properties on the unit side resistance and axial force.

2. An Analytical Solution of Load Transfer of Pile at the Crest of Rock Slope considering the Shear Behaviors of the Pile-Rock Interface

2.1. Initial Normal Stiffness Equation Based on Wedge Theory. The basic assumptions of this paper are as follows: For the pile at the crest of rock slope, because of slope, the normal stiffness of socket wall will decrease. The schematic of the slope-pile model analyzed is illustrated in Figure 1. (x, z) is the Cartesian coordinate system, and the y direction is perpendicular to the x - z plane. The stress of the rock around the pile under the self-weight is ρg .

Based on the wedge stress theory, the three-direction stress relationship of rock under the self-weight at the crest of slope is:

$$\begin{cases} \sigma_z = \rho g z, \\ \sigma_x = \rho g z \frac{2 - 2 \cos^2 \gamma}{\cos^2 \gamma}, \\ \sigma_y = \nu(\sigma_x + \sigma_z), \end{cases} \quad (1)$$

where σ_x, σ_y , and σ_z are the elastic stress solutions of the rock in the Cartesian coordinate system, ν is Poisson's ratio of rock, and γ is the complementary angle of α .

The initial tangent modulus equation of the pile at the crest of slope is:

$$E_0 = E_s(1 - \nu k_1 - \nu k_2), \quad (2)$$

where E_0 is the initial tangent modulus, E_s is the compression modulus, and k_1 and k_2 are the parameters defined as:

$$\sigma_x = k_1 \sigma_z, \quad (3)$$

$$\sigma_y = k_2 \sigma_z. \quad (4)$$

The initial tangent modulus equation of the pile in level ground is:

$$E_0' = \left(1 - \frac{2\nu^2}{1-\nu}\right) E_s. \quad (5)$$

The normal restraint stiffness of the pile in level ground can be expressed as:

$$K' = \frac{E_0'}{(1+\nu)r}, \quad (6)$$

where r is the radius of pile.

For the pile at the crest of rock slope, the normal stiffness of pile can be obtained by Eqs. (2)–(6):

$$K = R_{E_s} K', \quad (7)$$

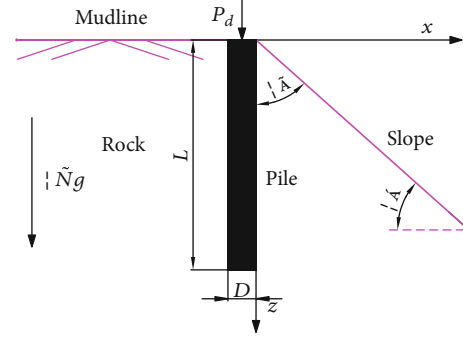


FIGURE 1: Schematic view of the slope-pile model.

where R_{E_s} is the ratio of the initial tangent modulus at the crest of slope to that in level ground; it can be expressed as:

$$R_{E_s} = \frac{(1 - \nu k_1 - \nu k_2)}{1 - (2\nu^2/(1 - \nu))}. \quad (8)$$

R_{E_s} is a function related to the Poisson's ratio ν , slope angle α , and embedded depth z . In order to obtain a more concise expression for $R_{E_s}(\alpha, z, \nu)$, calculate the value of R_{E_s} in various situations.

Figure 2 shows the corresponding value of R_{E_s} when Poisson's ratio $\nu = 0.2, 0.25, 0.3, 0.35, 0.4$; slope angle $\alpha = 0, 2.5^\circ, 5^\circ, 7.5^\circ, \dots, 30^\circ$; and embedded depths $z = 2 \text{ m}, 4 \text{ m}, 6 \text{ m}, \dots, 20 \text{ m}$. The distribution of R_{E_s} has a certain regularity, and it can be obtained.

R_{E_s} is negatively correlated with the slope angle α and positively correlated with the Poisson's ratio of the rock. The equation for $R_{E_s}(\alpha, z, \nu)$ was fitted by Matlab as:

$$R_{E_s}(\alpha, z, \nu) = \cos((1.654\nu + 0.129)\alpha). \quad (9)$$

For the pile at the crest of rock slope, the normal stiffness of pile can be obtained by Eqs. (7)–(9):

$$K = K' \cos((1.654\nu + 0.129)\alpha). \quad (10)$$

2.2. Shear Behavior of the Pile-Rock Interface

2.2.1. Assumption. Piles will be embedded in weathered rock of slopes, and its bearing capacity almost depends on side resistance. Relative slippage of concrete-rock interface occurs when the pile embedded in rocky slope is subjected to vertical load. Since the concrete-rock interface is rough, the slippage is often accompanied by radial expansion of the pile. The normal stress increases subsequently, and unit side resistance of pile is working. When pile embedded in slope is loaded, the sketch of relative shear motion of asperity is shown in Figure 3.

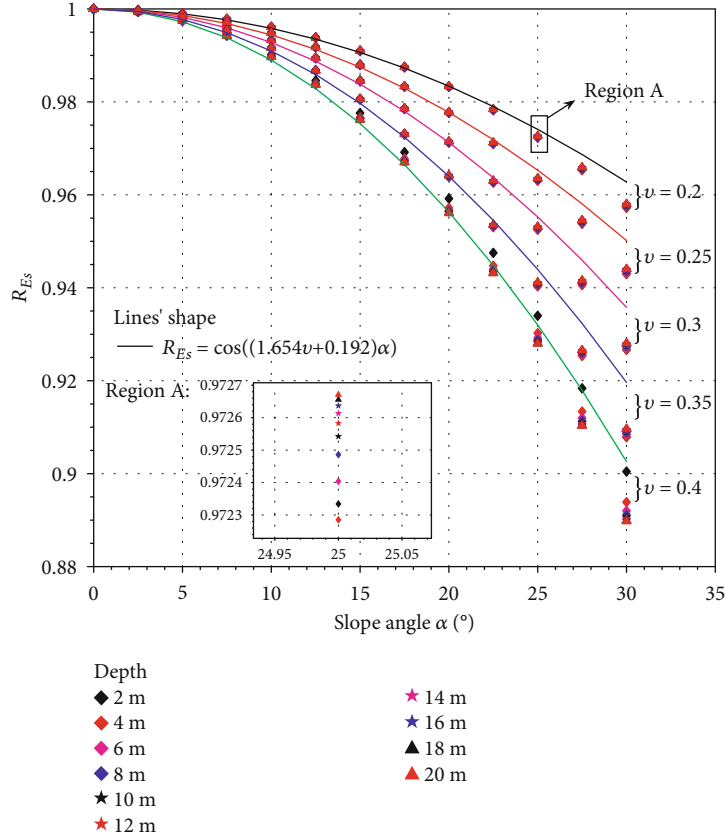


FIGURE 2: Fitting curve of R_{E_s} .

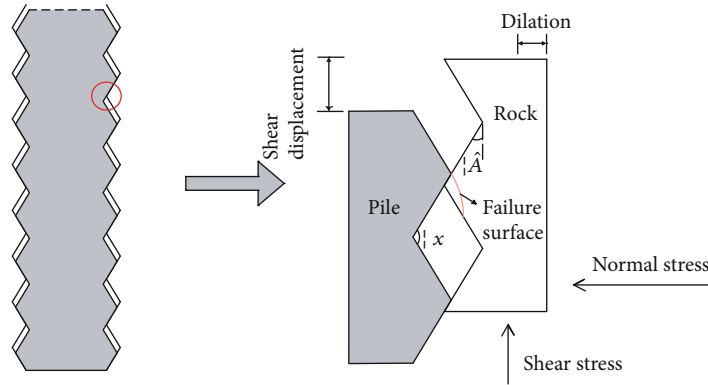


FIGURE 3: Shear motion of asperity.

To formulate shear behaviors of pile-rock interface and obtain solution of load transfer of pile at the crest of rock slope, assumptions of this paper are made in advance.

- (1) The pile-rock interface with regular triangular asperity is consistent, and the inclination of asperity is β
- (2) The cohesion of the pile-rock interface is small and cannot be accurately measured; the cohesion of the pile-rock interface is ignored. The initial normal stress could be ignored in the case of pile embedded

in rocky slope because of a release of the initial geostatic stresses [33]

- (3) The elastic modulus of the pile is greater than that of the rock; the surrounding rock is destroyed before the pile. The failure surface is curved, and the critical normal pressure of interface q_f can be expressed as

$$q_f = c \cot \varphi \left\{ \frac{1 + \sin \varphi}{1 - \sin \varphi} \exp [(2\psi - \pi) \tan \varphi] - 1 \right\}, \quad (11)$$

where c is the cohesion of rock, φ is the internal friction angle of rock, and ψ is vertex angle of regular triangle.

2.2.2. The Principal Mechanisms of Shear Transfer. The progress of shear behavior can be divided into dilation and residual periods. Dilation occurs when the shear displacement is small. With the development of the shear dilation, the pile-rock interface carries loads on the reach of critical stress, and the regular triangular asperity would be shorn off.

For the pile subjected to vertical load at the crest of rock slope, the slippage Δs is often accompanied with radial expansion of the pile Δr .

$$\Delta r = \Delta s \tan \beta, \quad (12)$$

where β is the dilation angle of rock.

And the normal stress will increase in the process of dilation; the incremental normal stress of pile-rock interface $\Delta\sigma_n$ can be expressed as:

$$\Delta\sigma_n = K' \cos((1.654\nu + 0.129)\alpha)\Delta r. \quad (13)$$

As mentioned in the previous assumption, the initial normal stress could be ignored. Therefore, stress acting normal to the direction along the pile σ_n can be expressed as:

$$\sigma_n = \Delta\sigma_n. \quad (14)$$

During progress of dilation, with the development of shear displacement, the normal stress increases continuously. Shear dilation for pile-rock interface is illustrated in Figure 4.

A classic theory for shear behavior is proposed, which was proposed by Patton et al. [34]. Shear stress for dilation can be expressed as:

$$\tau_d = \sigma_n \tan(\varphi_b + \beta), \quad (15)$$

where τ_d is the shear stress for dilation period and φ_b is the base friction angle of rock.

For the pile subjected to vertical load at the crest of rock slope, the unit side resistance for dilation can be obtained by Eqs. (12)–(15):

$$\tau_{(z)} = K' \cos((1.654\nu + 0.129)\alpha) s_{(z)} \tan \beta \tan(\varphi_b + \beta), \quad (16)$$

where $\tau_{(z)}$ is shear resistance for dilation at the depth z and $s_{(z)}$ is shear displacement at the depth z .

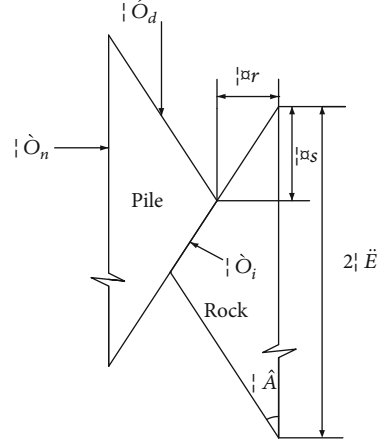


FIGURE 4: Schematic view of shear dilation for pile-rock interface.

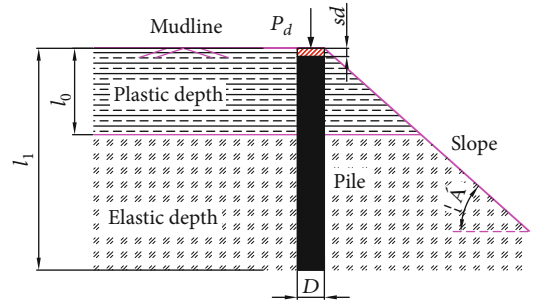


FIGURE 5: The sketch of plastic depth and elastic depth.

TABLE 1: The basic parameter values for verification.

Shaft diameter (D)	2.5 m
Shaft length (L)	32 m
Elastic modulus of pile (E_p)	30 GPa
Friction angle of interface (φ_b)	35°
Triangular half-chord length (λ)	3 mm
Cohesion of rock (c)	200 kPa
Internal friction angle of rock (φ)	25°
Elastic modulus of rock (E_r)	2.0 GPa
Poisson's ratio (ν)	0.25
Dilation angle of rock β	10°

With the development of the shear dilation, the pile-rock interface reaches the critical stress, and the regular triangular asperity would be shorn off. The condition of static equilibrium can be expressed as:

$$\frac{2\lambda(\sigma_n \cos \beta + \tau_d \sin \beta)}{(\lambda - \Delta s)} = \sigma_i, \quad (17)$$

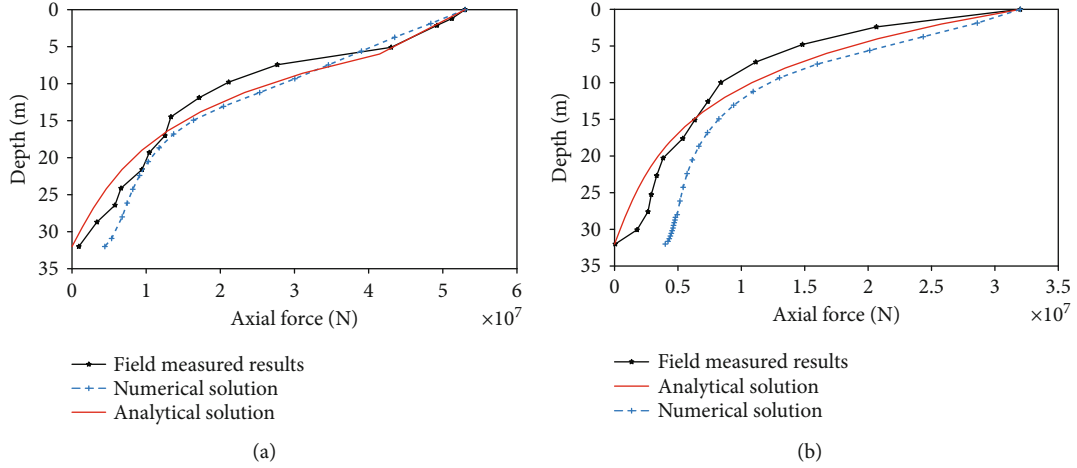


FIGURE 6: Verification in case of slope angle $\alpha = 0^\circ$: (a) comparison in depth with 53 MN vertical load; (b) comparison in depth with 32 MN vertical load.

where λ is the triangular half-chord length, σ_i is the normal stress perpendicular to the pile-rock interface, and Δs is the slippage.

When the normal stress perpendicular to the pile-rock interface σ_i reaches the critical normal pressure of interface q_f , the condition of static equilibrium can be rewritten as:

$$\frac{2\lambda(\sigma_n \cos \beta + \tau_d \sin \beta)}{(\lambda - \Delta s_0)} = q_f, \quad (18)$$

where Δs_0 is the critical shear displacement.

As a result, the critical shear displacement Δs_0 can be obtained by Eqs. (12)–(15) and (18):

$$\Delta s_0 = \frac{\lambda q_f}{2\lambda K' \cos((1.654\nu + 0.129)\alpha) \tan \beta \{\cos \beta + [\tan(\varphi_b + \beta) \sin \beta]\} + q_f}. \quad (19)$$

The interface is plastic when the relative shear displacement $s_{(z)}$ is more than the critical shear displacement Δs_0 . And the shear resistance for residual periods at the depth z would depend on residual parameters; the formulation of side resistance can be expressed as:

$$\tau_{(z)} = K' \cos((1.654\nu + 0.129)\alpha) \Delta s_0 \tan \beta \tan \varphi_r, \quad (20)$$

where φ_r is the residual friction angle of rock.

As a result, the equation of shear behavior for the pile subjected to vertical load at the crest of rock slope is generated as:

$$\tau_{(z)} = \begin{cases} K' \cos((1.654\nu + 0.129)\alpha) s_{(z)} \tan \beta \tan(\varphi_b + \beta) & (0 < s_{(z)} < \Delta s_0) \\ K' \cos((1.654\nu + 0.129)\alpha) \Delta s_0 \tan \beta \tan \varphi_r & (s_{(z)} > \Delta s_0) \end{cases}. \quad (21)$$

2.3. A Closed-Form Solution of Vertical Load Transfer of Pile at the Crest of Rock Slope

2.3.1. The Analytical Method of the Load Transfer. Generally speaking, the applied vertical load is supported by base resistance and side resistance. A number of related tests were conducted by scholars, and the experimental results illustrate that the bearing capacity almost depends on side resistance

for long pile embedded in rock. For simplicity, the base resistance could be neglected in the case of pile embedded in rocky slope.

In this investigation, shear behavior can be distinguished into two periods. As illustrated by Eq. (21), the pile-rock interface would behave plastic when the relative shear displacement $s_{(z)}$ is more than the critical shear displacement Δs_0 . In contrast, the pile-rock interface would be in elastic.

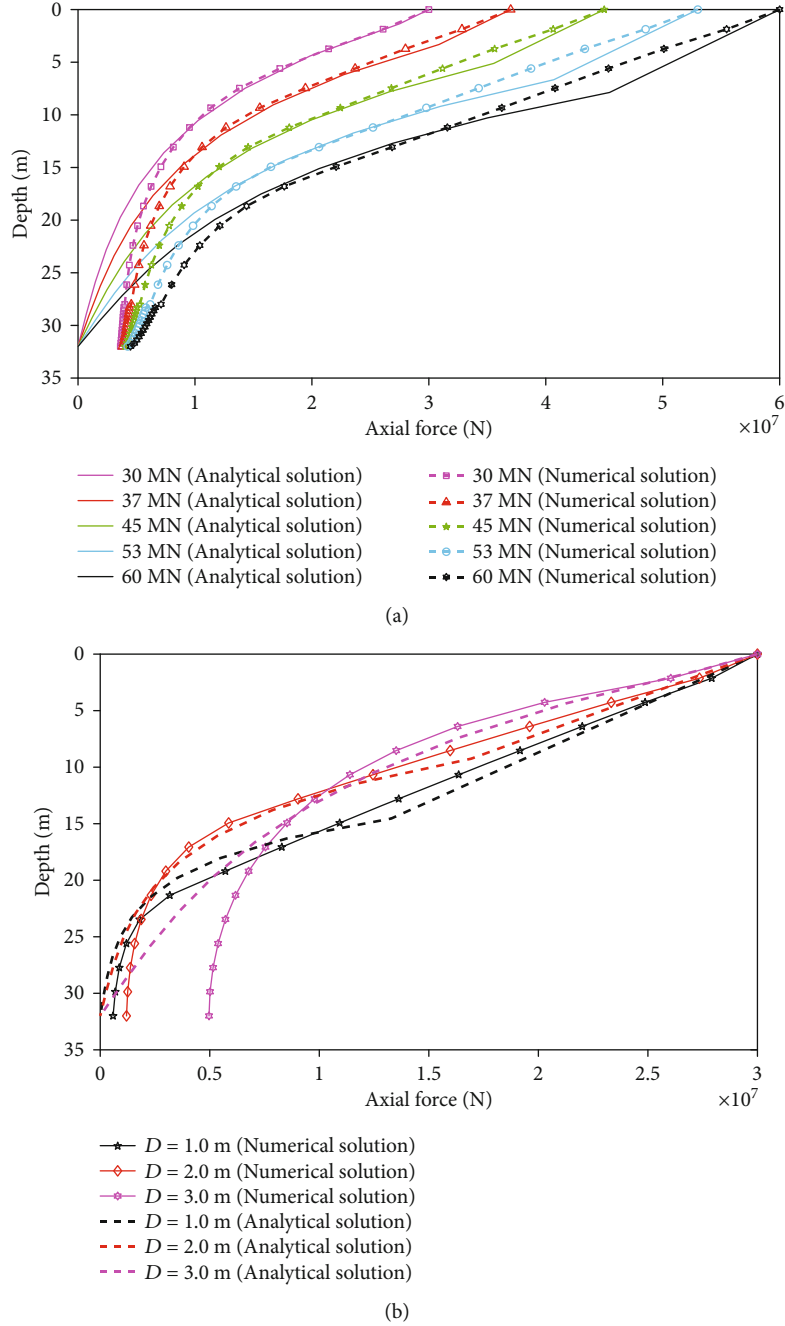


FIGURE 7: Verification in case of slope angle $\alpha = 30^\circ$: (a) the axial force distributions with different vertical load; (b) the axial force distributions in different diameter of pile with 32 MN vertical load.

To depict the distribution of side resistance exactly, the analytical method of the load transfer has been used. It can combine the shear behavior of pile-rock interface with side resistance of pile, and the static equilibrium of unit pile under the vertical load can be expressed as:

$$\frac{d^2 s_{(z)}}{dz^2} = \frac{U}{E_p A_p} \tau_{(z)}, \quad (22)$$

where $s_{(z)}$ is the shear displacement at the depth z , U is the perimeter of pile, E_p is the elastic modulus of the pile, and A_p is the sectional area of the pile.

As illustrated in Figure 5, l_0 is the plastic depth, and l_1 is the elastic depth; s_d is settlement of pile top, and P_d is vertical load of pile top.

2.3.2. Solution of Plastic State. The pile-rock interface would be behave plastic when settlement of pile top s_d is more than

TABLE 2: The basic parameter values for parametric study.

Shaft diameter (D)	0.61 m
Shaft length (L)	6.1 m
Elastic modulus of pile (E_p)	27.6 GPa
Friction angle of interface (φ_b)	30°
Triangular half-chord length (λ)	8 mm
Cohesion of rock (c)	1.2 MPa
Internal friction angle of rock (φ)	24.8°
Elastic modulus of rock (E_r)	232 MPa
Poisson's ratio (ν)	0.3
Dilation angle of rock β	10°

the critical shear displacement Δs_0 . The plastic solution for load transfer could be obtained by Eqs. (21) and (22):

$$\frac{d^2 s_{(z)}}{dz^2} = \frac{U}{E_p A_p} K' \cos((1.654\nu + 0.129)\alpha) \Delta s_0 \tan \beta \tan \varphi_r, \quad (23)$$

so, a general solution is expressed as:

$$s_{(z)} = \frac{UK' \cos((1.654\nu + 0.129)\alpha) \Delta s_0 \tan \beta \tan \varphi_r}{2E_p A_p} z^2 + c_1 z + c_2, \quad (24)$$

where c_1 and c_2 are constants.

The boundary conditions can be expressed as:

$$\begin{cases} s_{(z)} \Big|_{z=0} = s_d, \\ E_p A_p \frac{ds}{dz} \Big|_{z=0} = -P_d. \end{cases} \quad (25)$$

Substitution of Eq. (25) into Eq. (24) produces a solution:

$$\begin{cases} c_1 = \frac{-P_d}{E_p A_p}, \\ c_2 = s_d. \end{cases} \quad (26)$$

The plastic solution of vertical load in the case of pile embedded in rocky slope could be shown as:

$$s_{(z)} = \frac{UK' \cos((1.654\nu + 0.129)\alpha) \Delta s_0 \tan \beta \tan \varphi_r}{2E_p A_p} z^2 + \frac{-P_d}{E_p A_p} z + s_d, \quad (27)$$

$$\tau_{(z)} = K' \cos((1.654\nu + 0.129)\alpha) \Delta s_0 \tan \beta \tan \varphi_r, \quad (28)$$

$$P_{(z)} = P_d - UK' \cos((1.654\nu + 0.129)\alpha) \Delta s_0 \tan \beta \tan \varphi_r z. \quad (29)$$

The pile-rock interface is in conformity with continuity in displacements at the plastic depth l_0 . It could be seen

$$s_{(l_0)} = \Delta s_0. \quad (30)$$

The plastic depth l_0 can be obtained by Eqs. (19), (27), and (30):

$$l_0 = \frac{\sqrt{P_d^2 + 2UK' \cos((1.654\nu + 0.129)\alpha) \Delta s_0 \tan \beta \tan \varphi_r E_p A_p (\Delta s_0 - s_d)} - P_d}{UK' \cos((1.654\nu + 0.129)\alpha) \Delta s_0 \tan \beta \tan \varphi_r}. \quad (31)$$

Substituting Eq. (31) into Eq. (29) produces

$$P_{(l_0)} = P_d - UK' \cos((1.654\nu + 0.129)\alpha) \Delta s_0 \tan \beta \tan \varphi_r l_0. \quad (32)$$

2.3.3. Solution of Elastic State. The pile-rock interface would be in elasticity below the plastic depth. As the previously analysis of shear behavior proposed, the solution of elastic state for load transfer could be obtained by Eqs. (21) and (22):

$$\frac{d^2 s_{(z)}}{dz^2} = \frac{UK' \cos((1.654\nu + 0.129)\alpha) \tan \beta \tan(\varphi_b + \beta)}{E_p A_p} s_{(z)}. \quad (33)$$

According to the statements introduced above, a general solution is expressed as:

$$s_{(z)} = c_3 e^{Rz} + c_4 e^{-Rz}, \quad (34)$$

where R , c_3 , and c_4 are constant.

Substituting Eq. (34) into Eq. (33) produces

$$R = \sqrt{\frac{UK' \cos((1.654\nu + 0.129)\alpha) \tan \beta \tan(\varphi_b + \beta)}{E_p A_p}}. \quad (35)$$

The pile-rock interface is in conformity with continuity in axial force. And it can be expressed as:

$$\begin{cases} E_p A_p \frac{ds}{dz} \Big|_{z=l_0} = -P_{(l_0)}, \\ E_p A_p \frac{ds}{dz} \Big|_{z=l_1} = 0. \end{cases} \quad (36)$$

This leads to

$$s_{(z)} = \frac{P_d l_0 \cosh[R(l_1 - z)]}{RE_p A_p \sinh[R(l_1 - l_0)]}. \quad (37)$$

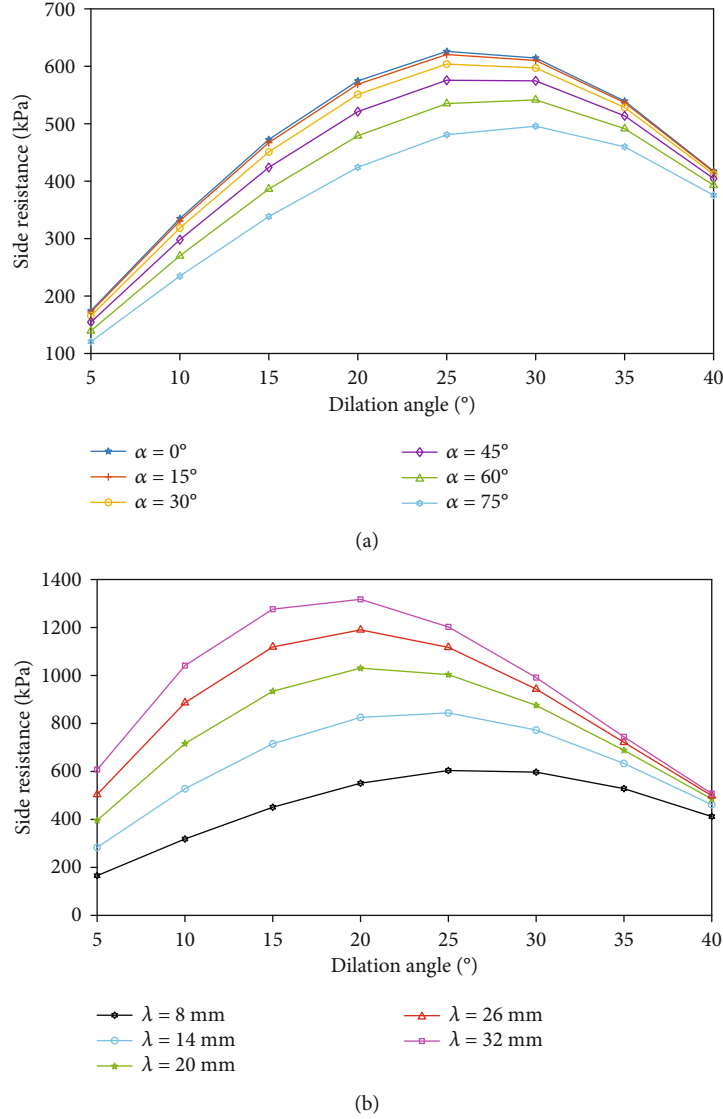


FIGURE 8: The influence of slope angle and interface roughness on residual unit side resistance: (a) the influence of slope angle; (b) the influence of the half-chord length.

The pile-rock interface is in conformity with continuity in displacements at the plastic depth l_0 . It could be seen

$$\Delta s_0 = \frac{P_d l_0 \cosh [R(l_1 - l_0)]}{RE_P A_P \sinh [R(l_1 - l_0)]}. \quad (38)$$

The elastic depth l_1 can be expressed as

$$l_1 = R^{-1} \operatorname{arccoth} \left[\frac{RE_P A_P \Delta s_0}{P_{(l_0)}} \right] + l_0. \quad (39)$$

The elastic solution of vertical load in the case of pile embedded in rocky slope could be shown as:

$$\begin{aligned} \tau_{(z)} &= \frac{RP_{(l_0)} \cosh [R(l_1 - z)]}{U \sinh [R(l_1 - l_0)]}, \\ P_{(z)} &= \frac{P_{(l_0)} \sinh [R(l_1 - z)]}{\sinh [R(l_1 - l_0)]}. \end{aligned} \quad (40)$$

3. Verification and Discussion

The mechanism of vertical load transfer is nonlinear and sophisticated for the pile at the crest of rock slope. It is difficult to study the progress of load transfer by conducting relative tests. To evaluate the accuracy of the new method, this method should be compared with the results of finite element analysis. The model of pile-slope is established with FLAC^{3D}. A pile embedded in the level ground for situ test was reported by Dong P et al. [35]. The basic parameter values of pile and slope for verification are showed in Table 1.

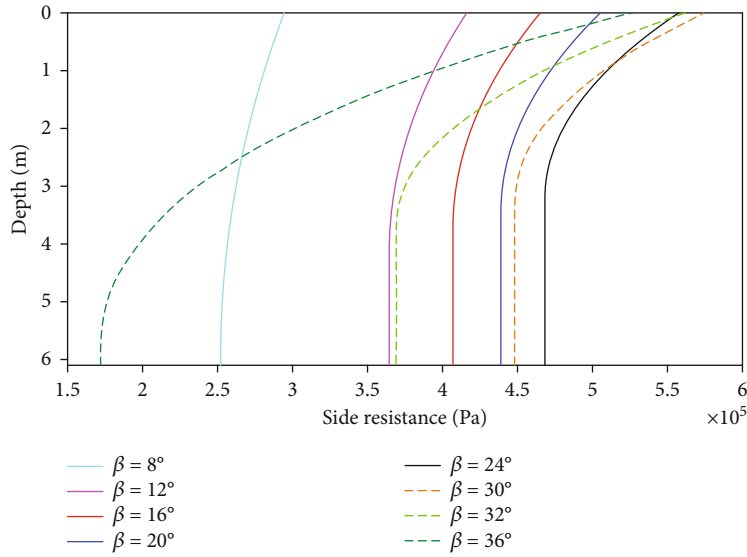


FIGURE 9: The influence of dilation angle on dilation unit side resistance.

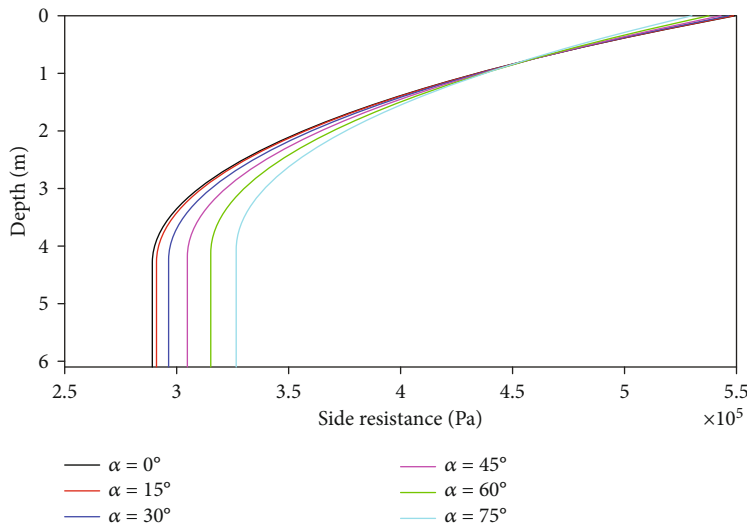


FIGURE 10: The influence of slope angle on dilation unit side resistance.

The reliability of the numerical simulation results should be demonstrated first. In case of slope angle $\alpha = 0^\circ$, the comparison of the results of numerical analysis, field measured results, and predict solution is shown in Figures 6 and 7.

Figure 6(a) illustrates the finite element results and the measured results of axial force distributions in depth with 53 MN vertical load. It is obvious that the regular triangular asperity has been shorn off, and part of the pile-rock interface has been in plasticity with 53 MN vertical load. The field measured result of the plastic depth l_0 is 5 m. By resolving the above equation, the plastic depth l_0 is 5.6 m, which matches closely with the field measured results. The numerical results of axial force distributions match more closely with the field measured results in the upper part of the pile. Figure 6(b) shows that the numerical results and the mea-

sured results of axial force distributions in depth with 32 MN vertical load. The numerical results of axial force distributions match closely with the field measured results. Since the base resistance has been neglected in analytical solution for simplicity, the base axial force of numerical results is larger than analytical results. Numerical simulation is more suitable to the actual working conditions, and the base resistance exists.

For the pile subjected to vertical load at the crest of rock slope, there are few relevant tests. Thus, the numerical method would be used to verify the accuracy of the theory.

In case of slope angle $\alpha = 30^\circ$, the comparison of the results of finite element analysis and predict solution is shown in Figure 7. As illustrated in Figure 7(a), the analytical results of axial force distributions match closely with the

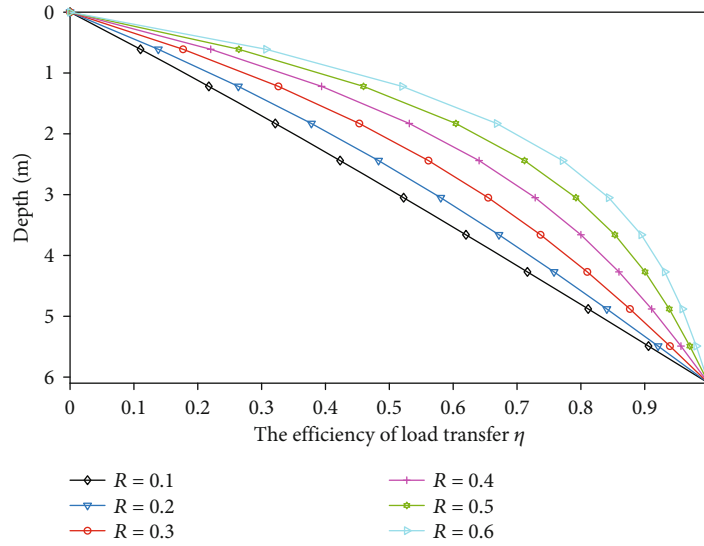


FIGURE 11: The influence of comprehensive parameters of slope-pile R on the efficiency of load transfer η .

numerical results in depth with any load. It is similar to the case of $\alpha = 0^\circ$ that the base axial force of numerical results is larger than analytical results. As explained in the previous section, the base axial force is 0 in analytical results while the base axial force exists in the actual engineering. The pile-rock interface would be in elastic when the vertical load is minimal. It would behave plastic when the vertical load is large enough, and the plastic depth l_0 would be larger with the increase of vertical load.

The highest axial force occurs in the upper part of the pile, which means the highest load transfer in the upper part of the pile correlates with highest values of shear displacements. The reduction of axial force is related to the shear displacement on the pile-rock interface. Figure 7(b) shows that the comparison of the results of finite element analysis and predict solution with different diameter of pile in case of $\alpha = 30^\circ$. It is obvious that the plastic depth l_0 has been larger with the reduction of diameter. And it seems that the higher load transfer in the upper part of the pile is associated with the smaller diameter. In other words, larger diameter piles have higher load carrying capacity.

In summary, the rationality of presented method has been explained by a series of numerical study for load transfer. And the analytical results of axial force distributions have a good match with the numerical results within the reasonable error range.

4. Parametric Study

There are many related parameters that affect the distribution of side resistance and axial force, especially for the vertical loaded pile at the crest of rock slope. Many scholars have focused on the issue of load transfer for pile at the level ground, and some conclusions are drawn. The effect of slope on the distribution of side resistance is an emphasis in this study. Therefore, a series of parametric analysis were conducted to further describe the presented method. The para-

metric study is investigated with the different parameters reported by O'Neill, as shown in Table 2.

4.1. Residual Period. The side resistance in plastic depth is constant, and it depends on the residual parameters and interface roughness. Figure 8 shows the effect of slope angle and roughness parameters on side resistance of residual periods in condition with 1296 kN vertical load. The values of half-chord length, dilation angle, and slope angle are varied from 8 mm to 32 mm, 5° to 40° , and 0° to 75° .

Figure 8(a) shows a tendency that the side resistance of residual periods decreases with the raised slope angle. At the same time, the higher slope angle, the greater reduction of the side resistance. This is because the larger slope angle, the smaller the normal constraint of pile. Figure 8(b) illustrates that the side resistance of residual periods increases and then decreases with the increase of dilation angle. It means that the simple increase of the dilation angle cannot enhance the side resistance; this may be caused by the quicker reduction of the contact area with the higher dilation angle. And it is obvious that the half-chord length is positively correlated with the side resistance.

4.2. Dilation Period. The value of side resistance in elastic depth is mobile on the method proposed previously, and the elastic depth is not immobile under different working conditions. As to the vertically loaded pile in dilation period, it is more difficult to describe the distribution of side resistance.

Figure 9 shows the effect of dilation angle on side resistance of dilation periods in condition of 4000 kN vertical load and 0.8 m diameter of pile. With the increase of dilation angle, the side resistance of dilation period increases initially and then decreases. This is similar to the behavior of residual period. As indicated previously, the smaller the dilation angle, the more uniform the distribution of side resistance. The values of dilation angle are varied from 8° to 36° .

Figure 10 illustrates the effect of slope angle on side resistance of dilation periods. The values of slope angle are varied from 0° to 75° . The smaller the slope angle, the more concentrated the distribution of pile lateral friction at the top of the pile, the greater the decreasing rate of the side resistance, and the deeper the plastic depth. This may be caused by the normal constraint of pile is small when the slope angle is large. As a result, the slope angle would give engineers a guidance to optimize designs.

To further study the load transfer, the term of “efficiency of load transfer η ” is referred in this paper. It can be expressed as $\eta = 1 - P_{(z)}/P_d$. According to the previous analysis of load transfer, R is a comprehensive parameter of slope pile. And it is a macroscopic composite index reflecting the bearing performance of pile embedded in the crest of the slope. Figure 11 illustrates the effect of comprehensive parameters of slope-pile R on the efficiency of load transfer η , and the values of R are varied from 0.1 to 0.6. The greater the R value, the greater the η value, and the upper pile bears more load. Therefore, the smaller the load ultimately transferred to the pile tip, the weaker the bearing capacity of the slope pile. As a result, the smaller R is beneficial to enhance the bearing capacity of piles.

5. Conclusion

In order to obtain the response of drilled pile under vertical load at the crest of rock slope. Efforts have been made in this paper to analysis the effect of slope on the normal stiffness of socket wall. The following conclusions can be drawn:

- (a) A modified model of normal stiffness of socket wall affected by the slope is obtained; the effect of slope angle and Poisson’s ratio on the reduce factor of normal stiffness of pile was proposed
- (b) Analyze the shear behaviors of the pile-rock interface, an analytical solution of load transfer of pile at the crest of rock slope is obtained. The response of the drilled pile at the crest of rock slope was obtained from the closed-form solution
- (c) The results of the new method were compared with the results of Flac^{3D}, which shows remarkable agreement
- (d) The simple increase of the dilation angle cannot enhance the side resistance, and the half-chord length is positively correlated with the side resistance
- (e) The side resistance of residual periods decreases with the raised slope angle, and the slope is a disadvantage for engineering. And the smaller comprehensive parameter of slope pile is beneficial to enhance the bearing capacity of piles

Data Availability

The data used to support the findings of this study are available from the corresponding author upon request.

Conflicts of Interest

The authors declare that there are no conflicts of interest regarding the publication of this paper.

Acknowledgments

This work is supported by the National Natural Science Foundation of China (Grant Nos. 51978665 and 51678570) and the Focus on research and development plan of Hunan province (No. 2015SK2053).

References

- [1] C. Jiang, W. Y. Wu, J. L. He, and L. J. Chen, “Computation method for the settlement of a vertically loaded pile in sloping ground,” *Advances in Civil Engineering*, vol. 2020, 10 pages, 2020.
- [2] C. Jiang, Z. Zhang, and J. L. He, “Nonlinear analysis of combined loaded rigid piles in cohesionless soil slope,” *Computers and Geotechnics*, vol. 117, p. 103225, 2020.
- [3] M. W. O’Neill, K. M. Hassan, and F. C. Townsend, “Load transfer for drilled shafts in intermediate geomaterials,” *FHWA-RD-95-172, Federal Highway Administration*, 1996McLean, VA, 1996.
- [4] M. Sahara, N. Akino, and K. Tominaga, “Experimental results and elasto-plastic analysis of the vertical behavior of a single model pile,” *Journal of Asian Architecture and Building Engineering*, vol. 1, no. 1, pp. 65–73, 2002.
- [5] J. H. Chung, J. Ko, H. Klammler, M. C. McVay, and P. Lai, “A numerical and experimental study of bearing stiffness of drilled shafts socketed in heterogeneous rock,” *Computers and Structures*, vol. 90-91, pp. 145–152, 2012.
- [6] Y. Wang, Y. F. Yi, C. H. Li, and J. Q. Han, “Anisotropic fracture and energy characteristics of a Tibet marble exposed to multi-level constant-amplitude (MLCA) cyclic loads: a lab-scale testing,” *Engineering Fracture Mechanics*, vol. 244, p. 107550, 2021.
- [7] Z. Y. Song, Y. Wang, H. Konietzky, and X. Cai, “Mechanical behavior of marble exposed to freeze-thaw-fatigue loading,” *International Journal of Rock Mechanics and Mining Sciences*, vol. 138, article 104648, 2021.
- [8] R. Oliver, “Numerical study of the bearing behavior of piled rafts,” *International Journal of Geomechanics*, vol. 4, no. 2, pp. 59–68, 2004.
- [9] R. C. Liu, B. S. Xu, B. Li, and Y. J. Jiang, “3-D numerical study of mechanical behaviors of pile-anchor system,” *Applied Mechanics and Materials*, vol. 580-583, pp. 238–242, 2014.
- [10] H. B. Seed and L. C. Reese, “The action of soft clay along friction piles,” *Transactions of the American Society of Civil Engineers*, vol. 122, no. 1, pp. 731–754, 1957.
- [11] E. D’Appolonia and J. P. Romualdi, “Load transfer in end-bearing steel H-piles,” *Journal of the Soil Mechanics and Foundations Division*, vol. 89, no. 2, pp. 1–25, 1963.
- [12] H. M. Coyle and L. C. Reese, “Load transfer for axially loaded piles in clay,” *Journal of the Soil Mechanics and Foundations Division*, vol. 92, no. 2, pp. 1–26, 1966.
- [13] J. P. Carter and F. H. Kulhawy, “Analysis and design of drilled shaft foundations socketed into rock,” EPRI EL-5918, Ithaca, New York, 1988.

- [14] R. Radhakrishnan and C. F. Leung, "Load transfer behavior of rock-socketed piles," *Journal of Geotechnical Engineering*, vol. 115, no. 6, pp. 755–768, 1989.
- [15] K. M. Hassan and M. W. O'Neill, "Side load-transfer mechanisms in drilled shafts in soft argillaceous rock," *Journal of Geotechnical Engineering*, vol. 123, no. 2, pp. 145–152, 1997.
- [16] L. Zhang and H. H. Einstein, "End bearing capacity of drilled shafts in rock," *Journal of Geotechnical and Geoenvironmental Engineering*, vol. 124, no. 7, pp. 574–584, 1998.
- [17] P. J. N. Pells, "State of practice for the design of socketed piles in rock," in *Proceedings of the Eighth Australia New Zealand conference on geomechanics*. Australian Geomechanics Society, pp. 307–327, Barton, ACT, 1999.
- [18] C. Zhan and J. Yin, "Field static load tests on drilled shaft founded on or socketed into rock," *Canadian Geotechnical Journal*, vol. 37, no. 6, pp. 1283–1294, 2000.
- [19] C. W. W. Ng, T. L. Y. Yau, J. H. M. Li, and W. H. Tang, "Side resistance of large diameter bored piles socketed into decomposed rocks," *Journal of Geotechnical and Geoenvironmental Engineering*, vol. 127, no. 8, pp. 642–657, 2001.
- [20] K. Georgiadis, M. Georgiadis, and C. Anagnostopoulos, "Lateral bearing capacity of rigid piles near clay slopes," *Soils and Foundations*, vol. 53, no. 1, pp. 144–154, 2013.
- [21] Q. Q. Zhang, R. F. Feng, Y. L. Yu, S. W. Liu, and J. G. Qian, "Simplified approach for prediction of nonlinear response of bored pile embedded in sand," *Soils and Foundations*, vol. 59, no. 5, pp. 1562–1578, 2019.
- [22] B. Ma, Z. Hu, Z. Li et al., "A three-section-settlement calculation method for composite foundation reinforced by geogrid-encased stone columns," *Advances in Civil Engineering*, vol. 2021, 10 pages, 2021.
- [23] B. Ma, Z. Li, K. Cai et al., "An improved nonlinear settlement calculation method for soft clay considering structural characteristics," *Geofluids*, vol. 2021, 7 pages, 2021.
- [24] M. Jesmani, A. Kasrania, and M. Kamalzare, "Finite element modelling of undrained vertical bearing capacity of piles adjacent to different types of clayey slopes," *International Journal of Geotechnical Engineering*, vol. 12, no. 2, pp. 147–154, 2018.
- [25] I. W. Johnston and T. S. K. Lam, "Shear behavior of regular triangular concrete/rock joints-analysis," *Journal of Geotechnical and Geoenvironmental Engineering*, vol. 115, no. 5, pp. 711–727, 1989.
- [26] J. P. Seidel and C. M. Haberfield, "Towards an understanding of joint roughness," *Rock Mechanics and Rock Engineering*, vol. 28, no. 2, pp. 69–92, 1995.
- [27] X. F. Gu, *Shear Behaviour of Sandstone-Concrete Joints and Pile Shafts in Sandstone*, [Ph.D. thesis], Department of Civil Engineering, Monash University Australia, 2001.
- [28] L. David Suits, T. C. Sheahan, J. P. Seidel, and C. M. Haberfield, "Laboratory testing of concrete-rock joints in constant normal stiffness direct shear," *Geotechnical Testing Journal*, vol. 25, no. 4, article 10416, 2002.
- [29] B. M. Basha and G. L. S. Babu, "Seismic rotational displacements of gravity walls by pseudodynamic method with curved rupture surface," *International Journal of Geotechnical Engineering*, vol. 10, no. 3, pp. 93–105, 2010.
- [30] M. H. Zhao, Y. Lei, and X. M. Liu, "Analysis of load transfer of rock-socketed piles based on characteristics of pile-rock structural plane," *Chinese Journal of Rock Mechanics and Engineering*, vol. 28, no. 1, pp. 103–110, 2009, [in Chinese].
- [31] H. F. Xing, M. H. Meng, and W. Y. He, "Analysis of the distribution of side friction resistance of rock-socketed piles based on the mechanical characteristics of structural surfaces," *Chinese Journal of Geotechnical Engineering*, vol. 12, pp. 2220–2227, 2012.
- [32] H. Zhao, Y. Xiao, M. Zhao, and P. Yin, "On behavior of load transfer for drilled shafts embedded in weak rocks," *Computers and Geotechnics*, vol. 85, pp. 177–185, 2017.
- [33] S. Y. Liu, J. Peng, and W. Jie, "Load transfer behavior of large diameter cast-in-place pile embedded in soft rock," *Chinese Journal of Geotechnical Engineering*, vol. 20, no. 4, pp. 58–61, 1998, [in Chinese].
- [34] F. D. Patton, "Multiple modes of shear failure in rock," in *Proceeding of the 1st Congress of International Society of Rock Mechanics*, Lisbon, Portugal, 1966.
- [35] P. Dong, "Bearing behavior of large-diameter rock-socket piles," *Chinese Journal of Rock Mechanics and Engineering*, vol. 22, no. 12, pp. 2099–2103, 2003, [in Chinese].

Research Article

Grouting Reinforcement Mechanism and Multimodel Simulation Analysis of Longwall Goaf

Xueliang Li ^{1,2}, Xiaoli Guo,^{2,3} and Guang Sun¹

¹China Coal Science and Technology Ecological Environment Technology Co., Ltd., Beijing 100013, China

²China Coal Research Institute, Beijing 100013, China

³CCTEG Beijing Research Institute of Land Renovation and Ecological Restoration Technology Co., Ltd., Beijing 100013, China

Correspondence should be addressed to Xueliang Li; cls9350@163.com

Received 31 March 2021; Accepted 5 May 2021; Published 24 May 2021

Academic Editor: Zhengyang Song

Copyright © 2021 Xueliang Li et al. This is an open access article distributed under the Creative Commons Attribution License, which permits unrestricted use, distribution, and reproduction in any medium, provided the original work is properly cited.

Grouting reinforcement is one of the most effective methods to enhance the stability of the goaf, and its scheme selection, hole location, and parameter determination directly affect the success or failure of goaf treatment. On the basis of discussion of the deformation mechanism and evolution law of the longwall goaf, this article comprehensively analyzed the grouting reinforcement mechanism of the goaf combined with filling theory, permeability theory, and fracturing theory and studied the physical and chemical reaction principles of two commonly used filling materials, cement-fly ash slurry and cement-clay slurry. Three grouting models have been established: whole grouting, local grouting in fracture zone, and strip grouting, and then simulated the grouting effect of the two more common methods of whole grouting and strip grouting by numerical simulation software (FLAC3D, tecplot, Surfer). Simulation analysis is carried out from the perspectives of settlement deformation, horizontal movement, vertical stress, and horizontal stress. Finally, the feasibility of grouting treatment in the goaf is verified by engineering example. The results show that a reasonable grouting scheme can effectively reduce the residual deformation of the goaf and its overlying rock and improve the poor stress state, so as to achieve the purpose of effective grouting.

1. Introduction

In recent years, construction land has gradually become a scarce resource in mining cities and their surrounding areas with the continuous acceleration of urbanization; sometimes, the land above the goaf has to be used to meet construction needs. However, the risk of secondary activation exists in the goaf because of its complex structure and susceptibility to groundwater, earthquake, external loads, and other factors; its stability degree directly restricts the size, volume, and safety of the proposed building [1–3]. In order to ensure safety, appropriate treatment measures must be taken as needed under the premise of scientific demonstration. At present, direct grouting in the goaf is one of the more widely used methods.

The grouting technology in developed industrial countries such as Britain, France, and America started relatively early, and the theoretical research and engineering practice have never stopped. The grouting technology has a wide range of applications in these countries. It has expanded from

simple foundation reinforcement and water plugging penetration in mines to hydraulic engineering, bridge and airport construction, and other fields. On the basis of the existing results, scholars have further applied grouting technology in the field of coal mine goaf management. Based on the analysis of the mechanism of residual settlement in the old goaf and the theory of mining subsidence, Deng et al. [4] studied the technical method of grouting and filling to control residual settlement in the old goaf. Xuan et al. [5] proposed a technical scheme for grouting and filling of old goafs to control dynamic disasters under huge thick igneous rocks and achieved good results. Pang et al. [6] explored a new way of alkali slag utilization for the grouting material of an alkali slag-fly ash system filled in the goaf. Wang et al. [7] established Bingham fluid constitutive model equations and performed a three-dimensional Bingham fluid turbulence simulation in the goaf of the South-to-North Water Transfer Project. In order to solve the problem that the goaf along the railway seriously threatens the safety of railway transportation, Li et al. [8]

carried out the experimental research on different grouting material ratios and determined the reasonable grouting material and slurry ratio. Lu et al. [9] established the relationship between the residual movement angle, the mining depth, and the equivalent mining thickness of the old goaf and proposed the determination method of the filling and grouting range in the old goaf. Yongliang et al. [10] carried out effective detection and evaluation of the grouting effect of a large and complex goaf combined with examples of goaf grouting engineering.

The grouting technology in the goaf is a concealed project, but there is no mature theoretical basis and technical support in the scientific community. Researchers still lack deep understanding of the mechanism of interaction between the grout and fractured rock mass in the goaf, the characteristics of grout migration, and the effect of grouting reinforcement. Based on the mechanism analysis, this study analyzed the grouting effect of different grouting models by means of numerical simulation.

2. Deformation Mechanism and Evolution Law of Longwall Goaf

2.1. Geological Mining Model of Goaf. The existing goafs are mainly those left by longwall collapse mining in China, and the existing mining methods of major production mines are also mainly longwall mining. After longwall continuous regular mining, the overlying rock has formed a caving zone, fracture band, and bending zone (Figure 1). Most of the rock mass structure in the caving zone is loose structure and fragmented structure, with a large residual swelling coefficient and void ratio. The above three moving belts behave obviously in horizontal mining or in gently inclined coal seams. Depending on different roof management methods, goaf size, mining thickness, rock properties, and mining depth, they may not exist simultaneously.

The cavities, separations, and cracks formed in the overlying rock after mining reach a certain compaction and stable state after a long period of physical and mechanical processes. However, the above weak structures cannot be completely eliminated, but they are in a relatively stable state. Instability and deformation will occur when the external force is greater than its resistance [11, 12]; the goaf is filled with broken rocks, gangue, crushed coal, and waste wood after mining. The mechanical properties of different filling materials are quite different, and the overall stability is poor; there are inevitable pores between the fillings, the middle part of the goaf has better compaction, and there may be larger cavities at both ends, especially the side close to the coal wall. Under the action of water erosion and weathering, the ability of the overall structure to resist external stress decreases.

In addition to the recompaction of residual cracks, the instability of the masonry rock beam structure, and the influence of the geological structure, the activation of the longwall goaf has obvious correlation with mining method, goaf size, and mining depth-thickness ratio. Whether there is a risk of activation in the goaf should be fully considered.

Most goafs are located in a complex geological environment, which determines the diversity of engineering geological conditions. Different types of goafs have different

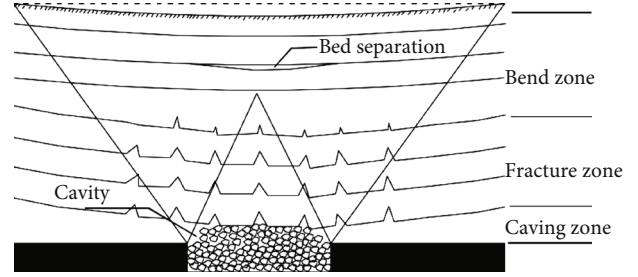


FIGURE 1: Damaged structure model of the overlying rock in the old goaf of the long wall.

engineering geological models. When dividing the engineering geological model of goaf, it is necessary to consider various factors such as mining method and roof management method, topography, geological structure, and final mining time [13–15]; each factor is very important to the stability of goaf. Combining different geological mining conditions and considering the above factors, the engineering geological model can be divided into the following types (Table 1).

From the perspective of engineering construction, the geological condition of stable goafs is relatively simple, the mining area is generally large, and surface movement and deformation are continuous and regular with little residual deformation and little impact on buildings; basically, a stable goaf has a short mining time, and the surface movement has not stabilized, which has a greater impact on ground buildings; an unstable goaf is prone to discontinuous ground deformation, which may have a serious negative impact on ground buildings. Measures such as filling old goafs and controlling ground collapse pits and cracks must be adopted.

2.2. Development Law of Residual Cavities in Goaf. Effective grouting reinforcement for the above-mentioned cavities, separation layers, and cracks is the key to successful grouting. It is very important to accurately grasp the location and size of the space, which can be comprehensively determined by combining geophysical and drilling. Theoretically, after the overlying rock strata breaks and collapses and fills the goaf, the uncracked rock strata will bend and sink [16–18]. The effective height of cavities and fissures in the goaf can be regarded as minus the mining thickness. The amount of subsidence and swelling of the collapsed rock mass

$$m(x) = m - W(x) - h_p(x), \quad (1)$$

where $m(x)$ is the total effective height of the cavity (m), m is the mining thickness (m), $W(x)$ is the subsidence of the overlying rock (m), and $h_p(x)$ is the breaking expansion of the collapsed rock mass (m).

Take the goaf formed by the horizontal coal seam mining where the collapsed rock mass is not full of goaf as an example (Figure 2). Assuming that the elastic foundation supporting the rock beam conforms to the Winkler foundation assumption, the vertical force R in the foundation is

$$R = ky, \quad (2)$$

TABLE 1: Classification table of geological mining model of goaf.

Model type	Mode of action	Specific conditions
Stable	Mainly for mining function, longwall mining; reaching or close to full mining, caving method to manage the roof; more than 3 years from the final mining time	(1) Depth-thickness ratio ≥ 30 ; (2) topography and stratum are close to level; (3) there are no faults or penetrating fissures within the range of mining influence; (4) thickness of loose ground layer > 10 m; (5) ground construction load does not affect the old goaf area
Basically stable	Mainly for mining, longwall mining; reaching or close to full mining, caving method to manage the roof; 1 to 3 years from the final mining time	(1) Depth-thickness ratio ≥ 30 ; (2) terrain level and shallow hills; (3) stratum dip $\leq 45^\circ$; (4) no faults or perforated fissures within the range of mining influence; (5) thickness of loose strata > 10 m; (6) the ground construction load has a certain influence on the old goaf
Unstable	Mainly mining, underground mining leads to fault slip and mountain slip; large deformed voids remain, which may cause discontinuous deformation of the ground; within 1 year from the final mining time	(1) Longwall caving method mining with depth to thickness ratio < 30 ; (2) pillar mining; (3) stratum dip $> 45^\circ$; (4) the ground is mountainous; (5) the strata contains quicksand layers; (6) the strata is loose and the thickness of the layer is less than 10 m; (7) the fault dip $\delta > 30^\circ$ and the mining area $S > 2000$ m ² ; (8) the ground construction load has a large impact on the old goaf

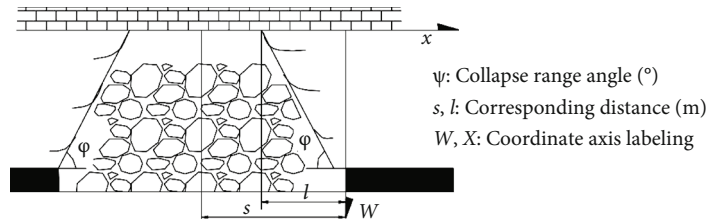


FIGURE 2: Rock mass model of collapsed rock mass not filled with goaf in horizontal coal seam mining.

where k is the Winkler foundation coefficient, which is related to the thickness of the foundation under the beam (h) and the elastic modulus (E) of the overlying rock mass. $k = \sqrt{E/h}$.

Taking the boundary of the goaf as the origin of the abscissa, the differential equation of the deflection curve of the beam can be obtained from the balance principle as

$$\begin{cases} E_1 I_1 y''' = q_1, & (-l \leq x \leq 0), (-l \leq x \leq 0) \\ E_1 I_1 y''' = q_1 - ky, & (0 \leq x \leq \infty), (0 \leq x \leq \infty) \end{cases} \quad (3)$$

where: q_1 is the distributed load concentration degree, $q_1 = E_1 h_1^3 \sum_{i=1}^n \gamma_i h_i / \sum_{i=1}^n E_i h_i^3$.

From the above formula and substituting the relevant boundary and continuity conditions, we can get

$$W(x) = \begin{cases} \frac{q_1}{E_1 I_1} \left[\frac{1}{24} x^4 + \frac{1}{6} s x^3 + \frac{1}{4} s^2 (1 - 2\alpha) x^2 + \frac{1}{6} s^3 (1 - 6\alpha) x + \left(\frac{\sqrt{2}}{\omega s} + \frac{1}{2} - \alpha \right) \frac{s^2}{\omega^2} \right], & -s < x < 0, \\ \frac{q_1 s^2}{E_1 I_1 \omega^2} e^{-(\omega/\sqrt{2})x} \left[\left(\frac{\sqrt{2}}{\omega s} + \frac{1}{2} - \alpha \right) \cos \frac{\omega}{\sqrt{2}} x + \left(\alpha - \frac{1}{2} \right) \sin \frac{\omega}{\sqrt{2}} x \right], & 0 < x < \infty, \end{cases} \quad (4)$$

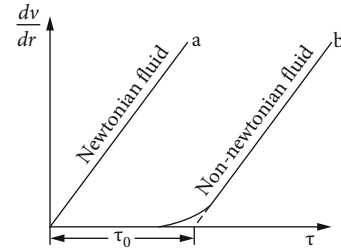


FIGURE 3: Rheological curve of grout.

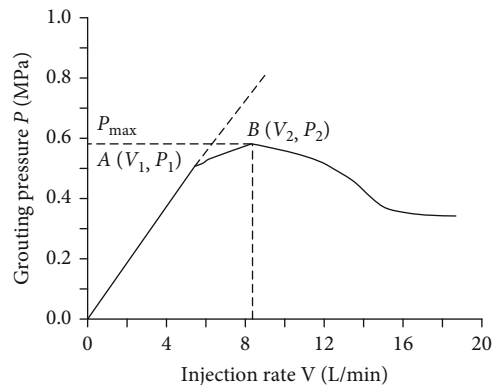
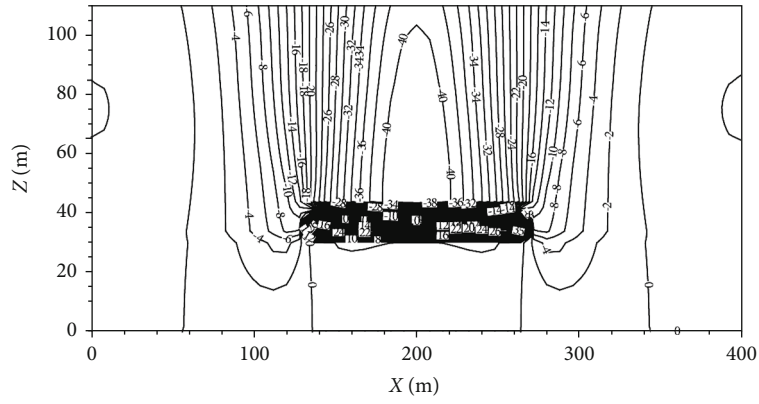
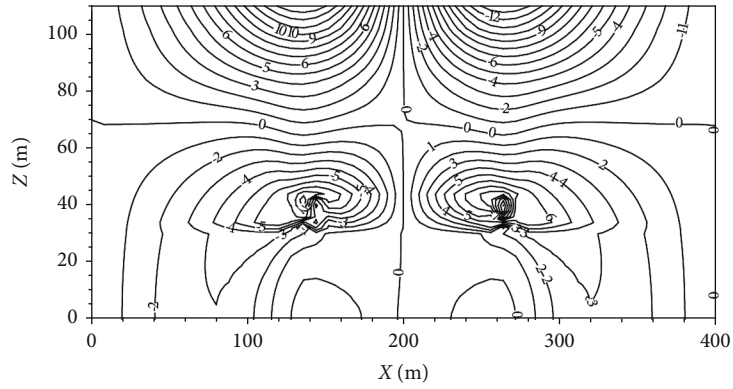


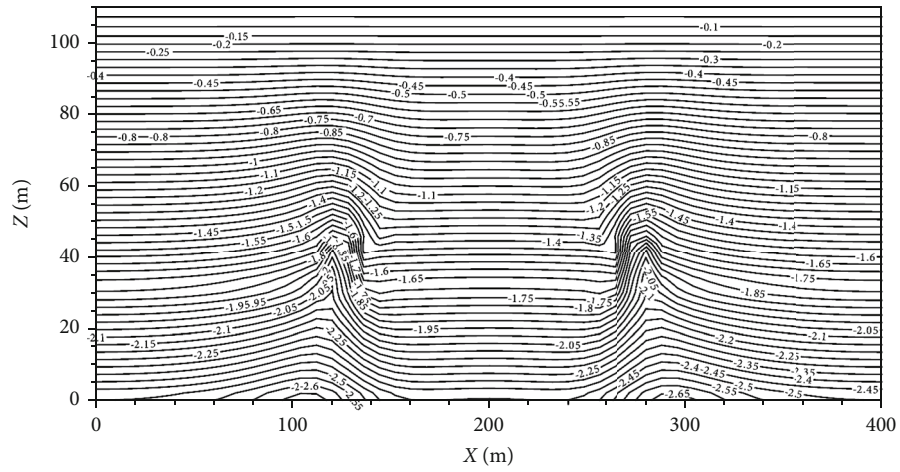
FIGURE 4: Relationship between grouting pressure and grouting speed.



(a) Settlement deformation when the goaf is untreated (mm)

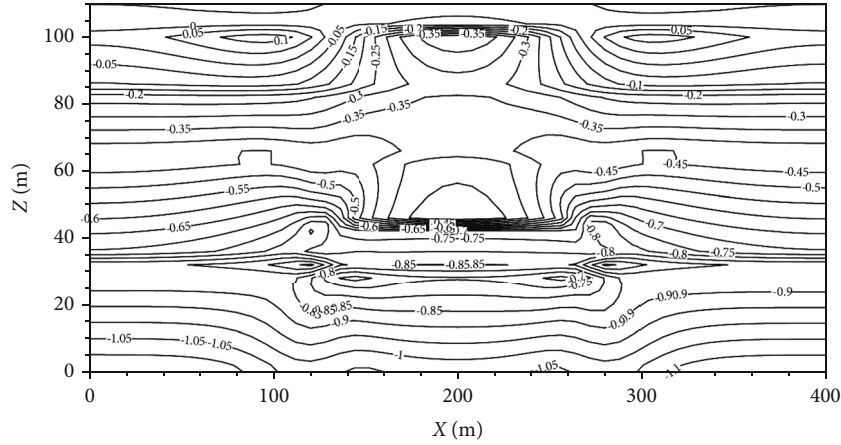


(b) Horizontal displacement change when the goaf is untreated (mm)



(c) The vertical stress when the goaf is untreated (MPa)

FIGURE 5: Continued.



(d) The horizontal stress when the goaf is untreated (MPa)

FIGURE 5: Displacement stress distribution diagram of goaf without grouting.

where $\omega = \sqrt[4]{k/E_1 I_1}$ and $\alpha = (\sqrt{2}\omega^2 s^2 + 6\omega s + 6\sqrt{2})/6\omega s (2 + \sqrt{2}\omega s)$.

The total height of old goaf voids formed by horizontal coal seam mining can be obtained from the above formulas as follows:

$$m(x) = \begin{cases} m - W(x) + (k - 1)x \tan \phi, & -l < x < 0, \\ m - W(x) - (k - 1)l \tan \phi, & -s < x < -l. \end{cases} \quad (5)$$

It can be seen from the above that the goaf cavity is the largest around the goaf and gradually decreases toward the center, and the mined-out area at the center is the smallest. The largest near the coal pillar, the height of the cavity gradually decreases with the distance from the coal pillar.

3. Mechanism of Grouting Reinforcement in Goaf

3.1. Analysis of Grouting Suitability. The ‘‘Code for Design of Coal Mine Building Structures’’ stipulates that it is advisable to use full filling grouting methods for goaf, collapsed area, and mining separation area with large coal mining scale and buried depth of less than 250 m, and according to its mining characteristics, hydrogeology, engineering geological conditions, and its degree of harm to the project, etc., it is necessary to adopt partial filling or full filling grouting schemes for goaf with a buried depth of more than 250 m.

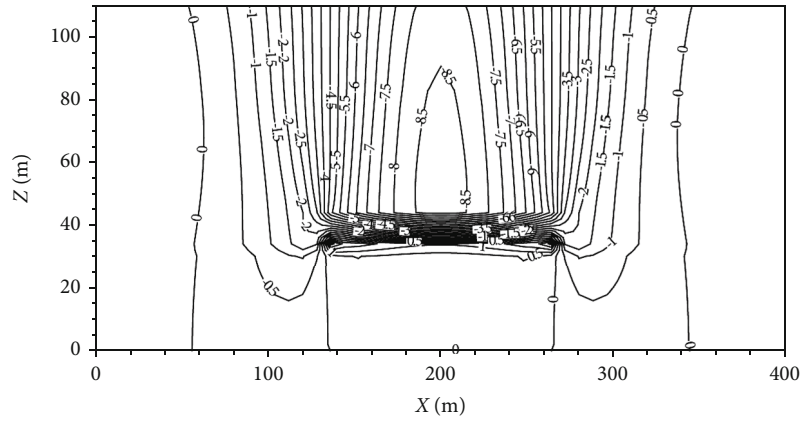
In actual design work, the influencing depth relationship between the falling crack zone and the building load is usually used to determine whether the goaf needs to be treated [19, 20]. When there is a certain distance or just contact between the impact depth of the building load and the top interface of the collapsed fissure zone, the stability of the collapsed fissure zone will not be affected. It is not necessary to treat goaf, but only to take antideformation measures for the surface buildings or to carry out conservative treatment (local grouting reinforcement) according to the importance of the buildings; when the depth of the building load affects the collapsed fissure zone, it will affect the stability of the

collapsed fissure zone, and it must be carried out on the surface of the building. While antideformation is designed, the mined-out area is grouted and reinforced to completely eliminate potential safety hazards.

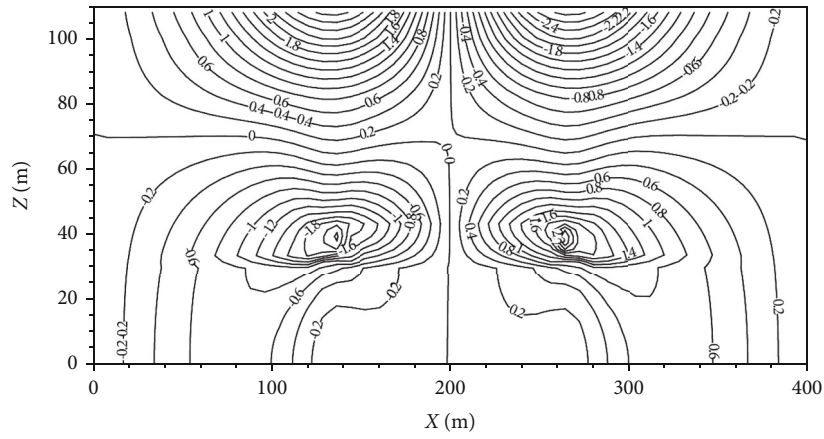
3.2. Theoretical Analysis of Grouting in Goaf. The purpose of grouting and filling is to make the grout reach the voids, separations, cracks, etc. of the mined-out area and its overlying rock and cement it as a whole [21–23]. The mechanical angle plays a supporting role and improves the self-strength and self-supporting ability of the mined-out area and its overlying rock; the structural angle ensures the stability of the original rock mass structure and avoids sudden instability of the surrounding rock structure system; the pressure angle is slow. The pressure relief allows the surrounding rock to slowly release the pressure, exerting pressure on the surrounding rock, and playing a flexible supporting role for the surrounding rock.

3.2.1. Penetration Theory. The slurry fills the residual space in the goaf under the action of pressure. Through physical and chemical reactions, the slurry forms stones with a certain strength and low water permeability in the pores and cracks, which play a role of reinforcement and antiseepage. At the permeation grouting angle in the goaf, the grout mainly acts on the water-conducting fracture zone and is used for the reinforcement of rock fissures, interrock fissures, and collapsed zone deposits. The grout can be divided into Newtonian fluid and non-Newtonian fluid according to the principle of rheology. The filling material used in the process of grouting treatment in the goaf usually belongs to the Bingham fluid in the non-Newtonian fluid, and its shear rate is not proportional to the shear stress. And only when the yield stress is exceeded can the slurry begin to flow [24–26] (Figure 3).

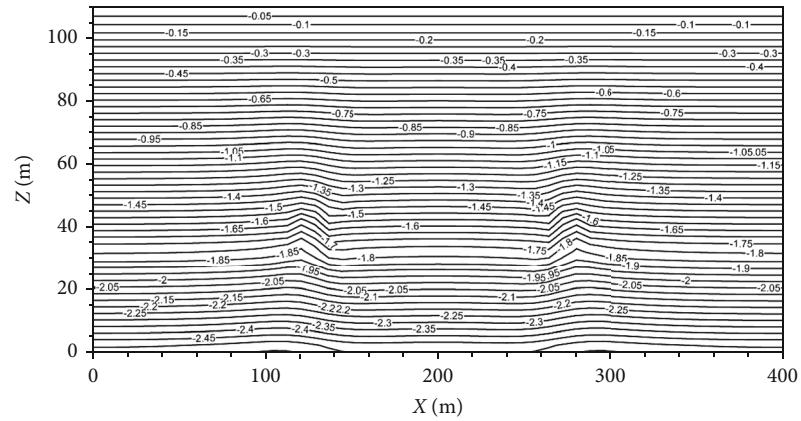
3.2.2. Split Theory. For the angle of splitting grouting in the mined-out area, the main reinforcement objects are bedrock, residual coal pillars, and residual roadway surrounding rocks. When splitting and grouting the bedrock, the existing



(a) Settlement deformation during full grouting in the goaf (mm)

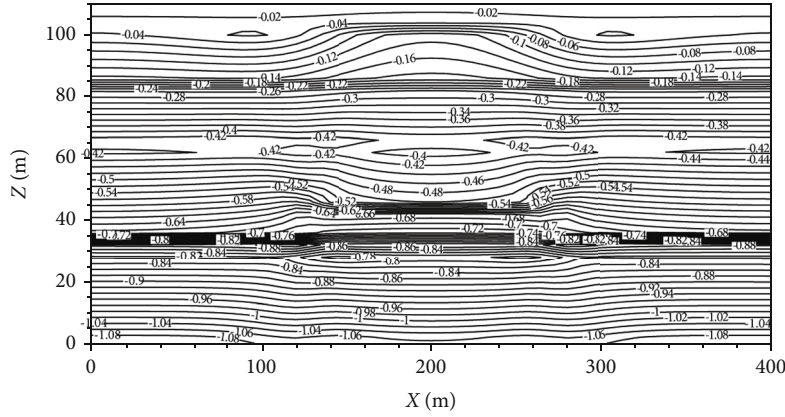


(b) Horizontal displacement change during full grouting in the goaf (mm)



(c) Vertical stress during full grouting in the goaf (MPa)

FIGURE 6: Continued.

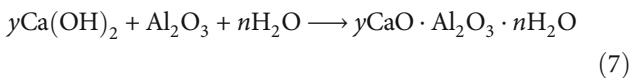
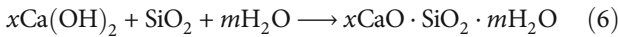


(d) Horizontal stress during full grouting in the goaf (MPa)

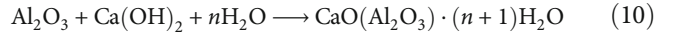
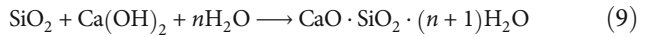
FIGURE 6: Displacement stress distribution diagram during full grouting in the goaf.

grouting technology has difficulty in splitting the fresh rock. When splitting the rock formation, the grout often enters the weak zone of the rock formation under pressure to cause splitting. The weak zone is mainly composed of joints and fissures, weak mud, and strong weathered layers [27–29]. On the contrary, when splitting and grouting the coal pillars and the surrounding rock of the remaining roadway, because the coal pillar itself has a low tensile strength, its ability to resist external mechanical action is low, and it is easy to produce a split surface, and the remaining roadway surrounding the rock in splitting surfaces can also be produced on the periphery. To realize split grouting, grouting pressure and grouting speed need to meet certain conditions. The relationship between grouting pressure and grouting speed during grouting is shown in Figure 4.

3.3. Analysis of Grout Reinforcement Mechanism. Fly ash is alkaline, mainly composed of SiO_2 and Al_2O_3 , and contains a small amount of Fe_2O_3 , CaO , Na_2O , K_2O , SiO_3 , etc. The density of fly ash is generally $2.0\sim 2.5\text{ g/cm}^3$, and the particle size is $0.5\sim 300\ \mu\text{m}$. The grouting reinforcement mechanism is chemically realized through the hydrolysis and hydration reaction of cement and the pozzolanic reaction of fly ash. Through this series of reactions, the slurry forms a continuous stone body with a certain strength and rigidity, thereby achieving the purpose of filling the cavities, separations, and cracks in the goaf. The chemical reaction formula involved is as follows:



When cement-clay slurry is used as the filling material, the clay itself undergoes a hydrolysis and ionization reaction before adding cement at the initial stage to form a certain activity and negatively charged clay particles. After adding cement, a series of reactions such as charge exchange and crystallization reaction occur and finally form a gel structure with a certain strength framework. The specific chemical reactions involved are as follows:

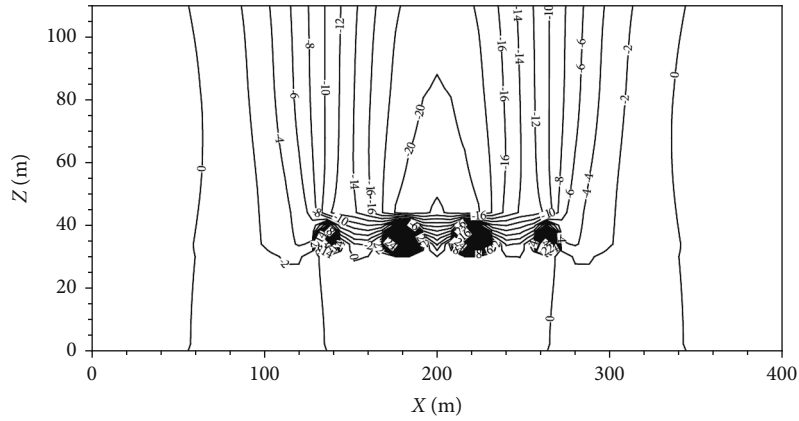


Through the above-mentioned physical and chemical reactions; the formation of grout stones is promoted; cracks, separations, and collapse zones in the mined-out area are filled and reinforced; and the purpose of effective reinforcement is finally achieved.

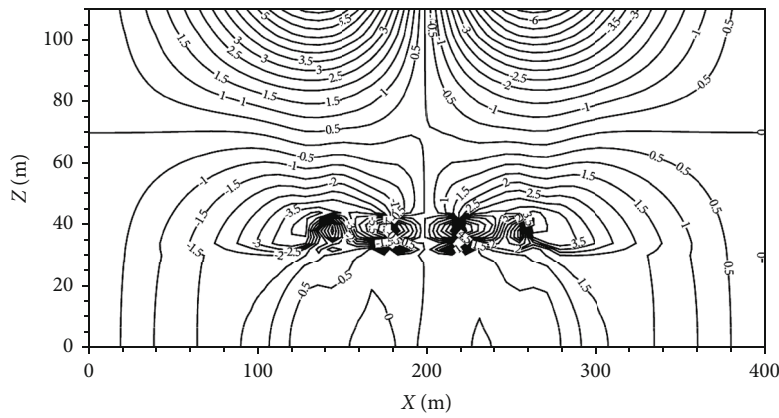
4. Numerical Simulation Analysis of Grouting Reinforcement in Goaf

4.1. Establishment of Grouting Reinforcement Model. According to theoretical analysis and field experience, under normal circumstances, whole grouting is a method of mixing filling materials in a certain proportion into the whole mined-out area and overlying rock cracks and separation layers to completely eliminate potential safety hazards; it is suitable for goaf areas, subsidence areas, and mining separation areas with a large coal seam mining scale and a buried depth of less than 250 m. Local grouting in the fracture zone is a method to recement the fractured rock blocks in the fracture zone into a layered whole, thereby improving the stability and bearing capacity of the overlying rock. It is suitable for reinforcing the situation where there are cavities or cracks on the boundary of the goaf. Strip grouting is a method of supporting the overlying rock mass together with the rock mass and the fractured rock mass under the premise that the strength of the grouted rock mass is sufficient to resist damage and the rigidity is sufficient to resist deformation; it is suitable for the case where the load transmission depth of the building does not touch the critical height of the water-conducting fissure zone. In this simulation, two situations of whole grouting and strip grouting are simulated and analyzed.

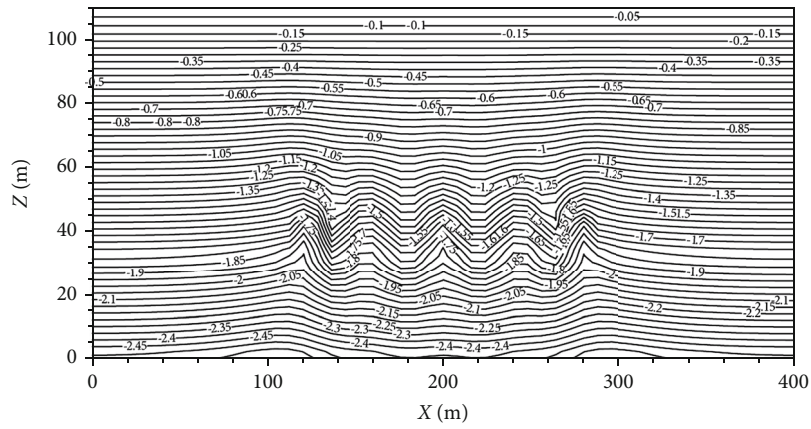
The model is based on the geological mining conditions of a subsidence area in Xingtai city, Hebei Province, China. Study area is generalized as a plane strain model along the coal seam incline. The model is 400 m long, 1 m wide, and



(a) Settlement deformation during strip grouting in the goaf (mm)

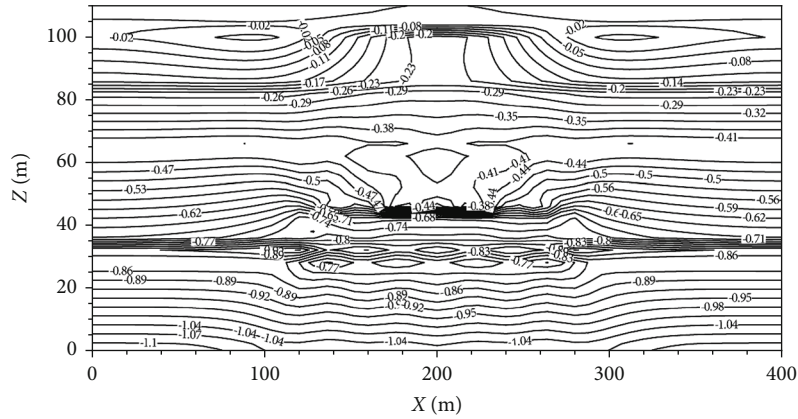


(b) Horizontal displacement change during strip grouting in the goaf (mm)



(c) Vertical stress during strip grouting in the goaf (MPa)

FIGURE 7: Continued.



(d) Horizontal stress during strip grouting in the goaf (MPa)

FIGURE 7: Displacement stress distribution diagram during strip grouting in the goaf.

TABLE 2: Observation of the depth statistics of borehole fracture development.

Drilling serial number	Depth of fissure development (m)	Detection depth (m)	Proportion of fissure (%)
4	31.0~38.5, 65.5~74.5, 128.5~130, 157.7~159.2, 162.2~163.7, 187.7~197.7, 234.2~237.2	28.0~245.4	15.6
8	40.5~45, 52.5~57, 64.5~70.5, 96~97.5, 100.5~102.0, 167.1~168.6, 170.1~177.6, 191.1~200.1	40.5~230.0	19.0
18	85.4~88.4, 89.9~92.9, 95.7~100.7, 113.7~116.7, 122.7~125.0, 128.7~134.7, 142.7~149.7, 169.7~175.7	85.4~193	32.8

110 m high, divided into $50 \times 1 \times 55$ units. In the model, coal thickness is 4 m, mining depth is 76 m, and mining area is 125 m~275 m, which has reached full mining. According to the calculation of the “three under” mining regulations, it can be seen that the heights of the caving zone and water-conducting fissure zone are about 10 m and 50 m, respectively.

This simulation generalized the model into a horizontal layered structure, with 6 layers of siltstone, coal, sandstone, and argillaceous sandstone from bottom to top. During the simulation process, the final results are mainly analyzed from the perspective of displacement and stress. The dynamic flow process of the slurry is not considered.

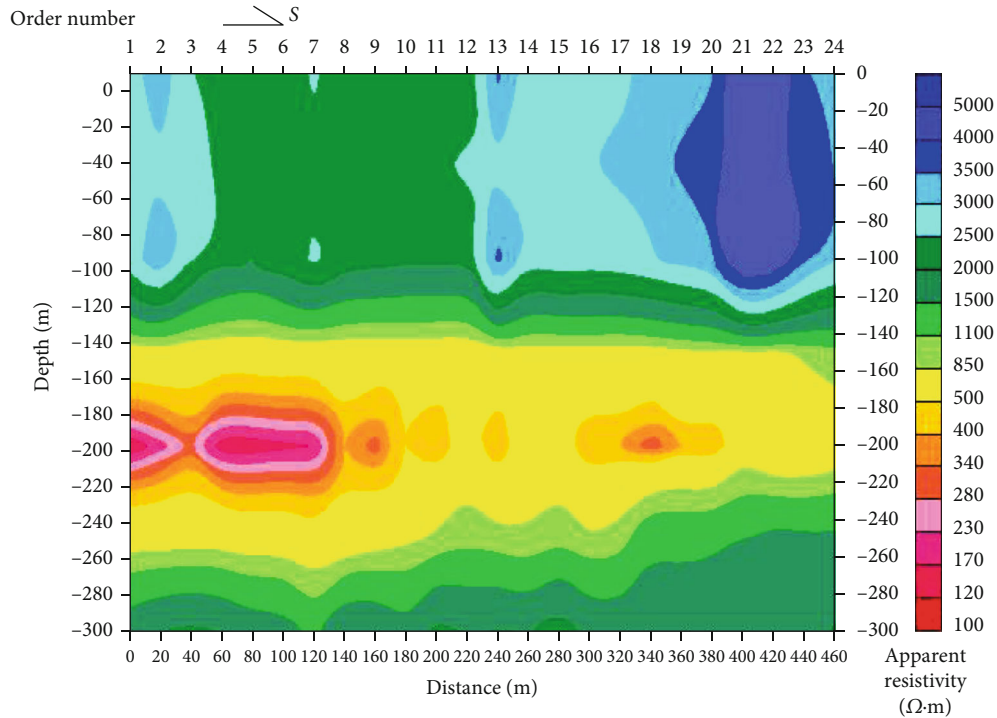
4.2. Simulation Method Selection and Process Determination.

In order to better analyze the grouting effect under each model condition, FLAC3D software is used to simulate the grouting reinforcement effect from multiple angles such as displacement and stress. The Mohr-Coulomb model is selected as a constitutive model due to need to consideration of loose media such as topsoil, rock, coal seams, and cemented granular media. The main parameters include elastic bulk modulus, cohesion, dilatancy angle, internal friction angle, elastic shear modulus, and tensile strength. In the simulation process, the collected physical and mechanical parameters of grouting stone bodies from previous projects are compared and corrected, and the physical and mechanical parameters of the grouted stone bodies are finally determined. On this

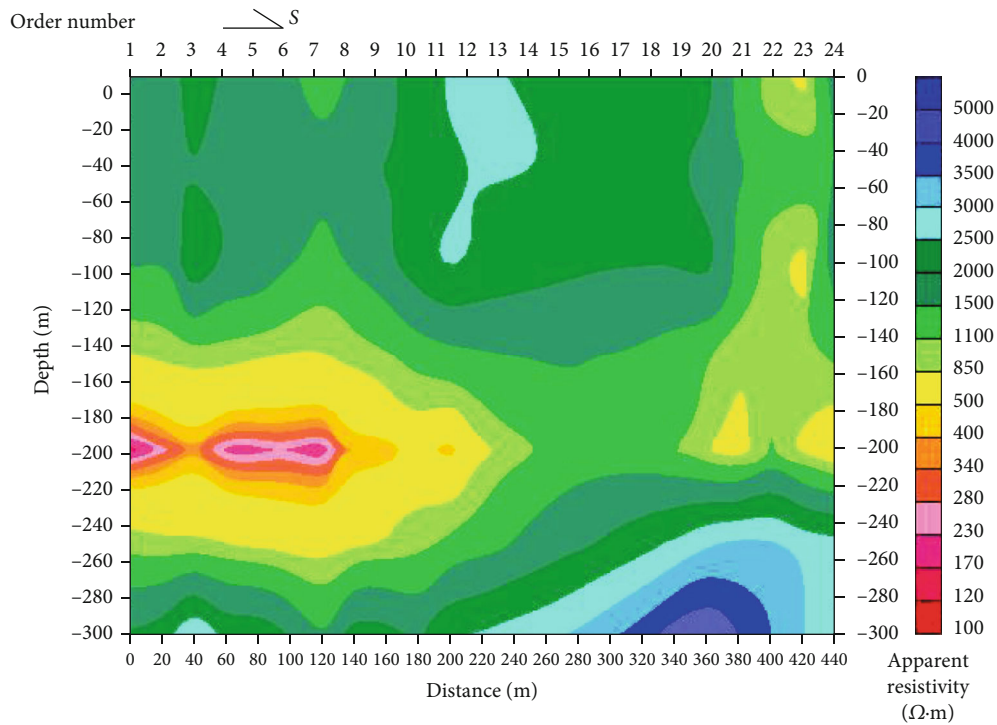
basis, the determined collapse zone, fracture zone, and separation zone are given “strengthening” treatment to obtain the settlement, horizontal movement, and force condition after grouting. In terms of postprocessing, FLAC3D has powerful postprocessing capabilities. The results can be displayed in the form of cloud diagrams, vector diagrams, curves, data, animations, etc. However, some professional calculation results cannot be directly obtained and need to combine with the embedded FISH language programming or with the help of other software. According to the actual situation, combined with tecplot software and Surfer software, the simulation results are postprocessed [30–32].

4.3. Analysis of Calculation Results.

After the initial model without grouting reaches a stable state (Figure 5), the maximum residual subsidence value of the ground surface is 43 mm, the residual subsidence coefficient is about 0.011, and the maximum subsidence value is located directly above the goaf, which is mainly due to further compaction of the rock mass in the goaf and caving zone and the closure of the separated layer and gap in the fracture zone; horizontal movement is mainly concentrated on both sides of goaf and the surface above the goaf. The maximum movement value on both sides of the goaf is 14 mm, which is mainly when the following phenomenon occurs, when the changing trend is gradually decreasing from above the goaf boundary to above the center of goaf, and the horizontal movement value



(a) Before grouting



(b) After grouting

FIGURE 8: Resistivity profile of the cooling tower area.

above the center of the goaf is zero. The change trend of vertical stress and horizontal stress corresponds to settlement deformation and horizontal displacement.

After whole grouting treatments (Figure 6), the maximum residual subsidence of the ground surface is reduced from 43 mm before grouting to 9 mm, and the horizontal

movement value is reduced from 13 mm before grouting to 3 mm. The subsidence of the ground surface mainly comes from the consolidation and deformation of the loose layer on the ground. The distribution of vertical stress and horizontal stress around the goaf is more uniform than before reinforcement, and the numerical value is greatly reduced.

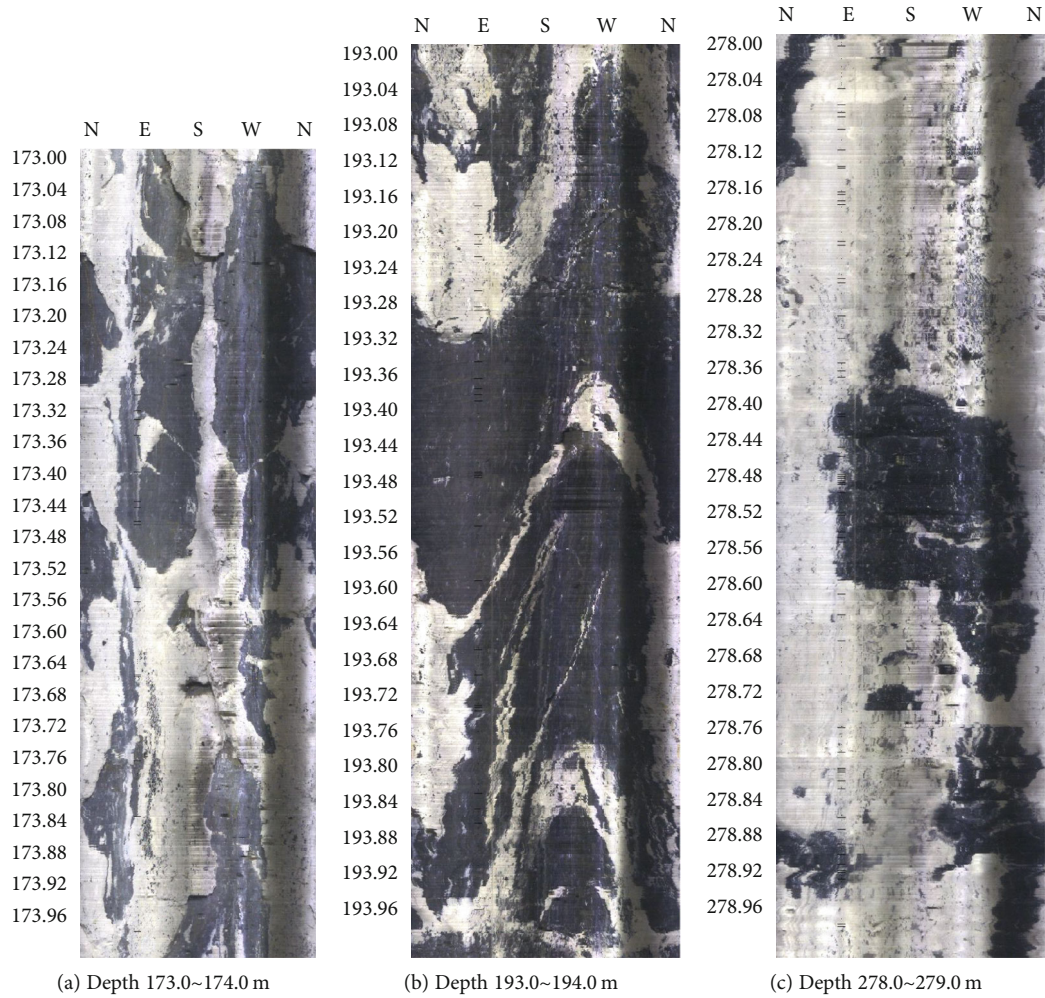


FIGURE 9: Filling situation of rock formation cracks below 170 m in No. II inspection hole.

After the strip grouting treatment in the goaf (Figure 7), the maximum surface subsidence is about 21 mm, which is between 43 mm before grouting and 9 mm after grouting. The vertical stress and horizontal stress are compared to the overall distribution before grouting. Although there is a stress concentration phenomenon at the edge of the belt-shaped filling body, the force on the edge of the coal pillar that is mined before the grouting is relatively small in value. The whole goaf is relatively stable, and the ability to resist interference from external force is much stronger than that without grouting.

5. Engineering Example

This study takes the construction site of the third phase of the Kailuan Tangjiazhuang Thermal Power Plant as an engineering example, which is located in the Guye District, Tangshan City, Hebei Province, China. Comprehensive analysis of drilling construction records and actual drilling data (Table 2) are used to determine that overlying rock in the goaf is affected by multiple seam mining. Although compacted for decades, its stability is still poor. The range of damage and fracture development in rock exceeds the

original estimate. Under the disturbance of surface load and other factors, secondary deformation may occur in the goaf and unstable rock mass above it. It is necessary to deal with unstable rock formations in the goaf under important buildings to ensure the safe operation of thermal power plants.

The grouting holes are arranged in multiple staggered rows, and the design hole distance is 50 m. Three rows of grouting holes are arranged on the annular foundation of the cooling tower (a total of 13 grouting holes); the main plant area is also arranged with three rows of 13 grouting holes, and the actual treatment area is about 51,000 m². Considering the destruction of the overlying rock strata in the goaf, the treatment project adopts the step-down grouting filling method.

A total of 3 north-south detection lines were set up according to the arrangement direction, location, and rock formation tendency of the grouting boreholes. After the goaf was treated by grouting, the apparent resistivity values of three survey lines are higher than those before grouting (Figure 8); the apparent resistivity profile basically disappeared or the range was obviously reduced after treatment (Figure 9), which indicated that the integrity and uniformity of rock mass in the goaf have been improved after grouting.

treatment, increasing the bearing capacity of the formation. Most areas have reached the treatment requirements, and additional grouting was carried out in time for some unfilled dense areas and finally achieved the expected goal of grouting treatment which was verified with inspection holes.

Since the construction and operation of the third phase of the thermal power plant, the relevant buildings (structures) have not shown obvious deformation and damage, and the operation is in good condition.

6. Conclusion

- (1) The goaf left by longwall mining has its unique complexity, and the damage status of the overlying rock layer is difficult to accurately predict and master, which brings great safety hazards to the project construction. When carrying out engineering construction above the goaf, the influence of residual deformation must be considered. On the basis of reasonable detection and scientific evaluation, necessary measures such as underground grouting reinforcement and surface construction antideformation shall be taken as needed
- (2) Numerical simulation reveals the changes in settlement deformation and horizontal movement of the goaf and its overlying rock before and after grouting under different grouting treatment conditions, as well as the distribution of vertical and horizontal stresses. The simulation results show that the whole grouting effect is the best, which can meet treatment requirements to the greatest extent; the strip grouting can also serve the purpose of reinforcing the goaf to a certain extent, and it can also be an effective method for goaf treatment under certain conditions
- (3) Grouting reinforcement is one of the effective methods to deal with the residual deformation of the goaf. There are still some shortcomings in the reinforcement mechanism and technical methods. This study only analyzed the effect before and after grouting and did not conduct real-time research on the whole process of dynamic grouting, which needs further research

Data Availability

The experimental data used to support the findings of this study are included within the article.

Conflicts of Interest

The authors declare no conflict of interest.

Acknowledgments

This research was funded by the Beijing Science and Technology Planning Project (Z181100005118012) and China Coal Science and Industry Group Science and Technology Innovation Venture Capital Special Key Project (2018-2-ZD007).

References

- [1] Z. Yang, Y. Q. Lv, and G. K. Sun, "Influence of multi-coal goaf on stability of upper proposed building," *Journal of Xi'an University of Science and Technology*, vol. 40, no. 5, pp. 862–868, 2020.
- [2] Z. X. Liu, C. X. Wang, L. L. Yang, Q. C. Sun, and N. Jiang, "Simulation analysis of key factors of activation instability in goaf," *Safety in Coal Mines*, vol. 50, no. 6, pp. 240–244, 2019.
- [3] G. L. Guo, K. Z. Deng, H. Y. Wang, Z. A. Huang, and S. J. Chen, "Research on the mechanism of foundation instability above the mined-out area and treatment measures," *Mine pressure and roof management*, vol. 17, no. 3, pp. 39–42, 2000.
- [4] K. Z. Deng, Z. X. Tan, and H. Z. Zhang, "Design method of strip grouting for old longwall mining goaf," *Journal of China Coal Society*, vol. 33, no. 2, pp. 153–156, 2008.
- [5] D. X. Xuan, G. L. Hu, W. B. Zhu, and L. Wang, "Field test on dynamic disaster control by grouting below extremely thick igneous rock," *Journal of China Coal Society*, vol. 37, no. 12, pp. 1967–1974, 2012.
- [6] Y. Z. Pang, C. Y. Liu, L. M. Zuo, X. H. Zhao, and Y. F. Liu, "Experimental study on preparation and properties of new grouting material for goaf filling," *Bulletin of The Chinese Ceramic Society*, vol. 36, no. 7, pp. 2268–2274, 2017.
- [7] X. L. Wang, Q. S. Wang, Z. Y. Zhou, and X. F. Ao, "Three-dimensional turbulent numerical simulation of Bingham fluid in the goaf grouting of the South-to-North water transfer project," *Journal of Hydraulic Engineering*, vol. 44, no. 11, pp. 1295–1302, 2013.
- [8] X. L. Li, L. G. Wang, N. Zhao, and Z. Hao, "Experimental research on mixing ratio of grouting material for goaf under railway," *Bulletin of The Chinese Ceramic Society*, vol. 33, no. 3, pp. 651–655, 2014.
- [9] Z. Lu, K. Z. Deng, and Y. Q. Jin, "Determination of grouting filling area in goaf with longwall mining," *Journal of Mining and Safety Engineering*, vol. 25, no. 4, pp. 499–501, 2008.
- [10] P. E. Yongliang, H. U. Xiewen, S. O. Dage, and H. E. Xin, "Inspection method for grouting effect in treating large complicated cavities due to mining," *Journal of Engineering Geology*, vol. 21, no. 4, pp. 664–671, 2013.
- [11] G. R. Feng, J. W. Bai, X. D. Shi et al., "Key pillar theory in the chain failure of residual coal pillars and its application prospect," *Journal of China Coal Society*, vol. 46, no. 1, pp. 164–179, 2021.
- [12] D. H. Wang, W. Li, and B. Zhang, "Present situation and prospect of research on prevention and control technologies of coal mine goaf instability disaster," *Safety in Coal Mines*, vol. 51, no. 3, pp. 188–193, 2020.
- [13] J. Zhang and B. Wang, "Stability of isolated coal pillar and overburden instability in shallow-buried interval gob," *Journal of Mining & Safety Engineering*, vol. 37, no. 5, pp. 936–942, 2020.
- [14] Y. Wang, Y. F. Yi, C. H. Li, and J. Q. Han, "Anisotropic fracture and energy characteristics of a Tibet marble exposed to multi-level constant-amplitude (MLCA) cyclic loads: a lab-scale testing," *Engineering fracture mechanics*, vol. 244, article 107550, 2021.
- [15] X. B. Xie, R. N. Deng, X. J. Dong et al., "Stability of goaf group system based on catastrophe theory and rheological theory," *Rock and Soil Mechanics*, vol. 39, no. 6, pp. 1963–1972, 2018.

- [16] Y. Wang, C. H. Li, H. Liu, and J. Q. Han, "Fracture failure analysis of freeze-thawed granite containing natural fracture under uniaxial multi-level cyclic loads," *Theoretical and Applied Fracture Mechanics*, vol. 110, article 102782, 2020.
- [17] H. Z. Zhang, K. Z. Deng, and W. Gu, "Distribution law of the old goaf residual cavity and void," *Journal of Mining & Safety Engineering*, vol. 33, no. 5, pp. 893–897, 2016.
- [18] G. L. Bai, S. Z. Li, and J. H. Gao, "Crack development characteristic of rock strata over abandoned gob and its activation mechanism," *Coal Mining Technology*, vol. 15, no. 5, p. 11, 2010.
- [19] Q. Xv, W. Zhu, H. Y. Teng, and Z. X. Tang, "Study on the construction technique of large-scale factory building above coal mining subsidence area," *Metal Mine*, vol. 54, no. 10, pp. 153–157, 2019.
- [20] Y. H. Teng and J. Y. Zhang, "Evaluation on stability of building foundation over goafs," *Journal of China Coal Society*, vol. 34, no. 5, pp. 58–62, 1997.
- [21] Z. P. Zhang, F. Li, and H. C. Zhang, "Stability analysis and evaluation of grouting treatment effect on goaf of steeply inclined thick coal seam," *Science Technology and Engineering*, vol. 21, no. 4, pp. 1312–1317, 2021.
- [22] W. J. Zhang and Y. Guo, "Study on grouting filling construction method of goaf in mountain area," *Modern Tunnelling Technology*, vol. 57, no. S1, pp. 1182–1186, 2020.
- [23] X. L. Li, S. Z. Li, and F. M. Li, "Research on grouting consolidation of foundation over abandoned mine goaf," *Metal Mine*, vol. 46, no. 11, pp. 33–36, 2011.
- [24] Q. S. Zhang, H. B. Wang, R. T. Liu et al., "Infiltration grouting mechanism of porous media considering diffusion paths of grout," *Chinese Journal of Geotechnical Engineering*, vol. 40, no. 5, pp. 918–924, 2018.
- [25] Y. A. Zhi-quan, H. O. Ke-peng, and W. Liang, "Study of diffusion parameters of Newtonian fluid based on column-hemispherical penetration grouting," *Rock and Soil Mechanics*, vol. 35, no. S2, pp. 17–24, 2014.
- [26] Y. Wang, C. H. Li, and J. Q. Han, "On the effect of stress amplitude on fracture and energy evolution of pre-flawed granite under uniaxial increasing-amplitude fatigue loads," *Engineering Fracture Mechanics*, vol. 240, p. 107366, 2020.
- [27] M. R. Zhou, G. W. Lu, T. Wang, and W. A. Jin-wei, "Mechanism analysis of structural loess fracturing grouting," *Engineering mechanics*, vol. 36, no. 3, pp. 169–181, 2019.
- [28] Z. Y. Song, Y. Wang, H. Konietzky, and X. Cai, "Mechanical behavior of marble exposed to freeze-thaw-fatigue loading," *International Journal of Rock Mechanics and Mining Sciences*, vol. 138, article 104648, 2021.
- [29] M. T. Zhu, Q. S. Zhang, S. C. Li, R. T. Liu, and L. Z. Zhang, "Numerical simulation and experimental study on soil split grouting reinforcement mechanism," *Journal of Central South University*, vol. 49, no. 5, pp. 1213–1220, 2018.
- [30] X. L. Li, "Numerical simulation method analysis for goaf problem," *Safety in Coal Mines*, vol. 43, no. 12, pp. 193–196, 2012.
- [31] H. W. Zhu, H. L. Zhu, K. P. Zhou, and X. Xiao, "Study on optimization of pre-processing and post-processing for numerical simulation based on FLAC3D," *Mining R&D*, vol. 28, no. 2, pp. 60–62, 2008.
- [32] X. L. Li, F. M. Li, and F. Zhou, "Band type grouting reinforcement mechanism and numerical analysis," *Coal Engineering*, vol. 59, no. 11, pp. 85–88, 2012.

Research Article

Shale Permeability under Shale Components' Thermal Swelling

Xiang Ao ^{1,2}, Jiren Tang,³ Hai Qu ^{1,2} and Zuping Xiang^{1,2}

¹Chongqing Key Laboratory of Complex Oil and Gas Field Exploration & Development, Chongqing University of Science and Technology, Chongqing 401331, China

²Chongqing Key Laboratory of Heavy Oil Exploitation, Chongqing University of Science and Technology, Chongqing 401331, China

³State Key Laboratory for Coal Mine Disaster Dynamics and Control, Chongqing University, Chongqing 400044, China

Correspondence should be addressed to Xiang Ao; aoxiang900409@gmail.com and Hai Qu; quhai729@163.com

Received 15 March 2021; Revised 6 April 2021; Accepted 17 April 2021; Published 11 May 2021

Academic Editor: Zhengyang Song

Copyright © 2021 Xiang Ao et al. This is an open access article distributed under the Creative Commons Attribution License, which permits unrestricted use, distribution, and reproduction in any medium, provided the original work is properly cited.

Permeability is one of the most fundamental reservoir rock properties required for modeling hydrocarbon production. However, shale permeability is not yet fully understood because of the high temperature of shale reservoirs. The third thermal stress that is caused by temperature change will decrease the permeability of shale. In this work, a theoretical model has been derived to describe the permeability of shale considering the third thermal stress; the principles of thermodynamics and the mechanics of elasticity have been employed to develop this model. The elastic modulus parameters of the shale were measured, along with Poisson's ratio, as required. Lastly, the permeability of shale was tested by transient pulse-decay. Isothermal flow experiments were carried out at 303, 313, 323, and 333 K to assess the effects of shale expansion and deformation on shale permeability caused by the third thermal stress. The permeability of shale samples, as predicted by the model, was found to agree well with experimental observations. The model may provide useful descriptions of the gas flow in shale. The correction accuracy of the permeability was found to increase at lower permeability. However, the development of completely predictive models for shale permeability will require additional experimental data and further testing.

1. Introduction

Shale gas is an unconventional but promising gas resource that has been used with significant success in the world. Permeability is one of the most fundamental properties of any reservoir rock, and it is required for modeling hydrocarbon production. Heller et al. [1] measured the permeability of the Barneet and Eagle Ford shales at low pressure (6.9 MPa) and reported the influence of confining pressure and pore pressure on permeability. Javadpour et al. [2] obtained nano-scale images of shale porosity using an atomic force microscope and then presented a model for gas flow in the nanopores of mudrocks based on the theory of Knudsen diffusion and slip flow. Kwon et al. [3] investigated the effect of effective stress on shale permeability using Wilcox shale. Chalmers et al. [4] measured the permeability of gas shale from the Liard Basin and assessed the effects of origin and

distribution, total organic carbon (TOC) content of minerals, porosity, and effective stress on the permeability of the matrix. Mahnaz et al. [5] used helium as a medium to measure the permeability of shale and assessed the Klinkenberg effect on the permeability of gas shale. The permeability of rock change by the wetting-drying cycles and freeze-thaw-fatigue loading was reported by Song et al. [6, 7].

The thickness of gas shales varies widely. For example, a study of five shale gas systems in the USA indicates a range in shale thicknesses of 2 to 700 m, and the maximum reported thickness of Chinese gas shales is 925 m [8–10]. Therefore, geothermal differences associated with depth will change the permeability of the shale. Zhang et al. [11] measured the permeability of Carrara marble at different temperatures. They found that marble permeability was significantly increased when the temperature rose to 600–700 K. Li and Xian [12] carried out coal permeability experiments under

different stress and temperature conditions using methane and helium. Liang et al. [13] measured the permeability of coal samples from Bang Xin Zu. They concluded that there is an exponential relationship between the permeability of coal and the temperature. Feng et al. [14] measured the permeability and deformation of the high-rank coal while increasing the temperature from 298 to 873 K.

Current studies mainly focus on the temperature effects on the permeability of rock. However, temperature effects on the permeability properties of rocks containing complicated components such as shale are comparatively unknown. Thermal stress can be divided into three categories [15]: (1) the first thermal stress, which is produced by the external deformation of homogeneous materials by heating; (2) the second thermal stress, which is produced as a result of the nonuniform temperature distribution within the same object that cannot freely deform; and (3) the third thermal stress, which occurs in materials comprised of multiple components with different linear expansion coefficients that produce thermal stress due to differences in expansion coefficients as the temperature changes. The thermal stress produced in a shale under the impacts of temperature generally consists of the third thermal stress. The reason for this is that shale accumulations in China are generally composed of organic matter and minerals (quartz, calcite, and clay minerals), and the linear expansion coefficients of these minerals do not have the same magnitude [16, 17].

In this paper, a model is proposed that is based on the principles of thermodynamics and mechanics of elasticity, to describe the temperature impacts of shale permeability under the third thermal stress conditions. The correction factor is tested by experimental measurements on the permeability of shale at 303, 313, 323, and 333 K.

2. Model

2.1. Calculation of the Third Thermal Stress. Since shale is composed of different mineral components, the linear expansion coefficient of shale α is calculated considering the linear expansion coefficients of the constituent minerals and organic matter:

$$\alpha = \sum v_i \alpha_i. \quad (1)$$

The thermal stress caused by temperature is expressed as follows [18]:

$$\sigma = \frac{3\alpha_i E}{1 - 2\mu} \Delta T, \quad (2)$$

where v_i is the percentage of the total volume of the various materials, α_i is the linear expansion coefficient of a particular material, the volume expansion coefficient is $3\alpha_i$, E is the elasticity modulus, μ is the Poisson's ratio, and ΔT is the change in temperature.

Thermal stress is a vector and its direction points from the region of largest expansion quantities to the region of smallest expansion, as shown in Figure 1.

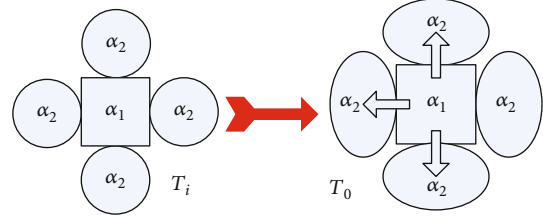


FIGURE 1: Schematic of the third thermal stress.

The direction of the thermal stress in bulk shale points from the organic matter to the minerals. Assuming that the minerals are fully mixed with the organic matter, the value of the thermal stress in small units can be calculated by the model of Figure 1. The thermal stress is expressed as follows:

$$\sigma_T = \left(\sum v_i \alpha_i - \alpha_2 \right) \frac{3E}{1 - 2\mu} \Delta T, \quad (3)$$

where α_i is the linear expansion coefficient of mixture material and α_2 is the linear expansion coefficient of small materials.

2.2. Balance Differential Equation for the Thermal Stress Field. Temperature change in shale formations can be determined by the depth of the shale. A shale formation at the same depth can be considered to have isothermal conditions because the temperature would not change at the same depth of shale burial. Additionally, shale can be assumed to be an isotropic solid for calculation simplicity [19]. Therefore, a planar coordinate system (x, z) is used to establish differential governing equations for the temperature and stress fields (Figure 2). The temperature T is determined by $T = \eta Z$, where η is the geothermal gradient, K/100 m.

The equilibrium, geometric, and physical equations in Cartesian coordinates are as follows [18]:

$$\begin{cases} \frac{\partial \sigma_x}{\partial x} + \frac{\partial \tau_{zx}}{\partial z} = 0, \\ \frac{\partial \tau_{xz}}{\partial x} + \frac{\partial \sigma_z}{\partial z} = 0, \\ \begin{cases} \varepsilon_x = \frac{\partial u}{\partial x}, \varepsilon_z = \frac{\partial w}{\partial z}, \\ \gamma_{xz} = \frac{\partial u}{\partial z} + \frac{\partial w}{\partial x}, \end{cases} \end{cases} \quad (4)$$

$$\begin{cases} \varepsilon_x = \frac{1}{E} (\sigma_x - \mu \sigma_z) + (\alpha - \alpha_2) T, \\ \varepsilon_z = \frac{1}{E} (\sigma_z - \mu \sigma_x) + (\alpha - \alpha_2) T, \\ \gamma_{xz} = \frac{2(1 + \mu)}{E} \tau_{xz}. \end{cases}$$

The equilibrium differential equation, using the displacement as the basic unknown function, is obtained through a transformation of Equation (4).

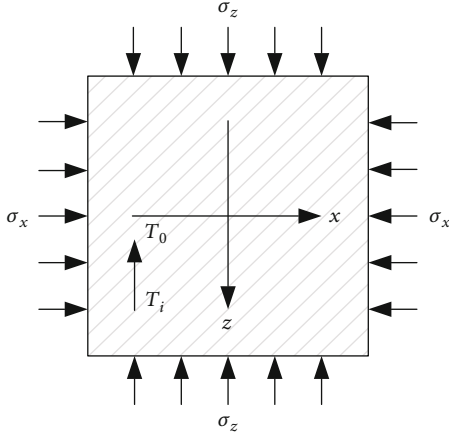


FIGURE 2: The thermal stress analysis diagram.

$$\left\{ \begin{array}{l} (\lambda + G) \frac{\partial \theta}{\partial x} + G \nabla^2 u = \frac{(\alpha - \alpha_2) E \partial T}{1 - 2\mu} \frac{\partial T}{\partial x}, \\ (\lambda + G) \frac{\partial \theta}{\partial z} + G \nabla^2 w = \frac{(\alpha - \alpha_2) E \partial T}{1 - 2\mu} \frac{\partial T}{\partial z}, \\ \theta = \varepsilon_x + \varepsilon_z = \frac{\partial u}{\partial x} + \frac{\partial w}{\partial z}, \\ \lambda = \frac{\mu E}{(1 + \mu)(1 - 2\mu)}, \\ G = \frac{E}{2(1 + \mu)}, \\ \nabla^2 = \frac{\partial^2}{\partial x^2} + \frac{\partial^2}{\partial z^2}. \end{array} \right. \quad (5)$$

The solution to Equation (5) is obtained by introducing the thermal elastic strain potential function $\Phi(x, z)$ ($u' = \partial\Phi/\partial x, w' = \partial\Phi/\partial z$).

A set of solutions to the equation of state of constant temperature, homogeneous plus, is the general solution of differential equations of equilibrium equations, boundary conditions to obtain simultaneous, displacement solution for determining:

$$\left\{ \begin{array}{l} u = \frac{f_x}{\lambda + 2G} x, \\ w = \frac{(1 - 2\mu)f_z + (\alpha - \alpha_2)E\eta}{(\lambda + 2G)(1 - 2\mu)} z^2 - \frac{1}{3}(\alpha - \alpha_2)\eta \frac{1 + \mu}{1 - \mu} z^3, \end{array} \right. \quad (6)$$

where f_z is the vertical crustal stress, f_x is the horizontal stress, and Z is the buried depth.

2.3. Correction Coefficient for Thermal-Hydro-Mechanics-Coupled Permeability. The shale strain in the x and y axes (horizontal plane) are the same, because the temperature of the shale is equal at the same depth. So, the shale volume

strain ε_v can be formulated as

$$\varepsilon_v = 2\varepsilon_x + \varepsilon_z = \frac{2(1 + \mu)}{(1 - \mu)} \left[\frac{(1 - 2\mu)(f_x + Tf_z)}{E} + (\alpha - \alpha_2) \left(T - \frac{T^2}{2\eta} \right) \right]. \quad (7)$$

The empirical formula $K = \sigma\phi^3/\Sigma^2$ can be used to calculate the permeability of the homogeneous medium under the fluid solid heat coupled conditions, where ϕ is the porosity, and Σ is the specific surface area, which is the ratio of value of pore surface area and the whole inner volume.

By introducing a modification coefficient ψ to consider the third thermal stress, the equation $K = \psi K_0$ can be obtained, where K_0 is the permeability without considering the third thermal stress.

$$\left\{ \begin{array}{l} \psi = \frac{K}{K_0} = \left(\frac{\phi}{\phi_0} \right)^3 \left(\frac{V}{V_0} \right)^2 \left(\frac{A_{P0}}{A_P} \right)^2, \\ \frac{V^2}{V_0^2} = \frac{1}{V_0^2} (V_0 + \Delta V)^2 = (1 + \varepsilon_v)^2 = 1 + 2\varepsilon_v, \\ \frac{A_{P0}^2}{A_P^2} = \left(\frac{A_{P0} + \Delta A_P - \Delta A_P}{A_{P0} + \Delta A_P} \right)^2 = 1 - 2 \frac{\Delta A_P}{A_{P0}}. \end{array} \right. \quad (8)$$

The shale porosity is not affected by the third thermal stress, so $\phi = \phi_0$. For the linear elastic strain of a homogeneous medium, an approximation of the internal surface area change is made, which is expressed as $\Delta A_P/A_{P0} \approx (2/3)\varepsilon_v$.

The above equations are simplified by omitting higher order terms because the linear elastic deformation is small:

$$K = K_0 \left(1 + \frac{2\varepsilon_v}{3} \right) \Rightarrow \psi = \frac{K}{K_0} = 1 - \frac{4(1 + \mu)}{3(1 - \mu)} \cdot \left[(\alpha - \alpha_2) \left(\frac{T^2}{2\eta} - T \right) - \frac{(1 - 2\mu)(f_x + Tf_z)}{E} \right]. \quad (9)$$

External factors that affect the correction coefficient of the shale permeability include the temperature difference, geothermal gradient, vertical stress, and horizontal stress. These factors are also related to the medium's elastic modulus, Poisson's ratio, coefficient of expansion, and the mass ratio of its mineral components.

Equation (9) shows that permeability decreases as temperature increases. Permeability decreases largely as a result of increasing the temperature when the difference in the expansion coefficient of shale components is higher and the organic matter content is higher.

2.4. The Permeability Test. It is very difficult to measure shale permeability using conventional steady-state measuring methods because the shale permeability is very low (10^{-3} to 10^{-6} mD). So, an alternative method such as the transient pulse-decay (TPD) method [20] or the beam-bending method [21] was proposed to measure the shale permeability. In contrast with conventional steady-state permeability test methods, the pulse-decay method does not need to record rock outlet velocity. It has the advantage of high

measurement accuracy and efficiency, but it has three disadvantages: (1) difficult sample preparation, (2) high sealing of the experimental device, and (3) a requirement for high-precision pressure sensors. Measurement precision with the beam-bending method is higher than with the conventional steady-state permeability test method. A permeability range of 0.009 to 400 nD can be measured by this method, but it also has three disadvantages: (1) complex mathematical models, (2) difficult sample cutting, and (3) small samples with poor representation.

In this work, the transient pulse-decay experiment was used to measure the permeability of shale samples affected by the temperature.

3. Experiment and Methods

3.1. Samples. The shale samples used in the laboratory experiments were collected from the lower Silurian Longmaxi Formation in Yibin City, Sichuan Province. The total organic carbon (TOC) content of the samples is 7.88%, and the vitrinite reflectance (R_0) of the samples is 2.85%. These values are in the range of most favorable conditions for the occurrence of shale gas ($\text{TOC} \geq 2\%$, $3\% \geq R_0 \geq 1\%$) [22]. Shale samples were prepared with $\Phi 25 \text{ mm} \times 50 \text{ mm}$ rock specimen blocks were obtained (Figure 3). Subsequently, the specimens were put into the oven and baked for 24 h at a temperature of 353 K. Then, the specimens were cooled and sealed in plastic bags.

The mineralogical compositions of shale samples were tested using X-ray diffraction. The X-ray diffraction data were obtained using a Siemens D5000 diffractometer, using $\text{CuK}\alpha$ radiation. The samples were scanned from 2 to $75^\circ 2\theta$, with a step time of 2 s per 0.02° step. The results are shown in Table 1.

The triaxial compression strength, elastic modulus, and Poisson's ratio of the samples were tested using MTS815. The results are shown in Table 2.

3.2. Apparatus. Figure 4 presents a schematic diagram of the permeability measurement apparatus. This apparatus consisted of a temperature control system, an experimental system, a data acquisition system, an auxiliary system, and a triaxial pressure chambers.

The maximum oil field thermostat system can be heated to 473 K, with a temperature control accuracy of 0.1 K. The servo loading system provides a maximum 3000 kN axial load to provide a maximum 200 MPa of confining pressure.

The experimental system consisted of a sample cell, two reference cell (5 mL), two pressure transducer (Rosemount, American, model 3051, range: 0 to 13.79 MPa, accuracy: 8 kPa), and a pressure difference sensor (Rosemount, American, model 3051, range: 0 to 0.68 MPa, accuracy: 0.68 kPa). The pore pressure is provided by the ISCO pump, with a maximum available gas pressure of about 5000PSI.

3.3. Procedure. Prior to measuring the permeability of shale samples, the apparatus was checked for pressure leaks. The helium was injected into the reference cell. If the values of pressure collected from the pressure transducer decreased less than the accuracy of the pressure transducer (8 kPa) in 24 h, then it was no leaks in the system [23].



FIGURE 3: The sample of shale.

TABLE 1: X-ray diffraction results of shale samples.

Quartz	Mineralogical composition (%) of shale samples					
	Potash-feldspar	Plagioclase	Calcite	Dolomite	Pyrites	Clay
53.5	1	3.1	20.3	8.7	3.6	9.8

TABLE 2: Mechanical indexes of shale under uniaxial compression.

	Data	Average
	Uniaxial strength (MPa)	158.88 154.95 160.14
Elastic modulus E (GPa)	46.5 48.5 47.5	47.5
Poisson's ratio μ	0.324 0.289 0.281	0.298

The sample was subsequently installed in the test cell. The system was allowed to reach thermal equilibrium at the target temperature, based on heating in the oil field, ensuring that any temperature-induced expansion took place. The swelling of the shale in response to increased temperature was considered to have reached its maximum when the strain gauges showed the strain of the sample had plateaued, at which point a vacuum was applied.

We apply a confining pressure of 9 MPa, then open the relevant valve of the pulse permeability instruments, and the N_2 was used to up to pressure of about 7 MPa to make the net confining pressure on the rock sample to 2 MPa. After the pressure of the instrument's upstream chamber, rock sample pores, and downstream chamber, it reaches thermal equilibrium according to the instrument prompts, manually lowering the pressure in the downstream chamber by about 70 kPa to form the initial attenuation pressure pulse.

4. Results and Discussion

4.1. Strain Caused by Gas. Kumar et al. [24] measured the permeability of shale samples with helium, methane, and carbon dioxide. They found that the permeability of samples

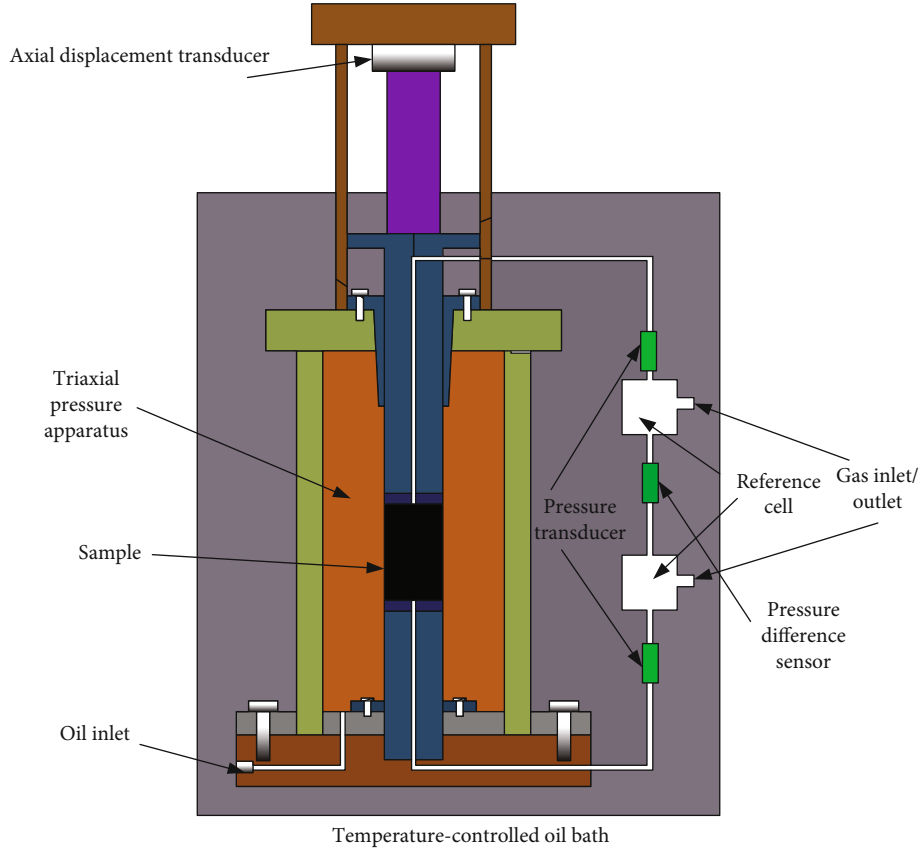


FIGURE 4: The schematic of the experimental apparatus.

decreased by 50% using carbon dioxide and decreased by 20% using methane. It is obviously that the strain on the shale caused by gas could affect the permeability of shale. According to the report by Ao et al. [25, 26], there are two effects that induce strain in the sample caused by gas. Gas was slowly adsorbed by the sample, and so the surface potential of the sample was reduced. The volume was also increased with increases in the thickness of the surface layer while free gas penetrated the pores and cracks. In addition, the gas infiltrated into cracks that were greater than or equal to the molecular size of the gas molecules. In this study, the N_2 was used to measure the permeability. The N_2 have not obviously adsorption ability, so the adsorption-induced strain on shale could not occur. In addition, the change in effective stress caused by gas pressure does not occur instantaneously. The experiment uses the transient method to measure the permeability, so the test time is very short. Therefore, it is difficult for the gas pressure to produce effective stress changes in this experiment. To sum up, there is no strain caused by the gas.

4.2. Experimental Results of Shale Permeability. The permeability was calculated as

$$K = \frac{c\mu\phi L^2 s}{f(a, b)}, \quad (10)$$

where K is the permeability, mD; c is the compressibility of

TABLE 3: The permeability of the sample.

Temperature (K)	303	313	323	333
Sample 1	0.278uD	0.268uD	0.250uD	0.239uD
Sample 2	0.256uD	0.246uD	0.234uD	0.223uD
Sample 3	0.233uD	0.228uD	0.216uD	0.209uD

the pore fluid of the rock sample, dimensionless; μ is the gas viscosity, mPa·s; ϕ is the porosity of shale, dimensionless; L is the length of shale, mm; s is the slope of the pressure difference between the upstream and downstream chambers and time of the pulse permeability tester tested in the single logarithmic graph, dimensionless; a, b is the ratio of the pore volume of the test rock sample to the volume of the upstream and downstream chambers of the pulse permeability meter, respectively; when the value of a is equal to b , the amount of $f(a, b)$ is 1.17. The results of the shale permeability determinations are shown in Table 3.

4.3. Verification of the Permeability Prediction Model. In this work, we have established a model to predict shale permeability. Eight parameters are included in this model, i.e., temperature difference T , geothermal gradient η , vertical stress f_z , horizontal stress f_x , the elastic modulus E , Poisson's ratio μ , the thermal expansion coefficient α , and the proportions of mineral components v_i . v_i was determined based on the

TABLE 4: Shale component parameter table.

Parameters	Data
Elastic modulus E (GPa)	47.5
Poisson's ratio μ	0.29
Geothermal gradient η ($K \cdot m^{-1}$)	0.03
Axial stress f_z (MPa)	30.0
Horizontal stress f_x (MPa)	20.0
The linear expansion coefficient of organic matter ($10^{-6} \cdot K^{-1}$)	30.0
The linear expansion coefficient of minerals ($10^{-6} \cdot K^{-1}$)	3.0

TABLE 5: Correction factor tables.

Temperature difference (K)	Correction factor	Temperature difference (K)	Correction factor
5	0.9995	25	0.9410
10	0.9932	30	0.9125
15	0.9813	35	0.8785
20	0.9639		

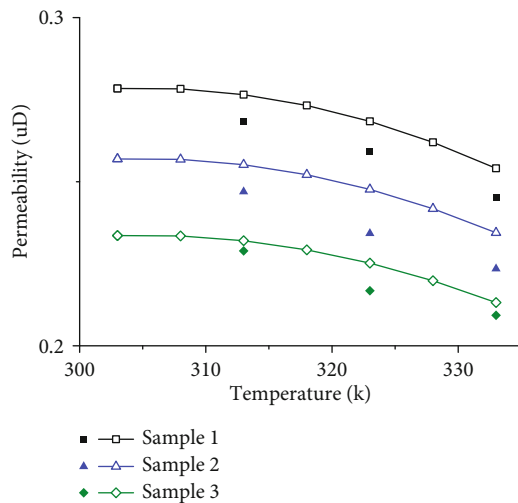


FIGURE 5: The relationship of temperature and permeability; the scatters were experiment data, while the curve was the model data.

results reported by Rahman [27], who pointed out that the TOC of shale is about 10%, whereas the mineral content of shale is about 90%. The parameters used in the model are shown in Table 4.

The correction coefficient for the temperature difference was calculated using equation (9) and reported in Table 5.

To eliminate the effect of the second thermal stress on the results, and based on the experimental conditions, the permeability at 303 K was considered the initial permeability of the model. Therefore, only the third thermal stress will affect the results. Figure 5 presents the model representations for the shale permeability.

Figure 5 compares the experimental and modeled shale permeability values. Note in the figure that the permeability predicted by the model is in good agreement with the mea-

sured data. In addition, the permeability was found to decrease as temperature increased. The model and experimental values were closer at lower permeabilities. This indicates that for a mixture of a hypotonic medium with a low permeability, the effect of the third thermal stress is higher as a result of the reduction in the permeability.

5. Conclusions

This paper presents a theoretical model to describe the impacts of temperature on shale permeability under the third thermal stress condition. This model was built on the principles of thermodynamics and mechanics of elasticity. All parameters included in this model have physical meanings, which provide a predictive basis for constraining the shale permeability.

The main constituents in the shale sample are minerals and organic matter. A shale sample will produce uneven swelling because the thermal expansion coefficients of the minerals and organic matters are different as a result of the effects of temperature change. The third thermal stress is caused by uneven swelling. Furthermore, shale permeability will change under the effects of matrix swelling, which is caused by both ground and thermal stresses. We have also modified the formula for the correction coefficient of the shale permeability. The shale permeability predicted by the model coincides with the experimentally measured permeability, which decreases as the temperature rises. Additionally, the accuracy of the permeability corrections was found to be higher when the permeability was reduced. The shale permeability decreased more rapidly when the temperature increased, particularly while the difference in the shale component expansion coefficients was larger and the organic matter content was higher.

Data Availability

The data used to support the findings of this study are available from the corresponding author upon request.

Conflicts of Interest

The authors declare that they have no conflicts of interest.

Acknowledgments

This study was funded by the National Key Basic Research Program of China (No. 2014CB239206), the Natural Science Foundation of Chongqing (Nos. cstc2019jcyj-msxmX0507 and cstc2019jcyj-zdxmX0024), and the Scientific and Technological Research Program of Chongqing Municipal Education Commission (KJQN20200).

References

- [1] R. Heller, J. Vermynen, and M. Zoback, "Experimental investigation of matrix permeability of gas shales," *AAPG Bulletin*, vol. 95, no. 5, pp. 975–995, 2014.
- [2] F. Javadpour, H. Singh, A. Rabbani, M. Babaei, and S. Enayati, "Gas flow models of shale: a review," *Energy and Fuels*, vol. 35, no. 4, pp. 2999–3010, 2021.
- [3] O. Kwon, A. K. Kronenberg, A. F. Gangi, and B. Johnson, "Permeability of Wilcox shale and its effective pressure law," *Journal of Geophysical Research: Solid Earth*, vol. 106, no. B9, pp. 19339–19353, 2001.
- [4] G. R. L. Chalmers, D. J. K. Ross, and R. M. Bustin, "Geological controls on matrix permeability of Devonian Gas Shales in the Horn River and Liard basins, northeastern British Columbia, Canada," *International Journal of Coal Geology*, vol. 103, pp. 120–131, 2012.
- [5] M. Firouzi, K. Alnoaimi, A. Kovscek, and J. Wilcox, "Klinkenberg effect on predicting and measuring helium permeability in gas shales," *International Journal of Coal Geology*, vol. 123, pp. 62–68, 2014.
- [6] Z. Song, Y. Wang, H. Konietzky, and X. Cai, "Mechanical behavior of marble exposed to freeze-thaw-fatigue loading," *International Journal of Rock Mechanics and Mining Sciences*, vol. 138, article 104648, 2021.
- [7] X. Cai, Z. Zhou, L. Tan, H. Zang, and Z. Song, "Fracture behavior and damage mechanisms of sandstone subjected to wetting-drying cycles," *Engineering Fracture Mechanics*, vol. 234, p. 107109, 2020.
- [8] C. Y. Fan and Z. L. Wang, "Geological factors and process in enrichment and high production of shale gas," *Petroleum Geology & Experiment*, vol. 32, no. 5, pp. 465–469, 2010.
- [9] R. Pan and X. Huang, "Shale gas and its exploration prospects in China," *China Petroleum Exploration*, vol. 3, pp. 1–7, 2009.
- [10] J. Y. Xu and A. J. Wu, "The development status of shale gas in the world and its exploration prospect in China," *Pecial Oil and Gas Reservoirs*, vol. 17, no. 5, pp. 1–9, 2010.
- [11] S. Zhang, M. S. Paterson, and S. F. Cox, "Microcrack growth and healing in deformed calcite aggregates," *Tectonophysics*, vol. 335, no. 1–2, pp. 17–36, 2001.
- [12] Z. Q. LI and X. Xian, "Study on experiment of coal permeability with temperature and stress changing," *Journal of Liaoning Technical University*, vol. 28, pp. 156–159, 2009.
- [13] B. Liang, H. M. Gao, and Y. M. Lan, "Theoretical analysis and experimental study on relation between rock permeability and temperature," *Chinese Journal of Rock Mechanics and Engineering*, vol. 24, no. 12, pp. 2009–2012, 2005.
- [14] Z. Y. Feng, Y. S. Zhao, Z. Y. Wan, G. W. Li, C. Wang, and Y. Zhang, "Law of permeability in the process of anthracite deformation with thermo-mechanical coupling," *Journal of China Coal Society*, vol. 35, pp. 86–90, 2010.
- [15] W. Li, B. Huang, and Z. Bi, *The Thermal Stress Theory and Application*, China Electric Power Press, Beijing, China, 2004.
- [16] H. G. Xu, Z. H. Shui, R. Zhang, W. Chen, and J. J. Zeng, "Effect of metakaolin on thermal expansion of hardened cement paste," *Bulletin Of The Chinese Ceramic Society*, vol. 30, no. 2, pp. 278–283, 2011.
- [17] B. B. Zhang, *Effect of Expansion Coefficient on the Quanlity of the Optical Glass*, Changchun University of Science and Technology, Changchun, China, 2005.
- [18] J. L. Wu, *Theory of Elastic Mechanics*, Higher Education Press, Beijing, China, 2001.
- [19] R. Gautam and R. C. Wong, "Transversely isotropic stiffness parameters and their measurement in Colorado shale," *Canadian Geotechnical Journal*, vol. 43, no. 12, pp. 1290–1305, 2006.
- [20] A. Sakhaee-Pour and S. Bryant, "Gas permeability of shale," *SPE Reservoir Evaluation & Engineering*, vol. 15, no. 4, pp. 401–409, 2012.
- [21] J. Zhang and G. W. Scherer, "Permeability of shale by the beam-bending method," *International Journal of Rock Mechanics and Mining Sciences*, vol. 53, pp. 179–191, 2012.
- [22] W. D. Zhang, M. Guo, and Z. X. Jiang, "Parameters and method for shale gas reservoir evaluation," *Natural Gas Geoscience*, vol. 22, no. 6, pp. 1093–1099, 2011.
- [23] C. Pongtorn, A. M. Sayeed, and L. Robert, "High-pressure adsorption of gases on shales: measurements and modeling," *International Journal of Coal Geology*, vol. 95, pp. 34–46, 2012.
- [24] H. Kumar, D. Elsworth, C. J. Marone, and J. Mathews, "Permeability evolution of shale and coal under differential sorption of He, CH₄ And CO₂," *Presented at the 2010 Fall Meeting of the American Geophysical Union*, 2010.
- [25] X. Ao, Z. Qi, Z. Xiang, Z. Li, H. Qu, and Z. Wang, "Swelling of shales by supercritical carbon dioxide and its relationship to sorption," *ACS Omega*, vol. 5, no. 31, pp. 19606–19614, 2020.
- [26] X. Ao, B. Wang, H. Qu, Z. Xiang, and Z. Luo, "Swelling of shales with slickwater in carbon dioxide," *Energy & Fuels*, vol. 35, no. 6, pp. 5122–5129, 2021.
- [27] W. M. Rahman, "Use classified kerogen," *Journal of Petroleum Geology*, vol. 8, no. 2, pp. 167–176, 1996.

Research Article

Fracture Characteristics and Fatigue Damage of Noncoplanar Fractured Rocklike Specimens under Uniaxial Graded Cyclic Loading and Unloading

Gui-cheng He,^{1,2} Wen-yuan Wu ^{1,2}, Yun Wang,^{1,2} Yong-ming Xue ^{1,2}, Bing Dai,^{1,2} and Zhi-jun Zhang ^{1,2}

¹School of Resources Environment and Safety Engineering, University of South China, Hengyang, China

²Hunan Province Engineering Technology, Research Center for Disaster Prediction and Control on Mining Geotechnical Engineering, 421001 Hengyang, China

Correspondence should be addressed to Wen-yuan Wu; wwyuan94@163.com

Received 27 March 2021; Accepted 26 April 2021; Published 10 May 2021

Academic Editor: Zhengyang Song

Copyright © 2021 Gui-cheng He et al. This is an open access article distributed under the Creative Commons Attribution License, which permits unrestricted use, distribution, and reproduction in any medium, provided the original work is properly cited.

To study the fracture characteristics and fatigue damage of fractured rock masses, noncoplanar fractured rocklike specimens prepared using cement mortar were used for a graded cyclic loading–unloading test. The results showed that the two ends of the horizontal crack were the main stress concentration areas, and they inhibited crack initiation of the inclined fracture. With increasing crack inclination, the inhibitory effect became more obvious. Under the condition that the lower limit stress is constant, as the upper limit stress increases, energy dissipation of the specimen increases, becoming relatively stable in each stage of the cycle. With increasing crack inclination, the increase in the energy dissipation value decreases. Specimens with large changes in the shape of their hysteresis loop tend to exhibit large fluctuations in the elastic modulus. As the loading progressed, the elastic modulus exhibited a downward trend, and the damping ratio tended to be stable. The change in the damping ratio is affected by the dynamic elastic modulus and area of the hysteresis loop. Based on the Weibull probability distribution function, the evolution curve of the damage variable of the specimen can be obtained. This curve reflects the trend of the damage change of the rocklike specimens under various levels of cyclic loading and unloading.

1. Introduction

Rock mass is the main bearing carrier in large-scale projects in fields such as mining, transportation, and water conservation. The rocks in special engineering locations such as mining areas, railways, bridges, tunnels, and other infrastructure are subject to complex loads. When subjected to periodic loads, such as repeated excavation and backfilling, blasting, and earthquakes, the bearing capacity and stability of rocks will decrease. The fatigue damage caused by the change in rock mechanical properties and the gradual deterioration of rock performance affect the safety of engineering activities. With the increasing construction scale of various engineering projects, rock mechanics problems are becoming increasingly complicated. Engineering accidents and economic losses caused by rock stability problems have attracted the

attention of many scholars [1–5]. To study the mechanical response and failure characteristics of rocks under periodic loads is vital to assess the stability and safety of rock mass engineering.

Various researchers [6–10] have found that, under the action of cyclic loading, the upper limit stress and amplitude are the main factors affecting the fatigue life of rocks, and they have put forward the viewpoint of fatigue threshold. By analyzing the mechanics, energy, and deformation characteristics of rocks under uniaxial cyclic loading and unloading, it was found that the unloading elastic modulus was greater than the loading elastic modulus under cyclic loading. In the aforementioned research, constant-amplitude cyclic loading and unloading of stress was mainly adopted, but the actual cyclic loading of the rock mass fluctuates within a certain range and is not a constant value. Therefore, some

scholars have studied the mechanical response and fatigue characteristics of rocks under the action of cyclic loading and unloading in stages. Peng et al. [11] studied the influence of the change in the lower limit of stress on the deformation characteristics of sandstone during cyclic loading and unloading and found that the elastic modulus and Poisson's ratio of the sample increased significantly with an increase in the lower limit of stress. Sun et al. [12] studied the evolution law of fatigue damage of rocks under different confining pressures under cyclic loading conditions and obtained an evolution curve. They found that the curve-fitting degree increased with an increase in the confining pressure. Li et al. [13] conducted uniaxial cyclic loading–unloading tests on sandstone, analyzed the evolutionary process of rock damage, established a theoretical model between the axial strain and the number of cycles, and derived the damage variable evolution equation. Other researchers considered the fatigue characteristics of rocks under different stress amplitudes of loading and unloading [14–16] but did not fully consider rock masses with structural planes, such as fractures and joints. In fact, most rock masses are neither complete nor completely discrete media. The fractured rock will undergo crack initiation, expansion, and penetration during the failure process. The evolution of the crack dominates the failure of the fractured rock mass. Therefore, in a study of intermittent fractured media under cyclic loading, Li et al. [17] established a fractured rock mass damage model from the perspective of energy dissipation and introduced the concept of an equivalent modulus. Liu et al. [18] and Li et al. [19] studied the mechanical properties of jointed rock masses under cyclic loading, explained the evolution of crack propagation, and established a jointed rock mass damage model.

In conclusion, few scholars have fully considered the strength characteristics, energy dissipation, and fatigue damage of fractured rock masses under the action of cyclic loading and unloading. Because rock masses are a geological material with initial defects, it is crucial to study the mechanical properties, crack propagation, and energy evolution of fractured rock masses under the action of nonconstant cyclic stress. Therefore, in this study, we used cyclic loading tests with varying stresses to study the guiding effect of different inclination angles of noncoplanar fractures on crack propagation and the fatigue damage caused by cyclic loading of different stress amplitudes to fractured rocks. The experimental conclusions were drawn by analyzing the hysteretic loop characteristics, energy dissipation, and fatigue damage characteristics. The research results should provide useful guidance for the safety and stability of geotechnical engineering construction projects.

2. Experimental Materials and Procedures

2.1. Sample Preparation. In [20–22], cement mortar was used as the rocklike material, with the ratio of white cement: fine sand: water = 5:5:2. First, oil was applied to the surface of a stainless steel sheet (of thickness = 0.4 mm) and inserted into a stainless steel mold with internal (length \times width \times height) dimensions of 150 mm \times 50 mm \times 200 mm; the mixed mortar was then poured and evenly vibrated. After the cement mortar was initially set, the embedded steel sheet was pulled out to

form a prefabricated crack, the mold was removed 24 h after the test piece was formed, and the qualified test piece was placed in the curing box for standard curing for 28 days. The test blocks were divided into groups A and B. Group A was a double-slit specimen, and group B was a three-slit specimen. The distance between the midpoints of the primary and secondary fissures remained unchanged at 20 mm, the fissure width was 0.4 mm, the main fissure was 30 mm long, and the secondary fissures were 20 mm long and rotated 0°, 30°, 45°, 60°, and 90° along their midpoints. The sample model is shown in Figures 1 and 2. (A00 indicates a double-crack specimen, in which the level of the main crack remains unchanged, and the angle α between the secondary crack and the horizontal plane is 0°.)

2.2. Test Scheme. The RMT-150 rock mechanics loading test machine was used for the indoor loading test, as shown in Figure 3. The test was conducted in two steps: first, each sample was subjected to uniaxial compression to obtain its uniaxial compressive strength and its stress–strain curve; second, the sample was subjected to a graded cyclic loading–unloading test. By taking 40% of the compressive strength of the sample obtained in the first step as the lower limit, the initial upper limit was 80%. During the loading process, the lower limit of stress remained unchanged. After every 300 cycles, the upper limit of stress was increased by 5% until the sample broke. Force control was used in the two-step test, with a loading rate of 0.5 kN/s, a sine wave used as a loading waveform during cyclic loading and unloading, and a loading frequency of 0.2 Hz.

2.3. Sample-Related Parameters. The relevant data obtained from the laboratory loading test on the specimens are listed in Table 1.

3. Results and Analysis

3.1. Characteristics of the Cyclic Loading–Unloading Curve. The uniaxial compression curves of a sample obtained in the test with the stress–strain curve under the action of a graded cyclic load are shown in Figures 4 and 5. Under the action of cyclic loading and unloading, the curves of the unfractured sample and that with cracks and the uniaxial compression curve roughly intersect in the postpeak area, and the uniaxial compression curve basically includes the grading cyclic loading–unloading curve. This phenomenon indicates that, under cyclic loading, the stress–strain curve of either unfractured or fractured rock is controlled by the uniaxial compression curve. The reason for the fatigue failure of the rock mass is that the deformation has reached the limit value, and the deformation of the fatigue failure is equivalent to the corresponding deformation in the postpeak zone under a static load. The fatigue deformation evolution of the intermittent fractured rock mass is consistent with that of unfractured rock and can be divided into three stages: initial deformation, constant-rate deformation, and accelerated deformation. When the load reached point A, the stress reached 80% of the peak stress, and the specimen entered the initial deformation stage of fatigue failure. In the AB stage,

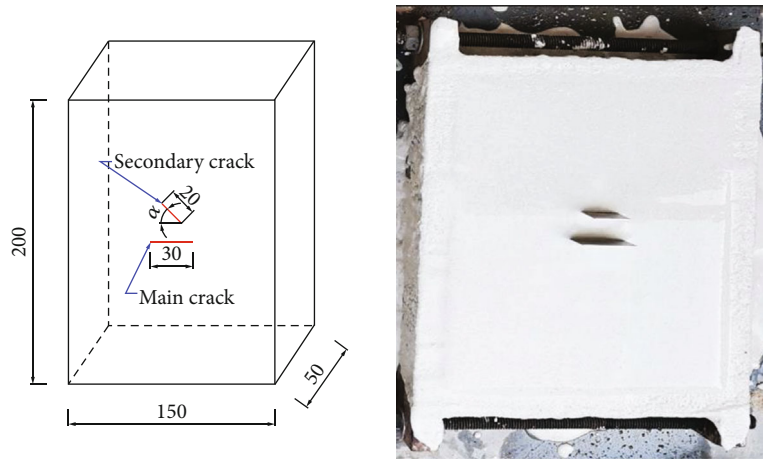


FIGURE 1: Model and production diagram of a group A specimen (in units of mm).

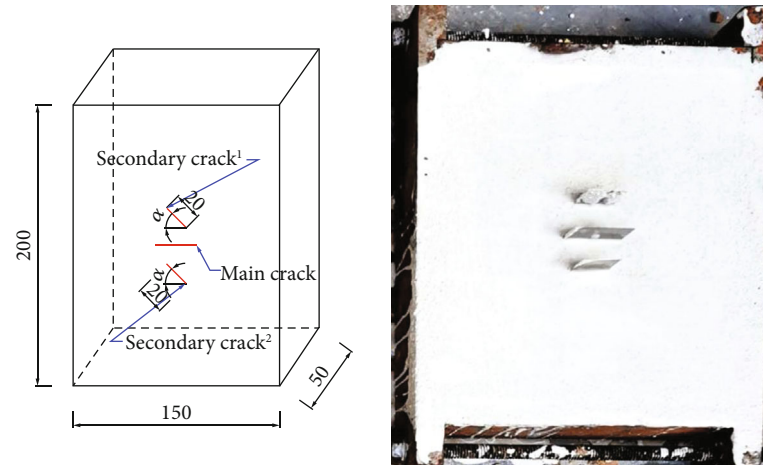


FIGURE 2: Model and production diagram of a group B specimen (in units of mm).



FIGURE 3: RMT-150 rock mechanics test system.

the area of the hysteresis loop was relatively small, the distribution was relatively sparse, and the curve formation rate was uniform; the prefabricated cracks began to crack, and the horizontal cracks were gradually compacted. As the loading-unloading cycle progressed, the sample entered segment BC of the constant-rate deformation stage. During this stage,

the maximum stress was 85% of the peak stress, the curve formation rate was relatively low, the shape of the hysteresis loop changed, the area increased, and the distribution was relatively dense. Observing the surface of the specimen reveals that the initiating cracks had further evolved, and the primary and secondary cracks had penetrated; segment

TABLE 1: Physical parameters of the samples.

Serial number	Length (mm)	Width (mm)	Height (mm)	Fracture dip angle ($^{\circ}$)	Failure strength under static load (MPa)	Cycle failure strength (MPa)	Number of cycles	Cyclic series (level)
Unfractured	149.6	50.0	199.5	/	43.210	38.357	626	3
A00	149.2	49.5	199.4	00-00	35.980	31.381	564	2
A30	150.0	49.2	198.8	30-00	37.549	31.917	336	2
A45	149.5	48.6	199.2	45-00	38.256	34.376	652	3
A60	149.4	49.5	198.6	60-00	36.387	34.568	873	3
A90	149.6	49.5	199.5	90-00	40.725	37.874	577	2
B00	149.5	49.6	199.3	00-00-00	36.520	33.613	522	2
B30	148.8	49.2	199.4	30-00-30	38.601	32.811	317	2
B45	149.2	49.4	199.5	45-00-45	39.621	35.499	615	3
B60	149.6	48.8	198.8	60-00-60	36.984	35.005	938	4
B90	149.5	49.6	199.5	90-00-90	40.301	36.883	1156	4

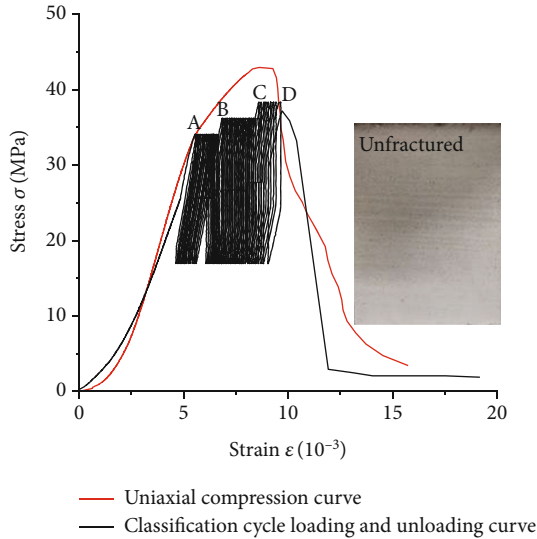


FIGURE 4: Stress–strain curves for the unfractured sample under two loading modes.

CD is the accelerated deformation stage. During this stage, the maximum stress reached 90% of the peak stress, the curve was formed rapidly, and the hysteric loop distribution became looser. The surface of the sample was partially lumped off until the whole sample broke and lost its bearing capacity. The stress drop of the cyclic loading–unloading curve when the specimen broke occurred faster than that under uniaxial compression, which means that the degree of damage to the rocklike specimen under cyclic load was greater, with obvious brittle failure characteristics.

3.2. Analysis of Intensity Characteristics. The existence of cracks destroys the integrity of the rock mass. Their size and location distribution greatly affect the failure mechanism of the rock mass and cause the strength of the rock mass to decrease. As shown in Figure 6, the peak strength of the cracked sample first increased, then decreased, and then increased with the change in the inclination angle, and the strength was lower than that of the unfractured sample.

The bearing capacity of the sample was the highest when the crack direction was consistent with the stress direction. In the samples of group B, the existence of secondary sub-cracks had a strengthening effect on the bearing capacity of the specimen. This strengthening is also reflected in the grading cyclic loading–unloading process. Samples with the same angle were destroyed in the same cyclic series. The failure strength of the specimen under cyclic loading was consistent with the variation under uniaxial compression. Under the action of grading cyclic loading and unloading, the number of cracks had only a minor effect on the number of cycles. As shown in Figure 7, the number of cycles for the two groups of AB samples increased with the inclination angle α when the main crack remained constant. For most of them, the number of cycles first decreased, then increased, and then decreased again, and the values were almost the same.

3.3. Crack Evolution and Failure Pattern. By combining the stress–strain curve and the overall situation of specimen failure, the deformation failure process of the specimen can be roughly divided into four stages: compaction, microcrack propagation, unstable fracture, and complete failure. Group A samples were selected to describe the crack evolution and failure morphology, as shown in Figure 8.

Crack growth of the specimens was simultaneously affected by the change in crack inclination and stress amplitude [23–27]. During the compression process, the prefabricated cracks in specimen A00 were gradually compacted. After the cyclic loading–unloading stage was entered, the vertical tensile cracks generated in the middle of the secondary cracks continued to expand upward as the loading progressed. The tensile cracks at the tips of the primary and secondary cracks produced lap joints, which evolved into shear cracks on both sides of the specimen after the lap joints and extended to the ends. A few far-field cracks were also observed. After specimens A30, A45, and A60 were compressed, the main cracks were gradually compacted, and the main cracks produced upward pull cracks at a certain distance from the tip of the cracks. The specific positions of the initiation were affected by the secondary cracks. The expansion has a guiding effect, and finally, the cracks overlap

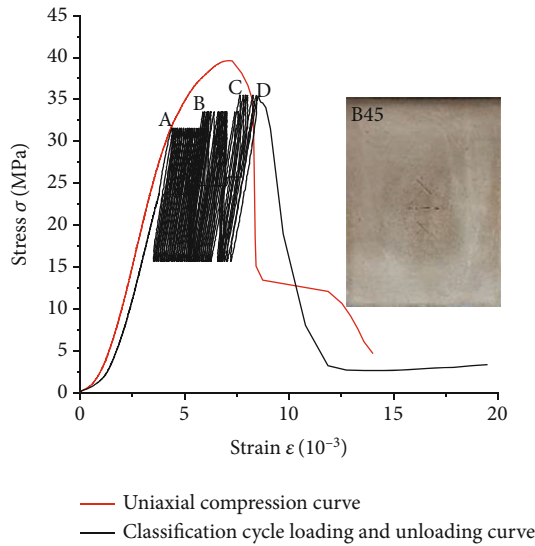


FIGURE 5: Stress–strain curves for the fractured sample under two loading modes.

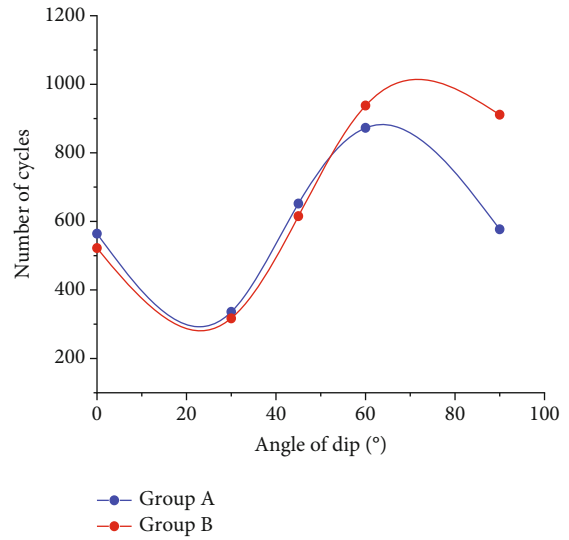


FIGURE 7: Variation of the number of cycles of group A and B samples as a function of the dip angle.

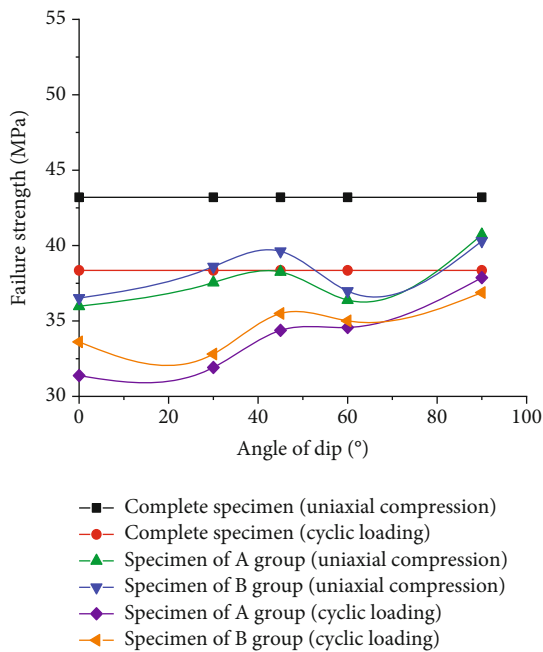


FIGURE 6: Failure strength of rocklike samples.

and penetrate the lower tip of the secondary fissure. However, as the loading progressed, the cracks initiating from the original main crack that overlapped with the inclined secondary cracks partially disappeared. It can be observed that airfoil cracks were generated at the tip of the secondary crack, and the tensile cracks generated at the tip of the main crack gradually evolved into shear cracks. These extended to the end of the specimen, and the upper tensile crack at the left tip of the main crack overlapped with the upper tip of the secondary crack to form a trough. The secondary crack of specimen A90 was in the same direction as the loading stress. During the loading process, the tensile crack in the middle of

the main crack penetrated the lower tip of the secondary crack, the upper tip of the secondary crack produced vertical cracks, and the upper and lower tensile cracks were generated at the tip of the main crack. As the loading progressed, the tensile cracks gradually extended and expanded. By observing the crack evolution process, it was found that the horizontal main crack inhibited crack initiation of the inclined crack. With an increase in the inclination angle, the inhibitory effect became more obvious. This is reflected in the fact that as the inclination angle increased, the distribution of cracks on the front of the specimen decreased, and, when the inclination angle was large, far-field cracks rarely appeared. When the inclination angles of the secondary fissures were 30°, 45°, and 60°, the stress concentration was mainly at the two ends of the horizontal fissure and at the distal end of the secondary fissure. The propagation of airfoil cracks generated by the inclined secondary cracks did not lead to the ultimate failure of the specimen; when the inclination angles of the secondary cracks were 0° and 90°, the stress was mainly concentrated at both ends of the horizontal cracks. With an increase in the loading stress, the tensile cracks generated at both ends evolved into shear cracks and expanded to the side of the specimen. During the compression process of the specimens in group B, like group A, the horizontal cracks are gradually compacted, and the secondary crack1 has a guiding effect on the crack initiation of the horizontal main crack. The specific position of the crack initiation is affected by the angle of the inclined crack. As the loading progresses, the tip of the primary fissure overlaps with the tip of the secondary crack1, as shown in specimens B30, B45, and B60. Airfoil cracks generated by inclined cracks will not lead to the final broken section. Parallel double cracks have a strengthening effect on the compressive strength of the specimens of group B, which is not only reflected in the final breaking strength but also reflected in the number of observable cracks on the surface of the specimens of group B than that of group A, as shown in Figure 8.

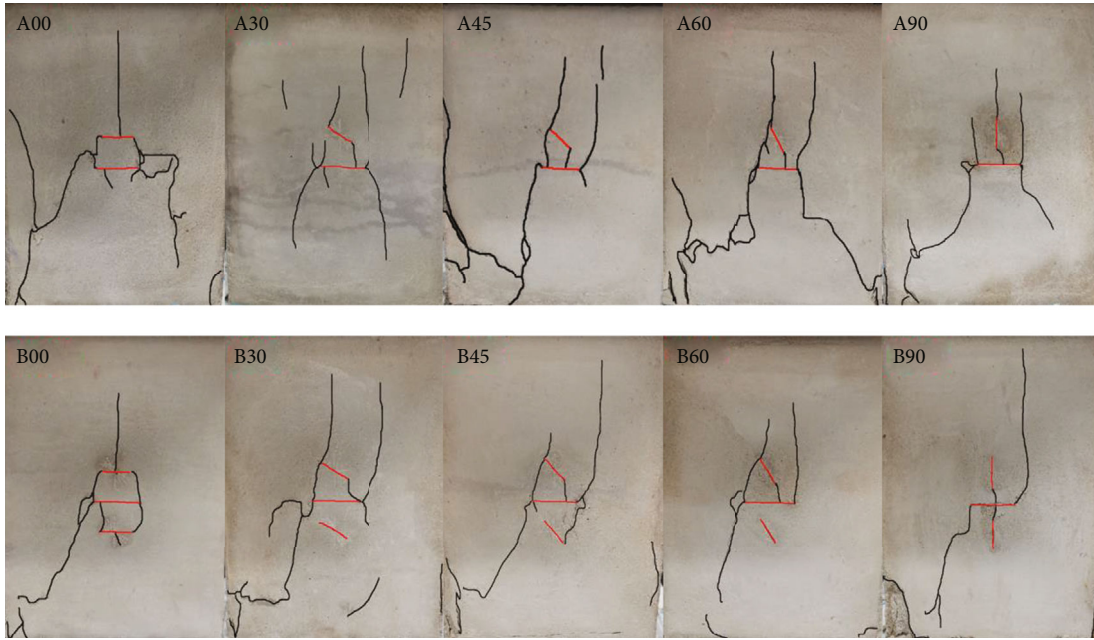


FIGURE 8: Crack propagation in the samples.

As the stress increased, cracks continued to occur, cracks penetrated through, and irreversible deformation increased. When the volume of the specimen began to expand, its end and the rigid cushion block will be subjected to an end effect owing to the frictional force. At this time, the specimen entered the unstable fracture stage, and it spalls and squeezes and expands at the main crack in the middle. When the failure strength was reached, the specimen entered the complete failure stage. At this stage, the fatigue damage of the rock specimen was severe, and the cracks expanded rapidly. The macroscopic sliding fracture surface was formed rapidly, even when the test block was broken and fragments collapsed, which is reflected in the curve falling rapidly. The specimen exhibited severe brittleness, accompanied by a “popping” sound when it was broken.

3.4. Analysis of Hysteresis Loop Characteristics. Numerous studies have been conducted on the shape of hysteresis loops [28–31]. There are certain disputes regarding their specific shapes. Rock properties affect the shape of the hysteresis loop, and the stress amplitude of loading–unloading cycles will also affect its shape. In this study, a rectangular parallelepiped specimen with prefabricated cracks was used to conduct a uniaxial-graded cyclic loading–unloading test. The hysteresis loop obtained in the test is neither an ellipse nor a crescent nor a long eggplant shape, but it is similar to a quadrilateral. Taking the stress–strain curve of the sample B90 as an example, as shown in Figure 9, we take the first hysteresis loop of each level cycle for comparative analysis.

During the cycle loading–unloading process, the unloading and reloading curves intersect under the unloading point to form a hysteresis loop. The relative relationship between the loading and unloading curves determines the area and shape of the hysteresis loop. The hysteresis loop generated

at the beginning of the first stage is relatively narrow and long, and the upper and lower ends of the hysteresis loop become sharp because of the hysteresis effect produced during the closing and opening of the cracks. After entering the second-level loading–unloading cycle, the shape of the hysteresis loop changes and resembles a parallelogram. It can be observed that the second- and third-level curves are more variable. Before the sample broke, the curve tended to be flat. This change is related to the friction of the particles inside the sample. Crack evolution is related to crack penetration, and the microdamage to the specimen causes residual deformation or irreversible deformation of the rock; consequently, the loading–unloading curve exhibits nonlinear characteristics.

After each cycle of loading and unloading, the endpoint of strain and stress on the hysteresis loop increased, and the specimen underwent plastic deformation. According to the stress–strain curve of sample B90, the change in strain at each level of cyclic loading and unloading can be obtained, as shown in Figure 10: the strain of the first cycle increased by a factor of 1.9. The initial cracks and microcracks in the structure of the specimen and the particle spacing were gradually compacted after 300 cycles of loading and unloading at a lower stress amplitude; therefore, the deformation of the specimen was relatively large. After the second-level cycle, the strain grew by a factor of 0.69. At this stage, because the specimen was quite hard, the strain change was much lower than that during the first stage. The amount of plastic deformation of the specimen was low, indicating a more obvious strain-hardening phenomenon. The growth in strain in the third-level cycle was a factor of 0.865, which was higher than that in the second-level cycle. The relatively hard specimens began to deteriorate under the higher stress amplitude loading and unloading, and obvious crack growth appeared on the surface. After the fourth cycle was entered, the highest

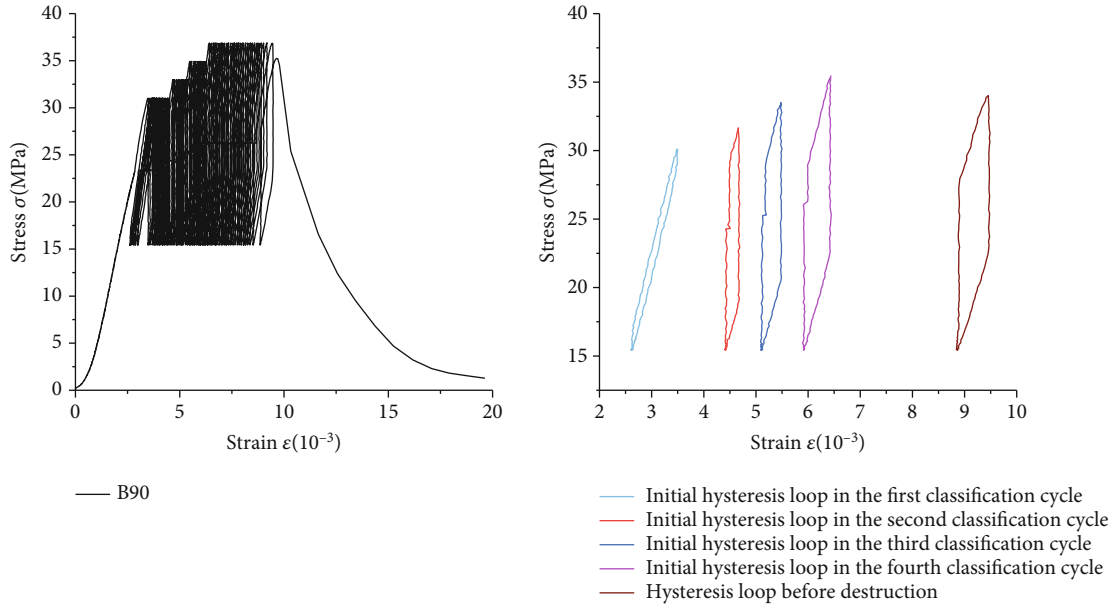


FIGURE 9: Comparison diagram of stress–strain curve and hysteresis loop for sample B90.

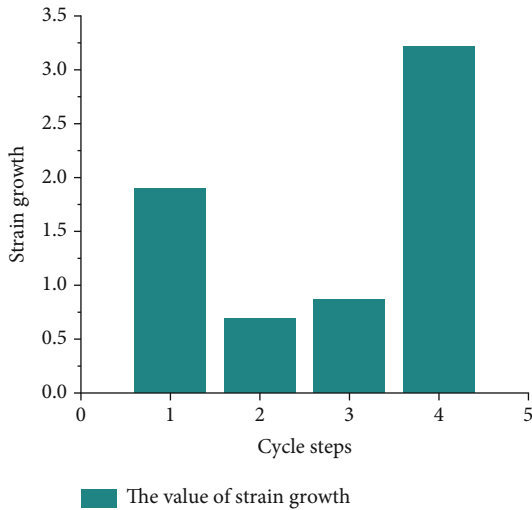


FIGURE 10: Variation in strain change versus cycle steps.

stress reached 95% of the peak stress, and the fatigue deformation of the specimen increased sharply and eventually failed. The strain grew by a factor of 3.215, and the larger the value, the greater was the degree of damage to the rock.

4. Analysis of Energy Dissipation, Dynamic Elastic Modulus, and Damping Ratio

Figure 11 shows that the hysteresis loop of cyclic loading and unloading is a closed loop. The area integral under the loading curve is the total work done by the external force on the rock sample, and the area integral under the unloading curve is the elastic strain energy of the rock. The total work minus the elastic strain energy is the energy dissipated in the rock, which is the area of the hysteresis loop. At each level of the

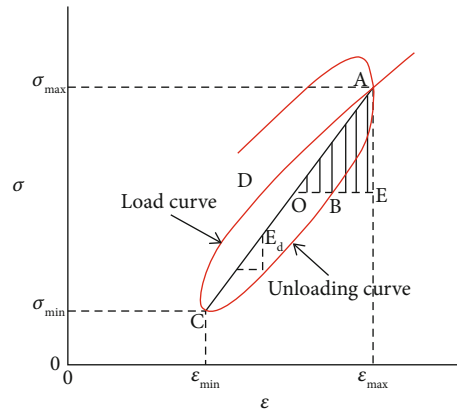


FIGURE 11: Stress-strain hysteresis loop.

loop curve, a part of the hysteresis loop is selected and applied to the calculation.

The damping ratio γ and dynamic elastic modulus E_d of a single cycle are defined as [32]

$$\gamma = A/(4\pi A_s), \tag{1}$$

and

$$E_d = (\sigma_{\max} - \sigma_{\min})/(\epsilon_{\max} - \epsilon_{\min}), \tag{2}$$

where A is the area of the hysteresis loop $ABCD$; A_s is the area of the triangle AOE ; E_d is the elastic modulus; σ_{\max} and σ_{\min} are the corresponding maximum and minimum stresses in the hysteresis loop, respectively; and ϵ_{\max} and ϵ_{\min} are the corresponding maximum and minimum strains in the hysteretic loop, respectively.

4.1. Energy Dissipation. The size of the hysteresis loop area indicates the amount of energy dissipation during the

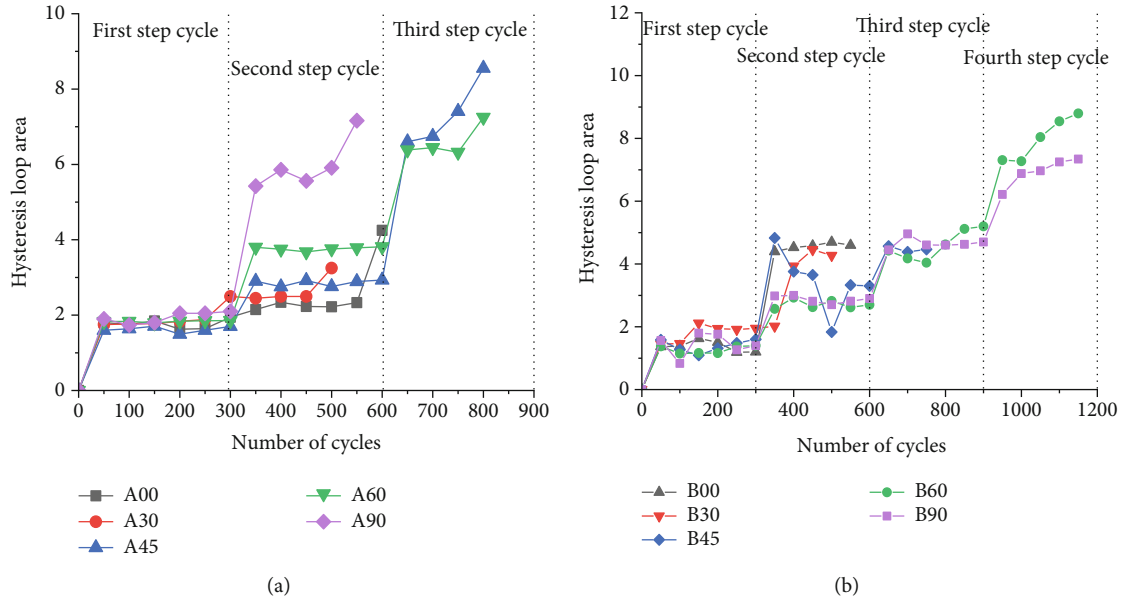


FIGURE 12: Hysteresis loop area curves for group A and B samples.

loading–unloading cycle. During cyclic loading and unloading, the initiation and expansion of microcracks and the penetration between prefabricated cracks consume part of the energy; the remaining energy is used to overcome the damping force and perform work. As shown in Figure 12, at each level of cyclic loading before the specimen was damaged, the hysteresis loop area curve was relatively flat, indicating that plastic deformation inside the specimen did not change significantly during the loading–unloading process at the same level and that energy dissipation was relatively stable. During the failure stage, the area of the hysteresis loop increased sharply, indicating that the energy of the specimen was unstable and that plastic deformation was more significant. Changing the upper limit of the stress changes the energy distribution. As the stress amplitude increased, the energy dissipation also increased. By combining these results with the observation of the stress–strain curve during the loading process, it is found that the hysteresis loops of some test blocks appear to change shape, overlap, and become offset during the loading process. These effects are related to the change in the crack inclination angle of the test specimen and the dispersion of internal particles. The shape of the hysteresis loop and the formation rate of the stress–strain curve were relatively constant. As the upper limit stress amplitude increased, the area of the hysteresis loop increased slightly.

4.2. Elastic Modulus. As shown in Figure 13, the sizes of the hysteresis loop areas of specimens A00 and A30 were essentially the same. As the number of cycles increased, the elastic modulus fluctuated slightly. Specimens A30, A60, and A90 exhibited obvious strengthening when entering the failure level cycle, B group specimens entering the second cycle exhibited an increase in their dynamic elastic moduli compared with their initial values, and specimens B30, B60, and B90 exhibited obvious strengthening in the first cycle. As

the loading progressed, the elastic modulus exhibited a downward trend in the failure level cycle, indicating that, when the macroscopic crack is at a higher stress level, the initiation, propagation, and penetration of the cracks will attenuate the elastic modulus of the specimen. The change in elastic modulus corresponds to the complicated change in the stress–strain relationship curve of the specimen. During the loading process, it can be found that the stress–strain curve exhibited a large lateral shift and hysteresis loop coverage.

4.3. Evolution of the Damping Ratio. The evolution of the damping ratio curve is affected by the area of the hysteresis loop and the dynamic elastic modulus. As shown in Figure 14, in the same cycle, the damping ratio of the group A specimens does not change significantly, while that of group B group specimens fluctuates relatively more. During the initial cycle, the damping ratios are all ~ 0.15 , and the damping ratios are all concentrated at ~ 0.4 at the final failure stage. After 300 cycles of loading and unloading under the first-level stress amplitude, the damping ratio increased after increasing the stress amplitude. Among them, the energy dissipation of specimens A00 and A30 was relatively stable during the loading process; consequently, the damping ratio was basically unchanged. Sample B45 exhibited complex changes during the second cycle, which may be due to damage leading to a greater deterioration of performance and unstable energy dissipation to overcome the damping force. Combined with the failure process, these findings also indicate that, when the crack inclination angle was 45° , the cracks in the specimen with three cracks evolved until the end of tensile–shear mixed penetration, which caused the specimen to exhibit different curve characteristics.

4.4. Damage Variable Analysis. If the initial damage caused by the prefabricated cracks is ignored, and we assume that the strength of the microelement of the rocklike specimen

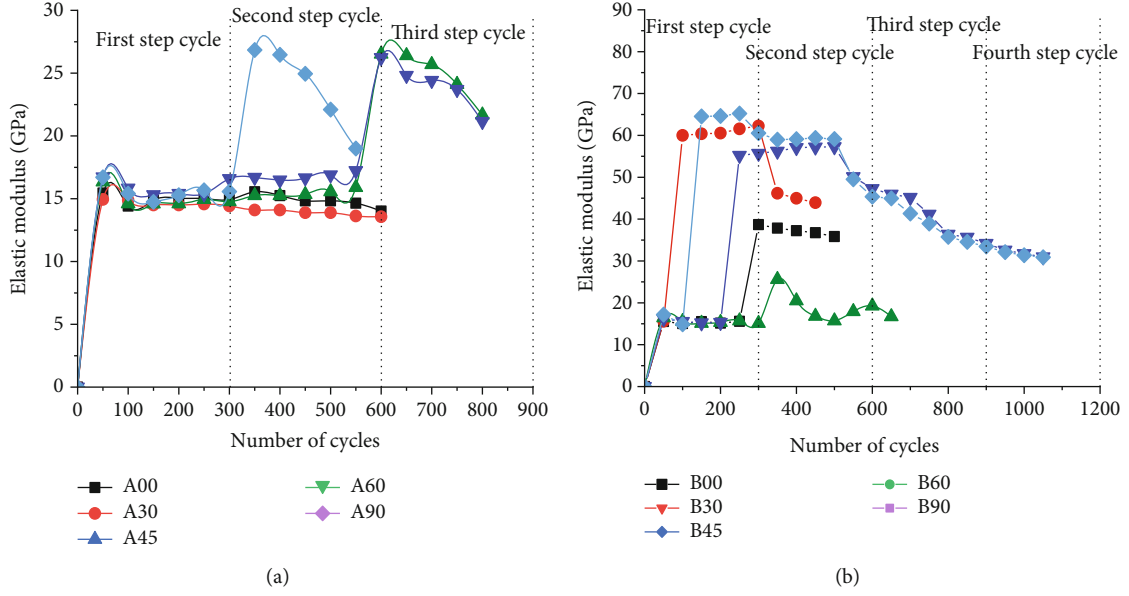


FIGURE 13: Dynamic elastic modulus curves for groups A and B.

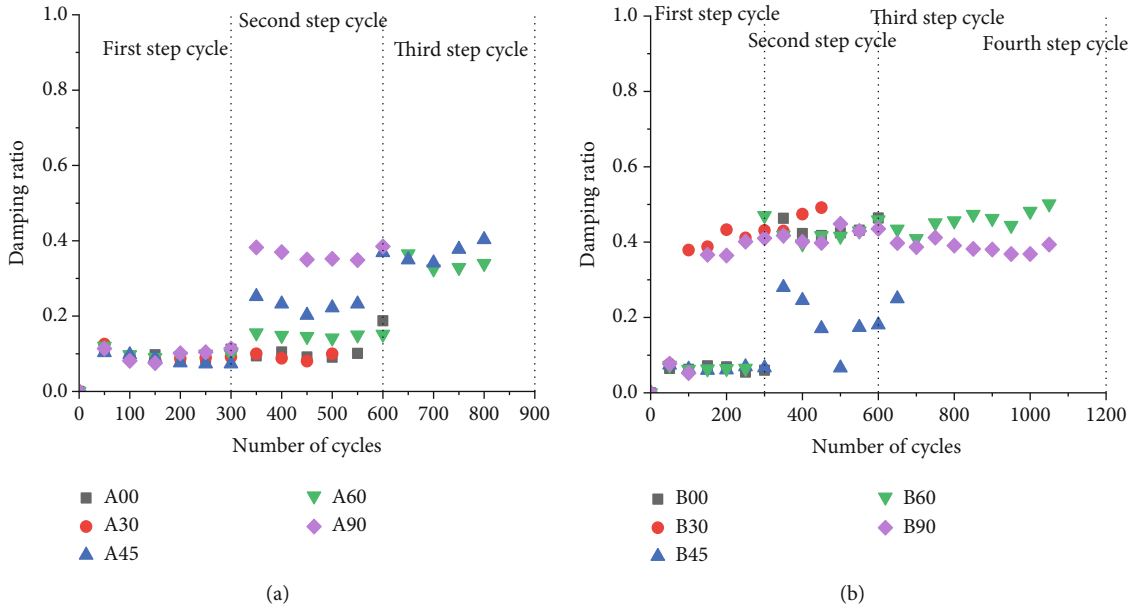


FIGURE 14: Damping ratio curves for groups A and B.

satisfies the Weibull distribution, then the probability density function is [33]

$$p(\varepsilon) = \frac{m}{\varepsilon_0} \left(\frac{\varepsilon}{\varepsilon_0}\right)^{m-1} \exp \left[-\left(\frac{\varepsilon}{\varepsilon_0}\right)^m \right], \quad (3)$$

where $p(\varepsilon)$ is the microelement strength distribution function of the rocklike specimen, ε is the strain, and m and ε_0 are the distribution parameters.

Let us introduce the damage variable D , which is defined as

$$D = \frac{n}{N}, \quad (4)$$

where n is the number of microelements damaged under a certain level of cyclic loading and unloading and N is the total number of microelements of rocklike specimens.

When cyclic loading and unloading reaches a certain strain ε , the number of broken cells is

$$n = \int_0^\varepsilon NP(\varepsilon)d\varepsilon = N \left\{ 1 - \exp \left[-\left(\frac{\varepsilon}{\varepsilon_0}\right)^m \right] \right\}. \quad (5)$$

Then, the damage variable is

$$D = 1 - \exp \left[-\left(\frac{\varepsilon}{\varepsilon_0}\right)^m \right]. \quad (6)$$

TABLE 2: Distribution parameters.

Cyclic loading–unloading series	m	ε_0
	1.365	5.376
First step cycle	1.223	5.494
	1.195	5.514
Second step cycle	0.530	1.784
	0.507	1.689
	0.470	1.511

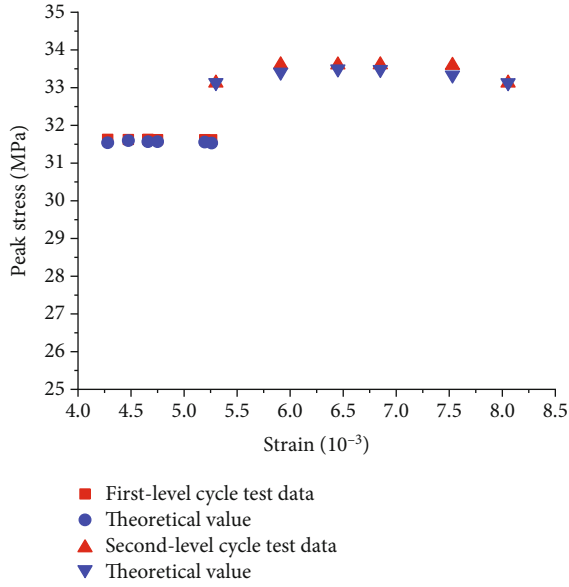


FIGURE 15: Comparison between experimental data and theoretical values.

When $D = 0$, the rocklike specimen is not damaged; when $0 < D < 1$, the rocklike specimen has different degrees of damage; when $D = 1$, the rocklike specimen is damaged.

From the rock damage constitutive model [34–37], under uniaxial compression, assuming that the microelement of the rocklike specimen satisfies the generalized Hooke's law before failure, we can obtain

$$\sigma = E\varepsilon(1 - D), \quad (7)$$

where E is the average dynamic elastic modulus of each number cycle and ε is the strain.

By substituting Equation (6) into Equation (7), the damage constitutive relation of the rocklike cyclic loading–unloading stage in the one-dimensional state can be obtained as

$$\sigma = E\varepsilon \exp \left[-\left(\frac{\varepsilon}{\varepsilon_0}\right)^m \right]. \quad (8)$$

The function $s(e)$ is derived as follows:

$$\sigma'(\varepsilon) = E \exp \left[-\left(\frac{\varepsilon}{\varepsilon_0}\right)^m \right] \left[1 - m \left(\frac{\varepsilon}{\varepsilon_0}\right)^{m-1} \right]. \quad (9)$$

Because the stress–strain relationship curve satisfies $\sigma_{\max}'(\varepsilon_{\max}) = 0$, then

$$m = \frac{1}{\ln(E\varepsilon_{\max}) - \ln \sigma_{\max}}, \quad (10)$$

$$\varepsilon_0 = \varepsilon_{\max} \sqrt[m]{m}. \quad (11)$$

In Equations (10) and (11), σ_{\max} and ε_{\max} are the peak stress and strain values of each level cycle of the rocklike specimen, respectively.

By taking specimen B00 as an example, three hysteresis loops were selected in the curve of each level. The distribution parameters m and ε_0 of the rocklike sample can be calculated according to Equations (10) and (11), and the results are listed in Table 2.

The average values of the distribution parameters m and ε_0 in Table 2 were used to calculate Equation (8), and the theoretical values obtained were compared with the experimental data to construct Figure 15. It can be found that the experimental values and the theoretical values basically coincide, indicating that the selection of the distribution parameters is relatively reasonable. Substituting the distribution parameters into Equation (6) to calculate the damage variable gives the fitting curve of the resulting damage evolution shown in Figure 16. The damage evolution curve reflects the change in damage to the specimen during the entire loading process. During the linear loading and the first cycle stage, the prefabricated cracks gradually compacted and cracks began to grow, but the stress on the specimen was at a lower amplitude and so the damage increased relatively steadily. As the loading progressed, microcracks within the specimen continued to develop, and the cracks expanded and combined. When the secondary cyclic loading stage was entered, the damage value rose sharply to 0.8. At this stage, there was a slight fluctuation in the damage value, and the surface of the specimen began to partially peel off and the crack extended to the side of the end of the specimen. When the damage accumulated to the 0.89, the specimen was destroyed instantaneously, demonstrating its obvious brittleness, but the specimen still had a certain residual strength after it was destroyed. Owing to the existence of prefabricated cracks, the specimen had initial damage; therefore, the damage value D did not reach 1 during the failure.

Based on the Weibull probability distribution function, the fitting curve of the damage variable of the specimen was obtained. As shown in Figure 17, the evolution curve can well reflect the damage variation trend of the rock-like specimen under various cycles. It can be found that the damage variable value of each specimen did not reach 1 after the failure. Due to the difference in the crack inclination of each specimen, the elastic modulus varies in the process of cyclic loading and unloading, which leads to the different amplitude of

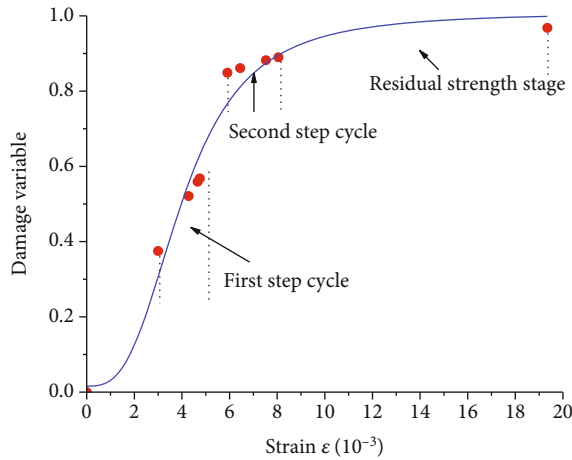


FIGURE 16: Damage evolution curve for specimen B00.

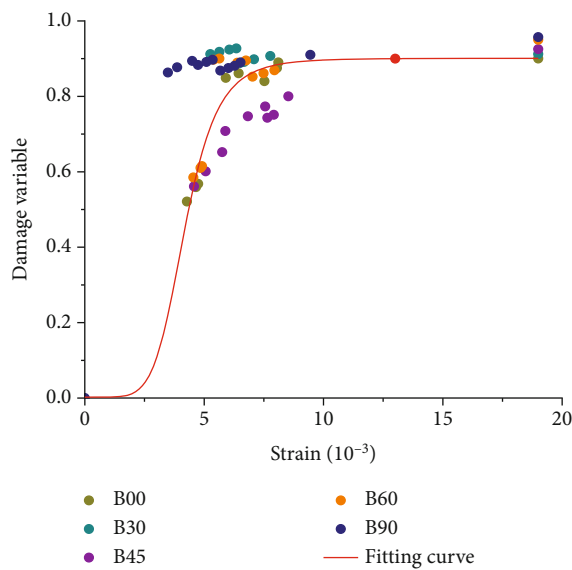


FIGURE 17: Damage evolution curve for specimens of group B.

the fluctuation of the damage variable of the specimen. For example, the elastic modulus of samples B30 and B90 increases sharply in the first-stage cyclic loading and unloading process, leading to a particularly large damage variable value, which is close to the value of failure.

5. Conclusions

(1) Under staged cyclic loading and unloading, the fatigue failure deformation of a noncoplanar intermittent fractured rock mass and an intact rock mass are basically the same as the deformation corresponding to the intersection point of the postpeak area under a static load, and with an increase in the stress amplitude, the fracture plastic deformation characteristics of the specimen become obvious. The trajectory distance of the loading–unloading curves increased, the shape of the hysteresis loop changed, and the area also increased

- (2) The fatigue failure of a rock mass with noncoplanar discontinuous fractures is affected by the distribution of fractures and penetration mode. Both ends of the horizontal main fractures are the main stress concentration areas, and they inhibited the initiation of cracks in the inclined fractures. As the inclination angle increased, the inhibitory effect became more obvious. Parallel double cracks have a certain strengthening effect on the failure strength of the specimen, and the failure of the specimen indicates significant brittleness
- (3) When the lower stress limit was constant, energy dissipation in the specimen increased with the increase in the upper limit stress, but the energy dissipation was relatively stable in each step cycle. As the inclination angle of the secondary crack increased, the increase in energy dissipation value decreased, the internal microstructure was adjusted because the pre-fabricated cracks were gradually compacted, and the cracks expanded and penetrated, resulting in greater fluctuations in the dynamic elastic modulus of the specimen. As the loading progressed, the dynamic elastic modulus exhibited a downward trend, and the change in the damping ratio was greatly affected by the dynamic elastic modulus and the area of the hysteresis loop. These factors overcome the energy dissipation of the damping force, and, along with changes in the degree of damage to the specimen, they determine the evolution form of the damping ratio curve
- (4) Based on the Weibull probability distribution function, the evolution curve of the damage variable of the specimen was obtained. The evolution curve reflects the damaged trend of the rocklike specimen under various cycles. However, the influence of the number of cycles and the amount of initial damage and the brittle–plastic transition of the specimen under staged cycle loading and unloading were not fully considered. This is also a problem to be addressed in future studies

Data Availability

All data used in this study can be obtained by contacting the corresponding author (Wen-yuan Wu), email address: wwyuan94@163.com.

Conflicts of Interest

The authors declare no conflicts of interest related to the publication of this paper.

Authors' Contributions

Wen-yuan Wu is responsible for the methodology and conceptualization. Gui-cheng He is responsible for the investigation and data curation. Yong-ming Xue is responsible for the writing of the original draft, validation, and visualization.

Yun Wang is responsible for the resources and writing of the review and editing. Bing Dai is responsible for the supervision.

Acknowledgments

This study was supported by the National Natural Science Foundation of China (51974163, 51804164, and 51774187) and the Key Scientific Research Foundation of Hunan Provincial Education Department (18A248 and 17A184). Thanks to the Hunan Province & Hengyang City Engineering Technology Research Center for Disaster Prediction and Control on Mining Geotechnical Engineering (2019TP2070) for providing experimental platform support.

References

- [1] Z. Rusin and P. Swiercz, "Frost resistance of rock materials," *Construction and Building Materials*, vol. 148, pp. 704–714, 2017.
- [2] M. P. Kuzmin, L. M. Larionov, V. V. Kondratiev, M. Y. Kuzmina, V. G. Grigoriev, and A. S. Kuzmina, "Use of the burnt rock of coal deposits slag heaps in the concrete products manufacturing," *Construction and Building Materials*, vol. 179, pp. 117–124, 2018.
- [3] S. Wang, S. Licheng, L. Xibing et al., "Experimental investigation of cuttability improvement for hard rock fragmentation using conical cutter," *International Journal of Geomechanics*, vol. 21, no. 2, p. 06020039, 2021.
- [4] Z. Song, T. Frühwirt, and H. Konietzky, "Inhomogeneous mechanical behaviour of concrete subjected to monotonic and cyclic loading," *International Journal of Fatigue*, vol. 132, p. 105383, 2020.
- [5] Y. Luo, F. Q. Gong, X. B. Li, and S. Y. Wang, "Experimental simulation investigation of influence of depth on spalling characteristics in circular hard rock tunnel," *Journal of Central South University*, vol. 27, no. 3, pp. 891–910, 2020.
- [6] Y. Wang, C. H. Li, and J. Q. Han, "On the effect of stress amplitude on fracture and energy evolution of pre-flawed granite under uniaxial increasing-amplitude fatigue loads," *Engineering Fracture Mechanics*, vol. 240, p. 107366, 2020.
- [7] J. Q. Xiao, D. X. Ding, G. Xu, and F. Jiang, "Waveform effect on quasi-dynamic loading condition and the mechanical properties of brittle materials," *International Journal of Rock Mechanics and Mining Sciences*, vol. 45, no. 4, pp. 621–626, 2008.
- [8] Z. Song, H. Konietzky, and M. Herbst, "Bonded-particle model-based simulation of artificial rock subjected to cyclic loading," *Acta Geotechnica*, vol. 14, no. 4, pp. 955–971, 2019.
- [9] M. N. Bang and V. Petros, "Fatigue properties of intact sandstone samples subjected to dynamic uniaxial cyclical loading," *International Journal of Rock Mechanics & Mining Sciences*, vol. 42, no. 2, pp. 237–250, 2005.
- [10] Z. Song, Y. Wang, H. Konietzky, and X. Cai, "Mechanical behavior of marble exposed to freeze-thaw-fatigue loading," *International Journal of Rock Mechanics and Mining Sciences*, vol. 138, p. 104648, 2021.
- [11] K. Peng, J. Q. Zhou, Q. Zou, J. Zhang, and F. Wu, "Effects of stress lower limit during cyclic loading and unloading on deformation characteristics of sandstones," *Construction and Building Materials*, vol. 217, pp. 202–215, 2019.
- [12] B. Sun, Z. Zhu, and C. Shi, "Dynamic mechanical behavior and fatigue damage evolution of sandstone under cyclic loading," *International Journal of Rock Mechanics & Mining Sciences*, vol. 94, pp. 82–89, 2017.
- [13] X. M. Li, C. Y. Liu, S. P. Syd, and Y. Lu, "Fatigue deformation characteristics and damage model of sandstone subjected to uniaxial step cyclic loading," *Journal of China university of mining and technology*, vol. 46, no. 1, pp. 8–17, 2017.
- [14] X. S. Liu, J. G. Ning, Y. L. Tan, and Q. H. Gu, "Damage constitutive model based on energy dissipation for intact rock subjected to cyclic loading," *International Journal of Rock Mechanics and Mining Sciences*, vol. 85, pp. 27–32, 2016.
- [15] E. Liu, R. Huang, and S. He, "Effects of frequency on the dynamic properties of intact rock samples subjected to cyclic loading under confining pressure conditions," *Rock Mechanics and Rock Engineering*, vol. 45, no. 1, pp. 89–102, 2012.
- [16] J. Liu, H. Xie, Z. Hou, C. Yang, and L. Chen, "Damage evolution of rock salt under cyclic loading in uniaxial tests," *Acta Geotechnica*, vol. 9, no. 1, pp. 153–160, 2014.
- [17] T. T. Li, X. J. Pei, and D. P. Wang, "Nonlinear behavior and damage model for fractured rock under cyclic loading based on energy dissipation principle," *Engineering Fracture Mechanics*, vol. 206, pp. 330–341, 2019.
- [18] M. X. Liu and E. L. LIU, "Dynamic mechanical properties of artificial jointed rock samples subjected to cyclic triaxial loading," *International Journal of Rock Mechanics and Mining Sciences*, vol. 98, no. 10, pp. 54–66, 2017.
- [19] N. Li, W. Chen, P. Zhang, and G. Swoboda, "The mechanical properties and a fatigue-damage model for jointed rock masses subjected to dynamic cyclical loading," *International Journal of Rock Mechanics and Mining Sciences*, vol. 38, no. 7, pp. 1071–1079, 2001.
- [20] S. Wang, X. Li, J. Yao et al., "Experimental investigation of rock breakage by a conical pick and its application to non-explosive mechanized mining in deep hard rock," *International journal of rock mechanics and mining sciences*, vol. 122, p. 104063, 2019.
- [21] J. JIN, P. CAO, Y. CHEN, C. Pu, D. Mao, and X. Fan, "Influence of single flaw on the failure process and energy mechanics of rock-like material," *Computers and Geotechnics*, vol. 86, pp. 150–162, 2017.
- [22] X. P. Zhang, Q. Zhang, and S. Wu, "Acoustic emission characteristics of the rock-like material containing a single flaw under different compressive loading rates," *Computers and Geotechnics*, vol. 83, pp. 83–97, 2017.
- [23] J. J. Zeng, Z. J. Zhang, X. X. Zhang, and C. Z. Pu, "Fracture test and analysis of horizontal fissure rock-like specimens influenced by apertures," *Chinese Journal of Geotechnical Engineering*, vol. 42, no. 3, pp. 523–532, 2020.
- [24] Y. Wang, W. K. Feng, R. L. Hu, and C. H. Li, "Fracture evolution and energy characteristics during marble failure under triaxial fatigue cyclic and confining pressure unloading (FC-CPU) conditions," *Rock Mechanics and Rock Engineering*, vol. 54, no. 2, pp. 799–818, 2021.
- [25] T. Liu, B. Lin, Q. Zou, C. Zhu, and F. Yan, "Mechanical behaviors and failure processes of precracked specimens under uniaxial compression: a perspective from microscopic displacement patterns," *Tectonophysics*, pp. 104–120, 2016.
- [26] S. Miao, P. Pan, Z. Wu, S. Li, and S. Zhao, "Fracture analysis of sandstone with a single filled flaw under uniaxial compression," *Engineering Fracture Mechanics*, vol. 204, pp. 319–343, 2018.

- [27] Y. Wang, W. K. Feng, H. J. Wang, C. H. Li, and Z. Q. Hou, "Rock bridge fracturing characteristics in granite induced by freeze-thaw and uniaxial deformation revealed by AE monitoring and post-test CT scanning," *Cold Regions Science and Technology*, vol. 177, p. 103115, 2020.
- [28] H. F. Deng, Y. Hu, J. L. Li, W. Zhe, Z. Xiao-jing, and Z. Heng-bin, "Effects of frequency and amplitude of cyclic loading on the dynamic characteristics of sandstone," *Rock and soil mechanics*, vol. 38, no. 12, 2017.
- [29] B. MCKAVANAGH and F. D. STACEY, "Mechanical hysteresis in rocks at low strain amplitudes and seismic frequencies," *Physics of the Earth and Planetary Interiors*, vol. 8, no. 3, pp. 246–250, 1974.
- [30] B. J. Brennan and F. D. Stacey, "Frequency dependence of elasticity of rock—test of seismic velocity dispersion," *Nature*, vol. 268, no. 5617, pp. 220–222, 1977.
- [31] M. L. Zhu, Z. D. Zhu, G. Li, Y. Qiu, Z. Chen, and J. Li, "Experimental study of dynamic characteristics of granite under cyclic loading," *Chinese journal of rock mechanics and Engineering*, vol. 28, no. 12, pp. 2520–2526, 2009.
- [32] J. F. Liu, J. Xu, Q. S. Li, and G. L. Li, "Experimental study of rock damping parameters under cyclic loading," *Chinese journal of rock mechanics and Engineering*, vol. 29, no. 5, pp. 1036–1041, 2010.
- [33] Z. L. Wang, Y. C. Li, and J. G. Wang, "A damage-softening statistical constitutive model considering rock residual strength," *Computers & Geosciences*, vol. 33, no. 1, pp. 1–9, 2007.
- [34] Y. Q. Zhao, H. Y. Liu, S. R. Lu, and L. Zhang, "Damage constitutive model of jointed rock mass based on coupling macroscopic and microscopic flaws," *Journal of central south university (natural science edition)*, vol. 46, no. 4, pp. 1489–1496, 2015.
- [35] N. Xie, Q. Z. Zhu, L. H. Xu, and J. F. Shao, "A micromechanics-based elastoplastic damage model for quasi-brittle rocks," *Computers and Geotechnics*, vol. 38, no. 8, pp. 970–977, 2011.
- [36] J. W. Zhou, W. Y. Xu, and X. G. Yang, "A microcrack damage model for brittle rocks under uniaxial compression," *Mechanics Research Communications*, vol. 37, no. 4, pp. 399–405, 2010.
- [37] N. Halakatevakis and A. L. Sofianos, "Strength of a blocky rock mass based on an extended plane of weakness theory," *International Journal of Rock Mechanics & Mining Sciences*, vol. 47, no. 4, pp. 568–582, 2010.

Research Article

Macro-Micro Response Characteristics of Surrounding Rock and Overlying Strata towards the Transition from Open-Pit to Underground Mining

Xiaoshuang Li,^{1,2,3,4} Shun Yang¹, Yunmin Wang,^{3,4} Wen Nie,¹ and Zhifang Liu¹

¹School of Resources and Environmental Engineering, Jiangxi University of Science and Technology, Ganzhou, Jiangxi 341000, China

²School of Civil Engineering, Shaoxing University, Shaoxing Zhejiang 312000, China

³State Key Laboratory of Safety and Health in Metal Mines, Maanshan, Anhui 243003, China

⁴Sinosteel Maanshan General Institute of Mining Research Co. Ltd., Maanshan, Anhui 243000, China

Correspondence should be addressed to Shun Yang; 18720720706@163.com

Received 13 January 2021; Revised 25 February 2021; Accepted 1 April 2021; Published 7 May 2021

Academic Editor: Rihong Cao

Copyright © 2021 Xiaoshuang Li et al. This is an open access article distributed under the Creative Commons Attribution License, which permits unrestricted use, distribution, and reproduction in any medium, provided the original work is properly cited.

The macro-micro mining response of the surrounding rock and overlying strata towards the transformation from open-pit to underground mining is examined in the present study, based on the engineering background of the Jinning phosphate mine (Yunnan Phosphate Chemical Group Co., Ltd.) via simulations involving similar materials, digital photographic measurement technology, and numerical simulation. The mining deformation of the surrounding rock underground, and of the overlying strata, is shown to develop in three stages, namely: (1) small and local deformation, (2) continuous linear increase, and (3) the violent nonlinear collapse of the entire system. The internal distribution of stress in the surrounding rock and adjacent overlying strata of the inclined mined-out area is complicated. The degrees of pressure increase and pressure relief have an important relationship with the size of the mining space. The pressure relief is more complete close to the mined area, and the stress reduction decreases with increasing distance. The cracks propagate in arc shapes and have a tendency to penetrate into the upper and lower ends of the stope. The size of the excavation space plays a key role in the generation, propagation, and penetration of the cracks. Due to the disturbance of the first mining level and the increase in excavation depth, the rate of damage to the surrounding and overlying rock increases in the second mining level. This process generates more cracks, which accelerate the instability of the surrounding rock and overlying strata.

1. Introduction

Most of China's open-pit mines were built in the 1950s. After several decades of continuous high-intensity mining, the vast majority of open-pit mines have entered the deep open-pit mining stage and even underground mining. The transition from open-pit to underground mining is a complex systems engineering problem, and the resulting deformation mechanism of the rock mass is highly complicated due to the effects of numerous stress fields. The process presents typical sudden and nonlinear characteristics and poses a serious challenge to the open-pit to underground mining project [1–5].

Research on the transition from open-pit to underground mining in China began around the 1990s, with many researchers conducting bottom friction modeling experiments [6, 7], physical modeling tests [8–10], numerical simulations [11–14], combined numerical and physical simulations [15–18], and field measurements [19–22]. Recently, a mathematical model was established to describe the attenuation of peak particle velocity (PPV) in the open-pit slope, which is used to evaluate the influence of underground mine blasting on the slope stability [23]. Cheng et al. used the Universal Distinct Element Code (UDEC) numerical method to simulate the movement of strata in the footwall caused by underground mining [24]. In addition, the discontinuous

deformation analysis (DDA) method has been used to study the process of slope instability induced by the caving method in rock structures of various mass during mining from open-pit to underground [25–27]. Regassa et al. used the equivalent discontinuity modeling method (EDMM) to simulate the rock movement and failure caused by mining under the end slope of the Western open pit of the Yanqianshan iron mine [28]. With advances in technology, researchers have used micro seismic monitoring, in situ monitoring, and true triaxial modeling [29–32] to investigate the deformation characteristics and failure mechanisms of the slope rock mass and the surrounding rock of the underground stope after the transition from open-pit to underground mining.

Nevertheless, few studies have examined the changes in the surrounding rock and overlying strata of the underground stope due to influences in slope and mining coupled. Due to major differences in the conditions, mining techniques, mining methods, and complexity of the open-pit slope and underground mining environments, it is necessary to study the macro-micro response characteristics of the surrounding rock and overlying strata to the transition from open-pit to underground mining. Therefore, taking the open-pit to underground mining project of the Jinning phosphate mine belonging to the Yunlin Group as an example, experiments on similar materials, numerical simulations, and theoretical analyses are used in the present study to investigate the mining response characteristics of the surrounding rock and overlying strata during such a transition.

2. Engineering Background

After more than 30 years of mining, part of the no. 2 pit in the Jinning phosphate mine belonging to the Yunnan Phosphate Chemical Group Co., Ltd. has formed a high and steep slope. Figure 1(a) is the second pithead of the Jinning phosphate mine. The mining area is low in the north and high in the south and inclined to the east and west. The highest point is 2320 m, and the general elevation is between +2200 and +2320 m. The average dip angle of the ore body is 36°. The thickness of the ore body is generally 3–15 m, with an average thickness of 6.8 m, and the firmness coefficient of the deposit is 7–9. The roof is composed of dolomite with argillaceous rock (firmness coefficient: 6–10), and the floor is composed of argillaceous dolomite with a thin layer of chert (firmness coefficient: 14–16). There are few weak interlayers in the rock layer of the open-pit slope; thus, the influence of faults and joints is small. At present, the total mining depth of pit 2 is over 120 m. The top slope angle is 45°, and the bottom slope angle is equal to the dip angle. Since only a small amount of geological reserves (above +2270 m) are available for open-pit mining, the levels below this will be transferred to the underground mining stage. The representative section of exploration line 59 has been selected as the test section for the present study, and Figure 1(b) is the engineering geological section of exploration line 59. According to the actual mining process, one mining level per 50 m is selected for the study. The underground ore body is mined at a level of 10 m in each mining level.

3. Macro Mining Response Characteristics: Similar Material Experiments

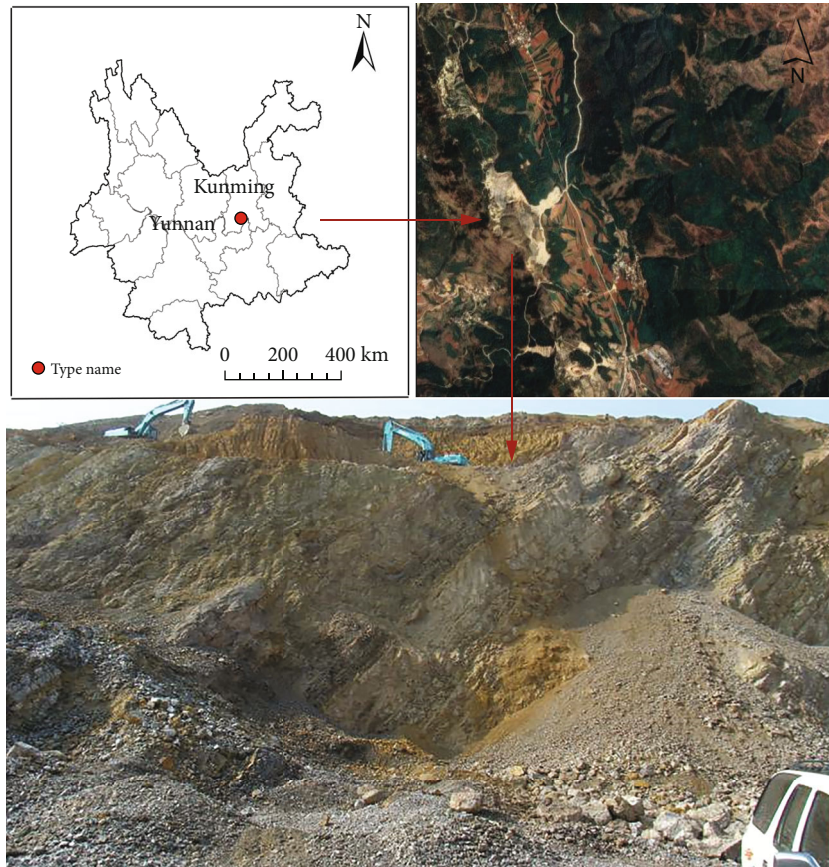
3.1. Simulated Excavation. Experiment is the most traditional method in the field of geotechnical engineering [33–48]. In order to simulate the excavation from the open pit to underground, the two middle sections were selected; Figure 2 shows the two middle sections. In the actual mine, mining extended only to the +2120 m level, and the maximum surface elevation was +2320 m (see Figure 1(b)). In the present study, the simulated maximum mining depth and width are 200 and 300 m, respectively. The overlying strata in the monitoring scheme area is uniformly divided into sixteen displacement observation lines at horizontal intervals of 0.1 m, with the initial observation line positioned at +2270 m at a horizontal distance of 0.116 m from the slope. In the vertical direction, the lowest observation point in each line is 0.1 m from the ore body, and the height of successive observation points increased in steps of 0.1 m. In total, 128 deformation observation points are arranged in this experiment, Figure 2 is the simulation monitoring scheme.

Mining is performed via the sublevel caving method, Figure 3 shows the mining method and steps. The ore blocks are arranged along the strike and divided into two middle sections, each with a height of 0.5 m. Both of the two middle sections are mined in 5 steps from bottom to top, with subsection heights of 0.1 m. And the mining process is completed in 10 steps.

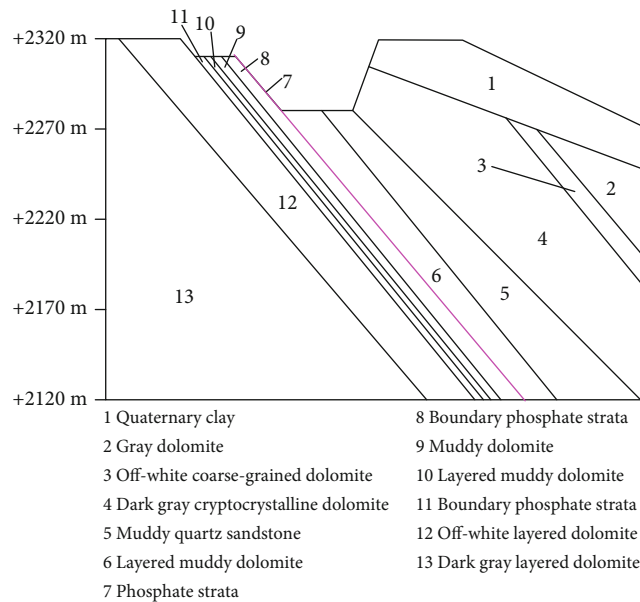
3.2. Model Design. The ore body is chiefly phosphate rock, with a footwall consisting primarily of boundary phosphate rock, mud-bearing dolomite, and layered dolomite. The upper section consists mainly of mudstone-bearing quartz sandstone, dolomite, and a quaternary clay layer. Table 1 shows the rock mechanical parameters measured by laboratory physical tests after field sampling, which reflects the mechanical properties of rock, and the similar physical model experiment material ratio is also based on the mechanical parameters.

Based on the principle of similar material simulation, the similarity parameters for each simulation test are as follows: geometry similarity ratio = 1 : 100, bulk density similarity ratio = 0.81 : 1, stress similarity ratio = 1 : 123.50, and time similarity ratio = 1 : 10. A plane stress model was used in the present work to simulate similar materials along the dip of the phosphate rock. The main components of the model materials were sand, gypsum, calcium carbonate, mica powder, soft glue, engine oil, fine wood chips, and water. The appropriate material ratios were selected via the orthogonal test method and the use of a material testing machine, and the dimensions of the plane model were 3.00 × 0.30 × 2.00 m (length × width × height).

3.3. Physical Modeling Result Analysis. The vertical displacement of the surrounding rock and overlying strata at various stages of the model excavation was measured using a digital camera system. Figures 4(a)–4(f) are the subsidence displacements after the first, third, fifth, sixth, eighth, and tenth excavation steps of the similar material model, respectively. Here,



(a) Second pithead of the Jinning phosphate mine



(b) Engineering geological section of exploration line 59

FIGURE 1: Engineering background.

the distance from the beginning of the ore body and the extent of subsidence are plotted as negative values.

These experimental results indicate that the deformation of the surrounding rock underground and the overlying strata during mining occurs in the following three stages:

(i) small and local deformations occur during the initial excavation steps (steps 1-3, see Figures 4(a) and 4(b)), (ii) a continuous linear increase in deformation occurs during the intermediate excavation stages (steps 4-8, see Figures 4(c)-4(e)), and (iii) a violent nonlinear collapse of the entire

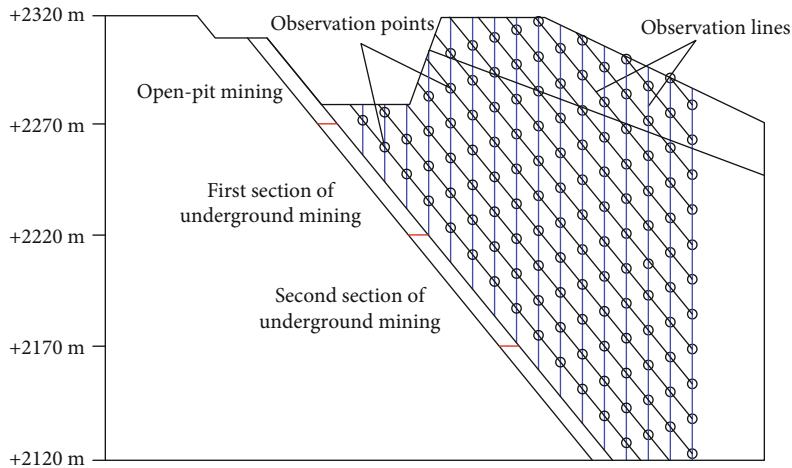


FIGURE 2: Simulation monitoring scheme.

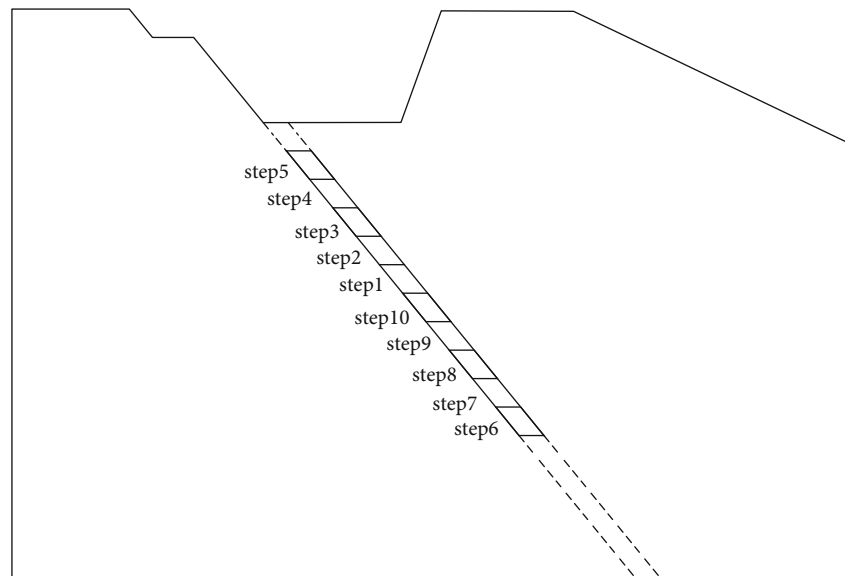


FIGURE 3: Mining method and steps.

structure occurs during the final excavation stages (steps 9–10, see Figure 4(f)).

In detail, an examination of Figure 4(a) indicates that only 10 observation points on lines 1–3 in the vicinity of the mined-out area are deformed, with a maximum subsidence of 5 mm in the central area of the stope. After steps 1–3 (see Figure 4(b)), small degrees of separation and caving have occurred in the rock mass, while it still remains intact and stable. As the mining process is continued (see Figure 4(c)), the underground mining space increases. The effects extend to line 5 on the right-hand side of the underground stope, and the disturbance becomes more serious. At this time, the maximum subsidence increases to 20.5 mm, and the deformation of the surrounding rock and overlying strata of the stope becomes intense in the area of stopes 2 and 3. The maximum vertical displacement has increased to 25.5 mm. After the eighth excavation step (see Figure 4(e)), the affected area extends to observation line 6, and the severe deformation is

mainly distributed along observation lines 1–2 on the upper left and lines 3–4 on the upper right. At this time, the maximum vertical subsidence has increased to 31.5 mm. After the tenth excavation step (see Figure 4(f)), the mined area of the two middle sections is connected, the old mined area is “activated,” and large numbers of macro through-cracks and large-scale pull-through microcracks are produced. At this time, the area affected by mining activity is seen to have increased sharply to 130 cm, the maximum displacement has increased to 33.2 mm, and the surface of the local area has collapsed.

In total, a gently inclined and thin- to medium-thick phosphate deposit was shown to transfer from the open pit to underground by the sublevel caving method, and the corresponding global subsidence curve (see Figure 4, the measure line 10 m and 20 m away from the stope) evolves from the irregular shape of a ladle to the final shape of a half-bowl. The results of the similar material model indicate that,

TABLE 1: Rock mechanical properties.

Lithology	Bulk density (γ) (kN·m ⁻³)	Modulus of elasticity (E) (GPa)	Compressive strength (σ_c) (MPa)	Poisson ratio (μ)	Tensile strength (σ_t) (MPa)
Quaternary clay	18.00	3.28	5.12	0.46	0
Gray dolomite	25.80	9.93	29.10	0.31	0.71
Off-white coarse-grained dolomite	25.28	9.99	31.50	0.29	0.78
Dark gray cryptocrystalline dolomite	25.80	9.93	29.10	0.31	0.89
Layered muddy dolomite	26.20	9.14	24.78	0.28	0.92
Muddy dolomite	24.79	6.06	17.10	0.34	0.67
Phosphatic bed	19.50	8.10	22.87	0.39	0.88
Boundary phosphate rock	26.60	13.80	37.96	0.30	1.46
Off-white layered dolomite	26.24	14.60	48.13	0.28	1.66
Charcoal gray layered dolomite	25.00	15.80	39.35	0.33	1.40

near the mined-out area, the surrounding rock and overlying strata of a gently inclined, thin- to medium-thick phosphate deposit begin to deform and break after 1-10 excavation steps. During this process, the rock will bend and sink under the influence of the gravity and mining stress, to finally collapse when the internal stress exceeds the limiting strength of the rock stratum. The failure modes of sinking, bending, and breaking are identical for the upper and lower strata, and failure of the surrounding and overlying rock gradually progresses from the bottom to the top.

4. Micro Mining Response Characteristics: Numerical Simulation

4.1. Model Geometry and Boundary Conditions. In recent years, computer technology has developed rapidly, and numerical simulation has become an important research method [49–70]. Based on the specific geological conditions and mechanical parameters of the deep inclined medium-thick phosphate ore body in the northern area of pit 2 (Jin-ning County phosphate mine), a particle flow code (PFC) numerical model was run with the same size as that of the similar material model, i.e., height \times width = 300 cm \times 200 cm; Figure 5(a) shows the particle flow code (PFC) model diagram, and Figure 5(b) shows the initial state of the model.

4.2. Physical and Mechanical Parameters of the Rock. The mesomechanical parameters of the PFC model were based on the measured mechanical properties of rock samples obtained on site. They account for the size effect and similarity ratio via repeated adjustments to make the simulated settlement close to that of the similar material model. Figure 6(a) shows the comparative picture of the experiment and simulation, Figure 6(b) shows the subsidence curve of the experiment and simulation, and Figure 6 shows the total comparative results of the similar material model and the PFC numerical model, the results illustrated the effectiveness of this simulation method, and this method can be used to analyze the mechanical behavior of surrounding rock and overlying strata during the mining process. Table 2 shows the final PFC mesoparameters of the rock samples, and the

PFC calculated results are consistent with the similar material model experiment.

4.3. Model Measuring Circle Layout. According to the mine pressure theory, after the underground mining, the surrounding rock and overlying strata are affected by mining stress and mined-out areas, and the in situ stress will redistribute. Figure 7 shows the in situ stress distribution after excavation step 1, step 2, step 5, and step 10, which illustrate the pressure increase and pressure relief zone of the surrounding rock and overlying strata near the goaf.

To analyze the stress changes in the surrounding rock and overlying strata at various locations after the first and second excavation steps, measuring circles were laid out in the surrounding rock, roof corner, and floor corner of the mined-out area, respectively. Figures 8(a) and 8(b) show the layout of survey points on the surrounding rock and overlying strata in the PFC model for the first excavation step and the second excavation step, respectively. The left measuring circles (5 and 51) and the right measuring circles (2 and 21) were 0.03 m away from the rock surrounding the excavation. The measuring line was arranged at an angle bisecting the roof and floor corner, with each measuring circle positioned 0.03 m away from the mined area (circles 1, 3, 4, and 6 and 11, 31, 41, and 61). Another six measurement circles (1, 7, and 8 and 11, 71, and 81) were set at vertical intervals of 0.09 m on the right-hand corner of the roof in order to analyze the changes in the internal stress of the overlying strata. All measuring circles had a radius of 0.03 m.

4.4. PFC Simulation Results and Analysis

4.4.1. Stress Characteristics of the Surrounding Rock and Overlying Strata after Each Excavation Step. Figures 9(a) and 9(b) show the stress evolution in the overlying strata at the upper right-hand corner of the roof and the lower left-hand corner of the floor after the first excavation step (measurement circles 1 and 4, respectively) and after the second excavation step (measurement circles 11 and 41, respectively). The stress evolution curves at the end of each excavation step indicate that the surrounding rocks experience three stress evolution stages: (i) unloading, (ii) fluctuation, and (iii)

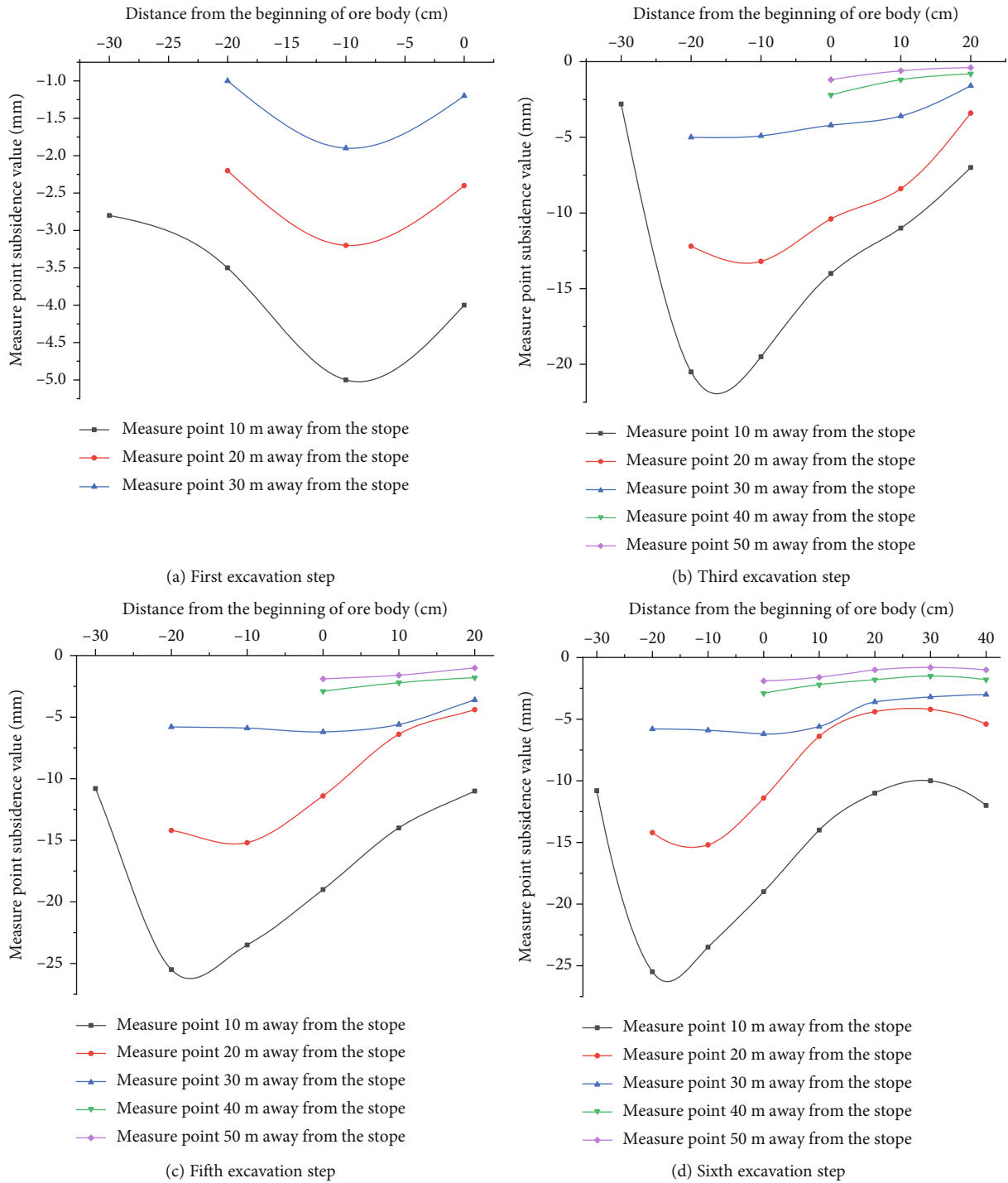


FIGURE 4: Continued.

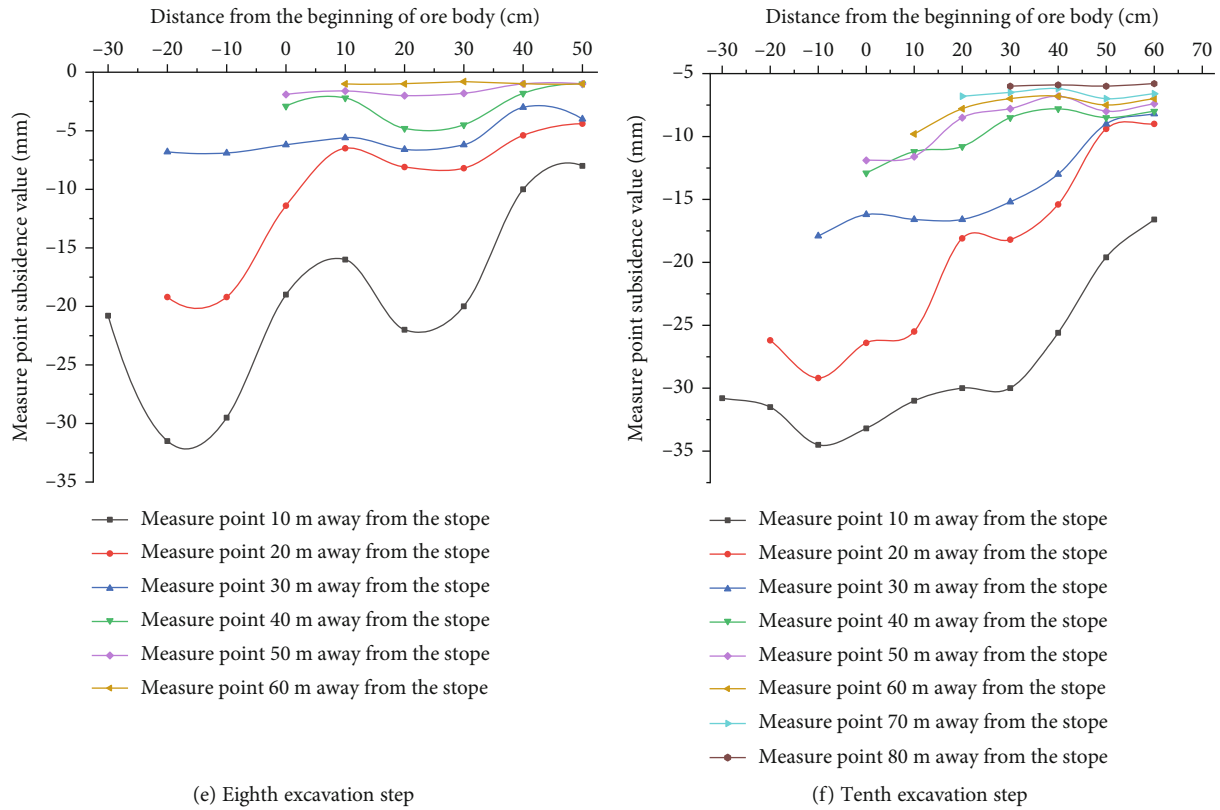


FIGURE 4: Subsidence displacements after each excavation step of the similar material model.

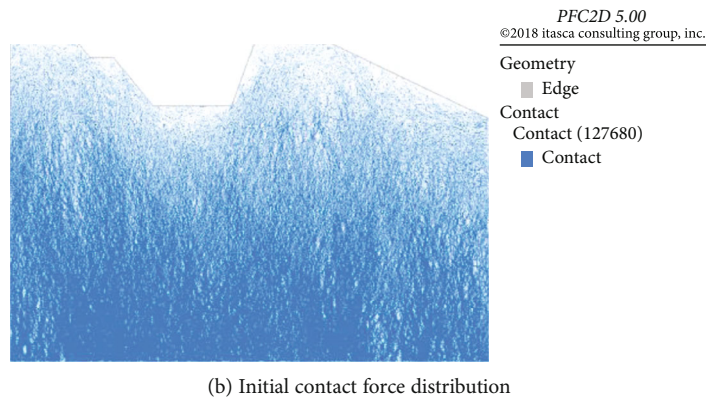
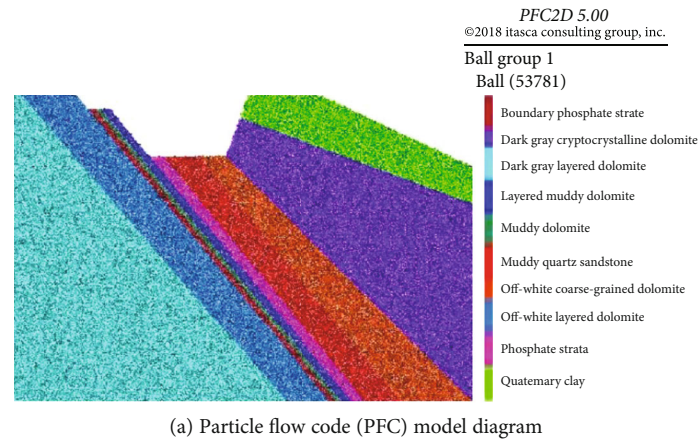
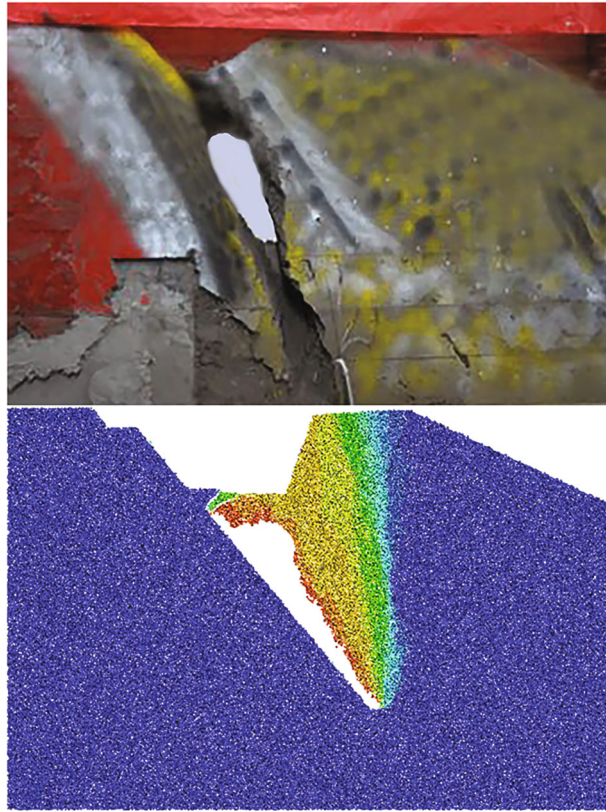
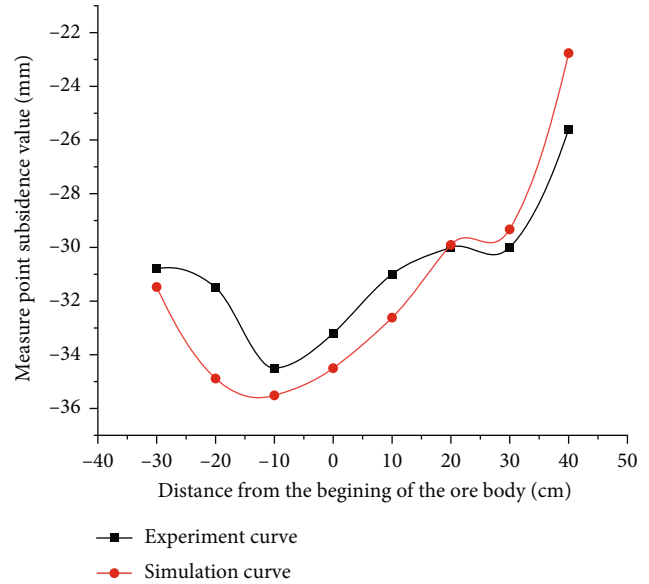


FIGURE 5: Particle flow code (PFC) model diagram and initial contact force distribution.



(a) Comparative picture



(b) Comparative curve

FIGURE 6: Comparative results of the similar material model and the PFC numerical model.

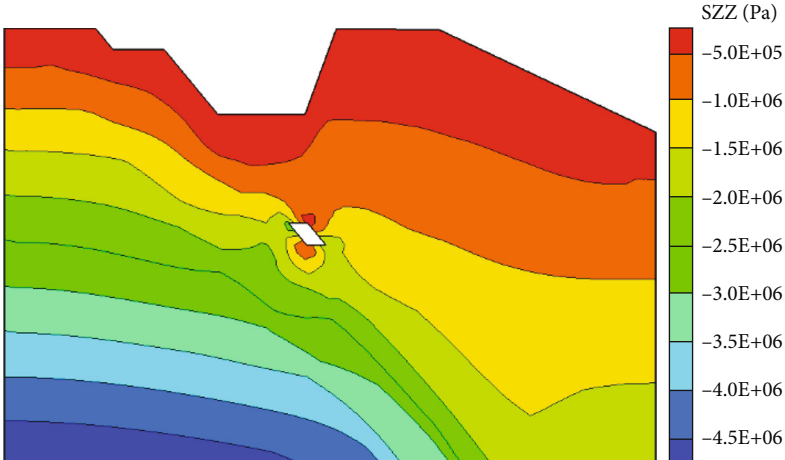
TABLE 2: The final PFC mesoparameters of the rock samples.

Rock type	Parallel bond modulus (gPa)	Cohesion (kPa)	Tension (kPa)	Friction (°)	Stiffness ratio	Density (kg/cm ³)
Quaternary clay	0.17	7.37	7.37	18.2	2.1	1458
Dark gray cryptocrystalline dolomite	0.19	8.42	8.42	30.20	2.1	2089
Off-white coarse-grained dolomite	0.21	7.04	7.04	29.66	2.1	2090
Muddy quartz sandstone	0.16	7.04	7.04	29.52	2.1	2122
Phosphate strata	0.23	10.14	10.14	30.53	2.1	2155
Layered muddy dolomite	0.24	13.44	13.44	30.17	2.1	2122
Muddy dolomite	0.25	11.32	11.32	33.23	2.1	2065
Boundary phosphate strata	0.26	11.81	11.81	30.89	2.1	2078
Off-white layered dolomite	0.29	21.86	21.86	47.23	2.1	2025
Dark gray layered dolomite	0.26	22.67	22.67	30.17	2.1	2125

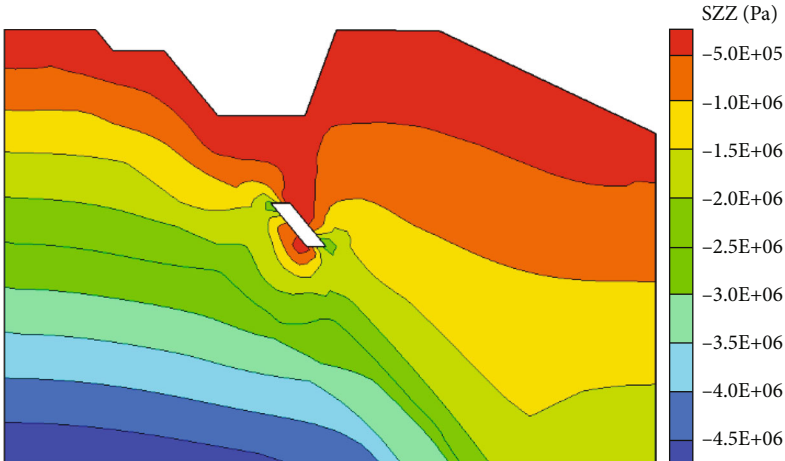
Note: the minimum particle radius is $4e - 3$ m, and the particle size ratio is 1.5.

stabilization. The larger the mining space, the longer the fluctuation time. In detail, the curves in Figure 9(a) reveal that the internal stress in the surrounding rocks at the upper right-hand corner of the roof (measurement circle 1, Figure 8(a)) and the lower left-hand corner of the floor (measurement circle 4, Figure 8(a)) decreases after the first excavation step, thus indicating a process of unloading. After the second excavation step (Figure 8(b)), the internal stress

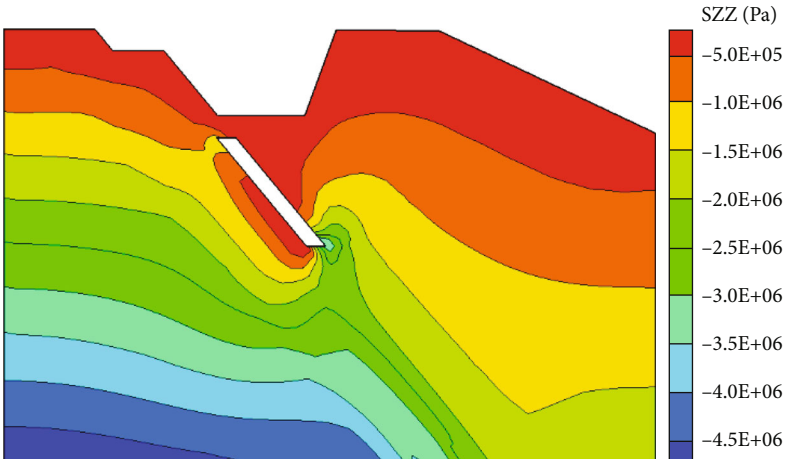
in the surrounding rock at the upper right-hand corner of the roof (measurement circle 11, Figure 8(b)) and the bottom left-hand corner (measurement circle 41, Figure 8(b)) continues to decrease, but the situation is no longer identical at the two locations. Thus, the amplitude of unloading of measurement circle 11 is 8 kPa, while the circle 41 is about 3 kPa. The final absolute stress value of measurement circle 11 after the second excavation step is about 0 kPa. This indicates that



(a) First excavation step



(b) Second excavation step



(c) Fifth excavation step

FIGURE 7: Continued.

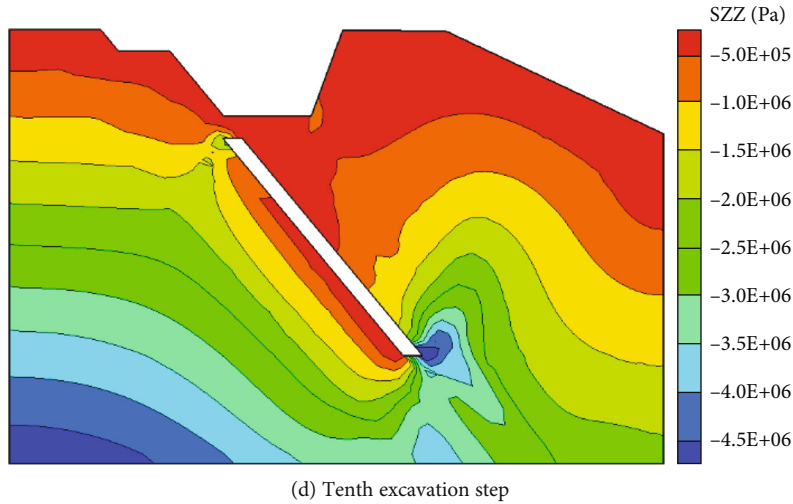


FIGURE 7: Stress distribution after underground excavation.

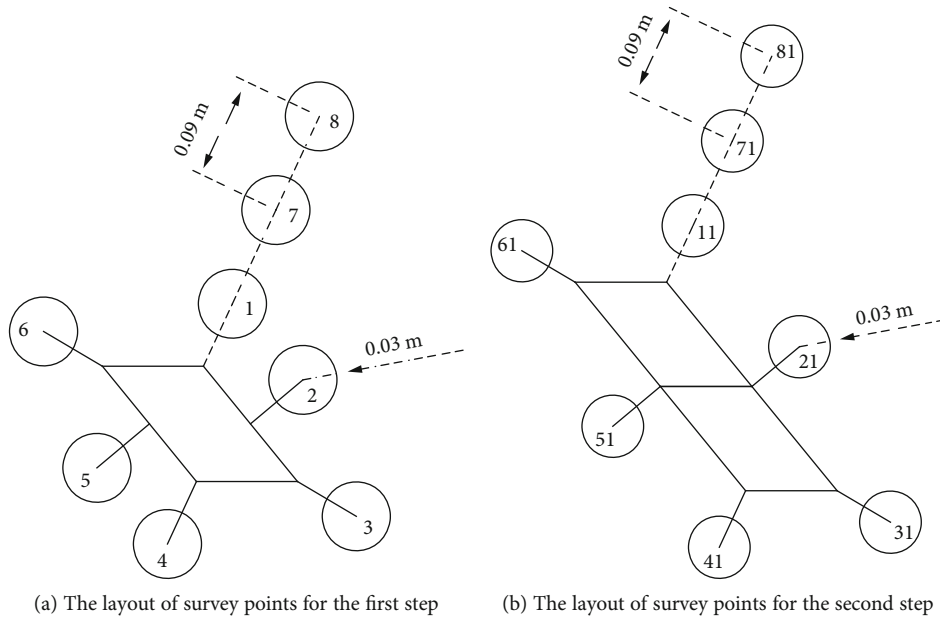


FIGURE 8: The layout of survey points on the surrounding rock and overlying strata in the PFC model for the first excavation step and the second excavation step.

the surrounding rocks at this location are now in a state of stress balance. However, as the excavation space increases during subsequent excavation steps, the unloading area will continue to increase. Hence, due to gravity, this part of the surrounding rock could be placed under tension accompanied by internal bonds breaking and cracks appearing.

Figures 10(a) and 10(b) show the stress evolution in the overlying strata on the right-hand side of the roof and the left-hand side of the floor after the first excavation step (measurement circles 2 and 5, respectively) and after the second excavation step (measurement circles 21 and 51, respectively). An examination of Figure 10(a) indicates that the internal stress of the surrounding rocks on the left and right sides is increased at the end of the first excavation step. In addition, the increase in stress on the left side of the floor

(measurement circle 5, Figure 8(a)) is more pronounced with a maximum amplitude of ~ 3 kPa, whereas that on the right (measurement circle 2, Figure 8(a)) increases slightly. As the mining space is increased during the second excavation step (Figure 10(b)), the pressure on measurement circle 21 continues to increase, whereas that on measurement circle 51 is significantly decreased, because the surrounding rock on the left side of the floor is continuously unloaded during the second excavation step. The absolute stress on the surrounding rocks on the right and left sides at the end of the second excavation step is about 8 kPa and 10 kPa, respectively, thus indicating that the rock mass was not damaged or moved. The above analysis indicates that the internal stress in the surrounding rocks on the left and right sides changes in a complicated manner as the excavation space is

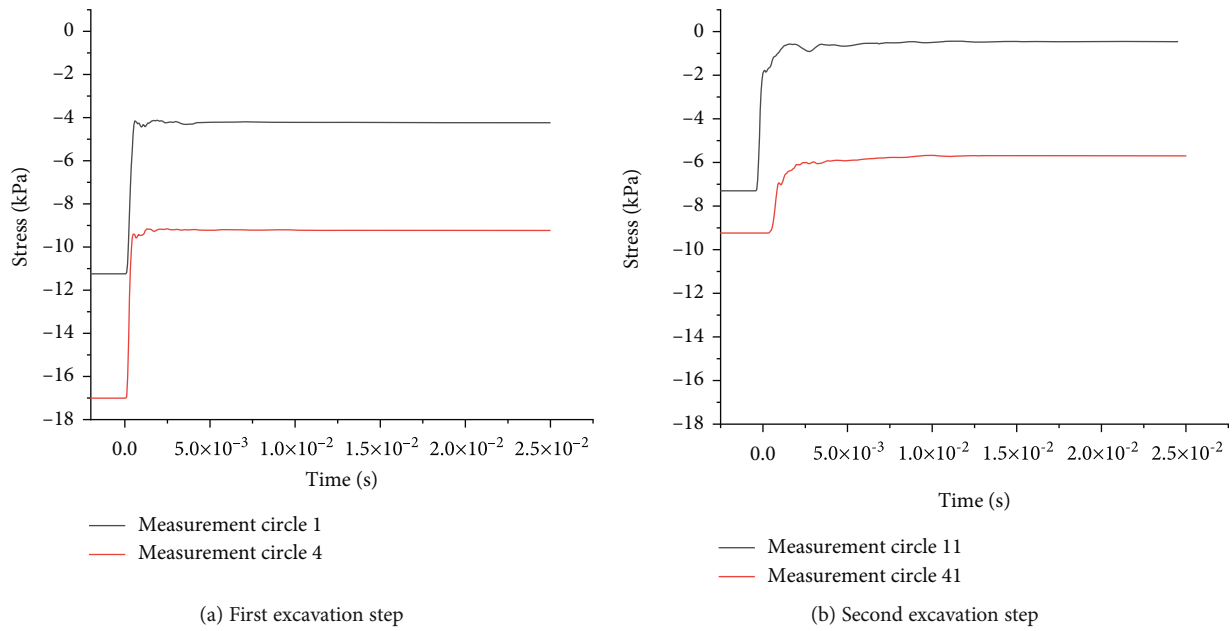


FIGURE 9: Stress evolution in the overlying strata at the upper right-hand corner of the roof and the lower left-hand corner of the floor after the first excavation step (measurement circles 1 and 4, respectively) and after the second excavation step (measurement circles 11 and 41, respectively).

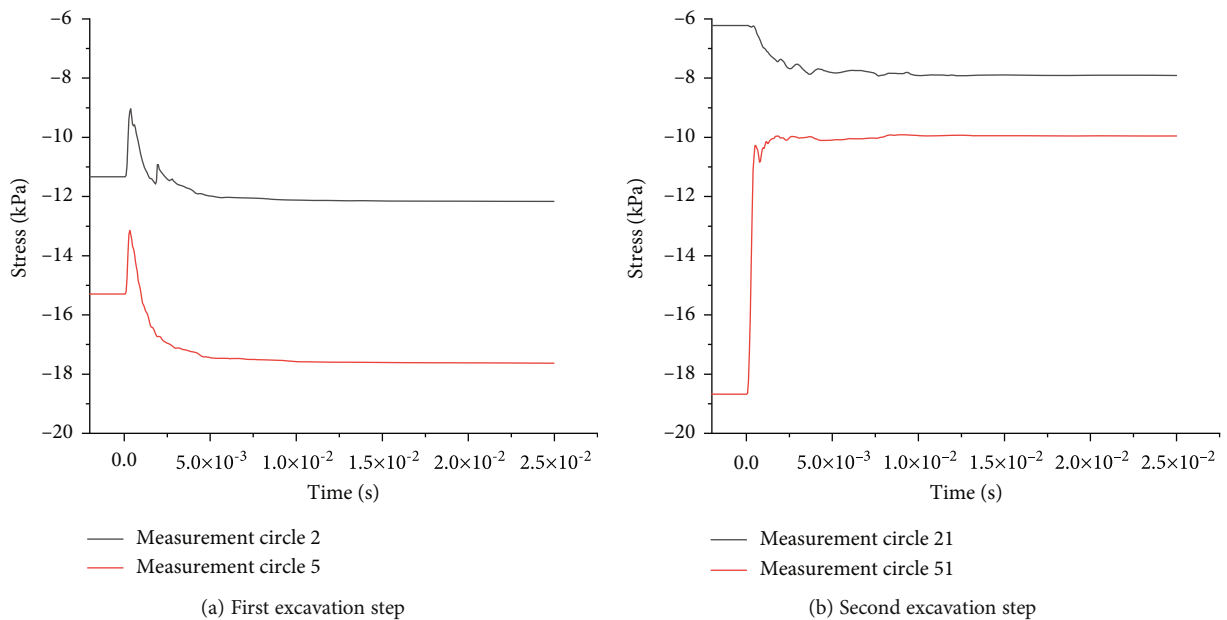


FIGURE 10: Stress evolution in the overlying strata on the right-hand side of the roof and the left-hand side of the floor after the first excavation step (measurement circles 2 and 5, respectively) and after the second excavation step (measurement circles 21 and 51, respectively).

increased. Hence, the scope of the mining space is a key factor affecting the increase in internal stress or the relief of the surrounding rocks.

Figures 11(a) and 11(b) show the stress evolution in the overlying strata at the upper left-hand corner of the roof and the lower right-hand corner of the floor after the first excavation step (measurement circles 3 and 6, respectively) and after the second excavation step (measurement circles 31 and 61, respectively). The results in Figure 11(a) show that

the internal stress in the surrounding rock at the upper left-hand corner of the roof (measurement circle 3, Figure 8(a)) and the lower right-hand corner of the floor (measurement circle 6, Figure 8(a)) increases during the first excavation step, thus indicating a concentration of stress at the two locations. During the second excavation step (Figure 11(b)), the internal stress in the surrounding rock at measurement circle 31 and circle 61 continues to increase with implementation of the excavation space. However, the increase in pressure is

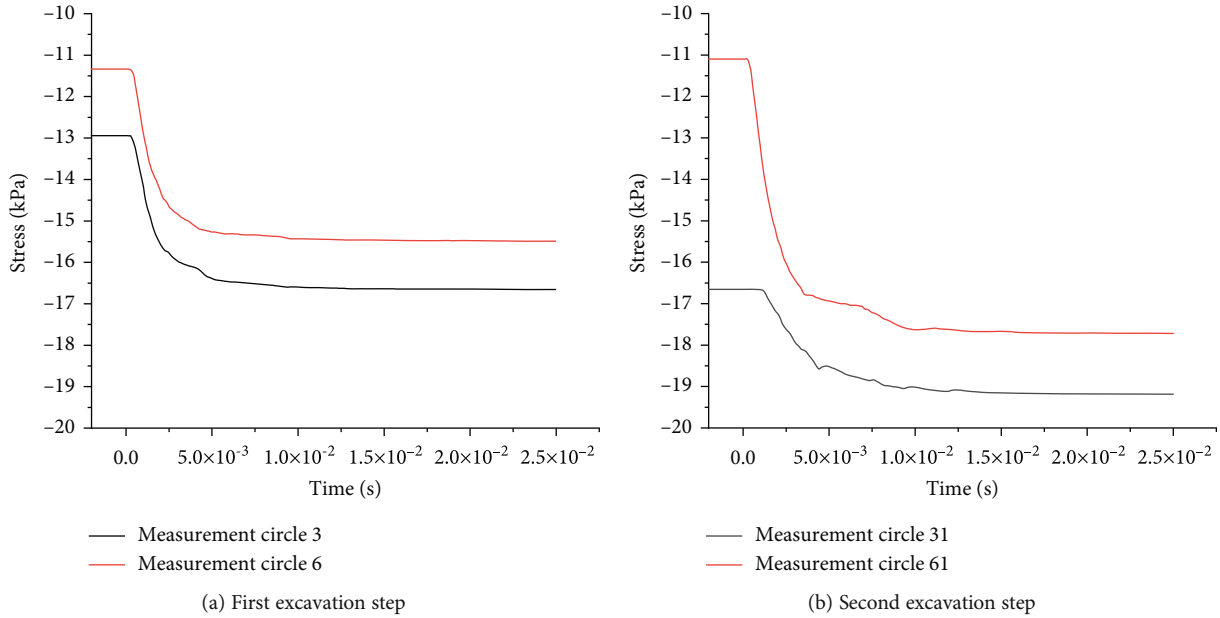


FIGURE 11: Stress evolution in the overlying strata at the upper left-hand corner of the roof and the lower right-hand corner of the floor after the first excavation step (measurement circles 3 and 6, respectively) and after the second excavation step (measurement circles 31 and 61, respectively).

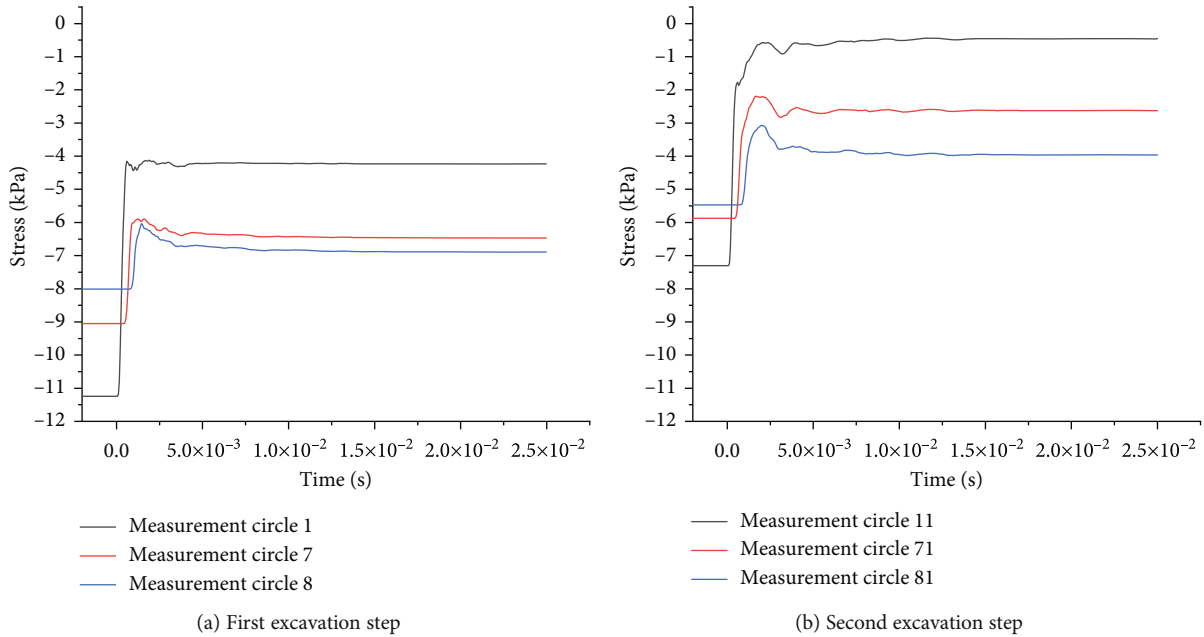


FIGURE 12: Stress evolution in the overlying strata at vertical intervals of 0.09 m on the upper right-hand corner of the roof after the first excavation step (measurement circles 1, 7, and 8) and after the second excavation step (measurement circles 11, 71, and 81).

more marked on the lower right, reaching about 6.5 kPa. In Figure 9(b), the unloading amplitude of the surrounding rock at the upper right-hand corner of the roof is greater during the second excavation. Hence, due to gravity, the roof has a tendency to move downwards and the stress concentrated in the upper left-hand corner. By contrast, the stress on the surrounding rock on the right-hand side is alleviated by the unloading of the overlying rock in the roof, thus limiting

the increase in the internal stress at the lower right-hand corner of the floor.

Figures 12(a) and 12(b) show the stress evolution in the overlying strata at vertical intervals of 0.09 m on the upper right-hand corner of the roof after the first excavation step (measurement circles 1, 7, and 8) and after the second excavation step (measurement circles 11, 71, and 81). During the first excavation step, the results in Figure 12(a) indicate

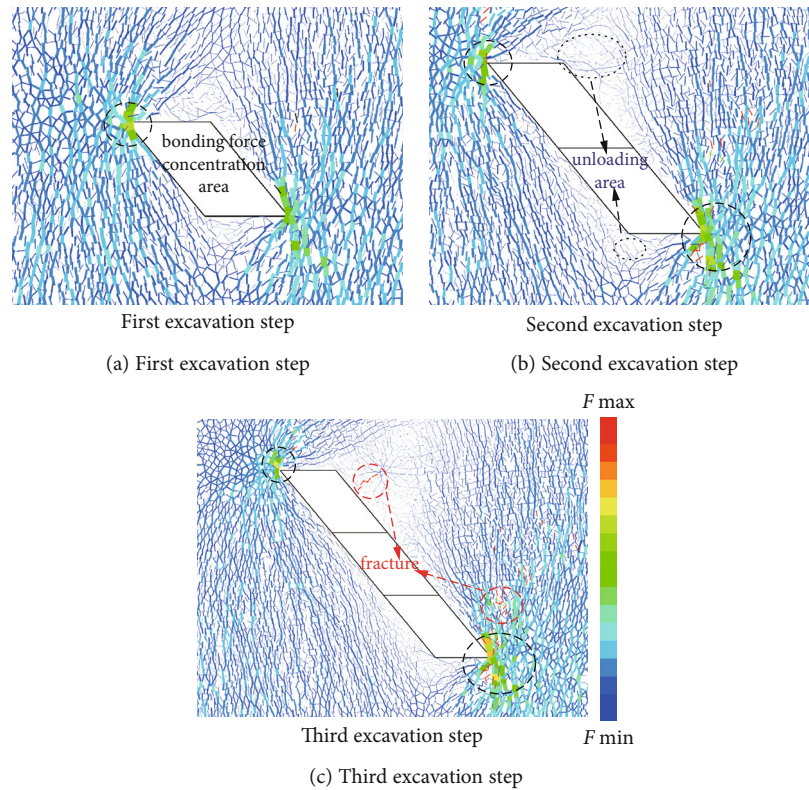


FIGURE 13: Mesoscale force field distribution and crack propagation during the first, second, and third excavation steps.

that the decrease in the internal stress on the overlying strata varies according to the vertical depth. Specifically, the degree of stress reduction decreases with increasing depth so that the original rock level of stress maintains at a certain depth. After the second excavation step (Figure 12(b)), the pattern of pressure relief with depth is like that at the end of the first excavation step. It is evident that the increase in the mined-out area results in a longer fluctuation time for the internal stress in the overlying strata; i.e., the larger the mining space, the longer the overlying rock stress stabilizes.

In brief, the stress evolution curves of overlying strata after various excavation steps (see Figures 8–11) demonstrate that a complicated pattern of internal stress distribution occurs in the adjacent overlying strata during the process of converting from open-pit to underground mining. Thus, both pressure-increasing and pressure-relieving zones exist and are exactly opposite for the roof and the floor. Moreover, the pressure-increasing and pressure-releasing zones in the roof are more severe than those at the floor. In addition, the surrounding rocks on each side form opposite pressure-increasing and pressure-relieving zones during the mining process, with that on the right side being more obvious. Thus, there is an important relationship between the size of the mining space and the pattern of pressure-increasing and pressure-relieving zones. The degree of stress reduction becomes weakened as the distance from the mined-out area increased, and, conversely, the pressure relief becomes more complete closer to the mined-out area, with the stress release being gradually completed towards the deeper parts.

4.4.2. Crack Propagation Behavior of the Surrounding Rock and Overlying Strata after Each Excavation Step. To investigate the mesomechanical characteristics of the surrounding rock and adjacent overlying strata after stepwise excavation, mesoscale distribution of contact forces between particles of binding force F and patterns of crack propagation around the mined-out area are diagrammed in Figures 13–15.

Figures 13(a)–13(c) show the mesoscale force field distribution and crack propagation during the first, second, and third excavation steps, respectively. During step 1, Figure 13(a) reveals the presence of concentrated areas of adhesion at the left-hand corner of the roof and the right-hand of the floor, whereas areas of weak adhesion (i.e., pressure-relieving areas) are indicated at the other two corners of the stope. As the excavation space increases during step 2 (see Figure 13(b)), the increase in pressure on the surrounding rocks becomes more marked. At the same time, the pressure-relieving areas become larger and the pressure relief is greater. As mining continues into step 3 (see Figure 13(c)), the internal tensile stress eventually exceeds the bonding tensile strength. The bonds break and microcracks appear in the pressure-relieving area. This result is consistent with the analyses in Figures 8–11 (physical modeling). Note that a few microcracks also appear in the surrounding rock on the bottom right-hand side of the mined-out area due to gravity. Since the mining space is small, there are no large-scale internal cracks, and the surrounding rock and adjacent overlying rocks remain stable after pressure relief.

Figures 14(a)–14(c) show the mesoscale force field distribution and crack propagation during the fourth, fifth, and

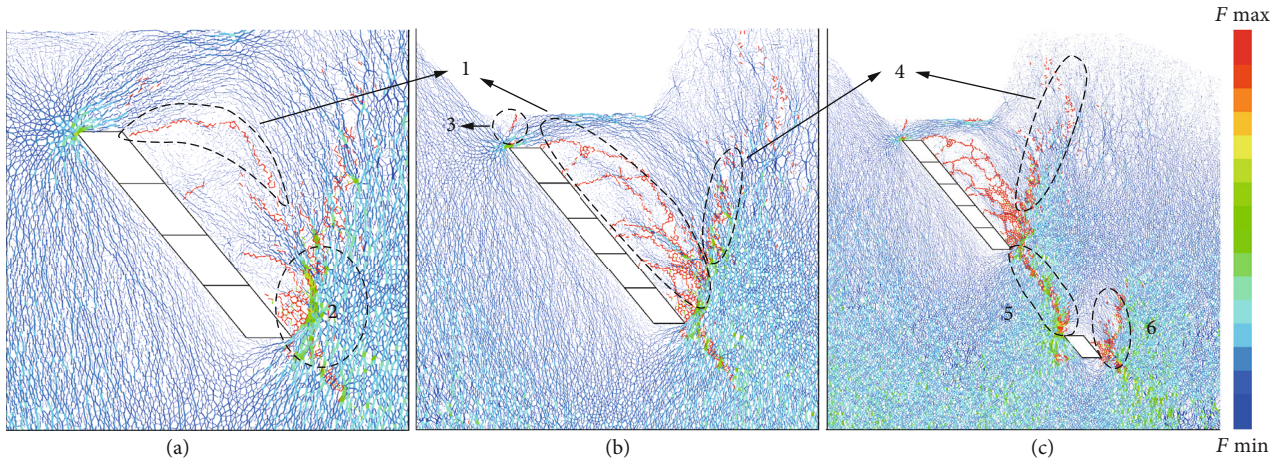


FIGURE 14: Mesoscale force field distribution and crack propagation during the fourth, fifth, and sixth excavation steps.

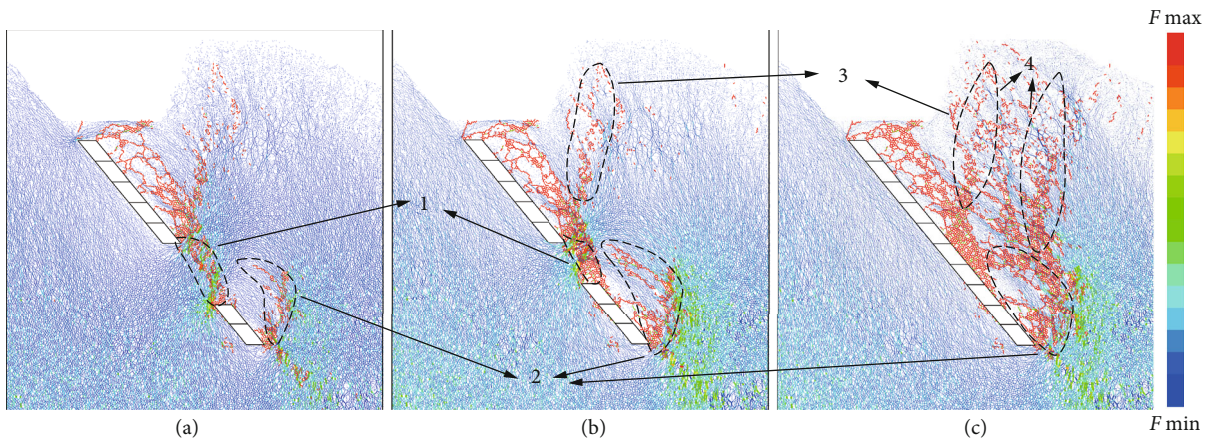


FIGURE 15: Mesoscale force field distribution and crack propagation during the seventh, eighth, and tenth excavation steps.

sixth excavation steps, respectively. With further progress in mining and further increase in the mined-out area during steps 4-6, the cracks expand more noticeably (see Figure 14). During steps 4 and 5, the cracks become arc-shaped and tend to penetrate and connect the upper and lower ends of the stope (labelled 1 in Figure 14). As the surrounding rock on the right ruptures and falls, the area of concentrated cohesive force at the bottom of the surrounding rock moves towards right (area 2 in Figure 14). As the roof of the excavation is close to the ground surface, unloading during mining causes the cracks in the roof, which firstly extend to the ground surface (the area labelled 3 in Figure 14(e)). After the lower part of the surrounding rock on the right-hand side falls and collapses, the cracks gradually expand upwards (area 4). When the next mining level is excavated during step 6 (see Figure 14(f)), the cracks between the upper and lower mining levels penetrated (area 5). Due to the greater depth of the next mining level, the original rock stress is correspondingly greater and, hence, more cracks form at the bottom of the surrounding rock on the right-hand side. Thus, it leads to faster destruction of the rock mass (area 6).

Figures 15(a)–15(c) show the mesoscale force field distribution and crack propagation during the seventh, eighth, and tenth excavation steps, respectively. During the process of mining the next level, the crack propagation behavior is roughly the same as that under the previous mining level; i.e., the cracks extend in arc shapes and penetrate the upper and lower ends of the stope (area 2 in Figure 15). Due to the increase in mining depth, the crack propagation rate is higher than that of the previous mining level such that the fissures around the two mining levels penetrate each other (area 1, see Figure 15) and subsequently propagate to the surface (areas 3 and 4, see Figure 15). At the end of the final excavation step, the relatively independent mined-out area has disappeared (see Figure 15(c)), causing the number of cracks to increase rapidly and propagate to the surface, thus resulting in overall instability of the mined-out area.

In brief, the crack propagation behavior is characterized by expansion in arc shapes and a tendency to penetrate the upper and lower ends of the stope. Moreover, the size of the excavation space is seen to play a key role in the generation, propagation, and penetration of the cracks. Thus, due to the disturbance of the first mining level and the increase in

excavation depth, the damage rate of the surrounding rock and overlying rock in the second mining level is greater and more cracks are generated, thus accelerating the instability of the surrounding rock and overlying strata.

5. Conclusions

The open-pit end slope, the surrounding rock of the pit bottom, and the underground mine constitute a compound mining system after the transfer from open-pit mining to underground mining. During the period of open-pit mining, the rock around the end of slope and the pit bottom is disturbed and, on this basis, the underground excavation leads to secondary disturbance. With the advancement of the excavation space, the dynamic superposition of this secondary disturbance influences the state of the underground surrounding rock and the overlying strata.

The present study has used similar material models and numerical simulation methods to analyze the settlement curves, stress changes, and crack propagation behavior of the surrounding rock and overlying strata during the process of converting from open-pit to underground mining. The fit of the settlement curve from the model experiment with the numerical calculation illustrated the effectiveness of this simulation method enabling an analysis of the internal stress changes and crack propagation behavior of the surrounding rock and overlying strata during the mining process, and the results can be concluded as follows:

- (1) When a gently inclined thin- to medium-thick phosphate deposit was transferred from open-pit to underground mining via a sublevel caving method, the surrounding rock and overlying strata gradually evolved from a stable state through a continuous linear failure state to a final large-scale nonlinear collapse state. The corresponding global subsidence curve was shown to evolve from an irregular ladle shape to a final half-bowl shape
 - (2) The internal stress distribution of the surrounding rock and adjacent overlying rock in the inclined mined-out area during the process of converting from open-pit to underground mining was shown to be complicated. The degrees of pressure increase and pressure relief on the internal stress of the surrounding rock and the adjacent overlying strata in the mined-out area were shown to have an important relationship with the size of the mining space. Specifically, the degree of stress reduction was weakened with increasing distance, and, conversely, the relief of pressure and the release of stress became gradually more complete towards the deeper part closer to the mined-out area
 - (3) The cracks were shown to expand in an arc shape and had a tendency to penetrate the upper and lower ends of the stope. The size of the excavation space was found to play a key role in the generation, propagation, and penetration of the cracks. Due to the disturbance of the first mining level and the increase
- in excavation depth, the rate of damage to the surrounding and overlying rock in the second mining level was greater and more cracks were generated, thus accelerating the instability of the surrounding rock and overlying strata
- (4) Many factors were shown to influence the evolution and dynamic characteristics of rock mass deformation and failure after the transition from open-pit to underground mining. It is therefore necessary to study the time-effect and space-time evolution of the mining response characteristics of the rock mass and the effects of various underground mining methods

Data Availability

Data are available from the authors upon reasonable request.

Conflicts of Interest

The authors declare that they have no conflict of interest.

Acknowledgments

The research work described herein was funded by the National Nature Science Foundation of China (NSFC) (Grant No. 41867033), State Key Laboratory of Safety and Health of Metal Mines Open Fund (Grant No. zdsys2019-005), China Postdoctoral Science Foundation program (Grant No. 2019M650144). These financial supports are gratefully acknowledged.

References

- [1] R. Q. Huang and S. W. Qi, "Engineering geology: review and prospect of past ten years in China," *Journal of Engineering Geology*, vol. 25, no. 2, pp. 257–276, 2017.
- [2] R. Q. Huang, Y. S. Li, and M. Yan, "The implication and evaluation of toppling failure in engineering geology practice," *Journal of Engineering Geology*, vol. 25, no. 5, pp. 1165–1181, 2017.
- [3] E. Bakhtavar, "Transition from open-pit to underground in the case of Chah-Gaz iron ore combined mining," *Journal of Mining Science*, vol. 49, no. 6, pp. 955–966, 2013.
- [4] C. Li, J. B. Zhu, B. Wang, Y. Z. Jiang, and P. Zeng, "Model tests for mechanical response of bedding rock during different excavation and anchoring process," *Chinese Journal of Underground Space and Engineering*, vol. 13, no. 1, pp. 271–278, 2017.
- [5] X. S. Li, Y. M. Wang, K. Zhao, and S. Yang, "Research progress on the key problems in transition from open-pit to underground mining for metal mines," *Metal Mine*, vol. 12, pp. 12–20, 2019.
- [6] S. G. Sun, M. F. Cai, and S. J. Wang, "Study of sliding mechanism for slope due to the excavation form open pit into underground mine," *Chinese Journal of Rock Mechanics and Engineering*, vol. 19, no. 1, pp. 126–129, 2000.
- [7] G. Z. Yin, X. S. Li, and Y. J. Li, "Simulation on the deformation and failure response features and stability of a slope from open pit mining to underground mining under the effecting of

- excavation goaf by the floor friction model,” *Journal of University of Science and Technology Beijing*, vol. 34, no. 3, pp. 231–238, 2012.
- [8] W. D. Song, J. H. Du, X. C. Yang, and D. D. Tannant, “Deformation and failure of a high steep slope due to transformation from deep open pit to underground mining,” *Journal of University of Science and Technology Beijing*, vol. 32, no. 2, pp. 145–151, 2010.
- [9] G. Z. Yin, X. S. Li, Z. A. Wei, Y. J. Li, and Q. S. Wang, “Similar simulation study of deformation and failure response features of slope and stope rocks,” *Chinese Journal of Rock Mechanics and Engineering*, vol. 30, Supplement 1, pp. 2913–2923, 2011.
- [10] X. S. Li, X. Y. Zhi, D. M. Zhang, and M. L. Wang, “Research on deformation and failure character and the thickness-effect of the overlying strata transition from open pit to underground mining,” in *National Engineering Geology Annual Conference*, Gui Lin City, Guang Xi province, China, 2017.
- [11] H. Liu, W. S. Chen, X. T. Feng, and Q. R. Chen, “Numerical modeling of Daye iron open-pit-mine transferring to underground mining by discrete element method,” *Rock and Soil Mechanics*, vol. 25, no. 9, pp. 1413–1417, 2004.
- [12] F. Han, F. Xie, and J. A. Wang, “3-D numerical simulation on the stability of rocks in transferred underground mining from open-pit,” *Journal of University of Science and Technology Beijing*, vol. 28, no. 6, pp. 509–514, 2006.
- [13] X. Z. Shi, G. H. Huang, S. Zhang, and J. Zhou, “Goaf surrounding rock deformation and failure features using FLAC3D in underground mining shifted from open-pit in complex situation,” *Journal of Central South University (Science and Technology)*, vol. 42, no. 6, pp. 1710–1718, 2011.
- [14] J. Y. Chen, X. Z. Shi, J. Zhou, and X. Y. Qiu, “Deformation prediction and reliability analysis of underground mining shifted from open-pit based on orthogonal experiment,” *The Chinese Journal of Nonferrous Metals*, vol. 26, no. 11, pp. 2383–2392, 2016.
- [15] Y. H. Li, “Study on digital photography-based deformation measurement technique and its application in geo-physical model experiment,” *Chinese Journal of Rock Mechanics and Engineering*, vol. 24, no. 7, p. 184, 2005.
- [16] W. D. Song, J. X. Fu, and D. X. Wang, “Study on physical and numerical simulation of failure laws of wall rock due to transformation from open-pit to underground mining,” *Journal of China Coal Society*, vol. 37, no. 2, pp. 186–191, 2012.
- [17] Y. F. Wang and F. P. Zhong, “Study on slope instability in transition from open-pit to underground mining by similar experiment and numerical simulation,” *Journal of China Coal Society*, vol. 38, Supplement 1, pp. 64–69, 2013.
- [18] D. B. Zhang, *Research of Similarity Model Test for Open Pit to Underground Mining with Super High-Steep Slope*, China University Of Geosciences, Wuhan, 2013.
- [19] Y. M. Zhang, F. S. Ma, J. M. Xu, and H. J. Zhao, “Deformation laws of rock mass due to transform from open-pit to underground mining in high stress area,” *Rock and Soil Mechanics*, vol. 32, Supplement 1, pp. 590–595, 2011.
- [20] J. Y. Cao, *The Deformation Behavior and Occurrence Mechanism of Pit Surrounding Rock after the Transition from Open-Pit Mining to Underground Mining*, Shandong University of Science and Technology, Shandong, 2015.
- [21] Q. H. Deng, J. Y. Cao, L. P. Zhang, F. S. Ma, and J. M. Xu, “Uplift mechanism of the bottom of open pit after the transition from open-pit mining to underground mining in Longshou mine,” *Journal of Mining and Safety Engineering*, vol. 32, no. 4, pp. 677–682, 2015.
- [22] T. B. Jia, “The dynamic prediction of environment damage induced by the excavation from open-pit into underground mine,” *Journal of Safety Science and Technology*, vol. 11, no. 3, pp. 99–104, 2015.
- [23] N. Jiang, C. B. Zhou, S. W. Lu, and Z. Zhang, “Propagation and prediction of blasting vibration on slope in an open pit during underground mining,” *Tunnelling and Underground Space Technology*, vol. 70, no. 1, pp. 409–421, 2017.
- [24] G. W. Cheng, C. X. Chen, L. C. Li et al., “Numerical modelling of strata movement at footwall induced by underground mining,” *International Journal of Rock Mechanics and Mining Sciences*, vol. 108, pp. 142–156, 2018.
- [25] X. M. Fan, F. Y. Ren, D. Xiao et al., “Improved induced caving mining method for hanging wall ore with deep concave features,” *Dongbei Daxue Xuebao/Journal of Northeastern University*, vol. 39, no. 9, pp. 1321–1326, 2018.
- [26] X. M. Fan, F. Y. Ren, D. Xiao, and Y. C. Mao, “Opencast to underground iron ore mining method,” *Journal of Central South University of Technology Science & technology of mining and metallurgy*, vol. 25, no. 7, pp. 1813–1824, 2018.
- [27] F. Y. Ren, B. H. Tan, Y. Fu, and Q. Zhu, “Slope failure caused by hanging-wall ores mining by induced caving method,” *Journal of Northeastern University (Natural Science)*, vol. 40, no. 2, pp. 273–277+283, 2019.
- [28] B. Regassa, N. Xu, and G. Mei, “An equivalent discontinuous modeling method of jointed rock masses for DEM simulation of mining-induced rock movements,” *International Journal of Rock Mechanics and Mining Sciences*, vol. 108, pp. 1–14, 2018.
- [29] K. Xia, C. Chen, Y. Deng et al., “In situ monitoring and analysis of the mining-induced deep ground movement in a metal mine,” *International Journal of Rock Mechanics and Mining Sciences*, vol. 109, pp. 32–51, 2018.
- [30] R. Yong, J. Ye, B. Li, and S. G. du, “Determining the maximum sampling interval in rock joint roughness measurements using Fourier series,” *International Journal of Rock Mechanics and Mining Sciences*, vol. 101, pp. 78–88, 2018.
- [31] Y. Zhao, T. H. Yang, M. Bohnhoff et al., “Study of the rock mass failure process and mechanisms during the transformation from open-pit to underground mining based on micro-seismic monitoring,” *Rock Mechanics and Rock Engineering*, vol. 51, no. 5, pp. 1473–1493, 2018.
- [32] Q. Y. Zhang, Y. Zhang, K. Duan, C. C. Liu, Y. S. Miao, and D. Wu, “Large-scale geo-mechanical model tests for the stability assessment of deep underground complex under true-triaxial stress,” *Tunnelling and Underground Space Technology*, vol. 83, no. 1, pp. 577–591, 2019.
- [33] C. Zhang, P. Zou, Y. Wang, T. Jiang, H. Lin, and P. Cao, “An elasto-visco-plastic model based on stress functions for deformation and damage of water-saturated rocks during the freeze-thaw process,” *Construction and Building Materials*, vol. 250, article 118862, 2020.
- [34] C. Zhang, Y. Wang, and T. Jiang, “The propagation mechanism of an oblique straight crack in a rock sample and the effect of osmotic pressure under in-plane biaxial compression,” *Arabian Journal of Geosciences*, vol. 13, no. 15, p. 736, 2020.
- [35] R. Cao, R. Yao, J. J. Meng, Q. Lin, H. Lin, and S. Li, “Failure mechanism of non-persistent jointed rock-like specimens under uniaxial loading: laboratory testing,” *International*

- Journal of Rock Mechanics and Mining Sciences*, vol. 132, article 104341, 2020.
- [36] R. H. Cao, R. Yao, T. Hu, C. Wang, K. Li, and J. Meng, "Failure and mechanical behavior of transversely isotropic rock under compression-shear tests: laboratory testing and numerical simulation," *Engineering Fracture Mechanics*, vol. 241, article 107389, 2021.
- [37] R. H. Cao, C. Wang, R. Yao et al., "Effects of cyclic freeze-thaw treatments on the fracture characteristics of sandstone under different fracture modes: laboratory testing," *Theoretical and Applied Fracture Mechanics*, vol. 109, article 102738, 2020.
- [38] Y. X. Wang, S. B. Shan, C. Zhang, and P. P. Guo, "Seismic response of tunnel lining structure in a thick expansive soil stratum," *Tunnelling and Underground Space Technology*, vol. 88, pp. 250–259, 2019.
- [39] Y. Chen, G. Wen, and J. Hu, "Analysis of deformation characteristics of fully grouted rock bolts under pull-and-shear loading," *Rock Mechanics and Rock Engineering*, vol. 53, no. 7, pp. 2981–2993, 2020.
- [40] Y. Zhao, L. Zhang, J. Liao, W. Wang, Q. Liu, and L. Tang, "Experimental study of fracture toughness and subcritical crack growth of three rocks under different environments," *International Journal of Geomechanics*, vol. 20, no. 8, article 04020128, 2020.
- [41] Y. Zhao, L. Zhang, W. Wang, Q. Liu, L. Tang, and G. Cheng, "Experimental study on shear behavior and a revised shear strength model for infilled rock joints," *International Journal of Geomechanics*, vol. 20, no. 9, article 04020141, 2020.
- [42] Y. Zhao, C. Zhang, Y. Wang, and H. Lin, "Shear-related roughness classification and strength model of natural rock joint based on fuzzy comprehensive evaluation," *International Journal of Rock Mechanics and Mining Sciences*, vol. 137, article 104550, 2021.
- [43] Y. Zhao, C. L. Wang, and J. Bi, "Analysis of fractured rock permeability evolution under unloading conditions by the model of elastoplastic contact between rough surfaces," *Rock Mechanics and Rock Engineering*, vol. 53, no. 12, pp. 5795–5808, 2020.
- [44] S. J. Xie, H. Lin, Y. Chen, R. Yong, W. Xiong, and S. Du, "A damage constitutive model for shear behavior of joints based on determination of the yield point," *International Journal of Rock Mechanics and Mining Sciences*, vol. 128, article 104269, 2020.
- [45] S. J. Xie, H. Lin, Y. Wang et al., "A statistical damage constitutive model considering whole joint shear deformation," *International Journal of Damage Mechanics*, vol. 29, no. 6, pp. 988–1008, 2020.
- [46] Y. Zheng, C. Chen, F. Meng, H. Zhang, K. Xia, and X. Chen, "Assessing the stability of rock slopes with respect to block-flexure toppling failure using a force-transfer model and genetic algorithm," *Rock Mechanics and Rock Engineering*, vol. 53, no. 8, pp. 3433–3445, 2020.
- [47] R. Jiang, F. Dai, Y. Liu, and A. Li, "Fast marching method for microseismic source location in cavern-containing rockmass: performance analysis and engineering application," *Engineering*, vol. 4, 2020.
- [48] C. Zhang, Y. Wang, H. Ruan, B. Ke, and H. Lin, "The strain characteristics and corresponding model of rock materials under uniaxial cyclic load/unload compression and their deformation and fatigue damage analysis," *Archive of Applied Mechanics*, 2021.
- [49] Y. Zheng, C. Chen, F. Meng, T. Liu, and K. Xia, "Assessing the stability of rock slopes with respect to flexural toppling failure using a limit equilibrium model and genetic algorithm," *Computers and Geotechnics*, vol. 124, article 103619, 2020.
- [50] Y. Zheng, C. Chen, T. Liu, H. Zhang, and C. Sun, "Theoretical and numerical study on the block-flexure toppling failure of rock slopes," *Engineering Geology*, vol. 263, article 105309, 2019.
- [51] Y. Zheng, C. Chen, T. Liu, D. Song, and F. Meng, "Stability analysis of anti-dip bedding rock slopes locally reinforced by rock bolts," *Engineering Geology*, vol. 251, pp. 228–240, 2019.
- [52] Y. Zheng, C. Chen, T. Liu, H. Zhang, K. Xia, and F. Liu, "Study on the mechanisms of flexural toppling failure in anti-inclined rock slopes using numerical and limit equilibrium models," *Engineering Geology*, vol. 237, pp. 116–128, 2018.
- [53] Y. Chen and H. Lin, "Consistency analysis of Hoek-Brown and equivalent Mohr-Coulomb parameters in calculating slope safety factor," *Bulletin of Engineering Geology and the Environment*, vol. 78, no. 6, pp. 4349–4361, 2019.
- [54] H. Lin, H. Yang, Y. Wang, Y. Zhao, and R. Cao, "Determination of the stress field and crack initiation angle of an open flaw tip under uniaxial compression," *Theoretical and Applied Fracture Mechanics*, vol. 104, article 102358, 2019.
- [55] Y. Wang, P. Guo, H. Lin et al., "Numerical analysis of fiber-reinforced soils based on the equivalent additional stress concept," *International Journal of Geomechanics*, vol. 19, no. 11, article 04019122, 2019.
- [56] X. Fan, Z. Yang, and K. Li, "Effects of the lining structure on mechanical and fracturing behaviors of four-arc shaped tunnels in a jointed rock mass under uniaxial compression," *Theoretical and Applied Fracture Mechanics*, vol. 112, p. 102887, 2021.
- [57] J. Meng, X. Zhang, J. Huang, H. Tang, H. Mattsson, and J. Laue, "A smoothed finite element method using second-order cone programming," *Computers and Geotechnics*, vol. 123, article 103547, 2020.
- [58] F. Wang, P. Cao, Y. Wang, R. Hao, J. Meng, and J. Shang, "Combined effects of cyclic load and temperature fluctuation on the mechanical behavior of porous sandstones," *Engineering Geology*, vol. 266, article 105466, 2020.
- [59] K. Li, Y. Cheng, Z. Y. Yin, D. Han, and J. Meng, "Size effects in a transversely isotropic rock under Brazilian tests: laboratory testing," *Rock Mechanics and Rock Engineering*, vol. 53, no. 6, pp. 2623–2642, 2020.
- [60] K. H. Li, Z. Y. Yin, Y. Cheng, P. Cao, and J. Meng, "Three-dimensional discrete element simulation of indirect tensile behaviour of a transversely isotropic rock," *International Journal for Numerical and Analytical Methods in Geomechanics*, vol. 44, no. 13, pp. 1812–1832, 2020.
- [61] H. Lin, Y. Zhu, J. Yang, and Z. Wen, "Anchor stress and deformation of the bolted joint under shearing," *Advances in Civil Engineering*, vol. 2020, Article ID 3696489, 10 pages, 2020.
- [62] C. Y. Zhang, C. Pu, R. Cao, T. Jiang, and G. Huang, "The stability and roof-support optimization of roadways passing through unfavorable geological bodies using advanced detection and monitoring methods, among others, in the Sanmenxia Bauxite Mine in China's Henan Province," *Bulletin of Engineering Geology and the Environment*, vol. 78, no. 7, pp. 5087–5099, 2019.
- [63] H. Lin, D. Lei, R. Yong, C. Jiang, and S. du, "Analytical and numerical analysis for frost heaving stress distribution within

- rock joints under freezing and thawing cycles,” *Environmental Earth Sciences*, vol. 79, no. 12, p. 305, 2020.
- [64] H. Lin, X. Zhang, R. Cao, and Z. Wen, “Improved nonlinear Burgers shear creep model based on the time-dependent shear strength for rock,” *Environmental Earth Sciences*, vol. 79, no. 6, p. 149, 2020.
- [65] Z. M. He, D. Xiang, Y. X. Liu, Q. F. Gao, and H. B. Bian, “Deformation behavior of coarse-grained soil as an embankment filler under cyclic loading,” *Advances in Civil Engineering*, vol. 2020, Article ID 4629105, 13 pages, 2020.
- [66] Z. M. He, Z. F. Liu, X. H. Liu, and H. B. Bian, “Improved method for determining active earth pressure considering arching effect and actual slip surface,” *Journal of Central South University*, vol. 27, no. 7, pp. 2032–2042, 2020.
- [67] X. Fan, X. Jiang, Y. Liu, H. Lin, K. Li, and Z. He, “Local stress distribution and evolution surrounding flaw and opening within rock block under uniaxial compression,” *Theoretical and Applied Fracture Mechanics*, vol. 112, article 102914, 2021.
- [68] H. Ozturk and D. Guner, “Laboratory and distinct element analysis of the deformability behaviour of thin spray-on liners,” *International Journal of Rock Mechanics and Mining Sciences*, vol. 123, article 104118, 2019.
- [69] Y. Zhou, D. Zhao, Q. Tang, and M. Wang, “Experimental and numerical investigation of the fatigue behaviour and crack evolution mechanism of granite under ultra-high-frequency loading,” *Royal Society Open Science*, vol. 7, no. 4, 2020.
- [70] J. C. Wang, W. J. Wei, J. W. Zhang, B. Mishra, and A. Li, “Numerical investigation on the caving mechanism with different standard deviations of top coal block size in LTCC,” *International Journal of Mining Science and Technology*, vol. 30, no. 5, pp. 34–42, 2020.

Research Article

Coupled Effects of Water and Low Temperature on Quasistatic and Dynamic Mechanical Behavior of Sandstone

Zilong Zhou, Yude E , Xin Cai , and Jing Zhang 

School of Resources and Safety Engineering, Central South University, Changsha 410083, China

Correspondence should be addressed to Xin Cai; xincai@csu.edu.cn and Jing Zhang; zjaimme@csu.edu.cn

Received 19 March 2021; Accepted 22 April 2021; Published 5 May 2021

Academic Editor: Dayang Xuan

Copyright © 2021 Zilong Zhou et al. This is an open access article distributed under the Creative Commons Attribution License, which permits unrestricted use, distribution, and reproduction in any medium, provided the original work is properly cited.

The mechanical behavior of rock materials is critically affected by water and temperature. To comprehensively study the coupled effects of water saturation and low temperature on the mechanical properties of sandstone, both quasistatic and dynamic compressive tests were performed on dry and water-saturated specimens under room temperature and -60°C . The results indicated that under the same strain rate, at room temperature, the compression strength and elastic modulus of the sandstone specimen are significantly reduced when the specimen becomes water-saturated. However, at -60°C , the compression strength and elastic modulus of the dry specimen notably increase compared to that at room temperature. Interestingly, these mechanical parameters of the saturated-frozen specimen are lower than that of the dry one but slightly higher than that of the saturated specimen under room temperature. Moreover, regardless of temperature, the saturated specimens have a higher strain rate dependence in terms of strength. The dual effects of water and subzero temperature of the mechanical behavior of rock are discussed.

1. Introduction

In China, a growing number of rock engineering projects (such as mining, tunneling, and railway) are constructed and proceeded in cold regions due to demands for resources and national strategies. The air temperature regularly falls below zero degrees Celsius in cold regions, where the rocks on the ground are frozen [1]. Furthermore, in some severe cold regions, such as Tibet plateau, Great Khingan mountains, the north Xinjiang area, and Inner Mongolian plateau, the lowest air temperature even can be below 60°C [2–4]. The extremely low temperature will lead to the changes of mechanical properties of rock especially with the presence of water [5, 6]. Therefore, an in-depth understanding of the freezing effects on rock performance is crucial for the security and stability of rock engineering projects in cold regimes.

In recent years, the mechanical and deformation properties of frozen rocks have been extensively studied. For instance, Winkler [7] conducted a lot of tests on rock at subzero temperature. He found that the lower the temperature, the greater the frost heave force generated by the pore ice. Inada and Yokota [8] carried out uniaxial compression and tension tests on granite and andesite specimens after being

frozen up to -160°C . They reported that at -160°C , the UCS and tensile strength of two tested rocks increase compared to that tested at room temperature. Aoki et al. [9] performed similar tests on five kinds of rock types. They however discovered that the mechanical properties of five rocks decrease in different extents after freezing. The UCS loss of rocks ranges from 20% to 70%, the loss in indirect tensile strength from 50% to 100%, and the loss in Young's modulus is about 20%. Yamabe and Neaupane [10] found that the UCS and Young's modulus decrease with the decline of temperature from 20°C to -10°C , while the UCS increases in temperature from -10°C to -20°C and Young's modulus further decreases. Moreover, Dwivedi et al. [11] conducted cracked chevron-notched Brazilian disc tests on eight kinds of rocks in temperature from -10°C to -50°C to study the temperature dependence of fracture toughness. They suggested that the fracture toughness of all tested rock types shows the negative linear relationship with temperature. Tang et al. [12] carried out triaxial compressive tests on granite specimens under -10°C to -50°C . Their test results showed that the compressive strength and cohesion of the granite are inversely proportional to temperature. The temperature of -40°C is the critical temperature below which the strength and cohesion

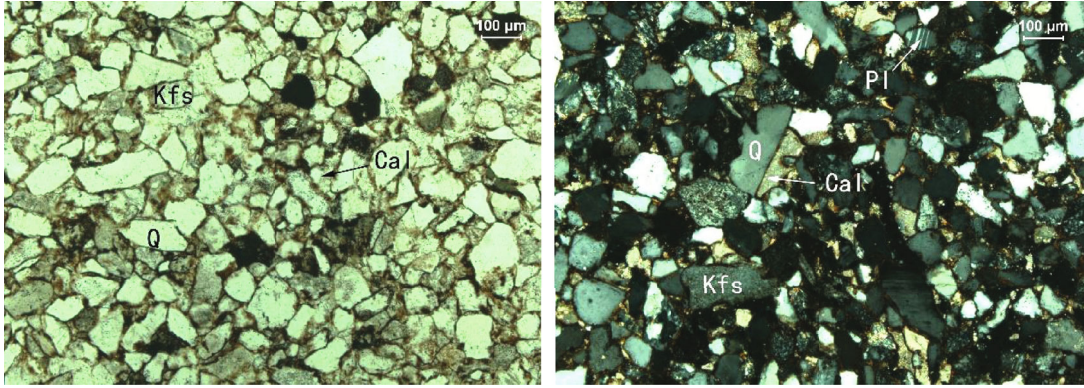


FIGURE 1: Optical microscopy analysis of the sandstone.

become stable. It is universally accepted that the mechanical behavior of rock materials tested under wet conditions is more sensitive to low temperature than that tested under dry condition [9]. For the wet rock under subzero temperatures, it can be considered as a water-ice-rock mixture [13]. Prior studies indicate that the mechanical response of frozen rock is very complicated, and the mechanical characteristics are controlled by the coupled effects of water weakening and ice enhancing. To be specific, the presence of water has weakening effects on rock strength and stiffness [14–18], whereas the ice can resist the rock deformation to enhance the rock integrity [19–21].

The abovementioned works mainly focus on the mechanical properties of rock under subzero temperatures tested in quasistatic loading conditions, in which the strain rate of rock specimen is very low around the magnitude of 10^{-4} s^{-1} . However, in some particular engineering projects constructed in cold regions, rock masses inevitably suffer from low-temperature weathering and dynamic disturbances concurrently [22]. The dynamic disturbances probably come from mining, drilling tunneling, or seismic activities [14, 15, 23–25]. As evidenced by previous studies [26, 27], the mechanical behavior of rocks under dynamic loadings is remarkably different from that under static ones [28]. Hence, it is necessary to study the dynamic mechanical properties of rocks at extremely low temperature.

The objective of the present study is to investigate the effects of low temperature on the dynamic mechanical behavior of rock. Series of high strain rate tests were conducted on dry and water-saturated sandstone specimens under room temperature and -60°C by using a split Hopkinson pressure bar apparatus. Quasistatic compressive tests were also performed for comparison. The effects of temperature and strain rate on dynamic strength, Young's modulus, failure strain, and energy dissipation were obtained. The water-weakening and ice-enhancing mechanisms for mechanical properties of water-saturated sandstone specimens at -60°C were discussed.

2. Experimental Material and Methodology

2.1. Description of Rock Material. The rock material used in this study is a sandstone collected from the southwest area of Sichuan province, China. Figure 1 presents microscopic

TABLE 1: Mineral composition of sandstone specimen.

Mineral composition	Content (%)
Quartz	46
Potash feldspar	18
Calcite	18
Plagioclase	8
Hematite	5
Chlorite	2
Sericite	2



FIGURE 2: MTS-322 used for quasistatic tests.

images of the sandstone using optical microscopy. The sandstone is fine-grained, and its cementation type is pore cementation. The mineral compositions of this sandstone

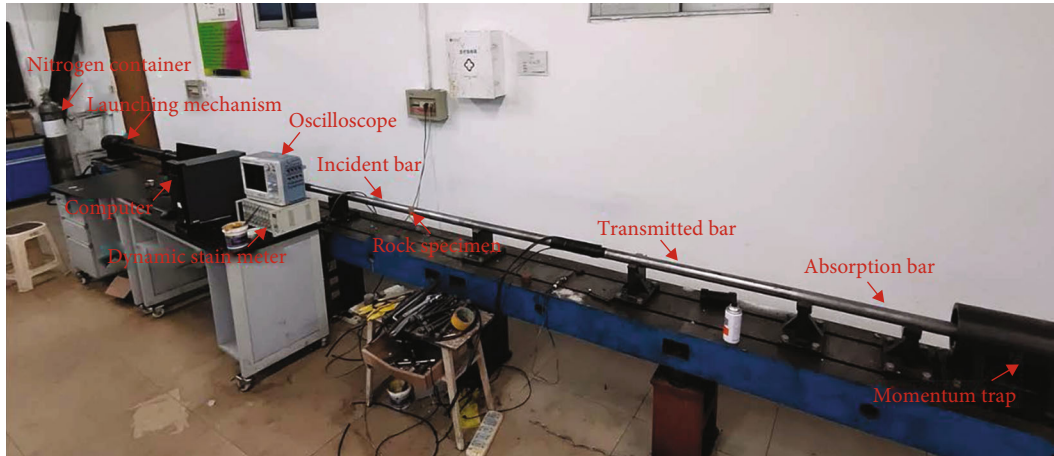


FIGURE 3: Photographic view of SHPB setup.

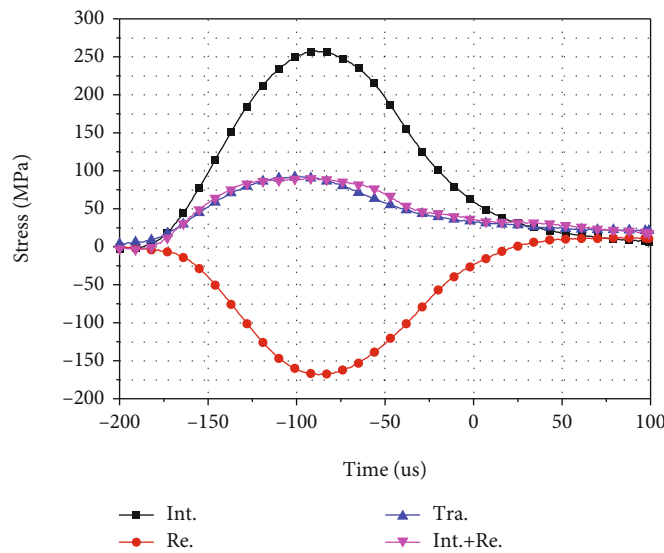


FIGURE 4: Dynamic force equilibrium.

and corresponding percentage were determined by the X-ray diffraction (XRD) technique. As listed in Table 1, the sandstone consists mainly of five minerals, including quartz (46%), potash feldspar (18%), calcite (18%), plagioclase (8%), and hematite (5%). The chlorite and sericite contents are less than 2% by weight. Crucial physical parameters of the sandstone were also measured as density of 2410 kg/m^3 , P-wave velocity of 3499 m/s , and water absorption of 3.37%.

2.2. Specimen Preparation. All specimens were manufactured in accordance with standards of the International Society for Rock Mechanics and Rock Engineering (ISRM) [29, 30]. To minimize the variation in properties across the specimens and reduce the dispersion of tested data, all cores in 50 mm diameter were first drilled from the same rock in the same direction. After which, rock cores were cut into the specified lengths. For quasistatic tests, the aspect ratio of specimens is about 2.0 while that for dynamic tests is 1.0. Then, the ends of all specimens were polished with a grinder to make the surface roughness less than 0.05 mm, and the end face was

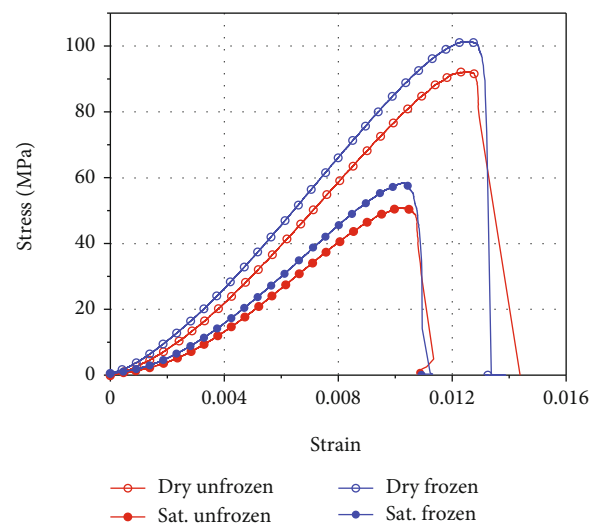


FIGURE 5: Stress-strain curves of dry and water-saturated specimens tested under uniaxial compression.

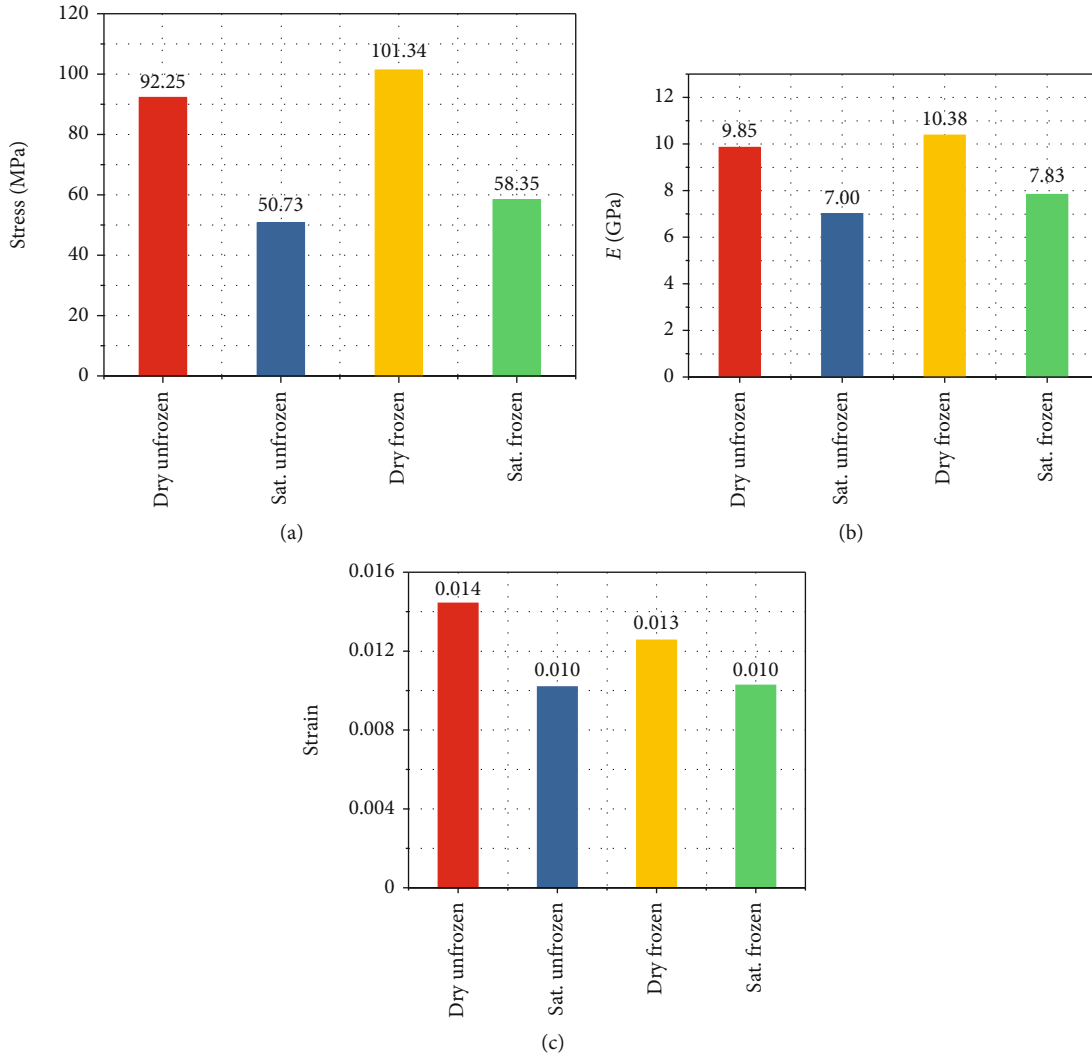


FIGURE 6: The (a) UCS, (b) E , and (c) failure strain values of specimens under uniaxial compression.

vertical to the axis of the specimen with a deviation less than 0.25° .

All specimens were placed in an oven set at the 105°C constant temperature for more than 48 h to remove the moisture in specimens. After that, they were taken out and placed in laboratory for air-cooling. Then, half of them were submerged in distilled water for at least 48 h for free soaking such that specimens can reach a water-saturation state [16, 31]. To prepare frozen specimens, half specimens were chosen from each dry and saturated set of specimens. They were put in a refrigerator at a constant temperature of -60°C for more than 48 h.

2.3. Experimental Apparatus

2.3.1. Quasistatic Test. Quasistatic uniaxial compression tests were conducted on an electrohydraulic servo material testing machine (MTS-322) housed in Advance Research Center of Central South University, China, as shown in Figure 2. The maximum vertical load of the device is up to 500 kN, and the overall stiffness is 1370 kN/mm. The machine can suc-

cessfully reproduce the failure process of rock under low strain rates and has been extensively used in the testing of rock mechanics [32–34]. In this study, the loading speed was maintained at 0.24 mm/min, i.e., the strain rate of specimens in quasistatic tests was $4 \times 10^{-5} \text{ s}^{-1}$.

2.3.2. Split Hopkinson Pressure Bar System. A split Hopkinson pressure bar (SHPB) device is used to conduct dynamic compressive tests [35]. It can realize the dynamic testing on rock materials within the range of strain rate from 10^0 to 10^2 s^{-1} [15, 36]. As shown in Figure 3, the SHPB system consists of a gas gun, a striker, three 50 mm diameter bars (called incident bar, transmitted bar, and absorption bar), and a momentum trap. The cone-shaped striker invented by Li et al. [37, 38] is applied to generate a half-sine wave for achieving stress equilibrium and avoiding premature failure of rock material. All of the bars and striker are made of high-strength 40 chromium alloy with a density of 7821 kg/m^3 , an elastic modulus of 233 GPa, and a longitudinal wave velocity is 5462 m/s. In tests, the specimen is sandwiched between the incident and transmitted bars. The

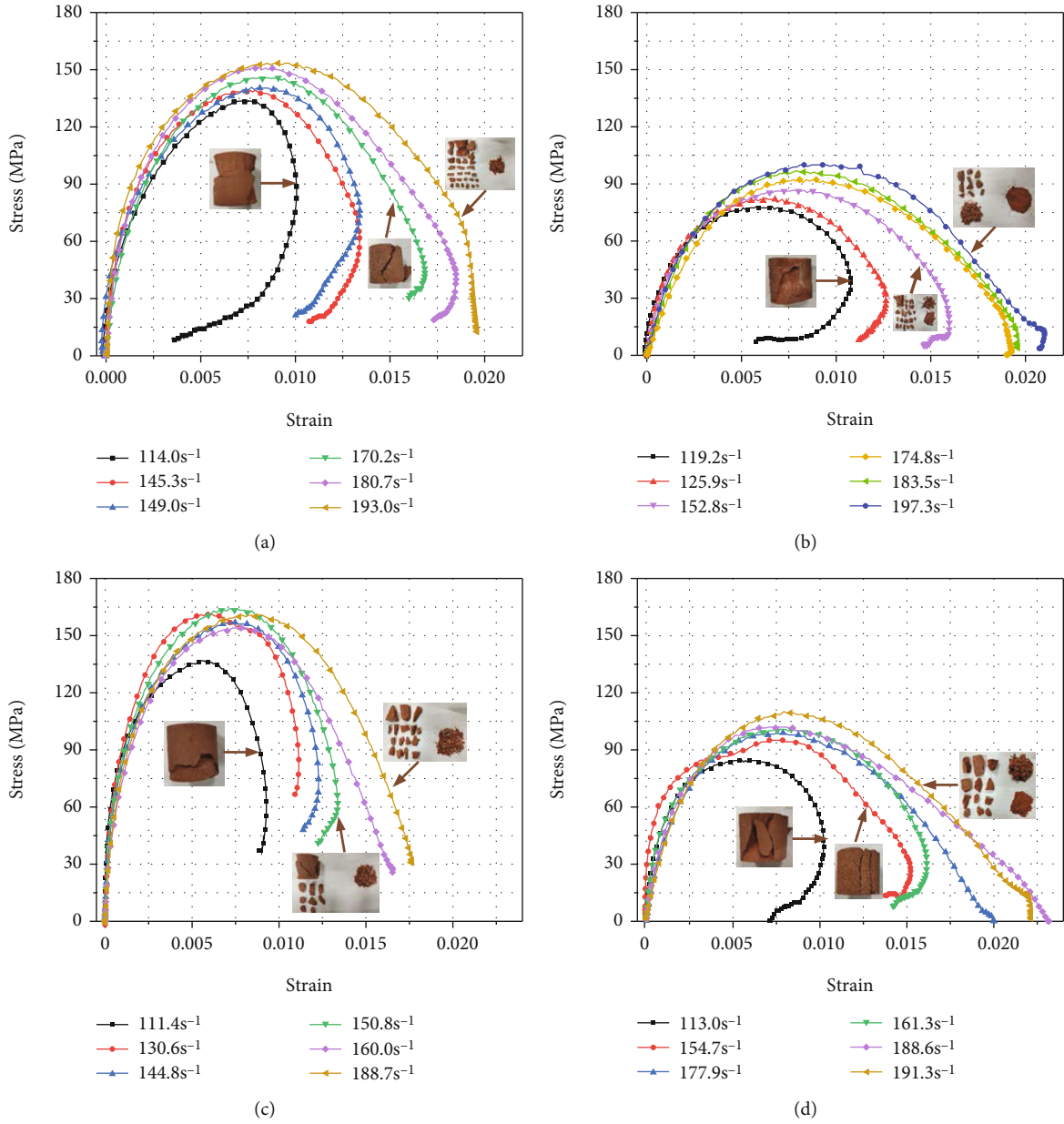


FIGURE 7: Dynamic stress-strain curves of (a) dry unfrozen, (b) saturated unfrozen, (c) dry frozen, and (d) saturated frozen specimens under different strain rates.

interfaces are smeared with sufficient lubricant to eliminate the end friction effect [27, 39, 40].

The cone-shaped striker is shot from the gas gun with a high velocity and impacts the end of the incident bar. Meanwhile, a slow-rising half-sine wave is produced and propagates along the incident bar (called incident wave). When the wave arrives in the interface between the incident bar and the specimen, a portion of it will be reflected to the incident bar (called reflected wave) due to the difference in wave impedance, and the other portion will pass through the specimen and transmitted into the transmitted bar (called transmitted wave). The three waves are monitored by strain gages glued on the middle of the incident and transmitted bars and then recorded by a digital oscilloscope.

2.4. Data Processing

2.4.1. Dynamic Stress Equilibrium. In SHPB tests, one of the prerequisites for test validity is the specimen reaching the stress equilibrium before failure. Herein, the dynamic stress equilibrium of the specimen is strictly examined by comparing the dynamic stress on both sides of the specimen. Figure 4 depicts the stress history on both sides of the specimen in a typical dynamic SHPB test. The time zeros of the incident wave and reflected wave are moved to the specimen/incident bar interface, and the time zero of the transmitted wave is shift to the specimen/transmitted bar interface. From Figure 4, the sum of the incident and the reflected stresses is almost equal to the value of transmitted stress during the

TABLE 2: Parameters and test results of the specimens in SHPB tests.

SN	Length (mm)	Diameter (mm)	P-wave (m/s)	Mass (g)	Strain rate (s ⁻¹)	UCS _d (MPa)	E _d (GPa)
DU-1	50.21	49.18	3536.15	230.07	114.01	133.54	13.56
DU-2	50.25	49.15	3513.99	230.98	145.28	139.16	13.32
DU-3	50.27	49.16	3490.74	229.54	149.05	140.75	13.62
DU-4	50.20	49.14	3510.26	228.76	170.18	145.68	13.65
DU-5	50.19	49.14	3509.56	229.83	180.68	151.18	13.93
DU-6	50.07	49.17	3525.82	228.56	193.00	153.43	14.02
SU-1	50.21	49.22	3511.19	229.52	119.20	78.19	9.71
SU-2	50.21	49.17	3487.04	229.55	125.90	82.66	9.98
SU-3	50.27	49.21	3490.97	229.80	152.80	86.57	10.23
SU-4	50.29	49.18	3541.55	230.51	174.80	92.26	9.95
SU-5	50.27	49.12	3442.92	231.11	183.50	96.98	10.56
SU-6	50.14	49.15	3434.47	229.03	197.30	100.01	10.79
DF-1	50.31	49.17	3493.75	230.88	111.39	136.76	15.62
DF-2	50.23	49.18	3613.43	229.90	130.57	161.07	16.30
DF-3	50.28	49.18	3516.32	229.36	144.82	156.86	16.00
DF-4	50.23	49.14	3587.86	231.13	150.76	164.07	16.02
DF-5	50.29	49.19	3492.13	231.08	159.97	154.04	15.70
DF-6	50.29	49.26	3468.51	229.98	188.68	160.69	16.33
SF-1	50.27	49.27	3490.97	228.97	113.03	84.72	10.26
SF-2	50.36	49.21	3571.63	229.64	154.69	95.02	9.98
SF-3	50.24	49.18	3513.05	230.14	177.85	98.98	11.09
SF-4	50.21	49.17	3438.81	229.04	161.33	100.75	10.78
SF-5	50.22	49.14	3416.33	229.28	188.63	102.04	11.05
SF-6	50.25	49.16	3514.22	230.05	191.26	110.10	11.22

Note: DU: dry unfrozen specimen; SU: saturated unfrozen specimen; DF: dry frozen specimen; SF: saturated frozen specimen; UCS_d: dynamic uniaxial compressive strength; E_d: dynamic elastic modulus.

whole loading process. In this case, the axial inertial effect can be ignored due to the fact that there is no overall force difference in the specimen to cause inertial force. Therefore, the SHPB test is valid.

2.4.2. *Determination of Stress, Strain, and Strain Rate.* According to the theory of one-dimensional wave, the histories of stress, strain rate, and strain in the specimen subjected to dynamic loading can be calculated by the three-wave method as [29, 41].

$$\begin{cases} \sigma_d(t) = \frac{A_b E_b}{2A_s} [\varepsilon_i(t) + \varepsilon_r(t) + \varepsilon_t(t)], \\ \varepsilon(t) = \frac{C_b}{L_s} \int_0^t [\varepsilon_i(t) - \varepsilon_r(t) - \varepsilon_t(t)] dt, \\ \dot{\varepsilon}(t) = \frac{C_b}{L_s} [\varepsilon_i(t) - \varepsilon_r(t) - \varepsilon_t(t)], \end{cases} \quad (1)$$

where σ_d , ε , and $\dot{\varepsilon}$ are the dynamic compressive stress, strain, and strain rate of the specimen, respectively; A_b , E_b , and C_b are the cross-sectional area, elastic modulus, and P-wave velocity of elastic bars; A_s and L_s are the cross-sectional area and length of the specimen; and ε_i , ε_r , and ε_t are incident, reflected, and transmitted wave signals. The strain rates of

specimens are controlled by the impact velocity of the striker, which can be adjusted to the actuating gas pressure in the gas gun.

3. Experimental Results

3.1. *Quasistatic Mechanical Behavior of Dry and Water-Saturated Sandstone.* Figure 5 presents the typical stress-strain curves of dry and water-saturated specimens tested under room temperature and -60°C. Apparent changes in the shape of the curve can be observed between dry and saturated specimens at the same temperature but not found between frozen and unfrozen specimens in the same water condition. This means that in quasistatic condition, the dominant factor controlling the rock properties is water rather than temperature. Average values of uniaxial compressive strength (UCS), Young's modulus (E), and failure strain of specimens are depicted in Figure 6. As shown in Figure 6(a), it can be clearly seen that the presence of water significantly weakens the UCS of sandstone specimens. At room temperature and -60°C, the water-induced loss percentage in UCS is 45.0% and 42.4%, respectively. However, for dry and water-saturated specimens, the UCS tested at -60°C is 8.97%, 13.1% higher than that tested at room temperature, respectively. The possible reason is that the frozen pore water can enhance the rock strength to some extent.

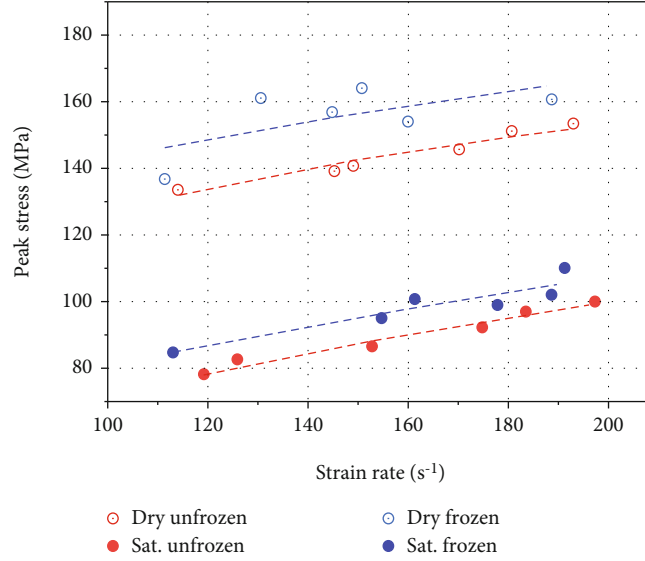


FIGURE 8: Variations in UCS_d against strain rate under four conditions.

From Figures 6(b) and 6(c), Young's modulus and failure strain follow a similar changing pattern as for UCS. This indicates that the water plays dual effects at subzero temperature.

3.2. Dynamic Mechanical Behavior of Dry and Water-Saturated Sandstone

3.2.1. Dynamic Stress-Strain Curves of Dry and Water-Saturated Specimens under Room Temperature and -60°C . Figure 7 presents the dynamic stress-strain curves of dry and saturated specimens tested at room temperature and -60°C . In each case, stress-strain curves obtained from six different strain rates are plotted. Before peak stress, the dynamic stress-strain curves show a similar pattern. However, the postpeak stress-strain curves are very different, indicating different final pattern. The apparent rebounding of postpeak curve means that the specimen is unbroken when subjected to dynamic loading, such as in Figure 7(a) curve with a strain rate of 114 s^{-1} . This is due to the fact that the incident energy is not enough to break the rock specimen [14]. The other curves in postpeak regime show strain softening, i.e., the stress decreases as the strain increases, leaving a large residual strain, such as Figure 7(a) curve with a strain rate of 193 s^{-1} . This indicates the specimen is fractured and loses its cohesion.

3.2.2. Dynamic Strength of Dry and Water-Saturated Specimens under Room Temperature and -60°C . According to dynamic stress-strain curves, dynamic parameters of each specimen are obtained as listed in Table 2.

The variations of peak stress versus strain rate for dry and water-saturated specimens under room temperature and -60°C are plotted in Figure 8. It can be seen that regardless of temperature and water conditions, the peak stress increases with the rise of the strain rate. Both low temperature and water saturation play crucial factors in controlling the peak stress of the specimen. When tested at the same

TABLE 3: Fitting parameters of the relationship between dynamic strength and strain rate.

	Fitting relationship
Dry unfrozen	$UCS_d = 35.6140\epsilon^{0.276}$
Saturated unfrozen	$UCS_d = 8.8165\epsilon^{0.458}$
Dry frozen	$UCS_d = 49.797\epsilon^{0.229}$
Saturated frozen	$UCS_d = 11.388\epsilon^{0.423}$

temperature, the peak stress of water-saturated specimen is much lower than that of dry ones at similar strain rates. This is caused by water-weakening effects.

The strength changes of these four types of rocks can be fitted with the exponential fitting relationship as follows:

$$UCS_d = a * \epsilon^b, \quad (2)$$

where a and b are the fitting parameters, b is the regression coefficient. The larger the absolute value of b , the higher the growth rate of the UCS_d . The specific fitting relationship is shown in Table 3.

A dynamic increasing factor (η), defined as the ratio of dynamic strength to quasi-static one ($\eta = \sigma_d / \sigma_s$), is introduced to quantify the strain rate effect on rock strength. From Figure 9, it can be seen that η apparently increases as the strain rate rises. Interestingly, η under different moisture and temperature conditions is very distinct. At the same strain rate, the saturated-unfrozen specimen has the largest value of η , followed by saturated frozen, dry frozen, and dry unfrozen specimens in descending order. This indicates that the presence of water plays a more important role in controlling the rate dependence of rock strength compared to low temperature.

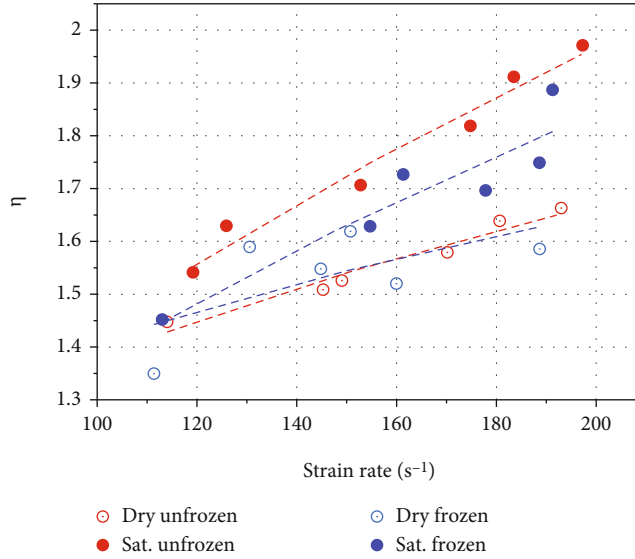


FIGURE 9: Variations of dynamic increasing factor against strain rate.

3.2.3. *Changes in E_d of Dry and Saturated Specimens at Room and Subzero Temperatures.* Figure 10 shows the variation in the dynamic elastic modulus of sandstone under different conditions versus strain rate. Unlike the dynamic strength, the dynamic elastic modulus nearly keeps constant in the testing range of strain rate for each condition. This implies that the dynamic elastic modulus is not sensitive to strain rate, which agrees with prior test results on other rock-like materials, such as concrete [41], sandstone [14], marble [42], limestone [43], and granite [44]. This is possibly due to the fact that the initial elastic modulus under dynamic loads is not affected by strain rate since no significant micro-crack creates during the initial loading stage, as shown in Figure 7.

From Figure 10, it can be also seen that, under each condition, the average dynamic elastic modulus is greater than the quasistatic value (see Figure 6(b)) probably due to the inertial effect. Moreover, no matter on frozen or unfrozen condition, the water-saturated specimen has the lower dynamic modulus than the dry one. The observation is contrary to many previous studies [14, 41], in which the dynamic elastic modulus will increase when the rock becomes water-saturated.

3.2.4. *The Energy Absorption of Dry and Saturated Specimens at Room and Subzero Temperatures.* To characterize the prepeak (e_f) and total absorbed (e_t) energy, the shadow areas under stress-strain curves before peak stress and during the whole loading process are calculated [45], as shown in Figure 11.

Figure 12 gives the results of energy absorbed in dynamic tests. It can be found that, for each condition, both of prepeak and total energy absorption rise with the increasing strain rate. There is no obvious difference in energy absorption between dry-frozen and dry-unfrozen specimens exposed to the same strain rate also between saturated-frozen and

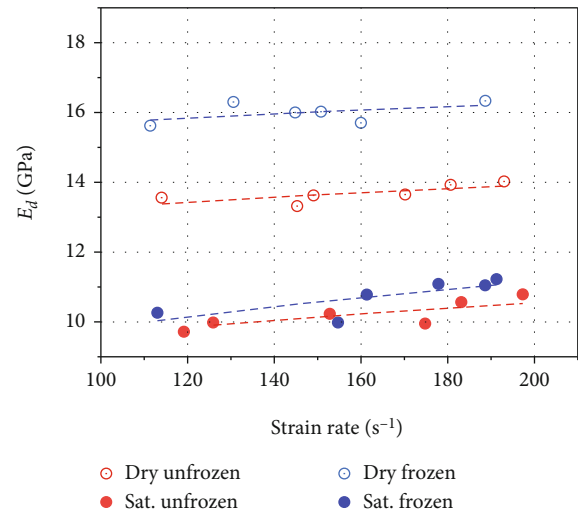


FIGURE 10: Variations in E_d against strain rate.

saturated-unfrozen specimens. In addition, regardless of temperature, dry specimens consume much more energy than saturated ones. These phenomena indicate that the water significantly lowers the energy needed to break the rock but the tested temperature has negligible effect.

4. Discussion

4.1. Effects of Water Saturation on Rock Strength

4.1.1. *Water-Weakening Effects.* At room temperature, water weakens rock strength in quasistatic tests [18]. Prior researchers proposed several mechanisms to reveal this phenomenon, such as (1) the reduction of fracture energy [17], (2) quartz hydrolysis [46–48], (3) friction reduction, and [31, 49] (4) chemical and physical deterioration [50, 51].

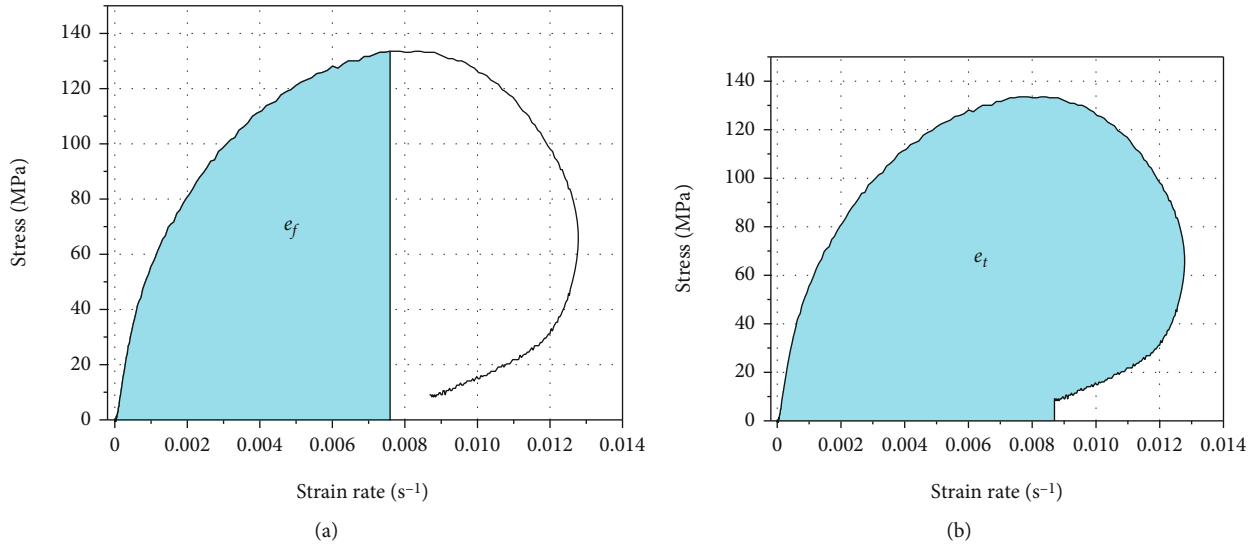


FIGURE 11: Calculation of energy absorption per unit volume: (a) absorption energy before peak stress and (b) total absorption energy.

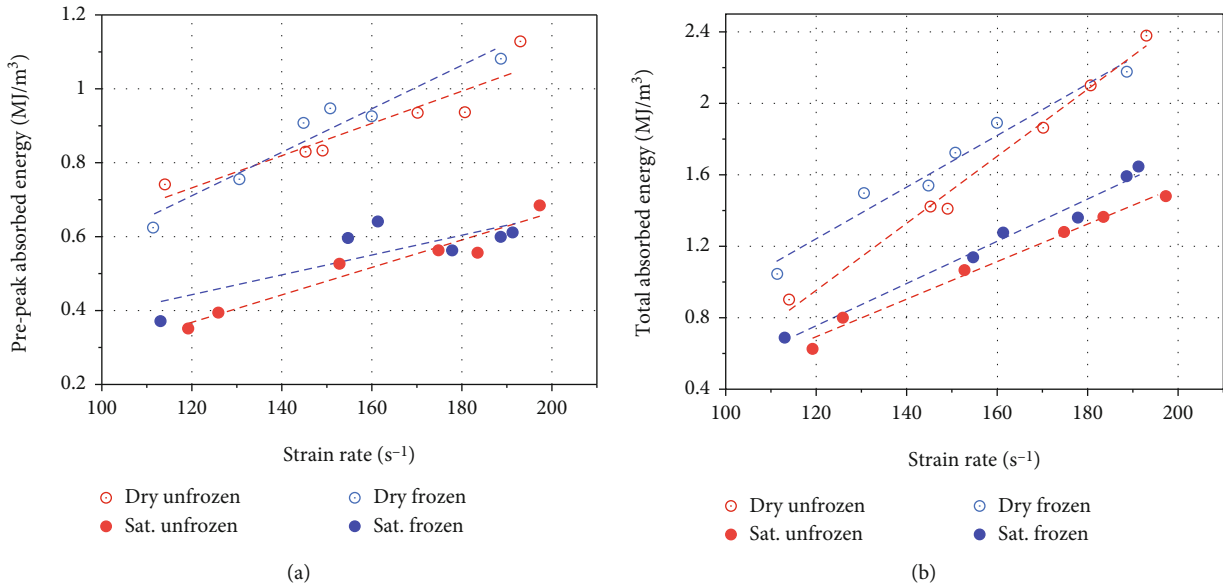


FIGURE 12: Variations of (a) e_f and (b) e_t versus strain rate.

For the sandstone, the friction reduction can be ignored because of the absence of minerals. Coupled effects of fracture energy reduction, quartz hydrolysis, and chemical and physical deterioration result in the loss of strength. Possible chemical reactions are listed in Table 4.

4.1.2. Water-Enhancing Effects. When the rock specimen is subjected to dynamic loading, free water in rock defects will hinder crack initiation and propagation through the following aspects: (1) the increase of inertia [15], (2) the reduction of local damage [52], (3) meniscus effect [53, 54], and (4) viscous effects [53]. These will increase the dynamic strength of rock to some extent and enhance the rate dependence of rock strength.

4.2. Effects of Subzero Temperature on Rock Strength

4.2.1. Subzero Temperature Enhancing Effects. Under subzero temperature condition, water in rock will be frozen. As a solid, ice can support external force with rock skeleton [6]. Also, ice can connect and tighten neighbouring grains and particles like binding agent [20]. In addition, subzero temperature makes the matrix group of mineral particles more compact and enhances the ability to resist deformation [20]. These are beneficial for rock strength.

4.2.2. Subzero Temperature Weakening Effects. When rock is completely saturated, water is filled with all connected pores. When the rock is exposed to subzero temperature, the dilation of frozen water will exert pore pressure to cause pore damage [20].

TABLE 4: Possible chemical reactions between water and minerals during water immersion.

Mineral	Chemical reaction formula
Quartz (46%)	$\text{SiO}_2 + \text{Al}_2\text{O}_3 + \text{H}_2\text{O} \longrightarrow [\text{mSiO}_2\text{g}2\text{H}_2\text{OgnSiO}_3^-]^{x-} + [\text{mAl}(\text{OH})_3\text{gnAl}(\text{OH})_2]^{x+}$
Potash feldspar (18%)	$\text{K}[\text{AlSi}_3\text{O}_8] + \text{H}^+ + \text{OH}^- \longrightarrow \text{Al}_4\text{Si}_4\text{O}_{10}(\text{OH})_8 + \text{H}_4\text{SiO}_4 + \text{K}^+$
Calcite (18%)	$\text{CaCO}_3 + \text{CO}_2 + \text{H}_2\text{O} \longrightarrow \text{Ca}(\text{HCO}_3)_2$
Plagioclase (8%)	$\text{CaAl}_2\text{Si}_2\text{O}_8 + \text{CO}_2 + \text{H}_2\text{O} \longrightarrow \text{CaCO}_3 + \text{Al}_2\text{Si}_2\text{O}_5(\text{OH})_4$

4.3. *Coupled Effects of Water Saturation and Subzero Temperature on the Compressive Strength of Sandstone.* Test results show that the sandstone under dry frozen condition has the maximum UCS, followed by that under dry unfrozen, saturated frozen, and saturated unfrozen conditions. For the dry frozen specimen, the subzero temperature enhancing effects dominates the increase of UCS. While for the saturated unfrozen specimen, water-weakening effects are responsible for the dramatic drop in UCS. When the saturated specimen is exposed to subzero temperature, the affecting mechanisms of rock strength are very complicated. On the one hand, water-weakening effects and subzero temperature weakening effects deteriorate rock skeleton and make serious damage in rock. On the other hand, the concretion and connection effects of ice can strengthen the rock. For the tested sandstone, the water-weakening effects are very significant. The subzero temperature enhancing effects are not enough to fully compensate for the UCS loss induced by water weakening. This leads to that the UCS of the saturated frozen specimen is evidently lower than that of the dry specimen but slightly greater than that of saturated unfrozen one.

In fact, when subjected to dynamic loading, the enhancing effects of free water work to rise the UCS. The rate dependence of UCS is primarily controlled by the content of liquid water in rock. Water will freeze under subzero temperature such that the content of liquid water decreases. Therefore, the saturated unfrozen specimen holds the maximum rate dependence of UCS while the UCS rate dependence of saturated frozen specimen, dry unfrozen specimen, and dry frozen specimen decreases in the cited order.

5. Conclusions

In this paper, quasistatic and dynamic compressive tests were performed on dry and water-saturated sandstone specimens under room and -60°C temperatures. The mechanical properties of specimens under different conditions were obtained. The coupled effects of water and low temperature on rock behavior were revealed. The following conclusions can be drawn:

- (1) At room temperature, in both quasistatic and dynamic loading condition, when the rock specimen becomes water-saturated from dry condition, its strength and elastic modulus are significantly decreased
- (2) The subzero temperature enhances the compressive strength and elastic modulus of dry and water-

saturated specimens, such that these mechanical parameters at subzero temperature are notably greater than that at room temperature. However, due to the water-weakening effects, the strength and elastic modulus of the saturated-frozen specimen are still lower than that of the dry-frozen and dry-unfrozen specimens

- (3) The compressive strength of sandstone is rate-dependent. The saturated unfrozen specimen has the highest rate dependence of strength, followed by the saturated frozen, dry unfrozen, and dry frozen specimens in degressive order. Contrarily, the elastic modulus of sandstone seems to be not sensitive to strain rate

Data Availability

The data used to support the findings of this study are available from the corresponding authors upon request.

Conflicts of Interest

The authors declare that there is no conflict of interest regarding the publication of this paper.

Acknowledgments

This work was supported by the National Natural Science Foundation of China (41772313), Hunan Science and Technology Planning Project (No. 2019RS3001), and the Graduated Students' Research and Innovation Fund Project of Central South University (2020zzts710). The authors are very grateful for the financial contributions and convey their appreciation to the organizations for supporting this basic research.

References

- [1] Z. Song, Y. Wang, H. Konietzky, and X. Cai, "Mechanical behavior of marble exposed to freeze-thaw-fatigue loading," *International Journal of Rock Mechanics and Mining Sciences*, vol. 138, article 104648, 2021.
- [2] H. Zhong-Wei, W. Jiang-Wei, L. I. Gen-Sheng, and C. Cheng-Zheng, "An experimental study of tensile and compressive strength of rocks under cryogenic nitrogen freezing," *Rock and Soil Mechanics*, vol. 37, no. 3, pp. 694–700, 834, 2016.
- [3] R. Yang, S. Fang, W. Li, Y. Yang, and Z. Yue, "Experimental study on the dynamic properties of three types of rock at

- negative temperature,” *Geotechnical and Geological Engineering*, vol. 37, no. 1, pp. 455–464, 2018.
- [4] W. Chen, X. Tan, H. Yu, K. Yuan, and S. Li, “Advance and review on thermo-hydro-mechanical characteristics of rock mass under condition of low temperature and freeze-thaw cycles,” *Chinese Journal of Rock Mechanics and Engineering*, vol. 30, no. 7, pp. 1318–1336, 2011.
- [5] H. Jia, F. Zi, G. Yang et al., “Influence of pore water (ice) content on the strength and deformability of frozen argillaceous siltstone,” *Rock Mechanics and Rock Engineering*, vol. 53, no. 2, pp. 967–974, 2020.
- [6] J. Kodama, T. Goto, Y. Fujii, and P. Hagan, “The effects of water content, temperature and loading rate on strength and failure process of frozen rocks,” *International Journal of Rock Mechanics and Mining Sciences*, vol. 62, pp. 1–13, 2013.
- [7] E. M. Winkler, “Frost damage to stone and concrete: geological considerations,” *Engineering Geology*, vol. 2, no. 5, pp. 315–323, 1968.
- [8] Y. Inada and K. Yokata, “Some studies of low temperature rock strength,” *International Journal of Rock Mechanics and Mining Sciences & Geomechanics Abstracts*, vol. 21, no. 3, pp. 145–153, 1984.
- [9] K. Aoki, K. Hibiya, and T. Yoshida, “Storage of refrigerated liquefied gases in rock caverns: characteristics of rock under very low temperatures,” *Tunnelling and Underground Space Technology*, vol. 4, no. 5, pp. 319–325, 1990.
- [10] T. Yamabe and K. M. Neaupane, “Determination of some thermo-mechanical properties of Sirahama sandstone under subzero temperature condition,” *International Journal of Rock Mechanics and Mining Sciences*, vol. 38, no. 7, pp. 1029–1034, 2001.
- [11] R. D. Dwivedi, A. K. Soni, R. K. Goel, and A. K. Dube, “Fracture toughness of rocks under sub-zero temperature conditions,” *International Journal of Rock Mechanics and Mining Sciences*, vol. 37, no. 8, pp. 1267–1275, 2000.
- [12] T. Mingming, W. Zhiyin, S. Yili, and B. Jinhong, “Experimental study of mechanical properties of granite under low temperature,” *Chinese Journal of Rock Mechanics and Engineering*, vol. 29, no. 4, pp. 787–794, 2010.
- [13] L. Weng, Z. Wu, A. Taheri, Q. Liu, and H. Lu, “Deterioration of dynamic mechanical properties of granite due to freeze-thaw weathering: considering the effects of moisture conditions,” *Cold Regions Science and Technology*, vol. 176, article 103092, 2020.
- [14] X. Cai, Z. Zhou, H. Zang, and Z. Song, “Water saturation effects on dynamic behavior and microstructure damage of sandstone: phenomena and mechanisms,” *Engineering Geology*, vol. 276, article 105760, 2020.
- [15] Z. Zhou, X. Cai, D. Ma et al., “Water saturation effects on dynamic fracture behavior of sandstone,” *International Journal of Rock Mechanics and Mining Sciences*, vol. 114, pp. 46–61, 2019.
- [16] X. Cai, Z. Zhou, L. Tan, H. Zang, and Z. Song, “Water saturation effects on thermal infrared radiation features of rock materials during deformation and fracturing,” *Rock Mechanics and Rock Engineering*, vol. 53, no. 11, pp. 4839–4856, 2020.
- [17] X. Cai, Z. Zhou, and X. Du, “Water-induced variations in dynamic behavior and failure characteristics of sandstone subjected to simulated geo-stress,” *International Journal of Rock Mechanics and Mining Sciences*, vol. 130, article 104339, 2020.
- [18] D. Ma, H. Duan, W. Liu, X. Ma, and M. Tao, “Water–sediment two-phase flow inrush Hazard in rock fractures of overburden strata during coal mining,” *Mine Water and the Environment*, vol. 39, no. 2, pp. 308–319, 2020.
- [19] T. C. Chen, M. R. Yeung, and N. Mori, “Effect of water saturation on deterioration of welded tuff due to freeze-thaw action,” *Cold Regions Science and Technology*, vol. 38, no. 2-3, pp. 127–136, 2004.
- [20] L. Weng, Z. Wu, and Q. Liu, “Dynamic mechanical properties of dry and water-saturated siltstones under sub-zero temperatures,” *Rock Mechanics and Rock Engineering*, vol. 53, no. 10, pp. 4381–4401, 2020.
- [21] S. Huang, Q. Liu, A. Cheng, Y. Liu, and G. Liu, “A fully coupled thermo-hydro-mechanical model including the determination of coupling parameters for freezing rock,” *International Journal of Rock Mechanics and Mining Sciences*, vol. 103, pp. 205–214, 2018.
- [22] L. Weng, Z. Wu, Q. Liu, and Z. Wang, “Energy dissipation and dynamic fragmentation of dry and water-saturated siltstones under sub-zero temperatures,” *Engineering Fracture Mechanics*, vol. 220, article 106659, 2019.
- [23] S. Wang, X. Li, K. Du, and S. Wang, “Experimental investigation of hard rock fragmentation using a conical pick on true triaxial test apparatus,” *Tunnelling and Underground Space Technology*, vol. 79, pp. 210–223, 2018.
- [24] Z. Song, T. Frühwirt, and H. Konietzky, “Inhomogeneous mechanical behaviour of concrete subjected to monotonic and cyclic loading,” *International Journal of Fatigue*, vol. 132, article 105383, 2019.
- [25] Y. Wang, W. K. Feng, R. L. Hu, and C. H. Li, “Fracture evolution and energy characteristics during marble failure under triaxial fatigue cyclic and confining pressure unloading (FC-CPU) conditions,” *Rock Mechanics and Rock Engineering*, vol. 54, no. 2, pp. 799–818, 2021.
- [26] X. Cai, Z. Zhou, L. Tan, H. Zang, and Z. Song, “Fracture behavior and damage mechanisms of sandstone subjected to wetting- drying cycles,” *Engineering Fracture Mechanics*, vol. 234, article 107109, 2020.
- [27] Q. B. Zhang and J. Zhao, “A review of dynamic experimental techniques and mechanical behaviour of rock materials,” *Rock Mechanics and Rock Engineering*, vol. 47, no. 4, pp. 1411–1478, 2014.
- [28] Y. Wang, C. H. Li, and J. Q. Han, “On the effect of stress amplitude on fracture and energy evolution of pre- flawed granite under uniaxial increasing-amplitude fatigue loads,” *Engineering Fracture Mechanics*, vol. 240, article 107366, 2020.
- [29] Y. X. Zhou, K. Xia, X. B. Li et al., “Suggested methods for determining the dynamic strength parameters and mode-I fracture toughness of rock materials,” *International Journal of Rock Mechanics and Mining Sciences*, vol. 49, pp. 105–112, 2012.
- [30] Z. T. Bieniawski and M. J. Bernede, “Suggested methods for determining the uniaxial compressive strength and deformability of rock materials,” *International Journal of Rock Mechanics & Mining Sciences & Geomechanics Abstracts*, vol. 16, no. 2, pp. 138–140, 1979.
- [31] X. Cai, Z. Zhou, K. Liu, X. Du, and H. Zang, “Water-weakening effects on the mechanical behavior of different rock types: phenomena and mechanisms,” *Applied Sciences*, vol. 9, no. 20, article 4450, 2019.
- [32] K. Du, X. Li, M. Tao, and S. Wang, “Experimental study on acoustic emission (AE) characteristics and crack classification

- during rock fracture in several basic lab tests,” *International Journal of Rock Mechanics and Mining Sciences*, vol. 133, article 104411, 2020.
- [33] K. Du, R. Su, M. Tao, C. Yang, A. Momeni, and S. Wang, “Specimen shape and cross-section effects on the mechanical properties of rocks under uniaxial compressive stress,” *Bulletin of Engineering Geology and the Environment*, vol. 78, no. 8, pp. 6061–6074, 2019.
- [34] Z. Zhou, X. Cai, W. Cao, X. Li, and C. Xiong, “Influence of water content on mechanical properties of rock in both saturation and drying processes,” *Rock Mechanics and Rock Engineering*, vol. 49, no. 8, pp. 3009–3025, 2016.
- [35] Q. Wu, X. Li, L. Weng, Q. Li, Y. Zhu, and R. Luo, “Experimental investigation of the dynamic response of prestressed rock-bolt by using an SHPB-based rockbolt test system,” *Tunnelling and Underground Space Technology*, vol. 93, article 103088, 2019.
- [36] X. Li, *Rock Dynamics: Fundamentals and Applications*, Science Press, Beijing, 2014.
- [37] X. Li, Z. Zhou, T. Lok, L. Hong, and T. Yin, “Innovative testing technique of rock subjected to coupled static and dynamic loads,” *International Journal of Rock Mechanics and Mining Sciences*, vol. 45, no. 5, pp. 739–748, 2008.
- [38] Z. Zhou, X. Li, Z. Ye, and K. Liu, “Obtaining constitutive relationship for rate-dependent rock in SHPB tests,” *Rock Mechanics and Rock Engineering*, vol. 43, no. 6, pp. 697–706, 2010.
- [39] Z. Zhou, X. Cai, X. Li, W. Cao, and X. Du, “Dynamic response and energy evolution of sandstone under coupled static–dynamic compression: insights from experimental study into deep rock engineering applications,” *Rock Mechanics and Rock Engineering*, vol. 53, no. 3, pp. 1305–1331, 2020.
- [40] Q. Wu, L. Chen, B. Shen, B. Dlamini, S. Li, and Y. Zhu, “Experimental investigation on rockbolt performance under the tension load,” *Rock Mechanics and Rock Engineering*, vol. 52, no. 11, pp. 4605–4618, 2019.
- [41] W. Ren, J. Xu, J. Liu, and H. Su, “Dynamic mechanical properties of geopolymer concrete after water immersion,” *Ceramics International*, vol. 41, no. 9, pp. 11852–11860, 2015.
- [42] M. Doan and A. Billi, “High strain rate damage of Carrara marble,” *Geophysical Research Letters*, vol. 38, no. 19, pp. 1066–1073, 2011.
- [43] D. J. Frew, M. J. Forrestal, and W. Chen, “A split Hopkinson pressure bar technique to determine compressive stress-strain data for rock materials,” *Experimental Mechanics*, vol. 41, no. 1, pp. 40–46, 2001.
- [44] X. B. Li, T. S. Lok, and J. Zhao, “Dynamic characteristics of granite subjected to intermediate loading rate,” *Rock Mechanics and Rock Engineering*, vol. 38, no. 1, pp. 21–39, 2005.
- [45] M. Zhang, L. Dou, H. Konietzky, Z. Song, and S. Huang, “Cyclic fatigue characteristics of strong burst-prone coal: experimental insights from energy dissipation, hysteresis and micro-seismicity,” *International Journal of Fatigue*, vol. 133, article 105429, 2020.
- [46] S. W. Freiman, “Effects of chemical environments on slow crack growth in glasses and ceramics,” *Journal of Geophysical Research: Solid Earth*, vol. 89, no. B6, pp. 4072–4076, 1984.
- [47] T. A. Michalske and S. W. Freiman, “A molecular interpretation of stress corrosion in silica,” *Nature*, vol. 295, no. 5849, pp. 511–512, 1982.
- [48] H. Dawei, Z. Hui, H. Qizhi, S. Jianfu, and F. Xiating, “A hydro-mechanical-chemical coupling model for geomaterial with both mechanical and chemical damages considered,” *Acta Mechanica Sinica*, vol. 25, pp. 361–376, 2012.
- [49] K. Kawai, H. Sakuma, I. Katayama, and K. Tamura, “Frictional characteristics of single and polycrystalline muscovite and influence of fluid chemistry,” *Journal of Geophysical Research: Solid Earth*, vol. 120, no. 9, pp. 6209–6218, 2015.
- [50] M. O. Ciantia, R. Castellanza, and C. di Prisco, “Experimental study on the water-induced weakening of calcarenites,” *Rock Mechanics & Rock Engineering*, vol. 48, no. 2, pp. 441–461, 2015.
- [51] M. O. Ciantia, R. Castellanza, G. B. Crosta, and T. Hueckel, “Effects of mineral suspension and dissolution on strength and compressibility of soft carbonate rocks,” *Engineering Geology*, vol. 184, pp. 1–18, 2015.
- [52] E. Cadoni, K. Labibes, C. Albertini, M. Berra, and M. Giangrasso, “Strain-rate effect on the tensile behaviour of concrete at different relative humidity levels,” *Materials and Structures*, vol. 34, no. 1, pp. 21–26, 2001.
- [53] P. Rossi, “A physical phenomenon which can explain the mechanical behaviour of concrete under high strain rates,” *Materials and Structures*, vol. 24, no. 6, pp. 422–424, 1991.
- [54] Z. Zhou, X. Cai, Y. Zhao, L. Chen, C. Xiong, and X. Li, “Strength characteristics of dry and saturated rock at different strain rates,” *Transactions of Nonferrous Metals Society of China*, vol. 26, no. 7, pp. 1919–1925, 2016.

Research Article

Numerical Study on the Mechanism and Application of Artificial Free Surfaces in Bedrock Blasting of Shield Tunnels

Yanjun Qi ^{1,2}, Linming Dou ², Zhaoxing Dong ¹, Zheng Jiang¹, Bo Meng¹, and Junzhong Zhang¹

¹School of Mechanics and Civil Engineering, China University of Mining and Technology, Xuzhou 221116, China

²State Key Laboratory of Coal Resources and Safe Mining, China University of Mining and Technology, Xuzhou 221116, China

Correspondence should be addressed to Linming Dou; lmdou@126.com

Received 23 March 2021; Revised 7 April 2021; Accepted 13 April 2021; Published 3 May 2021

Academic Editor: Yu Wang

Copyright © 2021 Yanjun Qi et al. This is an open access article distributed under the Creative Commons Attribution License, which permits unrestricted use, distribution, and reproduction in any medium, provided the original work is properly cited.

During the pretreatment construction of blasting in shield tunnel bedrock, in order to reduce the impact of blasting vibration on the surrounding environment and improve the effect of rock blasting, the method of creating an artificial free surface is proposed. From the point of creating an artificial free surface, this paper numerically studies the function mechanism and parameter optimization of artificial free faces in shield tunnel bedrock blasting construction. The propagation characteristics of explosion stress waves at the interface between the rock and the artificial free face and the effect of the artificial free face on the shield tunnel bedrock blasting were analyzed. The results indicate that, as the explosion stress wave transmits to the artificial free face, a part of the stress wave is reflected back to the bedrock, increasing the energy in the bedrock that needs blasting and improving the blasting effect and utilization rate of the blasting energy. The reduction degree of the peak velocity of the surface particle is more than 50%, and the reduction degree of the peak velocity of the particle near the artificial free face is more than 77%. The existence of the artificial free face reflects the stress wave and superimposes with the original stress waves, increasing the effective stress in the blasting area, and the effective stress can be increased by 5 MPa or more. The peak vibration velocity of the surface particle decreases with an increasing diameter of the empty holes and the distance between the empty holes and the blasting holes. The parameter design value of the artificial free face is put forward: the diameter of the hole is 200 mm, the distance between the empty holes and the center of the blasting holes is 60 cm, and the depth of the empty hole is the same as the blasting hole.

1. Introduction

With the continuous improvement of the urbanization level, urban transportation construction has developed rapidly, gradually developing in a multilevel and three-dimensional direction [1, 2]. Among them, the subway has been developed vigorously because it can effectively relieve the traffic pressure and reduce the road mileage to a certain place. The subway has become the main project of urban transportation construction [3]. Subway projects are characterized by long lines, variable geological conditions, and complex surrounding environments [4, 5], and along with the maturing of the shield construction technology, more and more

subway projects adopt shield construction to improve the construction efficiency and safety of subway projects [6]. Boulder groups and bedrock intrusion are the most representative cases in composite strata. This kind of rock mass is usually granite, and its strength is far greater than the strongly weathered surrounding rock mass, resulting in great security risks to shield engineering, which needs to be pretreated [7]. For the treatment of this situation, the blasting pretreatment technology of “ground drilling, millisecond blasting in the hole” is mainly used. Before the shield construction, a geological drilling machine is used to drill a hole vertically on the ground. A special charge is made to pretreat the boulder or bedrock intrusion in the composite stratum by



FIGURE 1: Rock sample preparation and the testing system.

blasting. The blasting pretreatment technology meets the requirements of the fragmentation in shield tunneling, which largely solves the difficulties encountered in shield construction and promotes the development of tunnel construction [8–11].

In actual engineering blasting, the vibration induced by the blast of the explosive is always a problem [12–15]; it can damage the buildings near the blasting resources [16, 17]. The artificial free surface is one of the important factors that affect the blasting effect, which has been widely studied by scholars all over the world [18–20]. In Ref. [21], it was found that empty holes between the blasting holes can control the expansion direction of the blasting lines. In Ref. [22], the authors investigated the influence of different intervals between blasting holes on crack propagation with a dynamic caustic test and numerical simulation. With the increase of intervals between the holes, the explosion cracks show no direct penetration anymore; rather, the deflection of cracks occurs in a “hand in hand” shape. In Ref. [23], the authors conducted a numerical study on deep-hole blasting and found that the explosion gas pressure has a significant impact on the formation and development of cracks in deep rocks without free faces. In Ref. [24], the authors found that a satisfactory blasting effect could be obtained when a free face exists and blasting efficiency could be improved to a large extent through field tests. In Ref. [25], the authors found that the existence of a free face could effectively improve the utilization rate of the explosion energy by studying the model test of single-hole blasting. In Ref. [26], the author believes that the charging hole should be as close to the free face as possible. If the free face is not flat and parallel to the gun hole, the effective utilization of the explosion energy can be improved, and similarly, the blasting effect can also be improved. Through numerical analysis, it was found that the free face has a strong control effect on the blasting vibration near it [27]. According to a similar law obtained in Ref. [28], the distance between the blasting source and the free face has a certain influence on the vibration velocity of the surface particles.

These previous researches provide good theoretical basis and research methods for the study of the mechanisms of an artificial free face in shield tunnel bedrock blasting. However, at present, the research on the mechanism of a rock burst mainly focuses on the construction of tunnel blasting and excavation. Research on the pretreatment technology of rock blasting in shield tunnels is still in its infancy. Besides, research on free faces mainly focuses on existing surfaces,

TABLE 1: Uniaxial compressive strength and axial strain of granites.

Sample no.	UCS (MPa)	Average UCS (MPa)	Axial failure strain	Average axial failure strain
DY1	117.21		0.0053	
DY2	112.41	114.01	0.0057	0.0055
DY3	123.67		0.0061	
DY4	102.72		0.0048	

and research on the action mechanisms of an artificial free face is relatively scarce. As the buildings around the blasting area become denser and the construction conditions become more complicated, the artificial free face will play an important role in any future construction.

This article takes the blasting construction of the shield tunnel in the Binhu section at Line 6 of the Fuzhou Metro as the engineering background to numerically analyze the propagation characteristics of the explosion stress waves in the rock mass and the effect of the artificial free face on the blasting of the shield tunnel bedrock. According to the actual engineering background, a series of numerical simulations were carried out to reveal the function mechanisms of the artificial free faces in the shield tunnel bedrock blasting, and the simulation results with and without a free face were compared. Then, based on the data and rules, the parameters of the artificial free face are studied, including the diameter of the empty holes and the distance between the empty holes and the blasting holes. The influence of different parameters on the effect of controlling the artificial free face is investigated. Finally, parameter optimization of the artificial free face was conducted.

2. Testing and Analysis of the Mechanical Properties of Granite

During the construction process of shield tunnel bedrock blasting pretreatment, the target objects are the bedrock and solitary stone groups in the stratum where the granite is the main lithology. There are dynamic loads such as explosion and shock impacts on granites in the process of ground drilling, bedrock blasting, and explosion stress wave propagation. Therefore, it is necessary to understand the mechanical properties of granites to fully grasp the fracture mechanism of granite under impact load and the stress wave propagation law to provide corresponding parameters for the numerical simulation.

TABLE 2: Deformation characteristics of granite samples.

Sample no.	Secant Young's modulus (MPa)		Tangent elasticity modulus (MPa)		Poisson's ratio	
	Single value	Average value	Single value	Average value	Single value	Average value
DY1	19493.8		25023.9		0.26	
DY2	17478.5	18959.6	26075.2	24713.3	0.25	0.26
DY3	17698.4		26302.5		0.31	
DY4	21167.7		21451.6		0.21	



FIGURE 2: Failure patterns of granite samples after uniaxial compression tests.

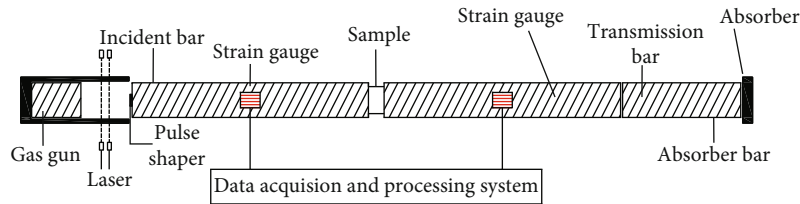


FIGURE 3: The SHPB testing system.

2.1. *Uniaxial Compressive Results of Granites.* The rock samples used in this paper were obtained from field drilling in the Binhu section at Line 6 of the Fuzhou Metro. Samples with relatively good integrity and homogeneity were selected. According to the suggested method of the International Society of Rock Mechanics (ISRM), uniaxial compression tests were conducted on granite samples with a diameter of 50 mm and a height of 100 mm (length diameter ratio of 2.0), and Split Hopkinson Pressure Bar (SHPB) tests were conducted on samples with a diameter of 50 mm and a height of 25 mm (length diameter ratio of 0.5). The error of nonparallelism and nonperpendicularity of the end surfaces for the samples should be controlled within 0.02 mm. Through the process of coring, cutting, and grinding, the rock samples were prepared, as shown in Figure 1.

Before the experiment, the prepared granite samples were first inspected, and the samples, which were smooth and flat, with parallelism, straightness, and perpendicularity all meeting the requirements, and with no obvious joints, cracks, and other defects, were finally selected. The uniaxial compression tests were conducted using the MTS-815 electrohydraulic servo rock testing system (Figure 1). The experimental

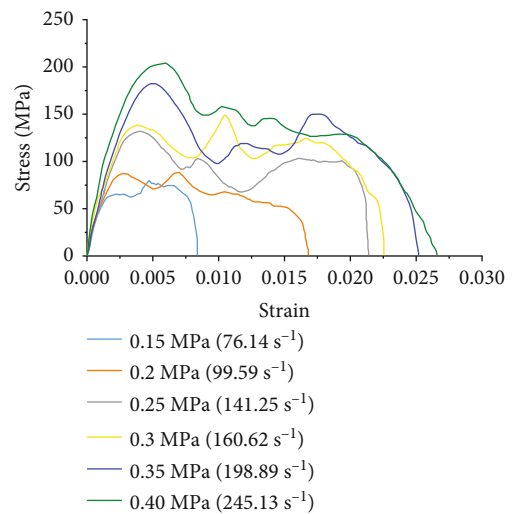


FIGURE 4: Stress-strain curves in the SHPB tests.

TABLE 3: Results of uniaxial impact compression tests of granites.

Excitation pressure (MPa)	Sample no.	Average strain rate (s^{-1})		Peak stress (MPa)		Peak strain	
		Single value	The average	Single value	The average	Single value	The average
0.15	A-1	80.991		70.974		0.0021	
	A-2	63.173		68.236		0.0032	
	A-3	83.269	76.137	60.498	64.78	0.0018	0.0023
	A-4	82.367		58.867		0.0025	
	A-5	70.236		65.324		0.0017	
0.2	B-1	115.596		99.497		0.0031	
	B-2	135.123		91.573		0.003	
	B-3	110.829	99.594	75.323	89.685	0.0026	0.003
	B-4	131.671		89.989		0.0025	
	B-5	120.346		92.043		0.0035	
0.25	C-1	142.131		130.748		0.0041	
	C-2	152.041		140.079		0.0039	
	C-3	144.572	141.25	144.217	141.055	0.0046	0.0042
	C-4	138.201		149.461		0.0035	
	C-5	129.311		140.771		0.0049	
0.3	D-1	159.509		166.638		0.0049	
	D-2	175.639		176.693		0.0051	
	D-3	160.438	160.62	138.864	158.961	0.0046	0.0053
	D-4	158.268		152.368		0.0057	
	D-5	149.235		160.235		0.0062	
0.35	E-1	203.609		157.269		0.0058	
	E-2	196.089		201.446		0.0065	
	E-3	207.223	198.9	183.247	178.105	0.0063	0.0062
	E-4	189.324		170.236		0.0057	
	E-5	198.235		178.327		0.0067	
0.4	F-1	251.935		200.583		0.0091	
	F-2	247.507		215.491		0.0078	
	F-3	237.496	245.13	193.679	203.599	0.0073	0.0083
	F-4	226.157		208.623		0.0083	
	F-5	262.548		199.623		0.0087	

results, including the uniaxial compressive strength (UCS), axial failure strain, secant Young's modulus, tangent elasticity modulus, and Poisson's ratio are, respectively, listed in Tables 1 and 2. The average UCS is 114.01 MPa, and the average axial failure strain is 0.0055. The average secant Young's modulus and average tangent elasticity modulus are 18959.6 MPa and 24713.3 MPa, respectively, with the average Poisson's ratio of 0.26. Ultimate failure modes of rock samples after uniaxial compression are displayed in Figure 2, which are characterized by typical splitting failure modes with tensile cracks along the loading direction.

2.2. Dynamic Mechanical Properties of Granites. The dynamic compression tests of granites were conducted using the SHPB device, which is composed of six units, including the dynamic system, bar system, supporting parts and guide rails, damper, velocimeter, and the data acquisition and processing systems, as shown in Figure 3. Due to the strain rate dependence and properties of the applied equipment, 6 sets

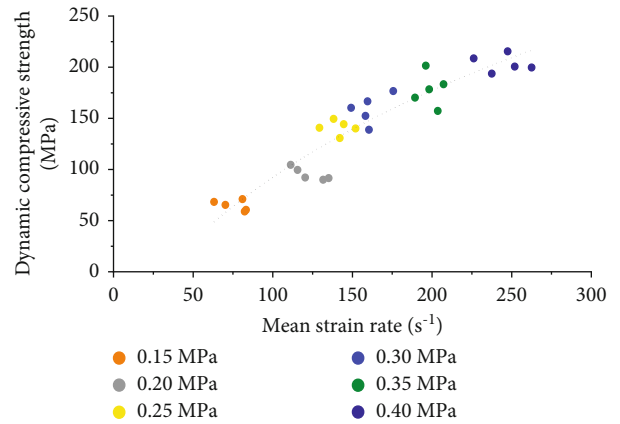


FIGURE 5: Relations between dynamic compressive strength and the average strain rate.

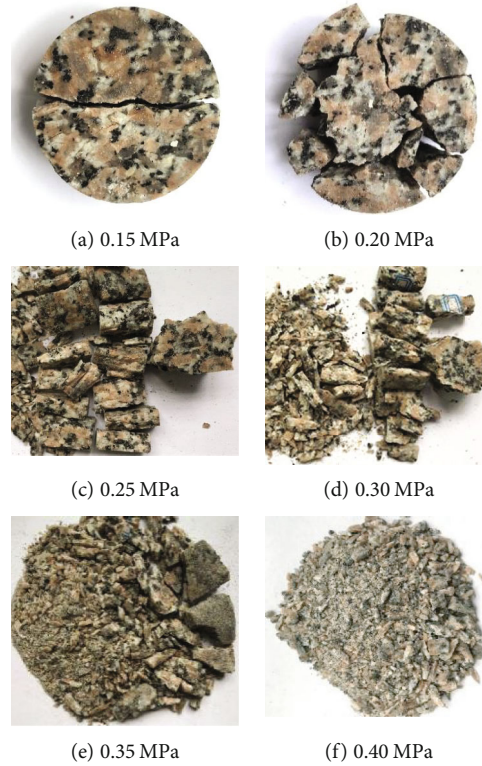


FIGURE 6: Granite crushing degree and crushing form with various excitation pressures.

of impact compression tests with various excitation pressures of 0.15 MPa, 0.20 MPa, 0.25 MPa, 0.30 MPa, 0.35 MPa, and 0.40 MPa were, respectively, performed. Each set of tests was repeated for 5 times, with the stress-strain curves displayed in Figure 4.

From Figure 4, the shape of stress-strain curves under various impact loads is similar, which includes the following 4 steps: the initial compaction stage, the elastic deformation stage, the nonlinear deformation stage, and the failure stage. When the strain rate is low, the proportion of the initial compaction stage in the prepeak curves is larger, mainly because when the strain rate is low, there is less energy obtained by the sample and the initial micro-crack closure is slower. With the increase of the strain rate, the proportion of the elastic stage in the prepeak curves gradually increases, more cracks are closed, and the closure speed is faster. After entering the nonlinear stage, the peak stress of the sample increases obviously, which shows that the granite has obvious strain rate characteristics under dynamic loads.

The average peak stress and peak strain under different impact loads of granite samples were calculated, as listed in Table 3.

Dynamic compressive strength and the strain rate are important parameters for analyzing the rock mechanical properties. According to the stress-strain time history curves, the relations between the two factors can be obtained, as shown in Figure 5.

Generally, the dynamic peak compressive strength of granites increases with the increase of the average strain rate.

TABLE 4: Classification of intervals of intrusion bedrock.

Classification of intrusive bedrock	Length (m)	Proportion
Small-volume bedrock	76	20.70%
Medium-volume bedrock	218	66.80%
Large-volume bedrock	40	12.50%

Curve fitting is performed to obtain the functional relationship between the two factors, as follows:

$$\sigma_d = 118.61 \ln \dot{\epsilon} - 450.32, \quad (1)$$

$$R^2 = 0.9324.$$

With the increase of the average strain rate, the dynamic compressive strength of granites gradually increases, indicating that the ultimate bearing capacity of granites increases correspondingly. However, at higher strain rates, the increased extent of the peak dynamic compressive strength gradually slows down.

After the dynamic compression tests, the ultimate failure modes of granites under different impact pressures are shown in Figure 6. Obviously, with an increasing excitation pressure, the fragmentation size of the sample decreases gradually and the number of fragments and the crushing degree increase gradually, indicating a strong strain rate effect.

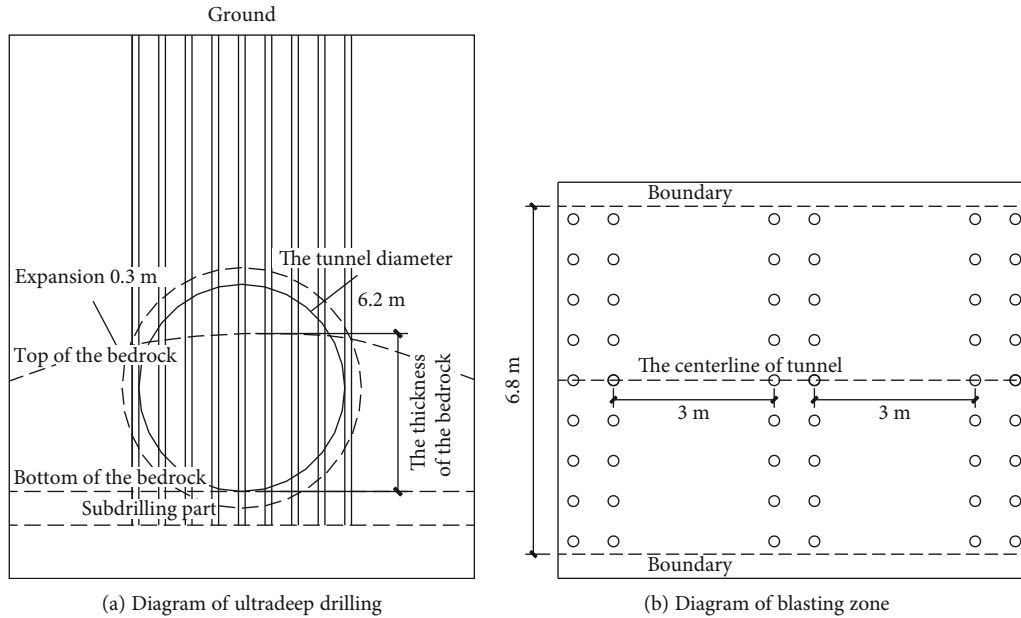


FIGURE 7: Layout diagram of the blasting holes.

TABLE 5: Bedrock blasting parameters.

Thickness of the bedrock (m)	Depth (m)	Pitch row (m)	Row spacing (m)	Hole depth (m)	Unit consumption (kg/m^3)	Charging mass (kg)	Charge structure
2	0.8	0.8	0.8	2.8	1.8	4.3	Continuous
3	1	0.8	0.8	4	1.9	7.6	Interval
5	1.5	0.8	0.8	6.5	2.1	10.3	Interval

3. Numerical Simulation of Bedrock Blasting in Shield Tunnels with Artificial Surfaces

3.1. Engineering Background. The Binhai Xincheng Station~Hujing Station of Fuzhou Rail Transit Line 6, referred to as the Binhu interval, is taken as the engineering background. The shield tunneling method was used to construct the tunnel. The diameter of the interval shield tunnel is 6.2 m, and the tunnel is covered with soil with a thickness of about 8.51 m~15.21 m. Detailed survey data show that there are large areas of moderately weathered granites and slightly weathered granites along the shield line. The uplift of bedrock (soft rock on top and hard rock at the bottom) can easily cause damage to the main bearing and cutter head of the shield tunneling machine, producing serious effects on the process of shielding and resulting in ground subsidence beyond the tolerated limit and in eventual collapse.

The intruded bedrock in the section is classified according to the thickness of the intrusive rock (i.e., the distance between the top surface of the bedrock and the bottom surface of the tunnel). The bedrock thickness below 2 m is called the small-volume bedrock, the bedrock thickness between 2 m and 4 m is called the medium-volume bedrock, and the bedrock thickness between 4 m and 6 m is called the large-volume bedrock. The statistics of bedrock in the section are

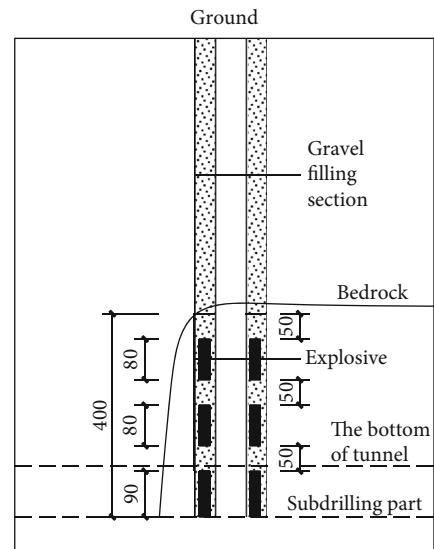


FIGURE 8: Schematic diagram of bedrock charge structures.

shown in Table 4, in which the medium-volume bedrock is the most prominent.

In order to ensure safe passage of the shield machine and meet the requirements of mucking out, it is necessary to blast

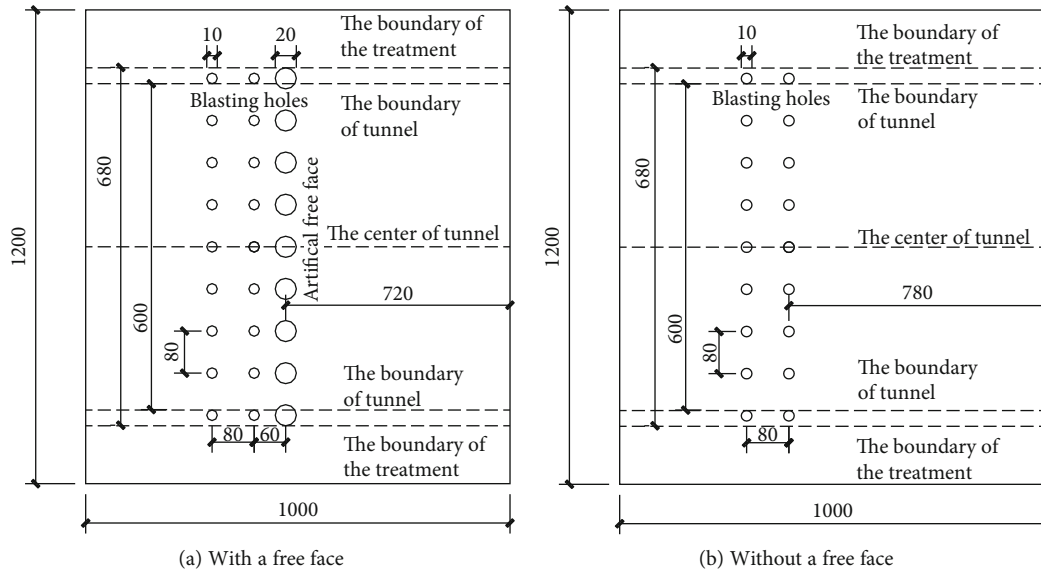


FIGURE 9: The numerical model plan (unit: cm).

the bedrock into fragments with a maximum length of less than 30 cm on one side. At the same time, it is also necessary to ensure that the buildings around the blasting area are not influenced by the construction. Combined with the corresponding provisions of the blasting safety regulations, the vibration velocity of the building foundation particles caused by the blasting pretreatment construction of the shield tunnel in the Binhu section should not be greater than 3 cm/s, and the vibration velocity of the building foundation particles directly above the right line should not be greater than 2.5 cm/s.

The diameter of the shield tunnel is 6.2 m, and both sides of the tunnel need to be expanded by 30 cm during the blasting treatment. The depth of the borehole is 0.8 m~1.5 m, and the charging depth is about 0.8 m~1 m deeper than the bottom of the tunnel. The blast holes are arranged in a rectangular layout, and the row spacing between the holes is 0.8 m × 0.8 m. Borehole blasting is carried out by blasting division, with 2 rows of blasting holes and an interval of about 3 m. The layout diagram of the blasting holes is shown in Figure 7. When the construction is near the building directly above the right line, it is necessary to add a row of empty holes near the charging hole at the side of the buildings to ensure the safety of the building structures.

According to actual construction experience, it is suggested that the shield machine should grind the rock directly when the bedrock thickness is more than 6 m. By calculating unit consumption, the charging parameters of different bedrock thicknesses are shown in Table 5.

It can be seen from Table 4 that the intrusive bedrock in the shield tunnel section is mainly medium-volume bedrock. Thus, the treatment depth of the bedrock is 4 m, as shown in Figure 8.

3.2. The Establishment of Model

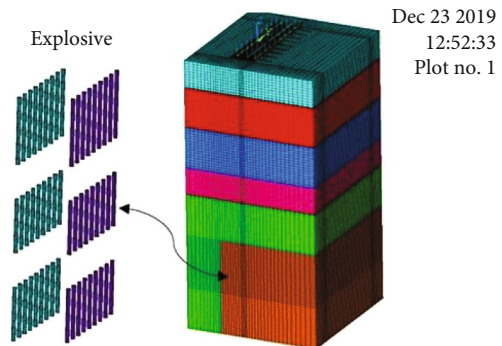


FIGURE 10: Bedrock blasting model.

3.2.1. Establishment of Numerical 3D Model. The main purpose of creating a free face is to reduce the damage caused by blasting vibration and improve the crushing effects of rock. According to actual construction experience, the artificial free holes should be arranged near the charging holes, and the artificial free face should be arranged on the side of the building that needs to be protected. In order to facilitate the actual construction, the empty holes are generally arranged in parallel with the charging holes, and the number of empty holes is the same as the number of charging holes. The diameter of the artificial empty holes should be larger than the diameter of the blast holes, and the distance between artificial empty holes and blast holes should be smaller than the row spacing of the blasting holes.

Combined with the engineering background of bedrock blasting pretreatment in the shield tunnel section, and considering the drilling diameter of the geological drill, the diameter of the artificial empty holes is selected as 200 mm, with the vertical distance from the blast holes of 60 cm. The depth of the empty hole is the same as the depth of the blasting hole. The numerical simulation includes two groups: one group

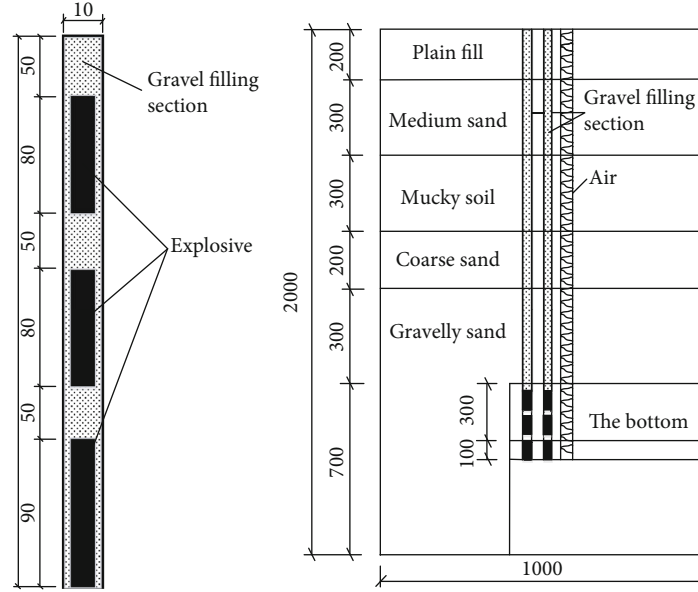


FIGURE 11: The vertical dimension and charging structures of the bedrock model.

TABLE 6: Explosive parameters.

Name	ρ (g/cm ³)	D (m/s)	P_{cj} (GPa)	A (GPa)	B (GPa)	R_1	R_2	ω	E (GPa)
Explosive	0.95	3400	5.3	162.7	10.82	5.4	1.8	0.25	4.1

TABLE 7: Material parameters of granites.

Rock types	Young's modulus E	Bulk modulus K	Shear modulus K_s	Lamme coefficient λ	Poisson's ratio λ_p	Density ρ
Granite	25 GPa	17 GPa	10 GPa	3.5	0.26	2.71 g/cm ³

with and the other group without artificial empty holes. The group with empty holes is taken as the control group, and the improvement of the blasting effect is obtained by analyzing the numerical results. The plan of the numerical model test is shown in Figure 9.

The software applied in this numerical simulation is LS-DYNA. According to the above engineering background and the diagram of bedrock explosion structures, a three-dimensional model of bedrock blasting is established, as shown in Figure 10. The vertical dimensions and charging structures of the bedrock model are shown in Figure 11.

According to Table 4, the medium-volume bedrocks were mainly distributed in this project, so medium-volume rocks were used as the bedrock in the simulation process. As shown in Figure 11, the thickness of bedrock intrusion into the tunnel is 3 m and the ultradeep drilling holes need to be 1 m below the tunnel bottom. Therefore, the actual thickness of the bedrock that needs to be treated is 4 m. Two rows of blasting holes are arranged according to the actual construction situation. The diameter of the shield tunnels is 6.2 m, and the actual treatment range is 6.8 m, based on the outward expansion of 30 cm on both sides. Nine blasting holes are set in each row, with a diameter of 100 mm and a spacing of 80 cm.

TABLE 8: Air parameters.

ρ (kg/m ³)	C_0	C_1	C_2	C_3	C_4	C_5	C_6	E_0	V_0
1.290	0	0	0	0	0.4	0.4	0	2.5×10^5	1

TABLE 9: Correlated parameters of the soil.

Name	ρ (cm ³)	E (MPa)	μ
Plain fill	1.8	20	0.26
Medium sand	2.05	37	0.25
Silty clay	1.95	15	0.35
Coarse sand	1.95	40	0.27
Gravelly sand	1.9	33	0.31

The arrangement of explosives is shown in Figure 11. The diameter of the charge is 60 mm. The uncoupled interval charge is adopted, and the initiation point is located at the 1/3 position above the bottom of the charge. When the bedrock thickness is 4 m, according to the blasting scheme, the charge is divided into three stages. The upper two explosive packages are 0.8 m, and the lower one is 0.9 m. The bedrock in the blasting interval near the buildings is located about

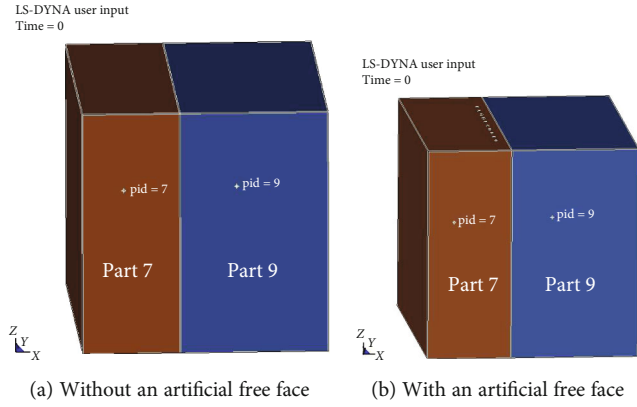


FIGURE 12: Bedrock model composition.

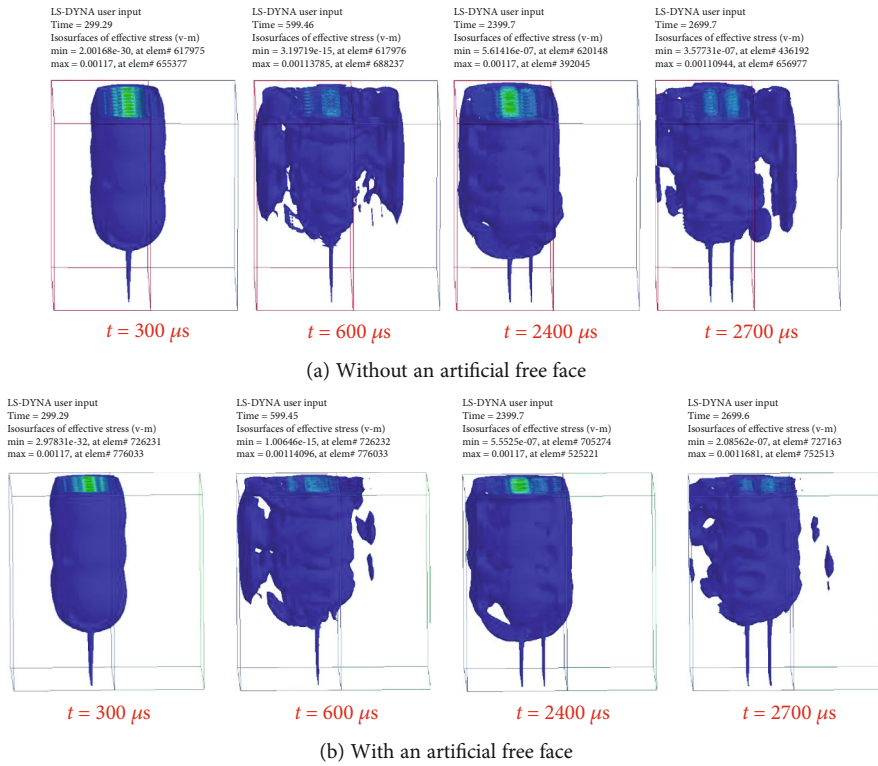


FIGURE 13: Comparison of bedrock stress clouds.

13 m below the surface, so the established bedrock in the numerical model is located 13 m below the surface, with the model height, width, and length of 20 m, 10 m, and 12 m, respectively.

Considering that the size of the numerical model is limited to a certain extent, the nonreflection boundary is applied to all the five boundaries except the surface of the model to prevent the reflection of explosion stress waves at the model boundaries. In the numerical calculation, if the grid size is too large, the calculation accuracy will decline. If the grid is too dense, the calculation time will be prolonged and the calculation efficiency will be affected. Generally, the minimum size of the unit should be less than 1/10 of the wave length, so

the maximum size of the grid in this model is 20 cm. At the same time, the explosive, bedrock, and air parts are refined and densified.

3.2.2. *Constitutive Model and Parameter Selection.* The explosive constitutive model provided by LS-DYNA was adopted, and the JWL state equation was used to simulate the detonation process of explosives, in the following form:

$$P = A \left(1 - \frac{\omega}{R_1 V} \right) e^{-R_1 V} + B \left(1 - \frac{\omega}{R_2 V} \right) e^{-R_2 V} + \frac{\omega E_0}{V}, \quad (2)$$

where P is pressure; V is the relative volume; E_0 is the initial

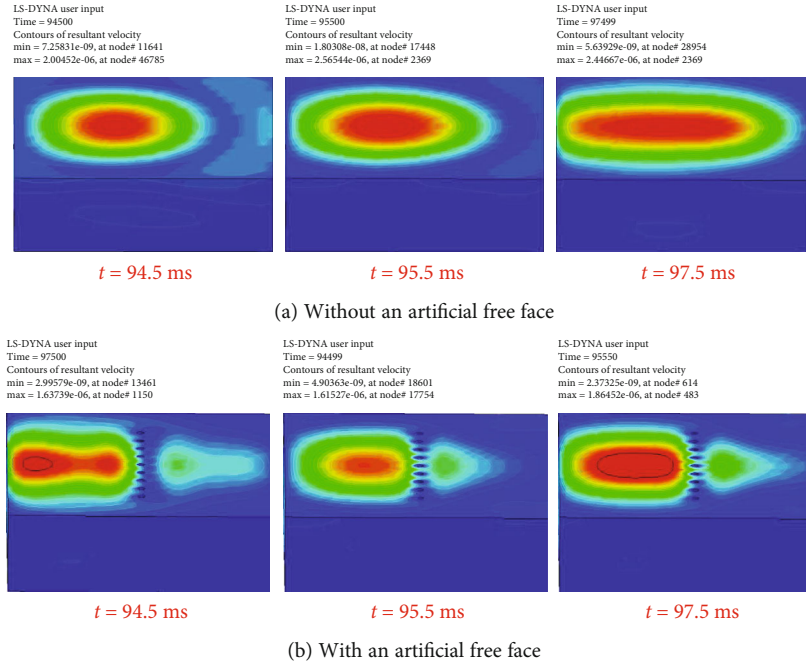


FIGURE 14: Surface velocity cloud images of the vibration (unit: ms).

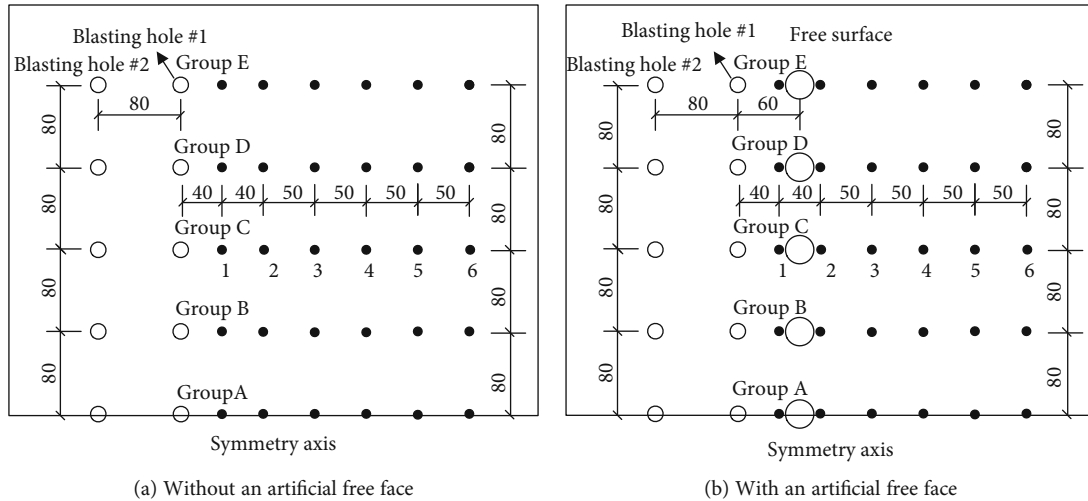


FIGURE 15: Schematic diagram of the selected surface particles.

specific internal energy; A , B , R_1 , R_2 , and ω are undetermined parameters. According to the actual situation of using explosives onsite, the selected parameters are shown in Table 6.

Under the action of dynamic loads such as impact and explosion, the mechanical properties of rock materials are much more complex than those under static loads, so the material constitutive model is selected as an isotropic bilinear elastoplastic model. The selected parameters according to the previous dynamic loading experimental results of granites are shown in Table 7.

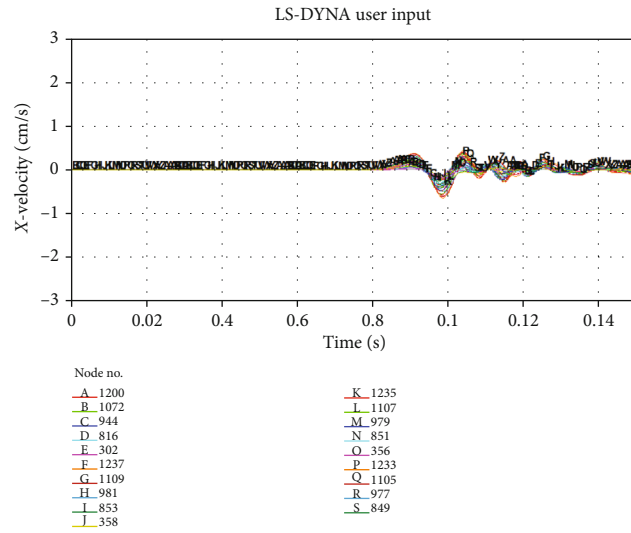
Air, which is also a kind of medium, exists in the artificial empty holes, so the parameters of air in the software need to be defined. In this test, MAT_NULL is used to simulate the

air material in the empty holes, and its polynomial state equation is as follows:

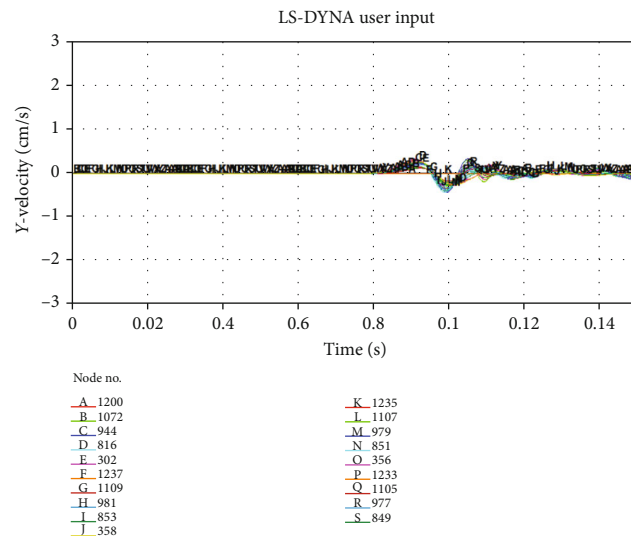
$$P = (C_0 + C_1\mu + C_2\mu^2 + C_3\mu^3) + (C_4 + C_5\mu + C_6\mu^2)E_0, \quad (3)$$

where $C_0 \sim C_6$ are constants; μ is the volume parameter; E_0 is the ratio of internal energy to initial volume, and the specific parameters are shown in Table 8 as follows:

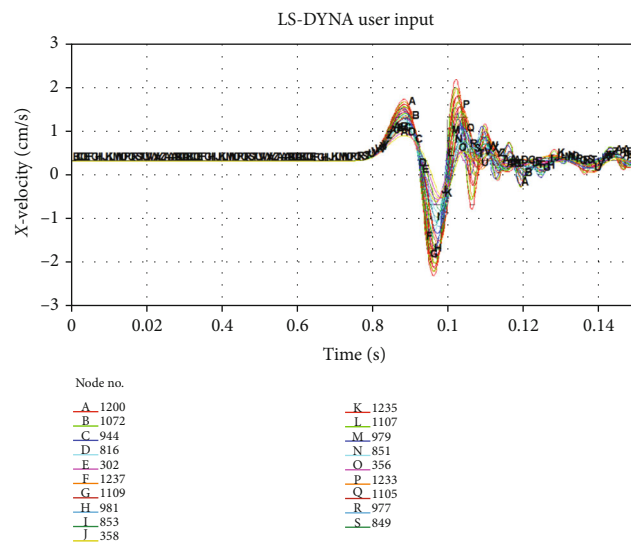
In order to improve the accuracy of the numerical tests, the elastoplastic model is also used for the analysis and calculation of the constitutive model of the soil layer, and its



(a) X direction



(b) Y direction



(c) Z direction

FIGURE 16: Time history curves of three-dimensional vibration velocity of particles.

TABLE 10: Peak values of the particle vibration velocity in the Z direction.

Free face	Particle no.	Distance from the center of the hole (cm)	Peak vibration velocity of a particle in the Z direction (cm/s)				
			Group A	Group B	Group C	Group D	Group E
With	1	40	1.31	1.16	0.82	0.51	0.32
	2	80	0.65	0.57	0.41	0.26	0.21
	3	130	1.27	1.13	0.81	0.54	0.38
	4	180	1.13	1.01	0.76	0.59	0.46
	5	230	0.86	0.78	0.58	0.5	0.41
	6	280	0.73	0.65	0.47	0.39	0.37
Without	1	40	2.96	2.84	2.48	1.79	1.11
	2	80	2.85	2.73	2.34	1.65	1.03
	3	130	2.76	2.64	2.21	1.55	0.99
	4	180	2.64	2.51	2.05	1.44	0.95
	5	230	2.45	2.31	1.86	1.35	0.94
	6	280	2.2	2.06	1.69	1.27	0.93

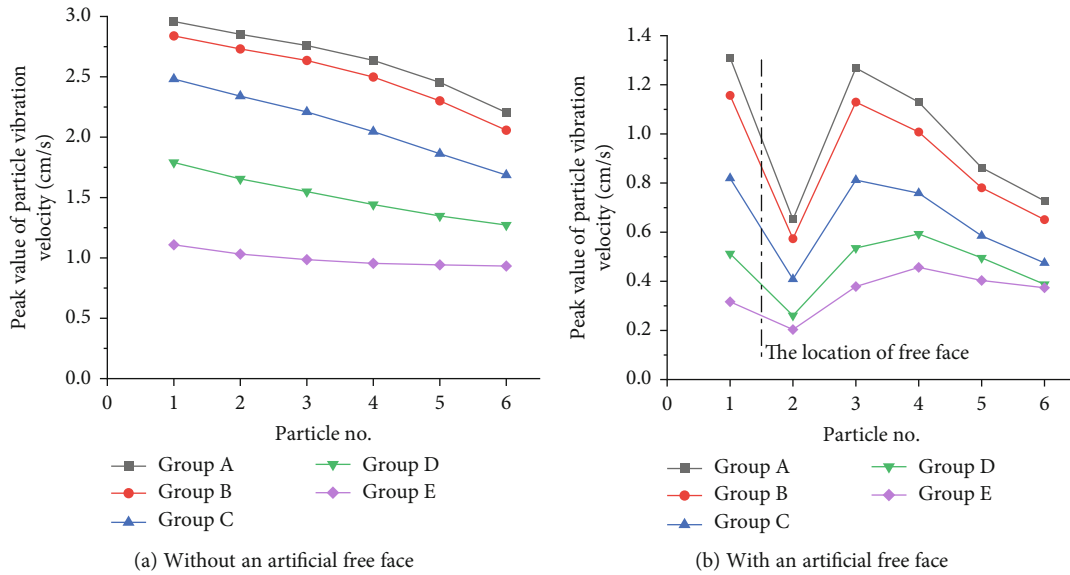


FIGURE 17: The peak vibration velocity curves of particles.

TABLE 11: Decreasing degree of the peak vibration velocity of particles.

Particle no.	Distance from the center of the hole (cm)	Reduction degree of the peak vibration velocity (%)				
		Group A	Group B	Group C	Group D	Group E
1	40	55.72	59.24	66.97	71.39	71.45
2	80	77.13	79.01	82.54	84.24	80.26
3	130	54.03	57.13	63.25	65.42	61.56
4	180	57.15	59.66	62.92	58.89	52.19
5	230	64.86	66.06	68.61	63.22	57.19
6	280	67.01	68.36	71.84	69.52	59.93

parameters refer to the geological prospecting data of the project, as shown in Table 9.

In blasting construction, each hole needs to be detonated at a certain time interval to ensure good construction effects. Langefors obtained a reasonable time interval formula to

improve the crushing effect by analyzing the field measured data, and it is shown as follows:

$$\Delta t = 3.3 \text{ kW}, \tag{4}$$

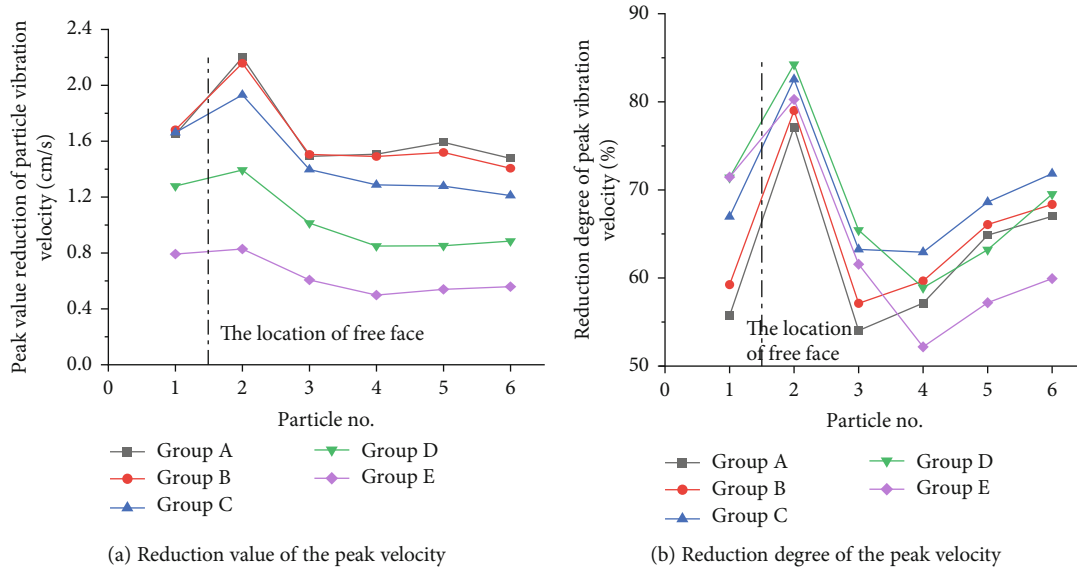


FIGURE 18: The difference between peak vibration velocities for cases with/without free faces.

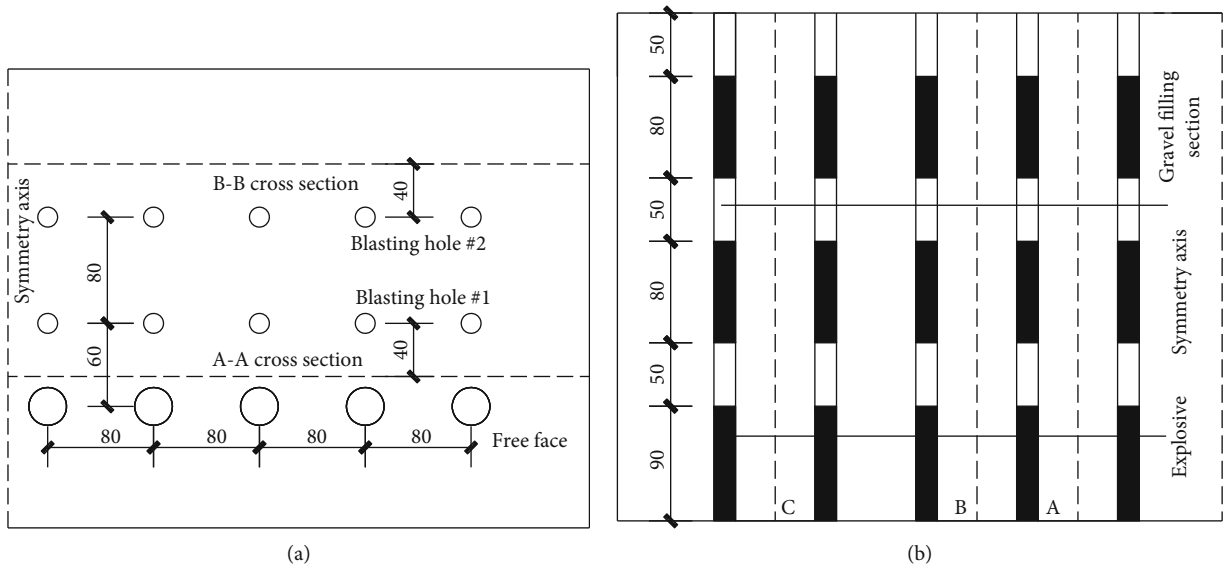


FIGURE 19: Cross section diagram (unit: cm).

where k can be taken as 1 ~ 2, considering the influences of site factors, and W is the minimum resistance line, which equals 0.6m in this study. From the formula calculation, the time interval is $\Delta t = 1.98 \sim 3.96$ ms, and in the numerical simulation, the time interval of 2 ms is selected.

3.3. Numerical Simulation Results and Analysis. In order to facilitate a comparative analysis, the bedrock part of the numerical model is divided into two parts by taking the artificial free face boundary as the interface, as shown by part 7 and part 9 in Figure 12. Part 7 is the bedrock needed to be treated by blasting, and this is where the explosive is buried.

Figure 13 shows the generation and propagation of explosion stress waves. After the explosive in the first row of holes is detonated, the explosion stress wave propagates outward in the shape approximately similar to a cylinder,

and the explosion stress waves formed by each section are superimposed. When $t = 300 \mu s$, the explosion stress wave propagates to the interface of part 7 and part 9, and there is not much difference between the two models. When the time is larger than $600 \mu s$, it can be seen that in the model with an artificial free face, the explosion stress wave presents a concentrated reflection at the position of the free face. Most explosion stress waves are reflected back to part 7, and only a small part of the explosion stress waves are transmitted to part 9 through the hole and the interval between holes. The action range of the stress waves in part 9 is relatively small, and stress waves decay with a fast speed. The artificial free surface hinders and weakens the propagation of explosion stress waves, and more energy is reflected back to part 7 and continues to act on the bedrock that needs blasting treatment.

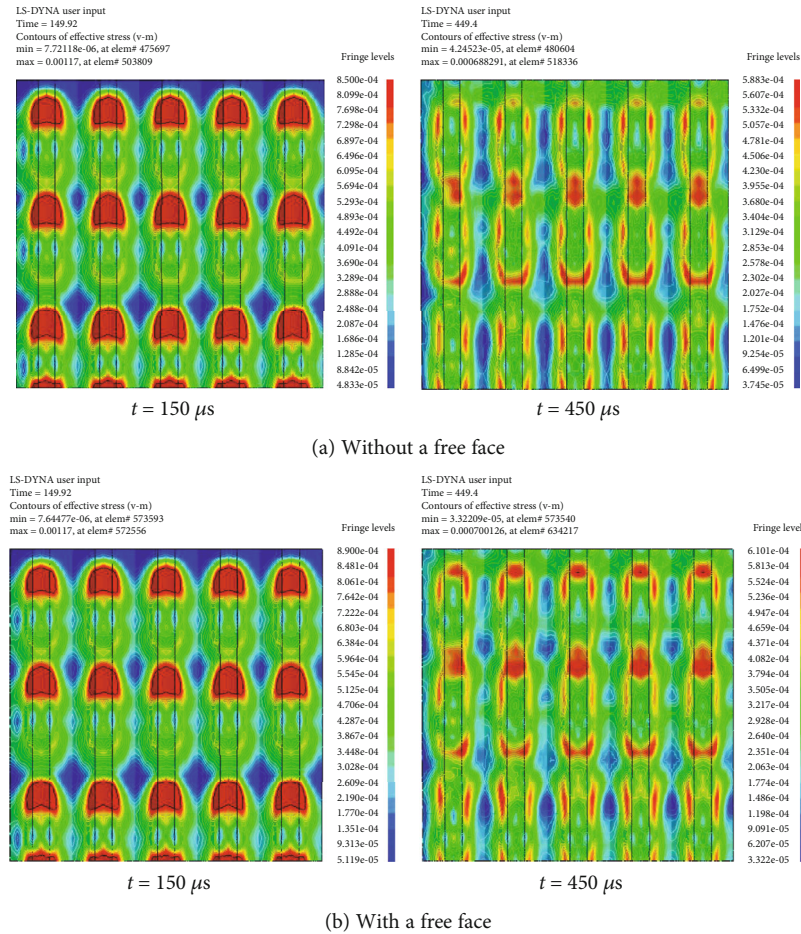


FIGURE 20: Effective stress cloud images of cross section A-A in the bedrock.

In the model without a free surface, there is no concentrated reflection, and the propagation speed of explosion stress waves in part 9 is relatively faster, with a larger action range. It shows that the existence of the artificial free face reflects more explosion stress waves back and continue to act on the bedrock that needs blasting treatment, which improves the utilization rate of explosion energy.

Studies have indicated that there is a good correlation between the vibration response law of building structures and the peak vibration velocity of particles. Therefore, the distribution of a vibration velocity field on the surface is qualitatively analyzed from the surface vibration velocity cloud images. The peak value of the particle vibration velocity is used as the judgment basis of the vibration control.

Figure 14 presents the vibration velocity cloud images of each particle on the surface obtained by the software. After the explosive in the bedrock is detonated, the explosion seismic wave reaches the surface at 94.5 ms, and the vibration intensity reaches its maximum at 95.5 ms. The explosion seismic wave propagates to the two sides from the center of the blasting holes. In the model without an artificial free face, the seismic wave diffusion is more uniform, and the vibration velocity on both sides of the hole is similar, with an axisymmetric distribution. In the model with an artificial free face, it can be found that when the explosion wave propagates towards the free face side, it is hindered by the free face,

and only a small part of the blast wave passes through the free face. The vibration velocity on the right side of the free face decreases significantly compared with the model without a free face. Most of the seismic waves are reflected back by the free face, resulting in the vibration velocity on the left side of the artificial face being significantly greater than that on the right side. Therefore, the existence of free faces hinders the propagation of seismic waves and significantly reduces the explosion vibration intensity in the areas that do not need to be blasted.

By recording the peak velocity of the selected surface particles, the weakening effect of the artificial free face on the explosion vibration intensity is quantitatively analyzed. Since the model is symmetric, half of the model is used for analysis. The buildings that need to be protected by the explosion are all on the right side. Six measuring points are taken from the right side, as shown in Figure 15. The horizontal distances between the blasting holes and the measuring points are 40 cm, 80 cm, 130 cm, 180 cm, 230 cm, and 280 cm, respectively, with group A to group E from bottom to top, and point 1 to point 6 from left to right, respectively.

According to the relevant provisions of blasting safety, three components of particle vibration perpendicular to each other should be measured simultaneously during blasting vibration monitoring. The direction of the maximum velocity is the principal vibration direction, and the vibration

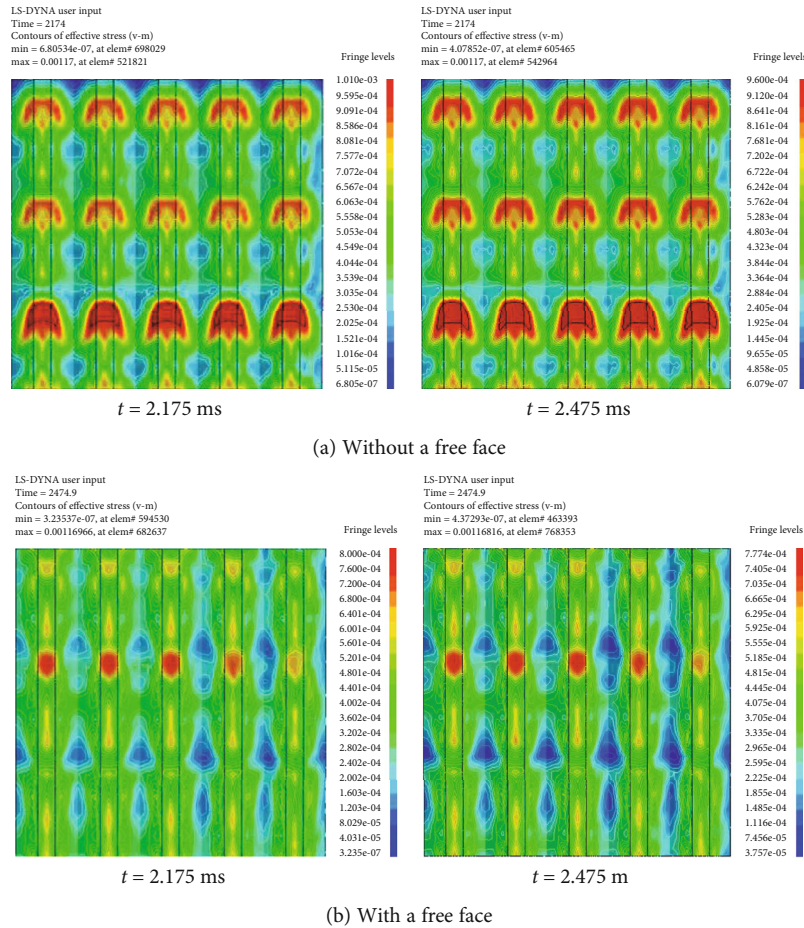


FIGURE 21: Effective stress cloud images of the cross section B-B in the bedrock.

frequency is the principal vibration frequency. The principal vibration velocity and the principal vibration frequency should be considered comprehensively. From the simulation results, it is found that the peak vibration velocity in the Z direction is much larger than that in the X and Y directions (Figure 16); thus, the peak vibration velocity value in the Z direction of the selected particle is mainly analyzed.

From Figure 16, the shapes of the three-dimensional vibration velocity curves of the particles are relatively similar. After the explosive in the bedrock is detonated, the explosion seismic wave is transmitted to the surface at 80 ms, and the surface blasting vibration intensity reaches the maximum at 95 ms, and then gradually decreases. When the time reaches 120 ms, the surface blasting vibration intensity is very small.

The peak vibration velocity of the selected particle in the Z direction is counted, as shown in Table 10, with the variation curves plotted in Figure 17.

From Table 10 and Figure 17, it can be found that the peak vibration velocity at each particle with a free face is lower than that without a free face. The peak value of the particle vibration is 2.96 cm/s without an artificial free face, but it is only 1.31 cm/s with an artificial free face. Obviously, the existence of a free face has a significant effect on reducing the blasting vibration intensity.

For the case without a free face, the peak vibration velocity values of the six points in each group decrease with an

increase in distance, and the decreasing range is smaller as the distance is closer to the boundary. The peak vibration velocity values of groups A and B, which are close to the axis of symmetry, are the closest, and are much larger than those of the other groups. This is because at the position of symmetry axis, the explosion effect is more concentrated, but to the direction of both sides, the vibration intensity declines gradually.

For the case with a free face, it can be found that the peak vibration velocity at midpoint #1 of each group is large. As the distance gets further, the peak velocity value decreases, which corresponds to the attenuation phenomenon of seismic waves in the case without a free face. It is worth noting that the peak vibration velocity of the five groups undergoes a sudden drop at point #2, because this point is the first point which is located at the right side of the empty holes and closest to the free face. The existence of the empty holes hinders the propagation of seismic stress waves, causing most of the stress waves to be reflected. It is found that the peak velocity at point #3 climbs significantly, because this is the part of the stress wave which propagates through the interval of the empty holes that causes vibration at point #3.

The reduction degree of the peak vibration velocity of each particle among the cases with/without a free face is calculated and listed in Table 11 and Figure 18.

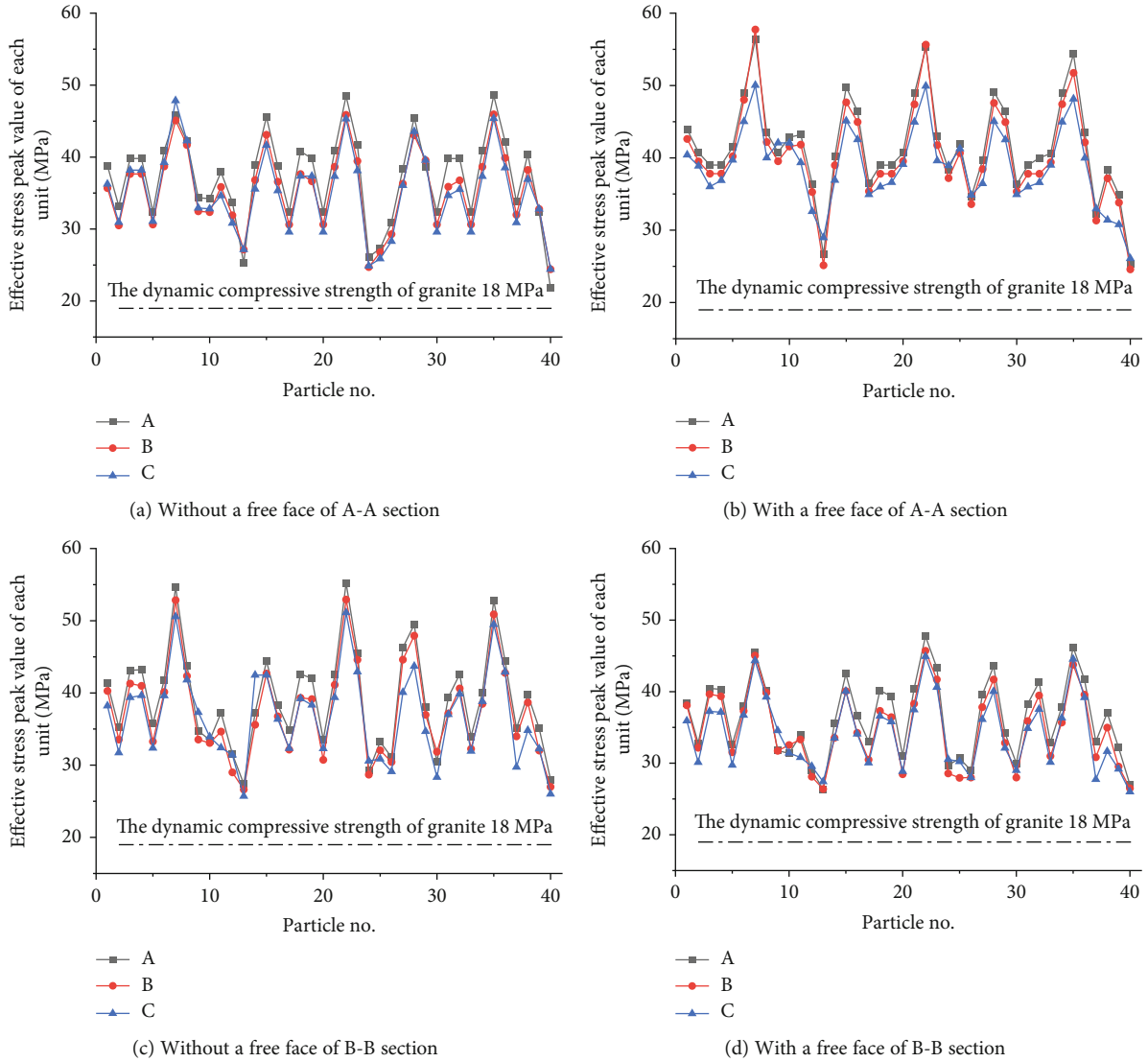


FIGURE 22: Peak effective stress values of the units.

From Table 11 and Figure 18, the artificial free face has a weakening effect on the peak values of the vibration velocity for each point, and the overall reduction degree is over 55%, among which, the reduction value of point #2 and the corresponding reduction degree are the largest. This is because the position of point #2 is closest to the empty holes at the right side, and an empty hole blocks and reflects most of the seismic stress waves; thus, the peak vibration velocity value of point #2 reduces greatly. With the increase of the distance between the empty holes and the measure points, the peak value reduction of the particle vibration velocity drops down and then stays at a relatively stable level, but the reduction degree of the peak vibration increases gradually; the reason is that the free face hinders the propagation of part of the explosion stress wave, so that the peak value of the latter 4 particles stays at a relatively stable level, while the peak velocity itself decreases with the increase of the distance, thus leading to the increase of the reduction degree.

The stress state of granites under blasting loads is very complicated—it is a three-dimensional stress state of a

tension-compression mixture. The Mises yield criterion is selected to analyze the stress state and failure characteristics of granites under an explosion load.

The effective stress at any point in the rock can be expressed as follows:

$$\sigma_e = \frac{1}{\sqrt{2}} \sqrt{(\sigma_1 - \sigma_2)^2 + (\sigma_1 - \sigma_3)^2 + (\sigma_2 - \sigma_3)^2}. \quad (5)$$

To judge whether rock failure occurs, the following formula is used:

$$\sigma_e \geq \sigma_0. \quad (6)$$

According to the different values of σ_0 , the rock has different failure modes:

$$\sigma_0 = \begin{cases} \sigma_{cd} \text{ (crushing circle),} \\ \sigma_{td} \text{ (crack circle),} \end{cases} \quad (7)$$

where σ_0 is the uniaxial failure strength, σ_{cd} and σ_{td} are the dynamic uniaxial compressive strength and tensile strength, respectively. The dynamic tensile strength of rock changes little with the loading strain rate; thus, we can take both σ_{td} and σ_t as equal to the tensile strength of rock. The tensile strength of the rock in this study is 18 MPa from the experimental results.

Because the volume of bedrock is too large, it is impossible to measure the effective stress state throughout the bedrock. Therefore, two cross sections (A-A and B-B) are, respectively, selected, as shown in Figure 19(a). Both sections are 40 cm away from the nearest blasting hole. The A-A section is located at one side of the first row of blasting holes; thus, the effective stress cloud images at 150 μ s and 450 μ s are selected (Figure 20).

From Figure 20, after the blast of the first row of boreholes, the stress wave is transmitted to the section at 150 ms, and the peak effective stress value reaches the maximum. Afterwards, the peak effective stress value begins to decline. It can be found that the peak stress near the explosive section is higher, while the peak stress near the gravel filling section and the gap area of the blast holes is relatively lower, due to the fact that the closer the blasting area is, the greater the intensity of the explosive stress waves and the greater the effective stress. Compared with the stress cloud images at the same time, the distribution of the effective stress field is roughly similar, while there is a certain difference between the maximum effective stress, with a difference of 4 MPa at 150 ms and a difference of 3 MPa at 450 ms. In the case without a free face, the effective stress value is smaller and the distribution range of the minimum value is larger, which indicate that the free face reflects a part of the stress waves back to the blasting area and enhances the explosion effects.

The B-B section is mainly affected by the second row of holes. The second row of holes is detonated 2 ms after the explosion of the first row of holes. The effective stress cloud maps at 2.175 ms and 2.475 ms are selected, respectively, as shown in Figure 21. The effective stress distribution of the B-B section is relatively similar to that of the A-A section. However, at the same time, it can be seen that the maximum effective stress of the B-B section is larger than that of the A-A section, because the stress waves generated by the second row of explosives overlaps with the stress waves generated by the first row of explosives.

To better analyze the distribution of the peak effective stress of bedrock, three positions of A, B, and C are, respectively, selected on the cross section. A and B are near the symmetry axis, and C is near the boundary, as shown in Figure 19(b). A total of 40 units from the bottom to the top of the bedrock, with a unit spacing of 10 cm, were selected. From the bottom to the top surface, the units were named No. 1~No. 40, respectively. The peak effective stress values of the units were calculated, as shown in Figure 22.

From Figure 22, all of the peak effective stress values of the units exceed the dynamic tensile strength of granites, which lead to the yielding and failing of the units. The peak effective stress for the case with an artificial free face is basically around or above 35 MPa, while the peak value of

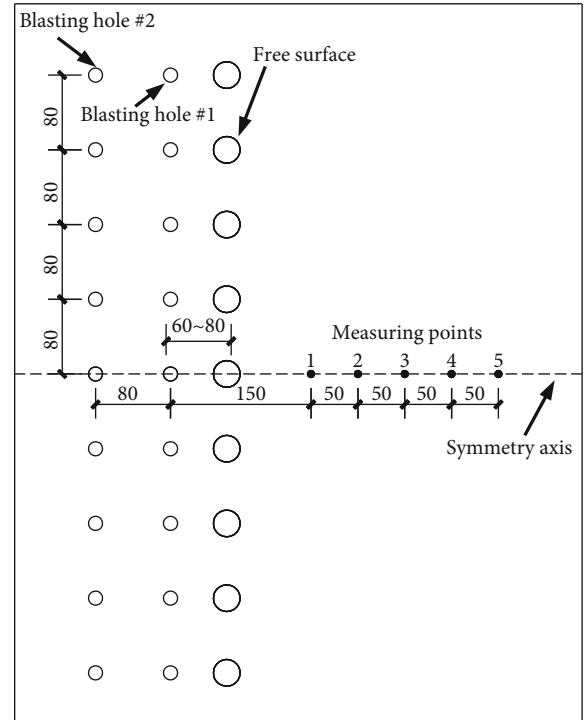


FIGURE 23: Particle selection diagram on the model surface.

the case without an artificial free face is concentrated around or above 30 MPa, which is lower than the case with a free face. It has been verified that the free face can reflect a part of the explosion stress waves, which increases the blasting peak stress value and improves the blasting effect. In the area perpendicular to the blasting interval, the effective stress of the unit is relatively larger, while in the area perpendicular to the blockage interval of the blasting holes, the effective stress is relatively small.

3.4. Parameter Optimization of the Artificial Free Face. The distance between the artificial free face and the center of blasting holes, and the size of the free face are the main factors affecting the effect of the artificial free face. According to construction experience, the row distance between the empty holes and blasting holes should be smaller than the row distance between the blasting holes, and the diameter of the empty holes should be larger than that of the blasting holes. Thus, two factors, including the row distance between empty holes and blasting holes, and the diameter of the empty holes, are selected in the simulation to analyze the influence of different artificial free face parameters on the blasting effects. The row distances are 60 cm, 65 cm, 70 cm, 75 cm, and 80 cm, respectively, and the diameters of the empty holes are 100 mm, 160 mm, 200 mm, 250 mm, and 300 mm, respectively. Five measuring points on the surface are selected to record the data, with the distances from the center of the first row of the blasting holes of 150 cm, 200 cm, 250 cm, 300 cm, and 350 cm, respectively (Figure 23). The peak vibration data in the Z direction of each point are recorded.

Using the postprocessing software LS-PrePost [29], the vibration velocity in the Z direction of each point without

TABLE 12: Peak values of the vibration velocity in the Z direction without a free surface.

Particle no.	No. 1	No. 2	No. 3	No. 4	No. 5
Peak velocity in the Z direction (cm/s)	2.64	2.45	2.16	2.08	1.89

TABLE 13: Peak values and average reduction degree of the vibration velocity in the Z direction.

Distance (cm)	Diameter (mm)	Peak vibration velocity of particle in Z direction (cm/s)					\bar{P} (%)
		No. 1	No. 2	No. 3	No. 4	No. 5	
60	100	1.27	0.96	0.88	0.91	1.01	54.8
	160	1.19	0.92	0.78	0.73	0.85	50.2
	200	1.13	0.81	0.63	0.74	0.79	63.2
	250	1.08	0.81	0.61	0.72	0.75	64.7
	300	1.05	0.78	0.59	0.72	0.76	65.2
65	100	1.39	0.98	1.01	0.86	0.95	53.9
	160	1.2	0.87	0.78	0.87	0.85	59.2
	200	1.15	0.88	0.75	0.71	0.76	62.3
	250	1.11	0.86	0.72	0.68	0.72	63.7
	300	1.06	0.88	0.69	0.65	0.71	64.6
70	100	1.54	1.12	0.95	0.95	1.04	50.2
	160	1.29	0.91	0.8	0.85	0.91	57.6
	200	1.18	0.89	0.72	0.79	0.83	60.6
	250	1.13	0.87	0.67	0.67	0.81	63.1
	300	1.09	0.85	0.71	0.66	0.78	63.5
75	100	1.67	1.18	1.08	1.01	1.09	46.4
	160	1.35	0.97	0.96	0.89	0.93	54.6
	200	1.24	0.91	0.76	0.79	0.85	59.5
	250	1.18	0.87	0.69	0.76	0.82	61.6
	300	1.14	0.86	0.72	0.77	0.79	61.9
80	100	1.76	1.18	1.06	1.05	1.08	46.1
	160	1.43	1.05	1.01	0.88	0.85	53.8
	200	1.32	0.94	0.83	0.79	0.77	58.9
	250	1.25	0.94	0.81	0.73	0.69	61.1
	300	1.19	0.91	0.83	0.72	0.68	62.2

and with an artificial free face is obtained. The average reduction degree of the peak stress values of particles is taken as the evaluation index, calculated using equation (8), and the calculated values are summarized in Tables 12 and 13.

$$\bar{P} = \frac{1}{n} \sum_{i=1}^n P_i, \quad (8)$$

where P_i is the reduction degree of the peak vibration velocity for the particle i , and n is the number of measuring points.

From Tables 12 and 13, the peak vibration velocity values of particles in the Z direction with a free face decreases significantly compared with the case without a free face, which is consistent with the previous conclusions. The average reduction degree is basically more than 50%, reflecting that the artificial free face significantly hinders the propagation of explosion stress waves. In order to further quantitatively represent the influence of a free face on the peak vibration veloc-

ity of each point, the peak vibration velocity and the reduction degree of peak values are drawn in Figures 24 and 25.

Figures 24 and 25 show that the peak value of particle vibration velocity generally presents a downward trend with the increasing diameter of the empty holes. As the diameter is increased from 100 mm to 200 mm, the curve is relatively steep, and then the downward trend of the curve gradually slows down in the diameter range of 200 mm to 300 mm. The decrease extent of the peak velocity is getting smaller and smaller, with the total decrease amplitude of less than 0.1 cm/s. However, the average decrease degree of the peak velocity shows an opposite trend, indicating a significant increase in the diameter range from 100 mm to 200 mm, and then a gentle increase trend as the diameter increases from 200 mm to 300 mm. This is because with the increase of the hole diameter, the effective area of the free surface will inevitably increase, which will hinder and weaken the stress waves more obviously, leading to the decrease of the particle

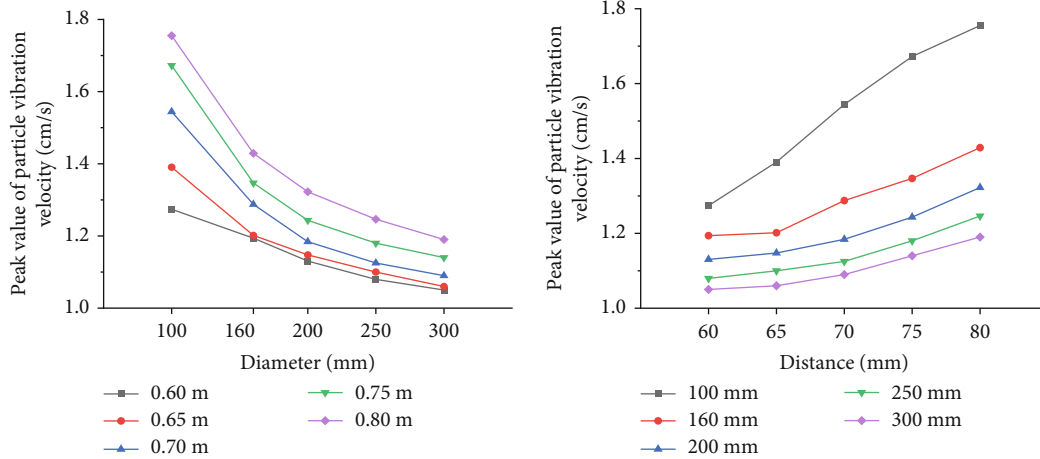


FIGURE 24: The influence of diameter and distance on the peak value of particle vibration velocity.

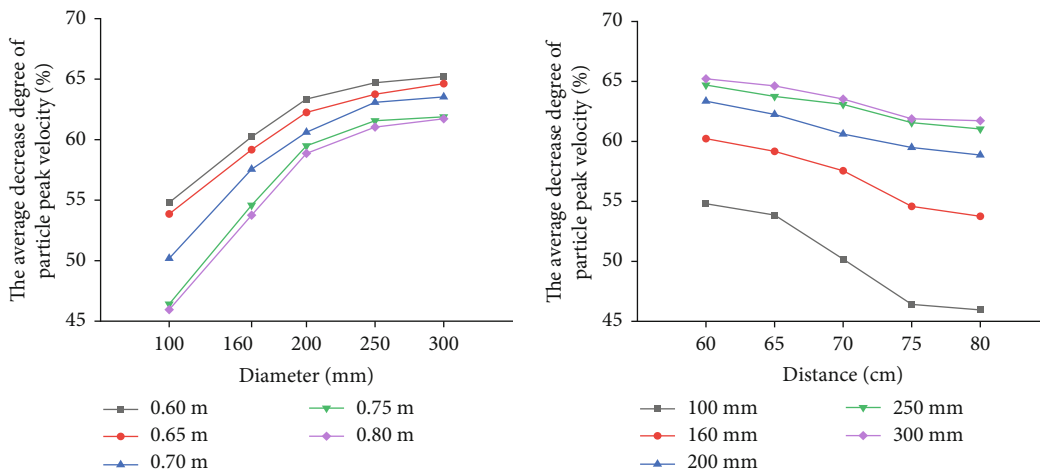


FIGURE 25: The influence of diameter and distance on the average decrease of peak velocities.

vibration velocity. When the hole diameter increases to a certain extent, the increase extent of the effective area of the free surface will slow down, which will lead to a reduction in the decrease extent of the peak vibration velocity.

When the distance between the artificial free faces and the blasting holes increases from 60 mm to 65 mm, the increase in the peak velocity is relatively small, while the increase extent of the peak velocity is large in the distance range of 65 mm to 80 mm. Variations in the average decrease degree present an opposite trend, which at first declines slowly in the distance range of 60 mm to 65 mm and then declines quickly in the range of 65 mm to 80 mm. This is mainly because when the distance between the artificial free face and the blasting holes is small, the energy carried by the explosion stress waves from the blasting holes to the free surface is correspondingly high. The artificial free face has a strong blocking and weakening effect on the explosion stress wave. However, when the distance between the free face and the blast holes is large, a considerable part of the explosion stress wave propagates around the free face. Therefore, the control effect on the blasting vibration intensity will be reduced to a certain extent.

The free face has a significant effect on the obstruction of the explosion stress waves, with an average reduction degree of 50% or more, which can greatly reduce the peak vibration velocity and play a protective role for the buildings. The larger the hole diameter, the better the blocking effect will be. However, considering the labor cost and the obtained blocking effect, 200 mm is the best diameter of the hole, and 60 cm is the best distance between the artificial free face and the blasting holes.

4. Conclusions

Through the numerical simulation method, the principle and influence of the artificial free face that hinder the propagation of explosive stress waves were explored. Two groups, one with artificial free faces and the other without, were set for comparison tests, and the effective stress on the bedrock and the peak vibration velocity of the measuring points were studied. Based on the numerical results, the influences of the diameter of the empty holes and distance between the empty holes to the blasting holes on the blasting effects of the bedrock were studied. The parameter optimization of the

artificial free surfaces in rock blasting are carried out. The main conclusions are drawn as follows:

- (1) Under an applied axial load, the granites are characterized by a typical splitting failure mode with tensile cracks along the loading direction. The average UCS, axial failure strain, secant Young's modulus, tangent elasticity modulus, and Poisson's ratio are 114.01 MPa, 0.0055, 18959.6 MPa, 24713.3 MPa, and 0.26, respectively. The dynamic peak compressive strength increases with the increasing strain rate. With an increasing excitation pressure, the number of fragments increases, and the failure degree increases gradually
- (2) Due to the reflection effect of the artificial free face, it can control the vibration intensity of the surface, and the reduction degree of the peak velocity of the surface particle can reach more than 50% and the reduction degree of the peak velocity of the particle near the artificial free face can reach more than 77%
- (3) The distribution of the effective stress field in the bedrock has a close relationship with the charging structure. The peak value of the effective stress near the charge area is larger than that near the gravel blockage area. The existence of the artificial free face makes the stress wave reflect and superimpose with the original stress waves, increasing the effective stress in the blasting area, and the effective stress can be increased by 5 MPa or more
- (4) The increase of the diameter of the empty holes can decrease the peak vibration velocity of the surface particle and improve the blasting effect. When the diameter of empty holes is 200 mm and 250 mm, the control effect is the most significant. The increase of the distance between the empty holes and the blasting holes can cause the decrease of the control effect
- (5) Based on the comprehensive consideration of blasting effects and construction cost, the parameter design value of the artificial free face is put forward, the diameter of the hole is 200 mm, the distance between the empty holes and the center of the blasting holes is 60 cm, and the depth of the empty hole is the same as the blasting hole. Two rows of blasting holes and one row of empty holes are adopted in the construction condition, and the artificial free face is located on the side of the building structure that needs to be protected

Data Availability

All data used during this study are available from the corresponding author by request.

Conflicts of Interest

The authors declare that they have no known conflicts of interests or personal relationships that could have appeared to influence the work reported in this paper.

Acknowledgments

The authors gratefully acknowledge the financial support from the National Natural Science Foundation of China (Nos. 51874292 and 51934007), the National Key Basic Research and Development Program of China (No. 2016YFC0801403), the Key Basic Research and Development Program of Jiangsu Province (No. BE2015040), and the Innovative Training Program for College Students of China University of Mining and Technology (No. 20200102cx).

References

- [1] Q. Wang and X. Yang, "Urbanization impact on residential energy consumption in China: the roles of income, urbanization level, and urban density," *Environmental Science and Pollution Research International*, vol. 26, no. 4, pp. 3542–3555, 2019.
- [2] J. Wu, H. Jing, Q. Yin, L. Yu, B. Meng, and S. Li, "Strength prediction model considering material, ultrasonic and stress of cemented waste rock backfill for recycling gangue," *Journal of Cleaner Production*, vol. 276, p. 123189, 2020.
- [3] R. Xu, X. Li, W. Yang, M. Rabiei, C. Yan, and S. Xue, "Field measurement and research on environmental vibration due to subway systems: a case study in eastern China," *Sustainability*, vol. 11, no. 23, pp. 1–12, 2019.
- [4] H. B. Amnieh, M. S. Zamzam, and M. R. Mozdianfar, "Geological hazards analysis in urban tunneling by epb machine (case study: Tehran subway line 7 tunnel)," *International Journal of Mining and Geo-Engineering*, vol. 50, pp. 1–12, 2016.
- [5] Q. Yin, R. Liu, H. Jing, H. Su, L. Yu, and L. He, "Experimental study of nonlinear flow behaviors through fractured rock samples after high-temperature exposure," *Rock Mechanics and Rock Engineering*, vol. 52, no. 9, pp. 2963–2983, 2019.
- [6] J. Lv, X. Li, Z. Li, and H. Fu, "Numerical simulations of construction of shield tunnel with small clearance to adjacent tunnel without and with isolation pile reinforcement," *KSCE Journal of Civil Engineering*, vol. 24, no. 1, pp. 295–309, 2020.
- [7] R. Coish, J. Kim, N. Morris, and D. Johnson, "Late stage rifting of the Laurentian continent: evidence from the geochemistry of greenstone and amphibolite in the Central Vermont Appalachians 1," *Canadian Journal of Earth Sciences*, vol. 49, no. 49, pp. 232–233, 2012.
- [8] J. Sun, P. Zhang, Y. Meng, Z. Li, Q. Wang, and C. Zeng, "Gray relational analysis on parameter sensitivity of blasting rock mass in soft-hard composite strata," *Highway*, vol. 6, pp. 314–318, 2018.
- [9] J. Wu, M. Feng, X. Mao et al., "Particle size distribution of aggregate effects on mechanical and structural properties of cemented rockfill: experiments and modeling," *Construction and Building Materials*, vol. 193, pp. 295–311, 2018.
- [10] J. H. Yang, W. B. Lu, Q. H. Jiang, C. Yao, and C. B. Zhou, "Frequency comparison of blast-induced vibration per delay for the full-face millisecond delay blasting in underground opening excavation," *Tunnelling and Underground Space Technology*, vol. 51, pp. 189–201, 2016.
- [11] Q. Yin, G. Ma, H. Jing, H. Su, Y. Wang, and R. Liu, "Hydraulic properties of 3D rough-walled fractures during shearing: an experimental study," *Journal of Hydrology*, vol. 2017, no. 555, pp. 169–184, 2017.

- [12] M. Khandelwal and T. N. Singh, "Prediction of blast induced ground vibrations and frequency in opencast mine: a neural network approach," *Journal of Sound and Vibration*, vol. 289, no. 4-5, pp. 711-725, 2006.
- [13] R. Kumar and K. Bhargava, "Determination of blast-induced ground vibration equations for rocks using mechanical and geological properties," *Journal of Rock Mechanics and Geotechnical Engineering*, vol. 8, no. 3, pp. 341-349, 2016.
- [14] R. Nateghi, "Prediction of ground vibration level induced by blasting at different rock units," *International Journal of Rock Mechanics and Mining Sciences*, vol. 48, no. 6, pp. 899-908, 2011.
- [15] Z. Wang, C. Fang, Y. Chen, and W. Cheng, "A comparative study of delay time identification by vibration energy analysis in millisecond blasting," *International Journal of Rock Mechanics and Mining Sciences*, vol. 60, pp. 389-400, 2013.
- [16] H. Li, X. Xia, J. Li, J. Zhao, B. Liu, and Y. Liu, "Rock damage control in bedrock blasting excavation for a nuclear power plant," *International Journal of Rock Mechanics and Mining Sciences*, vol. 48, no. 2, pp. 210-218, 2011.
- [17] P. K. Singh, "Blast vibration damage to underground coal mines from adjacent open-pit blasting," *International Journal of Rock Mechanics & Mining Sciences*, vol. 39, no. 8, pp. 959-973, 2002.
- [18] J. S. Lee, S. K. Ahn, and M. Sagong, "Attenuation of blast vibration in tunneling using a pre-cut discontinuity," *Tunnelling and Underground Space Technology*, vol. 52, pp. 30-37, 2016.
- [19] W. Lu, Z. Leng, H. Hu, M. Chen, and G. Wang, "Experimental and numerical investigation of the effect of blast-generated free surfaces on blasting vibration," *European Journal of Environmental and Civil Engineering*, vol. 22, no. 11, pp. 1374-1398, 2018.
- [20] X. Qiu, X. Shi, Y. Gou, J. Zhou, H. Chen, and X. Huo, "Short-delay blasting with single free surface: results of experimental tests," *Tunnelling & Underground Space Technology*, vol. 74, pp. 119-130, 2018.
- [21] B. Mohanty, "Explosion generated fractures in rock and rock-like materials," *Engineering Fracture Mechanics*, vol. 35, no. 4-5, pp. 889-898, 1990.
- [22] Z. Yue, S. Tian, and Z. Chen, "Influence of the interval between holes on crack propagation in slit charge blasting," *Chinese Journal of Rock Mechanics and Engineering*, vol. 37, no. 11, pp. 2460-2467, 2018.
- [23] W. Yuan, X. Su, W. Wang, L. Wen, and J. Chang, "Numerical study of the contributions of shock wave and detonation gas to crack generation in deep rock without free surfaces," *Journal of Petroleum Science and Engineering*, vol. 177, no. 2, pp. 699-710, 2019.
- [24] P. Rai, H. S. Yang, and B. S. Choudhary, "Formation of slot cut for creating free face in solid limestone bench: a case study," *Powder Technology*, vol. 228, pp. 327-333, 2012.
- [25] J. Tian and F. Qu, "Model experiment of rock blasting with single borehole and double free-surface," *Mining Science and Technology (China)*, vol. 3, pp. 395-398, 2009.
- [26] D. Hagan, "The importance of the shape, orientation and roughness of free faces in commercial blasting operations," *Cerebrovascular Diseases*, vol. 24, s1, pp. 181-188, 2007.
- [27] D. Johansson and F. Ouchterlony, "Shock wave interactions in rock blasting: the use of short delays to improve fragmentation in model-scale," *Rock Mechanics and Rock Engineering*, vol. 46, no. 1, pp. 1-18, 2013.
- [28] G. F. Brent, G. E. Smith, and G. N. Lye, "Studies on the effect of burden on blast damage and the implementation of new blasting practices to improve productivity at KCGMs Fimiston Mine," *Fragblast*, vol. 6, no. 2, pp. 189-206, 2002.
- [29] S. S. Aini, B. B. Sahari, A. Ali, A. A. Nuraini, A. A. Faieza, and T. T. Ismail, "Introducing fatigue contour plot in LS-Pre Post LSDYNA finite element crash simulation software," *Applied Mechanics & Materials*, vol. 165, pp. 275-279, 2012.

Research Article

Crack Evolution Characteristics and Cracking Mechanism of Red Beds in Central Sichuan during Seepage and Swelling

Zhe Zhou,^{1,2} Shanxiong Chen,¹ Yinhui Wang,^{1,2} and Zhangjun Dai¹ 

¹State Key Laboratory of Geomechanics and Geotechnical Engineering, Institute of Rock and Soil Mechanics, Chinese Academy of Sciences, Wuhan 430071, China

²School of Earth Sciences, University of Chinese Academy of Sciences, Beijing 100049, China

Correspondence should be addressed to Zhangjun Dai; zjdai@whrsm.ac.cn

Received 25 March 2021; Revised 2 April 2021; Accepted 9 April 2021; Published 28 April 2021

Academic Editor: Yu Wang

Copyright © 2021 Zhe Zhou et al. This is an open access article distributed under the Creative Commons Attribution License, which permits unrestricted use, distribution, and reproduction in any medium, provided the original work is properly cited.

Crack is one of the important factors affecting the engineering characteristics of expansive rock and soil. In order to study the evolution characteristics and cracking mechanism of red beds in Central Sichuan during seepage and swelling, multiple groups of cracking tests are conducted under different initial states with a self-made device. In addition, combining swelling-softening mechanism of expansive rock and numerical analysis, the swelling-cracking mechanism is studied. The following research results are obtained. (1) The evolution process of swelling cracks is divided into three stages: the generation stage, the rapid development stage, and the stabilization stage. In the rapid development stage, the increase in the crack degree accounts for 90% of the whole process. (2) The final crack degree of the sample is related to the initial water content, water absorption method, and clay mineral content. The lower the initial water content, the greater the final crack degree of the sample. The final crack degree under the soaking water absorption method is greater than that under the capillary water absorption method, and the final crack degree of mudstone is greater than that of argillaceous sandstone and sandstone. (3) The development of swelling cracks is controlled by three significant values of water absorption, which are w_1 , w_2 , and w_3 , respectively, representing the beginning of cracking, the starting of the rapid development stage, and the starting of the stabilization stage. Among them, w_2 is of great significance in engineering practice. It shows that the development of cracks has entered a stage of rapid development, and the crack degree in this stage will increase exponentially with water absorption. (4) Uneven water absorption and uneven distribution of clay minerals lead to uneven swelling of expansive rock, which in turn generates swelling stress. Under the combined action of swelling stress and water swelling-softening, the internal structure of the rock is destroyed, leading to the generation and development of the cracks. Due to the different causes of uneven expansion, the mechanical mechanism of cracking and the shape of the resulting cracks will be different.

1. Introduction

Crack is one of the important factors affecting the engineering properties of rock and soil. Previous studies have shown that cracks generate and expand under external stress, freeze-thaw, and dry-wet cycles, causing structural damage and strength attenuation of rock and soil, and changing the seepage characteristics of rock and soil [1–6]. Especially in expansive rock and soil engineering, fissures will cause serious deterioration of the engineering properties of the rock and soil mass, which will cause serious geological disasters and damage to engineering buildings and structures [7, 8].

Therefore, relevant geotechnical practitioners have conducted a large number of systematic studies on the expansive rock or soil cracks. These researches involve crack development characteristics and quantitative index analysis, influence factors of the development and expansion of cracks, and cracking mechanisms.

At present, there are a lot of research results on the crack development characteristics and quantitative description of expansive rock/soil. Chen [9] and Lu et al. [10] conducted CT test research on the crack evolution of expansive soil cracks. The research results show the process of crack development, new cracks connecting, and the formation of a crack

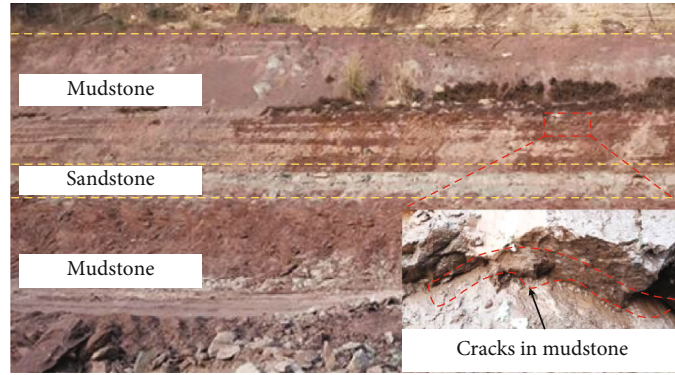


FIGURE 1: The red bed in Central Sichuan.

network. Yi et al. [11] studied the fractal characteristics of the fractured structure of expansive soils based on the fractal theory. Wang et al. [12] based on the numerical processing technology of image grayscale and binarization proposed the concept and quantitative description method of fissures in expansive rock. Li et al. [13] optimized and improved the image processing method of shrinkage cracks in expansive soil and the method of extracting crack features. Wei et al. [14] conducted a quantitative analysis of the cracks on the surface of expansive soil samples through indoor dry-wet cycle tests, and studied the variation of the geometric structure and morphological characteristics of the crack network with the number of cycles.

The evolution of cracks is greatly affected by the external environment. Tang et al. [15] studied the effect of temperature on the shrinkage cracks of expansive soil and found that the shrinkage cracks have obvious temperature effects. Mao et al. [16] studied the effects of different initial damage degrees, different numbers of dry-wet cycles, and coupled conditions of the two on the development and evolution of pores and fissures in expansive soils, as well as the corresponding soil deformation and mechanical behavior. Hu et al. [17] conducted a CT scan test on the undisturbed expansive soil through the dry-wet cycle, and studied the relationship between the three-dimensional space cracks and the dry-wet cycle from both qualitative and quantitative aspects. Lou et al. [18, 19] studied the influence of size and temperature on the evolution of cracks in expansive soils, and combined with the tensile failure theory of soil cracking and the shrinkage and evaporation of the sample, the cracking mechanism of soil under the influence of thickness is theoretically analyzed.

On the generation and propagation mechanism of cracks, many researchers have conducted considerable in-depth researches from the aspects of experiment, theory, and numerical model. Konrad and Ayad [20] established a theoretical model of clay cracking under the condition of surface evaporation through the field test results of clay dry cracking; Yao et al. [21] used elastic theory and fracture mechanics principle to put forward the mathematical expression of crack propagation depth, which basically determined the approximate depth of crack development. Ma et al. [22] studied the process of crack generation, propagation, and

expansion under the condition of dehumidification, and summarized the laws of crack generation, propagation, and expansion. Wu et al. [23] studied the development mechanism of initial cracks in expansive soil when water content changes, and established a theoretical model. Yin et al. [8] proposed that high shrinkage and low permeability are the basic reasons for the multicracks of expansive soils, and further discussed the generation mechanism and development process of cracks in expansive soils.

The above studies are mainly aimed at the shrinkage cracks of the expansive rock/soil under the condition of water loss. However, under the condition of water absorption, the expansive soil generally does not develop cracks, but the expansive rock will develop and expand cracks. Many scholars have observed the development and expansion of cracks in the expansion test and disintegration test of expansive rock [24–26]. In response to this phenomenon, the researchers only carried out some qualitative descriptions and analyses, and believed that the evolution of fissures was one of the reasons for the volume expansion and the disintegration of expansive rock. However, these studies did not quantitatively analyze the evolution characteristics of swelling cracks nor did they in-depth study of the mechanism of swelling cracks.

This work takes the red-bed mudstone in Central Sichuan as the research object. Through the self-made soft rock water absorption and cracking test device, multiple sets of unconfined swelling-cracking tests under different initial conditions were carried out. The crack field information is visualized through image recognition and interpretation technology. Combined with the analysis of fissure quantitative indicators, the evolution law and influencing factors of swelling cracks in red-bed mudstone are studied, and the relationship curve between the crack degree and water absorption is established. Finally, combining the swelling mechanism and numerical analysis, cracking mechanism of expansive rock under water swelling condition is studied.

2. Experimental Material and Methodology

2.1. Rock Material and Its Basic Physical Properties. The expansive rock materials studied in this work were acquired from red beds in Central Sichuan (Figure 1). The red bed is

TABLE 1: X-ray diffraction results (unit: %).

Lithology	Montmorillonite	Illite	Chlorite	Kaolinite	Calcite	Hematite	Quartz	Albite	Plagioclase
Mudstone	20	15		5		1	38	21	
Argillaceous sandstone	5	13	5		2	3	37	27	8
Sandstone		11	4	12	3		31	27	12

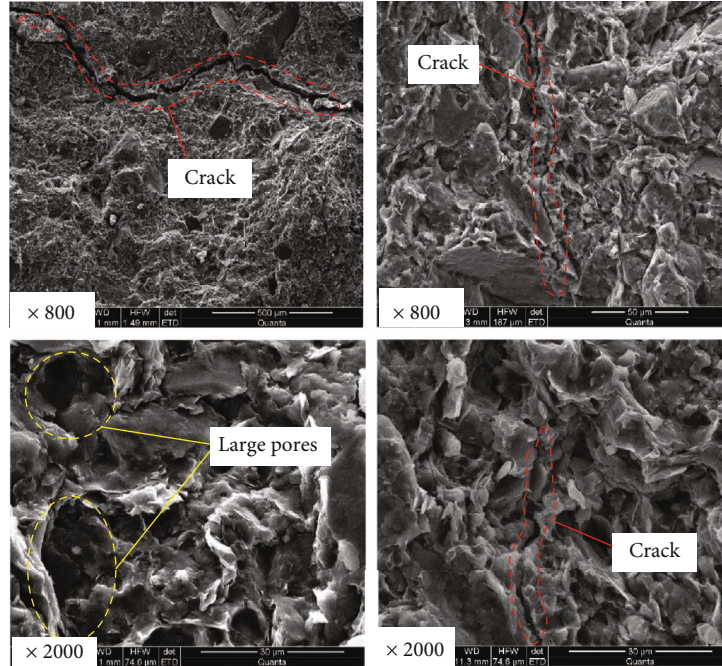


FIGURE 2: SEM results of mudstone.

the Middle Jurassic Upper Shaximiao Formation (J_2s) mudstone intercalated with sandstone. The mudstone is purple-red, argillaceous cemented, with well-developed fissures, contains more hydrophilic minerals, and is easy to disintegrate. Laboratory swelling test research shows that the average swelling force of the original rock is 700 kPa, and the average free expansion rate of rock powder is 27.9%, which has a large expansibility [27, 28]. The sandstone is gray-green/gray-white, mostly feldspar quartz sandstone, with medium-fine grain structure, argillaceous cement, hard texture, and nonswelling.

Table 1 shows the X-ray diffraction results of the test samples. From the results, mudstone contains 20% montmorillonite and 15% illite, argillaceous sandstone contains just 5% montmorillonite and 13% illite, and sandstone contains only 11% illite. According to SEM imaging analysis of mudstone sample in Figure 2, microcracks are developed, and clay minerals are stacked in flakes with no obvious orientation arrangement. In addition, there are some large pores and many small pores that can be observed.

2.2. Test Method. In the process of water swelling of mudstone, cracks must generate and develop in three-dimensional space. However, due to limited conditions, the sample cannot be scanned by three-dimensional CT (com-



FIGURE 3: Rock sample.

puted tomography) during the test. Therefore, the test mainly focuses on the observation and quantitative analysis of surface cracks on the sample. The sample is a rock cake obtained by cutting the core (Figure 3), and its size is $\phi \times h = 64.0 \text{ mm} \times 24.0 \text{ mm}$. The selection of the thickness

TABLE 2: Basic physical properties of samples.

Sample number	Lithology	Method of water absorption	Initial water content (%)	Thickness (mm)	Diameter (mm)	Natural density (g/cm^3)
1#	Mudstone	Capillary absorption	4.01	23.82	65.51	2.49
2#			2.95	24.23	63.17	2.51
3#			1.56	23.92	64.35	2.51
4#		Soaking absorption	4.01	23.94	64.35	2.51
5#			2.90	24.06	64.50	2.51
6#	Argillaceous sandstone	Soaking absorption	3.37	24.00	64.10	2.49
7#			2.56	24.30	64.66	2.49
8#	Sandstone		3.34	24.20	64.42	2.46

takes into account the need for surface crack observation (the thinner the sample, the easier the cracks to develop and the easier the observation) and the difficulty of sample preparation (the thinner the sample, the more difficult it is to prepare the sample).

A total of 8 samples were selected for this test, including 5 mudstone samples, 2 argillaceous sandstone samples, and 1 sandstone sample. The basic parameters of each sample are shown in Table 2, and the clay mineral composition is shown in Table 1.

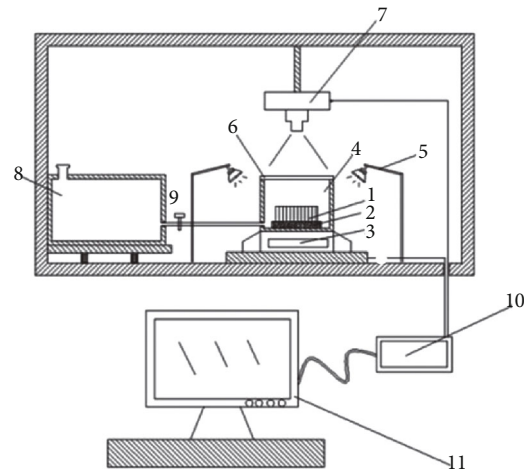
There are many factors influencing the swelling-cracking of expansive rock. The external factors include environmental conditions (temperature and humidity) and water absorption methods (capillary water absorption, soaking water absorption, and pressure). The internal factors include sample size and initial water content, density, clay mineral composition, and internal initial cracks. This test mainly analyzes the influence of initial water content, clay mineral content (different lithology), and different water absorption methods on the characteristics of swelling cracks under no confining condition.

Different initial water content is obtained by controlling the sample to air-dry at 45°C . Capillary absorption means that the sample absorbs water from the saturated permeable stone through capillary action. Soaking absorption means that the bottom and sides of the sample are immersed in water, and the top surface is left as observation surface without being immersed in water. The samples with the same lithology are all taken from the same rock core to ensure that the samples with the same lithology are uniform.

2.3. Test Device and Process. The soft rock water absorption and cracking test device is shown in Figure 4. The water tank provides the water source to the sample dish, and the sample gains weight by absorbing water. Then, the weight of the water absorbed is measured by the electronic balance, and the photo of swelling cracks on the surface of the sample is obtained with the camera. All collected photos and water absorption data are input to the computer via a data collector.

The main processes of the test are as follows:

(1) Before the test, fix the position of the camera to ensure that the focus direction of the camera is



- | | |
|------------------------|---------------------|
| 1 – Sample | 7 – Digital camera |
| 2 – Permeable | 8 – Water tank |
| 3 – Electronic balance | 9 – Control valve |
| 4 – Sample dish | 10 – Data collector |
| 5 – LED lamp | 11 – Computer |
| 6 – Sealing cover | |

FIGURE 4: Test device of soft rock water absorption and cracking.

perpendicular to the surface of the sample. At the same time, adjust the LED light sources on both sides to keep the vertical projection as much as possible to reduce the impact of shadows on photo quality

- (2) Set the shooting interval of the camera and the recording interval of the electronic balance at the specified time interval
- (3) In the capillary moisture absorption mode, pour distilled water into the water tank, and set the sample when the water level in the sample cuvette just surpasses the permeable stone
- (4) In the soaking water absorption mode, wrap the surface of the sample with plastic wrap and place it

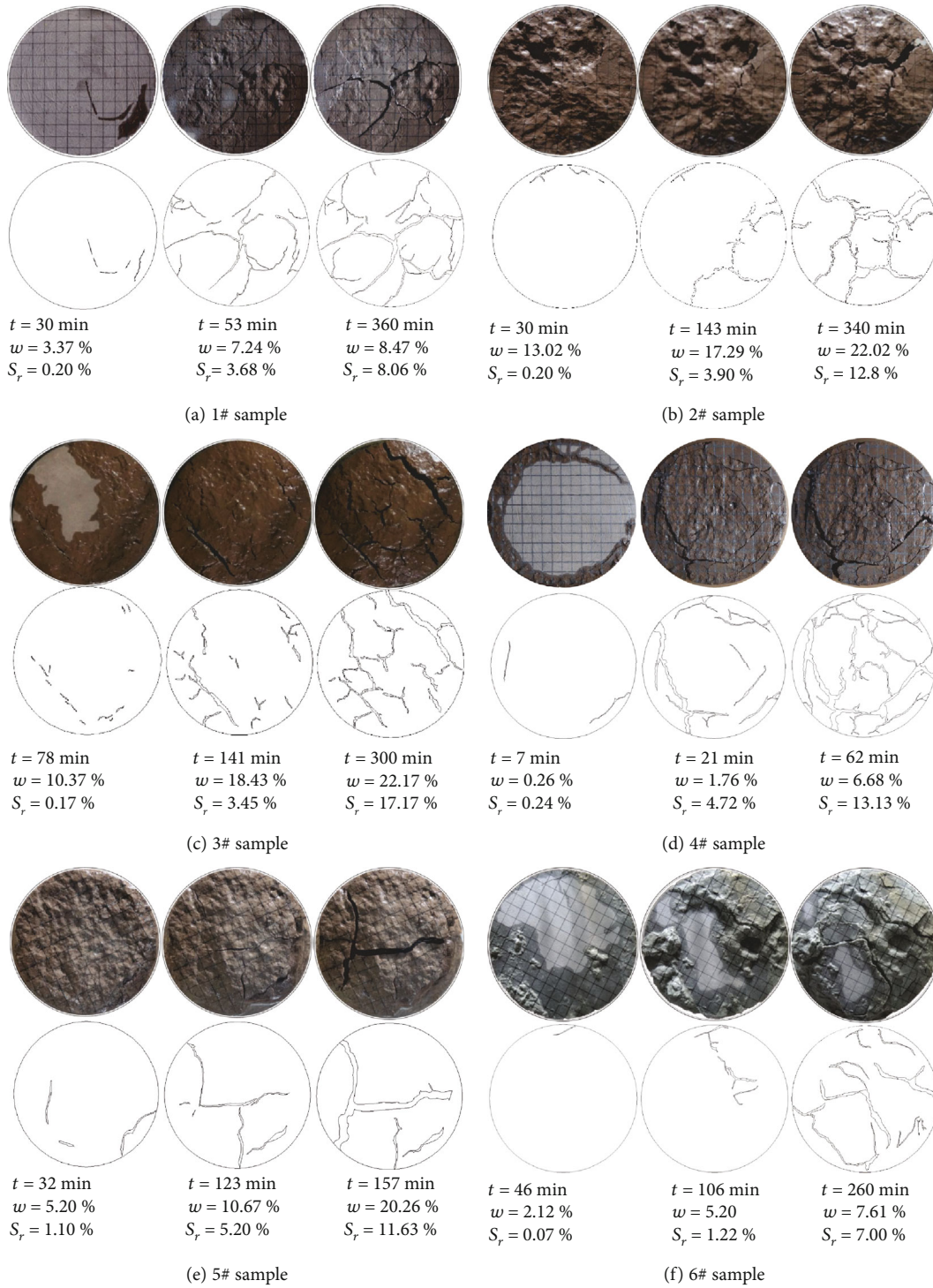


FIGURE 5: Continued.

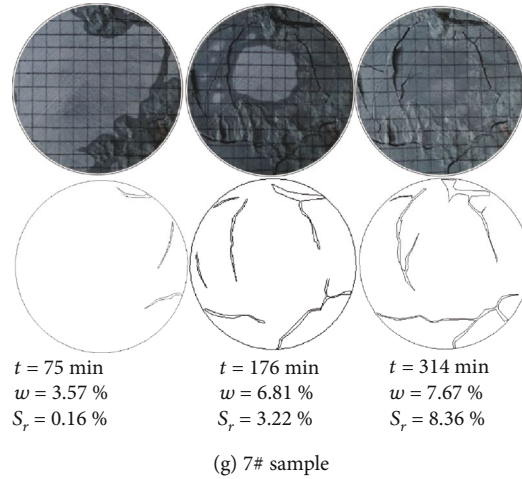


FIGURE 5: Cracking pictures of samples.

on the permeable stone, and then pour water into the water tank so that the liquid level in the water absorption dish is just under the upper surface of the sample. Close the control valve and remove the sample. Take it out and install the sample after removing the cling film, and open the control valve at the same time

- (5) Start collecting test data and observe the test process. When the water absorption does not increase and the cracks no longer change within 1 hour, the test is complete

3. Experimental Results and Analysis

3.1. Quantitative Indexes of Crack Field. By taking photos of the surface of the sample during the test, the spatial distribution and temporal changes of the cracks are recorded. Then use image processing technology to get the relevant crack indexes. There are many ways to implement crack image processing. However, considering that the cracks in this test are affected by the background environment (caused by water absorption), it is difficult to perform batch processing in accordance with conventional processing methods [8]. Therefore, the cracks in the photos of this experiment are all manually drawn by CAD. Due to the large amount of photos during the entire experiment, only the images with large fissure changes were processed. In addition, there are many small cracks on the surface of the sample, but due to the influence of swelling and mudding on the mudstone surface, it is difficult to count the small cracks. Therefore, only the cracks with larger width or later development are drawn.

Currently, the more commonly used crack indexes are total length of cracks, average width of cracks, maximum width of cracks, and the proportion of the area of cracks. In this test, the crack degree index was used to quantitatively analyze the evolution of the swelling cracks. This index comprehensively considers the degree of crack development

(length and width), and the calculation method is shown in Equation (1).

$$S_r = \frac{\sum S_i}{S_0}, \quad (1)$$

where S_r is the crack degree (%), S_i is the area of the i -th crack (mm^2), and S_0 is the initial upper surface area of the sample (mm^2).

3.2. Analysis of Crack Evolution Process. A large number of crack development photos were obtained from the experiment, and crack diagrams at different stages were drawn through CAD. Figure 4 shows the typical photos and crack diagrams of samples 1#~7# at different stages, and lists the state of the sample at each stage, including time t , the water absorption w , and the crack degree S_r . Since the 8# sample did not appear cracks during the water absorption process, it was not analyzed.

It can be seen from Figure 5 that the cracks of the specimens basically developed from the outside to the inside, gradually connected, and developed into a crack network. Each crack network is basically composed of 2 to 4 main fractures and several fine cracks. The basic morphology of the cracks is mainly arc or chord shape which develops circularly and short-line shape which develops radially.

In order to quantitatively analyze the swelling-cracking process of red-bed mudstone, taking the 2# sample as an example, the curve of the crack degree over time is shown in Figure 6. It can be seen from Figure 6 that the evolution process of the cracks can be divided into three stages, namely, the generation stage, the rapid development stage, and the stabilization stage.

Figure 7 shows the generation stage. During this stage, the sample begins to absorb water, and the surface becomes muddy and uplifted due to swelling and softening. A small amount of fine cracks are generated, but these cracks are

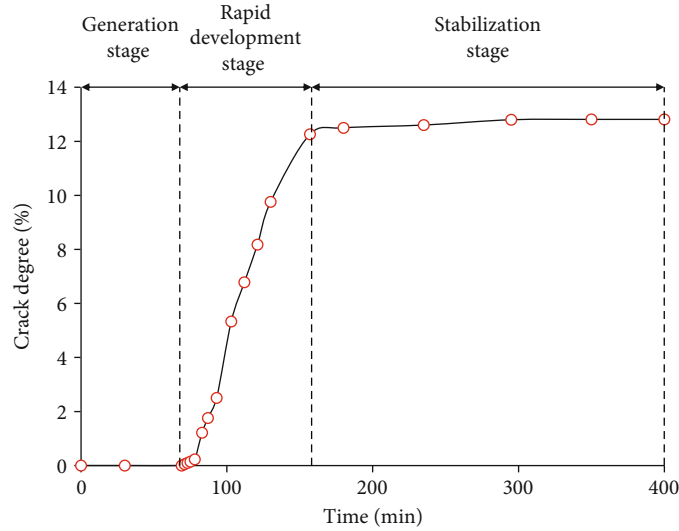


FIGURE 6: Curve of crack degree over time of 2# sample.

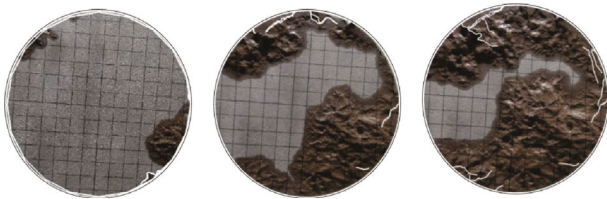


FIGURE 7: Generation stage.

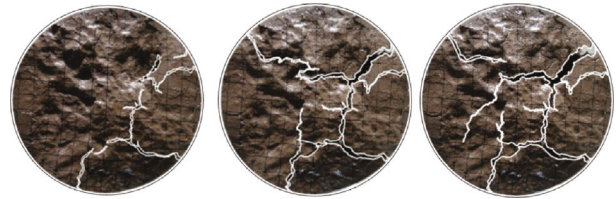


FIGURE 8: Rapid development stage.

short and local, independent and not connected to each other. The overall crack degree is small.

Figure 8 shows the rapid development stage of the cracks. In this stage, the old small cracks quickly grow and expand with new cracks forming. The old and new cracks are intertwined and connected with each other. In this stage, the crack degree has increased significantly.

Figure 9 shows the crack stabilization stage. During this stage, cracks grow slowly and the crack degree increases slowly to be constant.

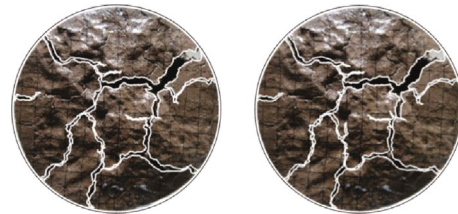


FIGURE 9: Stabilization stage.

3.3. *Influencing Factors of Crack Evolution Characteristics.* In order to analyze the influence of the initial state of the sample on the evolution characteristics of swelling cracks, plotting the time history curve of crack degree of different water absorption methods and different lithology samples is shown in Figures 10 and 11.

The following points can be obtained from Figures 10 and 11:

- (1) The three-stage characteristics of crack development are obvious. In the first stage, the crack degree did not increase. In the second stage, the crack degree increased rapidly. The duration of this stage was short, but the increased crack degree accounted for 90% of the whole process. In the third stage, the crack degree increased slowly, but eventually stabilized

- (2) Lithology, initial water content, and water absorption methods have a significant impact on the initial cracking time (as shown in Figure 12). Under capillary water absorption, the higher the initial water content of the sample, the earlier the cracks will appear. Under the same initial water content, the initial cracking time of soaking water absorption is significantly earlier than capillary water absorption. Under soaking water absorption conditions, mudstone started to crack earlier than argillaceous sandstone. This phenomenon may be related to the process of water swelling and softening. The initial water content is high, and the initial softening degree of the sample is large; in addition, the content of clay minerals such as montmorillonite is high, the greater the expansion and softening during the water

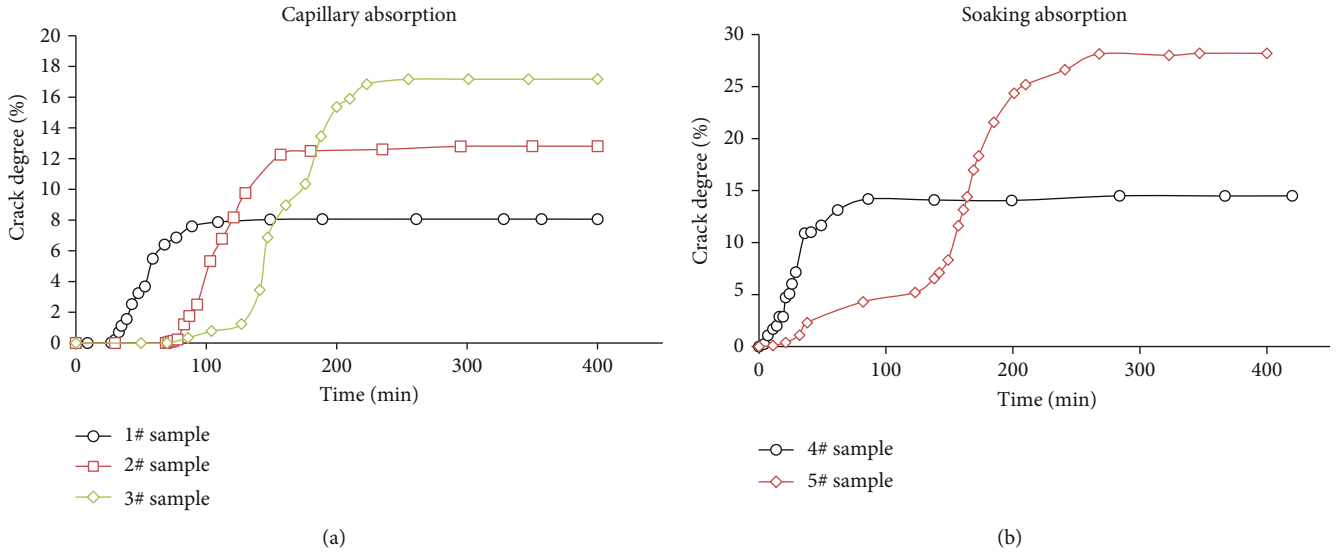


FIGURE 10: Time history curves of crack degree of 1#~5# samples.

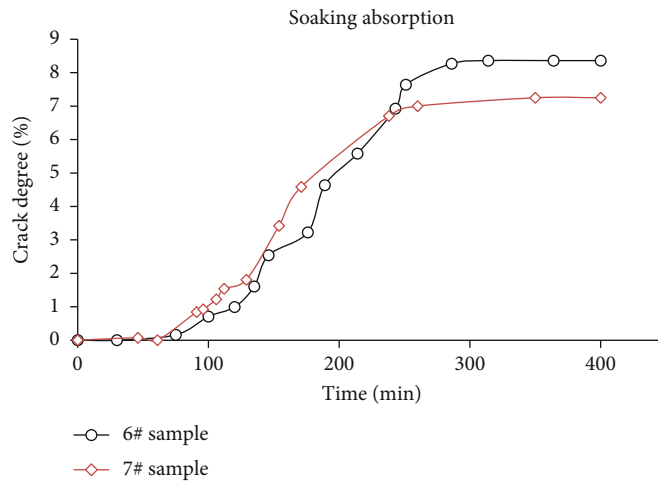


FIGURE 11: Time history curves of crack degree of 6#~7# samples.

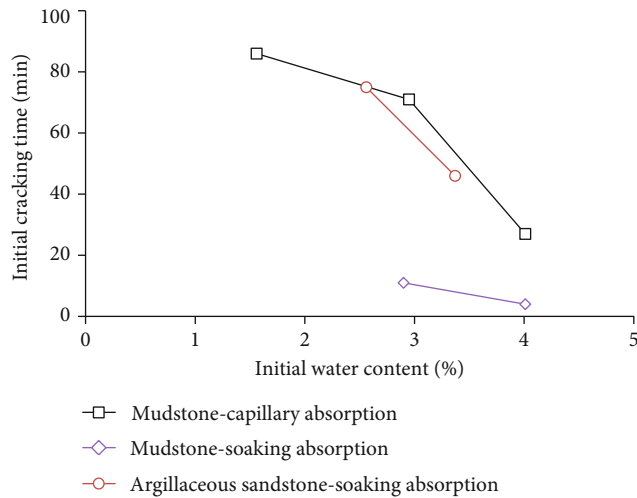


FIGURE 12: Curves between initial cracking time and initial water content

TABLE 3: Final crack degree of samples.

Sample number	Lithology	Method of water absorption	Initial water content (%)	Final crack degree (%)
1#	Mudstone	Capillary absorption	4.01	8.06
2#			2.95	12.81
3#			1.56	17.18
4#	Argillaceous sandstone	Soaking absorption	4.01	14.50
5#			2.90	28.20
6#			3.37	7.25
7#	Sandstone	Soaking absorption	2.56	8.36
8#			3.34	0

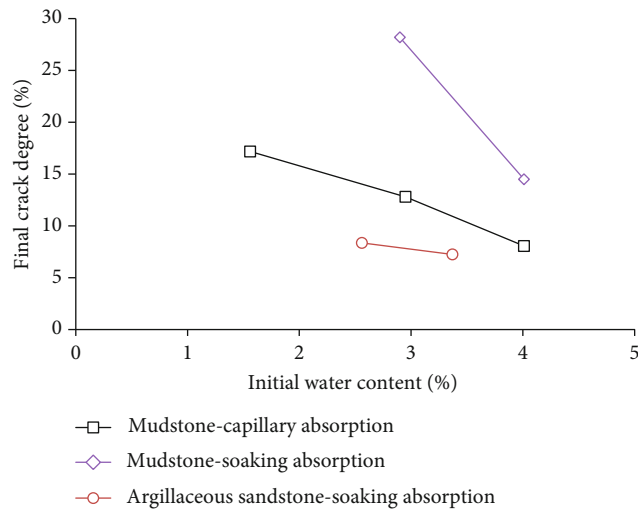


FIGURE 13: Curves of final fissure ratio and initial water content.

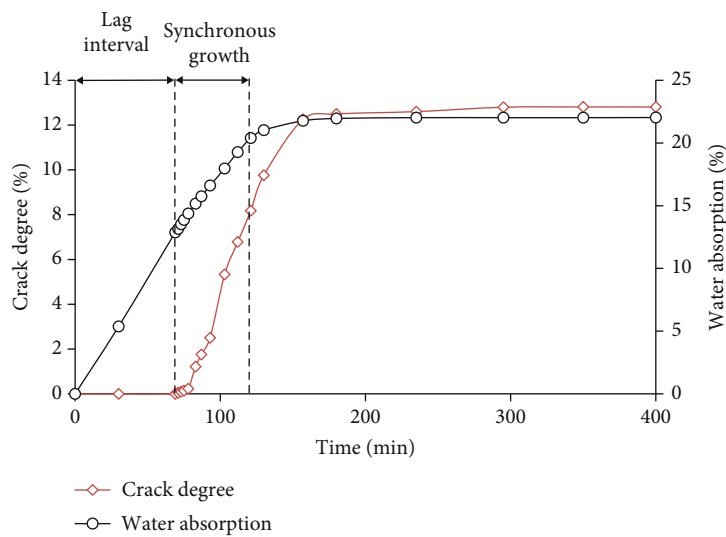


FIGURE 14: Curves of crack degree and water absorption over time of 2# sample.

absorption process; finally, the water migration is faster under soaking water absorption. These three reasons work together to make the cracking occurred earlier

(3) Lithology, initial water content, and water absorption methods also have a significant impact on the final crack degree. Table 3 shows the statistical results of the final crack degree after the test, and Figure 13

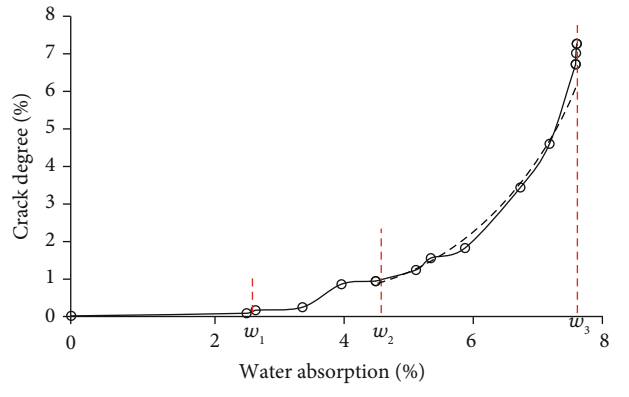
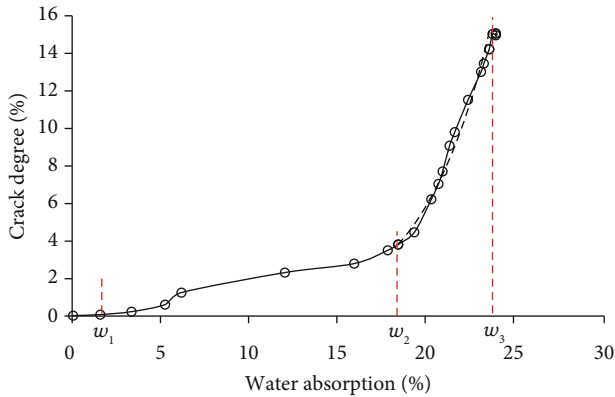
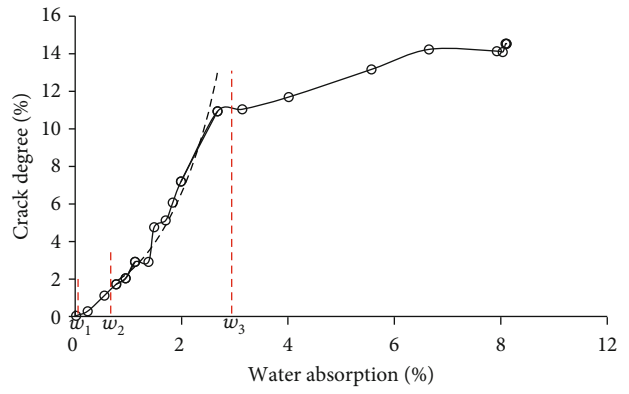
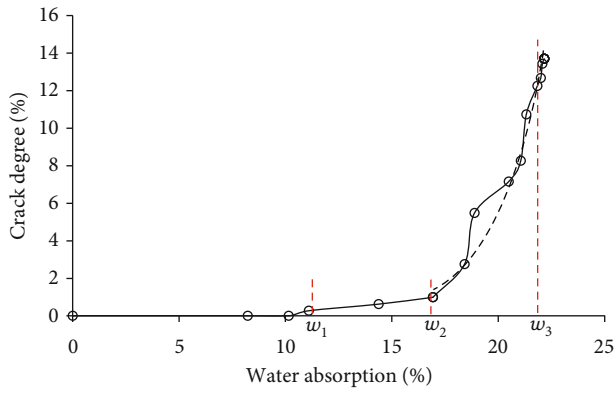
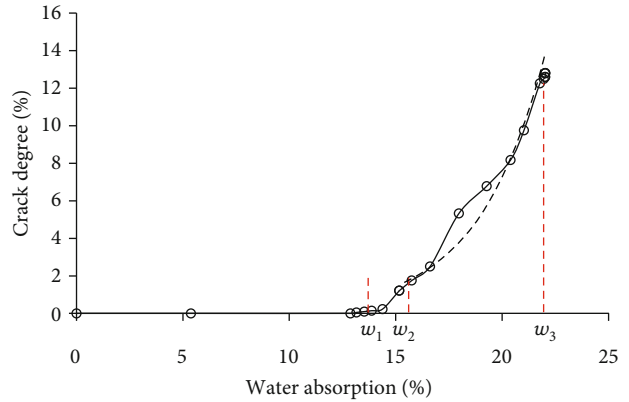
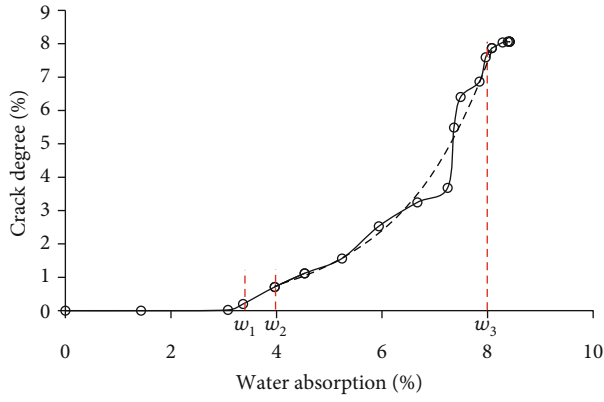


FIGURE 15: Continued.

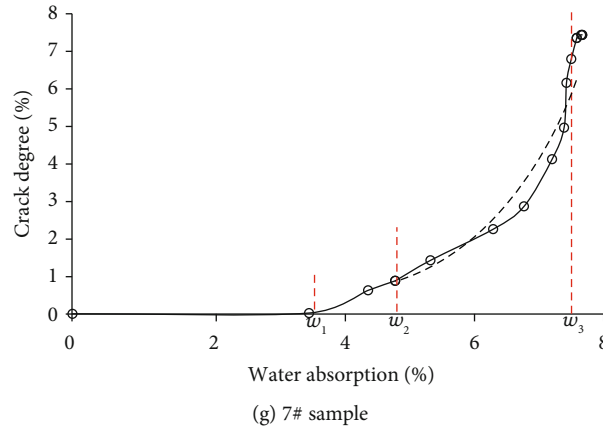


FIGURE 15: Relationship curves of crack degree and water absorption of 1#~7# samples.

TABLE 4: Characteristic values of water absorptions and fitting results.

Sample number	Characteristic value of water absorptions (%)			Fitting results ($S_r = ae^{bw}$) (S_r (%), w (%))		
	w_1	w_2	w_3	a	b	R^2
1#	3.08	3.97	8.29	0.0791	0.5683	0.98
2#	13.15	15.12	22.02	0.0119	0.3207	0.97
3#	11.10	16.94	21.86	0.0009	0.4468	0.95
4#	0.26	0.91	3.76	0.8509	0.8527	0.95
5#	1.54	18.38	23.71	0.0517	0.2687	0.98
6#	2.64	4.59	7.61	0.043	0.6509	0.99
7#	3.56	4.87	7.67	0.0283	0.7253	0.96

shows the relationship between the final crack degree and the initial water content

It can be seen from Figure 13 that the lower the initial water content, the greater the final crack degree of the sample, and the final crack degree under the soaking water absorption method is greater than the capillary water absorption. The final crack degree of mudstone is greater than that of argillaceous sandstone and sandstone.

The main reason for the development and expansion of swelling cracks is the uneven expansion of the sample during water absorption. The degree of this uneven expansion is controlled by the swelling potential of expansive rock.

The greater the swelling potential of the expansive rock is, the greater the internal stress caused by the uneven swelling deformation, and the resulting crack development and expansion will be more intense. The mudstone sample contains 20% montmorillonite, and its expansion potential is much greater than that of argillaceous sandstone, while sandstone has no montmorillonite mineral and has no obvious expansibility. Therefore, the swelling crack degree is generally larger than that of sandy mudstone. Due to the small expansibility of sandstone, the uneven expansion stress generated is not enough to cause the damage of the rock material, so no cracks are generated.

Even with the same expansion potential (such as 1~3# samples, 4~5# samples, and 6~7# samples), the initial water content of the sample is different, and the expansion energy

released under the condition of complete water absorption is also different. The lower the initial water content is, the greater the released expansion energy is, and the greater the swelling deformation and swelling stress are. Therefore, as the initial water content decreases, the final crack degree increases.

The water absorption method also affects the crack development of the sample. Compared with the capillary method, the sample absorbs water faster under the soaking method. Thus, the faster the water absorption is, the larger the internal water content gradient is, resulting more serious uneven expansion and softening. Therefore, the final crack degree under soaking method is higher than capillary method.

In summary, the degree of development of swelling cracks in expansive rocks is controlled by the swelling potential, and the basic material condition for swelling and cracking is swelling clay minerals.

3.4. Analysis of the Relationship between Crack Degree and Water Absorption. The swelling and cracking of red-bed mudstone is a process in which water absorption gradually increases, expansion occurs continuously, and cracks continue to develop. In order to analyze the time history change relationship between the crack degree and the water absorption in this process, the time history change curve of the 2# sample crack degree and water absorption was drawn in the same coordinate, as shown in Figure 14.

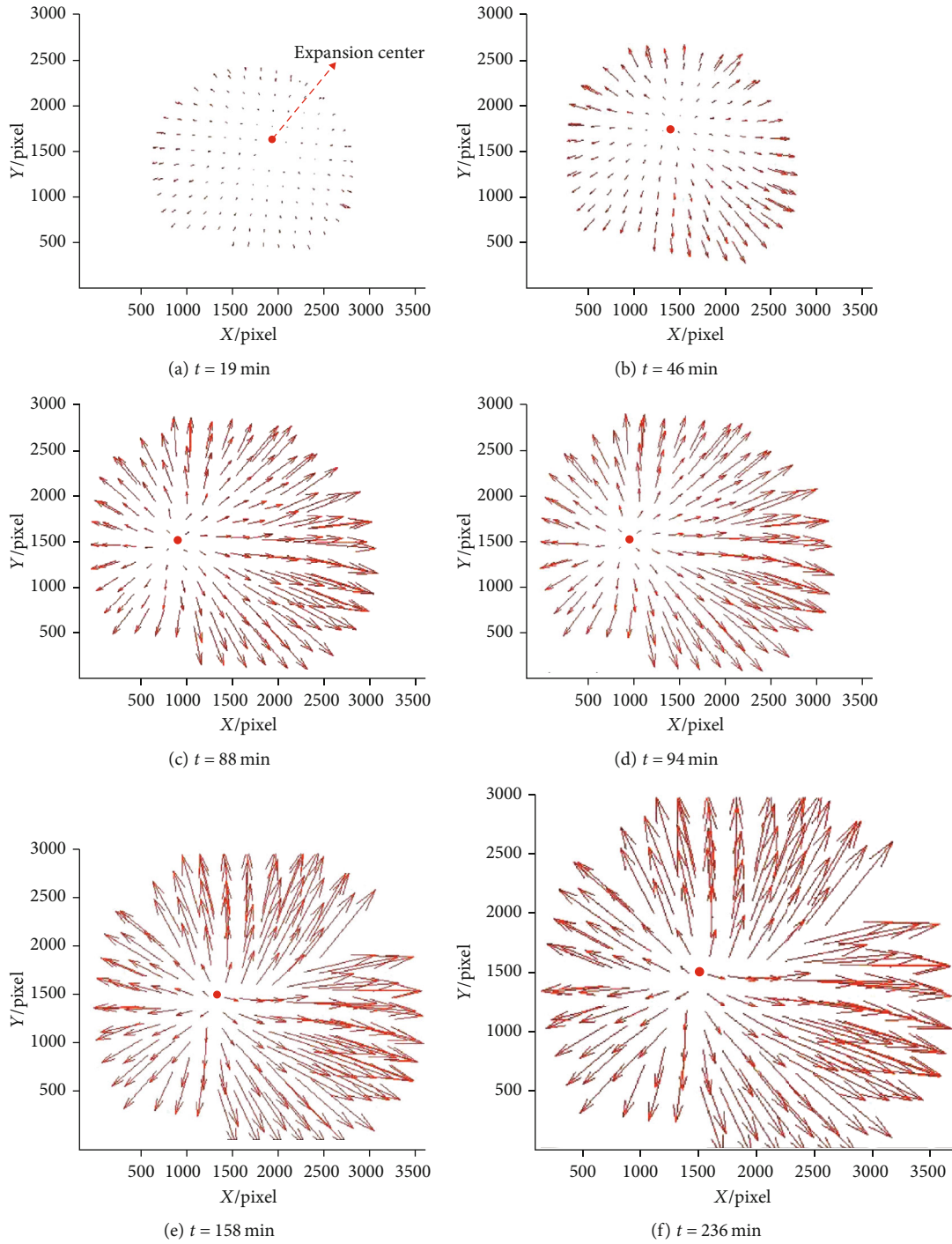


FIGURE 16: Displacement vector graph in different times of 2# sample.

It can be seen from Figure 14 that the crack degree is basically unchanged in the early stage of the test, while the water absorption increases rapidly. When the water absorption reaches a certain level, the cracks and the water absorption increase simultaneously. After the growth of water absorption gradually slows to stability, the cracks still grow, but eventually tend to stabilize. In general, the growth of the crack degree lags behind the increase of water absorption.

In order to further analyze the relationship between the crack degree and water absorption, the relationship curves of 1#~7# samples are plotted in Figure 15. It can be seen from Figure 15 that the crack degree of the seven samples changes with the water absorption basically similar, and there are three characteristic values of water absorption that control the development of the cracks. At the beginning of the test, the water absorption continued to increase, but the crack degree was always zero. When the water absorption increases

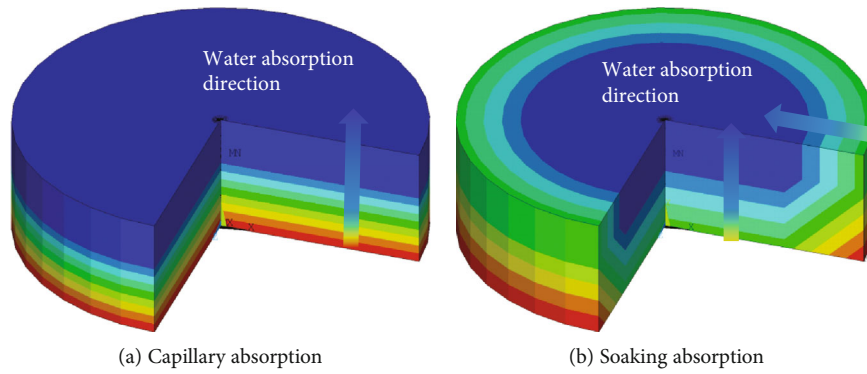


FIGURE 17: Numerical analysis model.

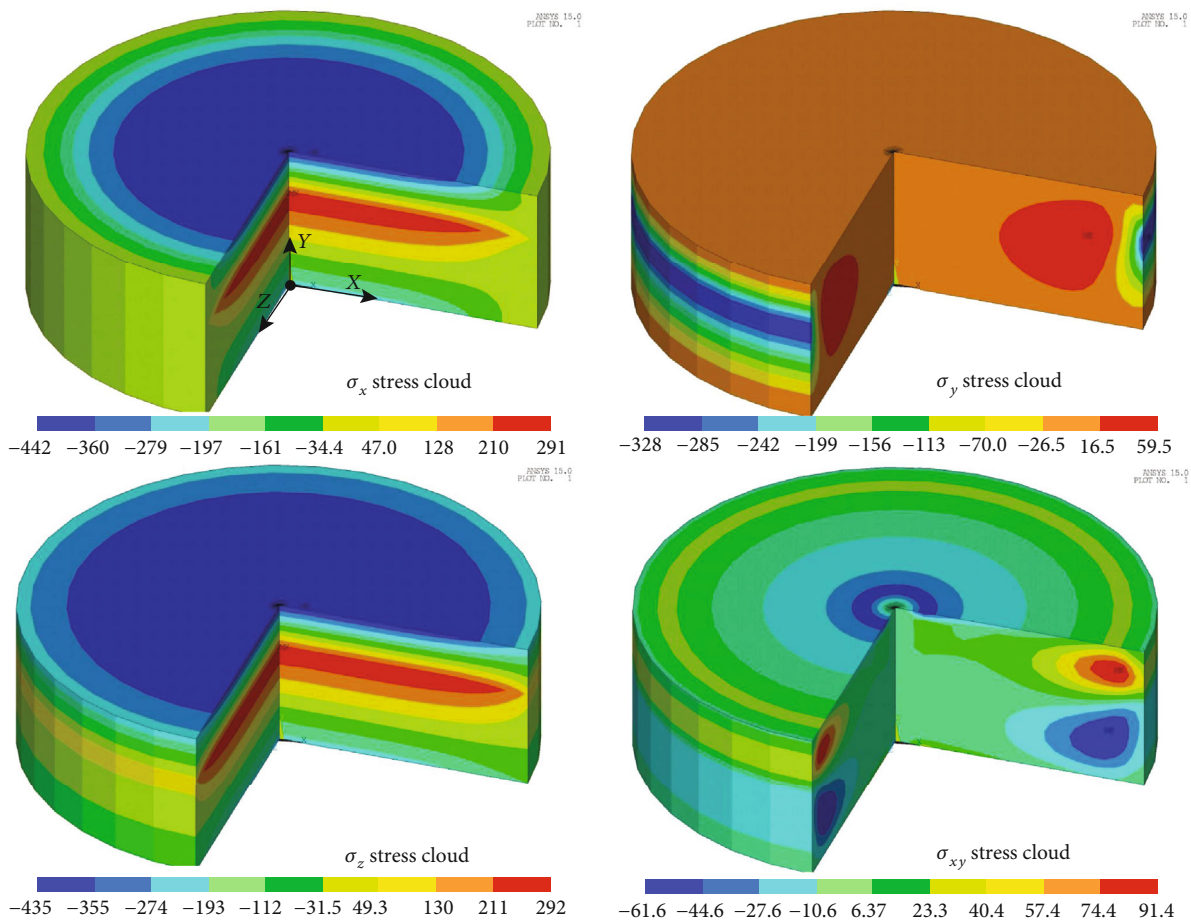


FIGURE 18: Stress cloud diagrams under capillary water absorption (unit: kPa).

to the first characteristic value w_1 , cracks begin to occur, and the crack degree slowly increases with the water absorption. As the water absorption increases to the second characteristic value w_2 , the crack degree begins to increase sharply with the water absorption. The growth trend is close to the exponential type, and the fitting correlation is good ($R^2 > 0.9$). When the water absorption is close to or reaches the third characteristic water absorption w_3 , the crack degree increases slowly to a stable value. Table 4 lists the characteristic values of

water absorption of each sample and the fitting results of the rapid development stage.

Among the three characteristics of water absorption, w_2 has a relatively large engineering significance. Under rainfall conditions, with the infiltration of water, the water absorption of swelling rock/soil slopes gradually increases. When the water absorption increases to w_2 , the cracks on the open surface such as the toe or shoulder of the slope will develop rapidly. As a result, the overall strength of the slope shoulder,

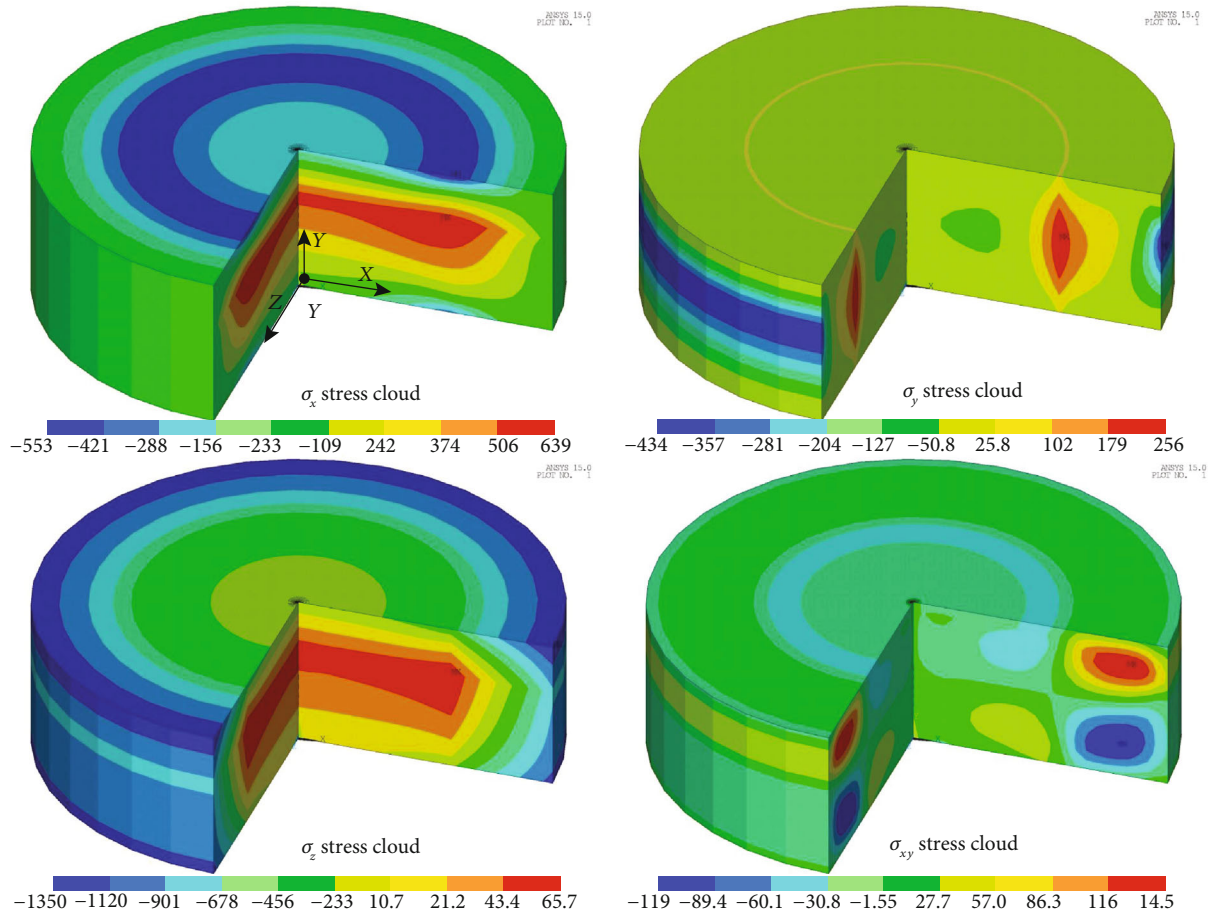


FIGURE 19: Stress cloud diagrams under soaking water absorption (unit: kPa).

especially the slope toe, is significantly reduced, leading to instability and failure of the slope.

4. Discussion on the Swelling-Cracking Mechanism

In the process of water loss and shrinkage of expansive rock/soil, tensile stress is generated on the surface due to the different evaporation degrees of the external and internal surfaces. When the tensile stress exceeds the tensile strength of the soil, tensile cracks will occur. The tensile stress caused by this inconsistent water loss of internal and external will make the cracks continue to develop in depth, and the cracks will develop and expand horizontally with the overall water loss and shrinkage of the soil. However, different from shrinkage cracks, swelling cracks of expansive rock are generated in the process of water absorption and swelling. In this process, on the one hand, the uneven expansion deformation leads to the internal swelling stress; on the other hand, the water swelling and softening decrease the bond strength between clay particles. From these two aspects, the swelling-cracking mechanism is completely different from the shrinkage cracking mechanism, so the mechanical mechanism of the swelling and cracking needs to be further studied.

4.1. Reasons for Uneven Expansion of Swelling Rock. In order to intuitively reflect the uneven expansion of the swelling rock during the water absorption process, the displacement of the black grid points in the 2# sample was calculated, and the displacement vector diagram is drawn in Figure 16.

It can be seen from Figure 16 that during the process of water absorption, the sample continuously expands outwards, and there is always a point in each vector diagram that does not shift, which is regarded as the center of expansion. As time changes, the center of expansion is constantly changing and it is not near the center of the sample. This shows that the water swelling process is an uneven expansion, and this uneven expansion is constantly changing over time.

The swelling potential of expansive rock is directly related to its clay mineral content, and the release of swelling potential is controlled by its water absorption. Therefore, from these two aspects, the uneven expansion of the sample may be caused by uneven water absorption and uneven distribution of swelling clay minerals.

4.2. Uneven Water Absorption Process. The process of water migration inside the sample inevitably determines the unevenness of water absorption. In the process of water absorption for a uniform and crack-free sample, the outer material preferentially absorbs water and expands. With the migration of water, the inner material expands later, so there

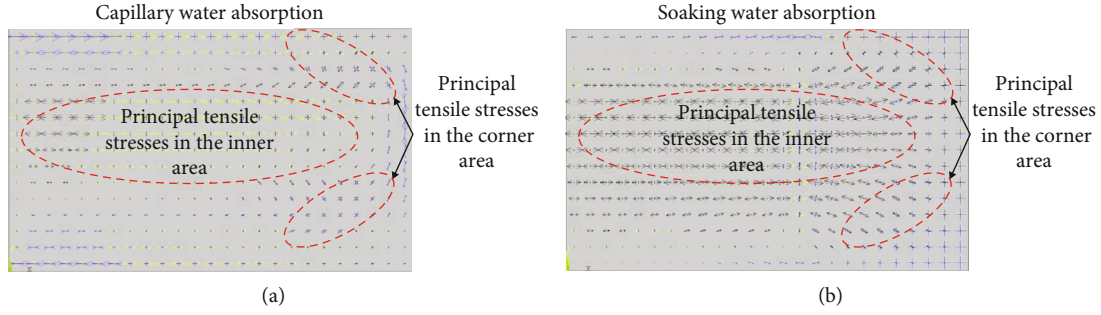


FIGURE 20: Principal stress vector diagram of XOY section.

is a sequential expansion difference in time. At the same time, the external has larger water absorption than the internal, meaning the released expansion energy of the external is greater than that of the internal. Therefore, there is an uneven expansion in space. In general, due to uneven water absorption, there is a humidity gradient field in the sample space, and the humidity gradient field changes with time.

In order to analyze the distribution law of the expansion stress caused by the humidity gradient field, an axisymmetric numerical analysis model was established using ANSYS software, as shown in Figure 17. The material parameters involved in the model refer to Dai et al. [29], and the calculated stress cloud diagrams are shown in Figures 18 and 19 (the X-axis is the radial direction, the Y-axis is the axial direction, and the Z-axis is the circular direction).

It can be seen from Figures 17 and 18 that the stress distribution law is basically similar in the two cases of soaking and capillary water absorption. The radial stress and the circular stress σ_z have similar distributions, and both change more uniformly along the radial direction. The outer area is compressive stress; the middle area is tensile stress. Axial stress σ_y changes from compressive stress to tensile stress from outside to inside in the radial direction, with obvious concentrated stress area. The shear stress σ_{xy} has an obvious concentration area in the outer edge, and the whole internal shear stress is much smaller than other stresses.

Since the internal area of the sample has not been softened by water, the horizontal tensile stress σ_x and σ_z needs to destroy the bond strength to produce vertical cracks. This is difficult when there is no internal water swelling and softening, and no structural defects (such as microcracks). The concentrated area of axial stress σ_y is on the outer surface, and prone to water softening. Therefore, this area is easier to damage and crack from the perspective of fracture mechanics. In addition, from the principal stress vector diagram of the XOY section (Figure 20), there are principal tensile stresses in the inner area and corner area of the specimen, which may provide mechanical conditions for the propagation of the cracks.

According to the above analysis, the sample swells during the process of water absorption, and compressive stress concentration area appears in the middle part of the side (see Figure 21). Due to compressive stress concentration σ_y and water softening of the rock material, shear failure is very

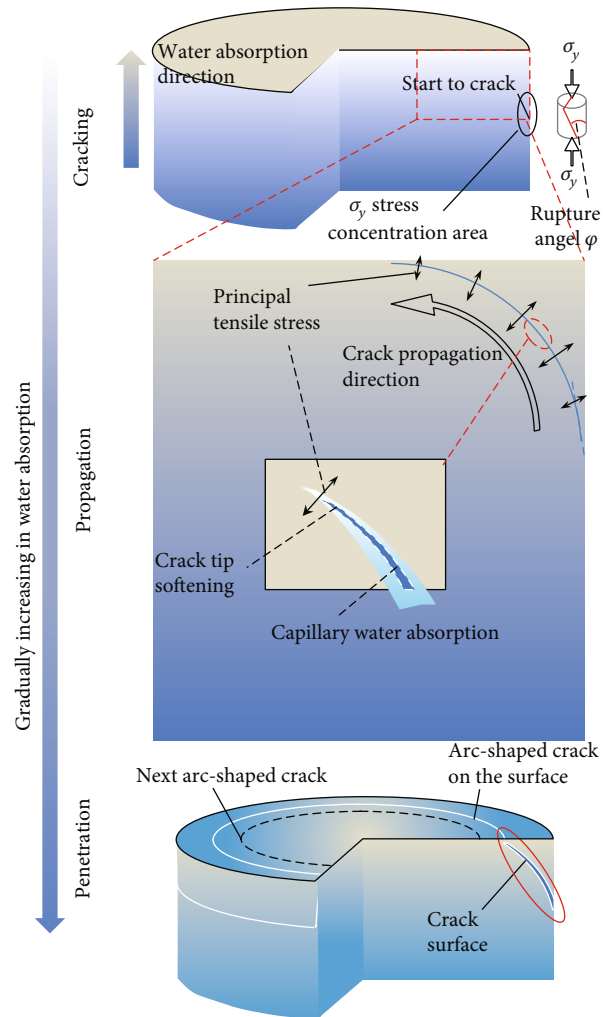


FIGURE 21: Processing of crack development.

likely to occur in this area, and the crack will form a certain angle (rupture angle φ) with the side face. Under capillary action, water will migrate to the tip of the crack, causing the tip to absorb water and soften. At the same time, under the action of the principal tensile stress in the corner area, the crack will continue to expand along the vertical direction of the principal tensile stress until it penetrates the upper surface of the sample, forming a crack surface as shown in

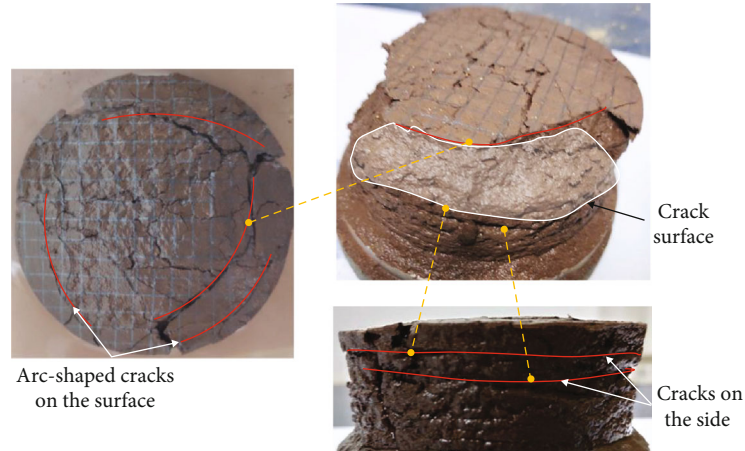


FIGURE 22: Cracks of 4# sample.

Figure 21. It is worth noting that, theoretically, this kind of crack can develop on the upper and lower surfaces, and the degree of softening and crack development on the lower surface should be more serious. But in fact, due to the friction between the bottom surface and the permeable stone and the action of gravity, the degree of development of cracks on the bottom surface is much lower than that on the upper surface.

The development mode of this crack will gradually move to the inside of the sample as the crack penetrates and softens by water absorption. In this way, during the whole test process, the sample will produce layer after layer of “wrapped” crack surface, which is a layer of arc-shaped cracks when observed on the surface of the sample. This type of arc-shaped cracks appears more often in the rapid development stage (Figure 22).

Finally, the model considers the case where the material is uniform and has no internal microcracks. In fact, according to the SEM results (Figure 2), it can be seen that there are obvious microcracks in the sample. These microcracks are fast passages for water swelling, aggravating the uneven degree of swelling and deformation. In addition, the cracks are also the locations of poor cementation inside the rock mass. Under the action of internal horizontal tensile stress and water softening, the microcracks will stretch and expand in the vertical direction, and the tendency of the cracks to develop is perpendicular to the direction of the horizontal principal tensile stress. After the microcracks expand to penetrate the surface, a visible chord-like macrocrack is formed, as shown in Figure 23.

4.3. Uneven Distribution of Swelling Clay Minerals. During the test, the surface of mudstone and argillaceous sandstone showed obvious mudding and uneven uplift (Figure 24). This indicates that the clay minerals in the sample are not evenly distributed. The degree of unevenness may be related to the size and distribution of clay particles and the composition of clay minerals during mudstone deposition.

The content of clay minerals in different areas of the sample is different, and the final water content of different areas will also be different under the condition of sufficient water

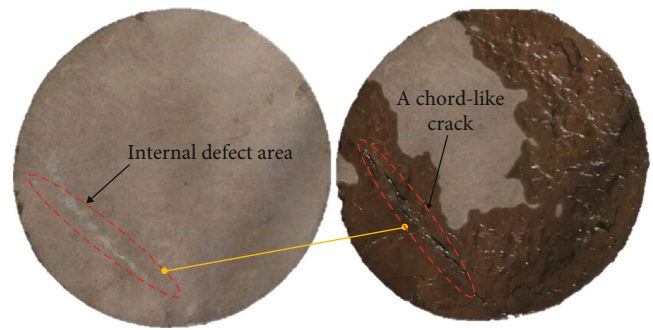


FIGURE 23: Surface chord cracks of 3# sample.

supply. Therefore, the sample after the test is divided into the upper layer and the bottom layer. The upper layer is divided into different areas with the cracks as the boundary to measure the water content, as shown in Figure 25 (take 2# sample as an example). Table 5 records the results of final water content in different areas of 1#~7# samples. The crack network of each sample is different, and the number (5~6) and size of the regions divided by the cracks are also different. It can be seen from Table 4 that the water content of different areas of the same sample is different. 1#, 3#, and 4# samples have relatively small differences in water content of different areas, while 2# and 6# have great differences. 2# is the difference between the upper and lower layers, while 6# is the overall difference, and its range is the largest, reaching 34.4%.

The uneven distribution of clay minerals on the one hand leads to differences in the degree of water absorption; on the other hand, it also leads to differences in swelling potential. Therefore, it is more likely to cause uneven expansion of the rock and aggravate the development and expansion of cracks. Especially when the internal clay mineral content of the sample is greater than the external one, the internal water swelling pressure is greater than the external one, resulting in external tension. And the outside is an easy-softening zone, which makes it easier to produce vertical tension cracks. With water absorption and softening, the cracks gradually develop inward along the radial direction.

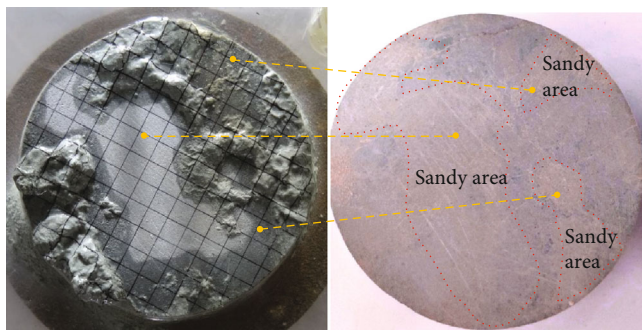


FIGURE 24: Uneven expansion on the surface of 6# sample.

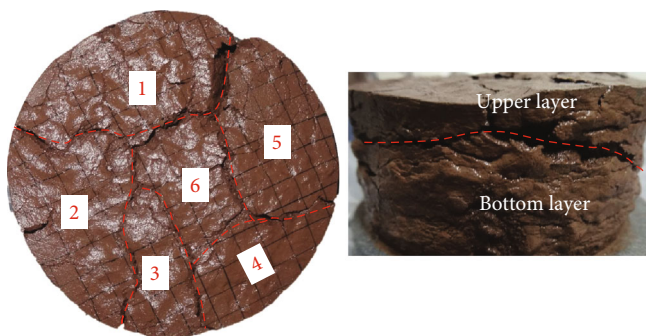


FIGURE 25: Measuring water content of 2# sample.

TABLE 5: Water content in different areas (unit: %).

Sample number	Distribution area						Bottom layer	Average value	Range
	1	2	3	4	5	6			
1#	11.20	11.86	12.43	12.29	13.00	12.69	15.21	14.51	4.01
2#	25.78	24.26	34.89	33.23	29.02	14.40	24.96	25.70	20.5
3#	32.70	31.35	29.74	27.34	29.67	—	27.35	28.60	5.36
4#	16.70	14.08	15.63	14.81	17.14	—	15.25	15.36	3.06
5#	27.40	26.49	35.20	32.03	31.60	—	31.62	31.46	8.71
6#	28.40	8.53	20.74	29.14	27.16	39.73	5.35	9.70	34.4
7#	12.97	11.33	9.14	11.49	11.78	10.62	8.69	9.32	4.28

Based on the above analysis, the swelling rock absorbs water and expands unevenly, causing internal swelling stress. Under the effect of structural defects such as internal microcracks and water softening, the expansion stress will destroy the internal structure, resulting in the generation and expansion of cracks. This uneven expansion is mainly caused by uneven water absorption and uneven distribution of clay minerals. Due to the different causes of uneven expansion, the mechanical mechanism of cracking and the shape of the resulting cracks will be different. When the material is uniform and has no internal structural defects, the cracks gradually develop from the outside to the inside, showing a “wrapped” shape. In the case of microcracks inside, it will cause vertical chord-like tension cracks. The uneven distribution of clay minerals will result in different degrees of water swelling. When the content of clay minerals inside is greater

than that of the outside, vertical tension cracks will be generated from the outside to the inside.

5. Conclusion

Through the swelling-cracking test of the expansive mudstone in the Central Sichuan red beds, the evolution characteristics of the swelling cracks were studied. The relationship between the water absorption and the crack degree during the evolution of the cracks was analyzed. Combined with a numerical analysis, the cracking mechanism of expansive rock is studied. The main conclusions are summarized as below:

- (1) The swelling-cracking process has obvious three-stage characteristics: the generation stage, the rapid

development stage, and the stabilization stage. Among them, the increase in the crack degree during the rapid development stage accounts for 90% of the total process

- (2) The final crack degree of swelling and cracking is related to the initial water content, water absorption method, and clay mineral content
- (3) The development of swelling cracks of expansive rock is controlled by three characteristic values of water absorption. The first characteristic value w_1 is the water absorption at the beginning of cracks; the second characteristic value w_2 is the initial water absorption at the rapid development stage of cracks; the third characteristic value w_3 is the water absorption when crack development reaches a stable level. The second characteristic value w_2 is of great significance in engineering practice. It indicates that the development of cracks has entered a stage of rapid development, in which the crack degree increases exponentially with water absorption. This has a certain reference for the study of swelling rock slope instability under rainfall conditions
- (4) Swelling and cracking of expansive rock is caused by uneven expansion, which is constantly changing over time. The main cause of uneven swelling is uneven water absorption and uneven distribution of swelling clay minerals. Due to the different causes of uneven expansion, the mechanical mechanism of cracking and the shape of the resulting cracks will be different

Data Availability

The data used to support the findings of this study are included within the article.

Conflicts of Interest

The authors declare no conflict of interest.

Acknowledgments

The authors are grateful for the financial support from the National Natural Science Foundation of China (Grant No. 41702337).

References

- [1] C. G. Bao, B. W. Gong, and L. T. Zhan, "Properties of unsaturated soils and slope stability of expansive soils," in *Proceedings of the Second International Conference on Unsaturated Soils*, vol. 2, pp. 81–108, Wuhan, China, 1998.
- [2] Y. Wang, C. H. Li, H. Liu, and J. Q. Han, "Fracture failure analysis of freeze-thawed granite containing natural fracture under uniaxial multi-level cyclic loads," *Theoretical and Applied Fracture Mechanics*, vol. 110, article 102782, 2020.
- [3] Y. Wang, C. H. Li, and J. Q. Han, "On the effect of stress amplitude on fracture and energy evolution of pre-flawed granite under uniaxial increasing-amplitude fatigue loads," *Engineering Fracture Mechanics*, vol. 240, article 107366, 2020.
- [4] Y. Wang, D. Q. Liu, J. Q. Han, C. H. Li, and H. Liu, "Effect of fatigue loading-confining stress unloading rate on marble mechanical behaviors: an insight into fracture evolution analyses," *Journal of Rock Mechanics and Geotechnical Engineering*, vol. 12, no. 6, pp. 1249–1262, 2020.
- [5] B. W. Gong, C. W. Ng, and C. Bao, "Field study of the effects of rainfall infiltration on channel slope of expansive soil," *Journal of Yangtze River Scientific Research Institute*, vol. 19, no. S1, pp. 94–97, 2002.
- [6] Y. Wang, Y. F. Yi, C. H. Li, and J. Q. Han, "Anisotropic fracture and energy characteristics of a Tibet marble exposed to multi-level constant-amplitude (MLCA) cyclic loads: a lab-scale testing," *Engineering Fracture Mechanics*, vol. 244, p. 107550, 2021.
- [7] Z. Z. Yin, J. Wei, J. P. Yuan, and X. S. Cao, "Mechanism of slope slide of expansive soil and reinforcement for the slope," *Journal of Hydraulic Engineering*, vol. 41, no. 1, pp. 1–6, 2010.
- [8] Z. Z. Yin, J. P. Yuan, J. Wei, X. S. Cao, H. Q. Liu, and B. Xu, "Influences of fissures on slope stability of expansive soil," *Chinese Journal of Geotechnical Engineering*, vol. 34, no. 12, pp. 2155–2161, 2012.
- [9] Z. H. Chen, "On basic theories of unsaturated soils and special soils," *Chinese Journal of Geotechnical Engineering*, vol. 36, no. 2, pp. 201–272, 2014.
- [10] Z. H. Lu, Z. H. Chen, and Y. B. Pu, "A CT study on the crack evolution of expansive soil during drying and wetting cycles," *Rock and Soil Mechanics*, vol. 23, no. 4, pp. 417–422, 2002.
- [11] S. M. Yi, Z. H. Li, and Y. Z. Zhang, "The fractal characteristics of fractures in expansion soil and its significance," *Chinese Journal of Geotechnical Engineering*, vol. 3, pp. 294–298, 1999.
- [12] J. Wang, B. W. Gong, J. J. Zhang, X. W. Zhou, and F. Y. Tan, "Field observation and description method of cracks development on expansive rock," *Journal of Yangtze River Scientific Research Institute*, vol. 27, no. 9, pp. 74–75, 2010.
- [13] W. Li, G. S. Liu, and T. Yao, "Improvement of methods for crack image processing and crack feature extraction of expansive soil," *Rock and Soil Mechanics*, vol. 35, no. 12, pp. 3619–3626, 2014.
- [14] B. X. Wei, B. Liu, and X. Liu, "Research on the quantitative basic index of expansive soil," *Hydrogeology & Engineering Geology*, vol. 42, no. 5, pp. 84–89, 2015.
- [15] C. S. Tang, Y. J. Cui, A. M. Tang, and B. Shi, "Shrinkage and desiccation cracking process of expansive soil and its temperature-dependent behaviour," *Chinese Journal of Geotechnical Engineering*, vol. 34, no. 12, pp. 2181–2187, 2012.
- [16] X. Mao, S. J. Xin, M. S. Cheng, Z. H. Chen, and X. Q. Wang, "Mechanical behavior of expansive soil under initial damage and wetting-drying cycles," *Rock and Soil Mechanics*, vol. 39, no. 2, pp. 571–579, 2018.
- [17] D. X. Hu, X. Li, C. Y. Zhou, L. Xue, and H. F. Liu, "Quantitative analysis of swelling and shrinkage cracks in expansive soil," *Rock and Soil Mechanics*, vol. 39, no. S1, pp. 318–324, 2018.
- [18] Z. G. Lou, S. J. Wang, and Z. B. Yang, "Quantitative analysis of fracture evolution of expansive soils under wetting-drying cycles," *Rock and Soil Mechanics*, vol. 41, no. 7, pp. 2313–2323, 2020.
- [19] Z. G. Lou, S. J. Wang, J. W. Zhang, and Z. B. Yang, "Thickness effect on crack evolution of expansive soil," *Chinese Journal of Geotechnical Engineering*, vol. 42, no. 10, pp. 1922–1930, 2020.

- [20] J. M. Konrad and R. Ayad, "Desiccation of a sensitive clay: field experimental observations," *Canadian Geotechnical Journal*, vol. 34, no. 6, pp. 929–942, 1997.
- [21] H. L. Yao, S. H. Zheng, X. R. Ge, and S. X. Yi, "Assessment on slope stability in cracking expansive soils," *Chinese Journal of Rock Mechanics and Engineering*, vol. 21, no. A02, pp. 2331–2335, 2002.
- [22] J. Ma, S. X. Chen, F. Yu, and M. G. Feng, "Experimental research on crack evolution process in fissured clay," *Rock and Soil Mechanics*, vol. 1, no. 10, pp. 2203–2208, 2007.
- [23] J. H. Wu, J. P. Yuan, and C. W. Ng, "Theoretical and experimental study of initial cracking mechanism of an expansive soil due to moisture-change," *Journal of Central South University*, vol. 19, no. 5, pp. 1437–1446, 2012.
- [24] D. X. Wu, H. J. Liu, and G. Q. Wang, "Laboratory experimental study of slaking characteristics of red-bed soft rock," *Chinese Journal of Rock Mechanics and Engineering*, vol. 9, no. S2, pp. 4173–4179, 2010.
- [25] Y. Pan, Z. Liu, and C. Y. Zhou, "Experimental study of disintegration characteristics of red-bed soft rock within water and its interface model," *Rock and Soil Mechanics*, vol. 38, no. 11, pp. 3231–3239, 2017.
- [26] S. K. Shan, X. L. Leng, and Q. Sheng, "Study on water swelling and softening characteristics of expansive rock," *Rock and Soil Mechanics*, vol. 41, no. 2, pp. 561–570, 2020.
- [27] Z. B. Zhong, A. H. Li, R. G. Rong, P. P. Wu, and J. Xu, "Experimental study on the time-dependent swelling characteristics of red-bed mudstone in Central Sichuan," *Chinese Journal of Rock Mechanics and Engineering*, vol. 38, no. 1, pp. 76–86, 2019.
- [28] F. Yu, X. X. Cui, S. X. Chen, Z. Zhou, and Z. J. Dai, "Experimental study on disintegration characteristics of swelling rock in Central Sichuan under dry-wet cycle," *Journal of Henan Polytechnic University (Natural Science)*, vol. 38, no. 4, pp. 130–135, 2019.
- [29] Z. J. Dai, J. H. Guo, Z. Zhou, S. X. Chen, J. Li, and F. Yu, "Inversion and prediction of long-term uplift deformation of high-speed railway subgrade in Central Sichuan red-bed," *Chinese Journal of Rock Mechanics and Engineering*, vol. 39, no. S2, pp. 3538–3548, 2020.

Research Article

Experimental Study on Fluid Properties of Cement-Fly Ash Slurry Subjected to Multifactors

Tian Huang , Feng Huang , and Huifeng Zhou

School of Engineering and Technology, China University of Geosciences (Beijing), 100083 Beijing, China

Correspondence should be addressed to Feng Huang; huangfeng@cugb.edu.cn

Received 11 March 2021; Revised 27 March 2021; Accepted 31 March 2021; Published 15 April 2021

Academic Editor: Zhengyang Song

Copyright © 2021 Tian Huang et al. This is an open access article distributed under the Creative Commons Attribution License, which permits unrestricted use, distribution, and reproduction in any medium, provided the original work is properly cited.

There are many factors affecting the characteristics of cement-fly ash slurry in practical engineering. Thus, this paper studies the influence of multifactors on the fluid properties of cement-fly ash slurry based on water-cement ratio (w/c) (0.75, 1, 1.25, and 1.5), fly ash content (0%, 10%, 20%, 30%, 40%, and 50%) and temperature (20°C, 40°C, 60°C, and 80°C). The bleeding ratio, initial setting time, final setting time, and viscosity were analyzed under coupling conditions. It is found that the water-cement ratio (w/c) is the main factor that affects the rheological properties and bleeding rate of slurry. The temperature affects the stability of the slurry in terms that the bleeding ratio of the slurry decreases as the temperature increases. The addition of fly ash enhances the stability of the slurry under different temperature conditions.

1. Introduction

Since the wide-scale combustion of coal for power generation, millions of tons of ash and related by-products have been produced. The current annual production of coal ash worldwide is estimated around 600 million tons, with fly ash constituting about 500 million tons at 75–80% of the total ash produced [1]. Therefore, the amount of fly ash released by factories and thermal power plants has been increasing worldwide, and the disposal of large amounts of fly ash has become a serious problem. Fly ash is a resource yet to be fully utilized. The geotechnical properties of fly ash (e.g., specific gravity, permeability, internal angular friction, and consolidation characteristics) make it suitable for use in construction of roads, embankments, and structural fill. The pozzolanic properties of the ash, including its lime-binding capacity, make it useful for the manufacture of cement and building material concrete and concrete-admixed products. Nowadays, fly ash has been used in many fields successfully [1–7]. Fly ash has many advantages to cement slurry, for example, reducing the cost and the rate of water separation [8]; the fly ash has been commonly used as a blending agent

to enhance various properties of slurry. At the same time, the slurry will be affected by many factors, resulting in changes of the characteristics of the slurry.

It is found that the viscosity of the slurry, as well as thickening time, rheology, and setting time, varied significantly with temperature [9, 10]. Thus, it is necessary to find how the temperature affects the characteristics of the slurry, which is important for the real projects. Du et al. [11] pointed that high temperature is the key factor in the formation of fly ash activity. Fly ash with activity and cement forms a stable cement body. Lee et al. [12] presented that the increase of temperature resulted in lower shear stress of the slurry mixtures. At the same time, the differences of shear stresses showed less sensitivity at high temperatures, indicating that the high temperature accelerated the hydration of fly ash. Alexandersson and Wallevik [13] analyzed the effect of pressure and temperature on cement slurry and found that temperature had a much larger effect on the loss of cement slurries than pressure, which revealed that elevated temperature accelerated the hydration reaction.

The flow behavior of slurry is controlled by the concentration and flocculating extent of the particles. The viscosity

increases with the increase of volume fraction of solids and degree of flocculation [14]. Bentz et al. [15] also pointed out that the rheological properties of cement-based slurry depend strongly on mixture proportions and the characteristics of the components. Thus, the concentration of particles which is usually represented by w/c is important for understanding the characteristics of the cement-fly ash slurry. The addition of fly ash can change the characteristics of the cement slurry; for example, the proper content of fly ash can reduce the yield stress and plastic viscosity of the slurry [16, 17]. Mirza et al. [18] indicated that the cement grout with fly ash reduced the flow time and drying shrinkage, improved the stability, and attained similar compressive and shear bond strengths as pure cement grouts. Lee et al. [19] investigated the effect of particle size distribution (PSD) of cement-fly ash on the fluidity of the slurry and found that the fluidity increases as the PSD becomes wider. A. Kashani et al. [4] obtained the similar results and found that a small addition of fly ash had a significant effect on workability because of its broad PSD. Xie et al. [20] analyzed the effects of fly ash on shearing thinning and thickening of cement slurry. It was presented that at the shear thinning stage, when fly ash content was less than 50%, the rheological parameters decreased with the increase of fly ash content, while the rheological parameters increased with increasing fly ash content when fly ash content was beyond 50%. At the shear thickening stage, the rheological parameters increased with increasing fly ash content.

In this paper, the properties of cement-fly ash slurry subjected to multiple factors were tested, which were aimed at providing references for underground engineering under complex conditions.

2. Materials and Methods

Portland cement (P.C 32.5R) and fly ash (class II) were prepared in this study, which are presented in Figures 1 and 2. The particle size distribution curves of cement and cement with different contents of fly ash are shown in Figures 3–8.

In this study, the cement with the fly ash content of 0%, 10%, 20%, 30%, 40%, and 50% was made into slurries with different w/c ($w/c = 1.5, 1.25, 1, \text{ and } 0.75$, respectively) for 24 kinds of slurry samples. The physical composition of the slurries in this study is shown in Table 1. The slurries were prepared by using WT-2000C frequency conversion high-speed mixer, whose maximum speed was 13,000 rpm. The mixing procedure was 10-minute mixing at low speed, 5-minute rest, and another 10-minute mixing at high speed to avoid false set.

In order to analyze the effect of temperature on slurry, the slurries were heated to 20°C, 40°C, 60°C, and 80°C, respectively, by constant temperature water baths. At constant temperature, pipettes were used to suck out bleeding once every 10 minutes and once every 20 minutes after 60 minutes, until there is no bleeding for three consecutive times. Bleeding rate measurement was completed. The bleeding rate test is shown in Figure 9. The slurries of standard consistency were prepared according to the specifications and cured at the set temperature. The initial setting time and final setting time



FIGURE 1: Portland cement.

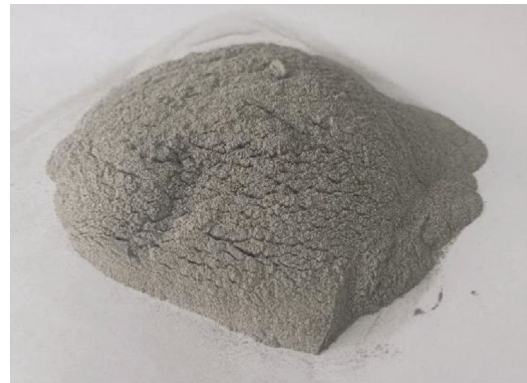


FIGURE 2: Fly ash.

of the slurry were measured with a Vicat apparatus. The setting time test is shown in Figure 10.

After heating the slurries to the set temperature, a six-speed rotary viscometer (ZNN-D6B) was used to measure the rheological properties of the slurries quickly. The slurries were measured from high speed to low speed (from 600 r/min to 3 r/min). The slurry viscosity test is shown in Figure 11.

3. Results and Discussion

3.1. Bleeding Ratio. Experiments were carried out to analyze the effect of different factors on bleeding ratio. The slurry was injected into the beakers with 200 ml volume, and then, the top of the beakers was sealed to prevent evaporation. The results of bleeding ratio are shown in Figures 12–17.

Figures 12–17 indicated that the bleeding ratio of all slurry samples decreased as the temperature increased. The magnitude curves of cement slurries without fly ash showed larger variation than that with fly ash. The bleeding rate curve of cement slurries with low fly ash content decreased greatly at 40°C and became relatively flat with the increase of fly ash content. At the same temperature, the bleeding ratio was positively correlated to the w/c . With the increase of fly ash content, the differences of bleeding ratio under each temperature condition gradually decreased, especially at the fly ash content of 40% and 50%. In addition, fly ash content had significantly larger influence on bleeding rate of high w/c than that

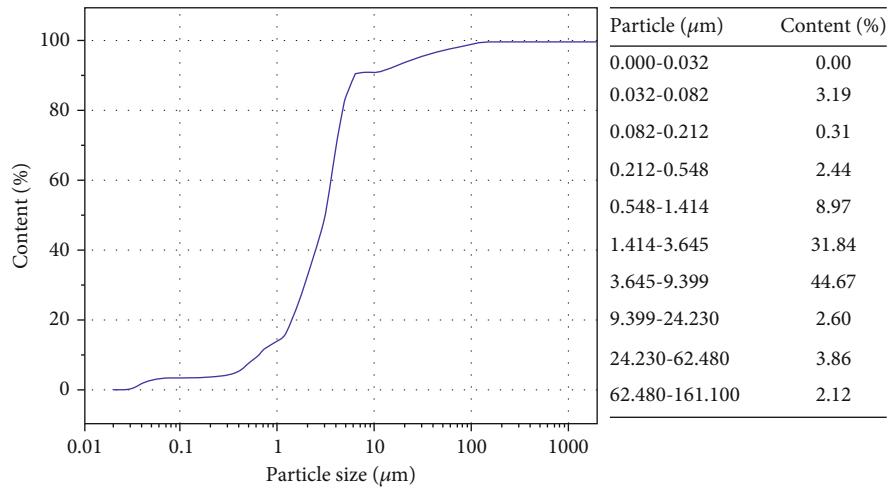


FIGURE 3: PSD of cement.

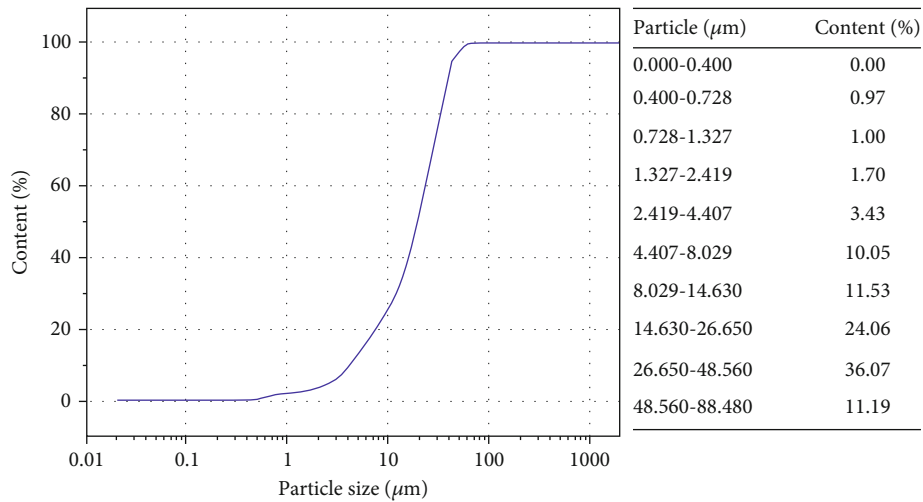


FIGURE 4: PSD of cement with 10% fly ash.

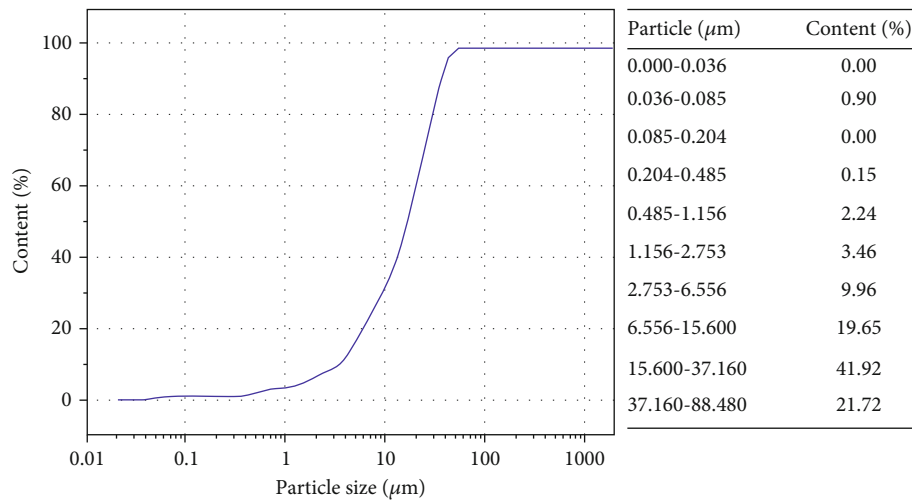


FIGURE 5: PSD of cement with 20% fly ash.

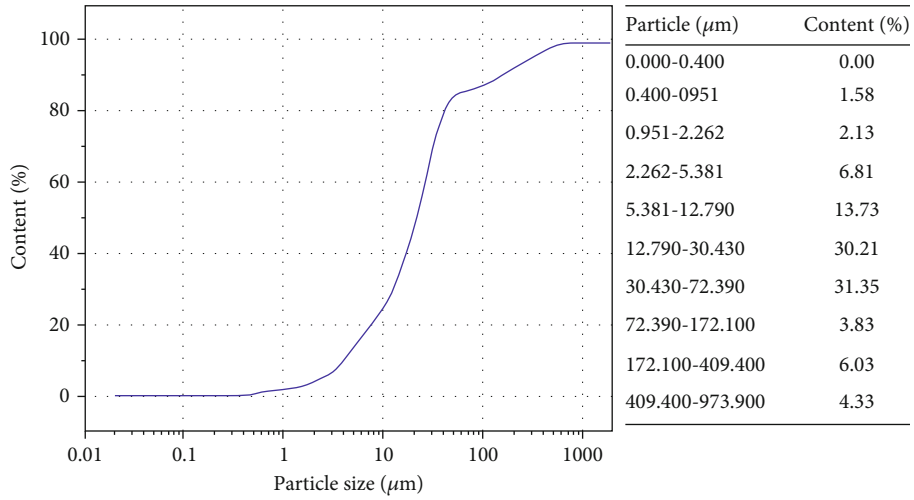


FIGURE 6: PSD of cement with 30% fly ash.

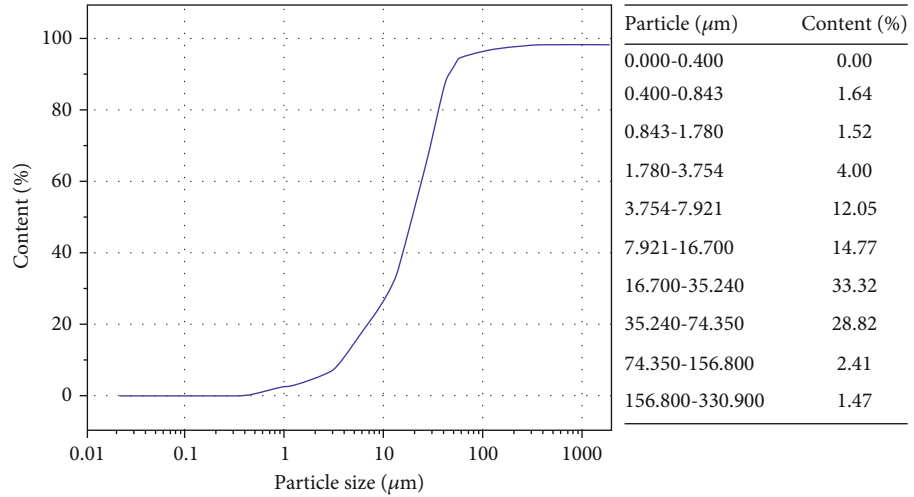


FIGURE 7: PSD of cement with 40% fly ash.

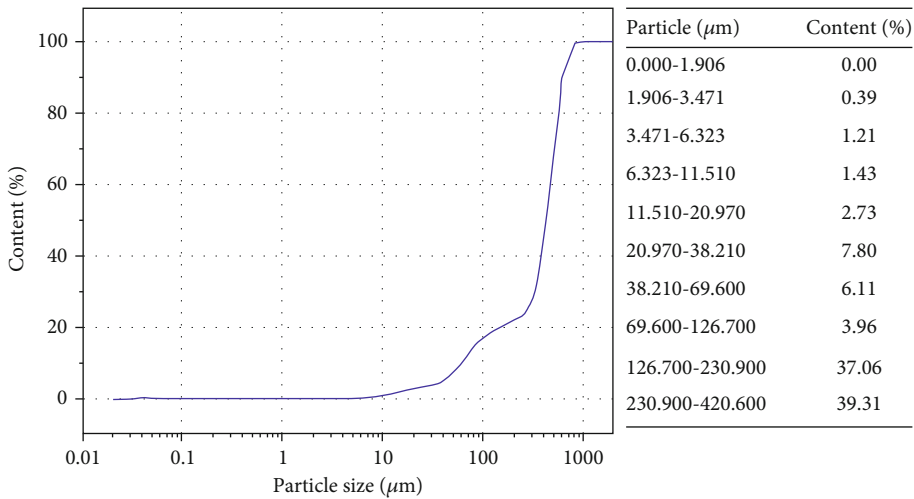


FIGURE 8: PSD of cement with 50% fly ash.

TABLE 1: Slurry materials and their notation in this study.

Water-cement ratio	Cement/fly ash content	Number
0.75	100% cement (571 g)/0% fly ash (0 g)	A1
	90% cement (514 g)/10% fly ash (57 g)	A2
	80% cement (457 g)/20% fly ash (114 g)	A3
	70% cement (400 g)/30% fly ash (171 g)	A4
	60% cement (343 g)/40% fly ash (228 g)	A5
	50% cement (286 g)/50% fly ash (285 g)	A6
1.00	100% cement (500 g)/0% fly ash (0 g)	B1
	90% cement (450 g)/10% fly ash (50 g)	B2
	80% cement (400 g)/20% fly ash (100 g)	B3
	70% cement (350 g)/30% fly ash (150 g)	B4
	60% cement (300 g)/40% fly ash (200 g)	B5
	50% cement (250 g)/50% fly ash (250 g)	B6
1.25	100% cement (444 g)/0% fly ash (0 g)	C1
	90% cement (400 g)/10% fly ash (44 g)	C2
	80% cement (356 g)/20% fly ash (88 g)	C3
	70% cement (312 g)/30% fly ash (132 g)	C4
	60% cement (267 g)/40% fly ash (177 g)	C5
	50% cement (222 g)/50% fly ash (222 g)	C6
1.50	100% cement (400 g)/0% fly ash (0 g)	D1
	90% cement (360 g)/10% fly ash (40g)	D2
	80% cement (320 g)/20% fly ash (80g)	D3
	70% cement (280g)/30% fly ash (120 g)	D4
	60% cement (240g)/40% fly ash (160 g)	D5
	50% cement (200 g)/50% fly ash (200 g)	D6

of low water-cement ratio slurry. Before the slurry solidifies, water appeared on the surface, which was a kind of water seepage realization. When the water and cement cannot

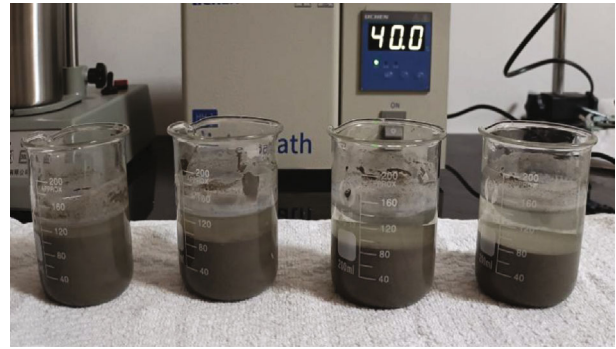


FIGURE 9: The bleeding rate test.



FIGURE 10: The setting time test.



FIGURE 11: The slurry viscosity test.

mix completely and the substance is in a fluid-solid dispersion state, water seepage will occur. The above description shows that cement cannot maintain a stable mixing state with water under low-temperature conditions. It can mix well under high-temperature conditions without separating, resulting in low bleeding rate. Fly ash can mix well with water under all temperature conditions. Thus, temperature is a key factor affecting the bleeding rate of the slurry, and fly ash is a very effective seepage reducer.

Figures 18–21 showed that under the condition of the same w/c , the bleeding ratio of the slurries had the largest change amplitude at 20°C in different fly ash content conditions. Compared to the slurries with fly ash, the bleeding rate

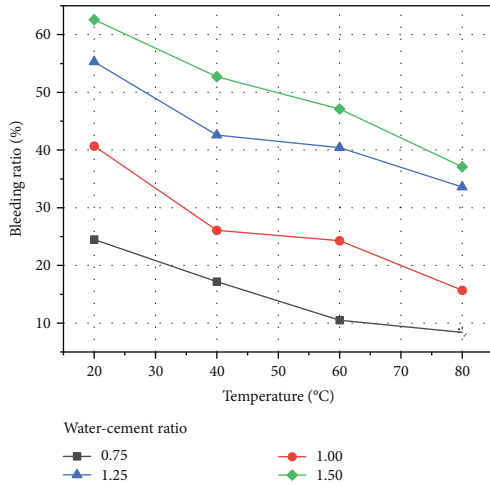


FIGURE 12: Relationship of bleeding ratio and temperature (0% fly ash).

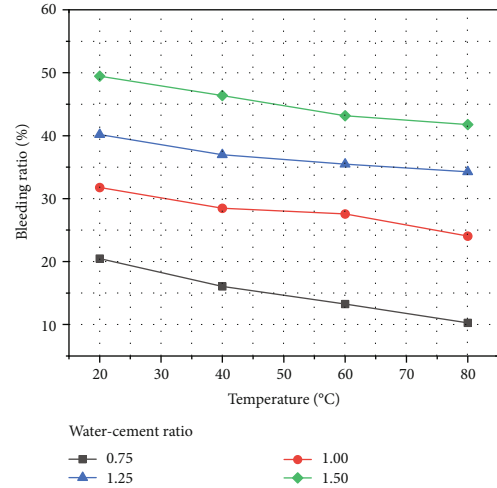


FIGURE 15: Relationship of bleeding ratio and temperature (30% fly ash).

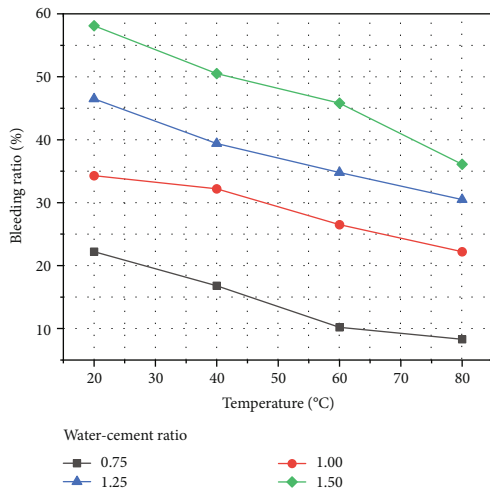


FIGURE 13: Relationship of bleeding ratio and temperature (10% fly ash).

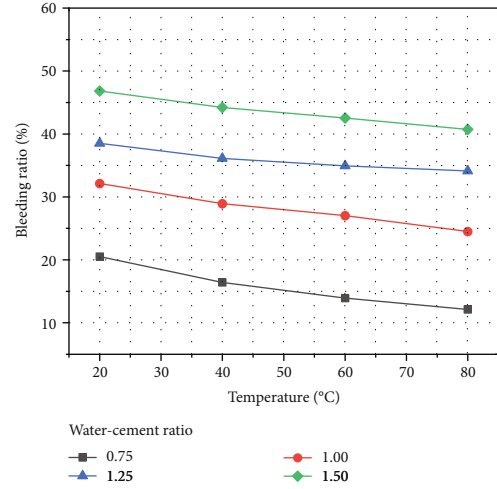


FIGURE 16: Relationship of bleeding ratio and temperature (40% fly ash).

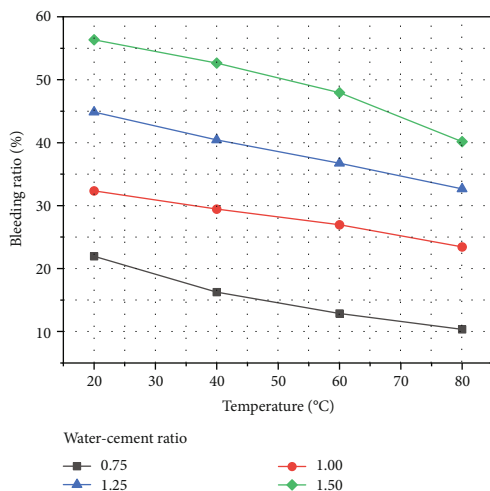


FIGURE 14: Relationship of bleeding ratio and temperature (20% fly ash).

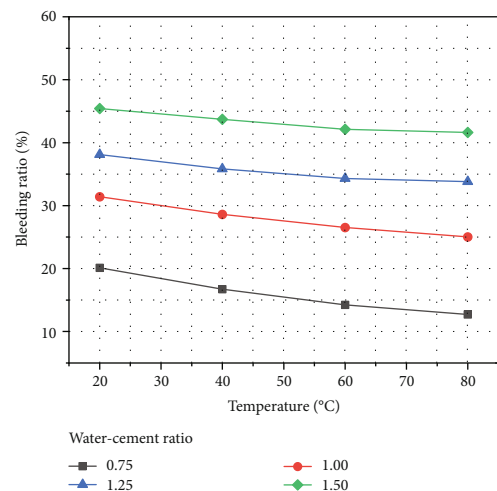


FIGURE 17: Relationship of bleeding ratio and temperature (50% fly ash).

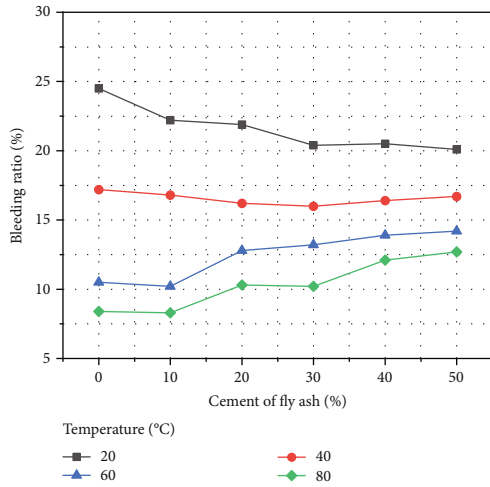


FIGURE 18: Relationship of bleeding ratio and fly ash content ($w/c = 0.75$).

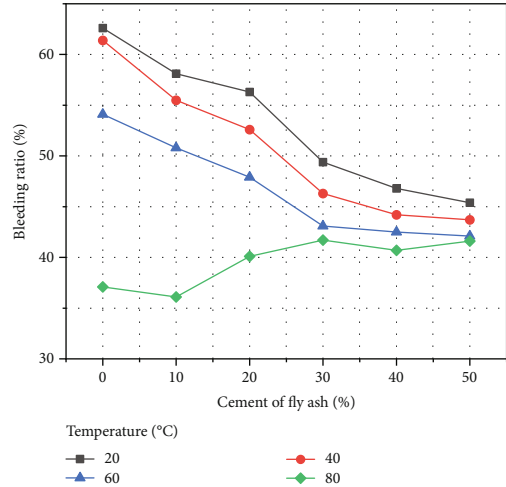


FIGURE 21: Relationship of bleeding ratio and fly ash content ($w/c = 1.5$).

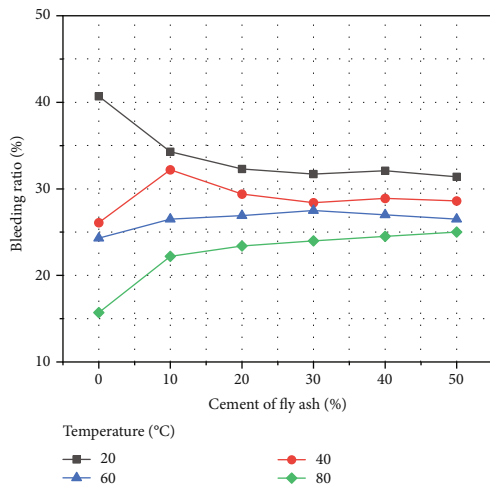


FIGURE 19: Relationship of bleeding ratio and fly ash content ($w/c = 1.0$).

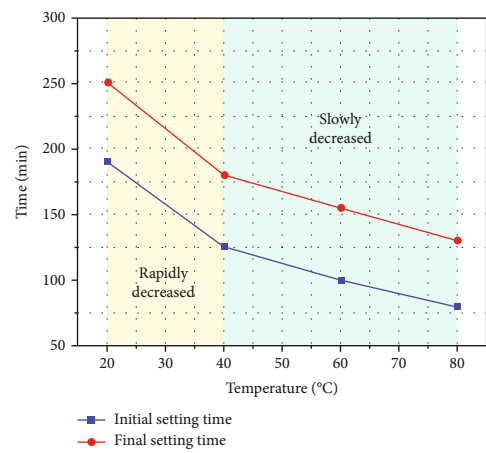


FIGURE 22: Relationship of setting time and temperature (0% fly ash).

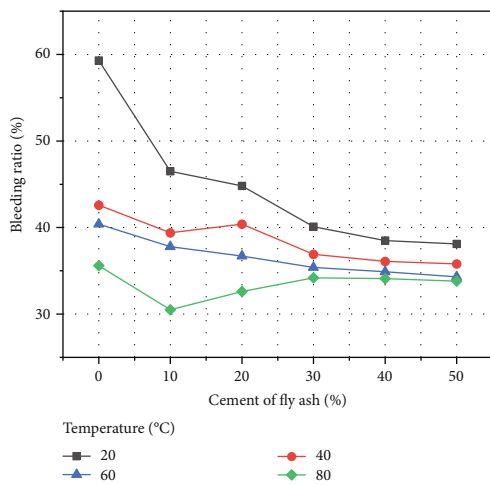


FIGURE 20: Relationship of bleeding ratio and fly ash content ($w/c = 1.5$).

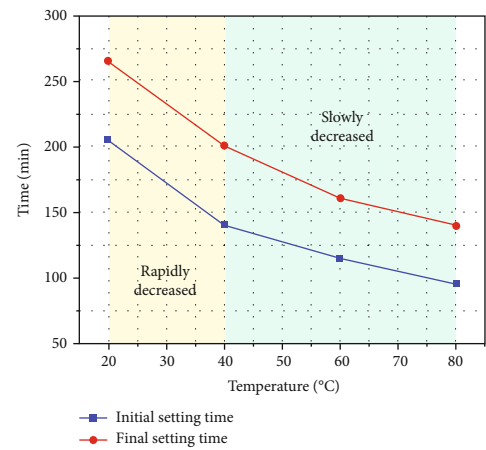


FIGURE 23: Relationship of setting time and temperature (10% fly ash).

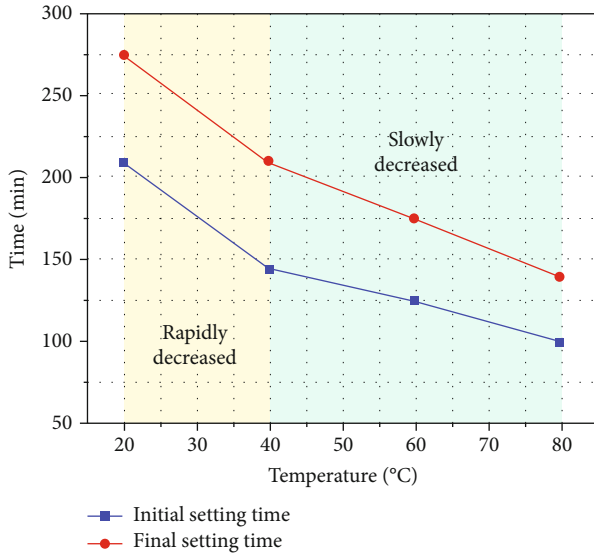


FIGURE 24: Relationship of setting time and temperature (20% fly ash).

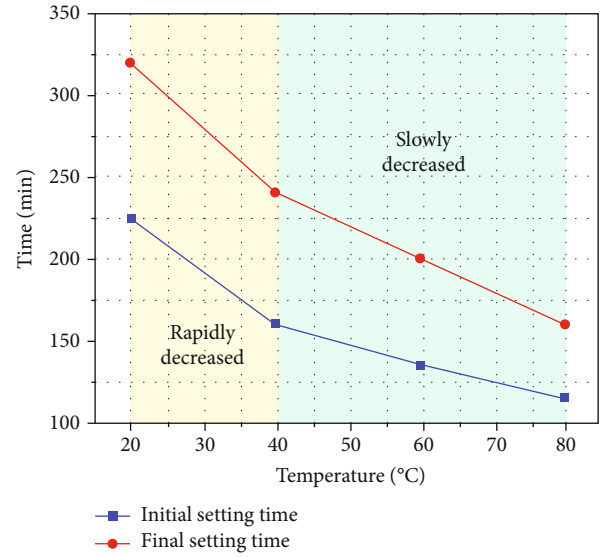


FIGURE 26: Relationship of setting time and temperature (40% fly ash).

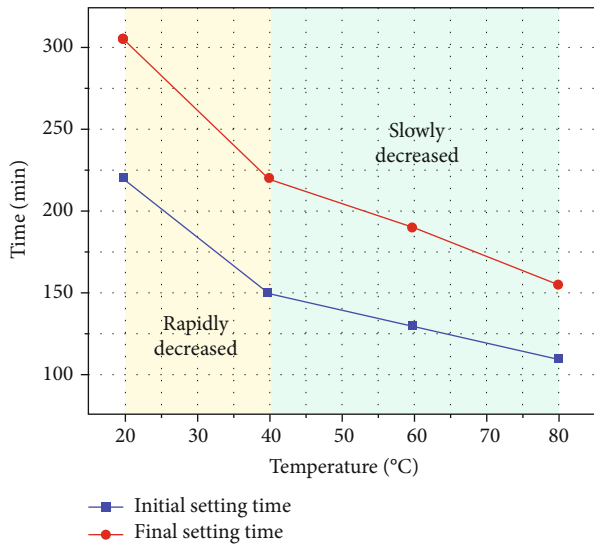


FIGURE 25: Relationship of setting time and temperature (30% fly ash).

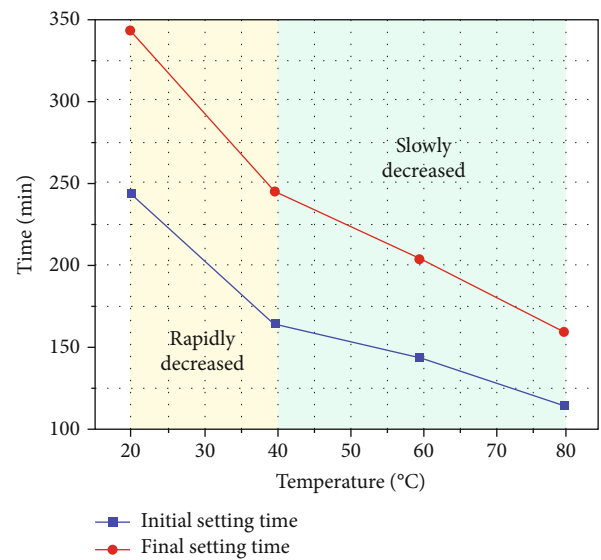


FIGURE 27: Relationship of setting time and temperature (50% fly ash).

presented greater variation range for cement slurries without fly ash. When the w/c was 0.75 or 1.0, at 20°C and 40°C, the bleeding rate of the slurries decreased with the increase of the content of fly ash. At 60°C and 80°C, the bleeding rate of the slurries increased with the increase of the content of fly ash. When the w/c was 1.25 or 1.5, at 20°C, 40°C, and 60°C, the bleeding rate of slurries decreased with the increase of fly ash content. The bleeding rate of slurry increased with the increase of fly ash content at 80°C. It can be seen from Figure 21 that under high w/c , the difference of slurries at different temperatures was obvious. Water and cement could not mix completely and were in a fluid-solid dispersion state. This phenomenon was more pronounced under high water-cement ratio. Under the condition of 20°C~60°C, the content of fly ash in the slurry increased, which greatly improved the

degree of mixing with water, and the bleeding rate dropped rapidly. At 80°C, cement and water were fully mixed, and the mixing degree was higher than fly ash. Meanwhile, the bleeding rate increased. This indicates that under low-temperature conditions, the cement with high fly ash content can maintain a low bleeding rate. Under high-temperature conditions, the mixing degree of fly ash and water is lower than that of ordinary cement, so cement with low fly ash content can maintain a low bleeding rate.

3.2. Setting Time. The initial and final setting times are basic parameters to evaluate the rheological stage. The setting time has been analyzed under different temperature and fly ash content conditions. The relationship between setting time and temperature is shown in Figures 22–27.

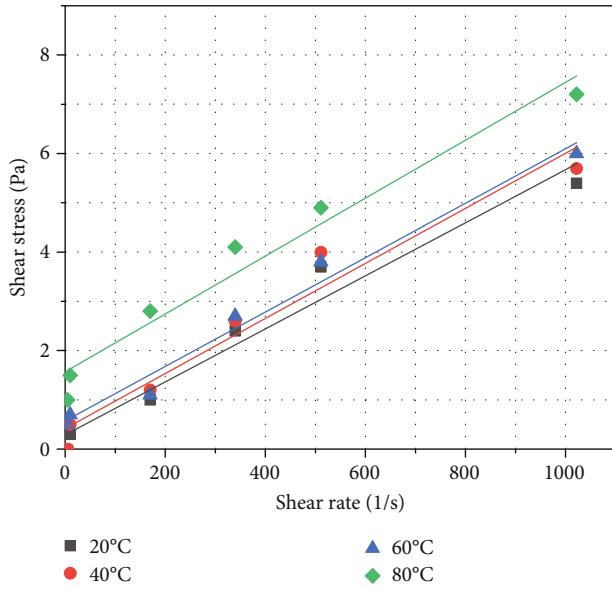


FIGURE 28: Viscosity of cement slurry with a w/c of 1.5.

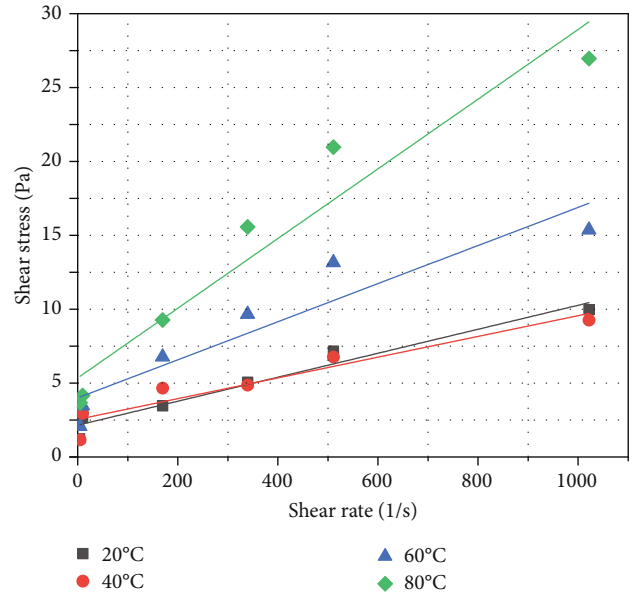


FIGURE 30: Viscosity of cement slurry with a w/c of 1.0.

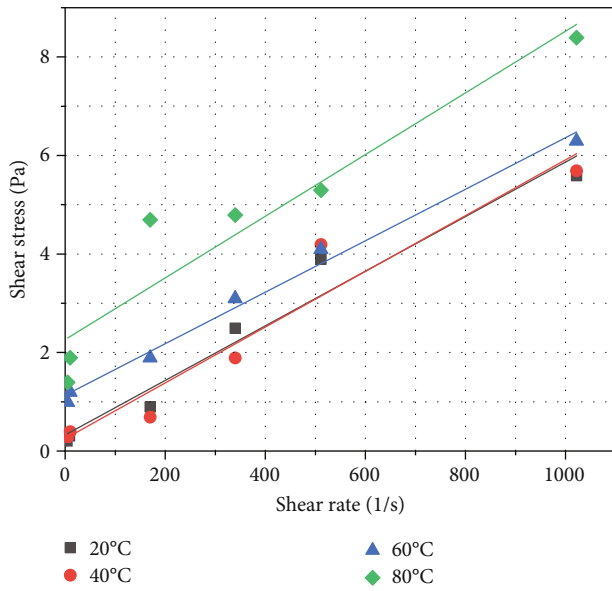


FIGURE 29: Viscosity of cement slurry with a w/c of 1.25.

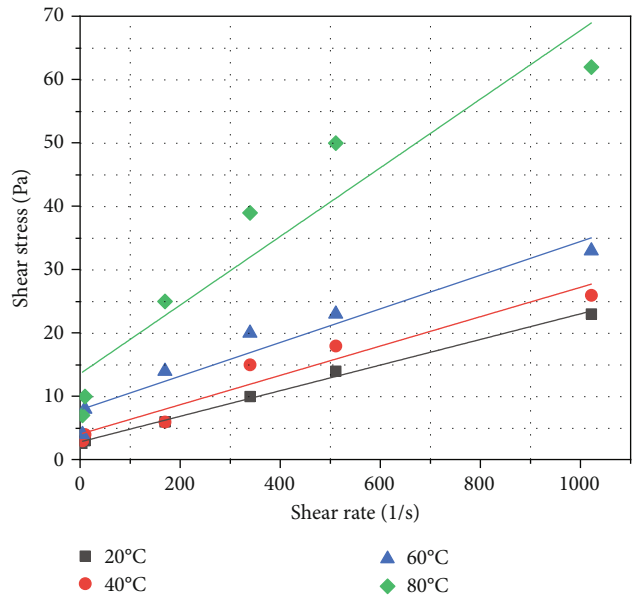


FIGURE 31: Viscosity of cement slurry with a w/c of 0.75.

It can be obtained that both the initial setting time and the final setting time decrease as temperature increases. Setting time decreased rapidly from 20°C to 40°C; the setting time decreased slowly from 40°C to 80°C. At the same temperature, the interval between the initial setting time and the final setting time also increased with the increase of the content of fly ash. At the same time, the initial setting time and the final setting time increased as the content of fly ash increased. The results show that the setting time depends on the speed of the hydration reaction between the particles and water. The hydration reaction of cement and water is active while fly ash is inert. The setting time of cement with a high content of fly ash is longer. Temperature has a great influence on the hydration reaction. Under high-temperature conditions, the hydration reaction activity of cement and fly ash increases.

3.3. *Viscosity.* Viscosity is one of the most important parameters in analyzing characteristics of slurry. The viscosity of slurry under different conditions was studied and presented in Figures 28–51. In fitting equations, τ represents the shear stress, and γ represents the shear rate. The relationship of shear stress and shear rate of cement slurry without fly ash is shown in Figures 28–31. The fitting line parameters of cement slurry are shown in Tables 2–5.

It can be seen that as w/c decreased, the shear stresses of the slurry gradually increased. The cement slurry was typically in Bingham type, except that under conditions of 1.5 of w/c , 20°C and 40°C, the slurries were Newtonian which is shown in Figure 28. At the temperature of 80°C, the shear stress was greater than that in other conditions, especially at

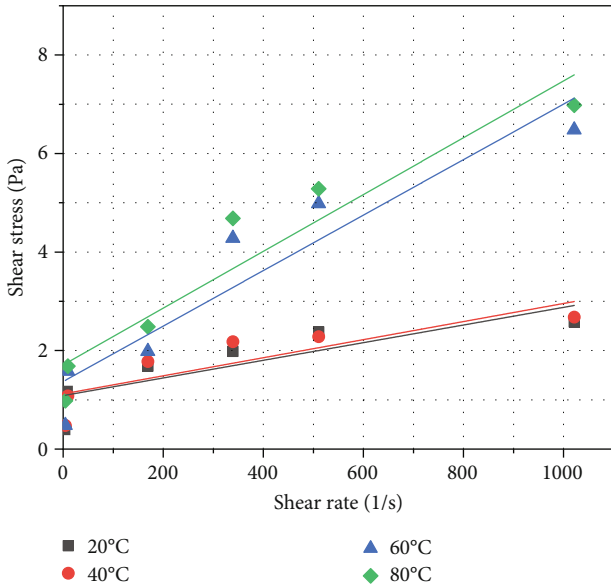


FIGURE 32: Viscosity of cement slurry with a w/c of 1.5 (10% fly ash).

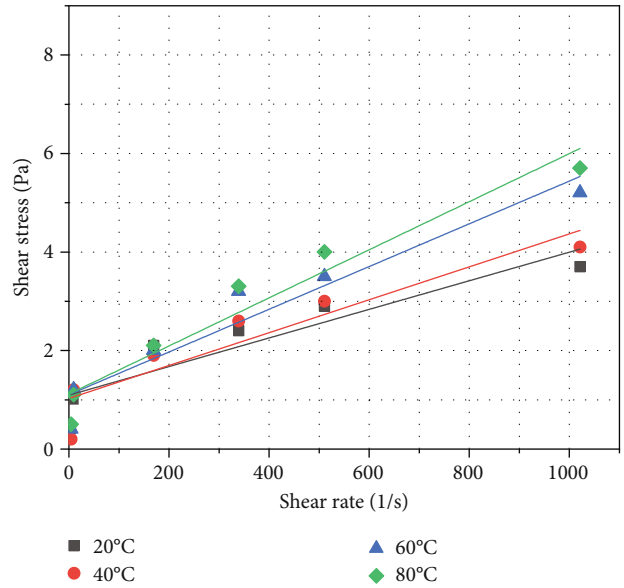


FIGURE 34: Viscosity of cement slurry with a w/c of 1.5 (30% fly ash).

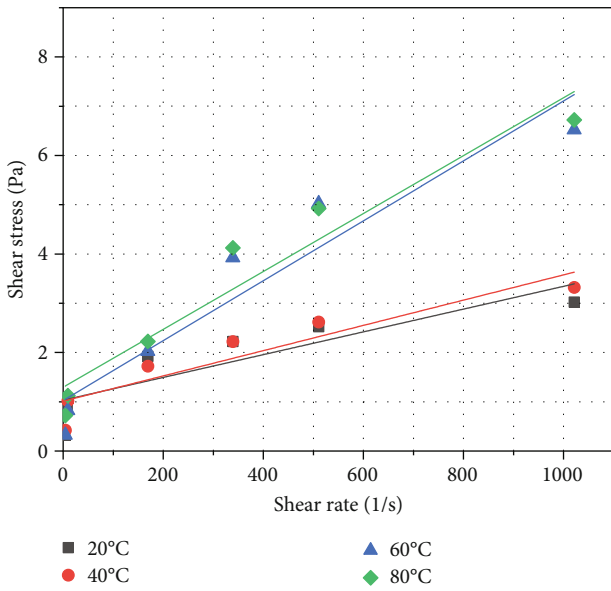


FIGURE 33: Viscosity of cement slurry with a w/c of 1.5 (20% fly ash).

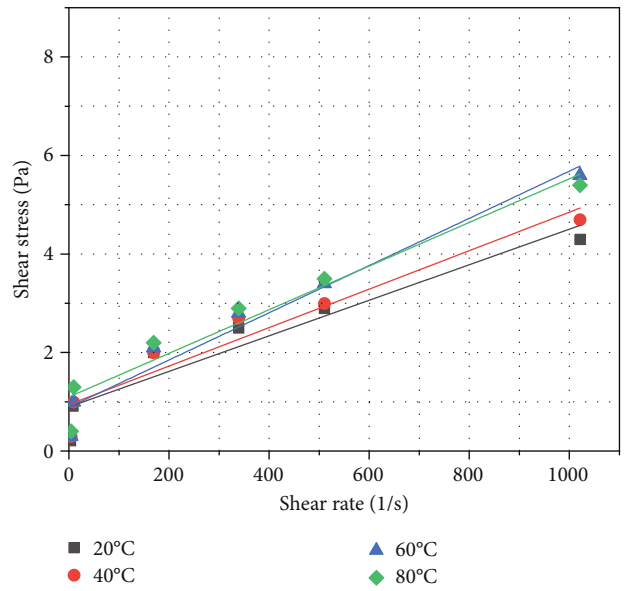


FIGURE 35: Viscosity of cement slurry with a w/c of 1.5 (40% fly ash).

0.75 of w/c , which is shown in Figure 31. Thus, it can be seen that the rheological properties of the cement slurries were significantly affected by high temperature. Except for the condition of 80°C, the shear stresses did not show significant difference at 20°C, 40°C, and 60°C. The slope of the fitting lines indicated the viscosity of the slurries. At high water-cement ratio, the viscosity of the slurries at different temperatures was approximately the same. At low water-cement ratio, the viscosity of high-temperature slurries was much greater than that of low-temperature slurries. The results show that the w/c affects the viscosity of the slurry. A decrease in the w/c means a high solid concentration, which directly leads to an increase in the number of particle-particle contacts, thereby increasing the gel formation rate. At the

same time, temperature also affects the viscosity of the slurry. Under high-temperature conditions, the hydration reaction accelerates, resulting in a large number of gel products, which increases the shear stress of the slurry.

The relationship of shear stress and shear rate of the slurry with w/c of 1.5 and different fly ash contents is shown in Figures 32–36. The fitting line parameters of cement slurry with a w/c of 1.5 are shown in Tables 6–10.

The slurries with a w/c of 1.5 were Bingham fluid under various temperature conditions regardless of fly ash content. When the slurries contained 10%, 20%, and 30% fly ash, the shear stress at 80°C was larger than that in other temperatures. The shear stress increased with the increase of temperature. However, when the slurries contained 40% or 50% fly

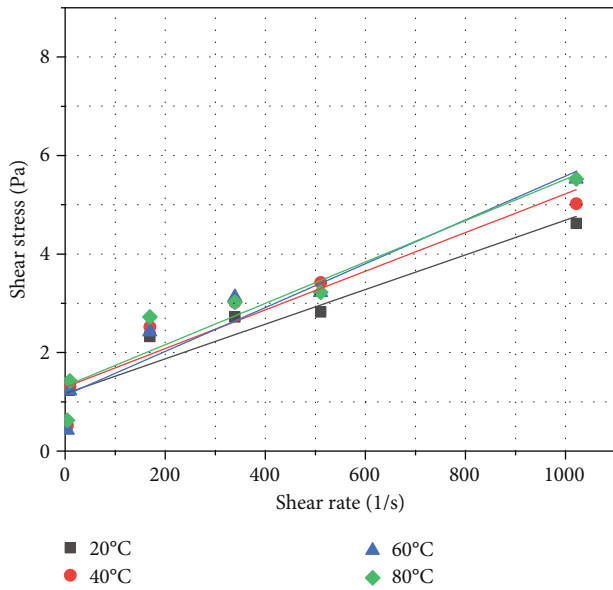


FIGURE 36: Viscosity of cement slurry with a w/c of 1.5 (50% fly ash).

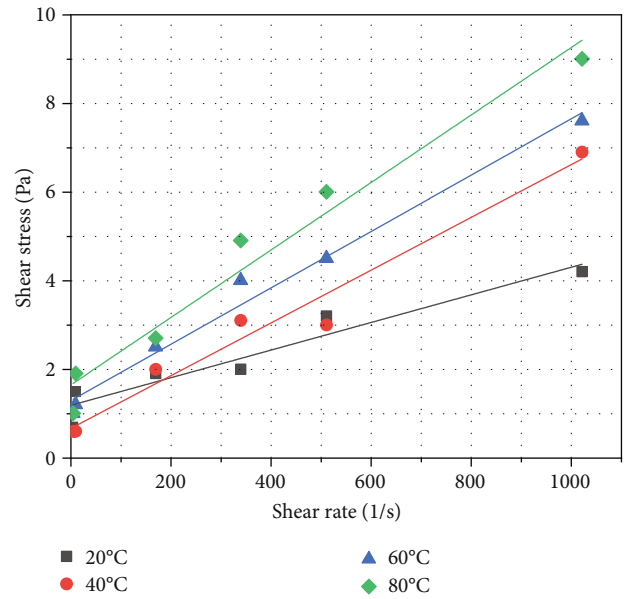


FIGURE 38: Viscosity of cement slurry with a w/c of 1.25 (20% fly ash).

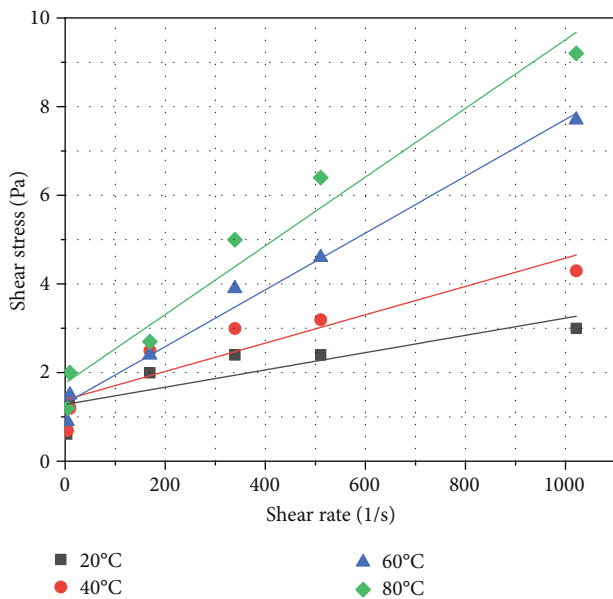


FIGURE 37: Viscosity of cement slurry with a w/c of 1.25 (10% fly ash).

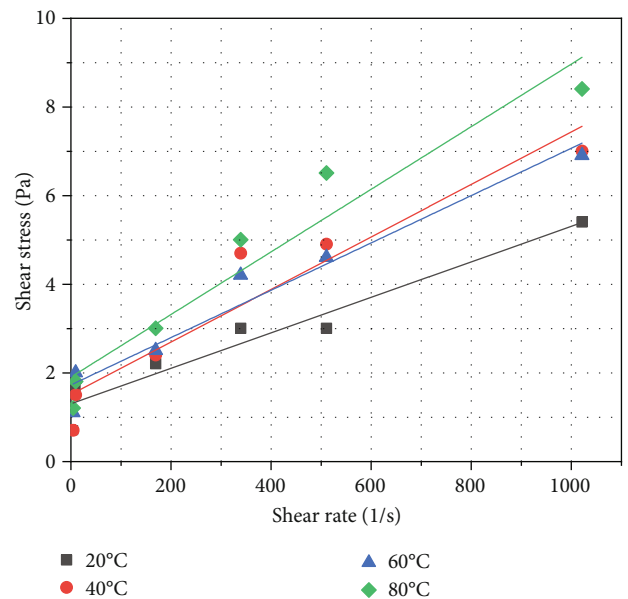


FIGURE 39: Viscosity of cement slurry with a w/c of 1.25 (30% fly ash).

ash, the change of shear stress was not obvious with temperature. It can be seen from the slope of the fitting lines that the viscosity of high-temperature slurries was much greater than that of low-temperature slurries at low fly ash content. With high fly ash content, the viscosity of high-temperature slurries was very close to that of low-temperature slurries. It is summarized that in slurries with high fly ash content, a large amount of fly ash is adsorbed on the surface of the cement particles, which acts as a lubrication for the mixed slurry. At the same time, steric hindrance forms between cement particles, which increases the distance between the particles, resulting in an insignificant effect of temperature on the slurry.

The relationship of shear stress and shear rate of the slurry with a w/c of 1.25 and different fly ash contents is shown in Figures 37–41. The fitting line parameters of cement slurry with a w/c of 1.25 are shown in Tables 11–15.

The slurries with a w/c of 1.25 were Bingham fluid under all temperature conditions regardless of fly ash content. With the increase of fly ash content, the influence of temperature on the shear stress of slurry became smaller. According to the fitting lines of slurries containing 40% or 50% fly ash, the shear stress and viscosity of slurry at 60°C were higher than those of other temperatures. This shows that under

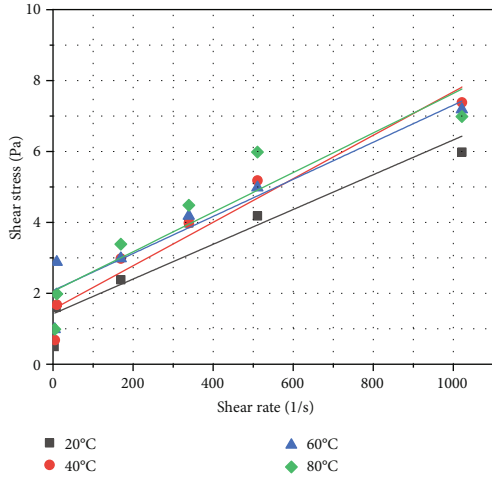


FIGURE 40: Viscosity of cement slurry with a w/c of 1.25 (40% fly ash).

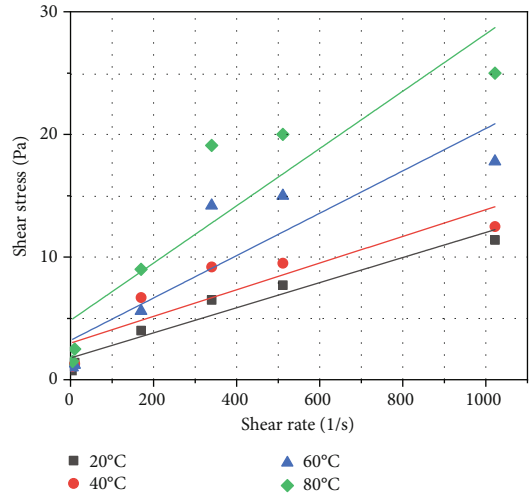


FIGURE 43: Viscosity of cement slurry with a w/c of 1.0 (20% fly ash).

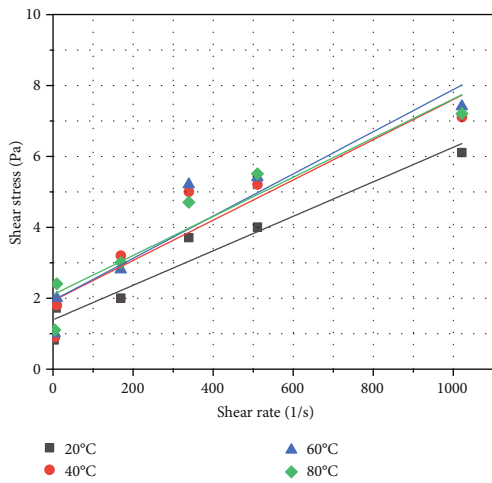


FIGURE 41: Viscosity of cement slurry with a w/c of 1.25 (50% fly ash).

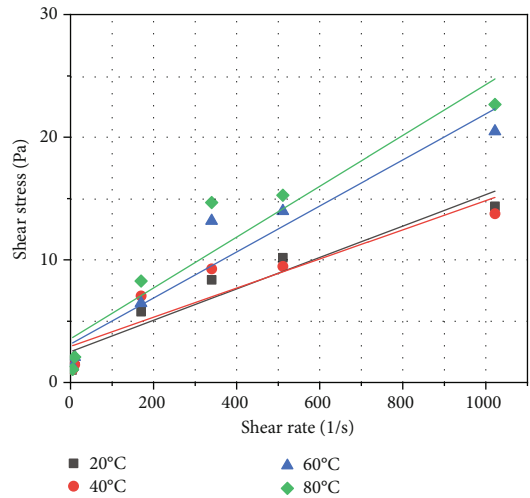


FIGURE 44: Viscosity of cement slurry with a w/c of 1.0 (30% fly ash).

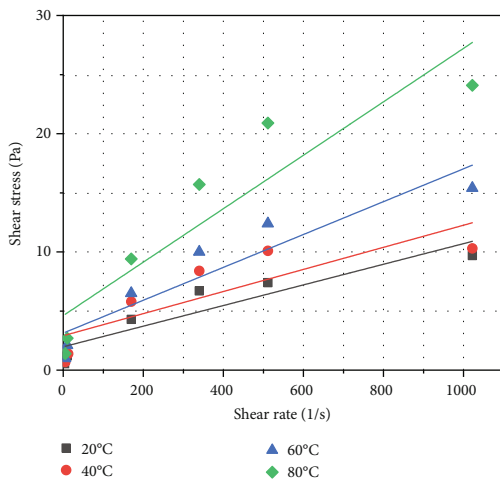


FIGURE 42: Viscosity of cement slurry with a w/c of 1.0 (10% fly ash).

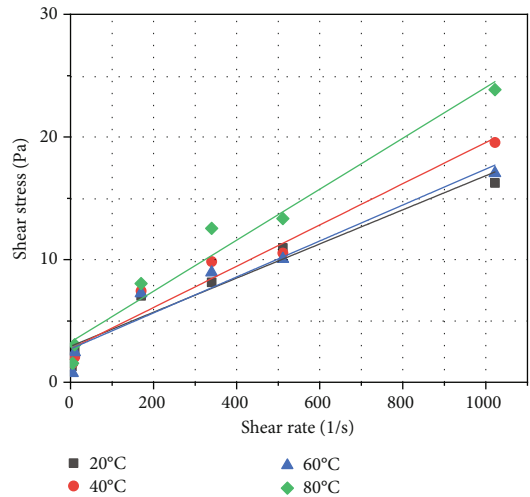


FIGURE 45: Viscosity of cement slurry with a w/c of 1.0 (40% fly ash).

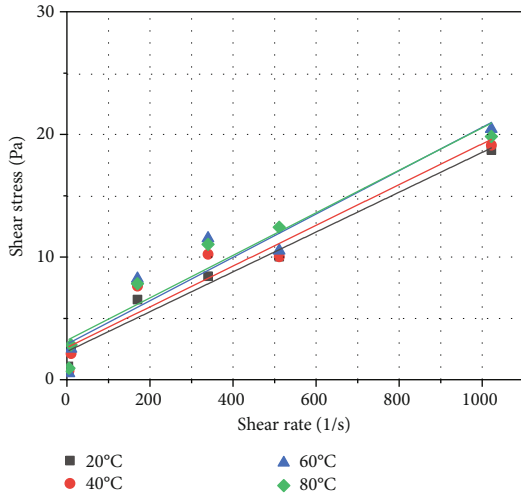


FIGURE 46: Viscosity of cement slurry with a w/c of 1.0 (50% fly ash).

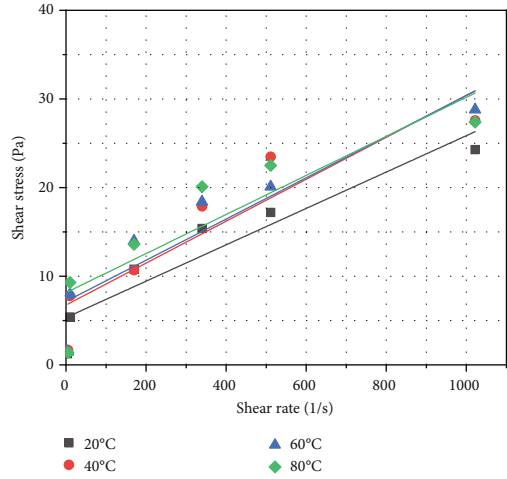


FIGURE 49: Viscosity of cement slurry with a w/c of 0.75 (30% fly ash).

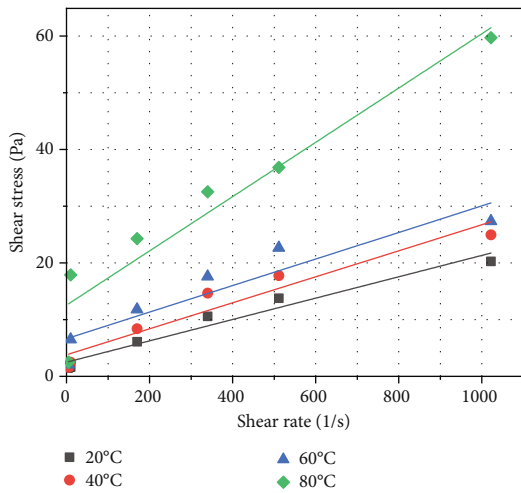


FIGURE 47: Viscosity of cement slurry with a w/c of 0.75 (10% fly ash).

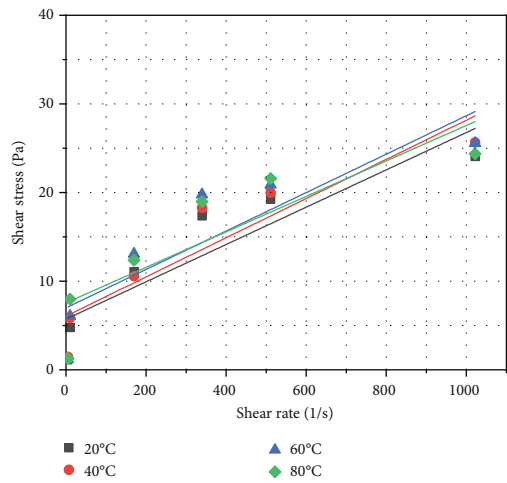


FIGURE 50: Viscosity of cement slurry with a w/c of 0.75 (40% fly ash).

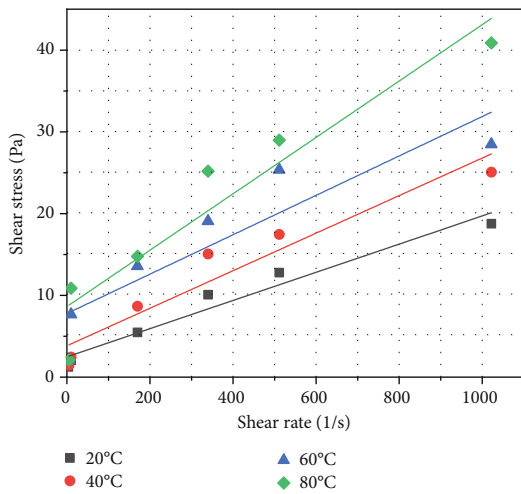


FIGURE 48: Viscosity of cement slurry with a w/c of 0.75 (20% fly ash).

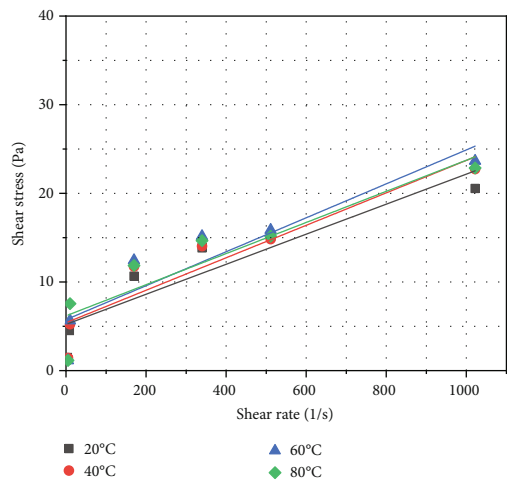


FIGURE 51: Viscosity of cement slurry with a w/c of 0.75 (50% fly ash).

TABLE 2: Fitting line parameters of cement slurry with a w/c of 1.5.

Fitting lines	Fitting equations	R^2
20°C line	$\tau = 0.00538\gamma + 0.28635$	0.95476
40°C line	$\tau = 0.00559\gamma + 0.41617$	0.94752
60°C line	$\tau = 0.00552\gamma + 0.57185$	0.97529
80°C line	$\tau = 0.00588\gamma + 1.56598$	0.95505

TABLE 3: Fitting line parameters of cement slurry with a w/c of 1.25.

Fitting lines	Fitting equations	R^2
20°C line	$\tau = 0.00554\gamma + 0.33160$	0.95006
40°C line	$\tau = 0.00566\gamma + 0.25790$	0.92251
60°C line	$\tau = 0.00523\gamma + 1.14035$	0.98817
80°C line	$\tau = 0.00626\gamma + 2.26900$	0.87904

TABLE 4: Fitting line parameters of cement slurry with a w/c of 1.0.

Fitting lines	Fitting equations	R^2
20°C line	$\tau = 0.00812\gamma + 2.18322$	0.94968
40°C line	$\tau = 0.00702\gamma + 2.57572$	0.88841
60°C line	$\tau = 0.01289\gamma + 4.02923$	0.85417
80°C line	$\tau = 0.02359\gamma + 5.37658$	0.91821

TABLE 5: Fitting line parameters of cement slurry with a w/c of 0.75.

Fitting lines	Fitting equations	R^2
20°C line	$\tau = 0.02023\gamma + 2.81153$	0.99473
40°C line	$\tau = 0.02317\gamma + 4.05143$	0.93401
60°C line	$\tau = 0.02656\gamma + 7.88834$	0.92246
80°C line	$\tau = 0.05422\gamma + 13.56824$	0.87535

TABLE 6: Fitting line parameters of cement slurry with a w/c of 1.5 (10% fly ash).

Fitting lines	Fitting equations	R^2
20°C line	$\tau = 0.00179\gamma + 1.10208$	0.64749
40°C line	$\tau = 0.00184\gamma + 1.13701$	0.67400
60°C line	$\tau = 0.00563\gamma + 1.38457$	0.92246
80°C line	$\tau = 0.00577\gamma + 1.72187$	0.87535

TABLE 7: Fitting line parameters of cement slurry with a w/c of 1.5 (20% fly ash).

Fitting lines	Fitting equations	R^2
20°C line	$\tau = 0.00231\gamma + 1.00712$	0.71350
40°C line	$\tau = 0.00256\gamma + 0.98716$	0.83594
60°C line	$\tau = 0.00608\gamma + 0.99677$	0.89206
80°C line	$\tau = 0.00588\gamma + 1.26649$	0.91687

TABLE 8: Fitting line parameters of cement slurry with a w/c of 1.5 (30% fly ash).

Fitting lines	Fitting equations	R^2
20°C line	$\tau = 0.00290\gamma + 1.08761$	0.81126
40°C line	$\tau = 0.00334\gamma + 1.02191$	0.84168
60°C line	$\tau = 0.00434\gamma + 1.09564$	0.91004
80°C line	$\tau = 0.00488\gamma + 1.10883$	0.93151

TABLE 9: Fitting line parameters of cement slurry with a w/c of 1.5 (40% fly ash).

Fitting lines	Fitting equations	R^2
20°C line	$\tau = 0.00361\gamma + 0.89554$	0.88311
40°C line	$\tau = 0.00391\gamma + 0.94384$	0.91420
60°C line	$\tau = 0.00479\gamma + 0.88938$	0.95390
80°C line	$\tau = 0.00443\gamma + 1.09727$	0.93335

TABLE 10: Fitting line parameters of cement slurry with a w/c of 1.5 (50% fly ash).

Fitting lines	Fitting equations	R^2
20°C line	$\tau = 0.00352\gamma + 1.14304$	0.88672
40°C line	$\tau = 0.00393\gamma + 1.26980$	0.88245
60°C line	$\tau = 0.00445\gamma + 1.10675$	0.91255
80°C line	$\tau = 0.00420\gamma + 1.29237$	0.90046

TABLE 11: Fitting line parameters of cement slurry with a w/c of 1.25 (10% fly ash).

Fitting lines	Fitting equations	R^2
20°C line	$\tau = 0.00195\gamma + 1.28122$	0.69199
40°C line	$\tau = 0.00320\gamma + 1.38678$	0.81746
60°C line	$\tau = 0.00641\gamma + 1.30169$	0.98364
80°C line	$\tau = 0.00775\gamma + 1.75856$	0.95716

TABLE 12: Fitting line parameters of cement slurry with a w/c of 1.25 (10% fly ash).

Fitting lines	Fitting equations	R^2
20°C line	$\tau = 0.00311\gamma + 1.18156$	0.89933
40°C line	$\tau = 0.00595\gamma + 0.65804$	0.96231
60°C line	$\tau = 0.00636\gamma + 1.28504$	0.98034
80°C line	$\tau = 0.00761\gamma + 1.63880$	0.96079

the conditions of high temperature and high fly ash content, the viscosity reduction effect caused by the lubricating effect of fly ash on the slurries is greater than the viscosity increase effect formed by the accelerated hydration at high temperature.

TABLE 13: Fitting line parameters of cement slurry with a w/c of 1.25 (30% fly ash).

Fitting lines	Fitting equations	R^2
20°C line	$\tau = 0.00400\gamma + 1.29423$	0.92171
40°C line	$\tau = 0.00593\gamma + 1.50078$	0.88866
60°C line	$\tau = 0.00534\gamma + 1.71827$	0.94231
80°C line	$\tau = 0.00706\gamma + 1.89435$	0.91920

TABLE 14: Fitting line parameters of cement slurry with a w/c of 1.25 (40% fly ash).

Fitting lines	Fitting equations	R^2
20°C line	$\tau = 0.00490\gamma + 1.43442$	0.87305
40°C line	$\tau = 0.00613\gamma + 1.56328$	0.93552
60°C line	$\tau = 0.00523\gamma + 2.08916$	0.88609
80°C line	$\tau = 0.00558\gamma + 2.06852$	0.83975

TABLE 15: Fitting line parameters of cement slurry with a w/c of 1.25 (50% fly ash).

Fitting lines	Fitting equations	R^2
20°C line	$\tau = 0.00486\gamma + 1.38172$	0.93241
40°C line	$\tau = 0.00567\gamma + 1.92097$	0.85749
60°C line	$\tau = 0.00595\gamma + 1.92628$	0.87013
80°C line	$\tau = 0.00552\gamma + 2.08999$	0.88634

TABLE 16: Fitting line parameters of cement slurry with a w/c of 1.0 (10% fly ash).

Fitting lines	Fitting equations	R^2
20°C line	$\tau = 0.00873\gamma + 1.97281$	0.82542
40°C line	$\tau = 0.00935\gamma + 2.90982$	0.65097
60°C line	$\tau = 0.01390\gamma + 3.13150$	0.84570
80°C line	$\tau = 0.02261\gamma + 4.61141$	0.82100

TABLE 17: Fitting line parameters of cement slurry with a w/c of 1.0 (20% fly ash).

Fitting lines	Fitting equations	R^2
20°C line	$\tau = 0.01024\gamma + 1.77198$	0.93237
40°C line	$\tau = 0.01087\gamma + 2.98772$	0.76588
60°C line	$\tau = 0.01727\gamma + 3.20856$	0.75302
80°C line	$\tau = 0.02335\gamma + 4.84051$	0.78841

The relationship of shear stress and shear rate of the slurry with a w/c of 1.0 and different fly ash contents is shown in Figures 42–46. The fitting line parameters of cement slurry with a w/c of 1.0 are shown in Tables 16–20.

Under the condition of low fly ash content, the viscosity of the slurries increased obviously with the increase of temperature. Under the condition of high fly ash content, the vis-

TABLE 18: Fitting line parameters of cement slurry with a w/c of 1.0 (30% fly ash).

Fitting lines	Fitting equations	R^2
20°C line	$\tau = 0.01280\gamma + 2.44399$	0.90944
40°C line	$\tau = 0.01187\gamma + 2.87701$	0.81806
60°C line	$\tau = 0.01877\gamma + 3.06304$	0.89622
80°C line	$\tau = 0.02073\gamma + 3.48845$	0.88291

TABLE 19: Fitting line parameters of cement slurry with a w/c of 1.0 (40% fly ash).

Fitting lines	Fitting equations	R^2
20°C line	$\tau = 0.01392\gamma + 2.87708$	0.93204
40°C line	$\tau = 0.01682\gamma + 2.67974$	0.95163
60°C line	$\tau = 0.01466\gamma + 2.67027$	0.92301
80°C line	$\tau = 0.02078\gamma + 3.22255$	0.95975

TABLE 20: Fitting line parameters of cement slurry with a w/c of 1.0 (50% fly ash).

Fitting lines	Fitting equations	R^2
20°C line	$\tau = 0.01624\gamma + 2.26215$	0.97222
40°C line	$\tau = 0.01662\gamma + 2.58418$	0.91850
60°C line	$\tau = 0.01768\gamma + 2.86857$	0.89714
80°C line	$\tau = 0.01734\gamma + 3.16830$	0.92767

TABLE 21: Fitting line parameters of cement slurry with a w/c of 0.75 (10% fly ash).

Fitting lines	Fitting equations	R^2
20°C line	$\tau = 0.01887\gamma + 2.37889$	0.95104
40°C line	$\tau = 0.02297\gamma + 3.68915$	0.91672
60°C line	$\tau = 0.02344\gamma + 6.54228$	0.84237
80°C line	$\tau = 0.04796\gamma + 12.45081$	0.89334

TABLE 22: Fitting line parameters of cement slurry with a w/c of 0.75 (20% fly ash).

Fitting lines	Fitting equations	R^2
20°C line	$\tau = 0.01724\gamma + 2.40494$	0.94987
40°C line	$\tau = 0.02296\gamma + 3.75665$	0.91150
60°C line	$\tau = 0.02409\gamma + 7.70212$	0.78470
80°C line	$\tau = 0.03448\gamma + 8.55536$	0.88627

cosity of the slurries at each temperature was almost the same. As the w/c of the slurries reduced, the viscosity of the slurries at different temperatures varied greatly when the fly ash content was 10%. The reduction of water-cement ratio resulted in a greater influence of physical composition and temperature on the viscosity of the slurries.

TABLE 23: Fitting line parameters of cement slurry with a w/c of 0.75 (30% fly ash).

Fitting lines	Fitting equations	R^2
20°C line	$\tau = 0.02052\gamma + 5.34630$	0.86686
40°C line	$\tau = 0.02366\gamma + 6.75101$	0.82060
60°C line	$\tau = 0.02322\gamma + 7.16873$	0.84023
80°C line	$\tau = 0.02203\gamma + 8.15868$	0.74869

TABLE 24: Fitting line parameters of cement slurry with a w/c of 0.75 (40% fly ash).

Fitting lines	Fitting equations	R^2
20°C line	$\tau = 0.02104\gamma + 5.64867$	0.79386
40°C line	$\tau = 0.02210\gamma + 5.98633$	0.82143
60°C line	$\tau = 0.02167\gamma + 6.91662$	0.73942
80°C line	$\tau = 0.02001\gamma + 7.48812$	0.70589

TABLE 25: Fitting line parameters of cement slurry with a w/c of 0.75 (50% fly ash).

Fitting lines	Fitting equations	R^2
20°C line	$\tau = 0.01694\gamma + 5.07298$	0.82282
40°C line	$\tau = 0.01831\gamma + 5.25300$	0.84752
60°C line	$\tau = 0.01915\gamma + 5.59929$	0.82224
80°C line	$\tau = 0.01755\gamma + 6.03016$	0.80373

The relationship of shear stress and shear rate of the slurry with a w/c of 0.75 and different fly ash contents is shown in Figures 47–51. The fitting line parameters of cement slurry with a w/c of 0.75 are shown in Tables 21–25.

When w/c is 0.75, the slurries were also Bingham fluid. The shear stresses of the slurries with 10% fly ash at 80°C were much larger than those of the slurry at lower temperature, which was similar to the rheological behavior of the cement slurries without fly ash. With the increase of fly ash content, the shear stress of slurries at 80°C decreased rapidly. When the slurries contained 30%, 40%, and 50% fly ash, the shear stress of slurries was almost the same at each temperature. The steric hindrance, which was formed by the adsorption of fly ash particles on the surface of cement particles, makes the slurry insensitive to temperature.

The slurries were Newtonian fluid only with a w/c of 1.5, no fly ash, at a temperature of 20 °C and 40°C. The slurries in all other cases were Bingham fluid. The w/c , slurry temperature, and fly ash content are the main factors affecting the rheological properties of the slurries. The w/c determines the solid concentration in the slurry, and the number of contacts between particles affects the rate of gel formation. The slurry temperature controls the rate of cement hydration reaction, thereby affecting the rate of gel product formation. Fly ash can be adsorbed on the surface of cement particles to lubricate the mixed slurry. At the same time, steric hin-

drance is formed between the cement particles, which increases the distance between the particles, resulting in insignificant influence of temperature on the slurry. The flowability is an important parameter relative to grout design. The slurry with high water-cement ratio and high fly ash content has good fluidity and low viscosity and is preferably injected into small cracks or increases the distance of penetration into the cracks. The slurry with a low water-cement ratio and a low fly ash content with a higher viscosity might be preferred to limit penetration or fill wider fractures.

4. Conclusions

This work considers the influence of multifactors on fluid properties of cement-fly ash slurry. The bleeding rate, setting time, and viscosity of slurry were tested and analyzed. The following conclusions can be drawn:

- (1) The water-cement ratio is a key factor affecting the rheology of the slurry. A low water-cement ratio means a high solid concentration and a large amount of particle contact, which is conducive to gel formation. In the case of low water-cement ratio, the slurry was Bingham fluid, and in the case of high water-cement ratio (water-cement ratio of 1.5), it was Newtonian fluid
- (2) The temperature affects the stability of the slurry. High temperature can increase the hydration reaction speed, leading to a rapid increase in gelling components, which can greatly shorten the initial setting time and final setting time, and increase the viscosity of the slurry. Therefore, the setting time of the cement slurry can be adjusted by the temperature and the fluidity of the slurry can be improved by the temperature
- (3) Fly ash can mix well with water under any temperature conditions. Fly ash can prolong the solidification time of the slurry. In addition, fly ash can be adsorbed on the surface of cement particles, increasing the steric hindrance between cement particles and reducing the influence of temperature on the rheological properties of the slurry

Data Availability

The data used to support the findings of this study are available from the corresponding author upon request.

Conflicts of Interest

The authors declare that there is no conflict of interest regarding the publication of this paper.

Acknowledgments

The authors are supported by the National Natural Science Foundation of China (Grant No. 41807230) and Fundamental Research Funds for the Central Universities (Grant No. 2-9-2018-090).

References

- [1] M. Ahmaruzzaman, "A review on the utilization of fly ash," *Progress in Energy and Combustion Science*, vol. 36, no. 3, pp. 327–363, 2010.
- [2] S. Horiuchi, M. Kawaguchi, and K. Yasuhara, "Effective use of fly ash slurry as fill material," *Journal of Hazardous Materials*, vol. 76, no. 2-3, pp. 301–337, 2000.
- [3] Z. T. Yao, X. S. Ji, P. K. Sarker et al., "A comprehensive review on the applications of coal fly ash," *Earth-Science Reviews*, vol. 141, pp. 105–121, 2015.
- [4] A. Kashani, R. S. Nicolas, G. G. Qiao, J. S. J. van Deventer, and J. L. Provis, "Modelling the yield stress of ternary cement-slag-fly ash pastes based on particle size distribution," *Powder Technology*, vol. 266, pp. 203–209, 2014.
- [5] A. K. Saha, "Effect of class F fly ash on the durability properties of concrete," *Sustainable Environment Research*, vol. 28, no. 1, pp. 25–31, 2018.
- [6] S. Antiohos and S. Tsimas, "Investigating the role of reactive silica in the hydration mechanisms of high-calcium fly ash/cement systems," *Cement and Concrete Composites*, vol. 72, no. 2, pp. 171–181, 2004.
- [7] S. R. Lo and S. P. R. Wardani, "Strength and dilatancy of a silt stabilized by a cement and fly ash mixture," *Canadian Geotechnical Journal*, vol. 39, no. 1, pp. 77–89, 2002.
- [8] W. H. Huang, "Properties of cement-fly ash grout admixed with bentonite, silica fume, or organic fiber," *Cement and Concrete Research*, vol. 27, no. 3, pp. 395–406, 1997.
- [9] Y. Tomita, L. C. Guo, Y. Zhang, N. Uchida, and K. Uematsu, "Effect of temperature on the slurry characteristics and green bodies of alumina," *Journal of the American Ceramic Society*, vol. 78, no. 8, pp. 2153–2156, 1995.
- [10] G. M. Nediljka, M. Davorin, and K. Gracijan, "Cement slurries for geothermal wells cementing," *Rudarsko-geoloSko-naftni zbornik*, vol. 6, no. 1, pp. 127–134, 1994.
- [11] J. Du, X. G. Shen, G. J. Feng, W. W. Zhu, and C. F. Xu, "Hydration mechanism of fly ash cement and grouting simulation experiment," *Chemical Engineering Transactions*, vol. 51, pp. 565–570, 2016.
- [12] J. K. Lee, J. Ko, and Y. S. Kim, "Rheology of fly ash mixed tailings slurries and applicability of prediction models," *Minerals*, vol. 7, no. 9, p. 165, 2017.
- [13] K. F. Alexandersson and S. Wallevik, "Effect of temperature and pressure on rheological measurements of cement slurries," *Annual Transactions of the Nordic Rheology Society*, vol. 22, pp. 125–130, 2014.
- [14] H. Justnes and H. Vikan, "Viscosity of cement slurries as a function of solids content," *Annual Transactions of the Nordic Rheology Society*, vol. 13, pp. 75–82, 2005.
- [15] D. P. Bentz, C. F. Ferraris, M. A. Galler, A. S. Hansen, and J. M. Guynn, "Influence of particle size distributions on yield stress and viscosity of cement-fly ash pastes," *Cement and Concrete Research*, vol. 42, no. 2, pp. 404–409, 2012.
- [16] W. Guan, M. H. Tan, H. Y. Yu, and K. R. Wu, "Rheological properties of cement pastes with fly ash," *Journal of Building Materials*, vol. 4, no. 4, pp. 339–345, 2001.
- [17] J. N. Zhang and X. B. Hu, "Effect of fly ash on rheological properties of cement paste," *Zhe Jiang Construction*, vol. S1, pp. 99–101, 2005.
- [18] J. Mirza, M. S. Mirza, V. Roy, and K. Saleh, "Basic rheological and mechanical properties of high-volume fly ash grouts," *Construction and Building Materials*, vol. 16, no. 6, pp. 353–363, 2002.
- [19] S. H. Lee, H. J. Kim, E. Sakai, and M. Daimon, "Effect of particle size distribution of fly ash-cement system on the fluidity of cement pastes," *Cement and Concrete Research*, vol. 33, no. 5, pp. 763–768, 2003.
- [20] Y. J. Xie, X. B. Cheng, K. L. Ma, J. Fen, and G. C. Long, "Effects of fly ash on shearing thinning and thickening of cement paste," *Journal of the Chinese Ceramic Society*, vol. 43, no. 8, pp. 1–7, 2015.

Research Article

Numerical Analysis of the Mud Inflow Model of Fractured Rock Mass Based on Particle Flow

Yongjian Pan,¹ Huajun Wang,¹ Yanlin Zhao ,² Qiang Liu ,^{2,3} and Shilin Luo ⁴

¹Zhejiang Engineering Survey and Design Institute Group Co. Ltd, Ningbo, 315010 Zhejiang Province, China

²Work Safety Key Lab on Prevention and Control of Gas and Roof Disasters for Southern Coal Mines, Hunan Provincial Key Laboratory of Safe Mining Techniques of Coal Mines, Hunan University of Science and Technology, Xiangtan, 411201 Hunan Province, China

³School of Resource Environment and Safety Engineering, Hunan University of Science and Technology, Xiangtan, 411201 Hunan Province, China

⁴School of Civil Engineering, Chongqing University, Chongqing 400045, China

Correspondence should be addressed to Yanlin Zhao; yanlin_8@163.com

Received 14 January 2021; Revised 25 February 2021; Accepted 27 March 2021; Published 9 April 2021

Academic Editor: Rihong Cao

Copyright © 2021 Yongjian Pan et al. This is an open access article distributed under the Creative Commons Attribution License, which permits unrestricted use, distribution, and reproduction in any medium, provided the original work is properly cited.

Water inrush and mud outburst are one of the crucial engineering disasters commonly encountered during the construction of many railways and tunnels in karst areas. In this paper, based on fluid dynamics theory and discrete element method, we established a fractured rock mass mud inflow model using particle flow PFC3D numerical software, simulated the whole process of fractured rock mass mud inflow, and discussed the effect of particle size and flow velocity on the change of pressure gradient. The numerical simulation results show that the movement of particles at the corner of the wall when the water pressure is first applied occurs similar to the vortex phenomenon, with the running time increases, the flow direction of particles changes, the vortex phenomenon disappears, and the flow direction of particles at the corner points to the fracture; in the initial stage, the slope of the particle flows rate curves increases in time, and the quadratic function is used for fitting. After the percolation velocity of particles reaches stability, the slope of the curve remains constant, and the primary function is used for fitting; the particle flow rate and pressure gradient are influenced by a variety of factors, and they approximately satisfy the exponential function of an “S” curve.

1. Introduction

Engineering construction under karst geological conditions often causes various disasters, such as water inrush, water gushing, and collapse. Among them, the problems of water inrush and mud outburst are particularly significant in fractured rock masses [1, 2]. Due to the complex dynamic process of water inrush and water gushing formation and time, the audience is influenced by many factors, such as formation lithology, hydrogeological conditions, construction methods, and change of mechanical behavior of rock mass [3]. The erosion of fluid reduces the strength and stability of engineering rock masses and brings serious threats to project construction and operation.

For underground engineering, the rock mass excavation not only involves the formation of a new equilibrium state after the original equilibrium state is broken [4] but also the rock masses in a certain range around the cavern will become loose under the influence of joints, fractures, and other structural surfaces slip and collapse. For this case, the particle discrete element PFC can be better simulated [5–9]. Yang et al. [10] performed a discrete element simulation of the fractured red sandstone under uniaxial compression and revealed the failure mechanism of the fractured red sandstone; Fan and Cao [11] established a numerical calculation model containing two fractures based on the particle contact adhesion model in the discrete element numerical analysis software PFC3D and discussed the effect of rock bridge angle

on the mechanical properties of defective rock; Liu et al. [12] studied the crack expansion of indented rock specimens numerically; Potyondy and Cundall [13] proposed a rock bonded particles numerical model (BPM) and used the discrete element numerical analysis software PFC to simulate; Zhu and Xu [14] considered the effects of blasting disturbance, geological conditions of surrounding rock, and tunnel cross-section form on tunnel collapse and carried out a series of numerical simulation calculations, and a series of numerical simulation calculations were carried out, the calculated tunnel collapse amount was compared with the commonly used loose load calculation results, and the closest calculation value was obtained. Furthermore, many scholars [15–17] conducted a great deal of research using PFC particle discrete elements in fluid-solid coupling calculations; Zhou et al. [18, 19] based on particle flow theory using the FISHTANK function library of the PFC software calculation program built-in FISH language successfully simulated the seepage and piping of sand and cohesive soil materials and obtained the variation law of pressure and flow velocity in the seepage process; Luo et al. [20] used the PFC particle flow platform and the built-in FISH language to compile a program to simulate the law of particles falling freely in the fluid and the change law of seepage gradient and flow rate under different pressure differences, and the results basically conform to Darcy's law; Bai [21] simulates the whole process of foundation pit water inrush through PFC2D; Wang et al. [22] used PFC3D numerical software to study and explore the influence of factors such as fault water pressure and rock fracture properties on the water inrush from tunnel and mud inrush.

Due to the complex nature of mud inflow seepage and the uncertainty of boundary conditions often make the numerical calculation of seepage impact far from the actual test results, and different numerical software has different scope of application, such as finite difference software for continuous nonlinear multifield coupling problems (FLAC3D), discrete element software has unique advantages in solving structural surface control problems (3DEC), and particle flow software is particularly suitable for brittle material fracture development and bulk flow deformation problems (PFC3D). Considering that the rock mass is a discontinuous medium to simulate the problem of large deformation of rock mass in underground engineering, PFC numerical software has the advantages of reasonable treatment of permeability boundary and effective application of multiple flow-solid coupling models. This paper uses the discrete element method, using particle flow software (PFC3D), combined with fluid dynamics theory, establishes a fractured rock mass mud inflow model, simulates the whole process of fractured rock mud inflow, and discusses the impact of particle size and flow rate on the change of pressure gradient, which provides positive guidance significance for underground engineering construction in karst areas.

2. Mud Inflow Theory

2.1. Basic Assumptions. Since there is no real fluid in the PFC3D program, a fluid unit containing a certain number of particles is used instead of a fluid for the calculation. The flow process and law of the particles in the fracture and the

indicators of pressure, velocity vector, and flow velocity on the fluid unit are obtained by the action of the particles rolling or flowing in the fracture. To facilitate the modeling of mud inflow in a single fracture rock, the following assumptions are proposed:

- (1) The force generated by fluid flow acts on the particle in the form of physical force and is applied to the fluid in the same magnitude
- (2) Particle units in the model are considered as rigid bodies, and the contact between particles occurs only in a small area, approximating point contact
- (3) The contact behavior is flexible, allowing a certain amount of superposition between the rigid particles at the contact, but the value is much smaller than the radius of the particles, and the contact force is linked to the superposition between the particles through the force-displacement law
- (4) The walls are parallel to each other, smooth and the width of the fracture can be adjusted by changing the distance between thin walls

2.2. Mud Inflow Theory and Its Implementation

2.2.1. The Force on the Particle. Figure 1 shows a fixed control volume, where $\Delta V = \Delta x \times \Delta y \times \Delta z$, and the number of particles in the fluid unit is n_p .

Assuming that the fluid flows only in the x -direction and there is a pressure gradient dp/dx in that direction, so that the forces on the particles inside the fluid element in the seepage direction are balanced, the total permeability on the particles is expressed as [23–25]:

$$f_{dsum} = \sum_{i=1}^{n_p} f_{dix} = -f_{int\ x} \Delta V - \frac{dp}{dx} \frac{\pi}{6} \sum_{i=1}^{n_p} d_{p_i}^3, \quad (1)$$

where $f_{int\ x}$ is the interaction force between the fluid and solid phases in the unit volume, d_{p_i} is the particle diameter, p is the seepage pressure, the negative sign of the first term on the right side of the equation indicates that the force acting on the fluid is positive, and the negative sign of the second term indicates that the pressure is gradually decreasing along the x -positive direction. $i = 1, 2, 3, \dots, n_p$, $j = x, y, z$.

Considering the porosity, it can be expressed as:

$$n = 1 - \frac{1}{\Delta V} \frac{\pi}{6} \sum_{i=1}^{n_p} d_{p_i}^3. \quad (2)$$

Substituting Eq. (2) into Eq. (1) yields:

$$f_{dsum} = \sum_{i=1}^{n_p} f_{dix} = - \left(\frac{f_{int\ x}}{1-n} + \frac{dp}{dx} \right) \frac{\pi}{6} \sum_{i=1}^{n_p} d_{p_i}^3. \quad (3)$$

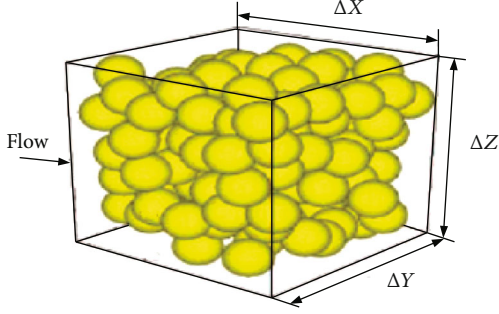


FIGURE 1: Fluid through the particle assemble.

Thus, the total force acting on the particle is

$$f_{dij} = - \left(\frac{f_{intj}}{1-n} + \nabla p_j \right) \frac{\pi}{6} d_{pi}^3. \quad (4)$$

The interaction force between the particle and fluid under fluid-solid coupling can be expressed as:

$$f_{intj} = n \cdot \nabla p_j. \quad (5)$$

Substituting Eq. (5) into Eq. (4), the total force on the particle under the action of fluid-solid coupling can be obtained as:

$$f_{dij} = - \frac{\nabla p_j}{1-n} \frac{\pi}{6} d_{pi}^3. \quad (6)$$

2.2.2. Pressure Gradient in Pore Media. The pressure gradient is used in pore media to represent the fluid-solid coupling interaction, which can usually be calculated by empirical equations. Darcy's law is widely used in the fluid phase of porous media, and the pressure gradient in the expression of Darcy's law is proportional to the apparent relative velocity as follows.

$$\frac{dp}{dx} = - \frac{\rho_f g}{K} u_{x0} = - \frac{\nu_f \rho_f}{k} u_{x0}, \quad (7)$$

where ν_f, ρ_f is the kinematic viscosity and density of the fluid, respectively, u_{x0} is the apparent relative velocity, K is the permeability coefficient, and k is the permeability.

According to the Kozeny-Carman equation, the permeability of the pore medium can be expressed as:

$$k = c \cdot \frac{\bar{d}_p^2 n^3}{(1-n)^2}, \quad (8)$$

where c is the Kozeny-Carman constant, generally taken between 0.003 and 0.0055; \bar{d}_p is the average diameter of the particles.

Darcy's law applies to laminar flows with Reynolds coefficients of 1 ~ 10. For relatively large Reynolds coefficients and nonlinear equations, the following equation can be used.

$$\frac{dp}{dx} = - \left(150 \cdot \frac{(1-n)^2}{n^3 \bar{d}_p^2} \nu_f \rho_f u_{x0} + 1.75 \cdot \frac{(1-n)}{n^3 \bar{d}_p} \rho_f u_{x0}^2 \right). \quad (9)$$

By substituting $nu_x = u_{x0}$ into Eq. (9) yields:

$$\frac{dp}{dx} = - \left(150 \cdot \frac{(1-n)^2}{n^2 \bar{d}_p^2} \nu_f \rho_f u_x + 1.75 \cdot \frac{(1-n)}{n \bar{d}_p} \rho_f u_x^2 \right). \quad (10)$$

Since the particle forces are generated by relative fluid flow, the relative velocity $u_{rx} = \bar{v}_x - u_x$ (where \bar{v}_x is the average velocity of particles in a given control area) is replaced by the absolute fluid velocity, which following formula can be obtained:

$$\frac{dp}{dx} = \left(150 \cdot \frac{(1-n)^2}{n^2 \bar{d}_p^2} \nu_f \rho_f u_x + 1.75 \cdot \frac{(1-n)}{n \bar{d}_p} \rho_f |\bar{v}_x - u_x| \right) \cdot (\bar{v}_x - u_x). \quad (11)$$

Equation (11) can be expressed as:

$$\nabla p_j = \left(150 \cdot \frac{(1-n)^2}{n^2 \bar{d}_p^2} \nu_f \rho_f u_x + 1.75 \cdot \frac{(1-n)}{n \bar{d}_p} \rho_f |\bar{v}_j - u_j| \right) \cdot (\bar{v}_j - u_j). \quad (12)$$

For large porosity ($n \geq 0.8$), the pressure gradient can be calculated by the following equation.

$$\nabla p_j = \frac{3}{4} \rho_f C_d \frac{(1-n) \cdot n^{-2.7}}{\bar{d}_p} |\bar{v}_j - u_j| \cdot (\bar{v}_j - u_j), \quad (13)$$

where C_d is the drag coefficient of the sphere, which is a function related to the Reynolds coefficient R_{ep} :

$$C_d = \begin{cases} \frac{24}{R_{ep}} (1 + 0.15 \cdot R_{ep}^{0.687}) & R_{ep} \leq 1000, \\ 0.44 & R_{ep} \geq 1000, \end{cases} \quad (14)$$

$$R_{ep} = \frac{n |\bar{v}_j - u_j| \bar{d}_p}{\nu_f}.$$

2.2.3. Navier-Stokes Equation and Continuity Equation. The Navier-stokes equation for a fluid in liquid-phase [24], non-turbulent, viscous incompressible fluid-solid two-phase, can be expressed as

$$\frac{\partial n}{\partial t} = -(\nabla \cdot nu), \quad (15)$$

$$\frac{\partial(nu)}{\partial t} = -(\nabla \cdot nuu) - \frac{n}{\rho_f} \nabla p - \frac{n}{\rho_f} \nabla \cdot \tau + ng + \frac{f_{int}}{\rho_f}, \quad (16)$$

TABLE 1: Mesoscopic parameters of numerical simulation materials.

Kinds	Particle size (mm)	Density (kg·m ⁻³)	Normal stiffness (N·m ⁻¹)	Tangential stiffness (N·m ⁻¹)	Coefficient of friction	Viscosity (MPa·s)
Ball	0.1 ~ 2.0	2300	1.0 × 10 ⁴	1.0 × 10 ⁴	0.5	
Fluid		1000				Functions related to runtime
Wall			1.0 × 10 ⁷	1.0 × 10 ⁷	0.3	

where u is the flow velocity vector, τ is the viscous stress tensor, g is the acceleration of gravity, f_{int} is the interaction force between the particle and the fluid in a unit volume, and ρ_f is the fluid density, where the viscous stress tensor τ can be expressed as:

$$\tau = \mu \cdot \dot{e}^{(d)}, \quad (17)$$

where μ and $e^{(d)}$ are the viscosity and the stress deflection tensor, respectively.

Expanding Eqs. (15) and (16) in the Cartesian coordinate system, we obtain:

$$\frac{\partial n}{\partial t} + \frac{\partial(nu_x)}{\partial x} + \frac{\partial(nu_y)}{\partial y} + \frac{\partial(nu_z)}{\partial z} = 0, \quad (18)$$

$$\begin{aligned} & \frac{\partial(nu_x)}{\partial t} + \frac{\partial(nu_x^2)}{\partial x} + \frac{\partial(nu_x u_y)}{\partial y} + \frac{\partial(nu_x u_z)}{\partial z} \\ &= -\frac{n}{\rho_f} \frac{\partial p}{\partial x} - \frac{1}{\rho_f} \left(\frac{\partial(n\tau_{xx})}{\partial x} + \frac{\partial(n\tau_{yx})}{\partial y} + \frac{\partial(n\tau_{zx})}{\partial z} \right) \\ &+ ng_x + \frac{f_{\text{int } x}}{\rho_f}, \end{aligned} \quad (19)$$

$$\begin{aligned} & \frac{\partial(nu_y)}{\partial t} + \frac{\partial(nu_y u_x)}{\partial x} + \frac{\partial(nu_y^2)}{\partial y} + \frac{\partial(nu_y u_z)}{\partial z} \\ &= -\frac{n}{\rho_f} \frac{\partial p}{\partial y} - \frac{1}{\rho_f} \left(\frac{\partial(n\tau_{xy})}{\partial x} + \frac{\partial(n\tau_{yy})}{\partial y} + \frac{\partial(n\tau_{zy})}{\partial z} \right) \\ &+ ng_y + \frac{f_{\text{int } y}}{\rho_f}, \end{aligned} \quad (20)$$

$$\begin{aligned} & \frac{\partial(nu_z)}{\partial t} + \frac{\partial(nu_z u_x)}{\partial x} + \frac{\partial(nu_z^2)}{\partial y} + \frac{\partial(nu_z u_z)}{\partial z} \\ &= -\frac{n}{\rho_f} \frac{\partial p}{\partial z} - \frac{1}{\rho_f} \left(\frac{\partial(n\tau_{xz})}{\partial x} + \frac{\partial(n\tau_{yz})}{\partial y} + \frac{\partial(n\tau_{zz})}{\partial z} \right) \\ &+ ng_z + \frac{f_{\text{int } z}}{\rho_f}. \end{aligned} \quad (21)$$

TABLE 2: Design of numerical experiment.

Water pressure (MPa)	Crack width (mm)	Number particles	Model size (mm)
0.5	8	116586	100 × 100 × 200
		155448	100 × 100 × 250
		174879	100 × 100 × 300
0.8	8	116586	100 × 100 × 200
		155448	100 × 100 × 250
		174879	100 × 100 × 300
1	8	116586	100 × 100 × 200
		155448	100 × 100 × 250
		174879	100 × 100 × 300
1.2	8	116586	100 × 100 × 200
		155448	100 × 100 × 250
		174879	100 × 100 × 300

The unit volume solid-liquid interaction force can be expressed as:

$$f_{\text{int } j} = \beta_{\text{int } j} (\bar{v}_j - u_j), \quad (22)$$

where the solid-liquid friction coefficient can be calculated by the following equation

$$\beta_{\text{int } j} = \begin{cases} 150 \cdot \frac{(1-n)^2}{n \cdot \bar{d}_p^2} u_f + 1.75 \cdot \frac{(1-n)}{\bar{d}_p} \cdot \rho_f \cdot |\bar{v}_j - u_j| & n \leq 0.8, \\ \frac{3}{4} \cdot \rho_f \cdot C_D \cdot \frac{(1-n) \cdot n^{-1.7}}{\bar{d}_p} \cdot |\bar{v}_j - u_j| & n > 0.8, \end{cases} \quad (23)$$

where $\beta_{\text{int } j}$ friction coefficient is defined as fluid, combining Eqs. (21) and (22), we can obtain that:

$$f_{\text{dij}} = -\left(\frac{\beta_{\text{int } j}}{1-n} (\bar{v}_j - u_j) + \nabla p_j \right) \frac{\pi}{6} d_{p_i}^3. \quad (24)$$

3. Numerical Analysis of Mud Inflow in Fractured Rock Masses

3.1. Establishment of a Numerical Model of Mud Inflow. The mud inflow model consists of walls and balls, where the

particles are simulated by small balls with certain dimensions, the fractures are realized by setting the distance between the walls, and the fluid is simulated by fluid units. Since the particles in the model are not directly assigned to the macroscopic parameters of the material, as shown in Table 1. It is necessary to calibrate the parameters of the particles to simulate four different groups of water pressure, with water pressure of 0.5 MPa, 0.8 MPa, 1.0 MPa, 1.2 MPa, and three different model sizes, $100 \times 100 \times 200$ mm, $100 \times 100 \times 250$ mm, and $100 \times 100 \times 300$ mm, as shown in Table 2.

3.1.1. Generated Particles. Since the model generation sequence and method are the same, only one example is used for illustration here. First, 6 walls are generated as faces, and the right-hand rule is used in PFC3D to determine the effective face of the wall (four fingers surround the 4 coordinate points of the wall, and the direction pointed by the thumb is the effective face); the 6 walls generated that are composed of dimensions is $0.3 \times 0.1 \times 0.1$ m (Length \times Width \times Height), as shown in Figure 2.

Then, the particles are generated in the hollow cuboid, the radius distribution of particles in PFC3D has normal distribution, uniform distribution, Gaussian distribution, etc. In order to better simulate the inhomogeneity of particle distribution, this numerical simulation adopts uniform distribution in random distribution, the distribution of particle radius R adopts from R_{\min} to R_{\max} uniform distribution, and the average radius of particles is $\bar{R} = (R_{\min} + R_{\max})/2$. Considering the calculation accuracy and calculation time, the minimum radius of particles $R_{\min} = 0.05$ mm, the maximum radius $R_{\max} = 1$ mm, and the number N of particles is determined by the porosity n .

$$N = (1 - n) \cdot \frac{V}{4/3 \cdot \pi \cdot \bar{R}^3}, \quad (25)$$

where n is the porosity; V is the cuboid volume, m^3 ; and \bar{R} is the average particle radius, m.

In order to make the particles randomly generated in the cuboid with a given porosity, ensure the uniformity of the particle distribution, and make the generated particles reach the initial equilibrium state in a short time, the particles are randomly generated by the expanding radius method, and the gravity method was used to make the particles reach equilibrium, as shown in Figure 3.

3.1.2. Generate Fractures. Delete one wall in the x -direction, while establishing multiple walls on that side to form a group, the gap width between the wall, and the wall $d = 6R_{\max}$, and the gap width is not less than 6 mm that a fracture; according to the fracture width $d = 6R_{\max}$ to establish the wall perpendicular to the wall group, the fracture width used in this paper are 8 mm, as shown in Figure 4.

3.1.3. Set up Fluid Unit. A total of 250 fluid units are set in this model, and the unit size is $2 \times 1 \times 1$ mm. The boundary condition of the side wall is smooth, and the fluid flow velocity parallel to the wall surface is not equal to 0. The water pressure P is applied at $x = 0$, and the water pressure P is

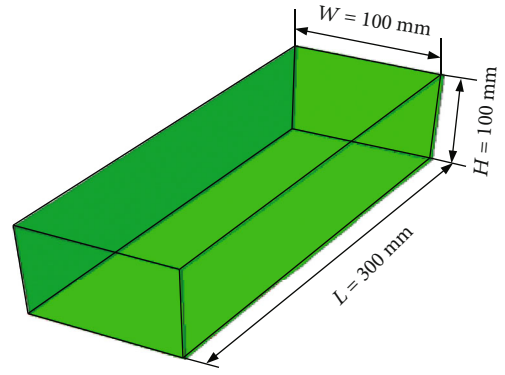


FIGURE 2: A hollow cuboid.

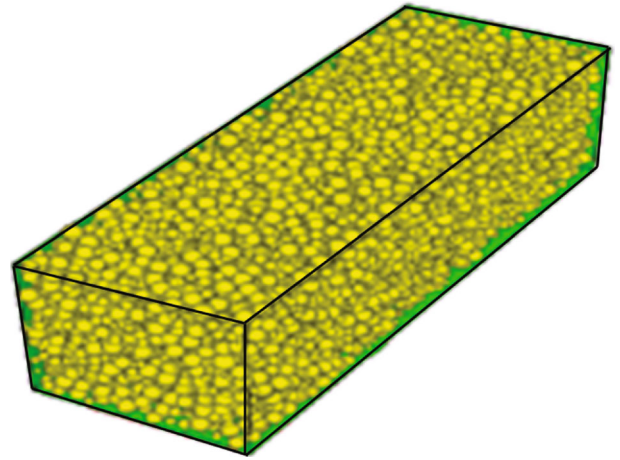


FIGURE 3: Particle assemble.

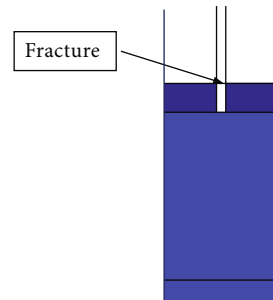


FIGURE 4: Numerical model of the fracture.

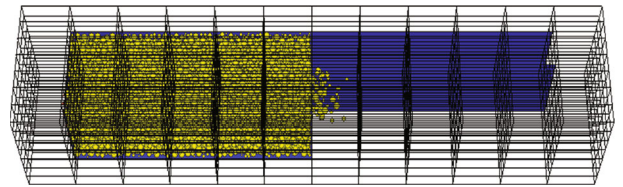


FIGURE 5: Schematic diagram of fluid unit model.

equal to 0 at $x = 0.3$, forming a water pressure difference ΔP . For computational simplicity and rapid convergence, the fluid time step is set to 5.0×10^{-4} s, as shown in Figure 5.

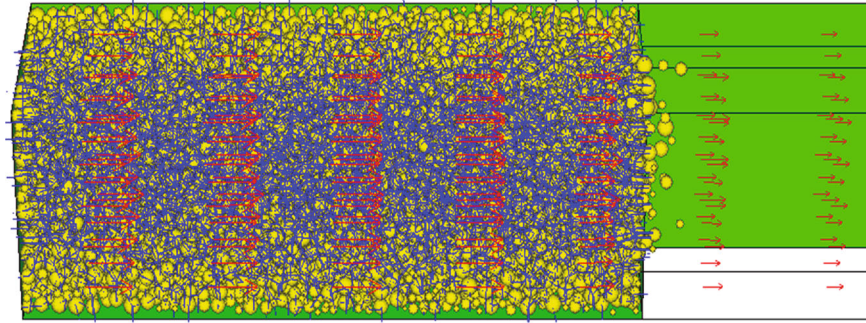


FIGURE 6: Model diagram of a moment of particle equilibrium disruption.

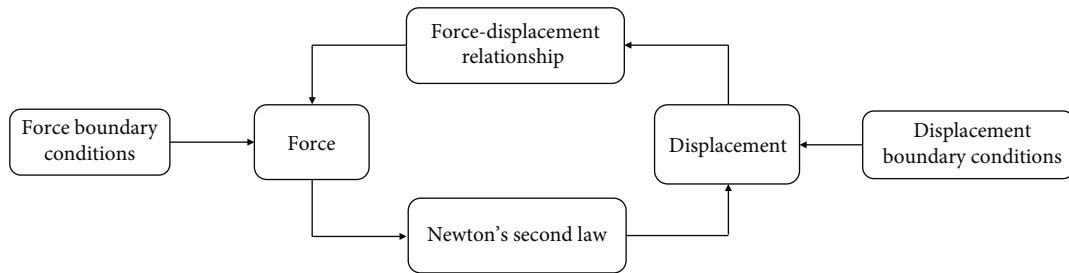


FIGURE 7: Schematic diagram of PFC iterative process.

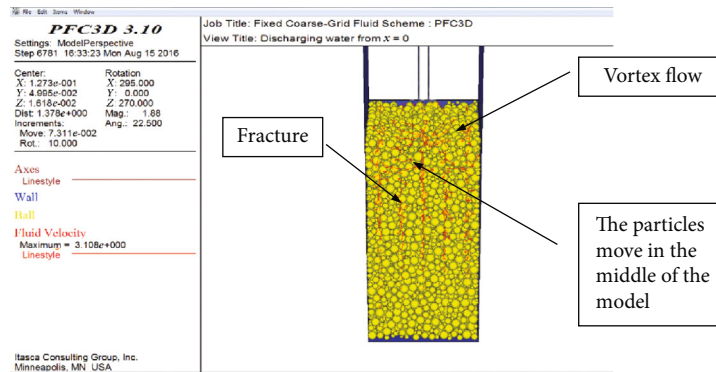


FIGURE 8: The vortex phenomenon and particle movement trend in the initial stage.

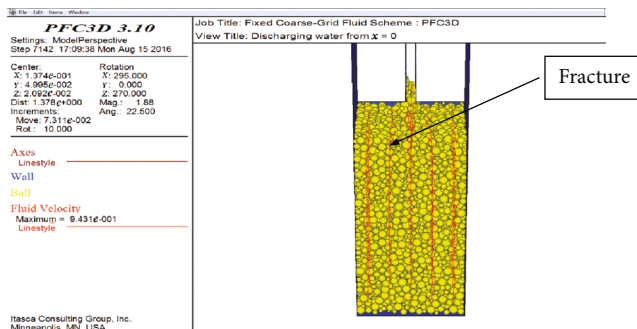


FIGURE 9: The change of the particle flow direction.

3.2. Initial Model Balance. The viscous damping coefficient is set at the solid connection for the energy consumption at the connection between the particles, and the ratio of the normal and tangential damping constants to the critical damping

constant is 0.1. The friction coefficient between the particles and the particles is 0.5, and the friction coefficient between the particles and the wall is 0.3. Numerically simulated material fine views parameters are shown in Table 1. The particles reach the equilibrium state under the action of gravity, and then the fracture is generated by deleting the wall and establishing the wall, the width of the fracture should exceed 6 times the radius of the largest particle, and water and particles are discharged from this fracture. The changes of water velocity, porosity, particle loss, and other parameters are also tracked and recorded. The specimen at a moment of particle equilibrium disruption is shown in Figure 6, where yellow represents clay, green represents the magnitude of the particle normal contact force, and red arrows represent the direction of fluid flow.

3.3. Solution Method. During the calculation of fluid circulation, Newton's second law and force-displacement law are

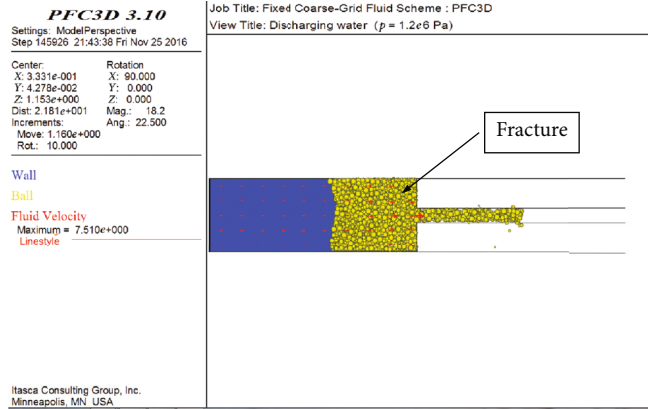


FIGURE 10: The overall increase in the process of particle flow.

applied repeatedly to the particles. Newton’s second law is used to update the position of the particles and the wall to readjust the contact relationship between the particles, while the force-displacement law is used to update the contact forces in the contacting parts. The two alternate, iterating, and traversing the entire particle set in time steps until equilibrium is reached or damage occurs, and the pressure and velocity vectors within each fluid unit are calculated by the semi-implicit PLE algorithm. The calculation process is shown in Figure 7. The conditions for convergence are set as follows.

$$\begin{aligned} \text{ratio}_{\text{sum}} &= \frac{\text{sum of average unbalanced forces of all particles}}{\text{sum of average contact forces of all particles}}, \\ \text{ratio}_{\text{max}} &= \frac{\text{maximum unbalanced force of particles}}{\text{maximum contact force of particles}}, \end{aligned} \quad (26)$$

when $\text{ratio}_{\text{sum}}$ and $\text{ratio}_{\text{max}}$ are both less than 0.0001, stop calculation.

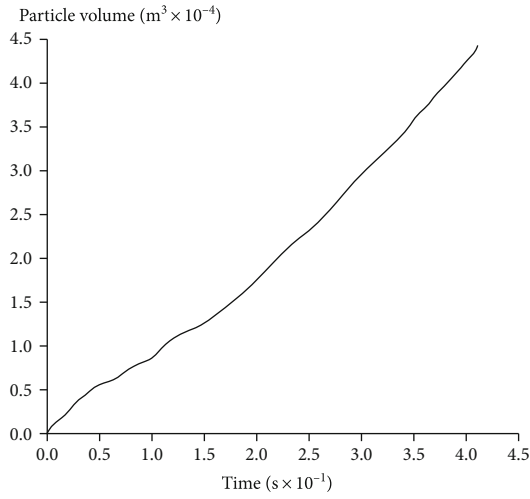
3.4. Analysis of Numerical Simulation Results

3.4.1. Analysis of Flow Law of Particle Seepage. According to the numerical simulation results, it can be found that most of the particles move to the middle of the model when the water pressure is first applied, and a very small number of particles immediately enter the fracture, meanwhile, the movement of particles at the corner of the wall will produce a phenomenon similar to vortex flow (Figure 8). As the numerical simulation calculation continues to advance, the particles gradually enter the fracture, the fluid viscosity keeps decreasing, the flow direction of the particles will change, the vortex flow phenomenon disappears, the particles at the corner of the wall flow toward the fracture, and the rest of the particles flow along the vertical direction (Figure 9). In addition, the outflow of particles, at the position $x = 0$ at the bottom of the model, is found to rise as a whole, which is the result of activating the buoyancy factor command during the simulation and setting the density of the fluid to be comparable to the density of the particles. Using the PFC3D program, com-

pared in the FISH language, the volume of flowing particles in the fracture was recorded in real time at different pressure, and the results of the numerical simulation are shown in Figure 10.

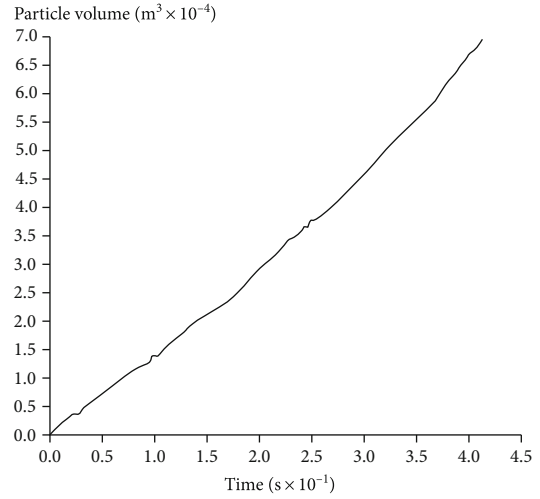
According to Figure 11, it can be found that the seepage flow of particles under different water pressure all increase with time, such as model size $100 \times 100 \times 300$ mm; with the increase of pressure gradient, the percolation volume of particles after 0.45 s are $4.4 \times 10^{-4} \text{ m}^3$, $6.9 \times 10^{-4} \text{ m}^3$, $9.2 \times 10^{-4} \text{ m}^3$, and $1.2 \times 10^{-3} \text{ m}^3$, and its adjacent two pressure gradient the percolation volume of particles under the difference increased by 56%, 33%, and 30%, respectively, with the model size of $100 \times 100 \times 250$ mm; and the percolation volume of particles after 0.35 s was $4.7 \times 10^{-4} \text{ m}^3$, $6.9 \times 10^{-4} \text{ m}^3$, $8.5 \times 10^{-4} \text{ m}^3$, and $1.4 \times 10^{-3} \text{ m}^3$ with the increase of pressure gradient, and the percolation volume of particles under the difference of its two adjacent pressure gradients were increased by 47%, 23%, 64%, and the model size of $100 \times 100 \times 200$ mm; with the increase of pressure gradient, the percolation volume of particles after 0.25 s was $3.7 \times 10^{-4} \text{ m}^3$, $6.9 \times 10^{-4} \text{ m}^3$, $9.2 \times 10^{-4} \text{ m}^3$, and $1.3 \times 10^{-3} \text{ m}^3$, and the percolation volume of particles under the difference of its two adjacent pressure gradients increased by 86%, 33%, and 42%. In addition, the model size and running time will increase the seepage volume of particles; in the case of the model size is large enough and the running time is relatively short, the seepage volume of particles increases and decreases with the increase of pressure gradient, which is due to the fact that when the particles enter the fracture, the width of the fracture remains the same, and the increase of the number of particles will make the crowding and friction between the particles and the friction between the particles and the wall, causing a certain degree of fracture. In the case of small model size and long running time, most of the particles enter the fracture in that running time, and the increase of seepage volume of particles will decrease first and then increase with the increase of pressure gradient, which indicates that the blocked particles in the fracture decrease, the porosity of the model increases, and the mobility of particles is enhanced, so the faster the speed of entering the fracture, the greater the increase of seepage volume of particles.

Job Title: Fixed Coarse-Grid Fluid Scheme: PFC3D
View Title: Making Assembly



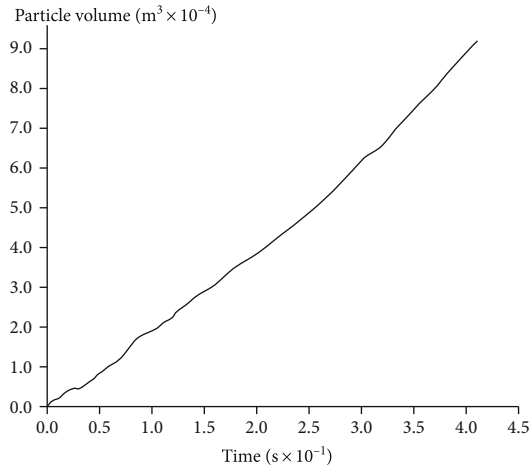
(a)

Job Title: Fixed Coarse-Grid Fluid Scheme: PFC3D
View Title: Making Assembly



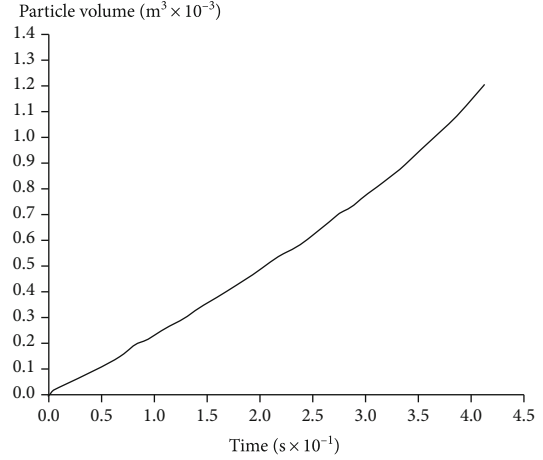
(b)

Job Title: Fixed Coarse-Grid Fluid Scheme: PFC3D
View Title: Making Assembly



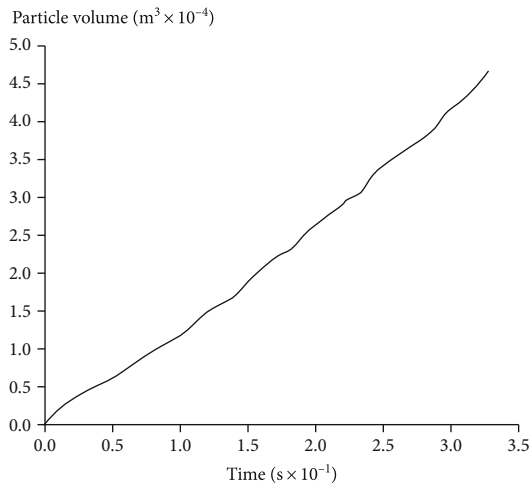
(c)

Job Title: Fixed Coarse-Grid fluid Scheme: PFC3D
View Title: Making Assembly



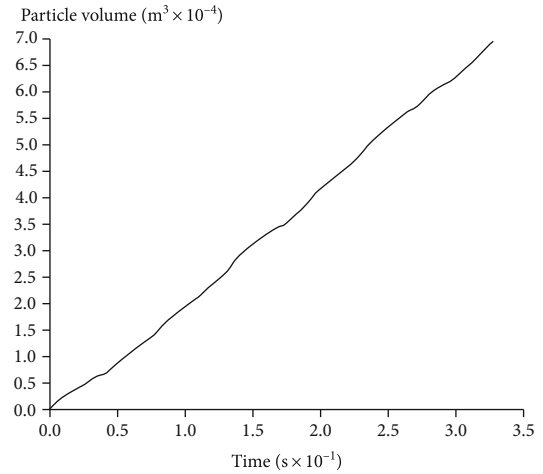
(d)

Job Title: Fixed Coarse-Grid Fluid Scheme: PFC3D
View Title: Making Assembly



(e)

Job Title: Fixed Coarse-Grid Fluid Scheme: PFC3D
View Title: Making Assembly



(f)

FIGURE 11: Continued.

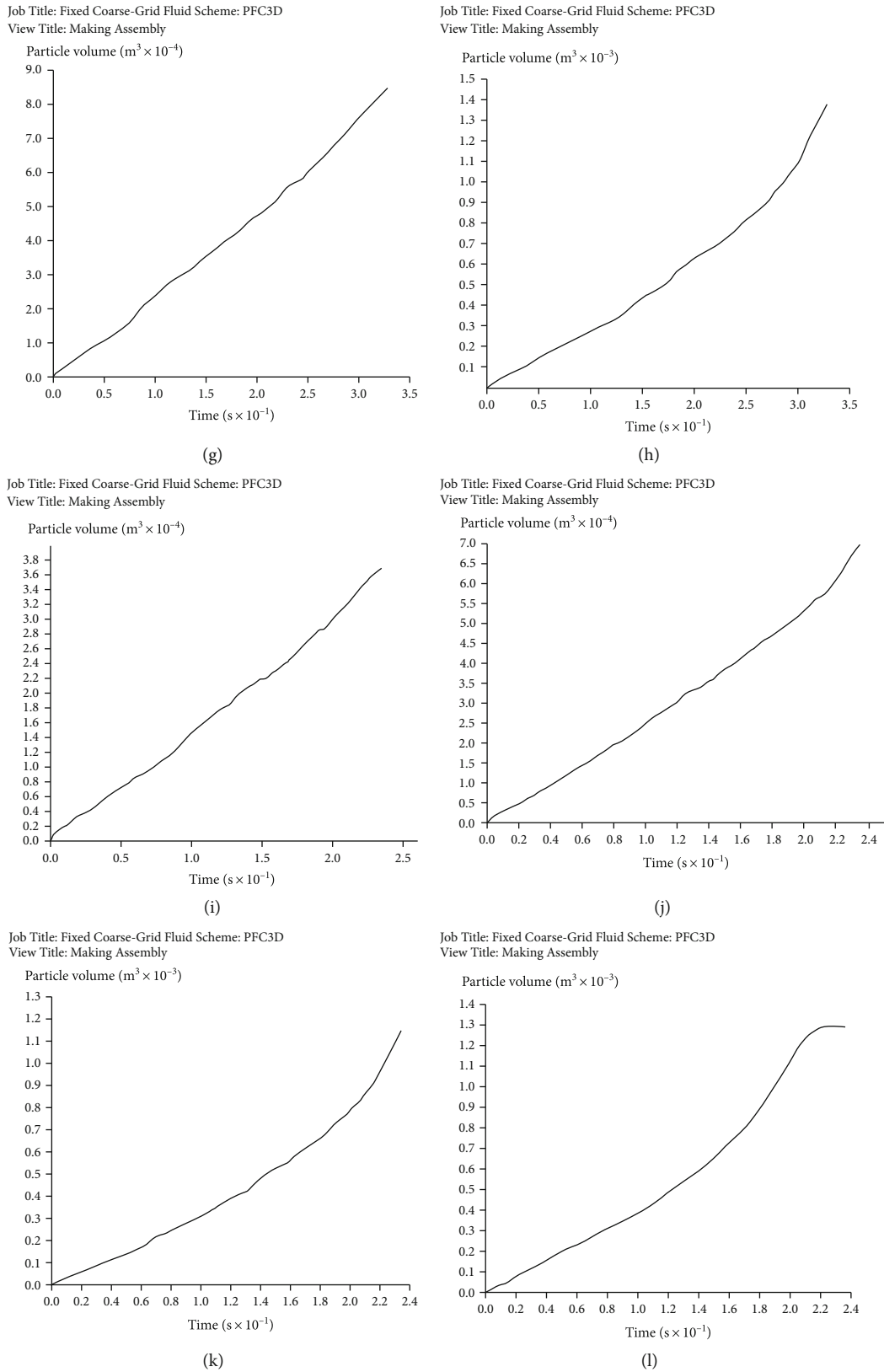
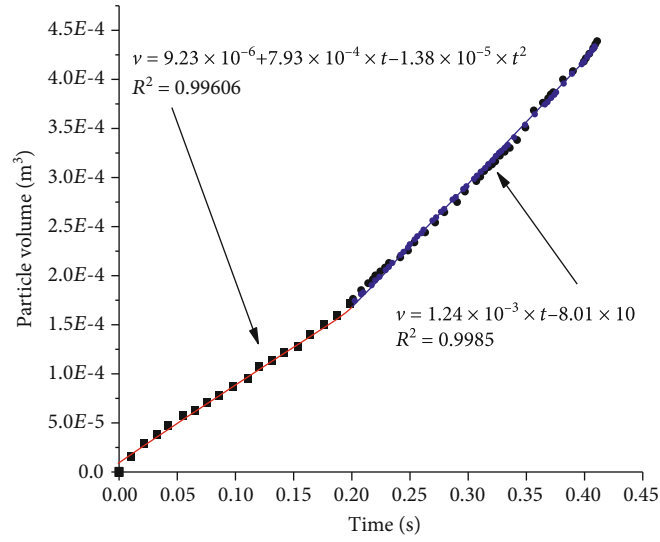
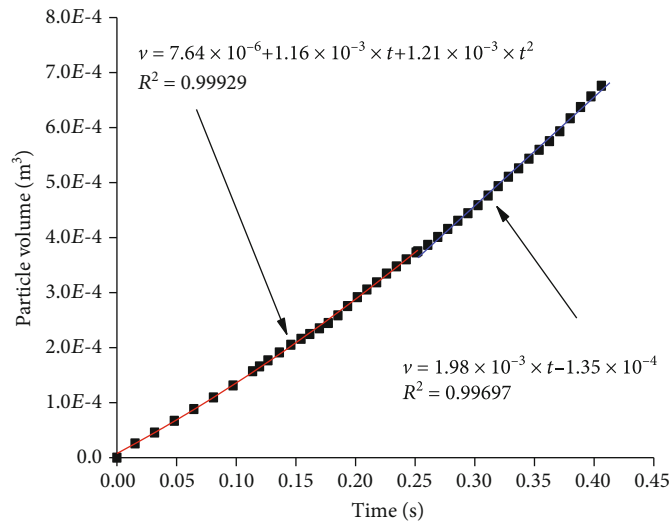


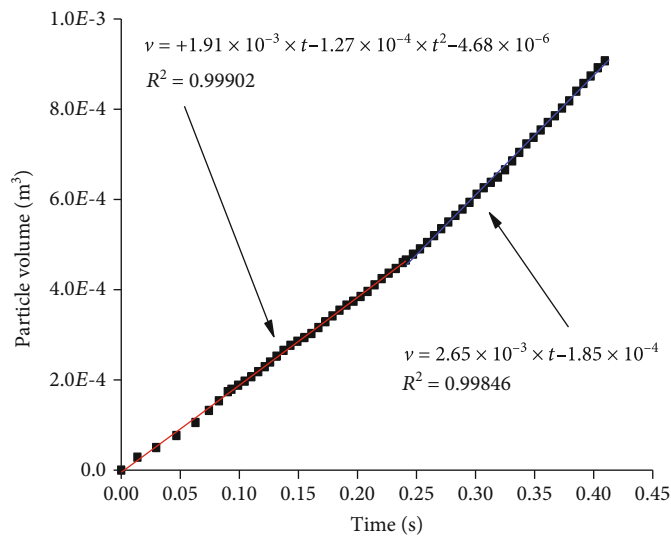
FIGURE 11: The relationship curve between seepage flow of particles and time under different water pressures for particle size of $100 \times 100 \times 300$ mm at (a) $P = 0.5$ MPa, (b) $P = 0.8$ MPa, (c) $P = 1.0$ MPa, and (d) $P = 1.2$ MPa; and particle size of $100 \times 100 \times 250$ mm at (e) $P = 0.5$ MPa, (f) $P = 0.8$ MPa, (g) $P = 1.0$ MPa, and (h) $P = 1.2$ MPa; and particle size of $100 \times 100 \times 200$ mm at (i) $P = 0.5$ MPa, (j) $P = 0.8$ MPa, (k) $P = 1.0$ MPa, and (l) $P = 1.2$ MPa.



(a)

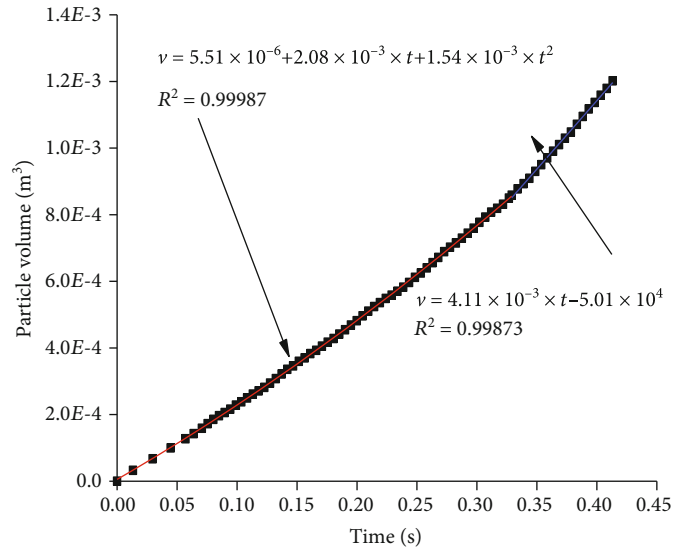


(b)

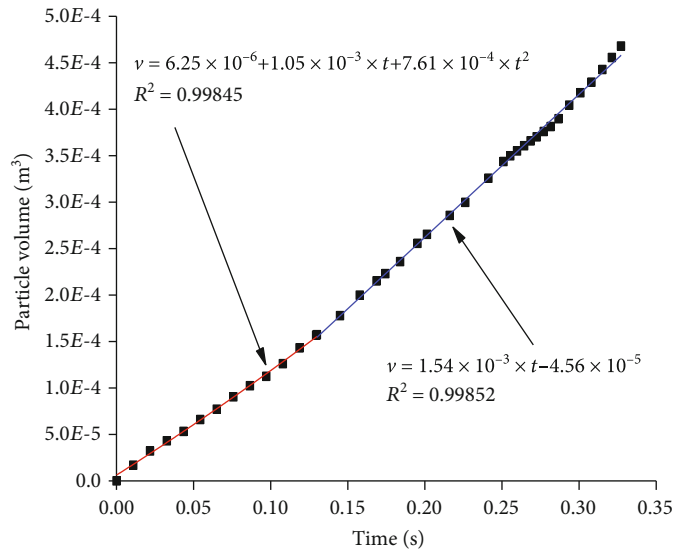


(c)

FIGURE 12: Continued.

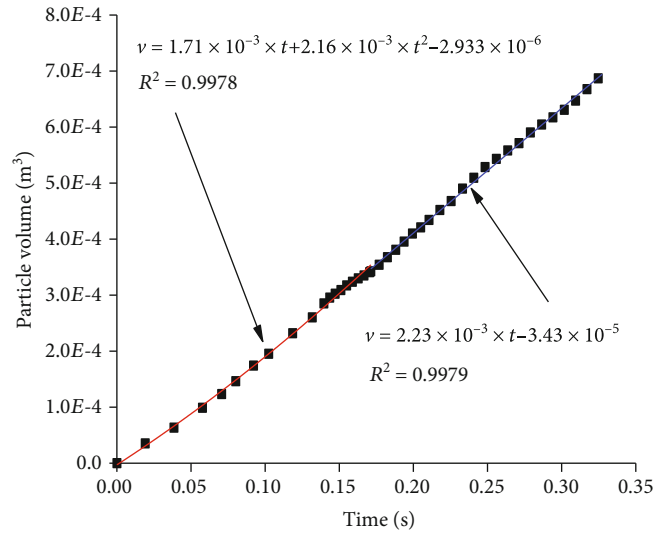


(d)

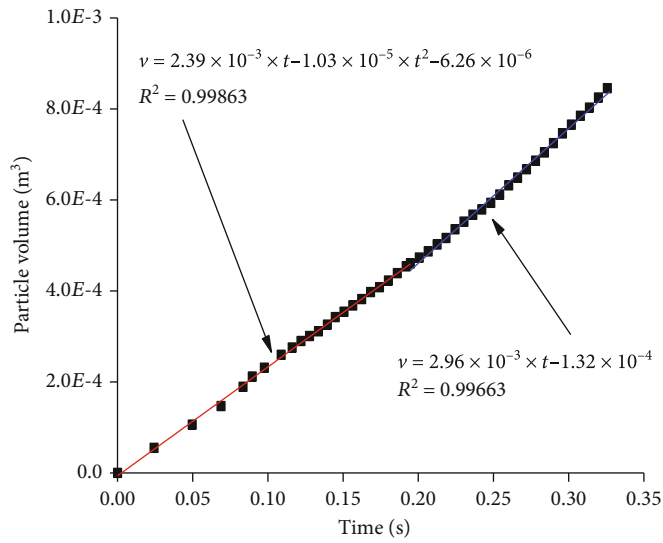


(e)

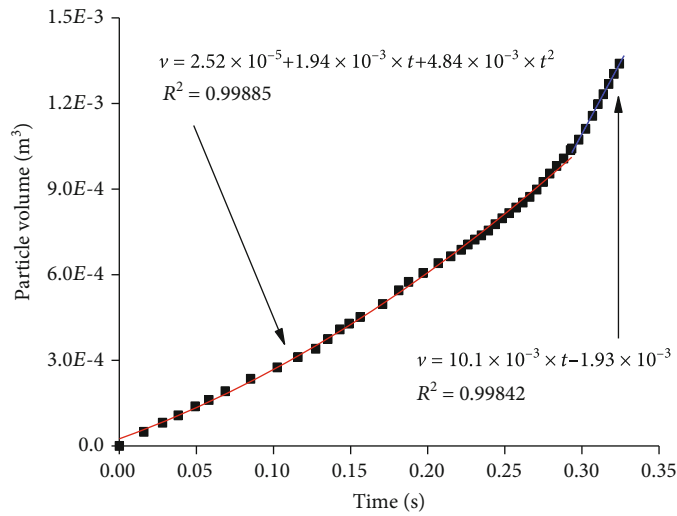
FIGURE 12: Continued.



(f)

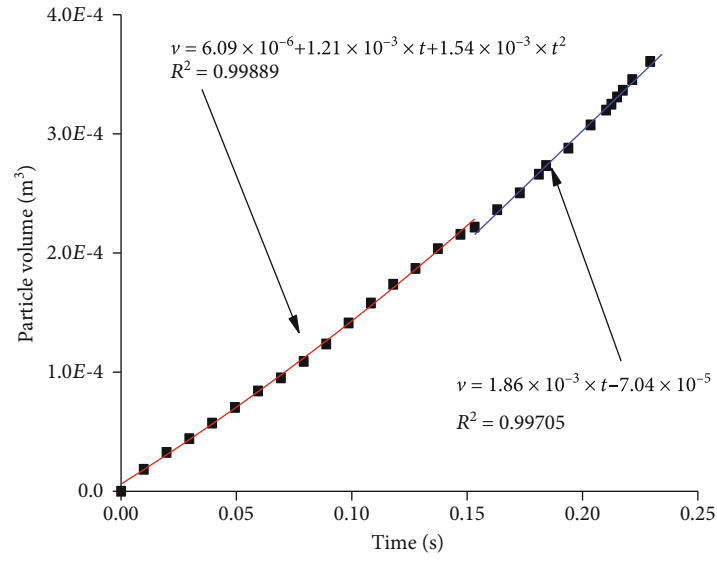


(g)

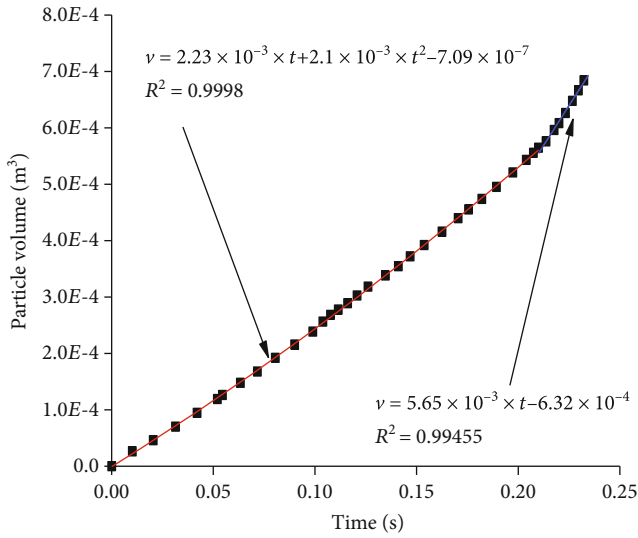


(h)

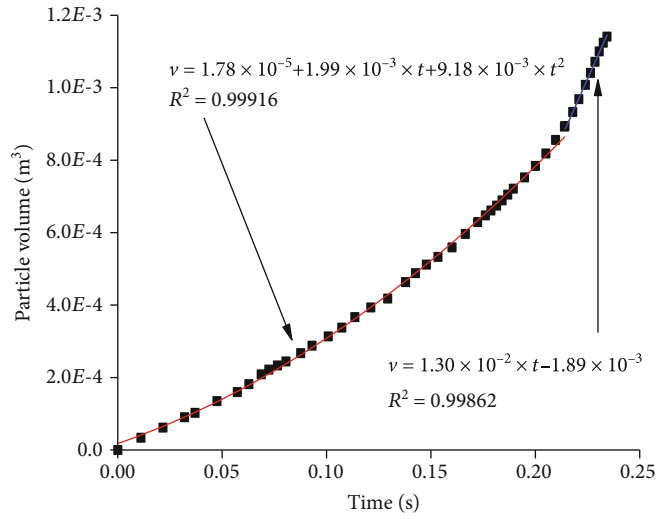
FIGURE 12: Continued.



(i)



(j)



(k)

FIGURE 12: Continued.

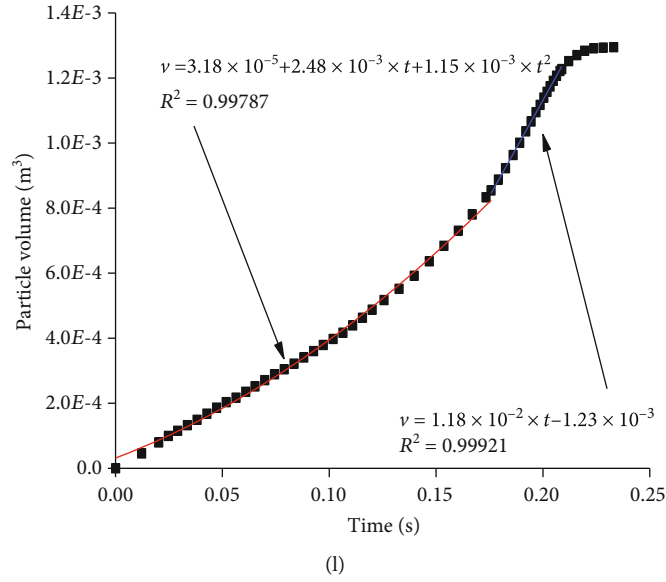


FIGURE 12: Simulated fitting curves for particle size is $100 \times 100 \times 300$ mm (a) $P = 0.5$ MPa, (b) $P = 0.8$ MPa, (c) $P = 1.0$ MPa, and (d) $P = 1.2$ MPa; and particle size is $100 \times 100 \times 250$ mm (e) $P = 0.5$ MPa, (f) $P = 0.8$ MPa, (g) $P = 1.0$ MPa, and (h) $P = 1.2$ MPa; and particle size is $100 \times 100 \times 200$ mm (i) $P = 0.5$ MPa, (j) $P = 0.8$ MPa, (k) $P = 1.0$ MPa, and (l) $P = 1.2$ MPa.

3.4.2. Analysis of Particle Seepage Rate. The particle percolation problem in the fracture is not really a water percolation problem in the fracture, and water is a continuous medium flowing in the fracture that almost satisfies Darcy’s law, while the motion of particles is approximately regarded as the motion between small balls, which collide with each other and there is friction; in addition to the characteristics of the flow, the small ball itself also has the nature of rotation. Therefore, the most fundamental difference between water and particle flow in a single fracture is that water is a continuum and particle is a discrete body, by compiling the FISH language program and using the Hist command to record the amount of particle percolation in the fracture at different running times, and using Origin software for fitting, the fitting results are shown in Figure 12.

Figure 12 shows that in the initial stage, the particle flow rate increases with the increase of running time, and the slope of the curve increases; consider fitting with a quadratic function, the fitting correlation coefficient R^2 is above 0.92, and the slope of the curve remains unchanged after the percolation rate of particles reaches stability; consider fitting with a primary function, the fitting coefficient R^2 is mostly above 0.90; and when the running time is long enough, the model after all the particles in the model are seeped out by the fracture, the particle flow rate is kept constant, and the slope is 0, as shown in Figure 12(l).

To analyze the relationship between pressure gradient and seepage velocity, the slope of the primary function (seepage velocity) was fitted for each model with different pressure gradients, and Figure 13 shows the fitted curves of pressure gradient and particle speed.

Figure 13 shows that the flow velocity is not exactly proportional to the pressure gradient (data points), and it does not conform to Darcy’s law. There are various reasons for

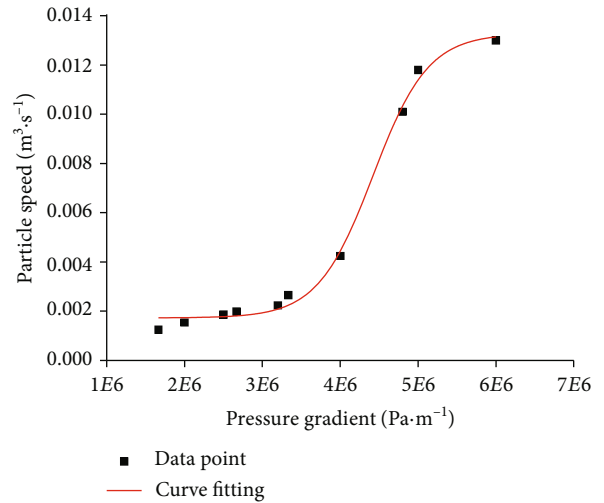


FIGURE 13: The relationship between pressure gradient and the particle speed.

this, such as changes in fluid viscosity, changes in model porosity, and collisions between particles and between particles and fracture walls or even the clogging effect of particles on fractures. When the pressure gradient is small, the flow velocity increases slowly with the increase of pressure gradient, after the pressure gradient exceeds a certain value, the flow velocity increases rapidly with the increase of gradient, and finally the region increases slowly, and the whole shows an “S” curve of growth. By further fitting the data (see the red curve in Figure 13), the pressure gradient and flow velocity approximately satisfy an exponential function relationship, and the fitted correlation coefficient R^2 equal to 0.9312, and the fitting formula is as follows:

$$v = 1.328 \times 10^{-2} - \frac{1.156 \times 10^{-2}}{1 + \exp(\Delta p - 4.42 \times 10^6 / 3.54 \times 10^5)}. \quad (27)$$

4. Conclusion

- (1) When the water pressure is first applied, the flow direction of the particles will show different, a small number of particles immediately into the fracture, the vast majority of particles are flowing toward the middle of the model, the movement of particles at the corners of the wall occurs similar to the phenomenon of vortex, with the increase in running time, the vortex phenomenon disappears, the flow direction of the particles at the corners point to the fracture, the rest of the particles flow along the vertical direction
- (2) In the initial stage, the flow rate of particles increases with time, the slope of the curve increases, and the quadratic function is used for fitting. After the percolation rate of particles reaches stability, the slope of the curve remains the same, and the primary function is used for fitting
- (3) In the beginning stage, the particle flow velocity increases with the increase of the pressure gradient. In addition, the particle flow rate and pressure gradient are influenced by many factors, such as the change of fluid viscosity, the change of model porosity, and the collision between particles, particles and fracture wall, so that they approximately satisfy an exponential function of "S" curve

Data Availability

All data and models generated or used during the study appear in the submitted article.

Conflicts of Interest

The authors declare that they have no conflicts of interest.

Acknowledgments

This research is supported by the National Natural Science Foundation of China (Nos. 51774131 and 51274097). The authors are thankful for all of the support for this basic research.

References

- [1] R. Q. Huang, X. N. Wang, and L. S. Chen, "Analysis of hydraulic fracturing in the process of water gushing in a deep tunnel," *Chinese Journal of Rock Mechanics and Engineering*, vol. 19, no. 5, pp. 573–576, 2000.
- [2] W. J. Wang, Y. L. Zhao, Q. F. Li, and W. Q. Peng, "Catastrophe mechanism of mine karst water inrush," *Journal of China Coal Society*, vol. 35, no. 3, pp. 443–448, 2010.
- [3] Y. X. Wang, H. Zhang, H. Lin, Y. L. Zhao, X. Li, and Y. Liu, "Mechanical behavior and failure analysis of fracture-filled gneissic granite," *Theoretical and Applied Fracture Mechanics*, vol. 108, article 102674, 2020.
- [4] C. Y. Zhang, C. Z. Pu, R. H. Cao, T. T. Jiang, and G. Huang, "The stability and roof-support optimization of roadways passing through unfavorable geological bodies using advanced detection and monitoring methods, among others, in the Sanmenxia Bauxite Mine in China's Henan Province," *Bulletin of Engineering Geology and the Environment*, vol. 78, no. 7, pp. 5087–5099, 2019.
- [5] Itasca Consulting Group, *Verification Problems and Example Applications*, Itasca Consulting Group, Minneapolis, USA, 2005.
- [6] P. A. Cundall and O. D. L. Strack, "A discrete numerical model for granular assemblies," *Geotechnique*, vol. 29, no. 1, pp. 47–65, 1979.
- [7] C. Shi, S. N. Wang, and L. Liu, "Numerical simulation of discrete element method for steep rock collapse under earthquake," *Chinese Journal of Rock Mechanics and Engineering*, vol. 32, no. S1, pp. 2798–2805, 2013.
- [8] U. Castro-Filgueira, L. R. Alejano, J. Arzúa, and D. M. Ivars, "Sensitivity analysis of the micro-parameters used in a PFC analysis towards the mechanical properties of rocks," *Procedia Engineering*, vol. 191, pp. 488–495, 2017.
- [9] C. O'Sullivan, "Particle-based discrete element modeling: geomechanics perspective," *International Journal of Geomechanics*, vol. 11, no. 6, pp. 449–464, 2011.
- [10] S. Q. Yang, Y. H. Huang, H. W. Jing, and X. R. Liu, "Discrete element modeling on fracture coalescence behavior of red sandstone containing two unparallel fractures under uniaxial compression," *Engineering Geology*, vol. 178, pp. 28–48, 2014.
- [11] X. Fan and P. Cao, "Numerical analysis of mechanical behavior of rock sample with two flaws under uniaxial compressive loading based on PFC-(3D)," *Journal of Central South University*, vol. 46, pp. 2635–2642, 2015.
- [12] J. Liu, J. Wang, and W. Wan, "Numerical study of crack propagation in an indented rock specimen," *Computers and Geotechnics*, vol. 96, pp. 1–11, 2018.
- [13] D. O. Potyondy and P. A. Cundall, "A bonded-particle model for rock," *International Journal of Rock Mechanics and Mining Sciences*, vol. 41, no. 8, pp. 1329–1364, 2004.
- [14] H. H. Zhu and Q. W. Xu, "Model test and analysis of loosening failure of surrounding rock of tunnel with weak interlayer," *Chinese Journal of Rock Mechanics and Engineering*, no. s1, pp. 2915–2924, 2016.
- [15] G. Zhang, *Model Test and Particle Flow Numerical Simulation Study on the Meso-Mechanism of Piping Phenomenon*, vol. 35, Tongji University, 2007.
- [16] W. Zeng, S. Q. Yang, W. L. Tian, and K. Wen, "Numerical investigation on permeability evolution behavior of rock by an improved flow-coupling algorithm in particle flow code," *Journal of Central South University*, vol. 25, no. 6, pp. 1367–1385, 2018.
- [17] Q. Wu, C. M. Wang, P. R. Song, H. B. Zhu, and D. H. Ma, "Rainfall scour test on loess steep slope and its three-dimensional particle flow fluid-solid coupling simulation," *Rock and Soil Mechanics*, vol. 35, no. 4, pp. 977–985, 2014.
- [18] J. Zhou, G. Zhang, and G. Kong, "Particle flow meso-level simulation of seepage flow," *Journal of Hydraulic Engineering*, vol. 37, no. 1, pp. 28–32, 2006.
- [19] J. Zhou, Z. X. Yao, and G. Zhang, "Research on piping mechanism of sand based on the theory of bulk medium," *Chinese*

- Journal of Rock Mechanics and Engineering*, vol. 27, no. 4, pp. 749–756, 2008.
- [20] Y. Luo, X. N. Gong, and R. Q. Wu, “Particle flow simulation and fluid-particle interaction analysis,” *Journal of Zhejiang University*, vol. 41, no. 11, pp. 1932–1936, 2007.
- [21] R. X. Bai, *Research on Inrush Failure Mechanism and Particle Flow Numerical Simulation of Foundation Pit Based on Groundwater Splitting PhD*, Tianjin University, 2012.
- [22] Y. Wang, Y. G. Lu, X. D. Ni, and D. T. Li, “Study on the mechanism of water and mud inrush during the construction of deep tunnels,” *Journal of Hydraulic Engineering*, vol. 42, no. 5, pp. 595–601, 2011.
- [23] J. Bear, *Dynamics of fluids in porous media*, New York: Elsevier, 1972.
- [24] G. Mavko and A. Nur, “The effect of a percolation threshold in the Kozeny-Carman relation,” *Geophysics*, vol. 62, no. 5, pp. 1480–1482, 1997.
- [25] S. Ergun, “Fluid flow through packed columns,” *Journal of Materials Science and Chemical Engineering*, vol. 48, no. 2, pp. 89–94, 1952.

Research Article

The Elastoplastic Solutions of Deep Buried Roadway Based on the Generalized 3D Hoek-Brown Strength Criterion considering Strain-Softening Properties

Rui Wang^{1,2}, Jian-biao Bai^{1,3}, Shuai Yan^{1,2}, Zhi-guo Chang³, Yuan-ba Song⁴, Wei-guang Zhang^{1,3} and Jun Xu⁵

¹State Key Laboratory of Coal Resources and Safe Mining, School of Mines, China University of Mining and Technology, Xuzhou, Jiangsu 221116, China

²Key Laboratory of Deep Coal Resource Mining, Ministry of Education of China, School of Mines, China University of Mining and Technology, Xuzhou, Jiangsu 221116, China

³Institute of Mining Engineering and Geology, Xinjiang Institute of Engineering, Urumqi 830091, China

⁴Rizhao Natural Resources and Planning Bureau, Shandong, Rizhao 276800, China

⁵School of Science, Yangzhou Polytechnic Institute, Yangzhou 225127, China

Correspondence should be addressed to Jian-biao Bai; bjianbiao@cumt.edu.cn and Shuai Yan; yanshuai@cumt.edu.cn

Received 24 February 2021; Revised 14 March 2021; Accepted 17 March 2021; Published 7 April 2021

Academic Editor: Yu Wang

Copyright © 2021 Rui Wang et al. This is an open access article distributed under the Creative Commons Attribution License, which permits unrestricted use, distribution, and reproduction in any medium, provided the original work is properly cited.

The deep underground roadways are widely used in the mining industries at present, but the relevant theoretical bases are not fully understood. In this paper, the numerical solutions for strain-softening surrounding rock under the generalized three-dimensional (3D) Hoek-Brown (GZZ) strength criterion are developed incorporating the confinement-dependent characteristics of ψ and η^* and their influences on the stress and displacement of equivalent circular roadway. On the basis of a finite difference method for the strain-softening model is proposed to consider the variation of ψ and η^* in analyzing the strain-softening behavior of rock masses. Combining the equilibrium equation and strength criterion, the stress conditions for each annulus are calculated analytically. The displacement for each step is obtained analytically by solving the differential equation through invoking flow rule and Hooke's law. The accuracy of the proposed method is verified through the comparison between the results and the previous studies. The effect of intermediate principal stress of GZZ strength criterion is considered; the rationality of the proposed method is verified by two aspects. First, by comparing with the two-dimensional narrow and generalized H-B strength criterion, the advantage of GZZ strength criterion that considers the effect of intermediate main stress is highlighted. On the other hand, compared with the three-dimensional linear D-P criterion, the advantage of GZZ strength criterion in the theoretical research of deep underground roadway in coal mine is highlighted. The results show that the strain-softening of the surrounding rock in the plastic zone of the roadway can reduce the pressure of the surrounding rock, but it will greatly increase its deformation. In the high field stress areas, the strain-softening of surrounding rock is the key reason for the destruction of the roadway. It is suggested that in the design and calculation of the support system of the roadway, the strain-softening characteristics of the surrounding rock should be considered, which is very important to avoid large deformation and damage of roadway.

1. Introduction

The deformation of rock mass is related to geological conditions, in situ stress, support technologies, and excavation disturbance. The prediction of rock mass deformation behavior is very useful for deep coal mining [1]. At great

depth with strong deep structural activity or high deformability, rock squeezing may occur, and the repair rate of large deformed roadways can reach 70% [2, 3]. In the deep coal mining, due to the influences of “three high and one disturbance” (high geo-stress, high ground temperature, high permeable pressure, and the disturbance of mining activities),

the unique stress characteristic and plastic yielding were engendered by the mechanics of roadway [4–6].

For deep underground engineering, the elasto-plastic [7–10], elasto-brittle-plastic [11–13], and strain-softening models [14–16] were established to finish off the issue of tunnel based on elasto-plastic approaches [17–19] in the past period. For the first two methods mentioned above, analytical solutions are available accounting to a simple point of view. However, experimental and field observation show that the deformation and failure mechanism of rock mass in the postpeak stage of rock was revealed by the strain-softening model [19–24]. Hence, lots of scholars have studied the strain-softening model in detail, especially for Brown et al. [17], Carranza-Torres [18], Alonso [7], and Lee and Pietruszczak [25]. There are two pivotal parameters, which are the critical softening parameter η^* and the dilatancy angle ψ , to research the features of strain-softening of deep underground engineering. It is worth noting that the confining stress acts on the above two parameters according to the existing findings [7, 8, 20, 26, 27]. In addition, the dilatancy angle was only deemed to a constant to research the features of strain-softening [7, 8, 25, 26]. Nevertheless, the variation of the critical softening parameter η^* and the dilatancy angle ψ should be seemed reasonable [20, 27, 28].

The above scholars mainly study the related problems of circular tunnel, but for deep underground engineering, there are similar problems in roadway in coal mine. Above all, five kinds of cross-section shape of roadway are commonly used in mining design, including rectangular, straight wall arch, trapezoidal, round, and oval [29]. The straight-wall semicircular arch roadway is widely used as the cross-section shape of underground roadway in coal mine because of its fast forming and high stability [30]. The impact of straight wall arch roadway on the surrounding rock was equal to the outer round with the same diameter of the circular roadway section [31]. In conclusion, for the convenience of analysis and calculation, the typical arched cross-section shape of the coal mine roadway with straight wall is equivalent to the outer circular cross-section roadway with the same diameter for the following specific analysis (as shown in Figure 1).

What is more, the elasto-plastic, elasto-brittle-plastic, and strain-softening models have been built based on Mohr-Coulomb (M-C) and Hoek-Brown (H-B) criteria [6–25, 32–36]. The Mohr-Coulomb criterion is linear which is relatively convenient to use, but the criterion does not reflect the nonlinear destruction characteristics of rock bodies. Since the Hoek-Brown strength criterion has been widely used in rock engineering, its prediction of rock behavior is sufficient and can be easily applied to a series of rock engineering problems. However, although many evidences show that in many cases, the intermediate principal stress does affect the strength of the rock, the H-B strength standard does not consider the influence of the intermediate principal stress. In order to overcome this shortcoming, the criterion proposed by Zhu [37] and Zhang [38] can predict the same strength as the original H-B strength criterion under triaxial compression and extension and is regarded as a true 3D version of the original H-B strength criterion. 3D Hoek-Brown strength criterion (GZZ strength criterion) was the strength

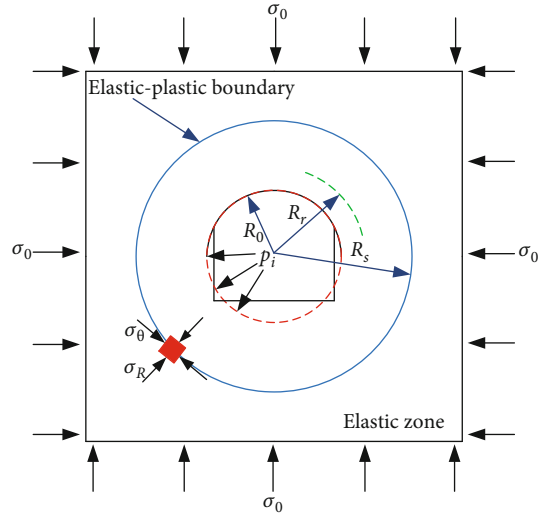


FIGURE 1: Plastic zone formed around equivalent circular roadway.

criterion suggested by International Society for Rock Mechanics (ISRM). Therefore, the GZZ strength criterion can be used as a failure criterion for constructing rock quality constitutive models and can be implemented in 3D finite element (FE) codes to perform 3D numerical analysis of rock engineering problems. The main objective of this study is to compare results considering the effect of a variable η^* and ψ on the strain-softening behavior of rock masses in equivalent circular roadways to select the correct combinative models under the GZZ strength criterion.

2. Description of Problem

For the convenience of analysis and calculation, the typical arched cross-section shape of the coal mine roadway with straight wall is equivalent to the outer circular cross-section roadway with the same diameter for the following specific analysis.

Based on the above analysis of roadway, for the sake of further study on the properties of surrounding rock stress, the following assumptions are required:

- (1) The roadway is equivalent circular
- (2) The rock mass is characterised as isotropic, continuous, infinite, and initially elastic, and its mechanical properties obey the GZZ strength criterion

As shown in Figure 2, the excavation radius of the equivalent circular roadway is R_0 . Here, the hydrostatic stress field σ_0 is applied to the whole area before excavation. At the areas where the magnitude of the internal support strength p_i is no larger than the critical value p_c , a plastic zone is assumed to be formed around the equivalent circular roadway. When $p_i < p_c^{**}$, p_c^{**} is deemed to the pivotal support pressures; the equivalent circular roadway was got into the plastic softening zone. When $p_i < p_c^*$, p_c^* is deemed to the pivotal support pressures, the equivalent circular roadway was got into the plastic residual zone. In the case of elastic-plastic behavior,

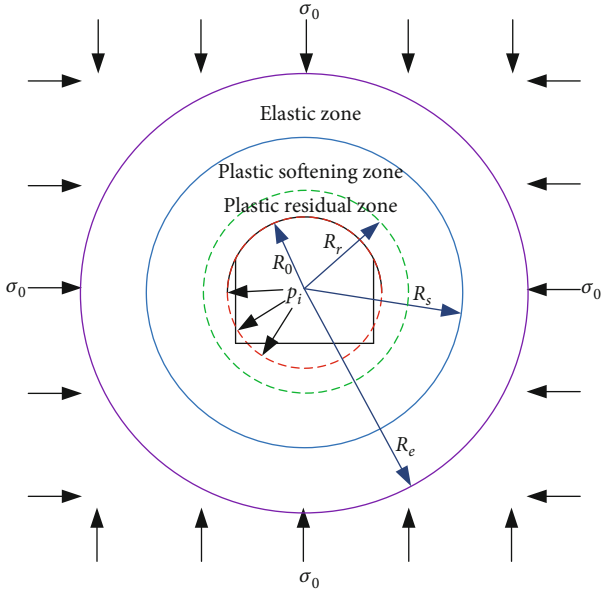


FIGURE 2: Partition diagram of an equivalent circular roadway after excavation.

the explicit expression of plastic radius R_p can be derived [9, 11]. Additionally, when consider the strain-softening behavior, the plastic zone can be separated by softening and residual zones through the application of an interface with radius R_s (as displayed in Figure 2). At the boundary of the elasto-plastic zones, $\sigma_{\theta p}$ and σ_{rp} are the tangential stress and the radial stress, respectively. Additionally, at the boundary of the softening residual zones, $\sigma_{\theta s}$ and σ_{rs} are the tangential and the radial stress. According to the stress equilibrium at the boundary of the elasto-plastic and the softening-residual zones, p_c^{**} and p_c^* are equal to σ_{rp} and σ_{rs} , while the R_p and R_s are the radii of plastic and plastic residual zone.

2.1. GZZ Strength Criterion. The standard Hoek Brown strength criterion can be used to calculate the three-dimensional stress state [33]. But the effects of intermediate principal stress is not considered in the initial form, which does influence the rock strength [39, 40]. Therefore, it is believed that the 3D Hoek-Brown strength criterion is more suitable for describing yield state of rock mass under 3D stress states. As is shown in Figure 3, the 3D Hoek-Brown strength criterion is established by Zhang and Zhu [37]. It is also the strength criterion suggested by International Society for Rock Mechanics (ISRM) and can be expressed as follows.

$$\frac{9}{2\sigma_c} \tau_{oct}^2 + \frac{3}{2\sqrt{2}} m_b \tau_{oct} - m_b \sigma_m = s \sigma_c. \quad (1)$$

In Equation (1), m_b , a , and s are all empirical parameters reflecting rock mass characteristics. a is rock mass characteristic parameter. m_b is the empirical parameter of the rock, which can be determined by experiment or rock types. s reflects the degree of rock fragmentation. σ_c is the uniaxial compression strength. τ_{oct} is the octahedral shear stress, and

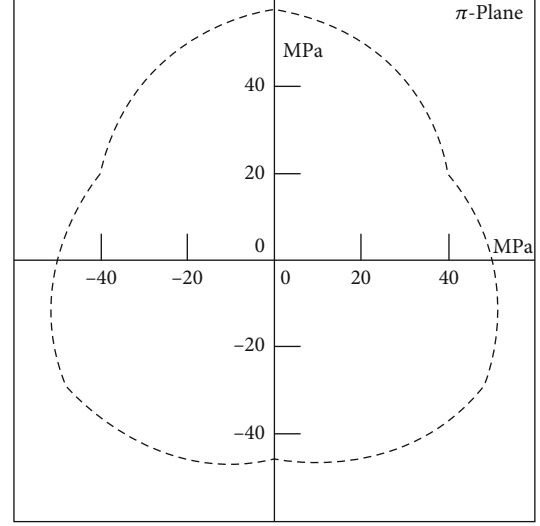


FIGURE 3: The yield surface of 3D strength criterion [37, 41].

σ_m is the average value of main stress. τ_{oct} and σ_m can be calculated by the Equations (2) and (3), respectively.

$$\tau_{oct} = \frac{1}{3} \sqrt{(\sigma_1 - \sigma_2)^2 + (\sigma_2 - \sigma_3)^2 + (\sigma_3 - \sigma_1)^2}, \quad (2)$$

$$\sigma_m = \frac{\sigma_1 + \sigma_2 + \sigma_3}{3}. \quad (3)$$

In Equations (2) and (3), σ_1 is the maximum principal stress, σ_2 is the intermediate principal stress, and σ_3 is the minimum principal stress. Where $\sigma_2 = [(1 + \sin \psi) \sigma_1 + (1 - \sin \psi) \sigma_3] / 2$, ψ is the dilatancy angle.

Where $m_b = m_i$ and $s = 1$ for intact rock, these quantities can be calculated by the geological strength index GSI and a factor D ,

$$m_b = \exp\left(\frac{GSI - 100}{28 - 14D}\right) m_i, \quad (4)$$

$$s = \exp\left(\frac{GSI - 100}{9 - 3D}\right),$$

where the value of D varies from 0 to 1. GSI is a factor that is related to the degree of disturbance caused by blast damage and stress relaxation, which varies between 10 and 100. m_i is determined by mechanical properties of rock mass. The values of m_i varies from 2 to 32, which is related to the compositions and mineralogical properties of rock mass.

2.2. Strain-Softening Behaviour. The strain softening is usually a transitional yield process or plastic potential, and its behaviour is dominated by a softening parameter η which can be described as follows:

$$\eta = \varepsilon_1^p - \varepsilon_3^p, \quad (5)$$

where ε_1^p and ε_3^p represent the major and minor principal

plastic strain, which are equal to the tangential ε_{θ}^p and radial strains ε_r^p . η is the plastic shear strain.

As displayed in Figure 4, the mechanical properties including the strength and deformation parameters is different when the deviatoric plastic strain change. This relationship can be described by a bilinear function with the application softening parameter η as follows:

$$\omega(\eta) = \begin{cases} \omega^p - (\omega^p - \omega^r) \frac{\eta}{\eta^*} (0 < \eta < \eta^*), \\ \omega^r (\eta \geq \eta^*), \end{cases} \quad (6)$$

where ω is one of the strength parameters and η^* represent the critical plastic softening parameter as shown in Figure 4. When η reaches critical plastic deviator strain, it begins to enter the residual state. Provided that the experiment data are available, the η^* may be assigned for each parameter. Here, for the purpose of the clarity, the single value η^* is assigned for each medium. The superscripts “p” and “r” represent the peak and residual strength. As displayed in Equation (6), at the stage of the plastic softening, the strength parameters has the negative linearly relationship with the η^* . Once the parameter increases to the value higher than the critical value η^* , the strength parameters remain stable.

The peak and residual values of m_b , s , and a can be obtained through the application of the geological strength index (GSI) [23]. The residual value of GSI is able to be obtained from the peak value of GSI [21, 22].

$$GSI^r = 17.25 \exp(0.0107GSI^p). \quad (7)$$

The nonassociated flow regulation is described as follows:

$$\Delta \varepsilon_r^p = -K_{\psi} \Delta \varepsilon_{\theta}^p, \quad (8)$$

where K_{ψ} is the dilatancy coefficient, $K_{\psi} = (1 + \sin \psi)/(1 - \sin \psi)$, and ψ is the angle of dilatancy, which are different with the change of the confining stress and mechanical properties of the rock [20].

2.3. Variable Path of σ_r . As described in the previous studies [7], the process of roadway excavation is simulated as the process of roof confining pressure decreasing gradually from σ_0 to p_i . Figure 5 shows the excavation stress path and yield criterion from the original hydrostatic stress to the state of the final support. Point A is defined as the state of the initial hydrostatic. At the stage of the excavation process, σ_r decreases gradually to the state of the elasto-plastic boundary (point B) where the confining stress σ_{rp} (referring to p^{**}) can be calculated by the elastic solution. Then, the status of the rock mass reaches the plastic softening area. During the process between point B and point C, since the strength parameters varies at the area of plastic softening, the GZZ function change with η ($0 < \eta < \eta^*$). Once the value of η reaches η^* , σ_r decreases to the values of σ_{rs} which refers to p^* . At this point, the state of the rock mass is transferred from the softening to the residual. During the process between point C and point D, the residual failure criterion can be employed with the

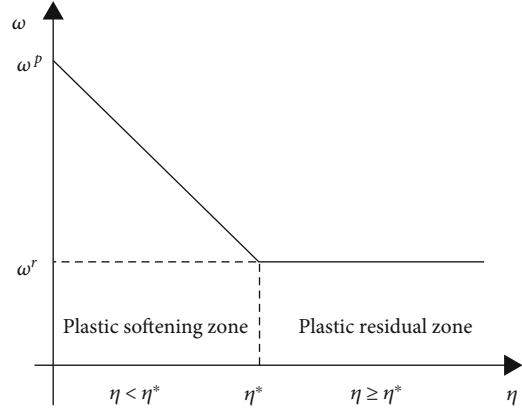


FIGURE 4: The relationship between strength parameters ω and η in plastic zone versus.

application of the parameter of residual strength ω^r . Then, if p_i is lower than the σ_{rs} , σ_r decreases from σ_{rs} at the boundary of the softening-residual to p_i on the surface of the excavation, which is imposed by the supporting systems. The results indicate with the application of the support systems, the σ_r decreases from σ_{rp} to p_i at the plastic zones.

For the soft rock masses after the excavation of the equivalent circular roadway, at the plastic zone, the values of the σ_r decrease from the boundary of the elasto-plastic to the of boundary excavation along the path of stress that displayed in Figure 5. The stress evolution in the equivalent circular roadway is different from that in the compression test. In the compression test, the confining pressure stress remains unchanged, while the axial stress increases until the occurrence of the failure. Therefore, if not conder the effects of the variable confining stress, the accuracy and practicability of the assumption that the critical plastic parameter η^* and dilatancy angle ψ remain unchanged should be taken with caution. Due to the variable property of σ_r in the plastic zone of strain softening behavior, the parameters related to the confining stress such as the η^* and ψ are also variable.

2.4. The Dilatancy Angle Model. The experimental results [26] show the angle of dilatancy angle is directly related to the failure of rock mass. Therefore, the dilatancy model is of great significance in the calculation of mine excavation displacement. In essence, in rock excavation engineering, in order to better reflect the mechanism evolution in the process of rock failure and study the potential dilatancy process in the process of rock plastic deformation, it is necessary to establish an appropriate dilatancy model.

Previous studies have described the dilatancy angle of rock mass is not constant, but decreases with the increase of confining pressure [42–45]. In addition, the dilatancy decreases gradually until it become constant at the residual strength during the failure process. If the plastic deformation is large enough, the dilatancy will gradually decrease to zero. The maximum values of the dilatancy angle appear near the peak strength at the elastoplastic boundary of plastic zone. Then, the angle of dilatancy decreases in the strain softening stage until it become stable at the residual strength.

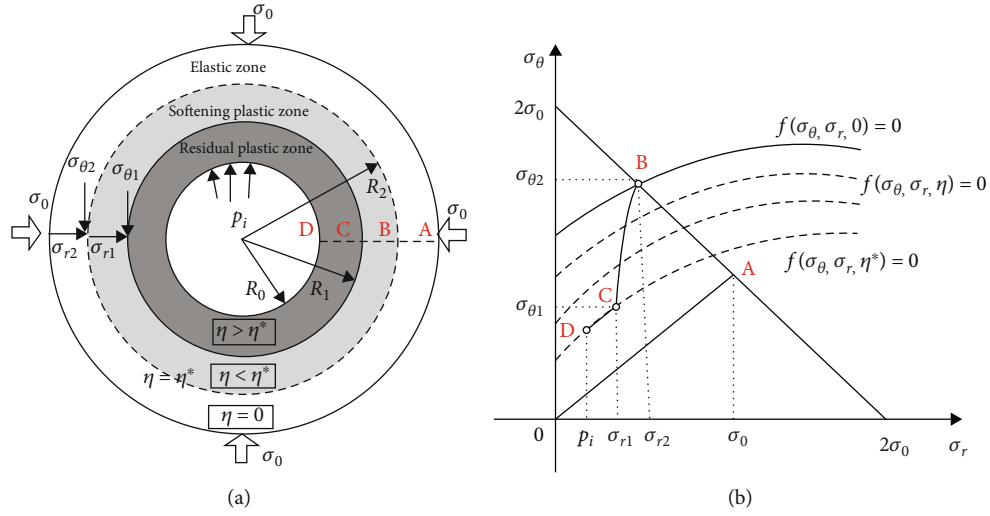


FIGURE 5: Variation path of the stress state modified [7].

In order to improve the understanding and calculation formula of rock dilatancy, many attempts have been made. Alejano and Alonso [20] described a feasible function of peak dilatancy angle of rock according to the equation of peak dilatancy angle of joint that obtained by Barton and Bandis [46]. The proposed function for the peak dilatancy angle of rock mass is described as follows:

$$\psi^p = \frac{\varphi^p}{1 + \lg \sigma_c} \lg \frac{\sigma_c}{\sigma_3 + 0.1}, \quad (9)$$

where ψ^p represents the angle of the peak dilatancy, φ^p represent the angle of the peak friction, and σ_3 represents the confining stress which refers to σ_r in underground roadways.

Based on the GZZ strength criterion, the peak friction angle variation with confining pressure can be obtained by using the derivative of peak failure criterion function to confining pressure [20]. In order to get the friction angle, the derivative of peak failure criterion function to confining pressure σ_3 can be described as follows:

$$K_{\varphi^p} = \frac{d\sigma_1}{d\sigma_3} = \frac{2\sqrt{2}s^p\sigma_c^2 - 9\sqrt{2}\tau_{oct}^2 - 3m_b^p\tau_{oct}\sigma_c}{\sqrt{2}m_b^p\sigma_c\sigma_3} - \frac{\sigma_2}{\sigma_3} - 1, \quad (10)$$

$$K_{\varphi^p} = \frac{1 + \sin \varphi^p}{1 - \sin \varphi^p}. \quad (11)$$

When combining Equations (10) and (11), the function of peak friction angle is obtained as follows:

$$\varphi^p = \arcsin \frac{Q-2}{Q}, \quad (12)$$

$$Q = \frac{2\sqrt{2}s^p\sigma_c^2 - 9\sqrt{2}\tau_{oct}^2 - 3m_b^p\tau_{oct}\sigma_c}{\sqrt{2}m_b^p\sigma_c\sigma_3} - \frac{\sigma_2}{\sigma_3}.$$

While incorporating Equation (12) into Equation (9), the function of peak dilatancy angle is reobtained as follows:

$$\psi^p = \frac{\arcsin ((Q-2)/Q)}{1 + \lg \sigma_c} \lg \frac{\sigma_c}{\sigma_3 + 0.1}. \quad (13)$$

From the equation, it can be seen that ψ^p is directly related to σ_3 as well as the mechanical properties of the rock.

In addition, based on the function of peak dilatancy angle as well as the results obtained by Detournay's [27], the coefficient of the decayed dilatancy is described as follows:

$$K_\psi = 1 + (K_\psi^p - 1)e^{-(\eta/\eta^*)}, \quad (14)$$

where K_ψ^p is the original dilatancy coefficient.

Equations (9)–(14) indicate that the dilatancy coefficient K_ψ changes with the change of η , η^* , and σ_3 , and the coefficient decays from the initial peak K_ψ^p , which also depends on σ_3 as well as the mechanical properties of the rock. Generally, the dilatancy model is nonlinear in the plastic region. Due to the complex dilatancy characteristics of rock mass, Hoek and Brown recommend that the dilatancy angles are $\phi/4$, $\phi/8$, and 0 are related to the rock mass with good quality, fair quality, and poor quality [19]. According to the recommendation, a more reasonable constant dilatancy model is proposed by Alejano et al. which can be applied to rock mass with different quality [8]. The equation is described as follows:

$$\psi = \frac{5GSI^p - 125}{1000}\varphi, \quad (15)$$

$$25 < GSI^p < 75.$$

where φ is the friction angle. GSI^p is the peak of GSI . Given the strength parameters of GZZ strength criterion, the optimal curve that is suitable for the GZZ strength criterion with

confining pressure from 0 to σ_{rp} can be carried out and thus obtained the value of φ [19, 23].

2.5. The Variable Critical Plastic Parameter. Through a large number of triaxial compression tests under different confining pressures, the deformation capacity of rock mass after failure is studied. Considering the strain softening characteristics, the strength parameters of rock mass are decreased (as shown in Figure 6). Figure 6 displays the geometry of the strain softening model with confining stress for the estimation of η^* , which can be calculated based on the equation described as follows:

$$\eta^* = \left(\frac{1}{E} + \frac{1}{M} \right) (\sigma_1^p - \sigma_1^r) \left(1 + \frac{K_\psi}{2} \right), \quad (16)$$

where E represent Young's modulus; M represent the drop modulus of the postpeak behaviour of rock mass; K_ψ is the coefficient of dilatancy.

Previous indoor and field test results show that the drop modulus M is directly related to the quality of rock mass quality [19, 22] as well as the confining pressure stress [24, 48]. Additionally, Alonso et al. [49] propose the function related to M as follows:

$$M = \begin{cases} E \left(0.0046 e^{0.00768 GSI^p} \right) \left(\frac{\sigma_3}{2\sqrt{s^p} \sigma_c} + 0.05 \right)^{-1}, \\ E \left(0.0046 e^{0.00768 GSI^p} \right) \left(\frac{\sigma_3}{\sqrt{s^p} \sigma_c} \right)^{-1}. \end{cases} \quad (17)$$

3. The Existing Model's Extension

3.1. Stress and Displacement Properties in the Elastic Zone. Based on the assumption of plane strain axial symmetry as well as the elastoplastic mechanics, the mechanical properties of the surrounding rock such as the stress-strain and displacement in elastic zone ($r \geq R_p$) is obtained using the function described as follows:

$$\begin{aligned} \sigma_r^e &= \sigma_0 - (\sigma_0 - \sigma_{rp}) \frac{R_p^2}{r^2}, \\ \sigma_\theta^e &= \sigma_0 + (\sigma_0 - \sigma_{rp}) \frac{R_p^2}{r^2}, \\ u^e &= \frac{1+\nu}{E} (\sigma_0 - \sigma_{rp}) \frac{R_p^2}{r^2}. \end{aligned} \quad (18)$$

In Equation (18), r is the distance between the calculated points and the median of the equivalent circular roadway. R_0 is the radius of the equivalent circular roadway, and σ_0 is the original rock stress. E and ν represent the Young's modulus and Poisson ratio, respectively.

3.2. Stress and Deformation Properties in the Plastic Zone. Based on the plane strain axial symmetry assumption for

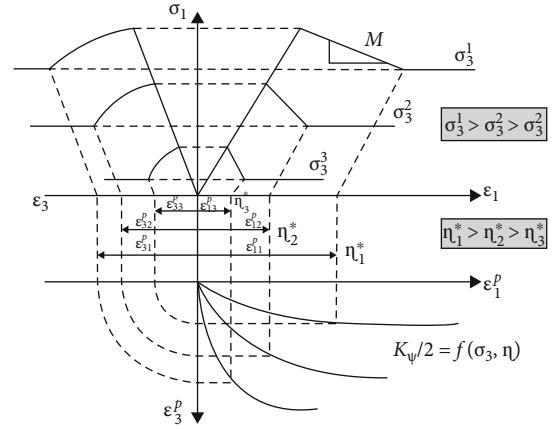


FIGURE 6: Geometrical diagram for estimating the value of η^* [8, 47].

the equivalent circular roadway, the equilibrium equation is described as follows:

$$\frac{d\sigma_r}{dr} + \frac{\sigma_r - \sigma_\theta}{r} = 0. \quad (19)$$

In Equation (19), σ_r and σ_θ represent radial and circumferential stress, respectively.

For the deep equivalent circular roadway, based on Hook's regulation, the tangential strain can be estimated by the stress conditions of the rock mass with the function provided as follows:

$$\begin{aligned} \frac{du_r}{dr} &= \varepsilon_r, \\ \frac{u_r}{r} &= \varepsilon_\theta. \end{aligned} \quad (20)$$

Since the variable strength parameters and the variables ψ and η^* caused by the change of σ_3 in the plastic softening area cannot be solved in closed form, especially for the rock mass that fails in the nonlinear failure patterns. Previous researchers use the methods of finite difference that is developed by Brown et al. [17] to identify the solution to the problem of strain softening in plastic zone [25, 50]. In the proposed method, the plastic zone is separated into a finite number of concentric rings, which is shown in Figure 7. In the process of the plastic deformation, the tangential strain ε_θ gradually increases while the radial strain increases in a nonflow manner with ψ . As shown in Figure 7, the plastic zone is separated into a finite number of the concentric rings as regards the radial stress [25]. The characteristic of adjacent rings is that the stress increment is very small.

The plastic zone is assumed to be formed by the concentric annuli n which is displayed in Figure 7. The ring of the number of i is defined by two circles of normalized radii $\rho_{(i-1)} = r_{(i-1)}/R_p$ and $\rho_{(i)} = r_{(i)}/R_p$. It should be noted that to satisfy the equilibrium conditions, the thickness of each

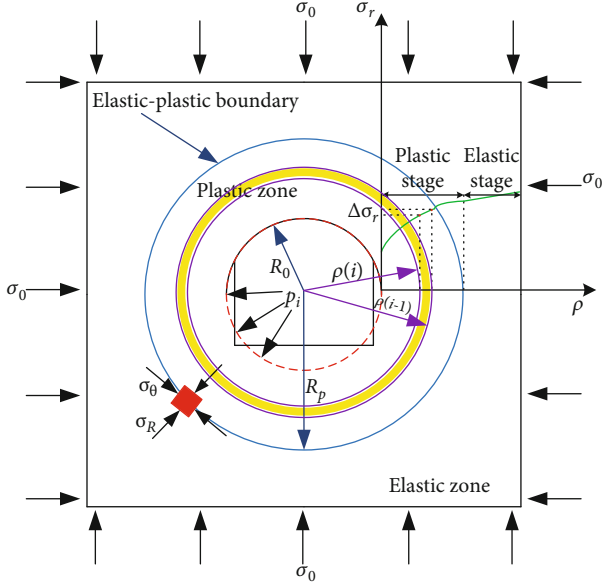


FIGURE 7: Radial stress distribution and plastic zone of equivalent circular roadway with finite number of annuli.

annulus is automatically defined in the numerical process, and its thickness is not equal.

For the convenience of calculation, all radius divided by the radius R_p of plastic zone are normalized (as shown in Equation (21)).

$$\rho = \frac{r}{R_p}. \quad (21)$$

Then, the radius of the inner and outer boundary of the number i ring are $\rho_{(i)}$ and $\rho_{(i-1)}$, respectively. At the outermost side of the plastic zone (which is the interface of the elastoplastic zone), $\rho_{(0)}$ is equal to 1. At the tunnel wall, $\rho_{(n)} = R_0/R_p$. It should be noted that the difference between the radial stresses on the inner and outer sides of each ring ($\Delta\sigma_r = \sigma_{r(i)} - \sigma_{r(i-1)}$) is defined as a constant value. In the study, the equivalent increment of confining pressure is applied for each annulus. This increment is described as follows:

$$\Delta\sigma_{r(i)} = \frac{p_i - \sigma_{rp}}{n}. \quad (22)$$

According to the calculation of increment of confining pressure using Equation (22), the radial pressure of the i th annulus is obtained using the function described as follows:

$$\sigma_{r(i)} = \sigma_{r(i-1)} + \Delta\sigma_{r(i)}. \quad (23)$$

Based on the equilibrium differential function (Equation (10)), when n is large enough, the tangential stress $\sigma_{\theta(i)}$ in the plastic zone is estimated with the equation described as follows:

$$\sigma_{\theta(i)} = \frac{\sigma_{r(i)} - \sigma_{r(i-1)}}{\rho_{(i)} - \rho_{(i-1)}} \rho_{(i)} + \sigma_{r(i)}. \quad (24)$$

If the number of annuli n is sufficiently large enough, the equilibrium equation can be related to the normalized radius $\rho = r/R_p$. For the convenience of calculation, all radius divided by the radius R_p of plastic zone are normalized. Then, the radius of the inner and outer boundary of the number i ring is $\rho_{(i)}$ and $\rho_{(i-1)}$, respectively. At the outermost side of the plastic zone (the interface of the elasto-plastic zone) $\rho_{(0)} = 1$. At the roadway wall, $\rho_{(n)} = R_0/R_p$. Therefore, the stress and strains at the boundary of the elasto-plastic can be obtained based on Brown et al. [17], which is described as follows:

$$\begin{Bmatrix} \sigma_{r(0)} \\ \sigma_{\theta(0)} \end{Bmatrix} = \begin{Bmatrix} \sigma_{rp} \\ 2\sigma_0 - \sigma_{rp} \end{Bmatrix}, \quad (25)$$

$$\begin{Bmatrix} \varepsilon_{r(0)} \\ \varepsilon_{\theta(0)} \end{Bmatrix} = \frac{1 + \nu}{E} \begin{Bmatrix} \sigma_{rp} - \sigma_0 \\ \sigma_0 - \sigma_{rp} \end{Bmatrix}. \quad (26)$$

Once the stress components are obtained, the strain parameters can be calculated according to the physical equation. The strain parameters including the elastic and plastic parts can be described as follows:

$$\begin{Bmatrix} \varepsilon_{r(i)} \\ \varepsilon_{\theta(i)} \end{Bmatrix} = \begin{Bmatrix} \varepsilon_{r(i-1)} \\ \varepsilon_{\theta(i-1)} \end{Bmatrix} + \begin{Bmatrix} \Delta\varepsilon_{r(i)}^e \\ \Delta\varepsilon_{\theta(i)}^e \end{Bmatrix} + \begin{Bmatrix} \Delta\varepsilon_{r(i)}^p \\ \Delta\varepsilon_{\theta(i)}^p \end{Bmatrix}, \quad (27)$$

where $\varepsilon_{r(i)}$, $\varepsilon_{\theta(i)}$, $\varepsilon_{r(i-1)}$, and $\varepsilon_{\theta(i-1)}$ represent the radial strains and tangential strains at the i th and $(i-1)$ th radius. $\Delta\varepsilon_{r(i)}^e$ and $\Delta\varepsilon_{\theta(i)}^e$ represent the increments of the elastic radial and tangential strain at the i th radius. $\Delta\varepsilon_{r(i)}^p$ and $\Delta\varepsilon_{\theta(i)}^p$ represent the increment of the plastic radial and tangential strain at the i th radius, respectively.

According to the Hooke's Law, the increments of the elastic strain can be calculated by the increments of the stress using the function as follows:

$$\begin{Bmatrix} \Delta\varepsilon_{r(i)}^e \\ \Delta\varepsilon_{\theta(i)}^e \end{Bmatrix} = \frac{1}{2G} \begin{pmatrix} 1 - \nu & -\nu \\ -\nu & 1 - \nu \end{pmatrix} \begin{Bmatrix} \Delta\sigma_{r(i)} \\ \Delta\sigma_{\theta(i)} \end{Bmatrix}, \quad (28)$$

where $\Delta\sigma_{\theta(i)}$ represent the increment of the tangential stress, $\Delta\sigma_{\theta(i)} = \sigma_{\theta(i)} - \sigma_{\theta(i-1)}$.

The increments of the plastic strain obey the nonassociated flow regulation as follows:

$$\Delta\varepsilon_{r(i)}^p = -K_{\psi(i)} \Delta\varepsilon_{\theta(i)}^p. \quad (29)$$

When both K_{ψ} and η^* are related to $\sigma_{r(i)}$, $K_{\psi(i)}$ can be calculated using the equation described as follows:

$$K_{\psi(i)} = 1 + \left(K_{\psi(i)}^p - 1 \right) \exp \left(-\frac{\eta_{(i-1)}}{\eta_{(i-1)}^*} \right). \quad (30)$$

Combining Equations (27) and (29), the following equation can be obtained:

$$\varepsilon_{r(i)} + K_{\psi(i)}\varepsilon_{\theta(i)} = \varepsilon_{r(i-1)} + K_{\psi(i)}\varepsilon_{\theta(i-1)} + \Delta\varepsilon_{r(i)}^e + K_{\psi(i)}\Delta\varepsilon_{\theta(i)}^e. \quad (31)$$

Then, the finite difference form of the equilibrium function (Equation (19)) can be expressed as follows:

$$\frac{\sigma_{r(i)} - \sigma_{r(i-1)}}{r_{(i)} - r_{(i-1)}} + \frac{\sigma_{r(i)} + \sigma_{r(i-1)} - \sigma_{\theta(i)} - \sigma_{\theta(i-1)}}{r_{(i)} + r_{(i-1)}}. \quad (32)$$

By combining Equation (18) and Equation (29), the rela-

tionship between $r_{(i)}$ and $r_{(i-1)}$ can be obtained as follows:

$$\frac{r_{(i)}}{r_{(i-1)}} = \frac{\sigma_{\theta(i)} + \sigma_{\theta(i-1)} - 2\sigma_{r(i-1)}}{\sigma_{\theta(i)} + \sigma_{\theta(i-1)} - 2\sigma_{r(i)}}. \quad (33)$$

For the purpose of solving the problem of the strain components, Equation (20) can be rewritten as follows:

$$\begin{aligned} \varepsilon_{r(i)} &= \frac{\Delta u_{(i)}}{\Delta r_{(i)}}, \\ \varepsilon_{\theta(i)} &= \frac{u_{(i)}}{r_{(i)}}. \end{aligned} \quad (34)$$

When combining Equations (28), (31), and (34), the radial displacement $u_{(i)}$ is obtained using the function described as:

$$u_{(i)} = \frac{\left\langle \varepsilon_{r(i-1)} + K_{\psi(i)}\varepsilon_{\theta(i-1)} + ((1+\nu)/E) \left\{ \Delta\sigma_{r(i)}(1-\nu - K_{\psi}\nu) + (\sigma_{r(i)} - \sigma_{\theta(i-1)})(K_{\psi} - K_{\psi}\nu - \nu) \right\} \right\rangle r_{(i)} (r_{(i)} - r_{(i-1)})}{r_{(i)} + K_{\psi}(r_{(i)} - r_{(i-1)})} + \frac{u_{(i-1)}r_{(i)}}{r_{(i)} + K_{\psi}(r_{(i)} - r_{(i-1)})}. \quad (35)$$

4. Calibration Examples

In order to verify and confirm the accuracy of the proposed methodologies, the results obtained from the proposed method are compared to that obtained using other methods. The verification of the proposed methods in this study is separated into three parts. The mechanical properties of rock mass used in the study are assumed to meet the strength criterion with strain-softening behavior. The first part focuses on showing the advantages of three-dimensional H-B strength criterion (GZZ), compared with two-dimensional H-B strength criterion (narrow H-B criterion and generalized H-B criterion). On the other hand, it focuses on the comparison of the current three-dimensional D-P criteria to show its correctness and rationality of the theoretical derivation.

Firstly, the differences between the three-dimensional H-B criterion and the two-dimensional H-B criterion (narrow H-B criterion and broad H-B criterion) are discussed. A series of data are selected from the publication by Sharan [51], which are $R_0 = 5$ m, $\sigma_0 = 30$ MPa, $p_i = 5$ MPa, $E = 5.5$ GPa, $\nu = 0.25$, $\sigma_c = 30$ MPa, $m_p = 1.7$, $s_p = 0.0039$, $m_r = 1.0$, $s_r = 0.0$, $a = 0.5$, $\psi = 30^\circ$, $n = 500$. The comparison between the three-dimensional H-B criterion and the two-dimensional narrow H-B criterion is carried out, and the specific change rule is shown in Figure 8. In addition, when $a \neq 0.5$, the difference between the three-dimensional H-B criterion and the two-dimensional generalized H-B criterion is compared and verified under the condition that the above data are kept unchanged. The specific change rule is shown in Figure 9.

It could be shown from Figures 8 and 9 with the increase of the ratio value of radius at a certain point to the radius of the equivalent circular roadways increases, the radial stress increases approximately linearly, while the circumferential stress increases approximately linearly first and then decreases gradually. As shown in Figures 8(a) and 9(a), the radial stress of GZZ criterion is generally lower than that of 2D H-B criterion obtained by Sharan [51], but the linear growth rate of GZZ criterion is higher, which highlights the role of intermediate main stress. As shown in Figures 8(b) and 9(b), the tangential stress of GZZ criterion is generally lower than that of 2D H-B criterion obtained by Sharan [51]. On one hand, the turning point of GZZ criterion is relatively later than that of 2D H-B criterion. On the other hand, the subsequent decreasing trend range of 2D H-B criterion is very small, which also shows the role of intermediate main stress. As shown in Figure 10, the three-dimensional H-B criterion and the three-dimensional D-P criterion were compared. Both of the calculation results produce the plastic zone, as shown in the dotted line part in the figure. The three-dimensional solution enters the state of elastic stress at the shallow depth of roadway, which is beneficial to the stability of roadway. This is mainly due to the favorable mechanical action of the intermediate main stress. With the decrease of the plastic zone's radius, the stress gradient in plastic zone and the stress value at the same depth are increased. In the plastic zone, the intermediate main stress increases with the increase of surrounding rock depth and converges to the original rock stress at the elastic-plastic interface.

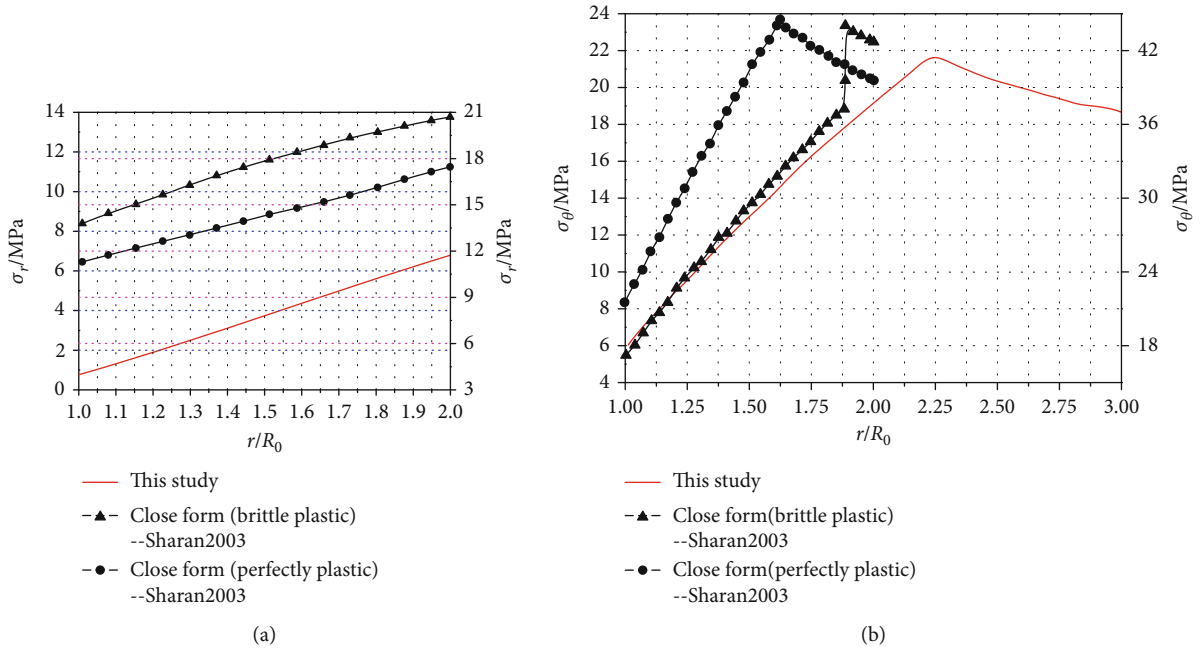


FIGURE 8: Comparison of stresses curves of GZZ criterion stress with narrow H-B criterion ((a) radial stress; (b) tangential stress).

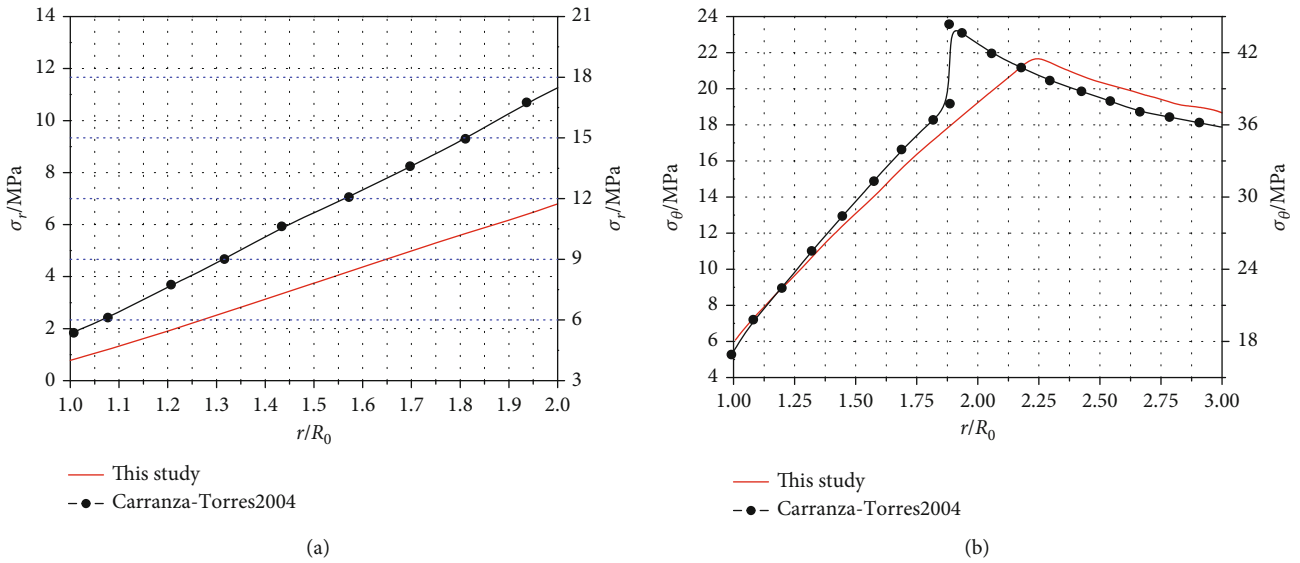


FIGURE 9: Comparison of stresses curves of GZZ criterion stress with generalized H-B criterion ((a) radial stress; (b) tangential stress).

In order to better verify the theoretical derivation, the calculation results based on this derivation are compared with the existing research results. Li et al. [52] deduced the analytical solution of circular tunnel based on GZZ strength criterion, but it did not consider the strain softening characteristics of surrounding rock. If ω^p in Equation (6) is equal to ω^r , the solution in this paper can be reduced to the solution without considering the strain softening characteristics of surrounding rock. In order to study the accuracy of the theoretical derivation, this solution is compared with the solution provided by Li et al. [52]. Figure 11 shows the comparison of radial and circumferential stress curves of surrounding rock under different uniaxial compressive strength.

Table 1 shows the comparison of plastic zone radius of surrounding rock under different uniaxial compressive strength. The uniaxial compressive strengths are 20, 30, 50, and 70 MPa, respectively. It can be seen that the calculation results in this paper almost coincide with the results given by Li et al. [52], and the radius of plastic zone is the same. Therefore, the correctness and rationality of the theoretical derivation are verified.

5. Discussion

Three-dimensional nonlinear GZZ strength criterion considered the influence of intermediate main stress. In this part,

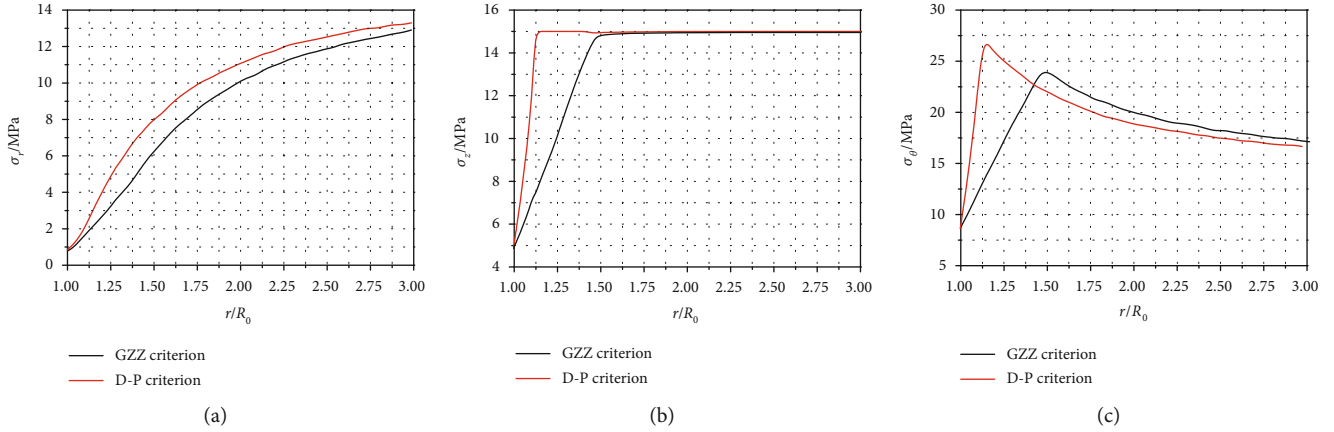


FIGURE 10: Stress distributions of surrounding rock under different strength criteria ((a) radial stress; (b) axial stress; (c) tangential stress).

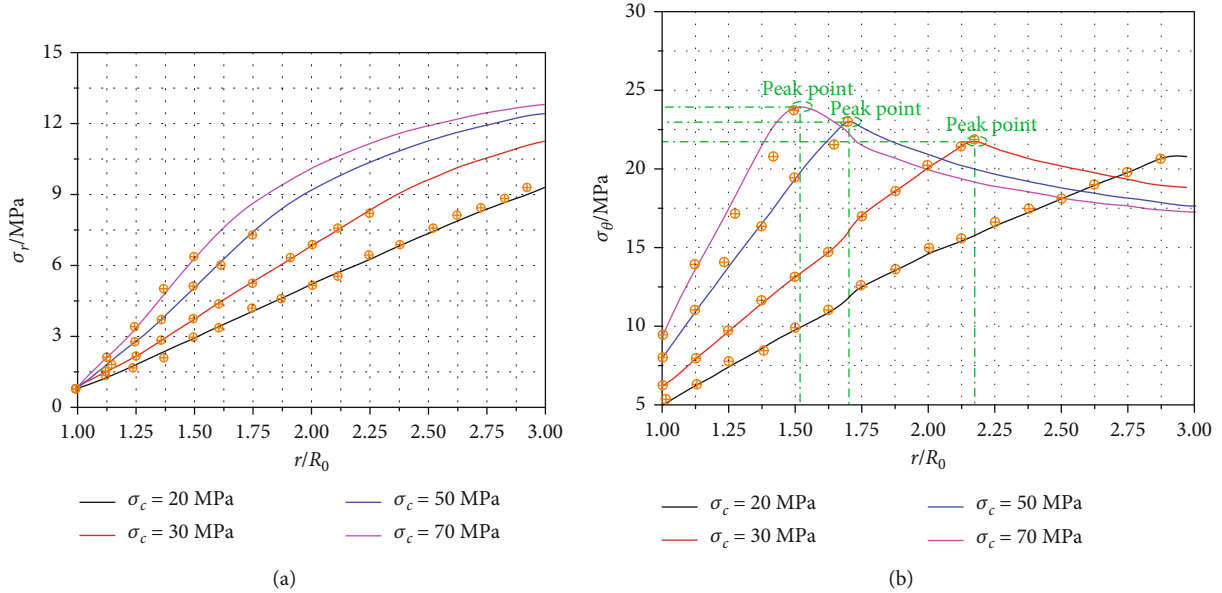


FIGURE 11: Curves of stresses under different uniaxial compressive strengths.

TABLE 1: Comparison for plastic zone radii of surrounding rock under different uniaxial compressive strengths.

	Plastic zone radii/m			
	$\sigma_c = 20$ MPa	$\sigma_c = 30$ MPa	$\sigma_c = 40$ MPa	$\sigma_c = 50$ MPa
This paper	8.92	6.69	5.06	4.39
Li et al. [52]	8.92	6.74	5.10	4.42

sensitivity analysis of intermediate main stress and the dilation angle are carried out on the stress, strain, and displacement of the surrounding rock.

According to the analysis of Xia et al. [53], the softening law of the surrounding rock strength parameters with strain involved in the GZZ guidelines is described as follows. The value a is increased with the increase of the tangential strain. When the tangential strain is between 0 and 0.001, the value a remains at 0.5; then, with the increase of strain, the value a increases linearly to 0.6, and the tangential strain is 0.003. After that, the value a remains constant with the increase of

the tangential strain; the s value is increased with the increase of the tangential strain. When the tangential strain is between 0 and 0.001, the value s remains at 0.0004. With the increase of strain, the s value decreases linearly until it is 0, and the tangential strain is 0.003. After that, the s value remains constant with the increase of the tangential strain; the m_b value is increased with the increase of the tangential strain. When the tangential strain is between 0 and 0.001, the m_b value remains at 0.5. Then, with the increase of strain, the m_b value decreases linearly to 0.25, and the tangential strain value is 0.003. After that, the m_b value remains constant with the

increase of the tangential strain; the ψ value is increased with the increase of the tangential strain. The softening law is that when the tangential strain is between 0 and 0.001, the ψ value is kept at 15° . With the increase of strain, the ψ value decreases linearly to 5° , and the tangential strain is 0.003. After that, the ψ value remains constant with the increase of the tangential strain.

In the sensitivity analysis, it is determined that the relevant parameters of the deep equivalent circular roadway are the original rock stress is $p_0 = 15$ MPa, the excavation radius of the equivalent circular roadway is $R_0 = 5$ m, $E = 20$ Gpa, $\mu = 0.35$, the strength parameter $m_i = 6$, the surrounding rock uniaxial compressive strength σ_c is 20 MPa, the initial value of the geological strength index GSI^p is 50, and the residual values GSI^r are 10, 20, 30, 40, and 50, respectively [53]. When GSI^r is 50, surrounding rock softening is not considered which is as the control group. Assuming the support reaction p_i is 1.5 MPa, the critical plastic deviator strain η^* of surrounding rock is 0.5%.

5.1. Impact of Rock Dilation. Dilatancy plays an important role in the deformation of the rock boundary of roadway excavation [54]. Previous studies described that the expansion of surrounding rock of the roadway has little impact on the stress distribution [55, 56]. However, the yield process of surrounding rock is accompanied by the expansion behavior. The volume of plastic zone keeping constant during the yield process is not consistent with the actual situation of rock mass [57]. In this paper, different dilatancy angles are introduced into the proposed theoretical calculation equation, and the influences of expansion on stress distribution are studied.

In addition, the main focuses of this paper are on the stability analysis of the roadway excavation process, and the rock mass involved is basically weak rock formations. Previous studies have divided rocks into soft rocks and hard rocks [58]. Since the mechanical characteristics of each rock are similar, the mechanical parameters of mudstone samples are selected to calculate the difference of stress and radius of plastic zone under different dilation angles. Compared with the change of main stress with dilation angle in Table 2, the sensitivity of stress distribution to dilation angle is weak. Considering the three-dimensional case of intermediate main stress, the dilation angle has little effect on the plastic zone of mudstone. It also verifies the conclusion that the dilation angle has little effect on the plastic zone stress [55, 56]. The results indicate the influence of the intermediate main stress and the strength potential of rock materials. The self-bearing capacity of materials is also considered to make sure that the analysis of the stability of the surrounding rock is reliable.

Figure 12 shows the distribution curve of displacement in plastic zone along the depth of surrounding rock under different dilatancy angles. It can be seen from Figure 12 that the displacement in the plastic zone of soft rock increases with the increase of dilation angle, which is consistent with the engineering practice. For soft rock, within 3 times of excavation radius, the expansion is very significant. When the dilatancy angle is large, the distribution of displacement in plastic zone along the depth of surrounding rock presents

TABLE 2: Parameters under different dilatancy angles for mudstone.

Lithology	$\psi/^\circ$	σ_R/MPa	R_p/m	β
Mudstone	0	9.21	8.92	1.00
	10	8.99	8.84	1.42
	20	8.85	8.92	2.04
	30	8.76	9.15	3.00

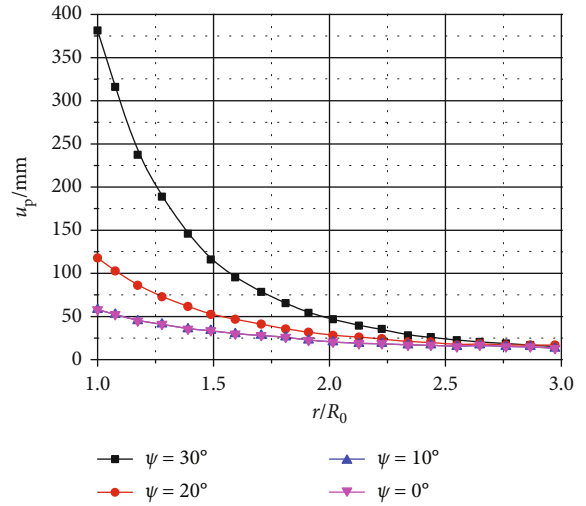


FIGURE 12: Effect of dilation angle on plastic zone of roadway surrounding rock displacement of the soft rock.

prominent nonlinear characteristics. The surrounding rock around the inner wall of the roadway is disturbed by the roadway excavation, and the strain energy stored in rock mass is also released along the disturbed area. As a result, the displacement distribution in plastic zone increases nonlinearly with the decrease of surrounding rock depth. The displacement of the inner wall of the tunnel develops the most. Therefore, for soft rocks such as mudstone, the plastic zone's displacement was affected by the increasing dilation angle, so attentions are needed to be paid to the influence of rock dilation in the calculation of stress distribution.

5.2. Effect of Softening Degree. Figure 13 shows the stress distribution of surrounding rock under different softening degree. For the radial stress (σ_r), under the same support pressure (p_i), the higher the softening degree of surrounding rock, the smaller the radial stress. However, due to the influence of the size of the plastic zone, the distribution of the tangential stress σ_θ in the elastic and plastic zone is not the same. In the inner wall of the roadway, the higher the softening degree of the surrounding rock, the smaller the tangential stress. It can be seen from Figure 13(b) that the softening degree of surrounding rock has a great influence on the scope of plastic area. The higher the softening degree, the greater the plastic zone of surrounding rock. However, regardless of the degree of softening, the maximum value of tangential stress is the same under various conditions. In other words, under the same support pressure (p_i), the strain softening of surrounding rock can change the stress distribution of

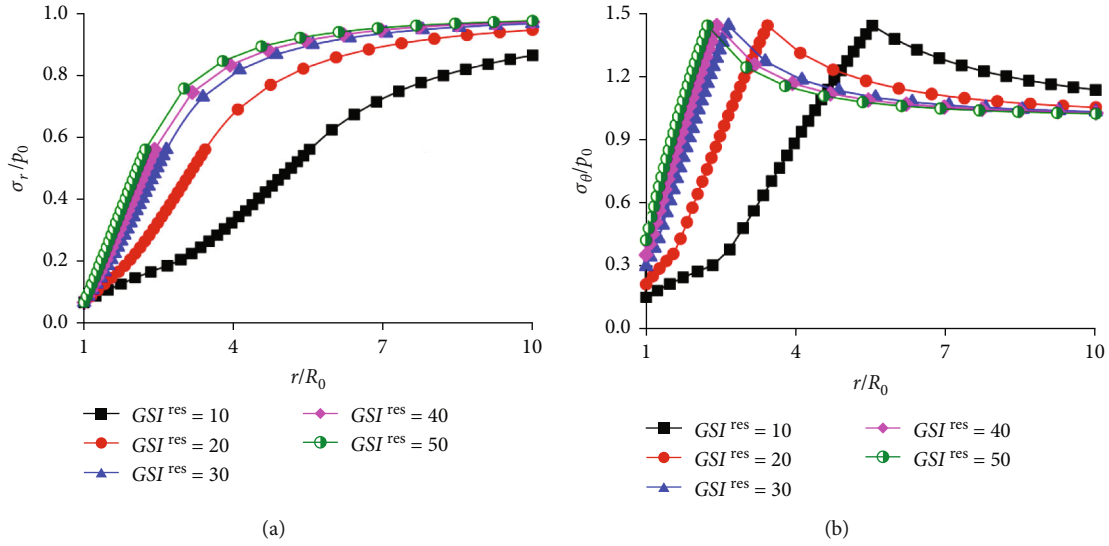


FIGURE 13: Stress curves with different GSI^{res} ((a) radial stress; (b) tangential stress).

surrounding rock, but cannot change the values of maximum stress. For the surrounding rock with high softening degree, the stress changes slowly due to the large radius of plastic zone. However, regardless of the degree of softening, the stress of surrounding rock at the boundary of plastic zone is constant.

In terms of the strain of surrounding rock, it can be seen from Figure 13 that the strain softening of surrounding rock has a great influence on its strain, and the strain of surrounding rock in plastic zone is particularly sensitive to softening. Under the same support pressure (p_i), when GSI^{res} are 40, 30, and 20, the radial strain at the inner wall of the tunnel is 1.2, 1.6, and 3.4 times of that without strain softening, respectively. When GSI^{res} is 10, the radial strain at the inner wall of the tunnel is 18.6 times larger than that under the condition of without strain softening. The change regulation of tangential strain is similar to that of radial strain. It can be seen that after the surrounding rock softens, although the stress in the plastic zone is relatively smaller, its strain increases exponentially, resulting in a large increase in the deformation of the surrounding rock.

Figure 14 shows the characteristic curve of surrounding rock under different softening degree. As can be seen from Figure 14, when the support pressure is large, the softening effect can be ignored due to the small deformation of roadway. However, with the decrease of support pressure, the deformation of surrounding rock changes significantly with the degree of softening. Under the same support pressure, the deformation of surrounding rock is several times or even dozens of times. For example, when the support pressure (p_i) is 1.5 MPa, the displacement of the inner wall of the roadway is 78 mm without considering the softening of surrounding rock. When GSI^{res} are 40, 30, and 20, the radial displacement at the inner wall of the roadway is 110 mm, 180 mm, and 500 mm, respectively. When GSI^{res} is less than 20, the displacement of the inner wall of the roadway is more than a few meters, which means the roadway lose its stability. In the same way, under the condition of the same deformation

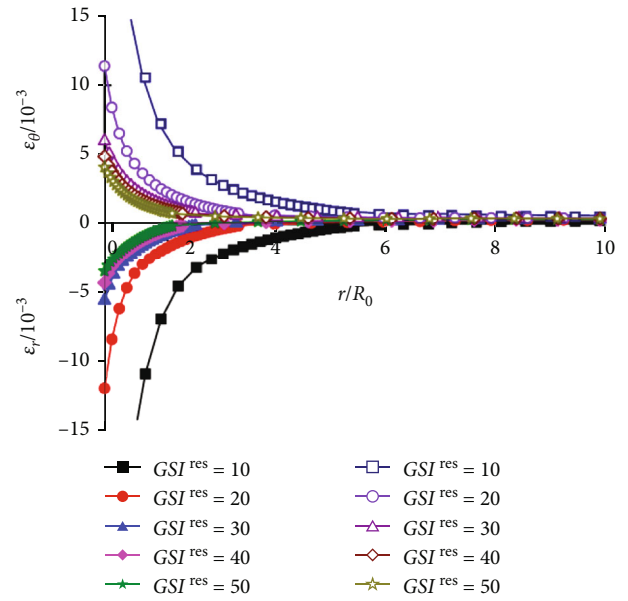


FIGURE 14: Strain curves with different GSI^{res} .

of roadway in the inner wall of the roadways, the support pressure required for the surrounding rock with different softening degree varies several times.

6. Conclusions

In this paper, based on GZZ strength criterion considering the impact of intermediate main stress, an equivalent circular roadway solution method which can reflect the strain-softening and dilatancy properties of surrounding rock is proposed. The stress, strain, and deformation of surrounding rock after the excavation of underground roadways are obtained by numerical method. The influence of the intermediate main stress on the mechanical behavior of the plastic

zone of the surrounding rock and the relationship between the mechanical properties of the surrounding rock and the softening parameters are studied. Then, the failure mechanism of roadway with soft rock is analyzed, and the main conclusions are as follows:

- (1) Compared with the traditional H-B strength criterion, the value of surrounding rock stress calculated by GZZ strength criterion considering the effect of intermediate main stress is smaller, while the radius of plastic zone, softening zone, and surrounding rock strain are larger. Therefore, it is more conservative to use the GZZ strength criterion for calculation
- (2) Under the same support pressure, the strain-softening of surrounding rock can change the stress distribution, but cannot change the value of the maximum stress. In other words, regardless of the degree of strain-softening, the stress of surrounding rock at the boundary of plastic zone is constant. But for the surrounding rock with high strain-softening degree, because of its large plastic zone radius, the surrounding rock stress near the inner wall of the tunnel is relatively small, and the displacement is large. When the support pressure is small, the deformation of surrounding rock changes significantly with the degree of strain-softening. Under the same support pressure, the deformation of surrounding rock is several times or even dozens of times. Similarly, under the condition of the same deformation of the surrounding rock in the inner wall of the roadways, the required supporting reaction force may increase several times or even dozens of times considering the soften of the surrounding rock
- (3) The dilatancy properties of rock have significant effects on the displacement of the plastic zone of the surrounding rock mass. Under the effects of dilatancy, the displacement of the plastic zone is obviously larger than that without considering the effects of dilatancy. The displacements of the plastic zone of the rock mass increase with the increase of the dilatancy angle
- (4) The stress of surrounding rock is redistributed due to the excavation and unloading of roadway. Shear slip failure of rock structure occurs under high ground stress, and the self-supporting capacity of the surrounding rock is greatly reduced. The deformation of surrounding rock of roadway increases rapidly when the support effect is enough. It is the main reason of large deformation and failure of deep underground roadway with soft rock. Therefore, in the design and calculation of roadway supporting system, the strain softening characteristics of surrounding rock should be properly considered to avoid large deformation and failure of roadway

Data Availability

The data used to support the findings of this study are available from the corresponding author upon request.

Conflicts of Interest

The authors declare no conflict of interest.

Acknowledgments

This research has been supported by the National Natural Science Foundation of China (grant no. 51927807), a Project Funded by the Priority Academic Program Development of Jiangsu Higher Education Institutions (PAPD), and National Natural Science Foundation of China (General Program:52074239).

References

- [1] K. Guan, W. C. Zhu, J. Wei, X. Liu, L. Niu, and X. Wang, "A finite strain numerical procedure for a circular tunnel in strain-softening rock mass with large deformation," *International Journal of Rock Mechanics and Mining Sciences*, vol. 112, pp. 266–280, 2018.
- [2] R. Wang, J. B. Bai, S. Yan, Z. G. Chang, and X. Y. Wang, "An innovative approach to theoretical analysis of partitioned width & stability of strip pillar in strip mining," *International Journal of Rock Mechanics and Mining Sciences*, vol. 129, article 104301, 2020.
- [3] W. Shen, G. Shi, M. Wang et al., "Method of entry layout under synergistic effects of abutment stress and dynamic stress," *Shock and Vibration*, vol. 2020, Article ID 6655293, 6 pages, 2020.
- [4] Y. Wang, W. K. Feng, H. J. Wang, C. H. Li, and Z. Q. Hou, "Rock bridge fracturing characteristics in granite induced by freeze-thaw and uniaxial deformation revealed by AE monitoring and post-test CT scanning," *Cold Regions Science and Technology*, vol. 177, article 103115, 2020.
- [5] Z. Guangchao, Z. Chuanwei, C. Miao et al., "Ground response of entries driven adjacent to a retreating longwall panel," *International Journal of Rock Mechanics and Mining Sciences*, vol. 138, article 104630, 2021.
- [6] F. Wang and D. Qian, "Difference solution for a circular tunnel excavated in strain-softening rock mass considering decayed confinement," *Tunnelling and Underground Space Technology*, vol. 82, pp. 66–81, 2018.
- [7] E. Alonso, L. R. Alejano, F. Varas, G. Fdez-Manin, and C. Carranza-Torres, "Ground response curves for rock masses exhibiting strain-softening behaviour," *International Journal for Numerical and Analytical Methods in Geomechanics*, vol. 27, no. 13, pp. 1153–1185, 2003.
- [8] L. R. Alejano, E. Alonso, A. Rodríguez-Dono, and G. Fernández-Manin, "Application of the convergence-confinement method to tunnels in rock masses exhibiting Hoek-Brown strain-softening behaviour," *International Journal of Rock Mechanics and Mining Sciences*, vol. 47, no. 1, pp. 150–160, 2010.
- [9] C. Carranza-Torres and C. Fairhurst, "The elasto-plastic response of underground excavations in rock masses that satisfy the Hoek-Brown failure criterion," *International Journal of Rock Mechanics and Mining Sciences*, vol. 36, no. 6, pp. 777–809, 1999.
- [10] C. Carranza-Torres and C. Fairhurst, "Application of the convergence-confinement method of tunnel design to rock masses that satisfy the Hoek-Brown failure criterion,"

- Tunnelling and Underground Space Technology*, vol. 15, no. 2, pp. 187–213, 2000.
- [11] K. H. Park and Y. J. Kim, “Analytical solution for a circular opening in an elastic-brittle-plastic rock,” *International Journal of Rock Mechanics and Mining Sciences*, vol. 43, no. 4, pp. 616–622, 2006.
 - [12] S. K. Sharan, “Elastic-brittle-plastic analysis of circular openings in Hoek-Brown media,” *International Journal of Rock Mechanics and Mining Sciences*, vol. 40, no. 6, pp. 817–824, 2003.
 - [13] S. K. Sharan, “Analytical solutions for stresses and displacements around a circular opening in a generalized Hoek-Brown rock,” *International Journal of Rock Mechanics and Mining Sciences*, vol. 45, no. 1, pp. 78–85, 2008.
 - [14] S. L. Wang, X. T. Yin, H. Tang, and X. Ge, “A new approach for analyzing circular tunnel in strain-softening rock masses,” *International Journal of Rock Mechanics and Mining Sciences*, vol. 47, no. 1, pp. 170–178, 2010.
 - [15] Q. Zhang, B. S. Jiang, S. L. Wang, X. R. Ge, and H. Q. Zhang, “Elasto-plastic analysis of a circular opening in strain-softening rock mass,” *International Journal of Rock Mechanics and Mining Sciences*, vol. 50, pp. 38–46, 2012.
 - [16] Q. Zhang, B. S. Jiang, and H. J. Lv, “Analytical solution for a circular opening in a rock mass obeying a three-stage stress-strain curve,” *International Journal of Rock Mechanics and Mining Sciences*, vol. 86, pp. 16–22, 2016.
 - [17] E. T. Brown, J. W. Bray, B. Ladanyi, and E. Hoek, “Ground response curves for rock tunnels,” *Journal of Geotechnical Engineering*, vol. 109, no. 1, pp. 15–39, 1983.
 - [18] C. Carranza-Torres, *Self-Similarity Analysis of the Elastoplastic Response of Underground Openings in Rock and Effects of Practical Variables*, Ph.D Thesis, University of Minnesota, 1998.
 - [19] E. Hoek and E. T. Brown, “Practical estimates of rock mass strength,” *International Journal of Rock Mechanics and Mining Sciences*, vol. 34, no. 8, pp. 1165–1186, 1997.
 - [20] L. R. Alejano and E. Alonso, “Considerations of the dilatancy angle in rocks and rock masses,” *International Journal of Rock Mechanics and Mining Sciences*, vol. 42, no. 4, pp. 481–507, 2005.
 - [21] Y. B. Zhang, X. R. Liu, X. Liu, S. Wang, and F. Ren, “Numerical characterization for rock mass integrating GSI/Hoek-Brown system and synthetic rock mass method,” *Journal of Structural Geology*, vol. 126, pp. 318–329, 2019.
 - [22] M. Cai, P. K. Kaiser, Y. Tasaka, and M. Minami, “Determination of residual strength parameters of jointed rock masses using the GSI system,” *International Journal of Rock Mechanics and Mining Sciences*, vol. 44, no. 2, pp. 247–265, 2007.
 - [23] Y. Wang, C. H. Li, and J. Q. Han, “On the effect of stress amplitude on fracture and energy evolution of pre-flawed granite under uniaxial increasing-amplitude fatigue loads,” *Engineering Fracture Mechanics*, vol. 240, article 107366, 2020.
 - [24] E. Hoek and M. S. Diederichs, “Empirical estimation of rock mass modulus,” *International Journal of Rock Mechanics and Mining Sciences*, vol. 43, no. 2, pp. 203–215, 2006.
 - [25] Y. K. Lee and S. Pietruszczak, “A new numerical procedure for elasto-plastic analysis of a circular opening excavated in a strain-softening rock mass,” *Tunnelling and Underground Space Technology*, vol. 23, no. 5, pp. 588–599, 2008.
 - [26] L. Cui, J. J. Zheng, R. J. Dong, and Y. K. Dong, “Elasto-plastic analysis of a circular opening in rock mass with confining stress-dependent strain-softening behaviour,” *Tunnelling and Underground Space Technology*, vol. 50, pp. 94–108, 2015.
 - [27] E. Detournay, “Elastoplastic model of a deep tunnel for a rock with variable dilatancy,” *Rock Mechanics and Rock Engineering*, vol. 19, no. 2, pp. 99–108, 1986.
 - [28] S. C. Yuan and J. P. Harrison, “An empirical dilatancy index for dilatant deformation of rock,” *International Journal of Rock Mechanics and Mining Sciences*, vol. 44, pp. 625–636, 2007.
 - [29] W. P. Huang, Q. Yuan, Y. L. Tan et al., “An innovative support technology employing a concrete-filled steel tubular structure for a 1000-m-deep roadway in a high in situ stress field,” *Tunnelling and Underground Space Technology*, vol. 73, pp. 26–36, 2018.
 - [30] D. P. Ma, Y. J. Yang, J. Cao, and L. Y. Xing, “Optimization design of cross section shape of deep roadways based on characteristics of energy release,” *Journal of Central South University (Science and Technology)*, vol. 46, no. 9, pp. 3354–3360, 2015.
 - [31] Y. Wang, W. K. Feng, R. L. Hu, and C. H. Li, “Fracture evolution and energy characteristics during marble failure under triaxial fatigue cyclic and confining pressure unloading (FC-CPU) conditions,” *Rock Mechanics and Rock Engineering*, vol. 54, pp. 799–818, 2020.
 - [32] S. L. Wang and S. Yin, “A closed-form solution for a spherical cavity in the elastic-brittle-plastic medium,” *Tunnelling and Underground Space Technology*, vol. 26, no. 1, pp. 236–241, 2011.
 - [33] S. L. Wang, Z. J. Wu, M. W. Guo, and X. Ge, “Theoretical solutions of a circular tunnel with the influence of axial in situ stress in elastic-brittle-plastic rock,” *Tunnelling and Underground Space Technology*, vol. 30, pp. 155–168, 2012.
 - [34] J. F. Zou, S. S. Li, Y. Xu, H. C. Dan, and L. H. Zhao, “Theoretical solutions for a circular opening in an elastic-brittle-plastic rock mass incorporating the out-of-plane stress and seepage force,” *KSCCE Journal of Civil Engineering*, vol. 20, no. 2, pp. 687–701, 2016.
 - [35] B. Ukritchon and S. Keawsawasvong, “Discussion of “lower-bound finite elements limit analysis for hoek-brown materials using semidefinite programming” by Jyant Kumar and Debasis Mohapatra,” *Journal of Engineering Mechanics*, vol. 144, no. 7, article 07018001, 2018.
 - [36] B. Ukritchon and S. Keawsawasvong, “Stability of retained soils behind underground walls with an opening using lower bound limit analysis and second-order cone programming,” *Geotechnical and Geological Engineering*, vol. 37, no. 3, pp. 1609–1625, 2019.
 - [37] L. Y. Zhang and H. H. Zhu, “Three-dimensional Hoek-Brown strength criterion for rocks,” *Journal of Geotechnical and Geoenvironmental Engineering*, vol. 133, no. 9, pp. 1128–1135, 2007.
 - [38] L. Zhang, “A generalized three-dimensional Hoek-Brown strength criterion,” *Rock Mechanics and Rock Engineering*, vol. 41, no. 6, pp. 893–915, 2008.
 - [39] X. D. Pan and J. A. Hudson, “A simplified three-dimensional Hoek-Brown yield criterion,” in *ISRM International Symposium*, Madrid, Spain, September 1988.
 - [40] A. M. Al-Ajmi and R. W. Zimmerman, “Relation between the Mogi and the Coulomb failure criteria,” *International Journal of Rock Mechanics and Mining Sciences*, vol. 42, no. 3, pp. 431–439, 2005.

- [41] J. F. Zou, Y. M. Sheng, M. Y. Xia, and F. Wang, "A novel numerical-iterative-approach for strain-softening surrounding rock incorporating rockbolts effectiveness and hydraulic-mechanical coupling based on three-dimensional Hoek-Brown strength criterion," *Tunnelling and Underground Space Technology*, vol. 101, article 103358, 2020.
- [42] P. Bésuelle, J. Desrues, and S. Raynaud, "Experimental characterisation of the localisation phenomenon inside a Vosges sandstone in a triaxial cell," *International Journal of Rock Mechanics and Mining Sciences*, vol. 37, no. 8, pp. 1223–1237, 2000.
- [43] F. P. Hassani, M. J. White, and D. Branch, *The Behaviour of Yielded Rock in Tunnel Design, Stability in Underground Mining II*, Lexington, Kentucky, 1984.
- [44] T. P. Medhurst, *Estimation of the in-situ strength and deformability of coal for engineering design*, Ph.D. Thesis, University of Queensland, Australia, 1996.
- [45] C. H. Scholz, "Micro-fracturing and the inelastic deformation of rock in compression," *Journal of Geophysical Research Atmospheres*, vol. 73, no. 4, pp. 1417–1432, 1968.
- [46] N. Barton and S. Bandis, "Effects of block size on the shear behavior of jointed rock," in *The 23rd U. S Symposium on Rock Mechanics (USRMS)*, pp. 739–760, Berkeley, CA, USA, August 1982.
- [47] L. R. Alejano, A. Rodriguez-Dono, E. Alonso, and G. Fdez-Manín, "Ground reaction curves for tunnels excavated in different quality rock masses showing several types of post-failure behaviour," *Tunnelling and Underground Space Technology*, vol. 24, no. 6, pp. 689–705, 2009.
- [48] S. D. Priest, "Determination of shear strength and three-dimensional yield strength for the Hoek-Brown yield criterion," *Rock Mechanics and Rock Engineering*, vol. 38, no. 4, pp. 299–327, 2005.
- [49] E. Alonso, L. R. Alejano, G. Fdez-Manin, and F. García-Bastante, "Influence of post peak properties in the application of the convergence-confinement for designing underground excavations," in *Proceedings of the 5th International Conference and Exhibition on Massive Mining Technology*, pp. 793–802, Lulea, Sweden, June 2008.
- [50] K. H. Park, B. Tontavanich, and J. G. Lee, "A simple procedure for ground response curve of circular tunnel in elastic-strain softening rock masses," *Tunnelling and Underground Space Technology*, vol. 23, no. 2, pp. 169–182, 2008.
- [51] S. D. Priest, "Three-dimensional failure criteria based on the Hoek-Brown criterion," *Rock Mechanics and Rock Engineering*, vol. 45, no. 6, pp. 989–993, 2012.
- [52] Y. G. Li, J. Yu, J. Z. Zhang, and S. H. Chen, "Three-dimensional nonlinear analysis of circular tunnel surrounding rock based on GZZ yield criterion," *Journal of PLA University of Science and Technology (Natural Science Edition)*, vol. 17, no. 5, pp. 445–452, 2016.
- [53] C. Xia, C. Xu, Y. Liu, and C. Han, "Elastoplastic solution of deep buried tunnel considering strain-softening characteristics based on GZZ strength criterion," *Chinese Journal of Rock Mechanics and Engineering*, vol. 37, no. 11, pp. 2465–2477, 2018.
- [54] X. G. Zhao, M. Cai, and M. F. Cai, "Influence of dilation on rock mass displacement around underground excavations—a case study of Donkin-Morien tunnels in Canada," *Chinese Journal of Rock Mechanics and Engineering*, vol. 29, no. 11, pp. 2186–2195, 2010.
- [55] R. Schuerch, A. Vrakas, and G. Anagnostou, "On manifestations of delayed failure and the effect of dilatancy in transient poro-elasto-plastic analyses of slopes and excavations," *Géotechnique*, vol. 67, no. 11, pp. 939–952, 2017.
- [56] Z. Guo, L. Zhang, H. Wang, S. Yin, T. Li, and X. Kuai, "Failure mechanism of bolts and countermeasures in swelling soft rock support," *Tehnički vjesnik*, vol. 25, pp. 1447–1456, 2018.
- [57] Z. Q. Liu and D. M. Yu, "Elastoplastic stress and displacement analytical solutions to deep-buried circular tunnels considering intermediate principal stress and dilatancy," *Engineering Mechanics*, vol. 29, no. 8, pp. 289–296, 2012.
- [58] T. Ogawa and Y. Lok, "Effects of dilatancy and yield criteria on displacements around tunnels," *Canadian Geotechnical Journal*, vol. 24, no. 1, pp. 100–113, 1987.

Research Article

Experimental Investigation into Compressive Behaviour and Preconsolidation Pressure of Structured Loess at Different Moisture Contents

Yali Xu ¹, Panpan Guo ², Chengwei Zhu ^{2,3}, Gang Lei ^{2,4} and Kang Cheng ^{2,5}

¹School of Urban Construction and Transportation, Hefei University, Hefei 230601, China

²Research Center of Coastal and Urban Geotechnical Engineering, Zhejiang University, Hangzhou 310058, China

³Institut für Geotechnik, Universität für Bodenkultur Wien, Feistmantelstrasse 4, 1180 Vienna, Austria

⁴Beijing Urban Construction Design & Development Group Company Limited, Beijing 100037, China

⁵China Railway 11th Bureau Group Co. Ltd., Wuhan 430061, China

Correspondence should be addressed to Panpan Guo; pp_guo@zju.edu.cn and Chengwei Zhu; zhuchengwei@zju.edu.cn

Received 22 January 2021; Revised 2 March 2021; Accepted 10 March 2021; Published 22 March 2021

Academic Editor: Yu Wang

Copyright © 2021 Yali Xu et al. This is an open access article distributed under the Creative Commons Attribution License, which permits unrestricted use, distribution, and reproduction in any medium, provided the original work is properly cited.

This paper investigates the influence of the structured property of loess on its compressive behaviour and proposes a new method for determining the preconsolidation pressure of structured loess soil. A series of oedometer tests were carried out on undisturbed and remoulded loess samples prepared at various moisture contents. The effects of moisture content on the structured yield stress, the preconsolidation pressure, and the structural strength were also captured. It was found that the influence of the structured property of loess on the compression behaviour is divergent between undisturbed and remoulded loess samples. The discrepancy before and after structural yielding is more remarkable for the undisturbed soil. The Casagrande method realized through the MATLAB program can effectively eliminate human factors and accurately calculate the corresponding preconsolidation pressure for undisturbed soil. The effects of moisture content on the method for determining the preconsolidation pressure considering the structured property of loess were discussed. The determination method can accurately evaluate the loess consolidation state in loess regions. The influencing rules which the moisture content exerts on the structured yield stress, the preconsolidation pressure, and the structural strength all conform to exponential functions. The study is of great significance to correctly differentiating the foundation consolidation states and calculating the ground settlement in loess regions.

1. Introduction

An accurate determination of the consolidation state of soil is significant for the calculation of foundation settlement and analysis of stability problems [1–4]. Moreover, the project quality, construction period, and cost are also affected by the accuracy of determination of the soil consolidation state [5–8]. Nevertheless, the soil consolidation state falls into three categories, i.e., the overconsolidation state, normal consolidation state, and underconsolidation state, according to the magnitude of the current pressure applied on soil compared to the preconsolidation pressure. Therefore, the core question of determining the consolidation state of the soil

layer is to accurately determine the preconsolidation pressure of soil.

Many investigations have been carried out into the determination of soil preconsolidation pressure. As to how to reasonably determine the preconsolidation pressure, many scholars at home and abroad have proposed various methods. These are such as the Casagrande method, Burmister method, Joes method, Mikasa method, “f” method, graphic method, and densitometric method [9, 10]. However, the calculated preconsolidation pressures using these methods are diverse and the structural effect of structured soil has not been well accounted for [11, 12]. The inflection point on the compression curve of soil was defined by Liu

[13] as the critical average pressure, which varied depending on the physical and mechanical properties of the loess and the age of its origin. Gong et al. [14] believed that the pressure corresponding to the inflection point on the compression curve of undisturbed soil can be regarded as the structured yield stress, which should be the sum of the preconsolidation pressure and the structural strength. By performing tests on old and red clays, Wang et al. [15] found that the preconsolidation pressure is related not only to the loading history of the soil but also to the material composition and the structural characteristics of the soil. Shi et al. [16] performed a research on the characteristics of engineering geological environment at Lingdingyang. Chen et al. [17] analyzed the influence of the structure on the compressive properties of compacted loess with different initial moisture contents. Li et al. [18] conducted a study on the soil-water and shear strength characteristics of unsaturated red clay. Li et al. [19] determined the preconsolidation pressure using quick direct shear tests. Jia and Lei [20] studied the anisotropic consolidation properties of Ariake clay in Japan by the constant rate of strain (CRS) consolidation test using vertically and horizontally cut specimens. Wang et al. [21] analyzed the law of stress-strain under different strain rates based on Lanzhou loess compressive tests. Zhang et al. [22] carried out compression-rebound tests and oedometer tests on specimens prepared at different moisture contents. Xu [23] performed an experimental investigation into the one-dimensional disturbed evolution law of Q3 loess. Jiang et al. [24] researched the consolidation and shear properties of seabed soft soil by means of the one-dimensional oedometer and conventional triaxial compressive tests.

Unfortunately, none of these methods take into account the structural properties of the soil. Therefore, if these methods were used to determine the preconsolidation pressure of structured soil, the accuracy of the determined preconsolidation pressure may be not satisfactory. As is known to all, most of the geomaterial has some certain structural properties, especially for the loess [25–29]. Due to the fact that the loess has the overhead or inlaid granular structural type which is formed under the special geological condition and in the special natural environment, the structure of the loess is particularly prominent. The preconsolidation pressure refers to the maximum effective stress which the natural soil has ever suffered in history. However, the soil is a special natural product, which has a strong “memorizing” function for its stress history. Its “memorizing” function can reflect or express, in the mechanical properties of the natural soil, the influence exerted by the factors, such as the generating environment, the geological history changes, and external forces. Therefore, proposing a method for determining the preconsolidation pressure of the structural soil is of great theoretical significance for and has far-reaching influence on correctly judging which consolidation state the soil layer belongs to, the settlement calculation, studying the structure of the soil, and constructing the constitutive model.

In order to explore the effects of the structural properties on the compression curves of the undisturbed and remoulded loess soil, a series of oedometer tests were performed on the undisturbed and remoulded loess soil speci-

TABLE 1: Material parameters of the loess.

Parameter	Magnitude
Specific gravity, G_s	2.71
Natural moisture content, w (%)	22%
Natural density, ρ (g/cm ³)	1.48
Dry density, ρ_d (g/cm ³)	1.20
Liquid limit, w_L (%)	31.30
Plastic limit, w_p (%)	18.90
Optimum moisture content, w_{opt} (%)	27.2
Maximum dry density, ρ_{mdd} (g/cm ³)	1.69

mens prepared at several moisture moistures. Secondly, according to the analysis of the compression test results, an investigation was made into the structured yield stress of the undisturbed soil, the preconsolidation pressure of the remoulded soil, and the influence of moisture content on the structured yield stress and the preconsolidation pressure. Finally, the determination of the preconsolidation pressure of the structural loess was carried out. The MATLAB program was used to implement the Casagrande method, which determined the preconsolidation pressure and the structured yield stress. On the basis of the reduction method and the concept of eliminating structural strength, the true preconsolidation pressure of the undisturbed loess can be determined with the help of the compression curve of the remoulded soil samples. The influence of moisture content on the preconsolidation pressure, the structured yield pressure, and the structural strength was further analyzed, and the influencing rules were studied.

2. Materials and Methods

2.1. Structured Loess Soil. The loess soil used in the tests was taken from a construction site in the suburb of Xi'an city with the overlying soil depth being 4.0–5.0 meters. The soil sample was yellowish-brown in colour and was in the plastic state which corresponds to a liquidity index ranging between 0 and 1. According to the Chinese standard for engineering classification of soil [30], the tested soil samples in this study were categorized as the typical Q3 loess. The physical and mechanical properties of the soil sample are shown in Table 1.

According to the test requirements, five different initial moisture contents, namely, 8%, 16%, 22%, 28%, and 46.5%, were adopted. The undisturbed loess sample with different initial moisture contents was prepared through the air seasoning method and the water dripping method and then was placed in a moisturizing cylinder for more than 24 hours so that the water was evenly distributed in the sample.

When the remoulded loess sample was prepared, the soil generated during the trimming of the undisturbed loess sample was crushed through a sieve of 1 mm in the aperture diameter. The remoulded loess sample was made using the method of stratified sample pressing. The saturated sample was prepared through the air pumping saturation method.

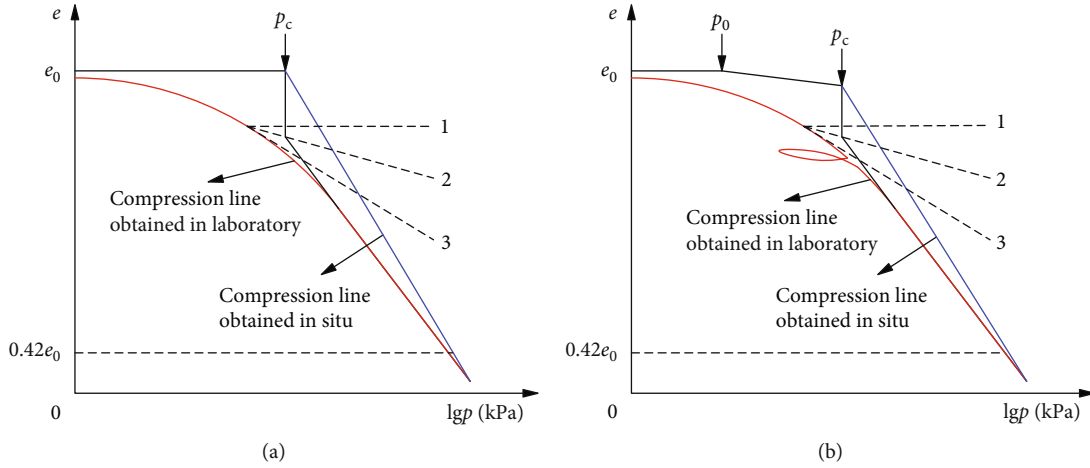


FIGURE 1: Schematic of compression lines obtained in the laboratory and in situ for (a) normally consolidated soil and (b) overconsolidated soil.

2.2. *Oedometer Tests.* To explore the effect of the structural properties on the compression curves of the undisturbed and remoulded loess soil and to study the influence of the structural property on the compressive behaviour, different oedometer tests were performed in accordance with the Chinese standard for geotechnical testing method [31]. These oedometer tests are as follows.

- (1) The oedometer tests on the undisturbed and remoulded loess soil
- (2) The loading-unloading oedometer tests on the undisturbed and remoulded soil samples
- (3) The loading-unloading-reloading oedometer tests on the undisturbed and remoulded soil samples with the load being 400 kPa and 800 kPa, respectively
- (4) The loading-unloading-reloading oedometer tests on the undisturbed soil samples with the load being 50 kPa, 100 kPa, 400 kPa, and 800 kPa

3. Preconsolidation Pressure Determination

3.1. *Conceptualization and Formulation.* The viewpoint proposed by Gong et al. [14] holds the opinion that the corresponding value of the inflection point of the compression curve of the undisturbed soil is the structured yield stress, which is the sum of the preconsolidation pressure and the structural strength, and that the corresponding value of the compression curve of the remoulded soil is the preconsolidation pressure. As is known to all, the traditional Casagrande method has the problem that human factors have great influence on it. The mathematical method which is used to realize the calculating process of this method can eliminate human factors to improve the accuracy of the method. On the basis of the basic theory of the Casagrande method, the MATLAB software was used to realize the Casagrande method, so that the problems caused by the traditional Casagrande method can be eliminated. For example, the maximum value of K can be obtained by the *fminbnd* function of the MATLAB

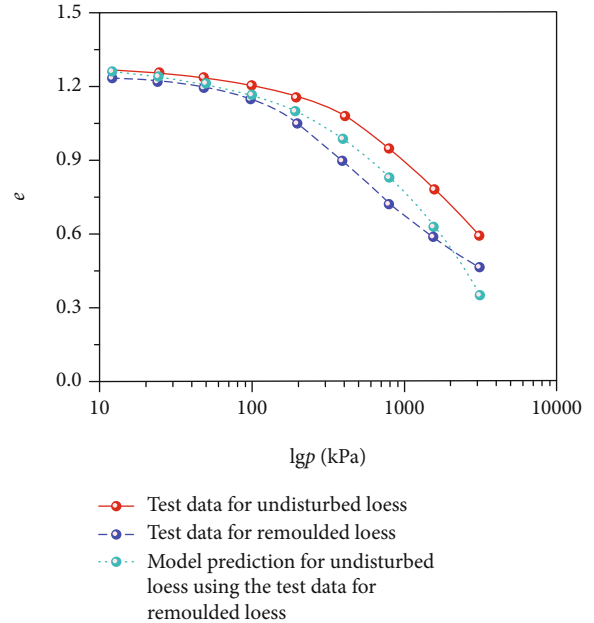


FIGURE 2: Comparison of the compression lines obtained by tests and model prediction.

software. Note that K is the minimum radius of curvature for a curve and *fminbnd* is a MATLAB function for finding the local optimized solution for a function. According to the form of the compression curve, the appropriate function can form the fitting curve and then select the appropriate function to solve or program to solve combined with the specific function form, which not only gets rid of human factors but also can carry out reasonable value according to the compression curve of specific soil samples. As to the disturbance caused by the sampling of the soil, Wei [32] had studied the influence of the disturbance on the strength and the compression characteristics of the soil sample. Some scholars have put forward different methods for deducing the preconsolidation pressure, such as on the basis of the concept of the reference state line through three

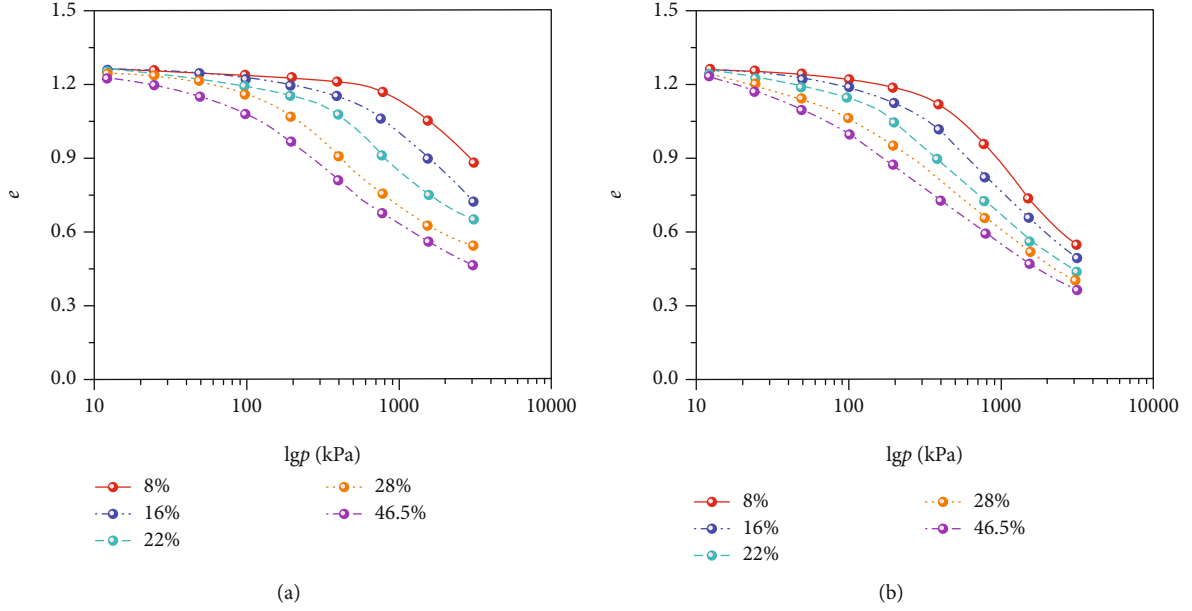


FIGURE 3: Compression lines at different moisture contents for (a) undisturbed loess and (b) remoulded loess.

corresponding test curves as the reference lines. There are also some domestic scholars, such as Li and Qian [33] who put forward the reduction method, Zou et al. [34] who put forward the iteration method, Wang [35] who put forward the four-stage or three-stage polygonal line analysis method, and Wang et al. [36] who put forward the ameliorating method for the mathematical model proposed by Li and Qian [33]. Umar and Sadrekarimi [37] proposed a method of determining the preconsolidation pressure on the basis of a lot of laboratory tests. Hammam et al. [38] presented the evaluation of preconsolidation pressure of undisturbed saturated clays.

Due to the unloading effect caused by sampling, the laboratory oedometer tests are equivalent to a process of recompression. Therefore, according to the conception of the reduction method and eliminating the structural strength, the real preconsolidation pressure of the structural loess can be determined through reducing the compression curve of the remoulded soil sample. As to this problem, Yang and Wei [39] also pointed out in the analysis of the compression deformation calculation that if the initial pressure which the soil layer bears, namely, the self-weight pressure of the overlying soil layer, falls within the bending section of the curve, the compression index of the straight-line section, must be relatively higher.

As is known to all, from the beginning of the soil sampling to the subsequent preparing and then to the specific tests, every section may have some disturbance of different degrees in the soil, resulting in some changes in its internal structure and stress. In addition, there are the human factors and the factors of test instruments in the process of testing. Therefore, the stress state of the current soil sample is not the stress state of the real in situ soil and it is also called the disturbed soil sample. It is inappropriate and inaccurate to deduce the preconsolidation pressure of the in situ soil by using the results of the oedometer tests at this time to judge

which consolidation state the in situ soil belongs to. At the same time, compared with the in situ soil, the sample in the laboratory test truly undergoes a process of unloading and reloading, which is also a disturbance to the original structure of the soil. Generally speaking, the in situ compression curve of the soil and the laboratory compression curve of the soil are shown in Figure 1. In Figure 1, “1” denotes the horizontal line from the inflection point on the compression line, “3” denotes the tangential line at the inflection point, and “2” denotes the angular bisector between “1” and “3.”

In addition, in the process of reduction, the influence exerted by the self-weight unloading of overlying soil and exerted by the recompression should be subtracted and should not pass for the influence exerted by the structural strength. Especially when the soil unloading depth is different, the disparity, which is caused by the self-weight of overlying soil that covers the soil, of this phase between the compression curves of the undisturbed soil sample and the remoulded soil sample will be also enormous, but in fact, it is not caused by the structure.

Particularly for the loess, the confined compression test results indicate that with the changing of the moisture content, the disparity between the compression curves of the undisturbed soil and the remoulded soil increases gradually. To solve this problem, this paper proposes the ameliorating model below:

$$e = e_1 - C_r (\lg p_L)^{1-A} (\lg p)^A + (C_c' - C_s') \lg p_0, \quad (1)$$

$$A = 1 + \frac{\lg (C_s/C_r)}{\lg (\lg p_0 / \lg p_L)}, \quad (2)$$

where p_0 is the overburden self-weight pressure, e_1 can be commonly replaced by the initial void ratio of the soil e_0 , C_r is the compression index of the remoulded soil, C_s is the

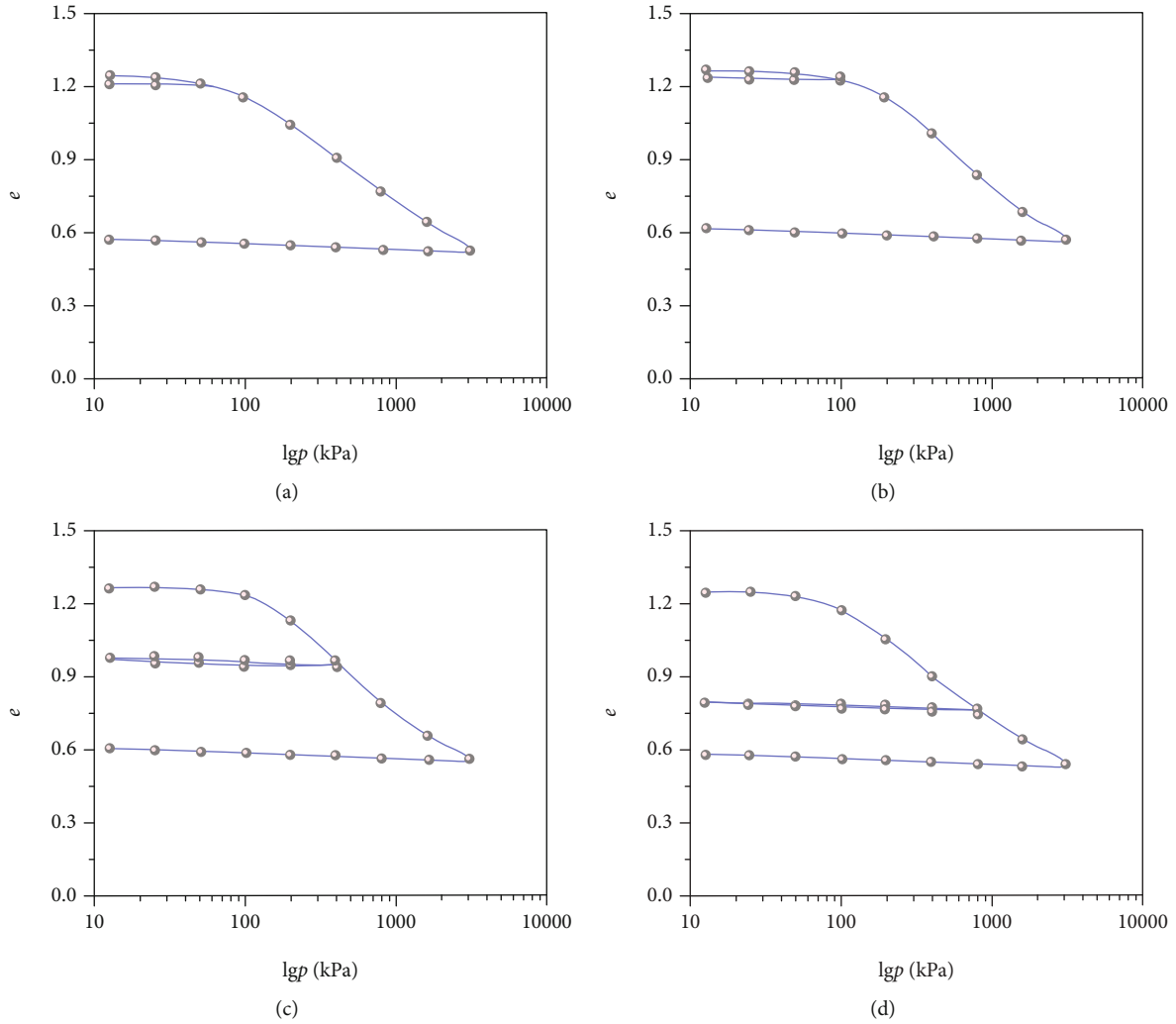


FIGURE 4: Loading-unloading compression lines for undisturbed loess with the first unloading excursion originating at (a) $p = 50$ kPa, (b) $p = 100$ kPa, (c) $p = 400$ kPa, and (d) $p = 800$ kPa.

unloading index of the remoulded soil, P_L is the corresponding pressure value at the intersection point L , C_c' is the compression index corresponding to the overburden self-weight pressure, and C_s' is the unloading index corresponding to the overburden self-weight pressure.

3.2. Verification. In this paper, the preconsolidation pressure of the undisturbed loess soil is deduced and calculated on the basis of the compression curve of the remoulded soil sample. The moisture moisture considered in the determination of the preconsolidation pressure is 22%.

According to the test results, the following parameters were derived: the compression index = 0.419, the unloading index = 0.0302, the intersection point $L = 12800$ (which can be obtained by extending the compression curves of the undisturbed soil and the remoulded soil), the initial void ratio of the soil sample = 1.258, and the overburden self-weight pressure = 59.2 kPa. Due to the proportion problem of the test load rate, here, p_0 was taken as 50 kPa, C_c' as

0.00343, and C_s' as 0.000416. All of the parameters above were substituted into equation (1), which yields

$$e = 1.258 - 0.00623472(\lg p)^{3.9786} + 0.005121. \quad (3)$$

Figure 2 compares the compression lines obtained by tests and model prediction using equation (3). From the comparison, it can be indicated that the determination of the preconsolidation pressure is affected by the sampling process which alters the structural effect of loess. Moreover, it is shown that the compression line of the undisturbed loess can be well predicted by the proposed formulation using the test data for remoulded loess.

4. Results and Discussion

4.1. Test Results. The compression lines at different moisture contents are presented in Figure 3 for the undisturbed and disturbed loess samples. It is found that the compression lines are composed of two stages: the flat stage and the sharp

drop stage. The first stage corresponds to a pressure lower than the structured yield stress. At this stage, the soil compressibility is relatively small and the deformation is dominated by the elastic deformation. The second stage corresponds to a pressure greater than the structured yield stress. At this stage, the structural strength, composed of the cementation effect between soil particles and the specific arrangement of soil particles, is incapable of resisting the external load. Therefore, the soil deformation increases greatly because of the internal collapse and the slippage of soil particles. Moreover, the proportion of the plastic deformation in the overall soil deformation is increasing as an increase in the external load.

Figure 3(a) indicates that the influence of moisture content on the compression line is relatively remarkable, especially for the evolution of the two stages. At a relatively low moisture content, the transition from the flat stage to the sharp drop stage is obvious. However, this transition becomes less obvious with an increase in the moisture content. This phenomenon demonstrates that water is the main factor affecting the bonding strength between soil particles and that the structured property of the undisturbed soil has been damaged by water.

From Figure 3(b), it can be indicated that the influence of moisture content on the compression line of remoulded loess soil is relatively small compared to that for the undisturbed loess soil. At a relatively low moisture content (i.e., 8% and 16%), the transition from the flat stage to the sharp drop stage is obvious for the compression line due to the effect of the secondary structure of loess. At other moisture contents, the compression lines are nearly linear without any inflection point. This also indicates that for the remoulded loess soil, the original structured property has been fully damaged by the compaction and sieving during sampling. Furthermore, the effect of moisture content on the compressibility of the remoulded loess soil where soil particles have been rearranged is relatively small.

A comparison of Figures 3(a) and 3(b) indicates that the compressive deformation of undisturbed loess is less than that for remoulded loess at some moisture content and pressure. Therefore, under this pressure, the compression line of undisturbed loess is more gradual than that of remoulded loess. When the loess structure has been fully damaged, the mechanical behaviour of loess is no longer affected by the structured property of loess. In this case, the compression line of undisturbed loess becomes similar to the compression line of remoulded loess. Consequently, a greater moisture content corresponds to a more similar compression line for the undisturbed and remoulded loess.

Figure 4 presents the loading-unloading compression lines for undisturbed loess with the first unloading excursion originating at various pressures. From this figure, it can be indicated that the difference between the slopes of the initial compression line and the unloading-reloading compression line is obvious when the first unloading excursion is originating at 50 kPa. This also demonstrates that the structured property of loess has a significant effect on the shape of compression line before the occurrence of damage to the structured property of loess. For undisturbed loess, when the

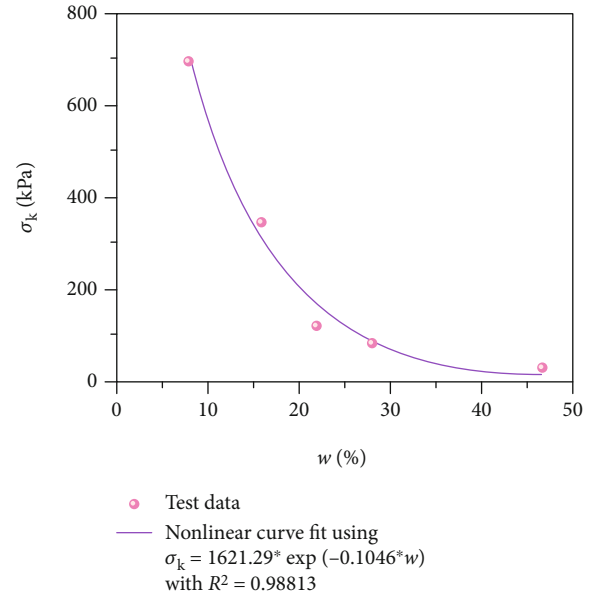


FIGURE 5: Relation between structural yield stress and moisture content for undisturbed loess.

unloading-reloading occurs at a pressure lower than the structured yield stress, the slope of the reloading line is approximately equal to that of the initial loading line. This means that the swelling index is the same as that of the initial loading line. However, when the pressure becomes greater than the structured yield stress, the slope of the unloading line (i.e., the swelling index) decreases with an increase in the pressure at which the unloading excursion originates, while it increases with an increase in the structured yield stress. This indicates that when the pressure is lower than the structured yield stress, the structured strength of undisturbed loess can resist a certain amount of pressure. In the meantime, the elastic deformation dominates and the plastic deformation is relatively small. Because of this, the swelling index of the unloading line is almost identical to that of the initial loading line. When the pressure is greater than the structured yield stress, with an increase in the pressure, the structured property of loess is gradually damaged by the increased pressure. Finally, the structure of loess is fully damaged, and thus, the slope of the compression line increases while the swelling ability decreases. In other words, the greater the pressure, the less the swelling line.

4.2. Discussion on Effects of Moisture Content. The relation between the moisture content and the structured yield pressure of the undisturbed soil samples is shown in Figure 5. As can be seen in Figure 5, the relationship between the structured yield pressure and moisture content can be well fitted by an exponential function. The function is expressed in equation (4). As can be seen in Figure 5, with an increase in moisture content, the structured yield stress decreases gradually. Nevertheless, the increase in moisture content, when the moisture content is relatively low, obviously has a greater influence on the decreasing extent of the structured

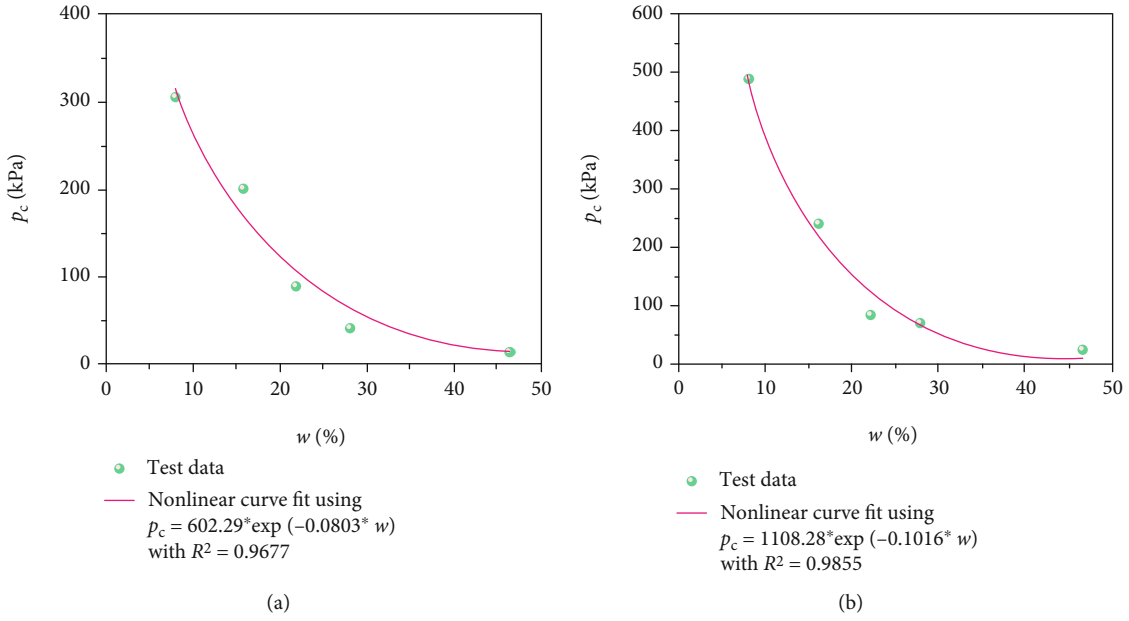


FIGURE 6: Relation between preconsolidation pressure and moisture content for (a) remoulded loess and (b) undisturbed loess.

yield stress than that when the moisture content is relatively high.

$$\sigma_k = a_k \exp(b_k w). \quad (4)$$

The relation between moisture content and the preconsolidation pressures of remoulded and undisturbed soil samples is presented in Figure 6. As can be seen in Figure 6, the relationship between the preconsolidation pressure of the remoulded soil and undisturbed soil and the moisture content can be expressed by an exponential function as presented in equation (5).

$$p_c = a_c \exp(b_c w). \quad (5)$$

As to the influence exerted by the moisture moisture on the structural strength, different scholars have obtained different research results, due to the fact that different scholars give diverse definitions for structural strength. For instance, Dang [40] defined the structural strength as the stress difference between the undisturbed loess and the corresponding remoulded loess when the natural structure was destroyed. It was found by him that there was an exponential relationship between the structural strength of the unsaturated loess and the moisture content. Tian et al. [41] made a research and found that the changing curve of the structural strength of the undisturbed loess with the initial degree of saturation of the sample conforms to the relationship of a power function. Xie et al. [42] pointed out that there was the relationship of an exponential function between the structural strength of the Q₂ loess and the moisture content. Chen et al. [43] stated that there was a relationship of the linear correlation between the structural strength and the structured yield pressure.

Based on the tests above, the values of the structural strength of the undisturbed soil under different moisture

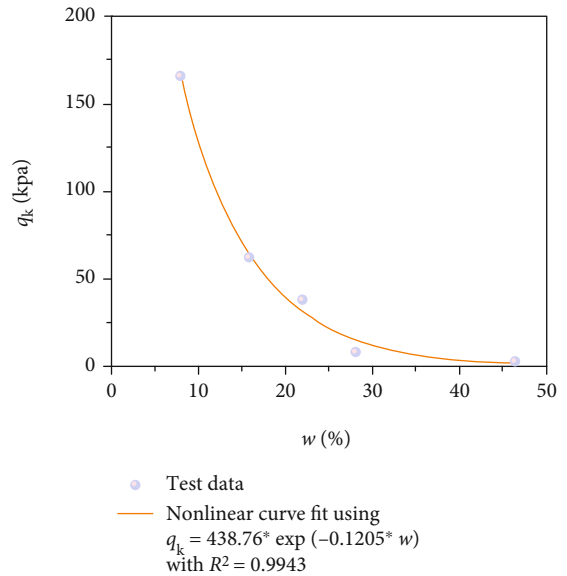


FIGURE 7: Relation between structural strength and moisture content for undisturbed loess.

contents are obtained. The influence which the moisture content exerts on the structural strength is shown in Figure 7. As can be seen in Figure 7, the relationship between the structural strength of the undisturbed soil and the moisture content can be fitted through an exponential function. The expression is expressed in equation (6).

$$q_k = a_q \exp(b_q w). \quad (6)$$

It can be seen from the above that due to the structure of loess formed in the special climatic conditions and geological environment, the microstructure of loess is characterized by

macrospores and high strength. However, it contains a lot of mineral components of soluble salts in the loess, which form cementation in the particles. At the same time, due to the different geological history, the particle arrangement shows strong structural strength. However, with the increase of water content, the cementation strength formed by various cementitious substances and water molecules at the contact point of coarse particles is gradually lost and the adsorption cohesion is also partially lost, so the structural strength between particles will rapidly decrease until it is completely lost. The remoulded soil sample had adjusted the cementation and arrangement of the particles completely, which does not have the cementation effect on the initial geological environment. In addition, the effect of the arrangement of particles on the whole structure is weaker than that of cementation, so the change of water content has a weaker impact on it. Therefore, the change of water content has an overall impact on the structural strength, structural yield pressure, and preconsolidation pressure of the undisturbed soil sample.

5. Conclusions

Confined oedometer tests were performed on undisturbed and remoulded loess soil samples prepared at different moisture contents to investigate the compressive behaviour of structural loess soil. A method of determining the preconsolidation pressure of structural loess soil was proposed. This method combines the MATLAB-based Casagrande method with the reduction method. Moreover, the influence of moisture content on the preconsolidation pressure of structural loess soil was analyzed. The conclusions drawn from this study can be summarized as follows:

- (1) The experimental results indicate that the influence of the structure of loess on the compression curves of undisturbed and remoulded loess soil is significant, especially for the range surrounding the structural yielding point on the compression curve
- (2) The proposed method for determining the preconsolidation pressure of structural loess soil is more accurate than the traditional Casagrande method as it considers the structural behaviour and eliminates the personal error
- (3) With an increase in the moisture content, the structured yield stress, the preconsolidation pressure, and the structural strength of the loess all decrease gradually, conforming to an exponential function

Data Availability

The data used to support the findings of this study are available from the corresponding authors upon request.

Conflicts of Interest

The authors declare that there is no conflict of interest regarding the publication of this paper.

Acknowledgments

This research was funded by the Natural Science Fund of the University of Anhui Province (grant numbers KJ2019ZD60 and KJ2013B223), the Excellent Young Talents Foundation Project in Anhui Province (grant number 2012SQRL195), the Talent Introduction in Hefei University (grant number 13RC10), the Provincial Quality Engineering Projects of the Education Department of Anhui Province (grant number 2017zhkt383), and the Undergraduate Education Quality Project in Hefei University (grant numbers 2018HFMOOC04 and 2018HFJC05).


References

- [1] J. Ju, "Prediction of the settlement for the vertically loaded pile group using 3D finite element analyses," *Marine Georesources and Geotechnology*, vol. 33, no. 3, pp. 264–271, 2014.
- [2] Y. Wang, S. H. Gao, C. H. Li, and J. Q. Han, "Energy dissipation and damage evolution for dynamic fracture of marble subjected to freeze-thaw and multiple level compressive fatigue loading," *International Journal of Fatigue*, vol. 142, p. 105927, 2020.
- [3] P. Guo, F. Liu, G. Lei et al., *Predicting Response of Constructed Tunnel to Adjacent Excavation with Dewatering*, Geofluids, 2021.
- [4] D. Wu, K. Xu, P. Guo, G. Lei, K. Cheng, and X. Gong, "Ground deformation characteristics induced by mechanized shield twin tunnelling along curved alignments," *Advances in Civil Engineering*, vol. 2021, Article ID 6640072, 17 pages, 2021.
- [5] T. M. Le, B. Fatahi, and H. Khabbaz, "Numerical optimisation to obtain elastic viscoplastic model parameters for soft clay," *International Journal of Plasticity*, vol. 65, no. 2, pp. 1–21, 2015.
- [6] Y. Wang, C. H. Li, and J. Q. Han, "On the effect of stress amplitude on fracture and energy evolution of pre-flawed granite under uniaxial increasing-amplitude fatigue loads," *Engineering Fracture Mechanics*, vol. 240, p. 107366, 2020.
- [7] H. Tang, D. Zhao, D. Wang, and Q. Dang, "Experimental investigation of creep behaviour of loess under different moisture contents," *Bulletin of Engineering Geology and the Environment*, vol. 79, no. 1, pp. 411–422, 2019.
- [8] P. Guo, X. Gong, and Y. Wang, "Displacement and force analyses of braced structure of deep excavation considering unsymmetrical surcharge effect," *Computers and Geotechnics*, vol. 113, p. 103102, 2019.
- [9] A. Sridharan, B. M. Abraham, and B. T. Jose, "Improved technique for estimation of preconsolidation pressure," *Géotechnique*, vol. 41, no. 2, pp. 263–268, 1991.
- [10] D. Demers and S. Leroueil, "Evaluation of preconsolidation pressure and the overconsolidation ratio from piezocone tests of clay deposits in Quebec," *Canadian Geotechnical Journal*, vol. 39, no. 1, pp. 174–192, 2002.
- [11] A. Soltani, A. Taheri, A. Deng, and M. Azimi, "A note on determination of the preconsolidation pressure," *Journal of Testing and Evaluation*, vol. 47, no. 6, pp. 4535–4550, 2019.
- [12] X. Cai, Z. Zhou, L. Tan, H. Zang, and Z. Song, "Fracture behavior and damage mechanisms of sandstone subjected to wetting-drying cycles," *Engineering Fracture Mechanics*, vol. 234, p. 107109, 2020.

- [13] Z. Liu, *Mechanics and Engineering of the Loess*, Shanxi Science and Technology Press, Shanxi, China, 1997.
- [14] X. Gong, C. Xiong, K. Xiang, and Y. Hou, "The formation of clay structure and its influence on mechanical characteristics of clay," *Journal of Hydraulic Engineering*, vol. 10, pp. 43–47, 2000.
- [15] Q. Wang, Y. Kong, X. Zhang, Y. Ruan, and Y. Chen, "Mechanical effect of pre-consolidation pressure of structural behaviour soil," *Journal of Southwest Jiaotong University*, vol. 51, pp. 987–994, 2016.
- [16] Y. Shi, S. Ma, N. Zeng, and Z. Xia, "Characteristics of engineering geological environment at Lingdingyang Estuary of Pearl River Mouth, South China Sea," *Journal of Coastal Research*, vol. 66, pp. 25–33, 2013.
- [17] C. Chen, X. Jiang, J. Yang, J. Zhang, and J. Xue, "Influence of soil structure on confined compression behaviour of compacted loess," *Chinese Journal of Rock Mechanics and Engineering*, vol. 33, pp. 1939–1944, 2014.
- [18] L. Li, S. Luo, H. Jiang, L. Song, B. Ding, and C. Li, "Soil-water and shear strength characteristics of unsaturated red clay," *Journal of Southwest Jiaotong University*, vol. 49, pp. 393–398, 2014.
- [19] H. Li, Y. Zhang, B. Shi, and L. Hu, "Determination of pre-consolidation pressure using quick direct shear tests," *Coal Geology and Exploration*, vol. 46, no. 1, pp. 115–118, 2018.
- [20] R. Jia and H. Lei, "Experimental research on anisotropic consolidation behaviour of Ariake clay," *Rock and Soil Mechanics*, vol. 40, pp. 1–8, 2019.
- [21] W. Wang, L. Wang, H. Liu, and M. Hu, "Test study on rate dependent characteristic of soil compression index-taken Lanzhou loess as study object," *Journal of Henan University (Natural Science)*, vol. 48, pp. 113–118, 2018.
- [22] Z. Zhang, Y. Xu, and Z. Liu, "Experimental research on the influence of the soil structure on the resilience of loess," *Journal of Xi'an University of Architecture and Technology (Natural Science Edition)*, vol. 48, pp. 500–504, 2016.
- [23] Y. Xu, "Experimental study on one-dimensional disturbed evolution law of Q3 loess," *Journal of West Anhui University*, vol. 34, pp. 110–114, 2018.
- [24] M. Jiang, Z. Li, P. Huang, and J. Liu, "Experimental study on microstructure and mechanical properties of seabed soft soil from South China Sea," *Chinese Journal of Geotechnical Engineering*, vol. 29, pp. 16–20, 2017.
- [25] Y. Xu, P. Guo, Y. Wang, C.-W. Zhu, K. Kang, and G. Lei, "Modelling the triaxial compression behavior of loess using the disturbed state concept," *Advances in Civil Engineering*, vol. 2021, Article ID 6638715, 17 pages, 2021.
- [26] Y. Wang, W. K. Feng, R. L. Hu, and C. H. Li, "Fracture evolution and energy characteristics during marble failure under triaxial fatigue cyclic and confining pressure unloading (FCCPU) conditions," *Rock Mechanics and Rock Engineering*, vol. 54, no. 2, pp. 799–818, 2020.
- [27] Z. Song, Y. Wang, H. Konietzky, and X. Cai, "Mechanical behavior of marble exposed to freeze-thaw-fatigue loading," *International Journal of Rock Mechanics and Mining Sciences*, vol. 138, p. 104648, 2021.
- [28] Y. Xu and P. Guo, "Disturbance evolution behaviour of loess soil under triaxial compression," *Advances in Civil Engineering*, vol. 2020, Article ID 4160898, 14 pages, 2020.
- [29] Y. Qian, P. Guo, Y. Wang, Y. Zhao, H. Lin, and Y. Liu, "Advances in laboratory-scale hydraulic fracturing experiments," *Advances in Civil Engineering*, vol. 2020, Article ID 1386581, 18 pages, 2020.
- [30] GB/T50145–2007, *Standard for Engineering Classification of Soil*, China Jihua Press, Beijing, 2007.
- [31] GB/T50123–2019, *Standard for Geotechnical Testing Method*, China Jihua Press, Beijing, 2019.
- [32] R. Wei, "Engineering behaviour of soft clay," *China Civil Engineering Journal*, vol. 19, pp. 73–85, 1986.
- [33] T. Li and S. Qian, "Evaluation of soil sample disturbance and determination of its preconsolidation pressure," *Journal of Geotechnical Engineering*, vol. 9, pp. 21–30, 1987.
- [34] Y. Zou, J. Wang, and M. Shao, "Study on iteration of ascertaining preconsolidation pressure," *Journal of Geotechnical Engineering*, vol. 16, pp. 34–37, 1994.
- [35] L. Wang, "Study on compressibility of structured soft soil," *China Civil Engineering Journal*, vol. 37, pp. 46–53, 2004.
- [36] G. Wang, S. Xiao, and W. Zhou, "Determination of preconsolidation pressure and structural strength of undisturbed structural soils," *Journal of Geotechnical Engineering*, vol. 25, pp. 249–251, 2003.
- [37] M. Umar and A. Sadrekarimi, "Accuracy of determining pre-consolidation pressure from laboratory tests," *Canadian Geotechnical Journal*, vol. 54, no. 3, pp. 441–450, 2017.
- [38] A. H. Hammam, A. I. Abel-Salam, and M. A. Yousef, "On the evaluation of pre-consolidation pressure of undisturbed saturated clays," *HBRC Journal*, vol. 13, pp. 47–53, 2019.
- [39] S. Yang and R. Wei, "Influence of sampling disturbances on strength and consolidation behaviour of normally consolidation clay," *Hydro-Science and Engineering*, vol. 1, pp. 70–83, 1992.
- [40] J. Dang, "Direct optimal dispatch of large scale water supply system," *Journal of Hydraulic Engineering*, vol. 7, pp. 79–83, 2001.
- [41] K. Tian, H. Zhang, B. Zhang, and Y. Luo, "Study on structural properties and structural strength characteristics of loess," *Journal of Hydraulic Engineering*, vol. 24, pp. 64–67, 2005.
- [42] X. Xie, D. Wang, and F. Zhao, "Damage constitutive model of structural Q2 loess under uniaxial compression," *Hydrogeology & Engineering Geology*, vol. 29, pp. 47–50, 2008.
- [43] L. Chen, J. Li, J. Wang, and Q. Li, "Relationship between structural strength of loess and structured yield pressure," *Journal of Geotechnical Engineering*, vol. 30, pp. 895–899, 2008.

Research Article

Investigation on Nonuniform Extension of Hydraulic Fracture in Shale Gas Formation

Zhiheng Zhao ¹, Youcheng Zheng,² Yili Kang,³ Bo Zeng,¹ and Yi Song¹

¹Shale Gas Research Institute, PetroChina Southwest Oil & Gas Field Company, Chengdu 610051, China

²PetroChina Southwest Oil & Gas Field Company, Chengdu 610051, China

³State Key Laboratory of Oil and Gas Reservoir Geology and Exploitation, Southwest Petroleum University, Chengdu 610500, China

Correspondence should be addressed to Zhiheng Zhao; bestznn@126.com

Received 3 February 2021; Revised 22 February 2021; Accepted 6 March 2021; Published 19 March 2021

Academic Editor: Zhengyang Song

Copyright © 2021 Zhiheng Zhao et al. This is an open access article distributed under the Creative Commons Attribution License, which permits unrestricted use, distribution, and reproduction in any medium, provided the original work is properly cited.

Hydraulic fracturing with multiple clusters has been a significant way to improve fracture complexity and achieve high utilization of shale formation. This technology has been widely applied in the main shale area of North America. In Changning shale block of China, it, as a promising treatment technology, is being used in horizontal well now. Due to the anisotropy of mechanical property and the stress shadowing effect between multiclusters, fractures would extend nonuniformly and even some clusters are invalid, leading to a poor treatment performance. In this work, based on the geology and engineering characteristics of Changning shale block, different cluster number, cluster spacing, perforation distribution, and flow rate were discussed by the numerical simulation method to clarify multifracture propagation. It is implied that with the reduction of cluster number and the growth of cluster spacing and flow rate, the length and average width of interior fractures are inclined to increase due to the mitigation of stress shadowing effect, contributing to the lower standard deviation (SD) of fracture length, but too small cluster number or too large cluster spacing is not recommended. Besides, the perforation distribution with more perforations in interior fractures can get larger length and average width of interior fractures compared with another two perforation distributions because of more fractional flow rates obtained, which results in more even fracture propagations. In Changning shale block, multicluster hydraulic fracturing with 4-6 clusters in a stage has been employed in 300-400 m well spacing, and diversion technology, limited-entry perforation (36-48 perforations per stage), high flow rate (16 m³/min), and small-sized ceramic proppant (100 mesh) are used to get better shale gas production. To promote the even propagation of fractures further, nonuniform perforation distribution should be introduced in the target shale area.

1. Introduction

Multistage hydraulic fracturing in horizontal well has been proved to be an efficient technology to stimulate shale formation with extremely low porosity and permeability [1–3]. To enhance production and realize beneficial development, multicluster hydraulic fracturing within a stage has been extensively employed in the main shale area of North America so far. Compared with conventional hydraulic fracturing, this technology can provide more flow paths by perforating more clusters, and takes advantage of induced stress during fracture propagation to increase the fracture complexity between

clusters and shorten the distance of gas flow from shale reservoir matrix to hydraulic fractures, improving the utilization of reservoir [4–7], which is shown in Figure 1. However, based on the data from production log and distributed acoustic sensor, one-third of perforation clusters do not extend and cluster efficiency is low, leading to undesirable shale gas production [8, 9].

Uneven extension of hydraulic fractures in multicluster fracturing has been investigated by many scholars. Germanovich and Astakhov and Olson pointed out that the flow rate was dynamically distributed in fractures, and the length and width of interior fractures were restricted during parallel

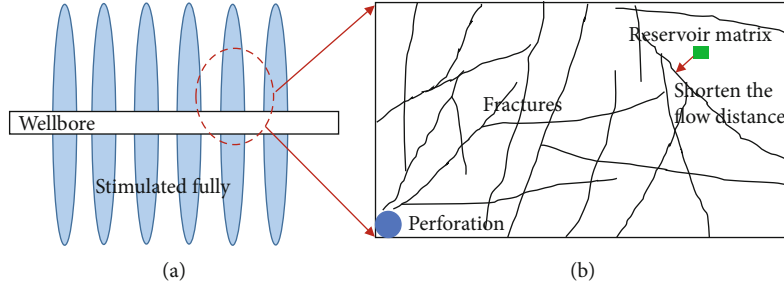


FIGURE 1: Mechanism schematic diagram of multistage hydraulic fracturing in shale.

fracture extension [10, 11]. Morrill studied the stress field around fracture tip and hydraulic fracture morphology by numerical simulation [12]. Afterwards, a 2D model setup through the displacement discontinuity method (DDM) was used by Bunger et al. and Cheng to discuss stress field distribution and fracture geometry [5, 13]. Peirce and Bunger developed a full coupling model and noted that nonuniform cluster spacing could decrease the uneven propagation of multiple fractures [14]. Shin and Sharma simulated the process of fracture extension by the finite element method and researched on the length and height of hydraulic fracture [15]. Then, Wu and Olson employed the DDM to build pseudo 3D model and demonstrated that fracture geometry was influenced by not only the stress shadowing effect but also the dynamic flow rate [16]. Zhao et al. established a multifracture simultaneous propagation model which coupled elastic deformation of rock, stress interaction, fluid flow, and flow distribution in fractures to optimize cluster spacing based on the sweep area of fractures [17]. Furthermore, a nonplanar 3D hydraulic fracturing simulator was developed by Wu et al. to study fracture width and fracture geometry due to induced stress among clusters [18]. In recent year, Lin et al. applied the DDM to calculate formation stress change and the finite difference method (FDM) to compute reservoir pressure rise, simulating nonplanar propagation of multiple hydraulic fractures [19]. And Wang et al. also studied fracture extension and evolution under different stress conditions [20–23]. As well, a phase-field modeling was used by Alotaibi et al. to study hydraulic fracture in heterogeneous formation with layers [24].

In multicluster hydraulic fracturing, though stress shadowing effect can improve the degree of fracture complexity due to fracture diversion, it restrains the propagation of interior fractures forward. Besides, mechanical properties and in situ stress of shale formation can also lead to uneven fracture extension [25, 26]. In the main shale area of North America, such as Haynesville, Permian Basin, Eagle Ford, and Bakken, multicluster hydraulic fracturing has now developed into a mature and reliable technology [25, 27–29]. And some effective measures, like limited-entry perforation, have been taken to increase perforation cluster efficiency and promote even propagation of fractures. In Changning shale block, one of the most promising shale gas production areas located in Sichuan Basin, China, multicluster hydraulic fracturing as an advanced treatment technology is being used in shale horizontal well. However, there are some different properties of

shale formation between two areas which are shown in Table 1, so the extension of multifracture and fracture geometry in the reservoir is likely to exhibit diversely. Additionally, few studies focus on the fracture extension in Changning shale block except Xie et al. who mostly discussed hydraulic fractures in only 3 clusters' perforation within one stage [30]. Therefore, based on the geology and engineering characteristics of Changning shale block, investigation of the effects of cluster number, cluster spacing, perforation distribution, and flow rate on fracture propagation in multicluster hydraulic fracturing by the numerical simulation method is indispensable.

2. Assumptions and Methodology

Hydraulic fracturing is a complex process with multifield coupling, showed in Figure 2. In this study, some assumptions are made to improve computational efficiency: (1) injection fluid is the incompressible Newtonian fluid; (2) the fluid is one-dimensional flow in the fractures, which is effected by Carter filtration; and (3) the formation rock is homogeneous, and it is the liner elastic material. [31, 32]. When multifracture is extended, the balance of flow pressure obeys Kirchoff's second law, including perforation friction, pressure drop in fractures, and wellbore friction [32]. Based on flow conservation in the clusters, the relationship of pressure and flow is expressed as follows [33, 34]:

$$P_i = P_{\text{perf},i} + \Delta p_{\text{frac},1} + \sum_{j=1}^i P_{f,j} - P_g (i \in 1 - n), \quad (1)$$

$$P_{n+1} = Q - \sum_{i=1}^n q_i, \quad (2)$$

where $P_{\text{perf},i}$ stands for the perforation friction, $P_{\text{frac},1}$ is the pressure of fracture inlet in cluster i , $P_{f,j}$ is the wellbore friction of segment j , P_g is the pressure in well heel, Q is the total flow, and q_i represents the flow of cluster i .

According to the principle of material balance, the injection flow equals fracture volume increment and fluid filtration [31]:

$$\int_0^t Q dt = \sum_1^N \int_0^{L_{f,i}(t)} \frac{\pi}{4} h_f w_f ds + \sum_1^N \int_0^{L_{f,i}(t)} \int_0^t q_v(s,t) dt ds, \quad (3)$$

TABLE 1: Comparison of the main reservoir geological parameters in Changning and North America shale area.

Shale area	Depth (m)	Total organic carbon (%)	Porosity (%)	Brittle mineral (%)	Pressure coefficient	Horizontal stress difference (MPa)
Changning	2000~4500	2.5~4.8	3.4~7.9	50~80	1.2~2.1	9~20
Haynesville	3000~4700	2.0~7.0	5.0~11.0	65~75	1.6~2.1	3~6
Eagle Ford	1300~3600	2.0~6.5	3.4~14.6	67~87	1.3~2.0	/
Duvernay	3000~4200	2.0~6.0	3.0~6.0	~40	1.8~2.1	/

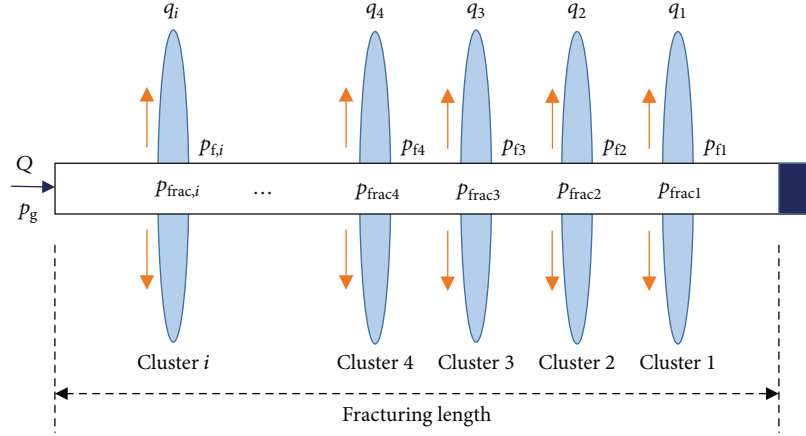


FIGURE 2: Schematic of multifracture propagation.

where $L_{f,i}$ stands for the fracture length in cluster i , N is the number of fractures, q_v is the viscosity of fluid filtration, h_f is the fracture height, w_f is the fracture width, s is the fracture element, and t is the fracturing time.

The induced stress is caused between clusters during multifracture propagation, and fracture elements are effected mutually. The equation of induced stress field is as follows [32]:

$$\sigma_n^i = \sum_{j=1}^N G^{ij} C_{nm}^{ij} D_n^j + \sum_{j=1}^N M^{ij} C_{ns}^{ij} D_s^j, \quad (4)$$

$$\sigma_s^i = \sum_{j=1}^N G^{ij} C_{ss}^{ij} D_s^j + \sum_{j=1}^N M^{ij} C_{sn}^{ij} D_n^j, \quad (5)$$

where σ_n^i and σ_s^i stand for the normal stress and shear stress, respectively, G^{ij} is the 3D correction factor, C^{ij} is the stress of fracture element, D_n^j and D_s^j are the strains of fracture element, and the value of i and j is 1 ~ N .

The stress intensity factor of fracture tip is calculated firstly when the fracture is extended. Fracture tip increases an element if meeting the condition of fracture propagation. The maximum circumferential stress criterion is expressed by the equivalent intensity factor [35, 36]:

$$K_e = \frac{1}{2} \left[K_I (1 + \cos \theta) \cos \frac{\theta_f}{2} - 3K_{II} \sin \theta_f \right] \geq K_{IC}. \quad (6)$$

Based on the DDM, the stress intensity factor of K_I and K_{II} can be calculated as follows [28, 29]:

$$K_I = \frac{\sqrt{2\pi}G}{4\sqrt{a}(1-\nu)} D_n, \quad (7)$$

$$K_{II} = \frac{\sqrt{2\pi}G}{4\sqrt{a}(1-\nu)} D_s, \quad (8)$$

where G stands for the shear modulus of formation rock, ν is the Poisson ratio, a is the half length of discrete fracture element, D_n and D_s represent the normal and shearing displacement discontinuities, respectively.

The normal and shearing displacements are calculated by the induced stress field, and nonlinear equations of stress- and flow pressure-coupled fields are calculated by the Levenberg-Marquardt iteration method.

3. Simulation Results

3.1. Basic Characteristics of Changning Shale. High-quality shale, belonging to the Upper Ordovician Wufeng Formation-Lower Silurian Longmaxi Formations, is well developed in Changning block. Its total organic carbon is 2.5~4.8%, the porosity is 3.4~7.9%, the gas content is 3.1~6.8%, and the brittle mineral content is 50~80%. And its Young's modulus is 34~47 GPa and Poisson's ratio is 0.21~0.3. The horizontal stress difference of shale formation in Changning is 9~20 MP, which is higher than that of North America area. Multicluster hydraulic fracturing technology is

being used to improve the efficiency of development in Changning shale block. Based on the geological characteristics and engineering parameters of target shale area in Changning, multifracture extension model was established to study the effects of clusters, cluster spacing, perforation distribution, and flow rate on fracture extension. The main basic model parameters are listed in Table 2.

3.2. Effects of Cluster Number on Fracture Propagation. Cluster number and cluster spacing are two vital parameters in the optimization design of multicluster hydraulic fracturing. In this part, effects of cluster number on fracture extension are discussed first. The cluster number is from 3 to 6 within a stage which is consistent with the completion design in Changning shale block. Cluster spacing (5 m), total injection rate ($14 \text{ m}^3/\text{min}$), and time are kept constant. The fracture geometries of various clusters simulated are showed in Figure 3.

Based on the stimulation results above, it is implied that the propagation of interior fractures is restricted compared with the exterior fractures. And with the increase in cluster number, the degree of restriction is inclined to heighten. Besides, the length and average width of interior fractures are smaller than those of the exterior fractures (Figure 4). It is likely that stress shadowing effect and stress superposition increase the flow resistance of interior fractures and less fracturing fluid flows into them, inhibiting the interior fracture extension.

3.3. Effects of Cluster Spacing on Fracture Propagation. In this section, effects of cluster spacing on fracture extension are investigated under the 6 clusters. In Changning shale block, the cluster spacing is decreasing in recent years, and the average cluster spacing is less than 20 m. In multifracture propagation model, the cluster spacing are 5 m, 10 m, and 15 m, respectively. Cluster number (6 clusters), total injection rate ($14 \text{ m}^3/\text{min}$), and time are kept constant. The fracture geometries of various cluster spacing are showed in Figure 5.

The fracture geometry is significantly influenced by cluster spacing according to Figure 5. With the decrease in cluster spacing, the restriction degree of interior fractures tends to strengthen remarkably. And the length and average width of two interior fractures are shorten compared with those of two exterior fractures in the case of cluster spacing 5 m (Figure 6). The main reasons are that when cluster spacing declines to 5 m, stress shadowing effect between clusters becomes stronger, inhibiting fracturing fluid entering into the interior fractures. Moreover, the interior fractures are squeezed intensively by the induced stress. Recently, cluster number has been growingly increasing and cluster spacing has been decreasing obviously in shale hydraulic fracturing at field, so the optimization design of construction parameter is particularly important for fracture extension and fracture propping.

3.4. Effects of Perforation Distribution on Fracture Propagation. Perforation parameters, including perforation number, perforation distribution, and phase angle, have a crucial influence on fracture extension in multicluster hydraulic fracturing. In order to promote fracture initiation and consider proper pumping pressure, 48 and 36 perfora-

TABLE 2: The main basic model parameters.

Parameters	Value
Average maximum horizontal stress (MPa)	88
Average minimum horizontal stress (MPa)	72
Young's modulus (GPa)	41
Poisson's ratio	0.26
Fracture height (m)	15
Total injection rate (m^3/min)	9-15
Cluster number	3-6
Cluster spacing (m)	5-15
Perforation number per stage	48
Fluid viscosity (mPa s)	2

tions per stage with uniform perforation distribution are widely used in Changning shale block. In these cases, 48 perforations with uniform and nonuniform perforation distribution are designed to study fracture extension in a stage with 6 clusters (Table 3). Cluster number (6 clusters), cluster spacing (10 m), total injection rate ($14 \text{ m}^3/\text{min}$), and time are kept constant. The fracture geometries of different perforation distributions are showed in Figure 7.

From Figure 7, it is clear that compared with the uniform perforation distribution (Case 1), the two interior fractures of Case 2 extend more evenly. But in Case 3, the two interior fractures are inhibited and cannot extend forward. Obviously, the length and average width of the two interior fractures of Case 2 are bigger than those of other two cases (Figure 8). The main reason is that under the same flow rate and total perforation number, the cluster with more perforations can get more fractional flow rates, minimizing the stress shadowing effect, so the fracture expands more easily compared with the fracture in cluster with less perforations.

3.5. Effects of Flow Rate on Fracture Propagation. In Changning shale block, flow rate is usually $10\text{-}16 \text{ m}^3/\text{min}$. Under the same other parameters, various flow rates ($9 \text{ m}^3/\text{min}$, $12 \text{ m}^3/\text{min}$, and $15 \text{ m}^3/\text{min}$) are set to research on fracture extension in a stage with multicluster. Cluster number (6 clusters), cluster spacing (10 m), and total injection volume (1200 m^3) are kept constant. The fracture geometries of different flow rates are showed in Figure 9.

It is obvious that the propagation of interior fractures is restricted severely at the small flow rate. With the growth of flow rate, interior fractures tend to expand forward with the exterior fractures. Furthermore, from Figure 10, the length and average width of interior fractures get larger as the flow rate becomes higher. Based on Equation (4), it is found that perforation friction pressure gets higher due to the increase in flow rate, contributing to higher bottom hole pressure and mitigating stress shadowing effect between clusters, which is beneficial for the even propagation of fractures.

4. Discussion

In multicluster hydraulic fracturing, cluster number, cluster spacing, perforation distribution, and flow rate are significant

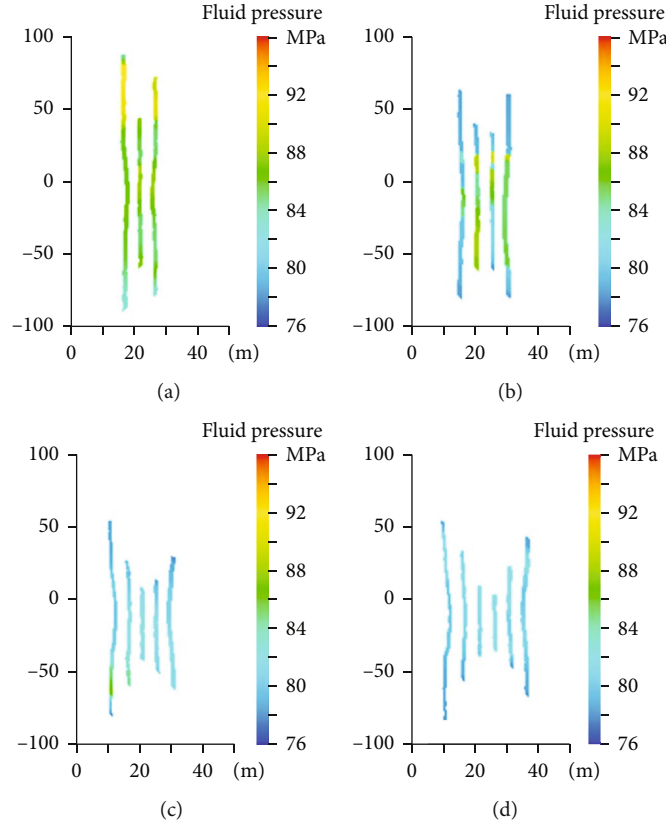


FIGURE 3: Effects of different numbers of clusters on fracture geometry: (a) 3 clusters, (b) 4 clusters, (c) 5 clusters, and (d) 6 clusters.

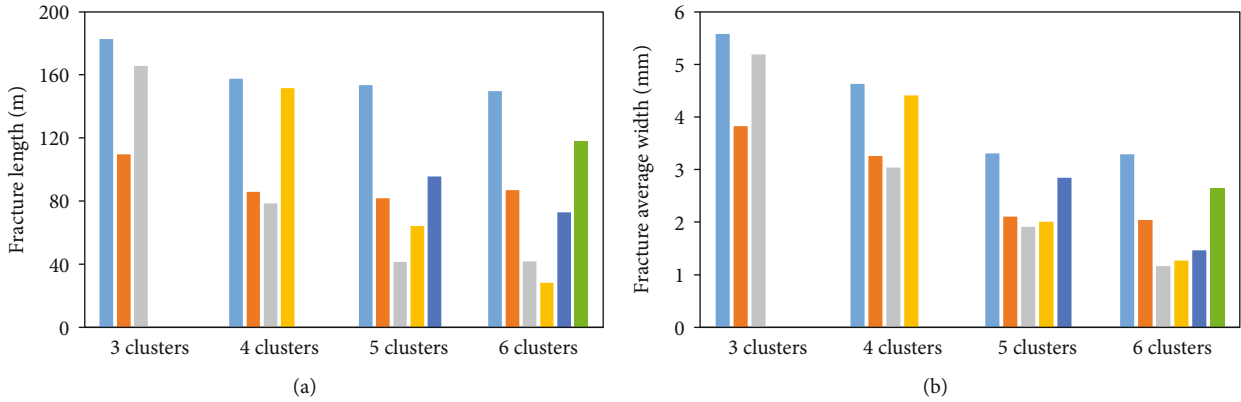


FIGURE 4: Length (a) and average width (b) of multifracture in a stage with different cluster numbers.

impact factors for fracture extension [18, 37–39]. Based on the simulation results above, standard deviation (SD) is employed to quantitatively evaluate the degree of fracture even extension. A high SD shows that data points distribute over a wider range of the average data value, while a low SD indicates the opposite situation [40].

$$SD = \sqrt{\frac{1}{N-1} \sum_{i=1}^N (X_i - X)^2}. \quad (9)$$

In this work, SD represents the standard deviation of fracture length and N stands for the number of fractures, and X_i is the length of each fracture and X is the average length of fractures. A lower SD means that fractures extend more evenly. Figure 11 shows the fracture length SD of different impact factors.

According to Figures 11(a) and 11(b), it is indicated that with the decrease in cluster number and the increase in cluster spacing, the SD of fracture length tends to be lower, which means the stress shadowing effect is mitigated and fracturing fluid entered into each cluster is more uniform, so the degree of fracture even propagation increases gradually. Similar

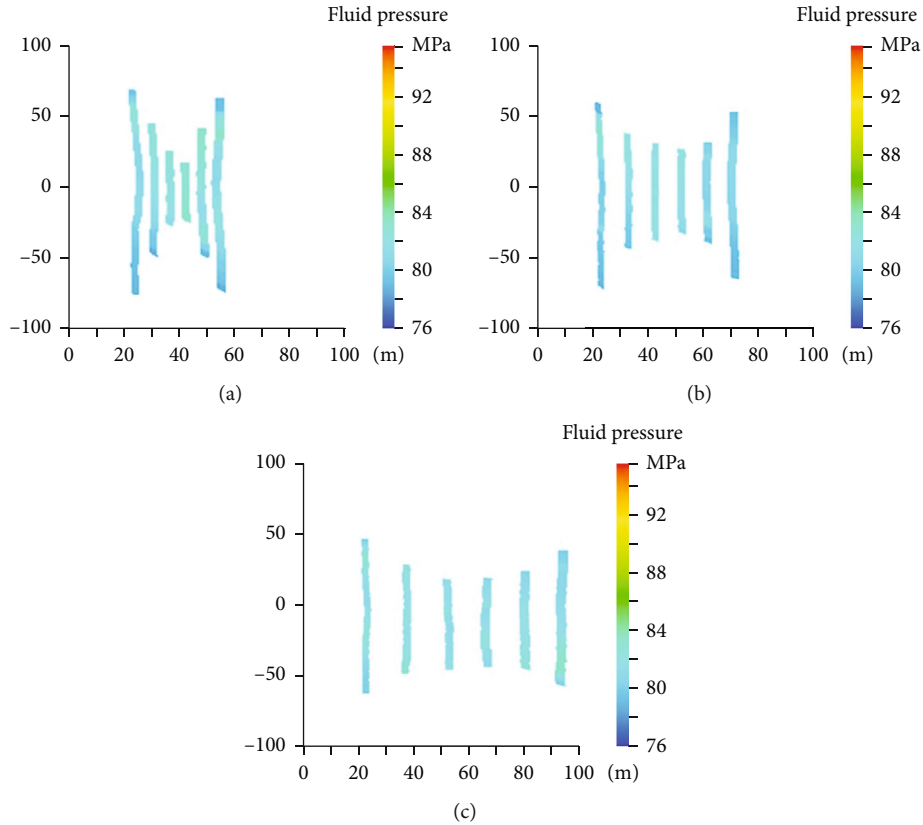


FIGURE 5: Effects of different cluster spacing on fracture geometry: (a) cluster spacing 5 m, (b) cluster spacing 10 m, and (c) cluster spacing 15 m.

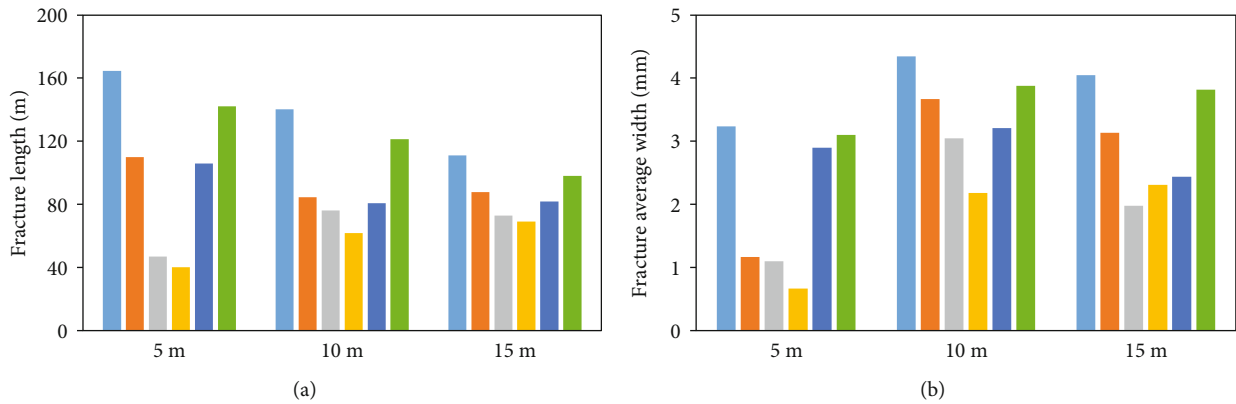


FIGURE 6: Length (a) and average width (b) of multifracture in a stage with different cluster spacing.

TABLE 3: Perforations of each cluster.

Case number	Cluster 1	Cluster 2	Cluster 3	Cluster 4	Cluster 5	Cluster 6
Case 1	8	8	8	8	8	8
Case 2	7	7	10	10	7	7
Case 3	9	9	6	6	9	9

stimulation results can be found by Lecampion et al. and Wu and Olson [16, 41]. However, it is not wise to design too small cluster number or too large cluster spacing which could lead

to low utilization of shale formation between clusters. Besides, Cheng et al. and Li et al. [42, 43] have discussed the effects of perforation distribution on fracture propagation and their study results are consistent with ours, which is that reducing the perforation number of exterior clusters and increasing the perforation number of interior clusters properly are beneficial for the even propagation of fractures (Figure 11(c)). For the flow rate, the lower SD of fracture length can be obtained with larger flow rate which is showed in Figure 11(d). At the smaller flow rate, the bottom hole pressure is lower relatively, which has a negative effect on fracture propagation. In the researches of Green et al. and

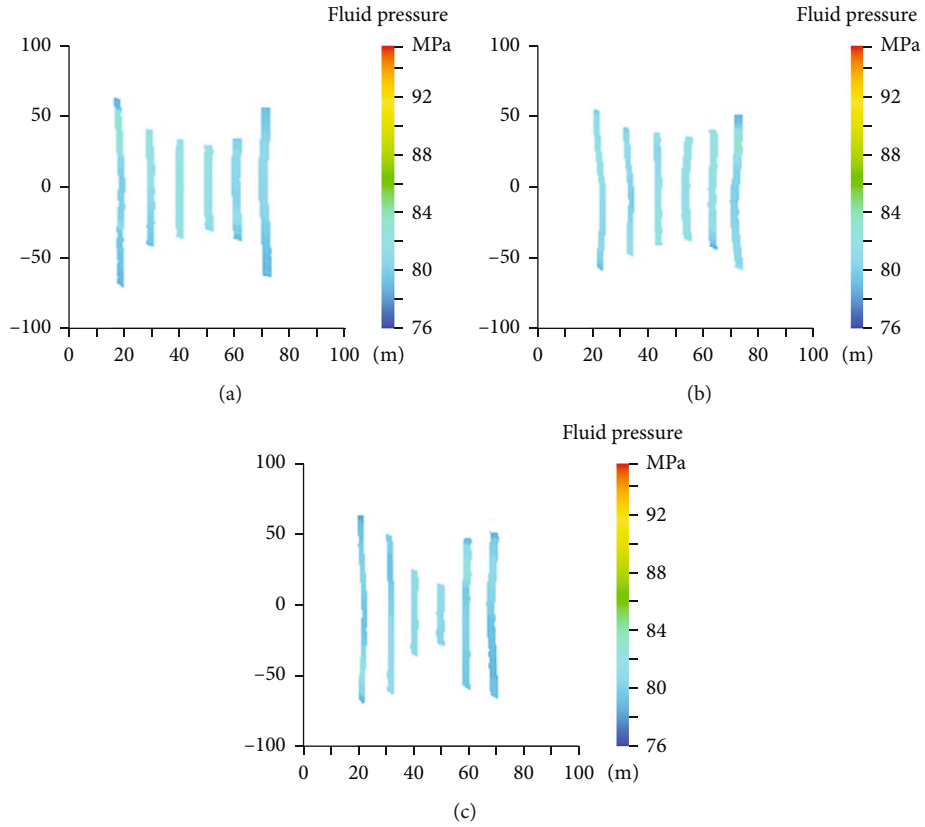


FIGURE 7: Effects of different perforation distributions on fracture geometry.

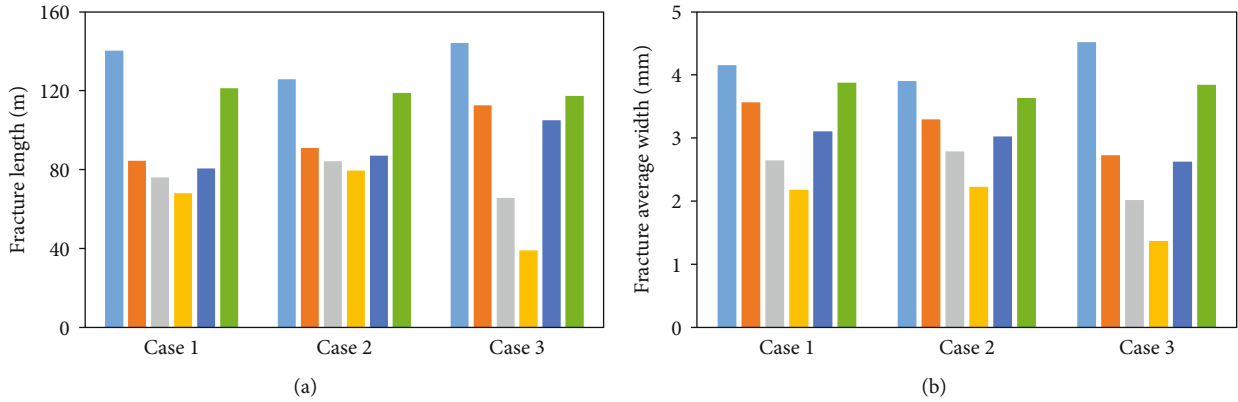


FIGURE 8: Length (a) and average width (b) of multifracture in a stage with different perforation distributions.

Xie et al. [30, 39], larger flow rate in multicluster hydraulic fracturing is recommended as well.

In the main shale area of North America, the well spacing is mostly about 100-300 m. The cluster spacing has shortened to less than 5 m, and the cluster number has increased to more than 15 clusters in a stage to obtain proper fracture length to match the small well spacing [44, 45]. In terms of fracture nonpropagation and fracture uneven propagation due to the mechanical property of shale formation and small cluster spacing, limited-entry perforation and diversion technology are introduced to enhance the cluster efficiency and fracture complexity. And through adopting multistep flow rate, original state of stress is unbalanced to promote fracture

propagation further [25, 46, 47]. However, due to the small well spacing and extreme limited-entry perforation, the flow rate is not usually expected to be high in some shale areas.

Compared with the North America area, the well spacing is larger in Changning shale block which is 300-400 m. With the growth of cluster number and the decline of cluster spacing, the average fracture length tends to be shorter. Under the conditions of the larger well spacing, multicluster hydraulic fracturing with 4-6 clusters in a stage has been employed to meet the demands for the well spacing and improve the utilization of shale formation in Changning block.

Also, when the 6 clusters within a stage are designed, diversion technology at the fracture inlet is widely used to

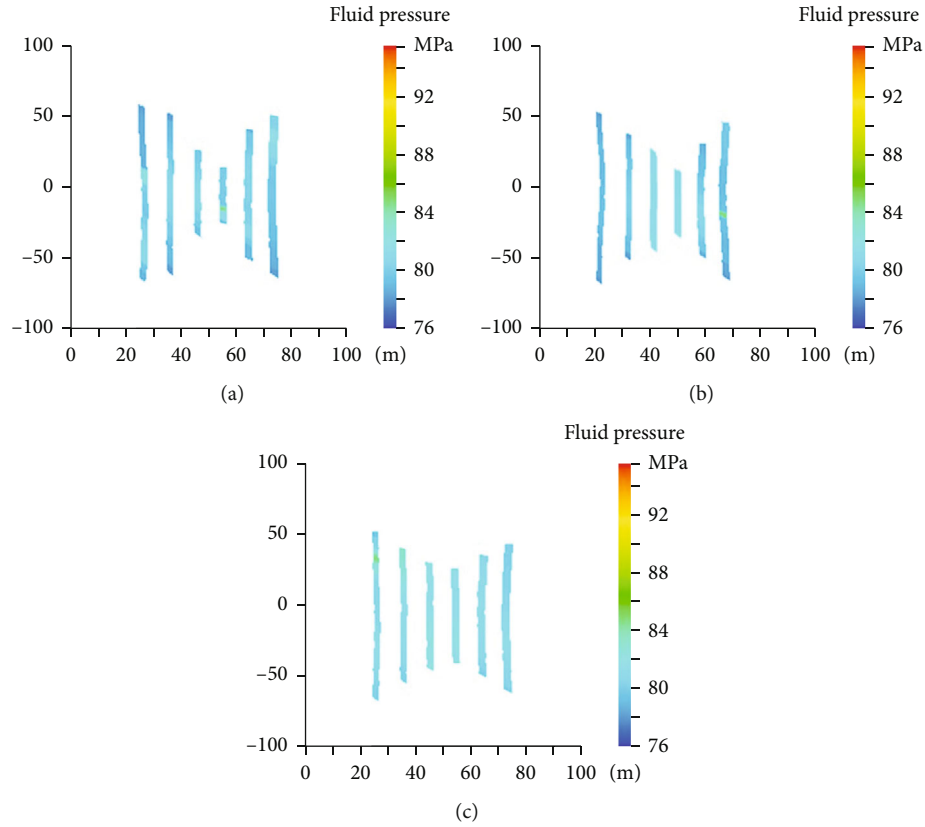


FIGURE 9: Effects of different flow rates on fracture geometry: (a) flow rate 9 m³/min, (b) flow rate 12 m³/min, and (c) flow rate 15 m³/min.

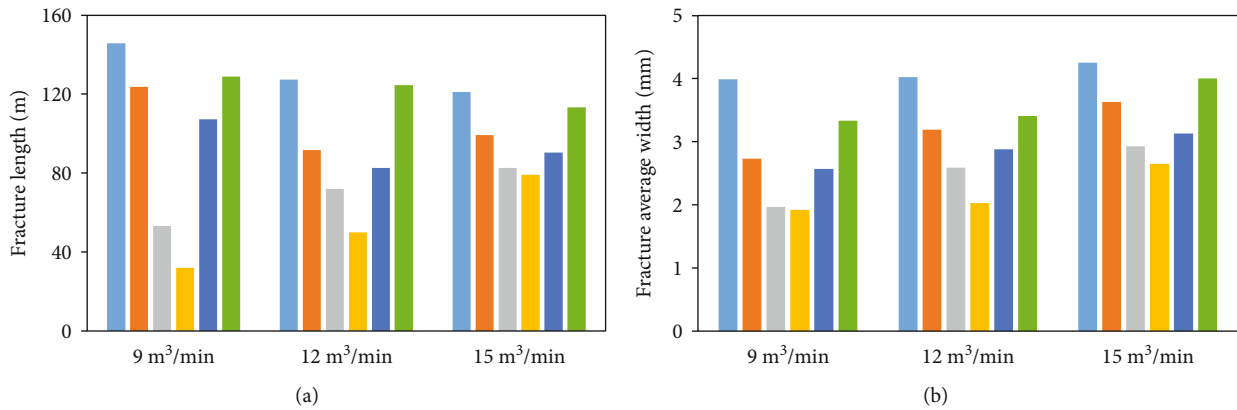


FIGURE 10: Length (a) and average width (b) of multifracture in a stage with different flow rates.

improve the cluster efficiency, promoting fracture propagation uniformly. The 15-19 mm diversion balls are used due to perforation hole erosion during hydraulic fracturing. Considering well extension of fractures, diversion balls are injected at the time of 50-60% total fracturing fluid within a stage to block the dominant fractures, facilitating recessive fractures to expand. Besides, in a certain stage, when the cluster spacing decreases to 10 m with the increase in cluster number, the width of interior fractures becomes smaller compared with exterior fractures based on the study above. In order to effectively prop fractures, small-sized ceramic

proppant (100 mesh) is introduced in field, which is beneficial to increase fracture conductivity. Additionally, flow rate is the significant influence factor for hydraulic fracturing effectiveness in this target area, so it should be as high as possible under the normal fracturing treatment at the large well spacing, contributing to the relatively even propagation of multifracture as the study result above shown.

The perforation number per stage decreases to 36 or 48 to enhance the cluster efficiency. Though extreme limited-entry perforation helps fracture to extend simultaneously, reducing perforations further would cause the high wellbore friction

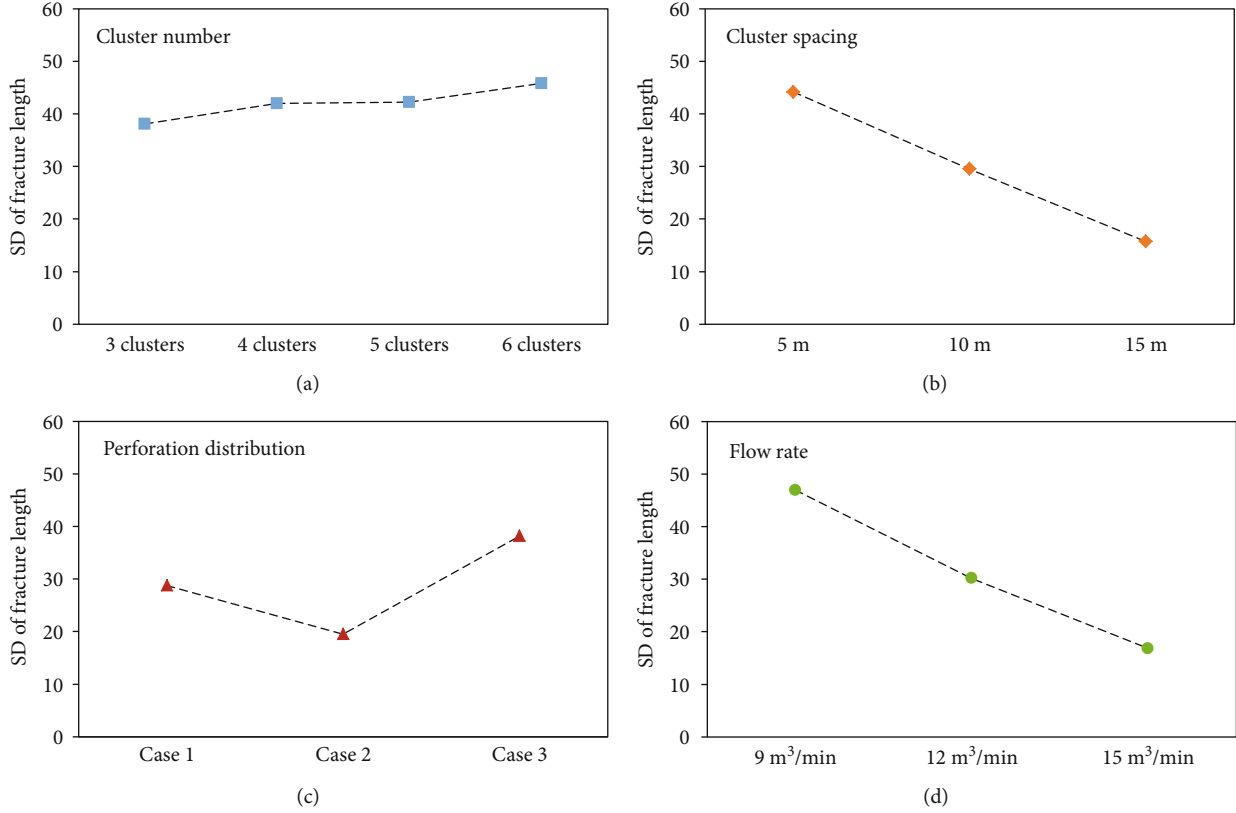


FIGURE 11: Standard deviation of fracture length: (a) cluster number, (b) cluster spacing, (c) perforation distribution, and (d) flow rate.

pressure P_{per} , increasing the pumping pressure which is not conducive to field operation in Changning shale block (Equation (10)).

$$P_{per} = 0.807 \frac{q^2 \rho}{N_{per} D_{per} C_{per}^2}, \quad (10)$$

where ρ represents the fluid density, N_{per} is the number of perforations, D_{per} is the perforation diameter, q is the flow rate, and C_{per} is the discharge coefficient.

Furthermore, nonuniform perforation distribution could not only promote cluster initiation simultaneously under different mechanical properties of shale formation but also render fractures extend more evenly. Therefore, a field test should be taken in target shale area to obtain better fracturing effectiveness and higher production.

5. Conclusion

There are many factors influencing the fracture propagation in multicluster hydraulic fracturing. Based on the geology and engineering characteristics of Changning shale block, cluster number, cluster spacing, perforation distribution, and flow rate were discussed to clarify the extension and geometry of multifracture by the numerical simulation

method. The main conclusions can be summarized as follows:

- (1) The fracture geometry is influenced by cluster number, cluster spacing, perforation distribution, and flow rate diversely. With the reduction of cluster number and the growth of cluster spacing and flow rate, the length and average width of interior fractures are inclined to increase due to the mitigation of stress shadowing effect between clusters. In the perforation distribution with more perforations in interior fractures, the length and average width of interior fractures are larger than those of another perforation distributions
- (2) The SD of fracture length is introduced to evaluate the degree of fracture even extension quantitatively. Employing small cluster number, large cluster spacing, nonuniform perforation distribution, and high flow rate can obtain the low SD of fracture length, which indicates that multifracture propagates more evenly. But too small cluster number or too large cluster spacing is not recommended in a stage because of the low utilization of shale formation between clusters
- (3) Multicluster hydraulic fracturing has now developed into a mature and advanced technology in the main

shale area of North America. In Changning shale block, multicluster hydraulic fracturing with 4-6 clusters in a stage has been in use based on its own geology and engineering characteristics, and diversion technology, limited-entry perforation, high flow rate, and small-sized ceramic proppant are employed to get better shale gas production. To promote fracture even extension further, nonuniform perforation distribution should be introduced

Data Availability

The data is available in the manuscript.

Conflicts of Interest

The authors declare no conflict of interest.

Acknowledgments

This research was funded by the Scientific Research Project of PetroChina Southwest Oil & Gas Field Company, grant number 20190302-18.

References

- [1] A. Daneshy, "Multistage fracturing using plug-and-perf systems," *World Oil*, vol. 232, no. 10, pp. 1–6, 2011.
- [2] J. B. Curtis, "Fractured shale-gas systems," *AAPG Bulletin*, vol. 86, no. 11, pp. 1921–1938, 2002.
- [3] X. Weng, "Modeling of complex hydraulic fractures in naturally fractured formation," *Journal of Unconventional Oil and Gas Resources*, vol. 9, pp. 114–135, 2015.
- [4] N. Modeland, D. Buller, and K. Chong, "Statistical analysis of the effect of completion methodology," in *North American Unconventional Gas Conference and Exhibition*, The Woodlands, Texas, USA, 2011.
- [5] Y. Cheng, "Impacts of the number of perforation clusters and cluster spacing on production performance of horizontal shale gas wells," in *SPE Eastern Regional Meeting*, Morgantown, West Virginia, USA, 2012.
- [6] Q. Wu, Y. Xu, X. Wang, T. Wang, and S. Zhang, "Volume fracturing technology of unconventional reservoirs: connotation, optimization design and implementation," *Petroleum Exploration and Development*, vol. 39, no. 3, pp. 352–358, 2012.
- [7] Y. Xu, Q. Lei, M. Chen et al., "Progress and development of volume stimulation techniques," *Petroleum Exploration and Development*, vol. 45, no. 5, pp. 874–887, 2018.
- [8] C. K. Miller, G. A. Waters, and E. I. Rylander, "Evaluation of production log data from horizontal wells drilled in organic shales," in *North American Unconventional Gas Conference and Exhibition*, The Woodlands, Texas, USA, 2011.
- [9] B. Wheaton, J. Miskimins, D. Wood, T. Lowe, and R. Barree, "Integration of distributed temperature and distributed acoustic survey results with hydraulic fracture modeling: a case study in the Woodford Shale," in *Unconventional Resources Technology Conference*, Denver, Colorado, 2014.
- [10] L. N. Germanovich and D. K. Astakhov, "Fracture closure in extension and mechanical interaction of parallel joints," *Journal of Geophysical Research*, vol. 109, no. 9, pp. 2208–2222, 2004.
- [11] J. E. Olson, "Multi-fracture propagation modeling: applications to hydraulic fracturing in shales and tight sands," in *42nd US Rock Mechanics Symposium and 2nd US-Canada Rock Mechanics Symposium*, San Francisco, 2008.
- [12] J. C. Morrill and J. L. Miskimins, "Optimizing hydraulic fracture spacing in unconventional shales," in *SPE Hydraulic Fracturing Technology Conference*, The Woodlands, Texas, USA, 2012.
- [13] A. P. Bunger, X. Zhang, and R. G. Jeffrey, "Parameters affecting the interaction among closely spaced hydraulic fractures," *SPE Journal*, vol. 17, no. 1, pp. 292–306, 2012.
- [14] A. Peirce and A. P. Bunger, "Interference fracturing: non-uniform distributions of perforation clusters that promote simultaneous growth of multiple hydraulic fractures," *SPE Journal*, vol. 20, no. 2, pp. 384–395, 2014.
- [15] D. H. Shin and M. M. Sharma, "Factors controlling the simultaneous propagation of multiple competing fractures in a horizontal well," in *SPE Hydraulic Fracturing Technology Conference*, The Woodlands, Texas, USA, 2014.
- [16] K. Wu and J. E. Olson, "Mechanisms of simultaneous hydraulic fracture propagation from multiple perforation clusters in horizontal wells," *SPE Journal*, vol. 21, no. 3, pp. 1000–1008, 2015.
- [17] J. Zhao, W. Xu, Y. Li, K. Cai, and M. Xu, "A new method for cluster spacing optimization of multi-cluster staged fracturing in horizontal wells of low-permeability oil and gas reservoirs," *Natural Gas Industry*, vol. 36, no. 10, pp. 63–69, 2016.
- [18] K. Wu, J. E. Olson, M. T. Balhoff, and W. Yu, "Numerical analysis for promoting uniform development of simultaneous multiple fracture propagation in horizontal wells," in *SPE Annual Technical Conference and Exhibition*, Houston, Texas, USA, 2015.
- [19] R. Lin, L. Ren, J. Zhao, Y. Tao, X. Tan, and J. Zhao, "Hydraulic fractures simulation and stimulated reservoir volume estimation for shale gas fracturing," in *SPE Europec Featured at 81st EAGE Conference and Exhibition*, London, England, UK, 2019.
- [20] Y. Wang, D. Liu, J. Han, C. Li, and H. Liu, "Effect of fatigue loading-confining stress unloading rate on marble mechanical behaviors: an insight into fracture evolution analyses," *Journal of Rock Mechanics and Geotechnical Engineering*, vol. 12, no. 6, pp. 1249–1262, 2020.
- [21] Y. Wang, W. Feng, and C. Li, "On anisotropic fracture and energy evolution of marble subjected to triaxial fatigue cyclic-confining pressure unloading conditions," *International Journal of Fatigue*, vol. 134, p. 105524, 2020.
- [22] Y. Wang, S. Gao, D. Liu, and C. Li, "Anisotropic fatigue behaviour of interbedded marble subjected to uniaxial cyclic compressive loads," *Fatigue & Fracture of Engineering Materials & Structures*, vol. 43, no. 6, pp. 1170–1183, 2020.
- [23] Y. Wang, C. Li, and J. Han, "On the effect of stress amplitude on fracture and energy evolution of pre-flawed granite under uniaxial increasing-amplitude fatigue loads," *Engineering Fracture Mechanics*, vol. 240, p. 107366, 2020.
- [24] T. E. Alotaibi, C. M. Landis, and M. J. AITammar, "Phase-field modeling of hydraulic fracture propagation in mechanically heterogeneous formations," in *International Petroleum Technology Conference*, Dhahran, Kingdom of Saudi Arabia, 2020.
- [25] B. Johnston and N. Volkmer, "Predicting success in the Haynesville Shale: a geologic, completion, and production analysis," in *SPE/AAPG/SEG Unconventional Resources Technology Conference*, Houston, Texas, USA, 2018.

- [26] Y. Wang, S. H. Gao, C. H. Li, and J. Q. Han, "Investigation on fracture behaviors and damage evolution modeling of freeze-thawed marble subjected to increasing - amplitude cyclic loads," *Theoretical and Applied Fracture Mechanics*, vol. 109, p. 102679, 2020.
- [27] J. Barraza, C. Capderou, C. J. Matthew et al., "Increase cluster efficiency and fracture network complexity using degradable diverter particulates to increase production: Permian Basin Wolfcamp Shale case study," in *SPE Annual Technical Conference and Exhibition*, San Antonio, Texas, USA, 2017.
- [28] S. Evans, S. Siddiqui, and J. Magness, "Impact of cluster spacing on infill completions in the Eagle Ford," in *The Unconventional Resources Technology Conference*, Houston, Texas, USA, 2018.
- [29] K. Ling, X. Wu, G. Han, and S. Wang, "Optimizing the multi-stage fracturing interval for horizontal wells in Bakken and Three Forks Formation," in *SPE Asia Pacific Hydraulic Fracturing Conference*, Beijing, China, 2016.
- [30] J. Xie, H. Huang, Y. Sang et al., "Numerical study of simultaneous multiple fracture propagation in Changning Shale Gas Field," *Energies*, vol. 12, no. 7, p. 1335, 2019.
- [31] U. C. GA, P. T. Huckabee, M. M. Molenaar, B. Wyker, and K. Somanchi, "Perforation cluster efficiency of cemented plug and perf limited entry completions; insights from fiber optics diagnostics," in *SPE Hydraulic Fracturing Technology Conference*, The Woodlands, Texas, USA, 2016.
- [32] S. T. Castonguay, M. E. Mear, R. H. Dean, and J. H. Schmidt, "September. Predictions of the growth of multiple interacting hydraulic fractures in three dimensions," in *SPE Annual Technical Conference and Exhibition*, New Orleans, Louisiana, USA, 2013.
- [33] R. Manchanda, E. C. Bryant, P. Bhardwaj, P. Cardiff, and M. M. Sharma, "Strategies for effective stimulation of multiple perforation clusters in horizontal wells," *SPE Production & Operations*, vol. 33, no. 3, pp. 539–556, 2017.
- [34] Q. Zeng, Z. Liu, T. Wang, Y. Gao, and Z. Zhuang, "Fully coupled simulation of multiple hydraulic fractures to propagate simultaneously from a perforated horizontal wellbore," *Computational Mechanics*, vol. 61, no. 1-2, pp. 137–155, 2018.
- [35] B. Lecampion and J. Desroches, "Simultaneous initiation and growth of multiple radial hydraulic fractures from a horizontal wellbore," *Journal of the Mechanics and Physics of Solids*, vol. 82, pp. 235–258, 2015.
- [36] A. Peirce and A. Bunger, "Interference fracturing: nonuniform distributions of perforation clusters that promote simultaneous growth of multiple hydraulic fractures," *SPE Journal*, vol. 20, no. 2, pp. 384–395, 2014.
- [37] G. Xu and S. Wong, "Interaction of multiple non-planar hydraulic fractures in horizontal wells," in *International Petroleum Technology Conference*, Beijing, China, 2013.
- [38] S. H. Fallahzadeh, M. M. Hossain, A. J. Cornwell, and V. Rasouli, "Near wellbore hydraulic fracture propagation from perforations in tight rocks: the roles of fracturing fluid viscosity and injection rate," *Energies*, vol. 10, no. 3, p. 359, 2017.
- [39] S. Green, G. Xu, B. Forbes, G. Green, J. McLennan, and D. Work, "Early time fracture growth and cluster spacing effects," in *52nd US Rock Mechanics/Geomechanics Symposium*, Seattle, Washington, 2018.
- [40] Z. Zhao, X. Li, J. He, T. Mao, B. Zheng, and G. Li, "A laboratory investigation of fracture propagation induced by supercritical carbon dioxide fracturing in continental shale with interbeds," *Journal of Petroleum Science and Engineering*, vol. 166, pp. 739–746, 2018.
- [41] B. Lecampion, J. Desroches, X. Weng, J. Burghardt, and J. E. Brown, "Can we engineer better multistage horizontal completions? Evidence of the importance of near-wellbore fracture geometry from theory, lab and field experiments," in *SPE Hydraulic Fracturing Technology Conference*, The Woodlands, Texas, USA, 2015.
- [42] C. Cheng, A. P. Bunger, and A. P. Peirce, "Optimal perforation location and limited entry design for promoting simultaneous growth of multiple hydraulic fractures," in *SPE Hydraulic Fracturing Technology Conference*, The Woodlands, Texas, USA, 2016.
- [43] X. Li, L. Yi, and Z. Yang, "Numerical model and investigation of simultaneous multiple-fracture propagation within a stage in horizontal well," *Environmental Earth Sciences*, vol. 76, no. 7, p. 273, 2017.
- [44] O. A. Jaripatke, J. G. Ndungu, G. W. Schein et al., "Review of Permian completion designs and results," in *SPE Annual Technical Conference and Exhibition*, Dallas, Texas, USA, 2018.
- [45] F. Alimahomed, R. Malpani, R. Jose et al., "Stacked pay pad development in the Midland Basin," in *SPE Liquids-Rich Basins Conference-North America*, Midland, Texas, USA, 2017.
- [46] P. Weddle, L. Griffin, and C. M. Pearson, "Mining the Bakken II – pushing the envelope with extreme limited entry perforating," in *SPE Hydraulic Fracturing Technology Conference and Exhibition*, The Woodlands, Texas, USA, 2018.
- [47] Y. Rodionov, C. Defeu, K. Gakhar et al., "Optimizing of infill well development using a novel far-field diversion technique in the Eagle Ford Shale," in *SPE/AAPG/SEG Unconventional Resources Technology Conference*, pp. 1160–1172, Austin, Texas, USA, 2017.

Research Article

Predicting Response of Constructed Tunnel to Adjacent Excavation with Dewatering

Panpan Guo ¹, Feifei Liu,² Gang Lei ^{1,3}, Xian Li ², Cheng-wei Zhu ⁴, Yixian Wang ^{2,5}, Mengmeng Lu,⁶ Kang Cheng ^{1,7} and Xiaonan Gong¹

¹Research Center of Coastal and Urban Geotechnical Engineering, Zhejiang University, Hangzhou 310058, China

²School of Civil Engineering, Hefei University of Technology, Hefei 230009, China

³Beijing Urban Construction Design & Development Group Company Limited, Beijing 100037, China

⁴Institut für Geotechnik, Universität für Bodenkultur Wien, Feistmantelstrasse 4, 1180 Vienna, Austria

⁵State Key Laboratory of Explosion Science and Technology, Beijing Institute of Technology, Beijing 100081, China

⁶School of Mechanics and Civil Engineering, China University of Mining and Technology, Xuzhou 221116, China

⁷China Railway 11th Bureau Group Co., Ltd., Wuhan 430061, China

Correspondence should be addressed to Gang Lei; 11812105@zju.edu.cn and Xian Li; 2012800022@hfut.edu.cn

Received 27 January 2021; Revised 25 February 2021; Accepted 2 March 2021; Published 18 March 2021

Academic Editor: Yu Wang

Copyright © 2021 Panpan Guo et al. This is an open access article distributed under the Creative Commons Attribution License, which permits unrestricted use, distribution, and reproduction in any medium, provided the original work is properly cited.

This paper proposes a new method for predicting the displacement and internal force of constructed tunnels induced by adjacent excavation with dewatering. In this method, the total excavation-induced additional stress on the constructed tunnel is derived by superposing the additional stresses induced by excavation unloading and dewatering effects. The additional stress induced by unloading effect is calculated using Mindlin's solution. The additional stress induced by dewatering effect is calculated using the principle of effective stress and the Dupuit precipitation funnel curve. With the beam on elastic foundation method, the total additional stress is then used for calculating the tunnel displacement and internal force caused by adjacent excavation with dewatering. Based on three well-documented case histories, the performance of the proposed method is verified. Moreover, a parametric analysis is also performed to capture the effects of excavation depth, tunnel-to-excavation distance, initial water level, excavation plan view size, and specific yield on the responses of the constructed tunnels. The results indicate that the effect of excavation depth on the tunnel maximum vertical displacement, maximum bending moment, and maximum shear force is more significant at an excavation depth greater than the cover depth of the constructed tunnel. The tunnel maximum vertical displacement, maximum bending moment, and maximum shear force decrease nonlinearly with an increase in the tunnel-to-excavation distance and the initial water level. Among the investigated parameters, the excavation dimension in the tunnel longitudinal direction affects most the tunnel responses. The effect of specific yield on the tunnel displacement and internal force induced by adjacent excavation with dewatering becomes more obvious as increasing the initial water level and excavation depth.

1. Introduction

The rapid development of urban rail traffic provides convenience of getting around for people. The development advantage along an urban rail traffic line has been stimulating the construction of high-rise buildings adjacent to the urban rail traffic line. Therefore, it is not rare to find an excavation that is adjacent to preexisting subway tunnels, piles, pipelines, or other shallowly buried facilities [1–5]. Inevitably, the adja-

cent excavation has an adverse effect on the constructed structures or facilities, and many studies have focused on this issue in recent decades [6–8]. It has been found that the excavation-induced redistribution of ground stress can lead to the generation of additional stress and deformation in the tunnel structure. If the induced tunnel deformation is excessive, the safe operation of the subway or other facilities will be affected [9–12]. As a result, an investigation into the excavation-induced internal force and deformation

characteristics of a constructed subway tunnel has great significance to the safe operation of the subway tunnel [13–15].

Many analysis methods for excavation-induced internal force and deformation in a subway tunnel have been proposed, which can be classified into the numerical analysis method [16–19], field monitoring method [20–23], and theoretical analysis method [24–26]. The numerical analysis method can simulate the complex process of excavation and is therefore a favored choice for engineers and researchers. However, this method suffers from several disadvantages such as cumbersome modelling, time-consuming computation, large discrepancy between the computed results using different numerical analysis software, and low reliability of the computed results. The field monitoring method can directly obtain the excavation-induced deformation behavior of the constructed tunnel during the whole excavation phase. However, this method is susceptible to the workers' operating skill and the quality of monitoring equipment. Moreover, the field monitoring method corresponds to only a specific engineering project and does not involve a discussion of the deformational mechanism and therefore has a limited guiding significance for the excavations in other areas.

The theoretical analysis method for excavation-induced internal force and deformation characteristics in a subway tunnel has been extensively investigated by many scholars. At the present time, the most common-adopted theoretical analysis method is the two-stage method [27, 28]. This method divides the considered problem into two separate stages: the excavation unloading stage and the tunnel responding stage. Depending on the concept of predicting the excavation-induced response of the constructed tunnel, the method for calculating the excavation-induced internal force in the constructed tunnel can be categorized into the additional load method and the additional displacement method [29–31]. The additional load method is performed in two steps. First, apply the excavation-induced additional stress in the tunnel position calculated by Mindlin's solution to the constructed subway tunnel. Second, calculate the internal force and deformation in the constructed tunnel under the effect of the applied excavation-induced additional stress, by adopting the beam on elastic foundation theory [32, 33]. The additional displacement method is also performed in two steps. First, calculate the excavation-induced ground displacement in the tunnel position by using Peck's formula [34]. Second, impose the calculated displacement in the first step on the constructed tunnel to predict the internal force and deformation in the constructed tunnel [35, 36].

The change of the initial stress field in the ground induced by an excavation is a rather complex phenomenon. This phenomenon is associated with not only the excavation unloading effect but also the excavation dewatering effect. Previous research has indicated that excavation dewatering affects significantly the internal force and deformation characteristics of the constructed facilities adjacent to the excavation [37–40]. Based on the effective stress principle, Ou et al. [41] proposed an analytical method for predicting the influence of excavation with dewatering on the response of the constructed tunnel underlying the excavation. This method

takes account of the excavation dewatering effect but is not applicable to the condition where the excavation is adjacent laterally to the constructed tunnel. In addition, based on Darcy's law and the Dupuit approximation, Anderson [42] derived a formula describing the steady flow of groundwater and determined the precipitation funnel curve using the groundwater surfaces on the external and internal boundaries.

In this paper, the excavation unloading effect and the excavation dewatering effect are modelled separately. Mindlin's solution is used to calculate the additional stress in the constructed tunnel induced by the excavation unloading effect. Based on the Dupuit precipitation funnel curve, the effective stress in the constructed tunnel induced by the excavation dewatering effect is obtained. The additional stress and the effective stress obtained above are then superimposed to derive the total additional stress in the constructed tunnel. After this, the additional load method is adopted to predict the internal force and displacement characteristics for the constructed tunnel adjacent to an excavation with dewatering. The innovation of this study lies in that the calculation of the excavation-induced additional stress takes account of not only the excavation unloading and dewatering effects but also the entire region subjected to the influence of dewatering by introducing the Dupuit precipitation funnel curve.

2. Total Additional Stress Induced by Excavation with Dewatering

In calculating the additional stress in the constructed tunnel induced by excavation with dewatering, the time effect involved in the excavation and dewatering process is not taken into account, and only the initial state and the final state of the excavation with dewatering have been considered. In general, the additional stress in the constructed tunnel induced by excavation with dewatering is composed of two parts: one is the effective stress effect induced by dewatering, and the other is the unloading effect induced by excavation.

2.1. Additional Stress Induced by Dewatering. It is assumed that the phreatic line induced by dewatering conforms to the Dupuit approximation [42]. In detail, the assumptions are as follows: (1) the aquifer is homogeneous, isotropic, isotropic, and horizontal; (2) the flow of the groundwater is laminar and stable and conforms to Darcy's law; (3) the static water level is horizontal; and (4) the contour of recharge of the pumping well is of fixed water level and is cylindrical in shape. A schematic of the dewatering during an excavation is presented in Figure 1.

The adopted water level lowering curve has the form

$$y^2 = h'^2 + (H^2 - h'^2) \frac{\ln x - \ln r}{\ln R - \ln r}, \quad (1)$$

where y = elevation of the phreatic line after dewatering (m), h' = distance between the water level of the dewatering well and the impermeable layer (m), H = elevation of the initial water level (m), r = radius of the dewatering well (m), R = radius of influence of dewatering (m), x = horizontal

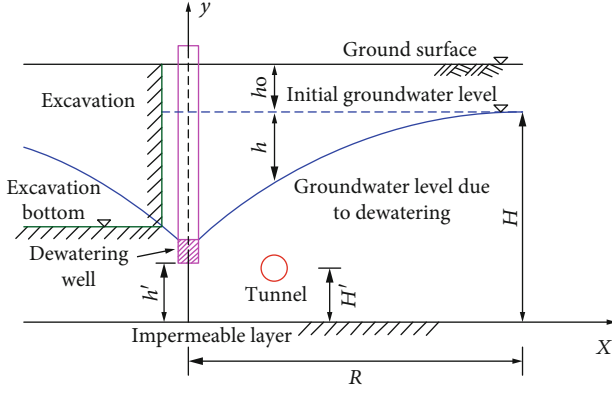


FIGURE 1: Schematic of dewatering during excavation.

distance to the axis of the dewatering well (m), and H' = distance between tunnel axis and impermeable layer.

The radius of influence of dewatering can be calculated using an empirical equation

$$R = 2s\sqrt{HK}, \quad (2)$$

where s = dewatering depth of the dewatering well (m) and K = permeability coefficient of the ground (m/d).

The change of the water level above the constructed tunnel can thus be estimated using Equations (1) and (2). The vertical additional stress applied on the constructed tunnel is calculated using the effective stress principle. Before dewatering, the constructed tunnel is subjected to earth pressure and pore water pressure, and the effective stress is calculated by

$$\sigma = h_0\gamma_0 + (H - y)(\gamma_{\text{sat}} - \gamma_w), \quad (3)$$

where h_0 = distance between ground surface and initial water level (m), γ_0 = dry unit weight of soil (kN/m^3), γ_{sat} = saturated unit weight (kN/m^3), and γ_w = unit weight of water (kN/m^3).

After dewatering, the effective stress applied to the constructed tunnel is given by

$$\sigma' = h_0\gamma_0 + (H - y)(\gamma_{\text{sat}} - (1 - \mu)\gamma_w), \quad (4)$$

where μ = specific yield. The magnitude of μ is associated with soil properties including the mineral composition, particle size, grain grading, degree of sorting, and void ratio. The mineral composition affects the specific yield by the adsorption force on the hydrone. A summary of the empirical values of the specific yield for various types of soils is presented in Table 1.

The dewatering-induced change of the vertical effective stress applied on the constructed tunnel is calculated by

$$\sigma_w^v = \sigma' - \sigma = \mu(H - y)\gamma_w = \mu h\gamma_w. \quad (5)$$

2.2. Additional Stress Induced by Unloading. The calculation of the additional stress in the constructed tunnel induced by excavation unloading effect is generally based on Mind-

TABLE 1: Empirical values of the specific yield for various types of soils.

Soil type	Specific yield
Clay	0.02–0.035
Loam	0.03–0.045
Sandy loam	0.035–0.06
Loess-like loam	0.02–0.05
Loess-like sandy loam	0.03–0.06
Silty sand	0.06–0.08
Silty fine sand	0.07–0.01
Fine sand	0.08–0.11
Medium-fine sand	0.085–0.12
Medium sand	0.09–0.13
Medium-coarse sand	0.10–0.15
Coarse sand	0.11–0.15
Clay cemented sandstone	0.02–0.03
Fractured limestone	0.008–0.10

lin's solution [43]. A schematic of the calculation model for the additional stress induced by unloading is presented in Figure 2. The assumptions involved in Mindlin's solution are as follows: (1) the ground is a homogeneous, elastic half-space, (2) the time and space effects involved in the excavation are overlooked, and (3) the influence of the constructed tunnel on the excavation unloading stress is not taken into account.

According to Mindlin's solution, under the effect of unit force $\sigma d\xi d\eta$ applied at the point (ξ, η) at the excavation bottom, the vertical and horizontal additional stresses at the point (x, y, z) on the tunnel axis are calculated by

$$\begin{aligned} \sigma_d^v = & -\frac{\gamma d}{8\pi(1-\nu)} \left[\frac{(1-2\nu)(z-d)}{R_1^3} - \frac{(1-2\nu)(z-d)}{R_2^3} \right. \\ & + \frac{3(z-d)^3}{R_1^5} + \frac{3(3-4\nu)z(z+d)^2 - 3d(z+d)(5z-d)}{R_2^5} \\ & \left. + \frac{30zd(z+d)^3}{R_2^7} \right], \end{aligned} \quad (6)$$

$$\begin{aligned} \sigma_d^h = & -\frac{\gamma d}{8\pi(1-\nu)} \left[-\frac{(1-2\nu)(z-d)}{R_1^3} + \frac{3(x-\xi)^2(z-d)}{R_1^5} \right. \\ & - \frac{(1-2\nu)[3(z-d) - 4\nu(z+d)]}{R_2^3} \\ & + \frac{\{3(3-4\nu)(x-\xi)^2(z-d) - 6d(z+d)[(1-2\nu)z - 2\nu d]\}}{R_2^5} \\ & + \frac{4(1-\nu)(1-2\nu)}{R_2(R_2+z+d)} \left[1 - \frac{(x-\xi)^2}{R_2(R_2+z+d)} - \frac{(x-\xi)}{R_2^2} \right] \\ & \left. + \frac{30(x-\xi)^2zd(z+d)}{R_2^7} \right], \end{aligned} \quad (7)$$

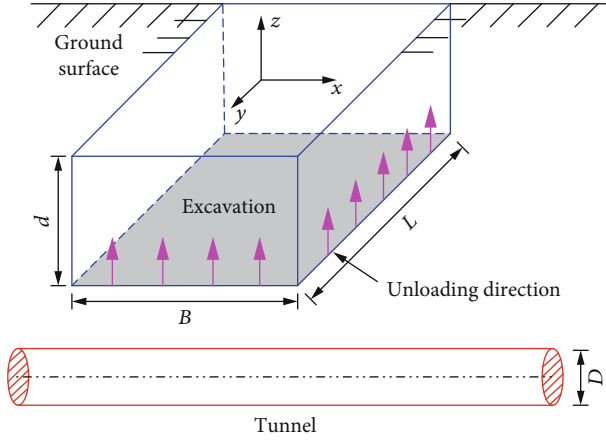


FIGURE 2: Schematic of the calculation model for additional stress induced by excavation unloading.

$$R_1 = \sqrt{(x - \xi)^2 + (y - \eta)^2 + (z - d)^2}, \quad (8a)$$

$$R_2 = \sqrt{(x - \xi)^2 + (y - \eta)^2 + (z + d)^2}. \quad (8b)$$

Similarly, under the effect of a unit force $K_0\gamma\tau d\eta d\tau$ applied at the point (η, τ) on the vertical side of the excavation, the vertical and horizontal additional stresses at the point (x, y, z) on the tunnel axis are calculated by

$$\begin{aligned} \sigma_c^v = & -\frac{K_0\gamma\tau S}{8\pi(1-\nu)} \left[\frac{-(1-2\nu)}{R_3^3} + \frac{3(z-\tau)^2}{R_3^5} + \frac{(1-2\nu)}{R_4^3} \right. \\ & + \frac{3(3-4\nu)(z+\tau)^2}{R_4^5} \\ & \left. + \frac{-6\tau}{R_4^5} \left(\tau + (1-2\nu)(z+\tau) + \frac{5z(z+\tau)^2}{R_4^2} \right) \right], \end{aligned} \quad (9)$$

$$\begin{aligned} \sigma_c^h = & -\frac{K_0\gamma\tau S}{8\pi(1-\nu)} \left[\frac{(1-2\nu)}{R_3^3} + \frac{3S^2}{R_3^5} + \frac{(1-2\nu)(5-4\nu)}{R_4^3} \right. \\ & + \frac{3(3-4\nu)S^2}{R_4^5} + \frac{4(1-\nu)(1-2\nu)}{R_4(R_4+z+\tau)^2} \left(3 - \frac{S^2(3R_4+z+\tau)}{R_4^2(R_4+z+\tau)} \right) \\ & \left. - \frac{6\tau}{R_4^5} \left(3\tau - (3-2\nu)(z+\tau) + \frac{5xS^2}{R_4^2} \right) \right], \end{aligned} \quad (10)$$

$$R_3 = \sqrt{(x - \xi)^2 + (y - \eta)^2 + (z - \tau)^2}, \quad (11a)$$

$$R_4 = \sqrt{(x - \xi)^2 + (y - \eta)^2 + (z + \tau)^2}, \quad (11b)$$

where γ = unit weight of soil (kN/m^3), d = excavation depth (m), ν = Poisson's ratio, K_0 = coefficient of lateral earth pressure at rest ($K_0 = 1 - \sin \varphi$, where φ is the angle of internal friction of soil), S = distance between the vertical side of the excavation and the axis of the constructed tunnel (m), and τ = depth of the calculation point on the vertical side of the excavation (m).

By integrating Equations (6) and (7) over the excavation bottom and integrating Equations (9) and (10) over the vertical side of the excavation, the excavation unloading-induced additional stress corresponding to the excavation bottom and to the vertical side of the excavation can be derived, respectively. In this case, the total vertical and horizontal additional stresses in the constructed tunnel induced by excavation with dewatering, σ^v and σ^h , have the forms

$$\sigma^v = \sigma_w^v + \sigma_d^v + \sigma_c^v, \quad (12a)$$

$$\sigma^h = \sigma_d^h + \sigma_c^h. \quad (12b)$$

3. Response of Constructed Tunnel

The internal force and displacement characteristics for the constructed tunnel under the effect of the additional stress induced by the adjacent excavation with dewatering are predicted in this section based on the beam on elastic foundation theory. To achieve this, it is assumed that (1) the constructed tunnel is equivalent to a long beam on an elastic foundation, (2) the contact between the constructed tunnel and the ground is perfect, and (3) compatibility of deformation is satisfied. A schematic of the calculation model for the response of the constructed tunnel under the additional stress is presented in Figure 3.

According to the Winkler foundation beam model, the equation of deflection curve for the constructed tunnel under the effect of the additional stress has the form

$$EI_{\text{eq}} \frac{d^4 w(x)}{dx^4} + Dkw(x) = p(x), \quad (13)$$

where EI_{eq} = equivalent longitudinal stiffness of the constructed tunnel ($\text{kN}\cdot\text{m}^2$), $w(x)$ = displacement of the constructed tunnel (m), D = external diameter of the constructed tunnel (m), k = coefficient of subgrade reaction ($\text{kN}\cdot\text{m}^3$), and $p(x)$ = additional stress applied on the constructed tunnel (kPa).

In Equation (13), $p(x)$ and EI_{eq} are given by

$$p(x) = \sigma D, \quad (14a)$$

$$EI_{\text{eq}} = \eta EI, \quad (14b)$$

where η = reduction coefficient and EI = actual longitudinal stiffness of the constructed tunnel ($\text{kN}\cdot\text{m}^2$).

The magnitude of the reduction coefficient η varies, depending on many factors such as the form of tunnel circumferential seam, bolt quantity, and tunnel lining thickness [44–46]. By performing a series of experiments, Xu [47] investigated the magnitude of the reduction coefficient η at various forms of tunnel circumferential seam. It was found that the magnitudes of the reduction coefficient η are, respectively, 0.145, 0.13, and 0.114 at homogeneous, staggered, and continuous forms of the tunnel circumferential seam.

A previous experimental study has indicated that the coefficient of subgrade reaction k is related to not only the soil strength but also the stiffness of the foundation beam

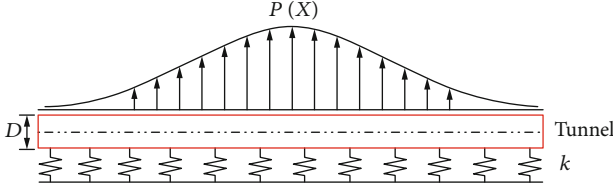


FIGURE 3: Schematic of calculation model for tunnel response under the additional stress.

[48, 49]. Therefore, the empirical equation proposed by Vesic [50] and Attewell et al. [51] was adopted to estimate the coefficient of subgrade reaction k :

$$k = 2k_{\text{Vesic}} = \frac{1.3E_s}{D(1-\nu^2)} \sqrt[12]{\frac{E_s D^4}{EI_{\text{eq}}}}, \quad (15)$$

where E_s = elastic modulus of the ground (MPa).

As Equation (13) is an inhomogeneous differential equation of fourth order with a constant coefficient, it is extremely difficult to derive directly its analytical solution. Therefore, the form of the analytical solution was assumed to be composed of two parts: the general solution part and the particular solution part. Let $p(x) = 0$, one can obtain the corresponding homogeneous differential equation

$$EI_{\text{eq}} \frac{d^4 w(x)}{dx^4} + Dk w(x) = 0. \quad (16)$$

Therefore, the general solution has the form

$$w(x) = e^{\lambda x} (C_1 \cos(\lambda x) + C_2 \sin(\lambda x)) + e^{-\lambda x} (C_3 \cos(\lambda x) + C_4 \sin(\lambda x)), \quad (17a)$$

$$\lambda = \sqrt[4]{\frac{DK}{4EI_{\text{eq}}}}, \quad (17b)$$

where $C_1, C_2, C_3,$ and C_4 = undetermined coefficients and λ = elastic characteristic coefficient.

Considering the symmetry of the beam on an elastic foundation, we have

$$w(x)|_{x \rightarrow \infty} = 0, \quad (18a)$$

$$\left. \frac{dw(x)}{dx} \right|_{x \rightarrow \infty} = 0. \quad (18b)$$

By manipulation of Equations (17) and (18), one obtains $C_1 = C_2 = 0$ and $C_3 = C_4$. Let $C_3 = C_4 = C$, the form of the general solution for Equation (16) can be transformed to

$$w(x) = C e^{-\lambda x} (\cos(\lambda x) + \sin(\lambda x)). \quad (19)$$

Assume that a point load P_0 is applied at the central section of the beam on an elastic foundation. Considering the equilibrium between the subgrade reaction and the external load, we have

$$2DkC \int_0^{\infty} e^{-\lambda x} (\cos(\lambda x) + \sin(\lambda x)) dx = P_0. \quad (20)$$

Manipulation of Equation (20) leads to

$$C = \frac{P_0 \lambda}{2Dk}. \quad (21)$$

Substituting Equation (21) into Equation (19), the form of the general solution becomes

$$w(x) = \frac{P_0 \lambda}{2Dk} e^{-\lambda x} (\cos(\lambda x) + \sin(\lambda x)). \quad (22)$$

For a tunnel subjected to an additional distributed load $q(x)$, the point load at the point ξ on the tunnel is $q(\xi)d\xi$. Under this point load, the induced displacement at the point x on the tunnel, $dw(x)$, is calculated, according to Equation (22), as

$$dw(x) = \frac{P(\xi)\lambda}{2Dk} e^{-\lambda|x-\xi|} (\cos(\lambda|x-\xi|) + \sin(\lambda|x-\xi|)) d\xi. \quad (23)$$

Integrating Equation (23) over the range of the distribution of the additional distributed load, the solution for Equation (13) is derived:

$$w(x) = \frac{\lambda}{2Dk} \int_{-\infty}^{+\infty} P(\xi) e^{-\lambda|x-\xi|} (\cos(\lambda|x-\xi|) + \sin(\lambda|x-\xi|)) d\xi. \quad (24)$$

Consequently, the bending moment and shear force at the point x on the tunnel axis are calculated, respectively, by

$$M = -EI_{\text{eq}} \frac{d^2 w(x)}{dx^2}, \quad (25)$$

$$Q = \frac{dM}{dx} = -EI_{\text{eq}} \frac{d^3 w(x)}{dx^3}. \quad (26)$$

The proposed method for predicting the response of a constructed tunnel to an adjacent excavation with dewatering treats the constructed tunnel as a long beam on an elastic foundation and calculates the internal force and deformation for the constructed tunnel by using the Winkler foundation model. The required parameters for the proposed method include the equivalent longitudinal stiffness of the constructed tunnel EI_{eq} , external diameter of the constructed tunnel D , and coefficient of subgrade reaction k . The advantages of the proposed method over other models are lesser parameters and convenient calculation process.

4. Verification

The performance of the proposed theoretical method for predicting the deformation and internal force characteristics of a constructed tunnel induced by an adjacent excavation with dewatering is challenged against three well-documented case histories. The predicted tunnel displacement characteristics are verified by the comparisons with the monitoring data obtained in the field and the three-dimensional finite element analysis results obtained in this study. The ability of the proposed method in well predicting the tunnel internal force characteristics is demonstrated by comparing it with the three-dimensional finite element analysis results.

4.1. Shanghai Dongfang Road Interchange Project. The first case history used for verifying the proposed method is the Shanghai Dongfang Road Interchange (SDRI) Project reported in Xu and Huang [52]. In this case history, the plan view showing the relative position of the excavation and the tunnels is presented in Figure 4. The soil parameters for this case history are listed in Table 2. The geometry of the excavation resembles a parallelogram of 26 m in length and 18 m in width. The short side of the excavation is oriented at 66° relative to the x -axis of the coordinate system. The excavation depth is approximately 6.5 m. The angle between the axis of the constructed tunnels and the y -axis of the coordinate system is 45° . The upline of the constructed tunnels is directly below the excavation. The minimum distance between the tunnel crown and the excavation bottom is 2.76 m, with the tunnel cover depth being approximately 9.26 m. The external diameter and the equivalent stiffness of the constructed tunnels are, respectively, 6.2 m and 3.93×10^7 kN·m². In theoretical calculation, it was assumed that the upline of the constructed tunnels was parallel with the excavation, considering the relatively small angle between the upline and the excavation.

In theoretical calculation for this case history, the horizontal additional stress in the upline of the constructed tunnels induced by excavation can be neglected because of the relative position of the upline and the excavation. In other words, the predicted tunnel deformation using the proposed method takes account of only the vertical additional stress induced by excavation.

Figure 5 presents the excavation-induced vertical displacements of the upline tunnel for the SDRI Project obtained by finite element analysis, field measurement, and theoretical calculation. The finite element analysis results presented in Figure 5 were obtained by Xu and Huang [52] using the MARC software. From Figure 5, it can be indicated that the distribution of the tunnel vertical displacement along the tunnel axis is similar for different methods. The distribution conforms approximately to a Gaussian distribution. The tunnel vertical displacements reach maxima in the middle of the upline tunnel axis intersecting with the vertical projection of the excavation. The maximum tunnel vertical displacements are, respectively, 11.5, 16, and 16.96 mm corresponding to the finite element analysis, field measurement, and theoretical calculation. The maximum tunnel vertical displacement calculated by the proposed method is more agree-

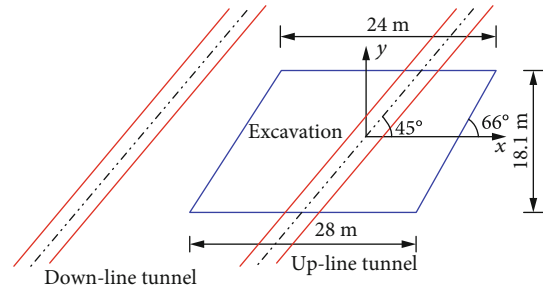


FIGURE 4: Site plan view for the SDRI Project.

TABLE 2: Soil parameters for the SDRI Project [52].

Soil layer	h (m)	γ (kN/m ³)	c (kPa)	μ	E_s (MPa)
Artificial fill	1.82	18.5	16	NA	NA
Silty clay ② ₁	1.13	18.4	10	0.4	6.43
Silty clay ② ₂	0.82	17.7	13	0.3	3.71
Silty clay ③ ₁	1.08	17.7	14	0.3	4.43
Sandy silt ③ ₂	2.28	18.3	3	0.35	9.72
Silty clay ③ ₃	2.46	17.2	13	0.35	3.63
Sandy silt	8.7	16.6	14	0.35	2.27
Clay ⑤ ₁	2.41	17.9	19	0.4	4.07
Silty clay ⑤ ₂	3.89	18.1	18	0.4	4.55
Silty clay	4.25	19.4	43	0.35	6.09

Note. h = soil thickness; γ = unit weight; c = cohesion; μ = Poisson's ratio; E_s = modulus of compressibility; NA = not available.

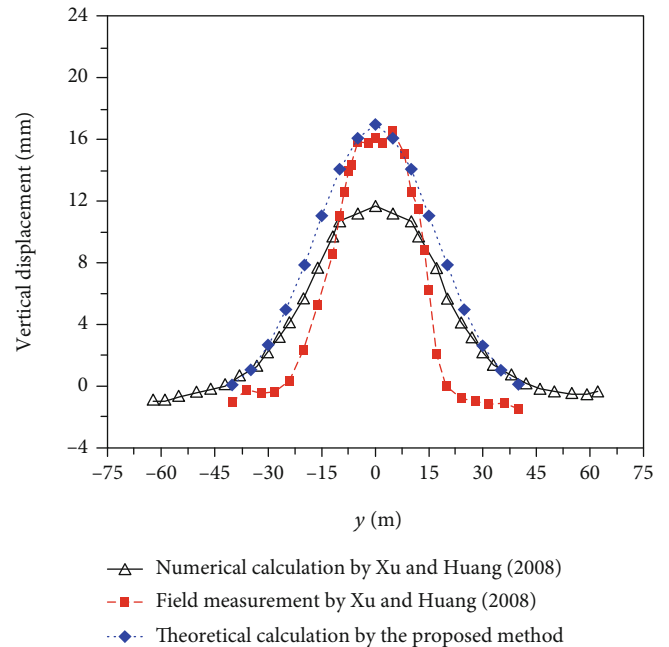


FIGURE 5: Excavation-induced tunnel vertical displacements for the SDRI Project.

able to the field measurement when compared with the finite element analysis result. Moreover, the predicted tunnel vertical displacements by the proposed theoretical method are generally greater than that by finite element analysis and field

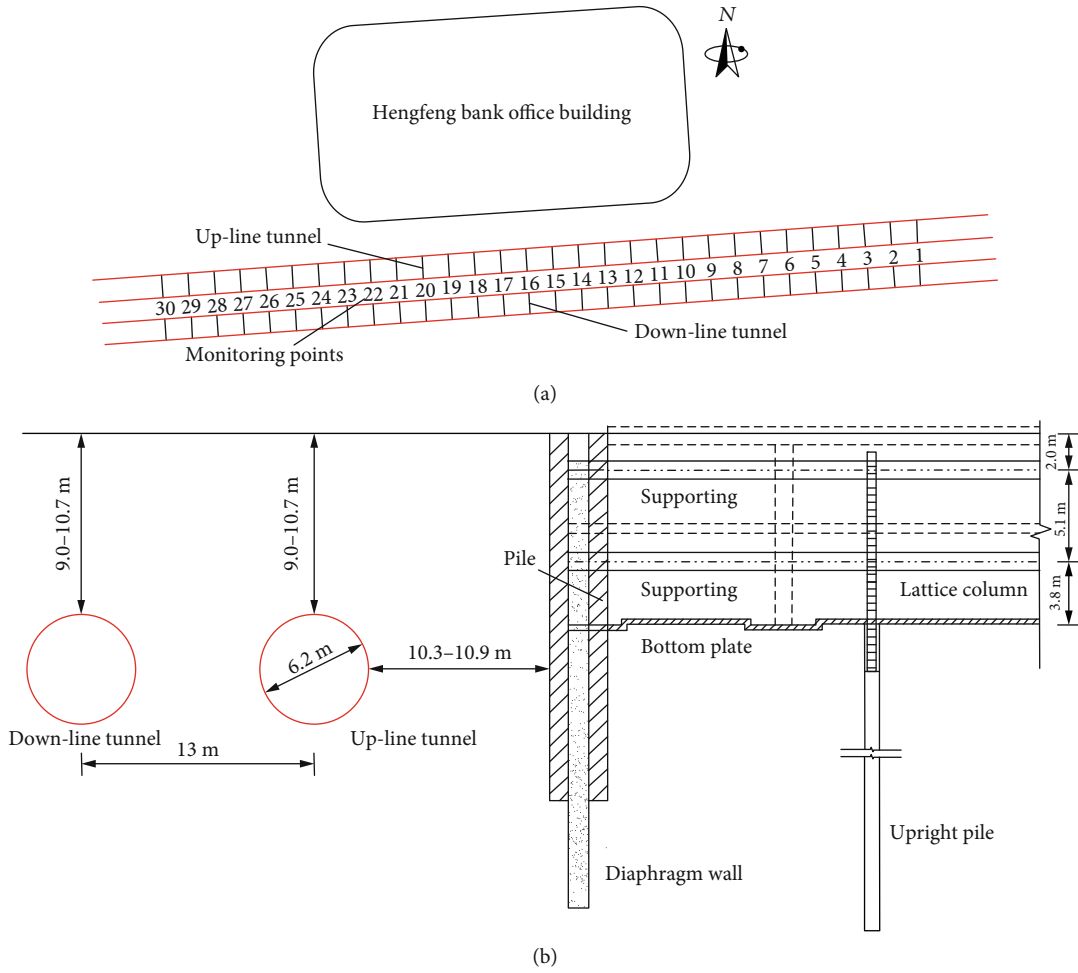


FIGURE 6: Schematic of the relative position of the excavation and the tunnel for the HBOB Project: (a) plan view and (b) cross-section view.

TABLE 3: Soil parameters for the HBOB Project [53].

Soil layer	h (m)	γ (kN/m ³)	c (kPa)	E_s (MPa)	φ (degree)
Plain fill ①	2.0–4.5	18.9	15	NA	10
Powder sticky clay ②	2.5–4.8	19.6	32.35	6.01	13.74
Silt ③	1.2–4.3	18.8	9.84	10.76	27.83
Silty clay ④ ₁	2.1–5.6	18.9	17.46	6.54	13.91
Silty clay ④ ₂	1.8–3.8	18.7	10.86	7.6	20.29
Silty clay ④ ₃	5.8–7.0	18.9	20.58	5.18	12.26
Clay ⑤	3.1–4.1	20.1	60.78	7.67	13.81
Silty clay ⑥	6.0–7.2	19.1	34.59	7.53	16.65
Silty clay ⑦	2.0–3.5	18.8	20.4	6.47	13.19
Silty clay ⑧	8.8–9.9	18.7	15.36	6.97	20.24
Silty clay ⑨	5.0–6.9	19.5	27.34	6.85	12.53
Silty clay ⑩	11.5–12.1	19.4	23.22	7.31	14.07

Note. h = soil thickness; γ = unit weight; c = cohesion; E_s = modulus of compressibility; φ = internal friction angle; NA = not available. Poisson's ratio was taken as 0.35 in the calculation for all the soil layers.

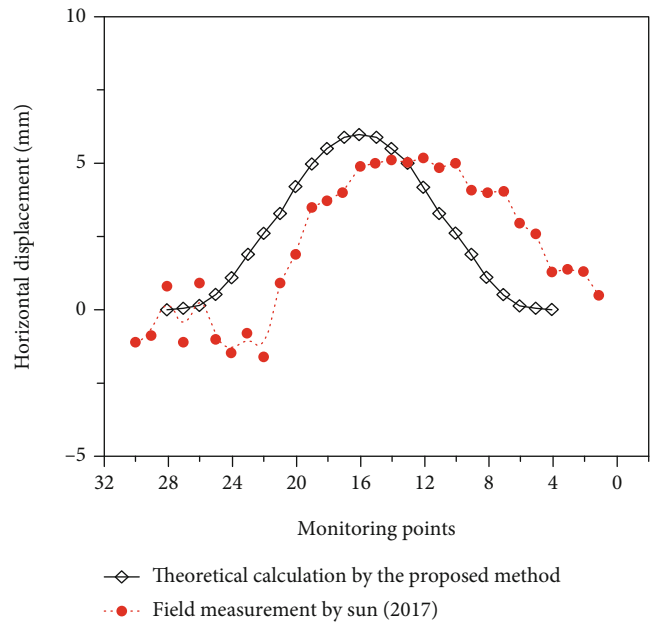


FIGURE 7: Excavation-induced tunnel horizontal displacements for the HBOB Project.

TABLE 4: Soil parameters for the HMLYRS Project.

Soil layer	h (m)	γ (KN/m ³)	c (kPa)	μ	E_s (MPa)	φ (degree)	k (m/d)
Miscellaneous soil	5.1	17.5	8	0.35	NA	10	0.001
Clay ₁	4.7	19.8	10	0.3	40	13	0.0006
Clay ₂	6.4	20.2	15	0.29	30	13	0.0004
Clay ₃	6.5	20.5	25	0.26	30	14	0.0004
SWS	1.1	21	30	0.26	70	20	NA
Weathered sandstone	NA	22	40	0.24	90	25	NA

Note. h = soil thickness; γ = unit weight; c = cohesion; μ = Poisson's ratio; E_s = modulus of compressibility; φ = internal friction angle; k = permeability coefficient; NA = not available; SWS = strongly weatherly sandstone.

measurement. For this, the primary reason is that the proposed theoretical method has not taken account of the influence of excavation supporting on the excavation unloading-induced additional stress.

4.2. Hengfeng Bank Office Building Project. The second case history used for verifying the proposed method is the Hengfeng Bank Office Building (HBOB) Project reported by Sun [53]. In this case history, an excavation adjacent to the Suzhou Metro Line 1 was made for the construction of an office building for Hengfeng Bank. The excavation geometry is approximately a rectangle with its length and width being, respectively, 85 m and 45 m. The average excavation depth is 10.6 m. To ensure stability and safety, diaphragm walls and concrete struts were used to support the excavation. The relative position of the excavation and the tunnel is depicted in Figure 6. Table 3 summarizes the soil parameters for the HBOB Project.

From Figure 6, it can be seen that the tunnel axis is approximately parallel with the south side of the excavation. The distance between the excavation side and the tunnel periphery ranges from 10.3 m to 10.9 m. The cover depth of the tunnel ranges from 9.0 m to 10.7 m. The minimum distance between the upline and downline tunnels is 6.8 m. The external and internal diameters and the equivalent stiffness are, respectively, 6.2 m, 5.5 m, and 3.45×10^7 kN·m². Monitoring was performed at 30 cross-sections of the upline and downline tunnels with the interval being 5 ring-lengths. For convenience, in theoretical calculation, it was assumed that the tunnels are parallel with the excavation and that the excavation is rectangular in shape.

A comparison of the excavation-induced horizontal displacements of the upline tunnel for the HBOB Project between the theoretical calculation and field measurement is made in Figure 7. It can be noted that a slight discrepancy exists between the theoretical calculation and field measurement. The maximum tunnel horizontal displacement occurs at a position corresponding to the middle of the excavation, both for the theoretical calculation and field measurement. The maximum tunnel horizontal displacements predicted by the proposed method and monitored by instrumentations are, respectively, 6 mm and 5.2 mm. The overestimate of the maximum tunnel horizontal displacement by the proposed method is attributed to the overlook of the influence of excavation supporting and stratigraphic distribution.

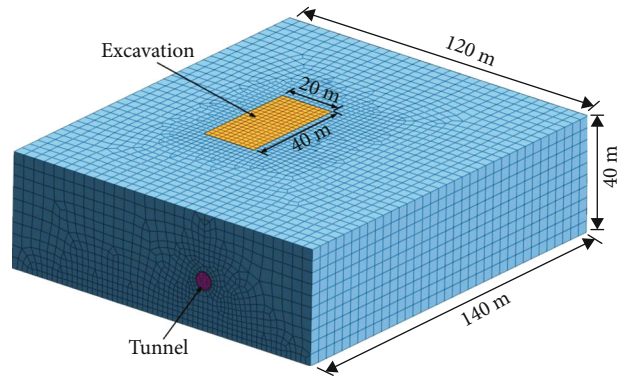


FIGURE 8: Meshing of numerical model for the HMLYRS Project.

4.3. Hefei Metro Line 1 Yungu Road Station Project. The third case history used for verifying the proposed method is the Hefei Metro Line 1 Yungu Road Station (HMLYRS) Project. An imaginary excavation is made adjacent to the HMLYRS Project. By performing three-dimensional finite element analysis, the excavation-induced tunnel internal force and deformation characteristics are compared between the theoretical calculation and numerical analysis results.

According to the drilling data in terms of age of deposition and genetic type as well as the laboratory testing results, the ground stratum for the HMLYRS Project are composed of six layers: miscellaneous fill, clayey soil I, clayey soil II, clayey soil III, highly weathered sandstone, and moderately weathered sandstone. The parameters for these soil layers are summarized in Table 4. The miscellaneous fill consists of construction waste, natural fibers [54–58], and other materials. The groundwater level is about 2.5 m below the ground surface. The specific yield was taken as 0.1 in the theoretical calculation.

In the three-dimensional finite element analysis, the plan view size of the excavation was assumed to be 40 m \times 20 m \times 10 m. The water level within the excavation after dewatering was assumed to be 0.5 m below the excavation bottom. The cover depth of the axis of the constructed tunnels for the HMLYRS Project is 20 m. The distance between the excavation boundary and the tunnel axis is 10 m. The external and internal diameters of the constructed tunnels are, respectively, 6.2 m and 5.4 m. Taking no account of the influence of the segment joint strength, the equivalent stiffness of the constructed tunnels was taken as 3.45×10^7 kN·m². In order to ensure that the numerical analysis results are consistent with

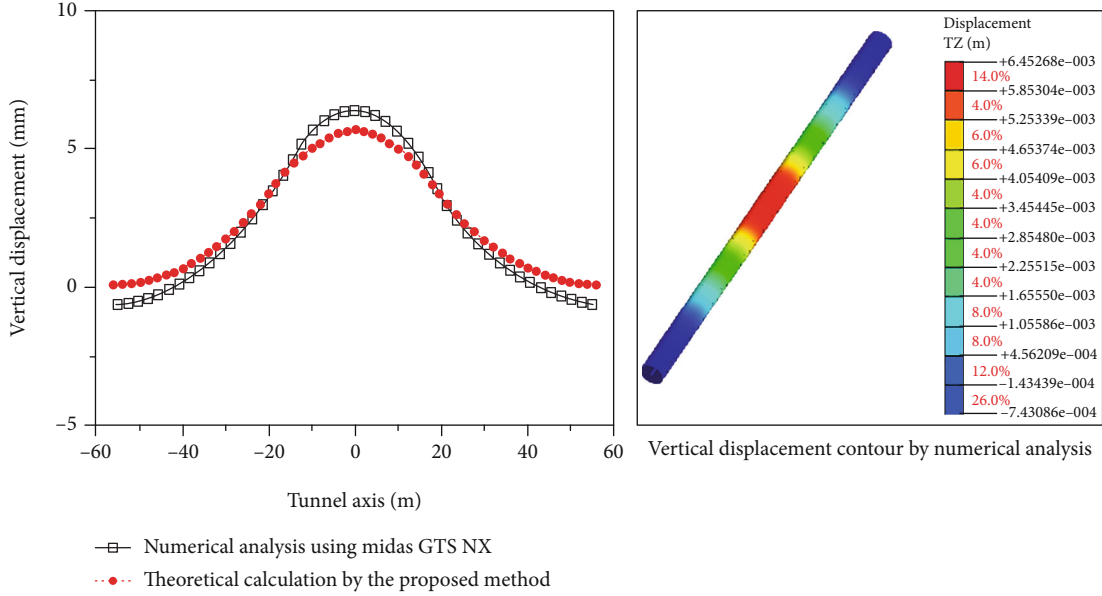


FIGURE 9: Excavation-induced tunnel vertical displacements by numerical and theoretical calculation.

the theoretical calculation results and to mitigate the influence of tunnel dimension on the excavation unloading, the one-dimensional beam element was used to represent the constructed tunnel in numerical modelling. Figure 8 shows the meshing of the numerical model for the HMLYRS Project. It is shown that the dimensions of the numerical model are 120 m \times 40 m \times 140 m. The Modified Mohr-Coulomb (MMC) model was used to simulate the stress-strain behavior of the soils. In the MMC model adopted by the present numerical analysis, the secant modulus by standard drained triaxial tests was estimated by Equation (27) for the miscellaneous fill and clay (i.e., E_{50}^{ref}) and by Equation (28) for the sandstone (i.e., $\tilde{E}_{50}^{\text{ref}}$); the unloading/reloading stiffness was estimated by Equation (29) for the miscellaneous fill and clay (i.e., E_{ur}^{ref}) and by Equation (30) for the sandstone (i.e., $\tilde{E}_{ur}^{\text{ref}}$):

$$E_{50}^{\text{ref}} = 2E_{\text{oad}}^{\text{ref}}, \quad (27)$$

$$\tilde{E}_{50}^{\text{ref}} = \tilde{E}_{\text{oad}}^{\text{ref}}, \quad (28)$$

$$E_{ur}^{\text{ref}} = 5E_{50}^{\text{ref}}, \quad (29)$$

$$\tilde{E}_{ur}^{\text{ref}} = 3\tilde{E}_{50}^{\text{ref}}, \quad (30)$$

where $E_{\text{oad}}^{\text{ref}}$ = tangential stiffness in uniaxial compression tests on miscellaneous fill or clay and $\tilde{E}_{\text{oad}}^{\text{ref}}$ = tangential stiffness in uniaxial compression tests on sandstone.

A comparison of the distribution of excavation-induced tunnel vertical displacement along the tunnel axis is made in Figure 9 between the numerical and theoretical calculation results. It is clear that the two distributions are similar in form. The maximum tunnel vertical displacements are, respectively, 6.45 mm and 5.70 mm for the numerical and theoretical calculation results. Moreover, both the magnitude

and incidence of the excavation-induced tunnel vertical displacement obtained by numerical analysis are greater than that obtained by theoretical calculation.

Figure 10 compares the distribution of excavation-induced tunnel vertical bending moment along the tunnel axis between numerical and theoretical calculation results. Note that the numerical analysis results in Figure 10 represent the incremental change of the tunnel vertical bending moment before and after the excavation. Clearly, a similar distribution of the excavation-induced tunnel vertical bending moment is found between the numerical analysis and theoretical calculation results. This distribution is almost w-shaped and symmetrical with respect to the middle of the tunnel axis. The maximum tunnel vertical bending moments are achieved at the middle of the tunnel axis with the magnitudes being, respectively, 608 kN·m and 560.31 kN·m for the theoretical calculation and numerical analysis results. With an increase in the distance between a point on the tunnel axis and the middle of the tunnel axis, the tunnel vertical bending moments decrease gradually both for the theoretical calculation and numerical analysis results. When this distance reaches about 20 m, the tunnel vertical bending moments reverse their direction. The negative tunnel vertical bending moment peaks, respectively, at the distance of about 30 m with a magnitude of -272 kN·m and at the distance of about 27 m with a magnitude of -302.83 kN·m for the theoretical calculation and numerical analysis results. The tunnel vertical bending moments become zero at the ends of the tunnel axis due to the limitation of the excavation depth and length.

Figure 11 presents a comparison of the distribution of excavation-induced tunnel vertical shear force along the tunnel axis between numerical analysis and theoretical calculation results. Note that the numerical analysis results in Figure 11 represent the incremental change of the tunnel vertical shear force before and after the excavation. It can be indicated that the distributions obtained by theoretical

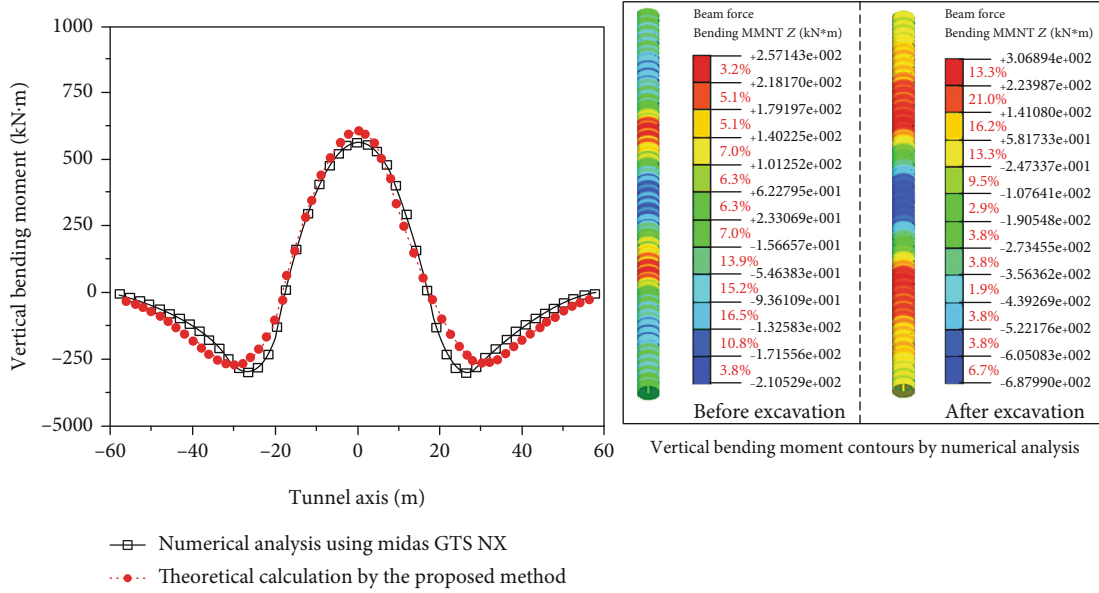


FIGURE 10: Excavation-induced tunnel vertical bending moments by numerical and theoretical calculation.

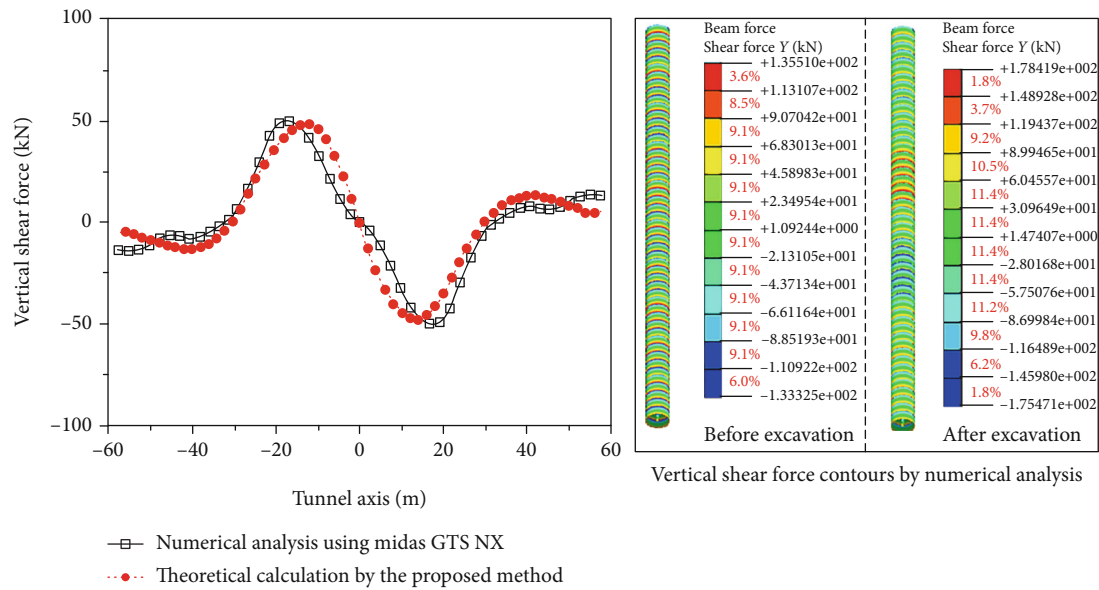


FIGURE 11: Excavation-induced tunnel vertical shear forces by numerical and theoretical calculation.

calculation and numerical analysis are similar in form. The distributions are nearly antisymmetric about the middle of the tunnel axis. The excavation-induced tunnel vertical shear force is zero in the middle of the tunnel axis and reaches the maximum at a distance of 14 m from the middle of the tunnel axis for the theoretical calculation result and at a distance of 18 m for the numerical analysis result. The maxima are, respectively, 48.12 kN and 50.55 kN for the theoretical calculation and numerical analysis results. The shear force stabilizes at a distance of approximately 50 m from the middle of the tunnel axis.

Based on the three case histories presented above, the performance of the proposed theoretical method in well predicting the excavation-induced internal force and deforma-

tion characteristics for a constructed tunnel is validated. Therefore, the proposed theoretical method may serve as a tool to provide a preliminary prediction of the response of a constructed tunnel to an adjacent excavation with dewatering.

5. Parametric Analysis

By performing parametric analysis, this section investigates the influence of excavation and tunnel parameters on the vertical displacement and internal force characteristics of a constructed tunnel induced by an adjacent excavation with dewatering. To this end, an imaginary case is considered where the longer side of a rectangular excavation is parallel

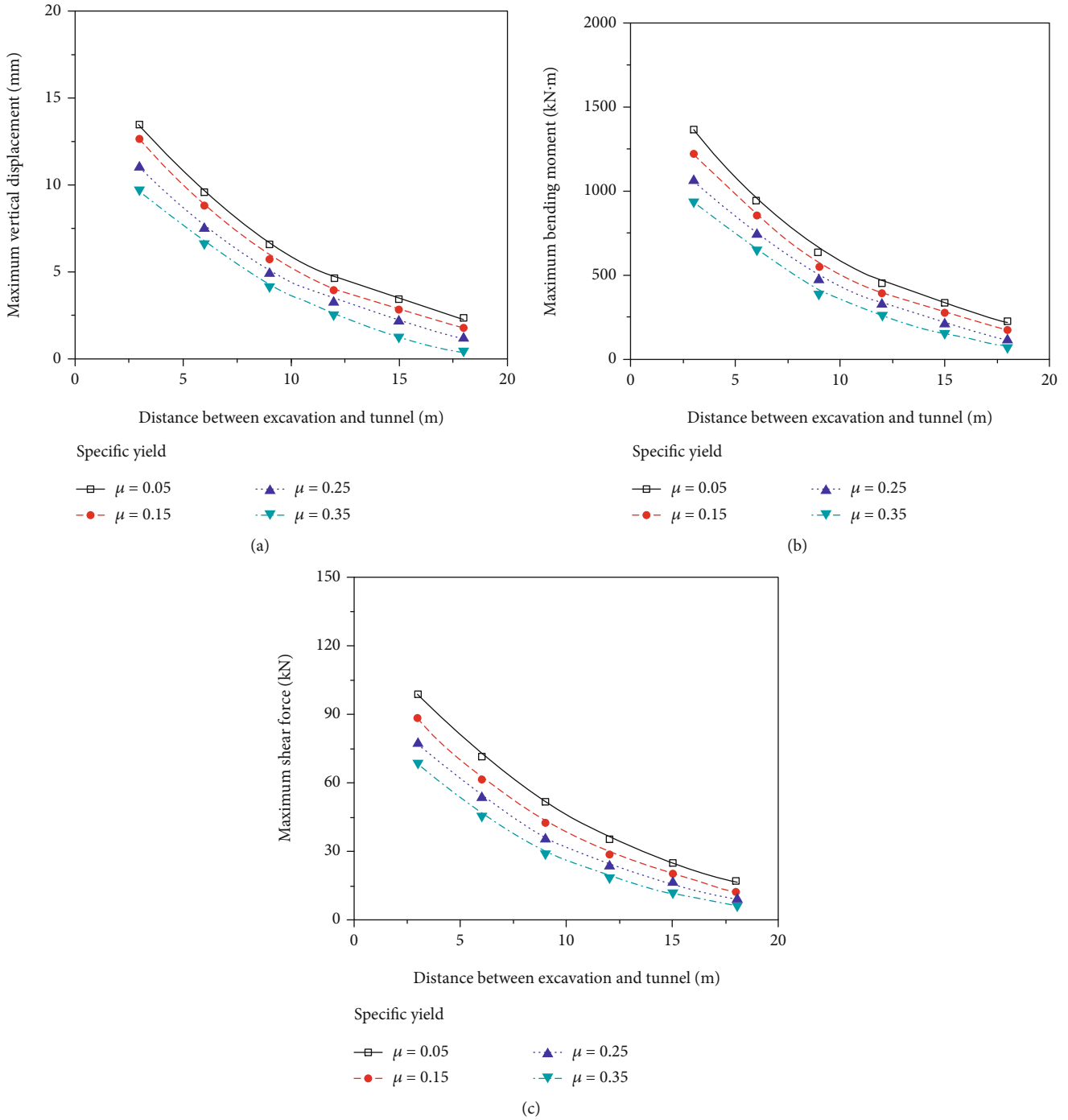


FIGURE 12: Effects of the distance between excavation and tunnel on (a) tunnel maximum vertical displacement; (b) tunnel maximum bending moment; (c) tunnel maximum shear force.

with the axis of the constructed tunnel. For this imaginary case, the soil and tunnel parameters are the same as in the HMLYRS Project described in the former section. In this parametric analysis, the investigated parameters are the distance between excavation and tunnel, initial water level, excavation depth, excavation plan view size, and specific yield.

5.1. *Effect of Distance between Excavation and Tunnel.* Six different distances are considered between the side of the

excavation and the periphery of the constructed tunnel: 3.0, 6.0, 9.0, 12.0, 15.0, and 18.0 m. Figure 12 presents the effects of the distance between excavation and tunnel on tunnel maximum vertical displacement, tunnel maximum bending moment, and tunnel maximum shear force. It can be indicated from Figure 12 that the tunnel maximum vertical displacement, maximum bending moment, and maximum shear force decrease nonlinearly with an increase in the distance between excavation and tunnel. This decreasing trend

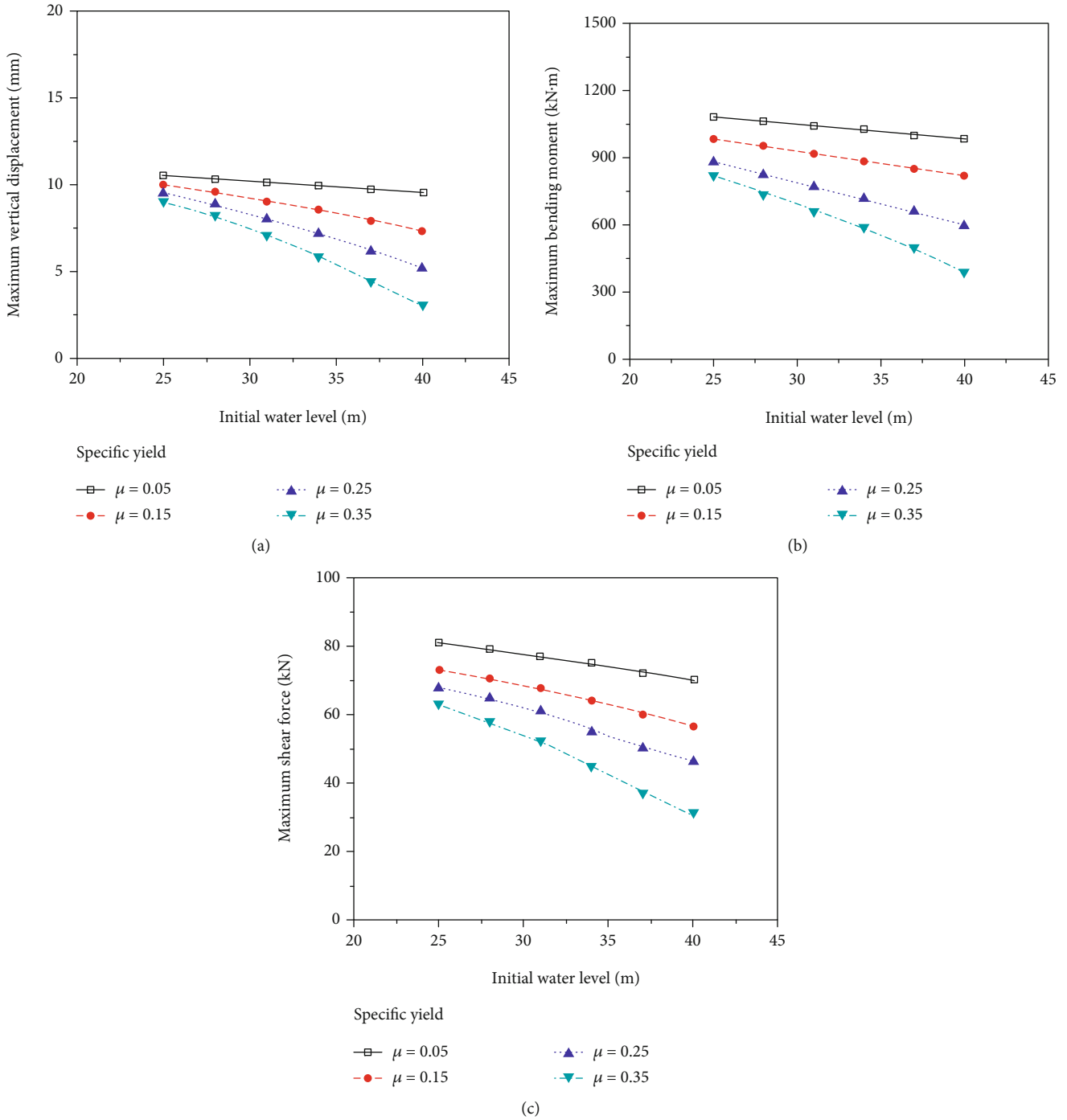


FIGURE 13: Effects of the initial water level on (a) tunnel maximum vertical displacement; (b) tunnel maximum bending moment; (c) tunnel maximum shear force.

is of a lower rate at a greater distance between excavation and tunnel. At the 18.0 m distance between excavation and tunnel, the tunnel maximum vertical displacement, maximum bending moment, and maximum shear force are, respectively, 2.2 mm, 220.0 kN·m, and 17.5 kN. When the distance between excavation and tunnel exceeds 18.0 m, the influence of excavation with dewatering on the responses of the constructed tunnel can be neglected. Moreover, it can also be indicated from Figure 12 that the tunnel maximum vertical

displacement, maximum bending moment, and maximum shear force decrease with increasing the specific yield, irrespective of the distance between excavation and tunnel. At the 3.0 m distance between excavation and tunnel, an increase in the specific yield from 0.05 to 0.35 leads to an approximately 30% reduction in the tunnel maximum vertical displacement, maximum bending moment, and maximum shear force. This reduction increases to approximately 65% when the distance between excavation

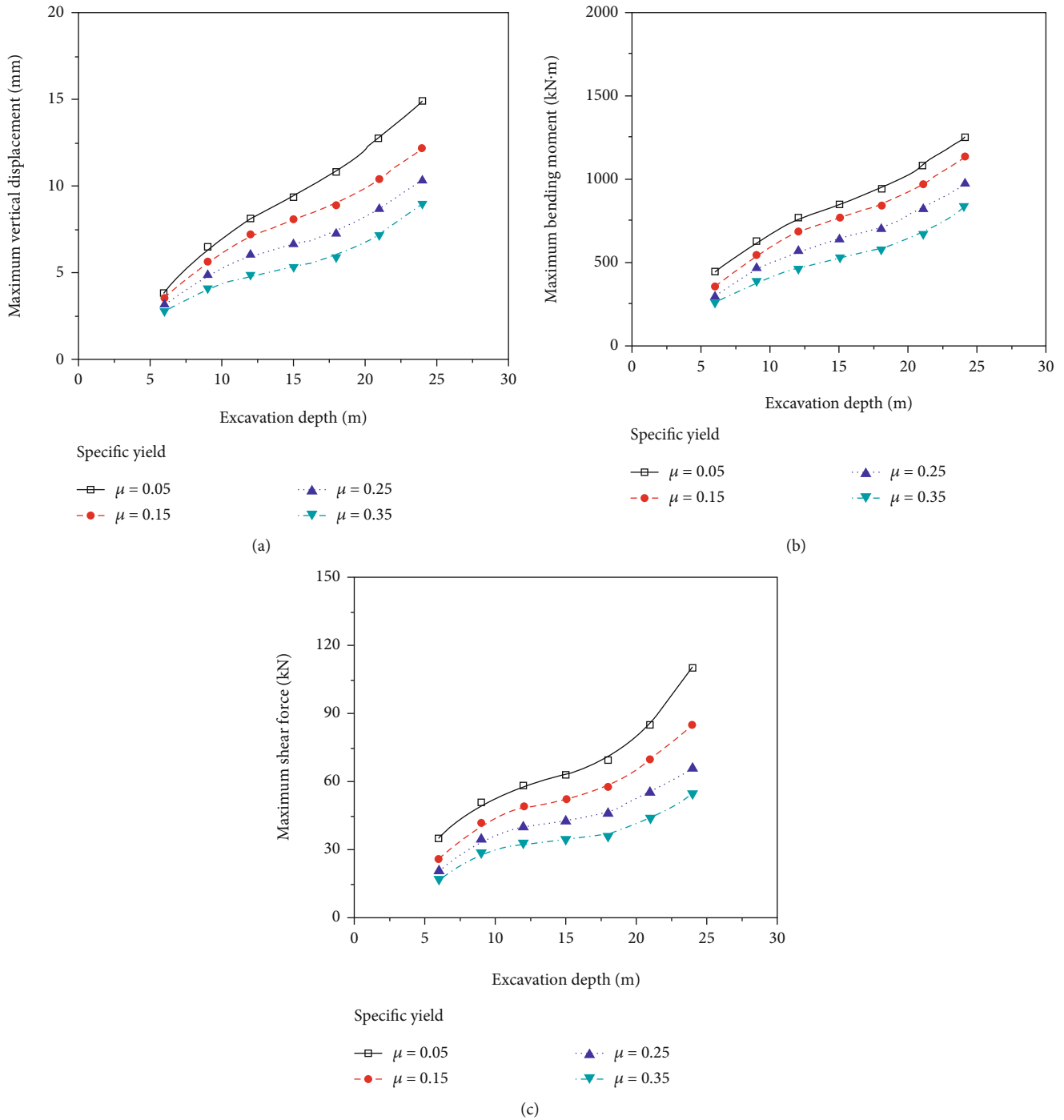


FIGURE 14: Effects of the excavation depth on (a) tunnel maximum vertical displacement; (b) tunnel maximum bending moment; (c) tunnel maximum shear force.

and tunnel reaches 18.0 m. This indicates that the specific yield has a significant effect on the tunnel maximum vertical displacement, maximum bending moment, and maximum shear force.

5.2. Effect of Initial Water Level. Six different initial water levels are considered in the parametric analysis: 25.0, 28.0, 31.0, 34.0, 37.0, and 40.0 m. The effects of the initial water

level on the tunnel maximum vertical displacement, maximum bending moment, and maximum shear force are presented in Figure 13. It can be indicated that the tunnel maximum vertical displacement, maximum bending moment, and maximum shear force decrease with an increase in the initial water level. This is attributed to the reduced vertical additional stress on the constructed tunnel at a higher dewatering depth. Moreover, at an initial water

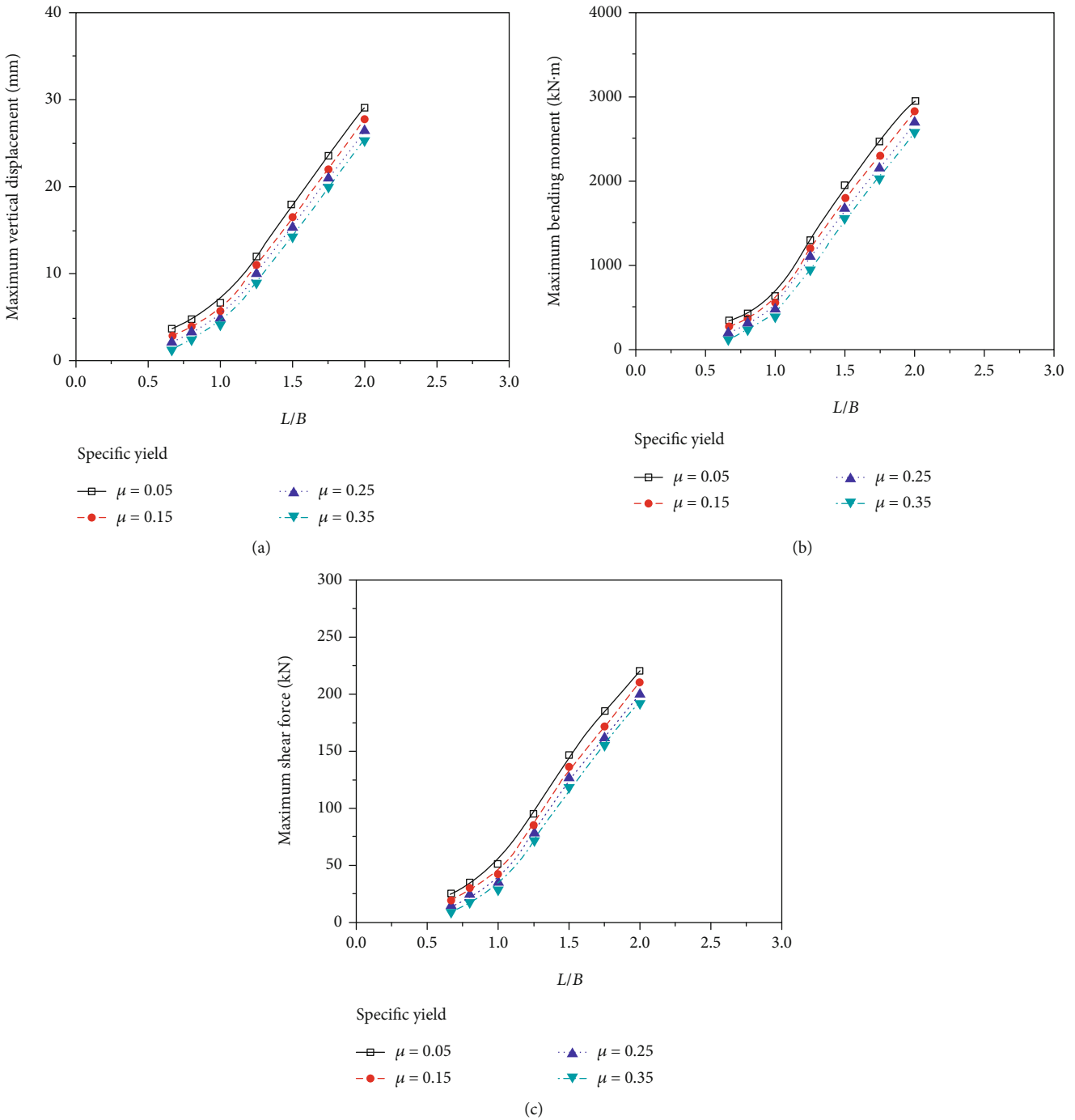


FIGURE 15: Effects of the excavation plan view size on (a) tunnel maximum vertical displacement; (b) tunnel maximum bending moment; (c) tunnel maximum shear force.

level, the tunnel maximum vertical displacement, maximum bending moment, and maximum shear force decrease with an increase in the specific yield. The rate of this decrease is higher at a greater initial water level. At the 25.0 m initial water level, an increase in the specific yield from 0.05 to 0.35 leads to, respectively, 9.6%, 24.1%, and 22.2% reductions in the tunnel maximum vertical displacement, maximum bending moment, and maximum shear force. The reductions are, respectively, 70.0%, 60.1%, and 74.0% at the 40.0 m initial water level. This indicates that at an excavation depth,

the influence of the specific yield on the tunnel displacement and internal force characteristics is more significant at a higher initial water level.

5.3. Effect of Excavation Depth. Seven different excavation depths are considered in the parametric analysis: 6.0, 9.0, 12.0, 15.0, 18.0, 21.0, and 24.0 m. Figure 14 depicts the effects of excavation depth on the tunnel maximum vertical displacement, maximum bending moment, and maximum shear force. It is shown that the rate of increase in the tunnel

maximum vertical displacement, maximum bending moment, and maximum shear force as increasing the excavation depth decreases until reaching the 15.0 m excavation depth and then increases after reaching this excavation depth. At an excavation depth greater than 15.0 m, a striking increase in the tunnel maximum vertical displacement, maximum bending moment, and maximum shear force can be observed with an increase in the excavation depth. This indicates that the effect of excavation depth on tunnel maximum vertical displacement, maximum bending moment, and maximum shear force is more significant at an excavation depth greater than the cover depth of the constructed tunnel. In addition, the tunnel maximum vertical displacement, maximum bending moment, and maximum shear force decrease with increasing the specific yield. At the 6.0 m excavation depth, an increase in the specific yield from 0.05 to 0.35 causes, respectively, 28.0%, 40.8%, and 48.0% reductions in the tunnel maximum vertical displacement, maximum bending moment, and maximum shear force. The reductions are, respectively, 27.4%, 38.0%, and 55.0% at the 24.0 excavation depth. This indicates that the specific yield has a significant effect on the tunnel maximum vertical displacement, maximum bending moment, and maximum shear force.

5.4. Effect of Excavation Plan View Size. The excavation plan view size is described with the ratio of excavation length to excavation width (i.e., L/B). In the parametric analysis, seven different excavation plan view sizes are considered: 0.67, 0.8, 1.0, 1.25, 1.5, 1.75, and 2.0. The excavation length is fixed at 40.0 m when $L/B < 1.0$; otherwise, the excavation width is fixed at 40.0 m. Figure 15 presents the effects of the excavation plan view size on the tunnel maximum vertical displacement, maximum bending moment, and maximum shear force. It can be indicated that at $L/B < 1.0$ or $L/B > 1.0$, the tunnel maximum vertical displacement, maximum bending moment, and maximum shear force increase approximately linearly with an increase in L/B . Moreover, the rate of increase is greater at $L/B > 1.0$ than at $L/B < 1.0$, indicating that the effect of changing the excavation width paralleling with the tunnel axis on the tunnel displacement and internal force characteristics is more significant than that for the excavation length perpendicular to the tunnel axis. In addition, with an increase in the specific yield, the tunnel maximum vertical displacement, maximum bending moment, and maximum shear force decrease. At an excavation depth and initial water level, the effect of specific yield on the tunnel displacement and internal force characteristics is not significant for all the considered excavation plan view sizes.

6. Conclusions

The safety operation of a constructed tunnel is affected by an adjacent excavation with dewatering. It is significant for practicing engineers to predict the displacement and internal force characteristics of a constructed tunnel induced by an adjacent excavation with dewatering. However, most of the previous theoretical studies relating to this topic focus on the excavation unloading effect and have neglected the effect of dewatering. In view of this, this paper proposes a new

method which can account for both the excavation unloading and excavation dewatering effects. The conclusions drawn from this study can be summarized as follows.

- (i) The proposed theoretical method taking account of the excavation unloading and dewatering effects is capable of predicting excavation-induced additional stress on the constructed tunnel that agrees well with the actual engineering. By adopting the beam on elastic foundation theory, the tunnel displacement and internal force under the action of the excavation-induced additional stress are derived. This derivation is simple in calculation. The derived results are reliable
- (ii) Based on three well-documented case histories, the predicted excavation-induced tunnel displacement and internal force characteristics using the proposed method are compared with the field monitoring and numerical analysis results. The comparison verifies the performance of the proposed method. The proposed method lay the theoretical foundations for the safety assessment and disaster prevention in similar engineering
- (iii) A parametric analysis is performed for the effects of excavation depth, distance between excavation and tunnel, excavation plan view size, initial water level, and specific yield on the tunnel displacement and internal force characteristics. It is found that the effect of excavation depth becomes significant when the excavation depth exceeds the cover depth of the constructed tunnel. The influence of adjacent excavation on the constructed tunnel can be overlooked if the distance between excavation and tunnel is greater than the tunnel cover depth. The effect of the excavation plan view size on the side parallel with the tunnel axis is more significant than that on the side perpendicular to the tunnel axis. A higher initial water level corresponds to a smaller excavation-induced additional stress on the constructed tunnel. An increase in the specific yield from 0.05 to 0.35 leads to an approximately 70% reduction in the tunnel displacement and internal force

Data Availability

The data used to support the findings of this study are available from the corresponding authors upon request.

Conflicts of Interest

The authors declare that they have no conflicts of interest.

Acknowledgments

This paper gets its funding from projects (51774107, 51774322, 51774131, and 51874112) supported by the

National Natural Science Foundation of China; Project (KFJJ21-03Z) supported by the State Key Laboratory of Explosion Science and Technology, Beijing Institute of Technology, and Project (2018JJ2500) supported by the Hunan Provincial Natural Science Foundation of China; the authors wish to acknowledge these supports.

References

- [1] R. J. Finno and L. S. Bryson, "Response of building adjacent to stiff excavation support system in soft clay," *Journal of Performance of Constructed Facilities*, vol. 16, no. 1, pp. 10–20, 2002.
- [2] Q. Zhang, B. Huang, M. He, and S. Guo, "A numerical investigation on the hydraulic fracturing effect of water inrush during tunnel excavation," *Geofluids*, vol. 2020, Article ID 6196327, 15 pages, 2020.
- [3] B.-C. B. Hsiung, "Geohazard caused by groundwater in urban underground excavation," *Geofluids*, vol. 2018, Article ID 5820938, 18 pages, 2018.
- [4] Y. Wang, Y. Zhang, and G. Wu, "Correlation research of TBM tunnel rock mechanical characteristics, chiseling specific energy, and abrasion performance: case study of Jiaozhou Bay Subsea Tunnel in Qingdao," *Geofluids*, vol. 2020, Article ID 6658878, 9 pages, 2020.
- [5] P. Guo, X. Gong, and Y. Wang, "Displacement and force analyses of braced structure of deep excavation considering unsymmetrical surcharge effect," *Computers and Geotechnics*, vol. 113, article 103102, p. 17, 2019.
- [6] T. Yang, L. Tong, H. Pan, Z. Wang, X. Chen, and H. Li, "Effect of excavation sequence on uplift deformation of underlying existing metro tunnel," *Journal of Performance of Constructed Facilities*, vol. 35, no. 2, article 04021003, p. 13, 2021.
- [7] C. W. W. Ng, M. Shakeel, J. Wei, and S. Lin, "Performance of existing piled raft and pile group due to adjacent multipropped excavation: 3D centrifuge and numerical modeling," *Journal of Geotechnical and Geoenvironmental Engineering*, vol. 147, no. 4, article 04021012, p. 13, 2021.
- [8] X. Shi, C. Rong, H. Cheng, L. Cui, and J. Kong, "An energy solution for predicting buried pipeline response induced by tunneling based on a uniform ground movement model," *Mathematical Problems in Engineering*, vol. 2020, Article ID 7905750, 12 pages, 2020.
- [9] H. L. Liu, P. Li, and J. Y. Liu, "Numerical investigation of underlying tunnel heave during a new tunnel construction," *Tunnelling and Underground Space Technology*, vol. 26, no. 2, pp. 276–283, 2011.
- [10] D. Wu, K. Xu, P. Guo, G. Lei, K. Cheng, and X. Gong, "Ground deformation characteristics induced by mechanized shield twin tunnelling along curved alignments," *Advances in Civil Engineering*, vol. 2021, Article ID 6640072, 17 pages, 2021.
- [11] C. Lin, M. Huang, F. Nadim, and Z. Liu, "Analytical solutions for tunnelling-induced response of two overlying pipelines," *Tunnelling and Underground Space Technology*, vol. 108, article 103678, p. 14, 2021.
- [12] C. Lin, M. Huang, F. Nadim, and Z. Liu, "Tunnelling-induced response of buried pipelines and their effects on ground settlements," *Tunnelling and Underground Space Technology*, vol. 96, article 103193, p. 17, 2020.
- [13] Y. Wang, C. H. Li, and J. Q. Han, "On the effect of stress amplitude on fracture and energy evolution of pre-flawed granite under uniaxial increasing-amplitude fatigue loads," *Engineering Fracture Mechanics*, vol. 240, article 107366, p. 17, 2020.
- [14] X. Z. Liu, Y. L. Sang, F. Zhao, G. Shi, and Y. Heng, "Evaluation of effects of static pile driving on existing metro tunnel structure," *Journal of Performance of Constructed Facilities*, vol. 33, no. 4, article 04019045, p. 11, 2019.
- [15] Y. Wang, W. K. Feng, R. L. Hu, and C. H. Li, "Fracture evolution and energy characteristics during marble failure under triaxial fatigue cyclic and confining pressure unloading (FC-CPU) conditions," *Rock Mechanics and Rock Engineering*, vol. 53, pp. 1–20, 2020.
- [16] J. W. Shi, C. W. W. Ng, and Y. H. Chen, "Three-dimensional numerical parametric study of the influence of basement excavation on existing tunnel," *Computers and Geotechnics*, vol. 63, pp. 146–158, 2015.
- [17] J. W. Shi, C. W. W. Ng, and Y. H. Chen, "A simplified method to estimate three-dimensional tunnel responses to basement excavation," *Tunnelling and Underground Space Technology*, vol. 62, pp. 53–63, 2017.
- [18] L. X. Li, J. J. Huang, and B. Han, "Centrifugal investigation of excavation adjacent to existing composite foundation," *Journal of Performance of Constructed Facilities*, vol. 32, no. 4, article 04018044, p. 12, 2018.
- [19] M. G. Li, X. Xiao, J. W. Wang, and J. J. Chen, "Numerical study on responses of an existing metro line to staged deep excavations," *Tunnelling and Underground Space Technology*, vol. 85, pp. 268–281, 2019.
- [20] Y. Wang, S. H. Gao, C. H. Li, and J. Q. Han, "Energy dissipation and damage evolution for dynamic fracture of marble subjected to freeze-thaw and multiple level compressive fatigue loading," *International Journal of Fatigue*, vol. 142, article 105927, p. 13, 2020.
- [21] R. P. Chen, F. Y. Meng, Z. C. Li, Y. H. Ye, and J. N. Ye, "Investigation of response of metro tunnels due to adjacent large excavation and protective measures in soft soils," *Tunnelling and Underground Space Technology*, vol. 58, pp. 224–235, 2016.
- [22] M. Zhu, X. N. Gong, X. Gao, S. M. Liu, and J. J. Yan, "Remediation of damaged shield tunnel using grouting technique: Serviceability improvements and prevention of potential risks," *Journal of Performance of Constructed Facilities*, vol. 33, no. 6, article 04019062, p. 14, 2019.
- [23] X. L. Gan, J. L. Yu, X. N. Gong, and M. Zhu, "Characteristics and countermeasures of tunnel heave due to large-diameter shield tunneling underneath," *Journal of Performance of Constructed Facilities*, vol. 34, no. 1, article 04019081, p. 13, 2020.
- [24] K. H. Chen and F. L. Peng, "An improved method to calculate the vertical earth pressure for deep shield tunnel in Shanghai soil layers," *Tunnelling and Underground Space Technology*, vol. 75, pp. 43–66, 2018.
- [25] G. Zheng, X. Y. Yang, H. Z. Zhou, Y. M. Du, J. Y. Sun, and X. X. Yu, "A simplified prediction method for evaluating tunnel displacement induced by laterally adjacent excavations," *Computers and Geotechnics*, vol. 95, pp. 119–128, 2018.
- [26] H. S. Sun, Y. D. Chen, J. H. Zhang, and T. S. Kuang, "Analytical investigation of tunnel deformation caused by circular foundation pit excavation," *Computers and Geotechnics*, vol. 201, pp. 193–198, 2019.
- [27] M. Huang, C. Zhang, and Z. Li, "A simplified analysis method for the influence of tunneling on grouped piles," *Tunnelling and Underground Space Technology*, vol. 24, no. 4, pp. 410–422, 2009.

- [28] Z. Zhang, M. Zhang, and Q. Zhao, "A simplified analysis for deformation behavior of buried pipelines considering disturbance effects of underground excavation in soft clays," *Arabian Journal of Geosciences*, vol. 8, no. 10, pp. 7771–7785, 2015.
- [29] Z. G. Zhang, M. S. Huang, and W. D. Wang, "Evaluation of deformation response for adjacent tunnels due to soil unloading in excavation engineering," *Tunnelling and Underground Space Technology*, vol. 38, pp. 244–253, 2013.
- [30] R. Z. Liang, T. D. Xia, Y. Hong, and F. Yu, "Effects of above-crossing tunnelling on the existing shield tunnels," *Tunnelling and Underground Space Technology*, vol. 58, pp. 159–176, 2016.
- [31] R. Z. Liang, T. D. Xia, M. S. Huang, and C. G. Lin, "Simplified analytical method for evaluating the effects of adjacent excavation on shield tunnel considering the shearing effect," *Computers and Geotechnics*, vol. 58, pp. 224–235, 2017.
- [32] J. F. Zhang, J. J. Chen, J. H. Wang, and Y. F. Zhu, "Prediction of tunnel displacement induced by adjacent excavation in soft soil," *Tunnelling and Underground Space Technology*, vol. 36, pp. 24–33, 2013.
- [33] J. W. Shi, Z. Z. Fu, and W. L. Guo, "Investigation of geometric effects on three-dimensional tunnel deformation mechanisms due to basement excavation," *Computers and Geotechnics*, vol. 106, pp. 106–116, 2019.
- [34] R. B. Peck, "Deep excavation and tunneling in soft ground," in *Proceedings of 7th International Conference on Soil Mechanics and Foundation Engineering*, pp. 225–290, Mexico, 1969.
- [35] G. T. C. Kung, C. H. Juang, E. C. L. Hsiao, and Y. M. A. Hashash, "Simplified model for wall deflection and ground-surface settlement caused by braced excavation in clays," *Journal of Geotechnical and Geoenvironmental Engineering*, vol. 133, no. 6, pp. 731–747, 2007.
- [36] Y. G. Tang and G. T. C. Kung, "Investigating the effect of soil models on deformations caused by braced excavations through an inverse-analysis technique," *Computers and Geotechnics*, vol. 37, no. 6, pp. 769–780, 2010.
- [37] J. H. Li, L. S. Zhu, and S. J. Zhang, "Numerical calculation of hydrodynamic characteristics of tidal currents for submarine excavation engineering in coastal area," *Water Science and Engineering*, vol. 9, no. 2, pp. 155–164, 2016.
- [38] J. X. Wang, Y. S. Deng, R. Q. Ma et al., "Model test on partial expansion in stratified subsidence during foundation pit dewatering," *Journal of Hydrology*, vol. 557, pp. 489–508, 2018.
- [39] Y. Tan, W. Z. Jiang, W. J. Luo, Y. Lu, and C. J. Xu, "Longitudinal sliding event during excavation of Feng-Qi Station of Hangzhou metro line 1: postfailure investigation," *Journal of Performance of Constructed Facilities*, vol. 32, no. 4, article 04018039, p. 27, 2018.
- [40] T. Ran, F. C. Dai, S. H. Mei, W. W. Wang, and L. H. Tan, "Performance of north anchorage excavation of Fuma Yangtze River Bridge in Wanzhou, China," *Journal of Performance of Constructed Facilities*, vol. 33, no. 3, article 06019002, p. 11, 2019.
- [41] X. F. Ou, X. M. Zhang, X. Q. Liu, J. S. Yang, J. Q. Liu, and X. F. Han, "Analytic calculation method of underlying tunnel deformation caused by excavation and dewatering of upper pit," *Journal of the China Railway Society*, vol. 41, no. 3, pp. 147–154, 2019.
- [42] E. I. Anderson, "Modeling groundwater-surface water interactions using the Dupuit approximation," *Advances in Water Resources*, vol. 28, no. 4, pp. 315–327, 2005.
- [43] R. D. Mindlin, "Force at a point in the interior of a semi-infinite solid," *Physics*, vol. 7, no. 5, pp. 195–202, 1936.
- [44] S. M. Liao, F. L. Peng, and S. L. Shen, "Analysis of shearing effect on tunnel induced by load transfer along longitudinal direction," *Tunnelling and Underground Space Technology*, vol. 23, no. 4, pp. 421–430, 2008.
- [45] R. Z. Liang, W. B. Wu, F. Yu, G. S. Jiang, and J. W. Liu, "Simplified method for evaluating shield tunnel deformation due to adjacent excavation," *Tunnelling and Underground Space Technology*, vol. 71, pp. 94–105, 2018.
- [46] J. Y. Han, W. Zhao, P. J. Jia, Y. P. Guang, Y. Chen, and B. F. Jiang, "Risk analysis of the opening of shield-tunnel circumferential joints induced by adjacent deep excavation," *Journal of Performance of Constructed Facilities*, vol. 32, no. 1, article 04017123, p. 12, 2018.
- [47] L. Xu, *Study on the Longitudinal Settlement of Shield Tunnel in Soft Soil*, Master Thesis, Tongji University, 2005.
- [48] G. R. Christian and J. T. Vanmarcke, "Tolerance of buildings to differential settlements," *International Journal of Rock Mechanics and Mining Sciences & Geomechanics Abstracts*, vol. 13, no. 11, pp. 137–150, 1976.
- [49] Y. C. Kog, C. Kho, and K. K. Loh, "Tunnel design and modulus of subgrade reaction," *Journal of Performance of Constructed Facilities*, vol. 29, no. 2, article 04014065, p. 8, 2015.
- [50] A. S. Vesic, "Bending of beams resting on isotropic elastic solid," *Journal of the Engineering Mechanics Division*, vol. 87, no. 2, pp. 35–53, 1961.
- [51] P. B. Attewell, J. Yeates, and A. R. Selby, *Soil Movements Induced by Tunnelling and Their Effects on Pipelines and Structures*, Blackie and Son Ltd, London, 1986.
- [52] L. Xu and H. W. Huang, "Effect of foundation pit excavation on underlying metro tunnels," *Chinese Journal of Geotechnical Engineering*, vol. 30, Supplement 1, pp. 164–166, 2008.
- [53] B. B. Sun, *Effects of Existing Subway Tunnels Due to Adjacent Excavation Construction of Foundation Pit*, Master Thesis, Soochow University, 2017.
- [54] Y. Wang, P. Guo, F. Dai, X. Li, Y. Zhao, and Y. Liu, "Behavior and modeling of fiber-reinforced clay under triaxial compression by combining the superposition method with the energy-based homogenization technique," *International Journal of Geomechanics*, vol. 18, no. 12, article 04018172, p. 22, 2018.
- [55] Y. Wang, P. Guo, H. Lin et al., "Numerical analysis of fiber reinforced soils based on the equivalent additional stress concept," *International Journal of Geomechanics*, vol. 19, no. 11, article 04019122, p. 17, 2019.
- [56] Y.-X. Wang, P.-P. Guo, W.-X. Ren et al., "Laboratory investigation on strength characteristics of expansive soil treated with jute fiber reinforcement," *International Journal of Geomechanics*, vol. 17, no. 11, article 04017101, p. 12, 2017.
- [57] Y. Wang, P. Guo, S. Shan, H. Yuan, and B. Yuan, "Study on strength influence mechanism of fiber-reinforced expansive soil using jute," *Geotechnical and Geological Engineering*, vol. 34, pp. 1079–1088, 2016.
- [58] Y. Wang, P. Guo, X. Li, H. Lin, Y. Liu, and H. Yuan, "Behavior of fiber-reinforced and lime-stabilized clayey soil in triaxial tests," *Applied Sciences*, vol. 9, no. 5, p. 900, 2019.

Research Article

Research on the Deformation Law of Jointed Surrounding Rock during Tunnel Excavation Based on Hydromechanical Coupling

Yan Wang  and Mingfei Li 

School of Civil Engineering, Qingdao University of Technology, Qingdao, Shandong 266033, China

Correspondence should be addressed to Yan Wang; wangyantumu@qut.edu.cn

Received 5 February 2021; Revised 24 February 2021; Accepted 8 March 2021; Published 18 March 2021

Academic Editor: Zhengyang Song

Copyright © 2021 Yan Wang and Mingfei Li. This is an open access article distributed under the Creative Commons Attribution License, which permits unrestricted use, distribution, and reproduction in any medium, provided the original work is properly cited.

The coupling of the joint network and groundwater in rock under bias conditions has a significant impact on the deformation and failure of the surrounding rock due to tunnel excavation. This paper studies the deformation and failure of surrounding rock after tunnel excavation under different joint network and groundwater conditions. A finite element-based composite joint network modeling method is proposed in this paper, and the typical parameters of the surrounding rock, such as the plastic zone size, vertical displacement, and lateral displacement, are analyzed and compared through numerical calculations. According to the different stratum and hydraulic conditions considered, four numerical models under four different working conditions are established and studied. The deformation and failure laws of the surrounding rock during tunnel excavation are obtained. The results show that with a single joint network, when there is no influence of groundwater, the surrounding rock mainly undergoes shear failure at the arch crown after tunnel excavation. When the influence of groundwater is considered, there are differences in the mode of damage between the left and right sides of the tunnel. The stratum approximately 1 m from the invert breaks, and the right sidewall fails approximately 1 m from the measuring point. In rock with a composite joint network, when groundwater is not considered, two kinds of failures occur in the surrounding rock near the tunnel; however, the surrounding rock far from the tunnel is dominated by shear failure. The stratum approximately 3.5 m from the arch crown fractures and the surrounding rock within approximately 5.5 m from the measurement point on the right sidewall undergoes separation failure. Under the dual effects of joints and groundwater, soft rock deforms considerably. The total hydraulic gradient decreases from left to right before and after tunnel excavation. The total hydraulic gradient of the composite joint network strata is generally smaller than that of the single joint network. In the composite joint network strata, the total hydraulic gradient near the tunnel changes dramatically. This research can provide a reference for tunnel engineering under similar conditions.

1. Introduction

In recent years, China's transportation infrastructure has developed rapidly. In particular, in Southwest China, the construction scale of mountain tunnels and railway tunnels continues to grow [1]. Because of the many mountains and hills in Southwest China and the corresponding geological processes, many discontinuous structures, such as joints, cracks, and faults, are present in the strata in this area. Boundaries between soft and hard strata also constitute a typical weak structural plane. Therefore, it is inevitable that a

tunnel built under these conditions crosses different types of weak structural surfaces. In addition, building tunnels in mountainous areas are often affected by bias load [2]. Under the combined action of the bias load and discontinuous structure, the deformation and failure laws of the rock surrounding a tunnel are very different from those of homogeneous layers. Another issue that cannot be ignored is the influence of groundwater. Weak structural surfaces such as joints, cracks, and faults act as conduits for water flow, and hydromechanical coupling has aggravated the destruction of tunnel-surrounding rock. The deformation law of jointed

rock surrounding a tunnel, considering the coupling of the mechanical behavior and hydraulic processes, needs to be further studied.

Many scholars have studied the failure modes and stability effects of tunnel excavation on jointed rock layers. Through orthogonal experiments, Chen et al. [3] discussed the failure mode of shallowly buried and large-span subway tunnels and analyzed the influence of rock mass structure parameters on tunnel failure. The results indicate that the failure modes of all the tested models are shear or tension failure of the overburden strata along weak planes corresponding to randomly distributed joints, which eventually leads to the occurrence of staggered traction slip collapses and clear slip surfaces. Based on the concept of representative elementary volume (REV) and synthetic rock mass (SRM) modeling technology, Wang and Cai [4] proposed a discrete fracture network-discrete element method (DFN-DEM) multiscale modeling approach for determining the response of jointed rock masses to excavation. Roy et al. [5] used the Voronoi subdivision scheme in a framework based on discrete elements to simulate massive rock masses. The prediction model of the convergent strain of a tunnel is constructed by considering the uncertainty in the joint parameters and field stress ratio. Deng et al. [6] used the DEM method to numerically simulate the damage of an existing circular tunnel under the action of an explosion shock wave. The size of disturbance areas such as the destruction area, open area, and shear area around the circular tunnel and the peak particle velocity (PPV) on the tunnel surface are used to analyze tunnel destruction. The direction of the joints in the rock mass around a tunnel has a great influence on the tunnel damage, while the initial stress around a tunnel has relatively little influence on the tunnel failure. Wang et al. [7, 8] studied the excavation of shield tunnels with joints in an upper soft unit and a lower hard unit and proposed a Bayesian network-based dynamic risk assessment method for deep tunnel construction. The results of previous research suggest that under these conditions, the surface settlement caused by tunnel excavation is mainly affected by the elastic modulus and cohesion of the surrounding rock. The above studies mostly focus on the stability of tunnel excavation under the influence of a single joint. Numerical methods are mostly used to study the influence of different angles, spacings, thicknesses, and other joint characteristics on the stability of surrounding rocks and tunnels. However, research on the effect of the joint network and surrounding rock properties on tunnel excavation is not comprehensive enough.

Many studies have been performed on the mechanical properties of jointed rock masses. Bahrani and Kaiser [9] used a unique particle element modeling method to simulate jointed rock masses with various joint interlocking degrees and studied the influence of block shape, joint strength, and joint surface condition on the finite peak strength. The results from this investigation confirm that strength equations based on the geological strength index (GSI) underestimate the confined strength of highly interlocked and nonpersistently jointed rock masses. Zhao et al. [10] deduced a three-point modeling method that can consider arbitrarily arranged

joints and applied it to discrete element simulation. The influence of joints on the mechanical behavior and failure modes of jointed rock specimens was studied. The results show that the joint angle (considering α , β , and γ) and resonant column apparatus (RCA) have a significant effect on the resulting $\sigma(t)$ and failure mode, while n has a significant effect on $E-t$. Changjiang et al. [11] established a jointed rock mass model of a tunnel in bedded strata. Using the finite element strength reduction method, the influences of the joint dip and joint spacing on the tunnel failure mode and stability were studied by assuming that the surrounding rock of the tunnel is a hard rock layer or interbedded hard rock and soft rock. After the tunnel in bedded strata is excavated, the surrounding rock will slide along a joint plane in the bedding direction and the surrounding rock with vertical bedding will bend and break. When the joint inclination angle changes, the damage degree and damage and range in these two directions will change accordingly, which affects the safety factor of the tunnel. The safety factor reaches its peak value when the inclination angle is 40° . The barrier function method based on the f_{min} -con optimization function in MATLAB was used to determine the function of mapping the tunnel boundary to the unit circle in the complex plane, and the structural failure criterion for mapping convergence was established according to the underground reliability theory. Wu et al. [12] approximated a joint as a crack around the tunnel, studied the anisotropy of the stress intensity factor caused by the inclination and position of the crack, and proposed a modified layered tunnel for the classification of rock geomechanics (RMR) joint scoring parameters. The crack with an inclination angle of 45° is the main structural surface of the jointed rock mass around the tunnel, and the corresponding cracks at various points around the tunnel have inconsistent effects on the tunnel. To study the mechanical properties of jointed rock masses, the physical and mechanical properties of prefabricated jointed specimens were measured mainly through indoor tests or numerical simulations. The previous research focuses on the mechanical properties of the rock itself and has little connection with engineering applications, such as tunnel excavation.

Some scholars have also conducted research on jointed rock tunnels by coupling the hydraulic processes and mechanical behavior. Maleki [13] introduced a new method for estimating the inflow of groundwater in a tunnel excavated in a rocky environment. The main advantage of this model is that it takes into account the joint conditions in the tunnel and the direct influence of the tunnel radius, to separate the study of the joint set and the role of the crack system in the diversion of groundwater to the excavation hole. The analysis and empirical methods used to estimate the flow into the tunnel in current engineering practice cannot fully consider the impact of groundwater level drop. Moon and Fernandez [14] proposed an analysis method for estimating the inflow of groundwater considering the drop in groundwater level in a jointed rock mass. The solution of the proposed analysis is similar to the results of field observations and numerical analysis using the unique element method. This method can fully simulate the coupling of the

hydraulic processes and joint behavior in the rock mass. Aiming at the problems that the inflow of water in fractured rock is greatly affected by the anisotropy of the rock and soil structure and that the assumed isotropic hydraulic coefficient is not efficient in calculating the amount of water that infiltrates into a tunnel in a jointed rock mass, Farhadian et al. [15] proposed a fractured rock empirical formula for describing the hydraulic conductivity in fractured rock masses. The empirical equation can be used to accurately predict the inflow of groundwater into a tunnel and thus the amount of water entering the tunnel.

Discrete element numerical simulations [16–20], mechanical tests [21–24], and model tests [25–28] have been used to study the surrounding rock deformation laws of jointed rock in underground engineering. As an emerging technology, 3D printing is also used in the research of jointed rock masses. Xia et al. [29] proposed and verified a new method to accurately reconstruct an irregular CJRM structure using 3D printing. This method can be used in the design of irregular CJRM in rock engineering. To overcome the deficiency of natural joint specimens with the same surface morphology for experimental studies, Jiang et al. [30] present a technical method for replicating natural joint specimens that incorporates two advanced techniques—three-dimensional (3D) scanning and 3D printing—using a computer-aided design (CAD) as the bridge. This method reduces the experimental error derived from the differences between replicate specimens containing natural joint morphology. Peridynamics, as a novel numerical method, is increasingly used in the study of rock fractures and joint crack propagation. Wang et al. and Zhou et al. [31–33] investigated crack propagation and coalescence behaviors in rock specimens containing preexisting open flaws under uniaxial compression using peridynamics. Most studies are limited to a single factor, such as the characteristic parameters of the joints, the size of the tunnel, or the volume of the water flow. The influence of multiple factors is commonly encountered in actual engineering. Therefore, it is necessary to study the deformation and failure laws of tunnel excavation in different rocks under the influence of both the joint network and hydromechanical processes. Compared with DEM, FLAC, PFC, and other numerical calculation methods, the FEM method has higher efficiency in linear solving. The DEM method is mostly used in the calculation of rock fractures. FLAC is widely used in the calculation of large deformation of soft rock. PFC is widely used in fluid calculations. The RS2 finite element software selected in this paper has a rich built-in joint network model and can perform hydraulic coupling calculations. Based on an engineering example of a railway tunnel in Southwestern China, the finite element method is used to establish a numerical model to study the deformation and failure laws of surrounding rock with different joint networks during tunnel excavation under a bias load. By comparing and analyzing the tunnel surrounding rock deformation parameters of tunnels located in rock with a single joint network and rock with a composite joint network, with and without hydraulic coupling, typical parameters such as the horizontal and vertical displacements and plastic zone size of the surrounding rock are analyzed

under different conditions. The stability of the surrounding rock of a tunnel under the combined action of groundwater flow and joint networks is discussed in this paper, which can provide a reference for similar tunnel projects.

2. The Joint Network Equivalent Model

According to the equivalent model of a joint network in strata summarized by Yabin [34] and Weihuan [35], the one-group joint model, two-group joint model and N -group joint model are analyzed.

2.1. The One-Group Joint Model. Suppose there is a group of joints in a two-dimensional coordinate system; the average distance between two joint surfaces is d , and the angle between the normal direction of the joint surface and the horizontal direction is φ , as shown in Figure 1.

The stress-strain relationship of the joint in the local coordinate system is as follows:

$$\begin{Bmatrix} \sigma_x' \\ \sigma_y' \\ \sigma_z' \end{Bmatrix} = M \begin{bmatrix} 1 - n\mu_2^2 & \mu_2(1 + \mu_1) & 0 \\ \mu_2(1 + \mu_1) & \frac{1 - \mu_2^2}{n} & 0 \\ 0 & 0 & \frac{G_2}{M} \end{bmatrix} \begin{Bmatrix} \varepsilon_x' \\ \varepsilon_y' \\ \varepsilon_z' \end{Bmatrix}, \quad (1)$$

or

$$\sigma' = [D'] \{ \varepsilon' \}, \quad (2)$$

where

$$\begin{aligned} M &= \frac{E_1}{(1 + \mu_1)(1 - \mu_1 - 2n\mu_2^2)}, \\ n &= \frac{E_2}{E_1}, \\ G_2 &= \frac{1}{[(2(1 + \mu)/E) + (1/K_s S)]}, \\ E_2 &= \frac{1}{[(1/E_1) + (1/K_n S)]}, \\ E_1 &= E, \\ \mu_1 &= \mu, \\ \mu_2 &= \left(\frac{E_2}{E_1} \right) \mu_1 = n\mu_1. \end{aligned} \quad (3)$$

E is the elastic modulus of the intact rock mass, and μ is the Poisson's ratio of the intact rock. K_n and K_s are the stiffness coefficients corresponding to the normal and tangential directions on the joint plane in the rock, respectively.

To convert the matrix $[D']$ from the local coordinate system x - y to the global coordinate system X - Y , the global

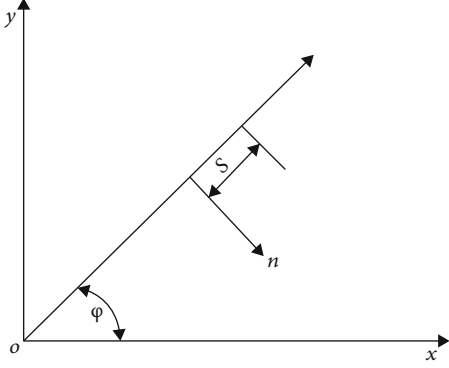


FIGURE 1: The one-group joint model in local and global coordinate systems.

coordinate system $[D]$ can be obtained as follows:

$$[D] = [L][D'] [L]^T, \quad (4)$$

where

$$[L] = \begin{bmatrix} \cos^2\theta & \sin^2\theta & -2 \sin \theta \cos \theta \\ \sin^2\theta & \cos^2\theta & 2 \sin \theta \cos \theta \\ \sin \theta \cos \theta & -\sin \theta \cos \theta & \cos^2\theta - \sin^2\theta \end{bmatrix}. \quad (5)$$

2.2. The Two-Group Joint Model. The two-group joint model is shown in Figure 2.

When there are two sets of joint planes in the surrounding rock, to simplify the calculation process, the interaction among joints is not considered. Instead, the contribution of each group of joints to the rock mass is calculated and algebraically superposed. In this case, the elastic matrix of the rock mass with joints can be written as follows:

$$\begin{aligned} [D] &= [D_0] + ([D_1] - [D_0]) + ([D_2] - [D_0]) \\ &= [D_1] + [D_2] - [D_0] = \sum_{i=1}^2 [D_i] - [D_0], \end{aligned} \quad (6)$$

where $[D]$ is the elastic matrix when the rock is intact, $[D_1]$ is the elastic matrix when only the first group of rock joints is present, $[D_2]$ is the elastic matrix when only the second group of rock joints is present, $[D_1] - [D_0]$ is the influence of the first group of joints on the rock mass, and $[D_2] - [D_0]$ is the influence of the second group of joints on the rock mass.

2.3. The N-Group Joint Model. According to the calculation process when one and two groups of joints exist, the elastic matrix for the N-group joint model in the X-Y coordinate

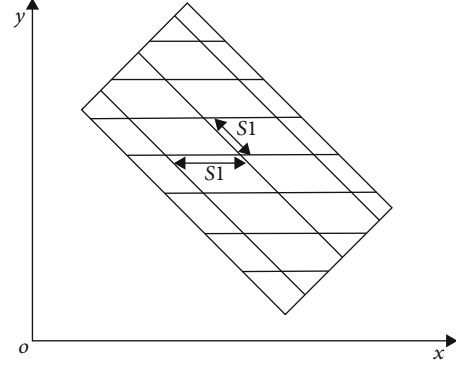


FIGURE 2: The two-group joint at global coordinate system.

TABLE 1: Numerical model conditions.

Working condition	Stratum condition	Hydraulic condition
I	Single joint network	Without groundwater
II	Single joint network	With groundwater
III	Composite joint network	Without groundwater
IV	Composite joint network	With groundwater

system can be calculated as follows:

$$\begin{aligned} [D] &= [D_0] + ([D_1] - [D_0]) + ([D_2] - [D_0]) = [D_1] \\ &+ [D_2] - [D_0] + \dots + [D_n] - [D_0] = \sum_{i=1}^N [D_i] - (n-1)[D_0], \end{aligned} \quad (7)$$

where $[D_i] = [L_i][D_i'] [L_i]^T$.

3. Numerical Simulation Methodology

3.1. Numerical Model Conditions. To study the deformation and failure laws of the surrounding rock with a single joint network and a composite joint network after tunnel excavation under the influence of the hydromechanical process, a comparative analysis numerical model was established with the finite element method. According to the two conditions of a single joint network and a composite joint network, the model is divided into two types. Among them, a single joint network corresponds to a hard rock stratum and a composite joint network corresponds to a hard rock stratum and a soft rock stratum. According to the two hydraulic conditions, including and excluding groundwater, the model is further divided into two types.

Therefore, according to the stratum conditions and hydraulic conditions, four working conditions, namely, working condition I, working condition II, working condition III, and working condition IV, are considered, as shown in Table 1. The groundwater is realized by setting different

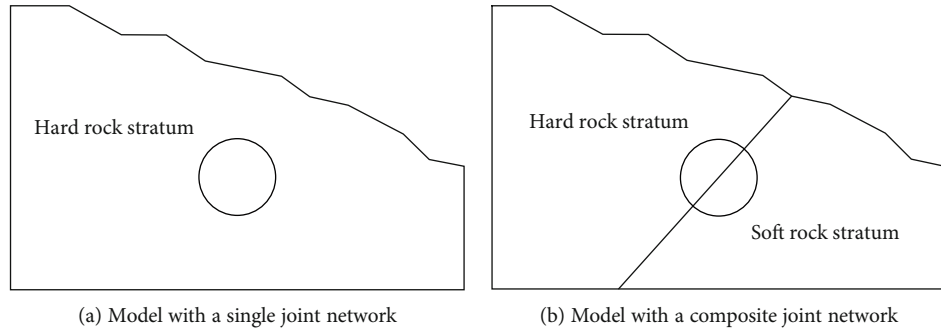


FIGURE 3: Schematic models.

TABLE 2: Stratum parameters.

Stratum	Density γ (kN/m ³)	Elastic modulus E (GPa)	Poisson's ratio ν	Cohesion c (MPa)	Internal friction angle φ (°)	Tensile strength t (MPa)
Hard stratum	26	20	0.3	1.6	55	0.8
Soft stratum	22	6	0.35	0.6	45	0.35

TABLE 3: Joint parameters.

Joint	Cohesion c (MPa)	Internal friction angle φ (°)	Normal stiffness N (MPa/m)	Shear stiffness S (MPa/m)
Joint 1	0.08	20	30000	3000
Joint 2	0.03	15	10000	1000

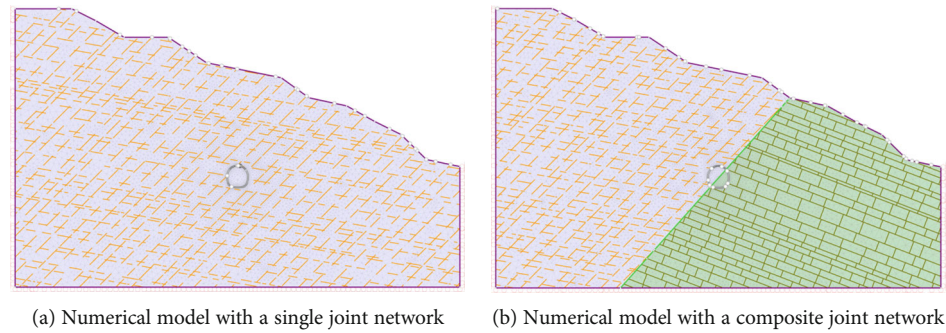


FIGURE 4: Numerical models.

total water heads at the left and right boundaries. According to the model boundaries, the water head on the left is 75 m and the water head on the right is 32.5 m. The groundwater is set after the initial balance.

3.2. The Numerical Simulation Model. For the example of a railway tunnel project, numerical models are established by considering the abovementioned working conditions. When simulating working condition I and working condition II, the tunnel is placed in strata with a single joint network (simplified as hard rock). When simulating condition III and condition IV, the tunnel is placed in strata with a composite joint network (simplified as hard rock and soft rock). By default, the intersection of the hard and soft rocks runs diagonally through the center of the tunnel. Different model heights

and initial stresses are used to achieve different bias loads. The models of a single joint network and a composite joint network are shown in Figure 3. For clarity, the tunnel is enlarged to a certain extent. The influence of the joint network on the direction of tunnel excavation has not been considered. The lining effect and excavation steps are not considered in the paper. Therefore, the 2D method was selected by the paper for calculation.

In the studied project, the width of the actual tunnel is 5.6 m and the height is 6.8 m. The tunnel in the model has a width of 120 m and a height of 75 m. The x direction is the horizontal direction, and the y direction is the vertical direction. The origin of the coordinates is at the center of the tunnel. The x direction displacement is fixed at the left and right boundaries, the y direction displacement is fixed at the lower

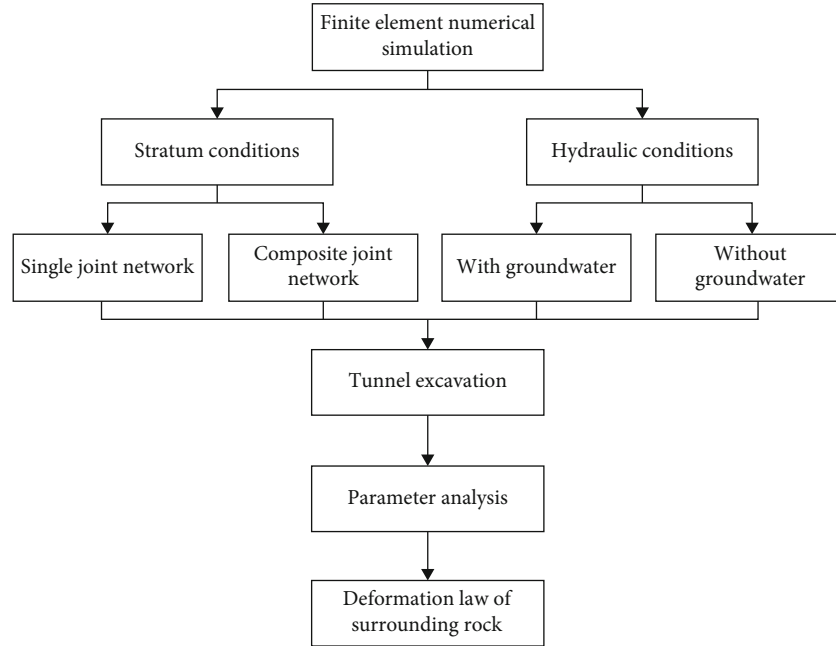


FIGURE 5: Numerical calculation steps.

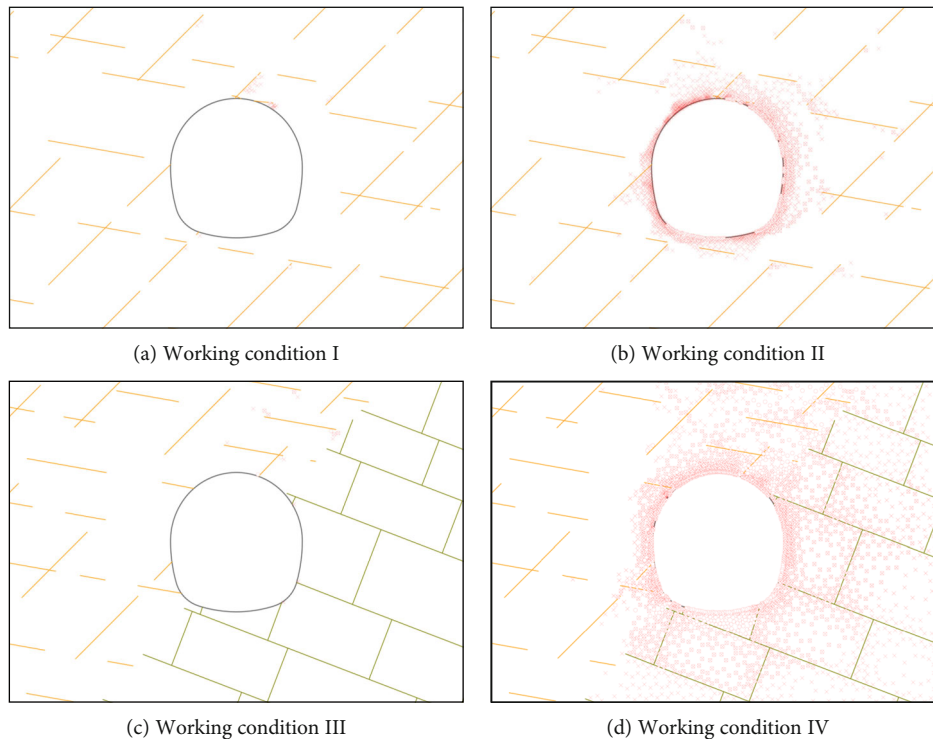


FIGURE 6: Surrounding rock plastic zone.

boundary, and the upper boundary is free. Each joint network is realized by setting different joint spacings and lengths and a joint inclination. Two hard rock joint networks are combined by combining two different parallel statistical models. Among them, one is generated according to a normal distribution with an average joint spacing of 3 m and a standard deviation of 0.8 m. The other is generated according to a normal distribution with a mean distance between joints

of 2 m and a standard deviation of 0.5 m. The network formed by the interweaving of the two parallel statistical models is the joint network. The soft rock joint networks are generated by creating a cross-jointed model with a normal distribution with a mean value of 2 m and a standard deviation of 0.8 m. The cross-joint spacing is generated according to a normal distribution with a mean value of 5 m and a standard deviation of 1 m. The method of setting

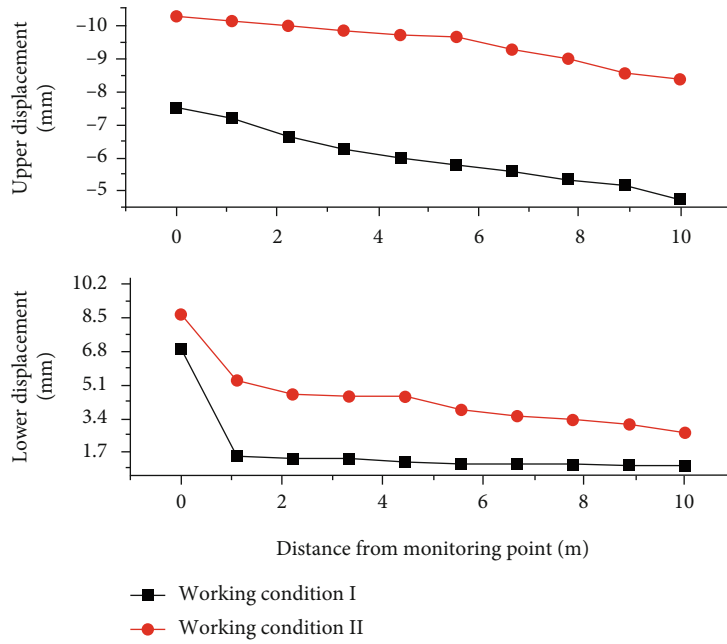


FIGURE 7: Vertical displacements of working conditions I and II.

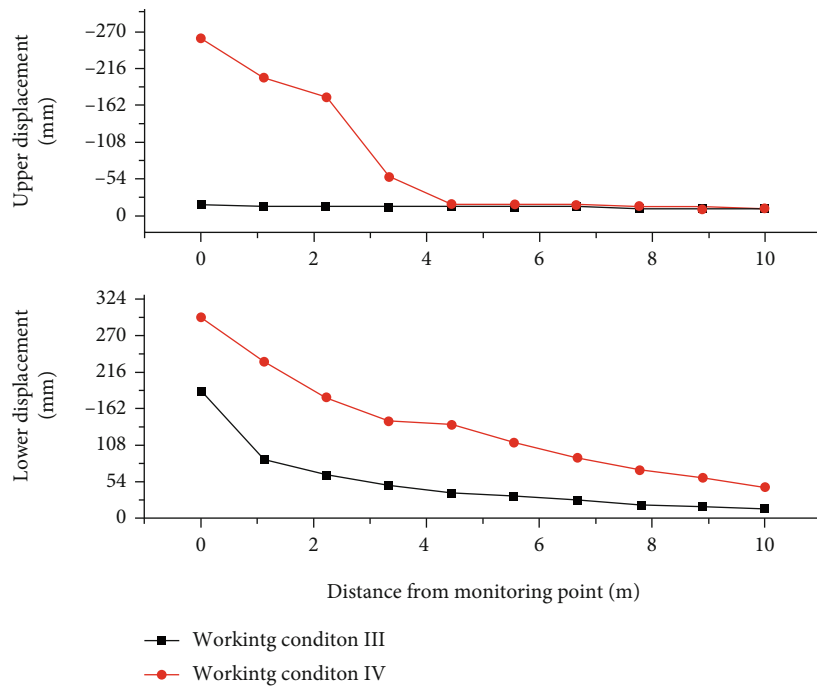


FIGURE 8: Vertical displacements of working conditions III and IV.

the water head is used to simulate groundwater. The model has 22,832 triangular elements and 13,232 nodes. The formation parameters and joint parameters are shown in Tables 2 and 3. Joint 1 represents the joints in the joint network in the hard strata, and joint 2 represents the joints in the joint network in the soft strata. The numerical models of the single joint network and composite joint network are shown in Figure 4.

When performing numerical calculations, according to the four different working conditions, the initial strata balance is performed and the initial displacement is reset. After tunnel excavation, the changes in the surrounding rock deformation parameters are analyzed and the surrounding rock deformation laws under the four working conditions are obtained. The full-face excavation method is adopted. The numerical calculation steps are shown in Figure 5.

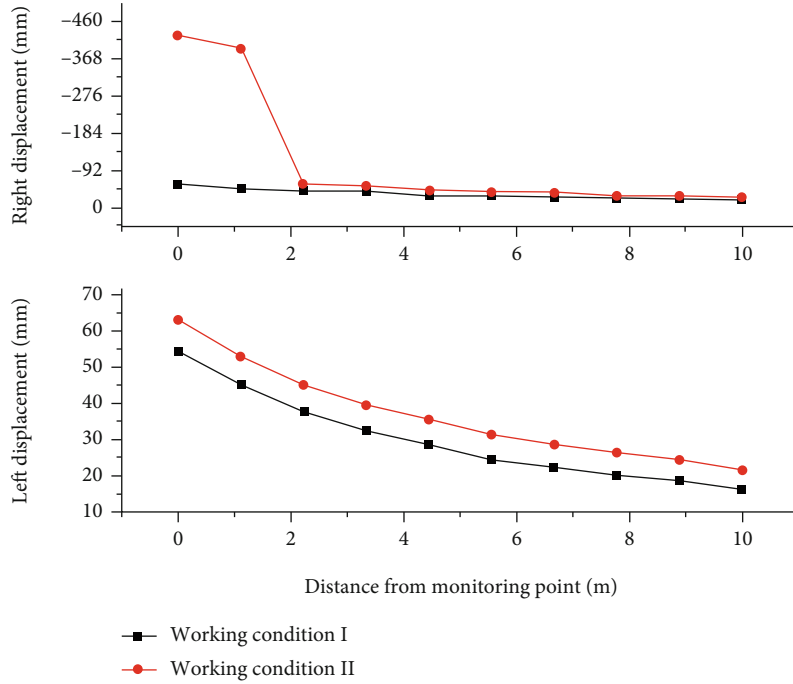


FIGURE 9: Horizontal displacements of working conditions I and II.

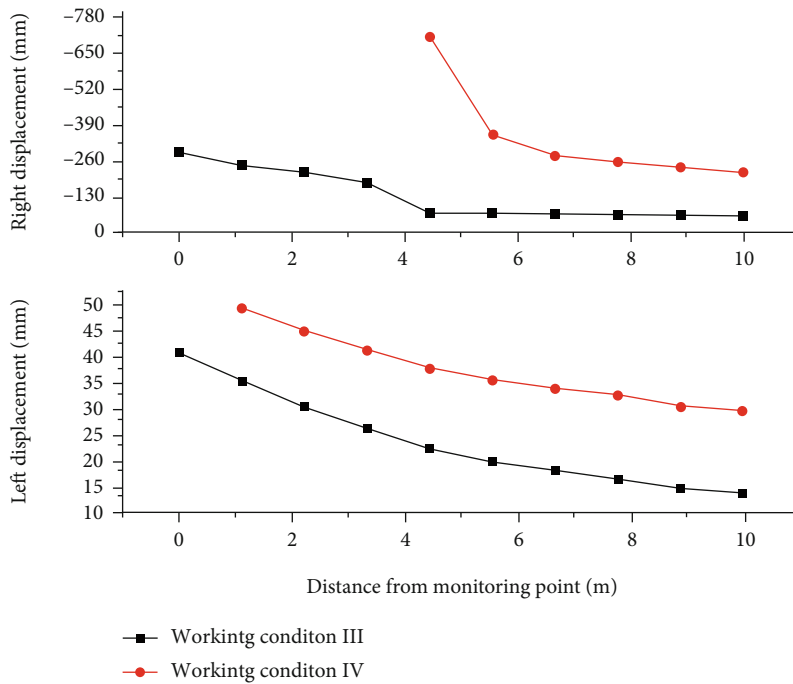


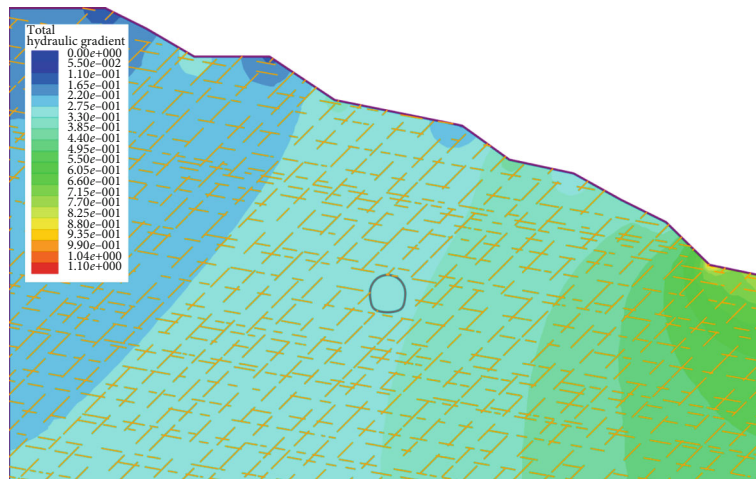
FIGURE 10: Horizontal displacements of working conditions III and IV.

4. Analysis of Numerical Simulation Results

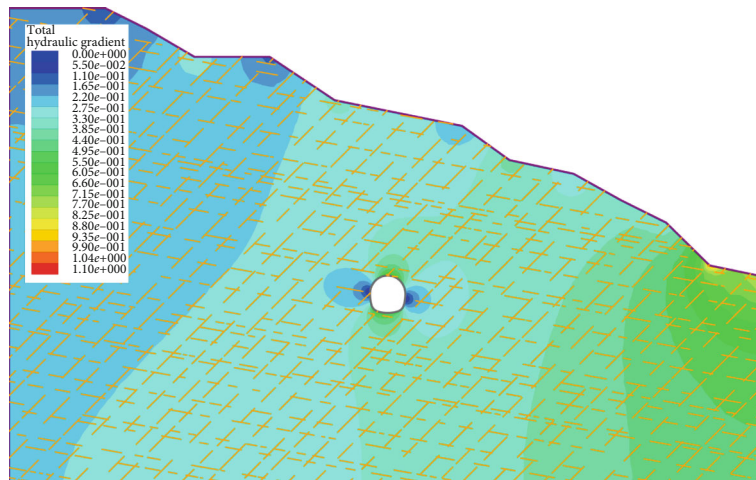
According to the four numerical models corresponding to the different working conditions, numerical calculations are carried out during the tunnel excavation in strata with joints and the surrounding rock deformation parameters are analyzed and compared.

4.1. *The Surrounding Rock Plastic Zone.* According to the calculation results, the shape of the plastic zone in the surrounding rock caused by tunnel excavation is obtained under the four working conditions, as shown in Figure 6.

The shape of the plastic zone in the surrounding rock shows that with a single joint network in hard rock and without the influence of groundwater, the surrounding



(a) Before tunnel excavation



(b) After tunnel excavation

FIGURE 11: Total hydraulic gradient with a single joint network.

rock mainly undergoes shear failure at the vault after tunnel excavation. Because of the existence of a set of cross-joints at the arch crown, the strength of the surrounding rock at the arch crown is weak, so shear failure occurs there. For the single joint network in hard rock under the influence of groundwater, the surrounding rock near the tunnel yielded but the yield range was not large. The surrounding rock on the left of the tunnel is dominated by shear failure, while the surrounding rock on the right undergoes both shear and tensile failure. For the composite joint network, without the influence of groundwater, tunnel excavation mainly produces a small amount of damage in the surrounding rock at the junction of the soft and hard strata. Under the influence of the composite joint network and groundwater, the surrounding rock near the tunnel suffers large-scale damage, mainly concentrated in the soft rock. The surrounding rock above the arch crown and below the invert yields in a large area. Two kinds of failures occur near the tunnel at the same time, whereas shear failure is the main failure at the rock far from the tunnel.

4.2. Vertical Displacement. To study the law of the vertical deformation of the surrounding rock caused by tunnel excavation under the four working conditions, two monitoring points are set at the midpoints of the tunnel arch crown and invert and the vertical displacements at 10 m above and below the two monitoring points are selected for analysis. The vertical displacements of working condition I and working condition II are shown in Figure 7. When only a single joint network is present, the vertical displacement affected by groundwater is greater than that without the influence of groundwater. The stratum displacement approximately 1 m from the invert decreases rapidly, indicating that the stratum fractures are there. The vertical displacement tends to be stable after the rock breaks.

The vertical displacements of working condition III and working condition IV are shown in Figure 8. In the rock with a composite joint network, the vertical displacement affected by groundwater is also greater than that without the influence of groundwater. The displacement of the surrounding rock at approximately 3.5 m from the arch crown decreases rapidly, indicating that the formation breaks.

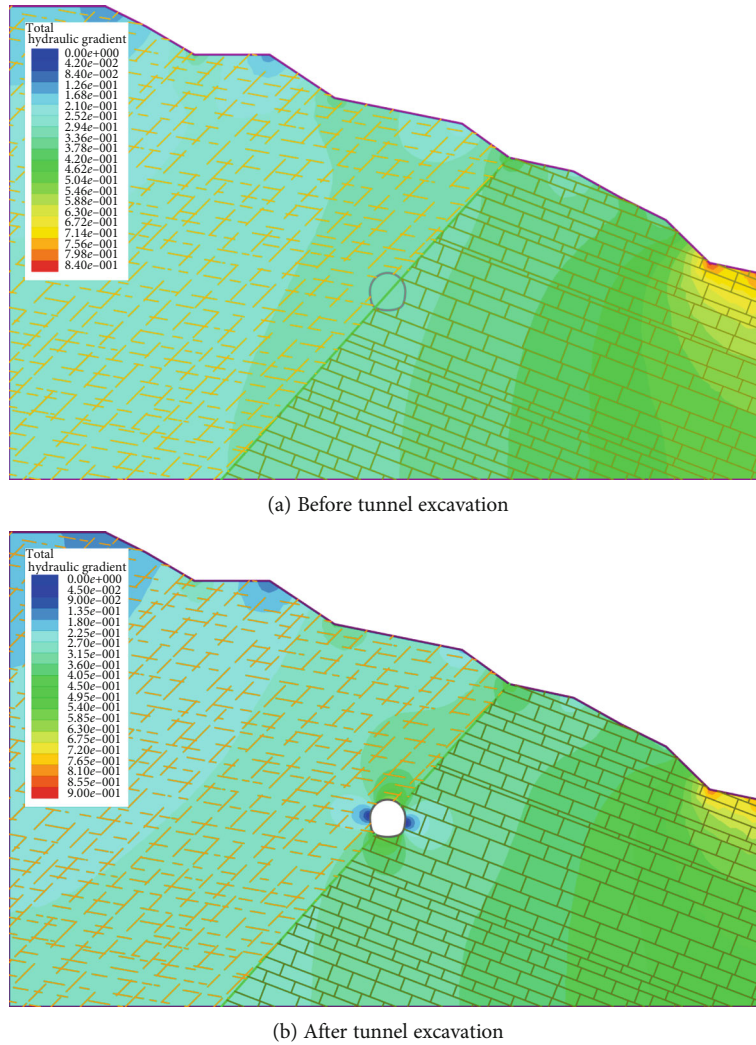


FIGURE 12: Total hydraulic gradient with a composite joint network.

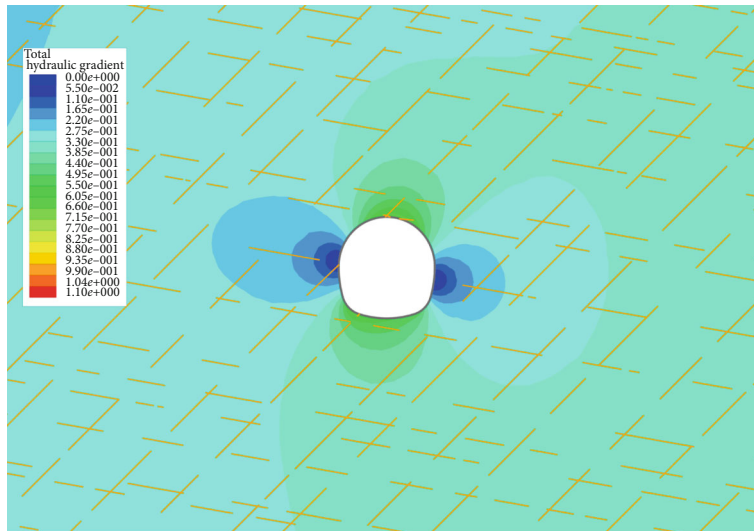
Comprehensive analysis suggests that the yield fractures of the strata may be affected by the joints, which are weak structural planes, resulting in a decrease in the strength of the strata. After the tunnel is excavated, under the influence of a coupled hydromechanical process, separation failure occurs.

4.3. Horizontal Displacement. To study the law of horizontal deformation of the surrounding rock caused by tunnel excavation under the four working conditions, two measuring points were set at the midpoints of the left and right sidewalls of the tunnel and the horizontal displacements within 10 m from the two measuring points were selected for analysis.

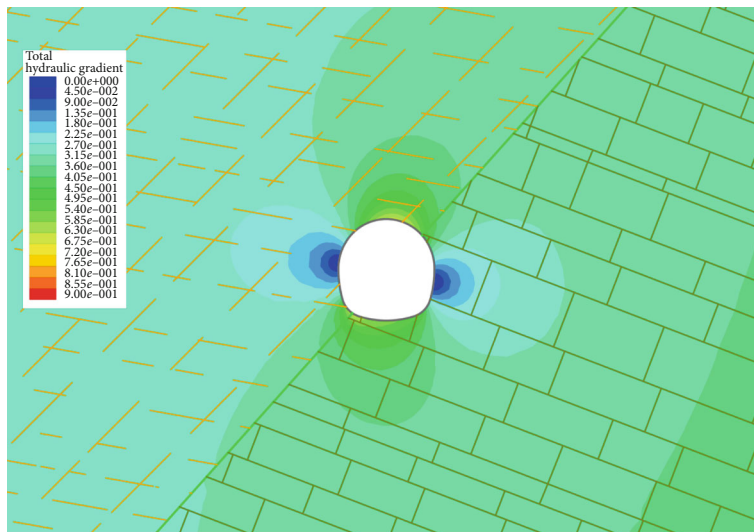
The horizontal displacements of working condition I and working condition II are shown in Figure 9. In the rock with a single joint network, the displacement at the right side of the tunnel sidewall approximately 2 m from the measuring point is relatively close. When there is groundwater, the right lateral displacement of working condition II suddenly decreases at approximately 1 m, indicating that the right sidewall is damaged at this time. Except for the large displacement of the surrounding rock within 2 m from the measuring point, there is little difference in the horizontal displacement on

the right with and without considering groundwater. The displacement of the sidewall on the left side of the tunnel changes more consistently under the influence of groundwater, and the displacement of the surrounding rock is larger under this condition. The difference in the displacement of the surrounding rock on both sides of the tunnel is clearly affected by not only the influence of groundwater but also the bias load.

The horizontal displacements of working condition III and working condition IV are shown in Figure 10. When the tunnel is located in rock with a composite joint network, due to the action of groundwater, the horizontal displacement of the surrounding rock on the right side of the sidewall has exceeded the limit, that is, the displacement is larger than the width of the tunnel. Therefore, after removing the limit value, the horizontal displacement curve of the surrounding rock on the right side of the sidewall is obtained with and without considering groundwater. The surrounding rock within approximately 5.5 m from the measuring point undergoes separation failure, indicating that the deformation of the jointed soft rock is significantly affected by the groundwater. When there is no groundwater effect, the horizontal



(a) Single joint network



(b) Composite joint network

FIGURE 13: Total hydraulic gradient after tunnel excavation.

deformation of the surrounding rock on the left sidewall is relatively consistent but there is also an overlimit value at the monitoring point on the left sidewall, indicating that the left sidewall is also damaged. The displacement of the jointed soft rock under the influence of groundwater increases significantly toward the monitoring point and is approximately 10 times that of the jointed hard rock. Under the dual effects of joints and groundwater, soft rock deforms considerably.

4.4. Total Hydraulic Gradient. Under the two conditions involving joint networks in strata, the hydraulic gradient cloud maps with groundwater after excavation are shown in Figures 11 and 12.

It can be seen from the figures that in the two joint network situations, due to the difference in water height on both sides of the model, the total hydraulic gradient decreases

from left to right before the tunnel is excavated. After the tunnel is excavated, the total hydraulic gradient of the two joint network situations still shows a decreasing distribution from left to right. Comparison of the total hydraulic gradient of the two joint network situations after tunnel excavation reveals that the total hydraulic gradient of the composite joint network is generally smaller than that of the single joint network. In the composite joint network, the total hydraulic gradient near the tunnel changes dramatically. Due to the two different joint networks, the hydromechanical effect is clearly observed in Figure 13.

5. Conclusions

Based on the modeling of rock with a single joint network and rock with a composite joint network, the deformation and failure laws of the surrounding rock after tunnel

excavation are studied under the influence of bias load and groundwater. Taking a railway tunnel as the engineering background, the finite element numerical simulation method is used. For the tunnels located in two different stratum conditions of a single joint network in hard rock and a composite joint network in soft and hard rock, comprehensively considering the groundwater and bias conditions, four numerical models were established, corresponding to working condition I, working condition II, working condition III, and working condition IV. Through numerical calculation, the typical surrounding rock deformation parameters, such as the plastic zone shape, vertical displacement, and horizontal displacement, under these four working conditions are analyzed and compared, and the deformation and failure laws of the surrounding rock after tunnel excavation are obtained under the different working conditions. The main conclusions are as follows:

- (1) In the hard rock with a single joint network and without the influence of groundwater, the surrounding rock mainly undergoes shear failure at the arch crown after tunnel excavation. When affected by groundwater, the failure of the surrounding rock on the left side of the tunnel is dominated by shear failure and the surrounding rock on the right side undergoes both shear and tensile failure. In the rock with a composite joint network and without the influence of groundwater, the surrounding rock after tunnel excavation mainly produces a small amount of damage at the junction of soft and hard strata. When the influence of groundwater is considered, large-scale damage occurs to the surrounding rock near the tunnel. Two types of damage occur at the same time close to the tunnel, while shear damage is the main damage in the surrounding rock far from the tunnel
- (2) For the rock with a composite joint network, the vertical displacements affected by groundwater are all greater than those without considering the influence of groundwater. The surrounding rock approximately 1 m from the arch crown is broken under the conditions of a single joint network and groundwater. The surrounding rock approximately 3.5 m from the arch crown is fractured and destroyed under the conditions of a composite joint network and groundwater
- (3) For the rock with a single joint network, when groundwater is considered, the right sidewall is destroyed approximately 1 m from the monitoring point. In addition to the influence of groundwater, the difference in the displacement of the surrounding rock on either side of the tunnel is obviously affected by the bias load. When the tunnel is located in a rock with a composite joint network, the deformation of the jointed soft rock is significantly affected by groundwater. The surrounding rock within approximately 5.5 m from the measuring point undergoes

separation failure. When there is no groundwater, the left sidewall is also damaged. Under the dual effects of joints and groundwater, the soft rock deforms considerably

Data Availability

All data supporting this study are included within the article.

Conflicts of Interest

The authors declare that there are no conflicts of interest regarding the publication of this paper.

Acknowledgments

The financial support for ongoing projects from the Open Fund of Innovation Institute for Sustainable Maritime Architecture Research and Technology (iSMART), Qingdao University of Technology (no. 2020-032), is greatly acknowledged.

References

- [1] H. Kairong and F. Huanhuan, "Development trends and views of highway tunnels in China over the past decade," *China Journal of Highway and Transport.*, vol. 33, pp. 62–76, 2020.
- [2] M. F. Lei, L. M. Peng, and C. H. Shi, "Model test to investigate the failure mechanisms and lining stress characteristics of shallow buried tunnels under unsymmetrical loading," *Tunnelling and Underground Space Technology*, vol. 46, pp. 64–75, 2015.
- [3] S. Chen, C. S. Qiao, Z. Yang, and C. Z. Qiao, "Application of stochastic joint network simulation to composite strata of shallow-buried long-span metro tunnels," *Bulletin of Engineering Geology and the Environment*, vol. 79, no. 4, pp. 2085–2107, 2020.
- [4] X. Wang and M. Cai, "A DFN-DEM multi-scale modeling approach for simulating tunnel excavation response in jointed rock masses," *Rock Mechanics and Rock Engineering.*, vol. 53, no. 3, pp. 1053–1077, 2020.
- [5] N. Roy, R. Sarkar, and S. D. Bharti, "Prediction model for performance evaluation of tunnel excavation in blocky rock mass," *International Journal of Geomechanics*, vol. 18, no. 1, article 04017125, 2018.
- [6] X. F. Deng, J. B. Zhu, S. G. Chen, Z. Y. Zhao, Y. X. Zhou, and J. Zhao, "Numerical study on tunnel damage subject to blast-induced shock wave in jointed rock masses," *Tunnelling and Underground Space Technology*, vol. 43, pp. 88–100, 2014.
- [7] Y. Wang, J. Su, S. L. Zhang, S. Y. Guo, P. Zhang, and M. Q. Du, "A dynamic risk assessment method for deep-buried tunnels based on a Bayesian network," *Geofluids*, vol. 2020, Article ID 8848860, 14 pages, 2020.
- [8] Y. Wang, Y. J. Zhang, Z. Zhu, M. Q. Du, and Y. Qi, "A novel method for analyzing the factors influencing ground settlement during shield tunnel construction in upper-soft and lower-hard fissured rock strata considering the coupled hydro-mechanical properties," *Geofluids*, vol. 2020, Article ID 6691157, 13 pages, 2020.
- [9] N. Bahrani and P. K. Kaiser, "Influence of degree of interlock on confined strength of jointed hard rock masses," *Journal of*

- Rock Mechanics and Geotechnical Engineering*, vol. 12, no. 6, pp. 1152–1170, 2020.
- [10] Y. Zhao, Y. Wu, Q. Xu et al., “Numerical analysis of the mechanical behavior and failure mode of jointed rock under uniaxial tensile loading,” *Advances in Civil Engineering*, vol. 2020, Article ID 8811282, 13 pages, 2020.
 - [11] H. Changjiang, F. Jun, J. Nan, Z. Yufeng, and H. Lin, “Analysis on the influence of rock joint characteristics on failure mode and stability of bedding tunnel,” *Chinese Journal of Underground Space and Engineering*, vol. 16, pp. 599–607, 2020.
 - [12] S. Wu, K. Li, Z. Yang et al., “Complex analytical study of the stability of tunnel-surrounding rock in a layered jointed rock mass,” *Mathematical Problems in Engineering*, vol. 2020, Article ID 5473059, 15 pages, 2020.
 - [13] M. R. Maleki, “Groundwater seepage rate (GSR); a new method for prediction of groundwater inflow into jointed rock tunnels,” *Tunnelling and Underground Space Technology*, vol. 71, pp. 505–517, 2018.
 - [14] J. Moon and G. Fernandez, “Effect of excavation-induced groundwater level drawdown on tunnel inflow in a jointed rock mass,” *Engineering Geology*, vol. 110, no. 3-4, pp. 33–42, 2010.
 - [15] H. Farhadian, H. Katibeh, and P. Huggenberger, “Empirical model for estimating groundwater flow into tunnel in discontinuous rock masses,” *Environment and Earth Science*, vol. 75, no. 6, 2016.
 - [16] C. Shi, B. Yang, Y. P. Zhang, and J. X. Yang, “Application of discrete-element numerical simulation for calculating the stability of dangerous rock mass: a case study,” *International Journal of Geomechanics*, vol. 20, no. 12, article 04020231, 2020.
 - [17] Q. B. Lin, P. Cao, J. J. Meng, R. H. Cao, and Z. Y. Zhao, “Strength and failure characteristics of jointed rock mass with double circular holes under uniaxial compression: insights from discrete element method modelling,” *Theoretical and Applied Fracture Mechanics*, vol. 109, article 102692, 2020.
 - [18] I. Vazaios, N. Vlachopoulos, and M. S. Diederichs, “Assessing fracturing mechanisms and evolution of excavation damaged zone of tunnels in interlocked rock masses at high stresses using a finite-discrete element approach,” *Journal of Rock Mechanics and Geotechnical Engineering*, vol. 11, no. 4, pp. 701–722, 2019.
 - [19] E. Wang, G. B. Chen, X. J. Yang, G. F. Zhang, and W. B. Guo, “Study on the failure mechanism for coal roadway stability in jointed rock mass due to the excavation unloading effect,” *Energies*, vol. 13, no. 10, p. 2515, 2020.
 - [20] G. C. Zhang, Y. L. Tan, S. J. Liang, and H. G. Jia, “Numerical estimation of suitable gob-side filling wall width in a highly gassy longwall mining panel,” *International Journal of Geomechanics*, vol. 18, no. 8, article 04018091, 2018.
 - [21] R. H. Cao, R. B. Yao, J. J. Meng, Q. B. Lin, H. Lin, and S. Li, “Failure mechanism of non-persistent jointed rock-like specimens under uniaxial loading: laboratory testing,” *International Journal of Rock Mechanics and Mining Sciences*, vol. 132, article 104341, 2020.
 - [22] Q. B. Lin, P. Cao, and R. H. Cao, “Experimental investigation of jointed rock breaking under a disc cutter with different confining stresses,” *Comptes Rendus Mécanique*, vol. 346, no. 9, pp. 833–843, 2018.
 - [23] P. L. P. Wasantha, P. G. Ranjith, and D. R. Viete, “Comparative study of the hydromechanical behavior of intact, horizontally jointed, and vertically jointed rocks under undrained conditions,” *Journal of Materials in Civil Engineering*, vol. 28, no. 9, article 04016083, 2016.
 - [24] G. C. Zhang, Z. J. Wen, S. J. Liang et al., “Ground response of a gob-side entry in a longwall panel extracting 17 m-thick coal seam: a case study,” *Rock Mechanics and Rock Engineering*, vol. 53, no. 2, pp. 497–516, 2020.
 - [25] R. S. Yang, C. X. Ding, L. Y. Yang, and C. Chen, “Model experiment on dynamic behavior of jointed rock mass under blasting at high-stress conditions,” *Tunnelling and Underground Space Technology*, vol. 74, pp. 145–152, 2018.
 - [26] Z. M. Chao, G. T. Ma, X. W. Hu, and G. Luo, “Research on anisotropic permeability and porosity of columnar jointed rock masses during cyclic loading and unloading based on physical model experiments,” *Bulletin of Engineering Geology and the Environment*, vol. 79, no. 10, pp. 5433–5454, 2020.
 - [27] H. W. Jing, S. Q. Yang, M. L. Zhang, G. A. Xu, and K. F. Chen, “An experimental study on anchorage strength and deformation behavior of large-scale jointed rock mass,” *Tunnelling and Underground Space Technology*, vol. 43, pp. 184–197, 2014.
 - [28] K. Wu, Z. S. Shao, and S. Qin, “An analytical design method for ductile support structures in squeezing tunnels,” *Archives of Civil and Mechanical Engineering*, vol. 20, no. 3, 2020.
 - [29] Y. Xia, C. Zhang, H. Zhou et al., “Mechanical behavior of structurally reconstructed irregular columnar jointed rock mass using 3D printing,” *Engineering Geology*, vol. 268, article 105509, 2020.
 - [30] Q. Jiang, X. T. Feng, Y. H. Gong, L. B. Song, S. G. Ran, and J. Cui, “Reverse modelling of natural rock joints using 3D scanning and 3D printing,” *Computers and Geotechnics*, vol. 73, pp. 210–220, 2016.
 - [31] Y. T. Wang, X. P. Zhou, and Y. D. Shou, “The modeling of crack propagation and coalescence in rocks under uniaxial compression using the novel conjugated bond-based peridynamics,” *International Journal of Mechanical Sciences*, vol. 128-129, pp. 614–643, 2017.
 - [32] X. P. Zhou, Y. T. Wang, Y. D. Shou, and M. M. Kou, “A novel conjugated bond linear elastic model in bond-based peridynamics for fracture problems under dynamic loads,” *Engineering Fracture Mechanics*, vol. 188, pp. 151–183, 2018.
 - [33] X. P. Zhou, Y. T. Wang, and Q. H. Qian, “Numerical simulation of crack curving and branching in brittle materials under dynamic loads using the extended non-ordinary state-based peridynamics,” *European Journal of Mechanics - A/Solids*, vol. 60, pp. 277–299, 2016.
 - [34] G. Yabin, *Study on Deformation Characteristics and Controlling Measures of Unsymmetrically Loading Tunnels in Bedding Strata [MD]*, Lanzhou Jiaotong University, Lanzhou, China, 2020.
 - [35] Z. Weihuan, *Advanced Rock Mechanics*, China Water Power Press, Beijing, China, 1990.

Research Article

Numerical Simulation on Mesoscale Mechanism of Seepage in Coal Fractures by Fluid-Solid Coupling Method

Kai Si ¹, Ruidong Peng ², Leilei Zhao ¹, Yan Zhao ¹, Yaheng Zhu ¹,
Zhendong Cui ^{3,4} and Jianyong Zhang ^{3,4}

¹School of Mechanics and Civil Engineering, China University of Mining and Technology (Beijing), Beijing 100083, China

²State Key Laboratory of Coal Resources and Safe Mining, China University of Mining and Technology, Beijing 100083, China

³Key Laboratory of Shale Gas and Geoengineering, Institute of Geology and Geophysics, Chinese Academy of Sciences, Beijing 100029, China

⁴College of Earth and Planetary Sciences, University of Chinese Academy of Sciences, Beijing 100049, China

Correspondence should be addressed to Kai Si; sky883636@163.com and Ruidong Peng; prd@cumtb.edu.cn

Received 14 January 2021; Revised 14 January 2021; Accepted 27 February 2021; Published 16 March 2021

Academic Editor: Rihong Cao

Copyright © 2021 Kai Si et al. This is an open access article distributed under the Creative Commons Attribution License, which permits unrestricted use, distribution, and reproduction in any medium, provided the original work is properly cited.

Trying to reveal the mechanism of gas seepage in coal is of significance to both safe mining and methane exploitation. A series of FEM numerical models were built up and studied so as to explore the mesoscale mechanism of seepage in coal fractures. The proposed mesoscale FEM model is a cube with micron fractures along three orthogonal directions. The distribution of velocity and pressure under fluid-solid coupling was obtained, and furthermore, the seepage flow flux and an equivalent permeability of the whole model were calculated. The influences of fracture width, outlet velocity, and in situ stress level on seepage were investigated. The numerical results show that nonlinear Darcy seepage occurs during low velocity zone. The permeability is increased linearly with the increasing of fracture width and outlet velocity. A certain change of lateral coefficient of in situ stress also affects seepage. The permeability is increased sharply once deviating the isotropic spherical stress state, but it is no longer changed obviously after the lateral coefficient has been increased or decreased more than 20%. The mesoscale seepage mechanism in coal fractures has been preliminarily revealed by considering fluid-solid coupling effect, and the key factors influencing fluid seepage in coal fractures were demonstrated. The proposed methods and results will be helpful to the further study of seepage behaviour in coal with more complex structures.

1. Introduction

In the process of coal mining, there is a kind of unconventional natural gas stored in coal seams, commonly known as coalbed methane (CBM). As an important energy in coal, environment pollution produced by using CBM is relatively much less than directly using coal resources, so its status is more and more important [1]. On the one hand, as an energy resource, CBM has a high utilization value; on the other hand, the outburst of gas during coal mining has become a serious geological disaster. Therefore, it is of great engineering significance to study the migration and seepage law of CBM in coal body and formulate reasonable extraction measures.

The migration and seepage laws of CBM are closely related to the deformation of coal matrix. Chen et al. [2] and Peng et al. [3] pointed out that stress and strain have a great influ-

ence on coal permeability. Geng et al. [4] and Cheng et al. [5] systematically studied the relationship between the stress sensitivity coefficient and permeability changes of briquette with different particle sizes. In coal reservoirs, the migration channel in the reservoir is regarded as a system of pores and fractures, and the permeability of this dual-pore and fracture structures has become one of the indicators of the success of CBM extraction engineering. The coal-bearing basin has undergone various periods and various degrees of compression and extension and other geological factors, which have reshaped the pore and fracture morphology of the coal, which have an important influence on the permeability of the coal seam. In addition, during the loading process of coal and rock, the microfracture structure inside coal and rock will change significantly [6–10]. From the perspective of acoustic emission, it shows that the cracks in the coal and rock masses gradually

expand with the increase of stress [11, 12]. Meng et al. [13] conducted a three-dimensional mesoscopic simulation study on the crack propagation inside the soil-rock mixture. In the process of CBM extraction, the change of internal pressure will cause the stress of coal to change, which in turn affects the characteristics of coal pores and cracks. Due to changes in the structural characteristics of pores and fissures, the deformation of coal will have an impact on fluid seepage [14]. Therefore, in the process of CBM extraction, fluid-solid coupling will be quite prominent. This means that the influence of interaction between fluid and solid matrix must be added in the process of various simulation studies. After recognizing this problem, most scholars have fully considered the influence of fluid-solid coupling on the seepage of CBM and other fluids and have achieved certain research results [15–18]. Majewska et al. [19] found that coal experienced a contraction trend after the initial expansion of adsorption, which was attributed to the compression effect of injection pressure. Yin et al. [20] studied the influence of different adsorbent gases on coal deformation and permeability and pointed out that the stronger the adsorption under the same gas pressure, the greater the deformation of the coal and the lower the permeability. Based on the double pore structure characteristics of coal and considering the influence of moisture on the adsorption characteristics of coal and rock, the seepage model under the condition of solid-liquid-gas coexistence was established [21]. Mitra et al. and Gu et al. [22–24] studied the non-Darcy phenomenon of gas migration in coal seams based on simplified coal seam physical models. These models mainly consider the compressibility of cleats and the impact of coal matrix shrinkage on the cleat opening. Shi et al. [25] conducted a large number of experimental studies and theoretical model derivation on the direction of coal matrix desorption-induced deformation and permeability changes under effective stress and tested coal under different uniaxial strain, displacement control, and pore pressure. Based on the mechanical properties of the coal sample and the deformation characteristics of the porous medium, a mathematical model of CBM flow solidification under various conditions is obtained.

According to the research results of many scholars mentioned above, both the experimental results and the numerical simulation results show that the seepage law of CBM in coal is subject to the interaction of fluid and solid, which is due to fluid-solid coupling. The study of fluid-solid coupling mechanism between fracture and solid matrix is helpful to better understand the seepage law of CBM in coal. However, most of those researches are resulted from phenomenological coupling between the pore and the solid matrix at the macro scale. Therefore, some mesoscale FEM models will be built to represent the characteristics of fluid-solid coupling, and the seepage law of CBM along microfractures will be investigated by changing different geometry features and boundary conditions.

2. Theoretical Equations and Model Construction

2.1. Equation for Fluid-Solid Coupling Calculation. The fluid-solid coupling effect in coal and rock mass is a kind of inter-

action between seepage field of fluid and stress field of solid, which belongs the interdisciplinary of solid mechanics and fluid mechanics. Therefore, the influence of fluid and solid interaction can be derived by coupling flow law in fractures and deformation law of coal matrices.

2.1.1. Governing Equations for Fluid Calculation. Fluid flow should follow the basic conservation principles, including the law of mass conservation, momentum conservation, and energy conservation law. If the fluid includes other different components of the mixture, the system also follows the component conservation law. The general compressible Newtonian conservation law is described by the following governing equations:

$$\text{Mass conservation equation : } \frac{\partial \rho_f}{\partial t} + \nabla \cdot (\rho_f \mathbf{v}) = 0. \quad (1)$$

$$\text{Momentum conservation equation : } \frac{\partial \rho_f \mathbf{v}}{\partial t} + \nabla \cdot (\rho_f \mathbf{v} \mathbf{v} - \boldsymbol{\tau}_f) = \mathbf{f}_f, \quad (2)$$

in which t is time, \mathbf{f}_f is volume force vector, ρ_f is fluid density, \mathbf{v} is fluid velocity vector, and $\boldsymbol{\tau}_f$ is shear force tensor, which can be expressed by the following equation:

$$\left. \begin{aligned} \boldsymbol{\tau}_f &= (-p + \mu \nabla \cdot \mathbf{v}) \mathbf{I} + 2\pi \mathbf{e}, \\ \mathbf{e} &= \frac{1}{2} (\nabla \mathbf{v} + \nabla \mathbf{v}^T), \end{aligned} \right\} \quad (3)$$

in which p represents pressure, μ represents dynamic viscosity, \mathbf{I} is unit tensor, and \mathbf{e} represents velocity stress tensor.

2.1.2. Solid Governing Equation. The equation of conservation of solids can be derived from Newton's second law:

$$\rho_s \ddot{\mathbf{d}}_s = \nabla \cdot \boldsymbol{\sigma}_s + \mathbf{f}_s. \quad (4)$$

The deformation of the solid matrix is assumed to be elastic, following Hooke's law:

$$\begin{cases} \sigma_1 = \lambda(\varepsilon_1 + \varepsilon_2 + \varepsilon_3) + 2G\varepsilon_1, \\ \sigma_2 = \lambda(\varepsilon_1 + \varepsilon_2 + \varepsilon_3) + 2G\varepsilon_2, \\ \sigma_3 = \lambda(\varepsilon_1 + \varepsilon_2 + \varepsilon_3) + 2G\varepsilon_3. \end{cases} \quad (5)$$

In Equations (4) and (5), ρ_s is the density of the solid; $\boldsymbol{\sigma}_s$ is the Cauchy stress tensor; $\ddot{\mathbf{d}}_s$ is the local acceleration vector in solid domain; $\sigma_1, \sigma_2, \sigma_3$ are the principal stresses; $\varepsilon_1, \varepsilon_2, \varepsilon_3$ are the principal strains, respectively; and λ and G are the Lamé constants.

2.1.3. Fluid-Solid Coupling Equation. On the fluid-solid coupling interface, the fluid pressure and solid stress (τ_f, τ_s)

and the displacements (d_f, d_s) must be equal or conserved; that is, the following equations should be satisfied:

$$\left. \begin{aligned} \tau_f \cdot n_f &= \tau_s \cdot n_s, \\ d_f &= d_s, \\ q_f &= q_s, \\ T_f &= T_s, \end{aligned} \right\} \quad (6)$$

in which the parameters of the lower corner band s represent the characteristics of solid parameters, while the parameters of the lower corner band f represent the characteristics of fluid parameters.

2.2. Fluid-Solid Coupling Analysis Method. At present, solving control equations of fluid-solid coupling problems are basically divided into two categories: direct coupled solving and separated solving. Direct coupled solving means integrate fluid constitutive equations, and solid constitutive equations combine into one equation matrix for solution, so the fluid constitutive equation and the solid constitutive equation are solved together in a solver. Although direct coupled solving method is perfect and advanced in theory, its calculation process is time-consuming and needs too large memory. Therefore, the direct coupled solving method is only suitable for some very simple situation. Separated solving does not require a fluid-solid coupling control equation. It calculates fluid control equations and solid control equations in one solver alternately or two different solvers parallel; hence, the solution can be obtained after several iterations. The sequence solving the flow field and the solid field need to be specified in advance. Although the synchronous solution is difficult to converge because the energy on the fluid-solid coupling interface cannot be completely conserved due to time lag, the separated solving can fully utilize the existing procedures of current computational fluid dynamics and computational solid mechanics, so as to retain the module of available computing program and reduce the required memory greatly. In this study, a separated solving method was adopted to handle the fluid-solid coupling problem.

The pressure of fluid field in fractures will act on solid field and result matrix deformation; meanwhile, the deformed matrix will transform the geometry of fractures and cause a change of fluid flow which means the pressure and velocity of the fluid will be altered. Therefore, bidirectional fluid-solid coupling calculation needs to be considered. At the same time, it is necessary to impose large deformation effect of solid field.

2.3. Model Constructing and Parameter Setting. A $40 \mu\text{m} \times 40 \mu\text{m} \times 40 \mu\text{m}$ cube with fractures along three orthogonal directions was constructed as shown in Figure 1. The side length of the model is tens of microns, and the width of the fracture is several microns. The fracture domain is designated fluid field indicated by the yellow part, and the residual matrix domain is designated solid field indicated by the blue part.

The flow field mesh needs to be divided more densely. In comparison, the solid field mesh can be appropriately relaxed. In addition, considering the calculation rate and convergence effect, dense tetrahedral meshes are used for the solid field near the fluid-solid coupling surface, and hexahedral meshes are used for the solid field away from the fluid-solid coupling surface. The elements and boundary conditions of one model are shown in Figure 2.

The fluid-solid interfaces are set as nonslip surfaces. The seepage channels are designed as three directions along the fractures, and hence, the inlets and outlets are assigned on different surfaces as shown in Figure 2(c). In order to simulate various seepage situations of these models, the kinds of pressure differences are assigned and studied. Three groups of inlet and outlet boundaries are defined as follows:

- (1) The seepage along z -axis-negative direction is from top (named as inlet $_z$) to bottom (named as outlet $_z$)
- (2) The seepage along y -axis-positive direction is from front (named as inlet $_y$) to back (named as outlet $_y$)
- (3) The seepage along x -axis-positive direction is from left (named as inlet $_x$) to right (named as outlet $_x$)

The solid matrices are denoted as coal, in which elastic modulus and Poisson's ratio are 1.4 GPa and 0.3, respectively. The in situ stress on each surface of a cube needs to be divided into matrix stress and fluid pressure, which can be calculated according to the area ratio of solid matrix and fluid field:

$$\sigma A = \sigma_s A_s + \sigma_\mu A_\mu, \quad (7)$$

where σ and A are the in situ stress and the total area of a cube side surface, respectively; σ_s and A_s are the effective stress and the area of surface solid matrix; and σ_μ and A_μ are, respectively, the fluid pressure and the area of surface fracture fluid. Commonly, the in situ stress adopted in this simulation is selected as 5 MPa.

3. Results and Discussion

3.1. Influence of Geometric Width of Fractures. In order to study the relationship between fracture structure and seepage at mesoscopic scale, it is necessary to investigate various models with different fracture width. Five groups of models were created under the same boundary conditions. Each cube has a size of $40 \mu\text{m} \times 40 \mu\text{m} \times 40 \mu\text{m}$, but the fracture width in these five groups of models was $2 \mu\text{m}$, $3 \mu\text{m}$, $4 \mu\text{m}$, $5 \mu\text{m}$, and $6 \mu\text{m}$, respectively.

The pressure on each inlet is set as 5 MPa. The inlet \rightarrow outlet $_z$ channel is set as the main flow channel. The velocity on outlet $_z$ V_1 is set as 0.1 m/s, and the velocity on other two outlets is $0.9 V_1$. The differential pressure of each flow channel between the inlet and the outlet can be calculated by subtracting the inlet pressure from the outlet pressure obtained from the numerical simulation results. The differential pressures under various fracture width are shown in Figure 3.

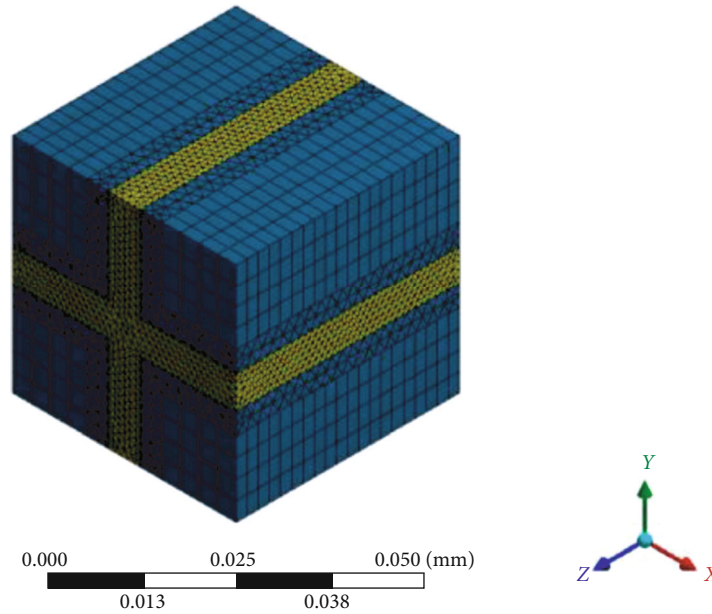


FIGURE 1: A three-dimensional fracture seepage model.

The pressure difference gradually decreases with the increasing of fracture width. The variation of differential pressure with fracture width increasing is basically coincident along three different directions, i.e., inletx-outletx, inlety-outlety, and inletz-outletz. An inflection point at the fracture width of about $4\ \mu\text{m}$ can be noticed from Figure 3. When the fracture width is greater than $4\ \mu\text{m}$, the differential pressures along three directions are almost same.

According to the traditional Darcy's linear seepage law, the pressure difference should be a certain value under the specified velocity. In order to explain the aforementioned variation of pressure difference, both the deformation of coal matrix and the flow of fracture fluid need to be learned.

Figure 4 shows the total displacements of coal matrix near fractures with different width. The displacements under large fracture width are smaller than those under small fracture width. It means the impact of matrix deformation becomes weaker with the increasing of fracture width.

The pressure on each outlet decreases evenly from one side to another side as shown in Figure 5(a). Therefore, the pressure on the fluid-solid interface (named as FSI) changes gradually along the diagonal direction as shown in Figure 5(b).

It can be seen from Figure 5(a) that the two horizontal flow channels are similar except that their flow directions are different, so a section parallel to the YOZ plane located at $x = 20\ \mu\text{m}$ can be selected to represent fluid flow, which is the middle plane of the inlet \rightarrow outlety flow channel (named as MPF). The velocity components along the X, Y, and Z directions on MPF are shown in Figures 5(c)–5(e), respectively, and Figure 5(f) shows the contour of total velocity.

The velocity contours on MPF indicate that flow in fractures is irregular. The velocity w mostly appears negative, so the fluid along Z direction is mainly from the top inlet to the bottom outlet. On the whole, the vertical flow along the Z

direction is relatively slower near the left horizontal inlet than in the right part. It is noticed that the velocity w of fluid near the horizontal inlet or the horizontal outlet is smaller owing to the restrictions of horizontal boundary conditions. The velocity u mostly appears positive, and thus, the fluid along the X direction is mainly from the left inlet to the right outlet. On the whole, the horizontal flow along the X direction is relative slower near the top inlet than in the bottom part. The velocity w mostly appears almost zero except in the middle intersection of two horizontal flow channels. It infers that some turbulent flow may occur in this middle zone as shown in Figures 5(e) and 5(f). The total maximum velocity appears in the corner between the inlet and the outlet, and the minimum velocity is in the corner between two inlets. The velocity decreases and increases gradually around the maximum and the minimum, respectively, and then an almost fixed value was retained which is distributed on the whole right-bottom part near the two outlets.

The distribution of fluid velocity on bottom outlet is shown in Figure 5(g). Since the outlet velocity has been specified as boundary conditions in advance, its distribution obeys laminar flow as expected. The velocity changes from the maximum in the middle to zero on both sides, and the average value is just the specified value.

Figure 5(h) shows the distribution of fluid velocity on top inlet. The changes along the X direction and Y direction are similar. The maximum velocity appears near the horizontal outlet, around which the velocity decreases continuously to zero. The velocity near horizontal inlets also retains zero owing that no pressure alteration occurs over there. The velocity distributions in fractures with different width are similar. However, the impacts of nonslip solid-fluid interfaces and the turbulent flow in middle zones become weaker with the increasing of fracture width, so the flow capacity is enhanced in large fractures. The actual velocity on each inlet

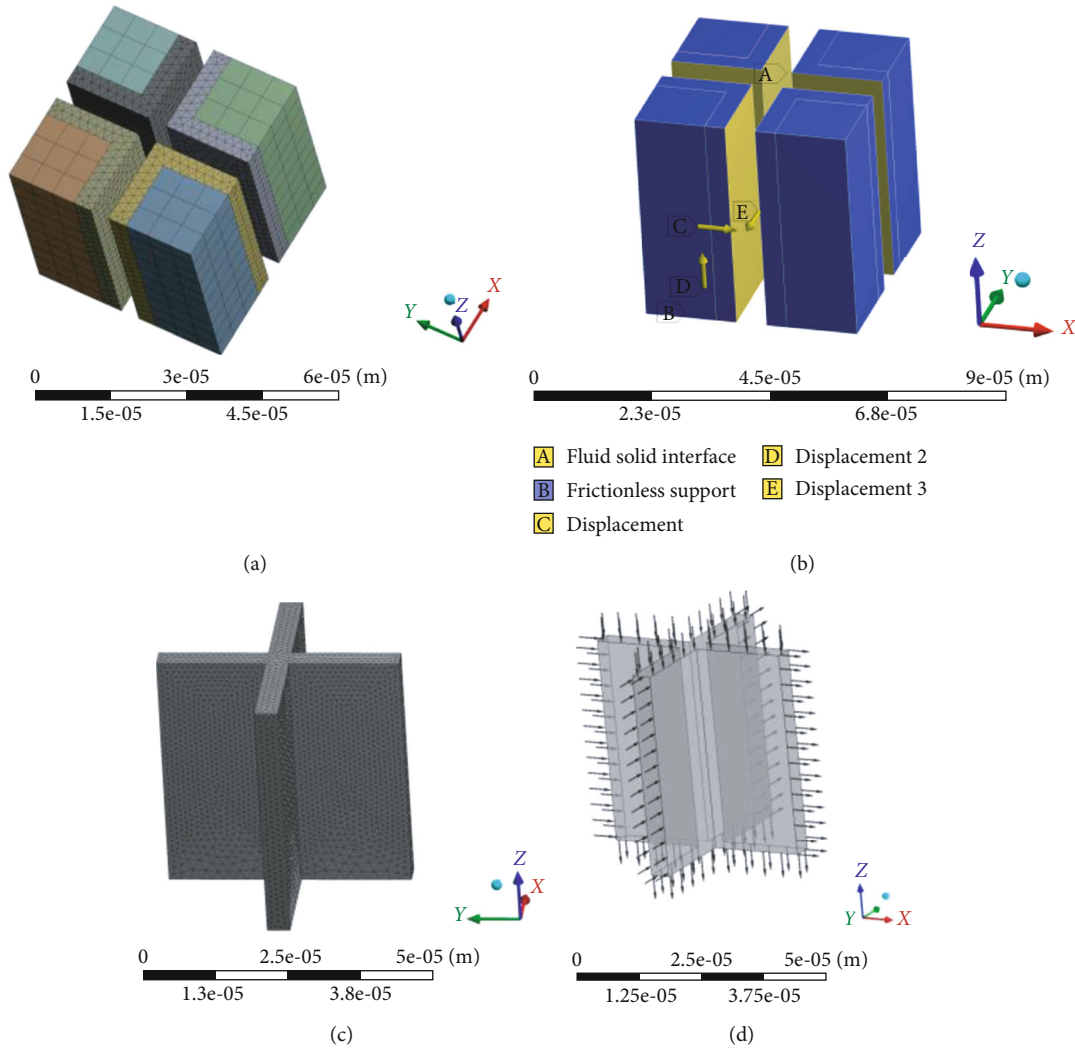


FIGURE 2: Meshing and boundary condition setting of flow field and solid field. (a) Mesh of solid. (b) Solid field loads and constraints. (c) Mesh of fluid. (d) Boundary condition of fluid.

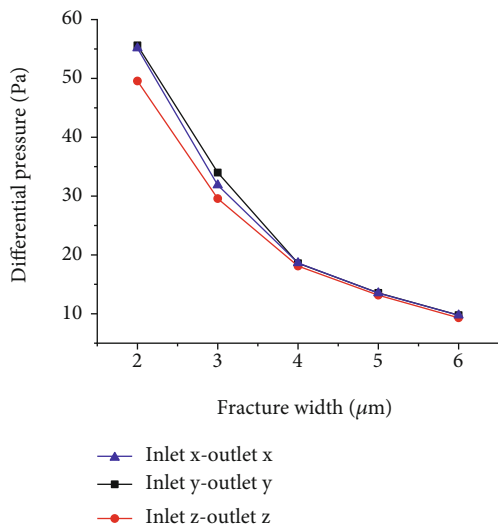


FIGURE 3: Differential pressure of fluid flow with different fracture width.

or outlet can be derived from the numerical simulation results. Furthermore, the flow flux of inlet or outlet can be calculated by surface integral of these velocity values. Figure 6 shows the flow flux of each inlet and outlet under different fracture widths. The flow flux increases with the increasing of fracture width. The increasing multiple of flow flux is not equal to the increasing multiple of the inlet or outlet area. Consequently, the impact of fracture width on the fluid flow cannot be neglected.

According to the Darcy's seepage law, an equivalent permeability k of fracture seepage can be defined as

$$k = \frac{\mu Q}{b \Delta p}, \quad (8)$$

in which μ is fluid viscosity, Q is flow flux, b is model length from the inlet to the outlet, and Δp represents differential pressure between the inlet and outlet.

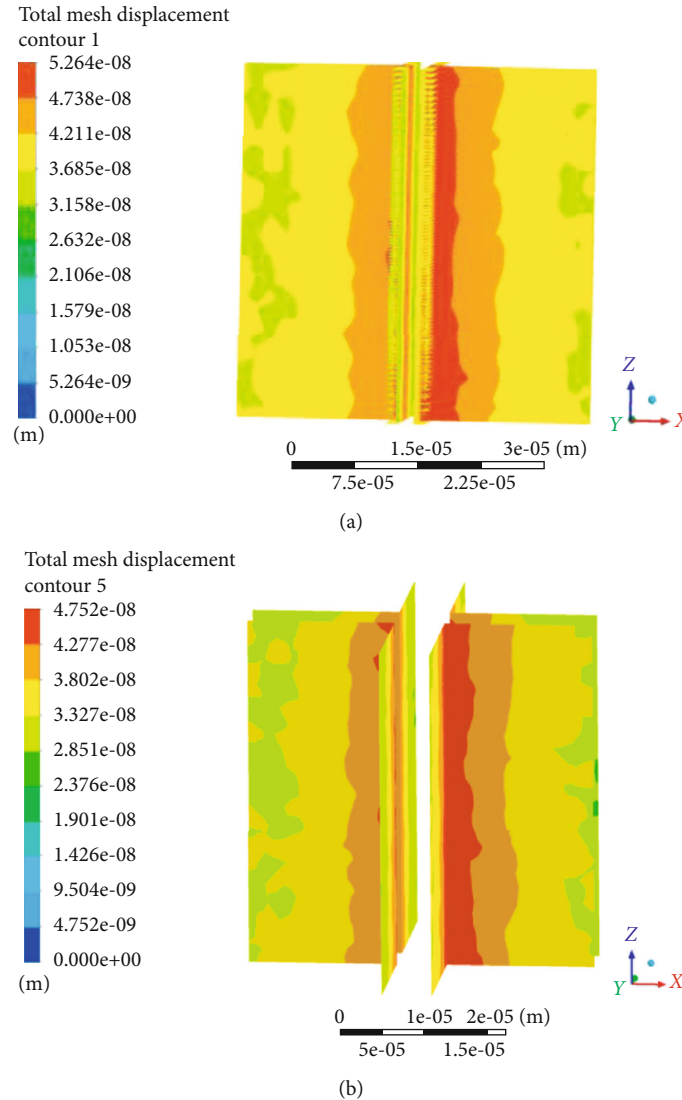


FIGURE 4: Total displacement of coal matrix with different fracture width: (a) $2 \mu\text{m}$ and (b) $6 \mu\text{m}$.

The equivalent permeability k under different fracture width can be calculated according to Equation (8), where the flow flux is from each outlet. The results are shown in Figure 7.

It can be seen that the equivalent permeability increases almost linearly with the increasing of fracture width, which indicates fluid seepage becomes easier for larger fractures. As mentioned previously, the horizontal flows along inlet \rightarrow outlet y and along inlet $x\rightarrow$ outlet x are similar, so their equivalent permeability is also the same. Because the velocity on outlet z is specified as a larger value than that on outlet x and outlet y , the equivalent permeability of inlet $z\rightarrow$ outlet z flow channel is greater than those of the other two flow channels. Therefore, such equivalent permeability will be influenced by both geometric width of fracture and flow pressure and velocity. It also means that the traditional linear Darcy's seepage law will become nonlinear due to the fact that the coefficient, i.e., permeability, is no longer a constant.

3.2. Seepage Law of the Model under Different Outlet Velocities. A series of models with a fracture width of $4 \mu\text{m}$

were taken to investigate the influences of outlet velocities. The inlet pressures of the X, Y, and Z directions are still set as 5 MPa. The inlet \rightarrow outlet z channel is set as the main flow channel, and the corresponding outlet velocity V_1 is 0.01 m/s and 0.025 m/s, 0.05 m/s, 0.075 m/s, 0.1 m/s, 0.5 m/s, 1.00 m/s, 5.00 m/s, or 10.00 m/s. The outlet velocity of the two horizontal flow channels inlet \rightarrow outlet y and inlet $x\rightarrow$ outlet x is $0.9 V_1$.

The distribution of pressure and velocity under different outlet velocities is roughly the same to those contours shown in Figure 8 only except that the values increase with the increasing of outlet velocity.

Since the pressure on inlet has been specified as 5 MPa and the pressure on outlet can be obtained from the numerical simulation results, the differential pressure along each flow channel can be calculated by subtraction. Figure 6 shows the differential pressure between each inlet and outlet under different outlet velocities.

It can be seen from Figure 8 that the differential pressure on each flow channel is basically proportional to the outlet

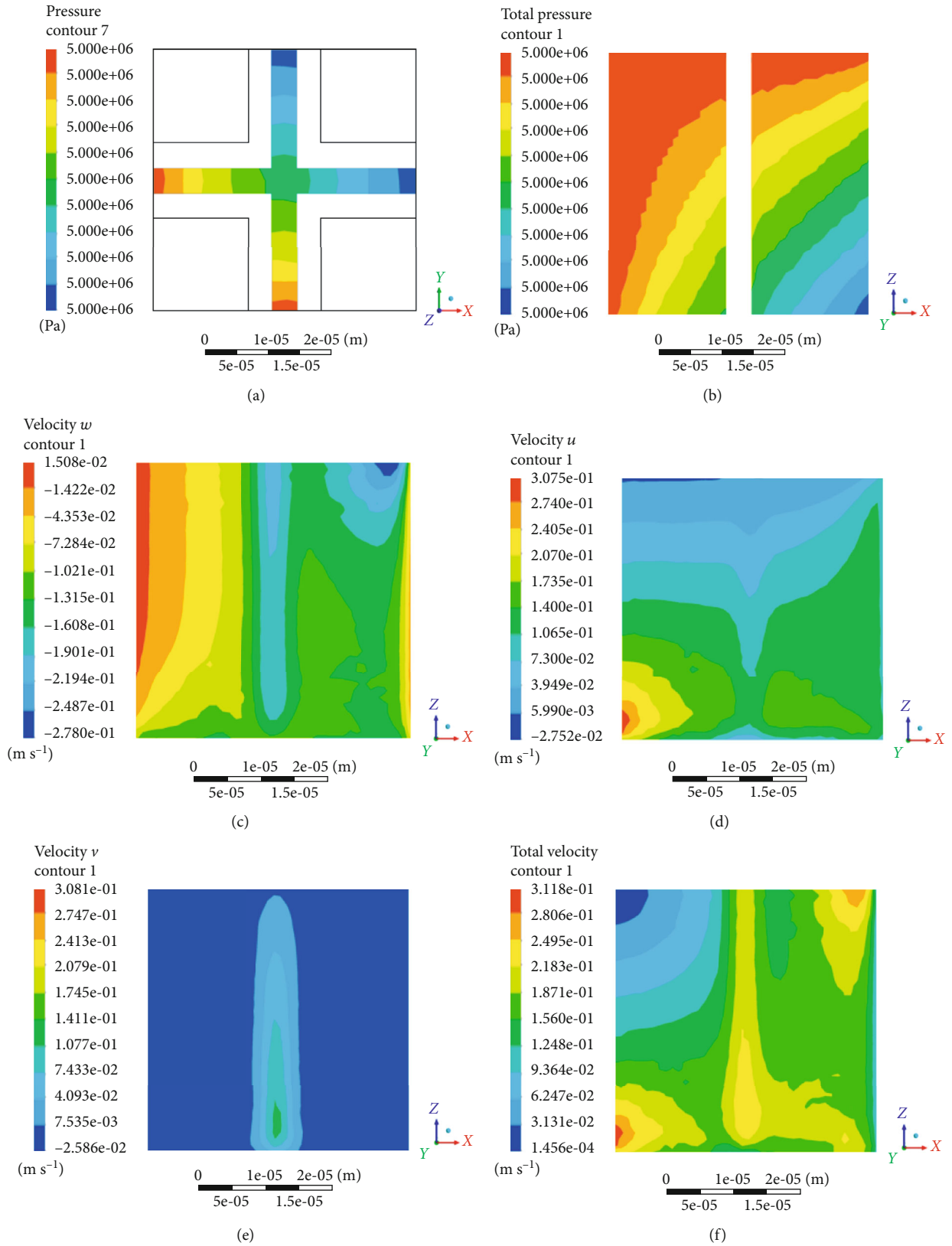


FIGURE 5: Continued.

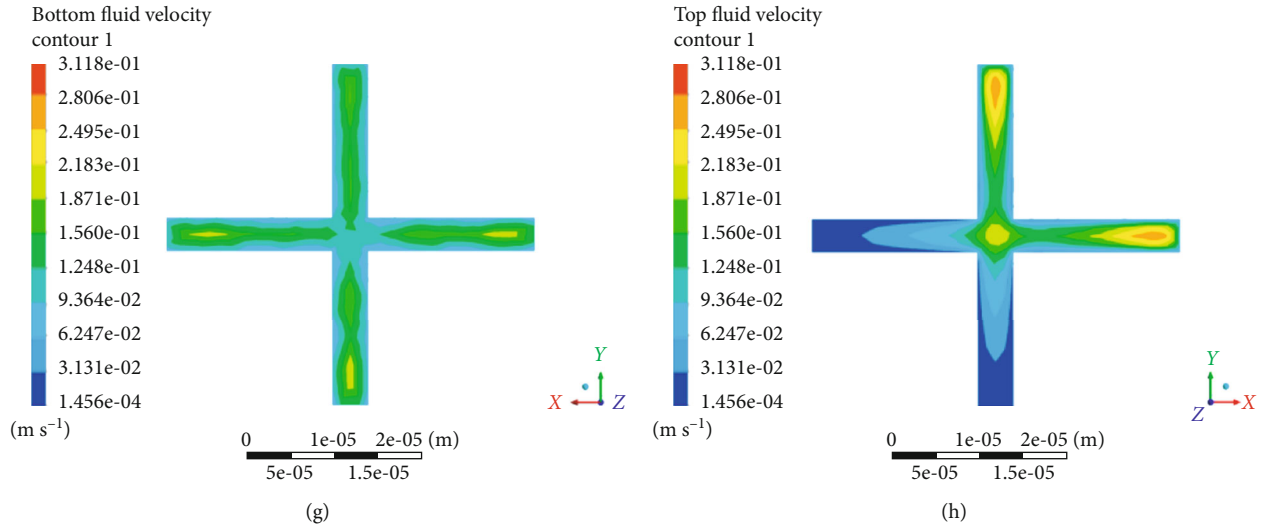


FIGURE 5: Pressure and velocity distribution of fracture fluid with $4\ \mu\text{m}$ width. (a) Pressure on outlet. (b) Pressure on FSI. (c) Velocity w on MPF. (d) Velocity u on MPF. (e) Velocity v on MPF. (f) Total velocity on MPF. (g) Fluid velocity on bottom outlet. (h) Fluid velocity on top inlet.

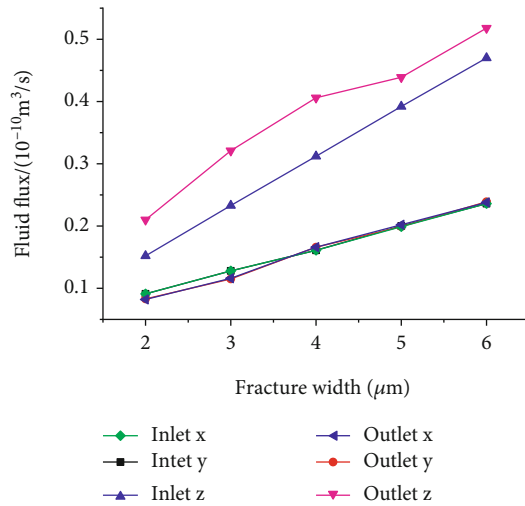


FIGURE 6: Flow flux of each inlet and outlet with different fracture widths.

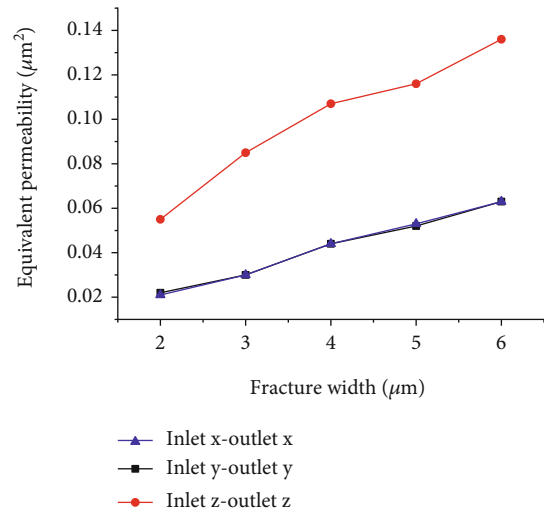


FIGURE 7: Curve of equivalent permeability with different fracture width.

velocity. Especially when the velocity is relatively large, the relationship between the increments of differential pressure and the increments of velocity is linear according a constant proportionality factor. It agrees with linear Darcy's law during these ranges. However, the relationship curve deviates from the straight line gradually when the velocity is relatively small. It indicates a phenomenon of nonlinear Darcy flow during low velocity zone.

The equivalent permeability k under different velocity can be calculated according to Equation (8). The results are shown in Figure 9. The equivalent permeability increases linearly with the increasing of velocity. It is also noticed that the equivalent permeability of inletz \rightarrow outletz flow channel is greater than those of the other two flow channels because the velocity on outletz is specified as a larger value than that on outletx and outlety.

3.3. Seepage Law under Different in-Situ Stress. In situ stress is the natural stress that exists in the stratum that greatly influences the mechanical behaviours of coal rock. According to current researches, it is generally believed that the formation of in situ stress is caused by the compression of continental plate boundaries, thermal convection in the mantle, and gravity and often disturbed by kinds of engineering activity. A large amount of measured data show that the ratio of the maximum horizontal principal stress to the vertical principal stress is about 0.5~5.0. In this study, a lateral coefficient γ is defined as the ratio of the principal stress in the horizontal plane to the principal stress in the vertical plane. The vertical stress is specified as 5 MPa, and the horizontal stress is specified as 3 MPa, 4 MPa, 5 MPa, 6 MPa, or 7 MPa; i.e., the value of γ is 0.6, 0.8, 1.0, 1.2, and 1.4, respectively.

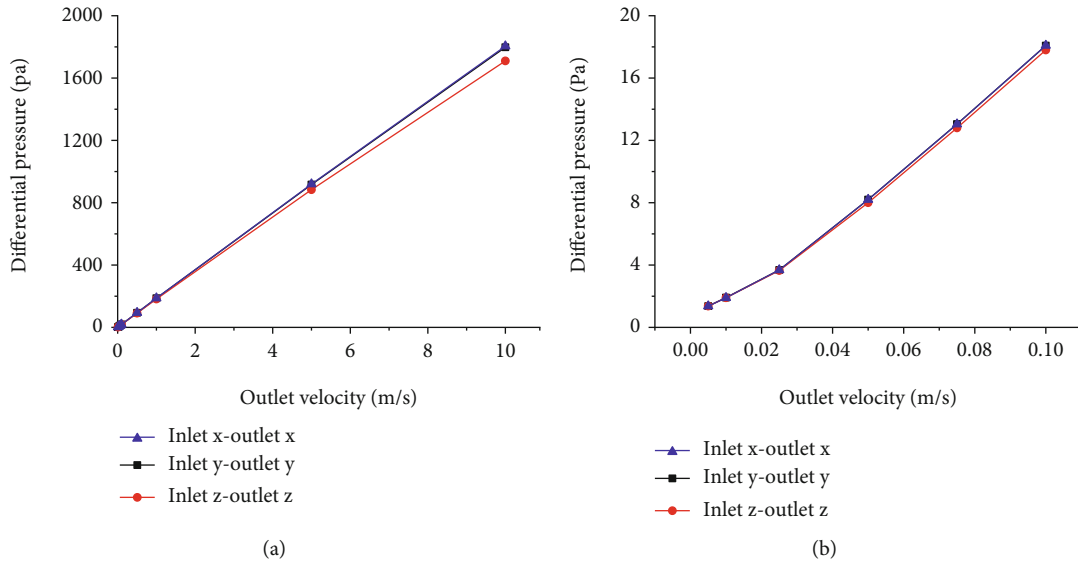


FIGURE 8: Curve of differential pressure in different outlet velocity.

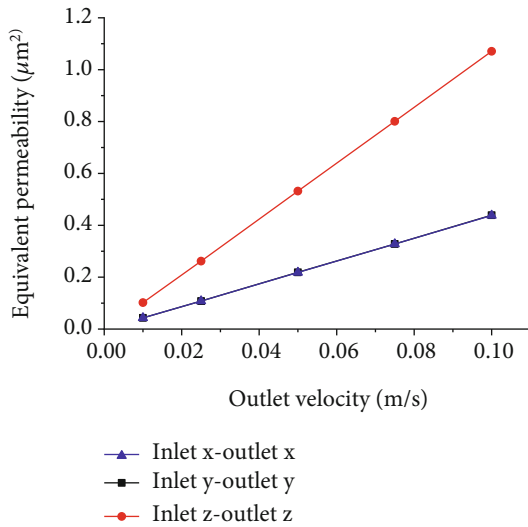


FIGURE 9: Relation curve of equivalent permeability with outlet velocity.

The previous models have fractures with equal width in which a certain difference pressure must be applied between the inlet and the outlet so that fluid can flow. In order to investigate the influences of in situ stresses, the pressure on each inlet needs to be equal to that on the opposite outlet so as to retain the specified in situ stress. Considering fluid in fractures with equal width cannot flow under constant pressure, the fractures with various width were introduced as shown in Figure 10. A series of models with fracture which width changes from $6.0 \mu\text{m}$ to $2.0 \mu\text{m}$ were constructed. Both the inlet pressure and the outlet pressure of each seepage channel are specified to equal to the in situ stress applied on the corresponding direction.

The distribution of velocity under different stress and pressure is roughly similar to that mentioned previously. Figure 11 shows the calculated velocity on each inlet and out-

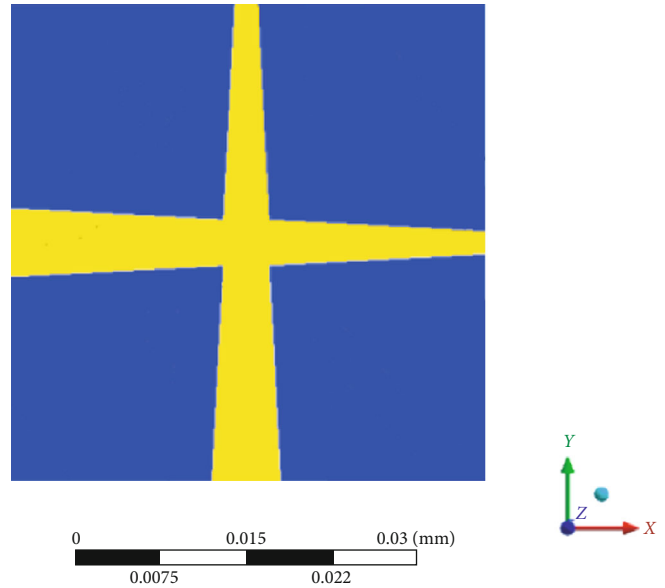


FIGURE 10: The cross-section of a model introducing fractures with various width.

let under different lateral coefficient. Furthermore, the corresponding equivalent permeability can be calculated according Equation (8) and shown in Figure 12.

When the in situ horizontal stress and the in situ vertical stress are not equal, the flow velocity of fracture fluids increases and the equivalent permeability of model becomes higher. A jump is noticed near the lateral coefficient of 1.0, which means the seepage fluid under the isotropic spherical stress is the weakest; i.e., the deviator stress can enhance the seepage in fractures obviously. But once the lateral coefficient has been increased or decreased more than 20%, its influences become very slight so that little variations can be noticed for higher or lower lateral coefficients. The seepage at the lateral coefficient γ of 0.7 and 1.3 is calculated as a supplement.

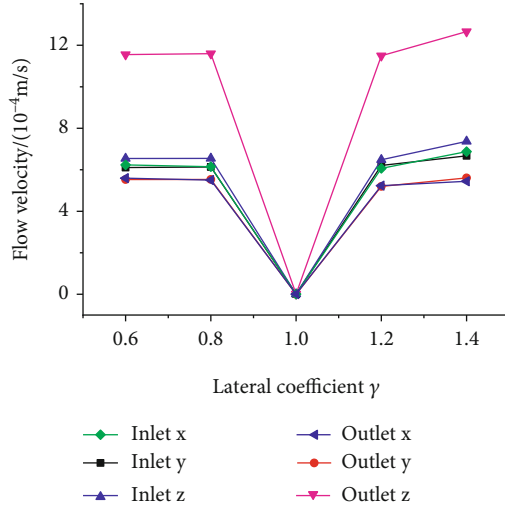


FIGURE 11: Relation curve of flow velocity with differential lateral coefficient γ .

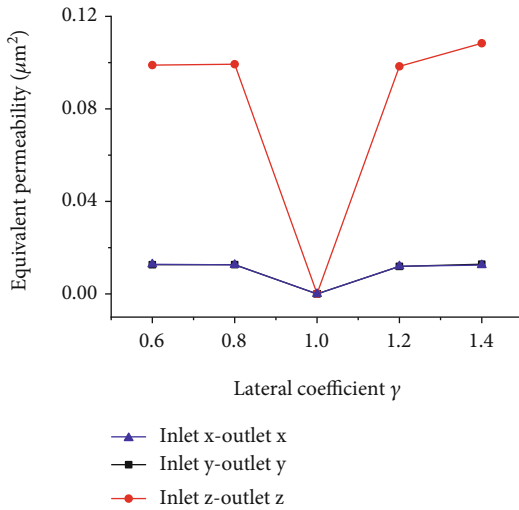


FIGURE 12: Curve of equivalent permeability with different lateral coefficient γ .

Numerical results show that the equivalent permeability of inlet y →outlet y is $0.01264 \mu\text{m}^2$ and $0.01231 \mu\text{m}^2$ and the equivalent permeability of inlet z →outlet z is $0.09911 \mu\text{m}^2$ and $0.09993 \mu\text{m}^2$, respectively. These results validate the jump occurs near the lateral coefficient of 1.0. It means the deviator stress will enhance the seepage once deviating the isotropic spherical stress state but such enhancement is limited and no longer takes effect even further increasing or decreasing lateral coefficients.

4. Conclusions

A series of FEM models representing seepage in coal fracture were built up and studied by means of ANSYS software. The proposed model is a cube with tens of microns side width containing three orthogonal fractures with several microns

width. By introducing fluid-solid coupling effect, the seepage law of gas in three-dimensional fractures was simulated and analyzed. The following conclusions can be drawn:

- (1) Even under the same specified outlet velocity, the pressure difference gradually decreases with the increasing of fracture width. It means the equivalent permeability calculated according traditional Darcy's seepage law is not a constant for different fracture widths. With the increasing of fracture width, the impact of matrix deformation becomes weaker, and the impacts of nonslip solid-fluid interfaces and the turbulent flow in middle zones also become weaker. Therefore, the flow flux through fractures increases with the increasing of fracture width, but the increasing multiple of flow flux is not equal to the increasing multiple of the inlet or outlet area. The equivalent permeability increases almost linearly with the increasing of fracture width, which indicates fluid seepage becomes easier for larger fractures
- (2) The linear Darcy's law is agreed with only when the outlet velocity is relatively large, while the nonlinear Darcy seepage occurs during low velocity zone. Although the differential pressure on each flow channel is basically proportional to the outlet velocity, it must be noticed that their relationship curve deviates from the straight line gradually when the velocity is relatively small. The equivalent permeability increases linearly with the increasing of outlet velocity
- (3) The influences of the in situ stress under different lateral coefficients on seepage are obviously nonlinear. A jump of the equivalent permeability is noticed near the isotropic spherical stress state, while little variations of the equivalent permeability can be observed for higher or lower lateral coefficients once the lateral coefficient has been increased or decreased more than 20%. Hence, the deviator stress will enhance the seepage, but such enhancement is limited

Data Availability

The data is limited to single case reports and falls under the protected health information. For more information regarding the data availability, please reach out to the corresponding author.

Conflicts of Interest

The authors declare no conflicts of interest.

Acknowledgments

This work was supported by the Second Tibetan Plateau Scientific Expedition and Research Program (STEP) (Grant No. 2019QZKK0904), the National Natural Science Foundation of China (Grant No. 51727807), and the Fundamental Research Funds for the Central Universities (Grant No. 2020YJSMT06).

References

- [1] X. F. Wang, C. G. Liu, S. J. Chen, L. Chen, K. Li, and N. Liu, "Impact of coal sector's de-capacity policy on coal price," *Applied Energy*, vol. 265, article 114802, 2020.
- [2] Z. W. Chen, J. S. Liu, Z. J. Pan, L. D. Connell, and D. Elsworth, "Influence of the effective stress coefficient and sorption-induced strain on the evolution of coal permeability: model development and analysis," *International Journal of Greenhouse Gas Control*, vol. 8, pp. 101–110, 2012.
- [3] Y. Peng, J. S. Liu, Z. J. Pan, L. D. Connell, Z. W. Chen, and H. Y. Qu, "Impact of coal matrix strains on the evolution of permeability," *Fuel*, vol. 189, pp. 270–283, 2017.
- [4] Y. G. Geng, D. Z. Tang, H. Xu et al., "Experimental study on permeability stress sensitivity of reconstituted granular coal with different lithotypes," *Fuel*, vol. 202, pp. 12–22, 2017.
- [5] W. M. Cheng, Z. Liu, H. Yang, and W. Y. Wang, "Non-linear seepage characteristics and influential factors of water injection in gassy seams," *Experimental Thermal and Fluid Science*, vol. 91, pp. 41–53, 2018.
- [6] Z. Li, S. G. Liu, W. T. Ren, J. J. Fang, Q. H. Zhu, and Z. L. Dun, "Multiscale laboratory study and numerical analysis of water-weakening effect on shale," *Advances in Materials Science and Engineering*, vol. 2020, Article ID 5263431, 14 pages, 2020.
- [7] R. Jiang, F. Dai, Y. Liu, and A. Li, "Fast marching method for microseismic source location in cavern-containing rockmass: performance analysis and engineering application," *Engineering*, vol. 4, 2021.
- [8] C. Zhu, M. C. He, M. Karakus, and Z. Tao, "Investigating toppling failure mechanism of anti-dip layered slope due to excavation by physical modelling," *Rock Mechanics and Rock Engineering*, vol. 53, no. 11, pp. 5029–5050, 2020.
- [9] C. Zhu, X. D. Xu, W. R. Liu et al., "Softening damage analysis of gypsum rock with water immersion time based on laboratory experiment," *IEEE Access*, vol. 7, pp. 125575–125585, 2019.
- [10] H. Y. Pan, D. W. Yin, N. Jiang, and Z. Xia, "Crack initiation behaviors of granite specimens containing crossing-double-flaws with different lengths under uniaxial loading," *Advances in Civil Engineering*, vol. 2020, Article ID 8871335, 13 pages, 2020.
- [11] F. Q. Ren, C. Zhu, and M. C. He, "Moment tensor analysis of acoustic emissions for cracking mechanisms during schist strain burst," *Rock Mechanics and Rock Engineering*, vol. 53, no. 1, pp. 153–170, 2020.
- [12] G. C. Shi, X. J. Yang, H. C. Yu, and C. Zhu, "Acoustic emission characteristics of creep fracture evolution in double- fracture fine sandstone under uniaxial compression," *Engineering Fracture Mechanics*, vol. 210, pp. 13–28, 2019.
- [13] Q. Meng, H. Wang, M. Cai, W. Y. Xu, X. Y. Zhuang, and T. Rabczuk, "Three-dimensional mesoscale computational modeling of soil-rock mixtures with concave particles," *Engineering Geology*, vol. 277, article 105802, 2020.
- [14] L. D. Connell, "A new interpretation of the response of coal permeability to changes in pore pressure, stress and matrix shrinkage," *International Journal of Coal Geology*, vol. 162, pp. 169–182, 2016.
- [15] S. Valliappan and Z. Wohua, "Numerical modelling of methane gas migration in dry coal seams," *International Journal for Numerical and Analytical Methods in Geomechanics*, vol. 20, no. 8, pp. 571–593, 1996.
- [16] P. D. Sun, "Numerical simulations for coupled rock deformation and gas leak flow in parallel coal seams," *Geotechnical and Geological Engineering*, vol. 22, no. 1, pp. 1–17, 2004.
- [17] Y. S. Zhao, Y. Q. Hu, B. H. Zhao, and D. Yang, "Nonlinear coupled mathematical model for solid deformation and gas seepage in fractured media," *Transport in Porous Media*, vol. 55, no. 2, pp. 119–136, 2004.
- [18] X. D. Zhang, Y. J. Wu, E. C. Zhai, and P. Ye, "Coupling analysis of the heat-water dynamics and frozen depth in a seasonally frozen zone," *Journal of Hydrology*, vol. 593, article 125603, 2021.
- [19] Z. Majewska, G. Ceglarska-Stefańska, S. Majewski, and J. Ziętek, "Binary gas sorption/desorption experiments on a bituminous coal: simultaneous measurements on sorption kinetics, volumetric strain and acoustic emission," *International Journal of Coal Geology*, vol. 77, no. 1-2, pp. 90–102, 2009.
- [20] G. Z. Yin, B. Z. Deng, M. H. Li et al., "Impact of injection pressure on CO₂-enhanced coalbed methane recovery considering mass transfer between coal fracture and matrix," *Fuel*, vol. 196, pp. 288–297, 2017.
- [21] P. Thararoop, Z. T. Karpyn, and T. Ertekin, "Development of a material balance equation for coalbed methane reservoirs accounting for the presence of water in the coal matrix and coal shrinkage and swelling," *Journal of Unconventional Oil & Gas Resources*, vol. 9, pp. 153–162, 2015.
- [22] A. Mitra, S. Harpalani, and S. Liu, "Laboratory measurement and modeling of coal permeability with continued methane production: part 1 - laboratory results," *Fuel*, vol. 94, pp. 110–116, 2012.
- [23] A. Mitra, S. Harpalani, and S. Liu, "Laboratory measurement and modeling of coal permeability with continued methane production: part 2 - modeling results," *Fuel*, vol. 94, pp. 117–124, 2012.
- [24] F. Gu and R. Chalaturnyk, "Permeability and porosity models considering anisotropy and discontinuity of coalbeds and application in coupled simulation," *Journal of Petroleum Science and Engineering*, vol. 74, no. 3-4, pp. 113–131, 2010.
- [25] J. Q. Shi, Z. J. Pan, and S. Durucan, "Analytical models for coal permeability changes during coalbed methane recovery: model comparison and performance evaluation," *International Journal of Coal Geology*, vol. 136, pp. 17–24, 2014.

Research Article

Laboratory Model Tests on Flow Erosion Failure Mechanism of a Slope Consisting of Anqing Group Clay Gravel Layer

Kang Huang,^{1,2} Haipeng Duan,³ Yuelin Yi,³ Fei Yu ,¹ Shanxiong Chen,¹ and Zhangjun Dai ¹

¹State Key Laboratory of Geomechanics and Geotechnical Engineering, Institute of Rock and Soil Mechanics, Chinese Academy of Sciences, Wuhan 430071, China

²University of Chinese Academy of Sciences, Beijing 100049, China

³Anhui Transportation Holding Group Co., Ltd, Hefei 230000, China

Correspondence should be addressed to Zhangjun Dai; zjdai@whrsm.ac.cn

Received 24 January 2021; Revised 13 February 2021; Accepted 1 March 2021; Published 15 March 2021

Academic Editor: Yu Wang

Copyright © 2021 Kang Huang et al. This is an open access article distributed under the Creative Commons Attribution License, which permits unrestricted use, distribution, and reproduction in any medium, provided the original work is properly cited.

The Anqing group clay gravel layer is a special geological body composed of gravel and clay. In excavation projects, involving this soil, such a gravel layer, is prone to slope collapse and instability under the influence of rainfall. To clearly understand the failure mechanism and influencing factors of clay gravel slopes, an indoor artificial rainfall erosion model testing was carried out to analyse the effect of various slope ratios, gravel contents, and rainfall intensities. The slope erosion damage form, runoff rate, infiltration rate, scoured material, and slope stability of the clay gravel slope were studied. The test results show that sloping surfaces of the gentle slope were mainly damaged by erosion, and the degree of damage gradually increased from the top to the bottom of the sloping surface; however, the stability of the surface was good. In the case of the sloping surface layer of the steep slope, large-scale landslides occurred, and the stability of the surface was poor. When the gravel content was small, the surface failure was manifested as a gully failure. When the gravel content was large, it was manifested as a “layer-by-layer sliding” failure. The degree of influence of different conditions on the stable runoff rate was as follows: rainfall intensity > slope ratio > gravel content. The degree of influence of the parameters on the stable infiltration rate was as follows: slope ratio > rainfall intensity > gravel content. On gentle slopes, the total mass of the scoured material was inversely proportional to the gravel content and directly proportional to the rainfall intensity; on a steep slope, the total mass of the scoured material increased with an increase in the rainfall intensity and gravel content. Moreover, the slope ratio was the key influencing factor to decide whether there was gravel in the scoured material.

1. Introduction

The clay gravel layer of the Anqing group is widely distributed in the Anqing section in the upper reaches of the Wanjia River. It is composed of clayey gravel alluvial strata from the Neogene to the quaternary early Pleistocene. It is a special engineering geological body comprising gravel as an aggregate and clay as a filling component and can be characterized as a typical fluvial alluvial earth–rock mixture.

Earlier researchers have predominantly investigated soil erosion of loess and collapsed hills; however, there

have been very few studies on the special clay gravel layers of the Anqing group. Currently, research on soil erosion is focused on studying the influence of rainfall intensity and slope on the development of rills and rill characteristics of the soil slopes [1, 2]. The development of rill networks varies [3, 4], and trichomonas point, rill head extension time, and average head erosion rate are representative indicators that reflect rill development better than the other indicators [5]. At the same time, the slope velocity is an important parameter for understanding the slope rill erosion process under rainfall conditions [6] and plays an

important role in the slope rill erosion dynamic process mechanism [7]. In addition, calculation of the hydraulic and hydrodynamic parameters of the slope runoff is crucial for evaluating the degree of slope erosion and the occurrence of debris flow [8–10]. In gravel and gravel mound areas, the gravel content has a significant influence on the hydrodynamic parameters and damage patterns of the slope runoff. Liang et al. [11] studied the relationship between the gravel content of the slope and runoff and sand production. Wang et al. [12] conducted an indoor artificial rainfall simulation to study the erosion process of red soil slopes with different rainfall intensities, slope ratios, and forms of gravel and compared the rainfall runoff time, runoff rate, runoff process, and sediment intensity of each slope. Jiang et al. [13] studied the effects of rainfall intensity and slope on runoff, infiltration, and sediment yield from landslides. Jiang et al. [14] studied the process of erosion and destruction of slope rills under a heavy rainfall. Liu et al. [15] quantified the hydraulic characteristics of the surface water flow on gravel-covered slopes through laboratory flume experiments. Qin et al. [16] used artificial rainfall simulation methods to study kinetic and rill morphological characteristics of erosion by water with different gravel contents and different rainfall intensities. It was concluded that the hydrodynamic parameters were significantly related to the degree of denudation through a power function relationship, and the water flow power had the best correlation. Rahardjo et al. [17] believed that the damage caused by rainfall was mainly through rainwater infiltration; however, the mechanism of rainwater infiltration has not been adequately understood. Therefore, understanding the response of slope soil under different rainfall conditions is crucial. Tahmasebi and Kamrava [18] based on the DEM model. A joined mathematical thermo-hydro-mechanical framework for studying the effects of external forces, the presence of fluid and thermal variation, is presented. The coupled method is based on a combination of Discrete Element Method and Computational Fluid Dynamics for simulating the solid and the fluid-flow, respectively. Researchers analysed the soil–rock distribution characteristics by test pitting, image analysis, and sieve test. Then, the PFC2D random structure models with different rock block size distributions were built. The stress evolution, damage evolution and failure, deformation localization (based on a principle proposed in this paper), rotation of rock blocks, and shear strength were systematically investigated [19]. These provide a theoretical basis for us to study the force, displacement, and movement mode between soil particles and water during rainfall.

The relative percentages of minerals in Anqing clay gravel layer are as follows: illite (12.3%), kaolinite (47%), and illite-smectite-mixed (40.7%); furthermore, the illite-smectite-mixed ratio is 58.3%. The mechanical properties of these hydrophilic minerals vary significantly when exposed to water. Compared to the general soil–rock mixtures, gravel and soil exhibit a better bonding force; however, under the action of rain, this cementing force will be significantly weakened [20]. Furthermore, the size distribu-

tion range of gravel in the clay gravel layer is wider, and the gravel content is higher. When studying slope erosion, researchers in the past focused on the shape of the slope rill erosion and its hydrodynamic parameters, and there have been only a few studies on the slope stability during the erosion process.

To mitigate the disasters caused by the instability of the clay gravel layer slope of the Anqing group, it is necessary to conduct research on the erosion mechanism and slope stability of special Anqing group clay gravel sloping surfaces under a rainfall. It is of imminent interest to study the main controlling factors, such as the rainfall intensity, slope ratio, and gravel content on slope erosion damage and slope stability. This study mainly investigates the erosion mechanism of slopes with different slope ratios and different gravel contents under heavy rainfall conditions. It is aimed at providing a reasonable theoretical basis for the protection and treatment of clay gravel slopes.

2. Materials and Methods

2.1. Overview of the Sampling Area. The sampling site is located in Wangjiang County, west of the urban area of Anqing City, Anhui Province, China (Figure 1). It has a subtropical and humid monsoon climate along the Yangtze River, with an abundant average rainfall of approximately 1385.0 mm and average annual temperature of 16°C. The sampled soil was from the Neogene to early quaternary Pleistocene Anqing group clay gravel layer, mainly distributed on the northern and southern banks of the Anqing section of the Yangtze River and mostly on the highest terraces (the upper part of the base terraces, that is, the fourth-level terraces, with some exposure to the third and second terraces (posts)). The stratum is of river alluvial type and mainly includes the Anqing gravel layer and Wangjiang gravel layer. Figure 2 shows the typical profile of the clay gravel layer. The basic colour of the stratum is yellow or greyish yellow; the layer thickness is 10–20 m; the main lithology is sand gravel with intercalated clay. The typical gravel diameter is 2–7 cm, with a gravel content of 55% to 75% (usually greater than 50%). The roundness is mainly subcircular, and its sortability is medium. The gravel is mainly composed of quartz gravel, followed by quartz sandstone gravel, siliceous rock gravel, jade, and limestone.

2.2. Test Materials. The clay gravel layer of the Anqing group is composed of gravel and clay with very varying particle sizes. To study the influence of gravel content on the rainfall failure mechanism of the slope, we were required to determine the soil–rock threshold of the clay gravel layer. Medley [21] carried out an extensive statistical analysis and showed that the particle size distribution of soil–rock mixture satisfied self-similarity within different research scales. The conceptual model of soil and rock threshold and rock content proposed by him was highly practical; however, it ignored the overall step-by-step characteristics of particle size. In this study, the fractal geometry theory was used to determine the threshold value of the clay gravel layer. This study adopted by Mandelbrot

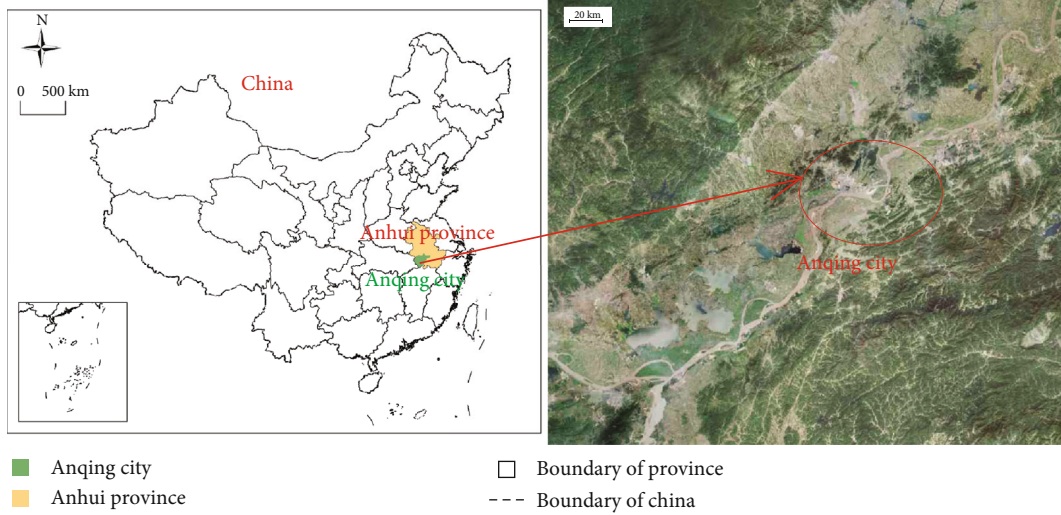


FIGURE 1: Topographic map of the upper reaches of the Wanjiang River in Anhui Province.



FIGURE 2: Typical profile of clay gravel layer.

[22] was based on the fractal structure expression of particle mass distribution derived from literature [23], and the fractal theory obtained is as follows:

$$\frac{M(d < r)}{M_T} = \left(\frac{r}{r_L}\right)^{3-D} \quad (1)$$

Here, M_T and r_L represent the total mass and maximum particle size of the particle system, $M(d < r)$ refers to the total mass with the particle size $d < r$, respectively, and $(3 - D)$ is the power exponent; d represents the radius of the particle; r represents the particle size; D is the fractal dimension. This formula represents the power function relationship between the mass fraction and the particle size ratio. The grain-size distribution of clay gravel layer at the sampling point was analysed, and the grain-size accumulation curve was denoted as PSD1, PSD2, and average PSD, as shown in Figure 3. In this experiment, two sets of particle size cumulative curves were selected for screening and were recorded as PSD1 and PSD2; the

average PSD of the gradation curve was obtained by averaging these two sets to calculate the fractal dimension, and the same was used in Equation (1). The mass cumulative percentage curve and the double logarithmic coordinate curve of the particle size are shown in Figure 4. It can be seen from the figure that the particle size distribution curve of the clay gravel layer did not satisfy a strict linear relationship within the research scale. With $r = 5 \text{ mm}$ as the point of separation, there was a strict scale-free interval on either side. The corresponding fitting formulae were $y_1 = 0.71x + 1.16$ and $y_2 = 0.28 + 1.46$; the corresponding fractal dimensions were $D_1 = 2.29$ and $D_2 = 2.72$, respectively. This shows that the particle size distribution of the clay gravel layer had a twofold fractal structure. Originally, “ $r = 5 \text{ mm}$ ” was considered as the “soil threshold” of the clay gravel layer.

2.3. Test Plan. From actual engineering experience and related results of rainfall erosion and destruction of soil slopes, the gravel content, slope ratio, and rainfall intensity all are considered to have an impact on the failure mechanism of clay gravel slopes. If the above three factors are comprehensively considered for a comprehensive test, 27 tests are required. Large-scale model tests can be expensive and entail time costs. Therefore, a more scientific, reasonable, and efficient orthogonal test method was adopted [24]. This method can design a variety of orthogonal tables for the tests, considering different factors and levels; it can screen several comprehensive tests according to certain mathematical rules and select nine typical tests from 27 tests. The orthogonal test scheme is shown in Table 1.

2.4. Test Device. The scouring device was composed of four components, as shown in Figure 5: the rainfall system, scour collection system, slope system, and camera system. The rainfall system could control the rainfall area according to the scope of the test and adjust the rainfall intensity, for example, light rain, heavy rain, and heavy rain in nature. At the same time, the uniformity of rainfall could reach more

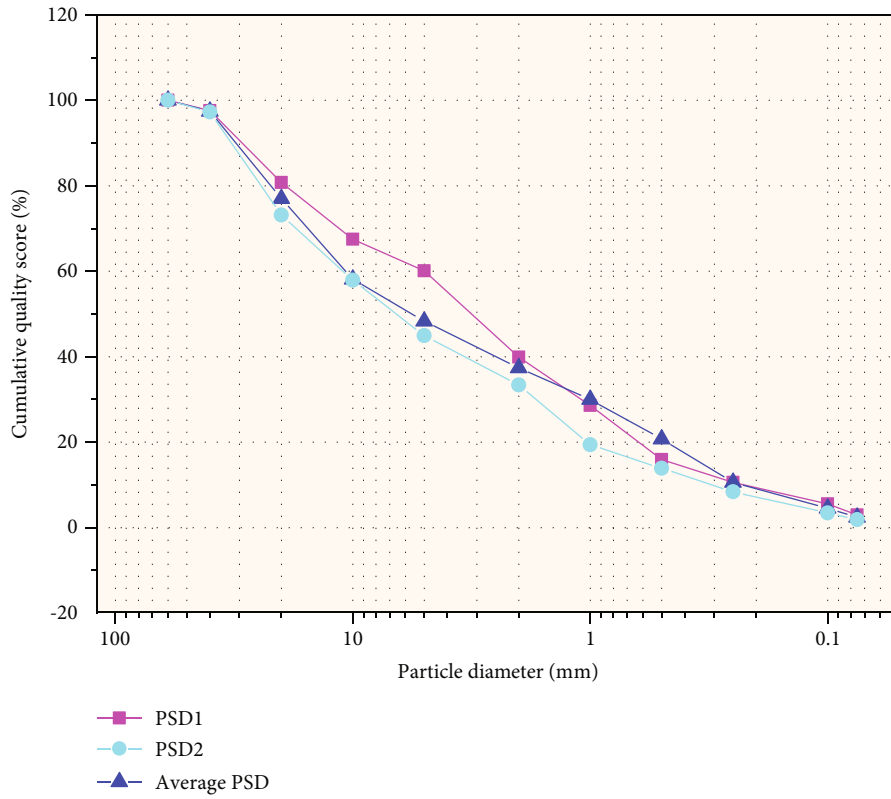


FIGURE 3: Nature grain-size distribution curve of clay gravel layer.

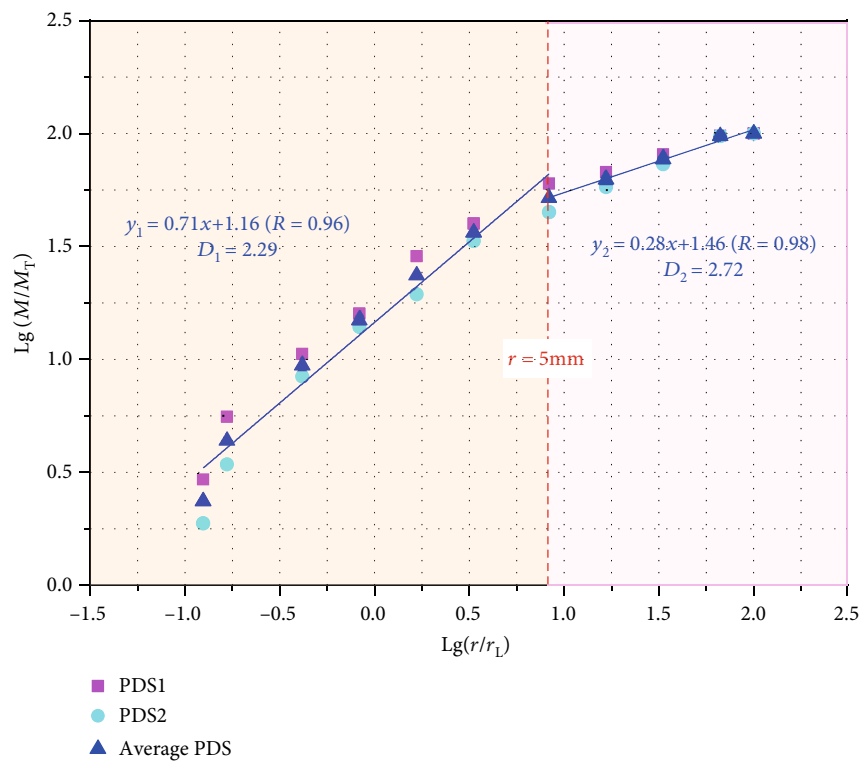


FIGURE 4: Calculation of the fractal dimension of the grain size of clay gravel and its analysis.

TABLE 1: Orthogonal test scheme.

Test number	Gravel content (%)	Slope ratio	Rainfall intensity (mm/h)
A	30	1:0.5	180
B	50	1:0.5	100
C	70	1:0.5	140
D	30	1:1.5	100
E	50	1:1.5	140
F	70	1:1.5	180
G	30	1:2.5	140
H	50	1:2.5	180
I	70	1:2.5	100

than 85%, and the sprayed water was similar to raindrops. The scour collection system could collect the mixture of rainwater and clay gravel, use an electronic scale to weigh the total mass of the scoured material, and then dry the saturated soil in an oven until the mass remained constant from which the dry mass was finally weighed. Using this system, the runoff rate and infiltration rate at different times could be calculated, and the total mass of the scoured material from the slope could also be obtained. The slope system comprised a model box with a variable slope ratio. The system could simulate a complete slope, including the slope top, slope surface, and slope angle. The width and length of the slope were 1 and 1.5 m, respectively. The camera system used a digital camera to capture the appearance of the slope at different times. Image recognition was used to extract the distribution of gullies on the slope as well as their depth and width. Thus, the development trend and change process of gullies at different times were studied. Through image processing slope surface images of different times, observe the change of slope failure, for analysis of slope rainfall erosion failure mechanism that provides a comprehensive efficient and strong operability, wide applicability, and can be more realistic simulation of the natural slope damage under different rainfall intensities, to clarify the slope rainfall erosion failure mechanism that provides an effective method and to lay a good foundation for the management of soil and water loss and the protection of the slope stability.

2.5. Test Procedure. The test procedure consisted of the following steps:

- (1) The clay gravel layer was retrieved from Wangjiang County to the west of Anqing city, and the matrix moisture content of the in situ clay gravel was measured to be 12.5%. In addition, the average value of the natural density of the clay gravel was measured to be 1.93 g/cm^3
- (2) The retrieved sample was dried and slightly ground so that there was no cementation between the clay and gravel. It was then passed through a 5 mm diameter sieve to separate the clay and gravel

- (3) According to the volume of the model box and the density of the clay gravel layer, the total mass of the clay gravel was calculated; the matrix moisture content of the clay gravel was controlled to 12.5% to ensure that the mechanical properties of the clay gravel were closer to those of the original soil. Based on the range of gravel content employed in the experiment, the water was weighed, with clay and gravel to obtain a corresponding quality
- (4) The clay and gravel were mixed with each other in required proportions; water of appropriate quality was sprayed evenly with a kettle. The stirring was repeated to ensure that the water content of the clay gravel matrix was evenly distributed
- (5) Using the layered filling method, the clay gravel was divided into several layers for filling. Each layer was filled with clay gravel of appropriate quality and then compacted to the original soil density. A PR2/4 soil profile moisture measuring instrument was buried successively at the top, two-thirds distance from the top, and one-third distance from the top of the slope
- (6) With regard to the rainfall, the corresponding rainfall intensity in the system was set, and the total rainfall time was 1 h (if the slope had a large area of collapse and instability, the test was terminated early)
- (7) The scoured material was collected every five minutes, and its mass was weighed. Then, the scoured material was allowed to stand still; the supernatant liquid was discarded; the remaining clay gravel was dried in an oven at 105°C . The clay gravel was weighed again, which was subtracted from the total mass to calculate the mass of the water. The total mass of the slope runoff was calculated back to calculate the slope runoff rate, and then, the slope infiltration rate was calculated by subtracting the slope runoff rate from the rainfall intensity
- (8) A digital camera was used to photograph the slope every five minutes to observe the changes in the width, depth, shape, number, and distribution of the gullies on the slope
- (9) After the rainfall, a slope water content measuring instrument was used to measure the matrix water content of the slope to obtain the immediate matrix water content after the rainfall. Then, the slope was allowed to stand for 24 h, and then, the matrix moisture content of the slope was measured

3. Erosion Failure Form of the Clay Gravel Slope

3.1. Slope Failure Morphological Characteristics. Figure 6 shows the slope failure morphology diagram for different test configurations. The slope of the test group with slope ratios of 1:2.5 and 1:1.5 was defined as a gentle slope, and the slope of the test group with a slope ratio of 1:0.5 was defined as a steep slope. The damage patterns of the slope surface of the

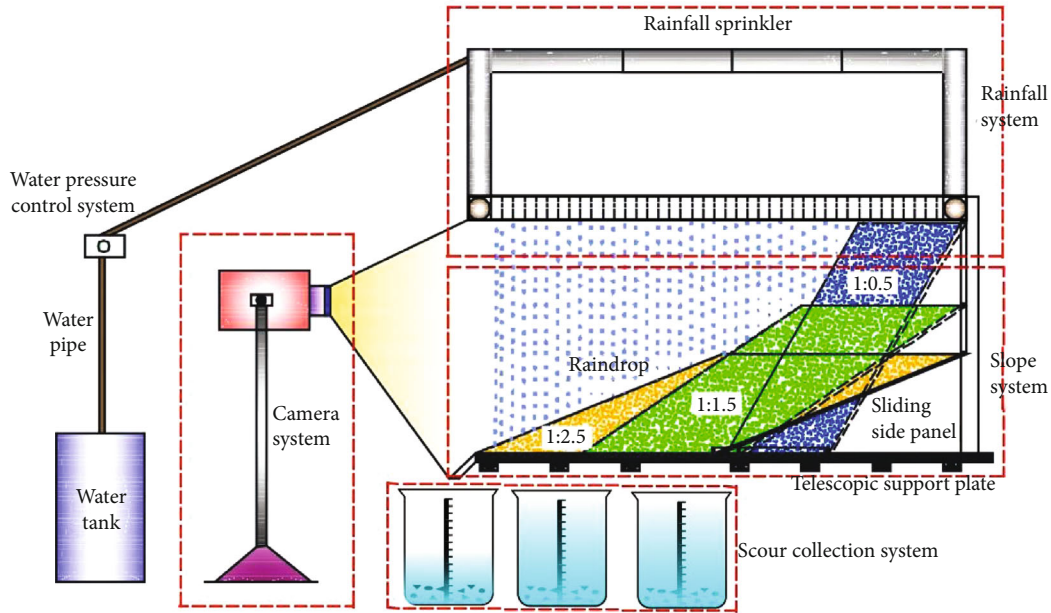


FIGURE 5: Schematic diagram of the test setup.

gentle slope of the clay gravel layer under different gravel contents, slope ratios, and rainfall intensities after 1 h of rainfall are shown in Figures 6(a)–6(f). It can be seen from the figure that the forms of gullies and pits on gentle slopes were affected by the gravel content. At the same time, the spatial distribution of gravel affected the position of the gullies and pits on the slope. The intensity of rainfall affected the depth of the gullies and size of the pits. Under different gravel contents, slope ratios, and rainfall intensities of the clay gravel steep slope, the slope failure patterns are displayed in Figures 6(g)–6(i). It can be seen from the figure that the difference in the gravel content determined the failure form of the slope. The steep slope with a low gravel content (30%) suffered a gully failure, and the steep slope with a high gravel content (50% and 70%) suffered “slip-by-layer” failure. However, upon comparing the damage patterns of gentle and steep slopes, it can be seen that the slope ratio was a key factor affecting the stability of the clay gravel sloping surface under rainfall conditions.

3.2. Gentle Slope Failure Form. The degree of damage at different positions of the slope surface is defined as $\omega_l = w_l/w_0$ (ω_l is the degree of damage of the slope surface; its value ranges from 0 to 1 and is a dimensionless constant; w_l is the width of the pit or rill on the slope when the distance from the point to the bottom of the slope is l , in centimeter; w_0 is the width of the slope when the distance from the bottom of the slope is l , in centimeter).

Figure 7 shows the degree of damage curves for different positions on the gentle slopes. It can be seen from the figure that under different gravel contents, slope ratios, and rainfall intensities, the degree of damage of the clay gravel sloping surface increased from the top to the bottom of the slope. In the gentle slope tests, when the rainfall intensity at different positions on the slope was the same, the rainfall

from the top of the slope to the bottom of the slope increased successively. The greater the rainfall on the slope, the greater the erosion damage to the slope. The curve was close to the bottom of all the curves, and the test E curve was close to the top of all the curves. It shows that the overall degrees of erosion of the slope in experiment I and experiment E were the smallest and the largest, respectively, among the gentle slope erosion tests. At the same time, the scours in experiment I and experiment E were the smallest and largest, respectively, in the gentle slope tests. This shows that the lower the overall erosion degree of the slope, the smaller the total mass of the scoured material, which would reflect the overall degree of erosion of the slope.

3.3. Steep Slope Failure Form. The shape of the erosion failure of the clay gravel slope was related to the gravel content, when the gravel content was 30%. For this case, the failure of the slope was a gully failure, which was similar to that of a gentle slope. At the beginning of the rainfall and before the runoff occurred, splash erosion on the slope played a major role. As the rainfall progressed, surface currents were formed and sheet erosion occurred. Then, the crater formed by the flaky erosion of the surface flow gradually transformed into a concentrated flow. On the path of the concentrated water flow, the erosion force of runoff gradually increased, and when soil particles could be washed away, a small waterfall was formed. The cascade further developed and evolved into a rill head, and rill erosion occurred accordingly. The side-cutting erosion of the head of the rill, forward erosion, and collapse and erosion of the ditch wall caused a discontinuity of the ditch. Therefore, multiple discontinuous rills on the same concentrated flow channel were connected by vertical erosion to form continuous rills. With the development of rainfall and rill erosion, the rill dip, rill density, degree of rill stripping, and bending complexity of the rills increased.

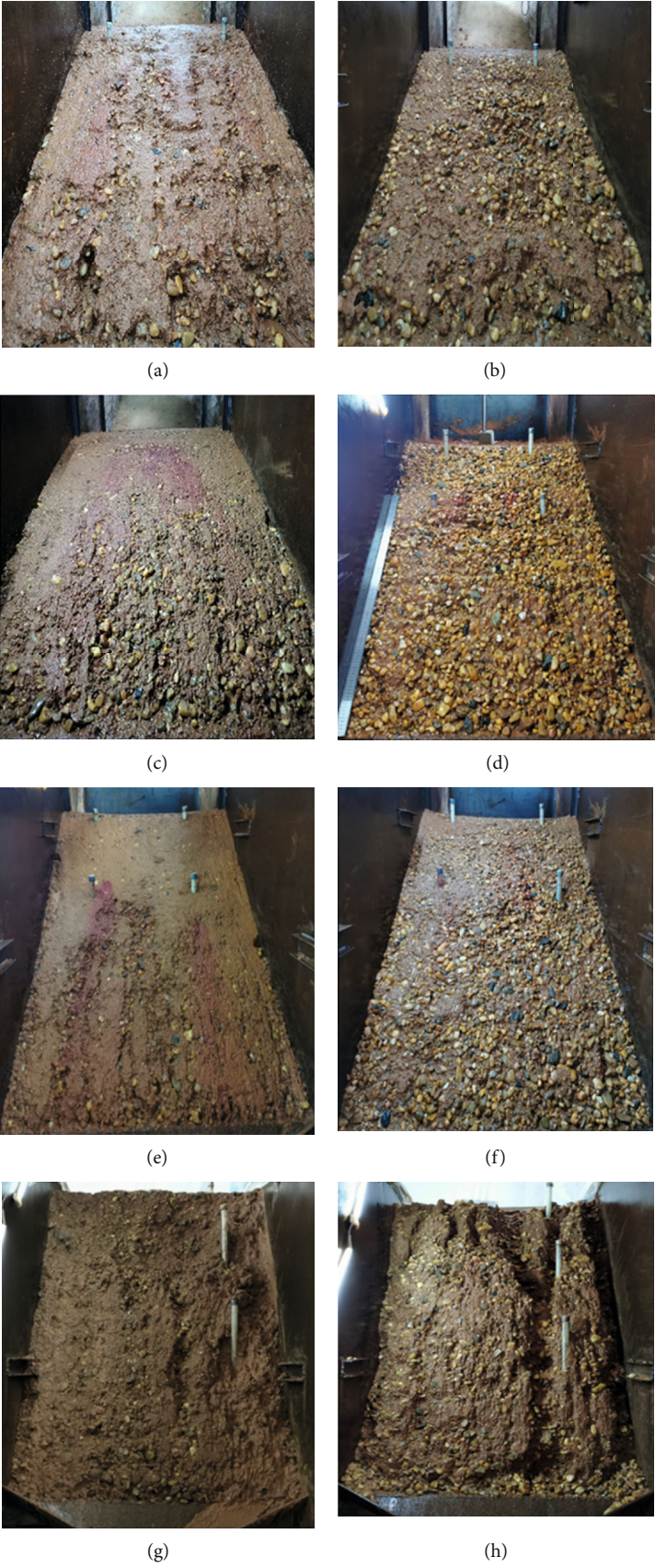


FIGURE 6: Continued.



(i)

FIGURE 6: Slope morphology diagram at the end of slope erosion: (a) 30%-1 : 2.5-140 (1 h); (b) 50%-1 : 2.5-180 (1 h); (c) 70%-1 : 2.5-100 (1 h); (d) 70%-1 : 1.5-180 (1 h); (h); (e) 30%-1 : 1.5-100 (1 h); (f) 50%-1 : 1.5-180 (1 h); (g) 50%-1 : 0.5-100 (20 min); (h) 30%-1 : 0.5-180 (1 h); (i) 70%-1 : 0.5-140 (13 min).

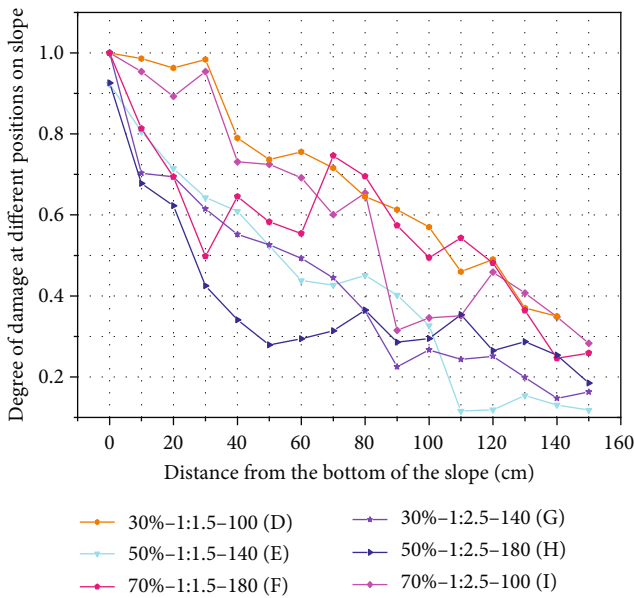


FIGURE 7: Curves representing the degree of damage at different positions of slope.

When the gravel content was either 50% or 70%, there was a significant difference in the failure mode of the sloping surface and the damage mode, compared to the case of 30% gravel content; there was almost no evidence of gullies forming on the slope surface. The sloping surface presented the failure form of “layer-by-layer” sliding mode. The reason was as follows: when the gravel content was high, initial cracks were formed between the gravel and the clay, which was the dominant channel for water seepage. At the same time, when the water flowed through a junction, a vortex with a stronger denudation capacity was formed, which would wash away the clay beside the gravel, and the gravel would fall into the erosion pit to form small steps under the action of gravity. These small steps consumed the energy of the runoff scouring in the vertical direction and hindered the runoff in that direction. At the same time, it promoted

a lateral flow of water, increased the lateral erosion ability of the water, and brought the vertical and lateral runoff forces at different positions of the slope close to each other, so that the degree of damage at different positions of the slope was similar. The phenomenon of “layer collapse” destroyed this form.

When the gravel content exceeds 70%, the failure mode of clay gravel slope is different from the previous two failure modes. Because the gravel content is sufficient, the gravel contacts each other to form a stable skeleton structure. The clay is filled in the pores of the gravel. When the clay is washed away, the skeleton structure of the slope is not affected much, and the stability of the slope is almost unchanged. In this case, the main factor affecting the stability of the slope is the slope ratio, because the change of slope ratio affects the stability of gravel and thus the stability of slope.

4. Runoff and Infiltration Characteristics of Clay Gravel Slope

4.1. Relationship between Slope Runoff, Infiltration, and Rainfall Time. Figures 8 and 9 show the simulated artificial rainfall, clay gravel layer slope runoff rate, and infiltration rate curves with time under different conditions. Under the conditions of different gravel contents, slope ratios, and rainfall intensities, the runoff rate and infiltration rate of the clay gravel layer slope changed similarly. When the rainfall time was less than 10 min, the slope runoff was in a rapid growth stage. When the rainfall time was more than 10 min, the slope runoff was in a stable stage; finally, when the rainfall time was less than 10 min, the slope infiltration was in a declining stage. When the rainfall time was more than 10 min, the slope infiltration is in the stable stage. At the beginning of the rainfall, the clay gravel slope was not sealed by water, and the erosion of the slope was mainly by raindrop splash erosion. Therefore, the slope runoff rate at this time was less than the later runoff rate, and the slope infiltration rate was greater than the later infiltration rate. With the formation of the slope water flow to promote the water sealing effect of the

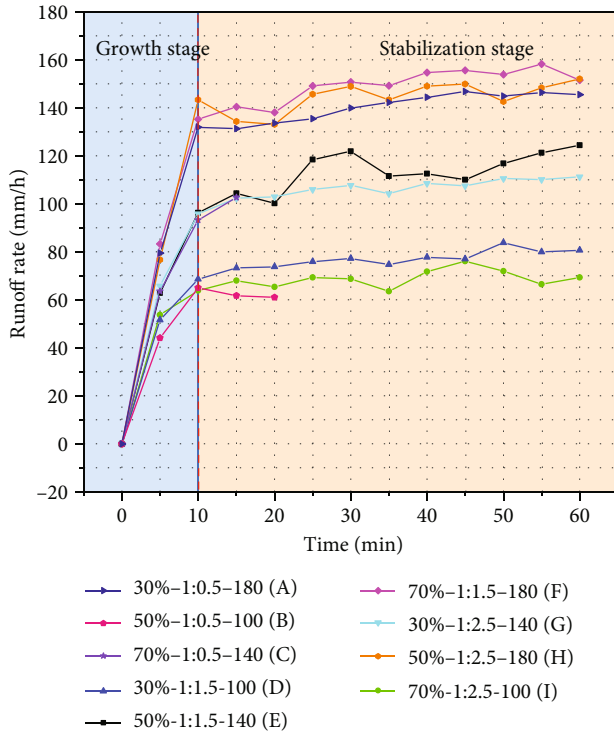


FIGURE 8: Runoff rate of the clay gravel slope.

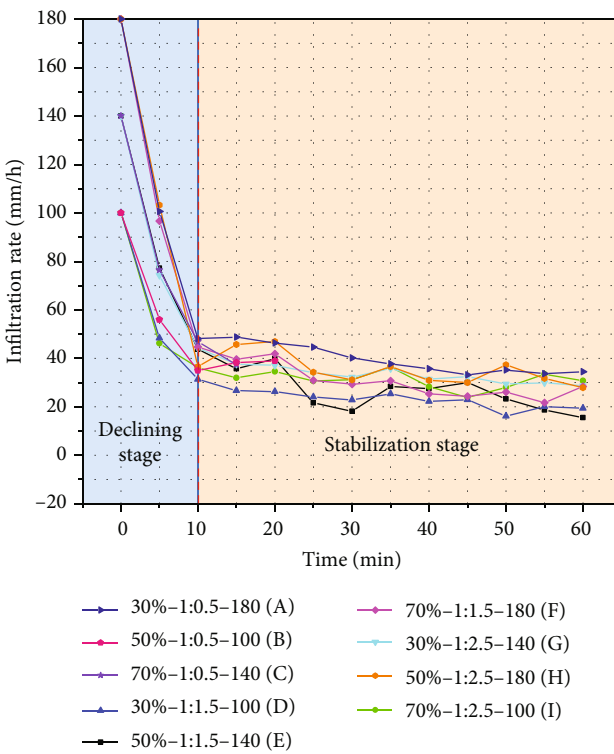


FIGURE 9: Infiltration rate of the clay gravel layer slope.

slope, the infiltration rate of the clay gravel slope gradually decreased, and the runoff rate gradually increased. When the rainfall time was approximately 10 min, the slope runoff

TABLE 2: Analysis of influencing factors of runoff rate in stable stage.

Test number	Gravel content (%)	Slope ratio	Rainfall intensity (mm/h)	The stable runoff rate (mm/h)
A	30	1:0.5	180	140.2
B	50	1:0.5	100	62.6
C	70	1:0.5	140	97.9
D	30	1:1.5	100	76.6
E	50	1:1.5	140	112.5
F	70	1:1.5	180	148.8
G	30	1:2.5	140	106.1
H	50	1:2.5	180	144.6
I	70	1:2.5	100	68.6
T1	322.9	300.7	207.8	
T2	319.7	337.9	316.5	
T3	315.3	319.3	433.6	
m1	107.63	100.23	69.27	
m2	106.57	112.63	105.5	
m3	105.1	106.43	144.53	
R	2.53	12.40	75.27	

Note that the “T1” line gives the sum of the average rates of the three tests in the stable phase under the condition of 30% gravel content; $T1 = 140.2 + 76.6 + 106.1 = 322.9$, and the average value = $T1/3 = 322.9/3 = 107.63$; it is listed in “m1.” Similarly, the average runoff rates of the three tests under 50% and 70% gravel content were 106.57 and 105.1, respectively. The ranges of the three average values were $R = \max [107.63, 106.57, 105.1 - \min] [107.63, 106.57, 105.1] = 2.53$, which is listed in the last row of the table. Corresponding numbers for the slope ratio and rainfall intensity were calculated similarly.

rate and infiltration rate reached relatively stable values. In the stable stage of the slope runoff, the runoff rate fluctuated over a small range, mainly owing to the unstable development of the slope erosion rills, for example, the widening of the rills, collapse of ditch walls, and blocking effect of gravel falling into the rills on runoff.

4.2. Analysis of Influencing Factors of Slope Runoff Rate in the Stable Stage. Table 2 summarizes the results from the analysis of the influencing factors of the runoff rate of the clay gravel layer sloping surface under different gravel contents, rainfall intensities, and slope ratios. It was assumed that the average value of the runoff rate in the stable stage with time was the stable runoff rate. The influences of gravel content, slope ratio, and rainfall intensity on the stable runoff rate were analysed. The R value of each factor in Table 2 indicates the maximum differences. The larger the range, the greater the influence of this factor on the stable runoff rate. Therefore, the order of the degrees of influence on the stable runoff rate was rainfall intensity>slope ratio>gravel content. Figure 10 shows the relationship between the average stable runoff rate and the gravel content, slope ratio, and rainfall intensity. It can be seen from the figure that as the gravel content increased, the average stable runoff rate kept decreasing. As the slope ratio increased, the average stable runoff rate first increased and then decreased. With an increase in the rainfall

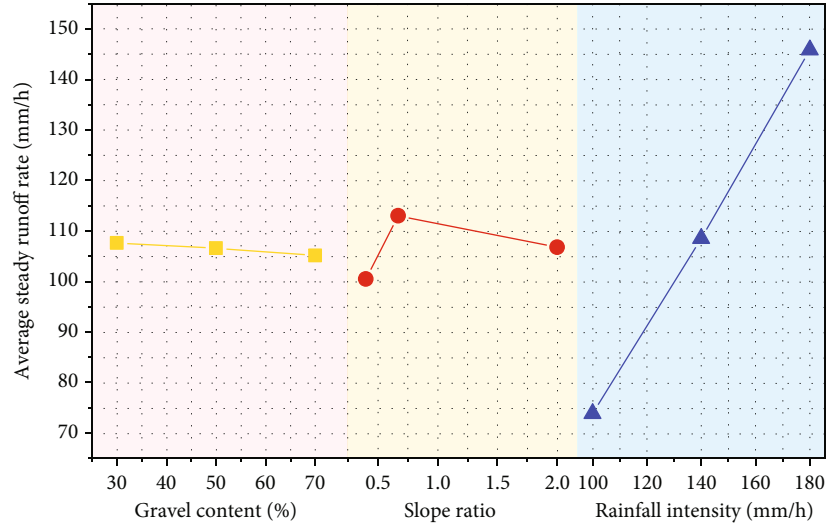


FIGURE 10: Relationship between the average steady runoff rate and gravel content, slope ratio, and rainfall intensity.

intensity, the average steady runoff rate kept increasing. Therefore, when the rainfall intensity was constant, the most favourable combination of the gravel content and slope ratio for a stable runoff of the slope was 30%-1:1.5. Under these conditions, the clay completely wrapped the gravel, and the gravel was embedded in the clay to form a compact structure. More runoff energy was needed to wash away the soil particles. In addition, the presence of gravel hindered the infiltration channels for the rainwater, and the slope was not conducive to the infiltration of rainwater. At the same time, the slope ratio of 1:1.5 was larger for the gentle slope, which was beneficial to the runoff of the slope. The interaction of these three factors promoted a direct flow of rainwater along the sloping surface, and at the same time, there were fewer soil particles entrapped in the runoff; therefore, the degree of slope damage was low, and the slope stability was high.

4.3. Analysis of Influencing Factors of Slope Infiltration Rate in the Stable Stage. Table 3 summarizes the influencing factor analysis of the infiltration rate of the clay gravel slope under conditions of different gravel contents, rainfall intensities, and slope ratios. Assuming that the stable infiltration rate was the average value of the infiltration rate in the stable phase over time, Table 3 summarizes the influence of gravel content, slope ratio, and rainfall intensity on the stable infiltration rate. The R value of each factor in Table 3 indicates the extreme differences. The larger the range, the greater the influence of this factor on the stable infiltration rate. Therefore, the order of the degrees of influence on the stable infiltration rate was slope ratio>rainfall intensity>gravel content. Figure 11 shows the relationship between the average stable infiltration rate and gravel content, slope ratio, and rainfall intensity. It can be seen from the figure that as the gravel content increased, the average stable infiltration rate increased. This result is consistent with previous research [25]; as the slope ratio increased, the average stable infiltration rate increased. The infiltration rate first decreased and

TABLE 3: Analysis of the influencing factors of the infiltration rate in stable stage.

Test number	Gravel content (%)	Slope ratio	Rainfall intensity (mm/h)	The stable runoff rate (mm/h)
A	30	1:0.5	180	39.8
B	50	1:0.5	100	37.4
C	70	1:0.5	140	42.1
D	30	1:1.5	100	23.4
E	50	1:1.5	140	28.91
F	70	1:1.5	180	31.2
G	30	1:2.5	140	33.9
H	50	1:2.5	180	35.4
I	70	1:2.5	100	31.4
T1	97.1	119.3	92.2	
T2	101.71	83.51	104.91	
T3	104.7	100.7	106.4	
m1	32.37	39.77	30.73	
m2	33.90	27.84	34.97	
m3	34.9	33.57	35.46	
R	2.53	11.93	4.73	

Note: T1, T2, T3, m1, m2, m3, and R have the same meanings and methods as in Table 2.

then increased; with an increase in the rainfall intensity, the average steady infiltration rate gradually increased; however, the rate of increase gradually decreased. It is generally believed that the infiltration rate of the soil slopes decreased with an increase in the slope ratio; that is, the infiltration rate of the steep slopes was less than that of the gentle slopes. However, the conclusion drawn in this study was that the steeper the slope, the greater the infiltration rate. The main reason for this phenomenon was that this test was carried

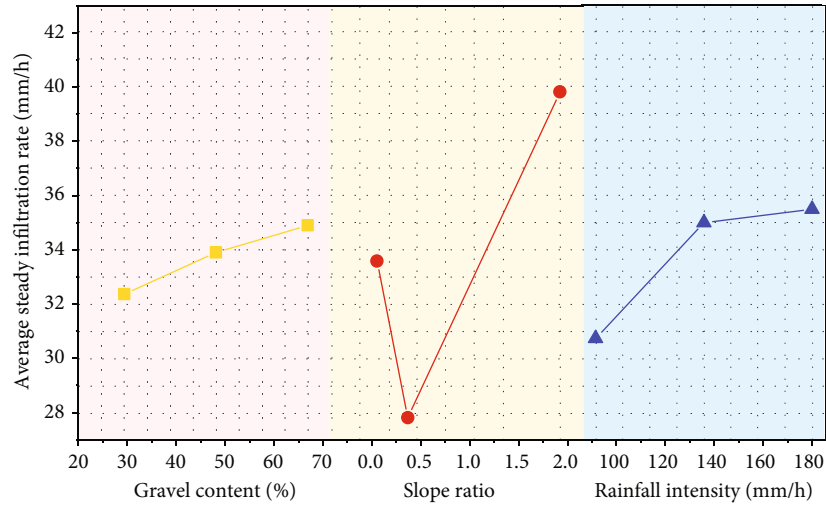


FIGURE 11: Relationship between the average steady infiltration rate and gravel content, slope ratio, and rainfall intensity.

out under heavy rain conditions. The slope of the clay gravel layer quickly formed pits and gullies under rainwater erosion, with an increase in the slope ratio, the pit area of the slope, and the width and depth of the gully expanded rapidly, and even landslides appeared to some extent. The fissures formed by these pits and gullies provided infiltration channels for further infiltration of rainwater. At the same time, the relative surface area of the slope increased, which increased the effective area of infiltration. As a result, the steeper the slope, the greater the infiltration rate. Therefore, when the rainfall intensity was constant, the combination of gravel content and slope ratio, which was most conducive to stable infiltration of the slope, was 70%-1:0.5. Under these conditions, the slope was most conducive to the infiltration of rainwater, the total mass of the slope-scouring material was the largest, and the slope stability was the lowest.

5. Scouring Characteristics of Clay Gravel Slope

5.1. Relationship between the Total Mass of Scoured Material on Gentle Slope, Gravel Content, and Rainfall Intensity. The quality of the scoured material of the clay gravel layer slope increased with an increase in rainfall time. When the slope was gentle, the quality of the scoured material was low, and there was almost no gravel; on the steep slope, the quality of the scoured material was larger and contained a significant amount of gravel. The slope was a key factor for the significant difference in the quality of the washed material.

Figure 12 shows the variation in the total mass of the scoured material over time on the clay gravel slope under artificial rainfall conditions. It can be seen from the figure that with an increase in the slope and rainfall intensity, the erosion force of the runoff increased; the erosion degree of the slope of different clay gravel layers increased, and the quality of the collected erosion material increased significantly. This was consistent with the research results of Jiang et al. [26]. Further analysis of the total mass of the scoured material of the clay gravel layer slope over time under differ-

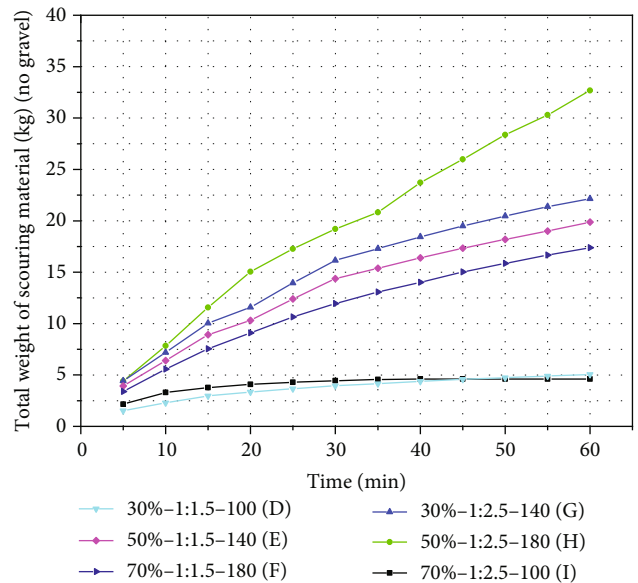


FIGURE 12: Time-history curve of the total mass of scoured material on gentle slopes.

ent conditions showed that when the slope was a gentle slope, it did not exhibit a large-scale landslide and instability, and the self-stability was good. Under these conditions, the total mass of the scouring material was inversely proportional to the gravel content and directly proportional to the rainfall intensity. This was because under gentle slope conditions, the slope was relatively stable under the given rainfall conditions, and there would be no large-scale landslides. The energy generated by the runoff was proportional to the intensity of the rainfall; however, the maximum energy at this time was not sufficient to wash away the gravel; it could only wash away the soil particles around the gravel, and the gravel collapsed into the pit under the action of gravity. The increase in the gravel content mainly hindered the runoff. Therefore,

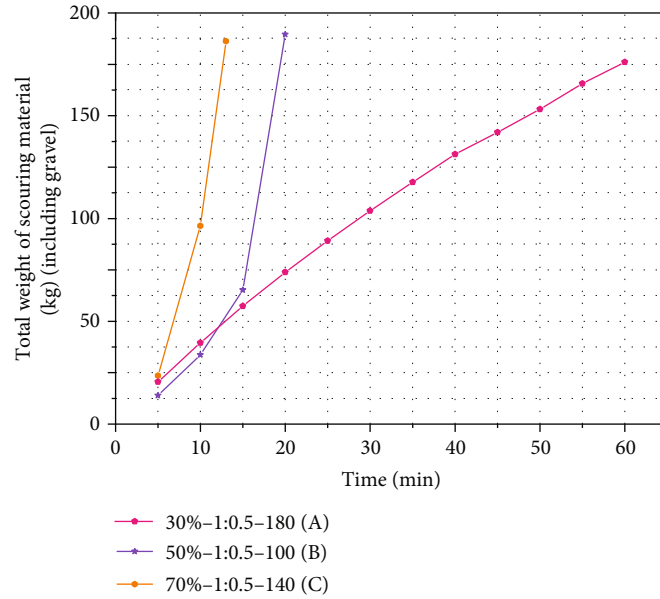


FIGURE 13: Time-history curve of the total mass of scoured material on steep slopes.

the total mass of the scouring material was affected by the two layers of gravel and rainfall intensity. The total mass of the scouring material decreased with an increase in the gravel content and increased with an increase in the rainfall intensity.

5.2. Relationship between the Total Mass of Scoured Material on Steep Slopes, Gravel Content, and Rainfall Intensity. As shown in Figure 13, when the slope is steep, test C had a large area of landslide and instability when the rainfall time was 13 min, while sample B exhibited the same phenomena when the rainfall time was for 20 min. We believe that the slope became unstable at this time, and the test was stopped. Under different rainfall conditions, all the steep slopes had a certain amount of landslide and instability, coupled with poor self-stability. The total mass of the scoured material increased with an increase in the rainfall intensity and gravel content. The reasons are as follows: (1) as the slope increased, the scouring force of the runoff along the slope increased; the scouring effect of the runoff increased; the antisliding force of the gravel on the slope decreased. In addition, when the content of gravel was high, the pores of the soil increased; the initial cracks increased in size; the clay could not completely wrap the gravel; the cohesive force of the clay gravel layer decreased; the erosion resistance decreased. Therefore, the clay gravel was more susceptible to erosion. (2) With an increase in the rainfall intensity, the scouring effect of the runoff was further strengthened and eddy currents with stronger denudation capability were easily formed around the gravel, and the scouring effect on the particles was enhanced. At the same time, the energy of the runoff was sufficient to wash away the gravel, and the slope was more prone to erosion.

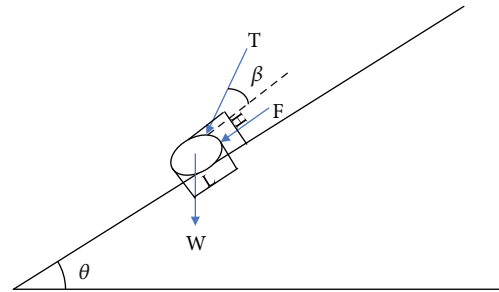


FIGURE 14: Presents a simplified diagram of the force on the gravel of the clay gravel slope.

5.3. Influencing Factors of Gravel Content in the Scoured Material. When the slope was gentle, there was no gravel in the scour from the clay gravel layer; however, when the slope was steep, the scour from the clay gravel layer contained gravel. Therefore, the key factor that decides whether gravel was contained in the scoured clay gravel layer was the slope ratio of the sloping surface. Based on Wang et al. [27], Figure 14 is a simplified diagram of the gravel stress on the clay gravel slope. The slope of the sloping surface is θ ; the cohesion of the clay gravel layer is C ; the friction angle is φ ; T is the impact force of raindrops on the gravel; F is the scour force of the runoff on the gravel; W is the gravity of the gravel; the angle between T and the slope direction is β . When rainfall on the slope surface formed a slope surface runoff, a water film was formed on the surface of the gravel, and the impact of raindrops on the gravel was very weak and could be ignored. After random statistics of 200 different elliptical gravels were considered, the short axis length H , long axis length $L = 0.73 : 1$, and the short axis length of the gravel in the width direction were almost equal to H . Therefore, the gravel was equivalent to a rectangular

TABLE 4: Stability coefficient of gravel fall of clay gravel layer slope.

Test number	Saturated cohesion of gravel layer (kPa)	Saturated friction angle of gravel layer (°)	Stability coefficient
A	15.8	19.3	0.829
B	16.4	18.6	0.850
C	13.6	17.3	0.717
D	15.8	19.3	1.513
E	16.4	18.6	1.541
F	13.6	17.3	1.313
G	15.8	19.3	2.316
H	16.4	18.6	2.356
I	13.6	17.3	2.012

parallelepiped, with its length (L), width (D), and height (H) equal to 1:0.73:0.73. Supposing that the volume of gravel was V and the area in contact with the sloping surface was S , the slip resistance of the gravel is

$$N = W \cdot \cos \theta \cdot \tan \varphi + C \cdot S. \quad (2)$$

The sliding force is

$$N_1 = W \cdot \sin \theta + F, \quad (3)$$

$$F = \gamma_{\text{water}} \cdot V \cdot \sin \theta. \quad (4)$$

Therefore, the stability factor of gravel is

$$F_s = \frac{N}{N_1}. \quad (5)$$

According to the indoor triaxial test, the cohesion and internal friction angle of the saturated clay gravel layer under different rock content conditions are summarized in Table 4. The stability coefficients of nine groups of clay gravel layer slope gravel slipping were calculated from the previous test. As shown in Table 4, the stability factor was less than 1, indicating that the antisliding force of the gravel on the slope was less than the sliding force, the gravel was in an unstable state under the action of the runoff on the slope, and the gravel would slip. On the contrary, when the stability factor was greater than 1, the gravel would run off on the slope. In a stable state under these conditions, the gravel would not slip off. The calculated results were consistent with the experimental observations. It shows that whether the gravel falls off of the clay gravel slope mainly depends on the slope ratio, and the gravel content also had a certain influence.

6. Conclusions

When the slope was gentle, the failure of the sloping surface appeared as an erosion damage. The degree of damage at different positions of the sloping surface increased from the top of the surface to the bottom of the surface. The overall degree

of erosion of the slope in test I was the smallest and had the greatest degree of overall erosion. When the slope was steep, it had a large area of collapse and instability. When the gravel content was 30%, the slope was revealed as a gully failure. When the gravel contents were 50% and 70%, the slope was revealed as a “layer-by-layer” sliding failure.

Under conditions of different gravel contents, slope ratios, and rainfall intensities, the runoff rate and infiltration rate of the clay gravel layer slope changed similarly. Taking 10 min of rainfall as the limit, the runoff on the slope was divided into a growth phase and a stable phase. The slope infiltration was divided into a descending phase and a stable phase. There were small-scale fluctuations in both the stable stages, which were mainly owing to the unstable development of the slope erosion, for example, the widening of rills, collapse of ditch walls, and blocking effect of gravel falling into the rills on the runoff. After 10 min of rainfall, the order of the degree of influence of each factor on the stable runoff rate was as follows: rainfall intensity > slope ratio > gravel content. The order of the degree of influence on the stable infiltration rate was slope ratio > rainfall intensity > gravel content. It is generally believed that the infiltration rate of a slope decreases with an increase in the slope ratio, and the test results in this study showed that the stable infiltration rate of the slope first decreased and then increased with an increase in the slope ratio, mainly because the slope was steep. The slope had a large area of collapse, which provided a passage for infiltration and increased the effective infiltration area of the slope.

When the rainfall intensity was constant, the most favourable combination of the gravel content and slope ratio for stable runoff of the slope was 30%-1:1.5. Under these conditions, the slope was not conducive to the infiltration of rainwater, and the rainwater flowed along the sloping surface. The quality of the clay in the middle wrap was low; the slope damage was low; the slope stability was high. The combination of gravel content and slope ratio that was most conducive to a stable infiltration of the slope was 70%-1:0.5. Under these conditions, the slope was most conducive to the infiltration of rainwater; the slope had a large area of collapse; the stability of the slope was the lowest.

When the slope was a gentle slope, the total mass of the scoured material was inversely proportional to the gravel content and proportional to the rainfall intensity. When the slope was steep, the total mass of the scoured material increased as the rainfall intensity and gravel content increased. At the same time, the key influencing factor that decided whether there was gravel in the scour was the slope ratio of the slope.

Data Availability

No data were used to support this study.

Conflicts of Interest

The authors declare no conflict of interest.

Acknowledgments

This research was funded by the National Natural Science Foundation of China, grant number 41702337.

References

- [1] J. De Vente and J. Poesen, "Predicting soil erosion and sediment yield at the basin scale: scale issues and semi-quantitative models," *Earth-Science Reviews*, vol. 71, no. 1-2, pp. 95-125, 2005.
- [2] S. Zhang, W. Qiao, Y. Wu, Z. Fan, and L. Zhang, "Experimental study on seepage characteristics of microfracture with different aperture," *Scientific Reports*, vol. 10, no. 1, p. 5452, 2020.
- [3] R. B. Bryan and D. L. Rockwell, "Water table control on rill initiation and implications for erosional response," *Geomorphology*, vol. 23, no. 2-4, pp. 151-169, 1998.
- [4] G. A. Mancilla, S. Chen, and D. K. McCool, "Rill density prediction and flow velocity distributions on agricultural areas in the Pacific northwest," *Soil & Tillage Research*, vol. 84, no. 1, pp. 54-66, 2005.
- [5] H. O. Shen, F.-l. Zheng, L. Wang, and L. L. Wen, "Effects of rainfall intensity and topography on rill development and rill characteristics on loessial hillslopes in China," *Journal of Mountain Science*, vol. 16, no. 10, pp. 2299-2307, 2019.
- [6] L. Zhao, R. Hou, F. Wu, and S. Keesstra, "Effect of soil surface roughness on infiltration water, ponding and runoff on tilled soils under rainfall simulation experiments," *Soil & Tillage Research*, vol. 179, no. 1, pp. 47-53, 2018.
- [7] J. An, F. Zheng, J. Lu, and G. Li, "Investigating the role of rain-drop impact on hydrodynamic mechanism of soil erosion under simulated rainfall conditions," *Soil Science*, vol. 177, no. 8, pp. 517-526, 2012.
- [8] D. Torri, M. Sfalanga, and G. Chisci, "Threshold conditions for incipient rilling," *Catena*, vol. 8, pp. 97-105, 1987.
- [9] G. Govers, "Relationship between discharge, velocity and flow area for rills eroding loose, nonlayered materials," *Earth Surface Processes and Landforms*, vol. 17, no. 5, pp. 515-528, 1992.
- [10] M. A. Nearing, L. D. Norton, D. A. Bulgakov, G. A. Larionov, L. T. West, and K. M. Dontsova, "Hydraulics and erosion in eroding rills," *Water Resources Research*, vol. 33, no. 4, pp. 865-876, 1997.
- [11] H. R. Liang, X. X. Yu, D. X. Fan, J. M. Sun, and Y. Chang, "Influence of gravel cover on sediment yield on slope surface," *Science of Soil and Water Conservation*, vol. 28, pp. 57-61, 2014.
- [12] H. Wang, D. B. Lu, D. J. Huang, and C. J. Shan, "On the erosion characteristics of red soil slope with different gravel existence forms," *Science of Soil and Water Conservation*, vol. 17, no. 4, pp. 49-58, 2019.
- [13] F. S. Jiang, Y.-h. Huang, M. K. Wang, J. S. Lin, G. Zhao, and H. L. Ge, "Effects of rainfall intensity and slope gradient on steep colluvial deposit erosion in southeast China," *Soil Science Society of America Journal*, vol. 78, no. 5, pp. 1741-1752, 2014.
- [14] F. S. Jiang, Z. Zhan, J. Chen et al., "Rill erosion processes on a steep colluvial deposit slope under heavy rainfall in flume experiments with artificial rain," *Catena*, vol. 169, pp. 46-58, 2018.
- [15] X. N. Liu, D. Fan, X. Yu, Z. Liu, and J. Sun, "Effects of simulated gravel on hydraulic characteristics of overland flow under varying flow discharges, slope gradients and gravel coverage degrees," *Scientific Reports*, vol. 9, no. 1, article 19781, 2019.
- [16] C. Qin, F. Zheng, X. Xu, H. Wu, and H. Shen, "A laboratory study on rill network development and morphological characteristics on loessial hillslope," *Journal of Soils and Sediments*, vol. 18, no. 4, pp. 1679-1690, 2018.
- [17] H. Rahardjo, T. Lee, E. Leong, and R. B. Rezaur, "Response of a residual soil slope to rainfall," *Canadian Geotechnical Journal*, vol. 42, no. 2, pp. 340-351, 2005.
- [18] P. Tahmasebi and S. Kamrava, "A pore-scale mathematical modeling of fluid-particle interactions: thermo- hydro-mechanical coupling," *International Journal of Greenhouse Gas Control*, vol. 83, pp. 245-255, 2019.
- [19] D. F. Cen, D. Huang, and F. Ren, "Shear deformation and strength of the interphase between the soil-rock mixture and the benched bedrock slope surface," *Acta Geotechnica*, vol. 12, no. 2, pp. 391-413, 2017.
- [20] K. Huang, Z. J. Dai, F. Yu, J. W. Wang, and X. X. Shan, "In situ strength characteristics of clay gravel layer in Anqing formation considering water environment and external load," *Rock and Soil Mechanics*, vol. 2, pp. 1-9, 2020.
- [21] E. Medley, "Orderly characterization of chaotic Franciscan Melanges," *Engineering Geology*, vol. 19, no. 4, pp. 20-33, 2001.
- [22] B. B. Mandelbrot, *The Fractal Geometry of Nature New Work*, WH freeman, New York, 1983.
- [23] Y. Wang and X. Li, "Study of mesoscopic fractal feature and mechanical properties for rock and soil aggregates samples," *Journal of Rock Mechanics and Engineering*, vol. 34, pp. 3397-3407, 2015.
- [24] K. T. Fang and C. X. Ma, *Orthogonal and Uniform Test Design*, Science Press, Beijing, China, 2001.
- [25] Z. Zhou, H. Yang, X. Wang, and B. Liu, "Model development and experimental verification for permeability coefficient of soil-rock mixture," *International Journal of Geomechanics*, vol. 17, no. 4, pp. 1-10, 2017.
- [26] F. S. Jiang, P. J. Chen, Y. H. Huang et al., "Experimental study on erosion hydrodynamic characteristics of concentrated flow on soil-rock mixed colluvial deposit slope," *Science of Soil and Water Conservation*, vol. 31, pp. 8-14, 2017.
- [27] X. Wang, W. K. Ni, H. S. Liu, P. Wu, and Z. Yuan, "Simulation experiment on loess slope rainfall erosion mechanism," *Chinese Journal of Geological Hazards and Prevention*, vol. 26, pp. 41-45, 2015.

Research Article

Model Test Study on Dynamic Response of Expressway Plastic-Reinforced Earth Embankment under Earthquake

Xue Han ¹, Pengyue Ji,² Qichen Gu,² and Guangsen Mu²

¹School of Civil & Architectural Engineering, Hunan University of Arts and Science, Changde 415000, China

²School of Architectural Engineering, Heilongjiang University of Science & Technology, Harbin 150022, China

Correspondence should be addressed to Xue Han; hanxue69@163.com

Received 10 January 2021; Revised 7 February 2021; Accepted 11 February 2021; Published 25 February 2021

Academic Editor: Yu Wang

Copyright © 2021 Han Xue et al. This is an open access article distributed under the Creative Commons Attribution License, which permits unrestricted use, distribution, and reproduction in any medium, provided the original work is properly cited.

Aiming at the seismic response of plastic geogrid-reinforced embankments, with Zhounan Expressway as the research engineering background, a self-designed seismic-rainfall coupled slope model test system was designed and used to produce 1 : 20 scale plastic geogrid-reinforced embankments. Moreover, the physical model of the unreinforced embankment under Hanshin wave, Wenchuan wave, Tianjin wave, etc. was also studied to carry out comparative analysis on seismic response and dynamic response on test model. The dynamic characteristics and dynamic response of the embankment model were tested from low to high seismic intensity; the changes of the embankment's natural frequency, damping ratio, acceleration at the measuring point, and dynamic earth pressure were analyzed; and the main influencing factors and damage to the embankment seismic response feature were discussed herein. The test results showed that the initial natural frequency of the reinforced embankment was 42.4% higher than that of the unreinforced embankment, and its initial damping ratio reduced by 19.4%. The attenuation effect of the natural frequency and damping ratio of the reinforced embankment with the loading history was significantly lower than that of the unreinforced embankment. Embankment reinforcement exhibited a very good inhibitory effect on the PGA amplification effect of the embankment, and the inhibitory effect on the interior of the slope was more significant than that on the slope. Moreover, the type of seismic wave, the amplitude of the seismic wave, and the frequency of the seismic wave significantly influenced the PGA amplification effect of the embankment. The peak dynamic soil pressure of the unreinforced embankment at the same location was significantly greater than that of the reinforced embankment. The two embankment models showed significantly different antivibration damage performance. After the peak acceleration of 2 m s^{-2} was loaded, no cracks were seen on the surface of the embankment model. When the peak acceleration of 3 m s^{-2} was loaded, on the slopes of the two embankment models, smaller cracks were observed in the middle and upper parts of the face. When the peak acceleration of 4 m s^{-2} was loaded, the failure of the unreinforced embankment model was obvious. Large cracks on the top of the slope could reach 16 mm in width, and 27 mm settlement appeared at the top, and the slope was convex. The reinforced embankment model was only on the slope shoulder. Moreover, there were fine cracks on the top, and the slope top settlement was less than 5 mm. The research results provide theoretical support for preventing and controlling the road embankment vibration diseases and improving highway durability design.

1. Introduction

China is located between the Pacific Rim seismic belt and the Himalayan-Mediterranean seismic belt. Since the 20th century, strong earthquakes have occurred in China and the frequency of earthquakes has been increasing year by year [1]. There are frequent reports on structural damage to highway subgrades during previous earthquakes. Moreover, subgrade subsidence, cracking, distortion, and slippage occur fre-

quently. The dynamic response characteristics of subgrades under earthquakes have an important impact on highway safety and durability.

Reinforced embankments have gradually been widely used in engineering practice. Reinforcement can limit the lateral deformation of the embankment to a certain extent, disperse the additional load and settlement of the embankment, inhibit the transmission of seismic loads, and finally improve the seismic resistance of expressways to varying degrees [2–

4]. Extensive research attention has been paid to the investigation of the dynamic response and seismic performance of reinforced soil slopes. Although there are few researches directly highlighting the dynamic problems of reinforced embankment slopes, numerous research reports are available on the study of reinforced slopes and retaining walls under earthquake action. For instance, Jianzhou et al. [5] used PLAXIS software numerical calculation method to study the dynamic characteristics of double-sided reinforced embankments under earthquake action and analyzed the maximum stress distribution of each layer of the embankment and the settlement form of the embankment. Lesniewska [6] used RES analysis software and the rigid-plastic theory of reinforced soil to analyze the differential boundary value of the bearing capacity of reinforced and unreinforced soil embankment slopes. Halder et al. [7] combined the lower bound finite element limit analysis method, anisotropic random field modeling method, and Monte Carlo simulation analysis to calculate the bearing capacity of the cohesive soil-reinforced embankment slope. Nouri et al. [8] used the limit equilibrium horizontal slice method to evaluate the pseudostatic acceleration and amplification effect of reinforced soil slopes and retaining walls. Furthermore, Lin et al. [9] compared the ground motion response of an unreinforced slope with that of a reinforced slope and found that the vertical acceleration magnification rate of the reinforced embankment slope was much smaller than that of the unreinforced embankment slope. Lihua et al. [10] conducted shaking table model experiments to study the dynamic response performance of unreinforced slope, waste tire strings and three-way geogrid composite reinforced slope, and tire strings and tire fragment composite-reinforced embankment slopes under earthquake action. The acceleration responses of the embankment slope model along the slope height distribution law under different seismic waves, acceleration peaks, and reinforcement methods were discussed. Hongwei et al. [11] carried out shaking table model tests for investigating the seismic performance of geobag-reinforced soil retaining walls under earthquake action. Lu [12] conducted a shaking table test on composite Gabion geogrid-reinforced soil retaining wall model with different similarity ratios, describing the macroscopic phenomenon of the test model under earthquake action, and they further studied the model retaining wall under earthquake action. Using the dynamic response, they tested the acceleration response and magnification of the backfill and tested the frequency spectrum characteristics at different heights of the model, the horizontal displacement of the wall, and the vertical settlement of the fill and finally compared and analyzed the parameters given in the design code. Jiang et al. [13] developed a combined panel reinforced soil retaining wall and conducted on-site filling tests and indoor shaking table model tests. Srilatha et al. [14] studied the influence of the fundamental vibration frequency on the dynamic response of unreinforced and reinforced soil slopes through shaking table tests and found that the acceleration and displacement responses of slopes with different reinforcement numbers and positions did not increase with frequency and linear growth. Bahadori et al. [15] conducted a shaking table test

study on the liquefaction problem of the liquefiable soil layer reinforced with geogrid and geocomposite and found that the antiliquefaction settlement performance of geocomposite reinforcement was significantly better than that of geogrid reinforcement. Panah et al. [16] conducted a series of 1 g shaking table tests on the 80 cm high reinforced soil retaining wall model and studied the effect of the length, distribution, and shape (sawtooth and parallel) of the steel bar on the failure mode of the retaining wall. Furthermore, displacement and acceleration magnification factor has also been studied. Wartman et al. [17] analyzed the mechanism of permanent displacement of the slope under the action of seismic load and commented on the Newmark slider displacement calculation method. Koseki et al. [18] analyzed the seismic performance and potential failure mechanism of reinforced earth retaining walls. Edinçliler et al. [19] used the shaking table test method to study the seismic performance of slag as a filler for reinforced soil retaining walls.

Plastic reinforced soil embankments are widely used in engineering practice. Although scientific and technological researchers have carried out certain research work on the seismic effects of reinforced soil slopes, the seismic effects of plastic geogrid-reinforced embankments have rarely been investigated [20–25]. The current seismic design of highways nor does the code evaluate the seismic performance of plastic-reinforced embankments. In-depth study of the dynamic response of plastic-reinforced embankment under earthquake action and its failure characteristics was used to qualitatively and quantitatively analyze the seismic performance and reinforcement effect of plastic-reinforced embankment. This study provides important theories and engineering design/guidelines for preventing and treating earthquake-induced damage and destruction of embankment.

2. Model Test Design

2.1. Model Test System. In this study, a self-designed and customized seismic action slope model test system (see Figure 1), including hydraulic servo power loading system, shaking table, model box, control system, data acquisition, and analysis and processing system, was adopted to perform the tests. The dimension of the slope model box was $2\text{ m} \times 1.5\text{ m} \times 1.8\text{ m}$, which can be used for various earthquake-induced slope scale model tests.

2.2. Engineering Background. The embankment model test considered the No. 8 section of Zhounan Expressway as the research engineering background, and the pile number section was K18+000–K42+600 and K42+600–K54+100. The upper part of the strata is dominated by Quaternary Holocene alluvial silt clay and silt soil, with some interbedded sand layers, and the upper part of the silty clay is soft plastic-plastic; and the lower part is an interbedded silty clay and silt soil. The sand layer is plastic-hard plastic. The earthquake fortification intensity is 7°. This is a section with a large embankment filling height, the maximum filling height of 10 m, the soil cohesion of the foundation bearing layer $c = 19.82\text{ kPa}$, the internal friction angle $\varphi = 27^\circ$, the natural

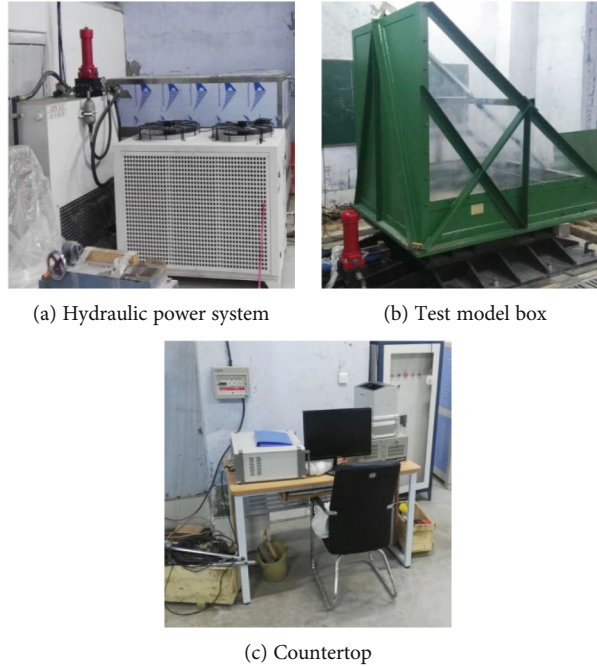


FIGURE 1: Earthquake physical model test system for slope.

density of 2074 kg m^{-3} , and the embankment earth pressure. The actual control dry density is 1790 kg m^{-3} , the cohesion force $c = 11.31 \text{ KPa}$, and the internal friction angle $\varphi = 24^\circ$.

2.3. Design and Production of Test Model. The embankment model design and the layout of the main measuring points are shown in Figure 2. Two types of embankment models were constructed: one was a filled embankment without reinforcement measures, and the other was a plastic-reinforced embankment. Owing to the symmetry of the cross section of the embankment, the two embankment models were designed in half width, and the geometric similarity ratio Cl was designed to be 20. Therefore, the total height of the prototype embankment after being scaled down was 800 mm, the cross-sectional direction of the foundation was 2000 mm, the thickness range was designed to be 300 mm, the height of the filled embankment was 500 mm, and the top cross-sectional dimension was 675 mm. The size of the foundation and the embankment along the road was 1500 mm according to the model box size. The slope angle of the embankment was the same as that of the prototype; using a broken line grading, the upper part was grading 1:1.5; and the lower part was grading 1:1.75. The ingredients and filling methods of the two embankment models were completely the same. The plastic reinforcement laying method of the reinforced embankment was horizontal through long bars, and the vertical spacing was 100 mm.

The model similarity design takes the embankment geometry size and packing density as the basic control quantities and determines the similarity relationship of other physical parameters of the embankment according to the Buckingham theorem to calculate the similarity law of the embankment model. The physical model test similarity design is presented in Table 1.

After the embankment model was designed, the soil was sieved to remove oversized, layered, and compacted particles. The foundation soil was evenly filled and compacted in six layers, the filled embankment was evenly filled and compacted in five layers, and the plastic geogrid was spread between each layer of the reinforced embankment model. Each layer of soil was compacted to control the dry density of 1790 kg m^{-3} . Corresponding sensors were embedded in the model making project based on the designed measuring points. The completed embankment model entities are shown in Figure 3.

3. Seismic Wave Selection and Test Loading System

Three typical seismic wave types, namely, Hanshin wave (code-named KOB) Figure 4, Wenchuan wave (code-named WC) Figure 5, and Tianjin wave (code-named TJ) Figure 6, were used for test loading. The peak acceleration of various waves was controlled to be at 0.5, 1, 2, 3, and 4 m s^{-2} five-level loading, and various waves were processed with four types of time compression ratios. The peak acceleration of white noise (code named WTN) was controlled to be at 0.3 m s^{-2} , as shown in Figure 7, to measure the initial dynamic characteristics of the model and its changes during the loading process. The loading of various seismic waves was carried out interspersed by magnitude, and the specific loading system is presented in Table 2.

4. Test Results and Analysis

Comparative analysis of the dynamic characteristics was carried out. Dynamic response and influencing factors of reinforced and unreinforced embankment models were studied,

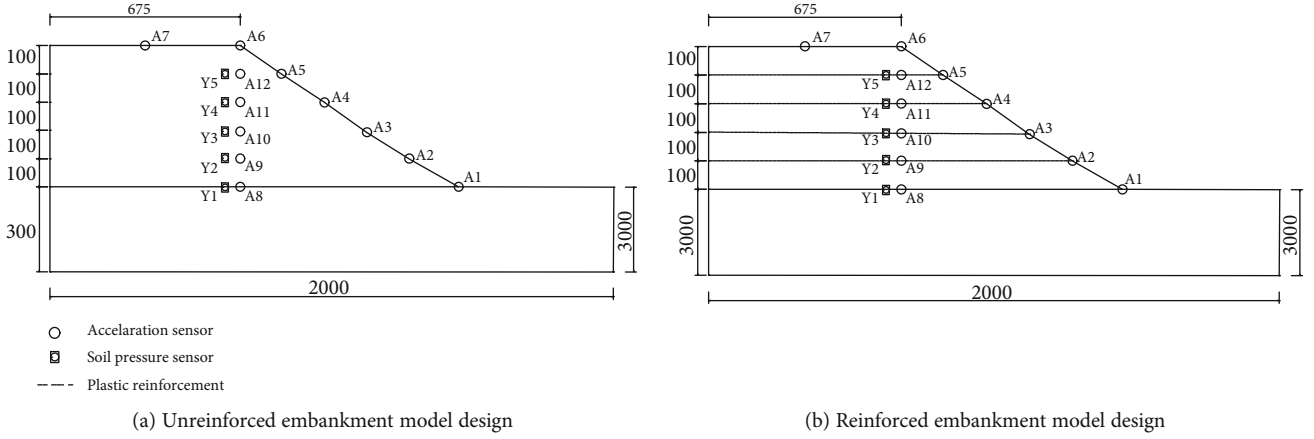
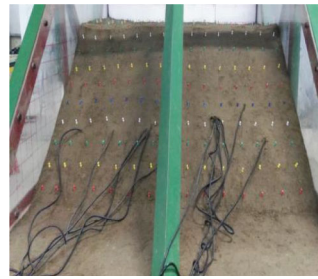


FIGURE 2: Embankment model and the layout of measuring points.

TABLE 1: Embankment physical model test similarity ratio summary.

Physical and mechanical parameters	Law of similarity	Similarity ratio (simplified)	Remarks
Geometric size l	C_l	C_l	Control amount
Acceleration a	$C_a = 1$	1	Utilization of prototype materials
Packing density ρ	C_ρ	1	Utilization of prototype materials
Internal friction angle φ	$C_\varphi = 1$	1	Utilization of prototype materials
Cohesion c	$C_c = C_\rho C_l$	C_l	—
Dimensionless coefficient K	C_K	1	Utilization of prototype materials
Stress σ	$C_\sigma = C_\rho C_l$	C_l	—
Strain ε	$C_\varepsilon = C_K^{-1} C_\rho^{1/2} C_l^{1/2}$	$C_l^{1/2}$	—
Displacement u	$C_u = C_K^{-1} C_\rho^{1/2} C_l^{3/2}$	$C_l^{3/2}$	Introduced in postprocessing similarity ratio
Speed v	$C_v = C_K^{-1/2} C_\rho^{1/4} C_l^{3/4}$	$C_l^{3/4}$	Introduced in postprocessing similarity ratio
Time t	$C_t = C_K^{-1/2} C_\rho^{1/4} C_l^{3/4}$	$C_l^{3/4}$	Scaling by time similarity



(a) Unreinforced embankment model



(b) Reinforced embankment model

FIGURE 3: Physical embankment model.

and the failure characteristics of the two embankment models were investigated.

4.1. Dynamic Characteristics of Embankment Model. The natural frequency and damping ratio are the main dynamic characteristic parameters of the embankment model. Before seismic waves were loaded in each working condition, the

embankment model was tested with white noise with an amplitude of 0.3 m s^{-2} , and the white noise transfer function of each measurement point was identified. Moreover, the average value of the identified natural frequency and damping ratio was taken as the characteristic natural frequency and damping ratio of the embankment model. The curves highlighting the variation in the natural frequency and

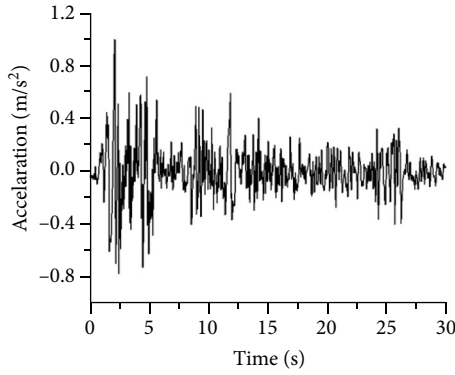


FIGURE 4: KOB wave acceleration time history curve.

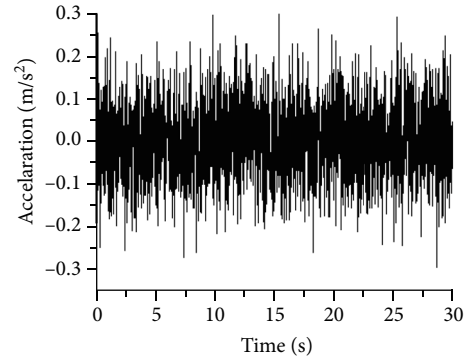


FIGURE 7: White noise acceleration time history.

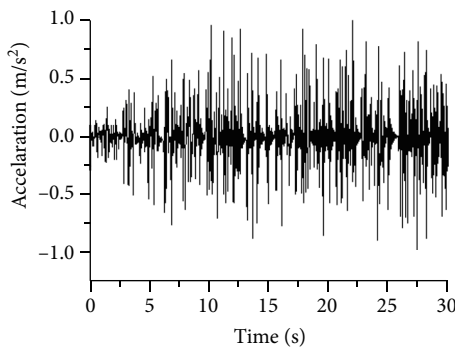


FIGURE 5: WC wave acceleration time history curve.

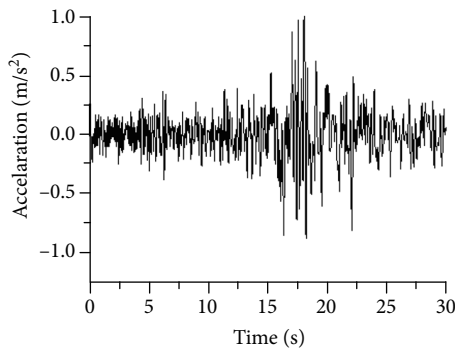


FIGURE 6: Wave acceleration time history curve.

damping ratio of the two embankment models with the loading history are shown in Figure 8.

Figure 8(a) demonstrates that the natural frequencies of the two embankment models gradually decrease with the loading process. The initial natural frequency of the unreinforced embankment is 12.63 Hz, until the seismic wave test conditions are loaded, and then its natural frequency is reduced to 9.23 Hz, corresponding to a drop of 26.9%. When the initial natural frequency of the reinforced embankment is 17.98 Hz, the load is completed. The frequency is reduced to 13.74 Hz, corresponding to a drop of 23.6%. Figure 8(b) illustrates that the damping ratio of the two embankment models gradually increases with the loading history. The initial

damping ratio of the unreinforced embankment was 0.098, and the damping ratio increased to 0.146; an increase of 49.4% after the seismic wave test conditions was loaded. The initial damping ratio of the reinforced embankment was 0.079, and the damping ratio increased to 0.106 after the loading was completed. This corresponded to an increase of 37.3%. The test data showed that reinforcement could effectively improve the dynamic characteristics of the embankment. The initial natural frequency of the reinforced embankment was 42.4% higher than that of the unreinforced embankment, and its initial damping was reduced by 19.4% compared to the unreinforced embankment. After the multi-condition loading process, the natural frequency decreased and the increase of damping ratio of the reinforced embankment model was smaller than those of the unreinforced embankment. Moreover, the dynamic damage resistance of the reinforced embankment was significantly better than that of the unreinforced embankment.

4.2. *Dynamic Response of Embankment Model.* The PGA amplification effect and dynamic earth pressure of the measuring points under different loading conditions were used as the main observation indexes of the dynamic response, and the analysis is presented in the subsequent sections.

4.2.1. *Analysis of PGA Amplification Effect at Measuring Point.* The PGA amplification factor of the measuring point was calculated according to the peak acceleration data of the measuring point in each working condition, that is, the ratio of the peak acceleration of each measuring point to the measured peak acceleration of the table. After comparing the data of multiple working conditions, the PGA amplification coefficients of the three seismic wave action measuring points exhibited similar characteristics. Herein, the KOB-18 and KOB-5 working conditions were used for analysis. The PGA amplification coefficients of the two embankment model measuring points were along the height. The change rule is shown in Figures 9 and 10.

The figure shows that from bottom to top along the height of the embankment, the PGA amplification coefficients of the slope measurement points of the two embankment models show an overall increasing trend, with the maximum value appearing at the top of the slope. The PGA amplification coefficients of the reinforced embankment at

TABLE 2: Embankment physical model test loading system.

Test number	Case code	Peak acceleration (m s^{-2})	Time compression ratio	Test number	Case code	White noise peak (m s^{-2})
				1	WTN-1	0.3
2	KOB-1	0.5	9.457	3	WTN-2	0.3
4	WC-1	0.5	9.457	5	WTN-3	0.3
6	TJ-1	0.5	9.457	7	WTN-4	0.3
8	KOB-2	0.5	4.472	9	WTN-5	0.3
10	WC-2	0.5	4.472	11	WTN-6	0.3
12	TJ-2	0.5	4.472	13	WTN-7	0.3
14	KOB-3	0.5	2.115	15	WTN-8	0.3
16	WC-3	0.5	2.115	17	WTN-9	0.3
18	TJ-3	0.5	2.115	19	WTN-10	0.3
20	KOB-4	0.5	1	21	WTN-11	0.3
22	WC-4	0.5	1	23	WTN-12	0.3
24	TJ-4	0.5	1	25	WTN-13	0.3
26	KOB-5	1	9.457	27	WTN-14	0.3
28	WC-5	1	9.457	29	WTN-15	0.3
30	TJ-5	1	9.457	31	WTN-16	0.3
32	KOB-6	1	4.472	33	WTN-17	0.3
34	WC-6	1	4.472	35	WTN-18	0.3
36	TJ-6	1	4.472	37	WTN-19	0.3
38	KOB-7	1	2.115	39	WTN-20	0.3
40	WC-7	1	2.115	41	WTN-21	0.3
42	TJ-7	1	2.115	43	WTN-22	0.3
44	KOB-8	1	1	45	WTN-23	0.3
46	WC-8	1	1	47	WTN-24	0.3
48	TJ-8	1	1	49	WTN-25	0.3
50	KOB-9	2	9.457	51	WTN-26	0.3
52	WC-9	2	9.457	53	WTN-27	0.3
54	TJ-9	2	9.457	55	WTN-28	0.3
56	KOB-10	2	4.472	57	WTN-29	0.3
58	WC-10	2	4.472	59	WTN-30	0.3
60	TJ-10	2	4.472	61	WTN-31	0.3
62	KOB-11	2	2.115	63	WTN-32	0.3
64	WC-11	2	2.115	65	WTN-33	0.3
66	TJ-11	2	2.115	67	WTN-34	0.3
68	KOB-12	2	1	69	WTN-35	0.3
70	WC-12	2	1	71	WTN-36	0.3
72	TJ-12	2	1	73	WTN-37	0.3
74	KOB-13	3	9.457	75	WTN-38	0.3
76	WC-13	3	9.457	77	WTN-39	0.3
78	TJ-13	3	9.457	79	WTN-40	0.3
80	KOB-14	3	4.472	81	WTN-41	0.3
82	WC-14	3	4.472	83	WTN-42	0.3
84	TJ-14	3	4.472	85	WTN-43	0.3
86	KOB-15	3	2.115	87	WTN-44	0.3
88	WC-15	3	2.115	89	WTN-45	0.3
90	TJ-15	3	2.115	91	WTN-46	0.3
92	KOB-16	3	1	93	WTN-47	0.3
94	WC-16	3	1	95	WTN-48	0.3

TABLE 2: Continued.

Test number	Case code	Peak acceleration ($m\ s^{-2}$)	Time compression ratio	Test number	Case code	White noise peak ($m\ s^{-2}$)
96	TJ-16	3	1	97	WTN-49	0.3
98	KOB-17	4	9.457	99	WTN-50	0.3
100	WC-17	4	9.457	101	WTN-51	0.3
102	TJ-17	4	9.457	103	WTN-52	0.3
104	KOB-18	4	4.472	105	WTN-53	0.3
106	WC-18	4	4.472	107	WTN-54	0.3
108	TJ-18	4	4.472	109	WTN-55	0.3
110	KOB-19	4	2.115	111	WTN-56	0.3
112	WC-19	4	2.115	113	WTN-57	0.3
114	TJ-19	4	2.115	115	WTN-58	0.3
116	KOB-20	4	1	117	WTN-59	0.3
118	WC-20	4	1	119	WTN-60	0.3
120	TJ-20	4	1	121	WTN-61	0.3

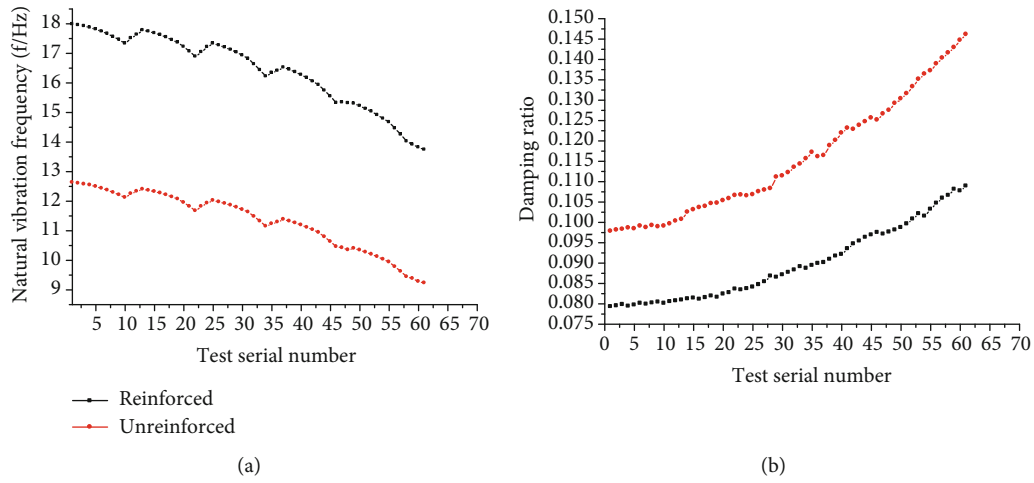


FIGURE 8: Variation curves of natural frequency and damping ratio with loading history. (a) Variation curve of natural frequency of embankment model with loading history (b) Variation curve of embankment model damping ratio with loading history.

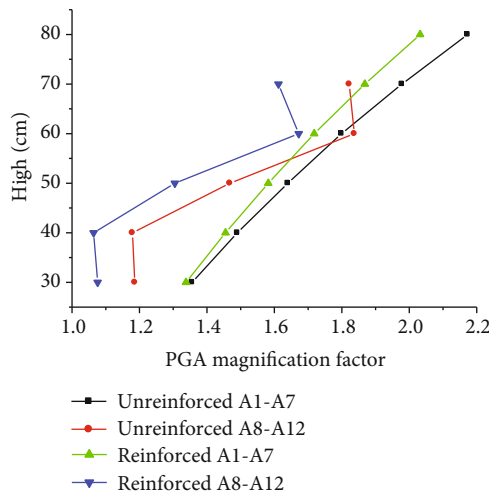


FIGURE 9: Comparison curve of PGA amplification factor under KOB-18 working condition.

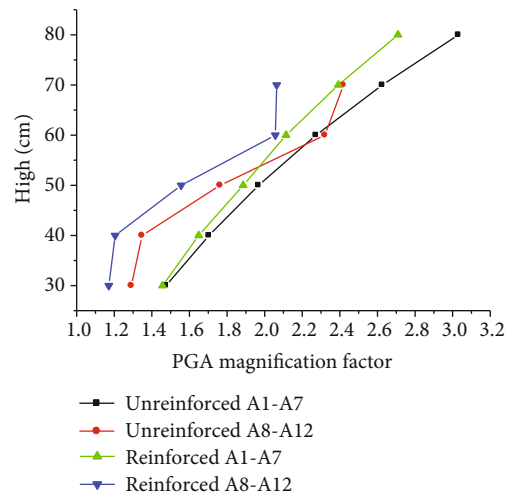


FIGURE 10: Comparison curve of PGA amplification factor under KOB-5 working condition.

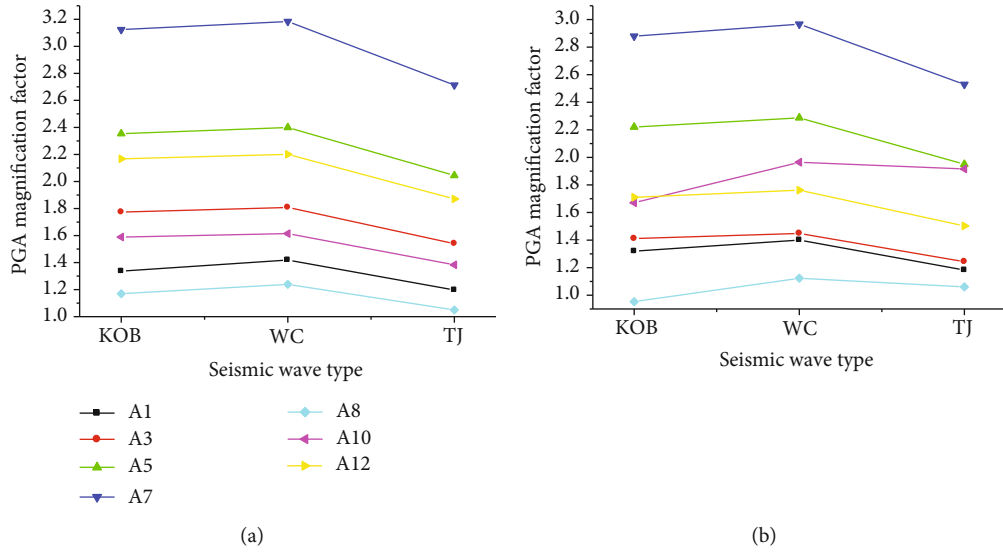


FIGURE 11: PGA amplification coefficients of measurement points on embankments under different types of seismic waves. (a) PGA amplification coefficients of measurement points on unreinforced embankments (b) PGA magnification coefficients of measurement points on reinforced embankments.

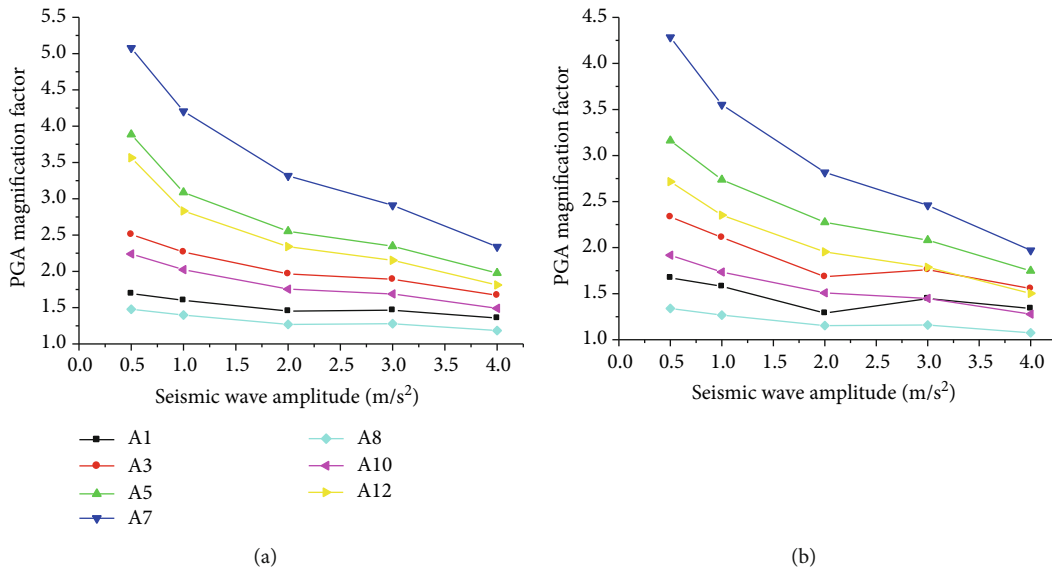


FIGURE 12: Changes in PGA amplification coefficient of measurement points on embankment with amplitude. (a) PGA amplification coefficient of measurement points on unreinforced embankment. (b) PGA amplification coefficient of measurement points on reinforced embankment.

the same height are less than those of the unreinforced embankment. The analysis of two types of embankment model slope body measuring points PGA amplification factor indicates that the lower and upper quarter height range of the slope body shows a small increase. The upper part even shows a decrease in a certain height range, and the middle part exhibits the fastest increase. Moreover, no increase is observed at the same height of the reinforced embankment. The PGA amplification factor of the A11 measurement point in the slope was greater than that of the slope A4; however, the reinforced embankment did not exhibit this phenomenon, indicating that the reinforcement exerted an inhibitory

effect on the PGA amplification effect of the embankment, in particular, the internal slope.

Based on the test data, the influences of seismic wave type, seismic wave amplitude, and seismic wave frequency on the PGA amplification factor are discussed below.

(1) *Influence of Seismic Wave Type.* In order to discuss the impact of seismic wave types on the acceleration response of the two embankment models, the KOB-10, WC-10, and TJ-10 working conditions were selected for analysis. The amplitude for all the three seismic waves was 2 m s^{-2} , and the time compression ratio was 4.472. Figure 11, respectively,

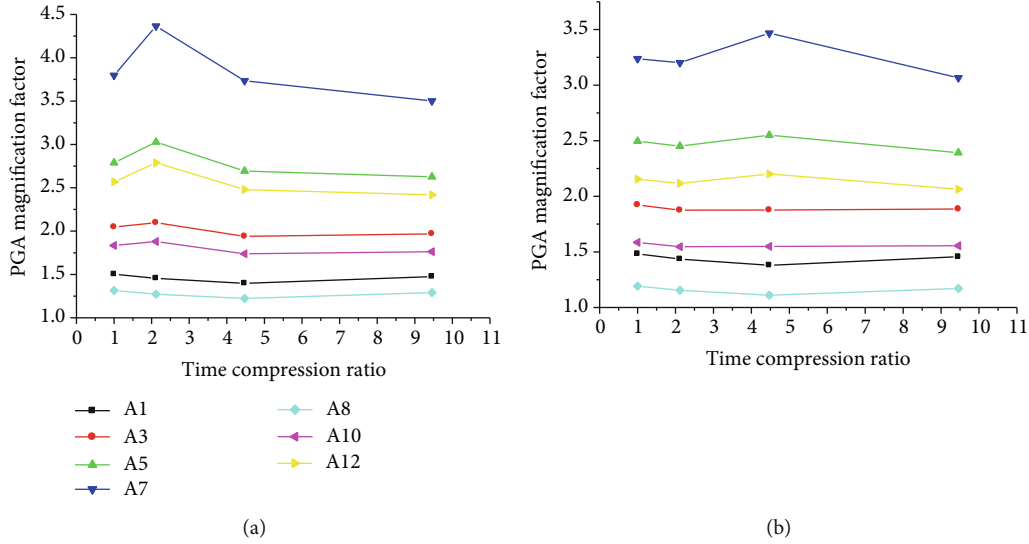


FIGURE 13: Variation curves of PGA amplification coefficients of measurement points on embankment with frequency. (a) Curve of PGA amplification coefficient at measuring point of unreinforced embankment (b) Curve of PGA amplification coefficient at measuring point of reinforced embankment.

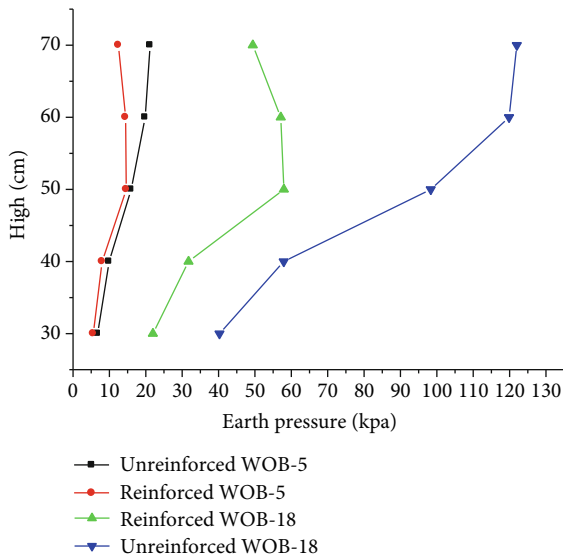


FIGURE 14: Peak earth pressure distribution of the two sets of embankment models.

shows the same amplitude and time compression ratio, the PGA amplification coefficients of two embankment slopes A1, A3, A5, A7 and A8, A10, and A12 on the slope of the slope.

The figure illustrates that at the same amplitude and time compression ratio, the PGA amplification factor of the embankment measurement point under the action of the WC wave is the largest, followed by that of the KOB wave, and that of the TJ wave is the smallest. Moreover, PGA amplification effects of other points exhibit the same rule as the given measuring points. It shows that when the types of seismic waves are different, the PGA amplification coefficients of the measurement points at the same location of

the embankment are also different. Furthermore, the PGA amplification factor of reinforced embankments is significantly lower than that of unreinforced embankments.

(2) *Influence of Seismic Wave Amplitude.* In order to discuss the impact of seismic wave amplitude on the acceleration response of the two embankment models, the Wenchuan waves WC-4, WC-8, WC-12, WC-16, and WC-20 with different amplitude operating conditions were selected for analysis. Moreover, the above-mentioned operating conditions show the same time compression ratio and seismic wave type; however, the acting amplitude is $0.5, 1, 2, 3,$ and 4 m s^{-2} , respectively. Figure 12 shows the PGA amplification coefficients of the two embankment models and the variation curves of seismic wave amplitude.

The figure shows that the PGA amplification coefficients of the two embankment model measuring points generally decrease with the increase of the seismic wave amplitude, and the PGA amplification coefficient of the slope top A7 measuring point shows the largest change. The two embankment seismic wave amplitudes are 0.5 m s^{-2} , and the PGA amplification factor of the A7 measuring point can reach 2.2 times that of the amplitude 4 m s^{-2} . The influence of KOB seismic wave and TJ seismic wave amplitude on PGA amplification coefficient is similar to that of WC seismic wave.

(3) *Seismic Wave Frequency.* In order to discuss the influence of seismic wave frequency on the acceleration response of the two embankment models, the Hanshin waves KOB-5, KOB-6, KOB-7, and KOB-8 were selected for the analysis of different frequency conditions, and the seismic wave amplitude of this condition was 1 m s^{-2} . The time compression ratios are $1, 20^{1/4}, 20^{1/2},$ and $20^{3/4}$, respectively. Figure 13, respectively, shows the PGA amplification coefficient of the two embankment measurement points versus frequency.

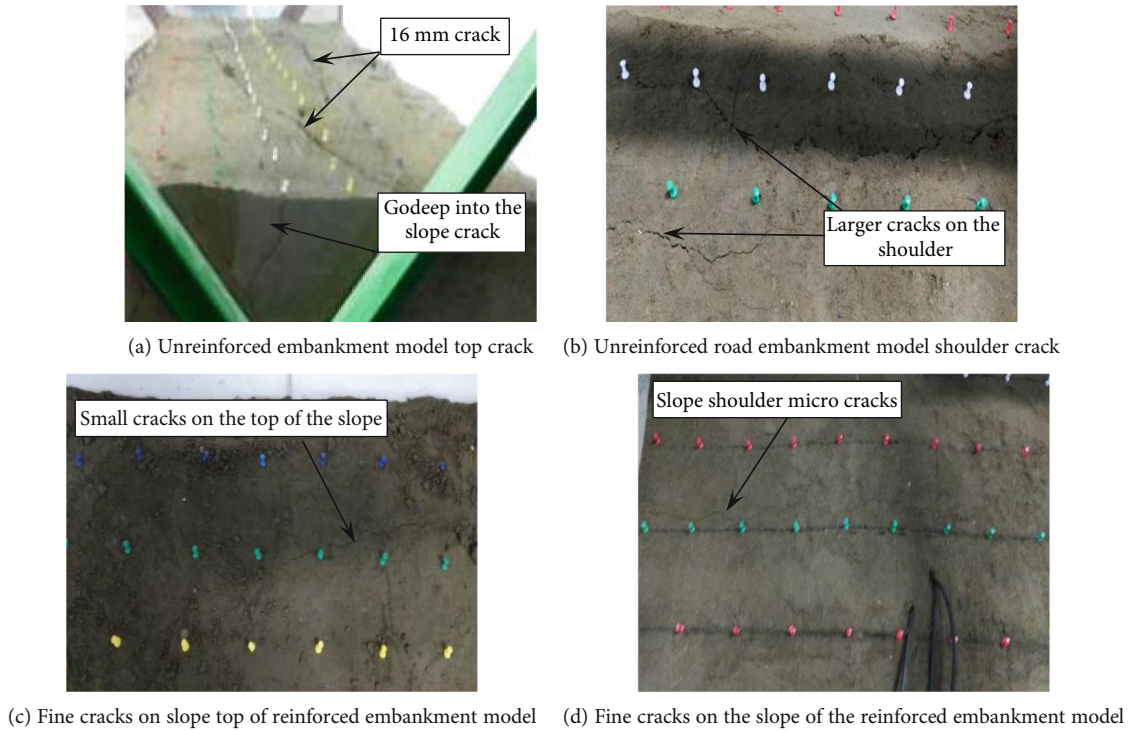


FIGURE 15: The damage and destruction patterns of the two embankment models.

The figure shows that the PGA amplification factor of the unreinforced embankment at the same input seismic wave frequency is greater than that of the reinforced embankment. Moreover, the PGA amplification factor of the two embankment measurement points changes with the input seismic wave frequency. The maximum value of the PGA amplification factor is on the upper part of the slope. For the measurement points, the maximum value of the PGA amplification factor of the measurement point of the unreinforced embankment appears in the range of the smaller time compression ratio, while the maximum value of the reinforced embankment is in the medium time compression ratio range. The influence of WC seismic wave and TJ seismic wave frequency on PGA amplification coefficient is similar to that of KOB seismic wave. It indicates that the resonance frequency of reinforced embankments is significantly higher than that of unreinforced embankments, and the frequency range of natural seismic action is closer to the natural frequency of unreinforced embankments. Therefore, reinforced embankments can effectively improve the seismic behavior of embankments.

4.2.2. Analysis of Measuring Point Dynamic Earth Pressure.

The dynamic earth pressure in the embankment under the action of earthquake is the main controlling factor to the damage and destruction of the embankment. In order to discuss the change law of the dynamic earth pressure along the height of the two embankment models, the KOB-5 and KOB-18 loading conditions were selected for analysis. The distribution curves of the peak dynamic earth pressure at the measuring point are shown in Figure 14.

The figure exhibits that the peak dynamic soil pressure at the measurement point of the unreinforced embankment at the same height is significantly greater than that of the reinforced embankment. For the KOB-5 and KOB-18 working conditions, the peak dynamic soil pressure at the Y5 measurement point of the unreinforced embankment is 1.7 times that of the reinforced embankment, respectively, and then 2.5 times. Clearly, the reinforcement can effectively reduce the peak dynamic earth pressure in the embankment. Moreover, the graph and curve reveal that reinforcement measures can effectively adjust the peak dynamic earth pressure distribution in the embankment, greatly reduce the dynamic earth pressure in the upper part of the embankment, and significantly improve the dynamic stability of the embankment.

4.3. Failure Characteristics of Embankment Model. During the test, the dynamic characteristics and dynamic response parameters of the embankment were collected and analyzed. At the same time, the deformation and crack failure characteristics of the embankment were observed and measured in detail. After the peak acceleration loading of 2 m s^{-2} was completed, no cracks were observed in the two embankment models. After the completion of the peak acceleration loading of 3 m s^{-2} , fine cracks appeared on the upper and middle slopes of the two embankment models. When the peak acceleration of 4 m s^{-2} was loaded, the cracks in the unreinforced embankment model became wider. The cracks were mainly distributed in the middle, and the upper part of the embankment and the slope shoulder. The width of the larger cracks reached 16 mm, and some cracks could be seen deep into the third part of the slope. The top of the embankment model

subsided to 27 mm, and the slope was convex. After the reinforced embankment model was loaded, only two small cracks appeared on the shoulder and top of the slope, and the slope top settlement was less than 5 mm. The damage and destruction patterns of the two embankment models are shown in Figure 15.

5. Conclusions

Aiming at the seismic response of plastic geogrid-reinforced embankment, with Zhounan Expressway as the research engineering background, a comparative model test of plastic geogrid-reinforced embankment and unreinforced embankment was designed and further conducted, and the embankment model was tested in various earthquake scenarios. The dynamic characteristics and dynamic response under loading conditions were analyzed. The change laws of the embankment's natural frequency, damping ratio, acceleration at the measuring point, and dynamic soil pressure were analyzed, and the main influencing factors and damage characteristics of the embankment seismic response were discussed. Through the systematic analysis of the test data, the following conclusions can be obtained:

- (1) The dynamic characteristics such as the initial natural frequency and damping ratio of the plastic-reinforced embankment were found to be significantly better than those of the unreinforced embankment. The reinforcement led to the increase in the initial natural frequency of the embankment by 42.4%, and the initial damping ratio decreased by 19.4%. The reinforcement reduced the embankment natural frequency by 3.3% with the loading history, and the damping ratio decreased by 12.1% with the loading history
- (2) Plastic reinforcement exhibited a good suppression effect on the PGA amplification effect of the embankment; in particular, the suppression effect on the interior of the slope was more significant than that on the slope. The type, amplitude, and frequency of seismic waves exhibited an important influence on the PGA amplification effect of the embankment
- (3) Plastic reinforcement significantly reduced the peak dynamic earth pressure of the embankment at the same location. The analysis of representative working conditions and measurement point data indicated that the peak dynamic earth pressure could be reduced to 40% of the unreinforced embankment. Reinforcement could not only effectively reduce the peak dynamic earth pressure but also effectively adjust the peak dynamic earth pressure distribution in the embankment, greatly reduce the dynamic earth pressure in the upper part of the embankment, and significantly improve the dynamic stability of the embankment
- (4) Reinforcement could effectively improve the anti-vibration damage performance of the embankment.

After loading with a peak acceleration of 3 m s^{-2} , relatively small cracks appeared in the upper part of the slope of the two embankment models. However, when the peak acceleration of 4 m s^{-2} was loaded, the cracks of the unreinforced embankment model evolved into cracks, and the cracks were mainly distributed in the embankment. In the middle and upper part and the slope shoulder, the width of the larger cracks reached 16 mm, and some cracks penetrated one-third of the height of the slope, and there was serious settlement at the top. The maximum settlement at the top of the embankment model was 27 mm, and the slope was convex. However, the reinforced embankment model only showed two small cracks on the slope shoulder and top, and the slope top settlement was less than 5 mm. Reinforcement can significantly improve the strong earthquake resistance of the embankment

Data Availability

The data are available and explained in this article; readers can access the data supporting the conclusions of this study.

Disclosure

I would like to declare on behalf of my coauthors that the work described is original research and has not been previously published.

Conflicts of Interest

The authors declare no conflict of interest. The manuscript is approved by all authors for publication.

Acknowledgments

This work was supported by the National Key Research & Development plan of China (2016YFC0600901).

References

- [1] J. Zhu, *Geogrid Reinforcement of Soft Soil Subgrade Time Effect and Seismic Dynamic Response Analysis*, Dalian Maritime University, 2017.
- [2] L. Jinbei, *Study on Seismic Performance of Highway Subgrade*, Beijing Jiaotong University, 2013.
- [3] W. Jian, Y. Lingkan, and C. Qiang, "Research on failure mode of road embankment in Wenchuan great earthquake and deformation control of geogrid reinforcement," *Chinese Journal of Rock Mechanics and Engineering*, vol. 29, Supplement 1, pp. 3387–3394, 2010.
- [4] Q. Yelin, P. Guo, J. Wang, W. Lu, S. Shengbiao, and Y. Wang, "A review of the dynamic response characteristics of fiber reinforced soil," *Geotechnical Foundation*, vol. 30, no. 6, pp. 705–713, 2016.
- [5] C. Jianzhou, L. Huabei, and F. Cheng, "Seismic response analysis of back-to-back mechanically stabilized earth (MSE) walls," *Chinese Journal of Geotechnical Engineering*, vol. 41, no. 5, pp. 918–926, 2019.

- [6] D. Lesniewska, "RES — a numerical program for reinforced-soil slopes based on the rigid-plastic theoretical model," *Geotextiles and Geomembranes*, vol. 12, no. 5, pp. 435–439, 1993.
- [7] K. Halder, D. Chakraborty, and S. K. Dash, "Bearing capacity of a strip footing situated on soil slope using a non-associated flow rule in lower bound limit analysis," *International Journal of Geotechnical Engineering*, vol. 3, pp. 1–9, 2017.
- [8] H. Nouri, A. Fakher, and C. J. F. P. Jones, "Evaluating the effects of the magnitude and amplification of pseudo-static acceleration on reinforced soil slopes and walls using the limit equilibrium horizontal slices method," *Geotextiles and Geomembranes*, vol. 26, no. 3, pp. 263–278, 2008.
- [9] Y. L. Lin, W. M. Leng, G. L. Yang, L. Li, and J. S. Yang, "Seismic response of embankment slopes with different reinforcing measures in shaking table tests," *Natural Hazards*, vol. 76, no. 2, pp. 791–810, 2015.
- [10] L. Lihua, R. Zengle, L. Guangxin et al., "Shaking table model tests for composite reinforced slopes," *Journal of Southwest Jiaotong University*, vol. 52, no. 3, pp. 496–504, 2017.
- [11] H. Zhu, Y. Lingkan, C. Xiaolong, and X. Qin, "Seismic behaviors and design recommendations of ecological bag-reinforced retaining wall," *Chinese Journal of Geotechnical Engineering*, vol. 39, no. 2, pp. 319–326, 2017.
- [12] T. Lu, *Shaking Table Test Analysis of Dynamic Characteristics of Composite Gabion and Geogrid Reinforced Soil Retaining Wall*, Institute of Disaster Prevention, 2019.
- [13] J. Guanlu, P. Xu, and W. Zhimeng, "Study on reinforced soil retaining wall with composite panels by model test[J]," *Railway Engineering*, vol. 58, no. 1, pp. 118–120, 2018.
- [14] N. Srilatha, G. Madhavi Latha, and C. G. Puttappa, "Effect of frequency on seismic response of reinforced soil slopes in shaking table tests," *Geotextiles and Geomembranes*, vol. 36, pp. 27–32, 2013.
- [15] H. Bahadori, H. Motamedi, A. Hasheminezhad, and R. Motamed, "Shaking table tests on shallow foundations over geocomposite and geogrid-reinforced liquefiable soils," *Soil Dynamics and Earthquake Engineering*, vol. 128, p. 105896, 2020.
- [16] A. Komak Panah, M. Yazdi, and A. Ghalandarzadeh, "Shaking table tests on soil retaining walls reinforced by polymeric strips," *Geotextiles and Geomembranes*, vol. 43, no. 2, pp. 148–161, 2015.
- [17] J. Wartman, R. B. Seed, and J. D. Bray, "Shaking table modeling of seismically induced deformations in Slopes," *Journal of Geotechnical and Geoenvironmental Engineering*, vol. 131, no. 5, pp. 610–622, 2005.
- [18] J. Koseki, R. J. Bathurst, E. Guler, J. Kuwano, and M. Mauerger, "Seismic stability of reinforced soil walls," in *8th International Conference on Geosynthetics*, pp. 51–77, Yokohama, Japan, 2006.
- [19] A. Edinçliler, G. Baykal, and A. Saygili, *Seismic Behavior of Geogrid Reinforced Slagwall*, American Institute of Physics, 2008.
- [20] Z. Li, S. G. Liu, W. T. Ren, J. J. Fang, Q. H. Zhu, and Z. L. Dun, "Multiscale laboratory study and numerical analysis of water-weakening effect on shale," *Advances in Materials Science and Engineering*, vol. 2020, Article ID 5263431, 14 pages, 2020.
- [21] T. Zhigang, Z. Chun, W. Yong, W. Jiamin, H. Manchao, and Z. Bo, "Research on stability of an open-pit mine dump with fiber optic monitoring," *Geofluids*, vol. 2018, Article ID 9631706, 20 pages, 2018.
- [22] Y. Wang, B. Zhang, S. H. Gao, and C. H. Li, "Investigation on the effect of freeze-thaw on fracture mode classification in marble subjected to multi-level cyclic loads," *Theoretical and Applied Fracture Mechanics*, vol. 111, article 102847, 2021.
- [23] Z. G. Tao, C. Zhu, M. C. He, and M. Karakus, "A physical modeling-based study on the control mechanisms of Negative Poisson's ratio anchor cable on the stratified toppling deformation of anti-inclined slopes," *International Journal of Rock Mechanics and Mining Sciences*, vol. 138, article 104632, 2021.
- [24] C. Zhu, Z. Yan, Y. Lin, F. Xiong, and Z. Tao, "Design and application of a monitoring system for a deep railway foundation pit project," *IEEE Access*, vol. 7, pp. 107591–107601, 2019.
- [25] Q.-X. Meng, W.-Y. Xu, H.-L. Wang, X.-Y. Zhuang, W.-C. Xie, and T. Rabczuk, "DigiSim — an open source software package for heterogeneous material modeling based on digital image processing," *Advances in Engineering Software*, vol. 148, p. 102836, 2020.

Research Article

Experimental Investigation of Permeability Evolution on Sandstone in Triaxial and Long-Term Dissolution Experiment

Ji Shi , Jianhua Zhang , Chunyang Zhang , Tingting Jiang , and Gang Huang 

Mining engineering, Wuhan University of Technology, 430070, China

Correspondence should be addressed to Ji Shi; shiji314@outlook.com

Received 12 January 2021; Revised 28 January 2021; Accepted 9 February 2021; Published 22 February 2021

Academic Editor: Yu Wang

Copyright © 2021 Ji Shi et al. This is an open access article distributed under the Creative Commons Attribution License, which permits unrestricted use, distribution, and reproduction in any medium, provided the original work is properly cited.

The temporal permeability and damage evolutions of low-permeability sandstone cores during triaxial and long-term dissolution experiments were measured using a triaxial-flow system. Three triaxial experiments were performed on sandstone cores having initial permeability ranging from $78 \times 10^{-18} \text{ m}^2$ to $120 \times 10^{-18} \text{ m}^2$. Two sets of long-term dissolution experiments were conducted on cracked sandstone cores. All dissolution experiments were performed at room temperature and using a 10 g/L H_2SO_4 and 0.2 g/L H_2O_2 input solution. Permeability evolution was determined using Darcy's law. The cores experienced an average increase of 25% in permeability in the dissolution experiment and 900%~1500% increase at the end of the experiment. The dissolution was fairly homogeneous during the long-term experiments whether on the 1 mm scale or the 10 μm scale. The relationship between damage and permeability was speculated and its correlation coefficient has been proved to be close to 1. These results suggest that hydraulic fracturing works well in permeability increase in low-permeability sandstone reservoir.

1. Introduction

Resource exploitation and engineering construction are influenced by the mechanical properties of rocks/soils [1–3]. Therefore, in some cases, their mechanical properties need to be changed according to requirements for exploitation [4–6]. How to increase the permeability of orebody artificially is the research front on many scientific topics such as petroleum engineering [7, 8], oil and gas storage [9–11], and in situ leaching mining.

Sandstone-hosted uranium deposits refer to the epigenetic and post exogenic deposits generated in sandstone, glutenite, and other clastic rocks. It is one of the earliest discovered and the most widely distributed uranium deposits in the world [12]. Those fine qualities of sandstone-hosted uranium deposits such as, for instance, medium-grade ore with a general value of about 0.1%~0.2%, high-quality ore, and stable occurrence, contribute to its great industrial value. Economic benefits of the deposits could be greatly improved by utilizing in situ leaching mining [13]. Low-permeability sandstone reservoir accounts for more than 50% of total reserves. However, the physical properties of low-permeability sandstone, like

developed microfissures, narrow pore radius, and small flow path, will lead to significant abrupt change in permeability in engineering process. Permeability is one of the most important evaluation criteria of exploitation and financial performance. Therefore, the permeability evolution in consolidated sandstone in engineering project is a research of great practical significance and requiring further study.

Many scholars have studied the permeability evolution of sandstone under different conditions. Lufeng et al. introduced a method to quantitatively evaluate the core permeability damage from a macroscopic perspective [7]. Liu et al. conducted an experiment to explore the gas porosity and permeability variation of sandstone at different levels of water saturation in loading-unloading cycles [14]. Odumabo investigated the fracturing fluid leakoff in low-permeability sandstones [11]. Zeng designed a simulation experiment for gas migration and accumulation in natural consolidated sandstone [15]. Fu et al. tried to explore the stress dependence of the absolute and relative permeabilities of some consolidated sandstones [9]. Wojtacki et al. presented a numerical method for estimating the stiffness-to-porosity relationships for evolving microstructures of Fontainebleau

sandstone [16]. These studies provide part of the theoretical basis for permeability evolution in low-permeability sandstone reservoir. In addition to the influence of engineering projects, the degradation of rock caused by leaching solution would also affect the permeability evolution in sandstone. Colón investigated the effect of dissolution on sandstone permeability, with the solution of NaOH (pH = 11.4) [17]. Mecchia et al. developed a hybrid model to estimate fracture karstification in quartz sandstone [18]. McKinley et al. calculated how porosity and permeability vary spatially with grain size, sorting, cement volume, and mineral dissolution in fluvial Triassic sandstones [19]. These studies have significant insights into the permeability evolution in sandstone under various states. At present, relatively few studies have explored long-term permeability evolution in sandstone during physicochemical processes. However, the long-term chemical reaction between leaching solution and acid soluble minerals in sandstone [20] will reduce strength and increase the permeability considerably [21].

The objectives of this study are to explore the permeability evolution and evaluate the damage caused by chemical reaction together with hydraulic fracturing, using triaxial experiment and SEM analysis. We establish a model and derive the equations to describe the relationship between damage and permeability in triaxial experiment and dissolution experiment.

2. Materials and Methods

2.1. Core Sample Preparation. Sample preparation is very important in the research process, which determines the reliability of the final results. The core samples were collected from the core of No. PD03 borehole in 2# stope of a uranium mine in Northwest China. The deposit is in the south of the Ili basin, the tectonic position of which is the east of the Ili microplate sandwiched by the Kazakhstan plate and the Tarim plate. The uranium metallogenic region is divided into two parts: the “roll” and the “tail.” The “roll” part is 45 m~205 m in length and relatively stable. The ore body is mainly composed of medium-coarse-grained and medium-fine-grained sandstone, most of which are grey, dark grey, and black grey. Clastic materials account for about 84.2% of the ore, while silty clay is about 15.77%. The main components of the clastic materials are quartz (51%~79%), cuttings (8%~20%), and feldspar (5%~15%). There is no easily-dilating montmorillonite in clay. The accessory minerals and authigenic minerals are mainly titanite (0.48%), pyrite (0.35%), limonite (0.22%), and pitchblende (0.18%). The effective porosity of the sandstone-hosted uranium ore is 12.2-13.1%, the main components of which are 76.38% SiO₂, 11.87% Al₂O₃, and 1.45% Fe₂O₃, as well as trace amounts of MnO, MgO, and CaO. Insoluble or difficultly soluble minerals account for 95.3% of the ore, and soluble minerals account for 1.5%~5.5%.

Refer to the rock mechanics standard GB/T50266-2013, the core samples are cylindrical cores with a diameter of 50 mm and a length of 100 mm. The diameter error of the core sample is no more than 0.3 mm, and the vertical deviation between the end face and the axis of the core sample is

no more than 0.25°. Typical core samples are shown in Figure 1. All the core samples were weighed up and recorded at first. Put all the core samples into drying oven and keep constant temperature drying at 105°C for 24 h. Take out the core samples and put them into a desiccator until they cool to room temperature. Record weight of every core sample, and duplicate the above steps until the D value of two adjacent weight records is no more than 0.1% of the last record. Put all the dried core samples into the vacuum saturation device, and make sure they are completely submerged in water. Set vacuum pressure as 100 kPa, pumping air for at least 6 h until no bubbles escape from water. Then, keep the core samples at atmospheric pressure in the vacuum saturation device for another 4 h. Make sure each core sample is fully saturated with water [22–27].

2.2. Experimental Method. TAW-2000 was utilized in experiments conducted in this study; it is a triaxial pressure-seepage system, as shown in Figure 2. The instrument can provide a maximum axial load of 2000 kN and a maximum confining pressure of 80 MPa. The measurement range of radial and axial displacement is 0~4 mm and 0~8 mm, and the resolution of pressure measurement is 1/180000. The system is equipped with a full digital servo controller, oil pump, and water pump that independently control axial pressure, confining pressure, and hydrostatic pressure. The axial strain is measured by the axial extensometer and linear variable differential transformer (LVDT), and the radial strain is measured by four radial strain gauges fixed to the center of the core sample, the measurement accuracy is $\pm 0.5\%$ FS. All displacement, stress, and strain data are displayed on the computer control system in real time [6, 28–42].

This experiment is divided into two main parts. In the first one, various confining pressure triaxial experiments were conducted. First, the saturated core sample was placed in the cylindrical chamber as shown in Figure 2 with confining pressure P_c (5 MPa, 10 MPa, and 15 MPa) and pore pressure P_p (4 MPa). The axial displacement increased at 0.02 mm/min until the ultimate strength was reached; the computer automatically recorded all the data including axial strain and circumferential strain. The purpose of part one is to gain an improved understanding of the permeability evolution of sandstone in triaxial experiment. In the second one, we conducted long-term flow experiments for 12 days. Two groups of saturated core samples were prepared, and each group contains eight core samples, similar to the first part except for confining pressure P_c which remained 5 MPa in both groups at first. The axial pressure stopped increasing and remained constant as soon as it reached ultimate strength. Core samples in group two were flooded with solution prepared before, while those in group one were flooded with double-distilled water as a control group. The input solution was pumped into the cell at a constant fluid flow rate until a stable differential pore pressure was achieved. Input solution for group two was prepared from reagent grade H₂SO₄ diluted in double-distilled water and concentrated reagent-grade H₂O₂ to produce a solution (10 g/L H₂SO₄ and 0.2 g/L H₂O₂). Record permeability every 12 h for both groups. Pore pressure increased from 4 MPa to

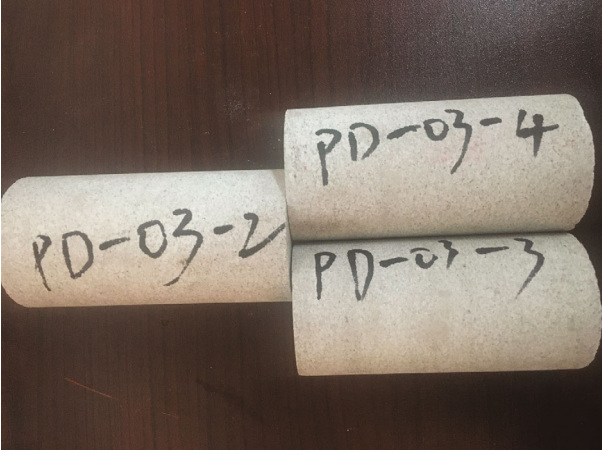


FIGURE 1: Typical sandstone core samples.

6 MPa on the 6th day. The purpose of part two is to investigate permeability evolution of sandstone in dissolution experiment after it reaches ultimate strength, thus providing feasibility assessment in permeability increase in low-permeability sandstone reservoir.

The steady-state method could be used for the measurement of rocks with relatively high permeability. According to Darcy's law, the permeability of the core sample could be calculated by measuring the liquid volume of the core sample in a period of time. The calculation method is as follows:

$$k = \frac{Q\mu L}{\Delta p A}, \quad (1)$$

where Q is the liquid flow rate per unit time, μ refers to viscosity coefficient of liquid, Δp represents pore pressure difference at both ends, A is cross-sectional area, and L is length of core sample.

The temporal porosity change during the dissolution of a sandstone core can be evaluated from the total soluble minerals removed by the reactive fluid in accord with

$$\phi_t = \phi_0 + \frac{V_m}{V_{\text{core}}} Q \int_{t=t_0}^t \Delta C_{\text{mine}} dt, \quad (2)$$

where ϕ_t represents porosity of the core at time t , ϕ_0 refers to the initial core porosity, t_0 denotes the time at the beginning of the experiment, V_m is molar volume of soluble minerals, and V_{core} denotes the total core volume. ΔC_{mine} refers to the difference in soluble minerals molal concentration between the inlet and the outlet solutions at steady-state, and Q corresponds to the mass flow rate of the reactive fluid.

Many equations aimed at estimating the permeability evolution of porous materials are based on permeability/porosity correlations. A commonly used correlation is expressed as follows:

$$k = k_0 \left(\frac{\phi}{\phi_0} \right)^n, \quad (3)$$

where k_0 stands for the permeability at the beginning of the dissolution experiment at an initial porosity of ϕ_0 . The exponent n is a constant, which is usually 2 or greater. It can be obtained by a curve-fitting procedure.

3. Results and Discussion

After the test, data analysis can be carried out, which is an important work in studies [5, 28, 43–59]. The temporal evolution of permeability and mechanical property during the various confining pressure triaxial experiments performed in TAW-2000 is illustrated in Figure 3. Three core samples experienced an initial permeability decrease followed by a continuous permeability increase during the experiments, which are attributed to fracture propagation. Permeability decreased along with pore throats size at the beginning of the experiment. Then, plastic deformation under dynamic loading in the core sample contributes to the occurrence of fractures, and volumetric strain began to decrease. The overall permeability increases during the experiments for samples 1, 2, and 3 in part one, which had initial permeability of $95 \times 10^{-18} \text{ m}^2$, $87 \times 10^{-18} \text{ m}^2$, and $82 \times 10^{-18} \text{ m}^2$, were 1500, 1000, and 900%, respectively. These different permeability increase rates are attributed in the present study to the confining pressure. For example, the permeability of core sample 1 increases at a faster rate than the other two core samples, which may stem from the relatively low confining pressure.

Mechanical properties of rock in triaxial experiment such as elastic modulus, deformation modulus, and Poisson's ratio are different from those in uniaxial experiment. The elastic modulus E and Poisson's ratio μ can be expressed as follows:

$$\begin{aligned} E &= \frac{\sigma_1 - 2\mu\sigma_3}{\varepsilon_1}, \\ \mu &= \frac{B\sigma_1 - \sigma_3}{\sigma_3(2B - 1) - \sigma_1}, \\ B &= \frac{\varepsilon_3}{\varepsilon_1}, \end{aligned} \quad (4)$$

where σ_1 stands for axial stress, σ_3 represents confining pressure, and ε_1 and ε_3 refer to axial and circumferential strain.

The volume strain of rock could not be measured directly in triaxial experiment, and hence, it is approximately expressed by the following formula:

$$\varepsilon_v = \varepsilon_1 + 2\varepsilon_3, \quad (5)$$

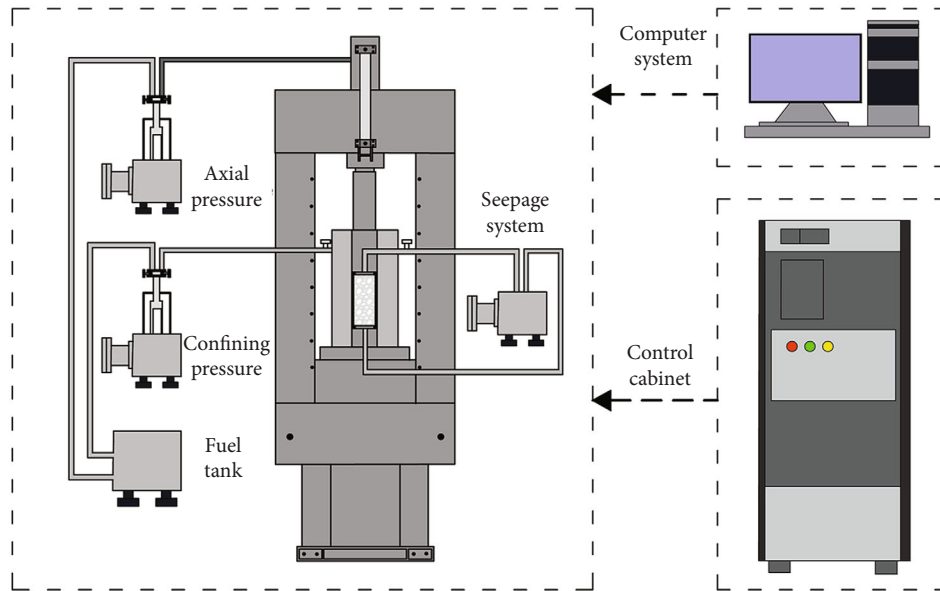
where ε_v designates volume strain and ε_1 and ε_3 represent axial and circumferential strain, respectively.

The circumferential strain can be regarded as the combination of two parts, namely elastic volume strain and the plastic strain result from rock failure. The elastic volume strain is shown as follows:

$$\varepsilon_2^e = \frac{1 - 2\mu}{E} (\sigma_1 + 2\sigma_3). \quad (6)$$



(a)



(b)

FIGURE 2: High temperature and high-pressure triaxial system. (a) Physical photograph. (b) Schematic diagram.

By subtracting the elastic volume strain from the total circumferential strain, the plastic strain result from crack ε_2^c , which reflects the propagation of axial crack, could be obtained, as follows:

$$\varepsilon_3 - \varepsilon_3^e = \varepsilon_3^c. \quad (7)$$

It can be seen from Figure 3 that there is a correlation between the crack circumferential strain and permeability. At the beginning of the experiment, microcracks in the core sample disappear and no new cracks grow. The increase of volume strain mainly stems from elastic deformation. Therefore, almost all circumferential strain is elastic strain, and the crack circumferential strain was almost nonexistent. The increase of elastic strain corresponds reasonably well with the small decline in permeability. As axial stress increases

and reaches the yield strength and ultimate strength, cracks begin to grow and coalesce until they merge into a sliding surface and cause rock failure. Crack circumferential strain increases rapidly at first and then shows no more change. Volumetric strain experiences a parabolic growth and the new fractures dramatically increase the permeability. The temporal evolution of permeability and crack circumferential strain are not synchronized; in general, the increase of permeability lags behind that of crack circumferential strain.

In the second part of the experiment, we conducted a long-term dissolution experiment to explore the temporal evolutions of permeability; we recorded permeabilities of 2 groups every 12 hours for 12 days. Results in long-term flow experiments are illustrated in Figure 4.

It can be seen in Figure 4(a) that most core samples experienced a decrease in permeability at the beginning except for

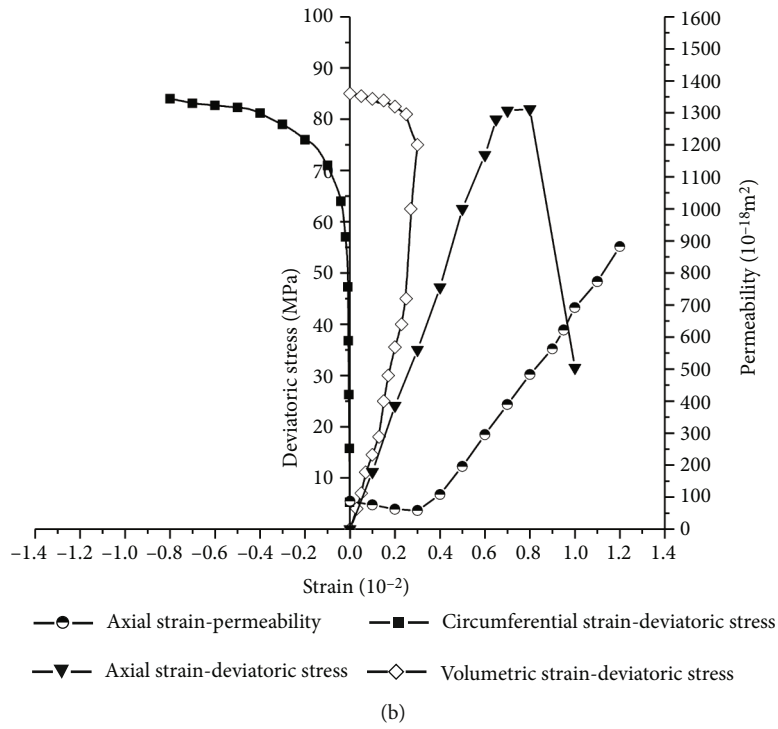
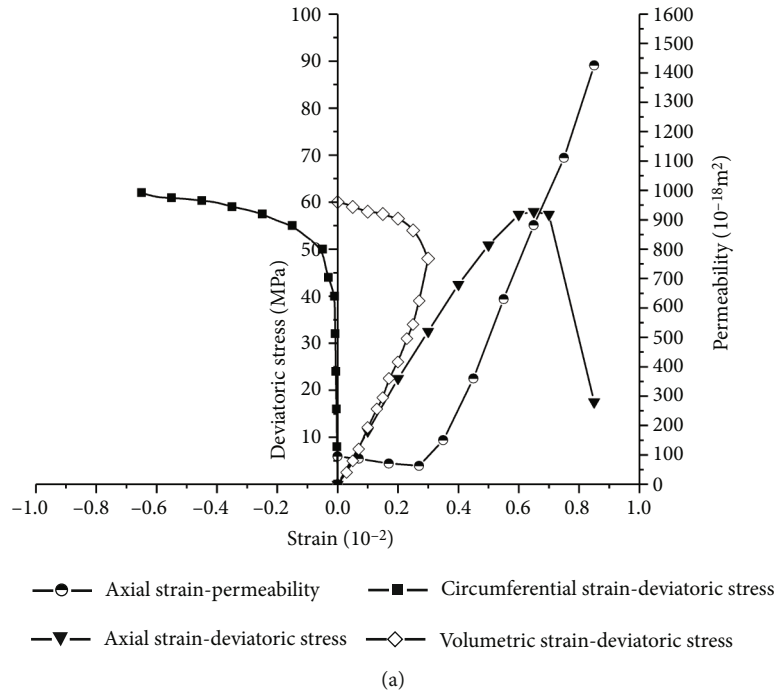


FIGURE 3: Continued.

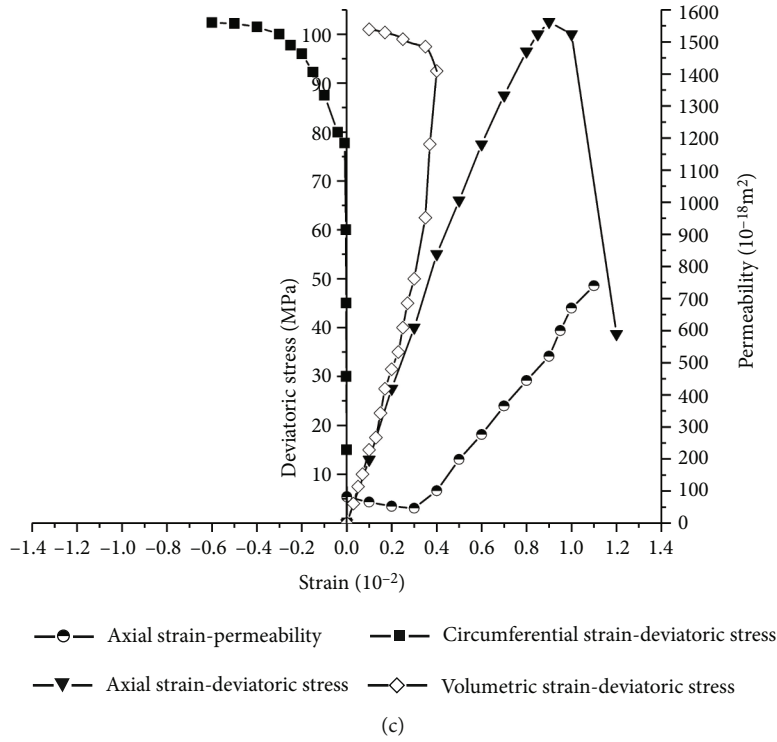


FIGURE 3: Temporal evolution of permeability and mechanical property during the various confining pressure triaxial experiments. (a) 5 MPa. (b) 10 MPa. (c) 15 MPa.

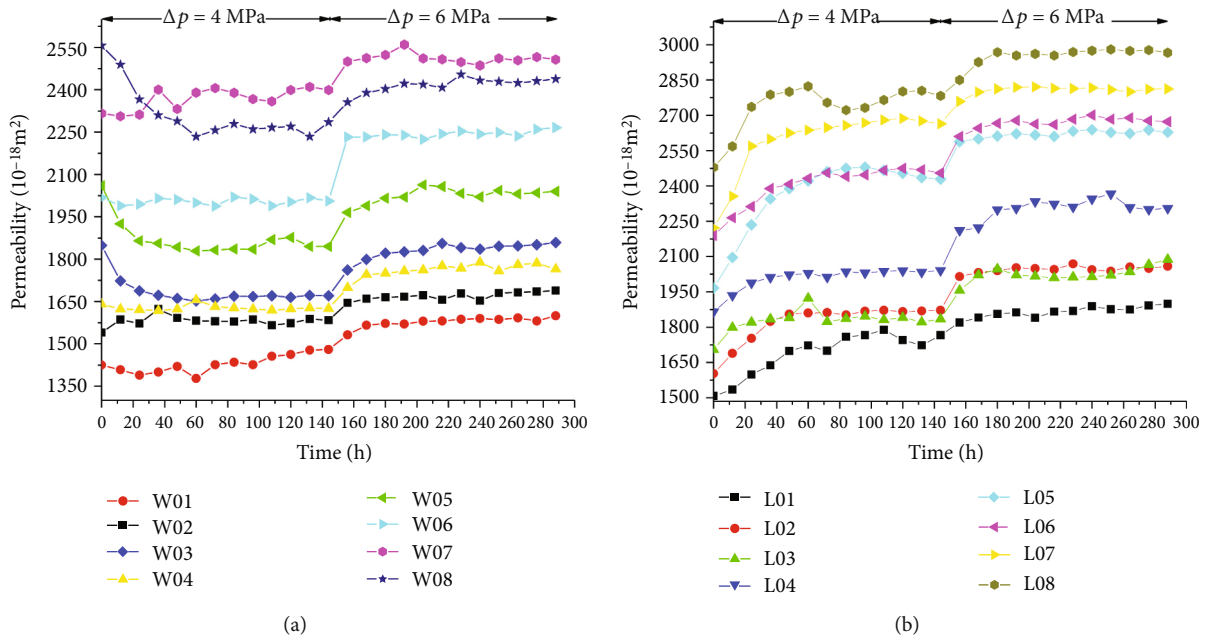


FIGURE 4: Temporal evolutions of permeability during the sandstone long-term dissolution experiments performed during the present study. (a) Group 1. (b) Group 2.

core sample W02, and a 15% decrease is achieved in core sample W08. Permeabilities of all cores tended to remain constant in about 48 hours and 72 hours. The decrease may stem from the tiny rock fragments that blocking the pore throats, which at the same time prevent the pore throats from

closing completely. Pore pressure changed from 4 MPa to 6 MPa on the 6th day, most core samples experienced a slightly increase except for core sample W06. This substantial permeability growth may stem from the rock fragments redistribution in fractures and pore throats.

The permeability evolution as a function of time during the long-time core dissolution experiment can be assessed with the aid of Figure 4(b). An overall average increase of 17% in permeability can be observed in the first part of the experiment, the largest increase is 26% and the smallest is 9%. Permeabilities of most cores tend to remain constant within 90 hours at most, including some short-term fluctuations in core samples L08 and L03. Pore pressure changed from 4 MPa to 6 MPa on the 6th day; all cores experienced a slight permeability increase from 3% to 13%.

The variations of measured permeabilities of group 2 are compared with those of group 1. At the end of the experiment, core samples of group 2 experienced a large permeability increase, which ranges from 18% for core sample L03 to 33% for core sample L05. Group 1 has an average increase of 5%, and permeabilities of core sample W03 and W05 are almost the same as its beginning separately.

Two conclusions can be drawn from the observations above. First, permeability evolution of cracked core sample during the long-term dissolution is affected by various factors, including location and direction of fractures and pore throats, tiny rock fragments, and pore pressure. These various factors can cause uncertainty in permeability increase. Secondly, dissolution can lead to an average increase of 25% permeability among cracked core samples.

Carlos et al. [17] conducted a long-term dissolution experiment of four Fontainebleau sandstone cores. Photomicrographs were taken of the full cross section of core sample 3 before and following the percolation experiments. Representative examples are illustrated in Figure 5.

This grain dissolution experiment was performed in a 0.1 mol/kg NaOH aqueous solution. The initial porosity of the core ranged from 7.03 to 8.63%, whereas those of the postexperiment ranged from 13.2 to 15.8%. It can be seen that quartz grain size and porosity distribution appear to be homogeneous on the 1 mm scale.

Yao et al. [28] explored permeability characteristics of sandstone in different chemical solutions. The SEM graphs of samples are illustrated in Figure 6.

This dissolution experiment was performed in 6 g/L H₂SO₄ acid solution (pH=2). It appears that the surface of the sample was generally smooth on the 10 μm scale before the dissolution, whereas the asperities of the postexperiment suggest the chemical reactions between acid and sandstone. Loads of pores and pore throats appeared on the surface, and the gap opening increases because the tiny fragments attached to the surface may slide down as the solution flows. The permeability increase may stem from the reasons mentioned above.

Several conclusions can be drawn from these observations. First, as all reactive fluids were the same temperature, pH, and H₂SO₄ concentration, and all core samples were fully saturated with water initially, these different permeability increase rates are attributed in the present study to the distinct fracture propagation and pore throats of each core sample. Secondly, the dissolution was fairly homogeneous during the long-term experiments whether on the 1 mm scale or the 10 μm scale. Thirdly, permeability increase stem from both the macroscopic fracture propagation and microscopic dissolution.

We consider the overall change of rock as damage to help describe the evolution of permeability during rock failure and dissolution. In order to describe the relationship between damage and permeability, we introduced a damage model and strength criterion for rock in triaxial experiment. Based on Terzaghi formula and hypothesis of strain equivalence, the effective stress tensor σ_e in joint action of rock failure and dissolution is defined as follows:

$$\sigma_e = \frac{\bar{\sigma} - p_w \delta}{1 - D}, \quad (8)$$

where $\bar{\sigma}$ refers to stress tensor, p_w represents pore pressure, δ is unit second-order tensor, and D represents degree of damage in rock materials. The degree of damage is related to the number and size of pores, pore throats, and fractures in rock materials, which directly affect the strength and permeability of rock. It is assumed that the strength of microelement in rock materials follows the power function distribution, and its probability density function is

$$P(F) = \frac{m}{F_0} \left(\frac{F}{F_0} \right)^{m-1}. \quad (9)$$

m , F_0 is the parameter in the distribution function which could be obtained by fitting of experimental data.

$$D = \int_0^F P(x) dx = \left(\frac{F}{F_0} \right)^m, \quad (10)$$

where $F \geq 0$. The three-dimensional constitutive relation of strength of microelement following normal distribution could be obtained.

$$\sigma_1 = E \varepsilon_1 \left[1 - \left(\frac{F}{F_0} \right)^m \right] + \mu (\sigma_2 + \sigma_3). \quad (11)$$

where E , μ refers to elastic modulus and Poisson's ratio of rock, respectively, ε_1 represents axial strain, σ_1 is axial stress, and σ_2 and σ_3 are confining pressure.

According to the generalized Hooke's law, the relationship between the axial elastic modulus and Poisson's ratio of rock in triaxial experiment is as follows:

$$\varepsilon_1 = \frac{1}{E} [\sigma_1 - \mu (\sigma_2 + \sigma_3)]. \quad (12)$$

Combined with the formula mentioned above, the stress-strain relationship of rock in seepage-triaxial experiment could be obtained:

$$\sigma_1 = E \varepsilon_1 (1 - D) + 2\mu \sigma_3 + (1 - 2\mu) p_w. \quad (13)$$

Loads of experimental results show that Mohr-Coulomb criterion satisfies the yield and failure characteristics of rock materials. However, the yield surface in the main stress space is a hexagonal pyramid with a sharp tip, which makes it quite difficult to calculate, and the effect of pore pressure is not

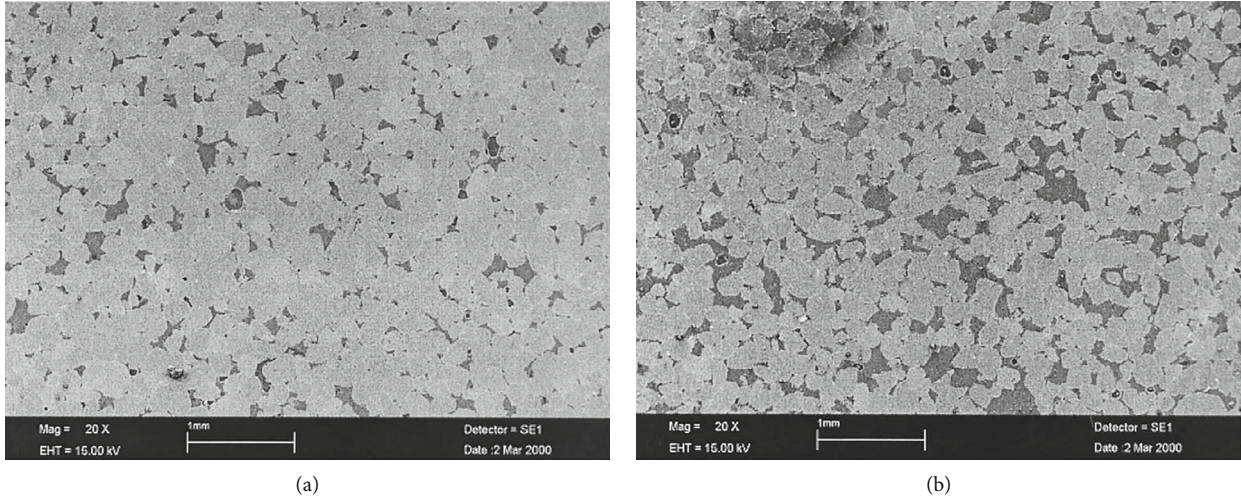


FIGURE 5: Photomicrographs of core sample 3 in research of Carlos et al. (a) before and (b) following its dissolution.

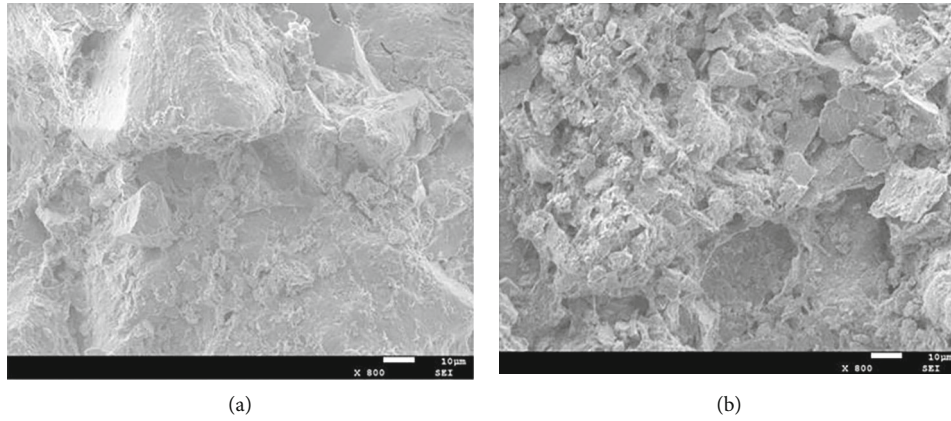


FIGURE 6: SEM graphs of sandstone core samples in research of Yao et al. (a) before and (b) following its dissolution.

considered. The yield criterion proposed by Drucker and Prager contains the effect of pore pressure, and its yield surface is a circle tangent to the hexagon in Mohr-Coulomb criterion. This criterion is as follows:

$$f(\sigma) = \alpha_0 I_1 + \sqrt{J_2}, \quad (14)$$

where I_1 is first invariant of stress tensor

$$I_1 = \sigma_1 + \sigma_2 + \sigma_3, \quad (15)$$

J_2 is the second invariant of deviatoric stress

$$J_2 = \frac{1}{6} [(\sigma_1 - \sigma_2)^2 + (\sigma_2 - \sigma_3)^2 + (\sigma_1 - \sigma_3)^2], \quad (16)$$

$$\alpha_0 = \frac{\sin \varphi}{\sqrt{9 + 3 \sin^2 \varphi}}.$$

φ is the angle of internal friction.

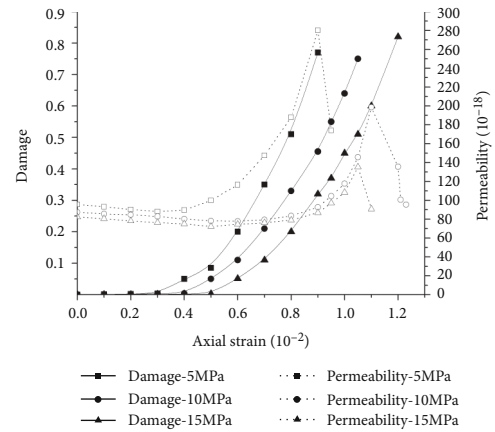


FIGURE 7: Permeability and damage evolution in the first part of the experiment.

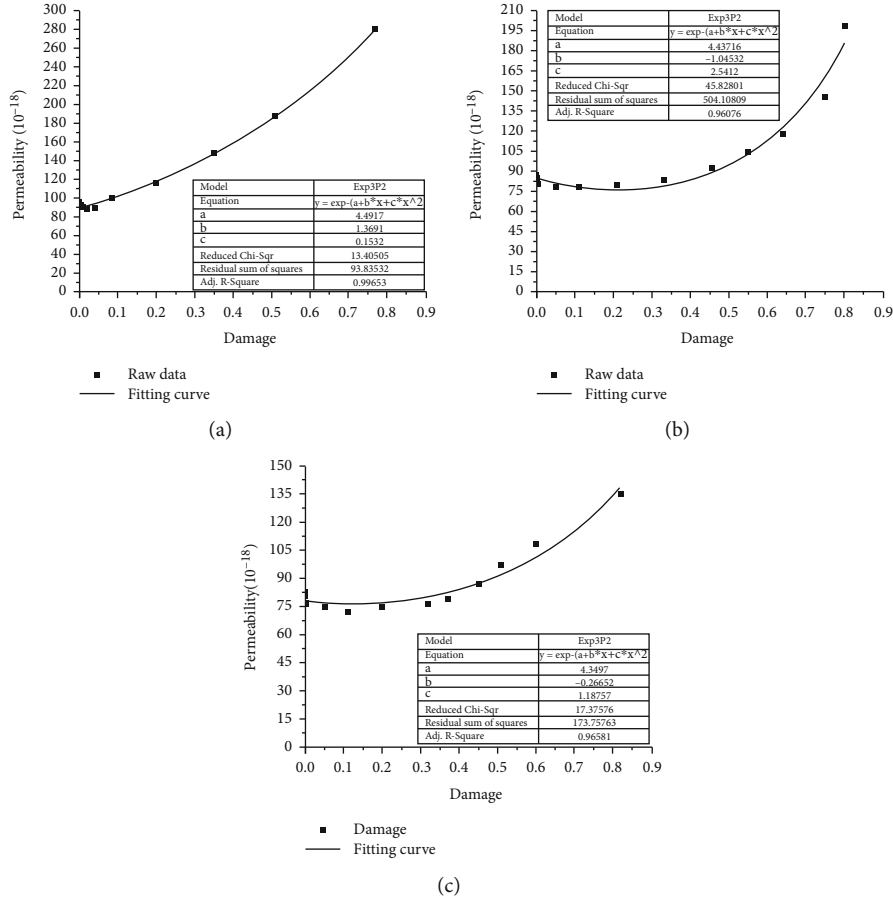


FIGURE 8: Fitting curve of the relationship between damage and permeability. (a) Confining pressure is 5 MPa. (b) Confining pressure is 10 MPa. (c) Confining pressure is 15 MPa.

Before the experiment started, the initial strain ε_0 due to confining pressure is expressed as follows:

$$\varepsilon_0 = \frac{1 - 2\mu}{E} (\sigma_3 - p_w). \quad (17)$$

The experimentally measured axial strain ε_t plus the initial strain is the total strain ε_1

$$\varepsilon_1 = \varepsilon_0 + \varepsilon_t. \quad (18)$$

Based on the above formulas, the functional relation between stress and damage can be obtained:

$$\sigma_d = [(1 - 2\mu)(\sigma_3 - p_w) + E\varepsilon_t] \left[1 - \left(\frac{F}{F_0} \right)^m \right] + (2\mu - 1)\sigma_3 + (1 - 2\mu)p_w. \quad (19)$$

Transform the above formula as follows:

$$D = \left(\frac{F}{F_0} \right)^m = \frac{E\varepsilon_t - \sigma_d}{E\varepsilon_t + (1 - 2\mu)\sigma_3 - p_w}. \quad (20)$$

According to the above formula and experimental data, the permeability and damage evolution is shown in Figure 7.

It can be seen from the figure that, at the beginning of the experiment permeability decreased slightly, while damage almost remained constant. This suggests that the opening of pores and pore throats decreased and few fractures were generated in this period. Then, damage started to increase while the evolution of permeability varies according to confining pressure. Core sample 1 experienced a synchronous increase of permeability and damage, while permeability increases of core sample 2 and 3 lag behind their damage increase, respectively. This may stem from the fact that once the new fractures generated inside the core sample, gap opening tended to decrease or be gone in a short time due to confining pressure.

According to the evolution of permeability and damage in the first part of the experiment, it can be speculated that the damage has an exponential relationship with permeability. A hypothesis of the relationship between damage and permeability was made as follows:

$$K = \exp(a + bD + cD^2), \quad (21)$$

where K is permeability, order of magnitude is 10^{-18} , D refers to damage, and a , b , and c are undetermined parameters. An exponential function curve-fitting procedure is conducted, as shown in Figure 8.

The results show that the relationship between damage and permeability remained exponential before permeability reaches a maximum value. The average correlation coefficient of each fitting curve is 0.972, and the highest value is 0.99653, which indicates that the fitting function correlates well with the experiment data. Once the permeability reaches the maximum value, with the continuous increase of axial strain, the closing of the sliding surface will lead to the decrease of permeability and the increase of rock damage continually. In real engineering practices, the cost and time to conduct large and long-term experiment to evaluate the geological parameters tend to be very high. In this paper, we establish the damage model and verify the hypothesis of the relationship between damage and permeability. Thus, by conducting a series of experiments, the permeability evolution of sandstone rock could be obtained. The derived equations could save loads of time as well as cost.

4. Conclusions

In this study, the core sample of a Uranium mine in Northwest China and TAW-2000 high-temperature and high-pressure triaxial experiment system developed by Wuhan University of Science and Technology were used. The experiment was divided into two parts; in the first part, we explored the temporal evolution of permeability and mechanical property in triaxial experiment with different confining pressure; in the second part, long time dissolution experiment was conducted; we established the relationship between damage and permeability and evaluated the correlation coefficient. Several conclusions are made:

- (1) Permeability evolution of cracked core sample during the long-term dissolution is affected by various factors, including location and direction of fractures and pore throats, tiny rock fragments, and pore pressure. These various factors can cause uncertainty in permeability increase. Dissolution can lead to an average increase of 25% permeability in the second part of the experiment
- (2) An average increase of 900%~1500% on permeability was observed in core samples at the end of the experiment, which indicates that hydraulic fracturing using solution works well in permeability increase in low-permeability sandstone deposit. Joint action of hydraulic fracturing and chemical reaction ensures that permeability increases in a reasonable interval
- (3) As all reactive fluids were the same temperature, pH, and H_2SO_4 concentration, and all core samples were fully saturated with water initially, the different permeability increase rates are attributed in the present study to the distinct fracture propagation and pore throats of each core sample. According to the previous research and SEM graphs, the dissolution was fairly homogeneous during the long-term experiments whether on the 1 mm scale or the 10 μm scale. Therefore, permeability increase stem from both the

macroscopic fracture propagation and microscopic dissolution

- (4) The function between damage and permeability works well in predicting permeability evolution before it reaches the maximum value. It provides a way for low-permeability sandstone deposits to evaluate the effect of permeability increase with less experiments and investment.

Data Availability

The permeability and dissolution data used to support the findings of this study are included within the article.

Conflicts of Interest

The authors declare that there is no conflict of interest regarding the publication of this paper.

Acknowledgments

This research was funded by the National Natural Science Foundation of China (Grant No. 51804236 and Grant 51804235).

References



- [1] C. Zhang, C. Pu, R. Cao, T. Jiang, and G. Huang, "The stability and roof-support optimization of roadways passing through unfavorable geological bodies using advanced detection and monitoring methods, among others, in the Sanmenxia Bauxite Mine in China's Henan Province," *Bulletin of Engineering Geology and the Environment*, vol. 78, no. 7, pp. 5087–5099, 2019.
- [2] Y. Zhao, Y. Wang, and L. Tang, "The compressive-shear fracture strength of rock containing water based on Druker-Prager failure criterion," *Arabian Journal of Geosciences*, vol. 12, p. 452, 2019.
- [3] H. Lin, X. Ding, R. Yong, W. Xu, and S. Du, "Effect of non-persistent joints distribution on shear behavior," *Comptes Rendus Mecanique*, vol. 347, no. 6, pp. 477–489, 2019.
- [4] X. Fan, K. Li, H. Lai, Y. Xie, R. Cao, and J. Zheng, "Internal stress distribution and cracking around flaws and openings of rock block under uniaxial compression: a particle mechanics approach," *Computers and Geotechnics*, vol. 102, pp. 28–38, 2018.
- [5] Y. Wang, P. Guo, H. Lin et al., "Numerical analysis of fiber-reinforced soils based on the equivalent additional stress concept," *International Journal of Geomechanics*, vol. 19, article 0401912211, 2019.
- [6] C. Zhang, Y. Wang, and T. Jiang, "The propagation mechanism of an oblique straight crack in a rock sample and the effect of osmotic pressure under in-plane biaxial compression," *Arabian Journal of Geosciences*, vol. 13, p. 736, 2020.
- [7] Z. Lufeng, Z. Fujian, Z. Shicheng, L. Zhun, W. Jin, and W. Yuechun, "Evaluation of permeability damage caused by drilling and fracturing fluids in tight low permeability sandstone reservoirs," *Journal of Petroleum Science and Engineering*, vol. 175, pp. 1122–1135, 2019.
- [8] C. Zhang, P. Zou, Y. Wang, T. Jiang, H. Lin, and P. Cao, "An elasto-visco-plastic model based on stress functions for

- deformation and damage of water-saturated rocks during the freeze-thaw process,” *Construction and Building Materials*, vol. 250, no. 118862, p. 118862, 2020.
- [9] X. Fu, F. Agostini, F. Skoczylas, and L. Jeannin, “Experimental study of the stress dependence of the absolute and relative permeabilities of some tight gas sandstones,” *International Journal of Rock Mechanics and Mining Sciences*, vol. 77, pp. 36–43, 2015.
- [10] B. Ghanbarian, C. Torres-Verdín, and T. H. Skaggs, “Quantifying tight-gas sandstone permeability via critical path analysis,” *Advances in Water Resources*, vol. 92, pp. 316–322, 2016.
- [11] S. M. Odumabo, Z. T. Karpyn, and L. F. Ayala H, “Investigation of gas flow hindrance due to fracturing fluid leakoff in low permeability sandstones,” *Journal of Natural Gas Science and Engineering*, vol. 17, pp. 1–12, 2014.
- [12] Y. Cheng, S. Wang, R. Jin, J. Li, C. Ao, and X. Teng, “Global Miocene tectonics and regional sandstone-style uranium mineralization,” *Ore Geology Reviews*, vol. 106, pp. 238–250, 2019.
- [13] S. Akhtar, X. Yang, and F. Pirajno, “Sandstone type uranium deposits in the Ordos Basin, Northwest China: a case study and an overview,” *Journal of Asian Earth Sciences*, vol. 146, pp. 367–382, 2017.
- [14] S. Liu, H. Wang, W. Xu, and Z. Xiang, “The influence of water saturation and confining pressure to gas porosity and permeability of sandstone,” *Environmental Earth Sciences*, vol. 78, no. 6, p. 182, 2019.
- [15] J. Zeng, Y. Zhang, S. Zhang, J. Qiao, X. Feng, and S. Feng, “Experimental and theoretical characterization of the natural gas migration and accumulation mechanism in low-permeability (tight) sandstone cores,” *Journal of Natural Gas Science and Engineering*, vol. 33, pp. 1308–1315, 2016.
- [16] K. Wojtacki, L. Daridon, and Y. Monerie, “Computing the elastic properties of sandstone submitted to progressive dissolution,” *International Journal of Rock Mechanics and Mining Sciences*, vol. 95, pp. 16–25, 2017.
- [17] C. F. J. Colón, E. H. Oelkers, and J. Schott, “Experimental investigation of the effect of dissolution on sandstone permeability, porosity, and reactive surface area¹,” *Geochimica Et Cosmochimica Acta*, vol. 68, no. 4, pp. 805–817, 2004.
- [18] M. Mecchia, F. Sauro, L. Piccini, A. Columbu, and J. De Waele, “A hybrid model to evaluate subsurface chemical weathering and fracture karstification in quartz sandstone,” *Journal of Hydrology*, vol. 572, pp. 745–760, 2019.
- [19] J. M. McKinley, P. M. Atkinson, C. D. Lloyd, A. H. Ruffell, and R. H. Worden, “How porosity and permeability vary spatially with grain size, sorting, cement volume, and mineral dissolution in fluvial Triassic sandstones: the value of geostatistics and local regression,” *Journal of Sedimentary Research*, vol. 81, no. 11-12, pp. 844–858, 2011.
- [20] M. I. Leybourne and E. M. Cameron, “Groundwater in geochemical exploration,” *Geochemistry-Exploration Environment Analysis*, vol. 10, no. 2, pp. 99–118, 2010.
- [21] M. Tanez and C. Hurel, “A review on the potential uses of red mud as amendment for pollution control in environmental media,” *Environmental Science and Pollution Research*, vol. 26, no. 22, pp. 22106–22125, 2019.
- [22] Y. Wang, W. K. Feng, R. L. Hu, and C. H. Li, “Fracture evolution and energy characteristics during marble failure under triaxial fatigue cyclic and confining pressure unloading (FC-CPU) conditions,” *Rock Mechanics and Rock Engineering*, 2020.
- [23] Y. Wang, C. H. Li, H. Liu, and J. Q. Han, “Fracture failure analysis of freeze-thawed granite containing natural fracture under uniaxial multi-level cyclic loads,” *Theoretical and Applied Fracture Mechanics*, vol. 110, article 102782, 2020.
- [24] Y. Wang, C. Li, J. Han, and H. Wang, “Mechanical behaviours of granite containing two flaws under uniaxial increasing-amplitude fatigue loading conditions: An insight into fracture evolution analyses,” *Fatigue & Fracture of Engineering Materials & Structures*, vol. 43, no. 9, pp. 2055–2070, 2020.
- [25] Y. Wang, C. H. Li, and J. Q. Han, “On the effect of stress amplitude on fracture and energy evolution of pre-flawed granite under uniaxial increasing-amplitude fatigue loads,” *Engineering Fracture Mechanics*, vol. 240, article 107366, 2020.
- [26] Y. Wang, W. K. Feng, H. J. Wang, C. H. Li, and Z. Q. Hou, “Rock bridge fracturing characteristics in granite induced by freeze-thaw and uniaxial deformation revealed by AE monitoring and post-test CT scanning,” *Cold Regions Science and Technology*, vol. 177, article 103115, 2020.
- [27] T. Wang, Z. Liu, Y. Gao, X. Ye, and Z. Zhuang, “Theoretical and numerical models for the influence of debonding on the interaction between hydraulic fracture and natural fracture,” *Engineering Computations*, vol. 36, no. 8, pp. 2673–2693, 2019.
- [28] H. Yao, Z. Zhang, and D. Li, “Experimental study on the permeability characteristics of sandstone in different chemical solutions,” *KSCE Journal of Civil Engineering*, vol. 22, no. 9, pp. 3271–3277, 2018.
- [29] C. Y. Zhang, P. Zou, Y. X. Wang, T. T. Jiang, and P. Cao, “An elasto-visco-plastic model based on stress functions for deformation and damage of water saturated rocks during the freezing-thawing process,” *Construction and Building Materials*, vol. 250, article 118862, 2020.
- [30] R. H. Cao, R. B. Yao, J. J. Meng, Q. B. Lin, H. Lin, and S. Li, “Failure mechanism of non-persistent jointed rock-like specimens under uniaxial loading: Laboratory testing,” *International Journal of Rock Mechanics and Mining Sciences*, vol. 132, article ???, 2020.
- [31] R. H. Cao, R. B. Yao, T. Hu, C. S. Wang, K. H. Li, and J. J. Meng, “Failure and mechanical behavior of transversely isotropic rock under compression-shear tests: laboratory testing and numerical simulation,” *Engineering Fracture Mechanics*, vol. 241, article 107389, 2021.
- [32] R. H. Cao, C. S. Wang, R. B. Yao et al., “Effects of Cyclic Freeze-thaw Treatments on the Fracture Characteristics of Sandstone under Different Fracture Modes: Laboratory Testing,” *Theoretical and Applied Fracture Mechanics*, vol. 109, article ???, 2020.
- [33] Y. X. Wang, S. B. Shan, C. S. Zhang, and P. P. Guo, “Seismic response of tunnel lining structure in a thick expansive soil stratum,” *Tunnelling and Underground Space Technology*, vol. 88, pp. 250–259, 2019.
- [34] Y. Chen, G. P. Wen, and J. H. Hu, “Analysis of deformation characteristics of fully grouted rock bolts under pull-and shear loading,” *Rock Mechanics and Rock Engineering*, vol. 53, no. 7, pp. 2981–2993, 2020.
- [35] Y. L. Zhao, L. Y. Zhang, J. Liao, W. J. Wang, Q. Liu, and L. Tang, “Experimental study of fracture toughness and sub-critical crack growth of three rocks under different environments,” *International Journal of Geomechanics*, vol. 20, no. 8, article 04020128, 2020.
- [36] Y. L. Zhao, L. Y. Zhang, W. J. Wang, Q. Liu, L. M. Tang, and G. Cheng, “Experimental study on shear behavior and a

- revised shear strength model for infilled rock joints,” *International Journal of Geomechanics*, vol. 20, no. 9, article 04020141, 2020.
- [37] Y. L. Zhao, C. S. Zhang, Y. X. Wang, and H. Lin, *Shear-Related Roughness Classification and Strength Model of Natural Rock Joint Based on Fuzzy Comprehensive Evaluation*, International Journal of Rock Mechanics and Mining Sciences, 2021, (Available online).
- [38] Y. L. Zhao, C. L. Wang, and J. Bi, “Analysis of fractured rock permeability evolution under unloading conditions by the model of elastoplastic contact between rough surfaces,” *Rock Mechanics and Rock Engineering*, vol. 53, no. 12, pp. 5795–5808, 2020.
- [39] S. J. Xie, H. Lin, Y. F. Chen, R. Yong, W. Xiong, and S. du, “A damage constitutive model for shear behavior of joints based on determination of the yield point,” *International Journal of Rock Mechanics and Mining Sciences*, vol. 128, article ???, 2020.
- [40] S. J. Xie, H. Lin, Y. X. Wang et al., “A statistical damage constitutive model considering whole joint shear deformation,” *International Journal of Damage Mechanics*, vol. 29, no. 6, pp. 988–1008, 2020.
- [41] Y. Zheng, C. Chen, F. Meng, H. N. Zhang, K. Z. Xia, and X. B. Chen, “Assessing the stability of rock slopes with respect to block-flexure toppling failure using a force-transfer model and genetic algorithm,” *Rock Mechanics and Rock Engineering*, vol. 53, no. 8, pp. 3433–3445, 2020.
- [42] Y. Zheng, C. Chen, F. Meng, T. Liu, and K. Xia, “Assessing the stability of rock slopes with respect to flexural toppling failure using a limit equilibrium model and genetic algorithm,” *Computers and Geotechnics*, vol. 124, article 103619, 2020.
- [43] Y. Zheng, C. Chen, T. Liu, H. Zhang, and C. Sun, “Theoretical and numerical study on the block-flexure toppling failure of rock slopes,” *Engineering Geology*, vol. 263, article 105309, 2019.
- [44] Y. Zheng, C. Chen, T. Liu, D. Song, and F. Meng, “Stability analysis of anti-dip bedding rock slopes locally reinforced by rock bolts,” *Engineering Geology*, vol. 251, pp. 228–240, 2019.
- [45] Y. Zheng, C. Chen, T. Liu, H. Zhang, K. Xia, and F. Liu, “Study on the mechanisms of flexural toppling failure in anti-inclined rock slopes using numerical and limit equilibrium models,” *Engineering Geology*, vol. 237, pp. 116–128, 2018.
- [46] Y. F. Chen and H. Lin, “Consistency analysis of Hoek-Brown and equivalent Mohr-coulomb parameters in calculating slope safety factor,” *Bulletin of Engineering Geology and the Environment*, vol. 78, no. 6, pp. 4349–4361, 2019.
- [47] H. Lin, H. Yang, Y. X. Wang, Y. L. Zhao, and R. H. Cao, “Determination of the stress field and crack initiation angle of an open flaw tip under uniaxial compression,” *Theoretical and Applied Fracture Mechanics*, vol. 104, article ???, 2019.
- [48] X. Fan, Z. Yang, and K. Li, “Effects of the lining structure on mechanical and fracturing behaviors of four-arc shaped tunnels in a jointed rock mass under uniaxial compression,” *Theoretical and Applied Fracture Mechanics*, vol. 112, article 102887, 2021.
- [49] J. J. Meng, X. Zhang, J. S. Huang, H. X. Tang, H. Mattsson, and J. Laue, “A smoothed finite element method using second-order cone programming,” *Computers and Geotechnics*, vol. 123, article ???, 2020.
- [50] F. Wang, P. Cao, Y. X. Wang, R. Q. Hao, J. J. Meng, and J. L. Shang, “Combined effects of cyclic load and temperature fluctuation on the mechanical behavior of porous sandstones,” *Engineering Geology*, vol. 266, article ???, 2020.
- [51] K. H. Li, Y. Cheng, Z. Y. Yin, D. Han, and J. J. Meng, “Size effects in a transversely isotropic rock under Brazilian tests: laboratory testing,” *Rock Mechanics and Rock Engineering*, vol. 53, no. 6, pp. 2623–2642, 2020.
- [52] K. H. Li, Z. Y. Yin, Y. M. Cheng, P. Cao, and J. J. Meng, “Three-dimensional discrete element simulation of indirect tensile behaviour of a transversely isotropic rock,” *International Journal for Numerical and Analytical Methods in Geomechanics*, vol. 44, no. 13, pp. 1812–1832, 2020.
- [53] C. Y. Zhang, C. Z. Pu, R. H. Cao, T. T. Jiang, and G. Huang, “The stability and roof-support optimization of roadways passing through unfavorable geological bodies using advanced detection and monitoring methods, among others, in the Sanmenxia Bauxite Mine in China’s Henan Province,” *Bulletin of Engineering Geology and the Environment*, vol. 78, no. 7, pp. 5087–5099, 2019.
- [54] H. Lin, D. Lei, R. Yong, C. Jiang, and S. Du, “Analytical and numerical analysis for frost heaving stress distribution within rock joints under freezing and thawing cycles,” *Environmental Earth Sciences*, vol. 79, no. 12, p. 305, 2020.
- [55] H. Lin, X. Zhang, R. Cao, and Z. Wen, “Improved nonlinear Burgers shear creep model based on the time-dependent shear strength for rock,” *Environmental Earth Sciences*, vol. 79, p. 149, 2020.
- [56] Z. M. He, D. Xiang, Y. X. Liu, Q. F. Gao, and H. B. Bian, “Deformation behavior of coarse-grained soil as an embankment filler under cyclic loading,” *Advances in Civil Engineering*, vol. 2020, Article ID 4629105, 2020.
- [57] Z. M. He, Z. F. Liu, X. H. Liu, and H. B. Bian, “Improved method for determining active earth pressure considering arching effect and actual slip surface,” *Journal of Central South University*, vol. 27, no. 7, pp. 2032–2042, 2020.
- [58] R. Jiang, F. Dai, Y. Liu, and A. Li, *Fast Marching Method for Microseismic Source Location in Cavern-Containing Rockmass: Performance Analysis and Engineering Application*, Engineering, 2021.
- [59] X. Fan, X. D. Jiang, Y. X. Liu, H. Lin, K. H. Li, and Z. M. He, “Local stress distribution and evolution surrounding flaw and opening within rock block under uniaxial compression,” *Theoretical and Applied Fracture Mechanics*, vol. 112, article 102914, 2021.

Research Article

Effect of Bedding Structure on the Energy Dissipation Characteristics of Dynamic Tensile Fracture for Water-Saturated Coal

Shuang Gong ^{1,2,3}, Lei Zhou ^{1,2,3}, Zhen Wang^{1,2,3} and Wen Wang^{1,3}

¹School of Energy Science and Engineering, Henan Polytechnic University, Jiaozuo 454000, China

²Henan Key Laboratory for Green and Efficient Mining & Comprehensive Utilization of Mineral Resources, Jiaozuo 454000, China

³Collaborative Innovation Center of Coal Work Safety, Jiaozuo, 454000 Henan Province, China

Correspondence should be addressed to Shuang Gong; gongcumtb@126.com

Received 21 January 2021; Revised 2 February 2021; Accepted 6 February 2021; Published 18 February 2021

Academic Editor: Zhengyang Song

Copyright © 2021 Shuang Gong et al. This is an open access article distributed under the Creative Commons Attribution License, which permits unrestricted use, distribution, and reproduction in any medium, provided the original work is properly cited.

The analysis of energy dissipation characteristics is a basic way to elucidate the mechanism of coal rock fragmentation. In order to study the energy dissipation patterns during dynamic tensile deformation damage of coal samples, the Brazilian disc (BD) splitting test under impact conditions was conducted on burst-prone coal samples using a split Hopkinson pressure bar (SHPB) loading system. The effects of impact velocity, bedding angle, and water saturation on the total absorbed energy density, total dissipated energy density, and damage variables of coal samples were investigated. In addition, the coal samples were collected after crushing to produce debris with particle sizes of 0-0.2 mm and 0.2-5 mm, and the distribution characteristics of different size debris were compared and analyzed. The results show that the damage variables of natural dry coal samples increase approximately linearly with the increase of impact velocity; however, the overall damage variables of saturated coal samples increase exponentially as a function of impact velocity. Compared with air-dry samples, the number of fragments with the particle size of 0-0.2 mm of saturated samples decreases by 14.1%-31.3%, and the number of fragments with the particle size of 0.2-5 mm decreases by 33.7%-53.0%. However, when the bedding angle is 45°, the percentage of fragment mass of saturated samples is larger than that of air-dry samples. The conclusions provide a theoretical basis for understanding the deterioration mechanism of coal after water saturation and the implementation of water injection dust prevention technology in coal mines.

1. Introduction

Coal is China's basic energy and fuel resource, accounting for 59.0% of the total energy consumption in 2019. The energy dissipation law and fragment distribution characteristics of coal in the dynamic tensile failure are directly related to the blasting scheme, coal roadway support, hazard prevention measures of rock burst, and gas outburst in top coal caving mining [1]. Energy is the essential characteristic of physical reaction and the internal factor of substance failure through the whole deformation and failure process of coal rock. Therefore, the energy dissipation can be analyzed to clarify the crushing mechanism of coal rock [2-7]. However, compared with the total input energy, the effective energy for rock crushing is quite low in mining techniques such as percus-

sion drilling, blasting, and cutting. For example, during the cutting and drilling, only about 10% of the input energy is used for the effective crushing, while most of the input energy is dissipated in heat or other forms [8]; during the blasting, the energy utilization rate for rock crushing is only about 5%-15% [9]. Chi et al. concluded that less than 1% of the input energy is used to crush rock and form a new fracture surface [10]. Therefore, further quantitative study on the energy dissipation law and fragment distribution characteristics of coal samples under dynamic tensile failure are of great significance for the dynamic disaster prevention, resource recovery rate, and energy efficiency in coal mines.

Up to now, many scholars have studied the deformation and failure process of rock from the perspective of energy and have achieved sound results [11-16]. Song et al. [17]

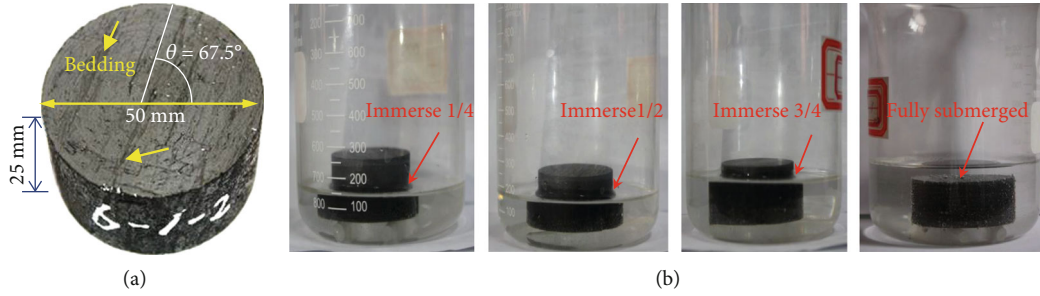


FIGURE 1: Schematic diagram of sample size and sample preparation. (a) The size and bedding angle of coal sample. (b) Water absorption process of saturated coal sample.

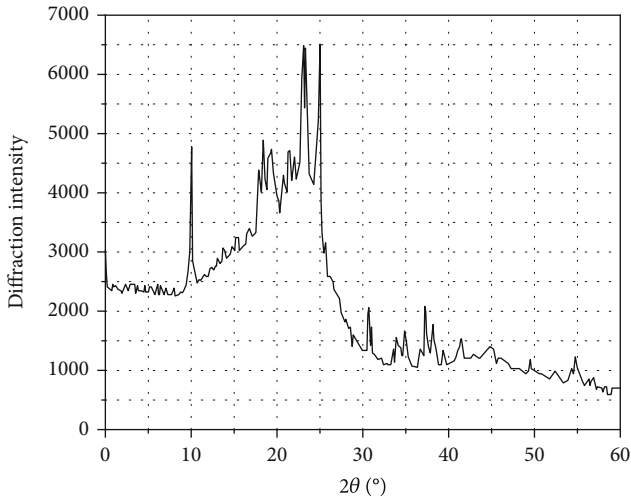


FIGURE 2: X-ray diffraction patterns of the coal specimen.

investigated the energy dissipation characteristics of concrete samples subjected to uniaxial cyclic loading based on the dissipated energy approach (DEA). The results show that the cumulative speed of energy dissipation and increasing growth rate of damage indicators in the continuum damage theory (CDT) follow an exponential function in relation to the maximum cyclic load level and follow a logarithmic function in relation to the minimum cyclic load level. Zhang et al. [18] studied the energy dissipation characteristics of the coal subjected to multilevel-frequency cyclic loading. Two hysteresis indexes were proposed according to the stress-strain relation during cyclic loading to predict the fatigue failure of coal samples. In addition, a lot of research works have been carried out by scholars in studying the deterioration mechanism of water on rocks. Cai et al. [19] investigate the effect of wetting-drying cycles on the fracture behavior of sandstone. Tests results indicate that both of fracture toughness and energy dissipation of sandstone significantly decrease with the increase of cycle number. Song et al. [20] studied the mechanical behavior of Tibet marble exposed to various freeze-thaw (FT) cycles and multilevel cyclic loading. A warning level is defined according to the evolution of radial strain and Poisson's ratio which can inform before dilation starts. The understanding of the energy dissipation characteristics of rock crushing is enhanced, and the development of mining technology is promoted. However, there are few

reports on the energy dissipation law of coal rock in the process of deformation and failure. Besides, the coal contains a certain amount of original moisture, bedding, and other primary structures, which increases the discreteness of dynamic tensile test results of coal rock [21]. Therefore, it is necessary to study the influence of bedding and water content on the energy dissipation characteristics of coal rock.

In this paper, the dynamic Brazilian splitting test was used to analyze the energy dissipation law of coal samples, and 90 disk-shaped coal samples were used for the SHPB impact splitting test. The effects of impact velocity, bedding angle, and saturated water content on the total absorbed energy density, total dissipated energy, total dissipated energy density, and damage variable of coal samples were discussed, and the distribution characteristics of the generated fragments with different sizes during the dynamic splitting of coal samples were compared and analyzed.

2. Experimental Setup

2.1. Sample Preparation. The coal samples were taken from the coal seam 11, panel 2, working face 8935 in Xinzhouyao mine, Datong, Shanxi Province. The coal was gathered from the Jurassic coal seam. To ensure the homogeneity of physical and mechanical properties of samples, all the samples were cut from a complete coal sample. A total of 90 coal samples with $\Phi 50 \text{ mm} \times 25 \text{ mm}$ was processed. The average diameter of coal samples was 49.29 mm, the average thickness was 25.27 mm, and the dimension error was $\pm 1 \text{ mm}$. The unevenness of both ends after grinding was $\pm 0.05 \text{ mm}$, and the end face was perpendicular to the axis. The maximum deviation was no more than 0.25° . The results showed that the uniaxial compressive strength, tensile strength, cohesion, internal friction angle, elastic modulus, and Poisson's ratio of coal samples were 27.64 MPa, 1.75 MPa, 7.85 MPa, 32.64° , 2.29 GPa, and 0.24, respectively. Through the proximate analysis of coal rock, the moisture content, ash content, and fixed carbon content of coal samples were 4.13%, 2.04%, and 69.17%, respectively.

As shown in Figure 1, a total of 90 Brazilian disc coal samples were finally processed, of which 45 coal samples were in the state of air-dry, and the remaining 45 coal samples were soaked in water for 161 hours to reach the state of saturated water content. According to the bedding angle (the angle between bedding plane and impact direction),

TABLE 1: Quantitative statistical results of coal samples' macerals.

Desmocollinites	Telocollinite	Telinite	Corpocollin-ite	Semifusinite	Fusinite	Inert detritus	Mineral
2.1	46.3	20.5	1.5	10.8	8.2	4.6	6.0

TABLE 2: Changes in parameters before and after saturation of coal samples.

Specimen ID	Diameter (mm)	Height (mm)	Mass (dry) (g)	Drying density ($\times 10^3 \text{kg/m}^3$)	Mass (saturated) (g)	Water absorption (%)
5-1-1	50.08	25.12	64.28	1.30	65.01	1.136
5-2-2	50.30	25.10	69.79	1.40	70.68	1.275
5-3-1	48.84	25.50	59.15	1.24	63.51	7.371
6-7-3	48.56	25.06	57.43	1.24	60.78	5.833
6-2-1	47.96	25.20	58.26	1.28	59.8	2.643

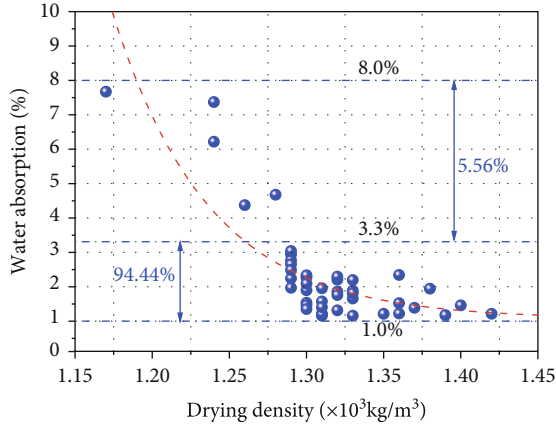


FIGURE 3: Relationship between saturated water absorption and density of coal sample.

the air-dry samples and saturated samples were divided into 5 groups (0° , 22.5° , 45° , 67.5° , and 90°). The results of X-ray diffraction (XRD) and maceral analysis of coal samples are shown in Figure 2 and Table 1, respectively. The changes of physical parameters of coal samples before and after water saturation are shown in Table 2. The water imbibition of 45 saturated samples was 1.2%-2.4%. Figure 3 shows the relationship between the water absorption of coal sample and its dry density. It can be concluded that 94.44% of the coal samples are in the water absorption rate of 1%~3.3%, and the distribution is relatively concentrated. Only 5.56% of the coal samples have water absorption of 3.3%~8.0%, and the distribution is relatively dispersed. Water absorption indirectly reflects the porosity of coal sample.

2.2. Split Hopkinson Pressure Bar (SHPB) Apparatus. The dynamic impact Brazilian splitting test of coal rock was carried out on the SHPB system (Figure 4). In the SHPB device, the diameter of the steel cylindrical bullet, the input rod, and the output rod were 50 mm, and the length of the steel cylindrical bullet, the input rod, and the output rod were 400 mm, 2000 mm, and 2000 mm, respectively. Strain gages were pasted at 1 m from the input rod and the output rod to the

end of the sample to record the rod strain. The muzzle velocity of the bullet was controlled by the air pressure in the air chamber, and the input rod velocity was measured by the photoelectric method.

2.3. Data Processing Method. The Hopkinson bar technique is based on the one-dimensional assumption and stress uniformity assumption. According to the stress uniformity assumption, the dynamic stress-strain relationship of the material is obtained by using the three-wave method [12]:

$$\left. \begin{aligned} \dot{\varepsilon}(t) &= \frac{c}{l_s} (\varepsilon_i - \varepsilon_r - \varepsilon_t) \\ \varepsilon(t) &= \frac{c}{l_s} \int_0^t (\varepsilon_i - \varepsilon_r - \varepsilon_t) dt \\ \sigma(t) &= \frac{A}{2A_s} E (\varepsilon_i + \varepsilon_r + \varepsilon_t) \end{aligned} \right\} \quad (1)$$

where E , c , and A are the elastic modulus, elastic wave velocity, and cross-sectional area of the compression bar; A_s and l_s are the initial cross-sectional area and initial length of the sample; and ε_i , ε_r , and ε_t are the incident strain, reflected strain, and transmitted strain in the bar, respectively.

From loading to unloading, the energy carried by the incident wave, reflected wave, and transmitted wave are W_i , W_r , and W_t , respectively. The total dissipated energy of the sample is W_d , and the total dissipated energy density is w_d . The calculation equation is as follows [11, 12]:

$$\left. \begin{aligned} W_i &= \frac{AC_b}{E_b} \int \sigma_i^2 dt = AE_b C_b \int \varepsilon_i^2 dt \\ W_r &= \frac{AC_b}{E_b} \int \sigma_r^2 dt = AE_b C_b \int \varepsilon_r^2 dt \\ W_t &= \frac{AC_{bt}}{E_{bt}} \int \sigma_t^2 dt = AE_{bt} C_{bt} \int \varepsilon_t^2 dt \end{aligned} \right\} \quad (2)$$

$$W_d = W_i - W_r - W_t, \quad (3)$$

$$w_d = \frac{W_d}{V}, \quad (4)$$

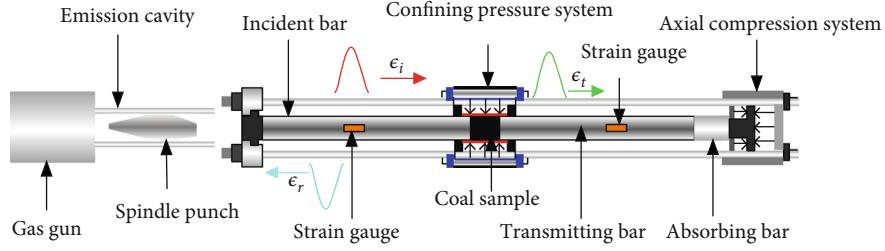


FIGURE 4: The Hopkinson pressure bar apparatus.

where σ_i , σ_r , and σ_t are the stresses of the incident wave, reflected wave, and transmitted wave on the pressure bar; V is the volume of the sample; C_b and C_{bt} are the propagation velocity of the sound wave in the input rod and output rod; and E_b and E_{bt} are elastic modulus of the input rod and output rod, respectively.

3. Results and Discussion

3.1. Definition of Damage Variable Based on Energy Dissipation. The split Hopkinson pressure bar test is based on one-dimensional elastic stress wave hypothesis and uniformity hypothesis. The stress-strain response characteristics of the sample are mainly reflected by the changes of the incident wave, reflected wave, and transmitted wave during the test. When the stress wave passes through the sample, the energy carried by the stress wave gradually decreases due to the existence of bedding and the formation and expansion of cracks in the sample. The energy carried by the incident wave minus the energy carried by the reflected wave and the transmitted wave is the energy consumed by the dynamic loading failure of the sample.

The research of damage can be based on two methods: micromechanics and macro phenomenology. In macroscopic phenomenology, different damage variables such as area, modulus, and energy can be defined. Li et al. [11] carried out dynamic SHPB impact test on sandstone samples and obtained the damage variables of sandstone samples under different impact velocities. Based on the understanding of constitutive energy and dissipated energy in material deformation, Jin et al. [15] defined the damage variable of material from the angle of energy dissipation, gave the theoretical formula of damage variable, and calculated the dissipated energy according to cyclic loading. Referring to the previous research, the damage variable d of dynamic impact tensile failure of coal sample is defined as follows:

$$d = \frac{w_d}{u}, \quad (5)$$

where u is the total absorbed energy density of the sample failure, i.e., the area enclosed by the stress-strain curve of coal samples.

$$u = \int \sigma d\varepsilon. \quad (6)$$

Figure 5 shows the typical stress-strain curves of air-dry

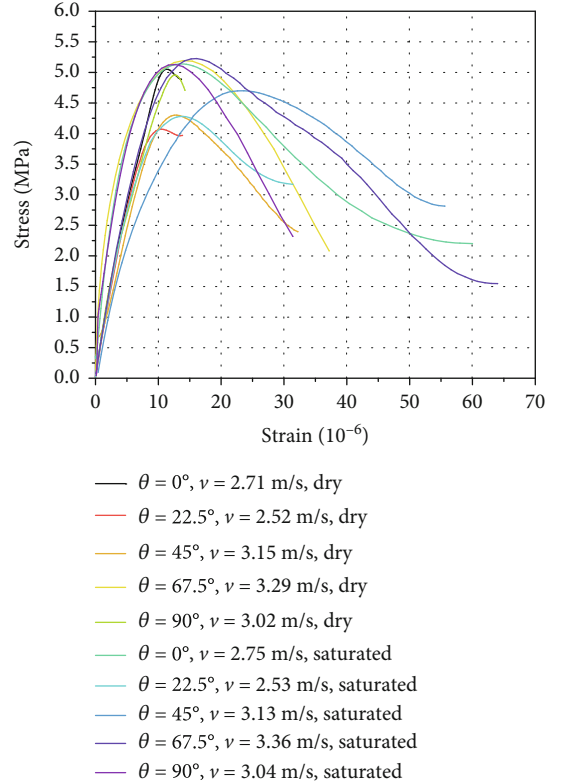


FIGURE 5: The stress-strain curves of coal specimens with different bedding angles.

and saturated samples with different bedding angles. In the stress-strain curve of saturated samples, there is a long post-peak curve, indicating that saturated samples have large deformation. In contrast, air-dry samples have lower peak strength and smaller deformation before failure. The total absorbed energy density can be obtained by integrating the corresponding stress-strain curves.

Figure 6 shows the dynamic tensile strength of coal samples with different bedding angles before and after water saturation. It can be concluded that when the bedding plane is perpendicular or parallel to the incident direction (that is, the bedding angle is 0 or 90 degrees), the test results before and after water absorption are more concentrated and less discrete than those of other groups. In addition, the change of tensile strength of coal sample before and after water absorption has no fixed trend, which may be higher or lower than that of natural coal

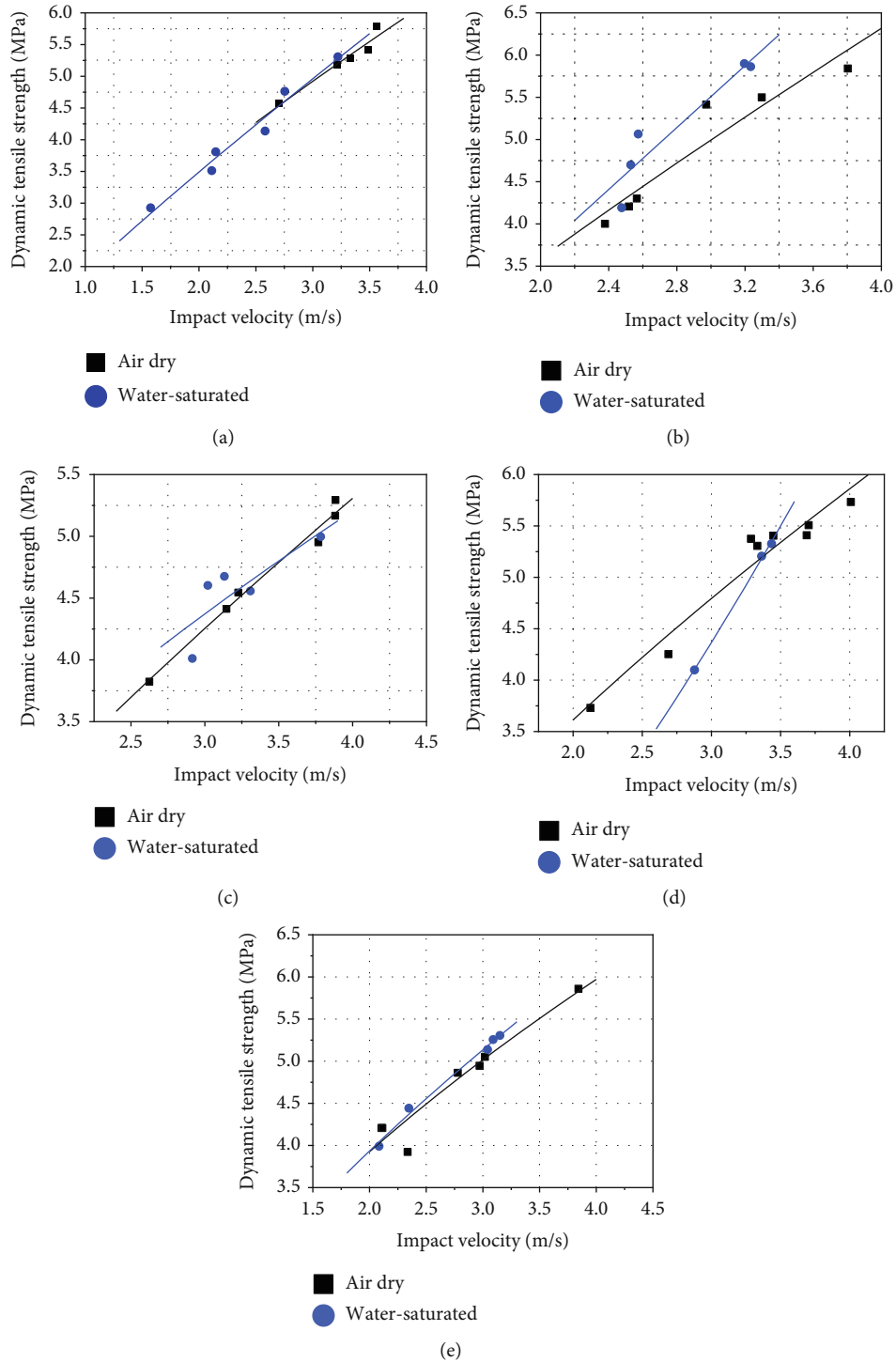


FIGURE 6: Comparison of relationship between dynamic tensile strength and impact velocity of coal rock specimens in natural state and water-saturated state. (a) $\theta = 0^\circ$. (b) $\theta = 22.5^\circ$. (c) $\theta = 45^\circ$. (d) $\theta = 67.5^\circ$. (e) $\theta = 90^\circ$.

sample. This is determined by bedding angle and water absorption factors at the same time.

3.2. Energy Dissipation Law of Coal Samples. To analyze the influence of the total absorbed energy density, total dissipated energy density, total dissipated energy density, and damage variables on the response characteristics of different impact velocities, bedding angles, and saturated water con-

tents of coal samples, the energy dissipation characteristic parameters of 41 samples were successfully obtained, as shown in Table 3. It is found that under the similar impact velocity, the total absorbed energy density of air-dry samples is the largest at a bedding angle of 45° and the smallest at a bedding angle of 90° ; the discreteness of coal samples with bedding angle of 0° is the largest and the discreteness of coal samples with a bedding angle of 22.5° is the smallest. For

TABLE 3: Energy dissipation parameters of air-dry and water-saturated coal specimens.

Water content	θ ($^{\circ}$)	v ($\text{m}\cdot\text{s}^{-1}$)	u ($\text{J}\cdot\text{m}^{-3}$)	W_d (J)	w_d ($\text{J}\cdot\text{m}^{-3}$)	d
Dry	0	3.213	8137.23	0.042	863.16	0.1061
		2.695	2932.36	0.011	229.32	0.0782
		3.565	8588.66	0.045	914.02	0.1064
		2.707	2242.11	0.009	184.26	0.0822
		2.378	3689.26	0.012	246.45	0.0668
	22.5	2.518	5781.86	0.024	499.22	0.0863
		2.565	4790.71	0.016	338.42	0.0706
		2.972	5609.13	0.025	509.45	0.0908
		3.803	6916.84	0.038	768.85	0.1112
		2.624	4796.75	0.017	355.85	0.0742
	45	3.146	7126.37	0.039	788.59	0.1107
		3.226	7496.42	0.040	813.23	0.1085
		3.286	3465.82	0.018	385.75	0.1113
		4.008	6885.24	0.038	795.93	0.1156
		3.332	3573.23	0.021	438.17	0.1226
	67.5	2.125	5712.75	0.023	461.78	0.0808
		2.689	5387.65	0.022	465.73	0.0887
		3.843	7132.59	0.041	838.88	0.1176
		2.97	2970.66	0.013	265.34	0.0893
		2.779	8090.98	0.036	747.61	0.0924
90	3.018	2273.96	0.010	207.83	0.0914	
	2.336	1966.50	0.007	139.82	0.0711	
	2.112	2684.75	0.009	190.35	0.0709	
	1.58	3365.76	0.011	226.52	0.0673	
	3.221	5051.66	0.026	542.48	0.1074	
Saturated	0	2.754	5276.99	0.021	438.16	0.0831
		2.851	4614.83	0.019	450.41	0.0850
		2.529	10055.36	0.044	907.12	0.0902
		3.233	8140.09	0.029	598.02	0.0735
		2.573	9821.71	0.044	891.06	0.0907
	22.5	2.476	4127.82	0.016	321.21	0.0778
		3.132	9910.17	0.055	1141.26	0.1152
		3.308	9611.25	0.058	1217.89	0.1267
		2.915	5429.54	0.029	597.93	0.1101
		3.363	7578.40	0.047	990.95	0.1308
	45	3.435	3472.94	0.026	545.56	0.1571
		2.878	7965.75	0.035	713.34	0.0896
		3.041	9484.67	0.048	997.61	0.1052
		3.09	3600.11	0.019	398.34	0.1106
		2.347	5490.83	0.021	450.85	0.0821
	67.5	2.084	3723.11	0.013	281.84	0.0751

Note: θ : bedding angle; v : impact velocity; u : density of total absorbed energy; W_d : total dissipated energy; w_d : density of total dissipated energy; d : damage variables.

saturated samples, the total absorbed energy density and discreteness are the smallest at a bedding angle of 0° , the total absorbed energy density is the largest at a bedding angle of 45° , and the discreteness is the largest at a bedding angle of 90° . The results show that the total dissipated energy density of air-dry coal sample is the highest at the bedding angle of

45° and the lowest at a bedding angle of 90° ; the total dissipated energy density of saturated samples is the highest at a bedding angle of 45° and the lowest at a bedding angle of 0° .

The fitting relationship between damage variables of coal samples with different bedding angles and impact loading velocity under air-dry and saturated conditions is shown in

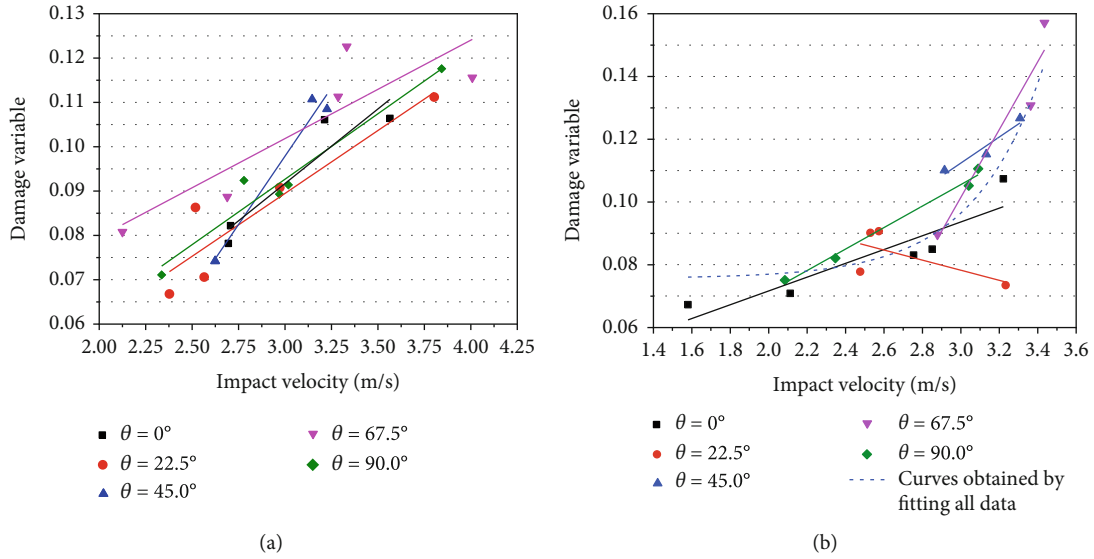


FIGURE 7: Relationship between damage variable and impact velocity of coal samples.

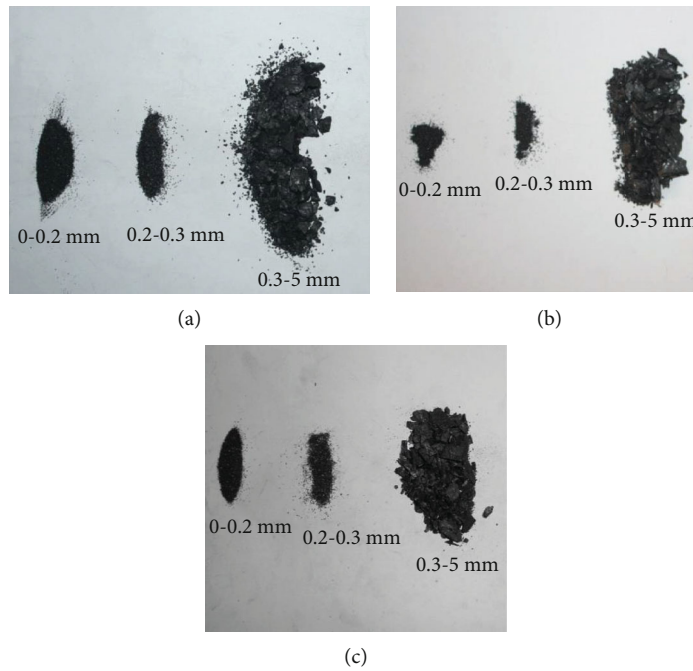


FIGURE 8: Size statistics of fragments of coal with different bedding angles under the impact loading. From (a) to (c), the bedding angle is 0°, 45°, and 90°, respectively.

Equations (7) and (8)

$$\left\{ \begin{array}{l} d_1 = -0.00915 + 0.03362v \quad (\theta = 0^\circ), \\ d_1 = 0.00436 + 0.02837v \quad (\theta = 22.5^\circ), \\ d_1 = -0.08702 + 0.06163v \quad (\theta = 45.0^\circ), \\ d_1 = 0.03525 + 0.0222v \quad (\theta = 67.5^\circ), \\ d_1 = 0.00411 + 0.02952v \quad (\theta = 90.0^\circ), \end{array} \right. \quad (7)$$

$$\left\{ \begin{array}{l} d_2 = 0.02771 + 0.02198v \quad (\theta = 0^\circ), \\ d_2 = 0.12654 - 0.01609v \quad (\theta = 22.5^\circ), \\ d_2 = -0.01215 + 0.04152v \quad (\theta = 45.0^\circ), \\ d_2 = -0.22251 + 0.108v \quad (\theta = 67.5^\circ), \\ d_2 = 0.00286 + 0.03423v \quad (\theta = 90.0^\circ). \end{array} \right. \quad (8)$$

Figures 7(a) and 7(b) show the relationship between damage variable and impact velocity of air-dry and water-

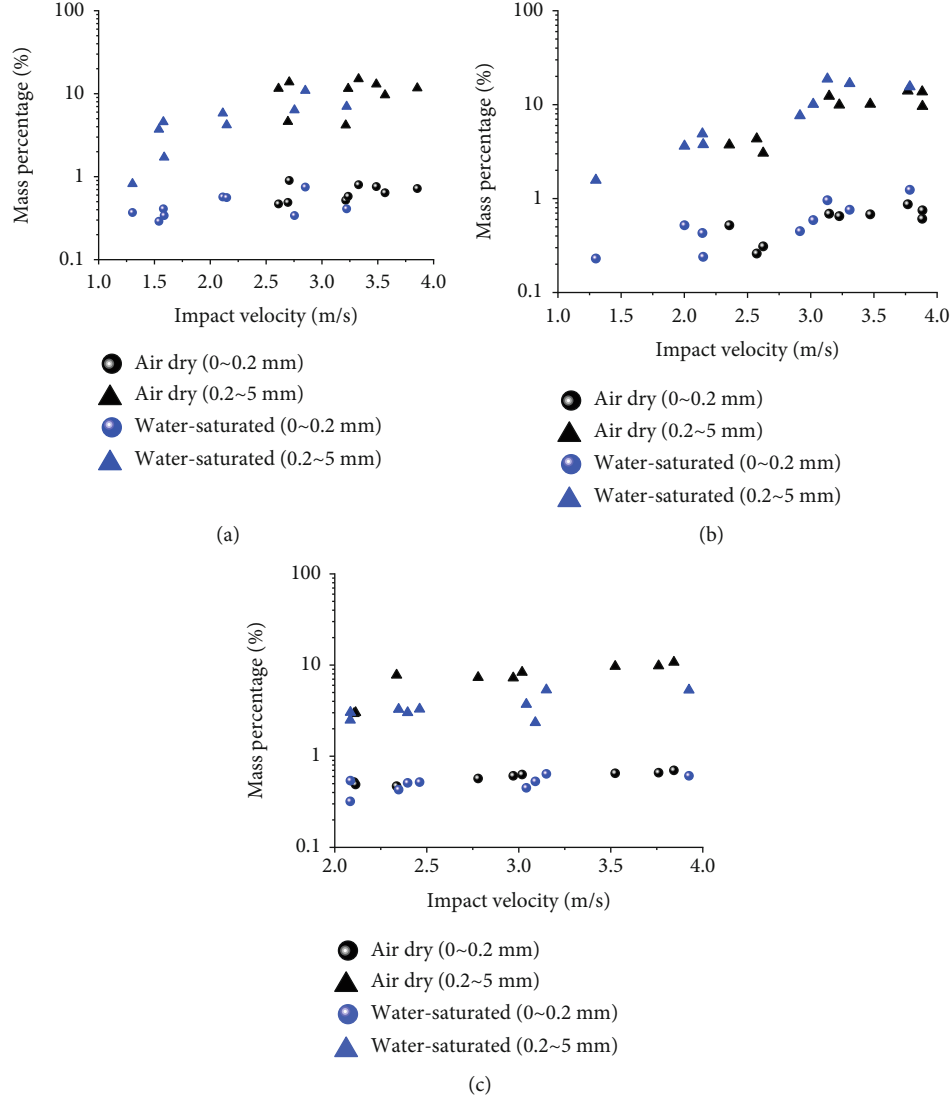


FIGURE 9: Size distribution of fragments of air-dry coal and water-saturated coal specimens after failure under the dynamic impact loading. From (a) to (c), the bedding angle is 0° , 45° , and 90° , respectively.

TABLE 4: Statistics of the average value of debris of two particle sizes for dry and water-saturated coal samples after impact loading.

θ	(0~0.2 mm, dry, W_{d1})	(0.2~5 mm, dry, W_{d2})	(0~0.2 mm, saturated, W_{w1})	(0.2~5 mm, saturated, W_{w2})	$(W_{d1} - W_{w1})/W_{d1}$ (%)	$(W_{d2} - W_{w2})/W_{d2}$ (%)
0°	0.653	10.551	0.4489	5.007	31.2557	52.54478
22.5°	0.617	9.004	0.4878	5.968	20.94003	33.71835
45°	0.593	8.97	0.602	9.183	-1.517707	-2.3746
67.5°	0.776	11.879	0.54	5.579	30.41237	53.03477
90°	0.589	7.4189	0.506	3.533	14.09168	52.37838

saturated samples. When the impact velocity is 2.0-4.25 m/s, the damage variable of air-dry coal sample is in the range of 0.06-0.13; when the impact velocity is 1.5-3.6 m/s, the damage variable of saturated samples is in the range of 0.06-0.16. Therefore, the damage variables of air-dry and saturated samples with the same bedding angle increase approximately linearly with the increase of impact velocity. When the

impact velocity is less than 3.1 m/s, the damage variable of air-dry samples with a bedding angle of 67.5° is the largest; when the impact velocity is greater than 3.1 m/s, the damage variable of air-dry samples with a bedding angle of 45.0° is the largest. The overall damage variable of saturated samples increases exponentially with impact velocity, and the fitting function is shown in Equation (9). However, for the saturated

samples with bedding angle of 22.5° , the overall damage variable shows a downward trend with the increase of the impact velocity, which may be caused by the increased heterogeneity of coal sample due to its full water content or the small number of successful samples.

$$d_2 = 5.692 \times 10^{-6} e^{v/0.3656} + 0.07565. \quad (9)$$

3.3. Fragment Distribution Characteristics. During the test, the generated fragments with particle sizes of 0-0.2 mm, 0.2-0.3 mm, and 0.3 mm-5 mm after the crushing of coal samples were collected and weighed. Figure 8 shows the particle size statistics of the fragments of coal samples with a bedding angle of 0° , 45° , and 90° under the impact velocity range of 1.58-3.882 m/s. With the increase of impact velocity, the number of fragments with the particle size of 0-0.2 mm and 0.2-0.3 mm increases after the failure of coal sample with the same bedding angle. This is because in the SHPB test, the greater the impact loading rate, the greater the energy carried by the incident wave, the greater the total dissipated energy density, and damage variable of the coal sample, and the more energy absorbed by the coal sample, the more fragments with the small size. The shape of fragments with the particle size of 0.3-5 mm is mainly flake, block, and granular.

Figures 9(a)–9(c) shows the fragment distribution with the particle size of 0 - 0.2 mm and 0.2-5 mm generated from air-dry samples and saturated samples with different bedding angles under dynamic impact loading. Since the distribution range of mass percentage of fragments with different particle sizes after crushing is large, a semilogarithmic coordinate is adopted in the figure to reflect its distribution characteristics. According to the scale characteristics of semilogarithmic coordinates, for fragments with the particle size of 0-0.2 mm generated from the air-dry and saturated samples, the percentage of fragment mass has little change with the increase of impact velocity (0.4489%-0.776%). However, for fragments with the particle size of 0.2-5 mm generated from the air-dry and saturated samples, the percentage of fragment mass increases significantly with the increase of impact velocity (3.533%-11.879%), and the percentage of fragments with the particle size of 0.2-5 mm generated from saturated samples is significantly less than that of air-dry samples under the same impact velocity. The previous research on the field dust prevention by the water injection [22–24] shows that the dust production in the water injection area is reduced by 38%-50%. This conclusion experimentally confirms the technical principle of water-injection dust-reduction technology in the mining process.

Table 4 shows the average value statistics of fragments with two particle sizes after impact loading on the air-dry and saturated samples. Compared with fragments generated from air-dry samples, the number of fragments with the particle size of 0-0.2 mm generated from saturated samples is reduced by 14.1%-31.3%, and the number of fragments with the particle size of 0.2-5 mm generated from saturated samples is reduced by 33.7%-53.0%. However, when the bedding angle is 45° , the percentage of fragment mass with the particle size of 0-0.2 mm and 0.2-5 mm generated from saturated samples is larger than that of air-dry samples. The reason

for this phenomenon needs to be further studied. However, previous field observations show that the effect of water-injection dust-prevention has a great relationship with the coal bedding, and the main joint system and the angle between the main joint system and the direction of working face in the longwall mining are the important factors [25].

4. Conclusions

- (1) There is a long postpeak section in the stress-strain curves of saturated samples, which indicates the occurrence of the large deformation in saturated samples. In contrast, air-dry samples have lower peak strength and smaller deformation before failure
- (2) The damage variable of coal samples under dynamic impact increases with the increase of impact velocity. And the overall damage variables of water-saturated coal samples increased exponentially with the increase of impact velocity
- (3) For fragments with the particle size of 0-0.2 mm generated from air-dry and water-saturated samples, the percentage of fragment mass has little change with the increase of impact velocity. However, for fragments with the particle size of 0.2-5 mm generated from the air-dry and saturated samples, the percentage of fragment mass increases significantly with the increase of impact velocity, and the percentage of fragments with the particle size of 0.2-5 mm generated from saturated samples is significantly less than that of air-dry samples under the same impact velocity
- (4) Compared with fragments generated from air-dry samples, the number of fragments with the particle size of 0-0.2 mm generated from saturated samples is reduced by 14.1%-31.3%, and the number of fragments with the particle size of 0.2-5 mm generated from saturated samples is reduced by 33.7%-53.0%. However, when the bedding angle is 45° , the percentage of fragment mass in saturated samples with the particle size of 0-0.2 mm and 0.2-5 mm is larger than that in air-dry samples

Data Availability

The data used to support the findings of this study are available from the corresponding author upon request.

Conflicts of Interest

The authors declare that they have no conflicts of interest.

Acknowledgments

This work was financially supported by the research fund of the National Natural Science Foundation of China (51604093), the Fundamental Research Funds for the Universities of Henan Province (Grant No. NSFRF200332), the Henan Key Laboratory for Green and Efficient Mining &

Comprehensive Utilization of Mineral Resources (Henan Polytechnic University) (KCF201804), the Key Scientific Research Project Fund of Colleges and Universities of Henan Province (21A610005 and 20B440001), and the Doctoral Foundation of Henan Polytechnic University (B2019-22). All supports are greatly appreciated.

References

- [1] S. Gong, *Study on Mechanical Characteristics of Dynamic Tensile and Mode I Fracture of Coal Samples under Impact Loading*, China University of Mining and Technology, Beijing, 2018.
- [2] L. Yuan and P. S. Zhang, "Development status and prospect of geological guarantee technology for precise coal mining," *Journal of China Coal Society*, vol. 44, no. 8, pp. 2277–2284, 2019.
- [3] W. Cai, L. Dou, G. Si et al., "A new seismic-based strain energy methodology for coal burst forecasting in underground coal mines," *International Journal of Rock Mechanics and Mining Sciences*, vol. 123, p. 104086, 2019.
- [4] A. Mottahedi and M. Ataei, "Fuzzy fault tree analysis for coal burst occurrence probability in underground coal mining," *Tunnelling and Underground Space Technology*, vol. 83, pp. 165–174, 2019.
- [5] D. Song, X. He, E. Wang, Z. Li, M. Wei, and H. Mu, "A dynamic ejection coal burst model for coalmine roadway collapse," *International Journal of Rock Mechanics and Mining Sciences*, vol. 29, no. 4, pp. 557–564, 2019.
- [6] I. Anthony and T. Stephen, "Occurrence, predication, and control of coal burst events in the U.S.," *International Journal of Mining Science and Technology*, vol. 26, no. 1, pp. 39–46, 2016.
- [7] X. W. Li and Y. J. Chai, "Determination of pillar width to improve mining safety in a deep burst-prone coal mine," *Safety Science*, vol. 113, pp. 244–256, 2019.
- [8] M. M. Carroll, "Mechanics of geological materials," *Applied Mechanics Division*, vol. 70, no. 38, pp. 1256–1260, 1985.
- [9] V. I. Revnintsev, "We really need revolution in comminution," in *XVI International Mineral Processing Congress*, pp. 93–114, Elsevier Science Publishers, Amsterdam, 1988.
- [10] G. Chi, M. C. Fuerstenau, R. C. Bradt, and A. Ghosh, "Improved comminution efficiency through controlled blasting during mining," *International Journal of Mineral Processing*, vol. 47, no. 1-2, pp. 93–101, 1996.
- [11] L. Y. Li, Z. J. Xu, H. P. Xie, Y. Ju, X. Ma, and Z. C. Han, "Failure experimental study on energy laws of rock under differential dynamic impact velocity," *Journal of China Coal Society*, vol. 36, no. 12, pp. 2007–2011, 2011.
- [12] J. Y. Xu and S. Liu, "Analysis of energy dissipation rule during deformation and fracture process of rock under high temperatures in SHPB test," *Chinese Journal of Rock Mechanics and Engineering*, vol. 32, no. S2, pp. 3109–3115, 2013.
- [13] B. Bohloli and E. Hoven, "A laboratory and full-scale study on the fragmentation behavior of rocks," *Engineering Geology*, vol. 89, no. 1-2, pp. 1–8, 2007.
- [14] A. Hua, Y. Kong, S. Li, and Y. Li, "Energy analysis of depressurized rock fracture," *Journal of China Coal Society*, vol. 4, pp. 389–392, 1995.
- [15] F. N. Jin, M. R. Jiang, and X. L. Gao, "Defining damage variable based on energy dissipation," *Chinese Journal of Rock Mechanics and Engineering*, vol. 23, no. 12, pp. 1976–1980, 2004.
- [16] Y. S. Zhao, Z. C. Feng, and Z. J. Wan, "Least energy principle of dynamical failure of rock mass," *Chinese Journal of Rock Mechanics and Engineering*, vol. 22, no. 11, pp. 1781–1783, 2003.
- [17] Z. Y. Song, T. Frühwirth, and H. Konietzky, "Characteristics of dissipated energy of concrete subjected to cyclic loading," *Construction and Building Materials*, vol. 168, pp. 47–60, 2018.
- [18] M. Zhang, L. Dou, H. Konietzky, Z. Song, and S. Huang, "Cyclic fatigue characteristics of strong burst-prone coal: experimental insights from energy dissipation, hysteresis and micro-seismicity," *International Journal of Fatigue*, vol. 133, p. 105429, 2020.
- [19] X. Cai, Z. Zhou, L. Tan, H. Zang, and Z. Song, "Fracture behavior and damage mechanisms of sandstone subjected to wetting-drying cycles," *Engineering Fracture Mechanics*, vol. 234, p. 107109, 2020.
- [20] Z. Song, Y. Wang, H. Konietzky, and X. Cai, "Mechanical behavior of marble exposed to freeze-thaw-fatigue loading," *International Journal of Rock Mechanics and Mining Sciences*, vol. 138, p. 104648, 2021.
- [21] S. Gong, Z. Wang, L. Zhou, and W. Wang, "Influence of cyclic impact loading and axial stress on dynamic mechanical properties of burst-prone coal," *Shock and Vibration*, vol. 2021, Article ID 6649308, 10 pages, 2021.
- [22] J. Cervik, A. Sainato, and E. Baker, *Water Infusion: An Effective and Economical Longwall Dust Control*, U.S. Department of the Interior, Bureau of Mines, Pittsburgh, PA, 1983.
- [23] J. J. McClelland, *Water Infusion for Coal Mine Dust Control: Three Case Studies*, USBM Final Report, Pittsburgh, PA, 1987.
- [24] G. A. Shirey, J. F. Colinet, and J. A. Kost, *Dust Control Handbook for Longwall Mining Operations*, USBM Final Report, Monroeville, PA, 1985.
- [25] F. N. Kissell, *Information Circular 9465 Handbook for Dust Control in Mining*, U.S. Department of Health and Human Services, Public Health Service, Centers for Disease Control and Prevention, National Institute for Occupational Safety and Health, DHHS (NIOSH), Pittsburgh, PA, 2003.